CERN-2004-003
4 June 2004

LHC DESIGN REPORT

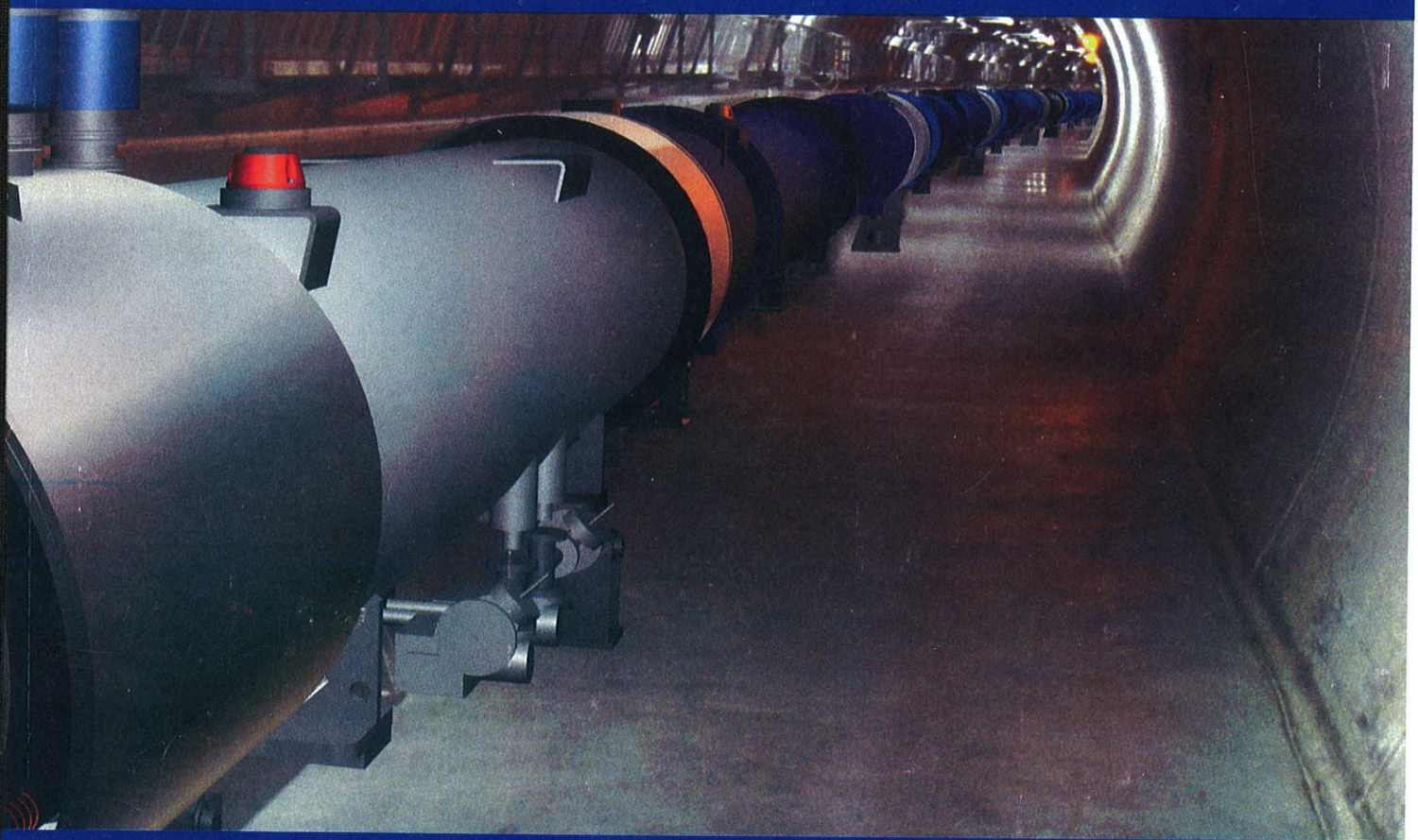

VOL. I **THE LHC MAIN RING**

EUROPEAN ORGANIZATION FOR NUCLEAR RESEARCH

ISSN 0007–8328
ISBN 92–9083–224–0

CERN-2004-003
4 June 2004

ORGANISATION EUROPÉENNE POUR LA RECHERCHE NUCLÉAIRE
CERN EUROPEAN ORGANIZATION FOR NUCLEAR RESEARCH

LHC Design Report
Volume I The LHC Main Ring

Editorial Board

**O. Brüning, P. Collier, P. Lebrun, S. Myers,
R. Ostojic, J. Poole, P. Proudlock**

GENEVA
2004

CERN – Scientific Information Service – 1300 – June 2004

Abstract

The LHC Design Report is presented in three volumes: the first concerns the main ring, the second the infrastructure and general services and the third, the injector chain. The conceptual design was published in 1995 and this report provides a snapshot of the detailed design as it stands at the time of writing – early 2004.

VOLUME I – CONTENTS

CHAPTER 1

INTRODUCTION

The Large Hadron Collider Project was approved by CERN Council in December 1994. However, in order to allow the machine to be built within a constant budget with no financial contributions from non-Member States, it was decided that the accelerator was to be built as a 2-stage project, the first stage with an energy of 10 TeV in the centre-of-mass, to be operational by 2004, with an upgrade to its final energy of 14 TeV by 2008. It was also decided that a comprehensive review of the Project would be made before the end of 1997 and that if sufficient extra contributions could be secured from non-Member States then it would be possible to re-examine the 2-stage project and revert to the immediate construction of a 14 TeV accelerator.

During the years 1995-1996, intense negotiations with non-Member States secured a substantial commitment to participate financially in the construction of the Machine. Consequently, the review foreseen before the end of 1997 was brought forward. In December 1996, Council passed a Resolution approving the construction of the 14 TeV accelerator in a single stage. The LHC will be the first machine built at CERN with substantial material contribution from non-Member States. Machine hardware is being constructed in National Laboratories in Canada, India, Japan, Russia and the USA.

In parallel with the diplomatic activity, a substantial redesign of the machine was undertaken in order to reduce cost and improve performance. This work culminated in the LHC Conceptual Design Report (the "Yellow Book") published in October 1995, which has served as the basis for the detailed design. The basic design of the machine and its performance projections have remained remarkably stable over the ensuing years, with a few exceptions mentioned below.

In the superconducting magnet system, the most significant change is in the design of the main dipoles. The Yellow Book design was based on the use of high-strength aluminium collars to contain the electromagnetic forces, with a gap in the yoke that closed when cold. After testing a number of models based on this concept it was decided to replace the aluminium collars with austenitic steel collars and to close the yoke gap at room temperature. The main reason for this was the much tighter tolerance requirements for the aluminium collars. It was considered that the cost of achieving these tolerance in an industrial environment would exceed the extra cost of the collar material. This choice has proved to be a very good one. Dipole production is proceeding smoothly, with consistent quality.

The design of the beam collimation systems has evolved considerably. Since the difficulties and performance goals are distributed in time, the collimation systems are designed so that they can be installed in three phases. In the first phase, robustness is favoured to ultimate performance. The primary collimator jaws are made from carbon, able to resist high beam loss. As experience with the system grows, further collimators will be installed to efficiently protect the machine and detectors at the highest intensity.

The RF and Beam Feedback systems have evolved somewhat since the "Yellow Book". The longitudinal damping will no longer be performed with separate damping cavities. In addition a new 200 MHz system to reduce capture losses and to ease operation has been designed, although recent success in controlling the longitudinal emittance in the SPS have shown that this system will only be required at the highest intensity.

The design of the vacuum system has remained unchanged in the cold regions of the machine except in the insertion regions, where beam screens have been introduced in all superconducting magnets in order to avoid cold traps. In the room temperature regions it has been decided to coat the chambers with Ti-Zr-V Non Evaporable Getter (NEG) which can be activated at low temperature (200°C). Considerable experience has also been accumulated in the SPS on the electron cloud instability, which will limit the luminosity in early operation. A "scrubbing" period will be needed to clean the vacuum chamber through electron bombardment before it will be possible to operate at full intensity.

The detailed optical design of the machine has been modified in the dispersion suppressor and insertion regions in order to improve the flexibility and tuneability of the machine.

Finally, a new small experiment for small angle scattering (TOTEM) has been approved to be installed in the region of CMS (Point 5). This has required a number of layout changes in order to integrate the "Roman Pot" detectors.

The present report, published in three volumes, is intended to serve as an accurate record of the machine and its experimental areas as constructed. The first Volume concerns the LHC Machine itself. In chapters 2 to 5, the main parameters are described and the many issues in accelerator physics that have to be taken into account in the design in order to achieve the required performance are discussed. Following chapters deal with the detailed hardware design of the main components.

A very considerable amount of modification of the existing LEP infrastructure has been necessary. On the surface, additional buildings are needed to house the huge cryogenic plants and other equipment. Underground, the most demanding civil engineering work has been the excavation of the experimental caverns for the two large detectors ATLAS and CMS. Other conventional infrastructure, including cooling, ventilation, access and safety systems, electrical infrastructure has all needed considerable modification. This is documented in Volume 2 of the report.

The LHC will be supplied with protons and Pb ions from the existing injector chain comprising linac, booster, PS and SPS. These accelerators have undergone a major upgrade in the last five years in order to meet the demanding requirements of the LHC. The upgrade project involved an increase in Linac2 current, new RF systems in the PS Booster and PS, increasing the Booster energy from 1 GeV to 1.4 GeV and the modification of the LEAR ring to allow Pb ion cooling and accumulation. In addition, a number of modifications of the SPS have been necessary, including an impedance reduction programme and the installation of a new extraction channel. Volume 3 of the report documents the work done on the LHC injectors.

CHAPTER 2

BEAM PARAMETERS AND DEFINITIONS

2.1 LHC BEAM PARAMETERMS RELEVANT FOR THE PEAK LUMINOSITY

This Chapter provides a summary of the main parameters for the nominal proton beam operation, a glossary and a list of definitions that are used throughout the chapters of the LHC design report. The equipment names and the circuit counts are summarized in dedicated tables at the end of this Chapter. A derivation and detailed explanation of the parameters can be found in Chapters 3 to 6 of Volume I of the design report. A discussion of the variation of the beam parameters from these nominal values in different operation scenarios is given in Chapter 20.

Table 2.1: LHC beam parameters relevant for the peak luminosity

		Injection	**Collision**
Beam Data			
Proton energy	[GeV]	450	7000
Relativistic gamma		479.6	7461
Number of particles per bunch		1.15×10^{11}	
Number of bunches		2808	
Longitudinal emittance (4σ)	[eVs]	1.0	2.5[a]
Transverse normalized emittance	[μm rad]	3.5[b]	3.75
Circulating beam current	[A]	0.584	
Stored energy per beam	[MJ]	23.3	362
Peak Luminosity Related Data			
RMS bunch length[c]	cm	11.24	7.55
RMS beam size at the IP1 and IP5[d]	μm	375.2	16.7
RMS beam size at the IP2 and IP8[e]	μm	279.6	70.9
Geometric luminosity reduction factor F[f]		-	0.836
Peak luminosity in IP1 and IP5	[$cm^{-2}sec^{-1}$]	-	1.0×10^{34}
Peak luminosity per bunch crossing in IP1 and IP5	[$cm^{-2}sec^{-1}$]	-	3.56×10^{30}

[a] The base line machine operation assumes that the longitudinal emittance is deliberately blown up at the middle of the ramp in order to reduce the intra beam scattering growth rates.

[b] The emittance at injection energy refers to the emittance delivered to the LHC by the SPS without any increase due to injection errors and optics mis-match. The RMS beam sizes at injection assume the nominal emittance value quoted for top energy (including emittance blowup due to injection oscillations and mismatch).

[c] Dimensions are given for Gaussian distributions. The real beam will not follow a Gaussian distribution but more realistic distributions do not allow analytic estimates for the IBS growth rates.

[d] The RMS beam sizes in IP1 and IP5 assume a β-function of 0.55 m.

[e] The RMS beam sizes in IP2 and IP8 assume a β-function of 10 m.

[f] The geometric luminosity reduction factor depends on the total crossing angle at the IP (see Sec. 3.1.1). The quoted number in Table 2.1 assumes a total crossing angle of 285 μrad as it is used in IR1 and IR5.

2.2 LHC BEAM PARAMETERS RELEVANT FOR THE LUMINOSITY LIFETIME

Table 2.2: LHC beam parameters relevant for the luminosity lifetime

		Injection	Collision
Interaction data			
Inelastic cross section	[mb]	60.0	
Total cross section	[mb]	100.0	
Events per bunch crossing		-	19.02
Beam current lifetime (due to beam-beam)	[h]	-	44.86
Intra Beam Scattering			
RMS beam size in arc	[mm]	1.19	0.3
RMS energy spread $\delta E/E_0$	[10^{-4}]	3.06	1.129
RMS bunch length	[cm]	11.24	7.55
Longitudinal emittance growth time	[hours]	30[a]	61
Horizontal emittance growth time	[hours]	38[a]	80
Total beam and luminosity lifetimes[b]			
Luminosity lifetime (due to beam-beam)	[hours]	-	29.1
Beam lifetime (due to rest-gas scattering)[c]	[hours]	100	100
Beam current lifetime (beam-beam, rest-gas)	[hours]	-	18.4
Luminosity lifetime (beam-beam, rest-gas, IBS)	[hours]	-	14.9
Synchrotron Radiation			
Instantaneous power loss per proton	[W]	3.15×10^{-16}	1.84×10^{-11}
Power loss per m in main bends	[Wm^{-1}]	0.0	0.206
Synchrotron radiation power per ring	[W]	6.15×10^{-2}	3.6×10^{3}
Energy loss per turn	[eV]	1.15×10^{-1}	6.71×10^{3}
Critical photon energy	[eV]	0.01	44.14
Longitudinal emittance damping time	[hours]	48489.1	13
Transverse emittance damping time	[hours]	48489.1	26

[a] IBS growth times are given without the 200 MHz RF system.

[b] lifetime estimates including the effect of proton losses due to luminosity production, IBS and vacuum rest gas scattering. It is assumed that the effect of the non-linear beam-beam interaction and RF noise are compensated by the synchrotron radiation damping.

[c] The desorption lifetime should be slightly better at injection energy because the cross sections for rest gas scattering decrease with energy. For more information see Chap. 28 and [1].

2.3 LHC MACHINE PARAMETERS RELEVANT FOR THE PEAK LUMINOSITY

Table 2.3: LHC machine parameter relevant for the peak luminosity

		Injection	**Collision**
Interaction Data			
Number of collision points		4	
Half crossing angle for ATLAS and CMS (IP1/IP5)	[μrad]	$\pm$160	$\pm$142.5
Half parallel separation at IP for ATLAS and CMS (IP1/IP5)	[mm]	$\pm$2.5	0.0
Half crossing angle at IP [a] for ALICE (IP2)	[μrad]	$\pm$240	$\pm$150
Half parallel separation at IP for ALICE	[mm]	$\pm$2.0	$\pm$0.178 (5 σ total separation)
Half crossing angle at IP [a] for LHCb (IP8)	[μrad]	$\pm$300	$\pm$200
Half parallel separation at IP for LHCb (IP8)	[mm]	$\pm$2.0	0.0
Plane of crossing in IP1		vertical	
Plane of crossing in IP2		vertical	
Plane of crossing in IP5		horizontal	
Plane of crossing in IP8		horizontal	
β at IP1 and IP5	[m]	18	0.55
β at IP2	[m]	10	0.5 for Pb / 10 for p
β at IP8	[m]	10	1.0 $\leftrightarrow$ 50

[a] The crossing angle in IP2 and IP8 is the sum of an external crossing angle bump and an 'internal' spectrometer compensation bump and depend on the spectrometer polarity. The values quoted above represent the maximum values from the different possible configurations. The external bump extends over the triplet and D1 and D2 magnets. The internal spectrometer compensation bump extends only over the long drift space between the two triplet assemblies left and right from the IP.

2.4 LHC STORAGE RING PARAMETERS

Table 2.4: LHC storage ring parameters

		Injection	Collision
Geometry			
Ring circumference	[m]	26658.883	
Ring separation in arcs	[mm]	194	
Bare inner vacuum screen height in arcs	[mm]	46.5	
Effective vacuum screen height (incl. tol.)	[mm]	44.04	
Bare inner vacuum screen width in arcs	[mm]	36.9	
Effective vacuum screen width (incl. tol.)	[mm]	34.28	
Main Magnet			
Number of main bends		1232	
Length of main bends	[m]	14.3	
Field of main bends	[T]	0.535	8.33
Bending radius	[m]	2803.95	
Lattice			
Maximum dispersion in arc	[m]	2.018 (h) / 0.0 (v)	
Minimum horizontal dispersion in arc	[m]	0.951	
Maximum β in arc	[m]	177 (h)/ 180 (v)	
Minimum β in arc	[m]	30 (h) / 30 (v)	
Horizontal tune		64.28	64.31
Vertical tune		59.31	59.32
Momentum compaction	10^{-4}	3.225	
Slip factor η	10^{-4}	3.182	3.225
Gamma transition γ_{tr}		55.68	
RF System			
Revolution frequency	[kHz]	11.245	
RF frequency [a]	[MHz]	400.8	
Harmonic number		35640	
Number of bunches		2808	
Total RF voltage	[MV]	8	16
Synchrotron frequency	[Hz]	61.8	21.4
Bucket area	[eVs]	1.46	8.7
Bucket half height ($\Delta E/E$)	[10^{-3}]	1	0.36

[a] A second optional low harmonic 200 MHz RF system can be installed after the initial running period.

2.5 GLOSSARY AND DEFINITIONS

2.5.1 Glossary

β^*: Optical β-function at the IP.

η: Machine slip factor.

η_D: Normalized dispersion: $\eta_D = D/\sqrt{\beta}$, where D is the machine dispersion.

γ: Optic gamma function: $\gamma(s) = (1 + \alpha^2(s))/\beta(s)$ where $\beta(s)$ is the optical betatron function along the machine and $\alpha(s) = -\frac{1}{2}\frac{d\beta}{ds}$.

γ_r: The relativistic gamma factor.

abort gap: Area without any bunches in the bunch train that fits the time required for building up the nominal field of the LHC dump kicker.

arc: The part of the ring occupied by regular half-cells. Each arc contains 46 half cells. The arc does not contain the dispersion suppressor.

arc cell: It consists of two arc half-cells and presents the basic period of the optic functions.

arc half-cell: Periodic part of the LHC arc lattice. Each half-cell consists of a string of three twin aperture main dipole magnets and one short straight section. The cryo magnets of all arc half-cells follow the same orientation with the dipole lead end pointing upstream of Beam 1 (downstream of Beam 2).

batch:

PS batch: Train of 72 bunches injected into the SPS in one PS to SPS transfer.

SPS batch: Train of 4×72 or 3×72 bunches injected into the LHC in one SPS to LHC transfer.

Beam 1 and Beam 2: Beam 1 and Beam 2 refer to the two LHC beams. Beam 1 circulates clockwise in Ring 1 and Beam 2 circulates counter clockwise in Ring 2. If colours are used for beams, Beam 1 is marked blue and Beam 2 red.

beam cleaning: Removal of the large amplitude (larger than 6 sigma) particles from the beam halo. The LHC has two beam cleaning insertions: one dedicated to the removal of particles with large transverse oscillation amplitudes (IR7) and one dedicated to the removal of particles with large longitudinal oscillation amplitudes (IR3). These insertions are also referred to as the betatron and momentum cleaning or collimation insertions.

beam crossing angle: Dedicated orbit bumps separate the two LHC beams at the parasitic beam crossing points of the common beam pipe of Ring 1 and Ring 2. The crossing angle bumps do not separate the beams at the IP but only at the parasitic crossing points. These orbit bumps generate an angle between the orbit of Beam 1 and Beam 2 at the IP. The full angle between the orbit of Beam 1 and Beam 2 is called the crossing angle. In IR2 and IR8 the crossing angle orbit bumps consist of two separate contributions. One external bump generated for the beam separation at the parasitic beam crossing points and one internal bump generated by the experimental spectrometer and its compensator magnets. The LHC baseline has vertical crossing angles in IR1 and IR2 and horizontal crossing angles in IR5 and IR8.

beam screen: Perforated tube inserted into the cold bore of the superconducting magnets in order to protect the cold bore from synchrotron radiation and ion bombardment.

beam types:

pilot beam: Consists of a single bunch with 0.5×10^{10} protons. It corresponds to the maximum beam current that can be lost without inducing a magnet quench.

commissioning beam: Beam tailored for a maximum luminosity with reduced total beam power (i.e. increased operational margins related to beam losses and magnet quenches) and possibly smaller beam sizes (i.e. increased mechanical acceptance in terms or the transverse beam size and larger tolerances for orbit and β-beat).

intermediate beam: Beam tailored for a high accuracy of the beam measurements with reduced total beam power (i.e. increased operational margins related to beam losses and magnet quenches).

nominal beam: Beam required to reach the design luminosity of $L = 10^{34}$ cm^{-2}s^{-1} with $\beta^* = 0.55$ m ($\rightarrow$ normalized emittance $\epsilon_n = 3.75$ μm; $N_\mathrm{b} = 1.15 \times 10^{11}$; $n_\mathrm{b} = 2808$).

ultimate beam: Beam consisting of the nominal number of bunches with nominal emittances (normalized emittance of 3.75μm) and ultimate bunch intensities ($I = 0.86$A $\rightarrow N_\mathrm{b} = 1.7 \times 10^{11}$). Assuming the nominal value of $\beta^* = 0.55$ m and 2808 bunches, the ultimate beam can generate a peak luminosity of $L = 2.3 \times 10^{34}$ cm^{-2}s^{-1} in the two high luminosity experiments.

BPM: Beam Position Monitor.

bunch: Collection of particles captured within one RF bucket.

bus bar: Main cable that carries the current for powering the magnets outside the magnet coil.

channel: The two apertures of the double bore magnets form two channels of the LHC. Each arc has one outer and one inner channel.

cold mass: The cold mass refers to the part of a magnet that needs to be cooled by the cryogenic system, i.e. the assembly of magnet coils, collars, iron yoke and helium vessel.

crossings: The two machine channels cross at the experimental insertions, i.e. at IP1, IP2, IP5 and IP8.

cryo magnet: Complete magnet system integrated into one cryostat, i.e. main magnet coils, collars and cryostat, correction magnets and powering circuits.

DA: See dynamic aperture.

damper: Transverse or longitudinal feedback system used to damp injection oscillations and / or multi-bunch instabilities of a beam.

decay and snap back: Persistent current decay is a change in the persistent current contribution to the total magnetic field in superconducting magnets powered at constant current (e.g. at injection). This effect varies among magnets and is a function of the powering history (i.e. previous current cycles). When the magnet current is changed (e.g. during the acceleration ramp) the magnetic field comes back to the original value before the decay. This effect is called snap back and occurs for the LHC main dipole magnets within the first 50 A change of the LHC ramp.

dispersion suppressor: The dispersion suppressor refers to the transition between the LHC arcs and insertions. The dispersion suppressor aims at a reduction of the machine dispersion inside the insertions. Each LHC arc has one dispersion suppressor on each end. The length of the dispersion suppressors is determined by the tunnel geometry. Each LHC dispersion suppressor consists of four individually powered quadrupole magnets which are separated by two dipole magnets. In the following this arrangement of four quadrupole and eight dipole magnets is referred to as two missing dipole cells. For the machine lattice these two missing dipole cells are referred to as one dispersion suppressor. However, reducing the dispersion at the IPs to zero requires a special powering of two more quadrupole magnets on each side of the arc. In terms

of the machine optics the dispersion suppressor refers therefore to the two missing dipole cells plus one additional arc cell.

dog leg magnets: Special dipole magnet used for increasing the separation of the two machine channels from standard arc separation. The dogleg magnets are installed in the cleaning insertions IR3 and IR7 and the RF insertion IR4.

dynamic aperture: Maximum initial oscillation amplitude that guarantees stable particle motion over a given number of turns. The dynamic aperture is normally expressed in multiples of the RMS beam size (σ) and together with the associated number of turns.

eddy currents: Eddy currents are screening currents that tend to shield the interior of a conductor or a superconducting cable from external magnetic field changes. In the case of a strand the eddy currents flow along the superconducting filaments in the strand (without loss) and close across the resistive matrix of the strand (copper for the LHC). In the case of a cable the eddy currents flow along the strands (without loss) and close resistively at the contact points among strands in the cable. Eddy currents are also referred to as coupling currents.

experimental insertion region: Insertion region that hosts one of the four LHC experiments.

filament: Superconducting filaments are fine wires of bulk superconducting material with typical dimension in the range of few microns. The superconducting filaments are embedded in the resistive matrix in a strand.

insertion region (IR): Machine region between the dispersion suppressors of two neighbouring arcs. The insertion region consists of two matching sections and, in the case of the experimental insertions, of two triplet assemblies and the separation / recombination dipoles.

interaction point (IP): Middle of the insertion region (except for IP8). In the insertions where the two LHC beams cross over the IP indicates the point where the two LHC beams can intersect. In IR8 the experimental detector is shifted by 3/2 RF wavelengths and the IP refers to the point where the two LHC beams can intersect and it does not coincide with the geometric centre of the insertion.

ions: The LHC will have collisions between heavy ions, $^{208}Pb^{82+}$ (fully stripped) during the first years (208 is the number of nucleons, 82 the number of protons of this particular nucleus).

Ions, early scheme: Approximately 60 bunches per beam, with 7×10^7 Pb ions each, are colliding to yield initial luminosity of $L = 5.0 \times 10^{25}$ cm^{-2}sec^{-1} with ($\beta^* = 0.5$ m).

ions, nominal scheme: Approximately 600 bunches per beam, with 7×10^7 Pb ions each, are colliding at 2.76 TeV/u to yield initial luminosity of $L = 1.0 \times 10^{27}$ cm^{-2}sec^{-1} with ($\beta^* = 0.5$ m).

lattice correction magnets: Correction magnets that are installed inside the Short Straight Section assembly.

lattice version: The lattice version refers to a certain hardware installation in the tunnel. It is clearly separated from the optics version and one lattice version can have more than one optics version.

left and right: See the definition under 'right and left'.

long range interactions: Interaction between the two LHC beams in the common part of the Ring 1 and Ring 2 where the two beams are separated by the crossing angle orbit bumps.

Long Straight Section (LSS): the quasi-straight sections between the upstream and downstream dispersion suppressor of an insertion, including the separation / recombination dipole magnets.

machine cycle: The machine cycle refers to one complete operation cycle of a machine, i.e. injection, ramp up, possible collision flat top, ejection and ramp down. The minimum cycle time refers to the minimum time required for a complete machine cycle.

magnet quench: Loss of the superconducting state in the coils of a superconducting magnet.

main lattice magnets: Main magnets of the LHC arcs, i.e. the arc dipole and quadrupole magnets.

matching section: Arrangement of quadrupole magnets located between the dispersion suppressor and the triplet magnets (or the IP for those insertions without triplet magnets). Each insertion has two matching sections: one upstream and one downstream from the IP.

n_1: The effective mechanical aperture n_1 defines the maximum primary collimator opening in terms of the rms beam size that still guarantees a protection of the machine aperture against losses from the secondary beam halo. It depends on the magnet aperture and geometry and the local optics perturbations.

N_b: Number of particles per bunch.

n_b: Number of bunches per beam.

nominal bunch: Bunch parameters required to reach the design luminosity of $L = 10^{34}\mathrm{cm}^{-2}s^{-1}$ with $\beta^* = 0.55$ m. The nominal bunch intensity is $N_\mathrm{b} = 1.15 \times 10^{11}$ protons.

nominal powering: Hardware powering required to reach the design beam energy of 7 TeV.

octant: An octant starts in the centre of an arc and goes to the centre of the next downstream arc. An octant consists of an upstream and a downstream half-octant. A half-octant and a half-sector cover the same part of the machine even though they may not have the same number.

optical configuration: An optical configuration refers to a certain powering of the LHC magnets. Each optics version has several optical configurations corresponding to the different operation modes of the LHC. For example, each optics version has different optical configurations for injection and luminosity operation and for the luminosity operation the optics features different optical configurations corresponding to different β^* values in the four experimental insertions of the LHC.

optics version: The optics version refers to a consistent set of optical configurations. There can be several different optics versions for one lattice version.

pacman bunches: Bunches that do not experience the same number of long-range beam-beam interactions left and right from the IP.

parallel separation: Dedicated orbit bumps separate the two LHC beams at the IP during injection, ramp and the optics squeeze. The total beam separation at the IP is called the parallel separation. The LHC baseline has horizontal parallel separations in IR1 and IR2 and vertical separations in IR5 and IR8.

parasitic crossing points: Positions in the common part of Ring 1 and Ring 2 where the two beams can experience long range interactions.

persistent currents: Persistent currents are eddy currents with (ideally) infinitely long time constants that flow in the bulk of the superconducting filaments of a strand and tend to shield the interior of the filament from the external magnetic field changes. These screening currents close inside the superconducting filament, with zero resistance (in steady state). Hence, for practical purposes, they do not decay in time and for this reason they are referred to as 'persistent'.

physics run: Machine operation at top energy with luminosity optics configuration and beam collisions.

pilot bunch: Bunch intensity that assures no magnet quench at injection energy for an abrupt loss of a single bunch but is still large enough provide BPM readings. The pilot bunch intensity of the LHC corresponds to 0.5×10^{10} protons in one bunch.

ramp: Change of the magnet current during the beam acceleration when the magnets are 'ramped up' and after the end of a physics store the magnets are 'ramped down'.

resistive matrix: One of the two main constituents of the strand. The resistive matrix embeds the filaments in the strand and provides a low resistance current shunt in case of quench (transition of the superconducting material to the normal state).

RF bucket: The RF system provides longitudinal focusing which constrains the particle motion in the longitudinal phase space to a confined region called the RF bucket.

right and left: Describes the position in the tunnel relative to an observer inside the ring looking out (same definition as for LEP).

Ring 1 and Ring 2: There are two rings in the LHC, one ring per beam. Ring 1 corresponds to Beam 1 which circulates clockwise and Ring 2 corresponds to Beam 2 which circulates counter-clockwise in the LHC.

satellite bunch: Collection of particles inside RF buckets that do not correspond to nominal bunch positions. The nominal bunch spacing for the LHC is 25 ns while the separation of RF buckets is 2.5 ns. In other words, there are 9 RF buckets between two nominal LHC bunch positions that should be empty.

sector: The part of a ring between two successive insertion points (IP) is called a sector. Sector 1-2 is situated between IP1 and IP2.

separation / recombination magnets: Special dipole magnets left and right from the triplet magnets that generate the beam crossings in the experimental insertions.

Short Straight Section (SSS): Assembly of the arc quadrupole and the lattice corrector magnets. Each SSS consists of one quadrupole magnet, one Beam Position Monitor (BPM), one orbit corrector dipole (horizontal deflection for focusing and vertical deflection for defocusing quadrupoles), one lattice correction element (i.e. trim or skew quadrupole elements or octupole magnets) and one lattice sextupole or skew sextupole magnet.

SPecial Straight Section (SPSS): Quadrupole assemblies of the insertion regions. The SPSS features no lattice corrector and sextupole magnets and has only orbit correction dipole magnets and BPMs.

spool piece correction magnets: Correction magnets directly attached to the main dipole magnets. The spool piece correction magnets are included in the dipole cryostat assembly.

strand: A superconducting strand is a composite wire containing several thousands of superconducting filaments dispersed in a matrix with suitably small electrical resistivity properties. The LHC strands have NbTi as superconducting material and copper as resistive matrix.

superconducting cable: Superconducting cables are formed from several superconducting strands in parallel, geometrically arranged in the cabling process to achieve well controlled cable geometry and dimensions, while limiting the strand deformation in the process. Cabling several strands in parallel results in an increase of the current carrying capability and a decrease of the inductance of the magnet, easing protection. The LHC cables are flat, keystoned cables of the so-called Rutherford type.

super pacman bunches: Bunches that do not collide head-on with a bunch from the other beam in one of experimental IPs.

TAN: Target Absorber Neutral: absorber for the neutral particles leaving the IP. It is located just in front of the D1 separation / recombination dipole magnet on the side facing the IP.

TAS: Target Absorber Secondaries: absorber for particles leaving the IP at large angles. It is located just in front of the Q1 triplet quadrupole magnet on the side facing the IP.

tune: Number of particle trajectory oscillations during one revolution in the storage ring (transverse and longitudinal).

triplet: Assembly of three quadrupole magnets used for a reduction of the optical β-functions at the IPs. The LHC triplet assembly consists in fact of four quadrupole magnets but the central two quadrupole magnets form one functional entity. The LHC has triplet assemblies in IR1, IR2, IR5 and IR8.

ultimate bunch intensity: Bunch intensity corresponding to the expected maximum acceptable beam-beam tune shift with two operating experimental insertions. Assuming the nominal emittance (normalized emittance of 3.75μm) the ultimate bunch intensity corresponds to 1.7×10^{11} protons per bunch.

ultimate powering: Hardware powering required to reach the ultimate beam energy of 7.54 TeV, corresponding to a dipole field of 9 T.

upstream and downstream: Always related to the direction of one of the two beams. If no beam is specified Beam 1 is taken as the default. This implies that stating a position as being 'upstream' without indicating any beam is equivalent to stating that the position is to the left.

2.5.2 Definitions

beam half-life: Time during beam collision after which half the beam intensity is lost.

luminosity half-life: Time during beam collision after which the luminosity is halved. The luminosity half-life is generally smaller than the beam half-life.

bunch duration: The bunch duration is defined as

$$\sigma_t = \frac{\sigma_s}{v}, \tag{2.1}$$

where σ_s is the bunch length and v is the speed of the particles in the storage rings.

bunch length: The bunch length is defined as the 'RMS' value of the longitudinal particle distribution in one RF bucket. The bunch length is denoted as

$$\sigma_s. \tag{2.2}$$

damping times: Time after which an oscillation amplitude has been reduced by a factor $1/e$. If no explicit explanation of the types of damping times is given the damping times refer to the amplitude damping times.

- **longitudinal emittance damping time:** Half of the longitudinal amplitude damping time for a Gaussian approximation of the bunch distribution.
- **transverse emittance damping time:** Half of the transverse amplitude damping time for a Gaussian approximation of the transverse bunch distribution.

synchrotron radiation damping times: If no explicit explanation of the types of damping times is given, the damping times refer to the amplitude damping times.

- **longitudinal amplitude damping time:** The ratio of the average rate of energy loss (energy lost over one turn divided by the revolution time) and the nominal particle energy.
- **transverse amplitude damping time:** Time after which the transverse oscillation amplitude has been reduced by a factor $1/e$ due to the emission of synchrotron radiation. For a proton beam it is just twice the longitudinal amplitude damping time due to the emission of synchrotron radiation.

energy spread: The energy spread is defined as the 'RMS' value of the relative energy deviations from the nominal beam energy in a particle distribution. The energy spread is denoted as

$$\sigma_{\delta E/E0}. \tag{2.3}$$

longitudinal emittance: The longitudinal emittance is defined as:

$$\epsilon_s = 4\pi\sigma_t\sigma_{\delta E/E0}E_0, \tag{2.4}$$

where σ_t is the bunch duration in seconds, $\sigma_{\delta E/E0}$ the relative energy spread.

transverse beam size: The transverse beam size is defined as the 'RMS' value of the transverse particle distribution.

transverse emittance: The transverse emittance is defined through the invariance of the area enclosed by the single particle phase space ellipse. The single particle invariant under the transformation through the storage ring is given by

$$A = \gamma x^2 + 2\alpha x x^{'} + \beta x^{'2}, \tag{2.5}$$

where α, β and γ are the optical functions. The area enclosed by the single particle phase space ellipse is given by

$$\text{area of ellipse} = \pi A \tag{2.6}$$

For an ensemble of particles the emittance is defined as the average of all single particle invariants (areas enclosed by the single particle phase space ellipsoids divided by π).

The transverse betatron beam size in the storage ring can be written in terms of the beam emittance as

$$\sigma_{x,y}(s) = \sqrt{\beta_{x,y}(s)\epsilon_{x,y}}, \tag{2.7}$$

where $\beta_{x,y}(s)$ is the optical β-function along the storage ring.

The transverse emittance is given by the following expression:

$$\epsilon_z = \sqrt{\langle z^2\rangle\langle z^{'2}\rangle - \langle zz^{'}\rangle^2}; z = x, y, \tag{2.8}$$

where it is assumed that the particle coordinates are taken at a place with vanishing dispersion and where $\langle\ \rangle$ defines the average value of the coordinates over the distribution. z and $z^{'}$ are the canonical transverse coordinates ($z = x, y$).

normalized transverse emittance: The beam emittance decreases with increasing beam energy during acceleration and a convenient quantity for the operation of a hadron storage rings (and linear accelerators) is the 'normalized emittance' defined as

$$\epsilon_n = \epsilon\gamma_r\beta_r, \tag{2.9}$$

where γ_r and β_r are the relativistic gamma and beta factors:

$$\beta_r = \frac{v}{c} \tag{2.10}$$

$$\gamma_r = \frac{1}{\sqrt{1-\beta_r^2}} \tag{2.11}$$

(v is the particle velocity and c the speed of light in vacuum).

The nominal normalized transverse emittance for the LHC is

$$\epsilon_n = 3.75\ \mu\text{m}. \tag{2.12}$$

2.6 LHC SYSTEM PREFIXES

Table 2.5: LHC system prefixes

LHC Systems Prefix Definitions [a]	
Letter	System description
A	Acceleration, RF and dampers
B	Beam instrumentation
C	Communication and controls
D	Electrical distribution
E	Electricity
F	Fluids (Demineralized water excluded)
G	Geodesy and geometry
H	Mechanics, supports and handling
I	Injection and transfer lines
J	Infrastructure
K	Civil engineering
L	Layouts
M	Magnetic elements
N	Particle sources
O	
P	Personnel safety
Q	Cryogenics
R	Power converters
S	General safety
T	Targets, dump and collimators
U	Ventilation and air conditioning
V	Vacuum
W	Demineralized water
X	Experiments
Y	Access systems
Z	Electrostatic systems

[a] No change has been introduced in system type identification. The first letter identifies a system as defined in the document 'Naming conventions for the LHC components', edited by P. Faugeras, AC.DI/FA Note 92-04.

2.7 LHC MAGNET SYSTEM EQUIPMENT NAMES AND CIRCUIT COUNT

Table 2.6: LHC magnet equipment names and circuit count

Magnet Type	Order	Description	Number of Magnets
MB	1	Main Dipole Coldmass	1232
MBAW	1	Alice Spectrometer (Muon Dipole)	1
MBLW	1	LHC-b Spectrometer	1
MBRB	1	Twin Aperture Separation Dipole (194 mm) D4	2
MBRC	1	Twin Aperture Separation Dipole (188 mm) D2	8
MBRS	1	Single Aperture Separation Dipole D3	4
MBW	1	Twin Aperture Warm Dipole Module D3 and D4 in IR3 and IR7	20
MBWMD	1	Single Aperture Warm Dipole Module Compensating Alice Spectrometer	1
MBX	1	Single Aperture Separation Dipole D1	4
MBXW	1	Single Aperture Warm Dipole Module D1 in IR1 and IR5	24
MBXWH	1	Single Aperture Warm Horizontal Dipole Module Compensating LHC-b Spectrometer	1
MBXWS	1	Aperture Warm Horizontal Dipole Short Module	2
MBXWT	1	Single aperture warm compensator for ALICE	2
MCBCH	1	Orbit Corrector in MCBCA(B,C,D)	78
MCBCV	1	Orbit Corrector in MCBCA(B,C,D)	78
MCBH	1	Arc Orbit Corrector in MSCBA(B,C,D), Horizontal	376
MCBV	1	Arc Orbit Corrector in MSCBA(B,C,D), Vertical	376
MCBWH	1	Single Aperture Warm Orbit Horizontal Corrector	8
MCBWV	1	Single Aperture Warm Orbit Verticall Corrector	8
MCBXH	1	Horizontal Orbit Corrector in MCBXA or MCBXB	24
MCBXV	1	Vertical Orbit Corrector in MCBXA or MCBXB	24
MCBYH	1	Orbit Corrector in MCBYA(B)	44
MCBYV	1	Orbit Corrector in MCBYA(B)	44
MCD	5	Decapole Corrector in MCDO, (Spool Piece Corrector)	1232
MCO	4	Octupole Corrector in MCDO, (Spool Piece Corrector)	1232
MCOSX	3	Skew Octupole Spool-Piece Associated to MQSX in MQSXA	8
MCOX	4	Octupole Spool-Piece Associated to MQSXA	8
MCS	3	Sextupole Corrector, (Spool Piece Corrector)	2464
MCSSX	3	Skew Sextupole Spool-Piece Associated to MQSX in MQSXA	8
MCSX	3	Sextupole Spool-Piece Associated to MCBXA	8
MCTX	6	Dodecapole Spool-Piece Associated to MCBXA	8
MKA	1	Tune kicker	2
MKD	1	Ejection dump kicker	30
MKI	1	Injection kicker	8
MKQ	1	Kicker For Q And Aperture Measurement	2

Table 2.7: LHC magnet equipment names and circuit count continued

Magnet Type	Order	Description	Number of Magnets
MO	4	Octupole Lattice Corrector in Arc Short Straight Section	336
MQ	2	Lattice Quadrupole in the Arc, (3rd character reserved)	392
MQM	2	Insertion Region Quadrupole 3.4 m	38
MQMC	2	Insertion Region Quadrupole 2.4m	12
MQML	2	Insertion Region Quadrupole 4.8 m	36
MQS	2	Skew Quadrupole Lattice Corrector in Arc Short Straight Section	64
MQSX	2	Skew Quadrupole (a2) in MQSXA	8
MQT	2	Tuning Quadrupole Corrector in Arc Short Straight Section	320
MQTLH	2	(MQTL Half Shell Type)	48
MQTLI	2	(MQTL Inertia Tube Type)	72
MQWA	2	Twin Aperture Warm Quadrupole Module in IR3 and IR7. Asymmetrical FD or DF	40
MQWB	2	Twin Aperture Warm Quadrupole Module in IR3 and IR7. Symmetrical FF or DD	8
MQXA	2	Single Aperture Triplet Quadrupole (Q1, Q3)	16
MQXB	2	Single Aperture Triplet Quadrupole (Q2)	16
MQY	2	Insertion Region Wide Aperture Quadrupole 3.4 m.	24
MS	3	Arc Sextupole Lattice Corrector Associated to MCBH or MCBV in MSCBA, MSCBB, MSCBC and MSCBD	688
MSDA	1	Ejection dump septum, Module A	10
MSDB	1	Ejection dump septum, Module B	10
MSDC	1	Ejection dump septum, Module C	10
MSIA	1	Injection septum, Module A	4
MSIB	1	Injection septum, Module B	6
MSS	2	Arc skew Sextupole Corrector Associated to MCBH in MSCBC and MSCBD	64

Table 2.8: LHC power converter circuit names and count

Type	Number of Circuits
B	8
BAWV	1
BLWH	1
BWMDV	1
BXWH	1
BXWSH	2
BXWTV	2
CBCH10	16
CBCH5	4
CBCH6	12
CBCH7	14
CBCH8	16
CBCH9	16
CBCV10	16
CBCV5	4
CBCV6	12
CBCV7	14
CBCV8	16
CBCV9	16
CBH11	16
CBH12	16
CBH13	16
CBH14	16
CBH15	16
CBH16	16
CBH17	16
CBH18	16
CBH19	16
CBH20	16
CBH21	16
CBH22	16
CBH23	16
CBH24	16
CBH25	16
CBH26	16
CBH27	16
CBH28	16
CBH29	16

Table 2.9: LHC power converter circuit names and count (continued)

Type	Number of Circuits
CBH30	16
CBH31	16
CBH32	16
CBH33	16
CBH34	8
CBV11	16
CBV12	16
CBV13	16
CBV14	16
CBV15	16
CBV16	16
CBV17	16
CBV18	16
CBV19	16
CBV20	16
CBV21	16
CBV22	16
CBV23	16
CBV24	16
CBV25	16
CBV26	16
CBV27	16
CBV28	16
CBV29	16
CBV30	16
CBV31	16
CBV32	16
CBV33	16
CBV34	8
CBWH4	4
CBWH5	4
CBWV4	4
CBWV5	4
CBXH1	8
CBXH2	8
CBXH3	8
CBXV1	8
CBXV2	8
CBXV3	8
CBYH4	10
CBYH5	8

Table 2.10: LHC power converter circuit names and count (continued)

Type	Number of Circuits
CBYH6	2
CBYHS4	16
CBYHS5	8
CBYV4	10
CBYV5	8
CBYV6	2
CBYVS4	16
CBYVS5	8
CD	16
CO	16
COSX3	8
COX3	8
CS	16
CSSX3	8
CSX3	8
CTX3	8
D1	6
D2	8
D3	2
D34	2
D4	2
MSD	2
OD	16
OF	16
Q10	12
Q4	12
Q5	14
Q6	18
Q7	10
Q8	12
Q9	12
QD	8
QF	8
QS	24
QSX3	8
QT12	32
QT13	32

Table 2.11: LHC power converter circuit names and count (continued)

Type	Number of Circuits
QT4	4
QT5	4
QTD	16
QTF	16
QTL10	8
QTL11	32
QTL7	8
QTL8	8
QTL9	8
QX	8
SD1	16
SD2	16
SF1	16
SF2	16
RSS	16

REFERENCES

[1] O. Gröbner, 'Overview of the LHC vacuum system', VACUUM **60**, pg. 25-34, 2001

CHAPTER 3

LAYOUT AND PERFORMANCE

3.1 PERFORMANCE

3.1.1 Performance goals

The Large Hadron Collider (LHC) is a two-ring, superconducting accelerator and collider to be installed in the 27 km long LEP [1] tunnel aiming at the discovery of the Higgs particle and the study of rare events with centre of mass collision energies of up to 14 TeV. The number of events per second generated in the LHC collisions is given by:

$$N_{\text{event}} = L\sigma_{\text{event}} \tag{3.1}$$

where σ_{event} is the cross section for the event under study and L the machine luminosity. The machine luminosity depends only on the beam parameters and can be written for a Gaussian beam distribution as:

$$L = \frac{N_{\text{b}}^2 n_{\text{b}} f_{\text{rev}} \gamma_r}{4\pi\epsilon_n \beta^*} F, \tag{3.2}$$

where N_{b} is the number of particles per bunch, n_{b} the number of bunches per beam, f_{rev} the revolution frequency, γ_r the relativistic gamma factor, ϵ_n the normalized transverse beam emittance, β^* the beta function at the collision point and F the geometric luminosity reduction factor due to the crossing angle at the IP:

$$F = 1/\sqrt{1 + \left(\frac{\theta_{\text{c}}\sigma_z}{2\sigma^*}\right)^2}, \tag{3.3}$$

where θ_{c} is the full crossing angle at the IP, σ_z the RMS bunch length and σ^* the transverse RMS beam size at the IP. (The above expression assumes equal beam parameters for both circulating beams). The exploration of rare events in the LHC collisions therefore requires both high beam energies and high beam intensities.

The LHC has two high luminosity experiments, ATLAS [2] and CMS [3], aiming at a peak luminosity of $L(\text{ATLAS\&CMS}) = 10^{34}\ \text{cm}^{-2}\text{s}^{-1}$. Tabs. 2.1 and 2.2 show the main parameters required to reach a peak luminosity of $L = 10^{34}\ \text{cm}^{-2}\text{s}^{-1}$ in the LHC in proton operation. In addition to these high luminosity experiments the LHC has two low luminosity experiments: LHCB [4] for B-physics aiming at a peak luminosity of $L(\text{LHCB}) = 10^{32}\ \text{cm}^{-2}\text{s}^{-1}$ and TOTEM [5] for the detection of protons from elastic scattering at small angles aiming at a peak luminosity of $L = 2\times10^{29}\ \text{cm}^{-2}\text{s}^{-1}$ with 156 bunches. In addition to the proton beams the LHC will also be operated with ion beams. The LHC has one dedicated ion experiment ALICE [6] aiming at a peak luminosity of $L(\text{ALICE}) = 10^{27}\ \text{cm}^{-2}\text{s}^{-1}$ for nominal Pb-Pb ion operation [6]. The parameters required for Pb ion operation are summarized in Chap. 21.

The high beam intensities implied by a luminosity of $L = 10^{34}\ \text{cm}^{-2}\text{s}^{-1}$ exclude the use of anti-proton beams and one common vacuum and magnet system for both circulating beams (as it is done in the TEVATRON) and implies the use of two proton beams. To collide two beams of equally charged particles requires opposite magnet dipole fields in both beams. The LHC is therefore designed as a proton-proton collider with separate magnet fields and vacuum chambers in the main arcs and with common sections only at the insertion regions where the experimental detectors are located. The two beams share an approximately 130 m long common beam pipe along the interaction regions (IR). The exact length is 126 m in IR2 and IR8 which feature superconducting separation dipole magnets next to the triplet assemblies and 140 m in IR1 and IR5 which feature normal conducting and therefore longer separation dipole magnets next to the triplet assemblies. Together with the large number of bunches (2808 for each proton beam), and a nominal bunch spacing of 25 ns, the long common beam pipe implies 34 parasitic collision points for each experimental insertion region (for four experimental IR's this implies a total of 136 unwanted collision points). Dedicated crossing angle orbit bumps separate the two LHC beams left and right from the central interaction point (IP) in order to avoid collisions at these parasitic collision points.

There is not enough room for two separate rings of magnets in the LEP tunnel. Therefore the LHC uses twin bore magnets which consist of two sets of coils and beam channels within the same mechanical structure and cryostat.

The peak beam energy in a storage ring depends on the integrated dipole field along the storage ring circumference. Aiming at peak beam energies of up to 7 TeV inside the existing LEP tunnel implies a peak dipole field of 8.33 T and the use of superconducting magnet technology.

3.1.2 Performance limitations for the LHC

The LHC machine performance is limited by seven main effects.

Beam-Beam limit

The maximum particles density per bunch is limited by the nonlinear beam-beam interaction that each particle experiences when the bunches of both beams collide with each other in the IR's. The beam-beam interaction is measured by the linear tune shift given by:

$$\xi = \frac{N_{\mathrm{bunch}} r_p}{4\pi\epsilon_n}, \tag{3.4}$$

where r_p is the classical proton radius $r_p = e^2/(4\pi\epsilon_0 m_p c^2)$. Experience with existing hadron collider machines indicates that the total linear tune shift (sum of all IP's) should not exceed 0.015. With three proton experiments requiring head-on collisions this implies that the linear beam-beam tune shift for each IP should satisfy $\xi \leq 0.005$. A detailed discussion of the limitations due to the beam-beam interaction can be found in Section 5.08.

Mechanical aperture

The geometrical aperture of the LHC arcs is given by the beam screen dimensions. The beam screen has a height of approximately 2×17.3 mm and a total width of 2×22 mm (a detailed description of the LHC beam screen is given in Chap. 12). Requiring a minimum aperture of 10 σ in terms of the RMS beam sizes and assuming tolerances for the linear machine imperfections and the magnet alignment and geometry implies a peak nominal beam size of 1.2 mm (a minimum mechanical aperture of 10 σ is prescribed by the LHC beam cleaning system which is described in more detail in Chap. 18). A detailed list of the assumed optics and mechanical imperfections is given in Sec. 4.03. Combined with a peak β-function of 180 m in the LHC arcs this implies a maximum acceptable transverse beam emittance of $\epsilon_n = 3.75$ μm. Combined with the limit on the linear beam-beam tune shift the mechanical aperture of the LHC therefore limits the maximum bunch intensity to $N_{\mathrm{bunch}}(\mathrm{nominal}) = 1.15 \times 10^{11}$.

Furthermore, the mechanical aperture of the triplet magnets limits the minimum attainable β^* value at the IP's and the maximum attainable crossing angle orbit bump in the experimental IR's. Both parameters can limit the peak luminosity in the LHC machine. A detailed description of the IR magnet parameters can be found in Chap. 8 and a description of the luminosity limitations due to the mechanical aperture in the IR's in Chap. 5.

Maximum dipole field and Magnet quench limits

The maximum γ_{r} that can be reached in the LHC is limited by the peak dipole field in the storage ring. The nominal field is 8.33 T corresponding to a beam energy of 7 TeV. However, the actual field attainable in the storage ring depends on the heat load and temperature margins inside the cryo-magnets and therefore on the beam losses in the machine during operation. A high dipole field therefore implies efficient operation with minimum beam losses. A detailed description of the limitations for the peak dipole field and the beam losses can be found in Chaps. 7 and 18.

Energy stored in the circulating beams and in the magnetic fields

A total beam current of 0.584 A corresponds to a stored energy of approximately 362 MJ. In addition to the energy stored in the circulating beams the LHC magnet system has a stored electromagnetic energy of

approximately 600 MJ yielding a total stored energy of more than 1 GJ. This stored energy must be absorbed safely at the end of each run or in the case of a malfunction or an emergency. The beam dumping system and the magnet system therefore provide additional limits for the maximum attainable beam energies and intensities (see Chaps. 7 and 17 for details on the above limits).

Heat load

Although the synchrotron radiation in hadron storage rings is small compared to that generated in electron rings it can still impose practical limits to the maximum attainable beam intensities if the radiation must be absorbed in a cryogenic system. In addition to the heat load due to synchrotron radiation, the LHC cryogenics system must absorb the heat deposition from the impedance issues (resistive wall effect) and electron cloud bombardment. The latter two effects are described in detail in Chap. 5.

Field quality and dynamic aperture

Field quality errors spoil the particle stability in the storage ring and loss-free operation of the machine therefore requires a high field quality. A characterizing feature of superconducting magnets is the decay of persistent currents and their 'snap back' at the beginning of the ramp. Small beam losses therefore require a tight control of the magnet field errors during magnet production and during machine operation. Assuming fixed limits for the beam losses due to the quench levels of the superconducting magnets, the accuracy of the field quality correction during operation limits the maximum attainable machine performance. A detailed description of the required magnet field quality can be found in Chap. 4. A description of the time dependent effects in superconducting magnets and the reference system for their correction during operation is given in Chaps. 7 and 20 while a discussion of the beam instrumentation available for beam based corrections of the field errors in Chap. 13.

Collective beam instabilities

The interaction of the charged particles in each beam with each other via electromagnetic fields and the conducting boundaries of the vacuum system can result in collective beam instabilities. Generally speaking the collective effects are a function of the vacuum system geometry and its surface properties. They are usually proportional to the beam currents and can therefore limit the maximum attainable beam intensities in the LHC beams. A detailed discussion of the collective effects in the LHC can be found in Chap. 5. High beam and bunch intensities, as implied by the nominal design luminosity for the LHC, therefore imply tight control of the vacuum system cross sections and surface properties. Both aspects are discussed in Chap. 12.

3.1.3 Luminosity lifetime

The luminosity in the LHC is not constant over a physics run but decays due to the degradation of intensities and emittances of the circulating beams.

The main cause for the luminosity decay for nominal LHC performance are the collisions themselves. The initial decay time of the bunch intensity, due to this effect, is:

$$\tau_{\text{nuclear}} = \frac{N_{\text{tot},0}}{L\sigma_{\text{tot}}k}, \tag{3.5}$$

where $N_{\text{tot},0}$ is the initial beam intensity, L the initial luminosity, σ_{tot} the total cross section ($\sigma_{\text{tot}} = 10^{-25}$ cm^{-2} at 7 TeV) and k the number of interaction points. Assuming an initial peak luminosity of $L = 10^{34}$ cm^{-2}s^{-1} and two high luminosity experiments the above expression yields an initial decay time of $\tau = 44.85$ h.

Eq. (3.5) results in the following decay of the beam intensity and luminosity as functions of time [7]:

$$N_{\text{tot}}(t) = \frac{N_{\text{tot},0}}{1 + t/\tau_{\text{nuclear}}} \tag{3.6}$$

$$L(t) = \frac{L_0}{(1 + t/\tau_{\rm nuclear})^2}. \tag{3.7}$$

The time required to reach 1/e of the initial luminosity is given by [7]:

$$t_{1/e} = (\sqrt{e} - 1)\tau. \tag{3.8}$$

yielding a luminosity decay time of $\tau_{\rm nuclear,1/e} = 29$ h.

Other contributions to beam losses come from Toucheck scattering and from particle losses due to a slow emittance blow-up. An emittance blow-up can be caused by the scattering of particles on the residual gas, the nonlinear force of the beam-beam interaction, RF noise and IBS scattering effects.

The synchrotron radiation damping in the LHC decreases the bunch dimensions at top energy and can partially compensate the beam size blow-up due to the above effects. Following the arguments set out in the Pink Book (the 1991 Design Study) [8] we assume here that the radiation damping process just cancels the beam blow up due to the beam-beam interactions and RF noise. Approximating further the decay due to the beam-beam interaction by an exponential decay process [9] one can estimate the net luminosity lifetime by:

$$\frac{1}{\tau_L} = \frac{1}{\tau_{\rm IBS}} + \frac{2}{\tau_{\rm rest-gas}} + \frac{1}{\tau_{\rm nuclear,1/e}}. \tag{3.9}$$

Inserting the exponential nuclear decay time, a transverse IBS growth time of $\tau_{\rm IBS} = 80$ h (see Chap. 5 for more details on the IBS growth time estimates) and a vacuum beam lifetime of $\tau_{\rm rest-gas} = 100$ h [10] (see Chap. 12 for more details on the vacuum beam lifetime estimates) on obtains a net luminosity lifetime of:

$$\tau_L = 14.9 \text{ h}. \tag{3.10}$$

3.1.4 Integrated luminosity

Estimating the integrated luminosity of a storage ring requires assumptions on the average turnaround time of the storage ring and the average number of luminosity fills per year. Having no operational data available for LHC, data from the HERA proton ring operation will be used as a reference [11].

3.1.5 Average Turnaround Time

Filling the LHC requires 12 cycles of the SPS synchrotron and each SPS fill requires 3 to 4 cycles of the PS synchrotron. The SPS and PS cycling time are 21.6 and 3.6 s respectively, yielding a total LHC filling time of approximately 4 mins per beam. Assuming that each LHC aperture requires additional 4 SPS cycles for the injection set up (3 pilot bunches and one nominal intensity) and that the LHC operators require at least 2 mins to evaluate the measurements of each pilot bunch shots and to readjust the machine settings, the total (minimum) LHC injection time becomes:

$$T_{\rm inj}(LHC) \approx 16 \text{ min}. \tag{3.11}$$

The minimum time required for ramping the beam energy in the LHC from 450 GeV to 7 TeV is approximately 20 minutes [12]. After a beam abort at top energy it takes also approximately 20 mins to ramp the magnets down to 450 GeV. Assuming a programmed check of all main systems of 10 mins [8] one obtains a total turnaround time for the LHC of [1]:

$$T_{\rm turnaround,min}(LHC) \approx 70\text{min}. \tag{3.12}$$

After 10 years of machine operation, on average, only every third proton injection in HERA leads to a successful proton fill at top energy [13]. The average time between the end of a luminosity run and a new beam at top energy in HERA is approximately 6 h compared to a theoretical minimum turnaround time of approximately 1 h. In the following analysis we consider therefore two cases for evaluating the integrated machine luminosity: i) the minimum theoretical turnaround time of the LHC, i.e. $T_{\rm turnaround}({\rm case1}) = 1.2$ h and ii) a turnaround time which is 6 times larger than the minimum theoretical turnaround time, i.e. $T_{\rm turnaround}({\rm case2}) = 7$ h.

[1] The pink book quotes a minimum turnaround time of 2 hours [8].

3.1.6 Integrated Luminosity

Integrating the luminosity over one luminosity run yields:

$$L_{\rm int} = L_0 \tau_L [1 - e^{-T_{\rm run}/\tau_L}] \tag{3.13}$$

where $T_{\rm run}$ is the total length of the luminosity run.

The overall collider efficiency depends on the ratio of the run length and the average turnaround time. Assuming that the machine can be operated during 200 days per year the total luminosity per year is given by:

$$L_{\rm tot} = \frac{200 \times 24}{T_{\rm run}[h] + T_{\rm turnaround}[{\rm h}]} L_{\rm int}. \tag{3.14}$$

The total luminosity per year attains a maximum if the run time satisfies the following equation

$$ln(\frac{T_{\rm turnaround} + T_{\rm run}}{\tau_L} + 1) = \frac{T_{\rm run}}{\tau_L}. \tag{3.15}$$

Assuming a luminosity lifetime of 15 h one obtains optimum run times of 12 h and 5.5 h for an average turnaround time of 7 h and 1.2 h, respectively. Inserting the nominal peak LHC luminosity and the optimum run times into Eqs. (3.13) and (3.14) one obtains for the maximum total luminosity per year between 80 fb^{-1} and 120 fb^{-1} depending on the average turn around time of the machine.

3.2 LATTICE LAYOUT

All lattice descriptions in this Chapter refer to the LHC Version 6.4 including the repositioning [1] of the Q3 triplet magnets which is part of Version 6.5. [2]

3.2.1 The LHC in the LEP tunnel

The basic layout of the LHC follows the LEP tunnel geometry and is depicted in Fig.3.2. The LHC has eight arcs and straight sections. Each straight section is approximately 528 m long and can serve as an experimental or utility insertion. The two high luminosity experimental insertions are located at diametrically opposite straight sections: the ATLAS experiment is located at point 1 and the CMS experiment at point 5. Two more experimental insertions are located at point 2 and point 8 which also contain the injection systems for Beam 1 and Beam 2, respectively. The injection kick occurs in the vertical plane with the two beams arriving at the LHC from below the LHC reference plane. The beams only cross from one magnet bore to the other at these four locations. The remaining four straight sections do not have beam crossings. Insertion 3 and 7 each contain two collimation systems. Insertion 4 contains two RF systems: one independent system for each LHC beam. The straight section at point 6 contains the beam dump insertion where the two beams are vertically extracted from the machine using a combination of horizontally deflecting fast-pulsed ('kicker') magnets and vertically-deflecting double steel septum magnets. Each beam features an independent abort system.

The LHC lattice has evolved over several versions. The Conceptual Design Report [14] was based on lattice version 4 which did not provide the required flexibility for the optics design. Significant improvements were introduced in version 5 and 6 of the LHC lattice [15] and [16] summarizes their main benefits. A summary of the different LHC lattice versions is given in [17].

The arcs of LHC lattice version 6.4 are made of 23 regular arc cells. The arc cells are 106.9 m long and are made out of two 53.45 m long half cells each of which contains one 5.355 m long cold mass (6.63 m long cryostat) short straight section (SSS) assembly and three 14.3 m long dipole magnets. The LHC arc cell has been optimized for a maximum integrated dipole field along the arc with a minimum number of magnet interconnections and with the smallest possible beam envelopes [18]. Fig. 3.1 shows a schematic picture of one LHC half-cell and Sec. 3.2.3 explains the functionality of the SSS in detail. The two apertures for Ring

[2] A summary of the differences between differnt LHC version can be found on the WWW under: http://slap.web.cern.ch/slap/MAC.pdf

1 and Ring 2 are separated by 194 mm. The two coils in the dipole magnets are powered in series and all dipole magnets of one arc form one electrical circuit. The quadrupoles of each arc form two electrical circuits: all focusing quadrupole magnets in Ring 1 and Ring 2 are powered in series and all defocusing quadrupole magnets of Beam 1 and Beam 2 are powered in series. The optics of Beam 1 and Beam 2 in the arc cells is therefore strictly coupled via the powering of the main magnetic elements.

A dispersion suppressor is located at the transition between an LHC arc and a straight section yielding a total of 16 dispersion suppressor sections. The aim of the dispersion suppressors is threefold [16]:

- adapt the LHC reference orbit to the geometry of the LEP tunnel;
- cancel the horizontal dispersion arising in the arc and generated by the separation / recombination dipole magnets and the crossing angle bumps;
- help in matching the insertion optics to the periodic solution of the arc.

A generic design of a dispersion suppressor uses standard arc cells with missing dipole magnets [19]. The LEP dispersion suppressor, which defines the geometry of the tunnel, was made of 3.5 cells with a 90° phase advance, optimized to suppress the dispersion. With the 2.5 times longer LHC dipole and quadrupole magnets, only two LHC cells can be fitted in the dispersion suppressor tunnel.

This layout can still accurately follow the LEP tunnel (see Sec 3.2.2). However, the shortened dispersion suppressor cannot fully cancel the horizontal dispersion if the dispersion suppressor cells are powered in series with the arc cells. Relying only on the missing dipole concept for the dispersion suppression the horizontal arc dispersion can only be reduced by a factor of 2.5 [20]. Full cancellation of the horizontal dispersion requires individual powering of the dispersion suppressor quadrupole magnets. To this end the dispersion suppressor cells are equipped with special, medium current, quadrupole magnets. A detailed description of the special insertion quadrupole magnets can be found in Chaps. 8 and 10. Fig. 3.3 shows the schematic layout of the LHC dispersion suppressors. The only exceptions to the above layout are IR3 and IR7 which do not have enough space to house the large 6000 A power supplies required for individual powering of the dispersion suppressor quadrupole magnets. Instead, the dispersion suppressor quadrupole magnets in IR3 and IR7 are powered in series with the arc quadrupole magnets and each dispersion suppressor quadrupole is equipped with a trim quadrupole magnet that requires only a small 500 A power supply. This solution solves the problem of limited space in the underground alcoves but limits the flexibility for the IR3 and IR7 dispersion suppressor insertions. Sec 3.2.6 describes in detail the consequences of the insertion quadrupole powering in IR3 and IR7.

The long straight sections in the LEP tunnel are approximately 528 m long. Assuming a quadrupole magnet spacing equivalent to the magnet separation in the LHC arc cells, provides sufficient space for approximately 10 insertion region quadrupole magnets. The exact number and arrangement of these quadrupole magnets in the insertion region might be further restricted by the special requirements in each insertion. Sec 3.2.4 to 3.2.9 describe the detailed insertion layout for each insertion type. Assuming a midpoint symmetry for the insertion optics this provides 5 independent parameters for matching 6 optics constraints (β_x, β_y, α_x, α_y, μ_x, and μ_y) at the transition points to the dispersion suppressors (assuming that the dispersion functions can be matched via the dispersion suppressor parameters). Even without additional optics constraints from the insertion region this minimum number of constraints exceeds the number of free parameters (Secs. 3.2.4 to 3.2.9 describe in detail the special requirements for each LHC insertion). [3] The dispersion suppressor therefore has to act as an optical buffer between the arc and the insertion optics which provides additional parameters for matching the insertion optics. In order to cope with this additional functionality the dispersion suppressors are extended into the neighboring arcs using the arc trim quadrupole magnets of the first arc cell next to each dispersion suppressor. This procedure adds four more parameters for matching the insertion optics to the arc (two parameters for each dispersion suppressor). The drawback of the above implementation is that it does not provide strictly separated functionality of the dispersion suppressor and the insertion regions.

[3] Up to Version 4 of the LHC lattice the experimental insertion featured only 4 functional quadrupole units on each side of the IP: an inner triplet powered in series as one unit left and right from the IP and an 'outer triplet' of three individually powered insertion quadrupole magnets on each side of the IP.

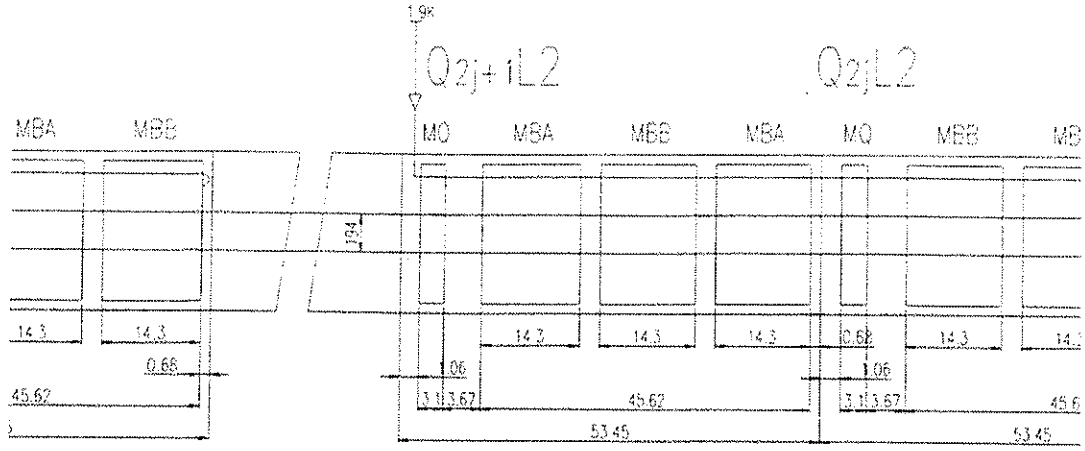

Figure 3.1: Schematic layout of an LHC half-cell

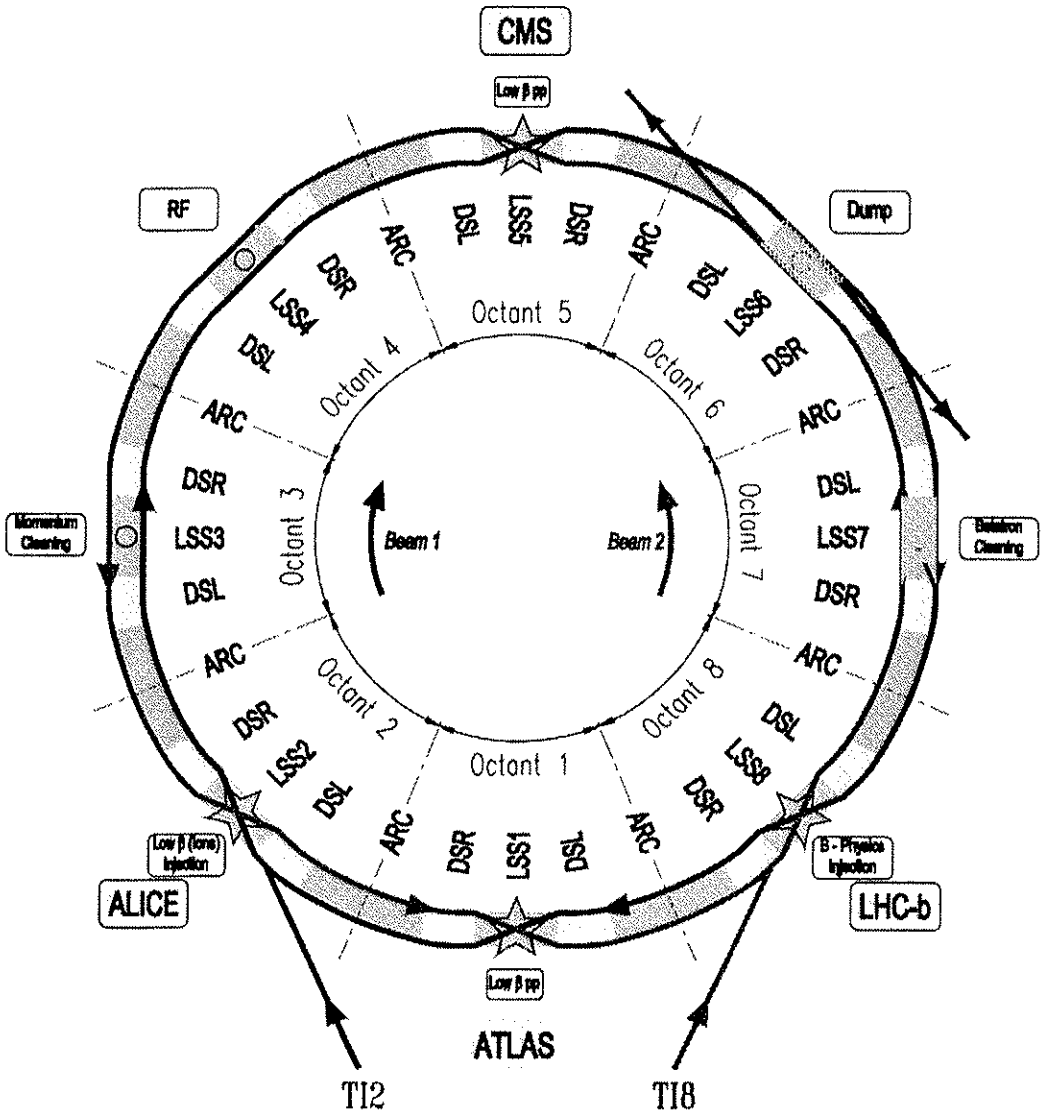

Figure 3.2: Schematic layout of the LHC. Beam 1 circulates clockwise and Beam 2 counter-clockwise.

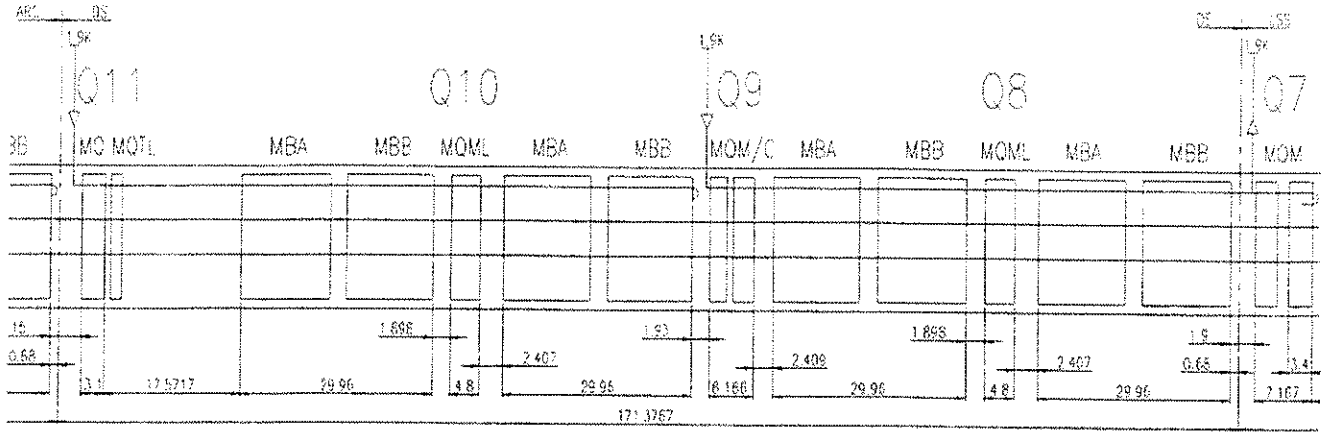

Figure 3.3: Schematic layout of LHC dispersion suppressor next to IR2

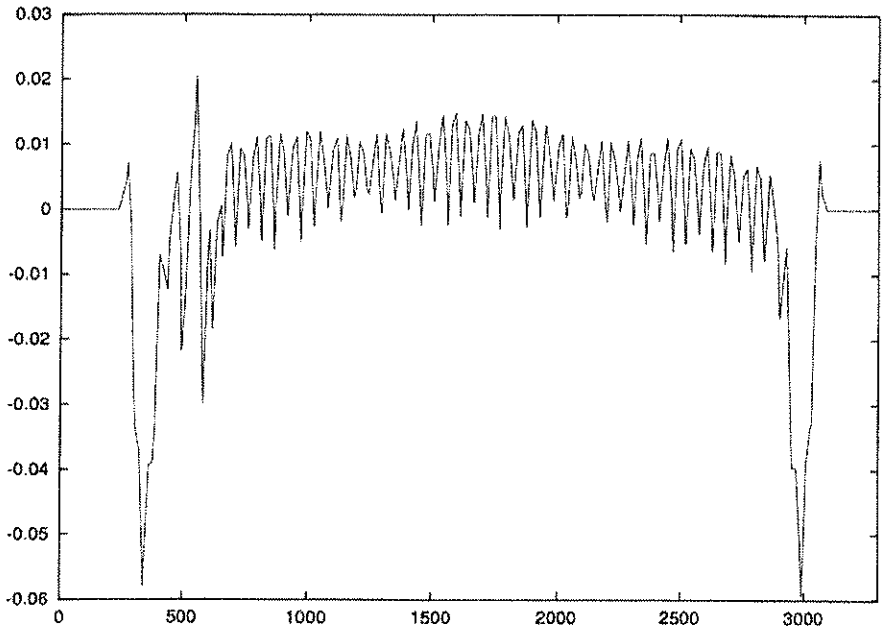

Figure 3.4: The horizontal position of the LHC compared to the LEP in one sector of the machine in metres.

3.2.2 Geometry

The LHC arcs tend to be radially exterior to the theoretical position of the LEP machine by up to 4 cm with the maximum excursions occurring near the arc transition to the dispersion suppressor. The total LHC circumference is kept equal to the LEP circumference and the positive offset of the LHC machine in the arcs is compensated by a larger excursion in the opposite direction inside the dispersion suppressor. The offset in the dispersion suppressor region reaches up to -0.1 m and is caused by the mismatch of the long LHC cells and the relatively short LEP dispersion suppressor section. Fig. 3.4 shows the horizontal position of the LHC compared to the LEP in one sector of the machine in metres.

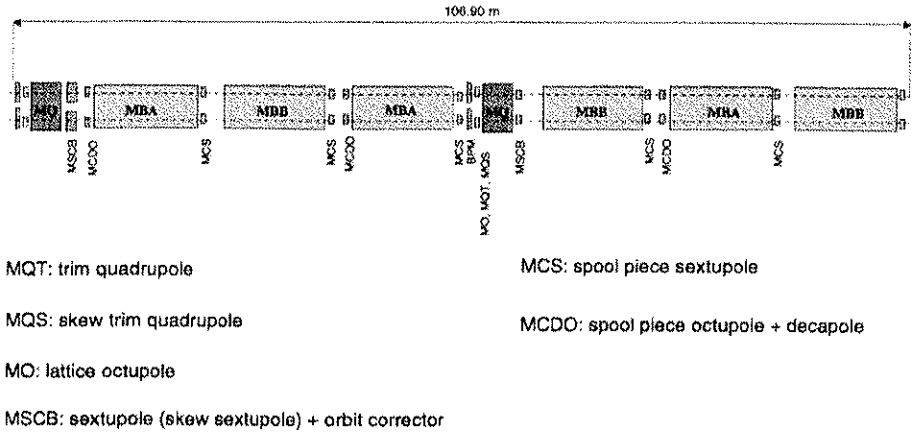

Figure 3.5: Schematic layout of the LHC arc corrector magnets

3.2.3 Functional description of the arc corrector circuits

The LHC correction circuits have evolved over the different LHC lattice versions [21][16]. The circuit description given in this Section is based on the LHC lattice version 6.4.

The corrector magnets located in the arcs of the LHC can be split into two distinct categories (see Fig. 3.5):

- The lattice corrector magnets attached on both sides of the main quadrupole magnets are installed in the Short Straight Section (SSS) cryostats.
- The spool-piece corrector magnets which are thin non-linear windings attached directly on the extremities of the main dipoles.

Contrary to the main dipole circuits and the two families (QF and QD) of lattice quadrupoles for which, in each sector, Ring 1 and Ring 2 are powered in series, the arc corrector magnets can be adjusted independently for the two beams.

The different types and main functionalities of the lattice corrector magnets are summarized below.

Arc orbit corrector magnets MCB

Horizontal and vertical orbit corrector magnets, MCBH and MCBV, are installed at each focusing (QF) and defocusing (QD) quadrupole, respectively, that is a total of 23 or 24 orbit correctors per ring, per arc and per transverse plane, depending on the polarity of the quadrupole at mid-arc. They are designed to achieve a maximum kick of 80.8 μrad at 7 TeV for a nominal current of 55 A (see for example, [22]).

Chromaticity or lattice sextupoles, MS

Chromaticity sextupoles, MS, will be installed at each focusing and defocusing quadrupole of the lattice. In a previous design these magnets were combined with the orbit corrector magnets MCB. The two windings are now well separated in the so-called MSCB assembly. The chromaticity sextupoles are split into four families in

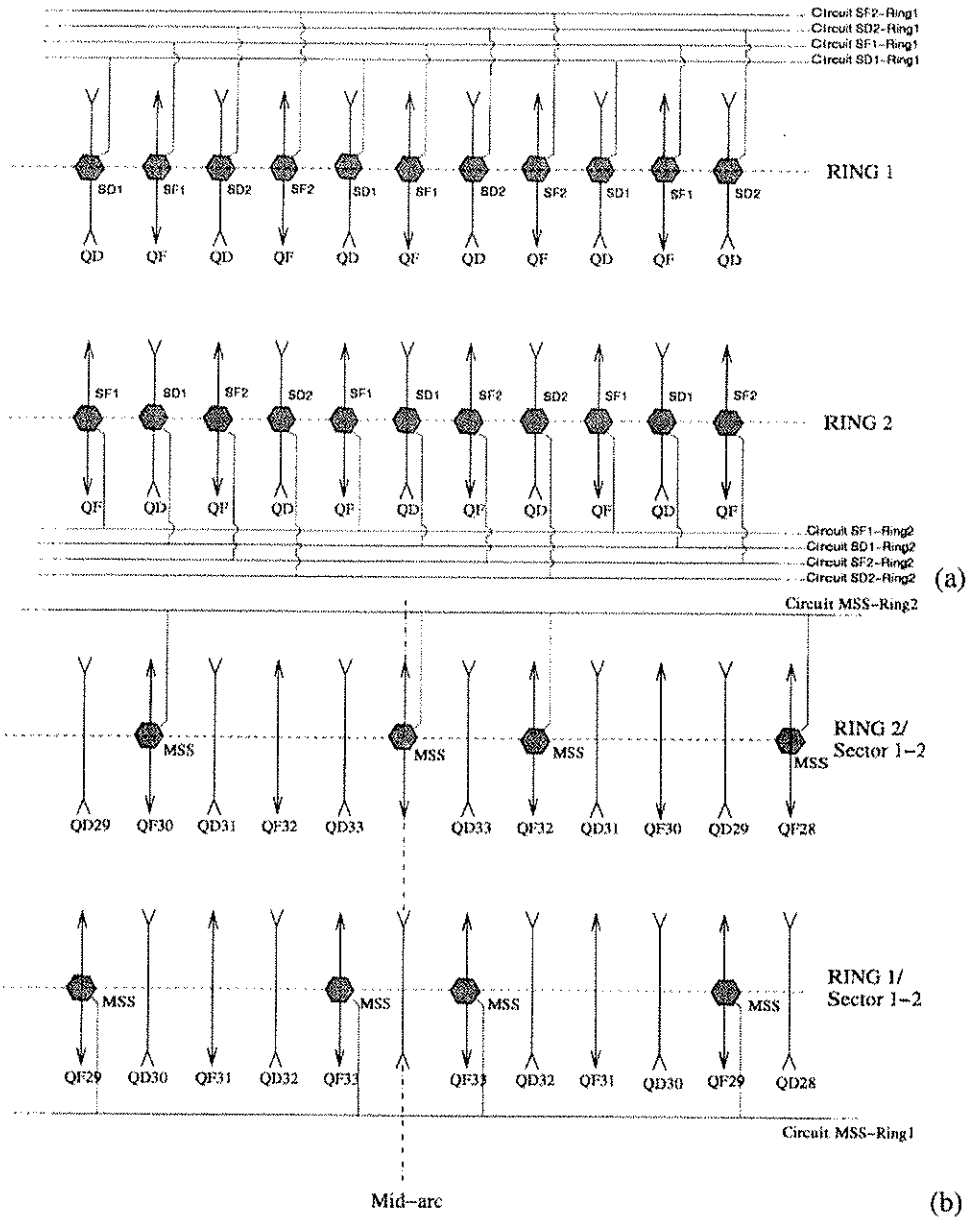

Figure 3.6: Arrangement in four families per ring and per sector for the chromaticity sextupoles MS in the LHC arcs (top) and dedicated location for the skew sextupole corrector MSS around the mid-arc in the case of Sector 1-2 (bottom).

each sector of each ring: that is two families, SF and SD installed at QF and QD, respectively. These are further divided into two interleaved sub-families '1' and '2' (see Fig. 3.6(a)). Only two SF and SD families are needed to correct the natural chromaticity of each ring. This includes the contributions from the arc ($Q'_{\text{nat.}} \sim -80$) and/or the contribution from the low-β insertions in collision ($Q'_{\text{nat.}} \sim -30$ for one experimental insertion squeezed to $\beta^* = 0.55$ m). Thanks to the phase advance close to 90° in the LHC arc cell, the present scheme has been designed to correct also the second order chromaticity $Q''_{x,y}$ and to minimize the off-momentum β-beating induced by the triplet magnets in collision (see [23] and [24] for more detail).
Note that the SF's and SD's are made of the same corrector magnets. Therefore, the integrated strength of the SD's sets the ultimate performance of the system as the dispersion function is smaller by a factor 2 compared to its value at the SF's.

Lattice skew sextupoles, MSS

In each ring and each sector of the machine, four focusing sextupoles (more precisely 2 SF1's and 2 SF2's) are tilted by 90° and are powered in series to generate a skew sextupole field for a compensation of the chromatic coupling induced by the a_3 component of the main dipoles. The MSS magnets are installed at Q29-Q33-Q33-Q29 in the sectors 1-2, 3-4, 5-6, 7-8 of Ring 1 (where the mid-arc quadrupole Q34 is defocusing for Beam 1) and in the sectors 2-3, 4-5, 6-7, 8-1 of Ring 2 (where Q34 is defocusing for Beam 2). For all other sectors they are installed at Q30-Q34-Q32-Q28 (see Fig. 3.6(b)). Such a scheme guarantees an extremely good compensation of the second order chromaticity induced by chromatic coupling with a minimum impact on the third order skew resonances and on the off-momentum β-beating (see [25] for more detail). Finally, as for the SF correction circuits, the efficiency of the MSS magnets is also doubled in terms of required strength since they are systematically installed close to a focusing quadrupole QF.

Tune-shift or tuning quadrupoles, MQT

Two families of 8 tuning quadrupoles per ring and per sector, QTF and QTD, equip the short-straight sections from Q14 to Q21 (left and right). Since the main quadrupole circuits are powered in series in Ring 1 and Ring 2, the phase advance per arc cell cannot be changed independently for the two rings. Therefore, independent tune adjustments for both beams can only be done by re-tuning the phase advances of the LHC insertions (essentially IR4, see Sec. 4.2.5) or by using the MQT corrector magnets. In principle, the latter are strong enough to achieve tune shifts of slightly more than one unit at 7 TeV. However, due to the large β-beating and dispersion mismatch induced they will be limited to much smaller tune shifts in nominal operation, of the order to $\Delta Q \sim \pm 0.1$ (see [26] for more detail).

Arc skew quadrupole corrector magnets, MQS

In both of the rings, each sector of the machine is equipped with 2 pairs of skew quadrupole magnets MQS at Q23 and Q27 (left and right) which are just MQT type magnets tilted by 45°. The two pairs are either powered in series, in sectors 1-2, 3-4, 5-6, 7-8 for Ring 1 and in sectors 2-3, 4-5, 6-7, 8-1 for Ring 2, or split into two independent families in the other sectors. This layout allows compensation of the coupling coefficient due to the systematic a_2 errors of the main dipoles for each sector but implies that only four corrector circuits are available for correction of the random coupling errors. Furthermore, the betatron phase advances between the MQS's of a same family ensures that the coupling compensation can be made without generating too large a vertical dispersion and with a minimum excitation of the sum coupling resonance, in order to minimize the β-beating possibly induced by the correction (see [27]).

Landau damping or lattice octupoles, MO

Each short straight section not equipped with MQT or MQS type magnets contains a lattice octupole MO, making a total of 168 MO type magnets per ring. These magnets will be powered in four families per sector, subdividing them into focusing and defocusing magnets, OF and OD, for Ring 1 and Ring 2. Assumed to have zero field at injection, the latter will Landau damp the coherent oscillations caused by collective effects [28].

Spool-piece corrector magnets

In addition to the lattice corrector magnets, each bore of the main dipoles will carry a small sextupole corrector magnet (MCS) at one end (Type B magnet) and every other dipole will be equipped with an octupole-decapole spool-piece (MCDO) at the opposite end (Type A magnet). The MCS magnets will be connected in series to form two families per sector, one for each ring. The same will apply for the octupole and decapole corrector magnets.
The MCS spool-pieces are designed to compensate the b_3 field integral of the main dipoles in each sector of the machine in order to correct its impact on the linear chromaticity up to the top energy. On the other hand the

Table 3.1: Arc corrector families and strength budget for the LHC Version 6.

Type	Name	Mag. length [m]	Nominal current [A]	Nominal field [T] at $R_r = 17$ mm	Family name	Number of families per ring	Number of magnets per ring	Max. integrated strength per ring at 450 GeV / 7 TeV
Lattice corrector magnets								
b_1 a_1	MCB	0.650	55	2.900	RCBH RCBV	188 188	188 188	376 / 24.17 units
b_2	MQT	0.320	550	2.040 (120 T/m)	RQTF RQTD	8 8	64 64	44.3 / 2.85 units
a_2	MQS	0.320	550	2.040 (120 T/m)	RQS	12	32	22.2 / 1.42 units
b_3	MS	0.369	550	1.280	RSF (SF1 & SF2) RSD (SD1 & SD2)	16 16	156 188	78.2 / 5.03 units 94.3 / 6.06 units
a_3	MSS	0.369	550	1.280	RSS	8	32	16.0 / 1.03 units
b_4	MO	0.320	550	0.290	ROF ROD	8 8	84 84	8.27 / 0.53 units
Spool-piece corrector magnets								
b_3	MCS	0.110	550	0.471	RCS	8	1232	67.7 / 4.35 units
b_4	MCO	0.066	100	0.040	RCO	8	616	1.73 / 0.11 units
b_5	MCD	0.066	550	0.100	RCD	8	616	4.31 / 0.28 units

MCDO spool-piece corrector magnets mainly preserve the dynamic aperture of the LHC at injection.

Corrector strength

The nominal strength of each arc corrector magnet is reported in Tab 3.1. In order to compare with the field imperfections of the main dipoles, the integrated strength per ring of each correction circuit has also been expressed in units of 10^{-4} relative field error in the main dipoles at a reference radius of $R_r = 17$ mm:

$$(BL)_{\text{Ring}}\,(x = 17\,\text{mm}) = 1\,\text{Tm}$$
$$\leftrightarrow$$
$$(BL)_{\text{Ring}} = \frac{1}{2\pi\,B\rho} \times 10^4 = \begin{cases} 1.061 \text{ units at 450 GeV} \\ 0.068 \text{ units at 7 TeV.} \end{cases}$$

With the exception of the multipoles b_3, b_4, b_5 for which the correction strategy consists effectively in a compensation of the field imperfection integrated per arc, the last column of Tab 3.1 is just indicative and generally underestimates the efficiency of the different correction circuits.

3.2.4 IR1 and IR5

General description

IR1 and IR5 house the high luminosity experiments of the LHC and are identical in terms of hardware and optics (except for the crossing-angle scheme: the crossing angle in IR1 is in the vertical plane and in IR5 in the horizontal plane). The small β-function values at the IP are generated with the help of a triplet quadrupole assembly [19]. A detailed description of the matching constraints for IR1 and IR5 can be found in [29]. The free space around the IPs is ± 23 m and the Q1 magnet stands in the tunnel instead of being supported by a cantilever inside the experimental cavern. At the IP, the two rings share the same vacuum chamber, the same low-beta triplet magnets and the D1 separation dipole magnets. The remaining matching section (MS) and the dispersion suppressor (DS) consist of double-bore magnets with separate beam pipes for each ring.

IR layout

Apart from the DS the insertions are comprised of the following sections, given in order from the interaction point:

- A 31 m long superconducting low-β triplet assembly operated at a temperature of 1.9 K and providing a nominal gradient of 205 T/m.
- A pair of separation / recombination dipoles separated by approximately 88 m. The D1 dipole located next to the triplet magnets has a single bore and consists of six 3.4 m long conventional warm magnet modules yielding a nominal field of 1.38 T. The following D2 dipole is a 9.45 m long, double bore, superconducting dipole magnet operating at a cryogenic temperature of 4.5 K with a nominal field of 3.8 T. The bore separation in the D2 magnet is 188 mm and is thus slightly smaller than the arc bore separation.
- Four matching quadrupole magnets. The first quadrupole following the separation dipole magnets, Q4, is a wide-aperture magnet operating at a cryogenic temperature of 4.5 K and yielding a nominal gradient of 160 T/m. The remaining three quadrupole magnets are normal-aperture quadrupole magnets operating at a cryogenic temperature of 1.9 K with a nominal gradient of 200 T/m.

Fig. 3.7 shows the schematic layout of IR1 and Tab 3.2 summarizes its main hardware parameters.

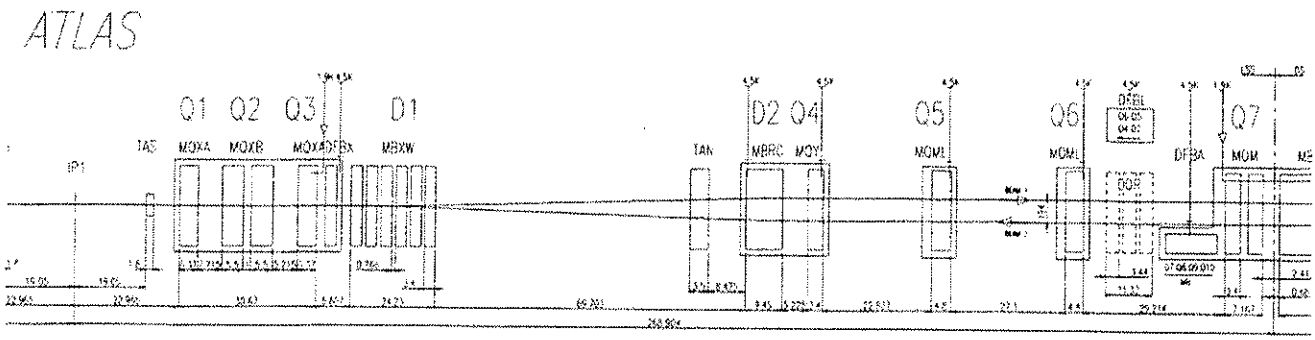

Figure 3.7: Schematic layout of the right side of IR1

Table 3.2: *Magnet parameters in IR1 and IR5.*

	LSS							Optical DS					
	low-β triplet			MS				DS				arc-cell	
Magnet	Q1	Q2	Q3	Q4	Q5	Q6	Q7	Q8	Q9	Q10	QT11	QT12	QT13
#	1	2	1	1	1	1	2	1	2	1	1	1	1
Type: MQ-	XL	X	XL	Y	ML		M	ML	M C	ML	TL	T	
L [m]	6.3	5.5	6.3	3.4	4.8	4.8	3.4	4.8	3.4 2.4	4.8	1.15	0.32	0.32
T [K]	1.9			4.5			1.9	1.9				1.9	
G [T/m]	200/205			160			200	200			110	110	
r [mm]	22.2 v17.3	28.95 24.05		27.2 22.3	20.6 15.75		22.2 17.3	22.2 17.3				22.2 17.3	

The triplet assembly features two different quadrupole designs: the outer two quadrupole magnets are made by KEK and require a peak current of 6450 A to reach the nominal gradient of 205 T/m, whereas the inner quadrupole block consists of two quadrupole magnets made by FNAL and requires a peak current of 10630 A. The triplet quadrupoles are powered by two nested power converters: one 8 kA power converter powering

all triplet quadrupole magnets in series and one 6 kA power converter supplying additional current only to the central two FNAL magnets. The Q1 quadrupole next to the IP features an additional 600 A trim power converter. The triplet quadrupoles are followed by the separation / recombination dipoles, D1 and D2, which guide the beams from the IP into two separated vacuum chambers. Q4, Q5, Q6, Q7, Q8, Q9 and Q10 are individually powered magnets. The aperture of Q4 is larger to provide sufficient aperture for the crossing-angle separation orbit. Two absorbers protect the cold magnets from particles leaving the IP. The TAS absorber protects the triplet quadrupole magnets and the TAN absorber, located in front of the D1 dipole magnet, protects the machine elements from neutral particles leaving the IP.

The matching section extends from Q4 to Q7 and the DS extends from Q8 to Q11. In addition to the DS, the first two trim quadrupoles of the first arc cell (QT12 and QT13) are also used for the matching procedure. All insertion and DS magnets are equipped with a beam screen [30]. The magnets left and right from the IP up to Q7 inclusive are placed symmetrically with respect to the IP. The positions of Q8, Q9 and Q10 left and right from the IP differ by approximately 0.5 m with respect to the IP due to the limited space in the DS.

3.2.5 IR2

The optics solutions in IR2 must obey a wide range of boundary conditions. A detailed description of these constraints can be found in reference [31].

The straight section at IR2 houses the injection elements for Ring-1 as well as the ion beam experiment ALICE. During injection the optics must obey the special constraints imposed by the beam injection for Ring-1 and the geometrical acceptance in the interaction region (IR) must be large enough to accommodate both beams in the common part of the ring with a beam separation of at least 10 σ.

IR layout

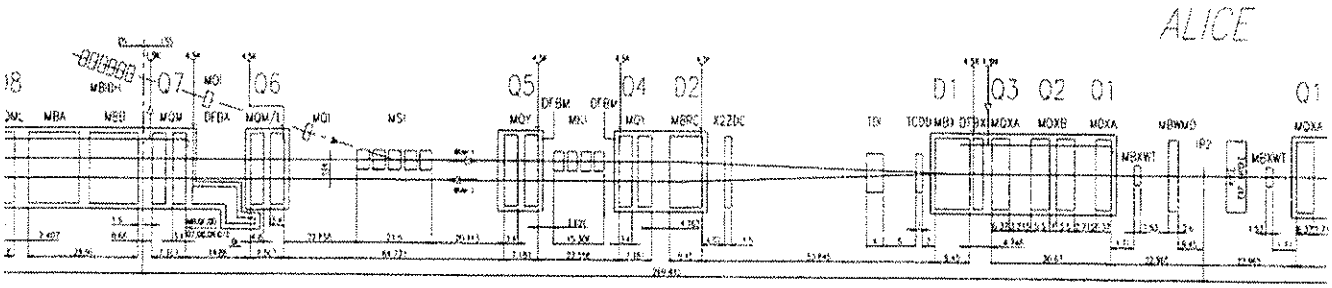

Figure 3.8: The left side of the matching section in IR2.

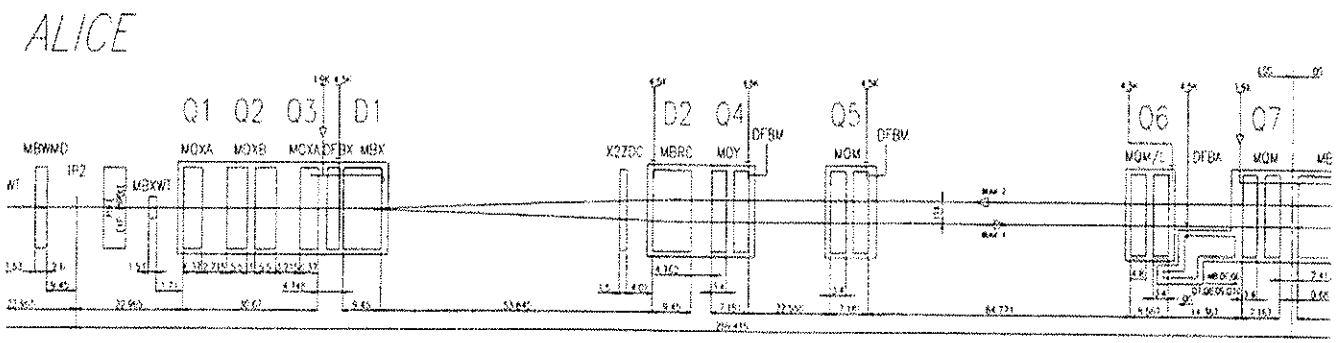

Figure 3.9: The right side of the matching section in IR2.

The triplet quadrupoles are powered in series and are followed by the separation / recombination dipoles D1 and D2, which guide the beams from the IP into two separated vacuum chambers. Q4, Q5, Q6, Q7, Q8, Q9 and Q10 are individually powered magnets. The aperture of Q4 is increased to provide sufficient aperture for the

crossing-angle separation orbit. The aperture of Q5 left of the IP is increased to provide sufficient aperture for the injected beam. The injection septum MSI is located between Q6 and Q5 on the left-side of the IP and kicks the injected beam in the horizontal plane towards the closed orbit of the circulating beam (positive deflection angle). The injection kicker MKI is located between Q5 and Q4 on the left-hand side of the IP and kicks the injected beam in the vertical plane towards the closed orbit of the circulating beam (negative deflection angle). In order to protect the cold elements in case of an injection failure a large absorber (TDI) is placed 15 m upstream from the D1 separation/recombination dipole left from the IP. The TDI absorber is complemented by an additional shielding element 3 m upstream of the D1 magnet and two additional collimators installed next to the Q6 quadrupole magnet. In order to obtain an optimum protection level in case of injection errors the vertical phase advance between MKI and TDI must be 90° and the vertical phase advance between the TDI and the two auxiliary collimators must be an integer multiple of $180° \pm 20°$.

The matching section extends from Q4 to Q7 and the DS extends from Q8 to Q11. In addition to the DS, the first two trim quadrupoles of the first arc cell (QT12 and QT13) are also used for the matching procedure. All magnets of the DS are equipped with a beam screen. The magnets left and right from the IP up to Q7 inclusive are placed symmetrically with respect to the IP. The positions of Q8, Q9 and Q10 left and right from the IP differ by approximately 0.5 m with respect to the IP due to the limited space in the DS.

Apart from the DS the insertions comprise the following sections, given in order from the interaction point:

- A 31 m long superconducting low-β triplet assembly operated at 1.9 K and providing a nominal gradient of 215 T/m.
- A pair of 9.45 m long superconducting separation / recombination dipole magnets separated by approximately 66 m.
- Four matching quadrupole magnets. The first two quadrupole magnets following the separation dipole magnets, Q4 and Q5, are wide aperture magnets operating at 4.5 K and yielding a nominal gradient of 160 T/m. The remaining two quadrupole magnets are normal aperture quadrupole magnets operating at 1.9 K with a nominal gradient of 200 T/m.

Figs 3.8 and 3.9 show the schematic layout of IR2 and Tab 3.3 summarizes its main hardware parameters.

Table 3.3: *Magnet parameters in IR2.*

	LSS								Optical DS					
	low-β triplet			MS					DS				arc-cell	
Magnet	Q1	Q2	Q3	Q4	Q5L	Q5R	Q6	Q7	Q8	Q9	Q10	QT11	QT12	QT13
#	1	2	1	2					1	2	1		1	
Type: MQ-	XL	X	XL	Y	Y	M	M		ML	M C	ML	TL	T	
L [m]	6.3	5.5	6.3	3.4					4.8	3.4 2.4	4.8	1.15	0.32	
T [K]	1.9			4.5			1.9		1.9				1.9	
B [T/m]	215 → 220			160			200		200			110	110	
r [mm]	22.2 17.3	28.95 24.05		27.2 22.3	27.2 22.3	20.6 15.75		22.2 17.3	22.2 17.3				22.2 17.3	

Hardware constraints

1. At the IP, the two rings of the LHC share the same vacuum chamber and the same low-beta triplet quadrupoles and the optics solutions for Ring 1 and Ring 2 must have the same triplet gradients.
2. The gradients must not exceed the maximum operating value (quench limit): 200 T/m for the insertion region quadrupoles at 1.9 K, 160 T/m for Q4 and Q5 which are operated at 4.5 K and 120 T/m for the trim

quadrupoles of the DS and 220 T/m for the triplet magnets without collisions (no heating from collision products) and 200 T/m with collisions at IP2.

3. The minimum gradient of the insertion quadrupoles which are powered by unipolar power converters must be larger than 3 % of the nominal gradient at injection energy.

4. The overall beam size must be small enough to fit into the tight aperture of the LHC. The aperture of the magnets is limited by the beam screen, and the aperture in the low-beta quadrupoles is further reduced by the vertical crossing-angle separation orbit. All magnets of the insertion are equipped with a race-track shaped beam screen, which is tilted by 90° wherever the required vertical aperture exceeds the required horizontal aperture. The aperture at the end of the MKI, the Q4 magnet and the D2 dipole magnet left from the IP, must be large enough to accommodate not only the circulating beam but also the mis-kicked injected and mis-kicked circulating beam.

3.2.6 IR3 and IR7

The insertion IR3 houses the momentum cleaning systems of both beams, while IR7 houses the betatron cleaning systems of both beams. Particles with a large momentum offset are scattered by the primary jaw of IR3. Particles with a large H, V or combined H-V betatron amplitudes are scattered by the primary collimator jaws in IR7. In both cases the scattered particles are absorbed by secondary collimators. The insertion layout and optics has been revised at the end of 2003 in order to reduce the impedance in the insertions and to make room for additional hybrid collimator jaws for the phase II of the LHC collimations system (see Chap. 18 for more details). The new layout drawings were not available at the time of writing. The layout given here therefore still corresponds to the old V6.4 lattice. However, all optics and aperture plots given in Chap. 4.2.4 and 4.2.7 correspond to the new optics that is based on the new layout and which will be part of the LHC V6.5 lattice.

IR7 layout

The dispersion suppressor extends from Q8 to Q11. In addition to the DS, the first two trim quadrupoles of the first arc cell (QT12 and QT13) are also used for the matching procedure. All cryo-magnets are equipped with a beam screen. In IR3 and IR7, the underground galleries are not wide enough to house many high current power supplies. Therefore, contrary to the layout of the other IR's, the DS quadrupoles (Q7,Q8,Q9 and Q10) are made of a MQ+MQTL assembly (MQ + 2 MQTL at Q9) where the MQ's magnets are powered in series with the main arc quadrupoles. To avoid producing two kinds of MQ+MQTL assemblies, the dispersion suppressors left and right from the IP are not mirror symmetric with respect to each other. Instead, the DS quadrupole assemblies have the same orientation in the dispersion suppressors left and right from the IP and the MQ positions differ by approximately 0.5 m with respect to the IP in the two DS.

The layout of the Long Straight Section between Q7L and Q7R is mirror symmetric with respect to the IP. The right side of IR7 is shown in Fig. 3.10. This allows the symmetrical installation for the collimators of the two beams and minimizes the space conflicts in the insertion. Starting from Q7 left, the quadrupole Q6 (made of 6 superconducting MQTL modules) is followed by a dog-leg structure made of two sets of MBW warm single bore wide aperture dipole magnets (2 warm modules each). The dogleg dipole magnets are labeled D3 and D4 in the LHC sequence with D3 being the dipole closer to the IP. The Primary Collimators are located between the D4 and D3 magnets, allowing neutral particles produced in the jaws to point out of the beam line, and most charged particles to be swept away. The inter-beam distance between the dogleg assemblies left and right from the IP is 224 mm, i.e. 30 mm larger than in the arc. This increased beam separation allows a substantially higher gradient in the Q4 and Q5 quadrupoles which are made out of 6 warm MQW modules. The space between Q5 left and right from the IP is used to house the secondary collimators at adequate phase advances with respect to the primary collimators.

The Q4 and Q5 quadrupoles left and right from the IP are powered in series. The warm dual-bore MQW quadrupole cannot be powered with different currents for each magnet aperture because the field quality is degraded to an unacceptable level even for a small imbalance in the field of the two apertures. The current

must be equal or of opposite value in the bores to provide a good field quality. In order to obtain the required flexibility for the optics, two different kinds of powering schemes are used for the Q4 and Q5 quadrupole units. The magnets are identical, but in the MQWA type magnet the field is identical in both apertures, $k_{\mathrm{Beam1}} = k_{\mathrm{Beam2}}$ while in the MQWB type magnet, the field is opposite for both apertures, $k_{\mathrm{Beam1}} = k_{\mathrm{Beam2}}$ [32]. Each Q4 and Q5 assembly is made of 5 MQWA and 1 MQWB module. The nominal gradient of the MQWB unit is limited to 29.6 T/m while it can reach 35 T/m in the MQWA unit. This powering scheme breaks the exact antisymmetry by 29% providing enough flexibility to satisfy all the optics constraints. Again, Q5AL+Q5AR and Q5BL+Q5BR respectively are powered in series. As a by-product, this freedom in the straight section allows the trim strength needed in the DS to be limited so that regular MQTL's can be used. Fig. 3.10 shows the OLD V6.4 schematic layout of the right-hand side of IR7. A detailed description of the layout of the collimators can be found in Chap. 18 (this volume).

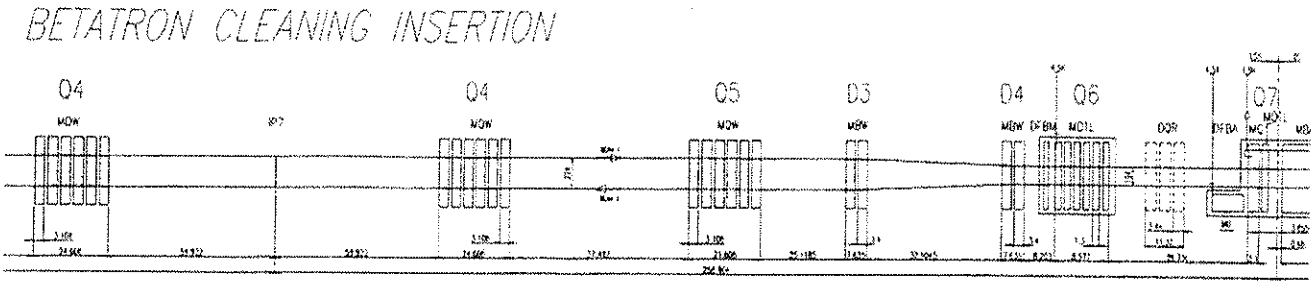

Figure 3.10: The right-hand side of the matching section in IR7.

IR3 layout

In IR3, the most difficult constraint was to generate a large dispersion function in the straight section. Since the layout of the DS cannot be changed in IR3 this constraint means that the natural dispersion suppression generated in the DS is over compensated. To this end Q6 and Q5 were moved towards each other by a substantial amount, thus shrinking the space granted to the dog-leg structure D4-D3. It was therefore necessary to add a third MBW element to D3 and D4 in IR3. Apart from this IR3 and IR7 are identical. Fig. 3.11 shows the OLD schematic layout of the right-hand side of IR3.

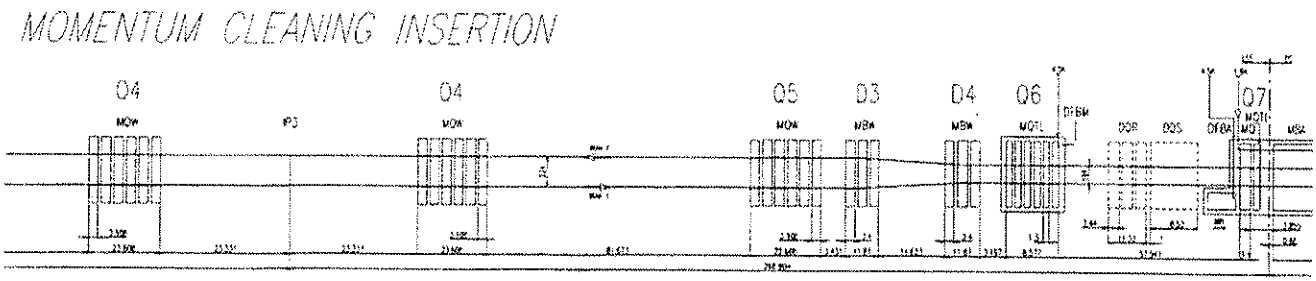

Figure 3.11: The right side of the matching section in IR3.

Hardware constraints

1. The MQWA may have gradients up to 35 T/m.
2. The MQWB may have gradients up to 29.6 T/m..
3. The maximum gradients must not exceed 120 T/m for the trim quadrupoles of the DS.
4. The overall beam size must be small enough to fit into the tight aperture of the LHC. The aperture of all cryo-magnets is limited by a beam screen, see Chap. 4.3. In the warm quadrupole the vacuum chamber

is elliptical with half main axis inner dimensions 25.5 × 14.5 mm. The shape of the vacuum chamber inside the MBW dipoles is not yet fixed. The present inner size has a race-track shape of half-dimensions 31.5 × 23 mm. This limits the maximum of the beta-functions to 400 m.

3.2.7 IR4

IR4 houses the RF and feed-back systems as well as some of the LHC beam instrumentation. In the first design described in the yellow book (the 1995 Conceptual Design)[14] the RF system was installed between Q5 and Q6 to leave room for an experiment. A detailed description of this insertion can be found in [33].

From 2001, the option of installing an experiment in IR4 has been dropped, allowing a simplification of the IR layout with respect to the previous version (e.g. to LHC V6.3). The RF is now installed in the ALEPH cavern, which provides a large space for the power supplies and klystrons. Because of the installation of both RF systems in this cavern, a large space is necessary between the quadrupole units surrounding the RF system. This makes the IR4 insertion look similar to the IR6 insertion. Furthermore, the two independent RF systems for Beam 1 and Beam 2 require a larger than nominal beam separation in the long straight section of IR4. The increased beam separation is provided by two pairs of dipole magnets. These dogleg dipole magnets are labeled D3 and D4 in the LHC sequence with D3 being the dipole magnets closer to the IP. The inter-beam distance between the dogleg magnets is 420 mm, i.e. 226 mm larger than in the arcs. In contrast to IR3 and IR7 the dogleg magnets in IR4 are superconducting magnets.

There are six superconducting quadrupole magnets in the straight section : Q5 Q6 Q7 on the left- and Q5 Q6 Q7 on the right-hand side of the IP. The outer dogleg dipoles, D4, sit next to the Q5 quadrupole magnets on each side of the IP. The RF cavities sit between the inner dogleg dipoles, D3. The layout of the DS, between Q7 and Q11, is identical to that in IR1 and IR5.

Fig. 3.12 shows the schematic layout of the right-hand side of IR4.

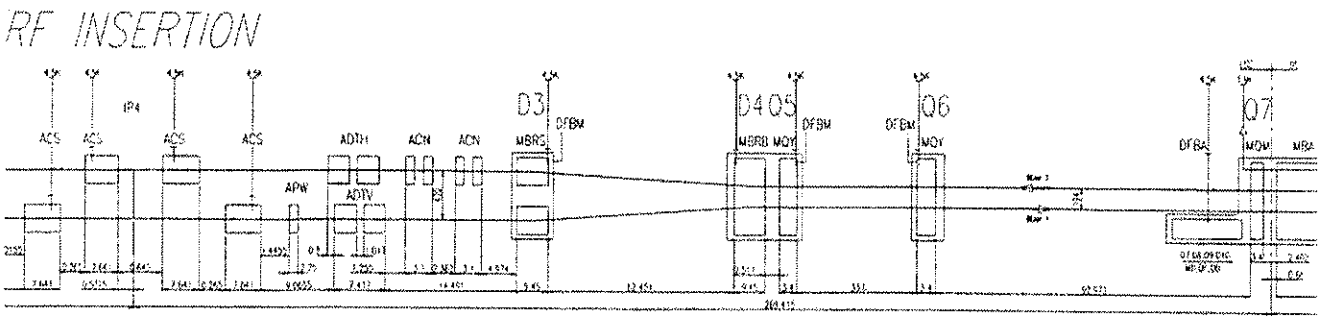

Figure 3.12: The right-hand side of the matching section in IR4.

3.2.8 IR6

IR6 houses the beam abort systems for Beam 1 and Beam 2. The beam extraction from the LHC is done by kicking the circulating beam horizontally into an iron septum magnet which deflects the beam in the vertical direction away from the machine components to absorbers in a separate tunnel. Each ring has its own system and both are installed in IR6.

In order to minimize the length of the kicker and the septum, large drift spaces have to be provided. Matching both β-functions between the ends of the left and right DS requires only four quadrupoles. Such a scheme was used in the first design [34] which was proposed a long time ago. Later on quadrupoles were added to achieve a phase advance equal to that of the other insertions, this was LHC Version 1 [35]. Eventually the design of the components of the beam dump system was based on similar optics labeled V4 [14].

For the nominal version 6 optics, there are four quadrupoles independently powered in the straight section of the insertion. This independent powering is possible as the gradients in the two apertures of the quadrupoles can have different values, i.e. they are no longer constrained to be exactly opposite, which was the case for LHC version 4. Fig. 3.13 shows the schematic layout of the right-hand side of IR6.

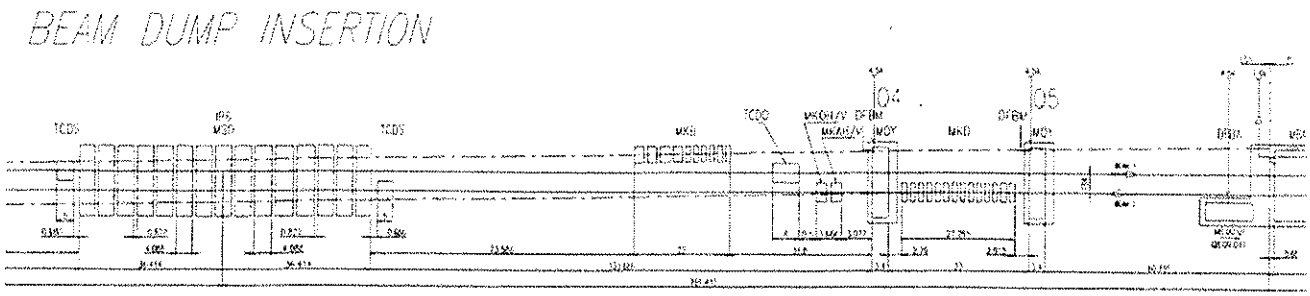

Figure 3.13: The right-hand side of the matching section in IR6.

In each of the dispersion suppressors up to six quadrupoles can be used for matching. The total of sixteen quadrupoles is more than necessary to match both β-functions, the dispersion (both at the crossing point and in the arc) and adjust the phases. Although this number of parameters seems considerable, their variation is strongly limited by the aperture constraints which set limits on the β-functions and the dispersion inside the insertion. Special detection devices protect the extraction septum and the LHC machine against losses during the extraction process. The TCDS absorber is located in front of the extraction septum and the TCDQ in front of the Q4 quadrupole magnet downstream of the septum magnet.

3.2.9 IR8

General description

IR8 houses the LHCb experiment and the injection elements for Beam 2. The small β-function values at the IP are generated with the help of a triplet quadrupole assembly [19]. A detailed description of the matching constraints for IR8 can be found in [36]. The free space around the IPs is ± 23 m and the Q1 magnet now stands in the tunnel instead of being supported by a cantilever inside the experimental cavern. At the IP, the two rings share the same vacuum chamber, the same low-beta triplet magnets and the D1 separation dipole magnet. The remaining matching section (MS) and the DS consist of double-bore magnets with separate beam pipes for each ring.

IR layout

Apart from the DS the insertions contain the following sections, given in order from the interaction point:

- Three warm dipole magnets compensate the deflection generated by the LHCb spectrometer magnet.
- A 31 m long superconducting low-β triplet assembly operated at 1.9 K and providing a nominal gradient of 205 T/m.
- A pair of separation/recombination dipole magnets separated by approximately 54 m. The D1 dipole located next to the triplet magnets is a 9.45 m long single-bore superconducting magnet. The following D2 dipole is a 9.45 m long, double bore, superconducting dipole magnet. Both magnets are operated at 4.5 K. The bore separation in the D2 magnet is 188 mm and is thus slightly smaller than the arc bore separation.
- Four matching quadrupole magnets. The first quadrupole following the separation dipole magnets, Q4, is a wide aperture magnet operating at 4.5 K and yielding a nominal gradient of 160 T/m. The remaining three matching section quadrupole magnets are normal aperture quadrupole magnets operating at 1.9 K with a nominal gradient of 200 T/m.
- The injection elements for Beam 2 on the right hand side of IP8. The 21.8 m long injection septum consists of 5 modules and is located between the Q6 and Q5 quadrupole magnets on the right-hand side of the IP. The 15 m long injection kicker consists of 4 modules and is located between the Q5 and Q4 quadrupole

magnets on the right-hand side of the IP. In order to protect the cold elements in case of injection failure a large absorber (TDI) is placed 15 m in front of the D1 separation/recombination dipole magnet right from the IP. The TDI is complemented by an additional shielding element between the TDI and D1 magnet (placed 3 m in front of D1) (TCDD) and by two additional collimators placed on the transition of the matching section left from the IP to the next DS section.

In order to provide sufficient space for the spectrometer magnet of the LHCb experiment IP8, is shifted by 15 half RF wavelengths (3.5 times the nominal bunch spacing $\rightarrow \approx 11.25$ m) towards IR7. This shift of the IP has to be recuperated before the beam returns to the dispersion suppressor sections and implies a non-symmetric magnet layout in the matching section.

Fig. 3.14 and 3.15 show the schematic layout of IR8 and Tab 3.4 summarizes the main hardware parameters.

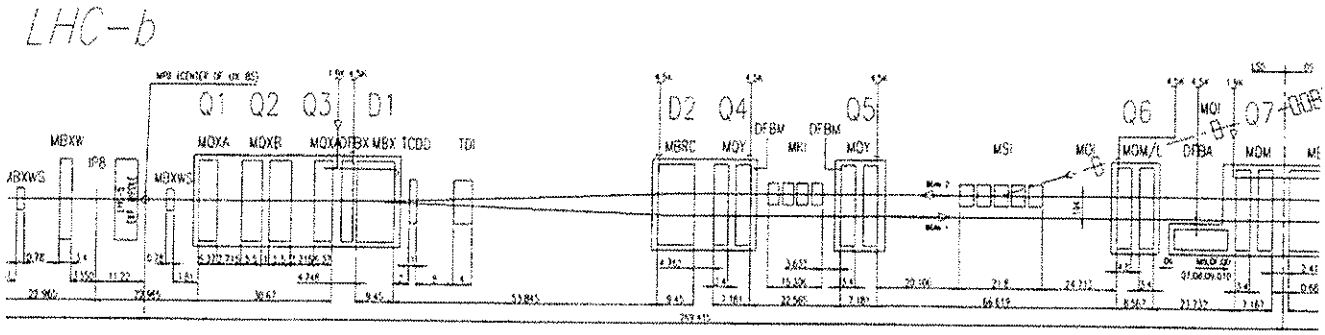

Figure 3.14: Schematic layout of the right side of IR8

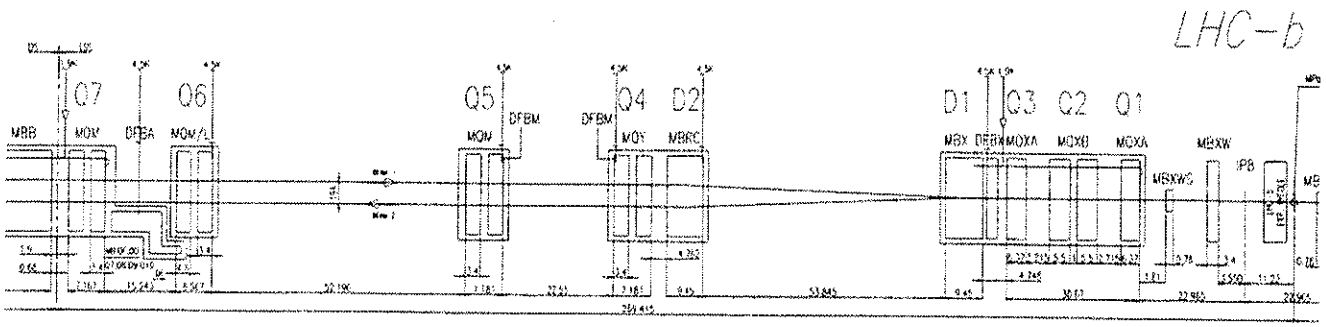

Figure 3.15: Schematic layout of the left side of IR8

Table 3.4: *Quadrupole magnet parameters in IR8.*

	LSS								Optical DS					
	low-β triplet			MS					DS				arc-cell	
Magnet	Q1	Q2	Q3	Q4	Q5R	Q5L	Q6	Q7	Q8	Q9	Q10	QT11	QT12	QT13
#	1	2	1	2					1	2	1		1	
Type: MQ-	XL	X	XL	Y	Y	M	M		ML	M C	ML	TL	T	
L [m]	6.3	5.5	6.3	3.4					4.8	3.4 2.4	4.8	1.15	0.32	
T [K]	1.9			4.5			1.9		1.9				1.9	
B [T/m]	215 → 220			160			200		200			110	110	
r [mm]	22.2 17.3	28.95 24.05		27.2 22.3	27.2 22.3	20.6 15.75		22.2 17.3	22.2 17.3				22.2 17.3	

The triplet assembly features two different quadrupole designs: the two outer quadrupole magnets are made by KEK and require a peak current of 6450 A for reaching the nominal gradient of 205 T/m and the inner quadrupole block consists of two quadrupole magnets made by FNAL and requires a peak current of 10630 A. The triplet quadrupoles are powered by two nested power converters. One 8 kA power converter powering all triplet quadrupole magnets in series and one 6 kA power converter supplying additional current only to the central two FNAL magnets. [4] The triplet quadrupoles are followed by the separation/recombination dipoles, D1 and D2, which guide the beams from the IP into two separated vacuum chambers. Q4, Q5, Q6, Q7, Q8, Q9 and Q10 are individually powered magnets. The apertures of Q4 and Q5 are increased to provide sufficient aperture for injected beam and the crossing-angle separation orbit.

The matching section extends from Q4 to Q7 and the DS extends Q8 to Q11. In addition to the DS, the first two trim quadrupoles of the first arc cell (QT12 and QT13) are also used for the matching procedure. All insertion and DS magnets are equipped with a beam screen [30]. The positions of Q8, Q9 and Q10 left and right from the IP differ by approximately 0.5 m with respect to the IP due to the limited space in the DS.

REFERENCES

[1] LEP Design Report; CERN-LEP/84-01; June 1984 and CERN-AC/96-01 (LEP2); June 1996

[2] ATLAS Technical Proposal; CERN / LHCC / 94-43; LHCC / P2; December 1994

[3] CMS Technical proposal; CERN-LHCC-94-38; LHCC-P-1; December 1994

[4] LHCB Technical Proposal; CERN/LHCC 98-4; February 1998

[5] Total Cross Section, Elastic Scattering and Diffractive Dissociation at the LHC, CERN / LHC 99-7, March 1999

[6] ALICE Technical Prposal; CERN/LHCC 95-71; December 1995

[7] H. Grote and W. Herr, Nominal and Ultimate Luminosity Performance of the LHC, LHC Project Note 275, January 2002

[8] Design Study of the Large Hadron Collider, CERN/91-03, 1991

[9] LHC Luminosity and Energy Upgrade: A Feasibility Study; LHC Project Report 626, December 2002

[10] O. Gröbner, 'Overview of the LHC Vacuum System', VACUUM **60**, pg. 25-34, 2001

[11] O. Brüning in the Chamonix 2000 proceedings

[12] A. Faus-Golfe, LHC Project Note 9, 1995

[13] O. Brüning in the Chamonix 2001 proceedings

[14] The LHC study group, The LARGE HADRON COLLIDER Conceptual design. CERN/AC/95-05(LHC), 20 October 1995.

[15] J.P. Koutchouk, Presentation to the 4. LHC Machine Advisory Committee 24/06/97

[16] A.Faus-Golfe, H. Grote, J-P Koutchouk, T. Risselada, A. Verdier, S. Weisz, 'A more robust and flexible lattice for LHC', LHC Project Report 107, 1997, and in the proceedings of PAC97, Vancouver, Canada

[17] Oliver Brüning, Presentation at the 10. LHC Machine Advisory Committee, http://slap.web.cern.ch/slap/MAC.pdf

[18] J.P. Koutchouk, W. Scandale and A. Verdier, Optimization of the LHC Lattice and Chromaticity. Proc. of the IEEE Part. Acc. Conf. Washington DC, March 1987.

[19] E. Keil, CERN 77-13, 1977 or R. Brinkmann, Insertions, CAS proceedings, pg. 45-61, CERN 87-10, Aarhus, Denmark, July 1987

[20] A. Faus-Golfe, J-P Koutchouk, A Verdier and S. Weisz, Modular Optics Design of the LHC Experimental Insertions, LHC Project Report 14, 1996 and in the proceedings of the EPAC96, Barcelona, Spain

[21] J.P. Koutchouk, Presentation to the 6. LHC Machine Advisory Committee 2/11/1998.

[22] A. Verdier, Revision of the Closed Orbit Corrector System of the LHC, CERN-LHC-Project-Report-397, Geneva, CERN (August 1, 2000).

[4] The Q1 quadrupole next to the IP features an additional 600 A trim power converter.

[23] S. Fartoukh, Second order chromaticity correction of LHC V6.0 at collision, LHC-Project-Report-308, Geneva, CERN (October, 1999).

[24] F. Schmidt, "Strength Requirements for the Arc Sextupoles of LHC Version 4.1", LHC Project Note 38

[25] S. Fartoukh, Chromatic coupling induced by skew sextupolar field errors in the LHC main dipoles and its correction, LHC-Project-Report-278, Geneva, CERN (March 1999).

[26] A. Verdier, Operational Q-shifts and $b2$ compensation in LHC, CERN-LHC-Project-Note-26, Geneva, CERN (January 8, 1996).

[27] O. Brüning, Linear coupling compensation for the LHC Version 6.1, EPAC 2000 Proc., 26-30 June 2000, Vienna and LHC-Project-Report-399, Geneva, CERN (August, 2000).

[28] J. Gareyte, J.P. Koutchouk, F. Ruggiero, Landau Damping, Dynamic Aperture and Octupoles in LHC, LHC-Project-Report-91 (revised), Geneva, CERN (April, 1997).

[29] O. Brüning, Optics Solutions in IR1 and IR5 for Ring-1 and Ring-2 of the LHC Version 6.0; 5LHC Project Note 187, April 1999

[30] 33. LCC meeting held on 20.11.2002: http://lhcp.web.cern.ch/lhcp/LCC/LCC_2002-18.htm

[31] O. Brüning, Optics Solutions in IR2 for Ring-1 and Ring-2 of the LHC Version 6.0; LHC Project Note 188, April 1999

[32] D.I. Kaltchev et al., M.K. Craddock, J.B. Jeanneret and A. Verdier, LHC Project Report 305 and PAC1999,1999.

[33] A. Verdier, A tunable insertion for point 4 in LHC. LHC Project Note 93 (June 1997).

[34] The large hadron collider in the LEP tunnel. Edited by G. Brianti and K. Hübner. CERN 87-05 (27 May 1987).

[35] Design study of the Large Hadron Collider, The LHC study group, CERN 91-03.

[36] O. Brüning, Optics Solutions in IR8 for Ring-1 and Ring-2 of the LHC Version 6.0; LHC Project Note 193, June 1998

CHAPTER 4

OPTICS AND SINGLE PARTICLE DYNAMICS

All optics descriptions in this Chapter refer to the LHC Version 6.4 including the repositioning [1] of the Q3 triplet magnets which is part of Version 6.5. [1]

The LHC optics design follows a modular approach where the functionality of each insertion is extended by one arc-cell on each side of the insertion [2]. This approach allows an optics matching with fixed and equal phase advances over the insertions for both beams that does not perturb the optics in the rest of the machine. The total tune of the machine is adjusted via the arc cell optics. In conjunction with the series powering of the Ring 1 and Ring 2 quadrupole magnets this approach automatically generates the same tunes for both beams. The flexibility of the phase advance over the insertions provides a measure for the flexibility of the total LHC optics and the range over which the phase advance between the main experimental insertions can be changed.

The common low-β triplets in the experimental insertions provide opposite focusing for the two counter-rotating beams. A strictly antisymmetric powering was adopted for the feasibility study as a natural symmetry for a proton-proton machine with common magnetic elements [3]. However, in the present optics design the antisymmetric powering is only approximately kept, except in the low-beta triplets where it is exact.

Table 4.1: Horizontal and vertical phase advances in the LHC for the injection optics. All values given below, except tor the phase advances given for IR3 and IR7, correspond to the LHC V6.4 optics. The values given for IR3 and IR7 correspond to the new cleaning insertion optics that will be part of V6.5. The new IR3 and IR7 optics have different phase advances for Beam 1 and Beam 2. The values for Beam 1 are given on top and the values for Beam 2 on the bottom of the double entries. The difference between the Beam 1 and Beam 2 phase advance needs to be compensated in the other insertions.

	1 arc (21 cells)	IR1/IR5	IR2	IR3	IR4	IR6	IR7	IR8	total insertions	LHC total
$\frac{\Delta\mu_x}{2\pi}$	5.497250	2.618	2.991	2.307 2.285	2.143	2.015	2.382 2.492	3.204	20.302	64.28
$\frac{\Delta\mu_y}{2\pi}$	5.099375	2.644	2.844	1.897 1.932	1.870	1.780	1.968 2.090	2.804	18.515	59.31

4.1 ARC OPTICS

The LHC arc cells feature a FODO lattice with approximately 90° phase advance per cell in both planes. A perfect 90° lattice generates equal tunes in the horizontal and vertical planes (apart from phase advance differences generated in the insertion regions) and minimizes the optics perturbations by tuning the trim quadrupole circuits at the end of each arc [4]. However, a correction of the systematic coupling generated by the main dipole field errors favors an optics with an integer tune split between the horizontal and vertical tunes [5] [6]. An integer tune split of 7 or 8 units is optimal for the compensation of the systematic resonances in each arc [7]-[10].

However, such a large tune split also implies a dephasing of the four sextupole families in each arc and reduces the margins for the magnet strength (in the plane with the higher tune value) and aperture (in the plane with the smaller tune value). Following V6.2 of the LHC lattice the optics is based on a total integer tune split of 5 units which is the combined results of the differences in the horizontal and vertical phase advances in the arcs and the insertion regions. This solution presents a good compromise between operational margins for the magnet strengths, aperture and a compensation efficiency of systematic resonances. Tab 4.1 summarizes the different contributions to the integer tune split and Fig 4.1 the corresponding optic functions of the LHC arc cells. All values given in Tab 4.1, except for the phase advances in IR3 and IR7, correspond to the LHC V6.4

[1] A summary of the differences between different LHC version can be found on the WWW under: http://slap.web.cern.ch/slap/MAC.pdf

optics. The values given for IR3 and IR7 correspond to the new cleaning insertion optics that will be part of V6.5. The new IR3 and IR7 optics have different phase advances for Beam 1 and Beam 2. The difference between the Beam 1 and Beam 2 phase advance needs to be compensated in the other insertions.

Fig 4.2 shows the mechanical acceptance of the arc cell in terms of n_1. The smallest acceptance depends on the spurious dispersion along the machine and Fig 4.2 shows the worst case of the mid-arc cells ($n_1 = 6.75$ for mid-arc cell-12 in Beam 2) for the nominal injection optics (a definition for n_1 can be found in Sec 4.3). This value is slightly smaller than the specification of $n_1 = 7.0$ (see Sec. 4.3 and Chap. 18 for details on the aperture specifications) and might require a revision of the mechanical tolerances for the dipole geometry.

Fig 4.3 and 4.4 show the variation of the horizontal and vertical tunes versus the relative beam momentum deviation for the perfect linear lattice with lattice sextupole magnets and a correction of the chromaticity for the injection and the collision optics with two squeezed IRs (IR1 and IR5) respectively. No magnetic field errors are considered here. One clearly sees how the chromaticity shows a strong third order dependence for the collision optics.

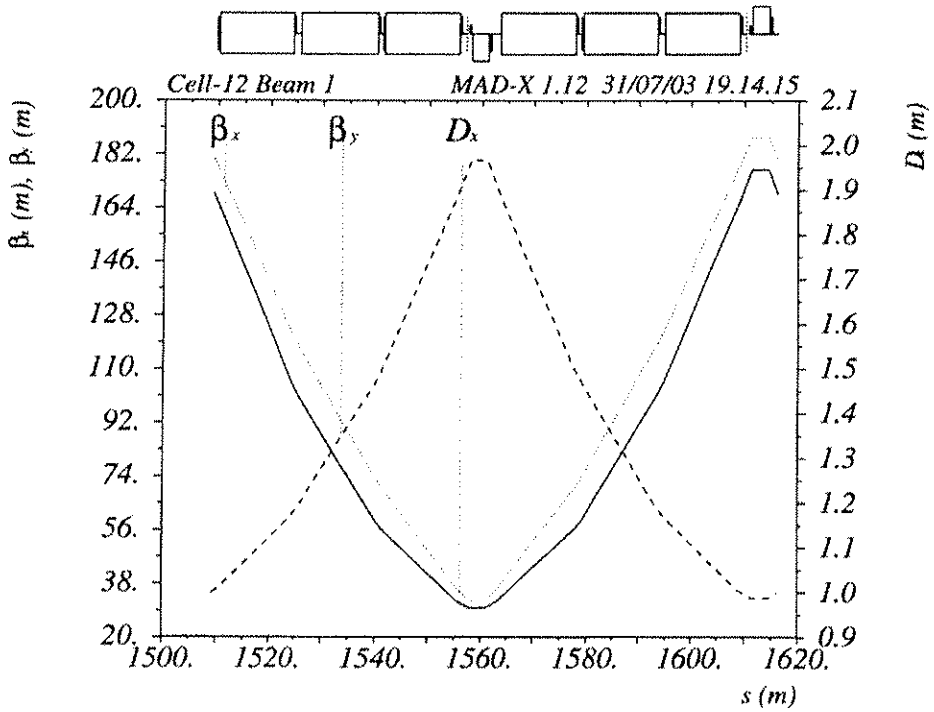

Figure 4.1: Periodic optics solution for the worst case LHC arc cell.

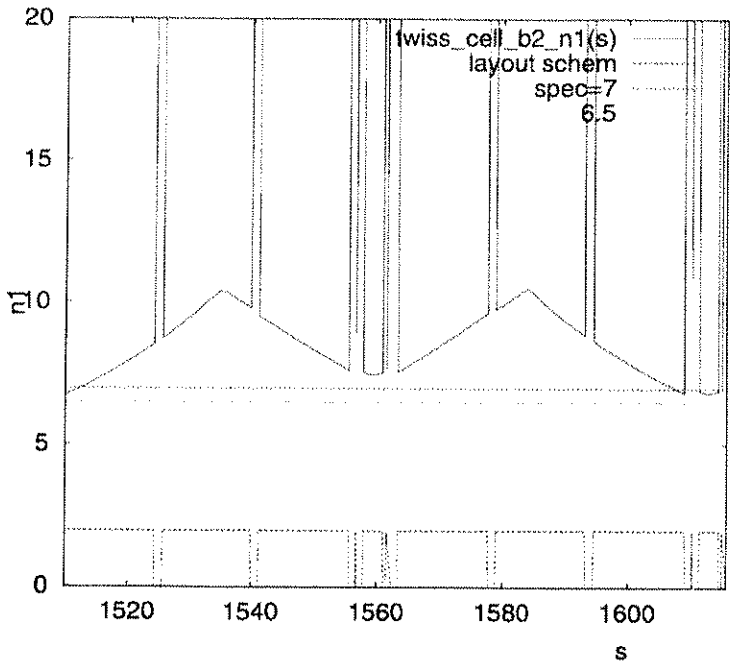

Figure 4.2: Periodic optics solution of a LHC arc cell

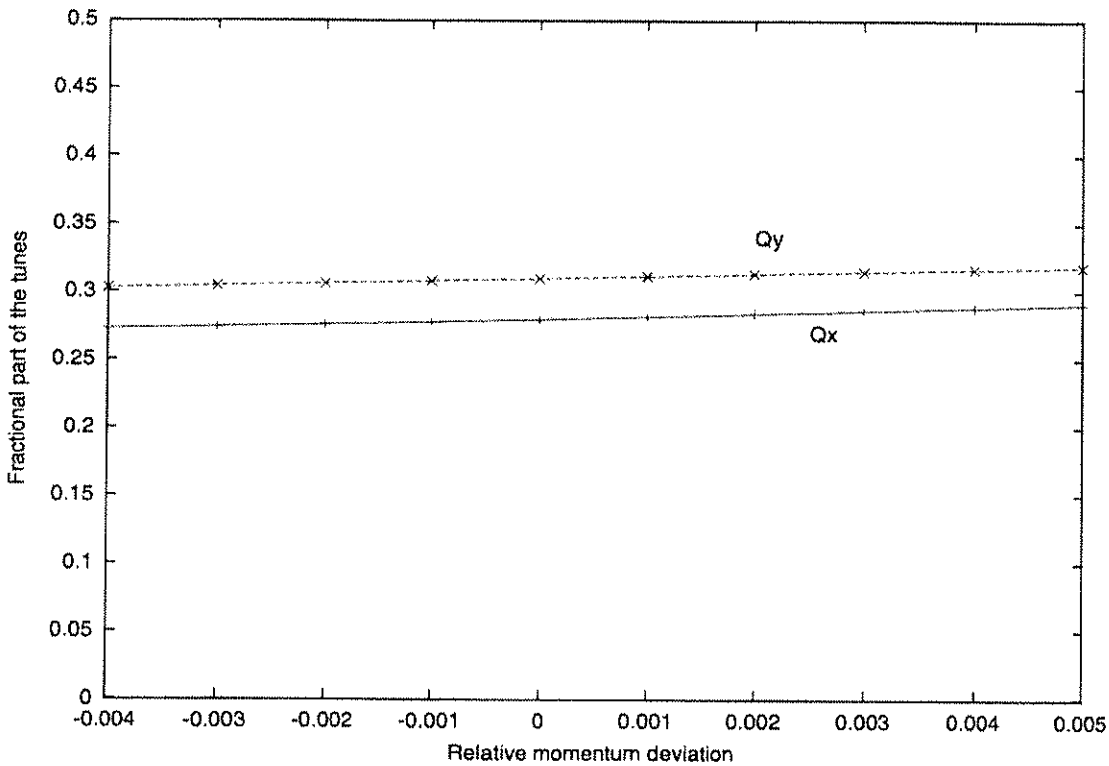

Figure 4.3: Tune variations versus the relative momentum offset for the unperturbed linear lattice with lattice sextupole magnets and corrected chromaticity for the injection optics without multipole errors.

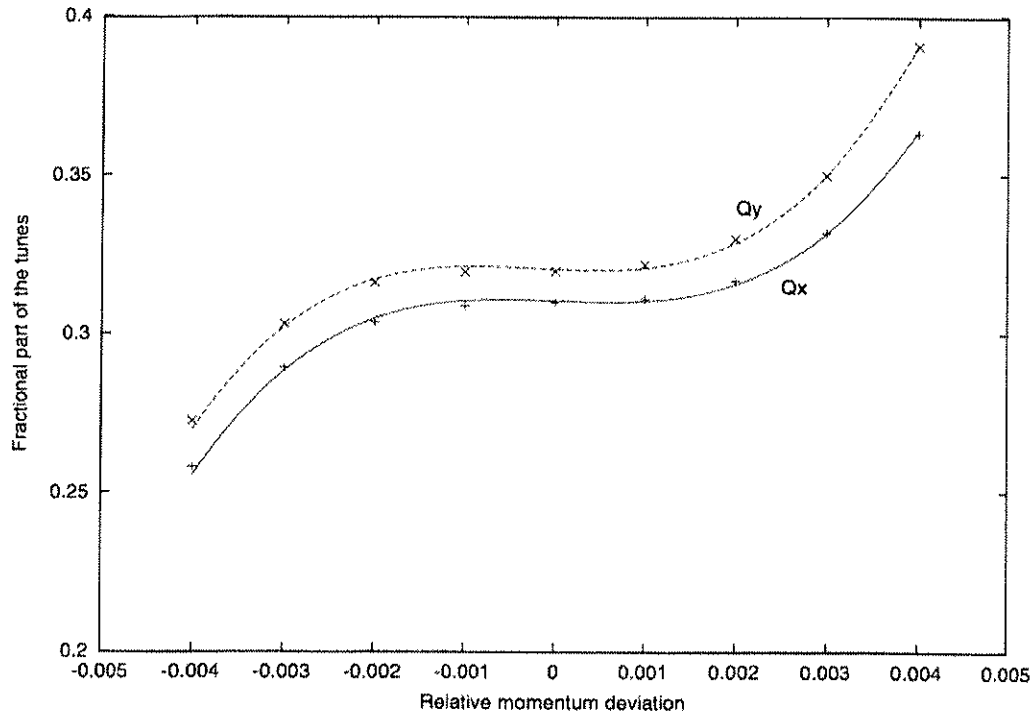

Figure 4.4: Tune variations versus the relative momentum offset for the unperturbed linear lattice with lattice sextupole magnets and corrected chromaticity for the collision optics with IR1 and IR5 squeezed to $\beta^* = 0.55$m without multipole errors.

Table 4.2: Crossing angle and orbit at IP1 for Beam 1 (half the total beam separation). The minimum separation between Beam 1 and Beam 2 is specified for one plane. The state 'Injection' refers to the optics configuration during injection, 'Ramp' to the configuration during ramp, 'Pre-Collision' to the optics at the end of the ramp but before the low-β squeeze and 'Collision' to the optics configuration at top energy after the low-β squeeze.

State	$\beta^*_{x,y}$ (m)	vertical crossing angle (μrad)	horizontal orbit (mm)	d_{IP} (σ)	d_{min} (σ)
Injection	18.0	+ 160.0	- 2.50	13.3	10.5
Ramp	18.0	+ 40.0	- 0.625	13.3	10.5
Pre-collision	0.55	+ 142.5	- 0.50	60	6.9
Collision	0.55	+ 142.5	- 0.0	0.0	6.9

4.2 INSERTION OPTICS

4.2.1 Crossing angle summary

The main limit on the bunch intensity will eventually come from beam-beam effects. To allow a maximum number of bunches, they are closely spaced (25 ns) and in order to avoid unwanted collisions in the part where the two beams share a common vacuum chamber in all experimental interaction regions, the beams must collide at a small crossing angle. Since the common part is much longer than the bunch spacing, parasitic collisions, so-called long-range interactions, of the separated beams cannot be avoided (see Sec. 5.9). With the present geometry, 15 unwanted long-range encounters occur on each side of a collision point, i.e. 120 for all collision points. The crossing angle has to provide a sufficient separation at all parasitic encounters to keep the effects small from long-range beam-beam interactions and should allow a quasi head-on collision at the central interaction point. This is true in particular for the two low β^* interaction regions IR1 and IR5 where the long-range effects are strongest (see Sec. 5.9). The normalized beam separation should not be smaller than 7 σ at any of the parasitic encounters. Before the two beams are brought into collision, i.e. for injection and the energy ramp, the central head-on collision must also be avoided. This is done with a parallel separation bump in the plane orthogonal to the crossing plane. This bump must also serve as a handle to push the beams into collision and to adjust the collision point in this plane, if necessary. To that purpose it is mandatory that the two beams can be steered independently. To compensate part of the unwanted beam-beam effects the crossing angles in the two low-β^* interaction regions IR1 and IR5 should be in orthogonal planes (see Sec. 5.9). At present it is assumed that the beams cross at a vertical angle in IR1 and in the horizontal plane in IR5. The boundary conditions and the strategy for the crossing scheme are summarized in [11].

Additional considerations are required for IR2 and IR8, housing the ALICE and LHCb experiments. The β^* in these interaction regions are much larger and the detrimental effects of long-range interactions are much smaller. However, the layout of the experiments constrain the choice of the beam separation scheme. Both experiments operate spectrometer magnets with magnetic fields orthogonal to the LHC beams. Together with their compensation magnets they form antisymmetric bumps with a crossing angle at the interaction points [12]. Furthermore, the separation schemes must allow a polarity change of both spectrometers. These internal crossing angles are in the vertical (ALICE, $\theta = \pm 70$ μrad) and horizontal plane (LHCb, $\theta = \pm 135$ μrad) but their longitudinal extension is not large enough to separate the beams at all parasitic encounters. Additional separation has to be provided by external crossing angles and parallel bumps similar to those in interaction points 1 and 5. In the present design these crossing angles are in the same plane as the angles from the spectrometer magnets. Their plane is therefore fixed by the direction of the magnetic field in the spectrometer magnets. The design principles and considerations on operational aspects are given in [12].

A complete summary of the crossing angles and the parallel separation in the four interaction points is given in Tabs. 4.2 to 4.5.

Table 4.3: Crossing angle and orbit at IP5 for Beam 1 (half the total beam separation). The minimum separation between Beam 1 and Beam 2 is specified for one plane. The state 'Injection' refers to the optics configuration during injection, 'Ramp' to the configuration during ramp, 'Pre-Collision' to the optics at the end of the ramp but before the low-β squeeze and 'Collision' to the optics configuration at top energy after the low-β squeeze.

State	$\beta^*_{x,y}$ (m)	horizontal crossing angle (μrad)	vertical orbit (mm)	$d_{\rm ip}$ (σ)	$d_{\rm min}$ (σ)
Injection	18.0	+ 160.0	+ 2.50	13.3	10.5
Ramp	18.0	+ 40.0	+ 0.625	13.3	10.5
Pre-collision	0.55	+ 142.5	+ 0.50	60	6.9
Collision	0.55	+ 142.5	+ 0.0	0.0	6.9

Table 4.4: Vertical crossing angle and horizontal orbit at IP2 for Beam 1 (half the total beam separation). Minimum separation between Beam 1 and Beam 2 is specified for one plane.

State	SPEC (ALICE) (μrad)	$\beta^*_{x,y}$ (m)	half external angle $\alpha_{\rm ext}$ (μrad)	half crossing angle α (μrad)	horizontal orbit separation (mm)	$d_{\rm ip}$ (σ)	$d_{\rm min}$ (σ)
Injection	0.0	10.0	$\pm$ 170.0	$\pm$ 170.0	+ 2.00	14.3	9.1
Injection	+ 70.0	10.0	+ 170.0	+ 240.0	+ 2.00	14.3	9.1
Injection	- 70.0	10.0	- 170.0	- 240.0	+ 2.00	14.3	9.1
Collision	+ 70.0	10.0	+ 80.0	+ 150.0	0.18	5	14.8
Collision	- 70.0	10.0	- 80.0	- 150.0	0.18	5	14.8

Table 4.5: Horizontal crossing angle and vertical orbit at IP8 for Beam 1 (half the total beam separation). Minimum separation between Beam 1 and Beam 2 is specified for one plane [a] at one unique position, everywhere else above 20 σ.

State	SPEC (LHCb) (μrad)	$\beta^*_{x,y}$ (m)	half external angle $\alpha_{\rm ext}$ (μrad)	half crossing angle α (μrad)	horizontal orbit separation (mm)	$d_{\rm ip}$ (σ)	$d_{\rm min}$ (σ)
Injection	0.0	10.0	- 170.0	- 170.0	- 2.00	14.3	9.0
Injection	+ 135.0	10.0	- 170.0	- 35.0	- 2.00	14.3	9.0
Injection	- 135.0	10.0	- 165.0	- 300.0	- 2.00	14.3	8.8
Collision	+ 135.0	10.0	- 210.0	- 75.0	0.0	-	6.5 [a]
Collision	- 135.0	10.0	- 65.0	- 200.0	0.0	-	12.8

4.2.2 The high luminosity insertions IR1 and IR5

The high luminosity insertions IR1 (ATLAS) and IR5 (CMS) house the main p-p experiments of the LHC and are identical in terms of hardware and optics, with the exception of the crossing plane, which was chosen vertical in IR1 and horizontal in IR5.

Optics goals

The optics design in IR1/5 is guided by two main requirements:

1. It must provide a range of accessible β^* values (18 m for the injection and 0.55 m for the collision optics) while keeping the total phase advance over the IR constant.

2. In order to have control over the beam size, the beam separation and the nonlinear chromaticity during the change from injection to collision optics, the quadrupole gradients must change smoothly with varying β^* (e.g. the slope of the quadrupole gradient versus time should not change its sign).

Hardware constraints

1. At the IP, the two rings of the LHC share the same vacuum chamber and the same low-beta triplet quadrupoles and the optics solutions for Ring 1 and Ring 2 must have the same triplet gradients.

2. The maximum gradients must not exceed the operating values given in Tab. 3.2.

3. The minimum gradient of the unipolar insertion quadrupoles at injection energy must be larger than 3% of the nominal gradient.

4. The overall beam size must be small enough to fit into the tight aperture of the LHC. The aperture of the insertions is limited by the crossing-angle separation orbit and the beam screen which is installed in all of the insertion region magnets.

Injection optics

At injection, the optics are detuned with a β^* of 18 m (see Fig. 4.5(a) and 4.5(b)). The phase advances across the IR, i.e. from Q13 left to Q13 right from the IP, are the same for both beams and equal to $\mu_x/2\pi = 2.618$ and $\mu_y/2\pi = 2.644$. They are kept constant along the ramp and are increased by $\Delta\mu_x/2\pi = 0.015$ and $\Delta\mu_y/2\pi = 0.005$ just before the squeeze in order to change from the injection tunes ($Q_{x,y} = 64.28/59.31$) to the collision tunes ($Q_{x,y} = 64.31/59.32$).
The recent implementation of beam-screens in the matching section quadrupoles [13] has reduced the mechanical aperture to $n_1 = 6.6 - 6.7$ at a few locations in the insertion which may require tighter mechanical tolerances and/or more frequent re-alignment of the most critical magnets in order to recover the intial IR tunability of $\Delta\mu_x/2\pi \sim 0.1$ and $\Delta\mu_y/2\pi \sim 0.2$ [14] (a detailed definition of n_1 can be found in Sec 4.3). The smallest aperture now occurs at Q5 for Beam 2 in IR1, see Fig. 4.8(a).
The crossing scheme, vertical in IR1 and horizontal IR5 is shown in Fig. 4.6. The sign of the vertical crossing angle in IR1 ($\theta_c = \pm 160\,\mu$rad) and of the vertical separation in IR5 ($\Delta y = \pm 2.5$ mm) can be chosen arbitrarily. On the other hand, due to the ring geometry (Beam 1 internal in sectors 4-5 and 7-8) and in order to maximise the beam-beam separation at injection, the (horizontal) parallel separation bump must be negative for Beam 1 in IR1 ($\Delta x = -2.5$ mm) and its (horizontal) crossing angle has to be positive at IP5 ($\theta_c = +160\,\mu$rad).

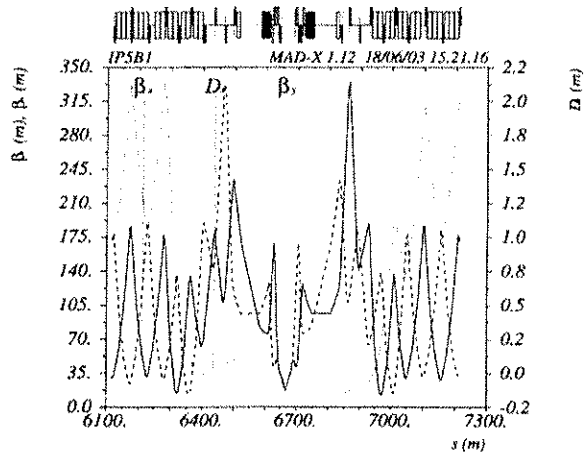

(a) Beam 1, injection optics

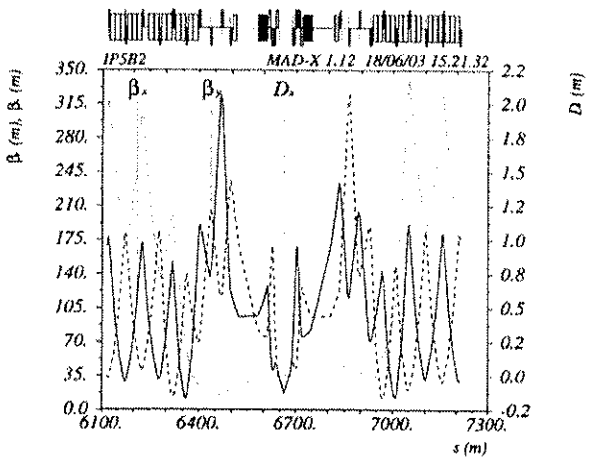

(b) Beam 2, injection optics

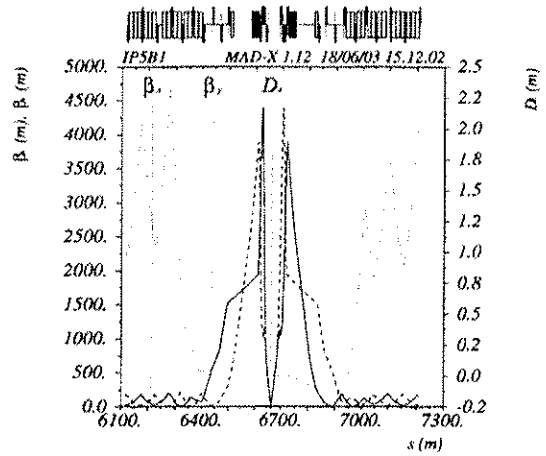

(c) Beam 1, collision optics

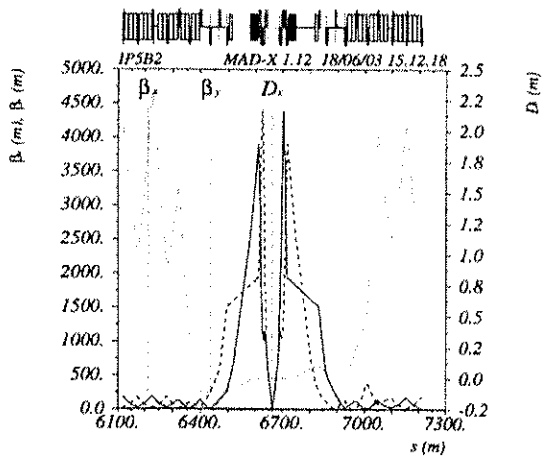

(d) Beam 2, collision optics

Figure 4.5: Injection (top) and collision (bottom) optics of the high-luminosity insertions at IP1 and IP5 for a β^* of 18 m and 0.55 m.

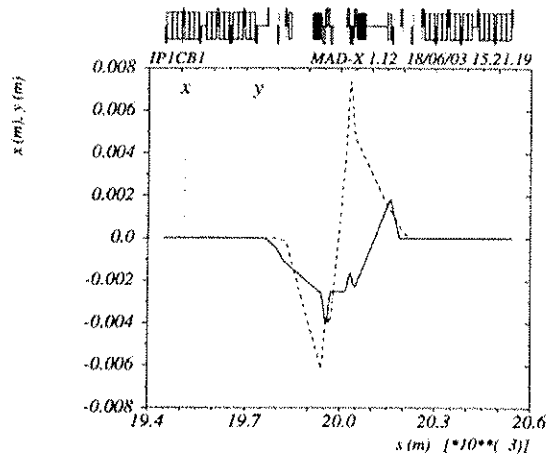

(a) Beam 1 in IR1

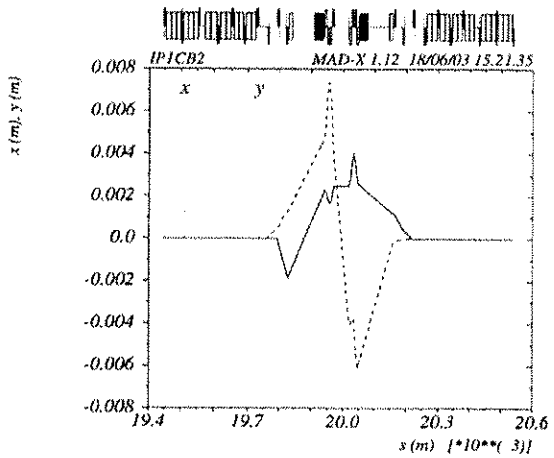

(b) Beam 2 in IR1

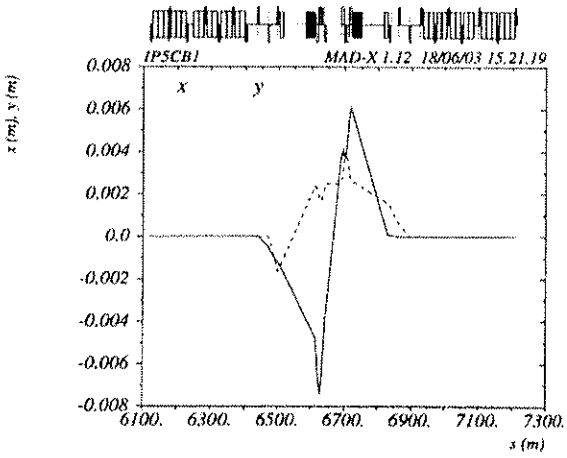

(c) Beam 1 in IR5

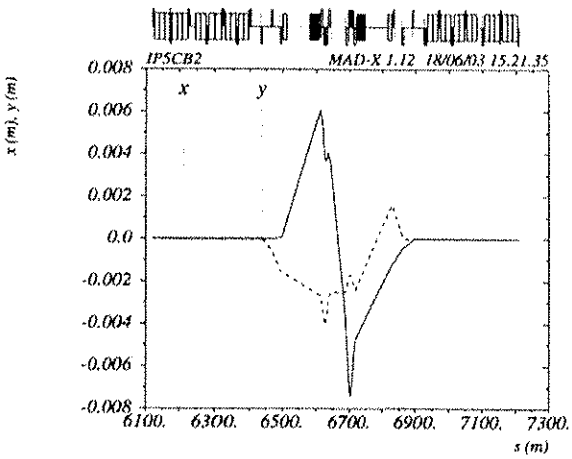

(d) Beam 2 in IR5

Figure 4.6: Crossing scheme for Beam 1 and Beam 2 at injection for the high-luminosity insertions IR1 (top) and IR5 (bottom).

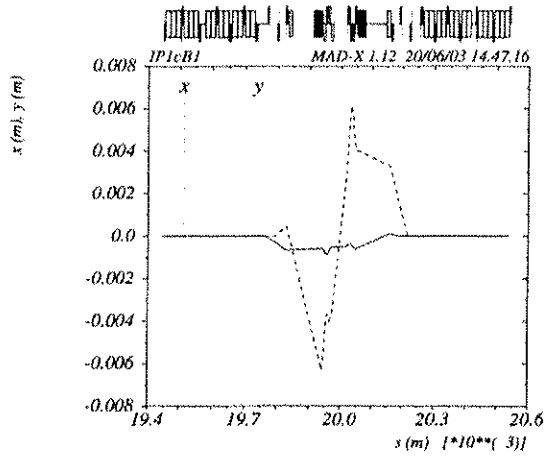

(a) Beam 1 in IR1

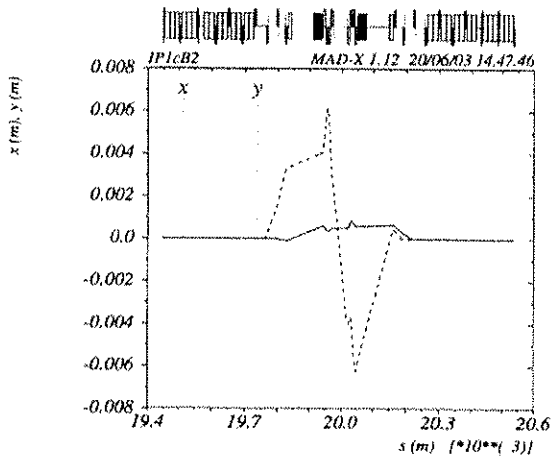

(b) Beam 2 in IR1

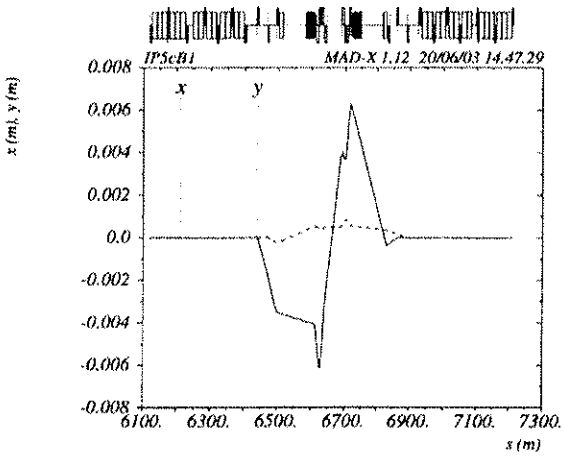

(c) Beam 1 in IR5

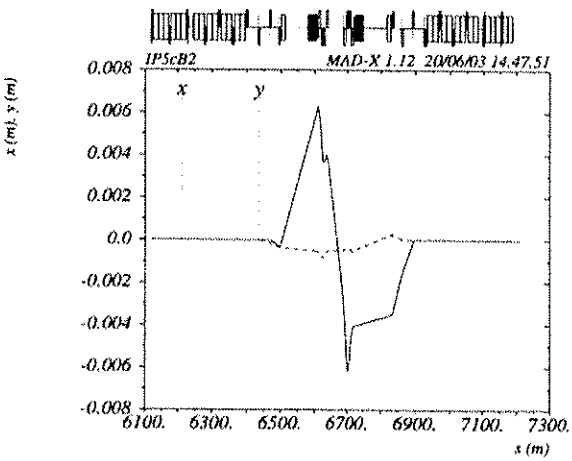

(d) Beam 2 in IR5

Figure 4.7: Crossing scheme for Beam 1 and Beam 2 in pre-collision for the high-luminosity insertions IR1 (top) and IR5 (bottom); IP is assumed to be shifted transversally by $\Delta y = -0.5$ mm in IR1 and $\Delta x = 0.5$ mm in IR5.

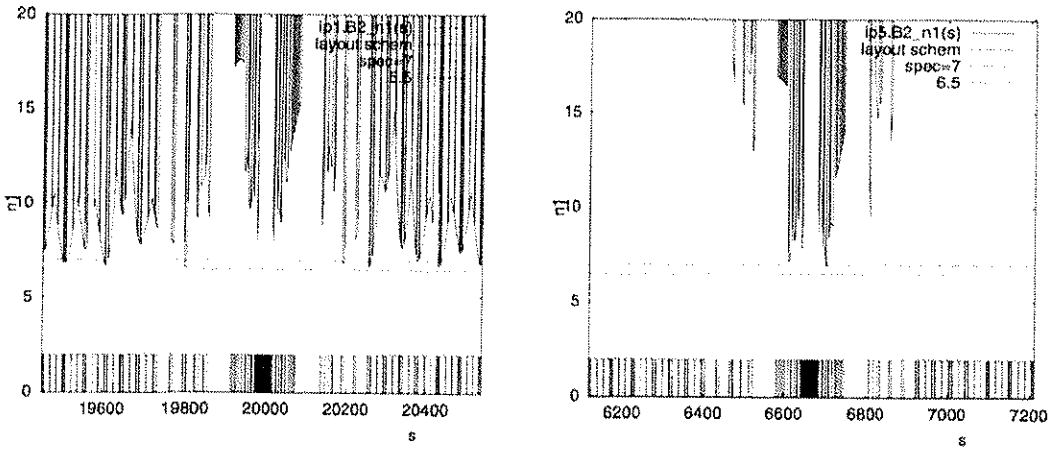

Figure 4.8: Typical figures for the mechanical acceptance of the high-luminosity insertions IR1 and IR5 expressed in terms of n_1 at 450 GeV (injection optics) (left) and 7 TeV (pre-collision optics) (right).

Collision optics

The collision optics of IR1 and IR5 is shown in Fig. 4.5(c) and 4.5(d) for a β^* of 0.55 m. In order to maximise the mechanical acceptance of the low-β quadrupoles, the interaction point can be shifted transversally, that is in the crossing plane, by $\Delta y = -0.5$ mm in IR1 and $\Delta x = 0.5$ mm in IR5, resulting in a net increase of the triplet aperture by $\Delta n_1 = 0.4$. As a result, in spite of the recent implementation of beam-screens in the low-β quadrupoles [13], the specification of $n_1 = 7$ can be met for both beams and both insertions (worst case obtained for Beam 2 in IR5 with $n_1 = 6.98$, see Fig. 4.8(b)).

The crossing schemes in IR1 and IR5 are shown in Fig. 4.7 for the pre-collision optics, i.e. collision optics with a half-parallel separation and crossing angle of ± 0.5 mm and $\pm 150\,\mu$rad, respectively. The crossing schemes ensure an average beam-beam separation of 9.4 σ over the IR, with a minimum separation of 6.6 σ inside the triplet assembly.

4.2.3 IR2

IR2 houses the ALICE experiment and the injection elements for Beam 1.

Optics goals

The optics design in IR2 is guided by three main requirements:

1. It must provide a range of accessible β^* values (0.5 m $< \beta^* <$ 50 m) while keeping the total phase advance over the IR constant.

2. The Ring 1 optics must satisfy the requirements imposed by the beam injection and provide a vertical phase advance of 90° between MKI and TDI, and a vertical phase advance of (360° − 20°) and (360° + 20°) between the TDI and the two auxiliary collimators. [2]

3. In order to have control over the beam sizes, the beam separation and the non-linear chromaticity during the change from injection to collision optics the quadrupole gradients must change smoothly with varying β^* (e.g. the slope of the quadrupole gradient versus time should not change its sign).

[2]The auxiliary collimators are incompatible with the space requirements for the DFB installation in the LHC lattice version V6.4. The TCL implementation is being revised for V6.5.

Hardware constraints

1. At the IP, the two rings of the LHC share the same vacuum chamber and the same low-beta triplet quadrupoles and the optics solutions for Ring 1 and Ring 2 must have the same triplet gradients.

2. The maximum gradients must not exceed the operating values given in Tab. 3.3

3. The minimum gradient of the unipolar insertion quadrupoles at injection energy must be larger than 3% of the nominal gradient.

4. The overall beam size must be small enough to fit into the tight aperture of the LHC. The aperture of the insertions is limited by the beam screen and the crossing-angle separation orbit. All magnets of the insertions are equipped with a beam screen.

5. For the large β^* optics the maximum achievable crossing angle is limited by the available orbit corrector strength. In fact, the orbit corrector strength limits the maximum acceptable β^* value in IR2 ($\beta^* \leq 50$ m).

Injection optics

At injection, the β^* value is determined by the injection constraints [15] which imply an optics with $\beta^* = 10$ m. Fig4.10(a) and 4.10(b) show the corresponding optics functions for Beam 1 and Beam 2 respectively. The phase advances across the IR (i.e. from Q13 left to Q13 right) are the same for both beams and equal to $\mu_x/2\pi = 2.991$ and $\mu_y/2\pi = 2.844$. The recent implementations of beam-screens in the matching section quadrupoles [13], and the optimisation of the DFB length [16] with the implied repositioning of the Q6 quadrupole magnets and the shift of the Q3 triplet quadrupole magnet position [1], has reduced the mechanical aperture with respect to the V6.0 solution presented in [15]. While the solutions presented in [15] had apertures larger than $n_1 = 7$ in all positions of the insertion it now drops to minimum values between $n_1 = 6.6 - 6.7$ at a few locations in the insertion. This may require tighter mechanical tolerances and/or more frequent realignment of the most critical magnets (a detailed definition of n_1 can be found in Sec. 4.3). The optics presented in Fig. 4.10(b) recuperated some of the aperture loss in Q6 by allowing larger than nominal optic functions at Q8 and relaxing the vertical phase advance constraints for the auxiliary collimators implying a further optimization of the auxiliary collimator positions. The vertical phase advance between the MKI and TDI is kept at 90°. This approach yields a minimum aperture of $n_1 = 6.68$ at Q6 and $n_1 = 6.71$ at Q8. Under this condition a large fraction of the IR tunability quoted in [15] is lost due to the reduced mechanical aperture imposed by the beam screen.
The crossing scheme, vertical crossing angle and a parallel separation in the horizontal plane is shown in Fig. 4.11. The sign of the vertical separation can be chosen arbitrarily. On the other hand, due to the ring geometry and in order to maximize the beam-beam separation at injection, the (horizontal) parallel separation bump must be positive for Beam 1 and negative for Beam 2.

Collision optics

The ALICE luminosity during proton beam operation assumes $\beta^* = 10$ m (equivalent to the injection optics) with a transverse beam separation of 5 σ. Because of the reduced beam size at 7 TeV there is no aperture problem for this configuration.

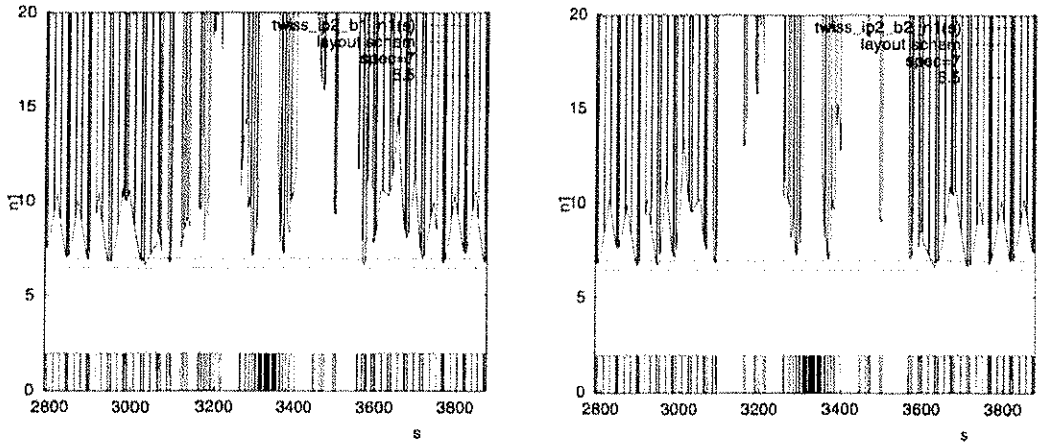

Figure 4.9: The mechanical acceptance in IR2 expressed in terms of n_1 at 450 GeV (injection optics) for Beam 1 (left) and Beam 2 (right). The minimum acceptance of $n_1 = 6.68$ occurs for Beam 1 in Q6.R2 and Q8.L2.

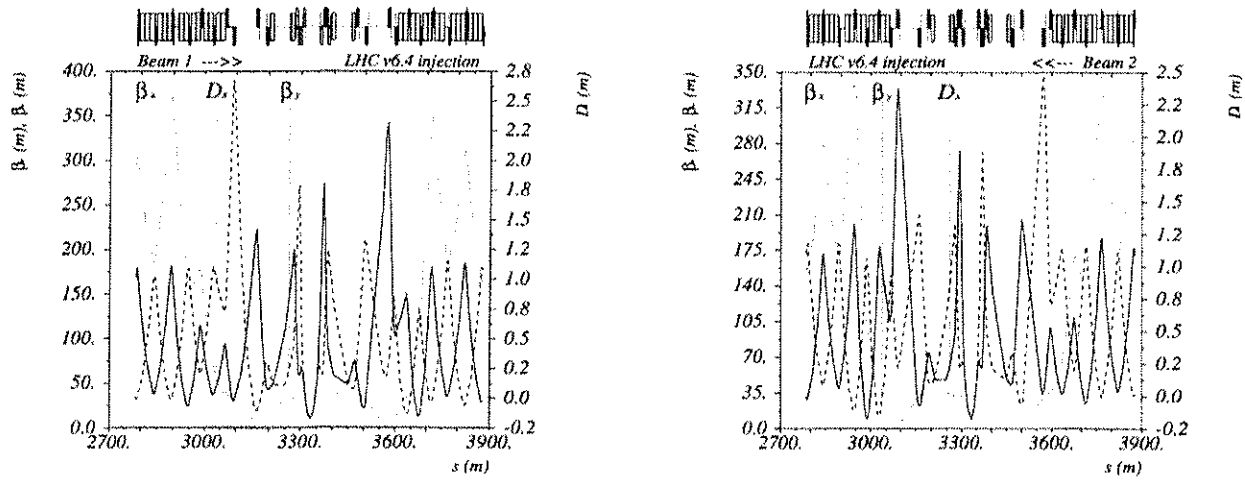

Figure 4.10: Injection (top) ($\beta^* = 10.0$ m) optics in IR2 for Beam 1 (left) and Beam 2 (right).

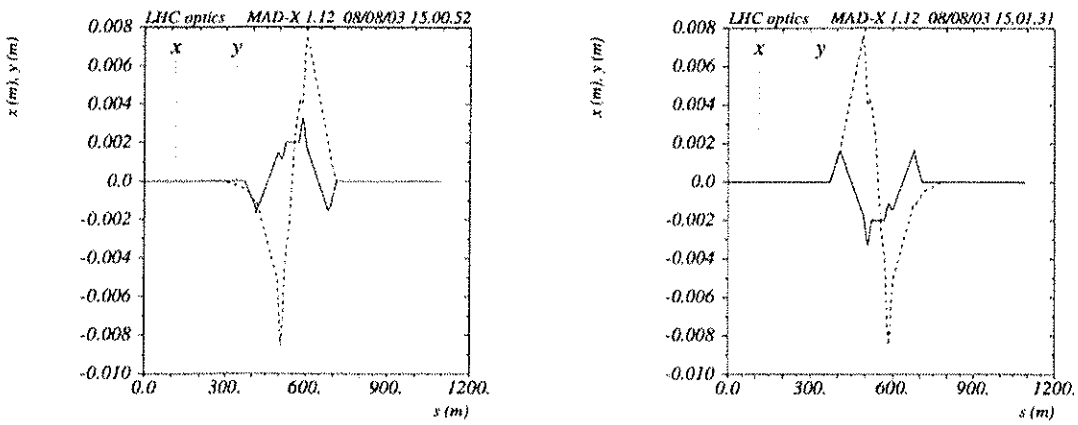

Figure 4.11: Crossing scheme for Beam 1 (left) and Beam 2 (right) at injection for IR2.

4.2.4 IR3

Insertion IR3 houses the Momentum Collimation system. The momentum range of the *nominal* circulating beam does not exceed $\pm 1\ 10^{-3}$. Particles outside this range must be absorbed in the momentum cleaning insertion before they can be lost in the arcs. This is done using a multi turn two stage collimation system (see Chap 18 for more details on the collimation system design). In order to decouple the momentum collimation in IR3 from the betatron-collimation in IR7, the primary collimator jaws in IR3 must be at a location with large dispersion and small betatron function. The optics design in IR3 therefore aims at maximizing the normalized dispersion:

$$\eta_{\mathrm{D}} = \frac{D_x}{\sqrt{\beta_x}}. \tag{4.1}$$

In order to protect the arc aperture from off momentum particle losses the normalized dispersion at the primary collimator must satisfy [17]:

$$\eta_{\mathrm{D,prim}}(n_1) \geq \frac{n_1\, \eta_{\mathrm{D,arc}}}{A_{\mathrm{arc,inj}}(\delta_p = 0) - (n_2^2 - n_1^2)^{1/2}} = 0.185\ \mathrm{m}^{1/2} \tag{4.2}$$

where $A_{\mathrm{arc,inj}}(\delta_p = 0)$ is the arc aperture for on-momentum particles ($A_{\mathrm{arc,inj}}(\delta_p = 0) = 12$), $\eta_{\mathrm{D,arc}} = 0.205\ \mathrm{m}^{1/2}$ with errors in the focusing quadrupole magnets (without errors one has $\eta_{\mathrm{D,arc}} = 0.16\ \mathrm{m}^{1/2}$). (See Sec 4.3 for more details.) n_1 and n_2 are the apertures of the primary and secondary collimator jaws in multiples of the RMS beam size ($n_1 = 7$ and $n_2 = 7n_1/6 = 8.2$) (a detailed definition of n_1 can be found in Sec 4.3). Requiring further that the cut of the secondary halo is independent of the particle momentum one obtains a second constraint for the optics at the position of the primary collimator [17, 18, 19, 20]:

$$\frac{D_x'}{D_x} = -\frac{\alpha_x}{\beta_x}. \tag{4.3}$$

Satisfying the constraints (4.2) and (4.3) can be facilitated by choosing convenient locations for the primary collimator jaws in the insertion. However, once the locations of the primary collimator jaw are fixed the positions of the secondary collimator jaws are constrained by the required phase advance between primary and secondary collimators. At least four secondary jaws are required to cut the secondary halo adequately [19] and it has been shown that six jaws offer a substantial further improvement [21]. The V6.4 layout features six secondary collimator jaws per beam. As the cleaning insertion provides only a limited range of acceptable positions for the secondary collimator jaws, the request for a given set of phase advances between the collimator jaws drastically limits the range of accessible optics solutions. Furthermore, the above constraints must be satisfied simultaneously for both beams.

The V6.4 optics solution shown in Fig. 4.12 provides a normalized dispersion value of $0.21\ \mathrm{m}^{1/2}$ at insertion quadrupole Q5 upstream of the IP. The primary collimator is located at the upstream side of the insertion between Q5 and Q6 [22][21]. This value is larger than the requested value in (4.2) and still provides some margin for optics errors. The total betatron phase advances in the normal conducting region available for the primary and secondary collimators are $0.5 * 2\pi$ and $0.2 * 2\pi$ in the horizontal and vertical plane respectively.

The optics in Fig. 4.12 shows a flat peak in the normalized dispersion function at the primary collimator. This provides efficient collimation over a large momentum error range [18]. This optical feature was obtained by moving Q6 closer to the IP and is the reason why the distance between the two groups of MBWs in IR3 is shorter than that in IR7.

Fig 4.15 shows the aperture of the insertion for Beam 1 in terms of the required primary collimator opening. One clearly recognizes the effect of the large dispersion near Q5 where the minimum aperture reaches a value of $n_1 = 5.5$. This is not problematic as long as the momentum collimators are in operation, because the primary betatronic amplitude cut at the edge of the bucket is $\approx 4\sigma$, see Fig. 4.13. At top energy, the normalized primary collimator aperture can be increased. While the dispersion function does not change with the beam energy, the betatronic beam size shrinks inversely with the square root of the beam energy allowing operation with a larger n_1 (see Fig. 4.14).

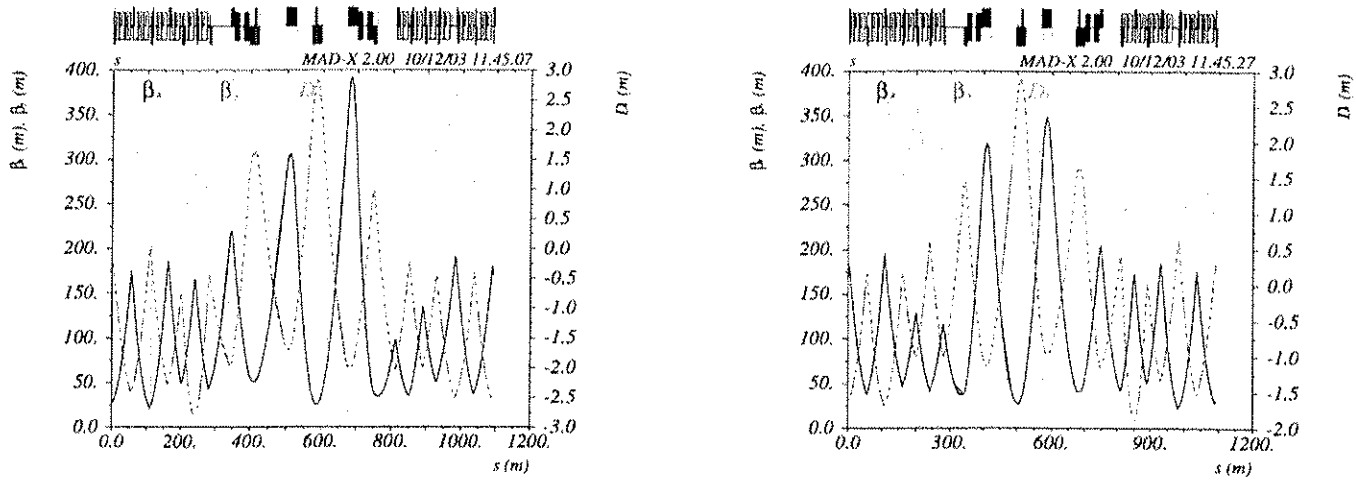

Figure 4.12: β functions and normalized dispersion $D_x/\sqrt{\beta_x}$ in IR3 for Beam 1(left) and Beam 2 (right). The optics corresponds to the new V6.5 layout.

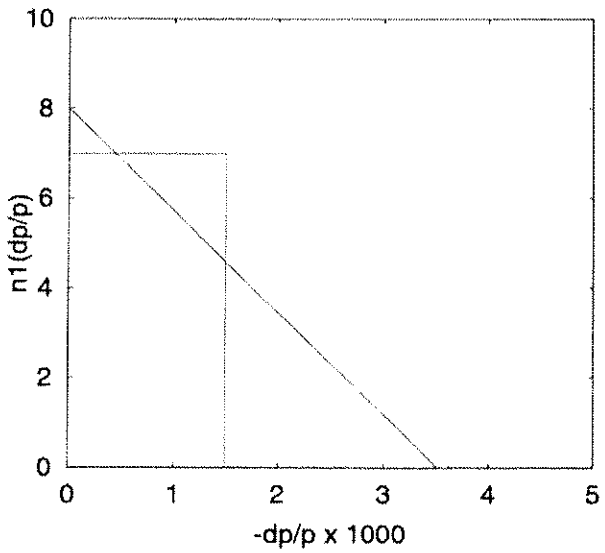

Figure 4.13: The betatron primary aperture as a function of the momentum as cut by the primary momentum collimator at injection, see text. Particles which drift beyond the line are captured and absorbed. The rectangle indicates the space occupied by circulating particles which are inside the bunch and which have an amplitude smaller than the cut made by the betatron collimation.

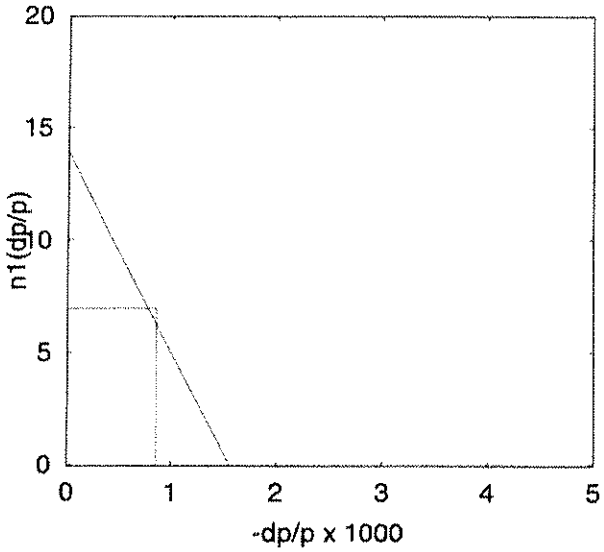

Figure 4.14: The betatron primary aperture as a function of the momentum as cut by the primary momentum collimator at top energy, see text and Fig. 4.13 for a description of the content.

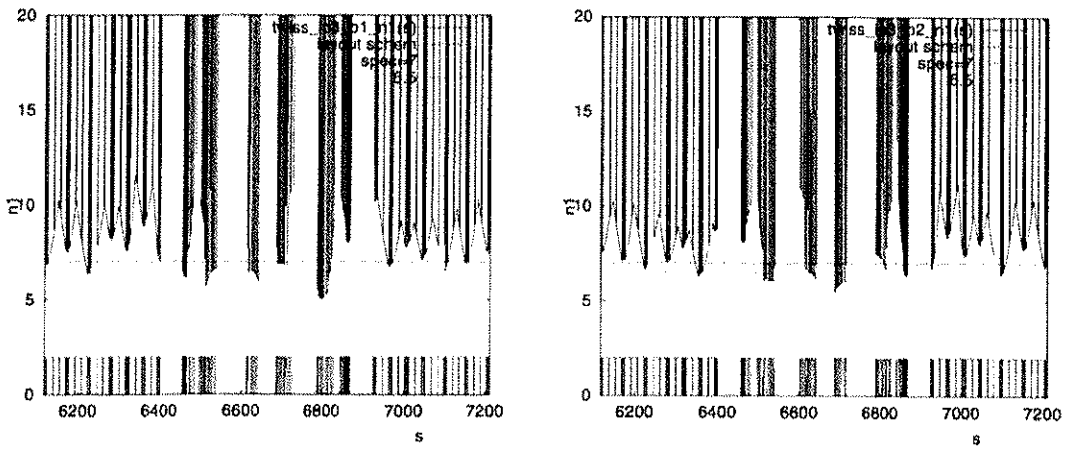

Figure 4.15: The normalized primary aperture plot in IR3 for Beam 1 (left) and Beam 2 (right). The reduced aperture at Q5 at the down stream side of the IP is caused by the increased dispersion. The aperture corresponds to the new V6.5 optics and layout.

4.2.5 IR4

IR4 houses the RF and feed-back systems as well as some of the LHC beam instrumentation. None of these systems impose serious constraints on the optics thus allowing a range of optics solutions with different phase advances for IR4. For this reason IR4 could be used to adjust the phase advances between IR1 and IR5 and to adjusts the tunes if the global LHC optics is constrained [23][24] (and see Sec. 4.6.2). However, the introduction of beam screens in all insertion regions imposes a strong aperture limitation that essentially removes the flexibility of the insertion optics that was available in previous optics versions. In fact the aperture limitation generated by the beam screens is so strong that several insertions can now no longer satisfy the intial goals of an aperture with $n_1 ge 7$ (see Sec. 4.3 for a description of n_1).

The matching in IR4 is done using all quadrupoles at the same time while constraining the maximum β-function in the dispersion suppressors (from Q7 to Q11) to the maximum value in the LHC arcs. The maximum β-function in the long straight section is limited to 600 m at Q5 and Q6 on both sides of the IP. The horizontal dispersion is matched to zero in the cavities.

Fig. 4.16 shows the optics functions for Beam1 in IR4 and Fig. 4.17 the range of accessible phase advances over IR4 for the case without beam screens in the insertion magnets. The decision to place beam screens inside all insertion magnets lowers the available mechanical aperture in IR4 and thus the accessible range of phase advances over the insertion.

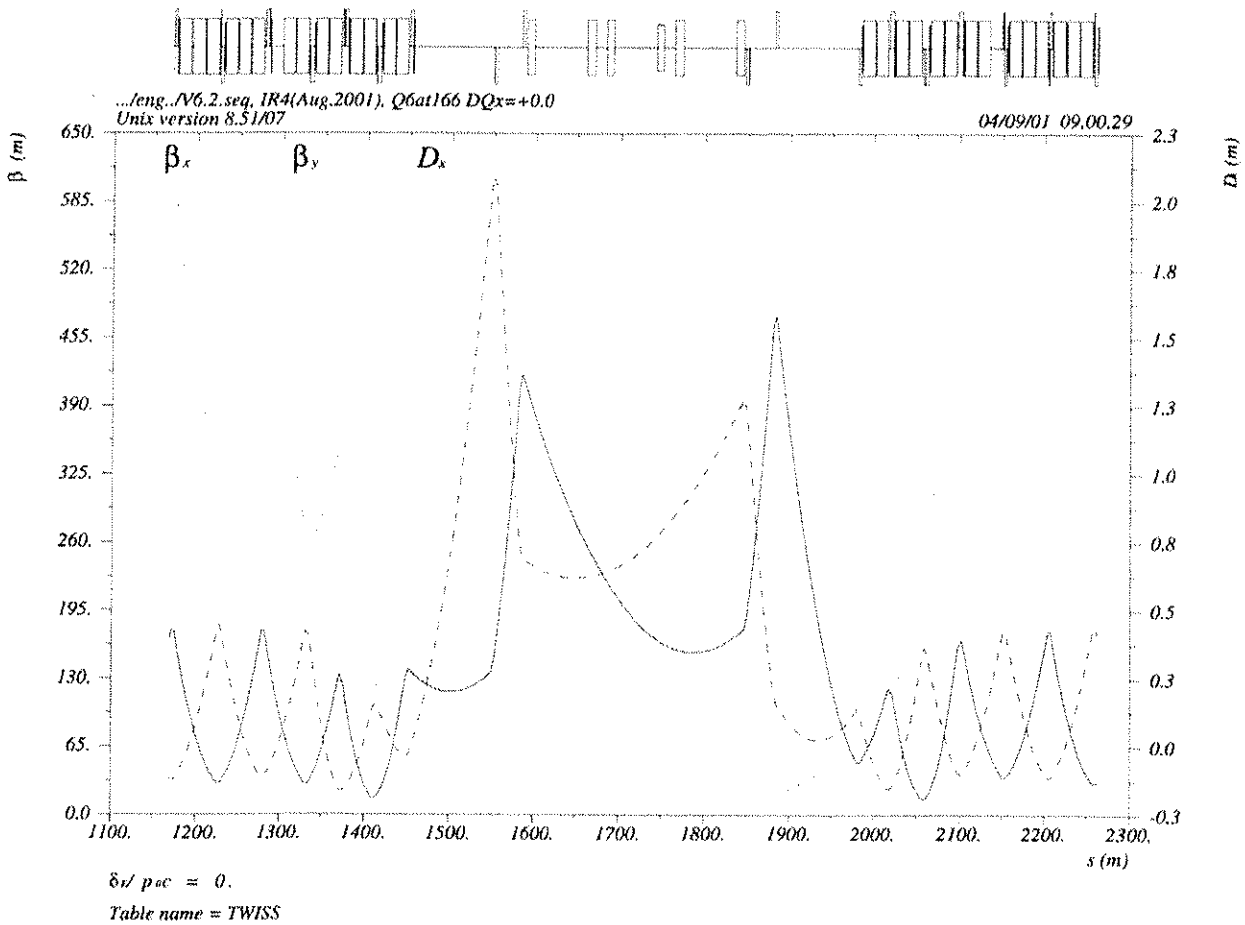

Figure 4.16: The optic functions for Beam 1 in IR4.

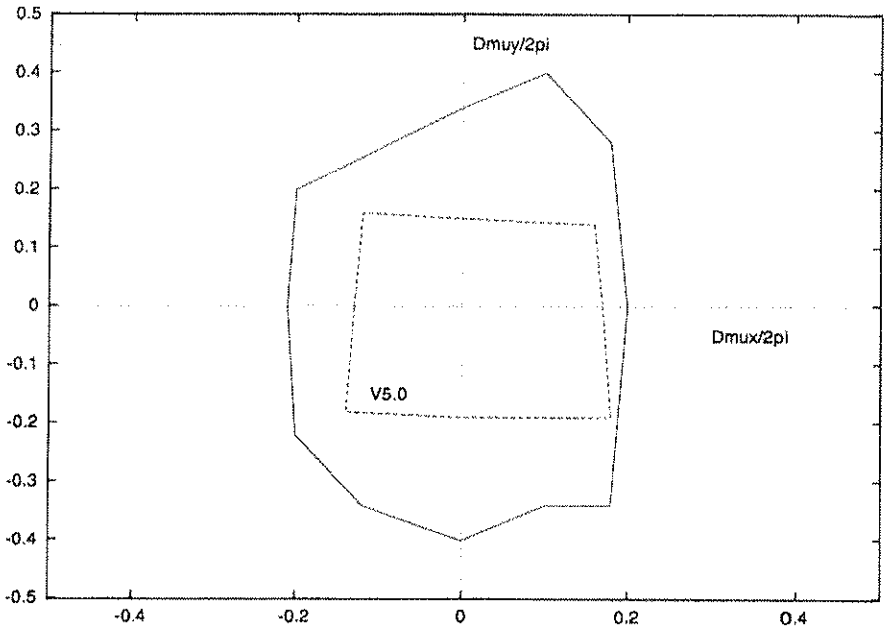

Figure 4.17: Outer figure: possible variations of the phase advance in IR4 without beam screens in the insertion magnets. The inner figure shows the same variation obtained with the old design.

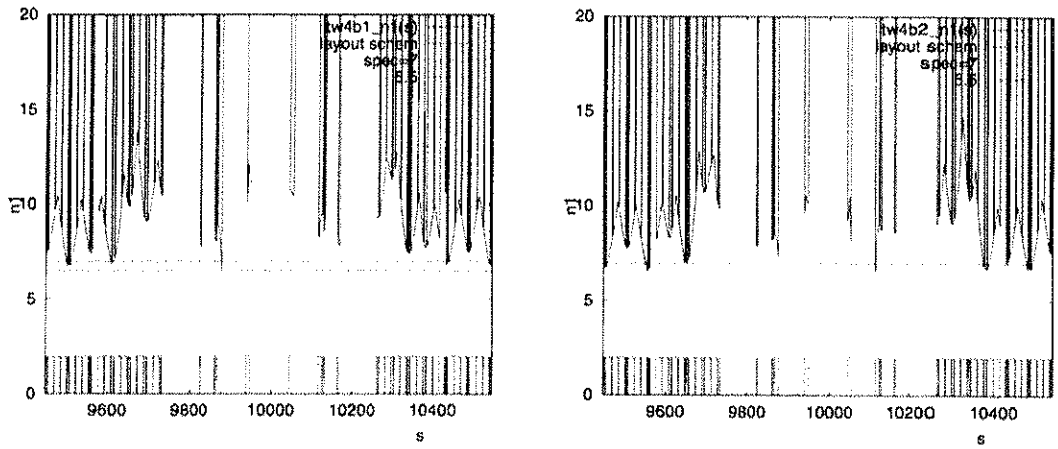

Figure 4.18: The mechanical acceptance in IR4 expressed in terms of n_1 at 450 GeV (injection optics). The minimum acceptance of $n_1 = 6.5$ occurs for Beam 1 and Beam 2 in the D4 dogleg dipole magnet (a detailed definition of n_1 can be found in Sec. 4.3).

4.2.6 IR6

IR6 houses the beam abort systems for Beam 1 and Beam 2. The optics in IR6 is constraind by the maximum aperture of the insertion quadrupole and septum magnets. The aperture constraint can be satisfied for a range of optics solutions. However, the introduction of beam screens in all insertion regions imposes a strong aperture limitation that essentially removes the flexibility of the insertion optics that was available in previous optics versions. Fig. 4.19 shows the optic functions for Beam1 in IR6 and Fig. 4.20 the range of accessible phase advances over IR6. Actually it is possible to change the phases by even larger amounts than indicated in 4.20 in a discontinuous way. This is discussed in [25]. However, it should be noted here that the tuneability in Fig. 4.20 was established under the assumption that the insertion magnets in IR6 are not equipped with beam screens. The decision to place beam screens inside all insertion magnets lowers the available mechanical aperture in IR6 and thus the accessible range of phase advances over the insertion.

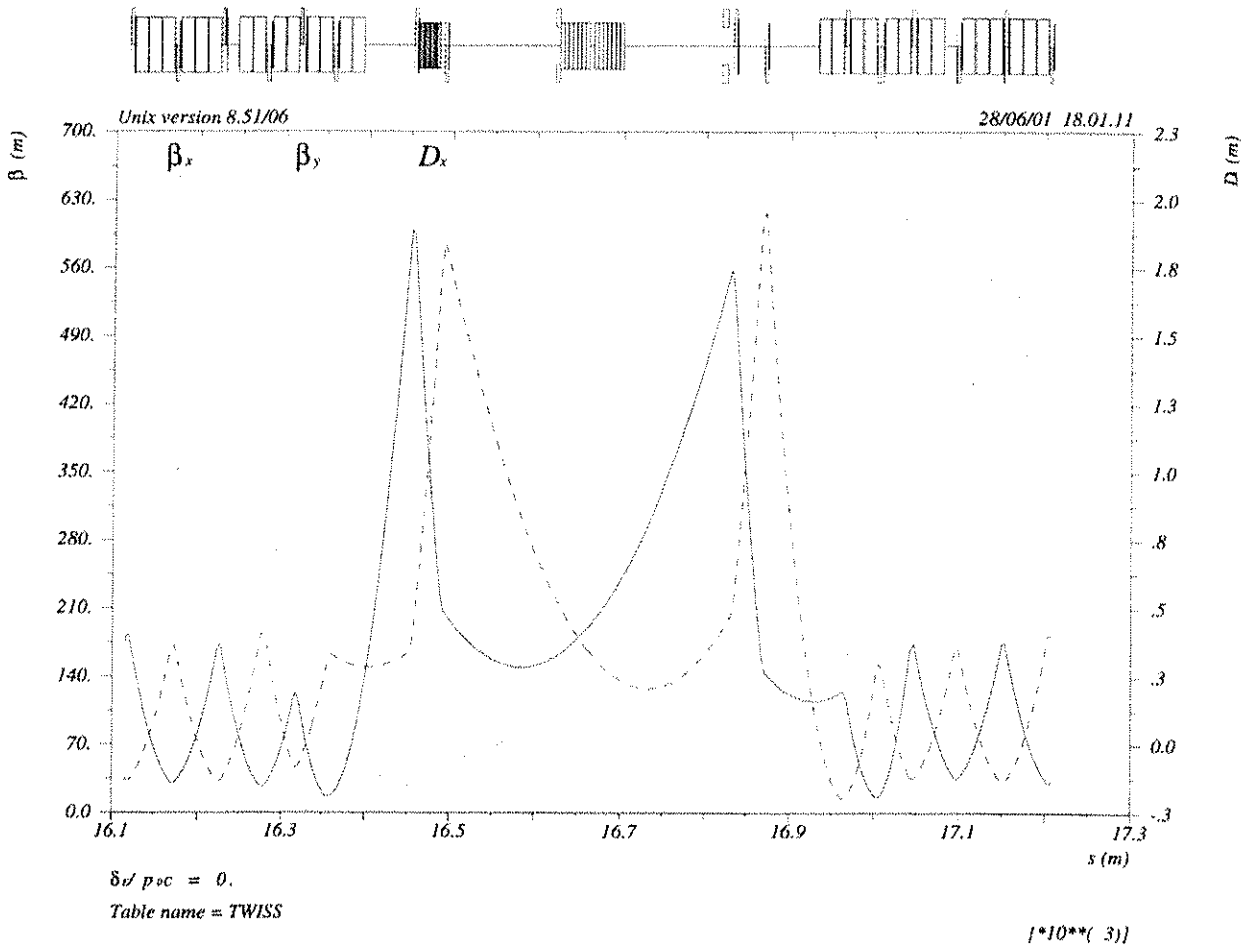

Figure 4.19: The optic functions for Beam 1 in IR6.

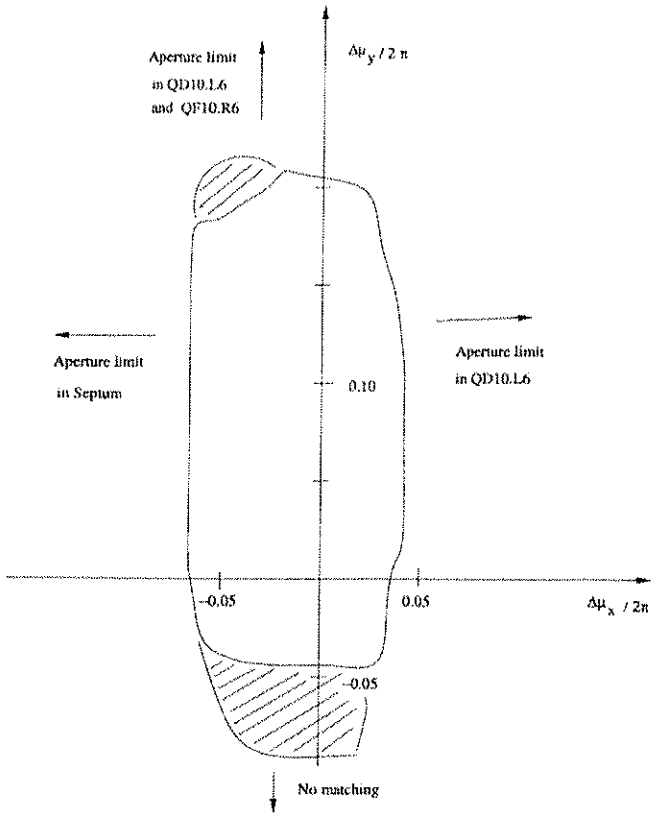

Figure 4.20: The range of accessible phase advances over IR6.

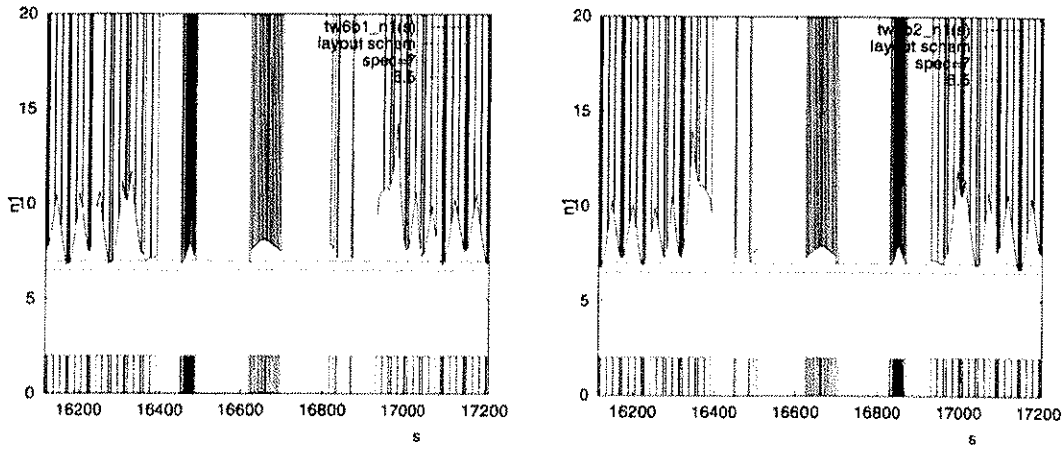

Figure 4.21: The mechanical acceptance in IR6 expressed in terms of n_1 at 450 GeV (injection optics). The minimum acceptance of $n_1 = 6.7$ occurs for Beam 2 inside the DS (a detailed definition of n_1 can be found in Sec. 4.3).

4.2.7 IR7

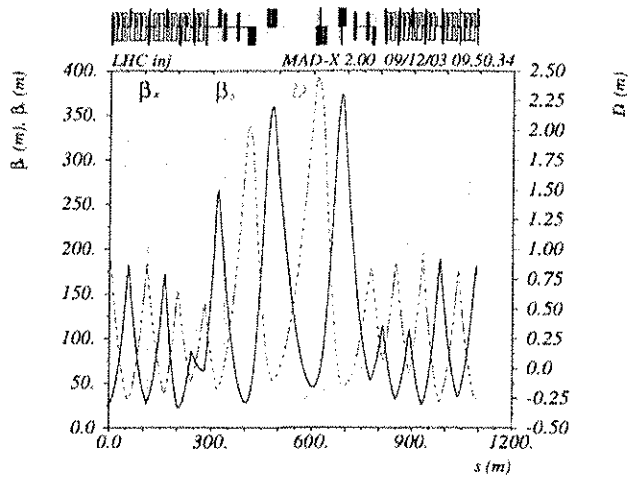

(a) Beam 1

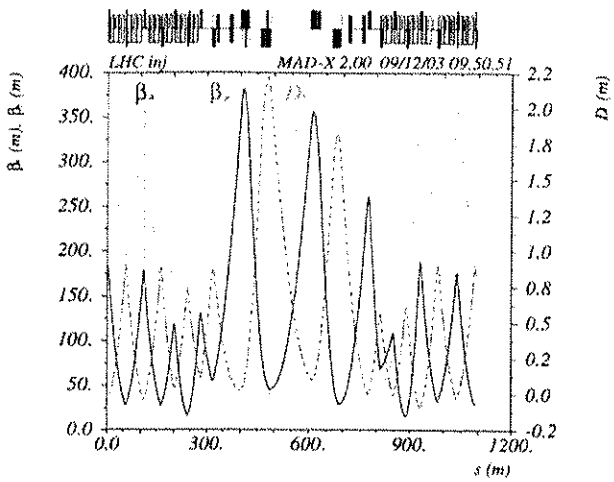

(b) Beam 2

Figure 4.22: Lattice functions in IR7. The optics corresponds to the new V6.5 layout.

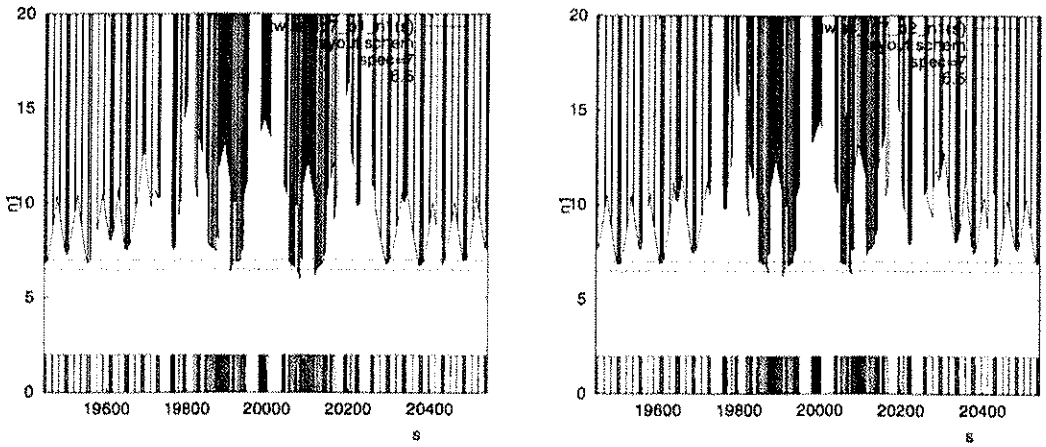

Figure 4.23: The normalized primary aperture plot in IR7 for Beam 1 (left) and Beam 2 (right). The plots correspond to the new V6.5 optics and layout.

Insertion IR7 houses the Betatron Collimation system. The dispersion function in the long straight section between Q7L and Q7R is kept small, in order to reduce the effect of the off-momentum motion on the collimation. The primary collimators are located at the upstream side of the IP, between Q5 and Q6. The total betatron phase advances in the normal conducting region of the insertion are $0.5 * 2\pi$ and $0.4 * 2\pi$ in the horizontal and vertical plane respectively. The primary betatron cleaning is made with three primary jaws, namely horizontal, vertical and skew. A detailed derivation for an ideal optics is found in [18, 19]. A reasonably good optimum is obtained with four secondary jaws per primary collimator. As the apertures of the LHC magnets in general have non-rectangular cross sections, collimation and aperture studies must take into account the combined horizontal and vertical particle motion. In this respect a problem arises for particles having large amplitudes in both transverse planes, because they can still escape through a series of collimators if the phases of their H and V betatron oscillations differ by 90 or 270° [26]. These particles may be lost outside the collimation region, at locations where the horizontal and vertical oscillations of the particles are again in phase. This problem is particularly severe if all collimators have approximately the same difference between the horizontal and vertical

betatron phases. Introducing fluctuations for $\mu_y - \mu_x$ in the region of the collimators reduces the above problem and particles having large amplitudes in both transverse planes are easier to intercept. To this end the minima of the β functions are made small, thus accelerating the phase advance alternatively in the horizontal and vertical planes [27].

In an insertion of finite length, the best correlation of the phase advances can never be reached. The optics was therefore optimized for maximum opening of the secondary collimators. For a fixed optics and given primary collimator opening, the required opening of the secondary collimator jaws is evaluated numerically with the code 'Distribution of Jaws', or DJ [20]. Once an optimum optics is obtained for one beam, a simultaneous matching of the two beams is performed, in order to find a common solution which is as close as possible to the initial solution of the single beam. This procedure typically generates an aperture loss of approximately 0.2 σ. Fig 4.22 shows the corresponding optics functions in IR7 for Beam 1 and Beam 2. The aperture of IR7 for this optics is shown in Fig 4.23. At some locations the equivalent primary aperture is as low as $n_1 \approx 6.3$ which is clearly smaller than the specified value $n_1 = 7$, see Sec 4.3. However, in warm elements this is still acceptable. It was also checked that the power deposition in the vacuum chamber is acceptable, w.r.t. to mechanical integrity and radiation.

Although the beam sizes, and thus the collimator apertures, decrease with increasing beam energy, the same IR7 optics will be used at all energies.

4.2.8 IR8

IR8 houses the LHCb experiment and the injection elements for Beam 2. It features a special layout where the IP is shifted by 3 half RF wavelengths ($\rightarrow \approx 11.25$ m) in order to provide enough space in the cavern for the spectrometer magnet. This shift of the IP has to be recuperated before the beam enters back into the dispersion suppressor sections and implies a non-symmetric magnet layout in the matching section.

Optics goals

The optics design in IR8 is guided by three main requirements:

1. It must provide a range of accessible β^* values (1.0 m $< \beta^* <$ 50 m) while keeping the total phase advance over the IR constant.

2. The Ring 2 optics must satify the the requirements imposed by the beam injection and provide a vertical phase advance of 90° betwen MKI and TDI, and a vertical phase advance of $(360° - 20°)$ and $(360° + 20°)$ bweteen the TDI and the two auxiliary collimators. [3]

3. In order to have control over the beam sizes, the beam separation and the non-linear chromaticity during the change from injection to collision optics the quadrupole gradients must change smoothly with varying β^* (e.g. the slope of the quadrupole gradient versus time should not change its sign).

Hardware constraints

1. At the IP, the two rings of the LHC share the same vacuum chamber and the same low-beta triplet quadrupoles and the optics solutions for Ring 1 and Ring 2 must have the same triplet gradients.

2. The maximum gradients must not exceed the operating values given in Tab. 3.4

3. The minimum gradient of the unipolar insertion quadrupoles at injection energy must be larger than 3% of the nominal gradient.

4. The overall beam size must be small enough to fit into the tight aperture of the LHC. The aperture of the insertions is limited by the crossing-angle separation orbit and the beam screen which is installed in all insertion magnets.

[3] The auxiliary collimators are incompatible with the space requirements for the DFB installation in the LHC lattice version V6.4. The TCL implementation is being revised for V6.5.

5. For the large β^* optics the maximum achievable crossing angle is limited by the available orbit corrector strength. In fact, the orbit corrector strength limits the maximum acceptable β^* value in IR8 to $\beta^* \leq 50$ m.

Injection optics

At injection, the β^* value is determined by the injection constraints [28] which imply a detuned optics with a β^* of 10 m. Fig 4.24(a) and 4.24(b) show the corresponding optics functions for Beam 1 and Beam 2 respectively. The phase advances across the IR (i.e. from Q13 left to Q13 right) are the same for both beams and equal to $\mu_x/2\pi = 3.204$ and $\mu_y/2\pi = 2.804$. The recent decision to install beam-screens in the matching section quadrupoles [13] and the optimization of the DFB length [16] with the implied repositioning of the Q6 quadrupole magnets and the shift of the Q3 triplet quadrupole magnet position [1], have reduced the mechanical aperture with respect to the V6.0 solution presented in [28]. While the solutions presented in [28] had apertures larger than $n_1 = 7$ in all positions of the insertion it now drops to minimum values between $n_1 = 6.6 - 6.7$ at a few locations in the insertion which might require tighter mechanical tolerances and/or more frequent re-alignment of the most critical magnets (a detailed definition of n_1 can be found in Sec. 4.3). The optics presented in Fig 4.24(b) recuperated some of the aperture loss in Q6 by allowing larger than nominal optic funtions at Q12 and relaxing the vertical phase advance constraints for the auxilliary collimators. For the V6.4 lattice layout the injection optics provides $(360° - 36°)$ and $(360° + 0.4°)$ for the vertical phase advances between the TDI and the auxilliary collimators. These values can be improved by optimizing the positions of the auxilliary collimators. Moving the collimator next to Q6 (TCL.6L8.B2) by 3.5 m closer to the Q6 magnet and the collimator next to Q7 (TCL.7L8.B2) by 8 m away from the Q7 magnet provides $(360° - 29°)$ and $(360° + 10°)$ for the vertical phase advances between the TDI and the auxilliary collimators. The vertical phase advance between the MKI and TDI is kept at 90°. This approach yields a minimum aperture of $n_1 = 6.65$ at Q6 and $n_1 = 6.68$ at Q12. Under this condition a large fraction of the IR tunability quoted in [28] is lost due to the reduced mechanical aperture imposed by the beam screen.
The crossing scheme, horizontal crossing angle and a parallel separation in the vertical plane is shown in Fig. 4.25. The sign of the vertical separation can be chosen arbitrarily. On the other hand, due to the ring geometry and in order to maximise the beam-beam separation at injection, the (horizontal) crossing angle bump must be negative for Beam 1 and positive for Beam 2. Depending on the polarity of the LHCb spectrometer magnet this implies either partial compensation or addition of the two crossing angle contributions coming from the external crossing angle separation orbit bump and the spectrometer compensation bump.

Collision optics

Fig 4.24(c) shows the collision optics with $\beta^* = 1.0$ m. The crossing scheme in IR8 is shown in Fig 4.26. Fig 4.27 shows the mechanical acceptance in IR8 for the injection and $\beta^* = 1.0$ m collision optics.

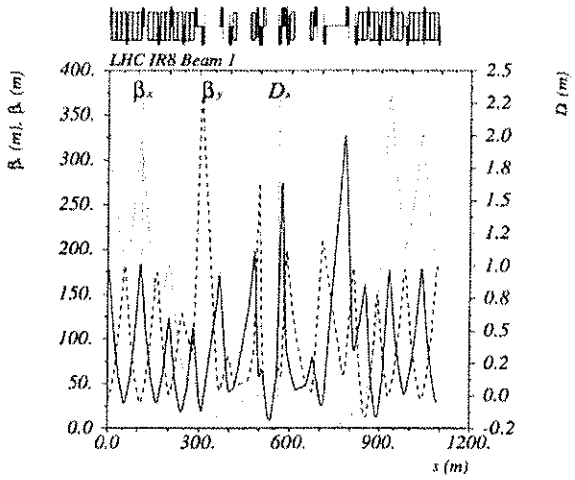

(a) Beam 1, injection optics

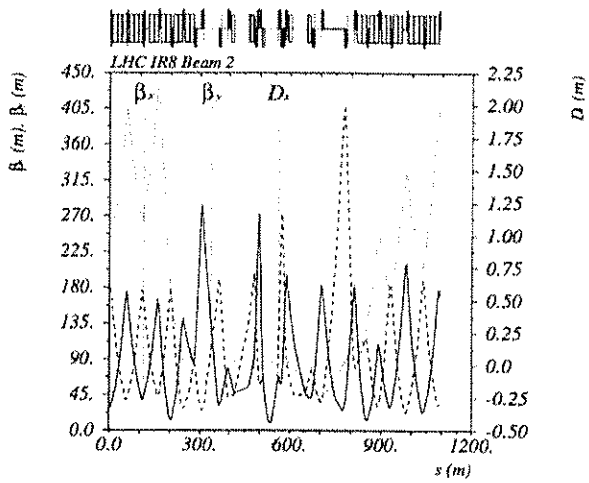

(b) Beam 2, injection optics

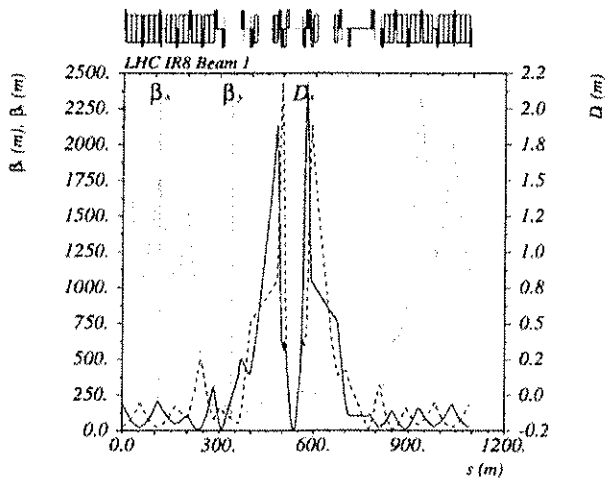

(c) Beam 1, collision optics

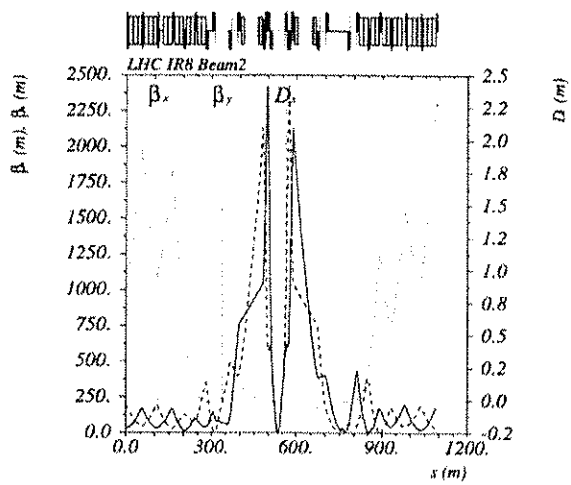

(d) Beam 2, collision optics

Figure 4.24: Injection (top) ($\beta^* = 10.0$ m) and $\beta^* = 1.0$ m collision (bottom) optics for IR8.

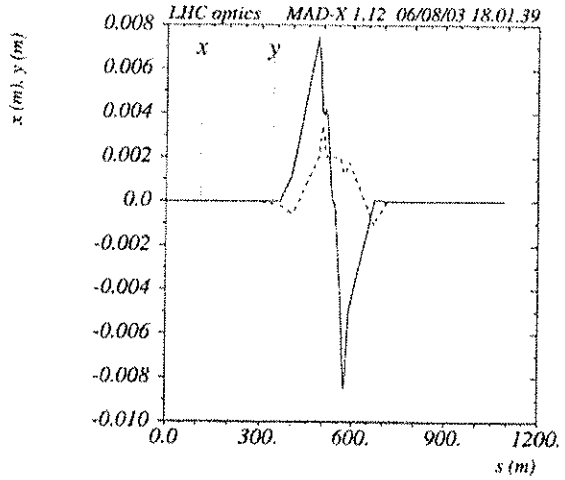

(a) Beam 1 in IR8

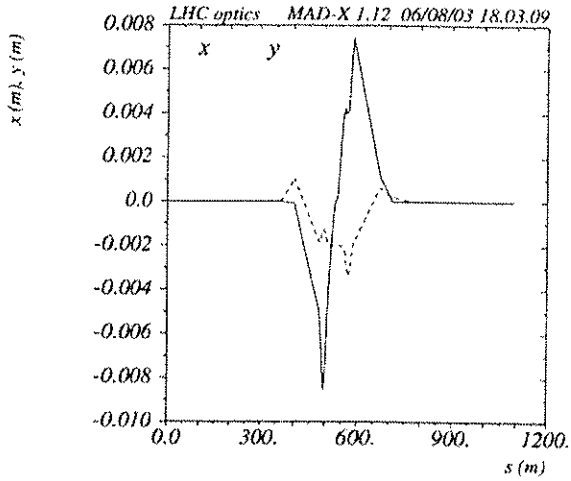

(b) Beam 2 in IR8

Figure 4.25: Crossing scheme for Beam 1 and Beam 2 at injection for the IR8.

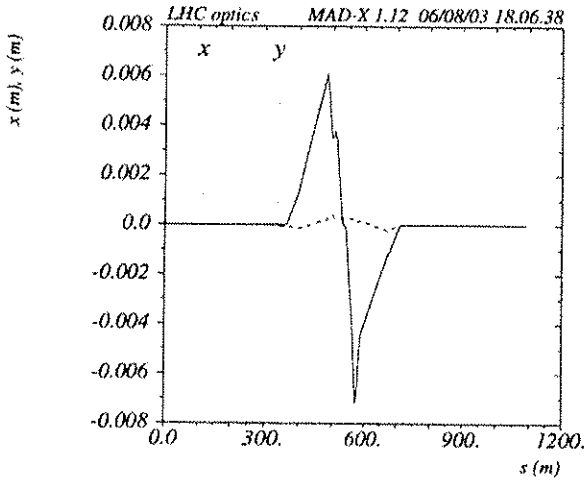

(a) Beam 1 in IR8

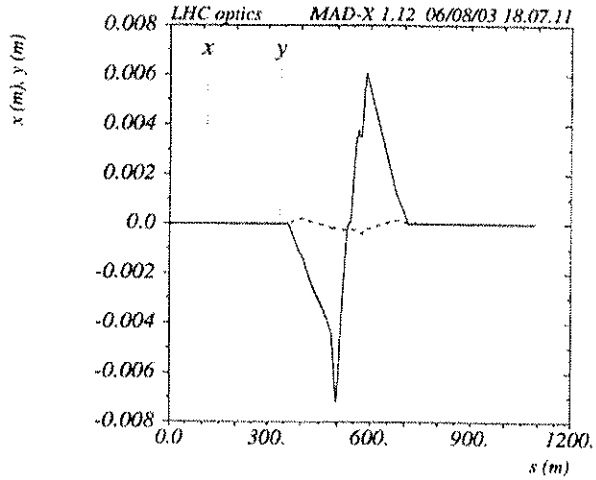

(b) Beam 2 in IR8

Figure 4.26: Crossing scheme for Beam 1 and Beam 2 at collision for the IR8 optics with $\beta^* = 1.0$ m.

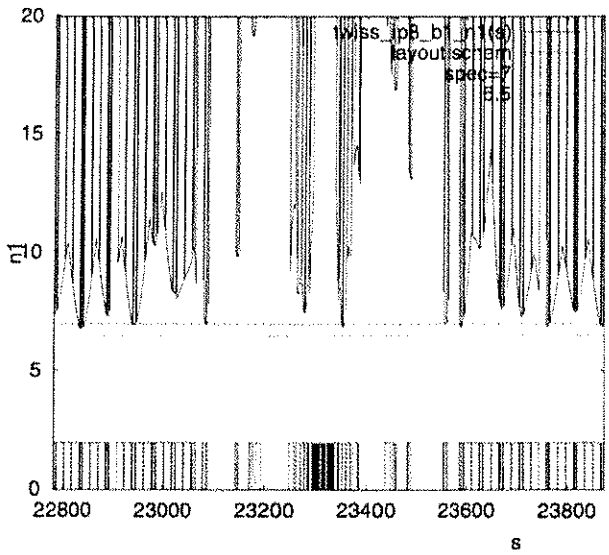

(a) Mechanical aperture of Ring 1 in IR8 at 450 GeV (injection optics)

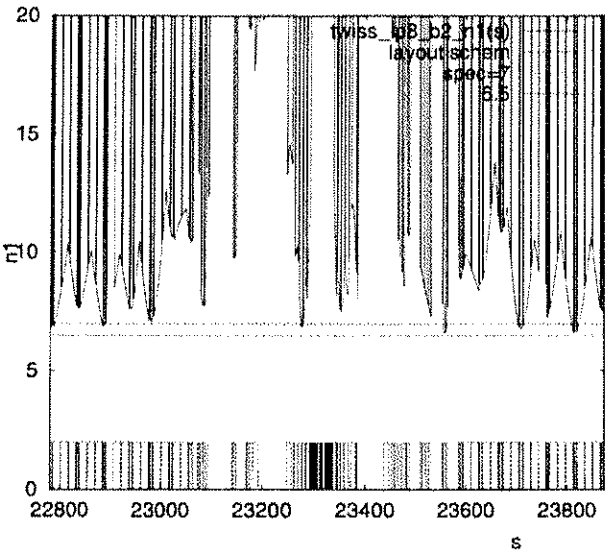

(b) Mechanical aperture of Ring 2 in IR8 at 450 GeV (injection optics)

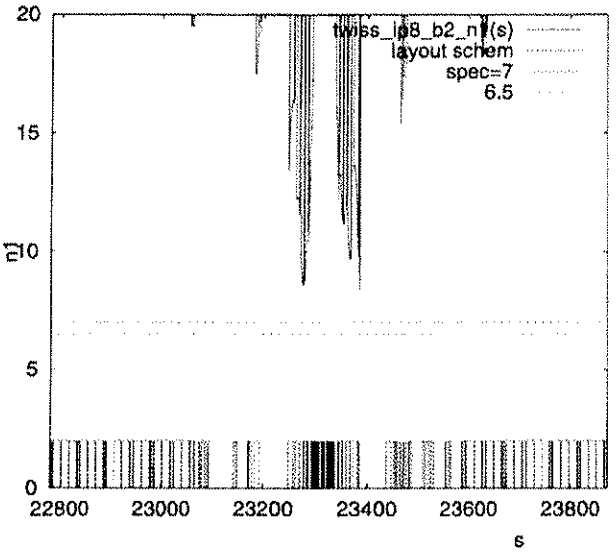

(b) Mechanical aperture of Ring 2 in IR8 at 7 TeV ($\beta^* = 1.0$ m)

Figure 4.27: The mechanical acceptance in IR8 expressed in terms of n_1 at 450 GeV (injection optics) and 7 TeV ($\beta^* = 1.0$ m). The minimum acceptance occurs for Beam 2 in Q6 and Q12 on the right-hand side of IP8.

4.3 MECHANICAL ACCEPTANCE

Expressed in beam size units, the effective aperture of the vacuum chambers of LHC are rather small, typically 10 σ. A precise two-dimensional approach is therefore used to compute the effective aperture which can be occupied by the beam. The beam shape itself deserves a particular treatment [29]. Except for a pilot beam, beam cleaning will always be in use, in particular to avoid quenches of the cryo magnets. The primary beam aperture will be delimited by the primary collimators. Secondary collimators will capture most of the secondary halo re-emitted by the primary collimators above an amplitude, which is defined as the edge of the secondary halo. The secondary beam aperture is defined by the edge of the secondary halo. The collimation efficiency will be high and thus limit the flux of the tertiary halo down to a harmless limit for the cryo magnets. It is therefore not considered in aperture calculations.

4.3.1 Beam size

All the quantities are defined in normalised coordinates:

$$X = \frac{x}{(1+k_\beta)\,\sigma_x} \quad , \quad Y = \frac{y}{(1+k_\beta)\,\sigma_y} \, , \tag{4.4}$$

with k_β being the beta-beat factor (see Tab 4.6) The primary collimators delimit the primary beam size to a regular octagon. The radius of the circle inscribed in the octagon is written:

$$X^2 + Y^2 = n_1^2 \tag{4.5}$$

with n_1 the primary collimator aperture. The secondary halo is contained in a circle of radius n_r and cut in the two principal directions at n_a (see Fig. 4.28), with:

$$n_r = 1.4 n_1 \quad , \quad n_a = 1.2 n_1 \tag{4.6}$$

These value are fixed by choosing the aperture of the secondary collimators to, see Chap 18 in this design report volume,

$$n_2 = \frac{7}{6} n_1 \tag{4.7}$$

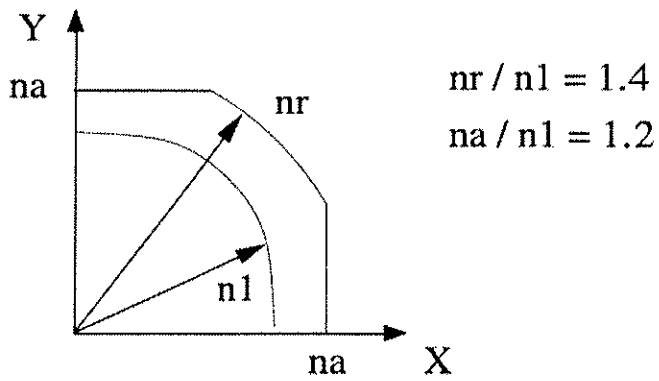

Figure 4.28: The geometry of the primary beam and its halo in normalised coordinates

At injection energy, the primary collimator aperture is specified as $n_1 = 7.0$, allowing space for the beam itself, injection oscillations and operational margins. At top energy, the same n_1 value is specified, but during the first years of operation, the secondary aperture will be $n_2 = 10$, yielding $n_r = 13.5$ (see the chapter on collimation for more details). It will be lowered down to $n_2 = 7$ after some upgrade of the cleaning system, see Tab. 4.6.

Table 4.6: Beam parameters related to aperture definitions

Variable	Name	Value	Units
Primary collimator aperture			
Injection	n_1	7	σ_β
Top energy	n_1	7	σ_β
Secondary halo			
Injection	n_r / n_a	10 / 8.4	σ_β
Top energy, early	n_r	13.5 / 11.3	σ_β
Top energy, nominal	n_r	10 / 8.4	σ_β
Radial closed orbit excursion :			
ARCs + D	CO_r^{peak}	4.0	mm
Exp.LSS at 7 TeV, Q7L to Q7R	CO_r^{peak}	3.0	mm
Beta beating	k_β	0.2	-
Relative parasitic dispersion	k_D	0.27	-
Momentum offset, injection	δ_p	1.5×10^{-3}	-
Momentum offset, collision	δ_p	0.86×10^{-3}	-

4.3.2 Beam errors

While beam dynamics is affected by random errors, the point of smallest aperture of the ring limits the performance. The aperture is therefore computed with the peak value of the errors, also called tolerance. These are listed in Tab. 4.6. Beam errors are discussed in Chap. 4.4. The maximum radial closed orbit error CO_r^{peak} is deduced from experience with LEP [30]. In collision, and in the experimental insertions, it is necessary to control the closed orbit better in order to maintain the beam in collisions. In a proton-proton collider, the superposition of the two beams is not inherently granted, contrary to e^+e^- or $\bar{p}p$ colliders. A smaller excursion is therefore used for aperture calculations.

Two sources contribute to the parasitic dispersion. A random source is dominated by orbit offsets in quadrupoles and by tilt errors of these elements. This effect is quantified by the parameter k_D given in Tab. 4.6. A substantial local effect occurs in the triplets of quadrupoles of the experimental insertions. The beams are offset by the beam-beam crossing scheme at locations where the quadrupole gradient is high and the β-functions are large. This generates a large parasitic dispersion in the other experimental insertions where the β-functions are also large. This latter contribution can be calculated by MAD and read by the code which computes the aperture. The momentum offset is made of two contributions: The aperture is computed for the particles which are at the edge of the bunch $\sigma_{\delta E/E_0}$ and the offset associated with the momentum sweep (5×10^{-4}) which will be used for chromatic measurements is added to $\sigma_{\delta E/E_0}$.

4.3.3 Mechanical tolerances

A mechanical tolerance is used for aperture calculations, instead of an r.m.s value, for the same reason given above for beam errors. Radial tolerances are given in Tab 4.7 where the quantity t_r is the transverse radial tolerance. It applies to the centre of the vacuum chamber (cold bore in cryo-magnets), w.r.t. the survey target and including a contribution from tunnel motion for one year. They differ for different kinds of elements. Cold magnets often have larger tolerances than warm ones. The presence of a cryostat implies a further shell of structure between the vacuum chamber and the survey target. A few elements, which are located in a particular area, or which must have a small aperture for performance issues, are designed in a way that allows smaller tolerances (MQX, TCDS). The tolerance of cryo-magnets are relative to the axis of the cold bore, i.e. they represent the expected error of centering of the cold bore with respect to the central beam trajectory. An additional tolerance is added for the beam screen. The beam-screen can distort inside the cold bore. The beam-screen and cold bore tolerances are added linearly. The effective beam-screen dimensions are given in Tab 4.8. The values quoted represent the nominal mechanical dimensions, from which the tolerance of the beam screen is subtracted. This table is extracted from the Tab 2 of the Functional Specification [31].

Table 4.7: Mechanical tolerance of critical machine elements. The quantity t_r is the transverse radial tolerance. It applies to the centre of the vacuum chamber (cold bore in cryo-magnets), w.r.t. the survey target and including a contribution from tunnel motion for one year, see text.

Element	Location	t_r [mm]
Dipoles		
MB	arc	2.0
MBX, MBRC	exp. IR	1.6
MBXW	IR1,IR5	1.0
MBW	IR3,IR7	1.6
MBRS, MBRB	IR4	2.0
Quadrupoles		
MQ, MQM	arc, IR's	1.5
MQX	exp. IR	1.2
MQW	IR3,IR7	1.6
Absorbers		
TAS	IR1,IR5	1.0
TAN	IR1,IR5	2.6
TCDS	IR6 absorbers	0.5
Kicker and Septa		
MKI	inj. kicker	1.0
MKD	dump kicker	2.0
MSI	inj. septum	2.0
MSD	dump septum	1.0
ADT	RF dampers	1.5

Table 4.8: Beam screen type with the corresponding cold bore inner/outer diameters, the effective inner diameter of the beam screen and the effective full inner width of the flat segments of the beam screen.

Beam screen type	Colb bore ID/OD [mm]	$d_{\rm bs}$ [mm]	$h, v_{\rm bs}$ [mm]
50A	50/53	44.0	34.3
50L	50/53	45.2	35.4
53	53/57	47.8	38.0
63	63/66.5	57.9	48.1
69	69.1/73	62.7	52.9
74	74/78	67.5	57.7

4.3.4 Effective aperture

The effective normalised aperture is calculated for each element at location s separated by ≈ 1 m. The beam centroid is shifted by the sum of all the transverse displacements of either the beam itself or the cold bore:

$$\vec{\Delta}(s) = \vec{d}_{\rm sep}(s) + \vec{d}_{\rm axis}(s) + \vec{d}_{\rm inj}(s)\ , \tag{4.8}$$

with $\vec{d}_{\rm sep}(s)$ the orbit generated by the beam-beam crossing scheme, $\vec{d}_{\rm axis}(s)$ the transverse displacement of separation and dog-leg dipoles with respect to the central trajectory, $\vec{d}_{\rm inj}(s)$ the beam displacement of the injected beam up to the injection kicker, and up to the TDI absorber in case of kicker misfire. The mechanical tolerance and the closed orbit displacement are defined radially. The corresponding offset is:

$$\vec{u} = (t_r + CO)(\cos\alpha, \sin\alpha) \quad \text{with} \quad \alpha\,\epsilon\,[0\,,\,\pi/2]\ , \tag{4.9}$$

Table 4.9: Cold bore size and beam screen and orientation in cryo-magnets. The first column indicates the temperature of the helium bath. The second one contains the cold inner and outer diameters and the corresponding beam screen type (in boldface). The orientation of the beam screen is given for each insertion and each element in the remaining columns. The beam screen dimension are given in Tab. 4.8.

C. B. T [K]	ID/OD [mm] **BS**	ir1	ir2	ir3	ir4	ir5	ir6	ir7	ir8
4.5	50/53 **50A**	Q6L VH Q5L HV Q5R VH Q6R HV	Q6L HV Q5R HV Q6R VH	Q6L VH Q6R HV		Q6L VH Q5L HV Q5R VH Q6R HV		Q6L VH Q6R HV	Q6L HV Q5L VH Q6R VH
1.9	50/53 **50L**	Q7 VV SM	Q7 VV SM	Q7 VV SM	Q7 VV SM	Q7 VV SM	SM	Q7 VV SM	Q7 VV SM
1.9	53/57 **53**	Q1 H	Q1 H			Q1 V			Q1 V
4.5	63/66.7 **63**	Q4 VV	Q5L HH Q4 HH		Q6L HV Q5L VH Q5R HV Q6R VH	Q4 VV	Q5L VH Q4L HV Q4R VH Q5R HV		Q5R HH Q4 HH
1.9	63/66.7 **63**	Q2 H Q3 H	Q2 H Q3 H			Q2 V Q3 V			Q2 V Q3 V
4.5	69.1/73 **69**	D2 VV	D2 HH		D4L VH D3L VH D3R VH D4R HV	D2 VV			D2 HH
1.9	74/78 **74**	DFBX	D1 V DFBX			DFBX			D1 V DFBX

see Tab. 4.7 for t_r and Tab. 4.6 for CO. The calculation is made for several values of α (default is 5). Finally the contribution of parametric dispersion is:

$$\vec{d}_{\text{disp}}(s) = (1 + k_\beta) \left[\vec{D} + k_D \frac{D_{\text{x,QF}}}{\sqrt{\beta_{\text{x,QF}}}} \sqrt{\vec{\beta}} \right] \delta_p, \tag{4.10}$$

with δ_p the relative momentum offset, see Tab 4.6. The total offset is then

$$\overrightarrow{OO'}(s) = \vec{\Delta}(s) + \vec{u} + \vec{d}_{\text{disp}}(s) \,. \tag{4.11}$$

Finally the aperture is calculated by first stretching the secondary halo, defined in Fig 4.28 and Tab 4.6, with the factor $(1 + k_\beta)\,\sigma_x$ and $(1 + k_\beta)\,\sigma_y$ along the X and Y directions respectively. Then it is shifted with $\overrightarrow{OO'}(s)$. Its size is adjusted to the largest value which is still inscribed in the beam screen or the vacuum chamber as shown in Fig 4.29. The normalised primary aperture is the corresponding value $n_1(s)$ which is the maximum acceptible primary collimator opening that still provides a protection of the mechanical aperture against losses from the secondary beam halo. An aperture plot for a section of the ring is produced, which displays the function $n_1(s)$. The aperture of this section is the minimum value of the function $n_1(s)$. The orientation of the beam screens inside the insertion regions is optimized for a maximum mechanical aperture and Tab. 4.9 lists the beam screen orientation for the insertion region elements. All beam screens have a race track shape and 'H' and 'V' indicate that the flat part of the beam screen lies in the horizontal or vertical plane.

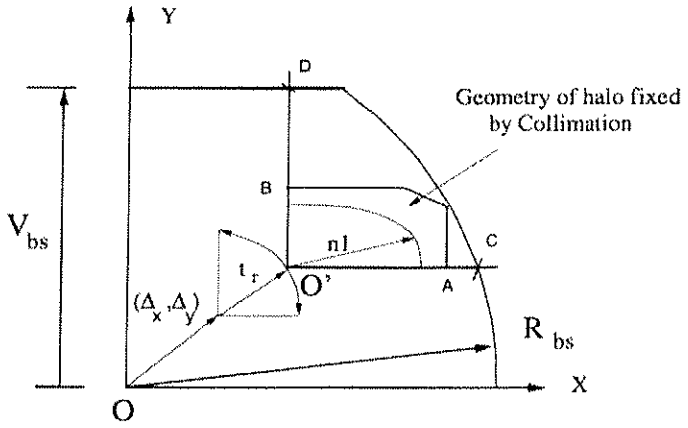

Figure 4.29: The largest secondary halo which fits to the inner edge of the beam screen, once shifted by the sum of the factors discussed in the text.

4.4 BEAM AND MACHINE PARAMETER TOLERANCES FOR OPERATION

The specification of the LHC beam and machine parameter tolerances for operation is based on simulation studies and past operational experience from existing hadron storage rings. Tab 4.10 summarizes the main optics tolerances and Tab 4.11 the main beam tolerances.

Table 4.10: *Operational optics tolerances.*

Parameter	tune	coupling	chromaticity	orbit (global)	orbit (local)	β-beat	dispersion spurious / normalized
Limit	$\pm 3 \times 10^{-3}$	$\lvert c_- \rvert \ll 3^{-3}$	± 2.0	4 mm	0.1 σ	20 %	27 %

Table 4.11: *Operational tolerances for the main beam parameters.*

Parameter	N_{bunch}	ϵ_{trans}	orbit (IP)	X-ing (IP)
Limit	10%	20%	10% of RMS beam size	10% of x-ing angle

4.4.1 Fractional tunes

Resonances of the horizontal and vertical particle oscillations limit the single particle stability and the control of the fractional tunes is of great importance for the preservation of the dynamic aperture. The choice for the fractional part of the base line LHC working point at injection ($Q_x = 59.28$ and $Q_y = 64.31$) is based on operational experience and various tracking studies. For example, Fig. 4.32 shows the 1000 turn dynamic aperture (DA) for the Version 5.0 lattice of the LHC and indicates that the injection tunes of the LHC lie at the centre of a plateau with sufficiently large DA [32]. The width of this plateau is approximately $\Delta Q \approx 10^{-2}$. Combining the width of this plateau with the total expected detuning from the field imperfections yields an operational margin of $\Delta Q_{\text{inj}}(\text{operation}) \approx \pm 3 \times 10^{-3}$ [33].

The choice for the fractional part of the tune at collision ($Q_x = 59.31$ and $Q_y = 64.32$) is based on the operational experience from the $Sp\bar{p}S$ collider [34]. The operational margin for the tunes during collisions is determined by the total tune spread due to the beam-beam interactions and field imperfections yielding an operational tolerance of $\Delta Q_{\text{col}}(\text{operation}) \approx \pm 2.5 \times 10^{-3}$ for the nominal beam parameters. This margin disappears for the operation with ultimate beam parameters.

4.4.2 Coupling

A proper tune control requires a machine coupling which is smaller than the tune separation in the horizontal and vertical planes. In the presence of coupling the minimum tune separation in the machine can be written as:

$$|Q_I - Q_{II}| = \sqrt{(Q_x - Q_y - p)^2 + |c_-|^2}, \tag{4.12}$$

where c_- is the coupling coefficient. For the LHC this requirement yields an operational tolerance for the global machine coupling of $|c_-| \ll 0.03$ and $|c_-| \ll 0.01$ for the injection and collision optics respectively.

4.4.3 Orbit

The maximum acceptable closed orbit perturbations are limited by the mechanical aperture and the feed-down effect of non-linear field imperfections. Both requirements limit the peak orbit perturbations to $|\Delta CO| \leq 4$ mm. This orbit tolerance is compatible with experience from the LEP operation [30]. Tighter orbit tolerances apply for special areas in the LHC (e.g. the collimation insertions and the beam dump area). These local tolerances require peak orbit deviations of $|\Delta CO(local)| \leq 0.1\ \sigma$ and are discussed in Chaps. 17 and 18.

4.4.4 $\beta - beat$

The maximum acceptable β-beat is limited by the available mechanical aperture and non-linear particle motions due to the magnet field imperfections. For the LHC the total tolerance for the β-beat has been specified as 20 %.

4.4.5 Chromaticity

The operational margins for the chromaticity are based on collective instabilities and the operational experience in existing hadron storage rings [34]. Stability of collective effects requires positive chromaticity values and operational experience chromaticity values smaller than 5 units yielding a target chromaticity of 2 units with an operational margin of $\delta Q^{'} = \pm 2$.

4.4.6 Spool piece powering

In order to maximize the DA, the LHC features spool piece correction circuits which aim at an arc-by-arc correction of the b_3, b_4 and b_5 field errors of the main dipole magnets. The DA reduction due to an imperfect spool piece circuit powering has been studied in [35] and [36]. Taking a DA reduction of more than 0.5 σ as a measure for the maximum tolerance of the spool piece circuit powering one obtains a minimum correction accuracy of 50 % for the powering of the b_3 circuits (assuming that the total chromaticity is corrected via the lattice sextupole circuits), 30 % for the octupole circuits (b_4) and 80 % for the b_5 circuits, where 100 % represents a perfect powering of the spool piece circuits and 0 % no powering at all.

4.5 FIELD QUALITY SPECIFICATION

4.5.1 Introduction

The magnetic field expansion used for the LHC magnets reads [37]:

$$B_y + iB_x = B_{ref} \sum_{n=1}^{\infty} (b_n + ia_n) \left(\frac{x+iy}{R_r}\right)^{n-1} \tag{4.13}$$

The subscript $n = 1$ refers to a dipole, $n = 2$ to a quadrupole and so on. The terms a_n and b_n indicate skew and normal harmonics respectively, and $B_{\rm ref}$ represents the magnetic field at the reference radius $R_r = 17$ mm. The multipolar harmonics, a_n and b_n can be classified as:

- those inherent to the *design geometry* (including the contribution of the beam-screen) are called 'systematic'.

They respect the coil symmetry (as b_1, b_3, b_5, ...for a dipole magnet and b_2, b_6, b_{10} for a quadrupole) or, at least, the symmetry given by the horizontal mid-plane (as the harmonics b_2 or b_4 which, due to the two-in-one design of the main dipoles, have opposite sign in the inner and outer bores of the magnet).

- those due to *fabrication tolerances* of the different components and of the tooling used during assembly. They are called 'uncertainty' errors in the following.

In principle, these errors do not respect any symmetry and are responsible for any skew harmonics such as the significant a_2 harmonics expected in the main dipole magnets. They are most likely random and/or lead to an average deviation with respect to the systematic components inherent to the magnet design. In this case, the 'uncertainty' will vary from production line to production line in the case of the short series of magnets (e.g. matching section quadrupoles MQMC, MQM or MQML, triplet quadrupoles or warm magnets). On the other hand, concerning the main dipole and quadrupole magnets, the concept of uncertainty must be interpreted as an average deviation per arc with respect to the systematic, changing from arc to arc and reflecting possible trends and/or modification of cross-section during the production and the fact that, for the main dipoles, the percentage of the magnets coming from three manufacturers might not be kept constant in each of the 8 sectors of the machine.

- those generated by the *persistent currents* in the superconducting cables.

They are responsible for systematic errors for the allowed harmonics (e.g. b_1, b_3, b_5, ...for a dipole magnet), possibly changing from arc to arc depending on the cable manufacturer equipping a given sector (i.e. source of uncertainty for the main dipoles and the main quadrupoles), but also for random errors for all other harmonics, a_n and b_n.

- those due to inter-strand *eddy currents* during the ramp, or ramp induced errors proportional to dI/dt.

They are inversely proportional to the inter-strand contact resistance R_c. The latter being presently much larger than targeted, the ramp induced errors measured in the first main dipole magnets have been found small enough to be neglected during the operation of the LHC and, therefore, will not be discussed in the following.

- finally, those induced at high field by *saturation*.

The first two sources of error, of purely geometric origin, are present at each stage of the LHC cycle (injection, ramp, collision), while the persistent current induced errors are maximum at the injection energy, these perturbations die away when raising the current (following a power law in $1/B^{1.5}$) and significant saturation effects can take place at nominal field, affecting in particular the sextupole component of the main dipoles.
To summarize, the multipolar content of each magnet installed in the ring is presently modeled as:

$$b_n = b_{n_S} + \frac{\xi_U}{1.5} b_{n_U} + \xi_R b_{n_R} \,, \tag{4.14}$$

where ξ_U and ξ_R denote random numbers with a Gaussian distribution cut at 1.5 and 3σ, respectively. Following the above discussion, b_{n_S} refers to a systematic error, b_{n_U} represents a maximum possible deviation with respect to the systematic, changing from sector to sector for the MB's or MQ's or from production line to production line for the other type of magnets produced in short series, and b_{n_r} denotes the standard deviation of the random errors varying from magnet to magnet. It is clear that each of these three quantities depends on the type of magnet considered but also on the operation mode of the LHC, that is, for instance, by summing the errors of geometric origin either with the persistent current induced errors at injection or with the saturation effects at high field.
Finally it is worth noting that the present modeling of the machine assumes that the uncertainty corresponds to

1.5 σ of a normal distribution cut at 1.5 σ. With this definition, the standard deviation related to the concept of uncertainty is then given by:

$$\begin{aligned} \sigma\left[b_{nU}\right] &= \left\{\frac{1}{\sqrt{2\pi}}\int_{-1.5}^{1.5} dx\, x^2\, e^{-x^2/2}\right\}^{1/2} \frac{b_{nU}}{1.5} \\ &= 0.69\,\frac{b_{nU}}{1.5} = 0.46\, b_{nU}\,. \end{aligned} \tag{4.15}$$

Since for the main dipole and quadrupole magnets, the uncertainty errors are assumed to be uncorrelated from arc to arc, with a confidence level of more than 99%, the bias induced is given by:

$$\langle b_{nU}\rangle = \pm\frac{3}{\sqrt{8}}\,\sigma\left[b_{nU}\right] = \pm\, 0.49 b_{nU}\,. \tag{4.16}$$

This relation will be of major interest, in particular to correctly interpret the specification concerning the uncertainty of b_2 and b_4 of the main dipole magnets. Indeed, due to the symmetry of the 2-in-1 design of the LHC dipole magnets both the systematic b_2 and b_4 errors have opposite signs in the inner and outer bores of the magnets. Because the particles of either beam travel an equal distance in the inner and outer apertures of the ring, these systematic errors inherent to the magnet design have no impact on the global beam observables such as the tune or the amplitude detuning, which is not the case for the uncertainty of b_2 and b_4.

4.5.2 Summary of the main dipole target field errors specifications

Concerning the injection optics, since the main dipoles occupy 66 % of the circumference of the LHC ring, they are the most demanding in terms of field quality while, in collision, the high β-function in the squeezed insertions makes the triplets and the separation-recombination dipoles D1/D2 the most critical magnets of the LHC ring (see Sec. 4.5.4). The performance of the main dipoles in terms of field quality have been analysed in detail in [33]. Starting from the expected field error table 9901 elaborated in 1999 by the Field Quality Working Group (see also [33, pp.65–67]) and based on criteria of a different nature such as the control of mechanical and dynamic aperture at injection and/or the correctability of the closed orbit, coupling and linear chromaticity up to 7 TeV. Hard limits have be found for the most critical multipoles and are reported in Tab 4.12. (More information on the field quality specification based on the DA evaluations can be found in Sec 4.7.3).
These specifications strongly depend on the misalignments of the different LHC components. The most sensitive ones are listed below.

- The tolerances on the multipoles a_1 and b_1 are directly linked to the positioning errors of the main quadrupole magnets in the LHC tunnel. According to [38], the quadrupole misalignments should not exceed 0.36 mm (rms) including the survey errors at installation and the effects induced by the ground motion after one year.

- The tolerance for the systematic b_3 component at injection is only based on the quadrupolar feed-down effects induced by the random misalignments of the MCS spool-piece with respect to the dipole. The latter have be specified to be lower than 0.5 mm (rms).

- The specification of the uncertainty of a_4 might be further tightened in case of systematic vertical misalignment of the b_5 spool-piece, MCD, of more than 0.3 mm.

Any deviation from these values could significantly relax or tighten the tolerances given for the field quality of the main dipoles. Inversely, if the field imperfections of the main dipoles significantly improve during the production, the above alignment tolerances could also be relaxed.
Finally, it is worth noting that the specification of 3 units for the systematic b_3 both at the end of the ramp (i.e close to 7 TeV with a maximum ramp rate of 10 A/s) and in collision, leaves a margin of 1.35 units for the MCS corrector strength at high field (see Tab. 3.1). In case of a failure of the MCS circuits in one or two sectors of the machine (for instance caused by repetitive quenches at high current of one single spool-piece per MCS circuit), this margin will just be sufficient to pursue the run of the LHC without requesting an intervention of 2 or 3 weeks to disconnect the pathological magnet.

Table 4.12: Specifications for the field quality of the main dipole magnets at injection, end of ramp and in collision (a_n and b_n given in units of 10^{-4} relative field error at a reference radius $R_{\text{ref}} = 17$ mm).

Harmonics a_n & b_n	Injection optics (450 GeV)	Injection optics (end of ramp)	Collision optics (7 TeV)	Systematic (max. value)	Uncertainty (max. value)	Random (r.m.s)	Criteria used
b_1	×	×	×	None	6.5	8.0	Closed orbit at injection and MCB strength at 7 TeV (with the MQ's misaligned by 0.36 mm r.m.s.)
a_1 (including MB roll angle)	×	×	×	6.5 (averaged per arc cell)		8.0	
b_2	×			1.4	0.8	0.7	β-beating and IP phasing
			×			0.8	
a_2	×	×			0.9	1.9	Vertical dispersion, linear coupling and MQS strength at 7 TeV
			×			2.3	
						1.6	
b_3	×			10.7 (including the		1.4	b_2 feed-down (with the MCS's misaligned by 0.5 mm r.m.s. w.r.t. the MB's) and DA at injection Correction of Q' and MCS strength at 7 TeV
			×	3.0 bias due to		none	
				3.0 uncertainty)		1.8	
a_3	×	×			1.5	0.7	Chromatic coupling inducing Q'' and MSS strength at 7 TeV
			×				
b_4	×			± 0.2 (from	0.4	0.5	DA and Q'' at injection, Detuning $\partial Q/\partial J$ and MCO strength at 7 TeV
			×	Table 9901)			
a_4	×				0.13	0.5 (from Table 9901)	DA at injection (considering the MCD's systematically) misaligned by 0.3 mm w.r.t. the MB's)
b_5	×			1.1 (including the		0.5	DA and Q''' at injection, Detuning $\partial^2 Q/\partial J \partial \delta$ and MCD strength at 7 TeV
			×	0.8 bias due to uncertainty)		0.4	
a_5	×				0.4	0.4 (from Table 9901)	Off-momentum DA at injection
b_7	×			$-0.3 < \langle b_7 \rangle < 0.1$		0.2 (from Table 9901)	DA at injection
a_6, b_6, a_7 and higher order multipoles	×			OK with the Error Table 9901			DA at injection

4.5.3 Main quadrupole and Short Straight Section assembly

The field quality of the elements of the short straight section (MQ, MQT, MS(S), MCB(H,V), MO) should be such that the effect on the relevant parameters is in the shadow of the effect of the main bending magnets. In this report the general procedure and the final results are reported, whereas details can be found in [33] and [39]. Two types of errors were considered: the field harmonic errors and the alignment errors. The cases considered are summarized in the following subsections.

Random b_2 errors in the MQ magnets

The effect of a random b_2 in the MQ has been analyzed numerically with the help of MAD [40]. A random b_2 error in the MQ magnets generates beta and dispersion beating. Mechanical aperture considerations [33] set the limits to 15% for the beta beating and 3.9 10^{-2} $m^{-1/2}$ for the normalized dispersion. Calculations with MAD for a random b_2 error of 10 units (target value in Tab 4.13 and 4.14) yield a maximum effect of 12 % for the beta beating and 2.6 10^{-2} $m^{-1/2}$ for the dispersion beating. Both values are within the tolerances.

Random b_3 errors in MQ magnets

The first order effect of a b_3 component in the MQ is the change of the chromaticity of the machine. This error can be compensated by the adjacent sextupoles MS. It has been verified that an error several times bigger than reported in the error Tab 4.13 and 4.14 can be correct with the sextupoles. The maximum allowed b_3 will be limited by DA considerations.

Multipoles higher than b_2 in the MQ magnets

The effect of the MQ higher order multipoles should not impact the reference dynamic aperture of 11.5 σ. This value is obtained by observing the behaviour of particles over 10^5 turns for 60 different MB error configurations as explained in 4.7 . The minimum DA for a machine without MQ errors and one with MQ errors has been compared : the MQ errors in Tab 4.13 and 4.14 do not significantly impact the dynamic aperture. However, tracking studies with slightly increased b_6 multipole errors showed a reduction of the DA indicating that the b_6 given in Tab 4.13 and 4.14 is at the limit of the acceptable field imperfections. Tab 4.13 and 4.14 summarize the MQ field errors which are referenced as error Table 0210.

Table 4.13: Normal Multipoles for MQ-table 0210. Columns 'p', 'g' and 'r' specify the persistent current, geometric and ramp induced errors respectively.

	mean			uncertainty			random		
n	p	g	r	p	g	r	p	g	r
1	0	0.483	0	0	0	0	0.747	0	0.941
2	-5.6	0	16.82	0.56	10	5.01	0.5	10	2.7
3	0	0.007	0	0	0.51	0	0.362	0.85	1.7
4	0	0.514	0.202	0	0.578	0	0	0.289	0.578
5	0	-0.005	0	0	0.246	0	0.133	0.231	0.246
6	-4.51	3.599	0.167	0.451	0.251	0.049	0.058	0.418	0.1
7	0	0	0	0	0	0	0	0.142	0
8	0	0.217	0	0	0	0	0	0.241	0
9	0	0	0	0	0	0	0	0.41	0
10	0.126	-0.418	-0.056	0.014	0.698	0.021	0	0.349	0
11	0	0	0	0	0	0	0	0.237	0

Tolerances on alignment

Tolerances from [38] are summarized in Tab 4.15

Table 4.14: Skew Multipoles for MQ-table 0210

	mean			uncertainty			random		
n	p	g	r	p	g	r	p	g	r
1	0	0	0	0	0	0	0.747	0	0.941
2	0	0	0	0	0	0	0	0	0.5
3	0	0	0	0	0.51	0	0.362	0.85	1.7
4	0	0	0	0	0.578	0	0.384	0.289	1.156
5	0	0	0	0	0.246	0	0.133	0.187	0.246
6	0	0	0	0	0.251	0	0	0.418	0.1
7	0	0	0	0	0	0	0	0.142	0
8	0	0	0	0	0	0	0	0.241	0
9	0	0	0	0	0	0	0	0.41	0
10	0	0	0	0	0	0	0	0.349	0
11	0	0	0	0	0	0	0	0.237	0

Table 4.15: Random and systematic alignment tolerances for the elements of the SSS

element	position x mm	position y mm	roll mrad
MQ	0.37	0.37	1.0 (r) / 0.3(s)
MS	1 (r) 0.1(s)	0.8 (r) 0.1(s)	1.5(r) 2.0(s)
MO	1.9 (r) / 0.16(s)	0.5 (r) / 0.1(s)	1.5(r) / 1.0(s)
CO			0.6

Higher order mutipoles in MQT,MS(S), MCB and MO

It has been verified that the multipoles generated by an error in coil positioning of 0.1 mm can be tolerated in the orbit correctors and in the sextupoles [39]. The maximum tolerable high order multipoles can be determined by rescaling from the MQ or the MB case with the following considerations:

- each MQ in the SSS is equipped with an MS or MSS. The MS(S) should not contribute to each multipole by more than 1% . Rescaling - over the integrated field at the reference radius - with respect to the target value in Tab 4.13 and 4.14 brings the value of Tab 4.16. The procedure is equivalent for MQT and MO.

- MCBH/V : due to the function of this corrector the rescaling is done with respect to the main bending magnets.

4.5.4 Insertion magnets

The approach used is not too different from the one applied for the main dipoles. Tolerances on the alignment of the insertion quadrupoles are given by considering the influence on closed orbit correctability (transverse misalignments and longitudinal tilt), coupling compensation and magnitude of spurious vertical dispersion (transverse tilt), beta-beating (longitudinal alignment). As far as the field errors are concerned, target intervals for the linear components (b_2, a_2) are found by imposing a bound on the beta-beating generated, while the ultimate criterium for determining the tolerances of the nonlinear field components is the outcome of detailed tracking studies. Normally, the field errors of the elements under study are compared to similar magnets for which tracking results are already known, taking into account the proper scaling given by the beta-functions. This is, for example, the case of the MQM, MQML, MQMC quadrupoles which are compared to the main quadrupoles requiring their contribution (to first order) be in the shadow of the main quadrupoles. Using these values as input for tracking allows the computations to be faster [41].

Table 4.16: Target field error tolerances for MQT, MS, MCB and MO units of the SSS assembly.

random	b1	b2	b3	b4	b5	b6	b7	b8	b9	b10	b11
MQT+MQS	1.34	18.02	1.66	0.52	0.481	0.76	0.26	0.43	0.74	063	0.43
MS+MSS	1.86	24.9	2.3	0.719	0.664	1.05	0.35	0.6	1.02	0.868	0.590
MO	9.59	128.6	12	3.817	3.576	5.73	1.96	3.37	5.81	5.02	3.41
MCBH/V	37.6	3.293	8.38	0.34	0.974	0.06	0.26	0.02	0.07	0.01	0.01
systematic	b1	b2	b3	b4	b5	b6	b7	b8	b9	b10	B11
MQT+MQS	0.869	-1.06	0.47	1.445	0.23	-1.18	0	0.39	0	0.103	0
MS+MSS	1.2	-1.47	0.65	1.997	0.318	-1.62	0	0.54	0	0.142	0
MO	6.2	-7.60	3.41	10.61	1.714	-8.87	0	3.03	0	0.819	0
MCBH/V	0	5.598	-14	0.052	2.766	-0.03	0.36	0.01	0.46	0	0.264
random	a1	a2	a3	a4	a5	a6	a7	a8	a9	a10	a11
MQT+MQS	1.34	0.00	1.66	0.87	0.41	0.75	0.26	0.43	0.74	6.28	4.27
MS+MSS	1.86	0.00	2.30	1.20	0.57	1.04	0.35	0.60	1.02	8.68	5.90
MO	9.59	0.00	12.03	6.35	3.07	5.68	1.96	3.37	5.81	50.16	34.06
MCBH/V	1.88	8.77	1.68	1.34	0.66	0.24	0.08	0.07	0.07	0.01	0.00
systematic	a1	a2	a3	a4	a5	a6	a7	a8	a9	a10	a11
MQT+MQS	0.00	0.00	0.46	0.52	0.22	0.22	0.00	0.00	0.00	0.00	0.00
MS+MSS	0.00	0.00	0.63	0.72	0.31	0.31	0.00	0.00	0.00	0.00	0.00
MO	0.00	0.00	3.32	3.82	1.65	1.70	0.00	0.00	0.00	0.00	0.00
MCBH/V	44.18	3.44	5.22	0.49	1.57	0.12	0.05	0.00	0.10	0.00	0.03

The detailed results of these studies can be found in [41, 42, 43, 44] here a qualitative summary of main conclusions is reported:

- MQM, MQMC, MQML [41]: these magnets are very similar to MQs not only as far as the mechanical structure is concerned, but also for the values of the optical functions. In the following we assumed the same field quality errors as for the MQ's (see Tabs. 4.13 and 4.14).

- MQY [41]: they are large bore quadrupoles, hence structurally different from MQs, and are located in regions where the beta-functions assume values larger than those in the arc-cell, both for the injection and collision optics. This implies that, at injection, the target values for the field quality are necessarily tighter than those of the MQs. At high-energy they should be compared, as far as the field errors are concerned, with the triplet quadrupoles with possibly some relaxed constraints due to the smaller beta-function than the triplet assemply.

- MQW [42, 43]: these warm quadrupoles are planned to be installed in the insertions 3 and 7. Saturation effects make the distance between the magnetic centre of the two quadrupole bores different from the nominal beam transverse separation, thus generating a dipole kick, inducing a closed orbit distortion. In addition, the dependence of saturation on beam energy induces a dynamic closed orbit distortion which however, seems not to be critical for the LHC operation and in particular, for the performance of the collimation system [42]. As far as higher order effects are concerned, the measured field errors [45] have been used in tracking studies and found to be compatible with the target value of dynamic aperture [43].

- D1/D2 [44]: the cold separation/recombination magnets have been studied in detail and their influence for the dynamic aperture evaluated using the expected error tables [46] to generate the nonlinear field errors. Also in this case, the error tables turned out to be compatible with the requirements on the value of the dynamic aperture.

Table 4.17: Multipole errors of the D1 magnet (main body).

n	Normal multipoles						Skew multipoles					
	Mean		Uncertainty		Random		Mean		Uncertainty		Random	
	p	g	p	g	p	g	p	g	p	g	p	g
1	0.0000	0.0000	0.0000	0.0000	0.0000	0.0000	0.0000	0.0000	0.0000	0.0000	0.0000	0.0000
2	-0.1088	0.1904	0.0000	0.5440	0.0000	0.1904	-0.2720	0.4080	1.5230	2.3596	0.1199	1.0540
3	-4.1431	-2.1825	1.9465	1.5860	0.3606	0.8416	0.1064	-0.1387	0.0000	0.2682	0.0000	0.0971
4	-0.0377	0.0220	0.0000	0.0786	0.0000	0.0283	0.0377	0.0063	0.1495	0.3396	0.0000	0.1321
5	0.0748	0.0599	0.0551	0.1732	0.0195	0.0877	0.0043	-0.0150	0.0000	0.0406	0.0000	0.0128
6	0.0189	-0.0189	0.0000	0.0174	0.0000	0.0058	0.0029	-0.0073	0.0000	0.0814	0.0000	0.0247
7	-0.1443	0.1058	0.0091	0.0198	0.0000	0.0109	0.0010	-0.0010	0.0000	0.0069	0.0000	0.0030
8	-0.0013	-0.0007	0.0000	0.0027	0.0000	0.0007	0.0000	-0.0007	0.0000	0.0101	0.0000	0.0034
9	0.0064	0.0014	0.0023	0.0055	0.0000	0.0023	0.0009	-0.0009	0.0000	0.0014	0.0000	0.0005
10	-0.0003	0.0016	0.0000	0.0019	0.0000	0.0006	-0.0006	0.0012	0.0009	0.0012	0.0000	0.0006
11	-0.0013	-0.0123	0.0006	0.0008	0.0000	0.0004	0.0000	-0.0002	0.0000	0.0004	0.0000	0.0002

Table 4.18: Multipole errors of the D1 magnet (lead end).

n	Normal multipoles						Skew multipoles					
	Mean		Uncertainty		Random		Mean		Uncertainty		Random	
	p	g	p	g	p	g	p	g	p	g	p	g
1	0.0000	0.0000	0.0000	0.0000	0.0000	0.0000	0.0000	0.0000	0.0000	0.0000	0.0000	0.0000
2	0.0952	-0.3196	0.0000	1.5368	0.0000	0.6732	-0.6596	-0.9656	0.0000	2.9036	0.0000	1.2036
3	-1.5953	10.3346	0.0000	1.3548	0.0000	0.5086	-0.0370	-4.5546	0.0000	0.4670	0.0000	0.1803
4	0.0031	0.0126	0.0000	0.2295	0.0000	0.0723	-0.0660	0.0283	0.0386	0.2358	0.0000	0.0912
5	0.0363	-0.0919	0.0252	0.1475	0.0000	0.0470	0.0064	0.4768	0.0167	0.0641	0.0000	0.0278
6	-0.0029	0.0029	0.0000	0.0422	0.0000	0.0174	-0.0044	0.0015	0.0159	0.0422	0.0000	0.0145
7	0.0138	0.0910	0.0000	0.0109	0.0000	0.0049	0.0030	-0.0850	0.0000	0.0129	0.0000	0.0059
8	0.0000	0.0000	0.0000	0.0040	0.0000	0.0020	0.0007	-0.0013	0.0000	0.0054	0.0000	0.0020
9	-0.0009	-0.0018	0.0000	0.0037	0.0000	0.0014	-0.0005	0.0114	0.0000	0.0023	0.0000	0.0009
10	0.0000	-0.0003	0.0000	0.0025	0.0000	0.0009	0.0000	-0.0003	0.0009	0.0012	0.0000	0.000
11	0.0000	-0.0013	0.0000	0.0006	0.0000	0.0002	0.0000	-0.0008	0.0005	0.0004	0.0000	0.0002

Table 4.19: Multipole errors of the D1 magnet (return end).

n	Normal multipoles						Skew multipoles					
	Mean		Uncertainty		Random		Mean		Uncertainty		Random	
	p	g	p	g	p	g	p	g	p	g	p	g
1	0.0000	0.0000	0.0000	0.0000	0.0000	0.0000	0.0000	0.0000	0.0000	0.0000	0.0000	0.0000
2	0.0136	0.1496	0.4555	1.2308	0.0000	0.4488	-0.8500	0.6188	0.5796	3.0600	0.0000	1.2988
3	-0.9849	2.8114	0.0000	1.2346	0.0000	0.5364	-0.0139	0.1341	0.0665	0.4763	0.0000	0.1572
4	0.0031	0.0000	0.0000	0.1132	0.0000	0.0503	-0.0755	0.0755	0.0000	0.2295	0.0000	0.0975
5	0.0321	0.0064	0.0000	0.1411	0.0000	0.0492	-0.0021	0.0000	0.0000	0.0663	0.0000	0.0235
6	-0.0073	0.0044	0.0000	0.0247	0.0000	0.0087	-0.0029	-0.0015	0.0000	0.0349	0.0000	0.0145
7	0.0099	-0.0040	0.0000	0.0129	0.0000	0.0059	0.0000	-0.0030	0.0000	0.0119	0.0000	0.0049
8	0.0000	-0.0020	0.0026	0.0047	0.0000	0.0020	0.0000	-0.0013	0.0000	0.0074	0.0000	0.0027
9	0.0000	-0.0078	0.0000	0.0037	0.0000	0.0014	0.0000	0.0000	0.0000	0.0023	0.0000	0.0009
10	0.0000	-0.0022	0.0000	0.0025	0.0000	0.0012	0.0000	-0.0006	0.0000	0.0031	0.0000	0.0016
11	0.0000	-0.0025	0.0000	0.0008	0.0000	0.0002	0.0000	0.0002	0.0000	0.0004	0.0000	0.0002

Table 4.20: Multipole errors of the MQWA magnet (left aperture (l) and right aperture (r) are given).

	Normal multipoles				Skew multipoles			
n	Mean		Random		Mean		Random	
	l	r	l	r	l	r	l	r
1	-227.8	-56.4	315.9	144.2	-115.2	-57.4	225.1	148.0
2	0.0	0.0	0.0	0.0	0.0	0.0	0.0	0.0
3	0.6	-0.1	6.3	1.8	-5.6	-3.5	3.6	7.6
4	1.3	1.7	0.7	0.8	0.4	0.0	0.4	0.8
5	3.0	-2.5	1.0	0.6	2.1	1.8	1.0	1.6
6	-0.2	-0.1	0.8	0.7	0.1	0.2	0.2	0.2
7	-0.3	1.2	0.3	0.5	-0.3	-0.5	0.1	0.1
8	0.0	0.0	0.1	0.2	0.3	0.3	0.1	0.2
9	0.0	0.0	0.0	0.0	0.0	0.0	0.0	0.0
10	0.8	0.8	0.1	0.1	0.1	0.0	0.0	0.1
11	0.1	0.1	0.0	0.1	0.1	0.0	0.1	0.1
12	0.0	0.0	0.0	0.0	0.2	0.0	0.1	0.0
13	0.1	0.1	0.1	0.0	0.0	-0.1	0.1	0.1
14	-0.2	-0.2	0.1	0.1	0.1	0.1	0.0	0.1
15	0.0	0.0	0.1	0.1	0.0	0.0	0.0	0.1

Table 4.21: Multipole errors of the MQWB magnet (left aperture (l) and right aperture (r) are given).

	Normal multipoles				Skew multipoles			
n	Mean		Random		Mean		Random	
	l	r	l	r	l	r	l	r
1	-413.90	243.70	242.60	215.10	-79.30	-128.90	256.00	185.30
2	0.00	0.00	0.00	0.00	0.00	0.00	0.00	0.00
3	-45.40	50.90	11.90	4.20	-5.20	-3.60	4.40	10.90
4	1.60	1.90	1.20	1.00	0.20	0.20	0.10	0.60
5	-0.20	1.20	0.90	0.70	2.10	1.80	0.90	2.00
6	-0.30	-0.30	0.60	0.70	0.20	0.20	0.10	0.20
7	0.90	-0.40	0.40	0.40	-0.40	-0.50	0.10	0.20
8	0.10	0.10	0.00	0.10	0.30	0.40	0.30	0.20
9	0.00	0.00	0.00	0.00	0.00	0.00	0.00	0.00
10	0.90	0.90	0.10	0.00	0.00	0.10	0.30	0.00
11	0.00	0.20	0.10	0.10	0.10	0.00	0.20	0.10
12	-0.10	-0.10	0.00	0.10	0.10	0.10	0.10	0.00
13	0.20	-0.10	0.00	0.10	0.00	0.00	0.10	0.10
14	-0.20	-0.20	0.10	0.10	0.10	0.00	0.10	0.00
15	0.10	0.00	0.10	0.00	0.00	0.00	0.00	0.00

The influence of the MQM, MQML, and MQMC elements, as well as the wide aperture quadrupoles MQY was tested in view of defining target errors complying with the requirements of the dynamic aperture. In order to distinguish between the contribution of the different elements, a tracking campaign was launched where the various types of elements are included one after the other. Two variants of the optics of IR8 have been considered, the difference being the maximum horizontal beta function. The results are summarised in Tab. 4.23 and show that tighter specifications have to be defined more for the target errors of the MQM and MQY elements than the MQs. In all cases we assumed the same error distributions for all the quadrupole types. The loss of dynamic aperture is due to the large value of the beta-functions at the locations of the MQM quadrupoles (IR8) and MQY (IR4 and IR6). The main results can be summarized as follows:

- The field errors of the cold D1 / D2 are in the shadow of the main dipole and quadrupole field errors at injection.

- Using an injection optics with $\beta_{max} \approx 500$ m in one single MQM quadrupole in IR8 and assuming the same field errors for the MQM magnets as for the arc MQ magnets shows a significant reduction of the minimum DA at injection indicating that the field quality of the insertion MQM quadrupole magnets must be better than that of the arc quadrupole magnets. Using an optics with $\beta_{max} \leq 400$ m the reduction of the minimum DA is not significant (e.g. within the resolution of the dynamic aperture tracking studies).

- Assuming the same field errors in the wide aperture MQY insertion quadrupole magnets as for the main arc (MQ) quadrupole magnets yields a significant reduction in the minimum DA at injection. This result indicates that the field quality of the insertion MQY quadrupole magnets must be better than that of the arc quadrupole magnets. At top energy the field quality specification should be comparable to the field quality specification of the low-β triplet quadrupole magnets (comparable β-function values).

4.6 SPECIAL OPTICS SOLUTIONS

4.6.1 Alignment Optics

The determination of the triplet misalignment by means of the beam, using an optics with the triplet turned off, can be used as a complementary method for its alignment. This technique was investigated for LEP in 1993 [47] and 1995 [48] (summary in [49]). It was not used in practice for LEP because the vertical misalignment of the low-β quadrupoles could be followed easily with a sufficient accuracy by hydraulic means. The case of LEP was quite simple as there were only two vertically focusing quadrupoles contributing to the machine performance (the horizontal misalignment by the survey was sufficient). For LHC the problem is more complicated as both planes have an equal importance. However this does not mean that both LHC planes should be realigned with the same accuracy as the LEP vertical plane. A bad closed orbit correction in physics results essentially in a parasitic dispersion and a β-beating. It is sufficient that they do not increase the beam size at the interaction point and do not make synchro-betatron resonances due to a non-zero dispersion at the IP.

The LHC triplets are the main contributor to the closed orbit distortion. They must be sufficiently well aligned not to overload their correctors. The triplet corrector strength is 1.5 Tm, while the nominal integrated gradient of a single Q2 is 1306 T. The corrector can just compensate a displacement of 1.1 mm of a single Q2. This shows the importance of the relative alignment of the triplet quadrupoles.

By means of the K-modulation it is possible to determine the misalignment of the average axis of a quadrupole with respect to the neighbouring BPM's within 0.05 mm [50]. Therefore the relative misalignment of the triplet quadrupole can be checked by means of the alignment optics provided the beam reference can be well established.

If the triplets are turned off, the value of the β-functions cannot be reduced below 550m because of the large drift space between the Q4 quadrupoles. This is a situation similar to that of IR6 [25]. As the maximum possible value of the β-functions in the insertion quadrupoles is 300m due to an aperture limit with the nominal beam, this optics can only be used with a normalized beam emittance 2.0 10^{-6}m. Such an emittance can be achieved easily by merely scraping the beam in the injectors [51].

This large value of the β-functions has another consequence that the phase advance in the region around the IR is much smaller than in the nominal optics. It is possible to partially recover this phase change, so that the tunes can be set one unit below the nominal values (Qx=63.28, Qy=58.31) if this alignment optics is set both in IR1 and IR5. The optics functions are shown on the left-hand side of Fig 4.30. The dispersion function is not set to zero at the interaction point as the tunes have been adjusted with QF and QD. This is unimportant as long as the maximum value of the β-functions in the insertion is not increased significantly. It is also possible to turn off Q5 and Q6 on both sides of the insertion. In this case, the value of the β-functions cannot be reduced below 800 m. This optics solution is shown on the right-hand side of Fig 4.30. According to the requirement at injection, the emittance has to be reduced to 1.4 10^{-6}m. This is a little more than the commissioning emittance, it can be achieved easily as said above.

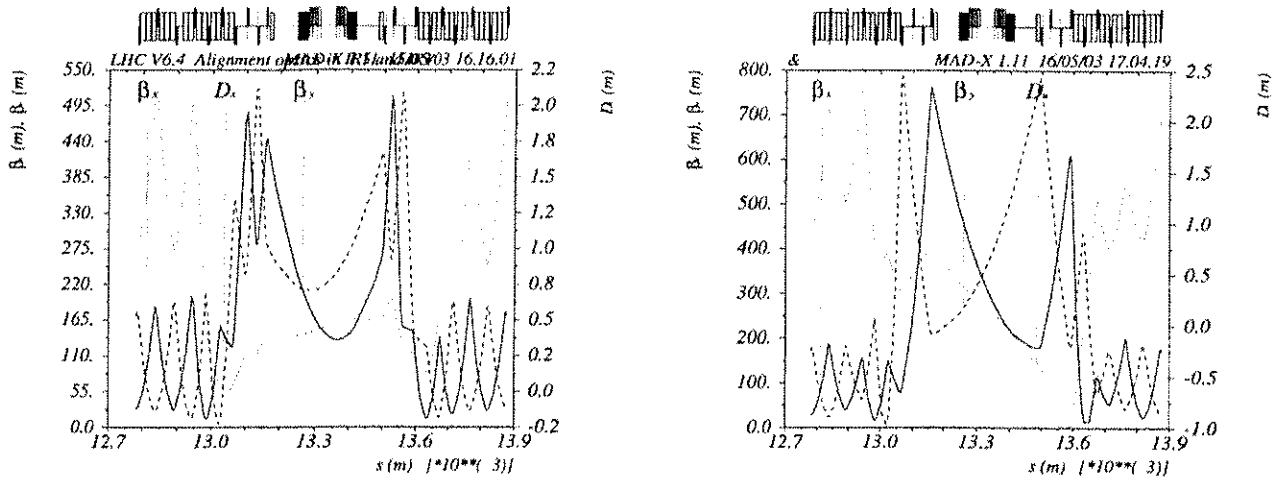

Figure 4.30: LHC alignment optics with the triplet turned off. Left: with powering of all other insertion quadrupole magnets. Right: without powering of Q5 and Q6.

For this optics the phases cannot be restored as there are not enough parameters to do it. The tunes Qx=63.72 (symmetric of the nominal tune with respect to the integer) and Qy=58.28 are obtained by changing the gradients in the main quadrupoles at the expense of introducing a β-beating of the order of one percent.

4.6.2 Resonance Free Lattices

The case where the systematic multipole components are larger than $\sim$3 limits the machine performance. This might be either because the field errors are larger than expected or because there are no correction circuits planned for the multipole type at hand. A resonance-free lattice can be used to increase the dynamic aperture. The idea behind such an optics is to adjust the phase advances per cell so that the driving terms of most non-linear resonances cancel in each arc [52]. For the LHC there are two possibilities:

- The horizontal phase advance per cell is $\frac{7}{25} \cdot 2\pi$ and the vertical one is $\frac{6}{25} \cdot 2\pi$. The associated total tunes including the insertions are Qx=68.28, Qy=59.31. The resonance free optics does not satisfy the aperture requirements in the arcs (see Sec. 4.3) and it has not been chosen as the base line optics. However, it could be run with a beam emittance reduced by 2 % and therefore presents an attractive backup solution in case the machine operation indicates performance limitations due to the systematic field errors.

  This lattice is free from resonances up to order 8 with the exception of the skew resonance 3Qy+Qx. In particular it has the nice feature of cancelling the second order chromaticity due to the systematic a_3 component.

- The horizontal phase advance per cell is $\frac{6}{25} \cdot 2\pi$ and the vertical one is $\frac{5}{25} \cdot 2\pi$. The associated total tunes including the insertions (with different insertion solution as for the previous case) are Qx=59.28, Qy=51.31. This lattice is free from resonances up to order 5. It also has the nice feature of cancelling the second order chromaticity due to the systematic a_3 component but is not limited by the mechanical aperture.

The fractional part of the tune can be adjusted by means of the phase advances over IR4 and IR6 for both cases. It has been shown that about two σ's of dynamic aperture can be gained for the case where the systematic octupole component is multiplied by a factor of three [53].

The benefits of the resonance-free lattice are preserved as long as the relative random gradient errors in the dipoles are smaller than 2×10^{-4} (three times the nominal value) [54].

4.6.3 Large β^* optics solution

The measurement of elastic scattering needs a high-β insertion so that the scattered protons have a trajectory far enough from the beam [55]. Several high-β insertions have already been studied for LHC [56][57]. The proposal made before 2003, based on the constraint that the elastic scattering measurement was done close to D2 in the vertical plane and close to Q6 in the horizontal plane, features a quasi doublet optics [57]. It has the drawback of needing special power supplies for the Q1 quadrupole in each triplet (the connections remain standard), as well as a high current switch.

The present optics generates $\beta^* = 1540$ m without the need for a special trim power converter. The optics is shown in Fig 4.31. The vertical phase advance at the detector placed close to Q6 (220 m from the IP) is $\pi/2$ and the horizontal phase advance is $\pi/2.1$. It has been checked that this is quite acceptable for the elastic scattering measurement.

The required luminosity is low, of the order of $2 \times 10^{29}\text{cm}^{-2}\text{s}^{-1}$, as the event cross section is large. Using 156 bunches per ring, the bunches are injected in batches of four. (Alternatively the TOTEM operation can use 43 bunches where the bunches are injected one by one resulting in a lower total luminosity of approximately $10^{28}\text{cm}^{-2}\text{s}^{-1}$.

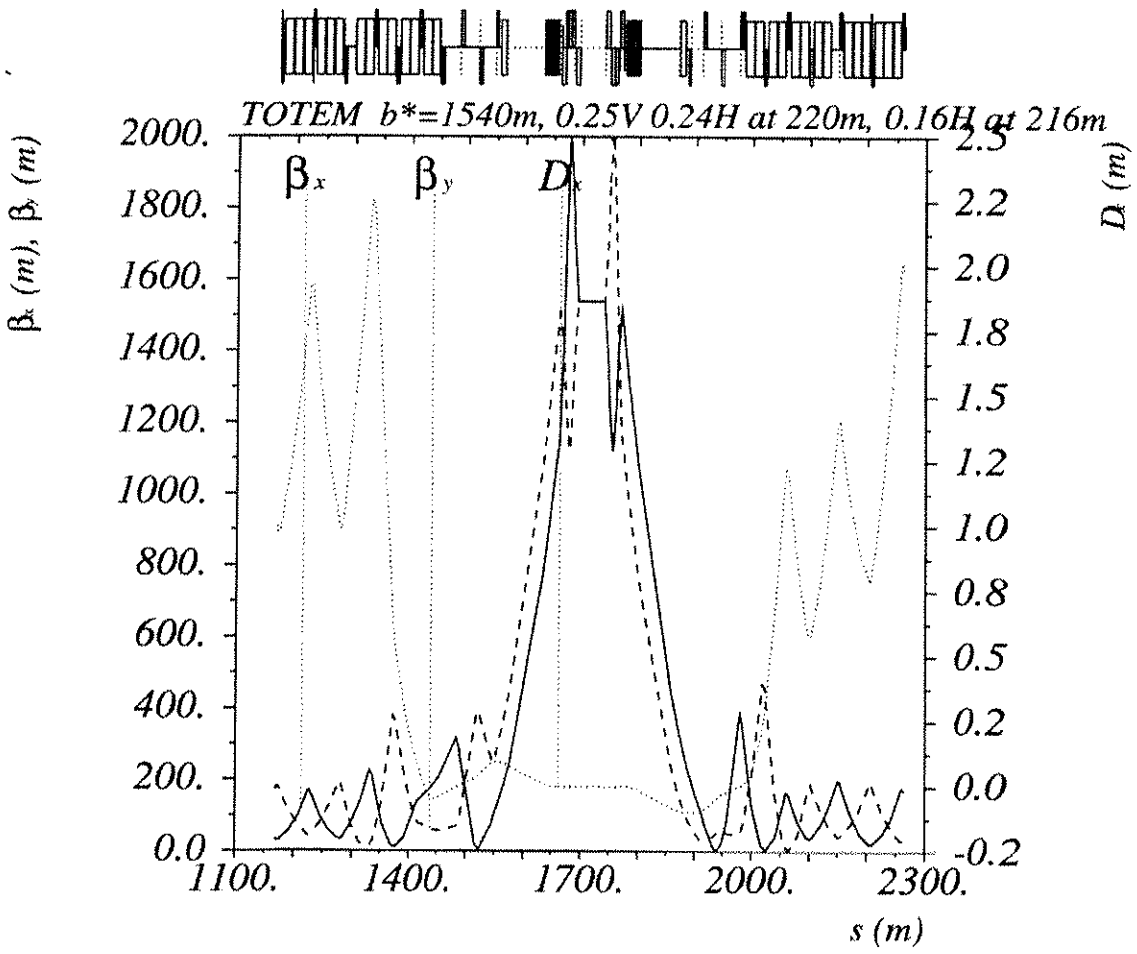

Figure 4.31: The TOTEM optics in IR5.

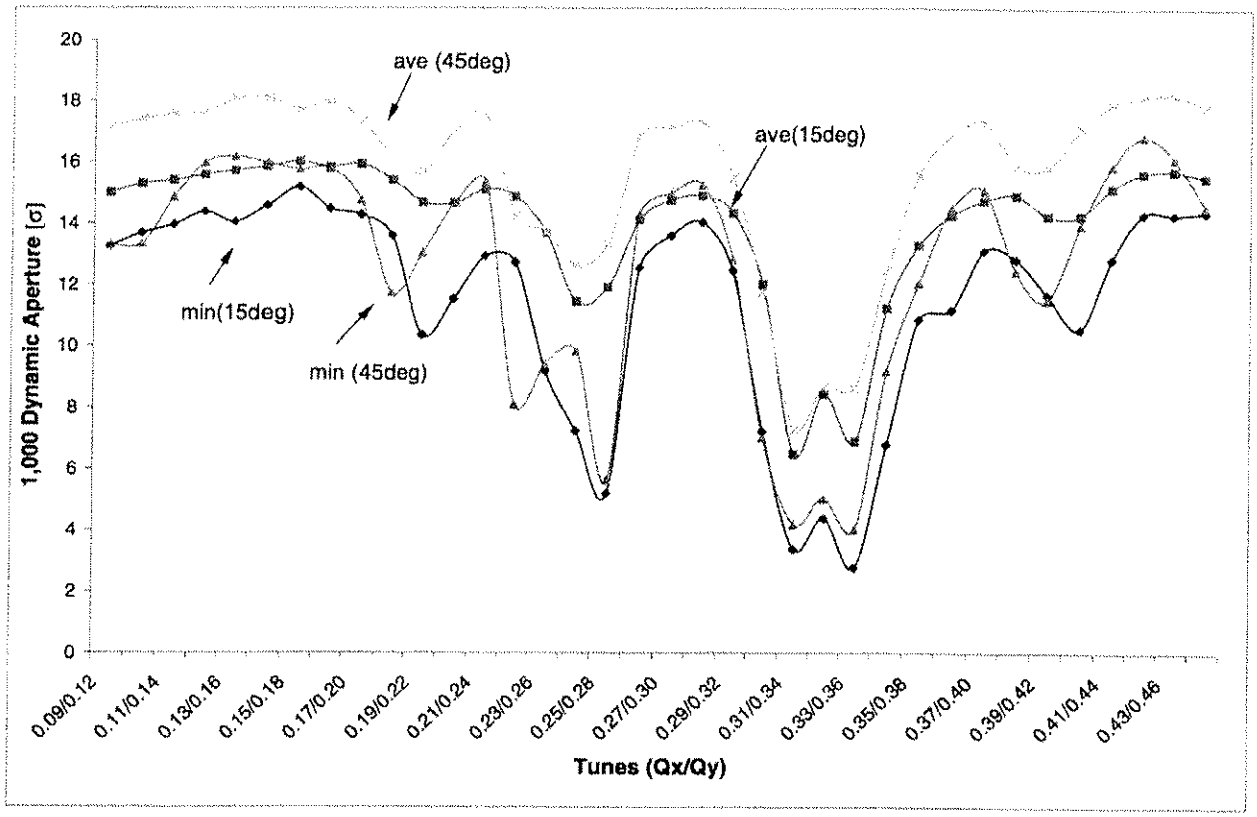

Figure 4.32: The 1000 turn DA as a function of the fractional tune for fixed distance to the (1:-1) coupling resonance.

4.7 DYNAMIC APERTURE

4.7.1 Tracking the LHC lattice

The dynamic aperture (DA) of the LHC is evaluated with the help of the SixTrack [59] simulation program. The input files for the fast tracking are generated via MAD-X [40] which is also used for the developement of the LHC optics. The dynamic aperture is defined as the maximum radius for which the particles are stable. The dynamic aperture depends on the number of turns that the simulations have been carried out for. For each phase space angle the minimum dynamic aperture is taken from 60 different sets of error distributions called seeds, in the following. This number of seeds allows the lower bound of the DA to be found with a 95% probability [60]. The phase space angle is defined as $\phi = \arctan(\sqrt{J_y/J_x})$, with ϕ =15°, 30°, 45°, 60° and 75°, where J_y and J_x are the vertical and horizontal single particle action variables [61] respectively.

The chaotic behavior of lost particles makes it impossible to predict their survival time. A typical survival plot is shown in Fig. 4.34. This also implies that the tracking mesh has to be sufficiently small to find the minimum value of the DA. For the LHC, the studies are typically performed over ranges of 2σ, each being subdivided into 30 amplitude steps. Fig. 4.32 shows the 1000 turn DA for the LHC injection optics as a function of the fractional tunes for a fixed separation between the horizontal and vertical tunes [32]. The results of such short term simulation studies have been used for optimizing the fractional part of the baseline tunes and evaluating the operational margins for the tune control at injection (see Sec. 4.4). All dynamic aperture values quoted for the LHC in the remaining part of this section are evaluated for 10^5 turns. Such intensive simulation studies have only been possible with the help of dedicated computing support [62].

Table 4.22: *Relation between target and D.A. calculated for* $x_i/y_i = 1$.

Source or Uncertainty	Impact	D.A. in σ
Target for tracking 10^5 turns		12
Finite mesh size	-5%	
Linear Imperfections[a]	-5%	
Amplitude ratio x_i/y_i plane	-5%	
Extrapolation to 4 10^7 turns	-7%	9.4
Time dependent multipoles	-10%	
Ripple	-10%	7.5
safety margin	-20%	6.0

[a] The DA reduction of 5% assumes an RMS orbit error of 0.5 mm. For an RMS orbit error of 1 mm the DA reduction can reach up to 10%.

4.7.2 Dynamic Aperture Safety Factor

Although there is a large arsenal of theoretical tools and fast tracking techniques and computers available [62], it remains impossible to track all relevant effects for sufficiently long times. Even with present day computers it is not possible to perform a full scale simulation over 4×10^7 turns, which corresponds to 1h of beam storage time. The DA obtained from simulations is typically 20% too optimistic when compared with dedicated beam experiments at several accelerators. Therefore, to ensure that particle motion is sufficiently linear at an amplitude relevant for the collimation system, i.e. roughly 6 σ, we estimate that the simulated DA should be a factor 2 larger. That this factor is valid in the absence of the very strong beam beam interaction which should be treated separately.

Typical simulation runs for the LHC DA are for 10^5 turns with non-linear field errors only, with empirical tune and chromaticity correction, and a 'perfect' powering of the non-linear lattice spool piece circuits based on the error distribution in the main dipole magnets. Tab 4.22 explains the different contributions which enter into this 'extrapolation' factor [63]. The DA reduction due to the linear imperfections and due to an imperfect spool piece circuit powering, have been studied in Ref. [35] and [36]. Assuming a perfect b_4 spool piece powering the linear field errors (quadrupole misalignment and closed orbit correction to 1 mm rms plus b_2 errors to generate a β-beat between 25 % and 35 %) reduce the minimum DA from 11.7 σ to 11.3 σ. Without b_4 correction via the b_4 spool piece circuits the same errors reduce the minimum DA from 11.2 σ to 9.6 σ. The DA reduction due to errors in the spool piece circuit powering is shown in Fig. 4.33. Depending on the spool piece circuit and the mispowering error scenarios the minimum DA can drop by, is up to 30 %.

Taking a conservative approach these contributions are added linearly. The 'finite mesh size', 'amplitude ratio' and the 'extrapolation' reflect the limited computing capacity which limits the speed of the computation and how fine a simulation mesh can be chosen. It is known from existing hadron storage rings that there are effects that limit the performance of any new machine. It is very hard to predict by how much the LHC will suffer from lattice imperfections, power supply ripple and transient effects. Finally a 20% margin is taken as a measure of the lack of predictability of tracking simulations. In the absence of beam-beam interaction the target DA for the simulations should therefore be about 12 σ.

4.7.3 Dynamic Aperture at Injection and Collision

Tab 4.23 and 4.24 summarize the dynamic aperture results for the LHC studies at injection and collision energy with luminosity optics respectively. Fig. 4.35 shows the case of non-linear main dipole, main quadrupole and warm quadrupole field errors as an example of the tracking results as a function of the angle of initial amplitudes. All tracking studies presented in this Chapter have been done with nonlinear field errors up to a_{11} and b_{11} and include tune and chromaticity (target $Q' = 2$), linear and chromatic coupling, b_3, b_4 and b_5 corrections. While tracking simulations provide the most accurate evaluation of the DA the tracking results as such are not well suited for guiding the evolution of the field quality specification in case of an insufficient DA [64]. The LHC tracking studies have therefore been complemented by studies on DA limitations due to single selected multipole components [65][66] and their first-order resonances (or sub-resonances) [7] and [8]

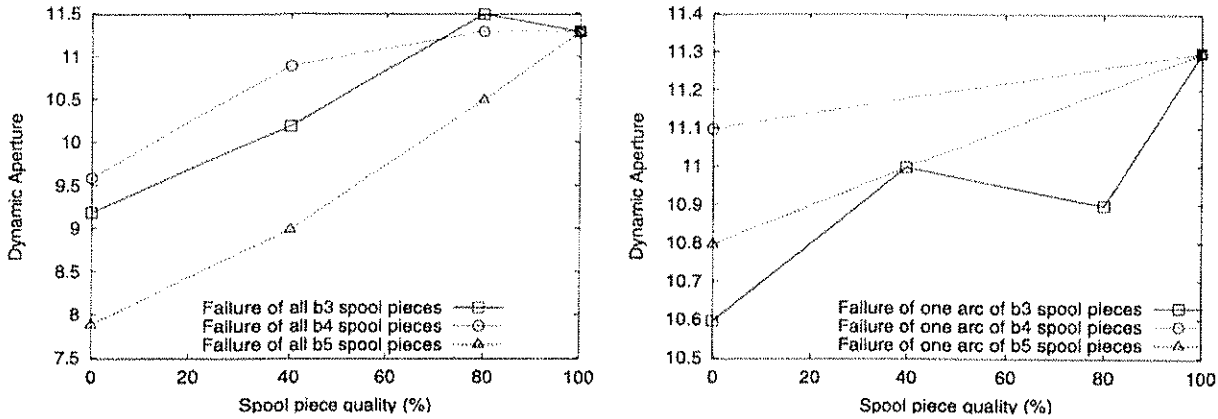

Figure 4.33: The minimum dynamic aperture (in units of the RMS beam size) as a function of b_3, b_4 and b_5 spool piece quality at injection. 100 % represents full correction and 0 % none. The chromaticity ($Q^{'}$) and the tunes are corrected to their nominal values in all cases using the lattice sextupole and tuning quadrupole circuits. Left: mispowering of all spool piece circuits. Right: mispowering of the spool piece circuits in the arc between IR2 and IR3.

and by frequency map, resonance strength and diffusion speed analysis [67]-[69] and other 'indicators' for the DA [70][71]. A summary of the different methods for calculating the DA can be found in [72] and a selection of references for the DA tracking studies at injection energy can be found in [73].

All results shown in Tab. 4.23 just satisfy the goal of a 12 σ DA for 10^5 turn tracking within the resolution of the numerical simulations (± 0.5 σ) indicating that the specified field errors are at their acceptible limits. The fact that the last case in Tab 4.23 for the cross section 2 is only 11.2 σ is related to the fact that the systematic b_5 and b_7 field errors are outside the specification of 1.4 and 0.33 units instead of 1.1 and 0.1 units respectively. All other multipoles, random and systematic, meet the specifications given in [33].

The nominal correction scheme of the low-beta triplet errors has been investigated for the LHC V6.2 in collision but without beam-beam interactions. Fig. 4.36 shows the average and minimum dynamic apertures among the 60 seeds for 10^5 turn tracking. The triplet errors reduce the average and minimum dynamic aperture to 12.9 σ and 8.8 σ respectively. This is mainly due to the large b_6 component of the triplet errors. After applying the local triplet corrections of b_3, b_4, b_6, a_3 and a_4 as described in Ref. [74], the average and minimum dynamic aperture increase to 16.8 σ and 12.9 σ respectively, i.e. larger by some 4 σ. We can therefore conclude that the triplet correction scheme is indeed effective for LHC lattice version V6.2.

In collision the DA is dominated by the beam-beam interactions and the goal for the field error specification is to keep the DA due to the magnet field errors in the shadow of the beam-beam interactions. The target DA for the 10^5 turn tracking for collision configuration is 10 σ. In collision the triplet errors are considered with and without their corrections and the D1/D2 field errors are treated without correction by the triplet corrector system. A comparison of these cases shows that the cold D1/D2 field error are in the shadow of the triplet field errors and that the triplet field errors are only relevant for $\beta^* \leq 0.75$ m [75]. For $\beta^* \geq 0.75$ m the DA is above 10 σ even without triplet field error correction. Studies including the beam–beam interactions are discussed in detail in Chap. 5.

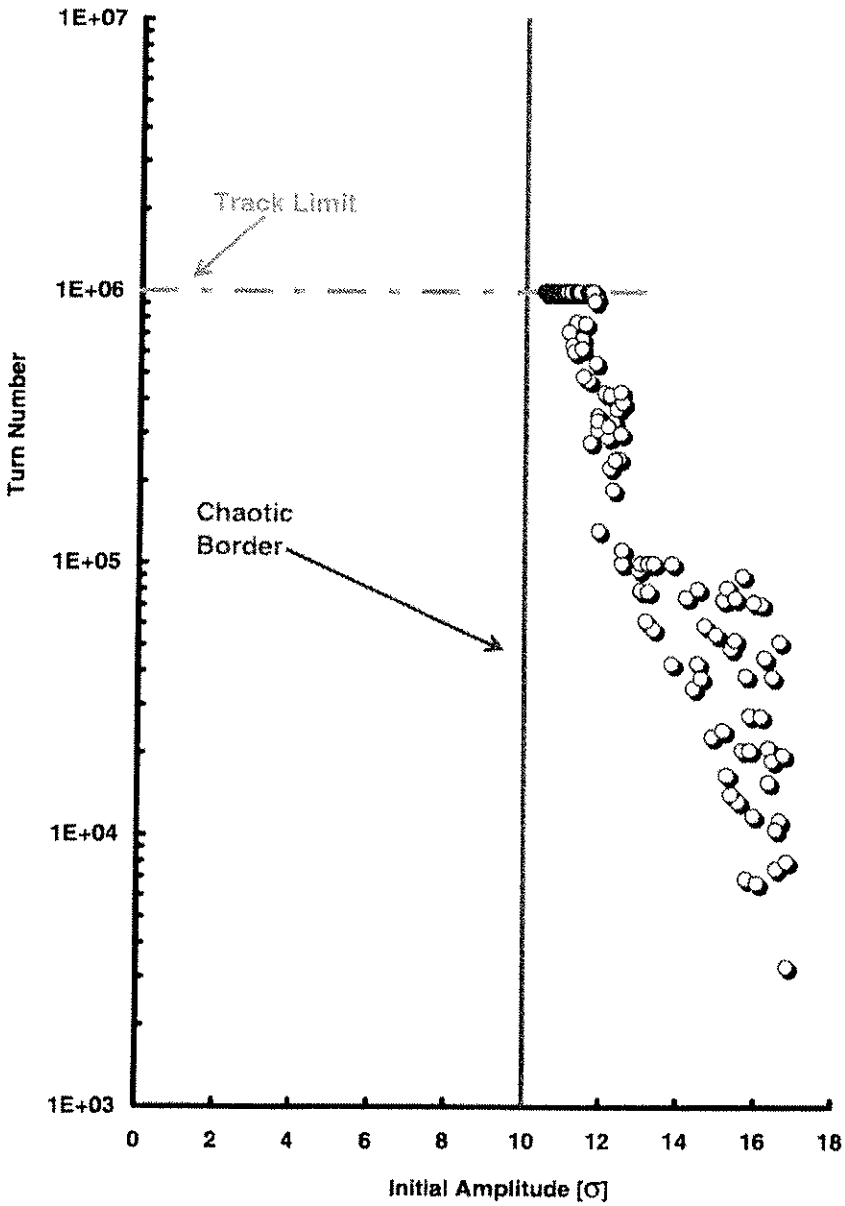

Figure 4.34: Typical Survival Plot

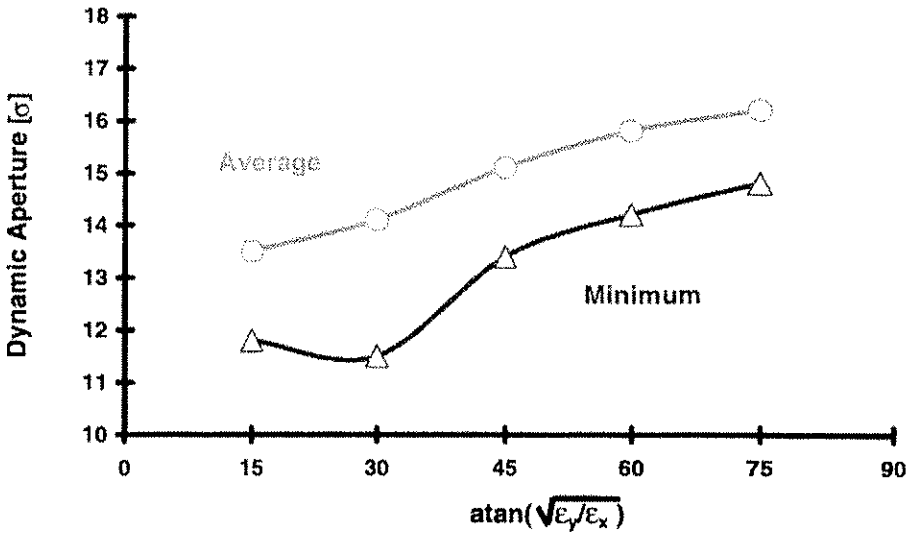

Figure 4.35: Average and minimum dynamic apertures of LHC V6.4 including realistic errors of the warm Quadrupoles MQW, the tracking has been performed for 10^5 turns.

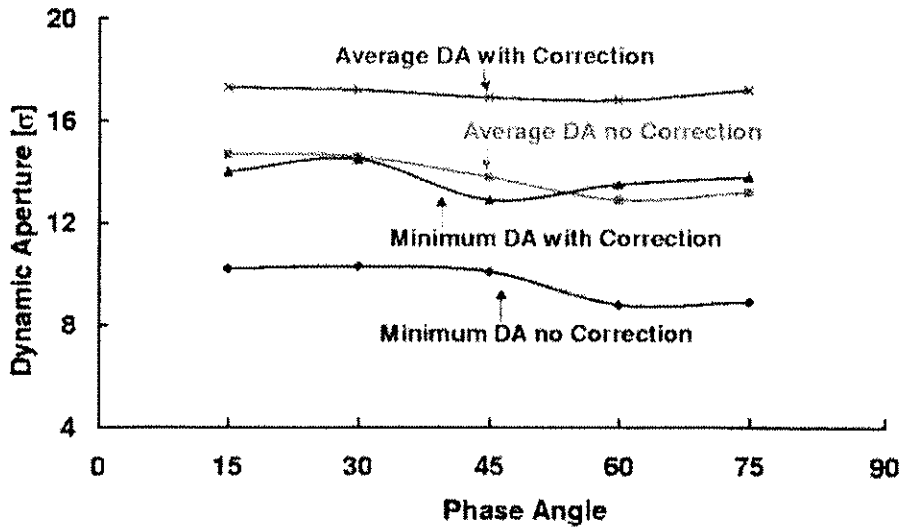

Figure 4.36: Average and minimum dynamic apertures with and without the correction of low–beta triplet field errors. The beam–beam interaction is not included and the tracking has been performed for 10^5 turns.

Table 4.23: Average and minimum 10^5 turns dynamic aperture at injection energy for 5 phase space angles $\phi = \arctan(\sqrt{J_y/J_x})$ of the phase space. All simulations were done for 60 seeds with lattice corrector circuit powering and refer to LHC injection optics Version 6.2 or 6.4 with nominal tunes $Q_x = 64.28$ and $Q_y = 59.31$.

Dyn. Aper. [σ]	15°	30°	45°	60°	75°
LHC V6.2, Error table 9901 [76] with errors in the MB and MQ elements					
Minimum	11.8	11.8	13.4	13.9	15.0
Average	13.3	13.6	15.3	15.5	16.1
LHC V6.2, Specification table [33] with errors in the MB and MQ elements					
Minimum	11.5	11.6	12.4	12.9	14.5
Average	12.7	13.1	$\geq$ 13.9	$\geq$ 14.0	$\geq$ 14.6
Minimum	9.3	10.1	11.4	11.1	11.7
Average	11.3	12.0	12.7	12.9	12.7
LHC V6.4, Field error expected after the production of 60 collared coils (X-section 2) with errors in the MB and MQ elements [77], [78]					
Minimum	**11.2**	12.0	13.3	15.2	14.8
Average	12.2	13.4	14.7	16.8	15.9
LHC V6.4, Error table 9901 [76] with errors in the MB and MQ elements plus field errors in warm quadrupole magnets [44]					
Minimum	11.7	11.2	13.0	13.8	14.3
Average	13.5	14.0	$\geq$ 15.0	$\geq$ 15.6	$\geq$ 16.0
LHC V6.4, Specification table [33] with errors in the MB and MQ elements plus field errors in the cold D1 and D2 dipole magnets [41]					
Minimum	11.3	12.2	13.9	16.3	15.5
Average	12.2	13.7	14.8	17.3	16.3
LHC V6.4, Specification table [33] with errors in the MB and MQ elements plus field errors in the cold D1 and D2 dipole and the MQM insertion quadrupole magnets using an IR8 optics with $\beta_{\max} = 500$ m at one MQM location (Q6) [41]					
Minimum	10.3	11.5	13.4	14.7	14.0
Average	12.0	13.2	14.5	16.3	15.2
LHC V6.4, Specification table [33] with errors in the MB and MQ elements plus field errors in the cold D1 and D2 dipole and the MQM insertion quadrupole magnets using an IR8 optics with $\beta_{\max} \leq 400$ m at one MQM location (Q6) [41]					
Minimum	10.8	11.9	13.5	14.9	14.1
Average	12.2	13.3	14.6	15.9	15.0
LHC V6.4, Specification table [33] with errors in the MB and MQ elements plus field errors in the cold D1 and D2 dipole and the MQM and MQY insertion quadrupole magnets [41]					
Minimum	9.27	10.1	11.4	11.1	11.7
Average	11.3	12.0	12.7	12.9	12.7

Table 4.24: Average and minimum 10^5 turns dynamic aperture at collision energy for 5 phase space angles $\phi = \arctan(\sqrt{J_y/J_x})$ of the phase space. All simulations are done for 60 seeds with different field error sources and correction schemes and refer to LHC collision optics Version 6.2 or 6.4 with nominal tunes Q_x =64.31 and Q_y =59.32.

Dyn. Aper. [σ]	15°	30°	45°	60°	75°
LHC V6.2, $\beta^* = 0.5$ in IR1 and IR5 with triplet field errors and NO correction [74]					
Minimum	10.2	10.3	10.1	8.8	8.9
Average	14.7	14.6	13.8	12.9	13.2
LHC V6.2, $\beta^* = 0.5$ in IR1 and IR5 with triplet field errors and correction [74]					
Minimum	14.0	14.5	12.9	13.5	13.8
Average	17.3	17.2	16.9	16.8	17.2
LHC V6.4, $\beta^* = 0.5$ in IR1 and IR5 and $\beta^* = 1.0$ in IR8 with triplet, MB, MQ and cold D1 and D2 field errors and b_3, b_4 and b_6 triplet field error correction (no correction for a_3 and a_4[44])					
Minimum	12.3	11.7	10.8	10.8	11.0
Average	14.7	14.4	14.1	14.0	14.1
LHC V6.4, $\beta^* = 0.5$ in IR1 and IR5 and $\beta^* = 1.0$ in IR2 with triplet and cold D1 and D2 field errors [44] and triplet field error correction					
Minimum	11.5	11.5	10.8	10.3	11.3
Average	15.4	15.0	14.1	14.4	15.1
LHC V6.2, $\beta^* = 0.5$ in IR1 and IR5 with triplet field errors and beam-beam interactions: NO triplet correction [74]					
Minimum	**6.6**	6.1	7.0	7.5	7.9
Average	8.4	8.4	8.7	8.6	9.2

REFERENCES

[1] Baseline chage request 53 approved by the U.S. LHC collaboration by summer 2003. An Engeneering Change Request is currently (August 2003) under preparation at CERN.

[2] A. Faus-Golfe et al, 'A more robust and flexible lattice for LHC', Proceedings for the 1998 European Particle Accelerator Conference, Stockholm Sweden, June 1998

[3] W. Scandale, 'Revisiting the Problem of the LHC Insertion Symmetry', CERN SL/Note 94-42 (AP), April 1994

[4] A. Faus-Golfe et al, 'Modular opticsal design of the LHC experimental insertions', Proceedings for the 1996 European Particle Accelerator Conference, Sitges Spain, June 1996

[5] J.P. Koutchouk, Alternative magnetic Optics for LEP1, CERN SL/91-23(DI), Chamonix 1991

[6] Jean-Pierre Koutchouk, 'Decoupling of a strongly coupled lattice with an application to the LHC', LHC Project Report 15, July 1996

[7] R. Talman, 'Tune optimization for maximum dynamic acceptance, 1, formulation', LHC Project Report 197, July 1998

[8] R. Talman, 'Tune optimization for maximum dynamic acceptance, 2: Qx=65, Qy=58', LHC Project Report 233, August 1998

[9] A. Verdier, 'Resonance free lattices for A.G. machines', Proceedings of the 1999 Particle Accelerator Conference, New-York, U.S.A, 1999

[10] D. Kaltchev, F. Schmidt and A. Verdier, 'Robustness of Resonance free lattices against gradient errors', LHC Project report 475, August, 2001

[11] O. Brüning, W. Herr and R. Ostojic; *A beam separation and collision scheme for IP1 and IP5 at the LHC for optics version 6.0*, LHC Project Report 315 CERN, (1999).

[12] O. Brüning, W. Herr and R. Ostojic; *A beam separation and collision scheme for IP2 and IP8 at the LHC for optics version 6.0*, LHC Project Report 367 CERN, (1999).

[13] V. Baglin, I. Collins and N. Kos, Beam Screens for the LHC Long Straight Sections, Functional Specification EDMS doc. 334961, LHC-VSS-ES-0002 rev 1.0, Geneva, CERN (April 2003).

[14] O.S. Brüning, Optics Solutions in IR1 and IR5 for Ring-1 and Ring-2 of the LHC Version 6.0, CERN-LHC-Project-Note-187, Geneva, CERN (April 1999).

[15] O. Brüning; *Optics solutions in IR2 for Ring 1 and Ring 2 of the LHC Version 6.0*, LHC Project Note 188 CERN, (1998).

[16] 'LHC Version 6.4: Layout of the DFBAs in the Insertion Regions', ECR LHC-LS64-EC-0002

[17] J.B. Jeanneret, CERN LHC Project Note 115,1997.

[18] T. Trenkler and J.B. Jeanneret, The principles of two-stage betatron and momemtum collimation in circular accelerators, Part.Acc., **50** , (1995) 287, January 1995.

[19] J.B. Jeanneret, Phys.Rev. ST-AB, **1**, 081001, Dec. 1998.

[20] D.I. Kaltchev et al., CERN LHC Project Report 134 and PAC1997,1997.

[21] D.I. Kaltchev et al., CERN LHC PRoject Report 305 and PAC1999,1999.

[22] D.I. Kaltchev et al., CERN LHC PRoject Report 194 and EPAC98,1998. CERN,1997.

[23] A. Verdier, A tunable insertion for point 4 in LHC. LHC Project Note 93 (June 1997).

[24] A. Verdier, Phases between IP's and non-linear chromaticity. LHC Project Note 103 (August 1997).

[25] A. Verdier, The LHC IR6 optics. LHC Project Note 146 (June 29, 1998).

[26] J.-B.Jeanneret and T.Trenkler, The principles of two stage betatron and momentum collimation in circular accelerators, LHC Note 312

[27] T. Risselada, Optical Requirements for an LHC Cleaning Insertion with Elliptical Collimators, SL/Note 95-67 (AP)

[28] O. Brüning; *Optics solutions in IR8 for Ring 1 and Ring 2 of the LHC Version 6.0*, LHC Project Note 188 CERN, (1998).

[29] J.B. Jeanneret and R. Ostojic, CERN LHC PRoject Note 111,1997.

[30] J.B Jeanneret at the 43rd PLC, October 1998 and decisions therein.

[31] V.Bagin,I.Collins and N.Kos, LHC-VSS-ES-0002 rev 1.0, EDMS doc 334961.

[32] L. Jin and F. schmidt, 'Dynamic aperture tune scan for LHC version 5 at injection energy', LHC Project Note 182, January 1999

[33] S. Fartoukh, O. Brüning, Field quality specification for the LHC Main dipole Magnets, LHC-Project-Report-501, Geneva, CERN (October 2001).

[34] Proceedings of the 'Workshop on Collective Effects in Large Hadron Colliders', Particle Accelerators, Volume 50, Numbers 1-3, 1995.

[35] M. Hayes, "The effect of spool piece mispowering on the dynamic aperture of the LHC during injection', LHC Project Report 522, December 2001

[36] M. Hayes, 'Tolerances of the spool piece correction system for the LHC', LHC Project Report 590, July 2002

[37] R. Wolf, Field Error Naming Conventions for LHC magnets, Engineering Specification LHC-M-ES-0001, Geneva, CERN (October 2001).

[38] A. Verdier (ed.) et al, Report on the mini-workshop on the LHC alignment, LHC-Project-Note-247, Geneva, CERN (February 2001).

[39] Jean-Pierre Koutchouk and Andre Verdier, 'Specification for the field quality of the LHC closed orbit correctors and sextupoles', LHC Project Note 210, January 2000.

[40] H. Grote and F. Schmidt, MADX an upgrade for MAD8. PAC03 Portland, Oregon, May 2003.

[41] S. Fartoukh, M. Giovannozzi, A. Verdier, Tolerances for the quadrupoles of the Special Straight Sections, in preparation.

[42] M. Giovannozzi, presentation at the 3rd LTC Meeting, http://lhcp.web.cern.ch/lhcp/ab-ltc/ltc_2003-03.html (2003).

[43] M. Giovannozzi, T. Risselada, F. Schmidt, 'Effect of the field quality of warm quadrupoles in IR3 and IR7 on LHC performance', in preparation.

[44] O. Brüning, S. Fartoukh, M. Giovannozzi, T. Risselada, 'Dynamic Aperture Studies for the LHC Separation Dipoles', in preparation.

[45] E. Boter, G. de Rijk, Multipole tables for the MQWA and MQWB magnets, LHC Project Note 289 (2002).

[46] E. Willen, Superconducting beam separation dipoles, LHC-MBR-ES-0001 rev. 2.0, (2000).

[47] F. Bordry, P. Collier and A. Verdier, Check of the BPM alignment with the LEP beam. SL MD Note 99 (September 6, 1993).

[48] A. Verdier, Estimation of the vertical misalignment of the low-β quadrupoles in IP2 and IP6. SL-MD Note 188 (October 24, 1995).

[49] A. Verdier and S. Weisz, Alignment of low-β with beam. Proc. of the fourth International Workshop on Accelerator Alignment. KEK Proceedings 95-12 (January 1996).

[50] I. Barnett et al., Dynamic beam based calibration of orbit monitors at LEP. Proc. of the fourth Int. Workshop on accelerator alignment IWAA95, KEK, November 1995. KEK Proceedings 95-12 (January 1996).

[51] G. Arduini, A. Verdier, Poor man pilot and TOTEM bunches. AB-Note-2003-017 MD (February 12, 2003).

[52] A. Verdier, Resonance-free lattices for A.G. machines. PAC 1999 New-York. Also divisional report CERN-SL-99-018 AP.

[53] F. Schmidt and A. Verdier, Optimisation of the LHC dynamic aperture via the phase advance of the arc cells. PAC 1999 New-York. Also LHC project report 297.

[54] F. Schmidt, A. Verdier, D. Kaltchev, Robustness of resonance-free lattices against gradients errors. PAC2001 Chicago USA (June 2001). Also LHC Project Report 475 (August 2001).

[55] The TOTEM collaboration, Technical proposal. CERN/LHCC 99-7, LHCC/ P5 (15 March 1999).

[56] A. Faus-Golfe, J. Velasco and M. Haguenauer, Precise measurements of the total cross section and the coulomb scattering at the LHC. EPAC 2000 (Vienna).

[57] A. Faus-Golfe, A. Verdier, Optics studies for diffractive physics at the LHC. EPAC 2002 (Paris).

[58] S. Weisz, An analytic approach to a high-β insertion and possible application for TOTEM at the LHC. LHC project note 164 (September 1998).

[59] F. Schmidt, "SixTrack, version 3, single particle tracking code treating transverse motion with synchrotron oscillations in a symplectic manner", CERN SL/94–56 (AP) (1994) F. Schmidt, "Run Environment for SixTrack", Beam Physics Note 53,

[60] H. Grote, "Statistical significance of dynamic aperture calculations", Beam Physics Note 34.

[61] L. Jin and F. Schmidt, "Tune Scan Studies for the LHC at Injection Energy", LHC Project Report 377.

[62] E. McIntosh, T. Pettersson and F. Schmidt, A Proposal for a Numerical Accelerator Project, Part. Acc. Vol. 54 (2-4) (1996).

[63] Jean-Pierre Koutchouk, 'The LHC Dynamic Aperture', Proceedings of the 1999 Particle Accelerator Conference, New York, 1999

[64] M Böge, H. Grote, Q. Quin and F. Schmidt, Dynamic Aperture Studies for the LHC Version 4, LHC Project Report 31, July 1996

[65] S. Wiesz and Q. Quin, Study of Systematic Multipolar Errors in LHC Version 4.1 and Spool Pieces Compensation, LHC Project Note 42, March 1996

[66] Y. Luo and F. Schmidt, "LHC Dynamic Aperture versus single Multipole Components", LHC Project Note 272,

[67] Y. Papahilippou, Correction Schemes for the Normal Octupole and Decapole Errors in the LHC Dipole, CERN LHC Project Report 411

[68] Y. Papaphilippou, Frequency Maps of LHC Models, CERN LHC PRoject Report 299

[69] Y. Papaphilippou and F. Schmidt, Normal Form Approached and Resonance Analysis of LHC Models, CERN LHC Project Report 255

[70] R. Bartolini, A. Faus-Golfe, M. Giovannozzi, E. Todesco, W. Scandale, Early Indicators of Long Term Stability in Hadron Colliders, LHC Project Report 41, July 1996

[71] M. Giovannozzi, W. Scandale, E. Todesco Prediction of Long-Term Stability in Large Hadron Colliders, LHC Project Report 45, July 1996

[72] M. Böge et al, Overview of the LHC Dynamic Aperture Studies, CERN LHC Project Report 106 and in the Proceedings of the 1997 Particle Accelerator Conference, New York, U.S.A.

[73] F. Schmidt and A. Verdier, "Optimisation of the LHC dynamic aperture via the phase advance of the arc cells", 1999 Particle Accelerator Conference - PAC '99 New York City, NY, USA , LHC Project Report 297 L. Jin, Y. Papaphilippou and F. Schmidt, "Improvement of LHC Dynamic Aperture via Octupole Spool Pieces for the Nominal Tunes", LHC Project Report 253 M. Böge, H. Grote, Q. Qin and F. Schmidt, "Dynamic Aperture Studies for the LHC Version 4", LHC Project Report 31, paper presented at the Fifth EPAC Conference, Barcelona, June 1996 W. Fischer and F. Schmidt, "Long–term tracking for the LHC including ripple", CERN SL/Note 94–75 (AP) F. Galluccio, Z. Guo, W. Scandale, F. Schmidt and A. Verdier, "Long–term stability studies for the Large Hadron Collider", CERN SL/91–20 (DI), LHC Note 147, in Conference Record of the 1991 IEEE Particle Accelerator Conference, San Francisco, California, May 1991, pp. 1669–1671 F. Schmidt, "First tracking results with SixTrack for the LHC", CERN SPS/AMS/FS (1988)

[74] Y. Luo and F. Schmidt, "Weak–Strong Beam–Beam Tracking for LHC V6.0 ", LHC Project Report 502 Y. Luo and F. Schmidt, "Dynamic Aperture Studies for LHC Optics Version 6.2 at Collision", LHC Project Note 310 H. Grote, L.H.A. Leunissen and F. Schmidt, "LHC Dynamic Aperture at Collision", LHC Project Note 197

[75] M. Hayes, 'The effect of triplet errors, misalignments and associated correction systems on dynamic aperture', LHC Project Note 291, April 2002.

[76] S. Fartoukh, Installation scenarios and dynamic aperture LHC-Project-Report-449, Geneva, CERN (December, 2000).

[77] E. Todesco et al., An Estimate of Multipolar Errors in the LHC Dipoles, LHC-Project-Report-625, Geneva, CERN (December 2002).

[78] S. Fartoukh, Session 6 of the Workshop on Field quality Steering of the LHC Dipole, `http://lhc-div-mms.web.cern.ch/lhc-div-mms/MMSPAGES/MA/fqwrkshp/fqwrkshp.html`, Geneva, CERN (March 2003).

CHAPTER 5

COLLECTIVE EFFECTS

5.1 INTRODUCTION

Collective effects, arising from the electromagnetic interaction of the beam particles among themselves, with their environment (possibly including 'foreign particles' such as electrons) and with the other beam, will ultimately limit the performance of the LHC. Depending on the beam intensity and on the bunch filling pattern, they give rise to parasitic losses, can cause beam instabilities or degrade the beam quality by emittance growth and poor lifetime of all or some specific bunches. A first summary of collective effects in the LHC was presented in [1], a systematic review of single beam effects can be found in [2], and intermediate reviews have been published in [3, 4, 5, 6, 7, 8, 9].

Collective effects include incoherent phenomena, concerning the behaviour of a single particle in the electromagnetic field produced by all the others, and coherent interactions of the beam with its surroundings, usually described in terms of coupling impedances. The LHC impedance budget is discussed in the next Section and a review of single-beam instability mechanisms is presented in Sec. 5.3. Cures against instabilities, discussed in Sec. 5.4, include feedback systems, chromaticity control, and Landau damping of the coherent beam oscillation modes, that takes place providing their tune shifts remain within the incoherent tune spread. Landau damping can be considered as a bridge between incoherent and coherent phenomena.

Examples of incoherent effects are direct space charge and Laslett tune shifts due to image currents, as well as residual gas and intra-beam scattering (IBS). The latter are discussed in Sec. 5.5, which contains a summary of the mechanisms leading to emittance growth. As discussed in [2], the magnetic Laslett tune shift at injection in the LHC is about 1.7×10^{-2}: this large tune shift, having opposite sign in the two betatron planes, can be compensated by adjusting the tuning quadrupoles. Effects associated with the incoherent synchrotron radiation are presented in Sec. 5.6. Coherent effects include parasitic losses, summarized in Sec. 5.7, and complex tune shifts of the beam oscillation modes.

Seed electrons created by ionization of the residual gas at injection or photo-electrons liberated by the large number of hard U.V. synchrotron radiation photons at 7 TeV are pulled towards the positively charged LHC proton bunches. When they hit the opposite wall, they generate secondary electrons which can in turn be accelerated by the next bunch if they are slow enough to survive. This mechanism can lead to the fast build-up of an *electron cloud*, discussed in Sec. 5.8, with potential implications for beam stability, emittance growth, and heat load on the cold beam screen. Electron cloud effects have been actively investigated at CERN since 1997 by analytic estimates, simulations, and experiments [10, 11, 12].

Beam-beam effects are discussed in Sec. 5.9. They include incoherent effects, such as betatron tune spreads associated with the nonlinear head-on and long range collisions as well as a reduction of dynamic aperture for insufficient beam separation at the parasitic encounters, and coherent effects affecting orbit, tunes, and chromaticities of the different bunches (depending on their different collision schedules) or coherent oscillation modes. The effect of long range beam-beam encounters can be compensated by electro-magnetic lenses [13], which are being experimentally investigated, and the luminosity can be optimized by increasing bunch length or crossing angle [14].

5.2 IMPEDANCE BUDGET

Single-bunch collective effects are associated with the broad-band impedance of low-Q structures, discussed in [8], while multi-bunch effects are dominated by the narrow-band impedance of high-Q resonators [9]. The narrow-band nature of the transverse resistive wall impedance at low frequency also leads to coupled-bunch instabilities.

5.2.1 Narrow-Band Impedance of High-Q Resonators

Detailed tables of damped and undamped higher order modes (HOM's) for 400 MHz and 200 MHz RF cavities, transverse damper system, and trapped modes in the CMS vacuum chamber can be found in [9].

5.2.2 Transverse Resistive Wall Impedance

In the LHC, about 90% of the circumference will be maintained at 5 to 20 K while the remaining 10% of the circumference will be at room temperature and will be generally equipped with a 2 mm thick copper beam pipe. The cryogenic part of the LHC beam pipe (mainly beam screen) will be copper cladded stainless steel to keep the resistance as low as possible both for instability and ohmic heating considerations. The resistivity of the cold copper is a function of the residual resistance ratio (RRR) and of the magnetic field B. The magnetic field increases the path length of the conduction electrons which leads to a substantial resistance increase at cryogenic temperatures. The final resistivity depends more on the field than on the RRR for very high magnetic fields. Past experience with co-laminating stainless steel with copper showed that the copper close to the steel gets contaminated during the fabrication process such that the surface impedance is increased. The increase of the resistance has been compensated by increasing the thickness of the copper layer from 50 to 75 μm. The equivalent thickness and RRR at low-B turn out to be 50 μm and 100, respectively, whereas the RRR reduces to 30 at high B [9]. The Yokoya factors [15] for the LHC beam screen geometry are derived from a geometry halfway between square and elliptical. Since the dimensions a and b of the beam screen in the two planes satisfy $(a-b)/(a+b) = 0.1$, vertical and horizontal Yokoya factors $Y_{\rm V} = 0.87$ and $Y_{\rm H} = 0.63$ respectively are assumed.

Tab. 5.1 gives the values of the transverse resistive wall impedance for each major LHC component, excluding collimators that will be treated separately. For easy comparison of the different components, the transverse impedance is normalised by a weighting factor $\beta/\langle\beta\rangle$, where β is the local betatron function in the relevant H or V plane, estimated based on LHC optics version 6.2, and $\langle\beta\rangle = 70$ m the average β-function defined as the ratio R/Q of the average machine radius to the betatron tune. These impedance estimates include the effect of the so-called inductive by-pass [16] and the Yokoya factors for non-cylindrical components. The 'effective' resistive wall impedances reported in Tab. 5.1 refer to the first slow wave at 8 kHz, corresponding to a non-integer part of the betatron tune equal to about 0.3, and to the slow wave at 20 MHz, corresponding to the frequency bandwidth of the transverse feedback system. The contributions at higher harmonics of the 40 MHz bunch frequency for these slow waves have been taken into account for the kickers and the TDI. It should be pointed out that for an easy comparison of the different impedance sources, including the collimators discussed in the next section, the sum over the higher harmonics of the coupled-bunch rigid mode spectrum is not normalized by the corresponding sum of the spectral densities. The resulting 'effective' impedance differs from the usual definition [17] by a factor $s_{\rm b}/2\sqrt{\pi}\sigma_z$, depending on the ratio of the bunch spacing $s_{\rm b}$ to the r.m.s. bunch length σ_z, and equal to about 28 for the LHC at 7 TeV. With this definition the coherent tune shifts[1] of the coupled-bunch modes are given by $\Delta Q = j\langle I\rangle\langle\beta\rangle Z_\perp^{\rm eff}/4\pi(E/e)$, where $\langle I\rangle$ is the *average* rather than the peak beam intensity.

The MQW and MBW are special types of magnets in the cleaning insertions. The MBW magnets have a circular chamber of radius 0.022 m. The MQW magnets have an elliptical chamber with $(a-b)/(a+b) = 0.275$ and an inscribed radius of 0.0145 m. The corresponding Yokoya factors are 0.85 and 0.5. Half of the major axes are in the horizontal plane, the other half in the vertical plane, following the value of the optical function β. The total resistive wall impedance is about equal in both planes for these magnet chambers and can be found with sufficient accuracy by assuming an average Yokoya factor of 0.7 and an average value for β.

The TDI is a special 'collimator' to be used for protecting the machine from a potential misfiring of the injection kickers. A thin 3 μm layer of Ti is assumed. The Yokoya factors are $\pi^2/12$ and $\pi^2/24$. The effect of the inductive by-pass is large due to the high surface impedance. As a consequence the contribution of the harmonics of the 40 MHz bunch frequency is relatively important.

Interconnects are the assemblies that contain the shielded bellows. The longitudinal resistance for one unit

[1] Oscillations are considered to be of the form $\exp(jQ\omega_o t)$, where $j = -i$ and ω_o is the revolution frequency. Therefore a beam instability corresponds to a coherent tune shift ΔQ with negative imaginary part and to an effective impedance with negative real part.

Table 5.1: Transverse resistive wall (low-frequency) impedance for the LHC without collimators. The first four columns report element name, latest relevant reference, total length in m and inner radius b in mm. The last two columns give the transverse 'effective' impedance $Z_\perp^{\rm eff}$ in MΩ/m for the slow waves at 8 kHz and at 20 MHz multiplied by $\beta/\langle\beta\rangle$, where $\langle\beta\rangle = 70$ m.

element	Ref.	length	b	$Z_\perp^{\rm eff}$ [8 kHz]	$Z_\perp^{\rm eff}$ [20 MHz]
		m	mm	MΩ/m	MΩ/m
Beam screen-H @low-B	[9]	23600	22	-21.4+6.3j	-1+0.3j
Beam screen-V @low B	[9]	23600	18	-29.5+8.6j	-1.5+0.5j
Beam screen-H @high-B	[9]	23600	22	-61+7.2j	-3+0.3j
Beam screen-V @high-B	[9]	23600	18	-84.4+9.9j	-4+0.5j
Interconnects	[19]	340	22	-5.3+0.5j	-
Cold-warm transitions		10	22	-0.6+0.3j	-
Warm pipe (pipe+etc.)		2400	40	-3.5+2.9j	-0.2+0.2j
MQW (2 mm Cu)		155	14.5	-4.3+4.8j	-0.3+0.3j
MQW (2 mm SS)		5		-1.4+1.6j	-0.1+0.1j
MBW (2 mm Cu)		70	22	-0.6+0.6j	-0.05+0.05j
MBW (2 mm SS)		2		-0.21+0.18j	-
TDI-H @injection		2.8		-	-0.8+4.5j
TDI-V @injection		2.8	5	-	-0.5+3j
Injection-Septum-H	[20]	22	22	-0.3	-
Injection-Septum-V	[20]	22		-0.5+0.1j	-
Dump-Septum	[20]	72	25	-1.3+0.2j	-
Injection-Kicker-H	[21]	15	19	-0.4+4j	-
Dump-Kicker-V		22.5	29	-1+5j	0+7.2j

with length 0.2 m is 100 $\mu\Omega$. For the cold-warm transitions, RRR=10 for the 3 μm thick copper layer, owing to pollution from SS are assumed.

The injection kickers are equipped with 5 μm thick Cu stripes covering 1/2 of the ceramic chamber. This is equivalent to a solid coating by a 2.5 μm thick copper layer [22]. The same remarks on the effect of inductive by-pass and 40 MHz harmonics as for the TDI apply for the injection and dump kickers.

The total resistive wall impedance at injection and at top energy, excluding collimators, is summarized in Tab. 5.2 for the slow waves at 8 kHz and 20 MHz. Most of this impedance depends on frequency as $1/\sqrt{\omega}$.

Table 5.2: LHC transverse resistive wall impedance budget in MΩ/m (no collimators).

	horizontal	vertical
TOTAL $Z_\perp^{\rm eff}$ @injection, 8 kHz slow wave	-40+22j	-49+26j
TOTAL $Z_\perp^{\rm eff}$ @injection, 20 MHz slow wave	-3+6j	-3+12j
TOTAL $Z_\perp^{\rm eff}$ @top energy, 8 kHz slow wave	-79+22j	-103+26j
TOTAL $Z_\perp^{\rm eff}$ @top energy, 20 MHz slow wave	-5+1j	-5+8j

Resistive wall impedance of the collimators

The impedance for a single graphite collimator has been estimated analytically and numerically in [16, 17]. The thick-wall approximation with 'inductive by-pass' has been used, since even at the lowest frequency around 8 kHz for the first slow wave the skin depth in graphite is about 2 cm and thus smaller than the 2.5 cm thickness of the collimator block. The corresponding analytic expression for a single collimator in [16] with a half-gap of 2 mm yields results in excellent agreement with the numerical results obtained using the code HFSS in [17]. A thin Cu coating of about 1 μm thickness would considerably reduce the real part of the coherent tune shift [17, 18] and improve beam stability, as discussed in Sec. 5.4.5. However such a thin coating may not

survive during machine operation.

The collimator scheme considered here corresponds to the baseline design described in Chap. 18 and including graphite collimators at all reserved spaces (some of which will not be installed for the LHC start-up), with 20 collimators in IR7 and 7 collimators in IR3 having lengths of 20 cm for the 5 primary collimators and 1 m for the 22 secondary collimators[2]. The β-functions at the collimators range from 27 m to 360 m and the range of collimator half-gaps is 4.7 to 11.1 mm for the injection optics and 1.2 to 3.8 mm for the squeezed optics. For our impedance estimate no metallic coating, a Carbon jaw resistivity $\rho = 14 \times 10^{-6}\,\Omega$m, and continuity of the electric contact with the beam pipe are assumed. The corresponding 'effective' resistive wall impedance is reported in Tab. 5.3 for the slow waves at 8 kHz and at 20 MHz. At injection the real part of the collimator impedance has a mild maximum around 0.2 MHz, while for the squeezed optics at 7 TeV the maximum is around 1 MHz. The 'effective' impedances for the corresponding most critical coupled-bunch modes are $(-11 + 55j)$ MΩ/m and $(-100 + 1400j)$ MΩ/m, respectively. The real part of the impedance for a single collimator varies approximately with $\sqrt{\omega}$ below the maximum and with $1/\sqrt{\omega}$ for frequencies well above the maximum. The frequency corresponding to the maximum of $\mathrm{Re}(Z_\perp)$ depends on ρ/b^2. The imaginary part of the impedance at low frequency tends to a constant value proportional to $1/b^2$. Also the maximum of $\mathrm{Re}(Z_\perp)$ is proportional to $1/b^2$.

Table 5.3: Vertical 'effective' impedance of the LHC collimators, normalized to $\langle\beta\rangle = 70$ m, for un-coated Carbon jaws with resistivity $\rho = 14 \times 10^{-6}\,\Omega$m. The effect of the inductive bypass, of the Yokoya coefficients, and the contribution at higher harmonics of the 40 MHz bunch frequency for the slow waves at 8 kHz and at 20 MHz have been properly taken into account.

	$Z_\perp^{\mathrm{eff}}$ [8 kHz]	$Z_\perp^{\mathrm{eff}}$ [20 MHz]
	MΩ/m	MΩ/m
injection optics	-7.6+74j	33j
squeezed optics	-42+1800j	-7.2+1160j

5.2.3 Broad-Band Impedance

Several elements contribute to the LHC broad-band impedance [8] and Tab. 5.4 gives a list of the corresponding effective longitudinal and transverse impedance, the latter being normalized to $\langle\beta\rangle = 70$ m. Roman pots (see the Glossary) are assumed retracted and shielded.

For the BPM's a 0.5 mm slit between electrode and body is assumed. The 'monitor' inductance per electrode is 4 pH, the 'slit' inductance 9 pH, and the 'cavity' inductance 4 pH, giving a total of about 60 pH or $Z/n = j\,4.2\,\mu\Omega$/monitor. 500 monitors, including some overhead for special and warm BPM's are considered.

The 1700 shielded bellows have a depth of 5 mm on 20 mm radius, corresponding to an inductance of 81 pH. 350 vacuum valves having an inner radius of 31.5 mm, a chamber radius of 40 mm and sloping edges at 15°, corresponding to an inductance of 0.2 nH per valve are considered.

The experimental chambers have inductances of 7.3 nH (CMS), 13.2 nH (Alice), 117 nH (LHCb), 75÷100 nH (vertex detector), and 15 nH for the rest of the IP. The total inductance is therefore 140 nH.

The shunt impedance for a 400 MHz cavity unit is $R/Q = 44.5\,\Omega$. Thus the total inductance for 8 units is 144 nH. The effective inductance is somewhat smaller. The shunt impedance for a 200 MHz cavity unit is $R/Q = 192\,\Omega$ and the total inductance for 4 units is therefore 600 nH, corresponding to $Z/n = j\,0.045\,\Omega$. The effective inductance is only a fraction of this, which is estimated at one third. The transverse impedance of the RF cavities is not included in the total broad-band impedance, since it does not extend beyond $\approx$ 1 MHz, while most of the remaining impedance extends up to about 5 GHz, corresponding to the cut-off frequency of the vacuum chamber.

The inductance of each of the 8 recombination chambers (Y-chambers) is 1.5 nH. Total length of the unshielded bellows is 2.6 m (0.36 m in Alice, 0.6 m in CMS, 0.75 m in ATLAS, and 0.9 m in LHCb) giving an

[2]The present baseline for Phase 1 includes only 4 primary and 15 secondary collimators per beam and the impedance is therefore somewhat reduced.

Table 5.4: LHC broad-band impedance budget. The first three columns report element name, latest relevant reference, and inner vertical aperture b in mm. The last two columns give the effective longitudinal and transverse impedance in the vertical plane, the latter being multiplied by $\beta/\langle\beta\rangle$, where $\langle\beta\rangle = 70$ m.

element	Ref.	b	Im(Z/n)	Im$(Z_\perp)$
		mm	Ω	MΩ/m
Pumping slots	[23]	18	0.017	0.5
BPM's	[24]	25	0.0021	0.3
Unshielded bellows		25	0.0046	0.06
Shielded bellows		20	0.010	0.265
Vacuum valves		40	0.005	0.035
Experimental chambers		-	0.010	-
RF Cavities (400 MHz)		150	0.010	(0.011)
RF Cavities (200 MHz)		50	0.015	(0.155)
Y-chambers (8)	[25]	-	0.001	-
BI (non-BPM instruments)		40	0.001	0.012
space charge @injection	[2]	18	-0.006	0.02
Collimators @injection optics		$4.4 \div 8$	0.0005	0.15
Collimators @squeezed optics		$1.3 \div 3.8$	0.0005	1.5
TOTAL broad-band @injection optics			0.070	1.34
TOTAL broad-band @squeezed optics			0.076	2.67

inductance of 65 nH.

24 BI instruments per ring other than BPM's, with inner radius of 0.04 m, outer radius 0.06 m, and sloping edges are assumed. This gives a total inductance of 12 nH. Special components like injection and dump kickers, septa and TDI are not expected to contribute significantly to the longitudinal impedance budget, since they are equipped with a thin metallic layer on their inner surface. Also the inductance of the beam screen sawtooth surface is negligible [26].

Space Charge Impedance

As discussed in [27], the transverse coherent tune of rigid dipole beam oscillations is not affected by the direct space charge effect. For a round beam with uniform density, one can formally define a direct space charge impedance giving rise to a collective tune shift which is compensated by the incoherent space charge tune shift $\Delta Q_{\perp,sc}^{\rm inc} = -\frac{N_{\rm b} r_{\rm p}}{4\pi B\beta\gamma^2\varepsilon_{\rm n}}$. Here $N_{\rm b}$ is the number of protons per bunch, $r_{\rm p}$ the classical proton radius, B the bunching factor, $\gamma = (1-\beta^2)^{-1/2}$ the Lorentz factor, and $\varepsilon_{\rm n} = \beta\gamma\varepsilon$ the normalized transverse beam emittance. Following Chao [28], the transverse space charge impedance can be written $Z_\perp = -j\,\frac{Z_0 R}{\beta^2\gamma^2}\left(\frac{1}{2a^2} - \frac{1}{b^2}\right)$. It has a direct effect, corresponding to a large capacitive contribution inversely proportional to the square of the average beam radius $a = \sqrt{\varepsilon\langle\beta\rangle}$, and a much smaller inductive contribution from the image currents on the beam pipe of radius b. Only the latter has been reported in Tab. 5.4, since the real tune shift induced by the direct space charge impedance for rigid dipole oscillations of a beam with *non uniform* transverse distribution i) is compensated by the incoherent tune shift for particles with small betatron amplitudes and ii) is unlikely to give rise to coherent instabilities thanks to the direct space charge tune spread for particles with larger betatron amplitudes (see also [29] and the discussion at the end of Sec. 5.4.4).

At injection energy, the incoherent space charge tune shift for nominal LHC bunch intensity is -1.36×10^{-3} and the direct space charge impedance is $-j\,6.35\,$MΩ/m. At 7 TeV these values become -7×10^{-6} and $-j\,0.41\,$MΩ/m, respectively.

Geometric Impedance of the Collimators

In the LHC the bunches are long and the collimator gaps after the β-squeeze are narrow. In addition the collimators are tapered at a small angle θ. (Wake fields for un-tapered collimators were computed in [30] and [31].) Therefore this is a regime, where $kb\theta \ll 1$ is fulfilled. For an ultra-relativistic particle, the wave number k is related to the frequency ω via $k = \omega/c$, and the maximum bunch frequency is of order c/σ_z. The above condition can be re-written as:

$$b\theta/\sigma_z \ll 1.$$

For example, with $\sigma_z = 7\,\mathrm{cm}$, $b = 2.5\,\mathrm{mm}$, and $\theta = 0.35$, the left side is 0.13, so that the inequality is still fulfilled.

The impedance of a round collimator for this regime was computed by Yokoya [32] and Stupakov [33]. The transverse impedance is:

$$Z_\perp = j\,\frac{Z_0}{2\pi}\int_{-\infty}^{\infty}\left(\frac{b'}{b}\right)^2 dz,$$

where $b = b(z)$ describes the evolution of the beam pipe aperture with longitudinal position and $b(-\infty) = b(\infty)$ is assumed.

If the beam passes the collimator with an offset y from the center of the collimator gap, it receives a centroid kick:

$$\Delta y' = \frac{N_\mathrm{b} r_\mathrm{p}}{\gamma}\kappa_\perp y,$$

where the coefficient $\kappa_\perp$ is the loss factor (or kick factor):

$$\kappa_\perp = -\frac{1}{\pi}\int_0^\infty d\omega |\tilde{f}(\omega)|^2 \mathrm{Im} Z_\perp(\omega),$$

and $\tilde{f}$ is the Fourier transform of the normalized longitudinal charge distribution (for a Gaussian $\tilde{f} = \exp(-\sigma_z^2\omega^2/(2c^2))$.

Considering the two sides of a tapered collimator and assuming that the collimator gap b is much narrower than the surrounding beam pipe, the loss factor is:

$$\kappa_\perp = \frac{2\theta}{\sqrt{\pi}\sigma_z}\frac{1}{b}.$$

For our example above, this evaluates to about 3000. An important parameter is the normalized deflection or jitter enhancement factor:

$$C \equiv \frac{\beta\Delta y'}{\Delta y} = \frac{\beta N_\mathrm{b} r_\mathrm{p}}{\gamma}\kappa_\perp.$$

Using the above numbers, and also $N_\mathrm{b} \approx 10^{11}$, $\beta = 200\,\mathrm{m}$, $\gamma \approx 7500$, gives $C \approx 10^{-5}$. This number applies to a single collimator with half-gap $b = 2.5\,\mathrm{mm}$. The corresponding impedance is $j\,\theta Z_0/(\pi b)$ or $j16.8\,\mathrm{k}\Omega/\mathrm{m}$. The broad-band impedance for 21 collimator units reported in Tab. 5.4 for the squeezed optics has been estimated by multiplying this value by a factor ≈ 2 to account for the weighted β-functions and by an additional safety factor of 2, in view of somewhat larger inductances obtained for similar tapered structures [24]. The impedance at injection is estimated to be 10 times lower. Further numerical estimates of the geometric collimator impedance are ongoing.

5.3 SINGLE-BEAM CONVENTIONAL INSTABILITY MECHANISMS

In this section rise times and thresholds for different single-beam conventional instabilities are reviewed. The imaginary part of the effective impedance is responsible for (real) coherent tune shifts and can lead to collective instabilities owing to mode coupling or to loss of Landau damping, while a negative real part of the effective impedance is related to the instability rise time.

5.3.1 Single-bunch coherent tune shifts

At injection with nominal LHC single bunch intensity, the inductive broad-band impedance summarized in Tab. 5.4 induces a transverse real coherent tune shift of the rigid ($m = 0$) mode $\Delta Q^{(0)}_{\perp,bb} = -1.7 \times 10^{-4}$. For the first few higher order head-tail modes of order m this tune shift is divided by $m + 1$. Similarly, at 7 TeV with squeezed optics and collimators in closed position $\Delta Q^{(0)}_{\perp,bb} = -3.82 \times 10^{-5}$.

5.3.2 Multi-bunch coherent tune shifts and resistive wall instability

The coherent tune shifts of coupled-bunch modes induced by the narrow-band impedance of damped and undamped HOM's for 400 MHz and 200 MHz RF cavities, transverse damper system, and trapped modes in the CMS vacuum chamber are listed in [9].

At injection, the vertical resistive wall 'effective' impedance for the slow wave at 8 kHz is $(-49+26j)$ MΩ/m plus $(-7.6+74j)$ MΩ/m for the collimators[3], giving a total of $(-56.6+100j)$ MΩ/m. The corresponding tune shift for a nominal LHC bunch population of 1.15×10^{11} protons, assuming a uniform machine filling with 3564 bunches, is $\Delta Q_{\mathrm{V}} = -(9.1 + 5.2j) \times 10^{-4}$. The vertical resistive wall instability rise time for the most unstable rigid coupled-bunch mode is therefore $1/(2\pi\,\mathrm{Im}(\Delta Q_{\mathrm{V}})) \simeq 308$ turns or 27.4 ms. For ultimate LHC beam intensity, corresponding to a bunch population of 1.7×10^{11} protons, the instability rise time becomes 208 turns or 18.5 ms.

5.3.3 Mode-coupling and microwave instability thresholds

The total broad-band longitudinal impedance $Z/n = j\,0.07\,\Omega$ at injection or $Z/n = j\,0.076\,\Omega$ at top energy is significantly lower than originally assumed in [2, 5]. The threshold single bunch intensity for loss of Landau damping of the longitudinal single-bunch modes at 7 TeV is about 9×10^{11} protons per bunch, well above the nominal and ultimate LHC bunch intensity, while the threshold for the longitudinal microwave instability is two orders of magnitude above the nominal LHC bunch intensity.

Similarly, the total transverse broad-band impedance is $j\,1.34$ MΩ/m at injection and $j\,2.67$ MΩ/m at 7 TeV. These values are lower than the transverse effective impedance assumed in [2, 8] and the transverse mode-coupling instability threshold at injection is now above 2×10^{12} protons per bunch. Mode-coupling for multi-bunch modes may occur at somewhat lower beam intensities, as discussed in [3] for an earlier impedance model. A systematic revision of all single- and multi-bunch effects with an updated LHC impedance model, including a detailed frequency dependence of the narrow and broad-band impedance and based on a dedicated impedance data-base [34], is taking place at the time of writing.

5.4 CURES AGAINST INSTABILITIES

5.4.1 HOM damping and controlled emittance blow-up

To ensure longitudinal stability at injection for nominal LHC beam intensity with a longitudinal emittance of 0.7 eVs, the shunt impedance of all the HOM's in high-Q cavity-like structures should be limited to 60 kΩ in the frequency range $100 \div 500$ MHz. The limitation for the shunt impedance then increases with frequency as $f_r^{5/3}$. As discussed in [7], a controlled emittance blow-up proportional to $\sqrt{E}$ is sufficient to avoid degradation of the longitudinal beam stability during acceleration to 7 TeV.

5.4.2 Transverse feedback system

A transverse feedback system is required to damp coupled-bunch instabilities caused by the narrow-band impedance, and in particular the resistive wall instability, at injection and during acceleration to 7 TeV. Since the feedback system can only dump rigid ($m = 0$) head-tail modes, higher order head-tail modes have to be stabilized by Landau damping or (slightly) negative chromaticity. On the other hand, operation with the

[3] This is a somewhat conservative estimate corresponding to an intermediate collimator layout.

transverse feedback and large betatron tune spread may lead to a significant emittance growth [35] and should be avoided. Therefore the LHC strategy is to switch off the feedback system before the end of the energy ramp and to ensure Landau damping of *all* the head-tail modes by proper control of the tune spread using the arc octupoles.

5.4.3 Tune spread: Landau damping octupoles and beam-beam

In addition to octupolar spool-pieces for the local b_4 correction of the superconducting dipoles, in the LHC arcs there are two families of magnetic octupoles to control the betatron detuning with amplitude and provide Landau damping of the coherent beam oscillation modes. The horizontal and vertical betatron functions at the 84 focusing octupoles are $\beta_{\rm x}^{\rm OF} = 180\,{\rm m}$ and $\beta_{\rm y}^{\rm OF} = 30\,{\rm m}$, respectively, and these values are swapped at the 84 defocusing octupoles. Each octupole has a magnetic length of 0.32 m and a maximum integrated strength $O_3 = 59100\,{\rm T\,m^{-3}}$. The amplitude-dependent incoherent horizontal tune can be written $Q_{\rm x} = Q_o + aJ_{\rm x} + bJ_{\rm y}$, where $J_{\rm x}$ and $J_{\rm y}$ are the betatron action variables. The maximum value of the anharmonicities is $a = 270000\,{\rm m^{-1}}$ and $b = -175420\,{\rm m^{-1}}$, with $c = b/a = -0.65$. Given the nominal beam emittance at 7 TeV $\varepsilon = 0.5\,{\rm nm}$, the corresponding maximum detuning at $1\,\sigma$ r.m.s. is $\Delta Q_{1\,\sigma} = a\varepsilon = 1.35 \times 10^{-4}$ in each plane. Landau damping for a pseudo-parabolic betatron distribution with $J_{\rm x} + J_{\rm y} \leq 5\sigma^2$, as discussed in [36, 37] is assumed. This is a somewhat conservative assumption, valid for a scraped beam with no tails beyond $3.2\,\sigma$. The corresponding stability curves at 7 TeV are shown in Fig. 5.1 for positive or negative values of the maximum anharmonicity a. Potentially unstable oscillation modes with negative imaginary tune shifts are stabilized by Landau damping provided their coherent tune shifts remain below these stability curves. It is interesting to remark that for real tune shifts, such as those induced by the broad-band impedance, modes with a maximum (negative) tune shift about 3.5 times the detuning at $1\,\sigma$ are still Landau damped. The tune spread associated with long range beam-beam encounters provides an additional (modest) stabilizing effect [38].

5.4.4 Coherent tune shifts and Landau damping at injection

As seen in Sec. 5.3.1, at injection the transverse coherent tune shifts of the single-bunch higher order head-tail modes with $m > 0$ are smaller than or equal to 0.85×10^{-4} in absolute value. The natural nonlinearities of the magnetic lattice still compatible with an adequate dynamic aperture correspond to a maximum detuning of 2×10^{-3} at $6\,\sigma$ [39], *i.e.*, about 0.56×10^{-4} at $1\,\sigma$. This provides Landau damping of coherent modes having real tune shifts up to about 3.5 times larger, corresponding to an effective tune spread of nearly 2×10^{-4}. Therefore all the single-bunch head-tail modes with $m > 1$ are Landau damped by the lattice nonlinearities, if these are pushed to the limit. The rigid $m = 0$ head-tail mode will be damped by the feedback system. In case the lattice nonlinearities need to be reduced to guarantee a sufficient dynamic aperture, the direct space charge tune spread of about 10^{-3} will provide additional Landau damping of the higher-order head tail modes[4].

5.4.5 Coherent tune shifts and Landau damping at 7 TeV after β-squeeze

The tune shift of the most unstable rigid coupled bunch mode at top energy is $-(0.13+0.42j)\times10^{-4}$ without collimators. The maximum tune shift induced by un-coated graphite collimators is $-(7.45 + 0.55j) \times 10^{-4}$ and that induced by graphite collimators with 1μm Cu coating, assuming a resistivity $\rho_{\rm Cu} = 1.5 \times 10^{-8}\,\Omega$m, is $-(2.83 + 0.84j) \times 10^{-4}$. Fig. 5.1 (left) shows the situation for the nominal LHC beam at 7 TeV without collimators and including collimators (either coated or un-coated), taking as an upper bound the sum of the maximum tune shifts. Also the small real tune shift $\Delta Q^{(0)}_{\perp,bb} = -4\times10^{-5}$ induced by the broad-band impedance has been added in all cases. The conclusion is that Landau damping may not be ensured, even for copper coated collimators: the upgraded, low-impedance collimation scheme described in Chap. 18 is needed to reach and exceed nominal LHC performance. For the baseline collimator design without copper coating, stability is

[4] This assumption needs experimental validation in the regime of the LHC at injection energy, where the space charge tune spread is somewhat larger than the tune spread associated with the natural nonlinearities of the magnetic lattice. Observations at the CERN PS with very long bunches and space charge detunings much larger than those associated with the lattice nonlinearities indicate that the direct space charge tune spread may not be effective in providing Landau damping of the higher-order transverse head-tail modes [29].

ensured up to about 40% of the nominal beam intensity, as shown in Fig. 5.1 (right), and up to about 65% of the nominal beam intensity for copper coated collimators.

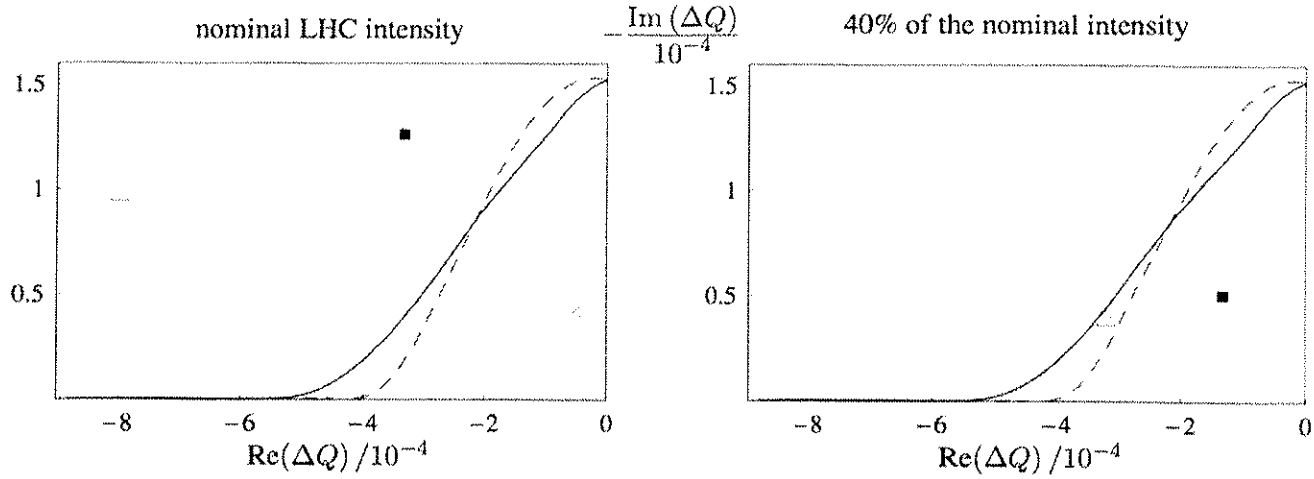

Figure 5.1: Stability limits for a detuning $\Delta Q_{1\,\sigma} = \pm 1.35 \times 10^{-4}$ and coherent tune shifts for the LHC at 7 TeV with squeezed optics and nominal LHC beam intensity (left) or 40% of the nominal intensity (right). The horizontal and vertical axes give the real part and minus the imaginary part, respectively, of the coherent tune shift for the most unstable coupled bunch rigid mode ($m = 0$): without collimators (cross), with copper coated graphite collimators (square), and with un-coated graphite collimators (triangle) at $\beta^* = 0.5\,\mathrm{m}$. The dashed (red) curve is the stability limit for maximum Landau octupole current with negative anharmonicity $a < 0$, the solid (blue) curve with positive anharmonicity $a > 0$.

5.5 SUMMARY OF EMITTANCE GROWTH AND BEAM LOSS MECHANISMS

5.5.1 Emittance growth caused by transverse injection oscillations

The effective overall damping time τ_{damp} of the LHC damper has to be significantly shorter than the decoherence time τ_{dec} of the injection oscillations to preserve the transverse emittance. For injection oscillations corresponding to a maximum transverse offset Δx, the relative emittance blow-up is given by [35]:

$$\frac{\Delta\sigma^2}{\sigma^2} \simeq \frac{1}{2}\,\frac{\Delta x^2/\sigma^2}{\left(1+\frac{\tau_{\mathrm{dec}}}{\tau_{\mathrm{damp}}}\right)^2}.$$

The LHC damping time for low intensity beams is 40 turns, corresponding to about 3.6 ms. At higher beam intensities, the damping rate is reduced by the resistive wall instability growth rate $1/\tau_{\mathrm{inst}}$, leading to an overall damping rate:

$$\frac{1}{\tau_{\mathrm{damp}}} = \frac{1}{40\,\mathrm{turns}} - \frac{1}{\tau_{\mathrm{inst}}}.$$

At nominal LHC beam intensity, the instability rise time is $\tau_{\mathrm{inst}} = 308$ turns and the overall damping time of the injection oscillations is 46 turns, corresponding to about 4.1 ms. After correction of the lattice nonlinearities at injection, it is thought that it is possible to reach a decoherence time around 750 turns, or 67 ms, corresponding to a full tune spread of about 1.3×10^{-3}. Assuming a maximum injection offset $\Delta x = 4\,\mathrm{mm}$, a modest emittance blow-up of about 1.9% is estimated.

At ultimate LHC beam intensity, the resistive wall instability rise time is $\tau_{\mathrm{inst}} = 208$ turns, or 18.5 ms, and the overall damping time of the injection oscillations becomes about 50 turns, or 4.4 ms. The corresponding emittance blow-up is 2.2%, i.e. still below 2.5%.

5.5.2 Intra-Beam Scattering

Small-angle particle-particle collisions within a bunch couple the horizontal and longitudinal particle oscillations and, above transition energy, give rise to an irreversible emittance growth in both planes. The horizontal IBS growth rate is approximately proportional to the particle density in the six-dimensional phase space. For nominal LHC beam parameters at top energy, the longitudinal IBS emittance growth time is 63 h and the horizontal growth time is 105 h. These values have been computed with the Bjorken-Mtingwa formalism implemented in MAD [40] for the LHC collision optics version 6.4.

The evolution of the LHC beam emittance during a physics store at 7 TeV is discussed in [41] and a plot including the effect of intra-beam scattering, particle consumption at the two high-luminosity IP's, and radiation damping is shown in Fig. 5.3.

5.5.3 Touschek Scattering

Touschek scattering refers to particle-particle collisions within a bunch, through which enough energy is transferred from transverse into longitudinal oscillations that the scattered particles leave the stable RF bucket. The loss rate due to Touschek scattering is quadratic in the bunch population and has been estimated for the LHC in [42]. For nominal beam parameters, coasting beam is produced at a rate per proton of $1.8 \times 10^{-4}\,\mathrm{h}^{-1}$ during injection and $8 \times 10^{-5}\,\mathrm{h}^{-1}$ at 7 TeV.

Once the protons are outside the RF bucket, they lose energy due to synchrotron radiation. If the collimators provide an energy aperture of 3.9×10^{-3}, a scattered proton is lost after about 390 hours at injection or after 6.5 minutes at top energy, respectively. While the energy drift due to synchrotron radiation is unimportant at injection, at 7 TeV it gives rise to a steady-state coasting beam component of about 10^{-5}.

5.5.4 Residual Gas Scattering

Residual-gas molecules reduce the proton beam lifetime due to nuclear scattering and they increase the beam emittance by multiple elastic Coulomb scattering. For the first time in an accelerator, beam loss due to the nuclear scattering represents a non-negligible heat load on the cold bore of the magnets. In consequence, a minimum beam lifetime of 100 h has been required, so as to ensure that the heat load due to nuclear scattering stays below 0.1 W/m for the two beams [43]. The beam lifetime τ is related to the cross section σ and gas density n via $1/\tau = c\sigma n$. Tab. 5.5 lists cross sections and the implied maximum allowed molecule densities for various gas species. Most of the cross sections were taken from [44]. The highest density of $1.2 \times 10^{15}\,\mathrm{m}^{-3}$ is permitted for hydrogen, corresponding to a 38-ntorr pressure at room temperature. The dipole magnet quench limit of 7×10^6 p/m/s at 7 TeV corresponds to a gas density about two orders of magnitude higher (see [45], p. 70).

The normalized emittance growth due to multiple scattering is:

$$\frac{d(\gamma\epsilon)}{dt} = \bar{\beta}\gamma \left(\frac{13.6\ \mathrm{MeV}}{\beta cp}\right)^2 \frac{cnm_{gas}}{X_0}\ ,$$

where m_{gas} is the mass of a molecule, X_0 the radiation length in units of $\mathrm{kg\,m}^{-3}$, and $\bar{\beta}$ the average beta function ($\bar{\beta} \approx 100$ m at injection, and $\bar{\beta} \approx 150$ m at top energy). The effect of multiple scattering is largest at injection. Emittance growth times expected at 450 GeV for the partial gas pressures corresponding to a 100 h nuclear-scattering lifetime are also included in Tab. 5.5. The emittance e-folding times are seen to range from 5 to 15 h, depending on the gas species. After some conditioning of the vacuum system, it is expected a fractional gas composition with less than 5% CO and CO_2 molecules. The emittance growth times will therefore be dominated by H_2.

5.5.5 Emittance Dilution caused by Collimators and Electron Cloud

If the beam passes a collimator with an offset y from the center of the collimator gap, it receives a centroid kick and an additional differential deflection along the bunch, which for a round collimator can be computed

Table 5.5: Nuclear scattering cross sections, the implied maximum allowed densities, and the accompanying emittance growth at injection for various gas species.

molecule	σ [barn] at 7 TeV	n [m^{-3}] at 7 TeV for $\tau_{\rm nucl} = 100$ h	equiv. gas pressure at 300 K [ntorr]	τ_ϵ [h] at 450 GeV for $\tau_{\rm nucl} = 100$ h
H_2	0.078	1.2×10^{15}	37.8	17.0
He	0.133	6.9×10^{14}	21.7	12.5
CH_4	0.511	1.8×10^{14}	5.6	7.6
H_2O	0.510	1.8×10^{14}	5.7	9.5
CO	0.751	1.2×10^{14}	3.8	7.5
CO_2	1.171	7.9×10^{13}	2.5	5.0

from the wake field:

$$w_\perp(s) = -\frac{j}{2\pi}\int_s^\infty \frac{e^{-s'^2/(2\sigma_z^2)}}{\sqrt{2\pi}\sigma_z}\int_{-\infty}^{\infty} d\omega e^{j(s-s')\omega/c} Z_\perp(\omega) = \frac{4\theta}{b}\frac{e^{-s^2/(2\sigma_z^2)}}{\sqrt{2\pi}\sigma_z},$$

where θ is the tapering angle and b the collimator gap. The rms spread of the kick (direct emittance growth) is $\sqrt{2}\sqrt{1/\sqrt{3}-1/2} \approx 0.4$ times smaller than the centroid kick. In other words, for a $1\,\sigma$ offset at the collimator, the beam emittance would blow up by 5×10^{-6}, so that after 2×10^5 turns it would be doubled, if the emittance growth were additive from turn to turn: this hypothesis needs further beam dynamics studies.

Considering a rigid oscillation or static displacement from the center of amplitude y, the deflection experienced by a particle at position s along the bunch passing the collimator is:

$$\Delta y'(s) = y\frac{N_b r_p}{\gamma} w_\perp(s).$$

For a flat collimator, a further emittance dilution arises from the quadrupole wake, which blows up the beam, even if the latter is perfectly centered between the jaws. This problem has also been studied by Stupakov [46]. In this case, the impedance depends on the offset of the local centroid (y_s) and the test particle (y_t), at the same longitudinal location. The generalized deflection under the condition that $\sigma_z \gg h^2\theta/b$ is [47]:

$$\Delta y'_t = \frac{\lambda_s r_p}{\gamma}\left(\frac{4\theta}{b}y_s - \frac{4\theta}{b}y_t + \frac{2\pi\theta h}{b^2}y_t\right),$$

where h is the half width of the beam pipe in the orthogonal transverse plane, and λ_s the local line density.

Preliminary results concerning the emittance growth caused by the electron cloud are discussed in Sec. 5.8.5. A quantitative estimate of the emittance dilution caused by collimators and electron cloud requires further investigations.

5.6 SYNCHROTRON RADIATION

The LHC is the first proton storage ring for which synchrotron radiation becomes a noticeable effect. At top energy, the synchrotron radiation gives rise to a significant heat load, which is intercepted by a beam screen at an elevated temperature of 5–20 K. The synchrotron radiation also leads to a shrinkage of the beam emittance during physics stores. Pertinent parameters are summarized in Tab. 5.6.

5.6.1 Photon Flux and Heat Load

Each of the two LHC beams emits 1.8×10^{21} photons per second, or on average 6.8×10^{16} photons per second and per metre of the ring. The proton energy loss per turn is 6.7 keV, at 7 TeV. The corresponding total power radiated per beam is 3886 W, with an average critical photon energy of 43.13 eV [48].

In the arcs, the average number of photons amounts to 8.2×10^{16} photons incident per metre length, second and beam. The synchrotron radiation power per metre bend and per beam is 0.22 W/m. In the long straight

Table 5.6: Synchrotron Radiation

parameter	450 GeV	7 TeV
total power / beam	0.066 W	3886 W
energy loss per turn	0.11 eV	6.7 keV
average photon flux per metre and second	0.4×10^{16}	6.8×10^{16}
photon critical energy	0.01 eV	43.13 eV
longit. emittance damping time	5.5 yr	12.9 h
transv. emittance damping time	11 yr	26 h

sections the average flux on the wall is 20 times smaller than in the arcs, or about 3.6×10^{15} photons per metre per second, as is illustrated in Fig. 5.2.

On the other hand, at injection energy, the synchrotron radiation stays negligible, with a total radiated power of only 0.066 W and a proton energy loss per turn of 0.11 eV.

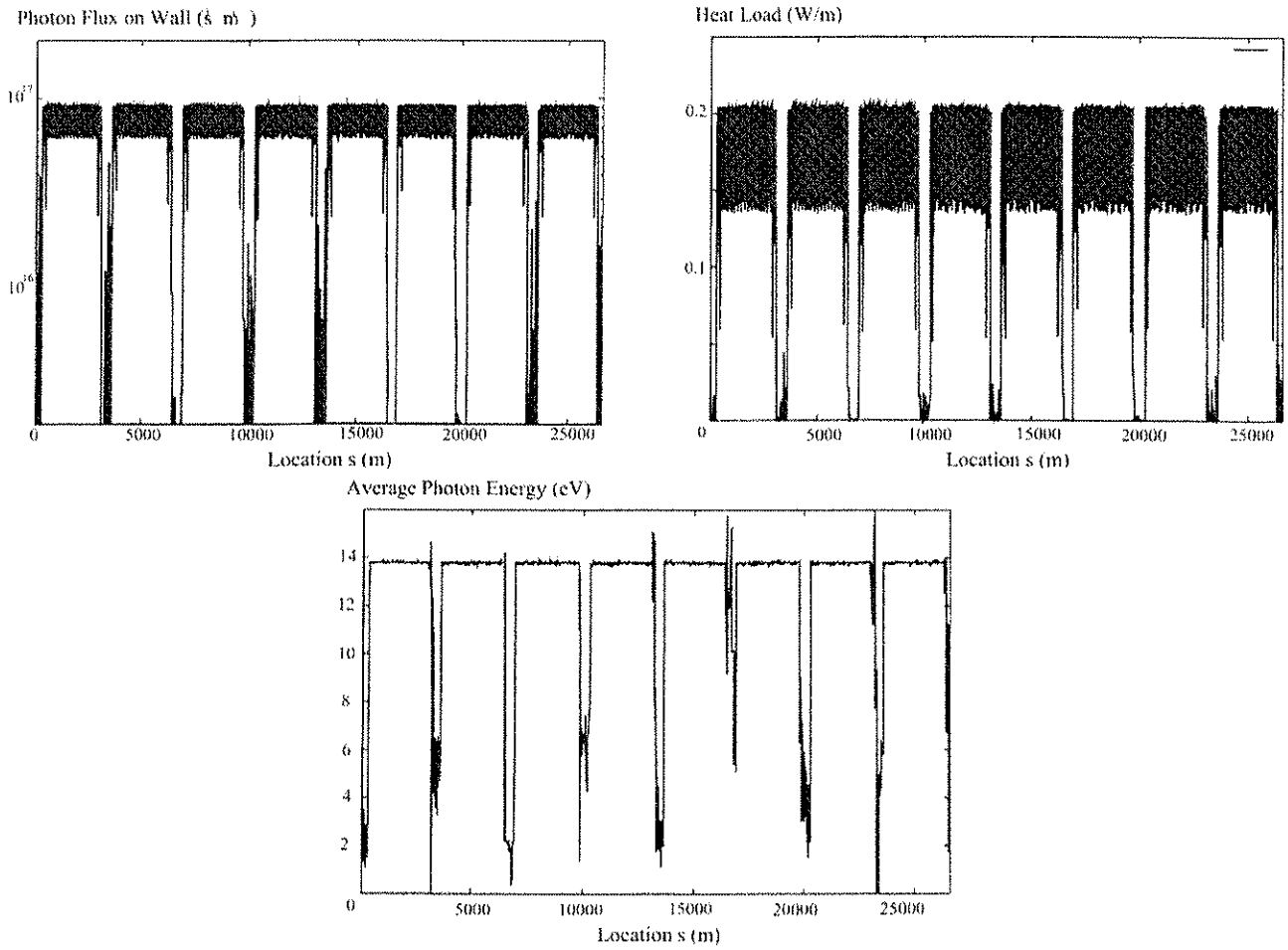

Figure 5.2: Synchrotron radiation as a function of position around the LHC: photon flux on wall per metre and per second (top left), heat load in W/m (top right), and average photon energy in eV (bottom) [48].

5.6.2 Emittance Damping

The synchrotron radiation gives rise to a continuous shrinkage of the beam emittances with exponential emittance-damping times of 26.0 h in the two transverse planes and 12.9 h in the longitudinal plane, at 7 TeV. The damping times scale with the inverse third power of the beam energy. For example, the damping is ten times weaker at 3.25 TeV. The damping times vary only by 1–2%, when either the crossing angles are turned

off or large optics errors are introduced.

In collision, due to the shrinkage of the emittance, the LHC luminosity decays less strongly than exponentially. The radiation damping may also compensate for emittance dilution due to other processes, such as beam-beam effects. However, if the transverse emittances decrease much more rapidly than protons are consumed at the collision points, the beam-beam tune shift may exceed the beam-beam limit, or the bunch length may become so short that the beam loses longitudinal Landau damping. Fortunately, this is not expected to be the case for the nominal LHC parameters with continually colliding beams, since the synchrotron-radiation damping is still moderate, and, in addition, it will partially be balanced by intra-beam scattering [49]. The expected evolution of key beam parameters and luminosity during a 10-h physics store is displayed in Fig. 5.3. If necessary, the balance of intra-beam scattering and synchrotron radiation can be modified by a judicious blow up of the longitudinal emittance using noise excitation.

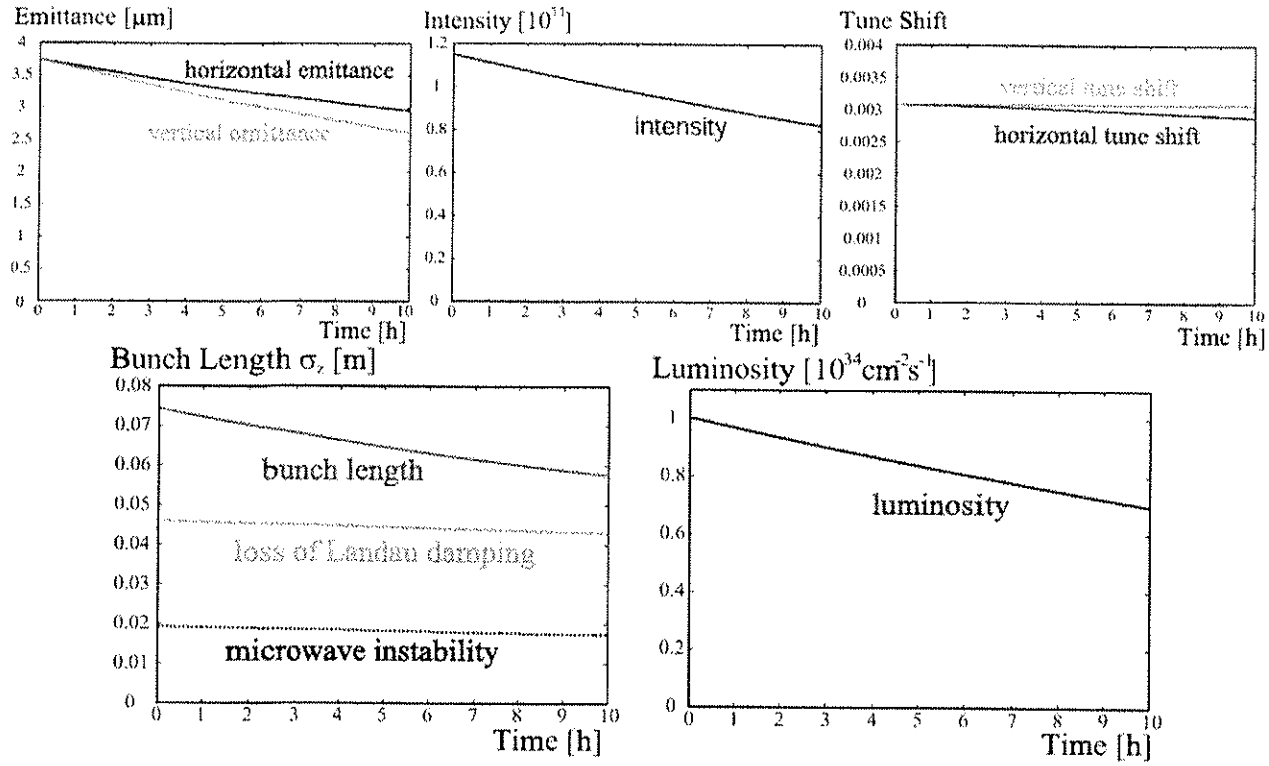

Figure 5.3: Evolution of normalized emittances (top left), bunch intensity (top centre), head-on beam-beam tune shift at the two high-luminosity IP's (top right), rms bunch length together with estimated limits for the loss of Landau damping and the onset of the longitudinal microwave instability (bottom left), and luminosity (bottom right) as a function of time during a nominal physics store at 7 TeV. The effect of intra-beam scattering (evaluated according to the approximate formulae in [50] and assuming a 10% vertical growth rate due to betatron coupling or vertical dispersion, corresponding to initial longitudinal/horizontal/vertical emittance growth times of 68/98/983 h), particle consumption at the two high-luminosity IP's (with a total inelastic cross section of 100 mbarn), and synchrotron radiation (with longitudinal/horizontal emittance damping times of 13/26 h) is included. The effect of residual gas scattering (with $\tau_{\mathrm{nucl}} \geq 100$ h) and other possible mechanisms leading to emittance growth, such as electron cloud, RF noise, ground motion, tune modulation or amplitude diffusion induced by the beam-beam interaction, is not included.

5.7 HEAT LOAD SUMMARY

A summary of the heat load induced on the arc beam screen by the nominal LHC beam at injection and at 7 TeV is shown in Tab. 5.7. The heat load caused by the electron cloud depends on the secondary electron yield of the beam screen surface and is discussed in Sec. 5.8.3.

Detailed estimates of the heat deposition by the nuclear scattering of the protons colliding in each of the two high luminosity LHC experiments can be found in [51]. These dynamic heat loads scale with the machine luminosity and, for nominal LHC luminosity of $10^{34}\,\mathrm{cm}^{-2}\,\mathrm{s}^{-1}$, they range between 5 and 13 W/m in the IR regions. In particular the power deposition in the inner triplet amounts to 30.7 W, 28.8 W, 26.6 W, and 27.7 W for the quadrupoles Q1, Q2a, Q2b, and Q3, respectively.

Table 5.7: Summary of heat load on the arc beam screen for nominal LHC beam at 7 TeV. The three columns give the source, the latest relevant reference, and the peak heat load in mW/m.

source	Ref.	Peak power [mW/m] at 7 TeV
Synchrotron Radiation	[48]	220
Ohmic Losses	[52]	110
Pumping Slots	[53]	10
Welds	[2]	10

5.8 ELECTRON CLOUD EFFECTS

A significant number of electrons can accumulate in the LHC beam pipe, due to the close bunch spacing of 25 ns [10]. This *electron cloud* could largely increase the heat load deposited on the LHC arc beam screen [11, 12]. It may also degrade the vacuum pressure, as observed, for example, in the ISR [54] and more recently in the SPS [55] and in RHIC [56], induce single- or multi-bunch instabilities [57, 58, 59, 60], and possibly cause long-term emittance growth. Electron clouds are presently limiting the performance of several operating storage rings, notably the two B factories, PEP-II and KEKB [61], the Los Alamos Proton Storage Ring [62], and RHIC [56]. An electron cloud occurs with LHC-type beam in the CERN SPS, where many of its characteristics, including heat load and conditioning effects, can be studied in situ for conditions resembling those of the LHC [55]. Primary electrons — the seed of the electron cloud — are created by a variety of different processes. The number of electrons then increases exponentially by a process known as *beam-induced multipacting*, in which the electron amplification is the result of secondary emission from the chamber wall.

In the LHC design, a number of countermeasures are incorporated, which aim either at suppressing an electron-cloud build up or at alleviating its effect. These measures include (1) a sawtooth chamber in the arcs, which reduces the photon reflectivity, (2) shielding the pumping holes inside the arc beam screen so as to prevent multipacting electrons from reaching the cold bore of the dipole magnets, (3) coating the warm regions by a special getter material, TiZrV, with low secondary emission yield, and (4) conditioning of the arc chamber surface by the cloud itself (*beam scrubbing*), which will ultimately provide a low secondary emission yield. During commissioning the bunch spacing can be increased and/or the beam energy be reduced to process the chamber while staying within the available cooling capacity.

5.8.1 Photoelectrons and Secondary Emission

An electron cloud builds up, if a modest number of primary electrons is amplified during the passage of a bunch train. This amplification occurs due to acceleration of electrons in the field of the beam and subsequent secondary emission with an average yield larger than one.

At injection energy, primary electrons are mainly generated by gas ionization or beam loss. At top energy, the primary electron flux is strongly enhanced, due to photoemission from synchrotron radiation. This latter process does not contribute to the electron seed at injection, since here the photon energies are too low to generate any photoelectrons. The number of photons emitted per radian is given by $5/(2\sqrt{3})\,\gamma/137$, which, at 7 TeV, is about 79 photons per proton and per radian deflection angle. For an LHC half cell of 53.45 m length and 15.3 mrad bending angle, this amounts to 0.023 photons incident per proton and per metre at 7 TeV. On the LHC Cu sawtooth chamber and with the LHC photon spectrum, the initial probability of photoemission is 5%, decreasing to about 2.5% after conditioning [63]. The primary synchrotron radiation at 7 TeV is incident on the outer wall of the chamber according to a Gaussian vertical distribution of about 1.4 mm rms in height. The

azimuthal distribution of the absorbed photons determines the region from where photo-electrons are emitted. In a dipole magnet, photo-electrons can reach the vicinity of the beam only if they come from the top or bottom of the chamber. Thus it is desirable to absorb the maximum number of photons at their primary impact point on the horizontally outward side of the beam pipe, and to keep the photon reflection as low as possible. One distinguishes forward, diffuse, and backward reflection. In the LHC a low forward reflectivity is accomplished by impressing a sawtooth surface on the beam screen (*i.e.*, the inner part of the beam pipe). However, about 20% of the incident photons are diffusely reflected from the sawtooth, roughly according to a $\cos^2\phi$ distribution (where ϕ denotes the angle of the reflected photon with respect to the horizontal plane), so that about 10% of the reflected photons (or 2% of the total) may be absorbed at the top and bottom of the chamber [64]. Preliminary experimental data on photon backward reflection indicate that this effect would only yield a small additional contribution [65]. In simulations, the measured energy distribution of the emitted photoelectrons [66] is approximated by a (one-sided truncated) Gaussian with a peak at 3 eV and an rms spread of 3 eV. The photoelectron emission angles are assumed to be distributed uniformly in spherical coordinates.

Secondary electron emission consists of two components: the true secondaries and the elastically reflected electrons. The true secondary yield as a function of the primary impact energy E_p is expressed by the Furman formula [67] $\delta_{\rm true}(E_p) = \delta_{\rm max} s E_p/E_{\rm max}/(s-1+(E_p/E_{\rm max})^s)$, where $s \approx 1.35$ and the two parameters $\delta_{\rm max}$ and $E_{\rm max}$ describe the maximum yield and the energy at which it is attained. These parameters vary with the angle of incidence. Laboratory measurements indicate that $E_{\rm max}(\theta) \approx E^0_{\rm max}(1+0.7(1-\cos\theta))$ [67] and $\delta_{\rm max}(\theta) \approx \delta^0_{\rm max}\exp(0.5(1-\cos\theta))$ [68], where quantities with superscript 0 refer to perpendicular incidence. The values of $\delta^0_{\rm max}$ and $E^0_{\rm max}$ characterize the degree of conditioning. In the laboratory, samples are fully conditioned after depositing an electron dose of 10 mC/mm^2 [69], and values of $\delta^0_{\rm max}$ below 1.3 can be obtained after a dose of 2 mC/mm^2 [69]. The final conditioning effect may depend not only on the total dose, but also on the electron flux during the processing [70]. Fully conditioned laboratory samples at room temperature sometimes exhibit maximum secondary emission yields as low as $\delta^0_{\rm max} \approx 1.1$. Similar yields after conditioning were also observed at cryogenic temperatures [71]. In-situ measurements with room-temperature detectors at the SPS in 2002 and 2003 showed $\delta^0_{\rm max} \approx 2.35$ and $E^0_{\rm max} \approx 260$ eV for the initial state, and $\delta^0_{\rm max} \approx 1.5$ and $E^0_{\rm max} \approx 240$ eV after about 2 days of dedicated 'beam scrubbing' [72]. Following this initial decrease, $\delta^0_{\rm max}$ remained approximately constant for several days until the end of the scrubbing period. This saturation at $\delta^0_{\rm max} \approx 1.5$ in the SPS is attributed to operational constraints on the available beam intensities and to the re-adsorption of the residual gas [70]. First preliminary measurements with cold detectors in the SPS suggest that the scrubbing time at cryogenic temperatures might be longer than at room temperature [73, 74]. For LHC simulation purposes, the value of $E^0_{\rm max}$ corresponding to a certain value of $\delta^0_{\rm max}$ has been estimated by linear interpolation from the above numbers for the SPS (see Tab. 5.8). The energy distribution of the true secondaries is concentrated at low energies, and can be parametrized as in [69], namely $D(E_s) \propto \exp(-(\ln E_s/E_0)^2/2\tau^2)$, where $E_0 \approx 1.8$ eV and $\tau \approx 1$ are two fitting parameters. For this distribution, the average emission energy of the true secondaries is $\bar{E}_s \approx 8.1$ eV. The initial angular distribution of the true secondaries in spherical coordinates, $dN/d\Omega$, is taken to be of the form $\cos\theta$, where θ denotes the emission angle of the secondary electron with respect to the surface normal [75].

For incident electrons of low energy, a significant portion of the secondary electrons are not true secondaries, but instead they are elastically reflected electrons. Depending on the interpretation of the experimental low-energy data, the yield of elastic reflection can be expressed in two different ways: First, one may write the elastic yield as $\delta_{\rm el} = f/(1-f)\delta^0_{\rm true}$, where f is the measured ratio of elastic reflections to the total number of secondaries, which may be parametrized as in [69]. Second, an alternative parametrization is derived from the assumption that the electron reflectivity is not affected by the conditioning process, and that it always approaches the value of 1 in the limit of zero primary energy. This assumption can be modelled by the parametrization $\delta_{\rm el} = (\sqrt{E_p+E_0}-\sqrt{E_p})^2/(\sqrt{E_p+E_0}+\sqrt{E_p})^2$. The single parameter $E_0 \approx 150$ eV has been fitted from measurements [76]. This second parametrization gives rise to a minimum in the total secondary yield, at around 10 eV, which appears consistent with many of the experimental data, *e.g.*, in [76], but it could still prove an artifact of the measurement apparatus. Fig. 5.4 displays alternative curves for the total secondary emission yield at perpendicular incidence, $SEY \equiv \delta_{\rm true}+\delta_{\rm el}$, as a function of the primary electron energy, corresponding to the different parametrizations. The centre curve assumes the first model of elastic

reflection, the top curve the second. For completeness, the bottom curve shows the Furman's formula for true secondaries only, using the parameters $\delta^0_{\max} = 1.06$ and $E^0_{\max} = 262\,\mathrm{eV}$ ($\delta_{\mathrm{el}} = 0$). Most simulations in this report have been performed for the first model (centre curve), which includes a moderate amount of elastic electron reflection. It is always assumed that, unlike for the true secondaries, the yield of the elastic reflection, δ_{el}, is independent of the angle of incidence.

Table 5.8: Typical LHC simulation parameters related to electron cloud build up at 7 TeV.

parameter	initial	final
maximum secondary emission yield $\delta^0_{\max}$	1.9	1.1
energy for which yield is maximum, $\epsilon^0_{\max}$	249 eV	230 eV
photo-electrons per absorbed photon	5%	2.5%
photo-electrons per proton and metre in the arc	0.00116	0.00058
photon reflectivity R	20%	20%
parameter for elastic electron reflection E_0	150 eV	150 eV

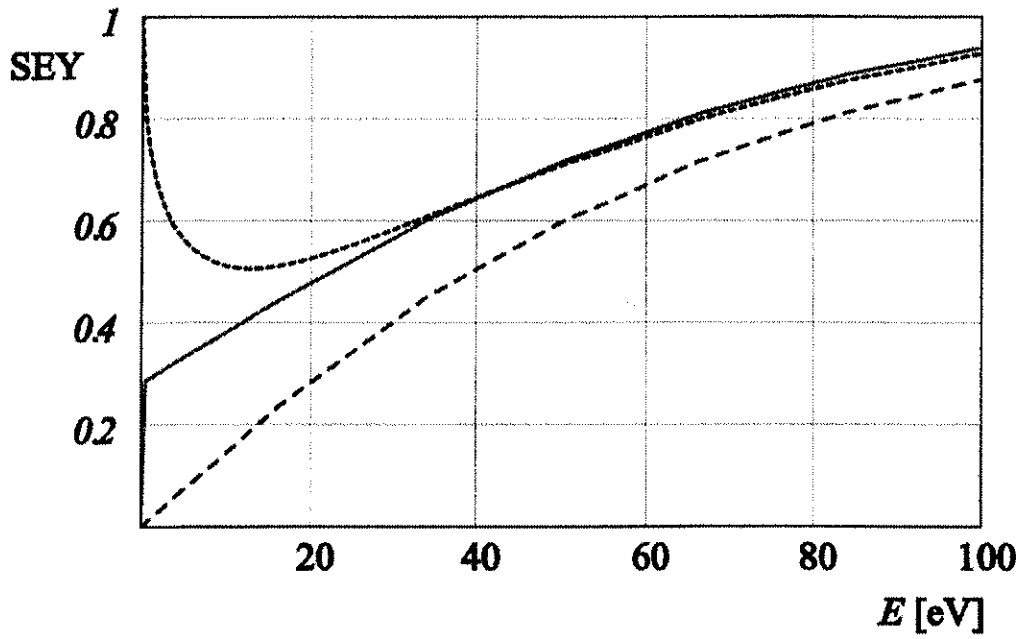

Figure 5.4: Model of the total secondary emission yield, $SEY = \delta_{\mathrm{true}} + \delta_{\mathrm{el}}$, at perpendicular incidence, as a function of the primary electron energy, assuming no elastic reflection (long dashes, bottom curve), a secondary emission that decreases at low energies towards about 0.3 (solid, centre curve), and the model that seems to best fit the measured data in [76], with a minimum near 10 eV and a reflection probability of one for incident energies approaching zero (short dashes, top curve). The other parameters for this graph correspond to the laboratory measurement of a fully scrubbed Cu surface at 9 K ($\delta^0_{\max} = 1.06$, $E_{\max} = 262\,\mathrm{eV}$) [76].

5.8.2 Build-Up and Saturation

If an electron amplification occurs, the cloud builds up until the growth is balanced by its own space charge. This limit can arise either if the average charge of the electrons equals that of the protons (neutralization) [10] or when, in the time interval between two proton bunches, the space charge potential exceeds the initial kinetic energy of the secondaries [77]. Thus, the estimated saturation density is the smaller value of [10, 77] $\rho_e^{(1)} \approx \bar{E}_s/(m_e c^2 b^2 r_e)$ and $\rho_e^{(2)} \approx N_b/(\pi b^2 L_{\mathrm{sep}})$, where L_{sep} denotes the bunch spacing in metres. For the nominal LHC parameters, these limiting densities are quite comparable: $\rho_e^{(1)} \approx 1.4 \times 10^{13}\,\mathrm{m}^{-3}$ and $\rho_e^{(2)} \approx 1.2 \times 10^{13}\,\mathrm{m}^{-3}$. As an illustration, Fig. 5.5 presents some simulations for the electron cloud build up in the LHC

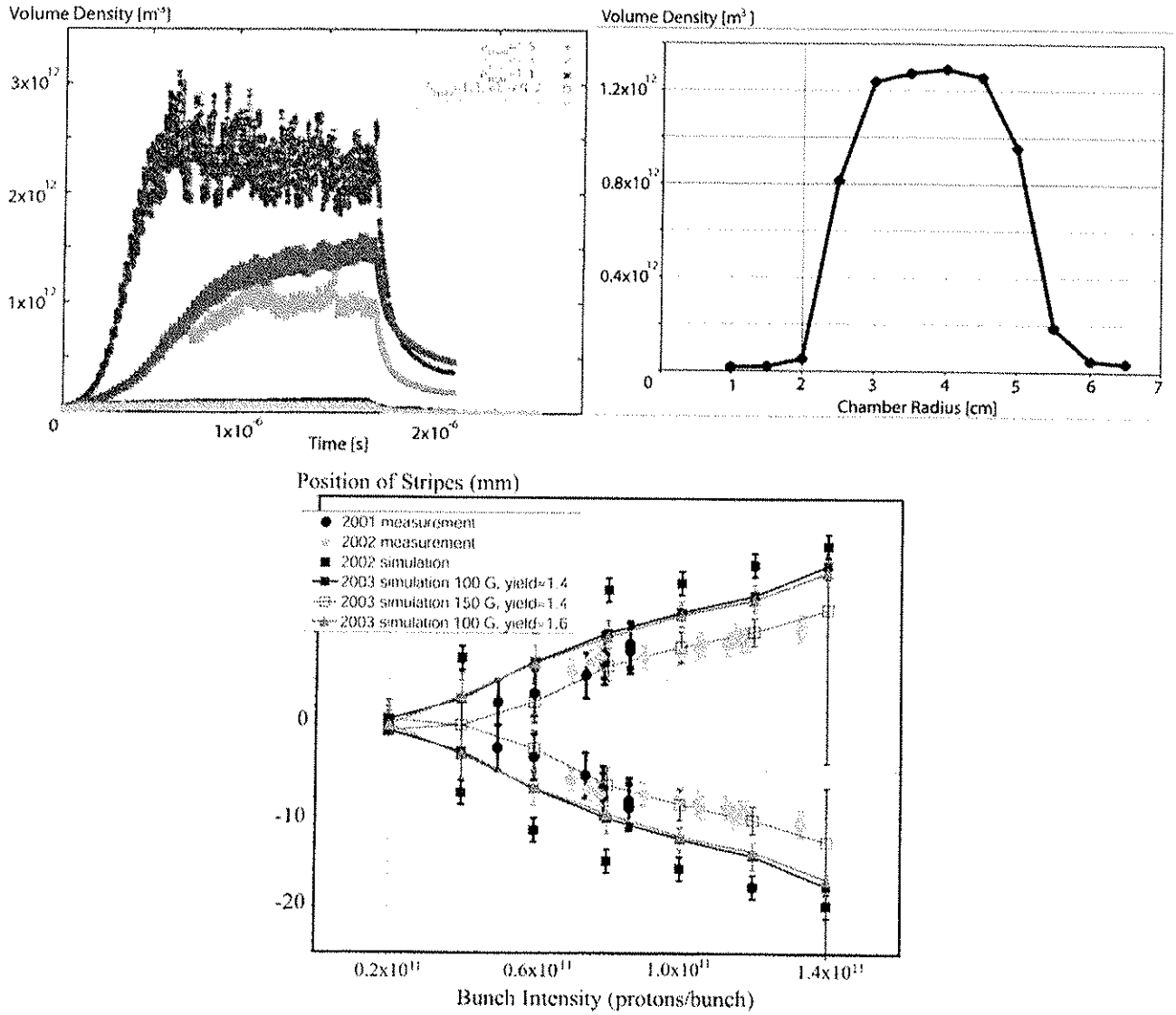

Figure 5.5: Top left: simulated electron volume density [m^{-3}] in an arc dipole as a function of time [s], for $N_b = 10^{11}$, various values of δ_{max}, two bunch spacings, and two models of the elastic electron reflection; top right: the simulated electron density [m^{-3}] in a circular field-free region of the long straight section as a function of beam pipe radius [cm], for $N_b = 1.15 \times 10^{11}$ and $\delta^0_{max} = 1.3$; bottom: the horizontal position of regions with high electron multipacting ("stripes") measured inside a dipole magnetic field at the SPS during 2001 and 2002 [55], as a function of bunch intensity, compared with simulations performed in 2002 and 2003. The effects of altering the magnetic field and using different values of δ^0_{max} are also shown [12].

and in the SPS, which were obtained using ECLOUD version 2.5. The top left picture shows the simulated build up of electron density during the passage of an LHC bunch train (a single PS batch) through an arc cell for a bunch population of $N_b = 10^{11}$. The various curves refer to different values of δ^0_{max}, to the two models of elastic reflection, and to two different bunch spacings. For the range of δ^0_{max} values considered here, the steady-state densities are determined by a balance of production and decay rates, and stay at least a factor of 10 below the ultimate space-charge saturation limit estimated above. The top right picture of Fig. 5.5 displays the simulated steady-state electron volume density as a function of aperture, for a field-free region, assuming $N_b = 1.15 \times 10^{11}$, and $\delta_{max} = 1.3$. The primary photo-electron flux in this simulation was taken to be 20 times smaller than in the arcs, which is representative of the long straight sections. The picture illustrates that for a single beam, radial apertures between 25 and 55 mm are most susceptible to an electron-cloud build up. Similar simulations have been performed for the SPS, where a reasonable agreement between various

simulated and measured electron-cloud properties, such as spatial structure, flux, energy spectrum, and heat load, was achieved [12, 55]. An example is shown in the bottom picture of Fig. 5.5, which illustrates the horizontal position of two narrow regions with high multipacting ("stripes"), as measured and simulated for an SPS dipole field. Since the vertical chamber dimension in the SPS is nearly the same as that for an LHC dipole, the location of the stripes is also expected to be similar in both accelerators, and, therefore, the observed and predicted variation of the stripe location with intensity in the SPS has motivated the addition of baffles at each LHC-beam screen pumping slot, which block the passage of electrons onto the cold bore of the magnets.

5.8.3 Heat Load

The heat load deposited by the electron cloud is a concern for the cold parts of the LHC, where it may quench the super-conducting magnets. Inside the 1.9-K cold bore of the magnets, the electron-cloud heat load is intercepted by a dedicated beam screen, which is held at a higher temperature of 5–20 K. As mentioned in Sec. 5.8.2, pumping holes in the beam screen are shielded by baffles, such that the electron cloud does not contribute to the heat load onto the 1.9-K cold bore. The heat load for the latter is then dominated by nuclear interactions, depositing about 0.035 W/m [43], which is to be compared with a cooling capacity of 0.32 W/m per beam at 1.9 K [78]. The total available cooling capacity for the warmer beam screen is 1.15 W/m per beam [78]. In addition to the heat from the electron cloud, this number must also accommodate the heat loads due to synchrotron radiation and impedance. The synchrotron-radiation heat load increases linearly with the total beam current, while the impedance contribution rises quadratically with the bunch population N_b. For the ultimate LHC intensity of $N_b = 1.67 \times 10^{11}$, the average arc heat load due to synchrotron radiation is 0.25 W/m, and that from impedance (res. wall, welds, pumping slots, shielded bellows, and BPMs) is estimated at 0.41 W/m [79]. The remaining cooling capacity, about 0.5 W/m at nominal intensity and energy, may be allocated to the electron cloud. The expected average electron-cloud heat loads in the arcs for various surface and beam conditions are computed by averaging simulation results over a 53.452-m long arc half cell, which comprises a field-free region of length 6.433 m, a dipole field of 42.9 m, and quadrupole plus sextupole fields extending over a length of 4.119 m.

Fig. 5.6 displays simulation results, obtained with ECLOUD version 2.5, for the steady-state electron density and the heat load generated during the passage of an LHC bunch train. The three pictures show the heat load and the electron volume density as a function of bunch population and also as a function of each other. The various curves refer to three different values of $\delta^0_{\max}$, to the two models of elastic electron reflection, and to both the nominal and twice the nominal bunch spacing. The available cooling capacity is also indicated, in the top left picture. For the nominal bunch spacing a maximum secondary emission yield of $\delta^0_{\max} = 1.1$ ensures sufficient cooling capacity, while for larger values of $\delta^0_{\max}$, *e.g.*, 1.3, doubling the bunch spacing reduces the heat load to an acceptable level. On the other hand, bunch spacings shorter than nominal likely increase the heat load to unacceptable values, so that enlarging the number of bunches does not appear a viable path towards ultimate LHC luminosities in a future upgrade [45]. Colliding a smaller number of long super-bunches, instead, would promise both a high luminosity and a much reduced electron-cloud heat load [80], but imply substantial detector upgrades.

5.8.4 Beam Stability

At various storage rings, for example the SPS, electron clouds have caused beam instabilites and disrupted operation. In the SPS a coupled-bunch instability is observed in the horizontal plane, and a single bunch instability in the vertical [59, 60]. The strengths of the electron-cloud single-bunch and multi-bunch wake fields ($W_{\rm sb}$ and $W_{\rm mb}$) are estimated as [58, 81] $W_{\rm sb} \approx 2W_{\rm mb} \approx 8\pi\rho_e C/N_b$, where C denotes the circumference, ρ_e the average electron density, N_b the bunch population, and the wakes are quoted in units of m^{-2}. The corresponding growth rate of the coupled-bunch instability is [81] $\tau_{e,\rm CB} \approx \gamma/(2\pi r_p c\bar{\beta}\rho_e)$, and the threshold of the single-bunch ('TMCI'-like) instability can be expressed as a threshold in the electron density as [58] $\rho_{e,\rm thr} \approx 2\gamma Q_s/(\pi\bar{\beta}r_p C)$, where Q_s denotes the synchrotron tune, and $\bar{\beta}$ the average beta function.

The instabilities are primarily a concern at injection, where the beam is less rigid. Here, the estimated multi-bunch instability rise times vary between 2 and 2000 turns, depending on the electron density. The effect

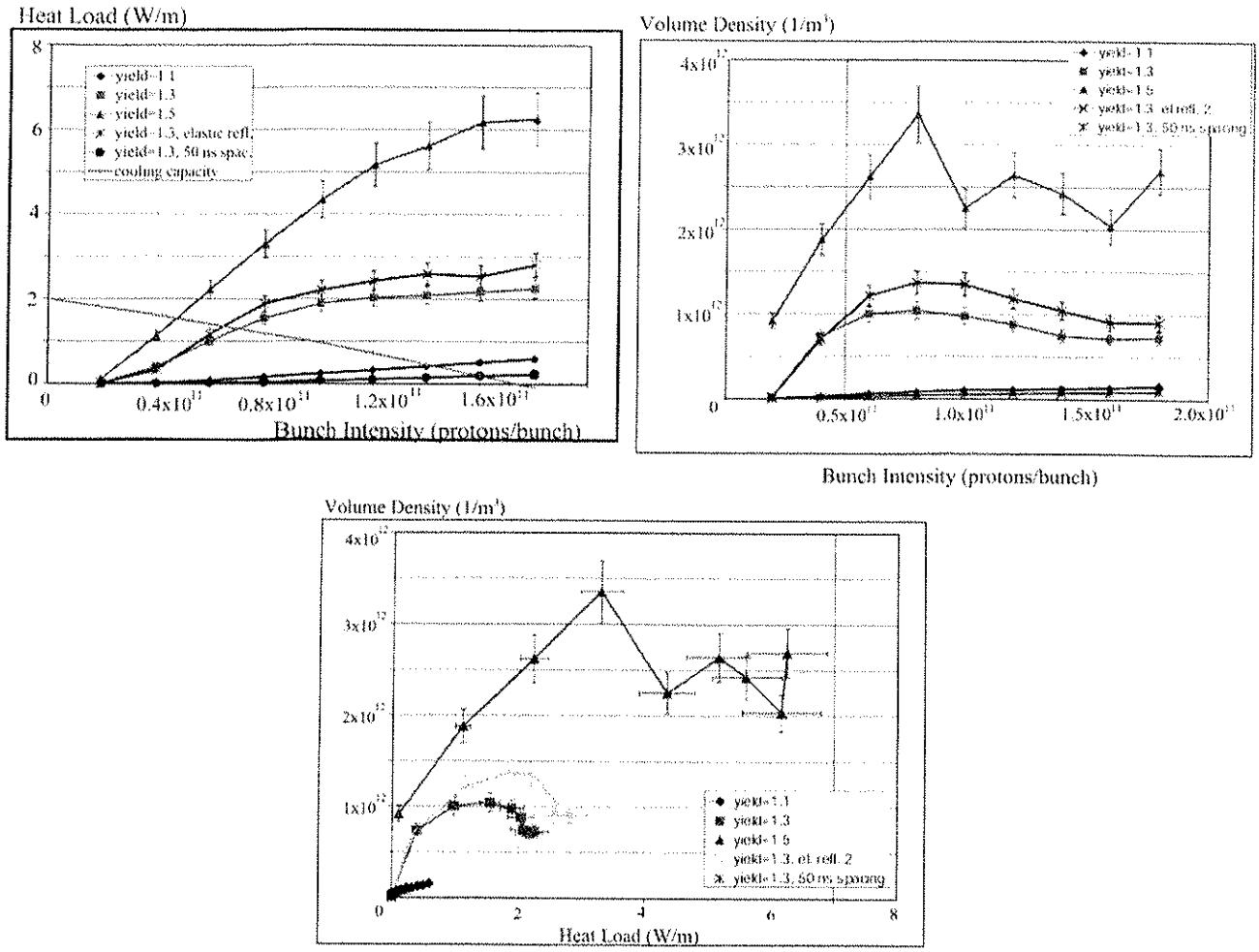

Figure 5.6: Simulated electron-cloud heat load and density for the LHC: average arc heat load and available beam screen cooling capacity (assuming an upgrade of the turbines for the four LEP cryoplants) as a function of bunch population (top left), simulated average electron volume density in the arc for the last bunch in a train as a function of the bunch population (top right), and simulated volume density as a function of simulated heat load for an LHC arc cell (bottom). Results for three different values of $\delta^0_{\max}$ (1.1, 1.3 and 1.5), using the first model of elastic reflection, are compared with those for the second model and for twice the nominal bunch spacing, at the intermediate value $\delta^0_{\max} = 1.3$.

of the electron cloud can be enhanced by the conventional impedance [82, 83], and also by the beam-beam interaction [84, 85]. Simulation studies of single-bunch instabilities driven by the electron cloud, with and without impedance, were performed using the code HEADTAIL for both the LHC and the SPS [82, 86]. For zero chromaticity, the simulations indicate an instability threshold at about $\rho_e \approx 5 \times 10^{11}$ m^{-3}. Above the threshold, the single-bunch emittance growth time decreases roughly inversely with the electron density. It is 160 turns for an average electron cloud density of $\rho_e \approx 10^{12}$ m^{-3}, and only 16 turns for $\rho_e \approx 10^{13}$ m^{-3}. Hence, if strong multipacting occurs in the arcs of the LHC, the strength of the vertical single-bunch instability may become comparable to that in the SPS. Both in the SPS experiments and in the simulations, the emittance growth is suppressed by a high positive chromaticity. This could also prove a viable cure for the LHC.

The actual magnitude of the electron density can be inferred from the induced coherent tune shift as [87] $\Delta Q \approx r_p \bar{\beta} \rho_e C/(2\gamma)$. For full saturation of the electron density ($\rho_e \approx 1.2 \times 10^{13}$ m^{-3}) the expected tune shift amounts to 0.05. As shown in Fig. 5.6, for $\delta^0_{\max} = 1.5$ a maximum electron density $\rho_e \approx 3 \times 10^{12}$ m^{-3} is expected and therefore a maximum tune shift at the end of a bunch train of about 0.015. The measured tune shifts in the SPS are of the order of 0.01.

5.8.5 Emittance Growth

Simulations indicate the possibility that the electron cloud may sustain long-term emittance growth [86]. The simulated emittance growth sensitively depends on the details of the simulation model, however, such as whether the beam-electron interaction is applied at random betatron phases or at the same constant phase from turn to turn. For the former case the growth seems to converge towards zero, as the number of beam-electron interaction points is increased in the code HEADTAIL [82, 86]. Nevertheless it is not excluded, that an incoherent emittance growth may occur due the incoherent tune spread induced by the pinched electrons or due to nonlinear resonances, *e.g.*, of order 3–10, which can be excited by the electron cloud [86]. This question can be investigated by QUICKPIC [88] simulations, which model the continuous interaction of the beam and the electrons.

5.8.6 Electron Cloud at Collimators

An electron cloud could also be generated at the collimators. In this case, the primary source of electrons are not photoelectrons, but electrons emerging from the nuclear and electromagnetic shower initiated by lost protons. In preliminary FLUKA simulations [89], 7-TeV protons impinged on a graphite collimator jaw with impact parameters uniformly distributed between 0 and 200 nm from the collimator edge. From the simulation, the fluence spectrum (*i.e.*, the flux weighted by $1/\cos\theta$) of charged hadrons, electrons and positrons emitted from the jaw was obtained, down to energies of 1 keV. Assuming a factor of 5 mg/(MeV cm^2) for the conversion efficiency of ionization energy into secondary electrons at perpendicular incidence [90], a beam lifetime of about 15 minutes yields an estimated total flux of low-energetic electrons emerging from a primary collimator jaw equal to 1.3×10^{14} s^{-1} [89], or, equivalently, 4×10^{-5} electrons per passing proton. This rate is comparable to the photoemission in the LHC arcs. More detailed studies of the lower-energy secondary electrons generated by the collimator shower and their longitudinal distribution may be needed. Assuming a maximum secondary emission yield $\delta_{\max} = 1.1$, the saturation level of the electron cloud density is about 2.5×10^{10} m^{-3}, *i.e.*, somewhat smaller than typical arc densities. The dependence on the collimator half-gap is weak.

5.8.7 LHC Strategy

The LHC design has adopted a fourfold strategy for suppressing the formation of an electron cloud:

(1) In the warm sections, which amount to about 10% of the total circumference, the beam pipe will be coated by a TiZrV getter developed at CERN [91]. This getter does not only provide an excellent pumping performance, but after activation, at only 180 centigrade, its maximum secondary emission yield drops down to $\delta^0_{\max} \approx 1.1$ [92, 93, 94], a value for which a significant electron cloud build up is no longer expected. The non-existence of an electron cloud in getter-coated regions has been confirmed in SPS experiments [95]. Even in the unlikely event that an electron-cloud builds up in the warm sections of the LHC, the getter still has its virtue. Namely, ionization of gas molecules by the low-energy electrons, with a high cross section of up to 400 Mbarn, and the subsequent absorption of the ionized molecules by the getter significantly increases the pumping speed in the affected regions. Therefore, different from past storage rings, the pressure in the LHC experimental areas is expected to improve, if a cloud develops.

(2) In the arcs, the outer wall of the beam screen, at 5–20 K, will be equipped with a sawtooth surface (a series of 30-μm high steps spaced at a distance of 500 μm in the longitudinal direction) such that the synchrotron radiation always impinges perpendicularly on the sawtooth surface. The sawtooth greatly reduces the forward reflectivity from about 80% to 2%. The largest residual reflectivity is a diffuse reflection of about 20%. A low reflectivity of the outer chamber wall is desired, since in bending magnets photoelectrons emitted from this outer region are confined by the strong dipole field and do not interact much with the beam (see also Sec. 5.8.1).

(3) The pumping slots in the beam screen are shielded by baffles, so that, in the dipoles, there is no direct electron path along magnetic field lines between the beam region and the cold bore, and, therefore, also no additional heat load onto the latter (see Secs. 5.8.2 and 5.8.3).

(4) Operating the LHC with nominal parameters relies on the surface conditioning (scrubbing) effect, akin to the processing of an RF cavity, by which the maximum secondary emission yield decreases from an initial

value of about 2 to about 1.4 or below, after depositing a sufficient dose of electrons on the chamber wall (see discussion in Sec. 5.8.1). During commissioning, when the yield is still high, an increased bunch spacing and/or a reduced bunch intensity will greatly reduce the heat load. However this will also slow down the scrubbing of the vacuum chamber.

5.9 BEAM-BEAM EFFECTS

An important limit to the luminosity comes from the beam-beam effect which can cause emittance increase, poor lifetime or instabilities. Different types of beam-beam effects can be distinguished and affect the performance in different ways:

- Incoherent beam-beam effects (lifetime and dynamic aperture).
- PACMAN effects (bunch to bunch variations).
- Coherent effects (beam oscillations and instabilities).

5.9.1 Relevant parameters

The high luminosity requires a large number of bunches (2808) and to avoid unwanted collisions, a crossing angle is needed to separate the two beams in the part of the machine where they share a vacuum chamber. The size of the crossing angle is limited by the available aperture in the final quadrupole triplet and for high luminosity operation a crossing angle of 285 μrad is planned. For $\beta^* = 0.55$ m this provides a separation $\mathrm{d_{sep}}$ above $9\,\sigma$. With the bunch spacing of 25 ns this leads to a total of 120 long-range beam-beam interactions in the four interaction regions. Both the head-on and the long-range interactions have to be considered when beam-beam effects are studied. The strength of head-on collisions is usually measured by the linear beam-beam parameter ξ which for small values and nominal betatron tunes is equivalent to the linear tune shift of small amplitude particles. It can be written as $\xi = N_\mathrm{b} r_\mathrm{p}/4\pi\varepsilon_\mathrm{n}$ where N_b is the number of particles per bunch, r_p the classical proton radius and ε_n the normalized emittance. With nominal parameters we get a value of 0.0033 for a single head-on collision in the LHC.

5.9.2 Incoherent effects

When the beam passes through the strong non-linear field of the opposing beam, the dynamics of single particles can be strongly distorted up to the point where they are lost from the beam. Different factors are shown which are used to quantify this behaviour. The experience obtained at the Tevatron and the SPS proton antiproton collider is very relevant although basic parameters such as the number of bunches and the importance of long-range collisions are very different.

Beam-beam induced tune spread: budget from past experience (SPS and Tevatron)

Due to its non-linear nature, the beam-beam interaction will lead to an amplitude dependent tune spread in both planes. This spread must be accommodated in the tune diagram without crossing dangerous resonance lines. Thus the total spread originating from head-on and long range beam-beam interactions is very important and must be kept as small as possible [96, 97]. Experience from the SPS and the Tevatron shows that the total tune spread including all other sources and the beam-beam effect, should not exceed 0.015 [98]. This allows about $\approx$0.01 for the overall beam-beam tune spread ΔQ_bb. The tune spread from a head-on collision, ΔQ_ho, is ξ, which is the maximum tune shift. For sufficiently large separation, i.e. above $6\,\sigma$, the tune spread from long-range interactions, ΔQ_lr, is approximately proportional to $\frac{\kappa_\mathrm{par} N_\mathrm{b}}{\varepsilon_\mathrm{n}}/d_\mathrm{sep}^2$. Here κ_par is the total number of long range (parasitic) interactions. As an example Fig. 5.7 shows the tune distribution (footprint) for the nominal proton parameters with three head-on collisions, one offset collision (IP2) and the full number of long-range interactions. Particles up to amplitudes of $6\,\sigma$ are included. The overall spread is slightly above 0.010 in agreement with the requirements.

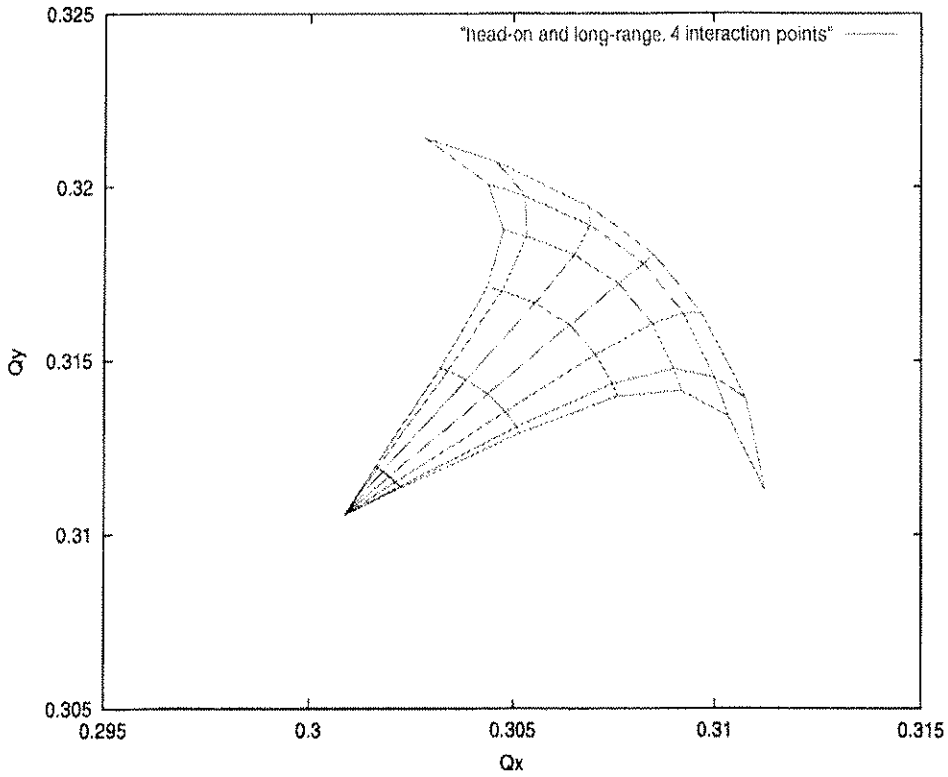

Figure 5.7: Two dimensional tune distribution versus amplitude (footprint) for nominal parameters in collision. Particles up to amplitudes of 6 σ are included.

Emittance variations from bunch to bunch will have implications for both long range and head-on beam-beam effects. In the first case they will reduce the normalized beam separation and therefore the available dynamic aperture for bunches with larger emittances. In the second case, head-on collisions of bunches with unequal sizes are known to lead to particle losses for the bunches with larger sizes [99]. Bunch-to-bunch emittance variations should therefore not exceed about 10%.

Dynamic aperture

An important single particle effect of the head-on and especially of the long range beam-beam interaction is the reduction of the beam lifetime due to the diffusion of large amplitude particles towards the aperture limit [100, 101]. The effects of the triplet errors together with the beam-beam interaction was intensively studied for collision as well as for injection [100]. In both cases the beam-beam interaction leads to a sizeable reduction of the dynamic aperture. Fig. 5.8 shows the results for 10^5 and 10^6 turns when the beam-beam interaction at collision is included. It was found that even very small non-linearities are sufficient to lead to particle losses when the beam-beam force is present. Therefore, the benefits of the triplet correction system are much reduced, in particular when longer term tracking is performed. Fig. 5.9 shows the results at injection. For comparison the dynamic aperture without beam-beam interaction is shown. The reduction of the aperture is very significant, in particular for a large number of turns. A more detailed discussion of the results can be found in [100]. Some approximate scaling [101] suggests that the reduction of dynamic aperture is proportional to $\sqrt{\frac{\kappa_{\rm par} N_{\rm b}}{\varepsilon_{\rm n}}}$, i.e. $\propto \sqrt{\Delta Q_{\rm lr}}$, which shows the relevance of the tune spread.

5.9.3 PACMAN effects

The bunches in the LHC do not form a continuous train of equidistant bunches spaced by 25 ns, but additional space must be provided to allow for the rise time of kickers. The whole LHC bunch pattern is composed of

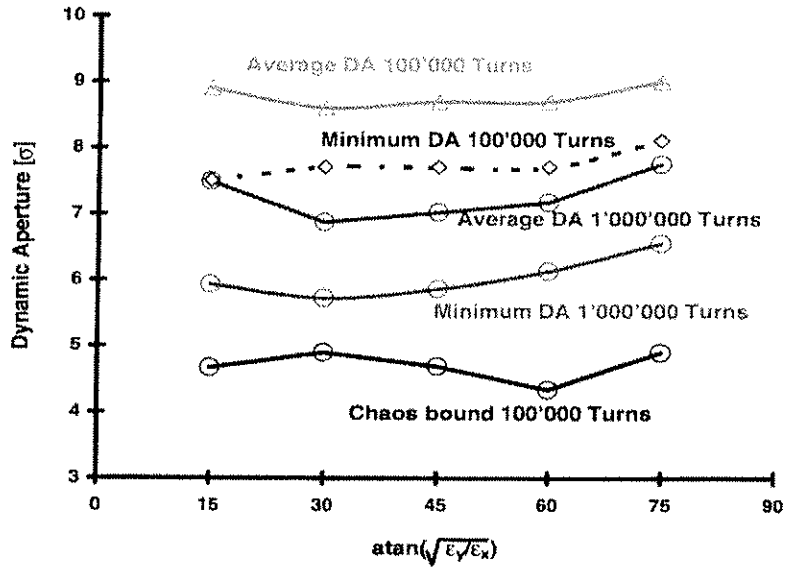

Figure 5.8: Dynamic aperture at collision including beam-beam interaction. Tracking is performed for 10^5 and 10^6 turns.

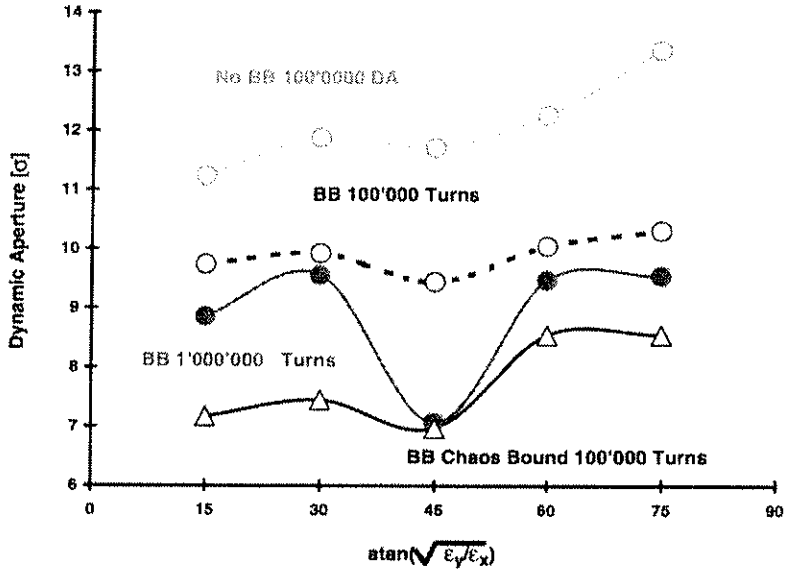

Figure 5.9: Dynamic aperture at injection with and without beam-beam interaction. Tracking is performed for 10^5 and 10^6 turns.

39 smaller trains of 72 bunches separated by gaps of various lengths (Fig. 5.10) including a large abort gap for the dump kicker. Due to the symmetric layout, all bunches collide head-on in interaction points 1 and 5. However, bunches at the beginning and end of a train suffer only half the long-range interactions at each interaction point [102]. As a consequence, they experience only half the accumulated beam-beam effects and may have a different dynamics [102]. The actual bunch filling scheme is presented in Fig. 5.10 and shows the various gaps in the train. Since the pattern does not have a complete fourfold symmetry, certain bunches will encounter the abort gap in points 2 and 8, therefore missing head-on collisions. A further complication is introduced by LHCb in interaction point 8 because the collision point is displaced by 11.22 m (corresponding to 15 RF buckets or 37.5 ns) from the symmetry point. Therefore the first three bunches of each train in one beam and the last three bunches of the other beam do not collide head-on in interaction point 8. As a consequence a significant number of bunches experience three (252 bunches) or only two (3 bunches) out of the four head-on collisions. Instead of 2808 bunch crossings per revolution as in interaction points 1 and 5, only 2736 will happen in interaction point 2 and only 2622 in 8. Bunches which do not have the regular collision pattern

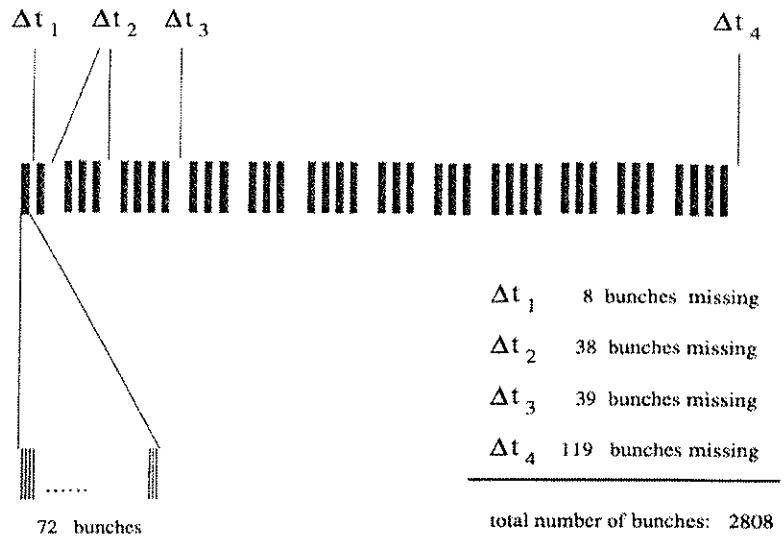

Figure 5.10: Bunch filling scheme for the LHC.

have been named PACMAN bunches in the literature. Only 1443 bunches are regular bunches with 4 head-on and 120 long range interactions, i.e. about half of the bunches are not regular. The identification of regular bunches is important since measurements such as tune, orbit or chromaticity should be selectively performed on them.

Bunch to bunch variation

As a result of the different accumulated beam-beam effects, a bunch to bunch variation of vital parameters such as orbit, tune and chromaticity must be expected. Such variations have been observed in LEP and have limited the performance [98]. While tune or orbit changes of the whole beam can be corrected, this is not possible on a bunch to bunch basis. It is therefore important to minimize these effects. A particular feature of long-range interactions helps in this case. The derivatives of the transverse force for head-on and long-range interactions have different signs and therefore the tune shift has a different sign in the plane of separation with respect to the orthogonal plane. This feature can be used for a partial compensation of beam-beam effects and becomes vital to minimize bunch to bunch variations. All calculations of bunch to bunch variations are done for nominal parameters, in particular for the nominal bunch intensity of 1.15×10^{11} particles per bunch.

Crossing schemes

It was already mentioned in the chapter on the optics that the crossings in the high luminosity regions (interaction points 1 and 5) occur in orthogonal planes [103, 104]. Since these regions are exactly opposite in azimuth, the same bunch combinations will experience long-range and head on interactions in the two regions, although in different planes. Having horizontal, respectively vertical, long-range interactions for the same bunch combinations can efficiently compensate their effects to first order. In particular the tune shifts of the bunches are compensated. To allow a good compensation, the two interaction regions should have a similar layout. The two other interaction regions in points 2 and 8 have a larger β^* and do not significantly contribute to long-range interactions. Therefore no compensation is required. More details and an evaluation of the stability of the compensation in the presence of imperfections are discussed in [105].

Orbit effects

The beam-beam kick for separated beams has a constant, i.e. amplitude independent contribution which changes the orbit of a bunch. The closed orbit of a beam can be corrected, however different orbits from bunch

to bunch, separated by 25 ns, cannot be corrected. In general, these patterns are not antisymmetric for the two beams and not all bunches can be made to collide head-on [102]. A small offset is therefore unavoidable which could lead to emittance growth [106]. One has to minimize these effects by a proper choice of the crossing schemes [105] and the filling pattern [107]. The compensation effect on the orbit of individual bunches is

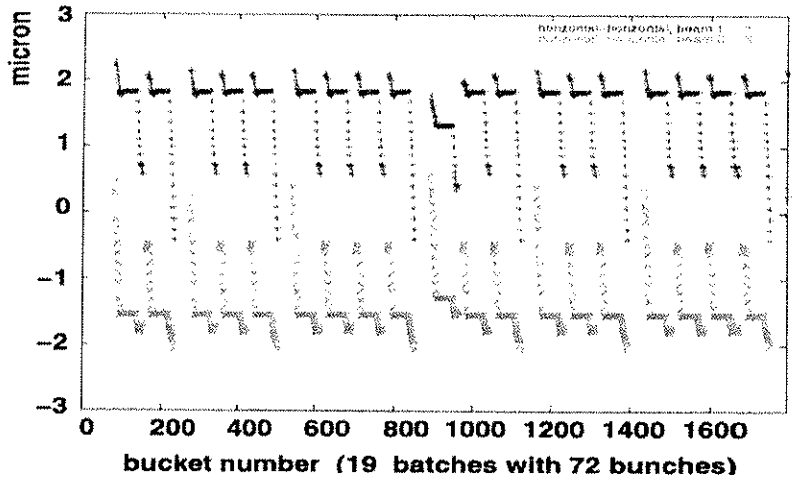

Figure 5.11: Horizontal orbit variation for beam 1 (upper trace) and beam 2 (lower trace) at interaction point 1 for horizontal-horizontal crossing. The first half of the whole bunch pattern is shown.

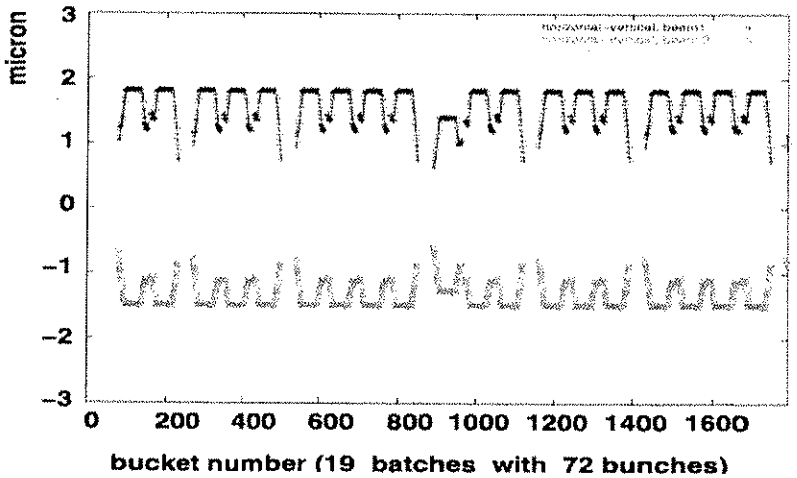

Figure 5.12: Horizontal orbit variation for beam 1 (upper trace) and beam 2 (lower trace) at interaction point 1 for vertical-horizontal crossing. The first half of the whole bunch pattern is shown.

demonstrated in Figs. 5.11 and 5.12. In both the calculated horizontal offset of the bunches along the bunch trains in interaction point 1 are shown. The calculation is done self-consistently using the full collision scheme and the beam optics of both beams [108]. The bunches are affected as a whole and the coherent beam-beam kick is calculated and applied. The first figure shows the closed orbits of the two beams for two horizontal crossings in interaction points 1 and 5 and the second for alternating, i.e. vertical (IP1) and horizontal (IP5) crossings [105]. The crossing planes in IP2 (vertical) and IP8 (horizontal) are the nominal for both cases. The beams in IP2 are separated to reduce the luminosity in proton-proton collisions. The different orbits of the leading and trailing bunches are very visible. The regular bunches all have the same closed orbit and appear on a straight line in the central part of the bunch trains. The orbit spread within the bunch train is significantly smaller in the second case. While in the first case the maximum orbit spread within the trains is approximately 2.5 μm, it is only around 0.9 μm for the case of alternating crossing planes. Only half of the whole bunch pattern is shown since no significant information is added for the full bunch pattern. The effect of the large abort gap is visible for the bunches with bucket numbers around 860. Due to the symmetry of the crossing

schemes, the vertical offsets in interaction point 5 show the same behaviour [105]. The vertical orbits in IP1 and the horizontal orbits in IP5 are antisymmetric due to the symmetry properties and the beams can collide head-on, although not in the centre of the collision point [105]. Since these effects are intensity dependent, the orbits may move and partially separate the beams at the interaction point during a typical LHC run when the intensity decays. A further source of beam separation is very low frequency ground motion. It was shown [109] that a separation of about 0.5 σ has to be expected during a typical 8 hours run. Both effects have to be corrected during an LHC run to maintain the maximum integrated luminosity.

Tune and chromaticity

In Figs. 5.13 and 5.14 results from the self-consistent calculation [108] for the horizontal tune (Fig. 5.13) and the horizontal chromaticity (Fig. 5.14) are shown. While all regular bunches have practically the same tune and chromaticity, the PACMAN bunches show significant differences. For the case of two horizontal crossings the spread is probably too large to ensure a safe operation. Similar results can be obtained for the vertical plane [105]. The compensation is very good and clearly demonstrates the necessity for the alternating crossing planes. The missing head-on collisions result in a different coherent tune of the bunches and the structure is very visible, showing the missing collisions of the first three bunches in each batch and the position of the abort gap. Additional spread is expected from unavoidable bunch to bunch fluctuations of the intensity and emittance. To keep the spread acceptable, the variation of both, intensity and emittance should not be larger than 10% [105]. It is therefore vital to minimize the systematic variations induced by beam-beam effects. For bunch intensities higher that the nominal, the alternating scheme is even more a necessity [110].

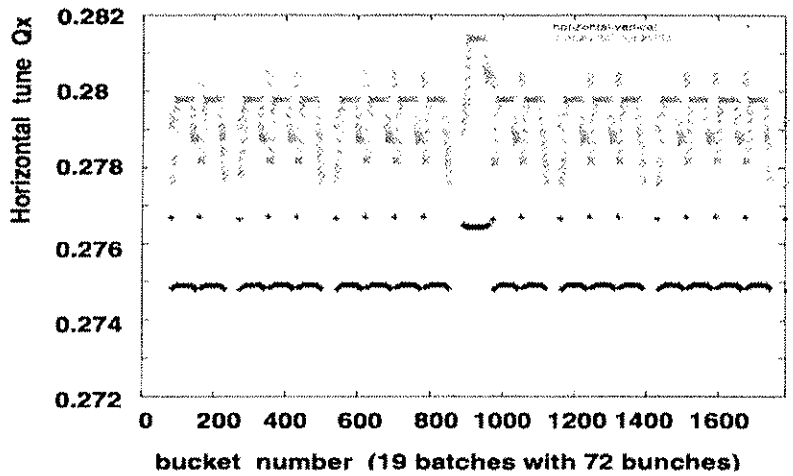

Figure 5.13: Horizontal tune variation along the first half of the batches. Horizontal-horizontal crossing in green (upper trace), vertical-horizontal crossing in red (lower trace).

5.9.4 Coherent effects

The LHC will be a machine with two equally strong beams and coherent beam-beam effects may be expected [111, 112]. Coherent modes of oscillations of the two counter rotating beams are coupled by the beam-beam interaction. They may become unstable depending on the strength of the beam-beam interaction and the other machine parameters. The most dangerous mode is the coherent dipole mode where a bunch oscillates as a rigid object around its nominal orbit. The predictions can be confirmed by multi-particle tracking [113]. The frequency spectrum of these coherent dipole oscillations is shown in Fig. 5.15 (left). The frequencies are shown as a tune change with reference to the unperturbed tune, normalized with the linear beam-beam tune shift. Fig. 5.15 (left) was produced with a multi-particle simulation using a recently developed algorithm for the field calculation [114] which gives quantitatively correct results. Only a single interaction point with one head-on interaction is considered to demonstrate the main features. The presence of long-range interactions

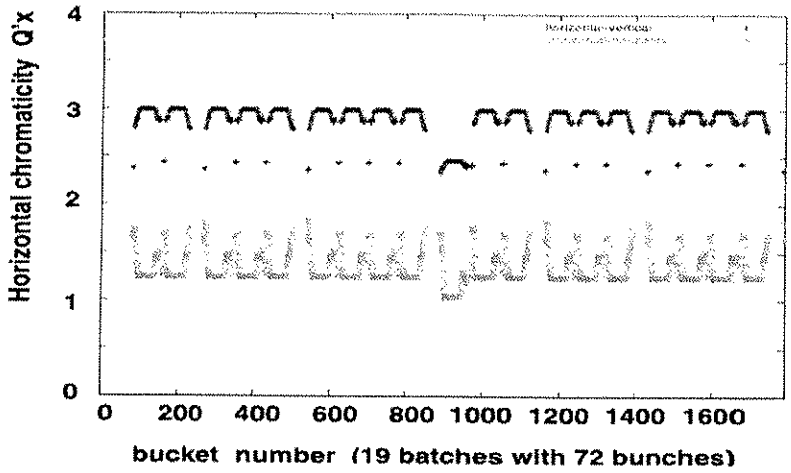

Figure 5.14: Horizontal chromaticity variation along the first half of the batches. Horizontal-horizontal crossing in green (lower trace), vertical-horizontal crossing in red (upper trace).

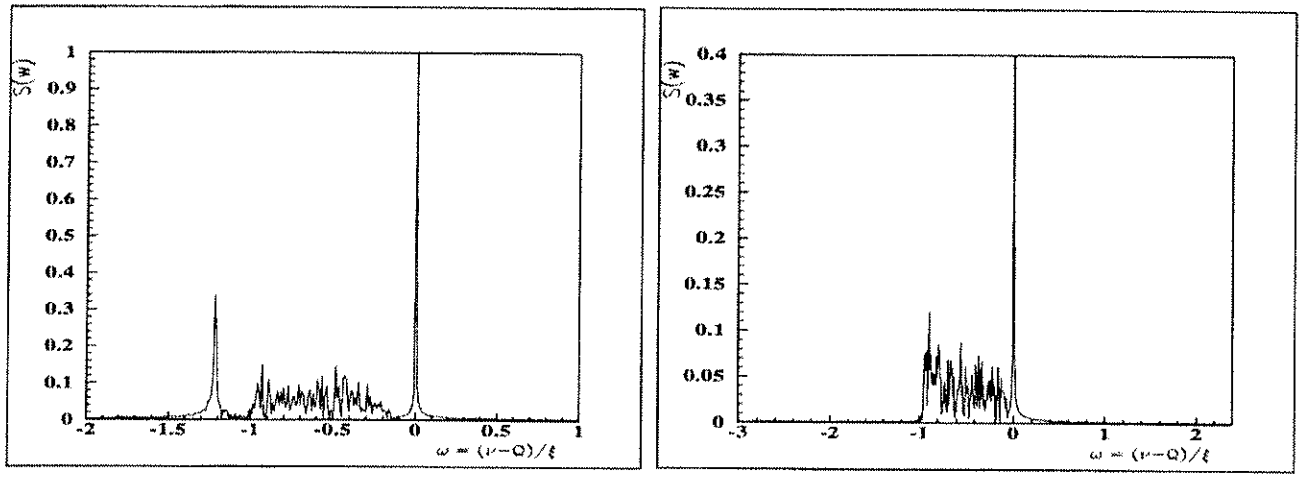

Figure 5.15: Frequency spectrum of dipole oscillation. One interaction point with a single bunch. Left figure shows spectrum for two identical beams. Right figure for an intensity ratio of 0.55 between the two beams.

complicates the picture and the underlying physics, but does not change the argument [114, 115]. All frequencies are contained in an interval limited by two discrete mode, the so-called σ- and π-modes. For the σ-mode the two beams oscillate exactly in phase, i.e. the distance between the two beams is constant when they collide and the beam-beam force cannot make this mode unstable. Furthermore, this mode oscillates with the unperturbed betatron frequency. In the π-mode the two beams oscillate exactly out of phase and this mode can become unstable and has the largest frequency shift with respect to the unperturbed tune. The tune shift of the π-mode is approximately $1.21\,\xi$ for round beams [111] (Fig. 5.15 left). Y. Alexahin predicted [112, 116] that for the nominal LHC parameters the π-mode will be outside the incoherent frequency spectrum which is due to beam-beam effects and extends from 0 to ξ for a single interaction region. This is reproduced by the simulation and clearly shown in Fig. 5.15 (left). Therefore the discrete π-mode will be outside this incoherent continuum and cannot be stabilized by Landau damping. The Landau damping can be restored when the symmetry between the two beams is broken [115], e.g. by different intensities (Fig. 5.15, right), different tunes [117], or broken symmetry for multiple interaction regions [118]. The frequency spectrum for two unequal beams with an intensity ratio of 0.55 is shown in 5.15 (right). The π-mode is now inside the continuum and is damped. This is quantitatively predicted in [112]. Additional degrees of freedom such a longitudinal motion and the overlap with synchrotron sidebands have been shown to effectively suppress the coherent π-mode [119]. It is believed that the symmetry breaking effects present in the LHC (multiple IPs, the already mentioned bunch to

bunch fluctuations etc.) are sufficient to suppress the excitation of coherent modes driven by the beam-beam interaction.

REFERENCES

[1] The LHC Study Group, *Design Study of the Large Hadron Collider (LHC)*, CERN report 91-03 (1991).

[2] F. Ruggiero, *Single-beam collective effects in the LHC*, CERN SL/95-09 (AP), LHC note 313 (1995) and Proc. Workshop on 'Collective Effects in Large Hadron Colliders', Montreux, 1994, eds. E. Keil and F. Ruggiero (Part. Accel. **50**, 1995), pp. 83–104, see also LHC Study Group, *The Large Hadron Collider, Conceptual Design*, eds. P. Lefevre and T. Pettersson, CERN/AC/95-05 (LHC) (1995).

[3] J.S. Berg, *Transverse instabilities in the LHC*, CERN LHC Project Report 16 (1996) and *Constraints imposed on LHC commissioning currents due to transverse collective modes and chromaticity*, CERN LHC Project Report 100 (1997).

[4] F. Ruggiero, J.S. Berg, O. Brüning, F. Caspers, M. Morvillo, and M. D'Yachkov, *Summary of the Single-Beam Collective Effects in the LHC*, PAC 97, Vancouver and CERN LHC Project Report 120 (1997).

[5] D. Boussard, D. Brandt, and L. Vos, *Is a longitudinal feedback system required for LHC?*, CERN LHC Project Note 205 (1999).

[6] D. Brandt and L. Vos, *Resistive wall instability for the LHC: intermediate review*, CERN LHC Project Note 257 (2001).

[7] E. Shaposhnikova, *Longitudinal phenomena during the LHC cycle*, Proc. Chamonix 2001, CERN-SL-2001-003 DI (2001).

[8] D. Angal, D. Brandt, and L. Vos, *Intermediate review of single bunch collective effects in the LHC*, EPAC 2002 and CERN LHC Project Report 587 (2002).

[9] D. Angal, *Review of Coupled Bunch Instabilities in the LHC* , CERN LHC Project Report 595 (2002), see also D. Angal, and L. Vos, *Coupled bunch instabilities in the LHC*, EPAC 2002 and CERN LHC Project Report 585 (2002).

[10] F. Zimmermann, *A Simulation Study of Electron-Cloud Instability and Beam-Induced Multipacting in the LHC*, CERN LHC Project Report 95 (1997).

[11] O. Gröbner, *Beam Induced Multipacting*, PAC 97, Vancouver, and CERN LHC Project Report 127 (1997), J.S. Berg, *Energy Gain in an Electron Cloud During the Passage of a Bunch*, CERN LHC Project Note 97 (1997), G. Stupakov, *Photoelectrons and Multipacting in the LHC: Electron Cloud Build-up*, CERN LHC Project Report 141 (1997), O. Brüning, *Simulations for the Beam-Induced Electron Cloud in the LHC beam screen with Magnetic Field and Image Charges*, CERN LHC Project Report 158 (1997), F. Caspers, J.-M. Laurent, M. Morvillo, and F. Ruggiero, *Multipacting tests with a resonant coaxial setup*, CERN LHC Project Note 110 (1997), F. Ruggiero, *Electron Cloud in the LHC*, CERN LHC Project Report 166 (1998), M. Furman, *The Electron Cloud Effect in the Arcs of the LHC*, CERN LHC Project Report 180 (1998), L. Vos, *Electron Cloud: an Analytic View*, CERN LHC Project Note 150 (1998), V. Baglin et al., *Beam-Induced Electron Cloud in the LHC and Possible Remedies*, EPAC 1998, Stockholm, and CERN LHC Project Report 188 (1998), F. Zimmermann, *Electron Cloud Simulations: An Update*, Proc. Chamonix 2001, CERN-SL-2001-003 DI (2001). See also World-wide web page on *Electron Cloud in the LHC* at the address `http://wwwslap.cern.ch/collective/electron-cloud/`.

[12] F. Zimmermann, *Electron Clouds – Operational Limitations and Simulations*, Proc. Chamonix 2003, CERN-AB-2003-008 ADM (2003).

[13] J.-P. Koutchouk, *Correction of the long-range beam-beam effect in LHC using electro-magnetic lenses*, CERN SL-2001-048-BI (2001) and Proc. IEEE Particle Accelerator Conference (PAC2001), Chicago, IL, USA, 18–22 June 2001, eds. P. Lucas and S. Webber (IEEE, Piscataway, NJ, 2001), pp. 1681–1683.

[14] F. Ruggiero and F. Zimmermann, *Luminosity optimization near the beam-beam limit by increasing bunch length or crossing angle*, CERN SL-2002-005-AP (2002) and Phys. Rev. ST Accel. Beams **5**, 061001 (2002).

[15] K. Yokoya, *Resistive wall impedance of beam pipes of general cross section*, KEK report 92-196 (1993).

[16] L. Vos, *The transverse impedance of a cylindrical pipe with arbitrary surface impedance*, CERN-AB-2003-005-ABP (2003).

[17] H. Tsutsui, *Resistive wall impedance of an LHC collimator*, CERN LHC Project Note 318 (2003).

[18] L. Vos, *The impedance of multi-layer vacuum chambers*, CERN-AB-2003-093-ABP (2003).

[19] S. Calatroni, et al., *Design aspects of the RF contacts for the LHC beam vacuum interconnects*, CERN LHC Project Report 491 (2001).

[20] M. Gyr, *Expected magnetic field quality of the LHC septum magnets used for injection (MSI) and for extraction to the beam dump (MSD)*, CERN LHC Project Note 129 (1998).

[21] F. Caspers and A. Mostacci, *Bench Measurements of the LHC Injection Kicker Low Frequency Impedance Properties*, CERN SL-Note-2002-030 AP (2002), see also L. Ducimetiere, et al., *Design of the injection kicker magnet system for CERN's 14 TeV proton collider LHC*, CERN SL-95-80 BT (1995).

[22] R. Gluckstern, L. Vos, and B. Zotter, *Shielding particle beams by thin conductors*, CERN SL-2002-014 AP (2002).

[23] R. Gluckstern, *Coupling Impedance of Many Holes in a Liner within a Beam Pipe*, CERN SL/92-06 (AP) (1992).

[24] D. Brandt, B. Spataro, and L. Vos, *Impedance of the LHC arc beam position monitors*, CERN LHC Project Note 284 (2002); L. Vos and A. Wagner, *Longitudinal impedance of LHC version-1 stripline beam position monitor*, CERN LHC Project Report 126 (1997).

[25] D. Brandt, et al., *Impedance of the LHC recombination chambers*, CERN LHC Project Note 254 (2001). See also D. Brandt et al., *On trapped modes in the LHC recombination chambers: numerical and experimental results*, CERN LHC Project Report 604 (2002) and L. Vos, *Considerations about the impedance of the Y-chamber*, SL-AP Beam Physics Note 50 (2000), `http://slap.web.cern.ch/slap/beam_physics.html`.

[26] M. D'Yachkov, *Impedance of the rough LHC beam pipe*, SL-AP Beam Physics Note 8 (1998), see `http://slap.web.cern.ch/slap/beam_physics.html`.

[27] J. Gareyte, *Impedances: Measurements and Calculations for Non-symmetric Structures*, EPAC 2002, Paris, and CERN SL-2002-028 (2002).

[28] A.W. Chao, *Physics of Collective Beam Instabilities in High Energy Accelerators*, (Wiley, New York, 1993).

[29] E. Metral, *Collective effects in the CERN-PS beam for LHC*, Proc. Workshop on 'Instabilities of high intensity hadron beams in rings', Upton, NY (AIP Conf. Proc. **460**, 1999), p. 116. There seems to be some disagreement in the community about the role of space charge impedance and tune spread in transverse instabilities, see same Proc. p. 398. Preliminary results on the combined treatment of direct space charge and lattice nonlinearities, to appear in a forthcoming report by E. Metral et al., indicate that the stability diagram is dominated by the space charge tune spread for negative real tune shifts and by the lattice nonlinearities for positive real tune shifts and imaginary tune shifts.

[30] K. Bane and P.L. Morton, *Deflection by the Image Currentand Charges of a Beam scraper*, Proc. 1986 Linac Accelerator Conference, Stanford, CA, SLAC-PUB-3983 (1986).

[31] F. Zimmermann, K. Bane, and C. Ng, *Collimator Wake Fields in the SLC Final Focus*, EPAC 1996, Sitges, Barcelona, SLAC-PUB-7137 (1996).

[32] K. Yokoya, *Impedance of Slowly Tapered Structures*, CERN SL/90-88 (AP) (1990).

[33] G. Stupakov, *Geometrical Wake of a Smooth Taper*, SLAC-PUB-95-7086 (1995).

[34] O. Brüning, *ZBASE User's Guide Version 1.1 : an Impedance Data Base Program*, CERN-SL-96-069 AP (1996).

[35] L. Vos, *Transverse Emittance Blow-up from Dipole Errors in Proton Machines*, EPAC 1998, Stockholm, and CERN LHC Project Report 193 (1998).

[36] J.S. Berg and F. Ruggiero, *Landau Damping with two-dimensional betatron tune spread*, CERN SL-96-71 AP (1996).

[37] J. Gareyte, J.-P. Koutchouk, and F. Ruggiero, *Landau Damping, Dynamic Aperture and Octupoles in LHC*, CERN LHC Project Report 91 (revised version, 1997); J.-P. Koutchouk and F. Ruggiero, *A Summary on Landau Octupoles for the LHC*, CERN LHC Project Note 163 (1998).

[38] W. Herr and L. Vos, *Tune distributions and effective tune spread from beam-beam interactions and the consequences for Landau damping in the LHC*, CERN LHC Project Note 316 (2003).

[39] O. Brüning and S. Fartoukh, *Field Quality Specification for the LHC Main Dipole Magnets*, CERN LHC Project Report 501 (2001), p. 7.

[40] H. Grote and F.C. Iselin, *The MAD Program, User's Reference Manual*, CERN SL/90-13 (AP) (Rev. 4) (1995), see also J. Bjorken and S. Mtingwa, Part. Acc. **13**, 115 (1983).

[41] F. Ruggiero, *Parameters for First Physics and for* 10^{33}, Proc. Chamonix 2003, CERN AB-2003-008 ADM (2003).

[42] F. Zimmermann and M.-P. Zorzano, *Touschek Scattering in HERA and LHC*, CERN LHC Project Note 244 (2000).

[43] O. Gröbner, *The LHC Vacuum System*, in CERN Accelerator School on 'Vacuum Technology for Particle Accelerators', Snekersten, Denmark, CERN Yellow Report CERN-99-05 (1999), pp. 291–306.

[44] The Particle Data Group, *Review of Particle Physics*, Eur. Phys. J. C**3**, 1–794 (1998).

[45] O. Brüning, et al., *LHC Luminosity and Energy Upgrade: A Feasibility Study*, edited by F. Ruggiero, CERN LHC Project Report 626 (2003).

[46] G. Stupakov, *Geometrical Wake of a Smooth Flat Collimator*, SLAC-PUB-7167 (1996).

[47] G. Stupakov, *High-Frequency Impedance of Small-Angle Collimators* and P. Tenenbaum et al., *Transverse Wakefields from Tapered Collimators: Measurements and Analysis*, PAC 2001, Chicago (2001).

[48] F. Zimmermann, *Synchrotron Radiation in the LHC Arcs — Monte-Carlo Approach*, CERN LHC Project Note 237 (2000); A. Rossi and F. Zimmermann, *Synchrotron Radiation in the LHC Experimental Insertions*, CERN LHC Project Report 675 (2003).

[49] F. Zimmermann, *Luminosity Limitations at Hadron Colliders*, Proc. 18th Conf. High Energy Accelerators (HEACC 2001), Tsukuba, and also CERN-SL-2001-009-AP (2001).

[50] K.L.F. Bane, *A Simplified Model of IntraBeam Scattering*, Proc. EPAC 2002, Paris, p. 1443 (2002).

[51] N. Mokhov, et al., *Protecting LHC IP1/IP5 Components Against Radiation Resulting from Colliding Beam Interactions*, CERN LHC Project Report 633 (2003).

[52] F. Caspers, M. Morvillo, F. Ruggiero, J. Tan, and H. Tsutsui, *Surface Resistance Measurements of LHC Dipole Beam Screen Samples*, EPAC 2000, Stokholm, and CERN LHC Project Report 410 (2000).

[53] A. Mostacci and F. Ruggiero, *Pumping slots and thickness of the LHC beam screen*, CERN LHC Project Note 195 (1999).

[54] O. Gröbner, *Bunch Induced Multipacting*, 10th Int. Conference on High Energy Accelerators, Protvino (1977).

[55] J.M. Jimenez et al., *Electron Cloud with LHC-Type Beams in the SPS: A Review of Three Years of Measurements*, CERN LHC Project Report 632 (2003).

[56] S.Y. Zhang et al., *RHIC Pressure Rise and Electron Cloud*, PAC 2003, Portland (2003).

[57] K. Ohmi, *Beam and Photoelectron Interactions in Positron Storage Rings*, Phys. Rev. Letters **75**, 1526 (1995).

[58] K. Ohmi and F. Zimmermann, *Head-Tail Instability Caused by Electron Cloud in Positron Storage Rings*, Phys. Rev. Letters **85**, 3821–3824 (2000).

[59] K. Cornelis, *The Electron Cloud Instability in the SPS*, Proc. ECLOUD'02, Geneva, 15–18 April, 2002, CERN Yellow Report CERN-2002-001 (2002).

[60] G. Arduini et al., *The Electron Cloud Instability of the LHC Beam in the CERN SPS*, PAC 2003, Portland, and CERN LHC Project Report 637 (2003).

[61] H. Fukuma, *Electron Cloud Effects at KEKB*, Proc. ECLOUD'02, Geneva 15–18 April, CERN Yellow Report CERN-2002-001 (2002).

[62] D. Neuffer et al., *Observations of a Fast Transverse Instablity in the PSR*, NIM A**321**, 1 (1992), and R. Macek, *Studies of the Electron Cloud at the LANL PSR*, Int. Workshop on Two-Stream Instabilities, Tsukuba, September 11–14 (2001).

[63] V. Baglin, I.R. Collins, O. Grobner, C. Grunhagel, B. Henrist, N. Hilleret, B. Jenninger, "Measurements at EPA of Vacuum and Electron-Cloud Related Effects," Proc. Chamonix 2001, CERN-SL-2001-003 DI, p. 141 (2001).

[64] I.R. Collins, private communication (2000), see also V.V. Anashin et al., *Magnetic and Electric Field Effects on the Photoelectron Emission from Prototype LHC Beam Screen Material*, CERN LHC Project Report 373 (1999).

[65] N. Mahne, V. Baglin, I.R. Collins, A. Giglia, L. Pasquali, M. Pedio, S. Nannarone, and R. Cimino, *Photon Reflectivity Distributions from the LHC Beam Screen and Their Implications on the Arc Beam Vacuum System*, 8th European Vacuum Conference, Berlin, and LHC Project Report 668 (2003).

[66] R. Cimino, I.R. Collins, and V. Baglin, *VUV Photoemission Studies of Candidate Large Hadron Collider Vacuum Chamber Materials*, Phys. Rev. ST Accel. Beams **2**, 063201 (1999).

[67] M. Furman and G. Lambertson, *The Electron-Cloud Instability in the Arcs of the PEP-II Positron Ring*, Proc. Int. Workshop on Multibunch Instabilities in Future Electron and Positron Accelerators (MBI 97), Tsukuba, KEK, KEK Proceedings 97-17 (1997).

[68] R. Kirby and F. King, *Secondary Electron Emission from Accelerator Materials*, 8th ICFA Beam Dynamics Mini-Workshop on 'Two-Stream Instabilities', SLAC-PUB-8380 (2000).

[69] V. Baglin, et al., *A Summary of the Main Experimental Results Concerning the Secondary Electron Emission of Copper*, CERN LHC Project Report 472 (2002).

[70] N. Hilleret, *SEY Measurements During the Scrubbing Run*, minutes of the CERN Accelerator Performance Committee meeting of 01.08.2003, `http://ab-div.web.cern.ch/ab-div/Meetings/APC/`.

[71] R. Cimino, I.R. Collins, *Vacuum Chamber Surface Electronic Properties Influencing Electron Cloud Phenomena*, 8th European Vacuum Conference, Berlin, and LHC Project Report 669 (2003).

[72] N. Hilleret, private communication (2003) and *SEY and Pick-up Calorimeter Measurements*, Mini-Workshop on 'SPS Scrubbing Run Results and Implications for the LHC', CERN, 28 June 2002, `http://sl.web.cern.ch/SL/sli/Scrubbing-2002/Workshop.htm`.

[73] J.M. Jimenez, *Vacuum Effects During the SPS Scrubbing Run*, minutes of the CERN Accelerator Performance Committee meeting of 01.08.2003, `http://ab-div.web.cern.ch/ab-div/Meetings/APC/`.

[74] V. Baglin, *Preliminary Results from COLDEX*, minutes of the CERN Accelerator Performance Committee meeting of 01.08.2003, `http://ab-div.web.cern.ch/ab-div/Meetings/APC/`.

[75] H. Seiler, *Secondary Electron Emission in the Scanning Electron Microscope*, J. Appl. Phys. **54**, 11 (1983).

[76] R. Cimino et al., *Can Low Energy Electrons Affect High Energy Physics Accelerators?*, CERN-AB-2004-012-ABP (2004).

[77] S. Heifets, *Electron Cloud at High Beam Currents*, Proc. ECLOUD'02, Geneva, 15–18 April, 2002, CERN Yellow Report CERN-2002-001 (2002).

[78] P. Lebrun, *Large Cryogenic Helium Refrigeration System for the LHC*, CERN LHC Project Report 629 (2003).

[79] Web site of the LHC heat load working group, `http://lhc-mgt-hlwg.web.cern.ch/`.

[80] F. Ruggiero, G. Rumolo, F. Zimmermann, Y. Papaphilippou, *Beam dynamics studies for uniform (hollow) bunches or super-bunches in the LHC: beam–beam effects, electron cloud, longitudinal dynamics, and intra-beam scattering*, RPIA2002 Workshop, KEK, Tsukuba, and CERN LHC Project Report 627 (2002).

[81] G. Rumolo and F. Zimmermann, *Two-Stream Problems in Accelerators*, Proc. 2nd APAC Conference, Beijing, 2001, and CERN-SL-2001-057-AP (2001).

[82] G. Rumolo and F. Zimmermann, *Electron-Cloud Simulations: Beam Instabilities and Wake Fields*, Proc. ECLOUD'02, CERN, Geneva, 15–18 April, 2002, CERN Yellow Report CERN-2002-001 and Phys. Rev. ST Accel. Beams **5**, 121002 (2002).

[83] K. Cornelis, *Interplay between SPS Impedance and Electron Cloud*, Mini-Workshop on 'SPS Scrubbing Run Results and Implications for the LHC', CERN, 28 June 2002, `http://sl.web.cern.ch/SL/sli/Scrubbing-2002/Workshop.htm`.

[84] G. Rumolo and F. Zimmermann, *Electron Cloud Instability with Space Charge or Beam Beam*, Proc. Int. Workshop on Two-stream Instabilities in Particle Accelerators and Storage Rings, Tsukuba, 11–14 September, 2001, and CERN-SL-2001-067-AP (2001).

[85] K. Ohmi and A. Chao, *Combined Phenomena of Beam-Beam and Beam Electron Cloud Effects in Circular e^+e^- Colliders*, Phys. Rev. ST Accel. Beams **5**, 101001 (2002).

[86] E. Benedetto et al., *Transverse Monopole Instability Driven by an Electron Cloud?*, Proc. PAC2003, Portland, May 2003, and CERN-AB-2003-036-ABP (2003).

[87] K. Ohmi et al., *Study of Coherent Tune Shift Caused by Electron Cloud in Positron Storage Rings*, Proc. 2nd APAC Conference, Beijing, 2001, and CERN-SL-2001-062-AP (2001).

[88] G. Rumolo, A.Z. Ghalam, T. Katsouleas, C.K. Huang, V.K. Decyk, C. Ren, W.B. Mori, F. Zimmermann, and F. Ruggiero, *Electron cloud effects on beam evolution in a circular accelerator*, Phys. Rev. ST Accel. Beams **6**, 081002 (2003).

[89] A. Ferrari, unpublished (2003).

[90] P. Thieberger et al., *Secondary-Electron Yields and Their Dependence on the Angle of Incidence on Stainless-Steel Surfaces for Three Energetic Ion Beams*, Phys. Rev. A**61**, 042901 (2000).

[91] C. Benvenuti et al., *Vacuum Properties of TiZrV Non-Evaropable Getter Films [for LHC Vacuum System]*, Vacuum **60**, 57–65 (2001).

[92] C. Scheuerlein et al., *The Secondary Electron Yield of TiZr and TiZrV Non-Evaporable Getter Thin Film Coatings*, Appl. Surf. Sci. **172**, 95–102 (2001), and CERN EST/2000-007 (SM) (2000).

[93] B. Henrist et al., CERN Vac. Tech. Note 98-08 (1998).

[94] B. Henrist and C. Scheuerlein, CERN Vac. Tech. Note 98-20 (1998).

[95] A. Rossi, *SPS electron cloud measurements with TiZrV NEG coating*, minutes of the CERN Accelerator Performance Committe meeting of 01.08.2003, `http://ab-div.web.cern.ch/ab-div/Meetings/APC/`.

[96] W. Herr and J. Miles, *A Comparative Study of Beam-beam Tune Footprints for Colliding Beams with a crossing angle and offset vertex in LHC V4.1*, CERN LHC Project Note 04 (1995).

[97] H. Grote and O. Meincke, *Tune footprints for collision optics 5.0*, CERN LHC Project Note 161 (1998).

[98] W. Herr, *Beam-beam issues in the LHC and relevant experience from the SPS proton antiproton collider and LEP*, in CERN LHC Project Report 502 (2001) and Proc. Workshop on Beam-Beam Effects in Circular Colliders, Fermilab, Batavia, IL, USA, 25–28 June 2001, eds. T. Sen and M. Xiao, FERMILAB-CONF-01-390 (2002).

[99] K. Cornelis, M. Meddahi, and R. Schmidt, *The beam-beam effect in the SPS proton antiproton collider for beams with unequal emittances*, CERN SL/90-73 (AP) (1990); W. Herr, *Beam-beam issues in the LHC and relevant experience from the SPS proton antiproton collider and LEP*, Proc. Workshop on 'Beam-Beam Effects in Circular Colliders', Fermilab, Batavia, IL, USA, 25–28 June 2001, eds. T. Sen and M. Xiao, FERMILAB-CONF-01-390 (2002), `http://www-ap.fnal.gov/~meiqin/beambeam01/beambeam01.html`.

[100] H. Grote, F. Schmidt, and L.H.A. Leunissen, *LHC Dynamic Aperture at Collision*, CERN LHC Project Note 197 (1999), Y. Luo and F. Schmidt, *Dynamic aperture studies for LHC optics version 6.2 at collision*, CERN LHC Project Note 310 (2003), see also Y. Luo and F. Schmidt, *Weak-strong beam-beam tracking for LHC v6.1*, CERN LHC Project Report 502 (2001) and Proc. Workshop on 'Beam-Beam Effects in Circular Colliders', Fermilab, Batavia, IL, USA, 25–28 June 2001, eds. T. Sen and M. Xiao, FERMILAB-CONF-01-390 (2002), `http://www-ap.fnal.gov/~meiqin/beambeam01/beambeam01.html`.

[101] Y. Papaphilippou and F. Zimmermann, *Weak-strong beam-beam simulations for the LHC*, in Proc. Workshop on 'Beam-Beam Effects in Large Hadron Colliders' (LHC99), CERN, Geneva, Switzerland, 12–17 April 1999, eds. J. Poole and F. Zimmermann (CERN SL-99-039-AP, 1999), pp. 95–107, see also Phys. Rev. ST Accel. Beams **2**, 104001 (1999) and Y. Papaphilippou and F. Zimmermann, *Estimates of diffusion due to long-range beam-beam collisions*, CERN LHC Project Report 600 (2002) and Phys. Rev. ST Accel. Beams **5**, 074001 (2002).

[102] W. Herr, *Effects of PACMAN bunches in the LHC*, CERN LHC Project Report 39 (1996).

[103] O. Brüning, W. Herr, and R. Ostojic, *A beam separation and collision scheme for IP1 and IP5 at the LHC for optics version 6.1*, CERN LHC Project Report 315 (1999).

[104] O. Brüning, W. Herr, and R. Ostojic, *A beam separation and collision scheme for IP2 and IP8 at the LHC for optics version 6.1*, CERN LHC Project Report 367 (2000).

[105] W. Herr, *Features and implications of different LHC crossing schemes*, CERN LHC Project Report 628 (2003).

[106] B. Muratori, *Study of Offset Collisions and Beam Adjustment in the LHC Using a Strong-Strong Simulation model*, CERN LHC Project Report 593 (2002).

[107] H. Grote, *Comparing beam-beam effects in three LHC injection schemes*, CERN LHC Project Note 267 (2001).

[108] H. Grote and W. Herr, *Self-consistent orbits with beam-beam effects in the LHC*, in CERN LHC Project Report 502 (2001) and Proc. Workshop on 'Beam-Beam Effects in Circular Colliders', Fermilab, Batavia, IL, USA, 25–28 June 2001, eds. T. Sen and M. Xiao, FERMILAB-CONF-01-390 (2002).

[109] L. Vos, *Effect of very low frequency ground motion on the LHC*, in Proc. Workshop on 'Beam-Beam Effects in Large Hadron Colliders' (LHC99), CERN, Geneva, Switzerland, 12–17 April 1999, eds. J. Poole and F. Zimmermann (CERN SL-99-039-AP, 1999), pp. 91–94.

[110] H. Grote and W. Herr, *Nominal and ultimate luminosity performance of the LHC*, CERN LHC Project Note 275 (2002).

[111] K. Yokoya et al., *Tune shift of coherent beam-beam oscillations*, Part. Acc. **27**, 181 (1990).

[112] Y. Alexahin, *On the Landau damping and decoherence of transverse dipole oscillations in colliding beams*, Part. Acc. **59**, 43 (1996).

[113] M.P. Zorzano and F. Zimmermann, *Coherent beam-beam oscillations at the LHC*, CERN LHC Project Report 314 (1999) and Phys. Rev. ST Accel. Beams **3**, 044401 (2000).

[114] W. Herr, M.P. Zorzano, and F. Jones, *A hybrid fast multipole method applied to beam-beam collisions in the strong-strong regime*, Phys. Rev. ST Accel. Beams **4**, 054402 (2001).

[115] Y. Alexahin, H. Grote, W. Herr and M.P. Zorzano, *Coherent beam-beam effects in the LHC*, CERN LHC Project Report 466 (2001).

[116] Y. Alexahin, *A study of the coherent beam-beam effect in the framework of the Vlasov perturbation theory*, Nucl. Inst. Meth. **A 380**, 253 (2002).

[117] Y. Alexahin and M.P. Zorzano, *Excitation of coherent beam-beam resonances for beams with unequal tunes in the LHC*, CERN LHC Project Note 226 (2000).

[118] W. Herr and M.P. Zorzano, *Coherent dipole modes for multiple interaction regions*, CERN LHC Project Report 461 (2001).

[119] W. Herr and R. Paparella, *Landau damping of coherent modes by overlap with synchrotron sidebands*, CERN LHC Project Note 304 (2002).

CHAPTER 6

THE RF SYSTEMS AND BEAM FEEDBACK

6.1 INTRODUCTION

The design of the RF and Beam Feedback systems has evolved in certain respects since the publication of the Conceptual Design, the "Yellow Book", in 1995 [1]. The injected beam will still be captured, accelerated and stored using the 400 MHz superconducting cavity system as before but longitudinal injection errors will now be damped using the same system. There will not be a separate longitudinal damper. Transverse injection errors will be damped by a system of electrostatic deflectors that will also ensure subsequent transverse stability. A new capture system at 200 MHz to reduce injection loss and ease operation has been proposed and designed and will be installed at a later stage if the injected emittance increases when intensities much higher than nominal are reached. The different RF and Beam Feedback systems are now concentrated around the centre of point 4 and extend from the UX45 cavern area into the tunnel on either side. The klystron power plant and racks of equipment for the different systems are in both the UX45 and US45 sides of the cavern. Previously the RF systems were in the tunnel and the old LEP klystron galleries were used for the RF power. IR4 is already equipped with klystron power converters from LEP.

6.1.1 Beam Parameters

The beam and machine parameters that are directly relevant to the design of the RF and Beam Feedback systems are given in Tab. 6.1. At nominal intensity in the SPS an emittance of 0.6 eVs has now been achieved giving a bunch length at 450 GeV of 1.6 ns. The phase variation along the batch due to beam loading is within 125 ps. This emittance is lower than originally assumed and is the result of a significant machine studies and upgrade programme in the SPS leading to reduced machine impedance, improved control of beam loading at the fundamental frequency with both RF feedback and feed-forward, and further instability control using both coupled bunch feedback for low-mode number instabilities and Landau damping of high order modes using a 4^{th} harmonic RF system. As a result, an RF system in the LHC of frequency 400.8 MHz, compatible with this bunch length, can be used to capture the beam with minimal losses and then accelerate and finally store it at top energy [2]. Higher frequencies, while better for producing the short bunches required in store, cannot accommodate the injected bunch length. At ultimate or higher intensities the emittance from the injector may increase and a separate 200 MHz RF system [3] can be used to capture the longer bunches. This system will not be installed for initial commissioning. However, space is allocated in the machine and certain preparatory work has been done. A brief description of this system will also be given below.

No separate longitudinal damping system is used. The main RF system provides some damping of injection errors and natural Landau damping is used to stabilise the beam against longitudinal beam coupled bunch instabilities during the cycle. This defines the maximum allowable machine impedance, in particular for higher order modes in cavities [4]. There will be some emittance increase at injection but this will be within the capabilities of the RF system for acceleration and in particular will be below the final emittance needed in storage. This final emittance is defined by intra-beam scattering lifetime in the presence of damping due to synchrotron radiation, RF lifetime and instability threshold considerations. Controlled emittance increase will be provided during acceleration by excitation with band-limited noise, the emittance increasing with the square root of the energy to optimise both narrow and broadband instability thresholds [4].

For the transverse plane, a feedback system damps the oscillations coming from injection errors to minimise emittance increase resulting from decoherence produced by magnetic and space-charge non-linearities and stabilizes the beam against the resistive wall instability [5].

Table 6.1: The Main Beam and RF Parameters

	Unit	Injection 450 GeV	Collision 7 TeV
Bunch area (2σ)*	eVs	1.0	2.5
Bunch length (4σ)*	ns	1.71	1.06
Energy spread (2σ)*	10^{-3}	0.88	0.22
Intensity per bunch	10^{11} p	1.15	1.15
Number of bunches		2808	2808
Transverse emittance V/H	μm	3.75	3.75
Intensity per beam	A	0.582	0.582
Synchrotron radiation loss/turn	keV	-	7
Longitudinal damping time	h	-	13
Intrabeam scattering growth time - H	h	38	80
- L	h	30	61
Frequency	MHz	400.789	400.790
Harmonic number		35640	35640
RF voltage/beam	MV	8	16
Energy gain/turn (20 min. ramp)	keV	485	
RF power supplied during acceleration/ beam	kW	~275	
Synchrotron frequency	Hz	63.7	23.0
Bucket area	eVs	1.43	7.91
RF (400 MHz) component of beam current	A	0.87	1.05

* The bunch values at 450 GeV are an upper value for the situation after filamentation, ~ 100 ms after each batch injection. The bunch parameters at injection are described in the text.

6.1.2 RF System Parameters and General Design

The final emittance at 7 TeV of 2.5 eVs and a maximum bunch length given by luminosity considerations in the experiments, leads to a required maximum voltage of 16 MV / beam. Transient beam-loading, coming from the high RF beam current (~ 1 A) combined with the long beam gap (~ 3 μs) due to the abort gap dominates the design of the LHC RF system and leads to the choice of SC cavities with wide beam aperture (30 cm). With high RF voltage per cavity and the low R/Q due to the wide aperture, the stored energy in the cavity is high and the cavity field phase swing due to reactive beam loading in the beam gap is minimized. Furthermore the required voltage is achieved with fewer cavities than with a copper system and, again due to the wide beam aperture, the R/Q of the Higher Order Modes in the cavity are lower. With strong HOM damping in the cavity the total machine impedance can be kept low.

During acceleration the real power supplied to the beams is relatively small (275 kW/beam) but the installed power required to control these beams is much larger. The challenge in the design of the RF system is to minimize the beam handling power in order to arrive at acceptable levels for the power couplers. If separate cavities can be used for each beam, the RF beam current and hence transient beam-loading in the cavities is halved and the coupler power requirement at injection also reduced to more realistic levels. An added advantage is the possibility of independent control of the beams. However, the standard distance between beams in the machine, 194 mm, is insufficient. Consequently the beam separation must be increased in the RF region to 420 mm by means of special SC dipoles. With this separation and also by staggering the cavities longitudinally, the "second" beam can pass outside the cavity. It must still, however, pass through the cryostat. In coast some static relative longitudinal displacement of the bunches can be tolerated to further relax the power requirements.

6.2 MAIN 400 MHZ RF ACCELERATING SYSTEM (ACS)

6.2.1 Parameter Specification

The two independent RF systems must each provide at least 16 MV in coast while at injection about 8 MV is needed. The frequency of 400 MHz is close to that of LEP, 352 MHz, allowing the same proven technology of niobium sputtered cavities to be applied.

All reactive beam power has to be carried by the RF couplers. The present design using single cell cavities each with 2 MV accelerating voltage, corresponding to a conservative field strength of 5.5 MV/m, minimizes the power carried by the RF window. Even so the peak power requirements for the coupler are significantly higher than previously achieved on SC cavities. A large tuning range is required to compensate the average reactive beam component. Each RF system has thus eight cavities, with $R/Q = 45\ \Omega$ and of length $\lambda/2$, grouped by four with a spacing of 3 $\lambda/2$ in one common cryostat [2].

Each cavity is driven by an individual RF system with klystron, circulator and load. Complex feedback loops around each cavity, described below, allow precise control of the field in each cavity, important for the unforgiving high-intensity LHC proton beam. The use of one klystron per cavity also avoids problems such as coupling between cavities and ponderomotive oscillations that plagued the LEP RF system when one klystron supplied eight cavities.

Energy and phase errors at injection require strong coupling between cavity and klystron (low external Q, Q_{ext}) but the higher field in coast demands a high Q_{ext} to limit the power needed. The power coupling must therefore vary during the ramp. The variable coupler has a range of $Q_{ext} = 10{,}000$ to $Q_{ext} = 200{,}000$.

To control the transient beam-loading the installed power is 300 kW – the average RF power being much lower. Simulations [6, 10] have shown that under some conditions the power to be handled can be even higher for a fraction of a μs; hence the RF drive has to be limited to avoid klystron saturation. Simulations also show that short reflected power spikes much larger than the installed RF power are possible, the energy being taken from the beam or the cavity stored energy. Therefore, the peak power capabilities of circulator and loads have to be increased correspondingly. Due to the staging of the 200 MHz capture system the 400 MHz RF system has to provide all injection damping. Simulations have verified that this is possible but the system's power-handling capabilities are stretched to the limits.

All higher-order modes (HOM) have to be damped as strongly as possible, partly for machine impedance reasons but also to avoid extracting excessive RF power from the beam through the coupler [2]. To couple to the different polarities of the multi-pole modes, two wide-band HOM couplers are used placed at 120° around the circumference. The wideband couplers have a notch filter at 400 MHz which causes reduced coupling to these modes. Two dipole modes at respectively ~500 MHz (TE_{111}) and ~534 MHz (TM_{110}) are particularly dangerous since they do not propagate in the tubes of the inter-cavity beam tubes with 700 MHz cut-off frequency. A second set of narrow band couplers is therefore needed for these two modes, resulting in a total of four HOM couplers for each cavity.

The recent choice of graphite as collimator material has caused some concern for the superconducting RF cavities. These are sensitive to any dust but especially to carbon dust. Charged dust particles, held by the beam electric field and travelling along the beam pipe, would be intercepted by an electrostatic dust-trap. The study of such a dust-trap has been launched.

6.2.2 SC Cavities, Modules and Couplers

Cavities and cryomodule

The use of niobium sputtering on copper for construction of the cavity has the important advantage over solid niobium that susceptibility to quenching is very much reduced. Local heat generated by small surface defects or impurities is quickly conducted away by the copper. During the low-power tests the 21 cavities produced all reached an accelerating field of twice nominal without quenching. The niobium sputtered cavities are insensitive to the Earth's magnetic field and special magnetic shielding, needed for solid niobium cavities, is not required.

Four cavities, each equipped with their helium tank, tuner, HOM couplers and power coupler, are grouped together in a single cryomodule. This reduces the overall static thermal losses and requires less total space

for installation compared to the previous bi-module configuration. The conception of the cryomodule is itself modular; all cavities are identical and can be installed in any position. If a problem arises with a cavity it can "easily" be replaced. The time taken to do this, from experience already gained with one module which suffered a degraded cavity after initial assembly, would be less than one month.

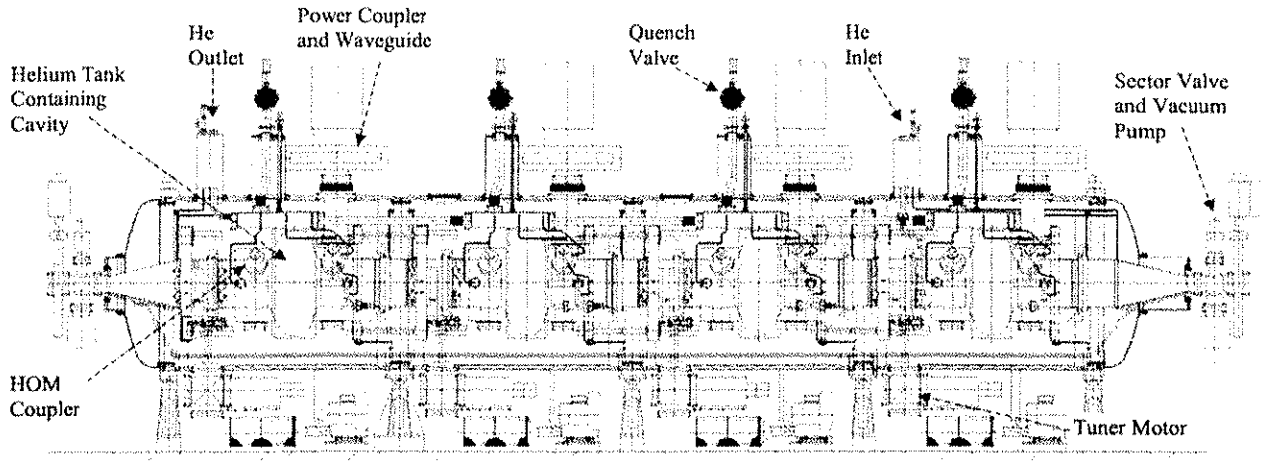

Figure 6.1: Four-Cavity Cryomodule

Tuning

The cavity is tuned by elastic deformation, by pulling on a harness using stainless-steel cables that are wound around a shaft. A stepping motor, fixed to the outside of the cryostat, drives the shaft. The motor therefore works in normal ambient conditions and can be easily accessed for maintenance or repair.

HOM Couplers

The HOM couplers have been designed to stand the 1 kW HOM power expected in the worst case and have been tested up to 600 W at 4.5 K without any evidence of overheating. The fundamental mode is almost completely rejected by a tuneable filter in the couplers. At nominal field, no more than 10 W fundamental power couples out of each HOM coupler.

Cryogenics

Each cryomodule has a single inlet for liquid helium and a single outlet for the helium evaporated by static and dynamic losses. The level is regulated by the input valve using feedback from superconducting wire level gauges in the cryomodule. The static losses are 150 W per module. At nominal field the RF losses are 100 W and at twice the nominal field 800 W per module, making the total losses 250 W and 950 W, respectively.

For operation at nominal field the pressure inside the helium tank has to be carefully controlled to avoid frequency variations of the cavity, the sensitivity being an appreciable 150 Hz/mbar. The maximum excursion around the nominal value of 1350 mbar has been fixed to ±15 mbar. The operation of the cavities will be very critical from the point of view of safety: they have been designed to withstand a maximum pressure of 2 bar and will be connected to the QRL line D in which pressure can rise to up to 20 bar if magnets quench. A pressure switch will therefore close the output valve if the pressure is above 1500 mbar. A possibility presently being studied is to provide a connection to the Warm Recovery Line (WRL) to ensure the safe discharge of evaporating helium in any operating mode. The cavities will in any case be equipped with safety (quench) valves to discharge the helium in case of insulating vacuum loss or inability to discharge into line D or the WRL.

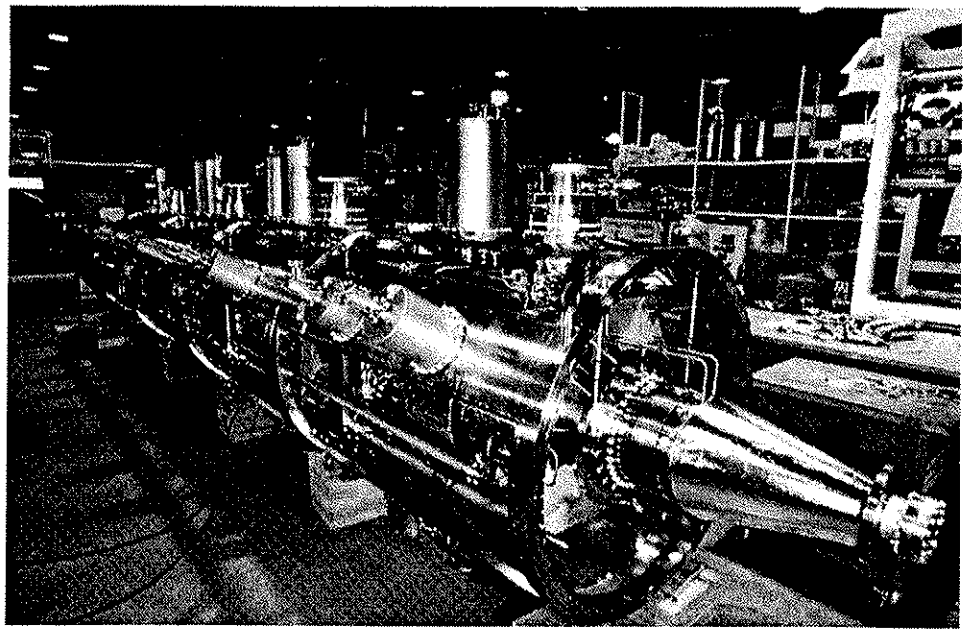

Figure 6.2: Four-Cavity Module during assembly

Variable Power Coupler

The LHC variable coupler, Fig. 6.3, is an upgraded version of the LEP2 fixed coupler. The general layout and improvements of the latter have already been described in detail [8, 9].

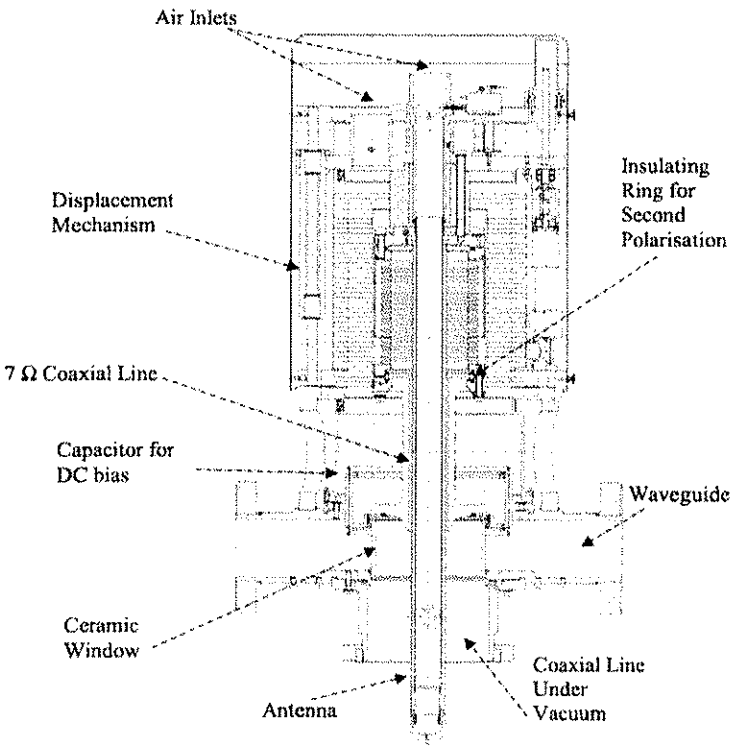

Figure 6.3: 400 MHz Variable Power Coupler

An open-ended coaxial line provides coupling to the cavity. The outer conductor, not shown in the figure, made of copper-plated stainless-steel (double walled) is cooled with 4.5 K helium gas. The inner conductor (antenna) is a copper tube cooled by forced air. A cylindrical ceramic air-cooled window, with solid copper rings brazed on its edges, is placed in the waveguide-to-coaxial transformer. This provides an excellent solution for RF heating but at the expense of more difficult technical manufacturing challenges, compared to

the use of kovar rings. A reduced height waveguide directly provides matching to the coaxial line, avoiding the usual "doorknob".

The antenna can be moved 60 mm by using bellows about $\lambda/4$ long, allowing changes in Q_{ext} of the cavity by a factor 20. A high precision assembly guides the antenna movement. In order to suppress multipactor during operation, two dc bias voltages are applied. A vacuum gauge and an electron pickup antenna are located close to the window and are used for coupler conditioning and interlocks.

High-power conditioning is done at room temperature with two couplers mounted horizontally on a 400 MHz copper test cavity. One coupler is connected to a 1.5 MW pulsed (1.0 MW average) 400 MHZ klystron via a circulator, the second either to a 500 kW load or to a mobile short circuit. After conditioning of the multipacting levels with a pressure limit of 5.0×10^{-7} Torr, the coupler sustains > 500 kW continuous forward power (2.0 MW travelling-wave equivalent), at full reflection for any phase and any coupling. The d.c. biasing is effective at all multipactor levels.

6.2.3 ACS Vacuum

The 400 MHz superconducting RF cavities have three different and independent types of vacuum systems: for the cavity, the secondary beam and the cryostat.

The cavities are pumped at room temperature by two 60 l/s ion pumps mounted at each end of the RF modules. At 4.5 K, an additional huge pumping speed of more than 300,000 l/s, for hydrogen, comes from the cryogenic pumping of the cavity walls. The background pressure, without RF, will be very low and not measurable using the Penning gauges ($<10^{-12}$ mbar). Pressure signals provided for RF control are a hardware interlock from the ion pumps to cut the high voltage and readout from the Penning gauges, one per coupler, to limit the RF power, for example during conditioning. Signals for vacuum control come from both Pirani and Penning gauges mounted on the pumping ports. The cavity vacuum can be isolated by two all-metal valves at the ends of each module, to maintain vacuum during transport and installation.

Due to the size of the cryostat the second beam has to pass in its own vacuum tube through the cryostat insulation vacuum. The second beam tube has been designed so as not to interfere with the removal of a faulty cavity. It is composed of two vacuum chambers of about 3 m in length connected by a shielded bellows. The chambers are made of stainless steel tube (ID 67 mm, 1.5 mm thick), coated by electro-deposition with a copper film 1 mm thick to give low impedance, and then coated with NEG to reduce the pressure and avoid electron cloud effects. The vacuum chambers are baked using thermo-coax heaters fixed onto the vacuum chamber by a sprayed aluminium coating. This 1.5 mm coating gives very good thermal contact. Two coaxial heaters are rolled around the chamber, the current leads and temperature measurements leaving via a special feed-through. The coating can resist a bake-out at 300 °C. A reflective aluminium film covers the heaters to reduce thermal radiation towards the super-insulation layers around the cryostat when at 4.5 K. At 250°C and after 24 h of bake-out, the temperature of the super-insulation layers in front of the baked chambers does not exceed 62 °C. A special spacer installed on the secondary beam tube prevents it coming into contact with the super-insulation during bakeout.

The insulation vacuum is less demanding in terms of pressure, the modules being pumped to 10^{-3} mbar before being cooled down. When cold, the insulation vacuum also benefits from the cryogenic pumping of the cold surfaces and the operating pressure will decrease to 10^{-7} mbar. Turbo molecular pumps are used and pressures are measured using Penning and Pirani gauges.

Intense gamma radiation is produced during cavity RF conditioning, which will be done *in situ*. Special radiation stoppers will be installed at the RF zone extremities to limit the radiation reaching nearby equipment and the machine tunnel. The use of the existing valves on the modules is excluded due to the risk of damage due to radiation. The stoppers will be modified versions of LEP sector valves, mounted independently and relatively easily removable in the event of problems.

6.2.4 RF Power System

A maximum of 4800 kW of RF power will be generated by sixteen 300 kW 400 MHz klystrons. Each klystron will feed, via a Y-junction circulator and a WR2300 (half height) waveguide line, a single-cell SC cavity. The average waveguide length will be about 22 m. The klystrons, the circulators and loads, the HV interface bunkers and the control racks will be located on the ground floor of the UX45 cavern, approximately 6 m below the level of the beam lines.

High-Voltage Interface

The four main 100 kV power converters, re-used from LEP, are located on the surface with transformers and rectifiers in the open air. Each converter will power four klystrons. The high-voltage interfaces will be located in four fireproof bunkers in the cavern. Each interface consists of high-voltage connections to the klystron guns, filament supplies, a fast protection unit (thyratron crowbar), a high-voltage commutator, smoothing capacitors, four hard tube modulators and insulation transformers. These components are immersed in oil. The klystrons are located about 30 m away from the HV bunker whereas the distance to the HV power converter at the surface is about 500 m.

Klystrons

The klystrons have been developed by a European company, according to CERN specifications. The main operating parameters at the rated output power are shown in Tab. 6.2.

An important parameter for the LHC klystrons is their group delay. This should be as short as possible since an RF feedback loop with total delay < 700 ns is required to ensure beam stability. Low group delay can be obtained by carefully tuning the klystron cavities (five per klystron). This increases the bandwidth of the klystron but reduces the RF gain to 37 dB.

The LHC klystrons are equipped with modulation anodes. Tetrode modulators set the klystron current to the best working point of the klystron. During operation the fast klystron power changes will be controlled by the RF drive signal level via the low-level control system.

Most auxiliary equipment for the klystrons has been recuperated from the LEP RF system, modified where necessary. This includes the power supplies for the focusing coils, the power supplies for the klystron vacuum pumps, the 200 W solid-state RF driver amplifiers and the arc detectors.

Table 6.2: Characteristics of the RF power equipment

Klystron:	
Output power	300 kW
Operating frequency f_0	400.8 MHz
dc to RF conversion efficiency	$\geq$ 62%
Operating voltage	$\leq$ 54 kV
Maximum beam current	9 A
Gain	$\geq$ 37 dB
Group Delay at $f_0 \pm$ 1MHz and 1 dB below rated output power	$\leq$ 120 ns
1 dB bandwidth	$\geq \pm$1 MHz
Circulator:	
Operating frequency f_0	400.8 MHz
Type	3-port junction circulator
Ports	WR2300 half-height waveguide
Maximum CW forward power	300 kW
Maximum CW reflected power	330 kW, at any phase
Insertion loss at rated forward power	$\leq$ -0.1 dB
Isolation: a) within frequency range $f_0 \pm$0.25 MHz b) within frequency range $f_0 \pm$12 MHz	 $\leq$ -28 dB $\leq$ -20 dB
Group delay at $f_0 \pm$ 0.25 MHz	$\leq$ 30 ns

Circulators and Loads

Each klystron will be protected against reflections by a three-port junction circulator. To ensure stable klystron operation a temperature control system will automatically adjust the circulator's magnetic field to

compensate for the ferrite temperature variations, keeping optimum input matching and isolation at all forward power levels.

For better performance and to reduce the size, 330 kW ferrite loaded waveguide absorbers will be used as the port 3 terminations, instead of water-loads. Other advantages of these ferrite loads are higher bandwidth and low variation in reflected phase with absorbed power.

Protection and Interlocks

The circulators must be protected against high reflected cavity power that may result under certain fault conditions and would cause arcing between the ferrite plates. This is done using fast interlocks (see section 6.6.3) on cavity reflected power and arc detection in the waveguides, to switch off RF power within several microseconds. Short transients with reflected power peaks considerably higher than the installed power but less than a few microseconds long will however occur during injection damping. These would not result in circulator arcing and must be tolerated by the interlock system. There are also fast interlocks on klystron reflected power to act in the event of circulator malfunction. Klystrons and high-voltage equipment are protected by the slower PLC based interlock system that acts on the power converter.

6.2.5 System Tests Before Installation

The installation of the RF system comes relatively late in the planning and the time for RF system testing before beam is very limited. A full system for the powering of one cavity will therefore be assembled in SM18. It will resemble the final machine installation as closely as is reasonably possible and will be used to test the operational reliability of all major components and the overall performance of the system. Particular attention will be paid to the RF power interlock system and to the operation of the low-level RF systems.

6.3 STAGED 200 MHZ CAPTURE SYSTEM (ACN)

6.3.1 Specification of the Staged Capture System.

If the injected bunch emittance from the SPS approaches 1 eVs, the resulting bunch length given by the maximum available voltage in the SPS, combined with the phase and energy errors expected, leads to unacceptable losses from the 400 MHz buckets in the LHC. Various schemes to cope with this have been studied: more voltage in the SPS, or a higher harmonic RF system in the SPS etc. but the solution retained is a separate 200 MHz capture system in the LHC. Studies and simulations [10] have shown that by installing 3 MV/beam, capture losses can be significantly reduced. Again transient beam-loading is the major issue and determines the installed power of 300 kW per cavity.

A full RF system using four standing-wave cavities has been designed [3], space has been reserved at IR4, basic civil engineering work has been undertaken and a complete power chain for one cavity will be tested, but due to the significant improvements in the longitudinal emittance of the beam from the SPS the 200 MHz system will not be installed in the machine for initial commissioning. Only later, at higher intensities than nominal when the beam emittance approaches 1 eVs, will the capture system be installed. In operation the system is used for both capture and injection damping. The beam is "transferred" to the 400 MHz RF system just before ramping, the 200 MHz voltage being reduced to zero and the cavities damped.

6.3.2 The Cavities

The cavity design is based on the SPS SWC 200 MHz standing-wave cavities. The nominal frequency is 200.210 MHz. The main constraints on the design were the reduced diameter imposed by the 420 mm separation between the two beams and the necessity of keeping essential monopole HOM frequencies away from multiples of the 40 MHz bunch frequency. These constraints result in slightly higher shunt impedance and lower quality factor. With $R/Q = 192\ \Omega$ and $Q_0 = 30{,}0000$ the power dissipated at a nominal field of 0.75 MV is 69 kW. Particular attention was therefore paid to the design of the cooling channels to evacuate this large amount of power. Components such as the four HOM couplers, the tuner (200 kHz range) and the two fundamental mode dampers will be recuperated from the SPS SWC cavities and refurbished. A new

power coupler, based on the new SPS TWC one, will be used. A low-power version has been built to validate the geometry and a full-power one will be built in 2004.

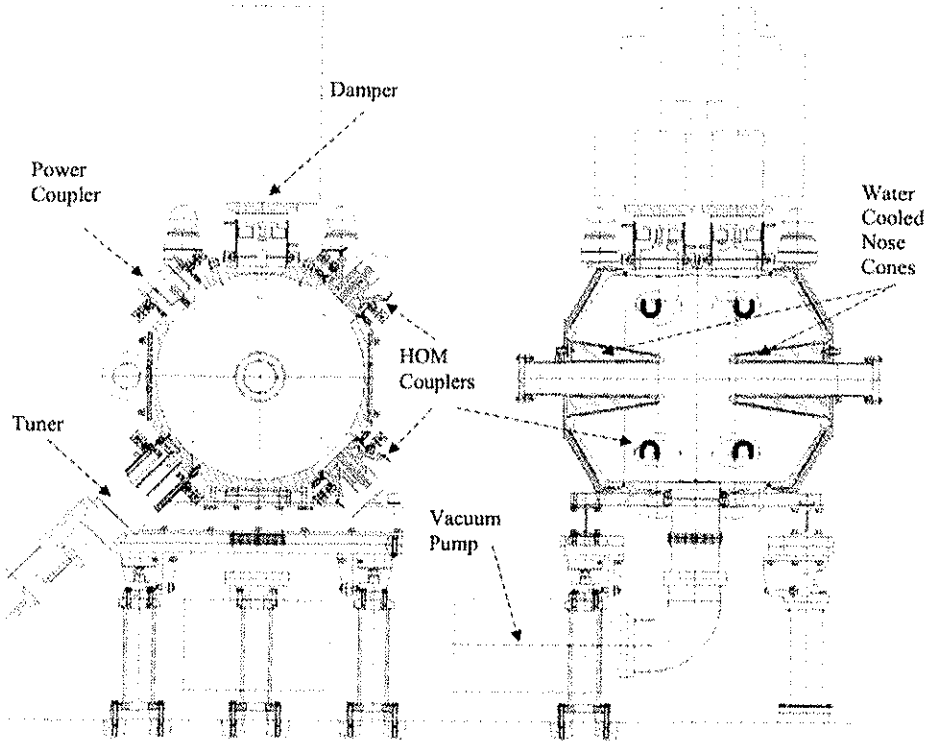

Figure 6.4: ACN 200 MHz Cavity mounted on its support

6.3.3 ACN Vacuum

Four ion pumps (400 l/s) are used, mounted underneath the cavities. A Penning gauge, also installed below the cavity, monitors the pressure. The pumps provide hardware interlocks to the RF system. The bake-out temperature of the cavities will be limited to 150 °C due to the use of conical flanges (SPS type). Heating is obtained by circulation of hot water in the cooling circuit of the cavity, the body being thermally insulated by an insulation film. These cavities will be isolated from the other equipment by two all-metal DN100 sector valves.

The second beam will pass very close to the cavity body. The length of the chamber, standard diameter NEG coated Cu tube (ID80/OD84 mm), is chosen to avoid conflict between the interconnecting bellows and the body of the cavities. Special supports will be used to support the second beam tube, their positioning taking into account the free space required to exchange a tuner.

6.3.4 RF Power

The cavity is connected to the power amplifier via a circulator, which directs the reflected wave to a terminating load. This configuration not only leads to the minimum RF installed power for a given cavity voltage and beam current, but also opens up the possibility of easily combining (in a 50 Ω matched system) several RF power amplifiers.

The solution chosen to provide the 300 kW per cavity is to recuperate four SPS-LEP SWC amplifiers (60 kW CW, up to 90 kW for 1 s) and use two stages of combiners to give the final power (three hybrids per cavity, each hybrid the same as those used with the SPS TWC systems) [11]. The driver amplifier will be the same with some modifications of the output circuitry. A pre-amplifier of 50 W and pre-driver of 1 kW are needed.

The amplifiers, combiners, circulator and load will be installed in the old LEP klystron gallery (UA). The reflected power from the cavity implies that the circulator must take 240 kW average with a peak of 400 kW during 1 s. The overall RF loop delay must be kept below 700 ns, as with the 400 MHz system.

Four existing HV power supplies (10 kV, 1.1 MVA each) will be re-used for the ACN (one for two ACN cavities) and installed in building SR4.

6.4 TRANSVERSE DAMPING AND FEEDBACK SYSTEM (ADT)

The LHC transverse feedback system (ADT) combines three principal functions: it damps transverse injection errors, prevents transverse coupled bunch instabilities (dipole modes) and can excite transverse oscillations for beam measurements [12,13,14,15].

6.4.1 Specification

There are four independent systems, one per plane and per ring. Each system comprises two modules, each consisting of two kicker units. Each kicker unit has one power amplifier with two tetrodes installed directly under the kicker vacuum tank. The horizontal kickers and power amplifiers for ring 1 are installed left of the IP4 and the vertical kickers and power amplifiers for ring 1 are to the right. The installation for ring 2 is asymmetric with respect to ring 1. Kickers and power amplifiers of ring 2 are interleaved with those of ring 1, as shown in Fig. 6.12. This arrangement optimizes the beta functions to maximize kick strength. Space has been left for a future upgrade of one extra module per ring and plane to boost the total system capability by 50%.

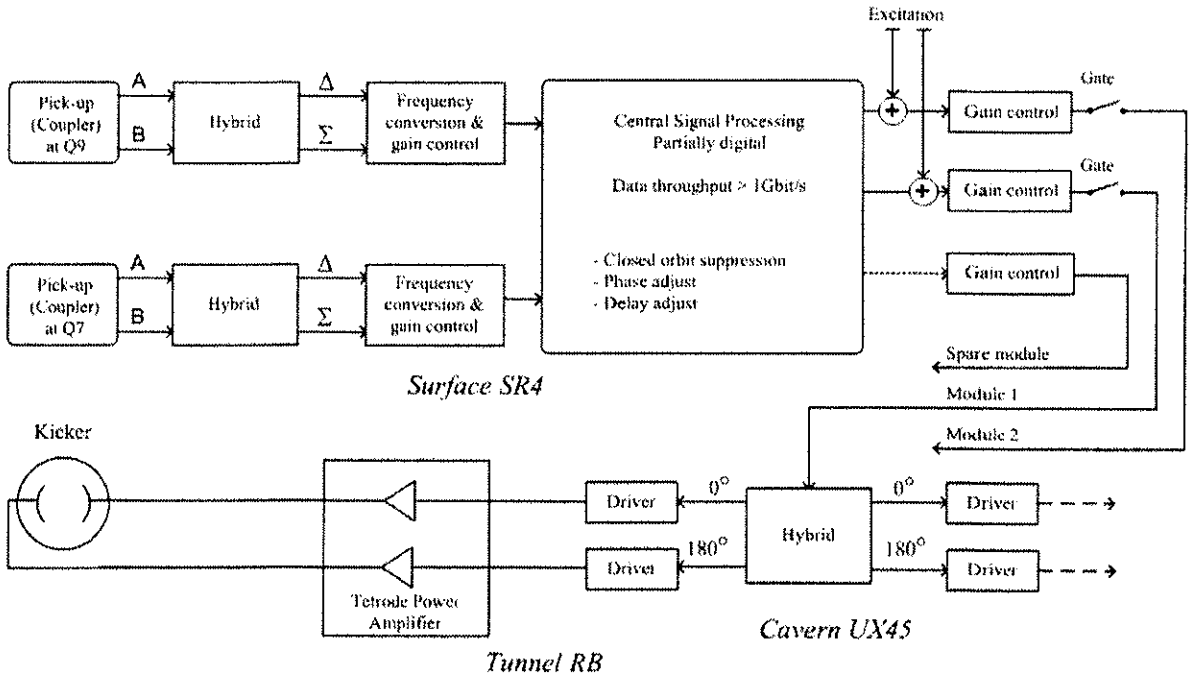

Figure 6.5: Block Diagram of an LHC Damper System.

Fig. 6.5 shows a schematic diagram of one system. Tab. 6.3 summarises the performance calculated for a β function of 100 m at the kicker and gives related hardware parameters for the four systems [5,14,15]. The ADT systems resemble the SPS damper for which considerable experience exists [16].

The systems work in base band, from below 3 kHz up to > 20 MHz. The lower frequency limit is given by the choice of fractional tune, $0.25 < Q_{frac} < 0.75$. The upper cut-off frequency is given by the necessary bandwidth to damp coupled bunch dipole oscillations at a bunch spacing of 25 ns. The lower frequency cut-off is limited in the hardware by the driver amplifier [17], and the upper frequency by the RC characteristics of the kicker-amplifier combination. LHC optics version 6.4, see Tab. 6.4, gives improved performance due to the higher β values at the kicker locations. Consequently in the vertical plane, damping times can be reduced easily to 2/3 of the values of Tab. 6.4. Note that the injection kicker in the LHC acts vertically.

Table 6.3: Nominal Performance and Hardware Parameters of LHC ADT Systems

Parameter	Value	Units
Injection beam momentum	450	GeV/c
Static injection errors (β=183 m)	2	mm
Ripple (β =183 m)	2	mm
Resistive wall growth time	27.4	ms
Tolerable emittance growth	2.5	%
Overall damping time	4.1	ms
Standard bunch spacing	25	ns
Minimum gap between batches	995	ns
Lowest betatron frequency	> 2	kHz
Highest frequency to damp	20	MHz
Aperture of kickers	52	mm
No. of kickers per plane & ring	4	
Length of kickers (electrodes)	1.5	m
Nominal voltage up to 1 MHz	± 7.5	kV
Kick / turn at 450 GeV/c (1 MHz)	2	μrad
Rise time 10-90%	350	ns
Rise time 1-99%	720	ns
Frequency range (gain)	0.001-20	MHz
Noise	< 1 LSB	with 10 Bit/2σ

Table 6.4: Performance with Optics 6.4, compared to β = 100 m (at 450 GeV/c), assuming 7.5 kV maximum kick voltage.

	β=100 m performance	Optics 6.4 performance
	Kick per turn in σ	Kick per turn in σ @ β in m
ADTH beam 1	0.23 σ	0.360 σ at β = 169 m
ADTH beam 2	0.23 σ	0.326 σ at β = 197 m
ADTV beam 1	0.23 σ	0.356 σ at β = 228 m
ADTV beam 2	0.23 σ	0.380 σ at β = 273 m

6.4.2 Kickers and Power Amplifiers

Kickers and power amplifiers, as well as their supports, form part of a contribution to the LHC by the Joint Institute for Nuclear Research (JINR), Dubna, Russia [18,5].

The kicker plates are directly coupled to the power amplifier tetrode anodes. They present a capacitive loading to the tetrode at low frequency in parallel with the anode resistor. At higher frequencies the distributed nature of the kicker capacitance behaves like a TEM line connected at the centre and open circuited at the ends [19]. Simulations, using a mathematical model developed for the kicker and the power amplifier circuit including the tetrodes [20] agree well with prototype measurements [20,15]. With 12 kV of anode voltage, 10.5 kV deflecting voltage is achieved at 100 kHz. The amplifier can be run with anode voltages of up to 15 kV DC further boosting the kick strength at low frequencies. At 1 MHz, however, the kick strength is limited by the capacitance of the kicker in parallel with the anode resistor. Not much more than the nominal 7.5 kV can be obtained beyond 1 MHz. The reserve kick strength at low frequencies is interesting for narrow band applications such as a beam exciter, for example as an ac dipole as demonstrated in the SPS [21]. At 15 kV anode voltage a maximum kick strength of around 4 μrad can be obtained at the lower frequencies for about 100 ms, limited by the power dissipation in the anode resistor. The feedthroughs are designed to withstand these high voltages [22]. Tab. 6.5 shows the maximum capabilities of the systems at different frequencies. These maximum values are only available in pulsed mode (50 ms at a duty cycle of 50%). In continuous mode about 50% of these values can be reached.

Table 6.5: Estimated Maximum Capabilities in Pulsed Mode (β=100 m)

	100 kHz	1 MHz	10 MHz	20 MHz
ADTH	0.47 σ	0.43 σ	0.14 σ	0.05 σ
ADTV	0.47 σ	0.43 σ	0.14 σ	0.05 σ

The auxiliary high-voltage equipment, including the anode voltage power converter, screen grid and control grid voltage converters, will be installed on the surface. All must be interlocked and remotely controlled. A distributed PLC system will be used for controls, slow interlocks and alarms. PLCs installed in UX45 and SR4 will communicate via a private bus for this purpose. They will also control the driver amplifiers in UX45 and monitor the power amplifiers in the tunnel. A fast hard-wired interlock chain is foreseen between SR4 and UX45.

Tab. 6.6 shows the most important higher order longitudinal modes contributing to the machine impedance with an estimate of their damped Q values.

Table 6.6: Higher-Order Longitudinal Modes in Kicker Structure (per Kicker); Estimates from Prototype Measurements.

Frequency (MHz)	R/Q in Ω	Q (damped)
89	2	256
176	3	110
296	< 0.1	47
357	9	46
436	13	104
488	11	42

There are some modes above 500 MHz including a cluster of modes at 800 MHz, but precise estimates of impedance require measurements on the final kicker. Damping is achieved using two capacitively coupled 50 Ω HOM couplers, one per plate (coupling capacity 2 pF). They can extract 500 W each, estimated to be sufficient even for ultimate beam intensities. The most critical case is when a mode falls exactly on a bunch frequency line (multiple of 40 MHz for 25 ns standard bunch spacing), and some modifications to the final geometry can be foreseen to push modes away from these dangerous lines.

6.4.3 ADT Vacuum

The dampers will be baked *in situ* at 250°C for 24 h. Each damper pair has two 30 l/s ion pumps, one at each end. A Penning gauge installed on each pair will provide a hardware interlock to the damper control system. The dampers and longitudinal pickups are between the same sector valves.

6.4.4 Damper pickups and RF Front End

Dedicated sets of two pickups per ring and plane will be used. These pickups are equipped with both buttons and strip-lines (See Sec. 13.11, Beam Position Monitors). The length of the strip-lines, short-circuited at one end, is 150 mm, giving a first transfer function maximum at 500 MHz. Hybrids in the tunnel provide the sum and difference signals, which will be transmitted via high quality 7/8" RF cables to the surface building SR4 where the signal processing is located.

6.4.5 Signal Processing and Interface with Computer Control

Signal processing will consist of an RF front end to down convert the pickup signals from a suitable harmonic of the revolution frequency to base-band, with a minimum bandwidth of ±20 MHz. Subsequent digital signal processing will be done with >80 MHz sampling rate and a minimum resolution of 12 bits for analogue to digital conversion. The main functions of the digital signal processing are to adjust the feedback phase [23,24] and adjust the overall delay to match the beam time of flight (1-turn delay). The processing is complemented by a post-mortem facility and a possibility for feedback gain adjustment. Correct system functioning can be tested by injecting a test-signal at the start of the signal processing and following it

through the chain up to the power amplifiers in the tunnel. Beam excitation signals can be added to the analogue part of the feedback loop or programmed in the digital part and triggered by timing.

6.4.6 System Operation and Limitations

At injection of a batch of proton bunches the dampers can be operated at the highest possible gain to achieve rapid damping of the lower frequency part of the injection error. During some tens of turns the systems can be operated in saturation, further reducing the damping time [25]. After initial damping the gain should be reduced to stay in a linear regime to provide feedback gain over the entire bandwidth of 20 MHz. Simulations show that the lower frequency part of the injection errors up to 1 MHz can be damped in the specified time, but small ripples in the strength of the injection kicks along the batch, both from the SPS extraction and LHC injection elements, which extend in frequency up to about 12 MHz, are damped more slowly and consequently lead to some emittance blow-up. Errors in timing of the kicker firing can also produce large bunch oscillations at the extremities of the batches.

Special care must be taken to limit noise injected by the ADT systems. Excess noise leads to emittance blow-up, the amount depending on the feedback gain and the betatron frequency spread [25]. Operation of the feedback in presence of strong non-linearities, such as octupoles, must be avoided. Stabilisation during the ramp and the flat top before colliding can be done by the feedback. Octupoles may be used instead; the overall strategy is described in Sec. 5.4 of this design report.

6.5 LOW-LEVEL RF

The low-level RF system comprises four sub-systems, the Cavity Controller, the Beam Control, RF Synchronization and the Longitudinal Damper. It also uses the longitudinal pickups (APW). The system described below is for the 400 MHz RF system. The requirements for the low level of the 200 MHz system are similar in many respects and the design will closely follow this system.

6.5.1 The Cavity Controller

There is one cavity controller for each individual cavity. It has two main functions; to provide adequate control of the phase and amplitude of the voltage in the cavity and to keep the power demanded at acceptable levels. To achieve this it comprises a number of separate loops (Fig. 6.6).

The Different Controller Elements

The Klystron Polar Loop keeps the gain and phase constant from the RF modulator input to the cavity main coupler input. It compensates the large change in phase shift when the klystron beam voltage is changed (~30°/kV) [29], the smaller phase shift variation with circulator temperature and the gain and phase modulation caused by power supply ripples (50 Hz, 600 Hz), on the power supply (~ 35° RF peak to peak measured on the second klystron). The loop bandwidth is approximately 1 kHz.

The RF Feedback Loop reduces the effects of the cavity impedance by compensating variations in the beam-induced voltage. The loop delay is ~ 650 ns. A 20 dB impedance reduction (open loop gain of 10) is specified at the exact RF frequency, reducing to zero at 1 MHz. The 1-Turn Feed-forward loop provides an extra 10-15 dB reduction of the beam loading at the RF frequency. In addition, a 1-Turn Feedback provides 20 dB gain on the revolution frequency sidebands to control transient effects. It reduces the impedance in a band extending to ~1 MHz on each side of the RF frequency.

The Tuner Loop maintains a given phase between incident power and cavity field. It has to be controlled in such a way that power transients due to the passage of batches and gaps are minimised (half-detuning).

The Set Point defines the desired voltage in the cavity. It should ideally be constant. However, some bunch-to-bunch variation is allowed as a compromise between an ideal voltage and the ability of the klystron to deliver transient power spikes. In addition to this function, the Set Point module also injects the drive from the Longitudinal Damper (see below).

Technology

All RF signals are first demodulated to generate base band I and Q signal pairs. The achievable range of impedance reduction with RF feedback depends on the overall loop delay and to minimize this a fast analogue path is used. Digital technology, inherently slower, is used to provide high precision control of 1° phase and 1% amplitude at the exact RF frequency. Digital I/Q Demodulators are used [30], implemented in Field Programmable Gate Arrays (FPGAs) or Complex Programmable Logic Devices (CPLDs). FPGAs are also used wherever bunch-by-bunch processing at 40 MHz is required (1-Turn Feedback, 1-Turn Feedforward and Set Point Generation).

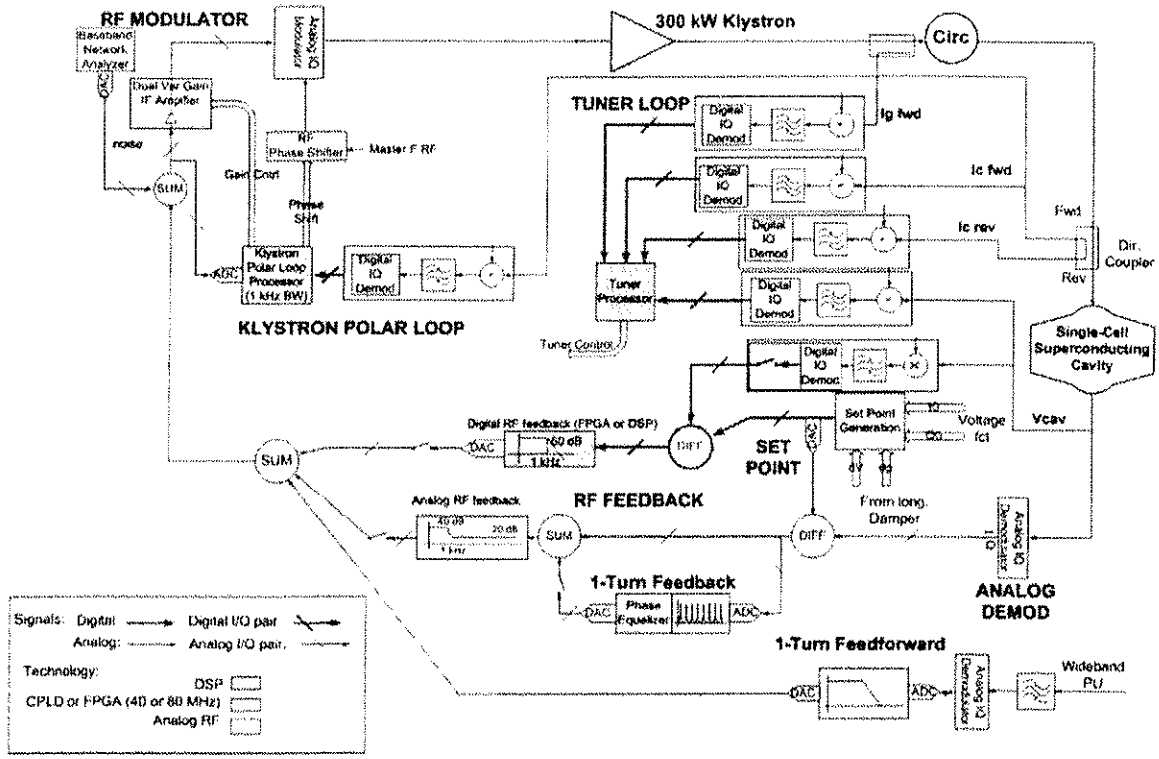

Figure 6.6: The Cavity Controller (One per Cavity).

Digital Signal Processors (DSPs) are used where the processing is very slow but complex. This is the case for the tuner where both hysteresis and non-linear characteristics are to be dealt with. Some parts, such as the Klystron Polar Loop and Digital RF Feedback can be implemented with either FPGA or DSP.

6U Euro crates with two backplanes will be used, the upper one (P1 connector row) being standard VME and the lower one custom designed to carry slow clocks, timing signals, interlock lines, serial data exchange between adjacent cards and separate linear power supplies reserved for the RF circuitry.

Diagnostics

All signals used in the loops are logged in two different memories, one for observation and one for post-mortem. For slow signals 6 s of data are kept with one sample /100 μs, whereas fast signals are logged at a rate of 40 MHz to observe the effects on each bunch, the last ten turns (~1 ms) being stored. In addition a base band network analyzer is included: an arbitrary function can be injected into the loops and the corresponding outputs at various points enable the transfer function to be obtained, as is done in PEPII [31]).

Layout

The cavity controllers are installed on a platform in UX45 on the opposite side of the tunnel from the klystrons to minimize the risk of signal contamination. There are four racks common to all cavities plus one rack per cavity. The latter contains the RF Feedback crate and the Klystron and Tuner Loop crate. A small pre-driver amplifies the 400 MHz output and sends it across the tunnel to the klystron driver amplifier.

6.5.2 Beam Control

The main functions of the beam control are to generate the beam centred RF reference, stabilize the beam against dipole oscillations and minimize noise effects - mainly phase noise - to optimize lifetime in coast. There is one separate system per ring, as shown in Fig. 6.7, but one single dual-frequency program, common to both.

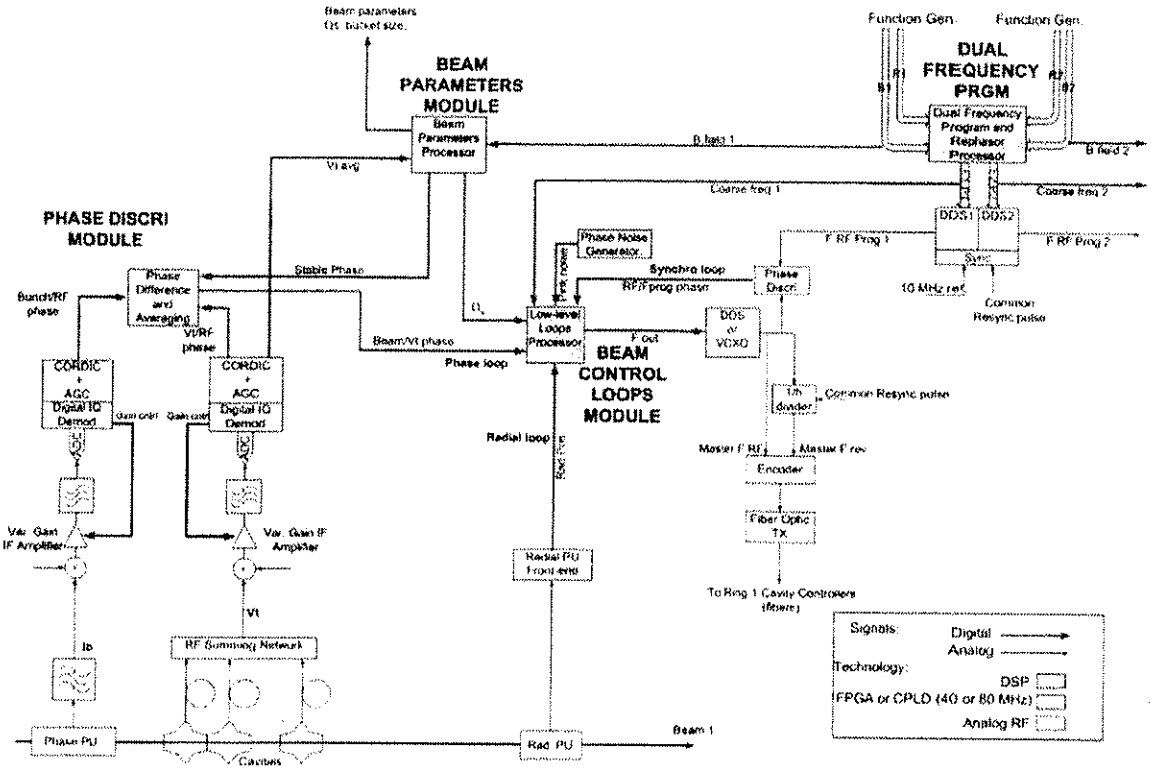

Figure 6.7: Beam Control System for One Ring

The dual frequency program pilots two Direct Digital Synthesizers (DDS) that generate the 400 MHz RF for each ring. The frequency is computed from the instantaneous value of the integrated B field, defined by a function, not a measurement, and the desired radial steering. The two rings can be ramped independently, but for physics to take place they will be ramped synchronously.

The Beam Control Loop module implements the classic three loops: phase, radial and synchronization. The last two are exclusive. If required, acceleration can be done with the radial loop. For physics, however, the frequency of each ring is locked in phase to the reference via the synchronization loop and both DDS have, at all instants, the same frequency. Acceleration with a synchronization loop is also used for LHC beams in the SPS [32].

The phase loop input is the phase error between the total cavity voltage and the beam phase, measured with a pickup. The Phase Discriminator Module measures the phase for each bunch and computes an average for the Beam Control Loop. The Beam Control thus deals with the beam as a whole, updating the RF frequency at each turn.

The dynamics of the synchronization loop must be adjusted as the synchrotron frequency changes [33]. The Beam Parameter Module computes the synchrotron frequency and passes the value to the Beam Control Loop module.

Technology

The processing is slow (update rate at the revolution frequency of 11 kHz) so that DSPs can be used. The Phase Discriminator uses a Digital I/Q Demodulator and transforms the cartesian coordinates (I,Q) into

(phase, amplitude) using the COordinate Rotation DIgital Computer (CORDIC) algorithm implemented in an FPGA. This is also used at RHIC [34]. The modules will reside in a VME crate.

Layout

The Beam Control system is installed in the Faraday Cage in SR4. It generates the Master f_{RF} and the revolution frequency and these are sent on fibres to the RF cavern in UX45.

6.5.3 RF Synchronization

The three main functions are the synchronisation of the SPS to LHC "bunch into bucket" transfer - with diagnostics of transfer faults, generation of beam synchronous signals (40 MHz bunch frequency, revolution frequency and injection kicker pulses) for users (experiments, Beam Instrumentation, Beam Transfer etc.) and fine re-phasing of the two rings before physics.

The method used for synchronizing the transfer is now classic at CERN, (PSB to CPS, CPS to SPS and also SPS to LEP [32, 35]). The LHC is the master machine, sending to the SPS a fiducial frequency train at the frequency f_c = SPS $f_{rev}/27$ = LHC $f_{rev}/7$ and a phase shifted LHC 400 MHz RF. The SPS locks its beam to these two signals. A delay box allows selection of the buckets to receive the SPS batch. The phase of the 400 MHz sent to the SPS can be fine adjusted to centre the received beam in the middle of the LHC bucket. All these adjustments are transparent to the SPS.

Layout and Distribution

The RF Synchronization systems will be installed in the Faraday Cage in SR4. The two signals sent to the SPS (BA3) go via thermally compensated fibre-optic links (re-used from LEP). Three pairs of bunch frequency plus revolution frequency references are also generated in SR4. There is one pair per ring for beam instrumentation equipment and one pair for the experiments. The links are under the responsibility of the AB Controls group. The LHC RF also generates pulses for the LHC injection kickers (transmitted on fibres). For fail-safe operation two dedicated fibres transmit the revolution frequency signals to the beam dump systems. The transmission is the responsibility of the AB Beam Transfer group.

When the LHC is ramped for physics, the two rings are locked from injection and the two DDS shown in Fig. 6.7 receive the same control word for their frequency register at all times. Before physics the relative phase of the two rings can be fine-adjusted by simply changing the control word of the phase register of one DDS.

6.5.4 Longitudinal Damper

The longitudinal damper reduces emittance blow-up due to filamentation following phase and energy errors at injection. This is important in the SPS-LHC transfer because the SPS bunch almost fills the LHC bucket [10]. The damper can also fight against slow longitudinal coupled-bunch instabilities but this should not be a concern [4,36]. It tries to damp the longitudinal oscillation of the bunch centre of charge (dipole mode) or the oscillations of the bunch shape (quadrupole and higher modes). Dipole mode damping is achieved by injecting a correction into the 400 MHz system to generate a cavity field in quadrature with the main accelerating field. Quadrupole damping, foreseen as an upgrade, can be achieved by varying the amplitude of the main accelerating field to modulate the bucket size.

Implementation and layout

The dipole mode damper will be similar to that proposed in [37]. Filtering will be done with a Finite Impulse Response (FIR) filter clocked at 40 MHz and implemented in an FPGA. The hardware will be located in the Faraday Cage in SR4 and will produce a signal in base band (momentum kick) extending from dc to a few MHz. This signal will be sent via a fibre-optic link to the RF cavern UX45, and hence to the Set Point module shown on Fig. 6.6.

6.5.5 Longitudinal Pickup (APW)

Two longitudinal monitors per beam will be installed. They are of the wall current type and are based on the coaxial-line designs used in the SPS and PS [38,39]. They will be used for the beam phase reference for the low level loops and also for longitudinal bunch and beam diagnostics. Their transfer impedance is ~8 Ω and their bandwidth ~170 kHz to ~3.7 GHz. As the pickups contain ferrite materials, they will be baked *in situ* at 250°C for 24 h and each pickup will have a 30 l/s ion pump at both ends. Before installation the ferrite will follow a special out-gassing procedure, presently being defined. No specific pressure hardware interlock is needed for these pickups.

6.6 EQUIPMENT CONTROLS

6.6.1 Hardware and Layout

Equipment controls for the LHC RF ACS, ADT and ACN systems will make extensive use of Programmable Logic Controllers (PLC), and industrial components. The ACS power system and SC cavities will be controlled by 20 midrange PLCs having 192 remote interface modules in total. Altogether the ACS control system will have to treat approximately 3400 signals, 1000 interlocks and 1 100 alarms. The ADT and ACN systems will each use eight PLCs. While commercial remote interface modules will mainly be used, a number of special signal conditioners have been developed, in industry-compatible form. These include a multi-sensor Pt100/Allen Bradley/CERNOX temperature conditioner, a liquid helium level measurement interface and a dual threshold level detector. The remote interface modules will be grouped near the equipment and connected to the PLCs via a field bus network (FIPIO). Special equipment, including that recuperated from LEP, e.g. RF amplifiers, power supplies and vacuum conditioners etc. will be fitted with this FIPIO. The PLCs will exchange data with each other and communicate with the supervision layer by Ethernet, over standard structured cabling. The layout for the ACS system is shown in Fig. 6.8.

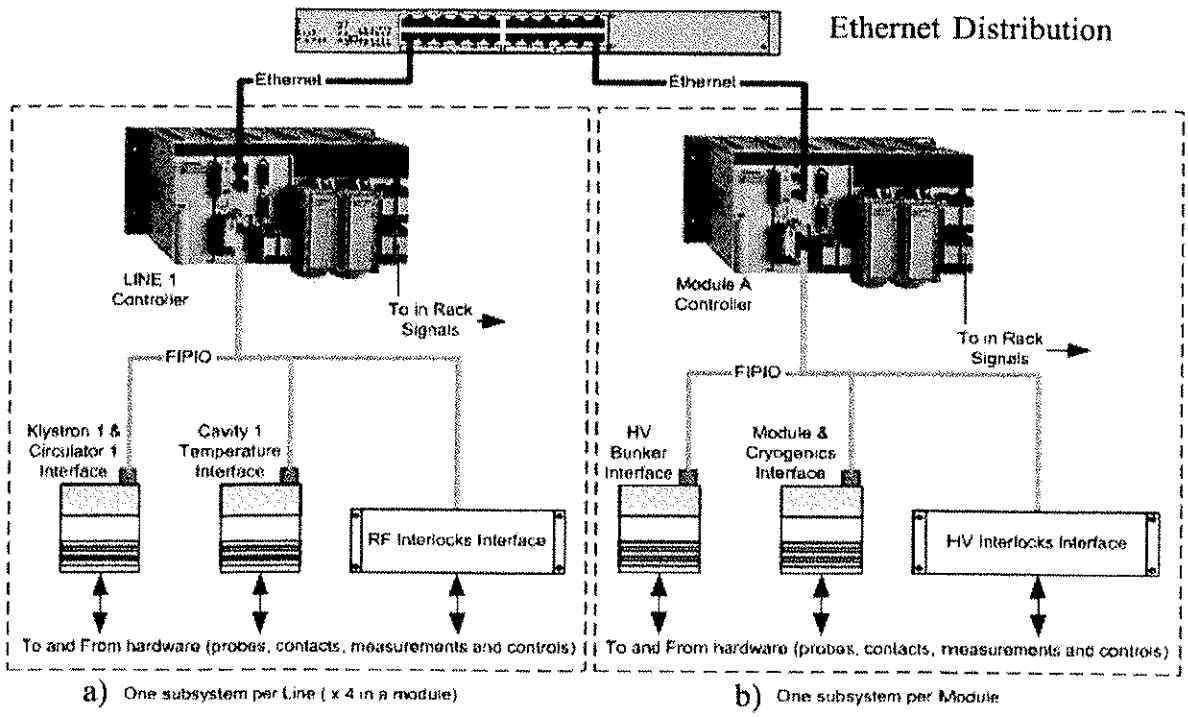

Figure 6.8: ACS Equipment Controls for a) One Klystron Cavity Line and b) One Cryomodule

There is one PLC for each cavity/klystron line and one for each SC module and HV system. The PLCs and remote interfaces for each system are distributed at the various equipment locations in UX45, SR4 and

machine tunnels so that cabling cost and complexity are minimized and problems with passing signals over long cables are avoided.

6.6.2 Software

The control software has been structured in an object-oriented manner right down into the PLC, as shown in Fig. 6.9. In the PLC each hardware device has its software counterpart. Global software devices have been defined allowing higher levels of abstraction. The software device contains properties (command, status code, values) that are the image of the hardware device parameters. The individual devices are controlled by a "sequencer" for automatic operation. The PLC devices are remotely accessible through an OPC server and a middleware gateway is used to implement Remote Device Access (RDA) based on Common Object Request Broker Architecture (CORBA), following the Common Middleware (CMW) approach. The "IOScan" mechanism is used to exchange predefined blocks of data between PLCs.

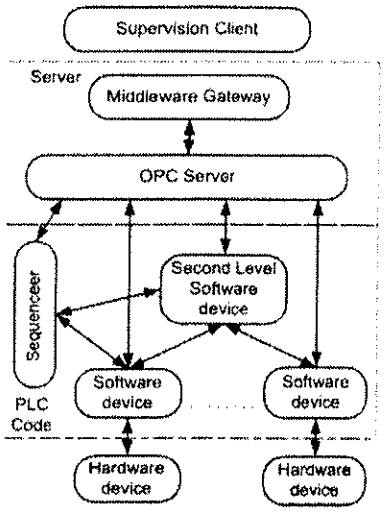

Figure 6.9: 'Object-Oriented' PLC Software Layout

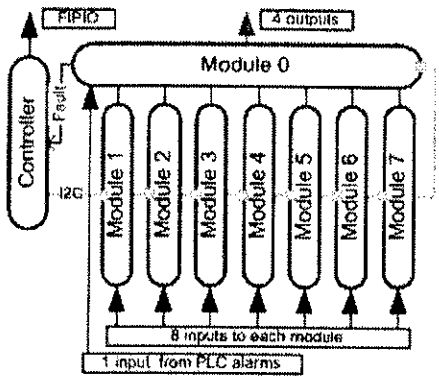

Figure 6.10: Modular Fast Interlock System

6.6.3 Interlocks

Fast interlocks (< 2μS) are treated by an independent hardware system based on that used in LEP. An interlock crate contains up to eight modules that can be interrogated by a local controller over an internal serial bus (I^2C). This is shown in Fig. 6.10. Information on the first fault in each module and the first active module in the crate is returned to the PLC over the fieldbus. A particular feature is that interlocks can be software inhibited by the PLC through a special command sequence. Crates and modules are chained to realise the full interlock system. In the ACS system there will be two chains: one for RF interlocks and one for HV interlocks. For the ADT, with interlock inputs in both UX45 and SR4, the HV chain is split into two parts.

6.6.4 Slow Interlocks and Alarms

Each PLC will generate an alarm code in the form of a coded integer (the 'code' property of each device) with an update period of <10 ms. The device codes are grouped to form a macro summary code used to toggle the PLC interlock output bit. A first fault detection mechanism is implemented in the PLC and fast interlock data and device codes are latched. An external reset is needed to restart. The supervision has full access to all alarm and interlock data.

6.6.5 Machine Protection

Simulations have shown that with nominal intensity the trip of one klystron will cause the beam to be lost. The RF systems will supply interlock signals to the Beam Interlock Controller (BIC) to provoke beam dump when serious fault conditions arise. Under certain conditions when there is no risk of damage to the machine, i.e. pilot beam, they will be inhibited by the BIC. Signals for the protection of the SC cavities will also be supplied to the BIC: these include HOM coupler temperatures, helium tank levels and pressures and insulation vacuum.

6.6.6 Low-Level RF Controls

The LHC low-level RF, damper feedback and beam control systems will make extensive use of digital technology in the form of FPGAs and DSPs. This allows the direct integration not only of all necessary remote control functionality but also of extensive diagnostics facilities.

6.6.7 Front End and Application Software

The local intelligence required for sequencing of complex equipment actions will reside where possible in the PLCs. Where non-PLC equipment is involved, such as in the RF low-level, damper feedback and beam control systems, the sequencing will be done in the front-end computer. There will be one front-end computer per ring for each system, which will be responsible for overall equipment control and will provide the interface to the accelerator control software via the Controls Middleware. The front-end computers will be AB/CO standard hardware, running software built on the standard AB/CO Front End Software Architecture (FESA). FESA is also being evaluated as the software platform for the VME crates housing the low-level system electronics.

Application software for the test stands and for expert diagnostic purposes in the LHC is being developed in Java, using tools provided by AB/CO such as the GUI Platform for user interfaces and CMW for communication.

The low-level RF, damper feedback and beam control systems represent a particular challenge. Many measurement and analysis tasks traditionally done with external instrumentation such as oscilloscopes and network analyzers will be done directly inside the systems themselves. Extensive software will be needed for setting up these facilities and for subsequent data acquisition, analysis and presentation.

6.6.8 Signal Observation and Post-Mortem

Since the RF equipment in UX45 will not be accessible when beam is circulating, operation of the RF systems will require remote observation of a number of signals. These signals fall into three categories: fast (RF) signals at and above 400 MHz, bunch frequency signals at 40 MHz and slow signals, below 100 kHz.

Many of these signals will be available directly from the RF low-level and damper feedback VME systems. The remaining signals will be acquired using commercial off-the-shelf digitizer and multiplexer modules based on Compact PCI, following the nAos replacement standard (OASIS). Data for the post-mortem system will be stored in circular buffers inside the digital parts of the low-level and feedback systems, as well as in the external Compact PCI acquisition crates. The arrival of a post-mortem trigger event will freeze the buffers, making the data available for readout via the control system. A second set of buffers will operate in parallel to provide data for non-post-mortem observation purposes. All diagnostics systems and systems containing diagnostics will be powered by Uninterruptible Power Supplies (UPS).

6.7 LAYOUTS AND INFRASTRUCTURE

Following the changes introduced by Optics version 6.4, all RF systems are now positioned closely around IR4, in UX45, RB44/46 and UL44/46. The 4800 kW power plant with its 16 klystrons, circulators and loads for the 400 MHz superconducting cavity RF system (ACS) is located in the cavern UX45, together with its HV equipment, auxiliary power supplies and control racks. The layout of the equipment is shown in Fig. 6.11.

The two accelerating modules for Beam 2 are positioned directly on either side of the centre of IR4, followed by the modules for Beam 1. This is to permit passage of the cryogenic line (QRL) which joins the bottom of the cavern UX45 after the Beam 2 modules.

While waveguides connecting the cavities to the klystrons are now more accessible than they were in the original layout, installation and access remains particularly difficult for the two modules of Beam 1, these being partly situated inside RB44 and RB46. The entrances into RB44 and RB46 cannot be enlarged, as they are steel-reinforced supporting structures for the cavern.

The machine tunnel crossing the cavern is shielded with 1200 mm thick concrete walls and an 800 mm thick concrete roof. Openings for the cryogenic lines and the 16 waveguides would allow passage of radiation from the tunnel into the cavern. While there is no access to UX45 for operation with beam, access to the control racks and the klystrons is necessary during RF conditioning which produces intense gamma radiation. An additional shielding wall (800 mm thick concrete) must therefore be installed. Simulations have confirmed that this wall reduces the radiation to safe levels.

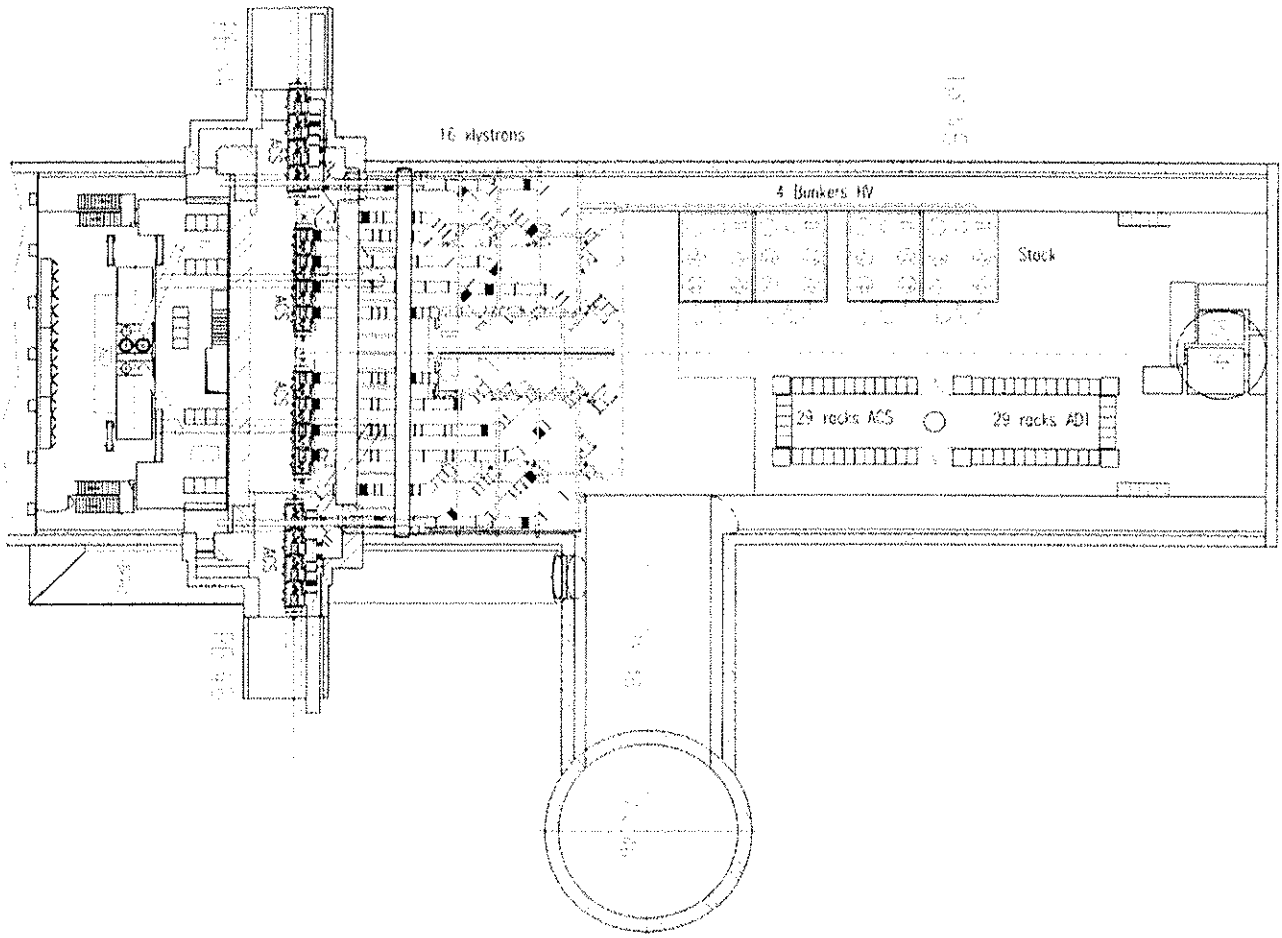

Figure 6.11 Layout of ACS and equipment in UX45

The other RF equipment is located in the tunnel areas symmetrically on either side of the IR. The layout on the right hand side is shown in Fig. 6.12. Equipment on the left hand side is identical. The RF pickup stations (APW) are at about 16 m, the transverse damper system (ADT) at about 23 m and the 200 MHz system (four cavities per beam) at about 24 m from the centre.

Although the 200 MHz system (ACN) is staged, it forms a normal part of the integration studies. Six holes for passing the coaxial power lines from the galleries UL44/46 and UA43/47 to the cavities in RB 44/46 have already been drilled.

The total dissipation of all RF systems into air is 490 kW (300 kW without the 200 MHz system). The existing ventilation plant in UX45 (100 kW), complemented by several additional local chilled water

ventilation units, is used to remove this heat. Two doors will separate the air volume of the RF areas from the machine tunnel.

The cooling of all RF systems requires 1300 m^3/hour water flow (930 m^3/hour without the 200 MHz system), supplied by two pumps, one for the left and one for the right side of Point 4.

The surface building SR4 is dedicated to RF. It houses the five 4 MW klystron power converters for the 400 MHz cavities and the power converters for the 200 MHz system and the transverse dampers. There will also be a Faraday cage for beam control equipment.

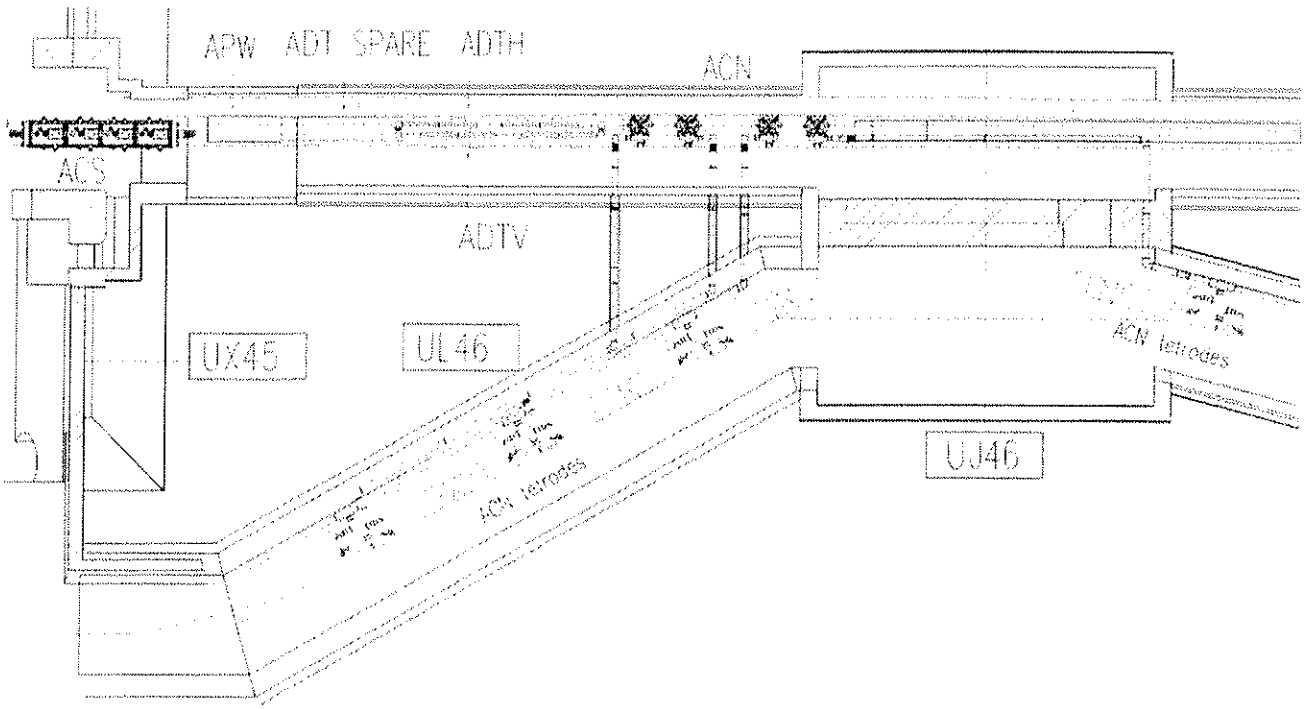

Figure 6.12: Layout of RF Systems on right-hand side of IR4

About 1100 cables of different kinds, totalling 160 km, connect the equipment in the machine tunnel, the power plants and the control racks. The cables for the 400 MHz modules are routed via two openings in the floor of the tunnel to the low level racks and the klystrons.

Most of the low-level and feedback electronics (20 racks) are located in the part of UX45 next to the cryogenic equipment, US45. This location has been chosen in order to reduce the lengths of the feedback cables as much as possible, and also to minimize possible cross-talk with the high-power RF installation (klystrons, circulators, power loads, and waveguides). Simulations indicate that the radiation level at the feedback electronics is 100 times lower than in the RRs where power converters and electronics will be installed. Nevertheless, there is a risk of single event perturbations and the susceptibility of the electronics is under study.

REFERENCES

[1] The LHC Study Group, *The Large Hadron Collider - Conceptual Design*, CERN/AC/95-05 (LHC).

[2] D. Boussard, T. Linnecar, *The LHC Superconducting RF System*, Cryogenic Engineering and International Cryogenic Materials Conference, July 1999, Montreal, Canada, and LHC Project Report 316.

[3] D. Boussard, E. Chiaveri, H.P. Kindermann, T. Linnecar, S. Marque, J. Tückmantel, *Design Considerations for the LHC 200 MHz System*, LHC Project Note 368.

[4] E. Shaposhnikova, *Longitudinal Beam Parameters during Acceleration in the LHC*, LHC Project Note 242.

[5] D. Boussard, W. Höfle, T. Linnecar, *The LHC Transverse Damper (ADT) Performance Specification*, SL-Note-99-055.
[6] J. Tückmantel, CERN, private communication.
[7] O. Brunner, H. Frischholz, D. Valuch, *RF Power Generation in LHC*, PAC 2003 and LHC Project Report 648.
[8] H.P. Kindermann *et al.*, *Status of RF couplers for SC cavities at CERN*, EPAC, Sitges (Spain), 1996.
[9] H.P. Kindermann, M. Stirbet, *RF Power Tests of LEP2 Main Couplers on a Single Cell Cavity*, 8th Workshop on RF Superconductivity, Padova (Italy), 1997 and CERN/SL/97-64 RF.
[10] J. Tückmantel, *The SPS/LHC Longitudinal Interface*, Chamonix IX, Jan 25-29, 1999, CERN-SL 99-007 DI.
[11] *Amplifier 240 kW CW 400 kW Pulsed* (EDMS LHCACNLA0003 v.0).
[12] "White" Book, CERN /AC/93-03 (LHC), page 67, CERN Geneva, 1993.
[13] "Yellow" Book, CERN /AC/95-05 (LHC), page 64, CERN Geneva, 1995.
[14] W. Höfle, *Operation of the LHC Transverse Damper (Feedback)Through Cycle*, Proceedings of the LHC Workshop, Chamonix XI, CERN-SL-2001-003 DI, pp. 317-319.
[15] E. Gorbatchev, I. Ivanov, V. Kossoukhine, N. Lebedev, V. Melnikov, S. Rabtsoun, W. Höfle, T. Linnecar, R. Louwerse, J. Tuckmantel, *Transverse Damping System for the Future CERN LHC*, PAC 2001, Chicago, Ill., USA, 2001.
[16] W. Höfle, *Towards a Transverse Feedback System and Damper for the SPS in the LHC Era*, Particle Accelerators, 1997, vol. 58, pp. 269-279.
[17] W. Höfle, R. Louwerse, *Technical Specification for Broadband Transistorised RF Amplifier*, LHC-ADTDA-CI-0001, EDMS No: 365359, CERN Geneva, 2002.
[18] CERN-JINR Agreement 29.05.1992, Protocol dated 28.04.1997, Addendum No. 1, 19.06.1997, http://ab-div-adm.web.cern.ch/ab-div-adm/Collaborations/Descriptions/LHCDamperCollab.html
[19] W. Höfle, R. Louwerse, *The Deflectors of the SPS Transverse Damper - Measurements and Calculations*, SL -45 (RF), CERN Geneva, 1997.
[20] E. Gorbatchev, W. Höfle, V. Melnikov, *Computer Simulation of the Electrical Circuit of the Wideband Power Amplifier for the Transverse Damping Systems of LHC*, LHC Project Note 259, CERN, Geneva, 2001.
[21] O. Berrig, W. Höfle, R. Jones, J. Koopman, J.-P. Koutchouk, H. Schmickler, F. Schmidt, *Excitation of Large Transverse Beam Oscillations without Emittance Blow-up Using the AC-Dipole Principle*, DIPAC 2001, Grenoble-France, 13-15 May 2001; CERN-SL-2001-019 BI, Geneva 2001.
[22] W. Höfle, J.-F. Malo, H. Preis, *Technical Specification for the Manufacture of High-voltage Vacuum-tight Ceramic Feedthroughs for the LHC ADT Kicker*, LHC-ADTKV-CI-0001, EDMS No. 378073, CERN Geneva, 2003.
[23] V. Rossi, *Digital Signal Processing Applications and Implementation for Accelerators - Digital Notch Filter with Programmable Delay and Betatron Phase Adjustment for the PS, SPS & LHC Transverse Dampers*, CERN-SL-2002-047 HRF, Geneva, 2002.
[24] V. Vendramini, *Traitement du Signal Numérique pour le Système de Contre-Réaction Transverse Utilisant un Seul Pick-up avec Application dans le SPS et dans le LHC*, SL -Note-2002-046 HRF, Geneva, 2002.
[25] W. Höfle, I.N. Ivanov, R. Louwerse, V.A. Melnikov, *Suggestion to increase the Transverse Damper Efficiency*, Particle Accelerators, 1997, vol. 58, pp. 281-286.
[26] R. Louwerse, J-F. Malo, H. Preis, *Electrical High-voltage and Vacuum Tests on Prototype Ceramic Feedthroughs for the LHC Transverse Damper*, unpublished, CERN Geneva, 1992.
[27] T. Bohl, W. Höfle, T. Linnecar, E. Shaposhnikova, J. Tuckmantel, *Observation of Parasitic Beam and Cleaning with Transverse Damper*, AB-Note-2003-021 MD, CERN, Geneva, 2003.
[28] D. Boussard, *Evaluation of Transverse Emittance Growth from Damper Noise in the Collider*, SL/Note 92-79 (RFS), LHC Note 218, CERN Geneva, 4.6.1992.
[29] H. Frischholz, private communication.
[30] C. Ziomek, P. Corredoura, *Digital I/Q Demodulator*, PAC 95, SLAC, May 1995.
[31] P. Corredoura, *Architecture and Performance of the PEP-II Low-Level RF System*, PAC 1999.
[32] P. Baudrenghien, *Beam Control for Protons and Ions*, Chamonix X, Jan 25-29, 1999, CERN-SL-99-007 DI.

[33] J.M. Brennan et al., *RF Beam Control System for the Brookhaven Relativistic Heavy Ion Collider RHIC*, EPAC 98.
[34] T. Hayes, BNL, private communication.
[35] P. Baudrenghien, T. Linnecar, D. Stellfeld, U. Wehrle, *SPS Beams for LHC: RF Beam Control to Minimize Rephasing in the SPS*, June 1998, CERN-SL-98-027-RF.
[36] D. Angal-Kalinin, *Review of Coupled Bunch Instabilities in the LHC*, July 15, 2002, LHC Project Report 595.
[37] D. Boussard, E. Onillon, *Damping of Phase Errors at Injection in the LHC*, PAC 1993, Washington DC.
[38] T. Linnecar, *The High Frequency Longitudinal and Transverse Pick-ups in the CERN SPS Accelerator*, IEEE Trans. Nuc. Sci. Vol. NS-26, No.3, June '79.
[39] J. Durand, A New Wall-Current Monitor for the PS, PS/PSR/Note 85-17.

CHAPTER 7

MAIN MAGNETS IN THE ARCS

7.1 OVERVIEW

7.1.1 Superconducting Technology for Accelerator Magnets

The Large Hadron Collider relies heavily on superconducting magnets which are at the edge of the present technology. There are presently three large accelerators that are based on superconducting magnets: the Tevatron (FNAL), HERA (Desy) and RHIC (BNL). All of these make use of classical Nb-Ti superconductors, cooled by supercritical helium at a temperature slightly above 4.2 K. In each case the nominal fields are below or around 5 T.

The challenge for the LHC magnet system is to make the most profitable use of the existing LEP tunnel and to obtain the highest possible bending strength whilst still making use of the well-proven technology based on Nb-Ti Rutherford cables. To increase the performance of Nb-Ti requires cooling of the superconductors to a temperature below 2 K, using superfluid helium. In practice, at 1.9 K an extra 1.5 T is attainable in the LHC dipole, i.e. from around 6.5-7 T to 8-8.5 T central field with corresponding 20% gain in beam energy.

He II technology for large magnet systems was demonstrated, though on a different geometry, in operation of the Tokamak, TORE SUPRA, at CEA-Cadarache (France). It has also been well confirmed in the two LHC strings, which eventually comprised a 107 m long series of magnets. He II has very low viscosity and very high heat conduction. These properties have to be fully exploited both in the magnet design and in the design of the cooling scheme.

On the other hand, reducing the temperature by more than a factor of two has the detrimental effect of reducing the heat capacity of the cable by almost an order of magnitude. For a given temperature margin (difference between the critical temperature of the superconductor and the operating temperature) the energy deposition that can trigger a quench is therefore substantially reduced; in the LHC magnets the temperature margin must be significantly larger than that used in previous projects. This also means that very tight control of movements and heat dissipation inside strands and cables is needed.

The electro-magnetic forces increase with the square of the field therefore, controlling conductor motion requires a stronger force-retaining structure than in earlier magnet designs. In addition, space limitations in the narrow LEP tunnel and the need to keep costs down have lead to the two-in-one design used for almost all of the LHC superconducting magnets. Two-in-one magnets have the windings for the two beam channels accommodated in a common cold mass cryostat and with magnetic flux circulating in the opposite sense in the two channels. This makes the magnet structure complicated, especially for the dipoles where the separation of the two beam channels is small enough that they are coupled both magnetically and mechanically.

The necessity to properly assess the above-mentioned design features, to validate the very demanding protection system (the energy density also increases with the square of the field) and to find the cheapest solution compatible with the required performance, needed a substantial R&D programme on magnets and associated technology. This was carried out by CERN in close collaboration with other European laboratories and with European industry during the years 1988 to 2001 [1, 2, 3, 4, 57].

7.1.2 The R&D Programme and New Features

The programme included development of software and design tools, construction of short models and full size prototypes and measurements of single magnets and two strings that simulated two half-cells of the LHC machine. The basic dipole design was frozen at the third generation.

The first generation [5] featured:

- an electro-magnetic design with 6 coil blocks
- use of two layers wound with 17 mm wide cable
- insulation with polyimide and pre-preg fibre-glass tapes
- collars in aluminium alloy

- iron yoke split vertically closing at cryogenic temperature
- separated flat iron insert
- 10 m cold mass length
- 50 mm bore
- 180 mm inter-beam distance
- cryogenic lines integrated in the dipole cryostat.

Despite the first generation cable, these magnets showed full reliability for field beyond 8 T and capability to attain 9 T [6]. Quenches were mainly in the ends which were not fully optimised at the time, especially for such big cables. The good behaviour of the structure was shown in a previous magnet, made with coils of HERA dipoles inserted in an LHC design cold mass [7].

The second generation (or "Yellow Book" [8]) design featured the following changes:

- an electro-magnetic design with 5 coil blocks
- use of 15 mm wide cables
- use of full polyimide tape insulation
- race-track collars in aluminium alloy
- flat iron insert embedded in the collar
- 15 m long cold mass
- 56 mm bore
- 194 mm inter-beam distance
- cryogenic line outside the dipole cryostat
- elimination of the radiation shield at 5 K.

This generation, introduced mainly for reasons of cost, went through various changes after its first introduction in 1995 that eventually resulted in a non ideal accommodation of the conductors. Performance was insufficient, although the last long model did have a good training curve [3].

The third and final generation [9, 10] presents the following main changes:

- an electro-magnetic design with 6 coil blocks
- use of 15.1 mm wide cables
- collars of austenitic steel
- inclined separated iron insert
- vertical iron gap closing at room temperature
- use of nested laminations at the end to reduce peak field on the ends while cancelling almost the field coupling at the extremities
- special polyimide insulation for the cold bore tube
- quench heater foils with 75 (rather than 125) μm thickness of polyimide and partial copper plating of the steel strips to control the resistance
- curved magnet obtained by welding curved half-shells in a press

The gain in performance with respect to the previous generation has been at least half a tesla and the model and prototype phase showed that 8.33 T operation is a target well within range for industrial construction.

The better conductor positioning of the 6 coil block (reducing shear stress among conductors), the better winding quality coming from increased experience and the main structural change, i.e. the use of stainless steel collars and closing the iron gap at room temperature, contributed to the improvement of quench performance. These structural changes have also helped ease the assembly tolerances [11].

The quadrupole design is practically unchanged from the "Yellow Book" [8]. The quadrupole magnet is the main element of the short straight section which accommodates a variety of other magnets and cryogenic functions. Since the last report was published the numerous variants of the short straight section cold masses and cryostats have been finalised and are reported in the quadrupole section.

In total there are some 18.7 km of main cryodipoles and about 2.7 km of short straight section cold masses, constituting more than 90% of the ~40,000 tons cold mass in the LHC tunnel.

7.2 SUPERCONDUCTING CABLE

7.2.1 The Cable

The transverse cross-section of the coils for the LHC 56 mm aperture dipole magnet (Fig. 7.1) shows two layers of different cables distributed in six blocks. The cable used in the inner layer has 28 strands, each having a diameter of 1.065 mm. The cable of the outer layer is formed from 36 strands, each of 0.825 mm diameter. The main parameters of the two cables are given in Tab. 7.1.

Table 7.1: Strand and cable characteristics of main dipoles (MB) and main quadrupoles (MQ)

	Inner Layer MB	**Outer Layer MB Both layers MQ**
Strand		
Coating type	Sn5wt%Ag	Sn5wt%Ag
Diameter after coating [mm]	1.065 ± 0.0025	0.825 ± 0.0025
Copper to superconductor ratio	1.65 ± 0.05	1.95 ± 0.05
Filament diameter [μm]	7	6
Number of filaments	~ 8900	~ 6500
RRR	≥ 150	≥ 150
Twist pitch after cabling [mm]	18 ± 1.5	15 ± 1.5
Critical current [A] 10 T, 1.9 K	≥ 515	
9 T, 1.9 K		≥ 380
ΔM at 0.5 T and 1.9 K [mT]	≤ 30	≤ 23
Cable		
Number of strands	28	36
Cable dimension (at room temperature)		
Mid-thickness at 50 MPa [mm]	1.900 ± 0.006	1.480 ± 0.006
Thin edge [mm]	1.736	1.362
Thick edge [mm]	2.064	1.598
Width [mm]	$15.10^{-0.02}_{+0}$	$15.10^{-0.02}_{+0}$
Keystone angle [degree]	1.25 ± 0.05	0.90 ± 0.05
Transposition pitch [mm]	115 ± 5	100 ± 5
Aspect ratio	7.95	10.20
MIITS [300 K] [MA^2 s]	45 [8T]	30 [6T]
Critical current I_c [A] 10 T, 1.9 K	> 13750	
9 T, 1.9 K		> 12960
dI_c/dB [A/T]	> 4800	> 3650
Inter-strand cross contact resistance [μΩ]	≥ 15	≥ 40
RRR	≥ 70	≥ 70
No cold welds and no cross-overs of strands allowed		

The filament size chosen (7 μm for the strand of the inner layer cable and 6 μm for the strand of the outer layer cable) allows the fabrication of superconducting wires by a single stacking process. The filament size for each type of strand is optimised in order to reduce the effects of the persistent currents on the sextupole field component at injection. The persistent current sextupole component (expressed in relative error at a reference radius of 17 mm) is -8.5×10^{-4} and the decapole component is 1.1×10^{-4} for these filament diameters. These error field components are corrected by small sextupole and decapole magnets located at the end of each dipole.

7.2.2 Definitions

The strand critical current is defined as the current measured at a resistivity of $\rho = 1.0 \times 10^{-14}$ Ωm in a magnetic field perpendicular to the strand axis with no correction made for the self-field effects and taking into account the strand cross section area.

The strand residual resistance ratio or RRR here is defined as the ratio of the resistance of the strand at 293 K to the resistance at 10 K just above the Nb-Ti superconductor transition temperature.

The width of the strand magnetization loop or ΔM is defined as the width of the hysteresis loop measured in an applied transverse field varying between 0 and 1 T.

The cable critical current is defined as the current measured at a resistivity of $\rho = 1.0 \times 10^{-14}$ Ωm taking into account the total cross section of the strands in an external magnetic field perpendicular to the large face of the cable, so that the highest total field occurs at the thin edge of the cable. The field is the maximum field seen by any strand, taking into account the effect of self-field averaged over the strand cross-section.

7.2.3 Strand Magnetization

To control the effects of the persistent currents at injection, a maximum value of the width of the strand magnetization loop at 0.5 T is required in the LHC cable specification. The width of the strand magnetization loop at 1.9 K and 0.5 T should not exceed 30 mT for the inner strand and 23 mT for the outer strand. In addition, by tight control of the manufacturing process, each strand manufacturer must keep the strand magnetization value within control limits of ±4.5% of the average value determined at the beginning of the production. To accommodate strand piece lengths with a magnetization value outside the control limits, CERN has requested restricting the use of these in a cable strand map to a limited number of strand positions. By a proper mixing of strands in cable, the variations of the magnetization from cable to cable for each manufacturer are kept within control limits of ±4.5%. [13, 14].

7.2.4 Cable Inter-strand Contact Resistance R_c

The inter-strand coupling currents are kept under control by oxidising the Sn-Ag layer on the strand surface, hence increasing the R_c value. The minimum allowed value for R_c is fixed at 10 μΩ. The duration of the heat treatment applied to the cables to oxidise the Sn-Ag layer is adjusted as a function of its thickness in order to get a target value of 15 μΩ for the dipole inner layer cable and 40 μΩ for the dipole outer cable. The field errors due to inter-strand coupling currents come mainly from the inner layer coils of dipoles; they are proportional to dB/dt and inversely proportional to R_c [15, 16].

7.2.5 Cable Dimensions

The tolerances on the cable dimensions have been specified to guarantee the requested field quality of the main magnets. The impact of cable dimensions is especially relevant for the even order skew field multipoles. The procedure established by CERN to control the cable dimensions guarantees an accuracy of 2 μm on the mid-cable thickness. To get the best field quality in a dipole, the cables for each layer are always selected from the same manufacturer. In addition, the cables for each layer in the same dipole aperture must be fabricated during the same cabling run and be heat treated together. To ensure this, CERN has requested that cabling runs are made with a multiple of 4 unit lengths and that cable heat treatments also take place with batches of 4 unit lengths. In the case of the quadrupole, the coils of one aperture are manufactured with the same cable unit length in such a way as to minimize the impact of the superconducting cable variations on the field quality.

7.2.6 Critical Current Densities in the Superconductor

Considerable experience was gained during the manufacture of cables for the R&D phase of the LHC programme for the dipole prototype. The manufacturing process for the strands and cables with 5 μm Nb-Ti filaments was optimised for high fields. The current densities in the non-copper part of the strand cross-section used in the present definition of the cables correspond to the critical currents measured on strands

extracted from the finished cables at the 3σ limit in the distribution curve of production. They are 1480 A/mm^2 at 7 T, 4.2 K, for the inner layer and 2000 A/mm^2 at 6 T, 4.2 K, for the outer layer. The critical current densities achieved for the mass production of LHC cables are more than 8% above the values used to specify the minimum critical current of the cables [17]. The R&D results show that the short-sample quenching field of the dipole (B_{ss}) is within ~2% of the cable short sample limit determined from strands extracted from the cables.

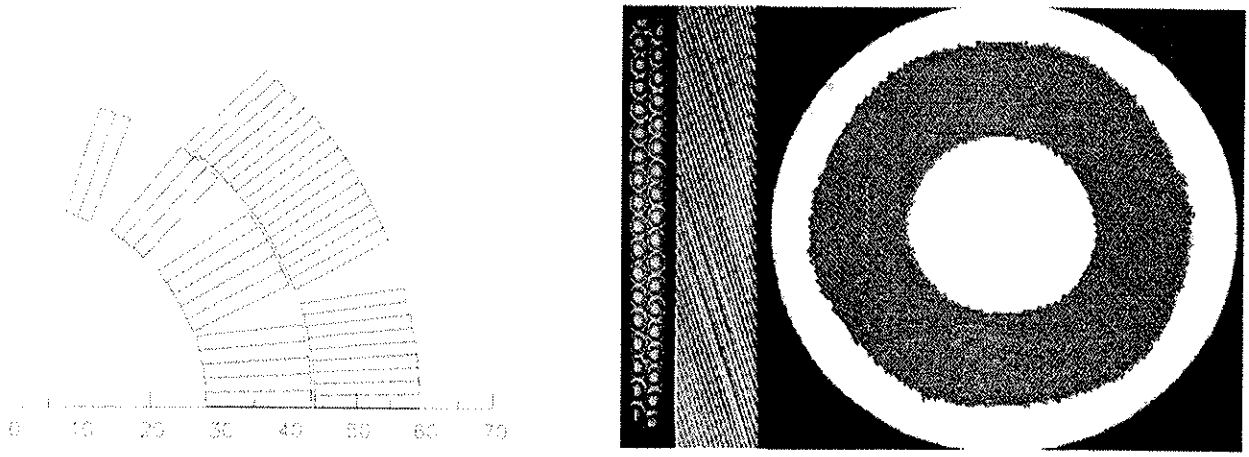

Figure 7.1: Conductor distribution in the dipole coil cross-section. X-axis in mm at left. Picture of cables and strand at right

7.2.7 Expected Quench Characteristics and Temperature Margin

Table 7.2: Expected quench performance and temperature margin (B_0 = 8.33 T, I_0 = 11800A, T_{bath} = 1.9 K)

Layer	B_p [T]	B_{margin} [%]	ΔT [K] margin	J_{cu} [A/mm^2]	T_{max} quench [K]	V_{max} [V]
Inner layer	8.57	85.7	1.51	760		
Outer Layer	7.46	85.8	1.57	928	375	500

Tab. 7.2 shows the peak field (B_p) for the two layers of cable, the field margin and the temperature margin when the magnet operates at 8.33 T. The field margin is defined as the ratio of the operating field to the expected quenching field at the short-sample limit (B_{ss}). The reference temperature of the bath is 1.9 K (helium between coil inner radius and cold bore). The current density in the copper at B_0 = 8.33 T in the case of a quench, the expected hot-spot temperature in the outer layer calculated in the adiabatic approximation and the maximum voltage across the outer layer calculated with the Quench Simulator QUABER [18] are given. The maximum voltage of 500 V corresponds to 20 V between turns (the inter-turn insulation is tested at room temperature with a voltage of 75 V). These two values have been calculated with an 80 ms delay for the quench detection and the active initiation of the quench triggered by the quench heaters over the volume of the outer layer. This time delay of 80 ms already produces 10.6 'MIITS' (MA^{2}s), corresponding to a hot-spot temperature of 60 K for a quench in the inner layer, or 80 K if the quench starts in the outer layer. The hot spot temperature is dominated by the choice of the copper to superconductor ratio and consequently the current density in the copper. For a quench in the outer layer at B_0 = 8.33 T, the hot-spot temperature can be related to the current density in the copper by the approximate formula

$$\int_{\Delta t_{delay}}^{\infty} J_{cu}^2 dt + J_{cu,0}^2 \Delta t_{delay} \cong 1.30 \times 10^5 \left(\frac{T}{375}\right)^{0.4} \left(1 + \frac{1}{\alpha}\right)$$

where α is the copper to superconductor ratio, T is the temperature of the hot spot, Δt_{delay} is the time delay for quench detection and heater initiated quench in the outer layer, and J_{cu} is the current density in the copper expressed in A/mm^2. The cable heat treatment applied for controlling R_c leads to an RRR value of up to 250.

This higher value of RRR allows a better voltage distribution between the poles of the two-in-one dipole but it generates an increase in the hot spot temperature of up to 4 %.

7.2.8 A.C. Effects

During ramping and discharge of the current in the dipole magnet, the main field errors and losses are generated by inter-strand coupling currents [19] and by persistent currents inside the filaments. The power losses due to inter-strand coupling currents depend strongly on the coating of the strands and the compression of the coils at low temperature. They are proportional to $(dB/dt)^2$ and inversely proportional to the inter-strand contact resistance R_c.

Losses for a twin-aperture dipole have been estimated at 180 mW/m for a charging time of 1200 s, corresponding to an energy of 220 J/m transmitted to the helium bath and to specific power dissipation in the cables of 0.077 mW/cm^3.

In the case of discharge of the machine, the upper limit of the time constant is given by the characteristics of the diode heat sink of the quench protection system and the quench propagation to other magnets via bus-bars. In the 10 m long magnets tested, a linear discharge from 8.33 T with dB/dt of 0.12 T/s did not initiate a quench. An exponential discharge with a time constant of 100 s leads to a load of 500 J/m. These values are mainly due to hysteresis losses and are calculated with an inter-strand contact resistance of 10 μΩ, the lowest expected.

7.2.9 Temperature Margin

A superconductor stays in the superconducting state when the temperature, the magnetic field, and the current density are below their critical value. The temperature margin shown in Tab. 7.2 corresponds to the difference between the bath temperature and the critical temperature at the design field and current. The temperature margin as a function of the operating field for the inner layers and for a bath temperature of 1.9 K is shown in Fig. 7.2.

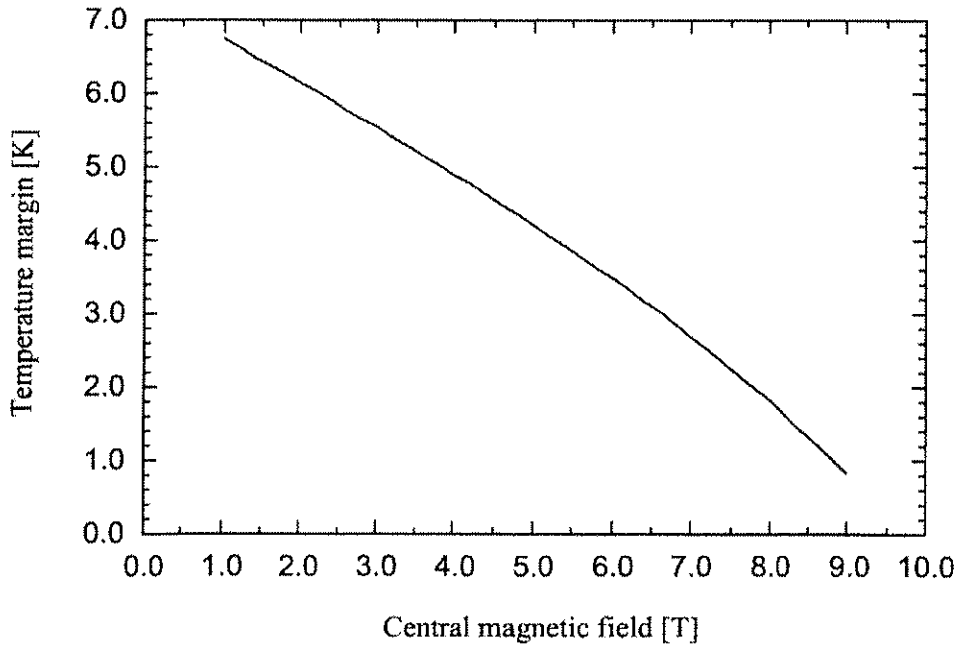

Figure 7.2: Variation of the temperature margin of the inner layer for T_{bath} = 1.9 K.

During the ramping tests on model magnets, the temperature of the superconductor was observed to stay at 4 K in steady-state conditions, i.e. above the λ point, without perturbation of the helium II bath. Experiments

made by CEA-Saclay show that with the existing insulation, the temperature difference between the conductor and the superfluid helium bath is 1 K for a power of 4 mW/cm^3 [20].

Tab. 7.3 illustrates the distribution of the temperature margin for the inner layer in a bath temperature of 1.9 K. The main part of the temperature margin will allow for beam losses.

Table 7.3: Use of temperature margin at 8.33 T and in a bath temperature of 1.9 K

Phenomenon	**Limits**	ΔT
J_c measurement precision	± 2.5 %	± 0.05 K
Dissipation at $\rho = 10^{-14}$ Ωm	< 0.5 mW/cm^3	0.27 K
Beam losses	4.5 mW/cm^3	1.12 K
Ramping losses at 1200 s	0.077 mW/cm^3	0.02 K
TOTAL		**~ 1.4 K**

7.2.10 Quality Assurance System

The QA system implemented to follow the manufacture of superconducting strand and cable relies on systematic tests performed by CERN on strand and cable samples [21]. The strand samples sent to CERN are cut from every strand piece length and are adjacent to the samples used by the manufacturer for the critical current test. They are used to perform acceptance tests at CERN and to cross-check the measurements done by the manufacturer. The data from the manufacturer concerning strand fabrication and electrical properties and the results of tests at CERN are recorded in an Oracle™ database. These data are monitored by CERN in order to assess the strand performance before giving approval to use the strands from a billet for cabling.

CERN's approval to use the strands from a billet for cabling is the first holding point imposed during manufacturing. To go ahead with the cable production, the manufacturer must also receive CERN's approval of the cable strand maps. CERN verifies that all the strand piece lengths are accepted and that the cable magnetization is within the limits and gives the duration of the heat treatment to be applied to the cable to get the required value for the cable inter-strand cross contact resistance. From a quality assurance perspective, the holding points imposed on the manufacturers before cabling are essential to check the manufacturing at key steps to ensure the required performance.

To obtain CERN's approval for shipment of the cables, the manufacturer must deliver a cable sample taken from each continuous length of cable, the cable fabrication and electrical data, the graphs of the cable dimensions, the graphs of the temperature variations during the cable heat treatment and a certificate of conformity for every unit length of cable.

At the beginning of the production, the dimensions of all cable unit lengths were measured by CERN to establish confidence in the manufacturer's quality assurance programme. During continuous production, the cable unit lengths are selected by sampling – taking at least one unit length per cabling run and taking into account the information on cable quality transmitted by the manufacturer. CERN will measure the cable dimensions and will also verify the absence of cold welds and cross-overs of strands. Measurements of cable inter-strand cross contact resistance, RRR and critical current in extracted strands will be performed on cable samples cut from every cable unit length selected for the measurement of cable dimensions. These measurements will be used to ensure the homogeneity of the production.

7.3 MAIN DIPOLE COLD MASS

7.3.1 Introduction

The LHC ring accommodates 1232 main dipoles: 1104 in the arc and 128 in the dispersion suppressor (DS) regions. They all have the same basic design. The geometric and interconnection characteristics have been targeted to be suitable for the DS region, which is more demanding than the arc. The cryodipoles are a critical part of the machine, both from the machine performance point of view and in terms of cost. Fig. 7.3 shows the cross section of the cryodipole.

The three European companies that have been collaborating with CERN throughout the prototype phase are now manufacturing the series cryodipole cold masses. To reduce costs, co-ordinate orders better and obtain the highest possible degree of uniformity in the three production lines, CERN supplies most of the critical components and some of the main tooling to the manufacturers. With CERN being at the same time the magnet designer, the supplier of the superconducting cables and most of the other main components, the dipole manufacturers are responsible for good quality construction that is free from faults. In order to help the cold mass manufacturers during the start-up phase, there have been two contracts with each manufacturer: firstly a pre-series contract (for the first 30 cold masses), then a series contract (for the remaining 386 cold masses). The components supplied by CERN for the two types of contract are shown in Tab. 7.4.

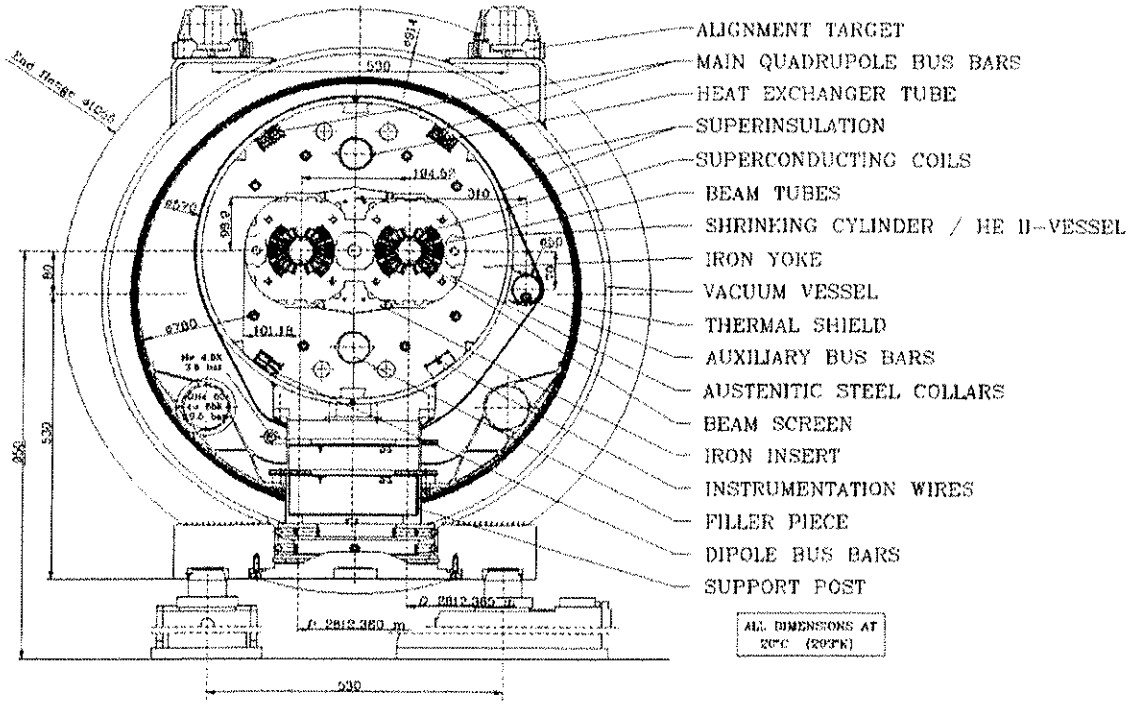

Figure 7.3: Cross-section of cryodipole

Tests on the first 15 m-long prototype of the second generation showed that transport of the fully assembled cryodipole is critical [12]. For this reason the cold masses are put in their cryostats at CERN. The surface transport of the entire cryodipole within CERN is done with a special vehicle (Rocla). Apart from the obvious cryogenics and vacuum considerations, the cryostating is also an important operation for the geometry and the alignment of the magnet, which is critical for the performance of the magnets in view of the large beam energy and small bore of the LHC. Moreover, the dipoles are longer than in previous superconducting accelerators and they are curved. All these factors result in stringent requirements for the dipole geometry.

Testing the cryodipoles is essential to validate the magnets for operation in the accelerator. It is also necessary to identify assembly faults (mechanical and/or electrical).

The core of the cryodipole is the "dipole cold mass", which contains all the components cooled by superfluid helium. Referring to Fig. 7.3 the dipole cold mass is the part inside the shrinking cylinder/He II vessel. The dipole cold mass provides two apertures for the cold bore tubes (i.e. the tubes where the proton beams will circulate) and is operated at 1.9 K in superfluid helium. It has an overall length of about 16.5 m (ancillaries included), a diameter of 570 mm (at room temperature) and a mass of about 27.5 t. The cold mass is curved in the horizontal plane with an apical angle of 5.1 mrad that corresponds to a radius of curvature of about 2812 m at 293 K, so as to closely match the trajectory of the particles. The main parameters of the dipole magnets are given in Tab. 7.5.

Table 7.4 CERN supplied components for the dipole cold masses

COMPONENT	"Pre-Series" Contract	"Series" Contract
Superconducting cables (for inner & outer layers)	x	x
Polyimide tapes for cable and Cu wedges insulation (two types)	x	x
Copper wedges (4 types)	x	x
Head spacers sets (for inner & outer layers)	x	
Inter-layer spacers	x	
Layer-jump boxes	x	
Layer-jump filling pieces	x	
Cable stabilisers (3 types)	x	
Quench heaters	x	
Polyimide (in rolls) for the coils ground insulation	x	x
Collars (6 types)	x	x
Cold Bore tubes (insulated)	x	x
Low-carbon steel half-yoke & insert laminations	x	x
Non-magnetic steel half-yoke & insert laminations	x	x
Busbars subassemblies (ready to be mounted)	x	x
Shrinking half-cylinders	x	x
Spool piece correction magnets (sextupole and decapole/octupole)	x	x
End covers	x	x
Helium heat exchanger tube	x	x
Interconnection bellows	x	x
Instrumentation (including the wires) for the Cold Mass	x	x
Auxiliary busbar pipe	x	x

The successful operation of LHC requires that the main dipole magnets have practically identical characteristics. The relative variations of the integrated field and of the field shape imperfections must not exceed ~10^{-4} and that their reproducibility be better than 10^{-4} after magnet testing and during magnet operation. The above properties are determined on the one hand by the coil geometry, which must be accurate, reproducible and symmetric to within a few hundredths of a millimetre and on the other hand by the structural stability of the magnet assembly in presence of large electromagnetic forces. Up to the short-sample field limit of the superconducting cable, the structural stability must prevent any coil movement which would cause quenches. This aspect is particularly important for magnets operated at 1.9 K, where the materials show little effective heat capacity and any energy dissipated must be removed via the superfluid helium.

The reproducibility of the integrated field strength requires close control of coil diameter and length, of the stacking factor of the laminated magnetic yokes and possibly fine-tuning of the length ratio between the magnetic and non-magnetic parts of the yoke.

The structural stability of the cold mass assembly is achieved by using very rigid collars and by opposing the electromagnetic forces acting at the interfaces between the collared coils and the magnetic yoke with the forces set up by the shrinking cylinder. A pre-stress between coils and retaining structure (collars, iron lamination and shrinking cylinder) is also built-in.

The dipole cold mass is assembled at room temperature, but will operate at 1.9 K. Because of the larger thermal contraction coefficient of the shrinking cylinder and austenitic steel collars with respect to the yoke steel, the force distribution inside the cold mass changes during cool down. The sensitivity of the above force distribution in the cold mass structure to the tolerances on all the major components and parameters (collars, laminations, inserts, coil pre-stress and shrinking cylinder circumferential stress) has been checked by finite element analysis computations, applying statistical methods. Some 3000 geometries were computed at high field conditions; in all cases strictly positive contact forces were found at the above interfaces between yoke halves and between the yoke and collared coils [11]. Detailed descriptions of the major dipole cold mass components are given in the next sections.

Table 7.5: Main parameters of the dipole cold mass

	Value	Unit
Injection field (0.45 TeV beam energy)	0.54	T
Current at injection field	763	A
Nominal field (7 TeV beam energy)	8.33	T
Current at nominal field	11850	A
Inductance at nominal field	98.7	mH
Stored energy (both apertures) at nominal field	6.93	MJ
Ultimate field	9.00	T
Current at ultimate field	12840	A
Stored energy (both apertures) at ultimate field	8.11	MJ
Maximum quench limit of the cold mass (from short samples)	9.7	T
Operating temperature	1.9	K
Magnetic length at 1.9 K and at nominal field	14312	mm
Distance between aperture axes at 1.9 K	194.00	mm
Cold mass sagitta at 293 K	9.14	mm
Bending radius at 1.9 K	2803.98	M
Inner coil diameter at 293 K	56.00	mm
Number of conductor blocks / pole	6	
Number of turns / pole, inner layer	15	
Number of turns / pole, outer layer	25	
Electromagnetic forces / coil quadrant at nominal field Horizontal force component (inner and outer layer) Vertical force component (inner and outer layer)	 1.8 0.81	 MN/m MN/m
Electromagnetic forces / coil quadrant at ultimate field Horizontal force component (inner and outer layer) Vertical force component (inner and outer layer)	 2.1 0.94	 MN/m MN/m
Axial electromagnetic force at each ends at nominal field	0.40	MN
Coil aperture at 293 K	56.00	mm
Cold tube inner diameter at 293 K	50.00	mm
Cold tube outer diameter at 293 K	53.00	mm
Cold mass length at 293 K (active part)	15.18	m
Cold mass diameter at 293 K	570.0	mm
Cold mass overall length with ancillaries	16.5	m
Total mass	~27.5	t

7.3.2 Electromagnetic Design

Multipolar expansion

The magnetic field is expressed according to the two-dimensional multipolar expansion where (x,y) are the horizontal and vertical transverse coordinates and s is the longitudinal coordinate:

$$B_y(x,y;s)+iB_x(x,y;s)=B_0(s)\sum_{n\geq 1}[b_n(s)+ia_n(s)]\frac{(x+iy)^{n-1}}{R_{ref}^{n-1}}$$

The reference radius is defined to be 17 mm, i.e. approximately two thirds of the magnet aperture radius of 28 mm. The expansion is valid locally along s where the main field is constant, or for values integrated along s, provided that the variation of the main field with respect to s is zero at the integration limits. The magnetic length, L, and the integrated multipoles, b_n, a_n are defined as:

$$L = \frac{\int B_0(s)ds}{B_c} \qquad b_n = \frac{\int b_n(s)B_0(s)ds}{\int B_0(s)ds} \qquad a_n = \frac{\int a_n(s)B_0(s)ds}{\int B_0(s)ds}$$

where B_c is the average field in the straight part. Reference system conventions can be found in [22].

Beam dynamics targets

The variation of field quality in a magnet over its length is considered negligible for beam dynamics. Therefore, only the mean values over its length for each magnet need be taken into account. For a set of magnets, the systematic error (average of mean values) and the random error (sigma of mean values) can be defined. In the LHC, corrector magnets in the dipoles are powered per octant and in order to minimize the random error along the machine, it would be better to install magnets with similar errors in the same octant. The following scenario was originally defined:

1) LHC dipoles produced by eight production lines, each having different systematic behaviour, but the same random characteristics.
2) Each production line to be installed in one octant.
3) Targets given as systematic over the machine, uncertainty (sigma of the averages of each octant), and random (sigma over each octant, the same for every octant).

At the beginning of the dipole pre-series production, measurements showed that the systematic difference between the three manufacturers was small and therefore the improvement in the random error resulting from this installation scenario can be neglected. For this reason, it was decided to change the baseline and allow allocating one third of the dipoles per firm and mixing magnets from different firms in the same octant.

Beam dynamics targets were reviewed in [23]. Since the work carried out in the prototyping phase [24], the systematic error has been specified with an acceptance range. This provides limits beyond which corrective actions should be taken.

Field quality model

In the collared coil, the field harmonics b_n^{cc} (at 300 K) are represented as the sum of the naked coil b_n^{coil} according to Biot-Savart law, plus the effect of the collar magnetization, $b_n^{collars}$, that can be evaluated using numerical methods such as the Boundary Element Method and the Finite Element Method (BEM and FEM) [25]). In addition, the contribution of the deformations, b_n^{ccdef} must be added. These deformations comprise the ovalisation of the collars and the radial deformations of the coil induced by the pre-stress. This contribution can be estimated by a FEM of the dipole mechanics [26].

$$b_n^{cc} = b_n^{coil} + b_n^{ccdef} + b_n^{collars}$$

In the cold mass, the collared coil contribution is rescaled by the main field increase. This factor, $k \cong 1.18$ is due to the iron yoke. Moreover the magnetic contribution of the iron yoke b_n^{iron} (evaluated through a magnetic BEM-FEM) and the contribution of the deformations induced by the yoke on the coil b_n^{cmdef} (evaluated through a mechanical FEM [27]) must also be added:

$$b_n^{cm} = \frac{b_n^{cc}}{k} + b_n^{cmdef} + b_n^{iron}$$

The geometrical contribution b_n^{geo}, is the multipole field due to the geometry of the coil and the magnetic effect of the materials around it at 1.9 K. In a first approximation it can be modelled as the sum of the cold mass contribution and an offset b_n^{cool} due to cooling down (using a mechanical FEM [6]). At low fields (injection), the multipoles will also be affected by the contribution of persistent current b_n^{pers}. This term can

be evaluated with a model that takes into account the measured magnetization and the coil geometry [28]. At high field the effect of iron saturation b_n^{satur} (evaluated through a magnetic BEM-FEM) and of deformation b_n^{emdef} induced by electromagnetic forces are also present:

$$b_n^{geo} = b_n^{cm} + b_n^{cool} \qquad b_n^{inj} = b_n^{geo} + b_n^{pers} \qquad b_n^{inj} = b_n^{geo} + b_n^{satur} + b_n^{emdef}$$

In Tab. 7.6 estimations of the different contributions are given. The naked coil component (b_n^{coil}) is estimated for the "6-block" layout denoted either by V6-1 [26, 29], or as cross-section 1 [30]. All data are based on models, with the exception of the deformation due to Lorentz forces for which no model was available and the results of magnetic measurements at 1.9 K are given [31]. A significant effect of collared coil deformation on b_3 and b_5, can be observed, but have a negligible effect of cool-down, saturation, and Lorentz forces. The persistent current gives by far the largest contribution to the multipoles of the naked coil b_n^{coil}.

Table 7.6: Contributions to allowed multipoles for cross-section 1. The methods used are identified as follows: Biot-Savart (1), magnetic BEM-FEM (2), mechanical FEM (3), computation based on magnetization (4), and measurements (5).

	Collared coil				Cold mass			Cryomagnet						
	x-s 1	ccdef	collars	Total	iron	cmdef	Total	cool	pers	satur	emdef	Geo	Inj	High
b3	3.90	-3.20	-1.36	-0.66	3.23	1.46	4.13	-0.22	-8.50	0.18	0.12	3.9	-4.6	4.2
b5	-1.04	0.80	0.37	0.13	0.00	0.01	0.12	-0.09	0.99	0.01	-0.16	0.03	1.02	-0.12
b7	0.75	0.12	-0.09	0.78	0.03	0.00	0.69	0.11	-0.44	0.00	0.00	0.80	0.36	0.80
b9	0.12	0.00	0.00	0.12	0.00	0.00	0.10	0.00	0.20	0.00	0.00	0.10	0.30	0.10
b11	0.68	0.00	0.00	0.68	0.00	0.00	0.58	0.00	0.03	0.00	0.00	0.58	0.61	0.58
Method	1	2	3		3	2		3	4	2	5			

The underlying hypothesis behind this "additive" linear model is that all effects can be independently added, i.e. they are not coupled.

Optimising systematic odd normal multipoles: coil cross-section design

The cross-section design aims at the optimal coil layout to minimize field imperfections. In principle, any combination of multipoles can be achieved with a careful choice of the coil layout. Indeed, a magnet with perfect field quality both at low field (i.e. injection) and at high field cannot be built since there is an offset between these two conditions coming from persistent currents, saturation and Lorentz force effects. It is therefore necessary to choose whether to optimise for low field (i.e. a geometric b_n^{geo} which compensates the persistent b_n^{pers}), at high field (i.e. a geometric b_n^{geo} close to zero, since b_n^{satur} and b_n^{emdef} are usually small), or somewhere in-between.

Models are usually not precise enough to give an absolute estimate of the multipoles in a given cross-section at the required level of accuracy. Therefore, a few iterations in coil design are usually needed. The coil used at the beginning of the production was designed in 1996. This was based on a six block layout and was denoted by 'V6-1' [29], or 'cross-section 1' as it will be called hereafter [30]. This coil design aimed at a 50% correction of persistent current b_3 and 80% of b_5, (as estimated in [25], i.e. –11.0 and 1.2 units respectively) by the coil geometry, neglecting the influence of all deformations. After 1996, a few changes to the magnet design were decided (stainless steel collars, different iron yoke). Design changes and neglected effects compensate each other for the b_3, where a 50% correction of persistent current with geometry is still found (see Tab. 7.6). The situation is different for b_5, for which the deformations play a very important role, leading to a geometric value of around zero, i.e. no compensation of persistent current at injection.

After 1996 a redefinition of the targets aimed at no correction of persistent current b_3 at injection, i.e. an optimal value close to zero at high field [25]. For b_5 the resulting target was kept to an 80% correction of persistent current effects with geometric effects [24]. As a result, cross section 1, used for the beginning of the pre-series, gave rise to systematic b_3 and b_5 outside the allowed ranges [30]. A fine tuning of the coil cross-section was carried out after the measurement of 9 collared coils (also integrating information coming from prototypes whenever possible). The copper wedges of the inner layer were changed by up to 0.4 mm

while keeping the same coil shape in order to avoid changes in the winding and curing tooling. The parameters of this second cross-section are given in Tab. 7.7. A total of 35 magnets were built with cross-section 1, and will be installed in the first octant. A second optimization of the coil layout based on the addition of 0.125 mm of mid-plane insulation (cross-section 3) has been implemented during construction of magnets for the second octant.

Table 7.7: Coil layout parameters in cross-sections 1 and 2

		Cross-section 1		Cross-section 2	
block	r (mm)	phi (deg)	alpha (deg)	phi (deg)	alpha (deg)
1	43.900	0.157	0.000	0.157	0.000
2	43.900	21.900	27.000	21.900	27.000
3	28.000	0.246	0.000	0.246	0.000
4	28.000	22.020	24.080	22.020	25.430
5	28.000	47.710	48.000	47.980	45.800
6	28.000	66.710	68.500	66.710	68.500

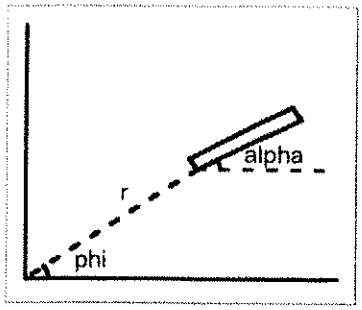

Optimizing even normal multipoles: iron yoke design

The main issues of iron yoke design are to minimize the effect of saturation by the geometry of the holes in the yoke [26] and to minimize the even normal multipoles b_2 and b_4 that naturally arise in a two-in-one collar design. During the final prototype phase, two changes were implemented.

Iron laminations in the coil heads were replaced by nested iron-stainless steel laminations to reduce the main field in the coil heads by 10%. This provides more margin for stability in a region prone to quenches. The nested laminations have an inner part of stainless steel and an outer one of iron. This option was preferred to having completely non-ferromagnetic laminations as it helped to reduce b_2 in the heads.

The yoke and insert implemented in the prototypes gave rise to a systematic b_2 of around 5 units coming from a mismatch between magnetic and mechanical design. A correction was implemented by reshaping the insert (see Fig. 7.4) between the yoke and collars [32], which reduced the systematic b_2 to a fraction of a unit.

Random components

Table 7.8: Target values for random, geometric and persistent current components together with results of Monte Carlo simulations

	Target geo	Target per	Mcarlo geo		Target geo	Target per	Mcarlo geo
b1	5.0	0.5		a1	5.0	0.4	
b2	0.68	0.31	0.66	a2	1.70	0.77	0.70
b3	1.45	0.29	0.42	a3	0.43	0.20	0.42
b4	0.49	0.15	0.22	a4	0.49	0.15	0.25
b5	0.42	0.09	0.14	a5	0.33	0.67	0.15
b6	0.085	0.023	0.077	a6	0.140	0.085	0.087
b7	0.220	0.027	0.050	a7	0.070	0.031	0.050
b8	0.041	0.012	0.029	a8	0.080	0.016	0.029
b9	0.070	0.014	0.016	a9	0.070	0.091	0.016
b10	0.000	0.000	0.011	a10	0.000	0.012	0.009
b11	0.000	0.000	0.005	a11	0.000	0.000	0.005

The random components limit the ability to adjust the allowed harmonics to the optimal values and to obtain zero for the non-allowed harmonics. Random components naturally arise from the tolerances on mechanical parts, on assembly procedures and on the magnetization of the superconducting cables. Therefore they define a scale to judge whether a multipole contribution is large or small. Tab. 7.8 gives an estimate of geometric and persistent random components (one σ) based on the experience of HERA, which are the upper limits targeted [24, 25]. Also shown are the results of a Monte Carlo simulation [33], where random

components are computed for random movements of the coil blocks having a sigma of 25 μm. This simulation provided the basis for relaxing the position tolerances for the conductor from 25 to 50 μm.

Adjusting integrated main field: the influence of laminations on magnetic length

The integrated main field, i.e., the magnetic length times the field in the central part, gives the strength of the dipole required for bending the beam. According to beam dynamics requirements, the random part of the integrated main field should not exceed 8 units (one σ). By fine-tuning the magnetic length to compensate differences in the central main field, one can reduce a large random component. Changing the length of the iron laminations can vary the magnetic length. Since the substitution of nested laminations with standard iron laminations increases the main field by about 10%, 100 mm more iron laminations will provide a coil with a magnetic length 10 mm longer, i.e. 7 units more. In the dipole specification manufacturers are allowed to adjust the length of iron lamination by up to ±100 mm, providing corrections of up to 14 units in the integrated main field.

Adjusting odd normal multipoles: the influence of pole shims

Pole shims are spacers of variable thickness placed between the collars and the coil poles. They can be used either to compensate for coil size variations in order to keep the nominal azimuthal pre-stress, or to vary the coil size as a way of changing multipoles. The nominal range for azimuthal pre-stress at 300 K is ±15 MPa, which corresponds to a variation of ±0.12 mm in the shim thickness for a fixed coil size. Therefore, if the coil has a nominal size, one can safely vary shims by up to 0.1 mm to improve field quality. An extra 0.1 mm shim thickness in the inner layer placed symmetrically around the aperture changes b_3, b_5 and b_7 by 1.6, -0.20 and 0.11 units respectively (values for the cold mass, based on tests performed on a short model [34]). For the outer layer, the effect is about 1.1 units of b_3 and negligible for the higher orders. This limits the possibility of acting on low order multipoles. It should be noted that a simultaneous change of b_3 and b_5 of the same sign is not possible due to the coupling between the multipoles. However, by changing the mid-plane insulation, it is possible to act on all odd multipoles. A change of shims in only one quarter of the coil would allow adjustments of the systematic values of the non-allowed multipoles. However, in all cases the value is close to zero as a consequence of the symmetry and no action of this type is foreseen in the baseline.

7.3.3 Mechanical Design

Description of the structure

The mechanical structure of the dipoles is designed to withstand the high forces generated in the magnet and limit the coil deformation over the range of operation as much as possible. The materials used for the most highly stressed components have a high load-bearing capacity, high elastic moduli, good fatigue endurance and a good behaviour at cryogenic temperatures. Fig. 7.3 shows the cross-section of the magnet cold mass. The coil support structure is composed of:

- Austenitic steel collars common to both apertures. The collars are made of 3 mm thick austenitic steel (tensile strength 700-800 MPa at 293 K, integrated thermal contraction between 293 K and 4.2 K $\alpha = 2.7 \times 10^{-3}$, $\mu_r \leq 1.003$ for $H \geq 8 \times 10^4$ A/m at 1.9 K). The coils are assembled inside the collars and pre-compressed at room temperature.
- An iron yoke split into two in the plane of vertical symmetry of the twin-aperture magnet. The yoke is made of 6 mm thick low-carbon-steel laminations.
- Iron inserts, punched out of the same low carbon steel as the yoke laminations, maintain the required field distribution at the different field levels and contribute to the mechanical stability of the structure.
- A stainless steel outer shrinking cylinder. This part is welded around the iron yoke in such a way that the required pre-stress is applied to the half-yokes at room temperature and in cold conditions.
- When powered, the coils must be under compressive stress in order to avoid movements. Displacements and deformations of the coils must be limited as much as possible (~few μm) to avoid a sudden release of energy. The necessary stiffness of the structure is assured when the following conditions are met:
    - the gap between the two iron yoke halves is closed during the entire life of the magnet,
    - good contact is ensured between the iron yoke and the collars.

To satisfy these conditions the relative dimensions of the components of the structure, the choice of materials, the pre-stress in the outer shrinking cylinder and the dimension of the gap between the two half-yokes have been carefully optimised.

The collars and the iron yoke are designed in such a way that they acquire the definitive and required shape at the operating temperature when subjected to the mechanical forces created by the clamped coils and the welded cylinder. For correct distribution of the mating force between the two half-yokes, the gap between them (iron gap, see Fig. 7.3) is not constant during assembly, but varies from 0.24 mm (inner part) to 0.46 mm (outer part). The yoke-insert contact is the inclined mating surface between the insert and the lamination. This guarantees a safe and firm contact between the two components transmitting the forces from the collared coil assembly to the cylinder and vice-versa.

Except for a short time during the collaring operation, the peak compressive stress in the coils at room temperature is limited to about 100 MPa to avoid creep of the insulation and of the copper. The structural behaviour of a dipole during the different production phases as well as in operation, is described below.

Collaring

The collars are pressed around the coils to obtain an average compression of about 70 MPa for the inner layer and 75 MPa for the outer layer at the end of the process. During the collaring process, coils are compressed up to 115 to 135 MPa, depending on the method used to apply the load in the press. Once the press force is released the compressed coils expand the collars and a part of the pre-stress is therefore lost. The collaring procedure includes the following main steps:

- approaching phase,
- cycling and insertion of the small rods,
- full load and insertion of the locking rods,
- release of the load.

Welding of the shrinking cylinder

The shrinking cylinder is welded to have an interference fit around the iron yoke. The interference generates a tensile stress of about 150 MPa in the cylinder and the vertical gap between yoke laminations is closed with mating force of 2400 N/mm. Thus the magnet has an intrinsic safety margin that guarantees the collar coil assembly will never be overstressed. The assembly procedure also provides a very efficient means of aligning the laminated structure. The pre-stress in the cylinder builds up a force reserve that guarantees the mechanical stability of the structure even when component and assembly tolerances combine unfavourably.

Cooling from 293 K to 1.9 K

During the cool-down, the mating forces along the iron yoke gap increase. The pre-stress in the cylinder reaches 335 MPa. At cryogenic temperatures the contact between the collars and yoke is almost lost due to the different thermal contractions of the materials. The pre-stress in the coil decreases by between 25 MPa and 40 MPa as a result of the higher contraction of the coils with respect to the collars. At 1.9 K the mating force between the two iron halves is around 6200 N per mm of length.

Excitation at nominal and maximum field

During excitation there is practically no change in the outer cylinder stress because the iron gap remains closed. For a field, B_o = 8.33 T, the outward electromagnetic force is 1700 N per mm length, per quadrant. This is shared between the collars and the outer structure. At this field excitation, the radial deformation in the median plane of the collared coils ion is about 0.07 mm. The coils reach minimum compression at their top (~5 N/mm^2) increasing at the mid plane up to ~70-80 MPa. This value is similar to the compression value during collaring. At B_o = 9.00 T the compression at the top of the coils drops to zero, but increases on the mid plane. The contact between the collars and iron yoke contact is maintained because of the collared coil deformation and this contact limits the deformation of the coils, thus avoiding the appearance of unwanted harmonics.

Coil ends

The bending of the cable blocks and the different directions of the electromagnetic forces make the situation in the coil ends different from that in the straight part. In this region, part of the iron yoke is replaced by special nested laminations. This feature reduces the magnetic field in the heads while controlling the stray field and the harmonic content. The longitudinal electromagnetic force is partly transmitted from the coils to the collars, yoke, and cylinder by friction. The remaining part directly loads the thick end plates welded at the extremities of the shrinking cylinder. Measurements performed on model and prototype magnets indicate that the end plates absorb 15-20% of the 400 kN axial load.

7.3.4 Collared Coils

The collared coils contain and restrain the superconducting coils that generate the required magnetic field. The different subassemblies and components are described below following the assembly process sequence.

The Insulated Cable:

The cable insulation has to satisfy different requirements:

- withstand the inter-turn voltage (turn-to-turn test voltage of 100 V).
- be sufficiently porous to allow the superfluid helium to carry away the heat. This heat is generated by dynamic loads resulting from losses during magnet ramping and by the energy deposited by lost particles and during current change.
- be robust, in order not to break during winding and curing.

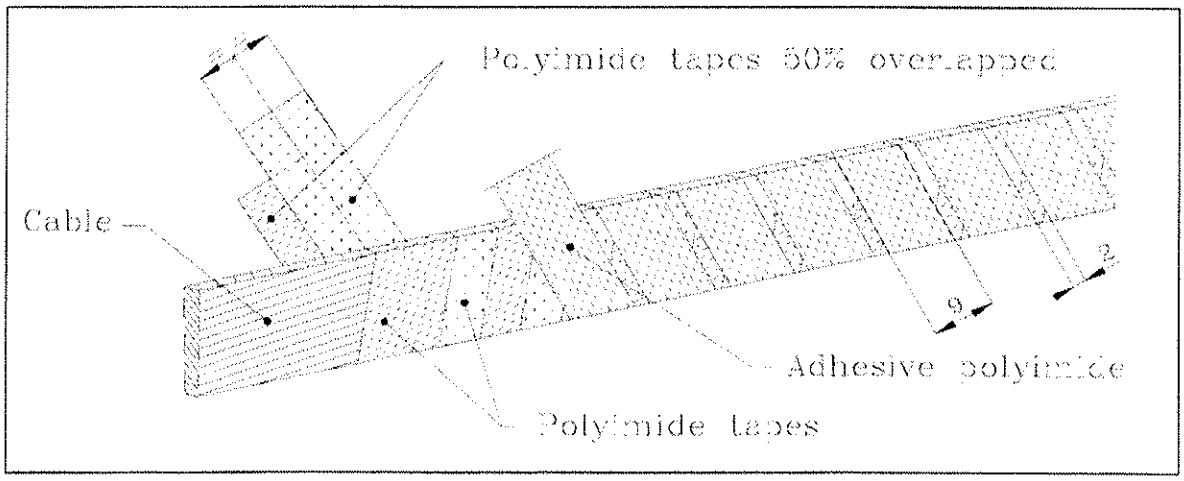

Figure 7.4: Superconducting cable insulation

The solution adopted consists of two polyimide layers wrapped around the cable with a 50% overlap, together with another polyimide tape wrapped with a spacing of 2 mm (Fig. 7.4). The resulting gap makes the coil porous by setting up channels for superfluid helium, without affecting the mechanical support between turns. The third layer presents an external surface coated with epoxy resin, which is necessary to provide mechanical rigidity and compaction to the coils during the curing process.

Two types of polyimide films are used (Fig. 7.4). The first is a "plane" tape, with a thickness of 50.8 μm ± 3%, is used for the first two wraps. The second film, having a thickness 68.6 μm ± 3%, is an all-polyimide adhesive film. This is applied as a covering wrap in a barber's pole fashion, i.e. leaving a gap between successive turns and with the adhesive directed outwards. It is made of a layer of plain film coated on one side with a layer of polyimide based adhesive. The adhesive coating as delivered has a nominal thickness of 5 μm. It is non-sticky at room temperature and bonds to itself at a minimum temperature of 185 °C and a moderate contact pressure.

The superconducting coils

A twin-aperture dipole consists of two single dipoles, each around a beam channel. Each dipole consists of an upper and a lower pole that are identical. Each pole consists of a coil wound in two layers, called inner layer and outer layer, wound with two cable types. Fig. 7.5 shows the flux plot as computed for the whole structure of the main dipole.

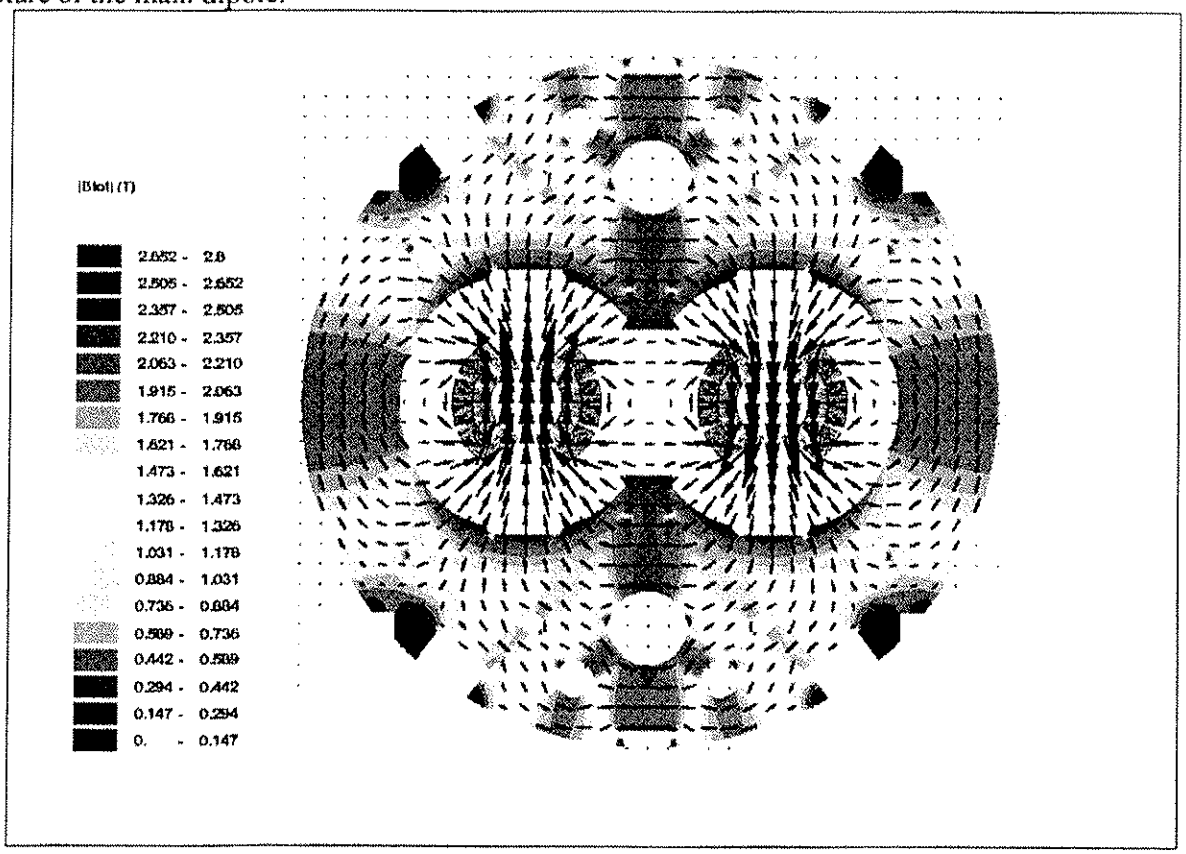

Figure 7.5: Dipole magnetic flux plot

The distribution of the cables in the two coil layers is shown in Fig. 7.1. The six sets of adjacent coil turns within the limits of the various copper wedges are defined as cable (or conductor) blocks. The precise azimuthal and radial position of the cables/blocks is of the utmost importance to achieve the nominal magnetic field and its homogeneity in the beam channels. The inner radius of the inner coil layer is 28 mm while the outer layer has an inner radius of 43.9 mm.

In addition to the insulated superconducting cable the following components are necessary in order to produce a coil (see Fig. 7.6):

- Copper wedges made from OF copper according to standard ASTM C102, DIN 1787. These wedge-shaped copper spacers are inserted between blocks of conductors in order to produce the desired field quality. In addition they approximate a quasi-circular coil geometry, thus compensating for the insufficient keystoning of the cables (see Figs. 7.1 left and 7.6 right). Before use they are insulated following the same procedure adopted for the superconducting cable.
- End spacers and end chips. These special saddle-shaped insulating fillers are designed to constrain the conductor to a consistent and mechanically stable shape.

For the end spacers satisfactory shapes were determined using a "constant perimeter" approach combined with empirical methods and refined during prototyping [35]. Several manufacturing techniques and materials are used for these elements. Large and thick pieces (end spacers) are produced by 5-axis machining of epoxy impregnated fibreglass thermoset while thin pieces, having a maximum wall thickness below 10 mm (end chips) are produced by injection moulding of polyetherimide resin with 30% loading by volume of glass fibre. This combination of techniques and materials has been instrumental in reducing the cost and the production time whilst maintaining quality.

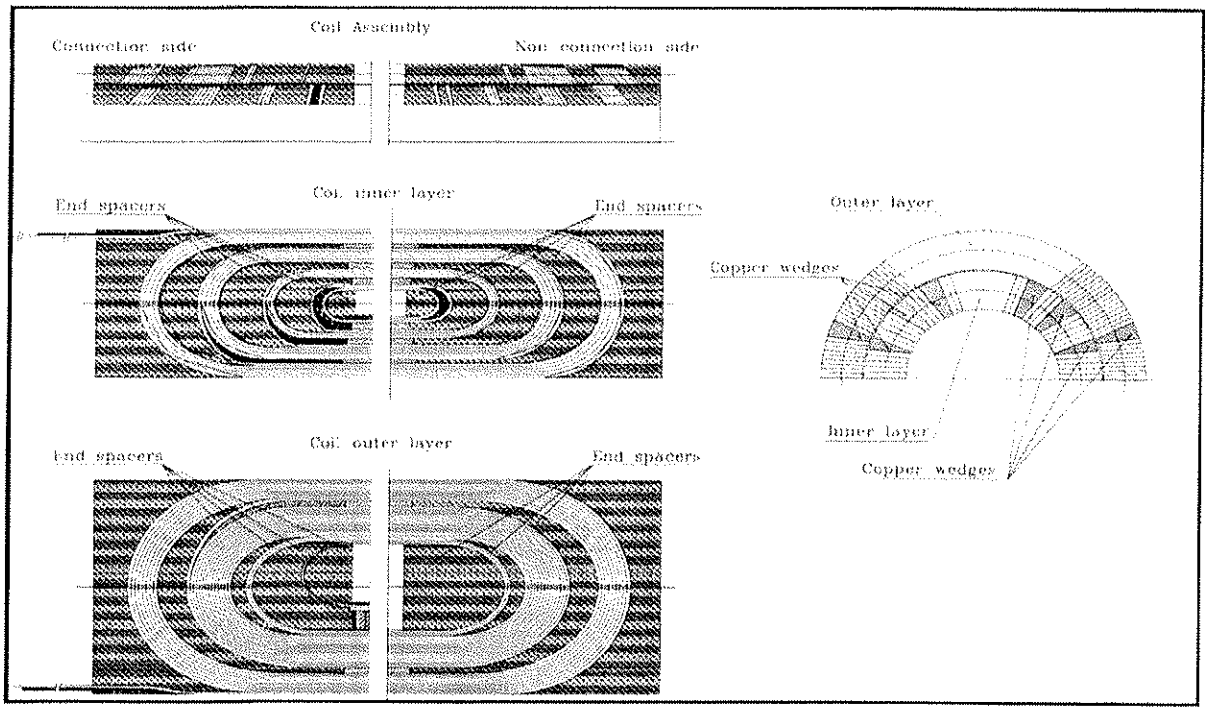

Figure 7.6: End spacers and end chips

The coils are manufactured in a clean area with adequate air circulation, air filtration and an airlock access. Coil winding is done with "winding machines" (Fig. 7.7) that are complex tools consisting of:

1. A table supporting the winding mandrel. For the winding of the layer ends, the mandrel is obliged to rock around its longitudinal axis.
2. A rotating support for the insulated cable spool and a brake which controls the tensile force on the spool. The tension applied to the cable is important to obtain reproducible and stable coils.
3. Mandrels with the inner layer and outer layer diameter in order to provide a rigid and safe support to the winding operation.

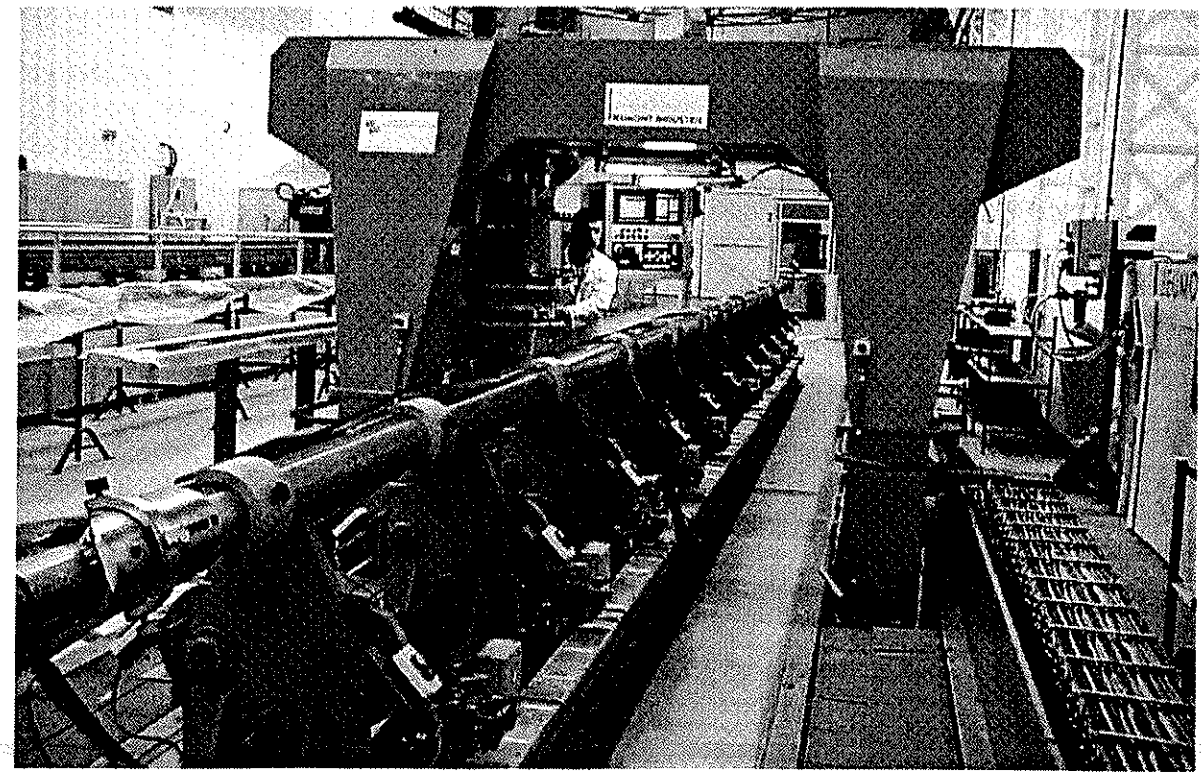

Figure 7.7: A winding machine for the superconducting coils

During winding, the conductors and spacers are maintained in place by tools designed for this purpose. In particular, the conductor must always be clamped in place in the straight parts before winding the ends. Special tooling for forming and pressing the conductors at the ends is also used.

The coil is prepared for the curing phase after winding whilst still lying on the mandrels. This operation takes place in a dedicated curing press. This press is equipped with moulds whose inner diameter is the outer diameter of either the inner or the outer layer. In addition, the moulds are equipped with heating systems that allow the coils to be cured at 190±3 °C under a maximum pressure of 80-90 MPa. The curing cycle is presented in Tab. 7.9.

Table 7.9: Characteristics of the pressing/curing procedure

	Starting temperature	Final temperature	Maximum rate of temperature change	Duration	Pressure
Warming 1	Ambient	100/135°C	< 3°C/min	60 min	10 MPa
Sizing	100/135°C	100/135°C	None	30 min	70 to 100 MPa
Warming 2	135°C	190°C	< 3°C/min	30 min	10 to 20 MPa
Curing	190°C	190°C	None	30 min	< 100 MPa
Cooling 1	190°C	140°C	< 3°C/min	30 min	< 100 MPa
Cooling 2	140°C	Ambient	< 5°C/min	50 min	< 100 MPa

The aim of the curing operation is to:

a) Activate the resin present on the 3rd insulation layer, gluing the turns together
b) Define the mechanical dimensions of the coils that must respect a tolerance of ±0.05 mm, with the average value having ±0.03 mm.

The superconducting pole

The coils are paired in inner and outer layers during the following operations:

a) Surfacing of the heads: this procedure fills voids in the extremity of the coils with loaded resin to guarantee the mechanical stability of the turns and provide a safe mechanical support when the outer layer is assembled on the top of the inner one.
b) Measurement of the azimuthal size of the coils under pressure: this operation is necessary to verify the coils dimensions and to compute the shims necessary for pre-loading the coils when assembled inside the collars.
c) Superposition of the outer layer onto the inner: a slotted interlayer spacer of polyetherimide net loaded 10% by volume with glass fibre (material ULTEM 2100TM) is positioned in the middle of the two layers. This provides channels for the superfluid helium flow and gives a precise mechanical support for the outer layer.
d) Connection of the two layers in series: at the beginning of the winding operation, the inner coil cable internal end is precisely formed to match up to the level of the outer layer. Later, after their complete assembly and curing, the two layers are soldered together to form the so-called "ramp-splice" region. A strip of high conductivity copper is soldered to the inner cable to thermally stabilize and mechanically stiffen the ramp and its curved portion. Different ways of making the ramp-splice have been investigated and tested in models. The solution chosen features the ramp and splice on the same side of the pole. Such a solution results in manufacturing simplicity, high reliability, and excellent performance. Copper strips are soldered to the superconducting cable to stabilize and reinforce the coil leads.
e) Shimming the heads: the pole heads are measured and shimmed in order to get a smooth transition of the mechanical pre-stress from the straight part (70-75 MPa) towards the extremity (20-30 MPa).

Assembly of the poles around the cold bore tubes

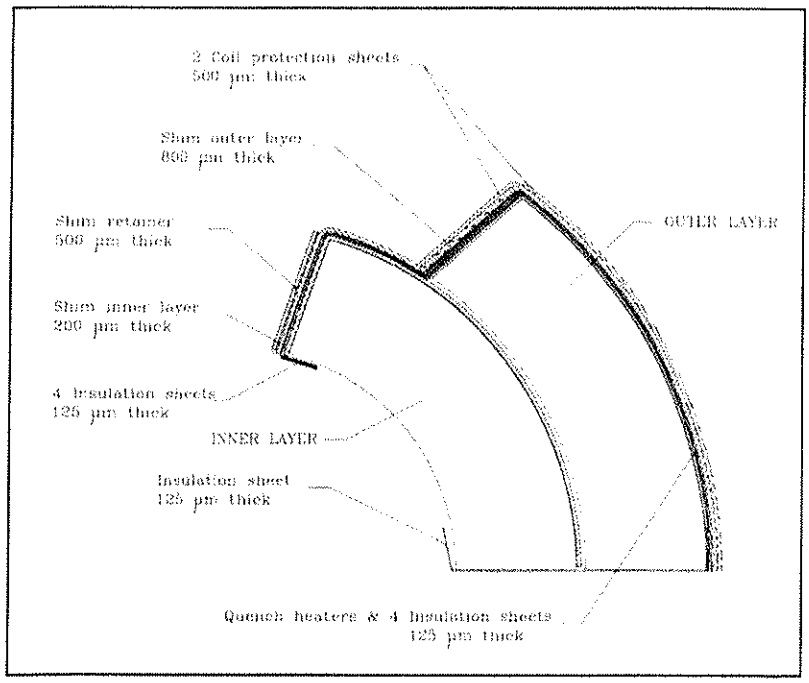

Figure 7.8: Pole assembly (half view)

The four poles are assembled in pairs around the cold bore tubes. Fig. 7.8 shows the pole assembly. The following components are added in this phase of the assembly process:

a) Quench heaters: When a quench occurs in the magnet, heaters are required to warm outer coil layers very rapidly raising the temperature above 10 K in ~20 ms. This forces the transition to the normal conducting state. The quench heaters consist of partially copper-plated stainless steel strips (thickness: 25±2 μm; 0.4 m with copper cladding alternating with 0.12 m without copper cladding). The strip is co-laminated in a sandwich of polyimide insulating foils (thickness: 75±4 μm per foil) with suitable electrical and mechanical properties to withstand high voltages, low temperatures, pressures and ionizing radiation. Special connections and wiring are present at each end of the stainless steel strips. The energy stored in a capacitor bank is discharged into the heater strips (±450 V with a mid connection to ground), providing a peak current of around 75 A. The time constant of the heater circuit is between 50 and 100 ms.
   The quench heater strips are assembled in pairs and are mounted on each coil quadrant outer surface. This gives 8 quench heaters in total per magnet assembly, each one containing two steel strips (16 strips in total per magnet). After collaring, at one side of the magnet, the quench heater wires are connected in series in pairs (on upper and lower poles) by manual soldering. The joint is insulated and inserted into a special groove in the end spacer, ensuring its safe insulation and protection of the joint. The total number of quench heater circuits per magnet is eight.
b) Additional electrical insulation: is required between poles and for the collars sitting at ground potential. The ground insulation is composed of several polyimide film layers which have to be cut azimuthally and longitudinally for assembly. Besides its electrical function of preventing shorts from coil to coil (tested at 3 kV in dry air) and from coil to ground (tested at 5 kV in dry air), it also has the role of providing good slip surfaces during collaring and a smooth surface over which both azimuthal and radial preloads are adequately distributed to avoid deterioration of the insulation. Adding an extra layer of polyimide insulation between the poles is an option for fine-tuning the magnetic field harmonics. This option (with an extra layer thickness of 125 μm on both inner and outer layers) is presently exercised in cross-section 3 (see Sec. 7.3.2).
c) The collaring shims are located at the layer poles and they provide a means to control the pre-loading of the coils and the field harmonics of the magnet. The shims are inserted inside special retainers on

the inner layers. These components are made of folded sheet metal and prevent the shims from slipping during assembly and collaring. On the outer layer, the shims lie directly on the ground insulation and they are protected from the collars by the prolongation of the coil protection sheets which are located between the outer layer ground insulation and the inner collar surface. These elements prevent damage to the insulation from contact with the serrated edges of the collars. In addition, the coil protection sheets help to avoid wrap breakdown and provide continuous support to the conductors.

Collaring

The two apertures are assembled inside a mechanical structure consisting of collars that are common to both apertures. Pre-assembled packs of 3 mm thick collars, made of a high Mn content austenitic grade steel (Nippon Steel YUS 130 S) are placed around the two insulated single dipoles, starting at the layer jump. The assembly operation is performed carefully to avoid damaging the ground insulation. At this stage, the collars are not closed because of the oversized dimensions of the coils which are not yet under compression. The coil/collar assembly is introduced into a collaring press having precise mechanical references to ensure the vertical alignment of the upper and lower collars during collaring and the horizontal alignment of the whole.

The collaring is performed in several steps, starting with a pre-stress phase when the collars are only partially closed. The pressure is increased until the locking rods can be inserted into the stack. The collared coil is then completed by adding end plates and making the electrical connections. At this stage the collared coil is ready to be installed in the magnetic yoke.

7.3.5 Magnetic Yoke

The design requirements of the magnetic yoke are related to magnetic field quality and to cryogenic considerations:

a) Magnetic steel with the minimum obtainable carbon content and controlled grain size guarantees a maximum magnetic permeability at low and intermediate field levels and a low and stable coercive field (max. coercivity after $H_{max} > 5000$ A/m: 75 A/m ±10 %).
b) The geometry of the yoke and its filling factor contribute to the required magnetic field multipole content at injection and at nominal field.
c) The yoke geometry and filling factor are also optimised to satisfy cryogenic requirements:
d) The yoke must contain sufficient helium to serve as a buffer during ramping up and running down the magnetic field.
e) The yoke geometry has also been optimised to allow for sufficient helium flow along the cold mass length, during cool down and warming up of the cold mass and sufficient free section for transverse heat conduction to the heat exchanger tube (see below) in static conditions.

The magnetic yoke (see Fig. 7.4) consists of precision punched laminations, split in the vertical symmetry plane, and a pair of smaller inserts between collars and yoke. A clear distinction is made between the cross section of the central part, where high magnetic field is required, and that of the extremities, where the field needs to be reduced. In the central part, the yoke is assembled using 5.80 mm thick steel laminations, made of low carbon mild steel, hot rolled and annealed, $\sigma_{0.2} \geq 140$ MPa, with a thermal contraction coefficient (integrated between 300 K and 1.9 K) of $\alpha=2.0\times10^{-3}$. They are riveted into sub-assemblies of short packs 1.50 m long. The packs are then mounted into half-yokes, with a uniform filling factor of 98.5%.

Packs with a standard length of 522 mm, composed of nested laminations 3.0 mm thick non-magnetic stainless steel laminations near the coils (high Mn content austenitic steel grade KHMN3CL.2B) and 5.80 mm thick low-carbon steel "rings" around them, are used at each end.

The inserts between the collars and the yoke are punched in the same raw material as the yoke , i.e. low-carbon steel in the central part and non-magnetic steel at the extremities.

After the assembly of the yoke around the collared coils and the longitudinal welding of the shrinking cylinder, the gap between both half-yokes is closed and will remain so during cool down to 1.9 K and excitation up to ultimate field.

7.3.6 He II Heat Exchanger Tube (HET)

The He II heat exchanger tube (see Fig. 7.9) is part of the cooling loop of the dipole and quadrupole cold masses. It extracts the heat loads during the cooling down of the cold mass from 4.2 to 1.9 K, as well as in operation at 1.9 K. In operation, the HET carries a two-phase flow of saturated superfluid helium at 1.6 kPa (16 mbar)

The He II heat exchanger tube is composed of a seamless round oxygen-free copper tube equipped with seamless austenitic stainless steel sleeves at both ends. The space available for the tube in the magnet yoke on one hand and the thermal and mechanical optimizations on the other hand, have resulted in a copper tube with an outside diameter of 58 mm and a wall thickness of 2 mm.

The working part of the HET is made of oxygen-free electrolytic refined copper (grade UNS C10200 according to ASTM B224) in order to provide adequate heat transfer at 1.9 K.

Stainless steel ends are required to weld the HET to the cryogenic lines (see Fig. 7.9). The ends are connected by vacuum brazing between a 316L tube and an OFE copper ring, followed by electron beam welding between the OFE copper ring and the OF copper tube.

The He II heat exchanger tube is designed to withstand an external radial pressure of 2 MPa under internal vacuum at 1.9 K. For this reason, the copper tube is made in the 1/4 hard temper status (H01), i.e. 21% cold-worked.

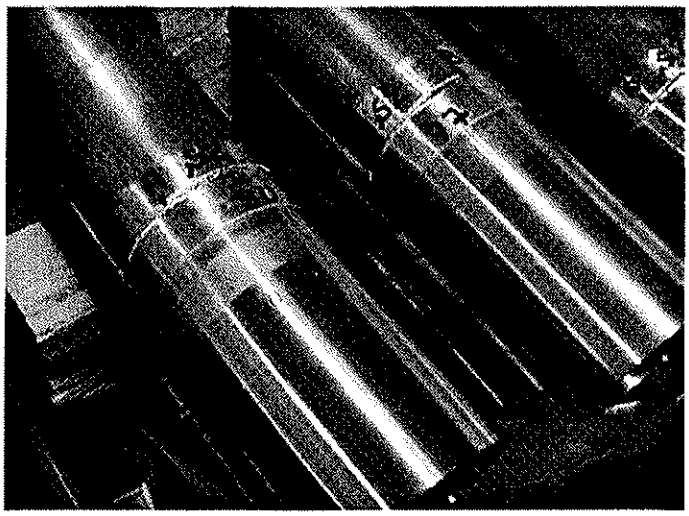

Figure 7.9: He II heat exchanger tube bi-metal extremities

7.3.7 Helium Enclosure and Longitudinal Welding

The helium enclosure is the envelope of the cold mass assembly. In operation at 1.9 K, it contains a static bath of atmospheric pressure He II, which can penetrate the smallest channels as a result of its very low viscosity.

The main components of the helium enclosure are the shrinking cylinder and the end covers that are thermally isolated from the ambient by the cryostat insulating vacuum (10^{-6} mbar) and the cold bore tubes that separate the helium volume from the ultra-high-vacuum necessary to particle beams (10^{-9} mbar).

The shrinking cylinder, which is made up of two welded half-shells, surrounds the yoke. The shrinking cylinder gives the necessary stiffness to the cold mass to resist the electromagnetic forces. It also provides the inertia needed to maintain the geometry of the cold mass on its supports against bending.

Longitudinal welding

The half-shells are assembled around the yoke and welded together in a purpose built welding press designed to introduce a circumferential stress exceeding 150 MPa at room temperature in the shrinking cylinder. During the longitudinal welding, the press applies compressive forces on the active part of the

assembly of the order of 500 tons per metre. The welding procedure is a combination of the STT®[1] process for the root pass with pulsed-MIG/MAG process for the 3 filling passes. The welding press is equipped with a laser camera that measures the curvature imposed on the cold mass and the welding gap between the shrinking cylinders. The reconstructed gap geometry is used to control the welding parameters during the execution of the root pass. These parameters can be modified, although calculations show that one obtains satisfactory results for variations of the gap between 2.7 and 4.3 mm. This range takes into account the unavoidable variation of the circumference of the shells and assembly tolerances. The welding parameters for the filling passes are constant.

The welding press imposes the desired curvature on the cold mass. To obtain a nominal sagitta of 9.14 mm, which corresponds to a chord of 14,343 mm (the magnetic length at room temperature), the active part is curved by about 12 mm in the welding-press. A relatively small spring-back occurs when the assembly is released from the press because the shells are pre-curved during manufacture.

The Ends

The end covers have openings that provide passages for the cold bores, the He II heat exchanger tube, helium flow and bus bars. On the downstream side (lyra side) of the cold mass, the outlets are equipped with bellows. These provide the necessary flexibility in the interconnections for movement during alignment and cool down. The end covers also carry the dowel holes that serve as fiducial points for the assembly of the cold mass inside its cryostat and for the adjustment of the cryostat fiducials that will be used for the installation and alignment of the cryomagnets in the tunnel.

The helium enclosure also contains ancillary parts (Fig. 7.10) such as the diode box, the N-line tube carrying the auxiliary bus bars along the magnets and the instrumentation feed-through system (IFS) that carries the instrumentation wiring from the inside of the cold mass to the outside of the cryostat insulating vacuum. The cold mass support bases are made of austenitic steel grades of the AISI-300 series to provide the necessary strength and toughness at low temperature. The most critical elements, e.g. the shrinking cylinder and the cold bore tubes, are made of nitrogen-strengthened grade AISI-316 LN steel.

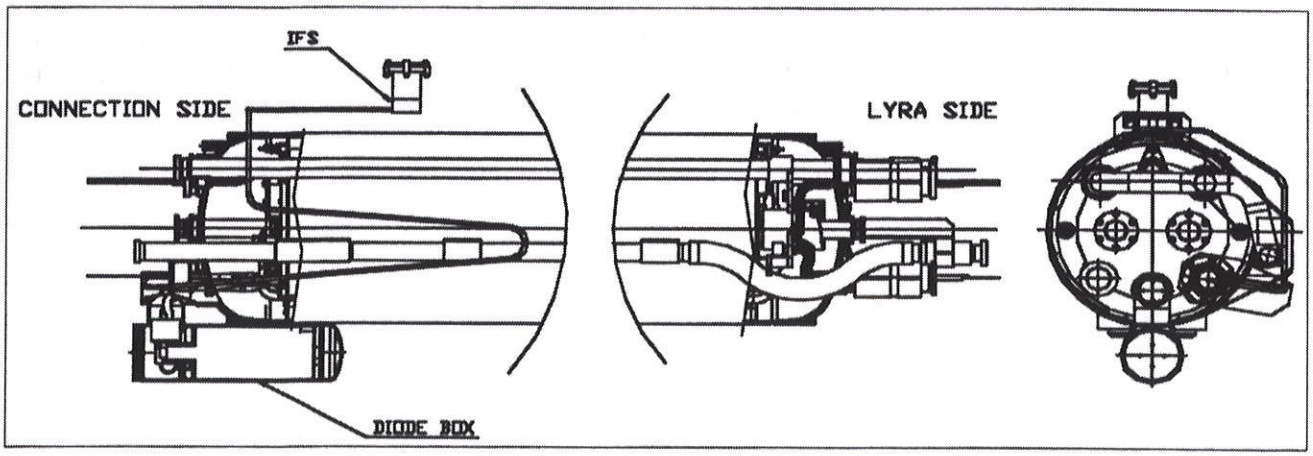

Figure 7.10: He Enclosure and ancillary equipment

The helium enclosure acts as a pressure vessel. However, its normal operational conditions do not allow it to be considered as such according to the European Directive 97/23/EC. Suitable design and structural safety requirements have been established in order to guarantee the dipole cold mass integrity in all operating conditions, including those arising from its operation as a pressure vessel.

The helium enclosure is made leak-tight with respect to ultra-high-vacuum and superfluid helium. A leak test is performed in conjunction with a mandatory pressure test with clean helium gas at 2.6 MPa (relative and absolute pressure). The helium enclosure satisfies the requirements stipulated in Tab. 7.10. The leak rate values are given at 293 K and the enclosure is at the test pressure with an atmosphere of 100% Helium.

[1] STT® stands for Surface Tension Transfer. The process was invented by Lincoln® Electric. It uses inverter-based power sources allowing variable current and voltage settings. These parameters are optimised for a better arc behaviour during the different phases of the typical welding cycles, allowing also an optimum control of the heat input.

Table 7.10: Maximum allowed leak rates at room temperature

Cold mass to insulation vacuum	$\leq 1x10^{-10}$ Pa m^3/s
Cold mass to beam vacuum	$\leq 1x10^{-11}$ Pa m^3/s
Cold mass to heat exchanger	$\leq 1x10^{-6}$ Pa m^3/s
Heat exchanger to insulation vacuum	$\leq 1x10^{-10}$ Pa m^3/s

7.3.8 Cold Bore Tubes

Table 7.11: Main characteristics of the bare cold bore tubes for the main LHC dipoles & SSS

Material	Seamless AISI 316 LN
External diameter	53 mm
Wall thickness	1.5 mm
Leak tightness	< 1.10-11 Pa m^3 s^{-1} with an external helium pressure of 2.6 MPa (absolute)

The cold bore tubes of the dipole magnets are seamless non-magnetic austenitic steel tubes 15.6 m long. The insulated cold bore tubes are placed in the aperture of the coils and form part of the inner wall of the helium vessel that contains the active part of the magnet. The cold bore tube is the passage for the circulating particle beams and as such, the tube wall separates the helium volume from the beam vacuum. The main characteristics of the cold bore tubes are summarised in Tab. 7.11.

The tubes are seamless in order to ensure both leak tightness and the homogeneity of the magnetic permeability. In addition to conventional cleaning, the tubes are subjected to a 24-hour vacuum bake-out at 150°C. The tubes are delivered by CERN already insulated and ready to be assembled.

The dipole coils are mounted and collared around the cold bore tubes, which are then submitted to high compression and shear stresses during the collaring procedure. In this case the insulation must be extremely robust mechanically. However, it must also provide a smooth external surface to allow coil and ground insulation adjustment around the tubes during collaring.

The insulation consists of three barriers (Fig. 7.11). The first one in contact with the tube is composed of two overlapped epoxy coated polyimide tape, the intermediate layer is made of an epoxy/fibre glass pre-preg tape and the external layer is made of a polyimide-coated polyimide tape. The first layer has specific epoxy glue, proving a good adhesion to the austenitic steel surface of the tube. The external layer has a polyimide glue to obtain a smooth external surface without drops of glue. The combination of polyimide and glass fibre ensures both the dielectric strength and mechanical robustness. The total thickness of the insulation is 0.65 mm.

Characteristics of the insulation materials used are summarised in Tab. 7.12.

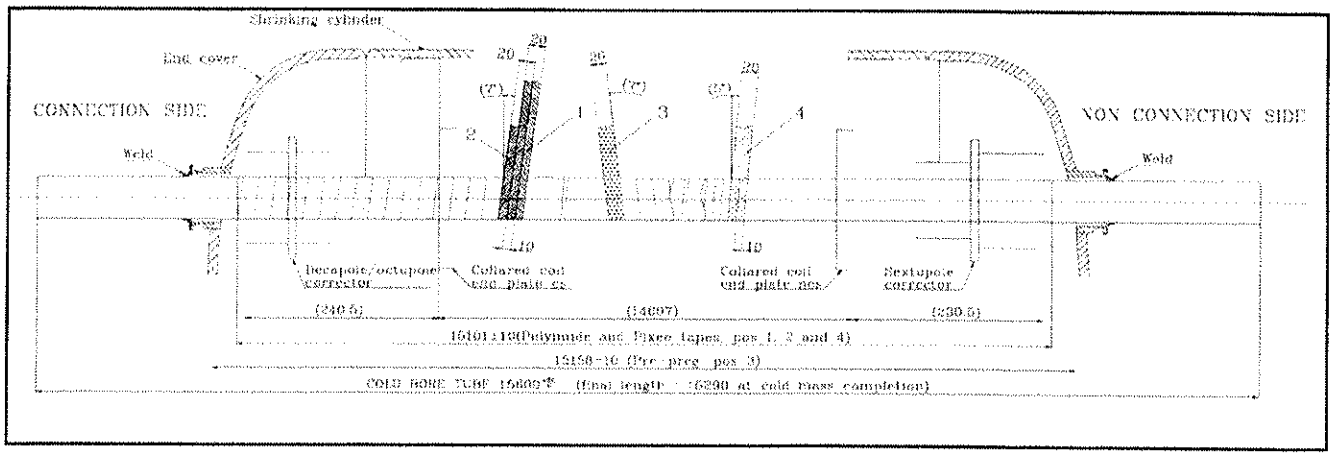

Figure 7.11: Layout of cold bore tube insulation for the main LHC dipoles

Table 7.12: Main characteristics of the insulating glass fibre tapes

Denomination	Width (mm)	Thickness (μm)	Composition
Tape1	220	770	Fast reacting epoxy glue, modified bisphenol-A, + polyimide tape
Tape 2	220	2200	Fast reacting epoxy glue/E-glass pre-preg tape, low-resin content for low flow
Tape 3	220	660	Polyimide glue of specific formulation, providing good bonding strength after thermal cycle at 190°C under moderate contact pressure

7.3.9 Spool Correctors

Requirements for the corrector magnets installed inside the dipole cold mass

Each dipole cold mass is equipped with corrector magnets. Type A dipoles have two sextupole correctors (MCS) on the lyra side and two combined decapole/octupole correctors (MCDO) on the connection side. Type B dipoles are equipped only with sextupole correctors.

In order to limit the field feed down effects to acceptable levels the corrector magnets must be positioned with a maximum deviation of ±0.3 mm systematic and 0.5 mm random errors (at 1 σ) from the geometrical axes[2] of the dipoles assuming that the magnetic[3] axes of the main coils is coincident with the mechanical[4] one to within 0.1 mm. There are errors contributing to this tolerance from the manufacturing of the corrector magnets and the assembly and installation of the correctors on the dipoles and finally the installation of the cryodipoles.

Manufacturing and assembly tolerances of the corrector magnets

The manufacturing tolerances of the correctors with respect to their magnetic axes are: 0.1 mm mean error and 0.1 mm random error at 1σ.

Once the half shells of a dipole cold mass have been welded, the end plates are fixed by welding them to the inside surface of the cylinders. The corrector magnet supports are positioned and fixed on the end plates. The radial error allowed for the position of the support is 0.3 mm with respect to the geometrical axes of the dipole cold mass. The corrector magnets are then placed onto their support and fixed by dowel pins in the holes previously used as reference for the positioning.

7.3.10 Cold Protection Diode

An essential element for the protection of the dipoles is a high current bypass diode mounted inside the liquid helium vessel and operating at a temperature of 1.9 K. The diodes will operate safely and reliably within a temperature range of 1.9 K to about 430 K throughout the life of the accelerator.

All diodes are tested at liquid helium temperatures (4.2 K) on the manufacturer's premises. After this test, they are hermetically sealed inside a capsule that is opened only at the moment of installation on the cold mass. A detailed procedure covers the handling and mounting of the diode with several precautions to avoid damage and pollution. Each twin aperture dipole is bypassed by one diode stack, consisting of two diodes in series clamped in a copper block.

The diodes are mounted under high pressure in clamping systems to ensure the required quality of thermal and electrical contact between heat sinks and the diode electrodes. When a magnet quench occurs, the diodes conduct a current pulse of up to 13 kA which decays exponentially with a time constant of about 100 s. This leads to a temperature rise inside the diode of up to 300 K.

2 The geometrical axes of the dipole cold mass are the theoretical (virtual) axes of the dipole

3 The magnetic axes of the dipole are the axes of a dipole with coils connected in a quadrupole scheme

4 The mechanic axes of the dipole cold mass are the axes of the cold bore tubes (measured)

7.3.11 Instrumentation

The instrumentation installed in the series and pre-series dipole magnets is much reduced compared to the prototypes. The following instrumentation is considered essential and is therefore installed on all pre-series and series magnets:

a) Voltage taps, to detect quenches of dipole windings and to permit diagnostics on the spool pieces and diode stack:
   - 14 voltage taps in a type A dipole cold mass,
   - 10 voltage taps in a type B dipole cold mass,
b) 2 current taps to power the protection diode stack during their annealing. These are installed on the bus-bar interconnections,
c) 2 current taps to allow the magnetic axis measurement by connecting coils in a quadrupole scheme (QCD),
d) 1 temperature sensor,
e) 1 cryo-heater to speed up the emptying and warming up of the cold mass.

Voltage taps

Voltage taps are installed at several locations on the superconducting bus bars of the cold mass. Two types of tap are used: the first type consists of tin-plated copper lugs, bent around and then soldered on the bare superconducting cable extremity and subsequently insulated. The ends of the lugs are formed as a solder lug to accept the connecting insulated wire. The second type consists of a standard lug fixed with a screw in a dedicated position on the bus bar copper stabiliser.

Temperature sensor

One temperature sensor (type CERNOX™) per cold mass is installed close to the connection side of the magnet. Each temperature sensor is already equipped with four connection wires arranged in a cable. The sensor is mounted with screws in one of the grooves of the outer surface of the iron laminations in the last lamination pack, close to the connection side of the cold mass (~1300 mm from the cold mass extremity).

Cryo-heater

A cryo heater is installed in the bottom of the connection side cold mass end on the end plate. It can be activated during warm-up of the magnet to vaporise the remaining helium present in the cold mass.

Instrumentation and quench heater wiring

All the instrumentation and quench heaters wiring (provided by CERN) is insulated with a polyimide film selected to withstand a service voltage of 1kV (5kV max. test voltage at room temperature). In addition it must be tolerant of the superfluid helium temperature and the expected level of radiation.

Instrumentation and feed-through system

The complete instrumentation feed-through system (IFS) is essentially an electrical communication path from inside the dipole magnet liquid helium bath to the outside of the cryostat. The electrical path is required for continuous and independent on-line monitoring of various diagnostics and control signals.

The complete IFS (Fig. 7.10) is made up of an extension to the cold mass, an interface-flange on the cryostat and a cover-flange with leak tight electrical feedthroughs. The extension to the cold mass, termed the IFS Tube consists of a stainless steel tube with specific end flanges through which run the 40 (type A dipole) or 36 (type B dipole) cold mass instrumentation wires. The installation of the IFS Tube is done during the cold mass manufacture. The IFS Tube is an integral part of the cold mass which can act as a cryogenic pressure vessel (Sec. 7.3.6) and must therefore fulfil the same design requirements and undergo the same pressure and leak test conditions as the helium enclosure.

7.3.12 Production QA and Tests

The cold masses are manufactured in compliance with the detailed CERN Technical Specification and are produced under a system of control checks agreed in advance with the manufacturers. CERN has specifically asked that, in addition to the complete application of the CERN Technical Specification, the manufacturers QA manual and plan should cover at least the planning, material, process control, inspection, testing, non-conformance control and objective evidence (documentation) of the inspection function.

Some of these documents are procured for each magnet produced and form part of the manufacturing and test documentation (the so-called "Traveller" folder, MTF) which contains all the test results, material traceability and manufacturing documentation for the magnet produced.

Tests during manufacturing

A considerable number of tests and inspections are mandatory during the course of the cold mass assembly. The aim of the intermediate tests at the manufacturers premises is to detect possible defects at the earliest possible stage.

These tests, together with their conditions and acceptance criteria are described in the contractual documents. The description of the mandatory tests is summarised in the Inspection and Test Plan (ITP) which systematically includes:

a) Verification of the integrity of the electrical insulation and the impedance of various electrical circuits at different steps of the assembly.
b) Verification of the dimensions of the coils.
c) Verification of other critical dimensions (such as the coil poles, coil extremities, collared coils, etc.).
d) Geometrical measurements, accurate to within 0.1 mm rms. These must include measurements of the horizontal curvature, the vertical straightness, the position of the ends of cold bore tubes and of other outlets for magnet interconnection, the position of the support bases, the minimum inner diameter of the cold bore tubes and the position of the spool pieces correction magnets.
e) The measurements of tilt of the magnetic mid-planes and the parallelism of the field direction in the two apertures.
f) The measurement of magnetic field quality and the integrated field strength. The purpose of these measurements is also to allow the possibility of fine-tuning the magnetic length (see Sec. 7.3.2).
g) Examination of welded joints (Safety Tests).
h) Room temperature pressure and leak tests (Safety tests).

In order to control the quality of magnets produced and to easily identify drift or similar problems, official "Holding Points" in the manufacturing are placed at:

1) Mounting of the collaring shim (indirect control of coil dimension).
2) Acceptance of the collared coils magnetic measurements (control of field quality expected).
3) Acceptance of the cold mass magnetic measurements.
4) Preparation of all the QA and tests result documentation prior delivery to CERN (general control on magnet conformity and traceability).

Magnetic measurements

The measurement of the magnetic field at room temperature is carried out on the whole of the production at the level of the collared coil and of the cold mass. These measurements are a powerful tool to control the quality of production and to steer the field quality towards the beam dynamics target. In the checks, acceptance ranges are fixed independently of the beam dynamics targets and are based on the statistics of a homogeneous set of pre-series measurements (around 30 for the collared coil, 15 for the cold mass). The aim of this control is to identify field anomalies that could be related to assembly errors or faulty components [36]. A warning is set at 3.5σ of the measured σ, and a red alarm at 7σ . Contrary to what is needed for beam dynamics, here the values along the magnet axis are monitored. Indeed, manufacturing errors are likely to affect only a short section of the 15 m-long magnets. The test for the cold masses is performed on the

difference with respect to the collared coil measurements [37]. This allows checking of the assembly phases between the collared coil and the cold mass only.

When a field anomaly is detected, the measurement system is first checked to ensure that the anomaly comes from a problem in the magnet. When the hypothesis of a measurement problem is rejected, simulations are carried out to estimate the coil movements that could have provoked the multipole shift. The symmetry of the error and its length along the axis are powerful indicators of the source of the anomaly. The decay of the error also indicates the distance from the centre of the aperture: if all multipoles are affected, the anomaly is likely to be in the inner layer, whilst if only the low orders are affected the problem is in the outer layer. All of these operations rely on the experience of the analysts, and an automatic analysis system has proved difficult to implement.

Inspection on arrival at CERN

The cold mass is submitted to the following reception tests within a 2 day period after its delivery to CERN:

a) Visual inspection
b) Mechanical checks
c) A simplified set of electrical tests
d) A simplified check of curvature and cold support position

Reception tests at CERN

The 1.9 K Reception tests at CERN systematically include:

a) Verification of the integrity of the electrical insulation and impedance of various circuits.
b) Training of the magnets above nominal field and then to ultimate field within a given number of quenches. Retraining after a thermal cycle if it takes more than 8 quenches to reach the ultimate filed.
c) The measurement of integrated field strength versus excitation, field quality at several field levels, tilt of the magnetic mid-planes, parallelism of the field direction in the two apertures and axis curvatures over a representative set of dipoles.
d) Leak tests.

7.4 DIPOLE CRYOSTAT

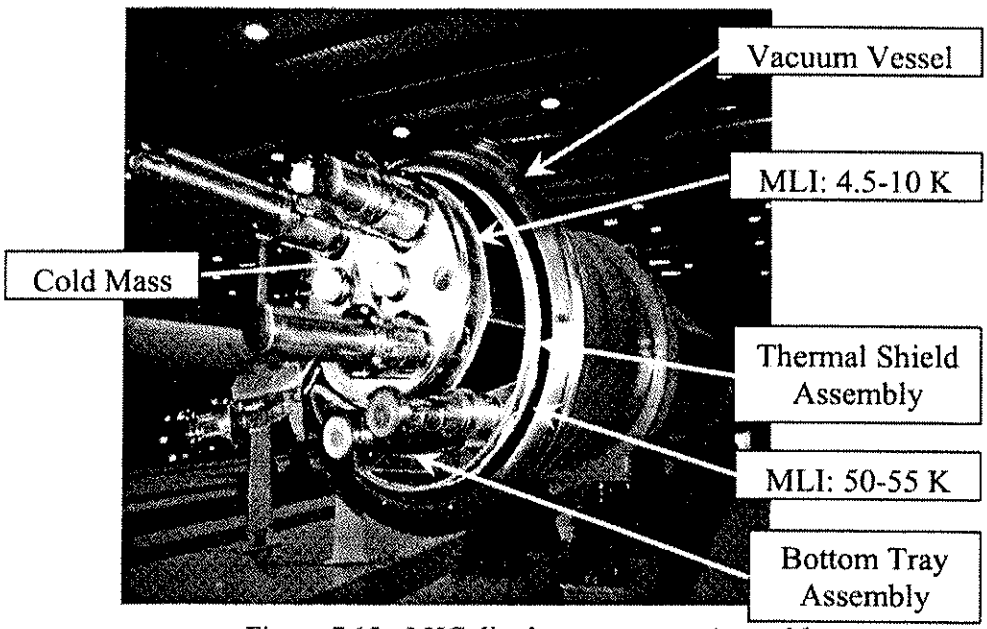

Figure 7.12: LHC dipole cryomagnet Assembly

7.4.1 Vacuum Vessel

The vacuum vessel consists of a long cylindrical standard tube with an outer diameter of 914 mm (36 inches) and a wall thickness 12 mm. It is made from alloyed low carbon steel and certified to conform to the general specification EN 10204/DIN 50049 3.1 B. The vessel has stainless steel end flanges for vacuum tight connection via elastomer seals to adjacent units.

Three support regions feature circumferential reinforcement rings. Upper reinforcing angles support alignment fixtures. An ISO standard flanged port is located azimuthally on the wall of the vessel at one end.

Lower cast cradles in DIN GS-21 Mn5 grade steel locally reinforce the vessel and allow the loads induced by the weight of the cold mass to be transmitted to the external jacks while minimising deformations of the vessel structure.

The dimensional precision and stability of the finished vacuum vessels with time is particularly important. Full stress-relieving heat treatment is not required. However, vibration techniques are used to reduce the internal stresses in all structural welds as far as possible.

In normal operation, the vessel will be under vacuum. In case of a cryogenic leak, the pressure can rise to 0.14 MPa absolute and a sudden local cooling of the vessel wall to about 230 K may occur. The steel selected for the vacuum vessel wall is tested to demonstrate adequate energy absorption during a standard Charpy test at -50 °C.

All flanges of the vacuum vessel are ring forged in AISI 304L stainless steel and welded to the vessel. One layer of anti-rust primer and 2 layers of epoxy paint are applied to protect the outer surfaces only. The inner surface is shot-blasted for high vacuum compatibility. A front view of the cryodipole is shown in Fig. 7.12.

7.4.2 Thermal Shielding, Bottom Tray Assembly and MLI

The thermal shield bottom tray assembly is essentially a long double-walled tray formed from two extruded profiles in series 6060 aluminium alloy. To achieve adequate overall stiffness and sufficiently uniform heat extraction from the complete extrusion the full-length extruded parts are joined with fully penetrating longitudinal welds uniformly distributed to occupy at least 25% of the total extrusion length. After longitudinal welding but before machining, the finished extrusions are heat-treated to ensure their long-term dimensional stability over repeated temperature cycling (25 times) between 293 K and 50 K. A minimum yield strength of 120 MPa is required in the base material and in the welds, including the zones of internal welds. Provisions for welding of the transition elements are machined at three locations along its length, at support interfaces and at each end. The tray incorporates two tubular channels. One is tested to be helium leak tight, used for the passage of cold gaseous helium at a temperature of about 60 K and serves to extract heat from the thermal shield and its support system. At each end of this cryogenic line, an industrially available aluminium-alloy-to-stainless-steel pipe transition element with an internal diameter of 80 mm is welded on using automatic orbital welding techniques. The position of these elements after welding and the quality of the connecting welds of the transition assemblies, separating vacuum from high-pressure cryogenic helium, is critical.

Sheets, in high purity (99.5%) aluminium are rolled into upper shells, fitted to the bottom tray assembly over its entire length and welded in place. Once wrapped in its MLI blankets, this becomes the thermal shield assembly, intercepting radiant heat at 50-65 K.

The set of MLI blankets including all blankets and pads needed to equip one dipole cryostat and its cold mass including the diode is obtained from industry as an installation kit. The blankets are manufactured with a layered structure of sheets of reflective polyethylene terephthalate (PET) film, coated with aluminium (minimum 40 μm) on each side, perforated with open areas of between 0.05% and 0.15% of their total area. The PET film is interleaved with polyester net spacing sheets. The thermal shield is equipped with two superimposed blankets of 15 layers each. The cold masses and the diodes are equipped with single blankets of 10 layers.

To obtain the required performance from the blankets, their overall thickness must be not less than 2 mm for the 10 composite layers and not less than 3 mm for the 15 composite layers. The length of each blanket takes into account their thermal contraction and an integrated thermal contraction of 4×10^{-3} has been used for all MLI blankets regardless of their operating temperature. The outermost layer of each blanket is a reflective film reinforced with a net of thickness of 12 μm.

All blankets are equipped with Velcro™ fasteners made of polyamide (Nylon 6.6) assembled on the cold inner side of the blankets and stitched to their edges, for ease of installation. The blankets are designed in such a way that they can be easily handled using clean cotton gloves and rapidly assembled using a minimum of tooling, by two trained technicians.

7.4.3 Support Posts

A dipole support post (Fig. 7.13), is composed of a monolithic 4 mm-thick tubular column in Glass Fibre Reinforced Epoxy resin (GFRE) material, chosen for its low thermal conductivity-to-stiffness ratio at reasonable cost. A top and a bottom flange serve as mounting interfaces to the cold mass and the vacuum vessel, respectively. Each support post is equipped with two external aluminium heat intercepts and internal stainless steel rings, glued to the composite column.

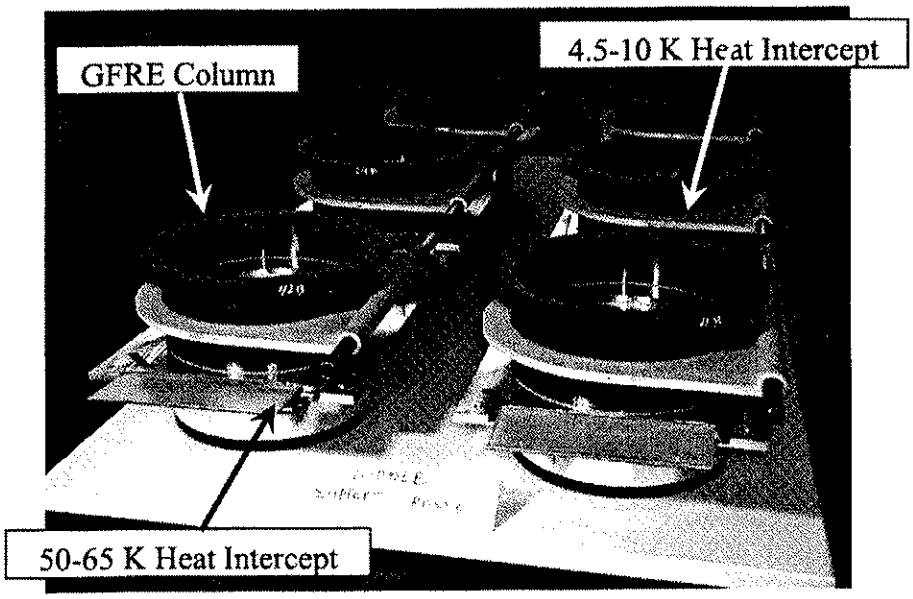

Figure 7.13: LHC dipole support post assemblies.

The lower heat intercept operating at 50-65 K is furnished with two aluminium multi-foil flexible straps to be welded to the bottom tray assembly whereas the upper intercept operating at 4.5-10 K integrates a low-thermal-impedance stainless steel tube insert to be later welded into the cryogenic supply line. Two aluminium radiation screen disks, fixed to the stainless steel rings and a radiation reflecting coating on the inner and outer walls of the lower portion of the composite column, provide thermal insulation from heat radiated from the vacuum vessel at room temperature.

The support posts are designed to sustain the thermo-mechanical loads of a cold mass (10 kN axial load, 50 kN in shear) during steady state operation and transients (transport, cool-down) with low, but sufficient, security margin. They must resist long term creep. They are designed to operate in an insulation vacuum of 10^{-4} Pa, to withstand exposure to a total integrated dose of ionising radiation of 100 Gy, to minimise heat in-leaks to the cryostats and to provide precise positioning of the cold mass within the cryostats. They are manufactured to tight dimensional, axial and shear stiffness tolerances and the dispersion of thermal contraction and mechanical properties are stringently controlled during production.

7.4.4 Dipole Cryomagnet Assembly

Specific tooling has been designed, built and installed in a purpose built factory complex to allow the industrial assembly of LHC Dipole Cryo-magnets (see Fig. 7.14). This tooling allows the Dipole Cold Mass to be equipped with its thermal insulation and other ancillary equipment before being integrated and positioned precisely inside its individual cryostat

Four tooling sets allow a normal assembly rate of 10 cryomagnets per week to be maintained when working one shift

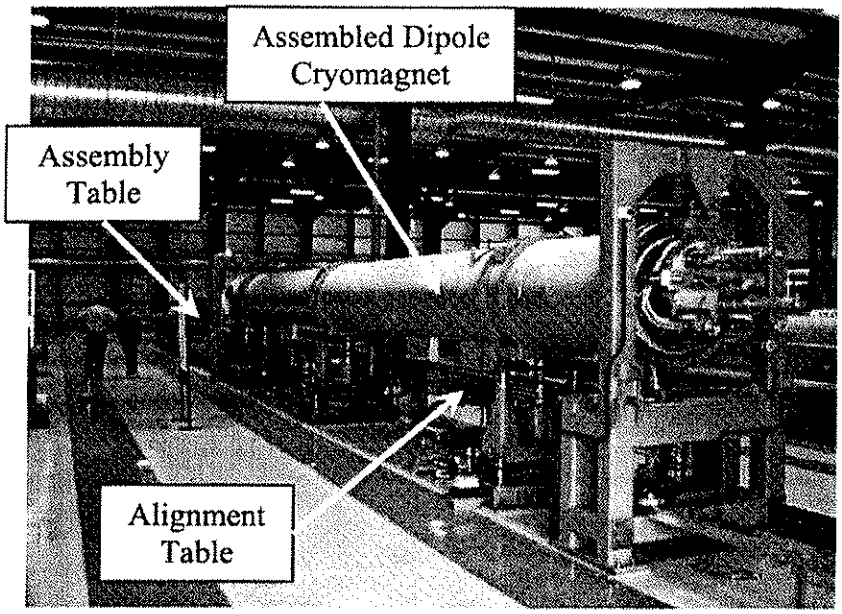

Figure 7.14: Specific tooling for assembly of LHC Dipole Cryomagnets.

7.5 SHORT STRAIGHT SECTIONS OF THE ARCS

7.5.1 General Design

Fig. 7.15 shows a perspective view while Fig. 7.16 illustrates the cross-section of a short straight section.

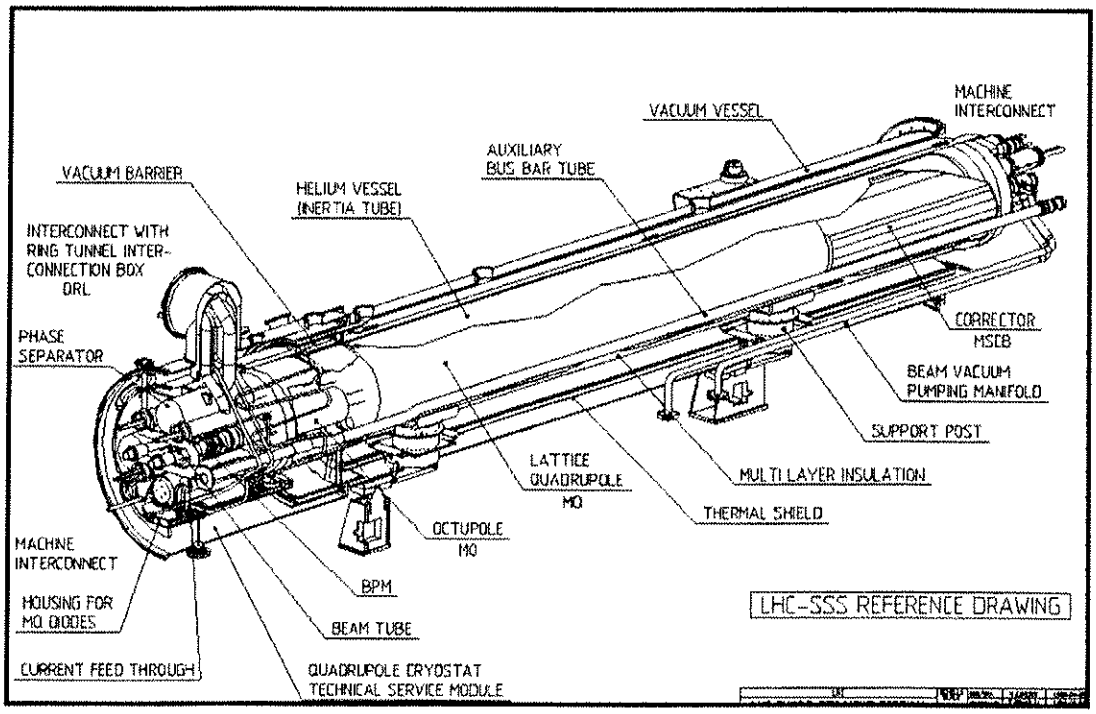

Figure 7.15: Short straight section with jumper

The cold masses of the arc short straight sections [43] contain the main quadrupole magnets, MQ, and various corrector magnets. On the up-stream end these can be either octupoles, MO, tuning quadrupoles, MQT, or skew quadrupole correctors, MQS. On the down-stream end the combined sextupole-dipole

correctors, MSCB are installed. These magnets are mounted inside a so-called inertia tube which is closed by end covers. This structure provides the helium vessel for these magnets and at the same time the mechanical stiffness of the assembly. The up-stream flat end cover also supports the beam position monitors and the container for the quench protection diode stack of the main quadrupoles. The down-stream, dished end cover, has the connection tubes mounted with bellows for the interconnections to the adjacent dipole cold mass. Running through the short straight sections are the two beam tubes, the heat exchanger tube and the main dipole and quadrupole bus-bars as well as the spool bus-bars which interconnect the correctors of the dipole cold masses. The powering of the corrector magnets inside the short straight section cold masses is made via bus-bars placed in a tube located outside the cold mass, called line N.

The cold masses are mounted into their cryostats to which the technical service modules, called QQS, are attached on the up-stream end. These modules house the interconnections to the adjacent up-stream dipole, the outlets of the wires for the instrumentation and local corrector powering. In every second unit, the interconnection to the separate cryogenic feed line, QRL, and the phase separators are present. One out of four straight sections is equipped with a vacuum barrier for sectorising the cryostat vacuum. At the same positions there are connection tubes and pressure plugs inside the up-stream bus-bars to separate the local helium circuits of the machine.

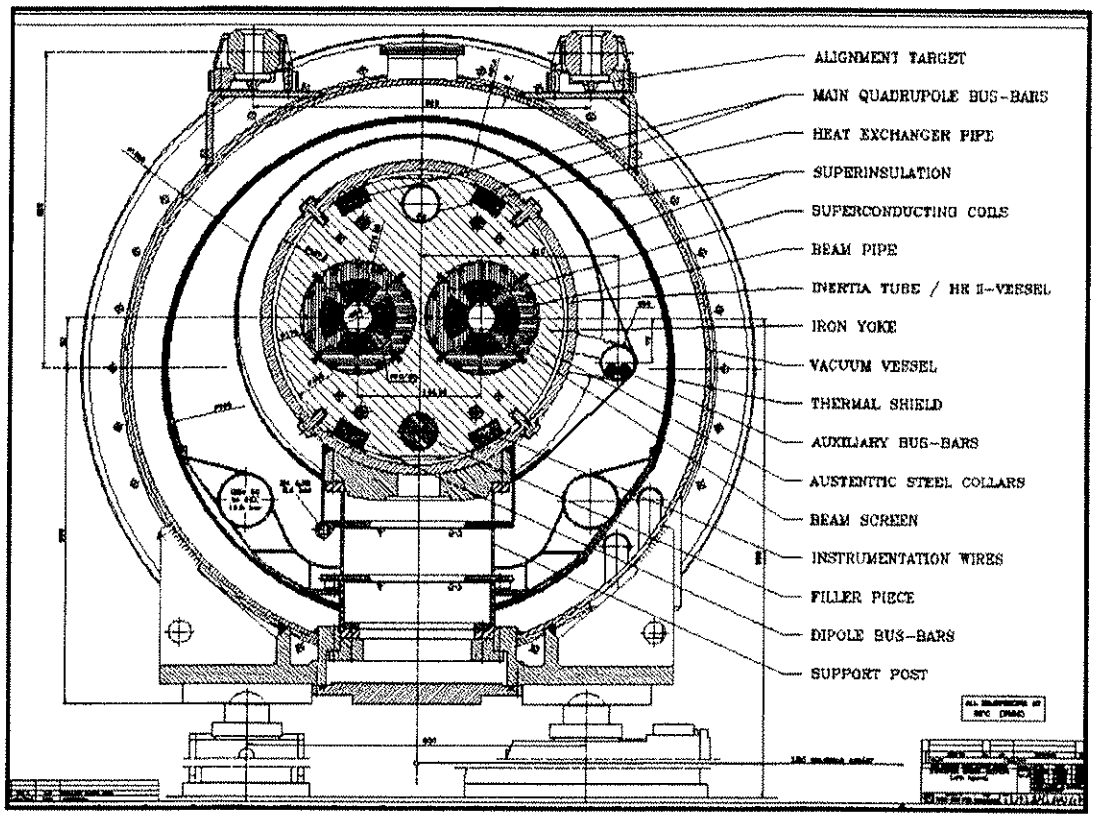

Figure 7.16: Cross-section of short straight section with quadrupole cold mass inside cryostat

7.5.2 Magnetic Design of the Quadrupole

The magnetic design of the main quadrupoles, MQ, has remained almost unchanged with respect to the design presented in the "Yellow Book" [8]. The increase of width of the bare cable by 0.1 mm to 15.1 mm had practically no effect on the magnetic design. The conductor distribution of two blocks in each of the two coil layers has remained the same, Fig. 7.17. The design features the two-in-one yoke concept, where a focusing and a de-focusing quadrupole are fitted in one common yoke.

Because of the lower electromagnetic forces, the two apertures are not combined but are assembled in separate annular collaring systems. This is in contrast to the case of the main dipoles. Computations, since confirmed by measurements, have shown that the magnetic coupling between the two apertures is negligible. This remains true even when the two apertures are excited with very different currents. Tab. 7.13 shows the design parameters of the quadrupole magnets

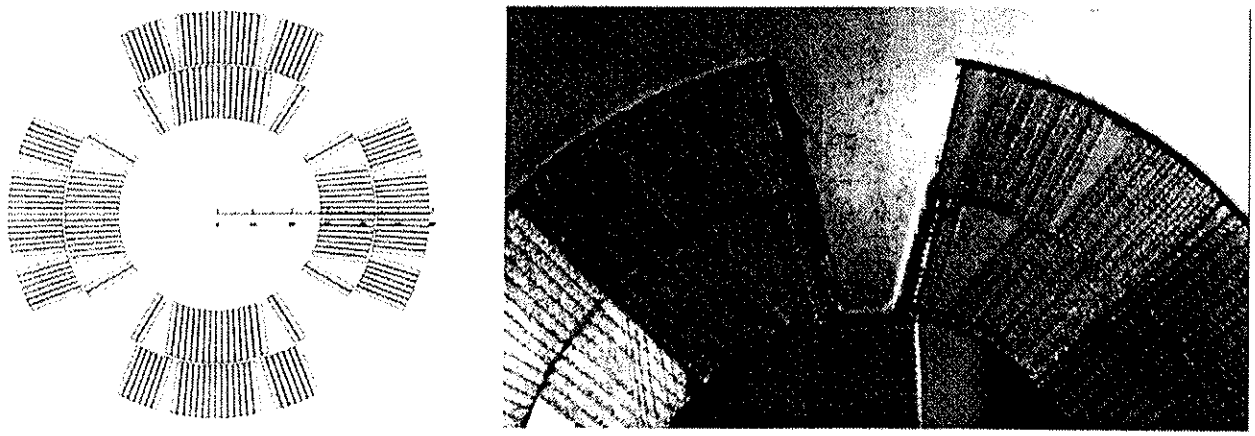

Figure 7.17: Conductor distribution in the main quadrupole

Table 7.13: Parameter list for main quadrupole magnets (MQ) at 7.0 TeV

Integrated Gradient	690	T
Nominal Temperature	1.9	K
Nominal Gradient	223	T/m
Peak Field in Conductor	6.85	T
Temperature Margin	2.19	K
Working Point on Load Line	80.3	%
Nominal Current	11870	A
Magnetic Length	3.10	M
Beam Separation distance (cold)	194.0	mm
Inner Coil Aperture Diameter (warm)	56.0	
Outer Coils Diameter	118.44	
Outer Yoke diameter	452	
Collar Material	Austenitic Steel	
Yoke Material	Low Carbon Steel	
Yoke Length including End Plates	3250	mm
Cold Mass Length Between End Covers	5345	mm
Total Mass Including Correctors	6500	kg
Number of turns per Coil (pole)	24	
Number of turns per coil inner layer (2 blocks)	2+8	
Number of turns per coil outer layer (2 blocks)	7+7	
Cable length per coil (pole)	160	m
Cable length per two-in-one quadrupole	1280	m
Bare Cable	Same as dipole outer layer	
Insulation Thickness 1st layer	50	μm
2nd layer	37.5	μm
3rd layer (adhesive)	50+5	μm
Self-inductance, one aperture	5.6	mH
Stored energy, one aperture	395	KJ
Electromagnetic forces: Resultant in x-dir	537	KN
Resultant in y-dir	-732	KN

The target values for the multipole content of the quadrupoles have been adapted to the newest results for the estimated and measured effects of the persistent currents in the superconducting filaments. Since the

"Yellow Book" [8] the dodecapole component, b_6, has been found to be smaller than earlier computed. The new target values also take into consideration the influence of the (low) permeability of stainless steel components, especially the collars and the beam pipe as well as the relatively small effect of the yoke. The target values are summarised in Tab. 7.14. The spread of the individual magnets must stay within the mean value tolerances plus twice the random error, σ. During the series fabrication any drift of the mean measured multipoles to beyond the limits should trigger corrective action.

Table 7.14: Expected multipoles at injection and nominal field, in units of 10^{-4} relative field error at 17 mm

n	At injection, 14.5 T/m				At nominal operation, 223 T/m			
	Mean		Random σ		Mean		Random σ	
	normal b_n	skew a_n	normal b_n	Skew a_n	normal b_n	skew a_n	normal b_n	skew a_n
3	±2.0	±2.0	1.0	1.0	±2.0	±2.0	1.0	1.0
4	±0.5	±0.5	0.7	0.7	±0.5	±0.5	0.7	0.7
5	±0.5	±0.5	0.6	0.6	±0.5	±0.5	0.6	0.6
6	±1.0	±0.3	0.5	0.5	2.5±1.0	±0.3	0.5	0.5
7	±0.15	±0.15	0.15	0.15	±0.15	±0.15	0.15	0.15
8	±0.1	±0.1	0.1	0.1	±0.1	±0.1	0.1	0.1
9	±0.1	±0.1	0.1	0.1	±0.1	±0.1	0.1	0.1
10	±0.2	±0.2	0.3	0.3	-0.3±0.2	±0.2	0.3	0.3

Superconducting cable

The cable used for the main quadrupole is the same as that for the outer layer of the dipole coils (see Section 7.2.1). Because of the much shorter cable length needed for one pole (160 m), use can be made of the shorter cable fabrication and thus avoid waste. Although this cable is not the optimum from the point of view of magnetic design its selection gives the advantage of standardization and hence important savings in cost.

The insulation consists of a layer of 50 μm polyimide wrapped edge to edge around the conductor followed by a second layer of 37.5 μm both 11 mm wide. The wrapping direction is the same as the cable twist orientation. This is covered by a so-called barber-pole wrapping in the opposite direction of a 50 μm thick polyimide, 9 mm wide with a spacing of 2 mm, covered on its outside with a adhesive layer of 5 μm.

The cable is the same for both coil layers, which allows the use of a true double-pancake winding technique, avoiding thus the need for an inter-layer connection.

Collared coils

Four coils, wound out of one single unit length of cable of 640 m, are assembled together with four layers of polyimide ground insulation and four quench heaters and the half-circle collars are piled around them. The collars are fine-blanked of austenitic stainless steel sheets of 2.0 mm thickness. The steel is specified to have a relative permeability of less than 1.005 at room temperature and at 1.9 K. Its yield strength is ≥620 MPa the tensile strength is ≥850 MPa, both specified at room temperature. These values are needed because the electromagnetic forces are taken by the collars only, without any support contribution of the yoke. The thermal contraction between 293 and 4.2 K is specified to be between 0.26 and 0.28% to ensure that the pre-stress of the coil is maintained. The collars are held together by eight stainless steel keys which are inserted by means of a specially designed collaring press. Care is taken to ensure that the coils are not compressed to values above 120 MPa during this operation. After the keys are fully inserted and the press is released, the residual pre-stress at room temperature amounts to around 100 MPa. Unlike the prototypes, the series magnets will be equipped with one-piece collar keys. This simplification was proposed by the series manufacturer after a number of mock-up tests and calculations.

After collaring, the conductors of the four coils are interconnected by means of copper channels fitted into a stack of glass-fibre plates.

Magnet yoke

The quadrupole magnet yoke is made of the same material as the yoke for the dipole magnets. However the 5.8 mm thick yoke laminations are not cut into two halves as for the dipoles, but punched from a single sheet. The laminations are stacked around the two pre-aligned collared apertures by having alternately the flat cut on top and on bottom of the assembly. The mechanical centring of the collared coils inside the yoke aperture is provided by four lines of stainless steel keys along the 45° plane of the coils. By progressively compressing the yoke laminations and by inserting keying rods the collared coils are locked inside the two yoke apertures. The yoke is compressed longitudinally by two end plates and four tie rods. The up-stream end-plate, 39 mm thick, contains a groove in its circumference into which the pins that fix the longitudinal position of the magnet inside the inertia tube are placed. The quadrupole (and the corrector magnets) are centred inside the inertia tube by means of stainless steel centring keys, placed in grooves in the yoke and fixed by means of pins and screws located in holes which are precisely machined along the 45° lines of the inertia tube.

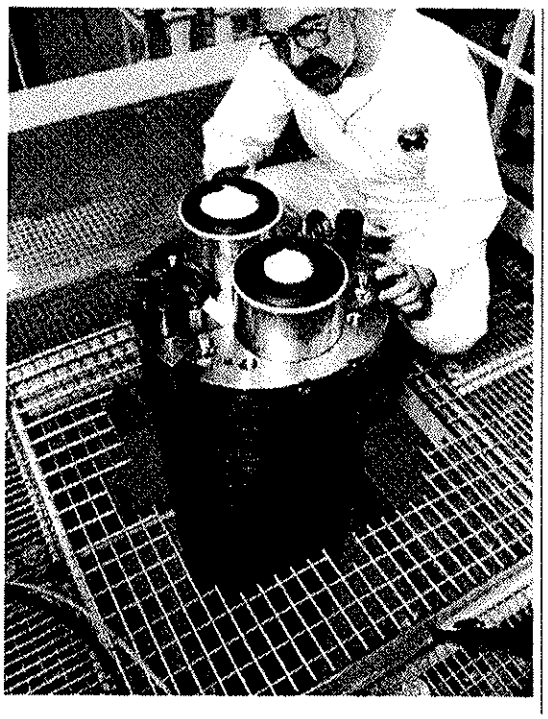

Figure 7.18: Assembled quadrupole yoke with end plate and tie rods

Over the whole length of the yoke, four 50 mm wide longitudinal grooves are present for the passage of the dipole bus-bar set and the focusing and de-focusing quadrupole bus-bar sets, including their insulation and the spool bus-bars. The fourth groove allows the passage of instrumentation wires and the auxiliary bus-bars for powering the sextupole-dipole corrector magnets.

Helium enclosure

The helium vessel consists of the inertia tube and its two end covers. The inertia tube is rolled from a 16 mm thick stainless steel sheet and features two enlargements welded to both ends. It is machined only at its ends and positioned using the rows of alignment holes. On the up-stream end it is closed by a flat end cover while on the down-stream end a dished end cover is welded on. Steel covers are welded over the holes of the alignment pins and screws. The inertia tube is completed with two base plates for the cold supports inside the cryostat and 12 geometrical reference points.

Before delivery, the function of the cold mass as the helium container and pressure vessel is verified by loading it with a helium gas pressure (absolute) of 2.6 MPa and by leak testing the tightness of the vessel and that of the various tubes, Fig. 7.19. For this purpose the cold mass is completely closed in the factory by welding separate closing covers onto the bus-bar connection tubes. A closing cover is attached by a flange

and tightened by means of a Helicoflex™ joint over the instrumentation feed-through. All closing covers are sent back to the factory for re-use after opening at CERN.

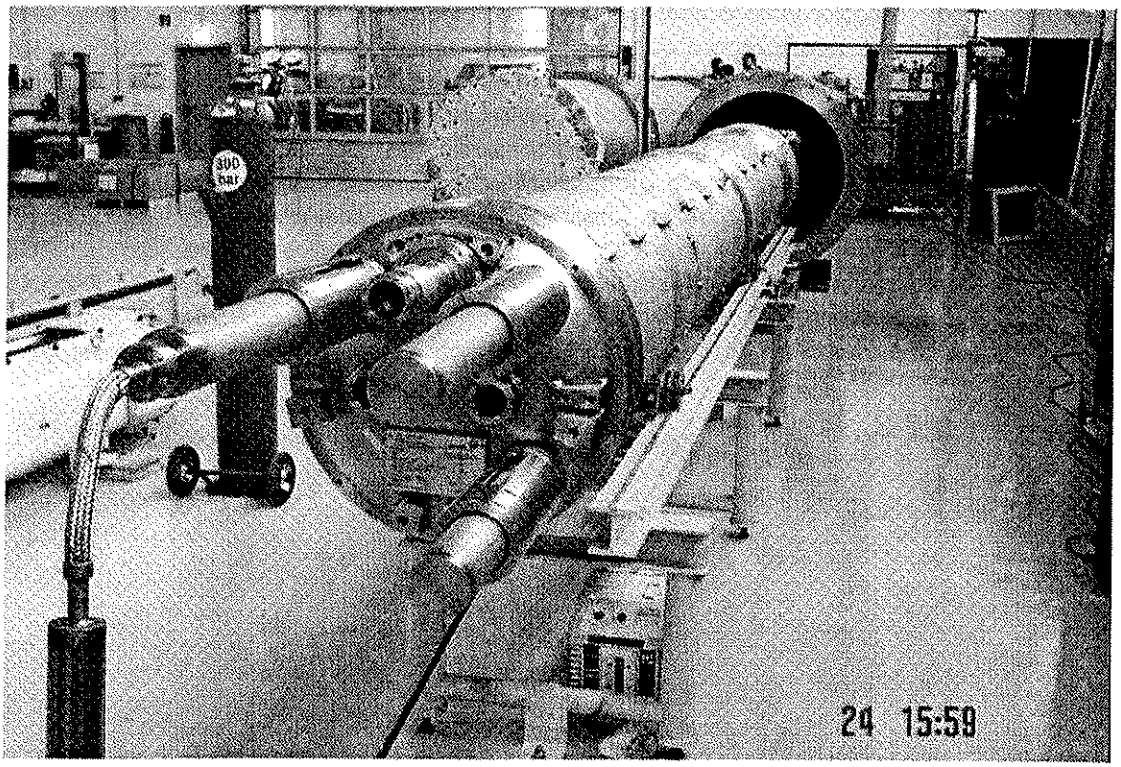

Figure 7.19: Cold mass in front of test vessel for pressure and leak tests in factory

To reduce the volume of the liquid helium, a number of filler pieces are mounted mainly around the corrector magnets, but also in the other void spaces. These fillers, where they have no mechanical function, are made out of high density polyethylene material.

Helium II heat exchanger tube

The heat exchanger tube passes through the top hole of the quadrupole yoke and beyond the full length of the cold mass in the same way as through the cold masses of the dipoles. It consists of a copper tubes to the end of which stainless steel sleeves are welded. These tubes can have two lengths depending on whether a phase separator is fitted in the technical service module, or not. The tube is welded to the dished end cover by means of a dedicated ring. This end is equipped with an inter-connection bellows.

Cold bore tubes

The two cold bore tubes pass through the two magnet apertures over the full length of the cold mass. The tubes have the same diameter as those for the dipoles. In the case of quadrupoles, the tubes are inserted after magnet assembly. The insulation thickness has to be further reduced with respect to that of dipoles and kept below 0.15 mm in order to allow the insulated tube to slide inside the cold masses. This is achieved by using one 50% overlapped layer of double sided adhesive polyimide tape (Tape 3 in Tab. 7.12). Their insulation consists of a wrapping of polyimide, Pixeo AST 252, of 60 mm thickness with a 48 % overlap.

On the up-stream end (flat end cover) the tubes are attached to the supports of the beam position monitors (BPM), while on the down-stream end they are fixed to the dished end covers. The beam screen will be installed into the cold bore before installation in the machine tunnel (see Chap. 12).

Corrector magnets

All short straight sections of the arcs are equipped with MSCB sextupole correctors on their downstream end. The two sextupole modules and two dipole corrector modules, one for each beam line, are aligned in a common yoke. The sextupoles alternate type with focusing and de-focusing sextupole polarity following the functions of the quadrupole apertures. A focusing sextupole is always combined with a horizontally

deflecting dipole corrector while a de-focusing sextupole will combine with a vertically deflecting dipole. There are, however, exceptions concerning these magnets. Eight of the sextupole-dipole correctors per arc will have one of their sextupole modules, the focusing one, rotated by 30° in order to form a skew sextupole magnet. Thus, in total four types of these magnets exist: MCSBA, MSCBB, MSCBC and MSCBD. The last two abbreviations indicate those with the skew sextupole modules in the outer and inner aperture, respectively.

The upstream end of a short straight section may have an octupole corrector magnet, a tuning quadrupole, or a skew quadrupole. The skew quadrupoles are similar to the tuning quadrupoles, just rotated by 45°. Mechanically these three types of magnets are of identical shape. The alignment of the corrector magnets inside the cold mass with respect to the axes of the quadrupole apertures has been determined to have a maximum displacement (3σ) of 0.17 mm. The main parameters of the correctors in the short straight sections are summarised in Tab. 7.15.

Table 7.15: Main parameters of corrector magnets in the arc short straight sections

	MO	MQT/MQS	MSCB (A,B,C,D)	
			Sextupole	Dipole
Nominal strength	6.3×10^4 T/m^3	123 T/m	4430 T/m^2	2.9 T
Nominal current	550 A	550 A	550 A	55 A
Magnetic length	320 mm	320 mm	369 mm	647 mm
Overall length	395 mm	395 mm	1260 mm	
Diameter of aperture	56 mm	56 mm	56 mm	56 mm
Outer diameter	514 mm	514	452 mm	
Mass	~250 kg	~250 kg	1000 kg	
Number of magnets in arcs	168	160/32	360 (Type A: 146, B: 150, C: 32, D 32)	

Protection diodes

The separate powering of the main focusing and de-focusing quadrupoles makes it necessary to have two diodes for each cold mass. The diode stack is housed in a can attached to the flat end cover which protrudes into the technical service module. Four dedicated copper bus-bars provide the electrical connection to the quadrupole apertures. The diode can is part of the cold mass and must therefore withstand the same leak tightness and pressure test as the cold mass itself.

Instrumentation

The instrumentation [44] consists of the voltage taps for quench detection, the quench heaters (and their wiring), a thermometer and a cryo-heater inside the cold mass.

The voltage taps are attached to the terminals of each quadrupole aperture and to the centre points of the coil assemblies. The voltage tap wires are duplicated for redundancy. The corrector magnets and diodes are also equipped with voltage taps.

The quench heaters are wired in two circuits. Each one connects two heaters of one aperture with two heaters of the other aperture. This gives redundancy to the quench protection system.

Each cold mass has a temperature sensor of the CERNOX™ type and a 100 W resistor for cryogenic heating mounted inside.

Production and quality assurance

The development of the quadrupole magnets and their cold masses was entrusted to CEA Saclay, France, who constructed and successfully tested a total of five prototypes. These prototypes were also operated highly satisfactorily in the two LHC strings at CERN. Thus, the design and method of construction were confirmed. The series production for the fabrication of the quadrupole magnets and the assembly of the cold masses [45] will be done in industry. In the same way as the dipoles, a number of components are supplied by CERN.

All material provided has to be accompanied by certificates of conformity. The complexity is illustrated by the fact that the corrector magnets come from different manufacturers in three European countries, the

fabrication of the bus-bars has been entrusted to BINP, Novosibirsk, Russia and that two critical operations (the insulation of cold bore tubes and brazing and e-beam welding of the heat exchanger tubes) are performed at CERN.

Table 7.16: Variants of cold masses in arc short straight sections

Cold-mass code	Quantity	Bus-bar-type	MSCB Type	MO, MQT or MQS	Diode type	Helium Vessel Type
LQMOC	2	de-focusing	B	MO	A	A: Two jumper studs, pressure plugs, short heat exchanger tube, vacuum barrier
LQMOD	2	de-focusing	B	MO	B	
LQMOO	6	focusing	A	MO	A	
LQMOP	6	focusing	A	MO	B	
LQMSA	4	de-focusing	B	MQS	A	
LQMSB	4	de-focusing	B	MQS	B	
LQMSC	12	focusing	A	MQS	A	
LQMSD	12	focusing	A	MQS	B	
LQMTC	4	de-focusing	B	MQT	A	
LQMTD	4	de-focusing	B	MQT	B	
LQMTI	12	focusing	A	MQT	A	
LQMTJ	12	focusing	A	MQT	B	
LQMOE	27	de-focusing	B	MO	A	B: No jumper studs, no pressure plugs, long heat exchanger tube, no vacuum barrier
LQMOF	27	de-focusing	B	MO	B	
LQMOK	12	de-focusing	D	MO	A	
LQMOL	12	de-focusing	D	MO	B	
LQMOQ	9	focusing	A	MO	A	
LQMOR	9	focusing	A	MO	B	
LQMOW	4	focusing	C	MO	A	
LQMOX	4	focusing	C	MO	B	
LQMTE	30	de-focusing	B	MQT	A	
LQMTF	30	de-focusing	B	MQT	B	
LQMTK	10	focusing	A	MQT	A	
LQMTL	10	focusing	A	MQT	B	
LQMOH	1	de-focusing	D	MO	A	C: One jumper stud, no pressure plugs, short heat exchanger tube, vacuum barrier
LQMOJ	1	de-focusing	D	MO	B	
LQMOT	3	focusing	C	MO	A	
LQMOV	3	focusing	C	MO	B	
LQMOA	2	de-focusing	B	MO	A	D: One jumper stud, no pressure plugs, short heat exchanger tube, no vacuum barrier
LQMOB	2	de-focusing	B	MO	B	
LQMOG	3	de-focusing	D	MO	A	
LQMOI	3	de-focusing	D	MO	B	
LQMOM	6	focusing	A	MO	A	
LQMON	6	focusing	A	MO	B	
LQMOS	9	focusing	C	MO	A	
LQMOU	9	focusing	C	MO	B	
LQMTA	6	de-focusing	B	MQT	A	
LQMTB	6	de-focusing	B	MQT	B	
LQMTG	18	focusing	A	MQT	A	
LQMTH	18	focusing	A	MQT	B	

In the quadrupole and cold mass assembly factory the technology transfer has been ensured by engineers and technicians from CEA Saclay in close collaboration with the CERN team. Each collared coil assembly and each quadrupole magnet undergoes warm magnetic field measurements after its integration into the cold mass. The various electrical circuits undergo systematic tests including high voltage insulation tests and tests for inter-turn shorts. All welds of the cold mass have been verified in advance and are executed by qualified

welders under the supervision of an authorised safety body and CERN's safety team. The finished cold masses are closed at their extremities and leak and pressure tested for operation at up to 2.0 MPa. The geometry of the cold masses, especially the interfaces to cryostats and adjacent magnets are verified by measurements with two commercial laser tracker systems provided by CERN. Magnetic measurements are carried out on each collared coil and each cold mass, in order to intercept manufacturing faults at an early stage and to have early indications on trends harmonics, in a similar manner as for the dipoles. The factory provides a record of tests and measurements which has to be accepted by CERN and CEA before delivery for each cold mass. These are integrated in the database at CERN via the manufacturing and test folder (MTF).

Cold mass variants

The series production and quality control of the cold masses is complicated by the existence of 40 different variants [46]. This variety is due to the different combinations of the magnets and the changing polarities, the presence or not of the two types of jumper connection interfaces, the vacuum barrier interface and pressure plugs. Tab. 7.16 lists the various types.

7.5.3 SSS Cryostat

The LHC contains 474 Short Straight Sections cryostats in total, 360 of the Arc type (10 variants), 64 of the Dispersion Suppressor type (7 variants) and 50 of the Matching Sections type (26 variants).

A standard section cryostat comprises three main sub-assemblies: the standard section cryostat, the cryogenic service module and the jumper connection. The standard section houses the cold mass and is of a similar design to the cryo-dipole cryostat (Sec. 7.4).

The cryogenic service module (QQS) contains the Beam Position Monitor (BPM), instrumentation and dipole corrector feed-through and, depending on the SSS variant, the insulation vacuum barrier. In combination with a jumper it houses the cryogenic interconnects to the LHC Cryogenic Distribution Line (QRL) and a helium phase separator together with its instrumentation.

For the SSS-Arc (see Fig. 7.15), the combination of one of two standard section cryostats with one of three different QQS units and one of two different jumpers leads to the 10 different cryostat variants. Similar cryostat modularity is achieved for the SSS-DS and SSS-MS cryostats.

Vacuum vessels

The vacuum vessel of the SSS standard section cryostat follows the same design as that of the cryodipole (Sec. 7.4.1) with the exception of the two-support posts version for the SSS-Arc and SSS-DS. The difference with the cryodipole vacuum vessel design used for the long SSS-MS, is that these vessels are made of a standard 36 inch tube of only 8 mm thickness and the cast steel cradle integrate also the lifting points for the SSS. No circumferential reinforcement rings are needed for this type.

Each SSS Standard Section vacuum vessel has two 36 mm diameter, 1 mm wall thickness stainless steel pumping tubes, allowing the pumping of the beam vacuum.

The vacuum vessel of the QQS section, made out of AISI 304L grade stainless steel, consists of a cylindrical tube of 6 mm thickness and an outer diameter of 1006 mm. Different ISO standard flanged ports allow a vacuum tight feed-through for the BPM coaxial cables, instrumentation capillary and thermometers. QQS with jumper units are completed with an interface weld flange of 365 mm diameter.

The dimensional precision and stability of the finished vacuum vessels is particularly important and must be better than 50 μm. Vibration techniques are used to reduce the internal stresses in all structural welds as far as possible.

In normal operation, the vessels will be under vacuum. In case of a cryogenic leak, the pressure can rise to 0.14 MPa absolute and in addition, sudden local cooling of the vessel wall to about 230 K may occur. The steel selected for the standard section cryostat vacuum vessel wall was tested to demonstrate adequate resilience during a standard Charpy test at -50°C.

All flanges of both vacuum vessel types are ring forged in AISI 304L stainless steel and welded to the vessel using TIG or MIG methods and according to ISO or Euro-norm standards. One layer of anti-rust primer and 2 layers of epoxy paint to RAL 7035 specification are applied to protect the outer surfaces only. The inner surface is shot-blasted for high vacuum compatibility.

Thermal shielding, bottom tray assembly and MLI

The thermal shield bottom tray assemblies for the SSS are of identical design and manufacture as the cryodipole type (Sec. 7.4.2). The SSS with an insulation vacuum barrier (about 25 %), have the bottom tray profile in two sections, welded together during cryostat assembly following integration of the vacuum barrier. The thermal shield of the SSS is of identical design and manufacture to the cryodipole type.

The set of MLI blankets including all blankets and pads needed to equip one SSS cryostat and its cold mass and the QQS, is obtained from industry as an installation kit. The blankets are of identical design and manufacture to those of the cryodipole. In addition to the Standard Section cryostats, MLI blankets are required for the QQS and the jumper tubes.

The insulation vacuum barrier has its MLI blankets installed before its integration into the SSS cryostat. The same technique is applied for the blankets of the two pumping tubes of the standard section cryostat vacuum vessel.

The blankets are designed in such a way that they can be easily handled using clean cotton gloves and rapidly assembled with a minimum of tooling by a maximum of two trained technicians. All other technical details, performance and fixation techniques are identical to those of the cryodipole.

Support posts

The SSS support posts are identical to those of the cryodipole (Sec. 7.4.3); only the overall height is adapted to the free distance between cold mass and vacuum vessel seats of the SSS. With two support posts, SSS-Arc and SSS-DS have the upstream post bolted onto the vacuum vessel to give the SSS the longitudinal reference point. In the case of SSS with three support posts, the central post acts as the longitudinal reference point.

Insulation vacuum barrier

The insulation vacuum barrier (Fig. 7.20) is a leak-tight, flexible thin-shell structure welded between the cold mass and the vacuum vessel of the SSS cryostat.

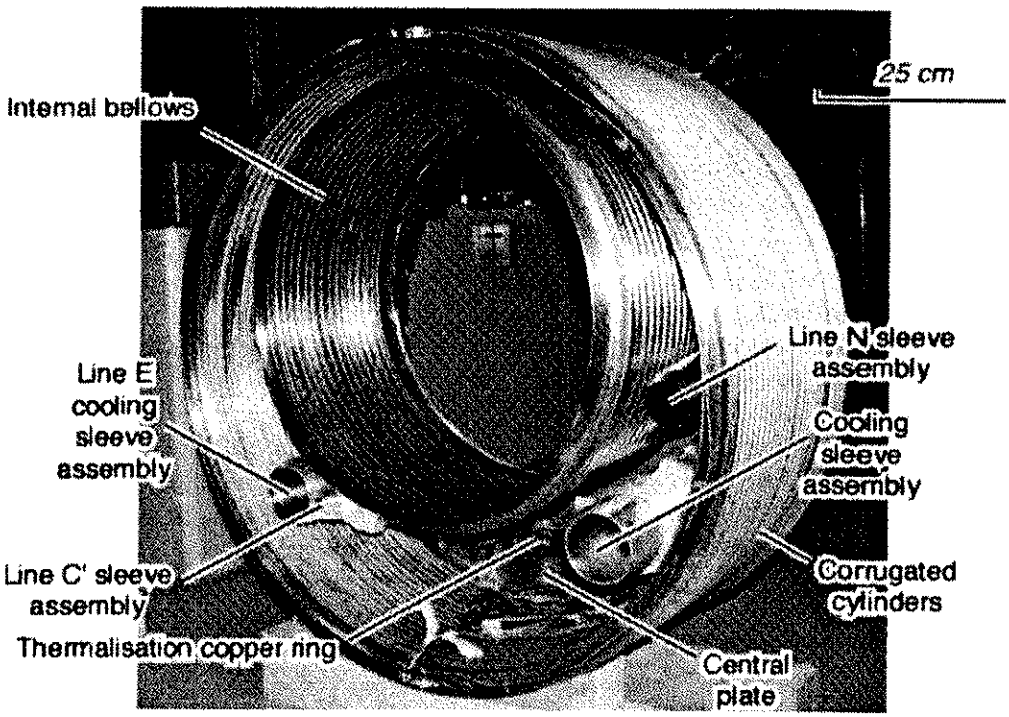

Figure 7.20: Insulation vacuum barrier

The function of the insulation vacuum barrier is to sectorise the insulation vacuum of the machine cryostats, facilitating machine installation and commissioning, and allowing the detection and containment of leaks in limited vacuum compartments of the machine during operation. The insulation vacuum barrier is designed to withstand the differential thermal contractions between cold mass, vacuum vessel and cryogenic

lines. As it constitutes a thermal bridge between the cold mass at 1.9 K and the vacuum vessel at ambient temperature, the vacuum barrier is also designed for low conduction and radiative heat in-leak.

The insulation vacuum barrier consists of two thin-walled corrugated cylinders and one large diameter internal bellows supported by a 6 mm thick central plate. The outer diameter is 950 mm and the inner diameter is 580 mm. Interface rings allow assembly by welding of the insulation vacuum barrier to the cold mass and the vacuum vessels of the SSS.

Four cylindrical sleeve assemblies with a bellows and welded onto the central plate, provide leak-tight feedthroughs for cryogenic lines across the insulation vacuum barrier. The two cooling sleeve assemblies are equipped with leak-tight bi-metallic transitions (stainless steel to aluminium).

A thermalisation copper ring, vacuum brazed to the central plate and to the cooling sleeves, extracts conduction heat from the central plate.

Helium phase separator

Helium phase separators form part of the 1.9 K refrigeration system. The plane of the LHC tunnel is tilted by 1.4% with respect to horizontal. The cryogenic architecture of the LHC imposes that the magnet string to be cooled is always upstream of the SSS-QRL. This implies that half of the SSS will have their helium phase separator cryogenically linked to the SSS housing them and the other half to the adjacent machine cryostats. At the lowest point of the LHC tunnel the helium phase separator has two internal filler tubes and is cryogenically connected on both sides.

The helium phase separator consists of upper and lower cylindrical helium enclosures, the latter is larger in order to obtain the 18 litre total helium storage capacity that is required. Both enclosures are linked together by a large size tube and a small back-up line on the top. The enclosure houses the helical wound filler tube entering from the jumper interconnect, passing through with its brazed copper section, which maximises heat exchange, and exiting through the interconnect tube to the upper enclosure. A pumping tube links the upper enclosure to the QRL.

Apart from the brazed copper section, all parts of the helium phase separator are of AISI 316L or 304L austenitic steel.

SSS cryostat assembly

Specific tools have been designed, built and installed in a purpose built factory complex to allow the industrial assembly of SSS (see Fig. 7.21). These assembly benches allow the SSS Cold Mass to be equipped

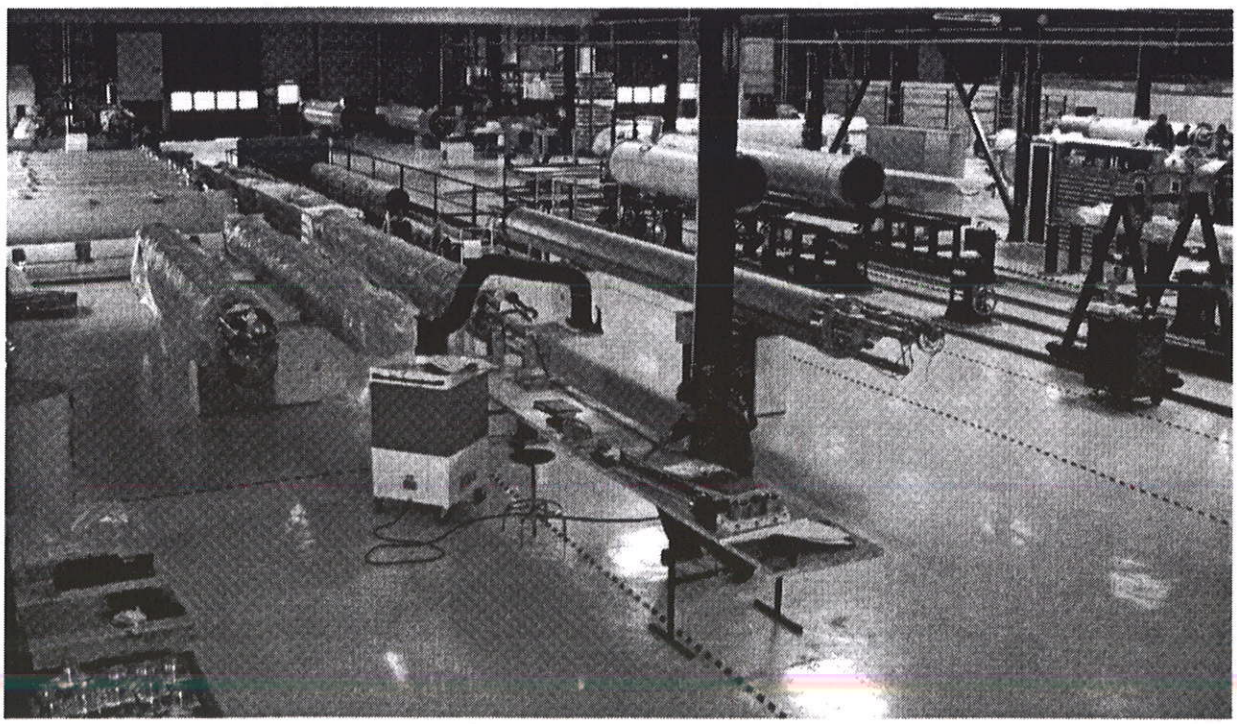

Figure 7.21: Hall 904 : SSS cryostat assembly at CERN

with its thermal insulation and other ancillary equipment before being integrated and positioned precisely inside its individual standard section cryostat. Individual work posts for the QQS assembly, and columns equipped with welding jigs and positioning gauges for the jumper connection assembly, complete the SSS cryostat assembly facility. The final tooling set allows a normal assembly rate of up to four SSS cryostats per week in one shift to be reached.

7.6 ORBIT AND MULTIPOLE CORRECTORS IN THE ARCS

7.6.1 General Design Principles

About 3800 single aperture and 1000 twin aperture corrector magnets will be used in the LHC. The 194 mm beam separation gives sufficient lateral space to build all correctors as single bore modules, with a nominal working point between 40 – 60 % along the load line. Twin aperture units are assembled by keying corresponding modules into laminated support structures. The assembly by keying ensures mechanical precision and allows flexibility during mounting, since the same type of module is used for a normal or skew magnet. To optimise the cost of the corrector magnets, common design and fabrication principles [47, 48, 49] are applied:

- Use of flat multi-wire ribbon to reduce the number of winding turns of a coil.
- Counter-rotating winding for automation of coil fabrication and suppression of layer jumps and spacers.
- Enhancement of the field using so-called scissor laminations placed close to the coils, made of magnetic material and which transfer the pre-stress.
- Pre-stress applied by shrinking rings so as to avoid the use of a press.
- Multipole correctors of higher order than the sextupole, i.e. octupole, decapole and dodecapole, are built with half the number of coils with respect to the number of poles, which is more economical. This only produces small asymmetries in the ends, which are acceptable.
- Quench protection [50] for series connected magnets is provided by parallel resistors combined with energy extraction systems.

A summary of the corrector magnet types is given in Tab. 7.17

Table 7.17: Overview of corrector magnet types and location

Name	**Description**	**Location**
MCS	Sextupole multipole corrector	Main MBA & MBB dipoles
MCDO	Nested Decapole-Octupole multipole corrector	Main MBA dipoles
MSCB	Sextupole-Dipole Corrector (lattice chromaticity & orbit). Exists in 4 variants with all combinations of normal & skew fields.	Main quadrupoles (SSS), dispersion suppressors
MQT, MQS	Tuning and Skew Quadrupoles	Main quadrupoles (SSS)
MO	Octupole Lattice Corrector (Landau damping)	Main quadrupoles (SSS)
MCBC, MCBY	Dipole correctors (orbit)	Insertion region and dispersion suppressors
MQTL	Long Trim Quadrupole	Insertion region and dispersion suppressors
MCBX MCBXA = MCBX+MCSTX	Inner Triplet nested Horizontal & Vertical Dipole Orbit corrector. MCBX with a nested 6-pole, 12-pole corrector insert.	Inner Triplets
MQSX	Skew quadrupole	Inner Triplets
MCSOX	Nested skew sextupole, octupole, skew octupole corrector package	Inner Triplets

Superconducting strands

The fabrication of coils for the different types of corrector magnets, which are rated for currents ranging from 50 A to 600 A, can be implemented by using only 4 different strands. Each strand consists of a multi-filamentary, Nb-Ti superconductor with a copper matrix, insulated by a layer of insulating enamel. The superconductor filaments have a nominal diameter in the range 6 to 7 μm. The strand cross-section is round for one type and rectangular for the others. The external dimensions of the strands are made with a precision of 0.01 mm. The main parameters for the superconducting wires are given in Tab. 7.18.

Table 7.18: Main parameters of the corrector magnet superconducting strands

	Type 1	**Type 2**	**Type 3**	**Type 4**
Overall dimensions (mm) (insulated)	∅ 0.435	0.38×0.73	0.73×1.25	0.97×1.65
Metal dimensions (mm)	∅ 0.375	0.32×0.67	0.61×1.13	0.85×1.53
Nominal Insulation Thickness (mm)	0.03	0.03	0.06	0.06
Critical current at 4.222 K and 5 T (A) Perpendicular to wire axis Perpendicular to broad face Parallel to broad face	>55	 >100 >110	 >630 >700	 >1190 >1320
Copper Matrix RRR	> 100			
Cu/Sc volume ratio	≥ 4.0-4.8	≥ 4.0-4.8	≥1.6-1.9	≥1.6-1.9
Superconductor	Nb-Ti with Ti = 47.0 % by weight			
High voltage insulation (V)	1000			
Insulation material	PVA enamel			

7.6.2 Spool Piece Corrector Magnets of the Main Dipoles

MCS

The MCS spool pieces [51] are single-aperture sextupole magnets mounted in pairs on both MBA and MBB main dipole cold masses. The main design parameters are given in Tab. 7.19. Each MCS magnet consists of six coils, a laminated iron yoke, an aluminium shrinking cylinder, an end plate that houses the electrical connections and an iron magnetic shield. A picture of an MCS magnet is shown in Fig. 7.22.

Table 7.19: MCS design parameters

Nominal main field strength	1630 T/m^2
Magnetic length	110 mm
Nominal operation current	550 A
Working temperature	1.9 K
Superconductor	Type 3
Short sample critical current at 4.2 K/1.9 K	950/1300 A
Self inductance	0.8 mH
Aperture diameter	58 mm
Overall length	155 mm
Mass	~10 kg

The coils are made by counter-winding a single superconducting strand wetted with epoxy around a G11 central post. After curing, the coils are assembled on a mandrel, wrapped with a glass-fibre/epoxy pre-preg bandage and cured again to make an MCS coil assembly. The MCS magnet module is built by stacking the eccentric yoke laminations (so-called scissor laminations) around the MCS coil assembly and shrink fitting the aluminium shrinking cylinder [3]. The radial interference between the inner diameter of the shrinking cylinder and the outer diameter of the yoke lamination stack is chosen such that the correct pre-stress is produced at operating temperature. This interference is obtained by precise machining of the cured coil assembly outer diameter. Precise dowel holes in the end plate allow accurate placement of the magnet module within the magnetic shield. The magnets are mounted on their support plate in the dipole cold mass by means of a bolted flange. This flange contains a pair of accurately drilled holes for dowelling to the support plate. Coil inter-connections are made by ultrasonic welding. Quench protection resistors are connected in parallel with each magnet and mounted in the gap between the shrinking cylinder and magnetic shield.

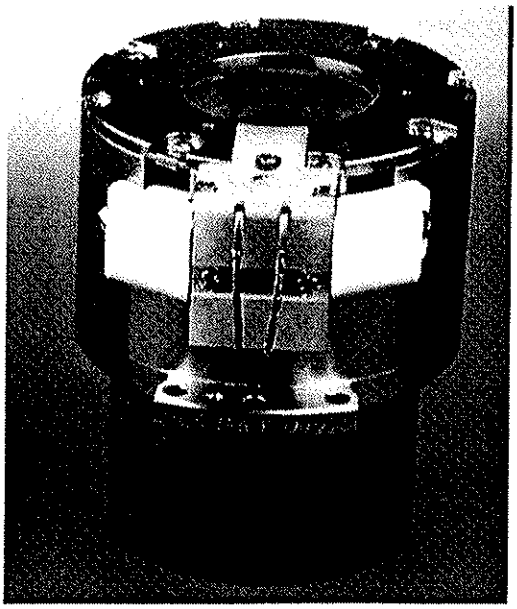

Figure 7.22: MCS magnet.

MCDO

The MCDO spool pieces [51] consist of an assembly formed of a single-aperture decapole (MCD) magnet with an octupole (MCO) insert. These spool pieces are mounted in pairs only on the MBA main dipole cold masses. The design parameters are given in Tab. 7.20.

Each MCD magnet module consists of five coils, a laminated iron yoke, an aluminium shrinking cylinder, an end plate that houses the electrical connections and an iron magnetic shield. It is built in a similar manner to the MCS magnets. The MCO insert is made from 4 coils, in a similar way to the MCS and MCD coil assembly. The MCO insert fits into the bore of the MCD magnet module. Precise dowel holes in the end plates of the MCD and MCO coil assemblies allow accurate location of the MCD and MCO within the magnetic shield.

Table 7.20: MCDO design parameters

	MCD	MCO
Nominal main field strength	1.2×106 Tm^{-4}	8200 Tm^{-3}
Magnetic length	0.066 mm	0.066 mm
Nominal operation current	550 A	100 A
Working temperature	1.9 K	1.9 K
Superconductor	Type 3	Type 2
Short sample critical current at 4.2 K	915 A	195* A
Short sample critical current at 1.9 K	1250 A	297* A
Self inductance (MCD/MCO)	0.4 mH	0.4 mH
Aperture diameter	58 mm	58 mm
Overall length	110 mm	110 mm
Total Mass	~ 6 kg	

*MCD powered with 550 A

7.6.3 Lattice and Orbit Correctors in the Short Straight Sections of the Main Arc

MQT and MQS

The tuning quadrupole (MQT) [52] and the skew quadrupole (MQS) each consist of a pair of single-aperture quadrupole modules mounted in a twin-aperture support structure. The MQS magnet modules are identical to the MQT magnet modules except that they are rotated by 45° with respect to the coil assembly end plate. Consequently, the MQS field is the same as the MQT field but rotated by 45°. Also, the completed MQT and MQS twin-aperture assemblies are externally identical. The design parameters of MQT are given in Tab. 7.21.

Table 7.21: MQT/MQS design parameters

Nominal main field strength	123 T/m
Magnetic length	0.320 m
Nominal operation current	550 A
Working temperature	1.9 K
Superconductor	Type 3
Short sample critical current at 4.2 K/1.9 K	670/945 A
Self inductance	0.03 H
Aperture diameter	56 mm
Overall length	380 mm
Module mass	25 kg
Total mass including the twin aperture support structure	250 kg

Each MQT or MQS magnet module consists of four coils, a laminated iron yoke, an aluminium shrinking cylinder in 2 sections and an end plate that houses the electrical connections. The coils are made by counter-winding three superconducting wires, pre-assembled as a flat cable, around a G11 central post. The flat cables are wet wound and the completed coil is cured in a mould. The finished coils are assembled on a precise mandrel together with the connection plate, wrapped with a glass-fibre/epoxy pre-preg bandage and cured to make an MQT or MQS coil assembly (the type is determined by the orientation of the connection plate with respect to the coils). The MQT/MQS magnet module is built by stacking the eccentric yoke laminations around the coil assembly and shrink fitting the aluminium shrinking cylinder sections [49]. The radial interference between the inner diameter of the shrinking cylinder sections and the outer diameter of the yoke lamination stack is chosen such that the correct pre-stress is produced at operating temperature. Accurately machined keyways on the outer diameter of the shrinking cylinder locate the magnet modules within the twin-aperture support structure. Coil inter-connections are made by ultrasonic welding. The support structure is assembled from stacked steel laminations dowelled together and compressed with tie-rods in between steel end plates. Quench protection is ensured by resistors connected in parallel with each module and mounted on the support-structure end plate at the connection end of the magnet assembly.

MO

The MO Landau damping octupole magnet assemblies consist of a pair of single-aperture octupole modules mounted in a twin-aperture support structure. The design parameters of the MO are given in Tab. 7.22.

Each MO magnet module consists of four coils, a laminated iron yoke, an aluminium shrinking cylinder and an end plate that houses the electrical connections. The coils are made by counter-winding a single superconducting wire around a G11 central post. The coil module and magnet assembly is similar to that of the MQT and MQS corrector magnets. Quench protection is ensured by resistors connected in parallel with each module and mounted on the support-structure end plate at the connection end of the magnet assembly.

Table 7.22: MO design parameters

Nominal main field strength	6.31×10^4 T/m^3
Magnetic length	0.320 m
Nominal operation current	550 A
Working temperature	1.9 K
Superconductor	Type 3
Short sample critical current at 4.2 K/1.9 K	15/1310 A
Self inductance	1.6 H
Aperture diameter	56 mm
Overall length	380 mm
Module mass	~ 8 kg
Total mass including the twin aperture support structure	~ 250 kg

MSCB

Table 7.23: Main parameters of MSCB correctors

	MCBM	MSM
Nominal main field strength	2.93 T	4430 T/m^2
Magnetic length	0.647 m	0.369 m
Nominal operation current	55 A	550 A
Working temperature	1.9 K	1.9 K
Turns per coil	1725 (25 x 69)	112 (8 x 14)
Superconductor	Type 1	Type 3
Peak field	3.15 T	4.37 T
Quench margin	43 %	38 %
Theoretical quench current	96 A	887 A
Stored energy	9.12 kJ	5.4 kJ
Self inductance	6.0 H	0.036 H
Overall length of individual modules	785.2 mm	455 mm
Overall length of MSCB	1260 mm	
Aperture	56 mm	56 mm
Individual mass of magnet modules	143 kg	83 kg
Total mass of MSCB	1000 kg	

The LHC Short Straight Sections (SSS) are equipped with 1260 mm long combined superconducting dipole and sextupole corrector magnet assemblies, MSCB [53, 54]. The dipole and sextupole magnets of the two rings are mounted in pairs in a common twin aperture support structure. The 0.465 m long MSM sextupole magnets and the 0.795 m long MCBM dipole magnets are fabricated as independent modules having an outer diameter of 192 mm. The sextupoles, which are grouped in families of 13 magnets, are used to correct the natural chromaticity produced by the focusing elements and the individually powered dipole is used for the closed orbit correction. Each dipole pair consists of a horizontal orbit corrector (vertical dipole field) for one aperture and a vertical orbit corrector (horizontal dipole field) for the other one, hereafter referred to as MCBH and MCBV respectively. The MCBV is realised by turning the MCBH by 90°.

The sextupoles in each MSCB are mounted so as to provide either a normal or a skew sextupole field, hereafter referred to as MS and MSS, respectively. The MSS is realised by turning the MS clock-wise by 90°. The design parameters of the MSCB are given in Tab. 7.23. Two cross-sections of the MSCB are shown in Fig. 7.23.

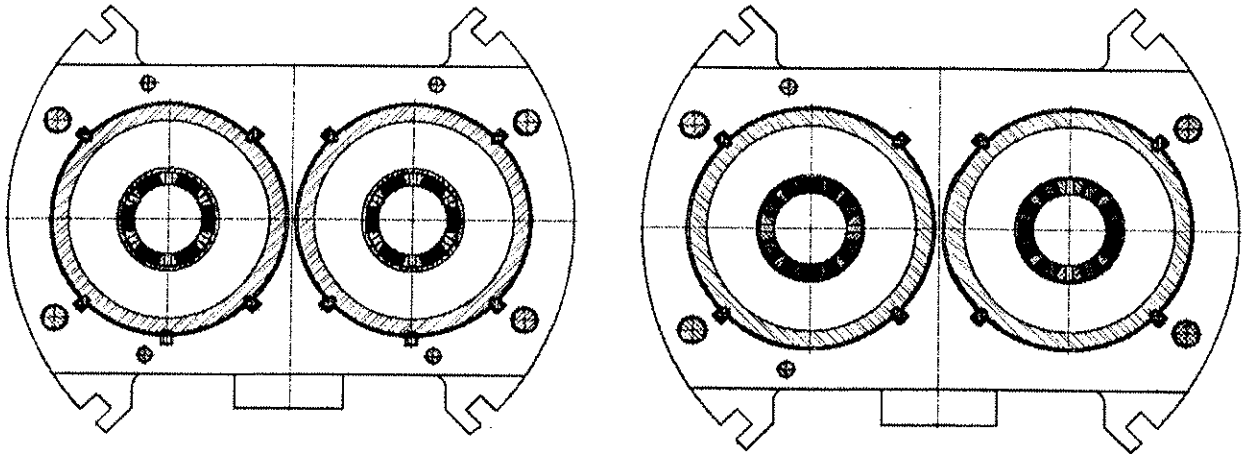

Figure 7.23: Cross-sections of MSCB. On the left at the MS location, on the right at the MCB location.

MSCB construction and assembly

Each dipole module consists of two vacuum impregnated dipole coils, a laminated iron yoke, aluminium shrinking cylinders and an end plate, which houses the electrical connections. The dipole coils are made by winding 25 superconducting wires, pre-assembled as a flat cable, around a copper central post and composite end-spacers. The superconductor has a round cross-section and is enamel insulated. The sextupole assemblies are constructed in the same way as the dipoles except that the six coils are counter-wound with 4 rectangular superconducting wires, pre-assembled as a flat cable.

Pre-compression is applied to the coils by shrink fitting an aluminium cylinder over the eccentric steel laminations that make up the yoke. The pre-compression is determined by the interference fit between the aluminium shrink ring and the yoke laminations around the coils.

Accurately machined keyways in the outer diameter of the shrinking cylinders are used to locate the modules within the twin-aperture support structure. Coil inter-connections of the dipole coils are soft-soldered and in the case of the sextupole they are made by ultrasonic welding.

The support structure is assembled from stacked steel laminations dowelled together and compressed axially with tie-rods in between thick steel end plates. Quench protection resistors are connected in parallel with each sextupole module and mounted on the support-structure next to the terminal for the bus-bar connections.

The MSCB assembly is a part of the cold mass of the SSS. It is centred in the inertia tube of the SSS by a set of keys located on the outer radius in a similar way as the main quadrupoles.

7.7 THE MAGNET TEST FACILITIES

7.7.1 General Goals

The LHC magnets must satisfy strict performance requirements throughout extensive tests in cold conditions prior to their installation in the machine. The SM18 test station at CERN is equipped with 12 benches and the necessary cryogenic infrastructure to operate for about 7000 hours per year in order to perform the power tests and magnetic measurements of the 1750 cold masses.

For the MB (main dipole magnets) it is required that the nominal field of 8.3 T is exceeded after the second training quench, the 9 T ultimate field after the 8th quench. Similar criteria are still under study according to results of pre-series magnets for the MQ MQM and MQY quadrupoles. The technology to localise weak points was developed during the prototyping phase of the LHC magnets [38]. The long coil-bearing shafts used for the magnetic measurements will be used as "quench antenna" for the series tests.

The magnetic measurement equipment has been developed and tailored to measure 100% of the main families of cold mass: the cryodipoles and the short straight sections (SSS's). For both, the main objective of the measurement is to provide the integrated field strength, the average field direction, the magnetic length and the steady state field error components as a function of the operating current. For the SSS's it is planned

in addition to measure the magnetic centre of the main quadrupoles and of the corrector packages in the cold mass, to provide the magnetic fiducialisation to be used for installation.

The measured field at relevant operating conditions, and in particular injection and flat-top, is used directly to accept the magnet for installation.

In addition, the measurements are used to quantify the main sources of field imperfections. These errors fall into two categories: errors which are of steady state nature (geometric errors, saturation effect, persistent current), and those which are dynamic (ramp rate effect, persistent current decay). The static errors are deduced from measurements at constant current along the magnet load-line, beginning at values of current below injection (e.g. 400 A for dipoles) and up to current above the nominal operating point (e.g. 12 kA for dipoles). The effect of the nominal ramp rate on the harmonics is obtained by cycling the magnets between the injection current and the nominal current. The effect of the persistent current decay at injection is quantified during a machine cycle with a simulated injection plateau. Finally, the measured field and in particular the geometric errors deduced from static measurements, are used to establish warm-cold correlations that are of paramount importance for steering the production (see warm measurements).

The electrical insulation at 1.9 K is systematically tested at 3.5 kV for the MB and 1.9 kV for the MQ with an allowed leakage current of 20 mA. The quench heaters protecting the magnets against high temperature and internal voltages during quenches are systematically tested, in particular the time delay needed to propagate the quenches.

7.7.2 The SM18 Test Infrastructure

The facility for cold testing of all LHC-main dipoles and quadrupoles is installed in the SM18 hall on the French site close to the border.

Once a magnet has undergone preliminary tests at room temperature it is prepared in the SMA18 hall, close to SM18, for cold tests. This preparation consists, among other things, of mounting an "anti-cryostat": a pipe fitted with electrical heaters inserted into each of the two apertures. The anti-cryostat allows the magnetic field measuring equipment (rotating coils) to be inserted and maintained at room temperature and atmospheric pressure along the magnetic field to be measured, while the magnet itself and its beam pipes are at cryogenic temperatures and under vacuum.

The twelve test benches form six pairs, each sharing one set of power converters (13 kA and 600 A), and the electronics for controls and data acquisition. After the cold test, warm up and disconnection, the magnet is transported back to the SMA18 hall where the auxiliary fittings, only required for the test, are removed.

Each of the twelve benches is able to receive either a main cryodipole or a much shorter SSS. The necessary bench reconfiguration requires a couple of days, therefore it is planned to minimize the number of reconfigurations. To test the 116 special SSS needed for the insertion and matching sections of the accelerator, special adapters are required in order to match their specific interfaces to those of the CFB, of the mechanical supporting structures and of the MRB.

7.7.3 Cryogenic System and Operational Performance Needed

Two cryoplants are used to supply liquid helium for the cold tests of the 1750 cold masses for the LHC. The PM18 18 kW plant already in his final location for the LHC is able to cover the full series test. A 6 kW plant installed in the SM18 hall and planned to be used to service the reference magnets systems once the LHC is in operation can be put in operation as a spare. Both can feed a 25000 litre, liquid helium dewar linked to the 12 test benches. A pumping capacity of 18 g/s at 12 mbar allows up to 9 sub-cooling cycles down to 1.9 K per day. This translates to a maximum of 3 cold masses per day with a maximum of two quenches per cold mass.

7.7.4 Operational Aspects Related to the 12 Benches

Optimisation of the test resulted in a split of the test sequence into 9 slices lasting 12 hours each. This optimisation takes care of the equipment for the cool-down and warm-up of the cold masses and will allow the testing of 2 cold masses per day on 9 of the 12 benches.

- 12 hours to connect a cold mass to the CFB,

- 12 hours to pump the vacuum enclosure of the CFB-Cryomagnet assembly,
- 12 hours to reach 90 K in the cold mass with circulation of gaseous helium at 80 K,
- 12 hours to reach 4.5 K, then to fill it with liquid helium and then make the first sub-cooling to 1.9 K
- 26 hours of cold tests including the magnet training (5 hours are needed to recover from a quench),
- 12 hours to warm-up the cold mass from 10 K to room temperature with circulation of gaseous helium at 320 K,
- 12 hours to disconnect and remove the cryomagnet from the test bench.

The remaining three benches will perform detailed test or thermal cycles in case of doubtful performance or will test the more complicated insertion and matching section, SSS. They will make use of the remaining cryogenic power. In this way, the overall throughput of the test station can be brought to 2.5 magnets a day. The standard cycle for dipole tests is shown in Fig. 7.24.

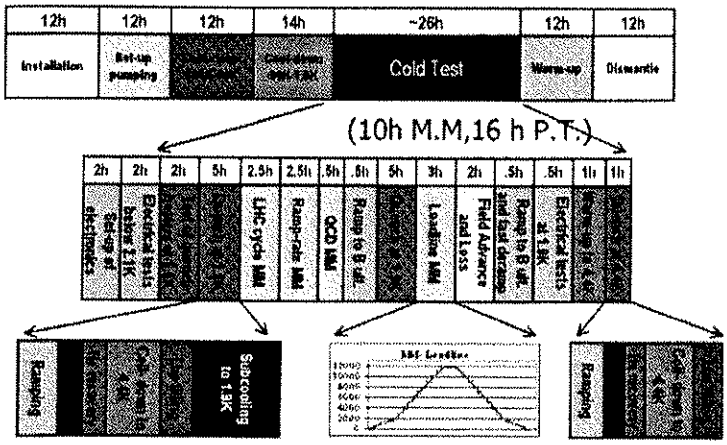

Figure 7.24: Standard Cold Tests foreseen for series MB's

7.7.5 The Test Station for Cold Tests of LHC Correctors and Prototype Magnets

Constantly upgraded over the past years, the former test facility for the LHC short model dipoles [39] is used in series production to validate the performance of the various types of the LHC quadrupoles (MQ, MQM, MQY) before their integration in the SSS, and all types of corrector magnets.

The full reception tests of two small series of correctors, MQSX and MCBX, will be performed, while for the quadrupoles and the other correctors it is foreseen to perform cold tests of a fraction of the series production.

Four vertical cryostats, of different sizes, three of which can operate at superfluid helium temperatures, give flexibility to test magnets with overall geometry up to 3.6 m in length and 0.54 m in external diameter, and mass up to 5 tons. Power performance and field quality measurements are routinely performed, at an average rate of one test per week.

The cryogenic architecture of the installation is composed of a central dewar of 2000 litre capacity for liquid helium which feeds the cryostats. The main parameters of the cryostats are given in Tab. 7.24. The processes of cool down, warm up, operation at set temperatures and recovery after quench are semi-automatic and remotely controlled. The helium circuit is integrated into the cryogenic network of the CERN North Area.

Magnetic measurements are performed by means of rotating coils with a system that covers 1300 mm maximum length. Calibrated pick-up coils are mounted on glass-fibre vertical shafts, rotating in liquid helium in the magnet bore (Fig. 7.25). The magnet-to-lambda-plate and cold-to-warm transitions are equipped with bellows which are torsionally stiff but which allow axial misalignments.

Table 7.24: Technical parameters of the four cryostats

Cryostat		Station 1	Station 2	Station 3	Station 4
Useful height	[mm]	1498	3800	2300	1000
Useful diameter	[mm]	800	600	300	500
Current leads	(18 kA)	2	2	-	2
Current leads	(2 kA)	-	2	4	-
Current leads	(800 A)	-	1	-	-
Current leads	(150 A)	4	-	-	-
Cool-down time	300 K - 4 K	20 hrs	30 hrs	12 hrs	5 hrs
Cool-down time	4 K – 1.9 K	7 hrs	10 hrs	3 hrs	-

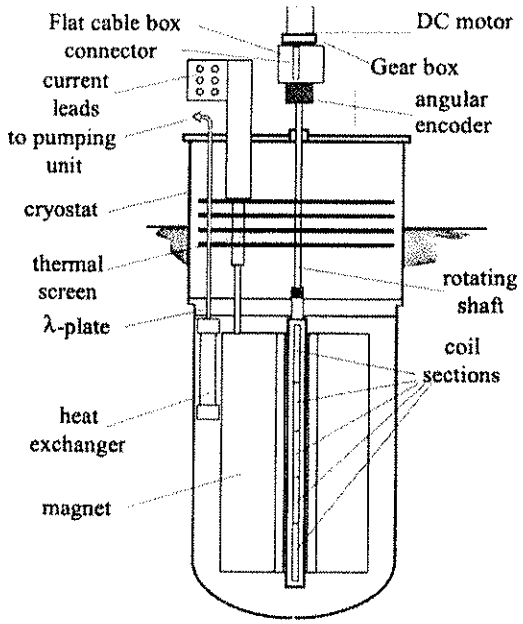

Figure 7.25: Magnetic measurement system in a vertical cryostat.

7.7.6 Field Quality Measurement Equipment

Based on the long standing experience of previous accelerators, the measurement technique of choice for the LHC magnets is the harmonic coil method [42]. The implementation of this principle is different depending on the magnet to be measured (dipole, quadrupole, corrector), the measurement conditions (warm, cold) and specific measurement requirements.

In addition to rotating coils, stationary coils and stretched wire systems provide field measurements and can be used either for the determination of the magnetic axis, or for cross calibration purposes.

Long shafts for cryodipoles

Cryodipoles are measured using modular assemblies of ceramic tangential coils that have a total length of 16 m, as shown in Fig. 7.27. This device is usually referred to as a long shaft. The 16 m long shaft is composed of 13 identical modules, each 1.26 m long when assembled, covering the total length of the magnet aperture. Each module consists of a ceramic pipe providing the necessary rigidity, on which two tangential (A, E) and one central (C) pick-up coils are mounted. The high order harmonics are obtained by suppressing the contribution of the dipole field. This is achieved by taking the difference of the signals from the A and C coils (compensated signal). The coil E is used as a spare.

The coil rotation radius (17 mm maximum, imposed by the available space in the anti-cryostats) and the width of the coils guarantee acceptable sensitivity up to the 12^{th}-order harmonic. The length of the pick-up

coils is 1.15 m. Between each module there is a 110 mm gap to house the rotating bearings and the cable inter-connects. The length of each coil and the sum of the gaps have been chosen to be equal to an integer multiple of the cable twist pitch so as to guarantee that the effect of the periodic field pattern cancels in the total field integral. The shaft covers the 15 m long LHC dipole and the adjacent corrector magnets.

The two coil shafts (one per aperture) are driven by a Twin Rotating Unit equipped with a stepping motor and an angular encoder rigidly connected to an electronic inclinometer. Voltage signals from the rotating coils are first pre-amplified and then read-out simultaneously by a set of 52 digital integrators. The accuracy that can be achieved by the system is 3 units on b_1, 0.16 mrad for the average field direction and 1 ppm of the main field for the harmonics. In order to achieve the absolute b_1 accuracy and the average field direction quoted above an accurate and laborious calibration is necessary.

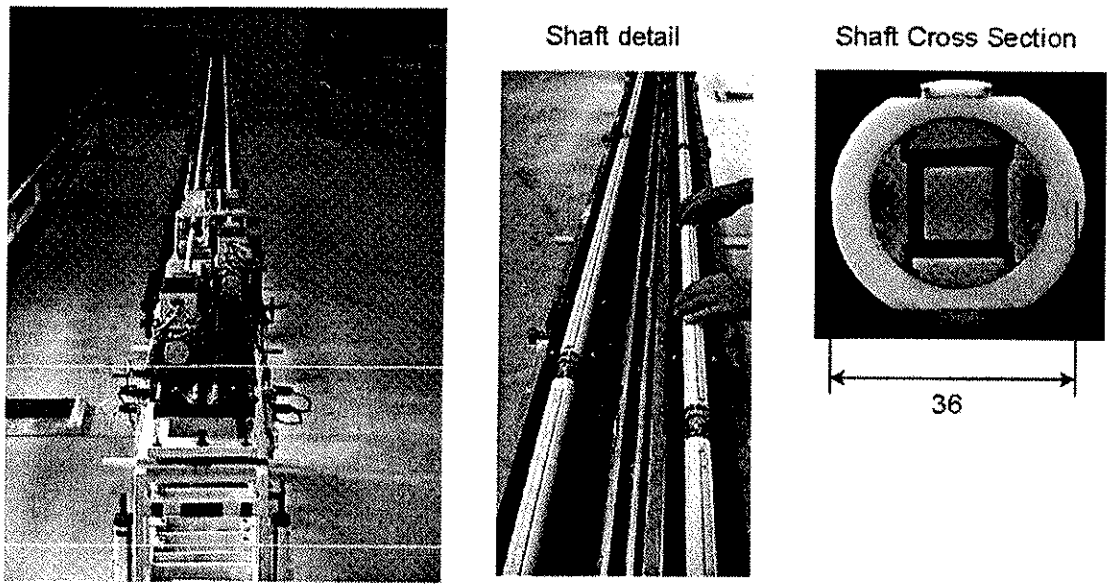

Figure 7.26: View of the pair of 16m long shafts used for the field measurement of cryodipoles. The cross section of the ceramic shaft, showing the coil winding, is also shown.

Scanner for SSS

The SSS scanner, shown in Fig. 7.27, measures both the magnetic field and the magnetic axis of quadrupole and corrector packages in the SSS. The core of the system is the probe, schematically shown in Fig. 7.28. It consists of two rotating coils supported against the anti-cryostat by ceramic ball-bearings which sit in bronze cages having spring-loaded longitudinal rollers. This support, the same used for the long dipole shafts, allows continuous and regular longitudinal displacement of the probe whilst still maintaining a well defined mechanical support. The two coils in the probe have different design and functions. The 0.6 m long harmonic coil contains five identical pick-ups placed radially in a fibre-reinforced epoxy composite. This coil is used for the measurement of the main field strength and harmonics. The 0.1 m long axis coil is assembled from four identical pick-ups placed tangentially on a fibre-reinforced epoxy support. A Light Emitting Diode (LED) is accurately positioned in the centre of this support, on its rotation axis, and can be surveyed from one end of the test bench. This short coil is used to measure the position of the local centre of the main field.

The rotation is transmitted to the coils from a computer-controlled rotating unit placed outside the magnet (stepping motor and gearbox, angular encoder) via a torsionally stiff 13 m long ceramic shaft. The angular encoder in the rotating unit provides the angular reference frame for the rotation of the measurement coils. The rotating unit can be displaced longitudinally on rails by a computer-controlled motorised transport system. The system has a reproducibility of 0.3 mm in longitudinal direction. As the rotating unit is moved longitudinally, a level meter mechanically fixed with respect to the angular encoder records the orientation of the rotating unit with respect to gravity.

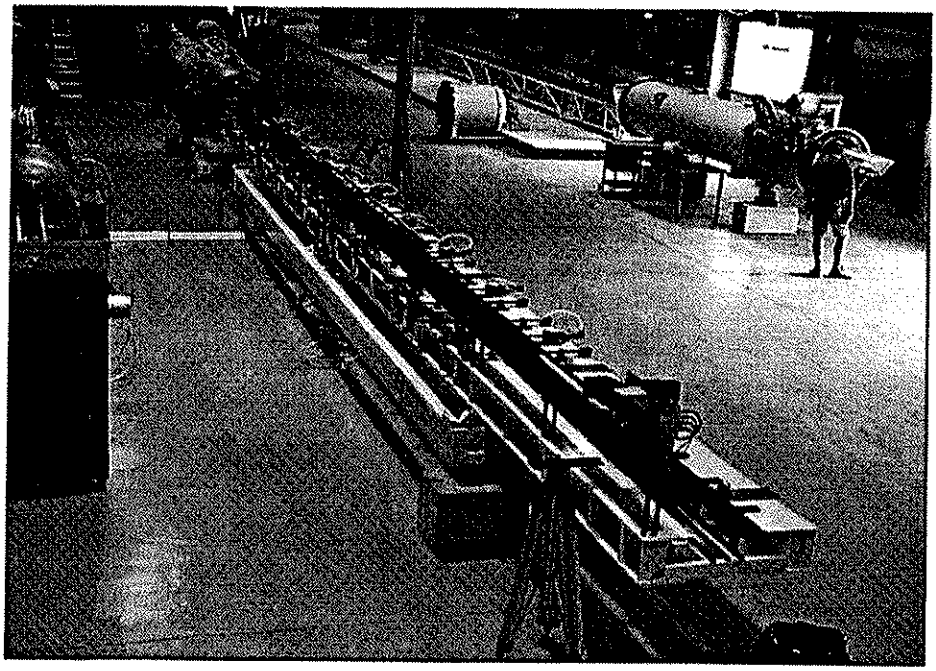

Figure 7.27: Automated scanner for the magnetic and axis measurement of the SSS.

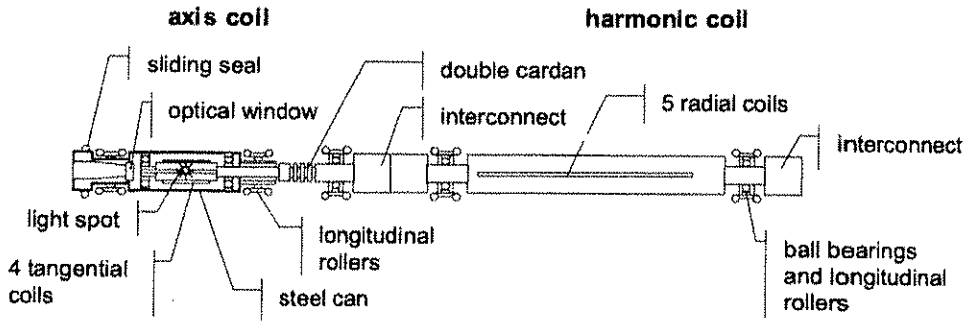

Figure 7.28: Schematic view of the SSS measurement probe consisting of an assembly of a 60 cm long harmonic coil and a 10 cm long axis coil.

To refer the centre coordinates to the SSS fiducials it is necessary to survey the location of the coil axis during the measurement. This is done by an alignment telescope equipped with a CCD camera and an on-board processor for image treatment mounted on the test bench, outside the SSS. The bore-sight is established prior to scanning the SSS using two reference positions, located ahead and behind the SSS in test. The reference locations are the magnetic axes of two short reference quadrupoles, whose fiducialisation is well known, stable and periodically checked. This intermediate step is necessary to establish the bore sight at the fiducial locations on the reference quadrupoles. The final step is then to measure the relative position of the SSS and reference quadrupoles fiducials. This is done using a LTD-500 laser tracker that operates in 3-D space around the test bench.

The target accuracy of the system is 5 units on B_2, 0.3 mrad for the average field direction and 1 ppm of the main field for the harmonics.

Long shaft for SSS

The scanner described above can measure all parameters of interest, but has the drawback of being relatively slow and cannot cope with all of the cold tests workload for the SSS production. For this reason a long rotating coil system (long shafts and twin rotating units) for field measurements of SSS's has been developed. This will provide the field, field direction and field harmonics in quadrupoles together with field and field direction in correctors.

The system is based on the same working principle as the long rotating coils for dipoles. It has the advantage of being able to measure the field in the two apertures with much higher efficiency than a scanner (simultaneous integral measurements in the two apertures). The drawback is that axis measurement is not possible with long coils, hence an additional measurement method is needed. For this the single stretched wire system will be used.

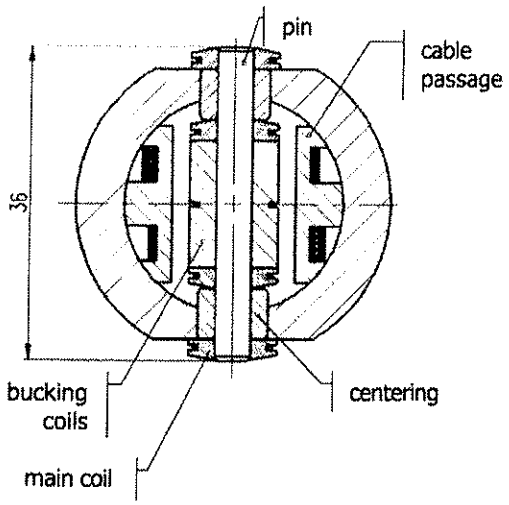

Figure 7.29: Schematic cross-section of an SSS measurement coil module, showing the location of the 5 coils.

Single stretched wire

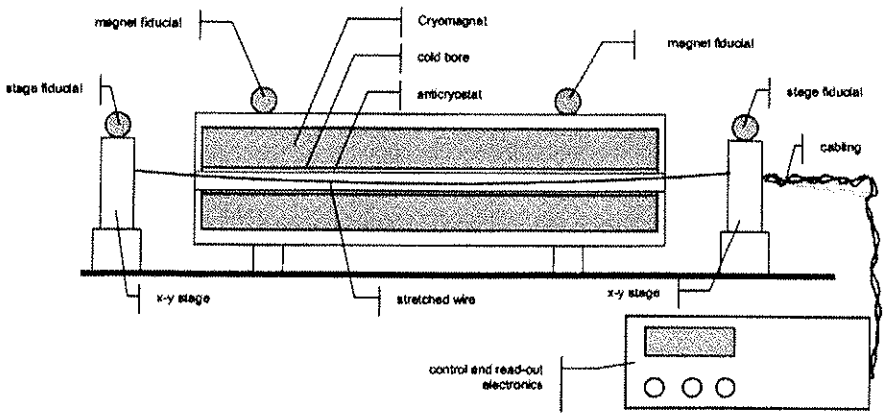

Figure 7.30 Schematic of the layout of a stretched wire system

A stretched wire system has been acquired through a collaboration with the Technical Division of FNAL, Batavia, USA. The principle of the system is based on moving a thin wire in the magnetic field to be measured, and integrating the voltage induced at the terminals. The voltage integral is equal to the flux change experienced by the wire from the initial to the final position. Using precision stages to move the wire, the motion itself can be known to high accuracy, thus allowing the calculation of the average field in the area spanned by the wire motion.

This system is used for the SSS axis measurement as a complement to magnetic measurements performed with long shafts and as a cross check of the rotating coil measurements of integrated gradient and direction. Fig. 7.30 shows the system schematically.

The system can measure dipoles (main field strength and average direction) and has been used to provide cross-calibration of the long shafts, as well as integrate information on field direction when calibration of the long shaft (a laborious procedure) is missing. The quoted accuracy of the system is 2×10^{-4} for the field integral, 0.1 mrad for the field direction and 10 m for the centre with respect to the system fiducials.

DIMM and QIMM moles for industry MB, SSS and MQW

Benches for warm magnetic measurements in industry have been designed and built for the dipoles (DIMM) and the quadrupoles (QIMM) [40, 41]. For the measurements, the magnets, which are in the normal conducting state, are excited with small currents ~10A. Both systems measure the field quality (harmonics and field angle) using the rotating coil method. The QIMM mole scans both apertures and is transported longitudinally by manual operation. DIMM has two moles working in parallel and the transport is motorised. In addition, it has a system to measure the longitudinal position of the mole in order to determine the magnetic length precisely. The DIMM system has been very useful in detecting assembly errors at very early stages: the result of these measurements is one of the holding points in the dipole production.

Moles for cold and warm axis measurements

The magnetic field axis is measured by means of a system with magnetic sensors (4 static tangential coils picking signals from the AC excited magnet) and position sensors (3D-laser tracker and light reflector) allow the detection of the magnetic field axis and the cold bore axis. Another capability of the system is to work for several field configurations (multipole of order n=1, 2, 3, 4 and 5). The system has been used to measure pre-series magnets and it has demonstrated that the mechanical and magnetic axis of the dipole agree within 0.2 mm. A second system has been designed to measure the field quality of the warm and cold main magnets by using the rotating coils method but under operational conditions (1.9 K, 8 Tesla). It can measure dipole field angle, harmonics and corrector axis, by a longitudinal scan inside an anti-cryostat. To detect the mole position inside the anti-cryostat it has an optical system (LED and external telescope) which needs to be operated under vacuum to avoid air temperature gradients that perturb the optical measurement.

Benches for warm measurements of correctors in industry

Benches for warm magnetic measurements have been designed and built in order to monitor the tolerances specified for the corrector magnets during fabrication. Besides providing accurate values for the coordinates of the magnetic centre and the main field angle with respect to magnet fiducials and field quality tables, the benches allow manufacturing errors to be detected during series production. In these measurements the magnets, which are in the normal conducting state, are excited with currents in the range of 0.1 to 1 A, depending on the type of wire employed for the winding. Three generations of benches have been developed to accommodate the mounting features of these correctors in their final location. Features common to all are the measurement technique based on rotating tangential coils with vertical axis, the acquisition software and the bench calibration technique based on magnet symmetries. These benches are designed to be simple and reliable enough to be operated and maintained by the staff of the corrector manufacturers.

The first generation measures the MCS, MCDO magnets that are positioned by means of pin holes, which define the reference frame for the magnetic measurement as well. A total of seven benches are operational at the premises of the different contractors for spool correctors in Europe and India.

The second generation of benches covers the MO, MQT, MCB, MS, MCBC and MQTL magnets. In each case the magnet is positioned by means of a system of longitudinal keys which are the reference system in which the bench measures the magnetic field. Pneumatic grippers precisely fixed to the bench housing hold the keys during the measurement. Three benches are operational to date (MO, MCB and MS).

The third generation of benches is for the inner triplet correctors MCBX, MQSXA. These correctors are positioned by means of pin holes. Only one of these benches has been produced, as all the series measurements will take place at CERN.

Software for data acquisition

A single, modular and configurable control and acquisition software system [42] has been developed for all rotating coils systems. The voltage signals from the rotating coils in a shaft are first pre-amplified and then read-out simultaneously by a battery of digital integrators. The integrators are triggered by an angular encoder connected to the rotating shaft. The integrated voltage signals delivered by the integrators are equal to the flux changes through each measuring coil for all angular steps. Rotation velocity variations during these measurements are compensated up to the first order. A real-time processor configures the integrators and reads the integrated voltages. In addition to the data acquisition from the digital integrators, the software

performs the overall control of the power supply, of the precision current reading, of the motor rotating the shaft, of the programmable gain amplifiers and finally auxiliary acquisitions (e.g. temperature, shaft torque).

7.8 REFERENCE MAGNET SYSTEM

7.8.1 Introduction

The requirements for the control of field quality of the main optics elements (dipoles, quadrupoles) are unprecedented in a superconducting accelerator. Because of this, the LHC will be equipped with several families of high-order multipole magnets that will be powered to correct the field errors in the main ring magnets (dipoles and quadrupoles) and in the interaction region magnets. Clearly, any correction scheme can only be effective when the errors are known to the desired accuracy. Although direct beam diagnostics are the ideal way to collect the information required on the field errors, a number of considerations make a system based solely on beam feedback far from ideal. In particular:

- Given an energy ramp, the required bandwidth depends on the magnitude of the error that requires correction. As an example, a beam-based correction of the sextupole change in the main dipole may result in unreasonable demands on the bandwidth for the chromaticity measurement (10 Hz and higher).
- Some beam measurements are destructive, as they cause an undesirable emittance growth.
- Some of the parameters cannot be determined easily from beam measurements, e.g. dynamic aperture that may be affected by high order multipoles such as normal decapole in the main bending dipoles.

Because of the above arguments, it is desirable to devise a method to bridge the gap between the magnet field errors as obtained from the production and installation and the requirements for operation. The conceptual design of a magnetic reference system that will track and provide information on the magnetic state has been started using three main elements:

- Knowledge of the magnetic field from the series measurements.
- Non-linear adaptation of the measured values based on physical or empirical models for injection decay and snap-back, established following dedicated measurements on prototype and series magnets.
- On-line reference magnets, equipped with suitable magnetic measurement systems.

The aim of the system is to provide the integral strength of the main field of dipole and quadrupole magnets on an octant-by-octant basis, as well as higher order harmonics for both magnet types. It is believed that it will be possible to achieve this at a frequency of few Hz (typically below 10 Hz), with a predicted (absolute) error of the order of 1 unit on the main dipole field, 10 units at 17 mm on the main quadrupole strength, and 0.1 units at 17 mm on the first harmonics of the main field. Initial cross calibration against dedicated beam based measurements, especially for orbit and tune, may be required to achieve this target. Reproducibility (random) errors for repetitive operation are expected to be one order of magnitude smaller. Achieving the above targets will decrease the bandwidth requirements for orbit, tune and chromaticity measurements to a feasible design range. A schematic representation of the concept of this system is shown in Fig. 7.31.

The system will communicate with the LHC control system, receiving operating conditions for the main dipoles and quadrupoles in the LHC octants as well as the powering history, needed to model non-linear memory effects. A field model, based on best interpolators of measured data for the different magnet families is planned. This can be used to predict the field strength and the higher order harmonics in each octant. In order to perform this calculation the field model requires the measured values of the field; either established during cold tests at CERN or deduced from warm measurements in industry and translated via warm-cold correlations. This information will be stored and retrieved from a reference database.

For non-linear effects, and in particular the injection decay and snap-back of allowed multipoles, scaling with the magnet powering history is trimmed using the information measured in a set of reference magnets. The reference magnets will be installed on the test benches presently used for series tests, and will be equipped with rotating coils, delivering harmonics throughout the cycle. In addition, other sensors will be installed. These include NMR probe couples, for accurate measurement of the dipole field and arrays of Hall plate sensors on rings, for fast sextupole and decapole measurements during snap-back.

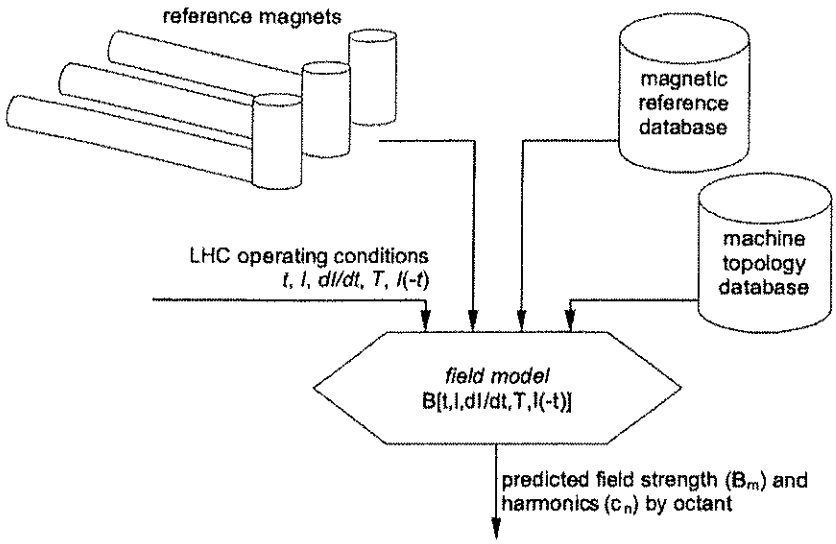

Figure 7.31: Block diagram of the LHC magnetic reference system

The main advantage of this architecture is that the function of the reference magnets is only to provide relative changes with respect to the expected behaviour, while the software interpolator remains the main element for control. Hence, in principle, reference magnets would not be needed for operation, provided the field model is sufficiently optimised through experience during operation to achieve the required prediction capability. This allows reference magnets to be taken off-line in case of faults, or for dedicated cycle optimization studies. The number and selection criteria for the reference magnets still needs to be decided, taking into account that the main effects are driven by superconducting cables (2 suppliers for inner cable, 5 suppliers for outer cable). Finally, information about the machine topology will be used to compute the averages by octant.

7.8.2 The field model

The field model is the core of the magnetic reference system, and will provide the desired field component C_n given the magnet operating condition and powering history:

$$\mathbf{C}_n = \mathbf{C}_n\left(t, I, \frac{dI}{dt}, T, I(-t)\right)$$

The functional dependence is centred on a physical decomposition of the effects that contribute to the total field in the magnet aperture of dipoles and quadrupoles. The following contributions have been identified, and are listed in approximate order of importance:

- Geometric: the deviation between the conductor placement in the real coil winding and the ideal distribution of current (i.e. producing the exact, desired multipolar field). This contribution is present at all field levels and is proportional to the operating current.
- Persistent currents, or dc magnetization in the superconducting filaments: this contribution is important at low operating field (e.g. injection in the main dipoles), where the superconductor magnetization is highest.
- Saturation due to changes of the magnetic permeability in the iron yoke surrounding the coils: this contribution is important at high field, mainly for the main field component.
- Decay: a long term ac effect due to cable internal field changes and flux creep in the filaments' magnetization – important during injection and in general current plateaus at low field
- Snap-back: the rapid re-establishment of the magnetization after its decay during a constant current plateau – important at the beginning of the acceleration ramp.
- Movements: displacements of the cables in the coil cross section. Cable movements can take place during cool-down and powering as a consequence of the changes in the force and stress distribution.

- Coupling currents: these are short term ac effects (ramp-rate dependent) due to inter-filamentary currents within the strand and inter-strand currents within the cable. This contribution is only present during changes in the operating field, e.g. during energy ramping.
- Residual magnetization of magnetic parts in the cold mass: this is mostly in the iron surrounding the coils and visible at low current, e.g. during warm measurements.

The functional dependences for each of the above effects have been established on either a physical basis, or through best fits of measured data [55]. This initial form for the functional dependencies will be refined using cold measurement results and information on orbit, tune and chromaticity accumulated from operation of LHC. Further developments, especially for cycle optimization and modelling of non-linear effects (decay and snap-back) will be based on dedicated measurement campaigns on one or more of the reference magnets taken off-line.

Once the average functional dependencies are established for a magnet type or family, the measured values stored in the reference database will be used to scale the known functional dependency to the particular behaviour of any magnet. This will greatly simplify interpolation work, as well as matching the fitting parameters (if needed) to reproduce the behaviour measured in the LHC through beam-derived quantities.

Last, but not least, a simplified form of the field model will provide the transfer function for implementation in the LHC control system of non-linearity or hysteretic behaviour that require special treatment when converting field corrections to current changes in the power converters. This transfer function, C_{n-1}, will contain contributions from geometric persistent currents and saturation effects. In this reduced form it will be suitable for direct implementation in the closed-loop control algorithm of magnets such as lattice correctors or spool pieces.

7.9 MAGNET INTERCONNECTIONS

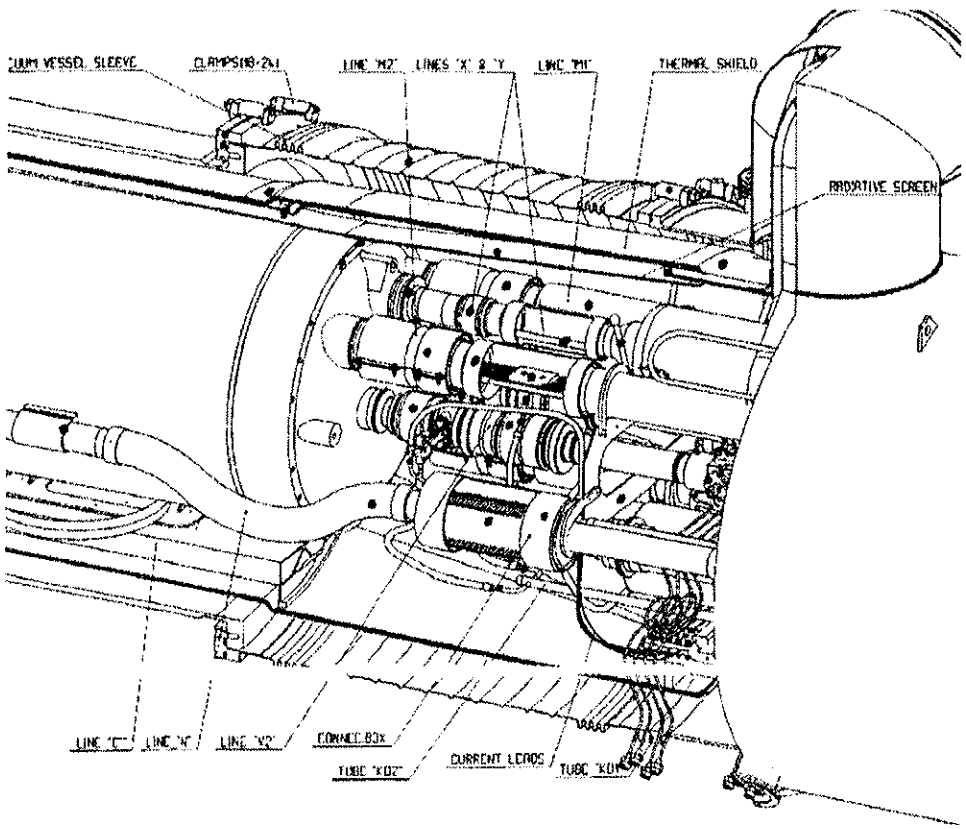

Figure 7.32: The interconnections between two dipoles with the quality assurance points indicated by dots

7.9.1 Electrical Interconnections

The electrical interconnections are inscribed into the powering scheme of the LHC. They start in the electrical distribution feed-boxes (DFB's) and are present in all the zones of the accelerator, including the insertion regions. Both the main and the auxiliary superconducting bus-bars cross each interconnection zone (Fig. 7.32). The main bus-bars power the main dipoles and quadrupoles and carry the current of up to 12 kA. They are housed in the interconnection channels M1-3 (see Fig. 7.32 for the labelling of the cryogenic channels and lines) and are connected by means of induction soldering. The particularity of this technology is the fact that a copper stabilizer of rectangular cross-section formed on the extremities of the Rutherford cables is heated by the induced currents. Three strips of Sn4wt%Ag solder per joint, accompanied by a colophony-based non-corrosive flux are applied. The structure of a single joint (splice) is shown in Fig. 7.33. In order to minimize dissipation of energy to superfluid helium by the Joule effect, the electrical resistance of each joint must remain below 0.6 nΩ. Thus, the heat generation rate per joint at nominal operating current does not exceed 100 mW, which amounts to a total of around 1 kW for interconnections in the 1.9 K zones of the whole accelerator.

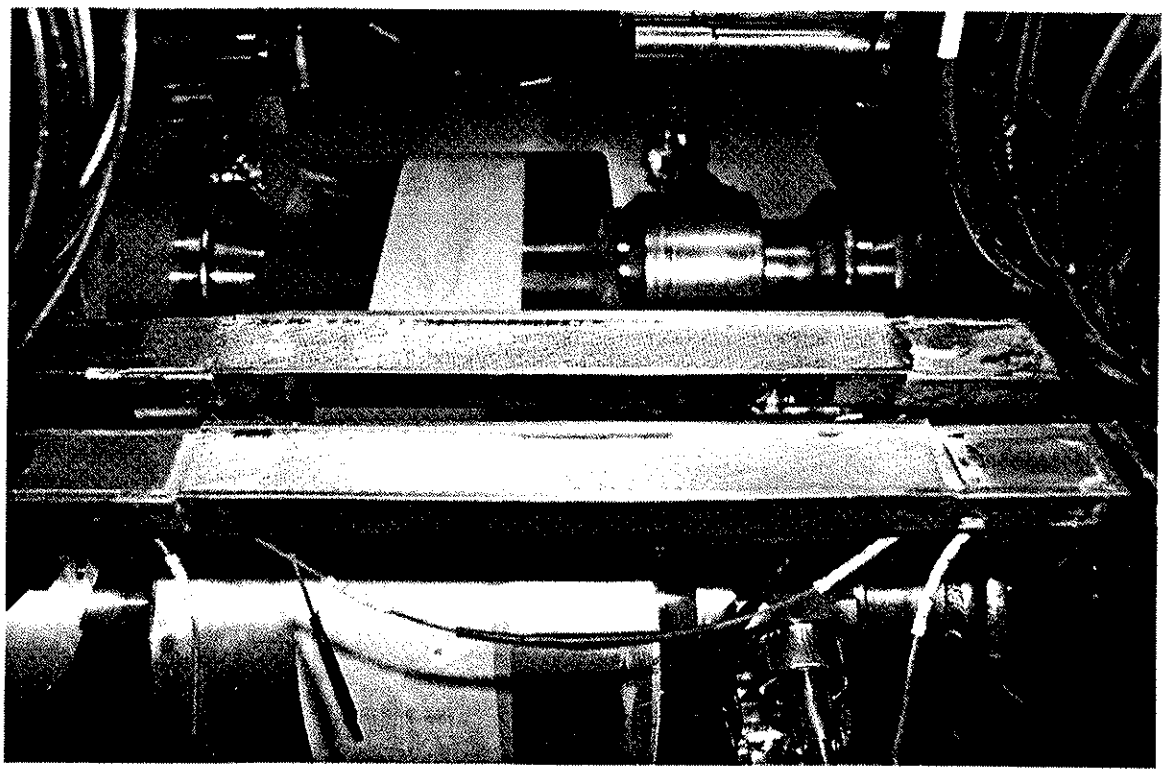

Figure 7.33: Superconducting bus-bars splices

The auxiliary superconducting bus-bars are in the channels M1-2 and in the so-called external auxiliary bus-bar routing (line N). The auxiliary bus-bars powering the spool pieces are located above the main bus-bars in the channels M1 and M2 (10 per channel). On the other hand, the bus-bars powering the array of correctors associated with the main quadrupole cold mass are located in line N (stainless steel braided cable containing 42 superconducting wires). All of them are connected by using an ultrasonic welding technique, specially developed for the LHC. This particular technology produces a combination of a very high mechanical and electrical reliability of the joints. The electrical resistance of a single splice does not exceed 3 nΩ at 1.9 K, which corresponds to a heat generation rate of around 1 mW per splice at nominal current. Given the fact that the auxiliary bus-bars of line N are connected every half-cell (46 joints) the maximum energy dissipation per interconnect amounts to around 670 mW at 1.9 K, for the interconnect between a dipole and a Short Straight Section and under assumption that all the bus-bars are simultaneously powered. Both the joints of main and auxiliary bus-bars are polyimide insulated and have to respect the voltage withstand levels defined for the electrical systems of the LHC. In the M1-2 channels the auxiliary bus-bars are separated from the main bus-bars by a set of composite spacers.

7.9.2 Interconnections of the Cryogenic Channels

The whole family of the cryogenic interconnections comprises both the magnet-to-magnet interconnections and the interconnections between the helium distribution line (QRL) and the string of magnets. The magnet-to-magnet interconnections (Fig. 7.35) include three main cryogenic channels (M1, M2, M3), that convey the gaseous or liquid helium from one magnet to another, the heat exchanger interconnect (channel X), an interconnect between two segments of line N, a bridge between two actively cooled thermal shield panels (channel E) and a bridge between the support post cooling channels (C'). Also, the cryogenic interconnections include flexible links between the beam screen cooling capillaries. All the main cryogenic channels (M1-3, X, E, N) are equipped with bellows expansion joints, which compensate for the thermal contraction and expansion of the magnets and the thermal shield panels. The bellows expansion joints are multi-ply, thin-walled, axi-symmetric, corrugated shells made of 316L grade stainless steel. As a result of advanced optimisation, the bellows expansion joints work in the elasto-plastic regime and develop high intensity plastic strain fields in the convolutions. In order to reduce the amount of plastic strain induced phase transformation ($\gamma \rightarrow \alpha'$) a special stainless steel grade [56], very stable at low temperatures, has been developed. Given the fact that the bellows work in the low-cycle fatigue regime, they have to fulfil very tight reliability requirements. Typically, each M1-3 bellows must have a failure rate below 5×10^{-8} [58, 59]. The pressure drop (for the gaseous and liquid helium) accumulated across three main cryogenic channels (M1-3) cannot exceed the equivalent pressure drop in a 50 mm ID smooth tube, under the same flow conditions. For this reason the composite spacers separating the polyimide insulated spool piece bus-bars from the main bus bars in the channels M1-2 were optimised in terms of cross-section. The helium flow in line N has been reduced to some 0.5% of the helium mass flow in the magnets by use of a special flow impedance located every half-cell within the dipole-SSS interconnect. The flow impedance is obtained by means of a 5 mm ID and 900 mm long corrugated metal hose that creates a link between line N and M2 interconnect. The thermal shield panels are connected by means of a special universal joint that contains two bellows and is equipped with an internal liner to reduce the flow impedance of helium at the temperature of 50-65 K. Finally, the cryogenic channels that cross the zone of interconnection between the QRL and the string of magnets are connected by means of small sleeves and the persistent rings, as shown in Fig. 7.35.

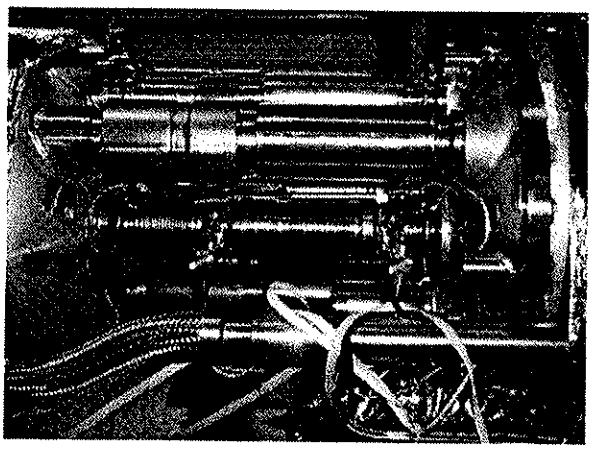

Figure 7.34: The vacuum and cryogenic interconnections

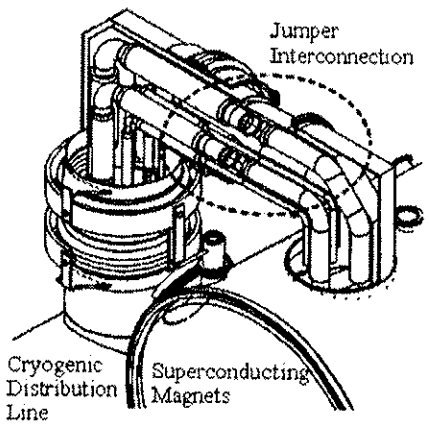

Figure7.35: QRL-SSS interconnection zone

7.9.3 Connection Cryostat

Located in dispersion suppressor zones between cryomagnet Q11 and the first dipole in half-cells 11Ri and 11Li, the 16 connection cryostat modules provide continuity of all the main electrical, vacuum, and cryogenic systems. Eleven variants of the cryostats are required to accommodate the variations due to different distances between virtual interconnection planes (13716.7 mm and 12774.7 mm), the different cryogenic schemes, the length of the large sleeves (840 mm and 1130 mm) and the orientations of the beam screens.

The overall design is similar to a standard cryomagnet (vacuum vessel, thermal shield, bottom tray, cold support posts, jacks) apart from the so-called cold mass which is an assembly of supporting plates, tubes, reinforcing shells (10 mm thick, 570 mm outer diameter) and the superconducting bus-bars. A special alignment mechanism has been developed to ensure that the cold bores stay within the alignment tolerance of 3.2 mm diameter along the cryostat when cold mass assembly is completed.

The cold bores are surrounded by cooling channels which are connected to the main cryogenic lines through corrugated tubes located at the extremities of the cryostat. These tubes reduce the helium flow during cool-down to about 10% of the total flow. Special elastic supports have been developed to maintain the cold bores in a fixed position inside the cooling channels under all circumstances. The maximum cold bore misalignment resulting from its own weight and external forces, is 0.25 mm.

The helium annular section around the cold bores has been designed to cope with the ultimate static and dynamic heat loads of 8.2 W. The cold mass shells and lead shielding plates do not stay directly in contact with pressurised liquid helium and therefore copper thermalisation strips have been included to enhance the cooling rate. The part of heat exchanger outside the shuffling module (which contains the bus-bars lyras) is made of stainless steel whilst the section which is inside the shuffling module is made of copper to ensure sufficiently rapid cooling of the whole cryostat. Standard dipole-type compensation lyras for the three main bus-bar sets are housed in the shuffling module which is located in the middle of the cold mass. These have been made by welding two standard dipole end covers together. The fixed points of the bus-bars are located on the upstream side of the module in the same way as the cryodipole.

Special elements have been developed to support the bus-bars to prevent buckling when interconnection operations are performed. The fixed points for cryogenic and beam pipes are located on the shuffling module which has the advantage that the elongation of the set of compensators is identical to that on a standard dipole/dipole interconnection. A special radiation shield, made from 15 mm thick lead plates, which is installed around the cold bore tubes will reduce the dose at the vacuum vessel surface from around 1000 Gy/y to some 30 Gy/y.

7.9.4 Vacuum Interconnections

Generally, the vacuum interconnections (Fig. 7.34) comprise both the sets of components integrated into the beam vacuum interconnects [60] which are located in the zones between the magnet extremities and the components that ensure continuity of the insulation vacuum. The envelope available for the majority of the beam vacuum [61] interconnects is restricted in all directions: the length is limited to 480 mm between dipole magnets and the radial space available for bellows and welding equipment is limited by the cryogenic lines.

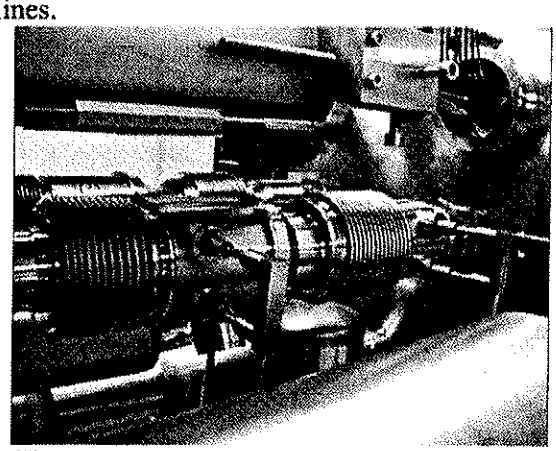

Figure 7.36: The beam vacuum interconnect

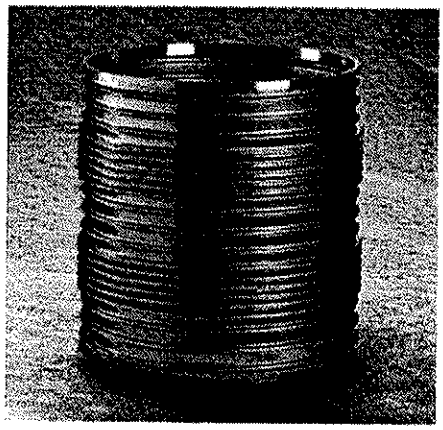

Figure 7.37: The large sleeves for LHC interconnections

The main function of the beam vacuum interconnects (Fig. 7.36) is to provide continuity of the beam vacuum inside the beam transport system. In addition they provide connections of the beam screens by means of the low impedance RF bridges. Also, in most cases the beam vacuum interconnects have four feedthroughs for the beam screen cooling tube crossovers. In order to compensate for the differential thermal contraction of the beam screens with respect to the magnets, a concept of nested bellows has been developed. The nested bellows are 0.2 mm thick very compact expansion joints, made of stainless steel grade 316L,

characterised by a specific "nested" profile of convolutions (Fig. 7.40). They are capable of absorbing thermal contraction/expansion of the order of their own convoluted length. In addition, each beam vacuum interconnect is equipped with an RF contact module, composed of 2 fixed and 1 flexible RF contact (RF contact fingers made of Cu-Be alloy with 5 mm layer of Au) and 0.2 mm thick stainless steel bellows expansion joint. The RF contact module will absorb the transient and steady state offsets due to both thermal contraction of the magnets and misalignment between them. All the components are integrated into the beam lines by using orbital welding technology, which ensures maximum reliability.

The beam lines and all the cryogenic lines are located in the insulation vacuum ($<10^{-4}$ Pa), obtained by connecting the cryostat ends by means of the vacuum vessel sleeves (Fig. 7.37). These large stainless steel corrugated shells (around 1 m in diameter) have two principal functions: they ensure continuity of the insulation vacuum and compensate for the misalignment of the vacuum vessels. Here, the necessary tightness is obtained by means of elastomer seals or metallic gaskets (used in the zones of enhanced radiation), located between the flanges of vacuum vessels and the corresponding flanges of interconnection sleeves.

7.9.5 Thermal Insulation

Thermal insulation in the interconnections is essentially an extension of the thermal insulation located inside the vacuum vessels. Each magnet (cold mass) is directly wrapped with the MLI blankets. In order to obtain a continuation of the radiation insulation across each interconnect a suitable support in the form of a bridge between two neighbouring magnets has been designed. The support consists of 1 mm thick stainless steel shell (cylindrical or conical), attached to the downstream extremity of magnet by means of stainless steel fixtures. The opposite side of the shell slides on the upstream extremity of the neighbouring magnet and in this way the thermal contraction/expansion of the magnets can easily be absorbed. The support is wrapped with a single MLI blanket containing 10 layers of aluminium coated reflective polyethylene terephthalate film, interleaved with polyester spacers. The heat flux through the MLI does not exceed 60 mW/m^2, in the zones where the MLI is not compressed. The radiation screen is not actively cooled and the main mechanism of cooling is based on conduction to the cold mass via the fixtures. The temperature of the shell stays in the range 2-20 K, whereas the temperature of the super-insulation ranges approximately between the temperature of the support and 60 K.

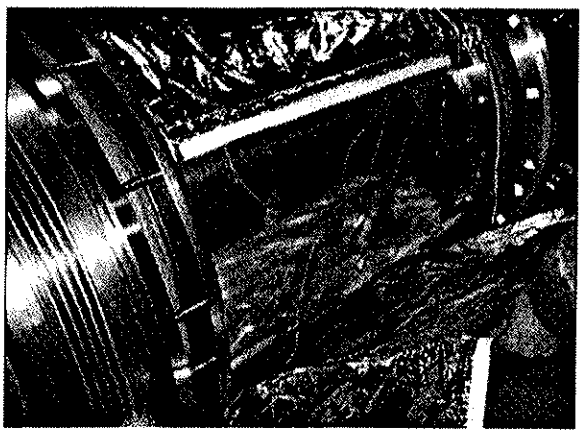

Figure 7.38: The support of MLI (thermal shield)

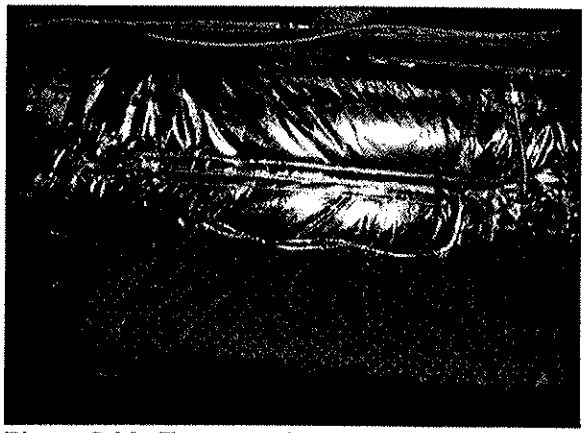

Figure 7.39: Two superimposed MLI blankets

The interconnection thermal shield, designed to intercept the radiant heat from the inner surface of the vacuum vessel, is composed of two 2.5 mm thick aluminium shells, joined together to form a cylinder (Fig. 7.38). The interconnection thermal shield is welded to the downstream extremity of the vacuum vessel thermal shield by means of a 100 mm wide pre-formed metal strip. The strip forms an expansion lyra and constitutes both a mechanical support and a thermalisation. The opposite extremity of the cylinder slides on the upstream end of the neighbouring thermal shield. Since the thermal shield is actively cooled by the flow of gaseous helium at a temperature of about 50-65 K in the channel E, the interconnection thermal shield is also cooled by solid conduction through the expansion lyra. The temperature gradient in the shell does not exceed around 5K. The shell is wrapped with two superimposed MLI blankets of 15 layers each (Fig. 7.39). All blankets are equipped with Velcro™ fasteners. The heat flux through the thermal shield insulation is

limited to around 1.1 W/m^2 in the non-compressed zones. The temperature across the MLI ranges between around 60-75 K and the room temperature on the outside surface of the insulation.

7.9.6 QA for the Interconnections

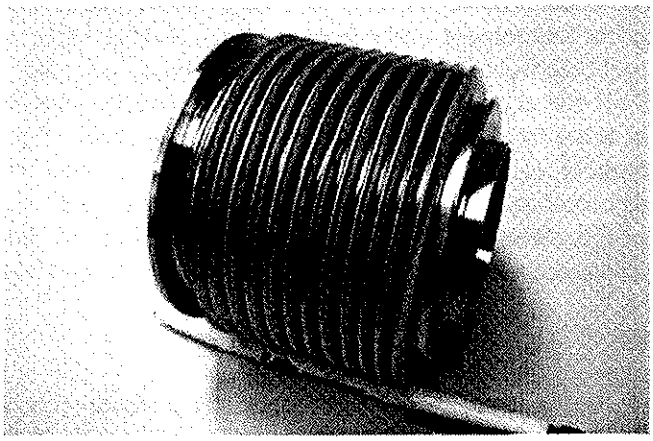

Figure 7.40: The 0.2 mm thick nested bellows for beam vacuum interconnections – the most fragile component.

The target availability of the LHC interconnections is based on the assumption of a maximum of one short intervention (10.5 days) per 10 years of the LHC operation. The availability function is understood as the ratio of the actual to the scheduled operating time of accelerator (excluding maintenance or scheduled servicing). This implies the required availability of the LHC interconnections equal to 99.5%. Generally, there are 3 groups of components that may fail in the interconnections: the compensation system (bellows expansion joints, flexible hoses), connections of the superconducting bus-bars (splices) and the RF contacts. It is assumed that the expected availability is apportioned to each of them on equal basis. Given the number of interconnections in the LHC, the expected failure rate for one interconnect is 10^{-6} per system (i.e. compensators, bus-bars and RF contacts). The LHC interconnections will consist of a total of around 250,000 components of different sizes and some 123,000 connections will be needed to integrate all these components. The main objective of the Quality Assurance (QA) for the LHC interconnections is to minimise the risk of frequent failures of the critical components and to reduce the associated number of interventions. The QA requirements apply to: interfaces and components, assembly technologies and assembly procedures. The quality control of the components starts at the manufacturing stage. The interfaces and the initially integrated components are checked during the preparation of the cryomagnet extremities. Finally, the quality control continues during the whole process of assembly of the interconnections in the tunnel. The most fragile components are the single-ply bellows expansion joints for the beam vacuum interconnections (Fig. 7.40) and the multi-ply bellows for the cryogenic cooling channels. As far as the assembly technologies are concerned, automatic processing is essential in order to eliminate human error. Therefore, for all the main technologies: inductive soldering, ultrasonic welding and orbital TIG welding a fully or semi-automatic approach has been specified with automatically generated process reports. Checking of the process reports combined with the sampling technique will lead to elimination of failures at the level of applied technologies. Finally, the QA refers to the assembly procedures. Correct application of the procedures, layouts and assembly drawings is fundamental for the reliability of the interconnections. Here, a relevant check list will be implemented and a number of check points will be verified (see Fig. 7.32).

REFERENCES

[1] R. Perin, D. Leroy, G. Spigo: "The First, Industry made, Model Magnet for CERN Large Hadron Collider" IEEE Trans. on Magn., vol 25 No.2 (March 1989)

[2] E. Acerbi et al. "Development and Fabrication of the First 10 m Long Superconducting Dipole Prototype for the LHC", IEEE Trans. on Magnetics, Vol 30, N. 4, July 1994, p. 1793

[3] J. Billan et al., "Test Results on Long Models and Full Scale Prototype of the Second Generation LHC Arc Dipoles" IEEE Trans. on Applied Superconductivity, Vol. 9, No. 2, June 1999, p. 1039-1044

[4] K. Artoos et al., "Status of Short Model program for the LHC", IEEE Trans. on Superconductiviy, Vol.10, no.1, March 2000, pages 49-52
[5] The LHC Study Group: "Design Study of The Large Hadron Collider", CERN Report 91-03 (1991);("The Pink Book")
[6] M. Bona et al., "Assessment of the Test Results of the Two CERN-INFN 10 m Long Superconducting Dipole Prototypes for the LHC", IEEE Trans. on Magnetics, Vol.32, N. 4, July 1996, p.2051
[7] M. Granier *et al.*: "Performance of Twin-Aperture Dipole for the CERN LHC" Proceed. of EPAC92 Berlin, March, 1992 Vol. 2.
[8] The LHC Study Group: "The Large Hadron Collider, Conceptual Design", CERN/AC/95-05 LHC Report (1995);("The Yellow Book")
[9] P. Fessia et al., "Selection of the Cross-Section Design for the LHC Main Dipole" *LHC Project Report **347*** (1999)
[10] M. Modena et al., "Final Prototypes, First Pre-series Units and Steps Towards Series Production of the LHC Main Dipoles" *LHC Project Report **487*** (2001)
[11] M. Bajko, "Statistical Studies of the Robustness of the LHC Main Dipole Mechanical Structure" *LHC Project Report **341*** (1999)
[12] C. Humberclaude, "Mesures photogrammétriques des extrémités de MBP1A1 avant et après transport Schio-CERN", LHC Project Note 133, 9.03.1998.
[13] S. Le Naour et al., "Magnetization measurements on LHC superconducting strands," *IEEE Trans. Appl. Superconduct.* 9 2, pt.2 1999 1763-1766.
[14] R. Wolf, S. Le Naour "The Expected Persistent Current Field Errors in the LHC Main Dipole and Quadrupole," *LHC Project Note 230*, CERN, Geneva, Switzerland, 2000
[15] D. Richter et al., "Strand Coating for the Superconducting Cables of the LHC Main Magnets", IEEE Trans. Appl. Supercond., Vol. 9, pp. 735-741, No. 2, 1999.
[16] D. Richter et al., "DC Measurement of electrical contacts between strands in superconducting cables for the LHC main magnets", IEEE Trans. Appl. Supercond., Vol. 7, pp. 786-792, No. 2, 1997.
[17] J.D. Adam et al., "Status of the LHC Superconducting Cable Production", IEEE Trans. Appl. Supercond. 12(2002) pp1056-1062 - MT-17 conference paper
[18] D. Hagedorn, F.Rodrigez Mateos, Modelling of the quenching process in complex superconducting magnet system, IEEE Trans. Magn. 28 (1992) pp366-399
[19] A. P. Verweij, R. Wolf, "Field errors due to interstrand coupling currents in the LHC dipole and quadrupole", CERN Internal Note AT/MA 94-97, 1995.
[20] C. Meuris et al., "Heat transfer in electrical insulation of lHC cables cooled with superfluid helium", Elsevier (ed.), published in Cryogenics 39 (1999) 921
[21] L. Oberli - https://edms.cern.ch/cedar/plsql/doc.download?document_id=310052
[22] R. Wolf "Field Error Naming Conventions for LHC Magnets", *LHC-M-ES-0001*, EDMS n.90250 (2001).
[23] S. Fartoukh, O. Bruning: *LHC Project Report* 501 (2001).
[24] L. Walckiers, private communication. http://edms.cern.ch/lhc_proj/plsql/lhcp.page?p_number=2555
[25] S. Russenschuck, *CERN* 99-01 (1999), pp 82-92.
[26] P. Ferracin et al., *LHC Project Report* 544 (2001).
[27] P. Ferracin, http://documents.cern.ch/archive/electronic/cern/preprint/thesis/thesis-2002-009.pdf Ph.D. Thesis, Politecnico of Torino (2001).
[28] R. Wolf, S. La Naour, *LHC Project Note* 230 (2000).
[29] S. Ramberger et al., "Genetic Algorithms with Niching for Conceptual Design Studies", IEEE Transactions on Magnetics, Vol 34, No. 5, Sept. 1998, 2944-2947.
[30] E. Todesco, et al : *LHC Project Report* **579** (2002).
[31] L. Bottura, et al : *LHC Project Report* **573** (2002).
[32] S. Redaelli, et al : *LHC Project Report* **578** (2002).
[33] P. Ferracin W. Scandale, E. Todesco, R. Wolf : *Phys. Rev. STAB* **3** (2000) 122403.
[34] P. Ferracin W. Scandale, E. Todesco, D. Tommasini: *Phys. Rev. STAB* **5** (2002) 62401.
[35] E. Farina et al., "Development and Manufacture of the Coil End Spacers of the LHC Pre-series Dipoles", *LHC Project Report* **535** (2001).
[36] S. Pauletta, http://doc.cern.ch/archive/electronic/cern/preprints/thesis/thesis-2003-002.pdf Master Thesis, Politecnico of Torino (2002).

[37] E. Todesco, E. Wildner, *LHC Project Report* (2003) in press.
[38] S. Jongeleen, D. Leroy, A. Siemko, R.Wolf, "Quench localization and current redistribution after quench in superconducting dipole magnets wound with Rutherford-type cables", CERN-LHC-Project-Report-59.
[39] Proceedings of the CAS on "Measurement and Alignement of Accelerator and Detector Magnets", edited by S.Turner, Geneva, 1998.
[40] J. Billan et al., "Magnetic measurements of the LHC quadrupole and dipole magnets at room temperature", LHC Project Note 283, 2002-01-07.
[41] J. Billan et al., "Development of a generic magnetic measurement system at room temperature and its application to the LHC quadrupoles", CERN LHC-MMS Internal note 99-01.
[42] L. Madaro et al., "A VME-based LabVIEW System for the Magnetic Measurements of the LHC Prototype Dipoles", Proc. EPAC 96, Sitges, Barcelona, 10-14 June 1996, pp 2246-2248.
[43] T. Tortschanoff et al., "The Short Straight Sections for the LHC", Proc. PAC97 Conference, Vancouver, Canada. 1997.
[44] Instrumentation and Wires for the Machine and QRL Cryostats in Arcs and Dispersion Suppressors, CERN-EDMS 111967
[45] R. Burgmer et al., "Performance of the First LHC Main Quadrupoles Made in Industry", Proc. PAC2003 Conference, Portland, Oregon, USA, May 2003
[46] L. Nielsen, Short Straight Section (SSS) Types in the Arcs from Q12 to Q12, CERN-EDMS 103939
[47] M. Allitt et al., "Principles Developed for the Construction of the High Performance, Low-cost Superconducting LHC corrector Magnets", CERN-LHC-Project-Report-528.- Geneva : CERN, 2002.
[48] J. Salminen et al., ".Experience with different constructions of superconducting corrector magnets for the LHC", LHC-Project-Report-254.- Geneva : CERN, 11 Nov 1998
[49] A. Ijspeert et al., "Superconducting coil compression by scissor laminations", EPAC-96, Sitges, Spain, June 1996, LHC-Project-Report-237.- Geneva : CERN, 25 Sep 1998 .
[50] R. Schmidt et al., "Protection of the Superconducting Corrector Magnets for the LHC", CERN-LHC-Project-Report-419 - Geneva : CERN, 23 Sep 2000 .
[51] M. Allitt et al., "Further Development of the Sextupole and Decapole Spool Corrector Magnets for the LHC", LHC-Project-Report-353.- Geneva : CERN, 1999 . and IEEE Trans. Appl. Supercond.: 10 (2000) no. 1, pp.162-5
[52] M. Allitt et al., "Development of Superconducting Tuning Quadrupole Corrector (MQT) Prototypes for the LHC", CERN-LHC-Project-Report-531.- Geneva : CERN, 06 Mar 2002.
[53] Z. Ang et al., "Further Development of the Sextupole Dipole Corrector (MSCB) Magnet for the LHC", LHC-Project-Report-356.- Geneva : CERN, 1999 and IEEE Trans. Appl. Supercond.: 10 (2000) no. 1, pp.158-61
[54] M. Bajko et al., "Training Tests on Single Superconducting Coils of Sextupolar Correctors for LHC", LHC-Project-Report-264.- Geneva : CERN, 1999.
[55] S. Amet et al., "The Multipole Factory: an Element of the LHC Control", IEEE Trans. Appl. Sup., 12(1), 1417-1421, 2002.
[56] A. Jacquemod et al.,"Inductive soldering of the junctions of the main superconducting bus-bars of the LHC", Proceedings of the 6th EUCAS Conference, Sorrento, Italy, 2003.
[57] Baze et al., "Design and fabrication of the prototype superconducting quadrupole for the CERN LHC project", Proc. 12th International Conference on Magnet Technology MT-12 , Leningrad, USSR , 23 - 28 June 1991 - pages 335-337.
[58] B. Skoczen, "Stability, fatigue and optimization of thin-walled structures under cryogenic conditions", CERN-2001-001.
[59] C. Garion, B. Skoczen, "Reliability oriented optimum design of the LHC interconnections – Part I: mechanical compensation system", LHC Project Note 245, CERN (EDMS 249793), 2000.
[60] R. Veness et al., "Beam vacuum interconnects for the LHC cold arcs", Particle Accelerator Conference, New York City, NY, USA, 1999.
[61] J.PH. Tock et al., "The interconnections of the LHC cryomagnets", Particle Accelerator Conference, PAC, Chicago, 2001.

CHAPTER 8

INSERTION MAGNETS

8.1 OVERVIEW

This chapter deals with the superconducting and normal conducting magnets used in the eight insertion regions of the LHC. Four of these insertions are dedicated to experiments, while the others are used for the major collider systems (one for the RF, two for beam cleaning and one for the beam dump system). The various functions of the insertions are fulfilled by a variety of magnets, most of them based on the technology of NbTi superconductors cooled by superfluid helium at 1.9 K. A number of stand-alone magnets in the matching sections and beam separation sections are cooled to 4.5 K, while in the radiation areas it is planned to install specialised normal conducting magnets. The different magnet types will be described in the frame of the machine sectors to which they belong.

Table 8.1: Types and number of magnets used in the LHC insertion regions

Magnet type	IR1 ATLAS	IR2 ALICE	IR3 Cleaning	IR4 RF	IR5 CMS	IR6 Dump	IR7 Cleaning	IR8 LHCb
Main dipoles and quadrupoles (DS)								
MB	16	16	16	16	16	16	16	16
MQ	2	2	10	2	2	2	10	2
Superconducting insertion quadrupoles and correctors (DS and MS)								
MQMC	2	2	-	2	2	2	-	2
MQM	6	10	-	4	6	2	-	10
MQML	8	6	-	4	8	4	-	6
MQY	2	6	-	4	2	4	-	6
MQTL	2	2	24	2	2	2	24	2
MSCB	2	2	2	2	2	2	2	2
MCBC	12	13	10	8	12	6	10	13
MCBY	6	9		4	6	4		9
Normal conducting quadrupoles (Cleaning insertions)								
MQWA/B(Q4,Q5)	-	-	24	-	-	-	24	-
Superconducting separation dipoles								
MBX (D1)	-	2	-	-	-	-	-	2
MBRC (D2)	2	2	-	-	2	-	-	2
MBRS (D3)	-	-	-	4	-	-	-	-
MBRB (D4)	-	-	-	4	-	-	-	-
Normal conducting separation and correction dipoles								
MBXW (D1)	12	-	-	-	12	-	-	-
MBW (D3)/(D4)	-	-	12	-	-	-	8	-
MCBWH/V	-	-	8	-	-	-	8	-
Inner triplets and associated correctors								
MQXA (Q1, Q3)	4	4	-	-	4	-	-	4
MQXB (Q2)	4	4	-	-	4	-	-	4
MCBX	6	6	-	-	6	-	-	6
MQSX	2	2	-	-	2	-	-	2
Multipole packages	2	2	-	-	2	-	-	2
Normal conducting compensator dipoles in ALICE and LHCb experiments								
MBWMD	-	1	-	-	-	-	-	-
MBXWT	-	2	-	-	-	-	-	-
MBXWH	-	-	-	-	-	-	-	1
MBXWS	-	-	-	-	-	-	-	2

The type and distribution of magnets amongst the eight insertions are summarized in Tab. 8.1. The dispersion suppressors (DS), from Q8 to Q11, include main dipoles, main quadrupoles in the two beam

cleaning insertions and special matching quadrupoles and corrector magnets in all other insertions. The matching sections (MS), from Q4 to Q7 (except in the IR6 where Q6 and Q7 are non-existent), include special insertion type quadrupole and corrector magnets. All of these magnets are superconducting, except in the beam cleaning insertions, where normal conducting quadrupoles and corrector magnets are used. The separation dipoles are partly superconducting magnets and partly normal conducting magnets. The magnets of the inner triplets (Q1 to Q3) consist of special high-gradient large-aperture superconducting quadrupoles, together with a number of specific corrector magnets. For the ALICE and LHCb experimental insertions, which both feature large spectrometer dipoles, specific orbit compensator dipoles are used.

8.2 DISPERSION SUPPRESSORS

8.2.1 Main Dipoles in the Dispersion Suppressors

The main dipoles in the dispersion suppressors have the same characteristics and the same cryostats as for the arc, as described in Sec. 7.3 and 7.4 (with a minor difference in the cryogenic circuits in some of the cryodipoles). These dipoles are installed two per half-cell. The half-cell from Q10 to Q11 is longer than the others and the extra length is bridged by a connection cryostat, which is adjacent to quadrupole Q11 in all IRs. The connection cryostats (Sec. 7.9.3) ensure the continuity of the beam pipes, the cryogenic fluids and the electrical bus-bars.

8.2.2 Dispersion Suppressor Quadrupoles

The superconducting quadrupoles in the dispersion suppressors are based on the MQ and MQM-type magnets. The design of these magnets is described in Sec. 7.5 and 8.3.1, respectively. In all insertions, the first quadrupole of the dispersion suppressors next to the arc (Q11) consists of a cold mass containing an MQ quadrupole, an individually powered MQTL trim quadrupole and an MSCB dipole-sextupole corrector. The main parameters of the dispersion suppressor quadrupole cold masses are given in Tab. 8.2. Their cryostats closely follow the design of the SSS cryostat, where the standard section of the vacuum vessel is modified in accordance with the length of the cold mass. The main components of the cryostat are discussed in Sec. 7.5.3.

Table 8.2: Main parameters of the dispersion suppressor quadrupole cold masses

Cold mass position	Magnets	Operating temperature (K)	Length (mm)	Mass (kg)	No. units
Q11	MQ+MQTL+MSCB	1.9	6620	7416	16
Q10, Q8 (other than IR3/7)	MQML+MCBC	1.9	6620	7416	24
Q10, Q8 (IR3/7)	MQ+MQTL+MCBC	1.9	6620	7416	8
Q9 (other than IR3/7)	MQMC+MQM+MCBC	1.9	8020	9310	12
Q9 (IR3/7)	MQ+2 MQTL+MCBC	1.9	8020	9310	4

Quadrupoles Q8 to Q10 in the Insertions IR 1/2/4/5/6/8

In the experimental, dump and RF insertions, the focusing from Q8 to Q10 is achieved by using twin aperture quadrupoles of MQM-type operating at currents below 6 kA. Each aperture is individually powered which allows the flexibility required for beam optics to be obtained in a cost effective way. The cold masses of the corresponding short straight sections contain one or two MQM-type quadrupoles and one MCBC dipole corrector, as shown in Tab. 8.2.

Quadrupoles Q8 to Q10 in the Insertions IR 3/7

In the cleaning insertions IR3 and IR7, the focusing from Q8 to Q10 (including Q7) is achieved using main arc quadrupoles with the addition of an individually powered MQTL trim quadrupole to provide the required optical tuning. The corresponding cold masses therefore include one MQTL trim quadrupole (except Q9 which has two) and one MCBC for closed orbit correction, in addition to the MQ quadrupoles. The MQ quadrupoles in these two insertions are powered in series with the corresponding main quadrupole circuits in the arc.

8.3 MATCHING SECTIONS

The tuning of the LHC insertions is provided by the individually powered quadrupoles in the dispersion suppressor and matching sections. The matching sections consist of stand-alone quadrupoles arranged in four half cells, but the number and parameters of the magnets are specific for each insertion. Apart from the cleaning insertions, where specialized normal conducting quadrupoles are used in the high-radiation areas, all matching quadrupoles are superconducting magnets. Most of them are cooled to 4.5 K, except Q7 quadrupoles which are the first magnets in the continuous arc cryostat and are cooled to 1.9 K as are the rest of the arc magnets.

8.3.1 Superconducting Matching Quadrupoles

CERN has developed two superconducting quadrupoles for the matching sections: the MQM quadrupoles featuring a 56 mm aperture coil, which are also used in the dispersion suppressors and the MQY quadrupole with an enlarged, 70 mm coil aperture. Both quadrupoles use narrow cables, so that the nominal current is less than 6 kA, substantially simplifying the warm and cold powering circuits. Each aperture is powered separately, but a common return is used so that a three-wire bus-bar system is sufficient for full control of the apertures.

MQM

The MQM quadrupole, Fig. 8.1, consists of two identical, independently powered apertures, which are assembled together in a two-in-one yoke structure. Three versions of the MQM quadrupole are required for the LHC, with magnetic lengths of 2.4 m, 3.4 m and 4.8 m. The main parameters of the quadrupole are listed in Tab. 8.3. In total, 84 MQM magnets are required for the LHC dispersion suppressor and matching sections.

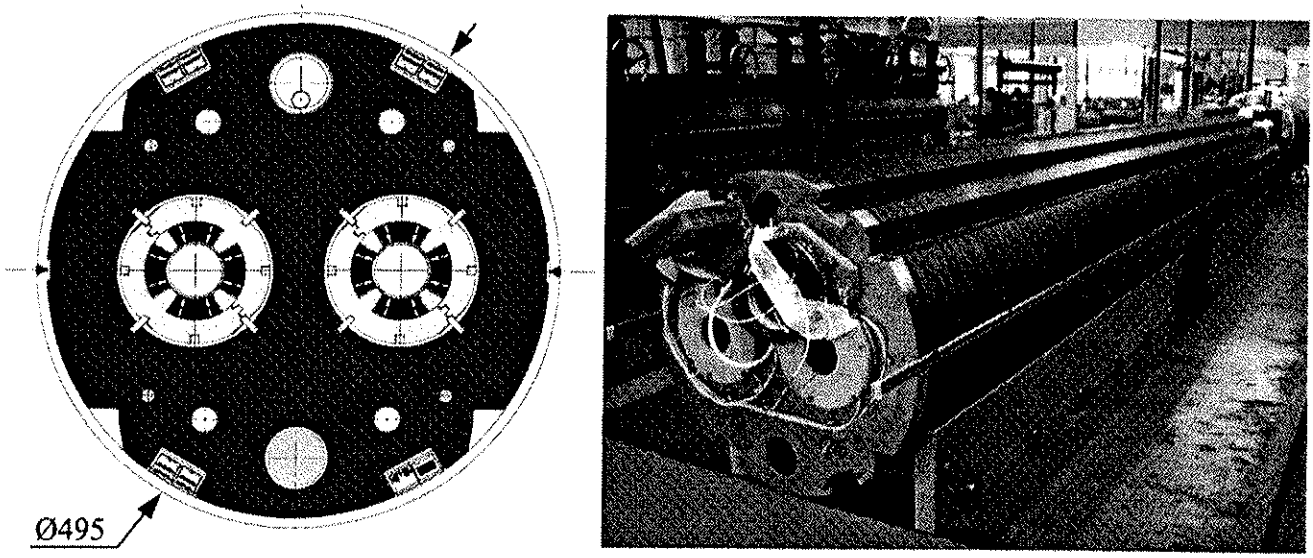

Figure 8.1: Cross-section of MQM quadrupole (left) and a 5 m long MQM magnet on the test stand (right).

The superconducting cable used for MQM quadrupoles is an 8.8 mm wide Rutherford-type NbTi cable formed of 36 strands, each 0.475 mm in diameter. The filament diameter of 6 μm was chosen in order to minimize the effects of the persistent currents at low fields. The cable is insulated with three layers of polyimide film. The first two layers are made of butt wrapped polyimide film (11 mm wide and 25 μm thick), with the second layer offset by half the tape width. The third insulation layer is a 9 mm wide 50 μm thick polyimide film with a 5 μm thick coating of adhesive which cures at 185°C, wrapped with a 2 mm gap.

Table 8.3: Main parameters of the MQM-type quadrupoles

Coil inner diameter	56 mm
Magnetic length	2.4/3.4/4.8 m
Operating temperature	1.9/4.5 K
Nominal gradient	200/160 T/m
Nominal current	5390/4310 A
Cold bore diameter OD/ID	53/50 mm
Peak field in coil	6.3 T
Quench field	7.8 T
Stored energy per aperture	64.3 kJ/m
Inductance per aperture	4.44 mH
Quench protection	Quench heaters, two independent circuits
Cable width	8.8 mm
Mid-thickness	0.84 mm
Keystone angle	0.91 deg.
No of strands	36
Strand diameter	0.475 mm
Cu/SC Ratio	1.75
Filament diameter	6 μm
j_c, (4.2 K and 5 T)	2800 A/mm^2
Mass (2.4/3.4/4.8 m)	3100/4300/6000 kg

The MQM coils are wound out of a single length of insulated cable as a double layer which is cured in a single cycle. The coil design was optimized for the highest transfer function and operational margin and a geometrical b_6 multipole which partially compensates the term due to persistent currents at low currents [1]. The coils are assembled into a collared aperture using 2 mm thick collars, fine-stamped from sheets of high-strength low-permeability steel (yield strength > 620 MPa, relative permeability less than 1.005, both at room temperature). The collars are locked with four full-length tapered keys and provide the necessary compressive stress to withstand the magnetic forces up to the ultimate current.

The protection of the magnet during a quench is assured by eight strip quench heaters placed on the outer layer of each coil octant. For redundancy, the heaters are connected in two circuits, such that each circuit covers all four poles and are powered by independent power supplies.

Each collared aperture carries its own connection box. Two completed apertures are assembled in the iron yoke by vertically stacking single-piece laminations. The yoke laminations are similar in design to the LHC arc quadrupole, but are slightly larger (OD 475 mm), so that the outer diameters of the helium vessels are identical. The outer contour of the laminations has alignment and other features necessary for cold mass assembly and longitudinal welding. As the stack is gradually built up, the yokes are compressed and locked with elastic pins, centring at the same time the apertures with four lines of alignment keys. The longitudinal rigidity of the magnet is provided by four tie-rods which link the two end plates.

Measurements of the pre-series MQM magnets have shown that the field quality of the series production can be expected to follow the guidelines set for the arc quadrupoles (see Tab. 7.14). This is in particular the case for non-allowed harmonics of low order where the azimuthal size of the coils plays a dominant role. At the LHC injection energy, the largest fraction of the b_6 multipole is due to the persistent currents, which strongly depend on the powering cycle. Contrary to arc quadrupoles, the MQM quadrupoles have a significant range of currents at injection. Compensation of the persistent current part of the b_6 multipole error with its geometric part is therefore limited in efficiency.

MQY

The MQY wide-aperture quadrupole, Fig. 8.2, consists of two individually powered apertures assembled in a common yoke structure. The coil aperture of the magnet is 70 mm and its magnetic length 3.4 m. The main parameters of the quadrupole are given in Tab. 8.4. In total, 24 MQY magnets are required for the LHC matching sections.

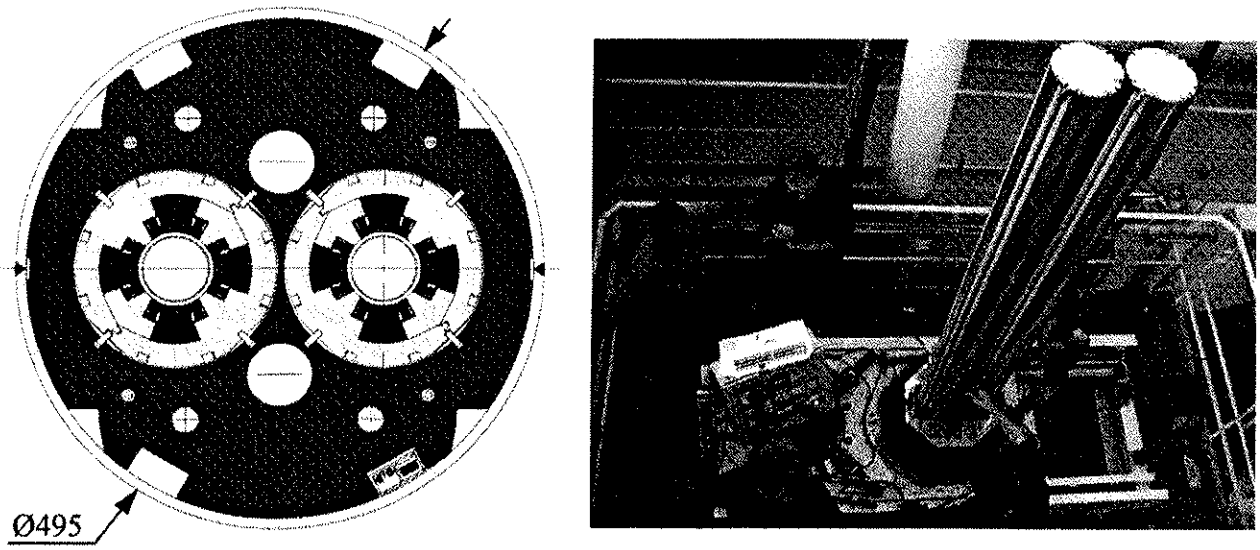

Figure 8.2: Cross-section of MQY quadrupole (left) and assembly of the magnet (right).

Table 8.4: Main parameters of the MQY matching quadrupole

Coil inner diameter	70 mm
Magnetic length	3.4 m
Operating temperature	4.5 K
Nominal gradient	160 T/m
Nominal current	3610 A
Cold bore diameter OD/ID	66.5/62.9 mm
Peak field in coil	6.1 T
Quench field	7.5 T
Stored energy	479 kJ
Inductance	73.8 mH
Quench protection	Quench heaters, two independent circuits
Cable width, cable 1/2	8.3/8.3 mm
Mid-thickness, cable 1/2	1.285/0.845 mm
Keystone angle, cable 1/2	2.16/1.05 deg.
No of strands, cable 1/2	22/34
Strand diameter, cable ½	0.735/0.475 mm
Cu/SC Ratio, cable 1/2	1.25/1.75
Filament diameter, cable 1/2	6/6 μm
j_c, cable 1/2, (4.2 K and 5 T)	2670/2800 A/mm^2
Mass	4400 kg

Two Rutherford-type NbTi superconducting cables are used for winding the MQY coils. They are both 8.3 mm wide, but are made of two types of strands, each strand containing 6 μm filaments. Apart from the diameter (0.735 mm and 0.475 mm), the strands have a different Cu/SC ratio (1.25 and 1.75). The strand and cable parameters were chosen so that the current density in Cable 2 (mid-thickness 0.845 mm) is 1.5 times higher than in Cable 1 (mid-thickness 1.285 mm) for the same current in the cables. The cables are insulated using the same polyimide films and insulation layout as the MQM cable.

The 70 mm aperture MQY coils have four layers, optimized for the highest transfer function and operational field quality [2]. The inner two layers are wound using both types of cable. The first layer and part of the second layer are wound using Cable 1. The transition between the cables is made in an internal joint in the middle of the second layer. Once the winding of the second layer is completed with Cable 2, the two layers are cured together in a single cycle. The outer two layers are wound out of a single length of Cable 2 as a double layer and cured in a single cycle. The connections between the layers, as well as between the poles, are made in the connection box mounted on the end plate of the collared aperture.

As is done for other LHC quadrupoles, the MQY coils are assembled in a collared aperture using 2 mm thick collars fine-stamped from high-strength low-permeability steel. However, due to the large aperture of the coil and the spacing between apertures of 194 mm, the width of the collars is only 22 mm and they need to be locked with eight full-length tapered keys to minimize deformation. In this configuration, the collars provide the necessary compressive stress to withstand the magnetic forces up to an ultimate current of 3800 A at 4.5 K.

The protection of the MQY quadrupole during a quench is assured by sixteen strip quench heaters of two different widths. Eight wide quench heaters are mounted between the second and third layers and the narrow heaters on the outer surface of the fourth layer. This number of heaters is required to limit the voltage during quench in case of failure of some of the heaters. Both the inner and outer heaters are connected in two circuits, each circuit covering all four poles and powered by independent power supplies.

Two completed apertures are assembled in the iron yoke by vertically stacking single-piece laminations (Fig. 8.2). The outer contour of the yoke laminations is identical to the MQM laminations. The position of the heat exchanger hole, however, is displaced towards the centre. Due to the close proximity of the apertures in the two-in-one configuration, the coupling at high currents is considerable and the field quality rapidly degrades above 4000 A. For this reason, the MQY is limited to 3800 A, which in turn means that it can operate at 4.5 K. The internal heat exchanger is therefore not required and its position in the yoke lamination was used to optimize the saturation effects.

The MQY quadrupole was designed with highest field quality in mind. As in the MQM quadrupole, the b_6 multipole has a non-zero geometrical part used to compensate the persistent current effects at injection. However, due to its operation at 4.5 K and larger coil aperture, these effects are smaller than in MQM so that compensation with geometrical b_6 is more effective. Measurements of the pre-series MQY magnets have shown that the field quality of the series production can be expected to follow the specification error tables for the low-β triplet quadrupoles (Sec. 8.5).

Matching Section Cold Masses

The main parameters of the matching section cold masses, which range in length from 5.35 m to 11.45 m, are given in Tab. 8.5. All cold masses (except Q7 in IR3 and 7) are assembled using two welded half-shells as MQM-type helium vessels. Apart from the differences in length, the construction features of the cold masses depend on the operating temperature (1.9 K for Q7 and 4.5 K for all other assemblies), on the powering scheme (e.g. powering through the superconducting link in IR1 and 5) and on the interface details to surrounding elements (e.g. Q4-D2 interconnect).

Table 8.5: Main parameters of the matching section cold masses

Cold mass position	Magnets	Operating temperature (K)	Length (mm)	Mass (kg)	No. units
Q7 (IR4)	MQM+MCBC	1.9	5345	5820	2
Q5, Q6 (IR4) Q4, Q5 (IR6)	MQY+MCBC	4.5	5345	5820	8
Q7 (IR3, 7)	MQ+MQTL+MCBC	1.9	6620	7416	4
Q5, Q6 (IR1, 5)	MQML+MCBC	4.5	6620	8210	8
Q4 (IR1, 5)	MQY+3MCBY	4.5	8020	9310	4
Q7 (IR1, 2, 5, 8)	MQM+MQM+MCBC	1.9	8995	11090	8
Q6 (IR2, 8)	MQM+MQML+MCBC	4.5	10400	12300	4
Q6 (IR3, 7)	6 MQTL+MCBC	4.5	10400	12300	4
Q4, Q5 (IR2, 8)	2 MQY+3 MCBY	4.5	11355	14070	8

MQM-type Helium Vessel

The cold masses containing MQM and MQY quadrupoles are assembled in the Magnet Assembly Facility at CERN in a helium vessel which by its principle is similar to that of the main dipoles. The central elements of the assembly are two 10 mm thick half-shells made of AISI 304L steel which serve for alignment of the various magnetic elements, provide the rigidity and serve as a helium pressure vessel. Contrary to the main dipoles, once welded the half-shells do not participate in compressing the coils or containing the magnetic forces. The vessel is closed with two end covers, which also support the elements required for interconnecting the string of LHC cryo-magnets. In particular, the main 13 kA electrical bus work and 1.9 K helium lines are guided by the end covers and the beam position monitors (BPM) and beam vacuum interconnects are precisely positioned with end covers as reference.

The alignment of the magnets is performed in two steps. In the first step, precision alignment cradles are used to individually align the MQM and MQY magnets, which are not aligned during yoke assembly. The yoke laminations have alignment flats designed as contact surfaces and also as references for control. After compressing the cradles, the alignment of individual magnets is completed by tack welding the alignment keys to the laminations. Subsequently, the individually aligned magnets are placed in the half-shell and aligned relative to each other using the alignment cradles which span the full length of the assembly. The operation is completed with tack welding of the alignment keys to the chamfer of the half-shell.

Several electrical circuits and their instrumentation are installed during assembly. In the first instance, the 13 kA main LHC dipole and quadrupole bus work, although not used for powering the insertion quadrupoles, must be installed in Q7-Q10 cold masses to provide continuity of the arc circuits. Although the design of the bus-bars follows closely that of the main magnets, there are a number of differences, particularly in the position of the expansion loops, Fig. 8.3. Furthermore, as the main quadrupole bus-bars are pulled through after the magnets are aligned in the half-shell, their lead ends have to be bent to their final position in situ.

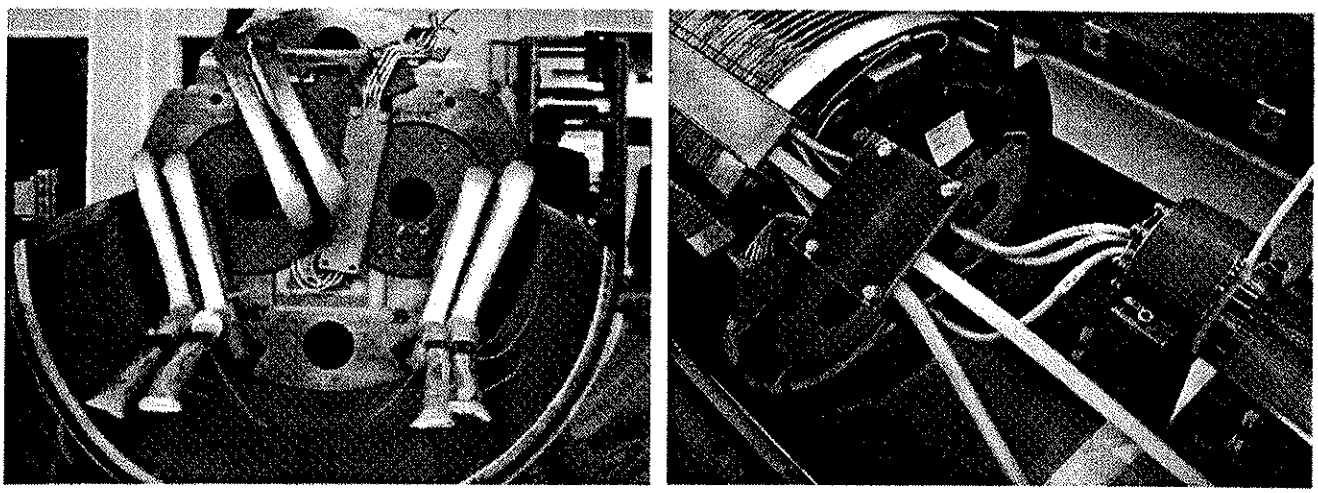

Figure 8.3: (Left) Non-connection side of the Q9 quadrupole showing the MCBC corrector aligned in the half-shell and the expansion loops of the three 13 kA bus-bars. (Right) Lead end of the Q9 quadrupole after completion of the 6 kA splices. The helium tight feed-through for the three 6 kA round wires to line-N is shown on the right. The 13 kA main quadrupole bus bars, bent in situ to their final positions, are in the bottom of the half-shell.

The insertion quadrupoles are powered with three 6 kA round cables routed through line-N (Sec. 7.3.7). In those quadrupoles which comprise two magnets, the apertures are powered in series and the bus-bars connecting the magnets are also 6 kA round cables. Several splices between the 6 kA round cables and the magnet Rutherford-type cable are therefore required. The connections on the lead end of the quadrupole, Fig. 8.3, are particularly challenging due to the large number of splices and tight space. The same technique is used for interconnecting the 6 kA bus-bars with the leads of the second magnet.

The cold bore tubes and heat exchanger tubes are mounted after magnet alignment and before longitudinal welding of the cold mass. The cold bore tubes for the MQM quadrupoles have the same dimensions as those for the arc quadrupole (Sec. 7.5). For the MQY quadrupoles, cold bore tubes have an outer diameter of 66.5 mm and wall thickness of 1.8 mm. Both types of cold bore tubes are insulated with 60 mm wide

polyimide tape AST 252 with a 48% overlap. The heat exchanger tubes (mounted in the cold masses cooled at 1.9 K) are copper tubes equipped with stainless steel sleeves at both ends. Apart from the length, they are identical to those mounted in the arc quadrupoles.

The longitudinal welding of the half-shells is performed in the 17 m welding press, previously used for the main dipole prototypes. The welding procedure is a MIG process with three passes. The weld is performed in a cavity formed by the shell chamfers and the alignment key, having the function of a backing strip, Fig. 8.4. Before welding, the press is activated to bring the root faces of the two half-shells in contact over the full length (Fig. 8.4, left). Since the inner circumference of the half-shells is slightly larger than the yoke by 3 mm (corresponding to the weld shrinkage) there is no force on the magnet structure. After welding, the shells and the laminations are brought in contact around the circumference by a small azimuthal stress.

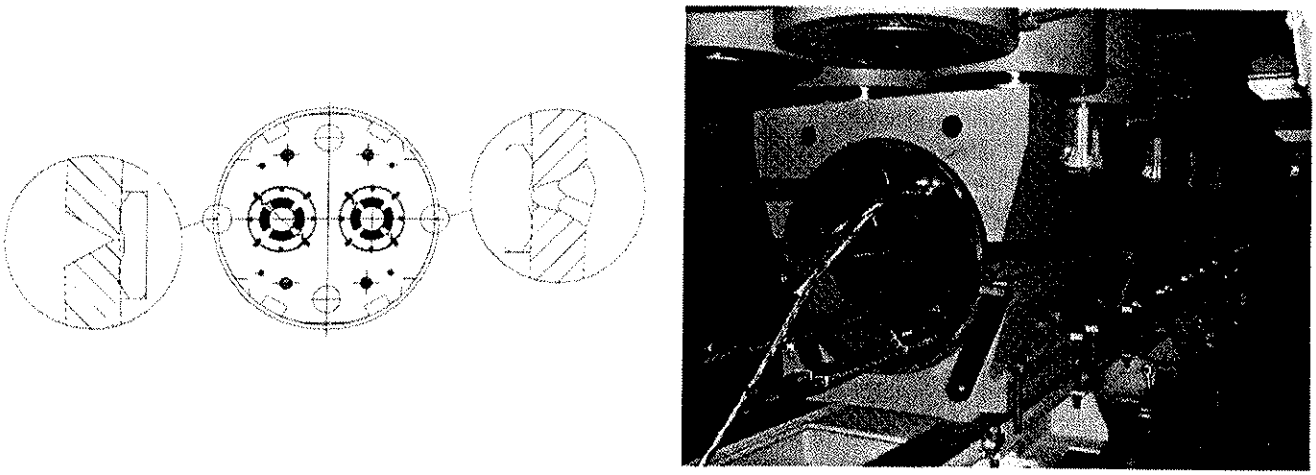

Figure 8.4: (Left) Geometry of the longitudinal weld: detail at left is before welding, detail at right shows the position of the three welding seams. (Right) Q9 quadrupole in place for longitudinal welding.

The end covers of the helium vessel are similar to those of the LHC main dipole. However, many of their features are quadrupole-specific (e.g. cryogenic pipes, BPM supports). As the tolerances are very tight, special tools and procedures are necessary for their assembly. One of the most critical assembly stages is the welding of the end covers. Prior to this operation, the shells are cut to precise length and machined for mounting of the adapting rings, which compensate for the difference in outer diameters of the shell and the end covers. Due to the importance of the final positions of the cryogenic pipes, the positioning of the end covers is controlled with a laser tracker. Before the final orbital weld, the end covers are tack welded and their position adjusted, as shown in Fig. 8.5. The last step in completing the quadrupole extremities is the mounting of the BPM supports, also precisely controlled with a laser tracker.

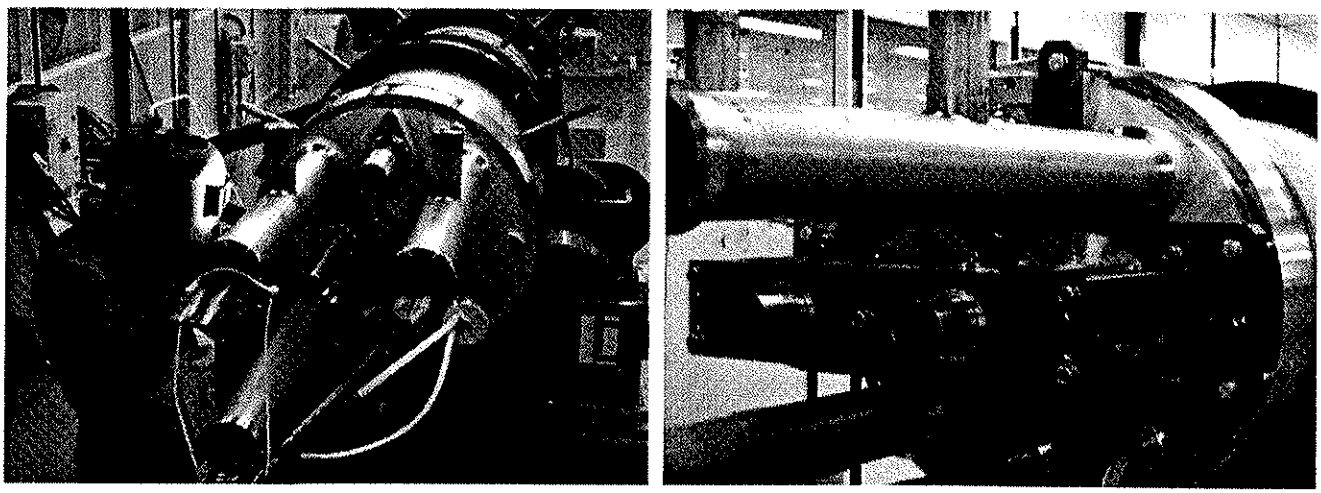

Figure 8.5: (Left) Positioning of the end covers before final orbital welding. (Right) Positioning of the BPM supports on the connection end of the Q9 quadrupole.

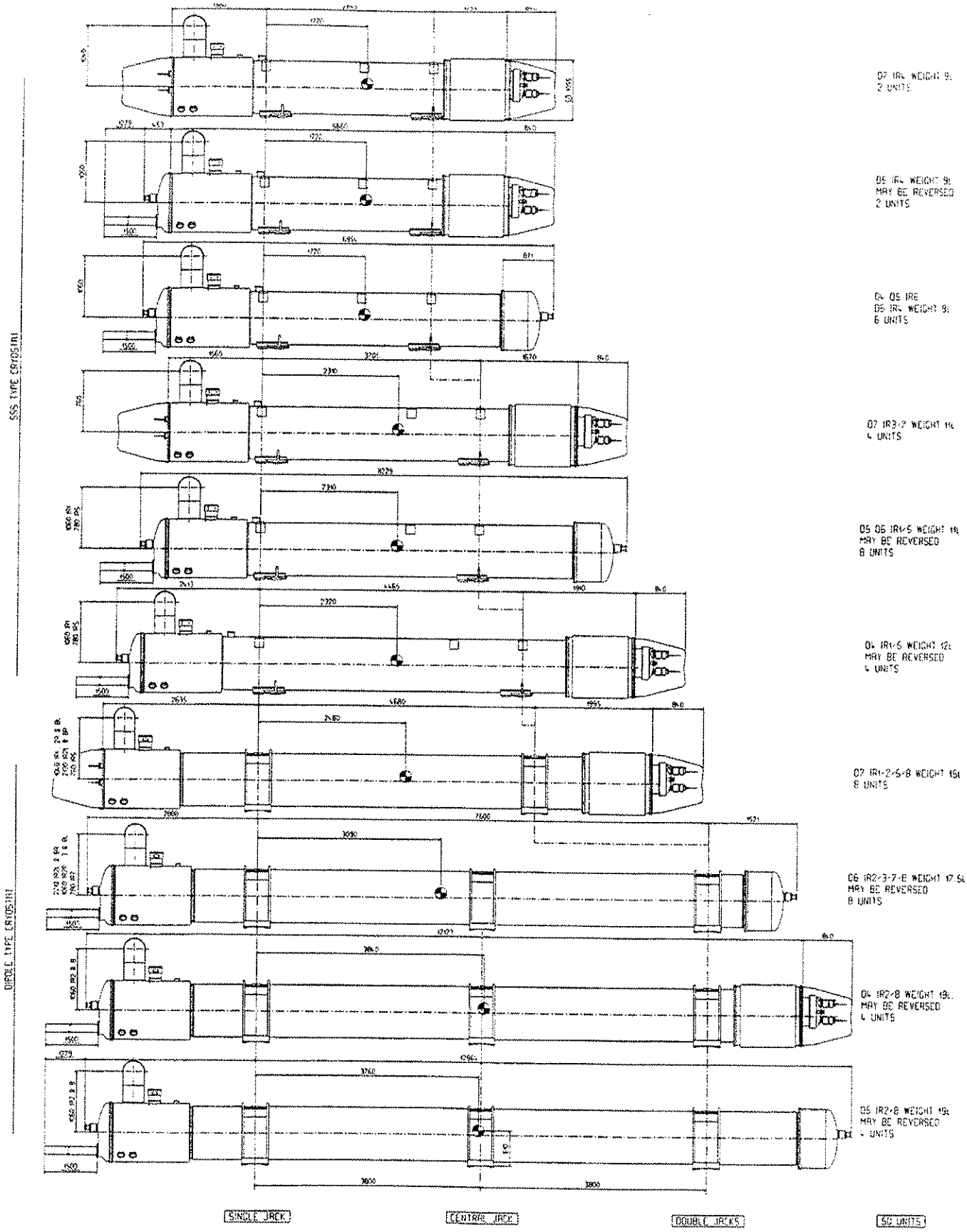

Figure 8.6: Longitudinal view of the matching section cryostated quadrupole assemblies.

Matching Section Cryostats

The cryostats of the matching section quadrupoles were designed by extending the solutions developed for the arc cryostats as far as practical. In particular, the cross-section features of the cryostat (vacuum vessel diameter and thickness), the thermal shields, the MLI blankets and composite support posts were all kept the same. For all cold masses where the length and mass allowed, a two-point support design developed for the arc SSS was preferred. For the longest and heaviest cold masses, however, a three-point support of the dipole vacuum vessels had to be adopted in order to limit the cold mass deflection. As a result, there are six lengths of cryostats, Fig. 8.6, including the additional variants for the stand-alone units.

In addition to the variety of cold masses, the SSS for the matching sections have to accommodate the very specific features imposed by the topology of the machine. For instance, the Q6 quadrupole cryostats in the injection areas (IR2 and IR8), as well as in IR6, must be modified to allow sufficient clearance for the injection and ejection beam lines, respectively. On the other hand, due to the LHC tunnel slope, stand-alone units have to be positioned in such a way as to allow clear venting paths for the boil-off from the 4.5 K saturated helium baths. Also due to the tunnel configuration, the Q7 quadrupoles on the left side of IR4, 5 and 7 are cooled by heat conduction to the 1.9 K heat exchanger of the upstream dipole. In spite of considerable effort to standardize the design, the specific features of the cold masses and cryostats result in 20 different types of cold mass assemblies and 26 different types of cryo-assemblies for a total of 50 matching section quadrupoles [3].

Testing of the Matching Section Quadrupoles

The large number of variants of the dispersion suppressor and matching section quadrupoles raise the issue of their final cold testing. Although in principle the infrastructure and the test capacity exist in the SM18 hall (see Sec. 7.7), the tests of these special magnets is made more difficult because they require additional equipment and in particular the length of time necessary for setting-up and execution of the tests. It is therefore not excluded that the test programme for a subset of these magnets is considerably reduced, or even that some magnets are installed without testing. In order to partially compensate for this possibility, the individual MQM and MQY magnets are tested as far as possible in the vertical cryostat in Block 4 before their assembly and closure in the helium vessel. These tests are focused on the electrical integrity and quench training. The magnetic field quality of the magnets, as well as the alignment of the cold masses are checked by warm measurements, which are used for inferring the performance of the magnets at operating temperatures, in case these are not directly measured.

8.3.2 Normal Conducting Matching Quadrupoles

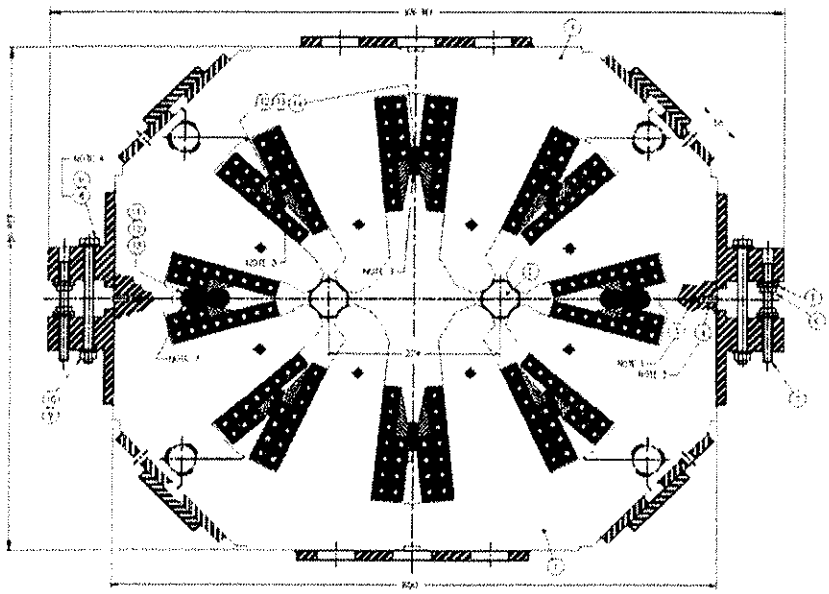

Figure 8.7: Cross-section of the MQW twin aperture normal conducting matching quadrupole.

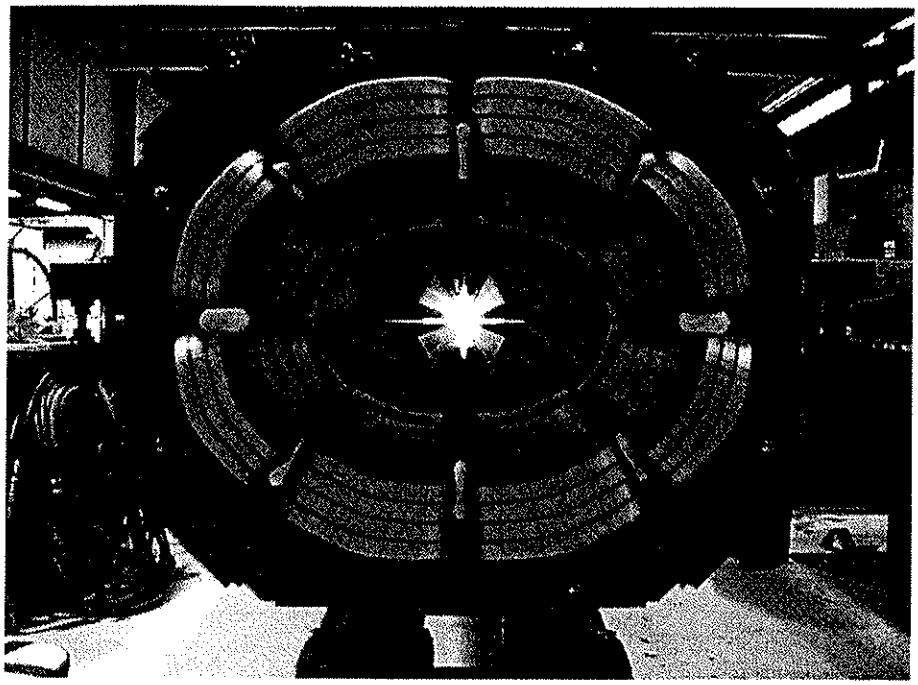

Figure 8.8: End view of the MQW twin aperture normal conducting matching quadrupole.

Table 8.6: Main parameters of the MQW normal conducting quadrupole magnet.

Magnet type	**MQWA**	**MQWB**
Magnetic length	3.1 m	
Beam separation	224 mm	
Aperture diameter	46 mm	
Operating temperature	< 65° C	
Nominal gradient	35 T/m	30 T/m
Nominal current	710 A	600 A
Inductance	28 mH	
Resistance	37 mΩ	
Conductor X-section	20.5 x 18.0 mm² inner poles 17.0 x 17.0 mm² outer poles	
Cooling hole diameter	7 mm inner poles, 8 mm outer poles	
Number of turns per magnet	8 x 11	
Minimum water flow	28 l/min	
Dissipated power at I_{nom}	19 kW	14 kW
Mass	11700 kg	

In the cleaning insertions IR3 and IR7, each of the matching quadrupoles Q4 and Q5 consists of a group of 6 normal conducting MQW magnets. This choice is dictated by the high radiation levels due to scattered particles from the collimation system and therefore the use of superconducting magnets is not possible. The cross-section of the quadrupole is shown in Fig. 8.7 and features two apertures in a common yoke (2-in-1), which is atypical for normal conducting quadrupole magnets but is needed because of transverse space constraints in the tunnel. The two apertures may be powered in series in a standard focusing/defocusing configuration (MQWA), or alternatively in a focusing/focusing configuration (MQWB) in order to correct asymmetries of the magnet. In a functional group of 6 magnets, 5 are configured as MQWA corrected by one configured as MQWB. As in most normal conducting magnets, the field quality is iron-dominated and therefore defined by the shape of the magnetic poles. In order to achieve the necessary field quality, the

separation between poles is adjusted and verified to within a tenth of a millimetre by tightening rods along the length of the magnet. The total number of quadrupole magnets in each of the two insertions is 24. Altogether 52 magnets of this type including 4 spares have been built by Canadian industry in collaboration with TRIUMF and CERN. A view of the end of such a quadrupole is shown in Fig. 8.8. The design is given in [4, 5, 6] and the design parameters in Tab. 8.6. The field quality of the production magnets, based on measurements made on 22 quadrupoles is given in Tab. 8.7.

Table 8.7: Field quality of the production MQW quadrupoles at 35 T/m (units of 10^{-4} at 17 mm).

	Measured Average	Measured rms.
b1	-16.11	58.62
b2	10 000	0
b3	39.13	5.60
b4	4.12	2.09
b5	5.74	0.64
b6	-1.09	0.26
b7	-1.81	0.17
b8	0.05	0.07
b9	0	0
b10	0.97	0.03
a1	5.05	46.36
a2	0	0
a3	0.33	3.99
a4	-0.08	1.31
a5	-0.04	0.69
a6	-0.04	0.17
a7	0.01	0.07
a8	0.01	0.17
a9	0	0
a10	-0.02	0.04

8.4 SEPARATION DIPOLES

The separation dipoles are used in several insertions to change the beam separation from the nominal 194 mm in the LHC arcs. In the experimental insertions the pair of D1-D2 dipoles brings the two beams onto a colliding orbit at the interaction point and then separates the beam again beyond the collision point. To reduce the beam-beam effects, the first separation dipole D1 is placed immediately upstream of the low-β triplet. In the high-luminosity insertions, high radiation levels are expected and more robust normal conducting magnets, MBXW, are used. In the ALICE and LHCb insertions, D1 is a stronger superconducting magnet, MBX, allowing more space for the injection systems. In all cases, the D2 separation dipole, MBRC, is a twin-aperture superconducting magnet. In the cleaning insertions, the pair of D3-D4 dipoles separates the beams to 224 mm to accommodate the collimation system, while in the RF insertion the beam separation is 420 mm so that individual RF cavities can be installed for each beam. The radiation levels in the cleaning insertions require the use of normal conducting dipoles, MBW (both for D3 and D4), while superconducting dipoles, MBRB (D4) and MBRS (D3), are used in the RF insertion.

8.4.1 Superconducting Separation Dipoles

The MBX (D1), MBRB/C (D4/D2) and MBRS (D3) dipoles are designed and built by BNL (USA) on the basis of the RHIC lattice dipole [7]. The MBX magnets are designed with one RHIC-style cold mass in a RHIC-style cryostat and the MBRS magnets are designed with two such cold masses side-by-side in a common cryostat. The cold masses are built straight, without the 47 mm sagitta of the RHIC magnets. The MBRB and MBRC magnets are built with coils that are pre-stressed with stainless steel collars. These

collared coils are assembled into yokes with common outside dimensions but with two aperture spacing, depending on the type. The main parameters of the magnets are given in Tab. 8.8.

Table 8.8: Main parameters of the MBX, MBRB/C and MBRS superconducting separation dipoles

Coil inner diameter Magnetic length Nominal field	80 mm 9.45 m 3.8 T
Operating temperature	1.9 K (MBX) 4.5 K (MBRB/C, MBRS)
Nominal current	5750 A (MBX, MBRS) 6050 A (MBRB/C)
Aperture separation	188 mm (MBRC) 194 mm (MBRB) 414 mm (MBRS)
Cold bore diameter OD/ID	78/74 mm (MBX) 73/69 mm (MBRB/C, MBRS)
Peak field in coil Quench field Stored energy per aperture Inductance per aperture	4.2 T 4.8 T 470 kJ 25.8 mH
Quench protection	Quench heaters, two independent circuits per aperture
Cable width Mid-thickness Keystone angle No of strands Strand diameter Cu/SC Ratio Filament diameter j_c	9.73 mm 1.166 1.2 deg. 30 0.648 mm 1.8 6 μm 2500 A/mm^2 (4.2 K and 5 T)
Mass	4500 kg (MBX) 13500 kg (MBRS) 24500 kg (MBRB/C)

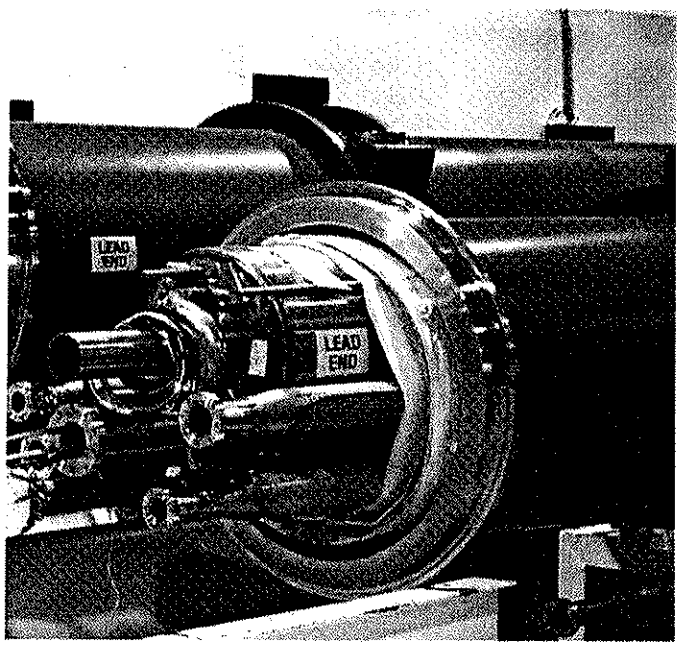

Figure 8.9: The MBX (D1) cryo-dipole, viewed from the lead end.

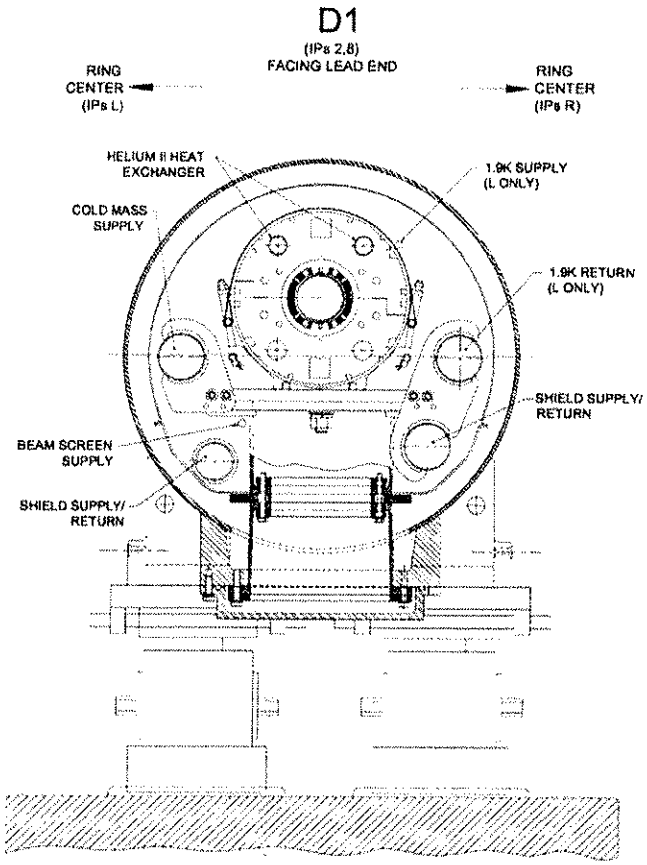

Figure 8.10: Cross-section of the MBX (D1) cryo-dipole, of same design as the RHIC main dipoles.

Table 8.9: Field quality of the MBX magnets at 3.8 T (units of 10^{-4} at 25 mm)

	Measured average	Reference Table <b> +- Δb		Measured rms	Reference σ(b)
b2	-0.19 +-0.24	0.25 +-0.79	b2	0.53	0.28
b3	-3.10 +-0.98	-1.71 +-3.57	b3	2.20	1.70
b4	0.14 +-0.08	0.07 +-0.21	b4	0.18	0.08
b5	0.99 +-0.17	0.24 +-0.80	b5	0.37	0.39
b6	0.030 +-0.036	-0.120 +-0.100	b6	0.080	0.040
b7	1.160 +-0.031	1.170 +-0.190	b7	0.070	0.100
b8	-0.010 +-0.009	-0.020 +-0.030	b8	0.020	0.010
b9	-0.070 +-0.013	0.010 +-0.120	b9	0.030	0.040
b10	0.040 +-0.009	0.040 +-0.050	b10	0.020	0.020
b11	-0.680 +-0.004	-0.600 +-0.040	b11	0.010	0.020

	Measured average	Reference Table <a> +- Δa		Measured rms	Reference σ(a)
a2	-3.16 +-1.02	0.54 +-3.71	a2	2.29	1.51
a3	-0.83 +-0.04	-1.31 +-0.55	a3	0.09	0.18
a4	-0.58 +-0.28	0.06 +-1.08	a4	0.62	0.41
a5	0.17 +-0.04	0.16 +-0.17	a5	0.10	0.06
a6	0.050 +-0.072	-0.050 +-0.550	a6	0.160	0.160
a7	-0.110 +-0.013	-0.110 +-0.060	a7	0.030	0.020
a8	0.050 +-0.013	-0.010 +-0.150	a8	0.030	0.050
a9	0.020 +-0.009	0.010 +-0.030	a9	0.020	0.010
a10	0.060 +-0.009	0.040 +-0.040	a10	0.020	0.020
a11	-0.010 +-0.004	-0.010 +-0.010	a11	0.010	0.010

MBX

The MBX dipole as seen from its lead end is shown in Fig. 8.9 and its cross-section is shown in Fig. 8.10. Many of its design features are identical to the RHIC main dipoles. However, the magnet is equipped with two heat exchangers allowing it to be cooled to 1.9 K and it has a larger cold bore (OD 78 mm) than the RHIC dipole. Another feature is the use of quench heaters as active protection elements. All these modifications require additional cryogenic and electrical instrumentation, described in [8].

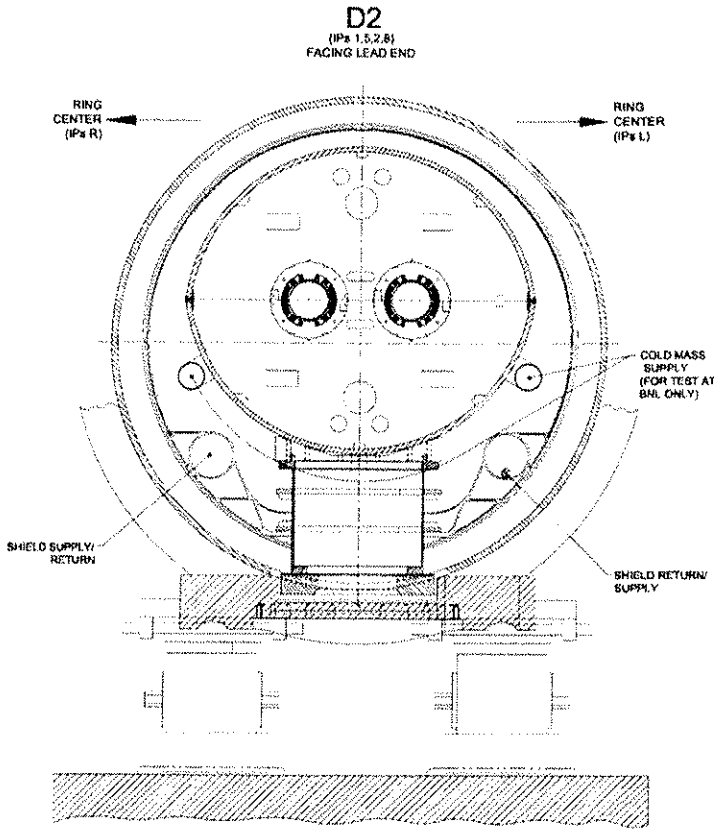

Figure 8.11: Cross section of the MBRC (D2) cryo-dipole at a support post location.

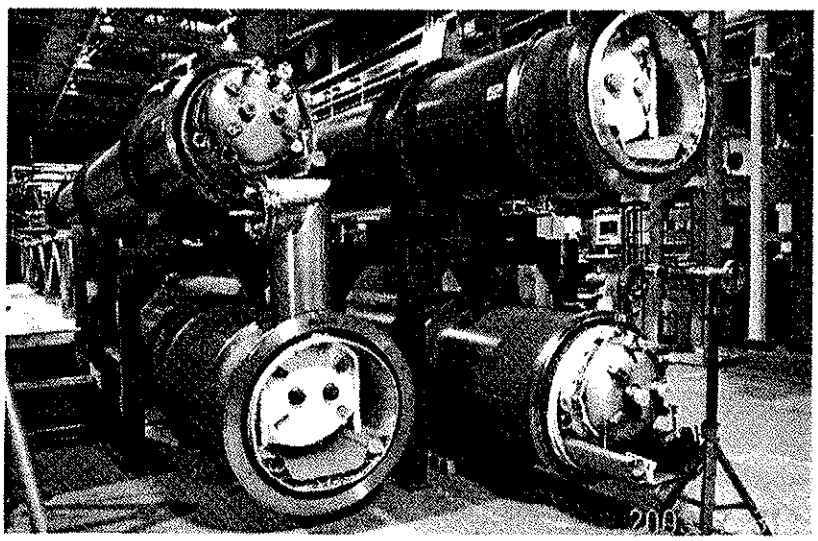

Figure 8.12: MBRB cryo-dipoles ready for shipment. The lower left unit is equipped with a QQS module.

BNL has completed all four MBX dipoles necessary for the LHC and an additional unit as a spare. All magnets were tested in BNL, including cold checkout and quench training at 4.5 K. All magnets were

powered to well above the ultimate current at 4.5 K, leaving considerable margin for operation at 1.9 K in the LHC. One magnet was fully tested for static and dynamic field quality. The field quality of the other magnets was obtained on the basis of cold-warm correlations established during the RHIC production. The field quality of the as-produced magnets is compared in Tab. 8.9 to the reference field error table [9].

Table 8.10: Field quality of the MBRB/C dipoles at 3.8 T (units of 10^{-4} at 25 mm)

	Measured average	Reference Table <b> +- Δb		Measured rms	Reference σ(b)
b2	-0.18 +-0.10	-0.07 +-0.79	b2	0.36	0.28
b3	-0.49 +-0.39	1.99 +-3.57	b3	1.36	1.70
b4	0.07 +-0.10	-0.21 +-0.21	b4	0.35	0.08
b5	0.05 +-0.10	0.04 +-0.80	b5	0.34	0.39
b6	-0.006 +-0.042	-0.050 +-0.100	b6	0.145	0.040
b7	0.179 +-0.024	0.060 +-0.190	b7	0.083	0.100
b8	-0.008 +-0.010	-0.010 +-0.030	b8	0.036	0.010
b9	-0.154 +-0.009	0.000 +-0.120	b9	0.033	0.040
b10	-0.001 +-0.004	0.030 +-0.050	b10	0.012	0.020
b11	-0.644 +-0.004	-0.560 +-0.040	b11	0.013	0.020
	Measured average	Reference Table <a> +- Δa		Measured rms	Reference σ(a)
a2	-0.65 +-0.38	0.55 +-3.71	a2	1.31	1.51
a3	-1.14 +-0.08	-1.07 +-0.55	a3	0.26	0.18
a4	0.04 +-0.19	0.06 +-1.08	a4	0.67	0.41
a5	0.17 +-0.02	0.19 +-0.17	a5	0.08	0.06
a6	0.070 +-0.059	0.000 +-0.550	a6	0.206	0.160
a7	-0.086 +-0.007	-0.110 +-0.060	a7	0.025	0.020
a8	0.020 +-0.015	-0.010 +-0.150	a8	0.052	0.050
a9	0.026 +-0.003	0.010 +-0.030	a9	0.009	0.010
a10	0.043 +-0.004	0.030 +-0.040	a10	0.013	0.020
a11	-0.002 +-0.002	-0.010 +-0.010	a11	0.006	0.010

MBRB and MBRC

The MBRB magnet is a two-in-one magnet with parallel fields in the two apertures. The MBRC is very similar in design (its cross-section is shown in Fig. 8.11) and differs only by the nominal aperture spacing (188 mm). In addition, to allow installation of the beam screens, the cold bore in MBRB is slightly off-centred on the IP side [10]. The cross-talk between parallel fields in the two apertures is reduced by additional iron around the median plane, resulting in an oval shape of the cold mass. Its outer dimensions are identical in the vertical plane to the LHC main dipole, so that standard LHC support posts and other cryostat elements are used in a 9.8 m long vacuum tank. The MBRB/C magnets are equipped with QQS service modules, Fig. 8.12, which provide cryogenic connections to the QRL for the 4.5 K operation of the Q4-D2 (Q5-D4) string of magnets, as described in [11].

BNL has completed the construction of eight MBRC and two MBRB magnets for installation in the LHC, as well as one spare of each type. All magnets were tested at 4.5 K in BNL and showed very good training behaviour. The field quality of nine magnets was measured extensively and warm-cold correlations established. The correlations were used for extrapolating the field quality of the spare magnets. The field quality of as-built magnets is compared in Tab. 8.10 to the reference field error table [9].

MBRS

The MBRS separation dipole consists of two MBX-like cold masses assembled in a 9.6 m long cryostat, as shown in Fig. 8.13. The cold masses are aligned to a separation of 414 mm using three transverse beams, connected to the upper plates of standard LHC dipole posts. Other cryostat elements are identical to MBRB. The magnet interfaces on the non-IP side with the QQS service module, which provides the connection to the cryogenics and powering services. On the IP side, provisions are made for interconnecting MBRS with the MSRU undulator [12].

Three MBRS magnets are built by BNL, two of which are installed in the RF insertion and one is a spare. All magnets are fully tested at 4.5 K, including field measurements. The field quality of the MBRS magnets follows closely that of MBX, as shown in Tab. 8.9.

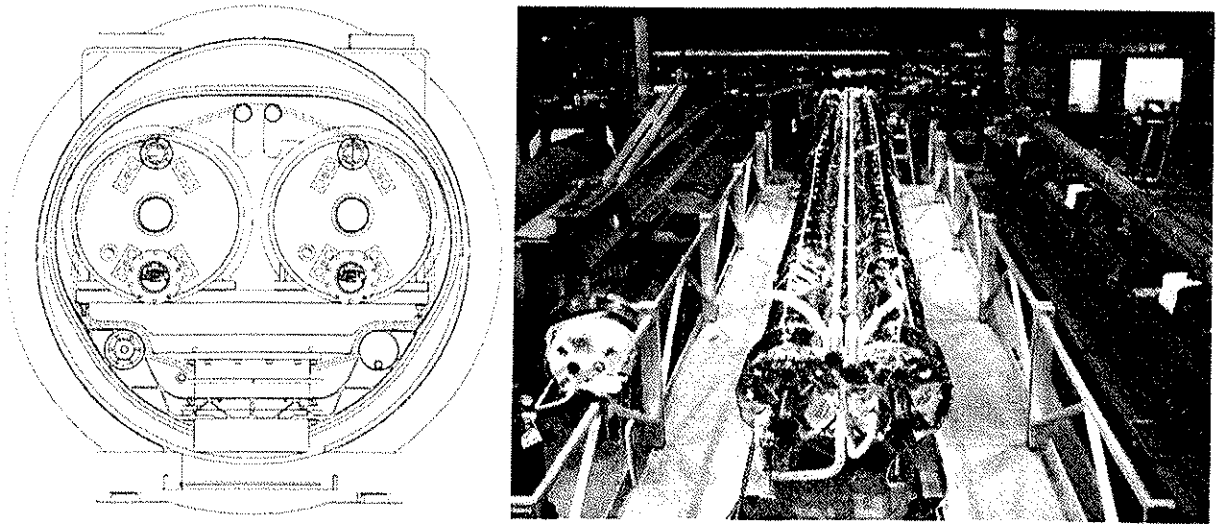

Figure 8.13: (Left) Cross-section of the MBRS dipole. (Right) Assembly of the MBRS cold masses at BNL.

8.4.2 Normal Conducting Separation Dipoles

The MBW and MBXW dipoles are designed and built by BINP (Novosibirsk, Russia) employing a well-established technology of epoxy-impregnated coils in a laminated window-frame steel yoke (Figs. 8.14, 8.15 and 8.16). The two coils of both types of magnet consist of three pancakes that are wound from a hollow rectangular copper conductor. The conductor is insulated with glass-fibre tape and impregnated with epoxy resin. The yoke is laminated from insulated magnetic steel sheets of 1.5 mm thickness to reduce eddy currents that are generated during ramping of the magnets. The laminations are held together by welded plates. The shape of the end-plates and shims is adjusted to compensate the magnetic end effect. The coils are fixed in the yoke by stainless steel clamps at the end of the magnet and further supported by separation blocks in the mid-plane. The magnets are manufactured as two half-cores that are clamped together with studs and nuts along the side cover plates. The main parameters of the magnets are given in Tab. 8.11.

The field quality of normal conducting magnets is defined by the shape of the steel poles. In order to guarantee good field quality, punching of laminations is controlled to within 0.05 mm in the vicinity of the apertures. Also, lamination stacks and the clamping of the two half-magnets are assembled within a tenth of a millimetre. Access to the laminations on the top and the sides of the magnet allows the verification of the magnet assembly after production. Specifications require a sag of less than 0.5 mm and a twist of less than 1 mrad. All these parameters are checked to assure the quality during production and to guarantee the required field quality. Magnetic field quality measured at BINP and at CERN is given in [13].

Table 8.11: Main parameters of the MBW and MBXW separation dipoles

Magnet type	**MBW**	**MBXW**
Magnetic length	3.4 m	
Beam separation	194-224 mm	0-27 mm
Gap height	52 mm	63 mm
Coil Protection temperature	< 65° C	
Nominal field	1.42 T	1.28 T
Nominal current	720 A	690 A
Inductance	180mH	145 mH
Resistance	55 mΩ	60 mΩ
Conductor X-section	18 x 15 mm²	
Cooling hole diameter	8 mm	
Number of turns per magnet	2 x 42	2 x 48
Minimum water flow	19 l/min	
Dissipated power at I_{nom}	29kW	29 kW
Mass	18000 kg	11500 g

MBW

The MBW magnet, Fig. 8.14, features a pole shape with varying gap height and two positions for the beam pipes (194 to 224 mm) while employing a standard H-type dipole construction. The two coils consist of three pancakes with 14 windings. The overall number of MBW magnets produced by BINP is 24, including 4 spares. The expected field quality is given in reference [14].

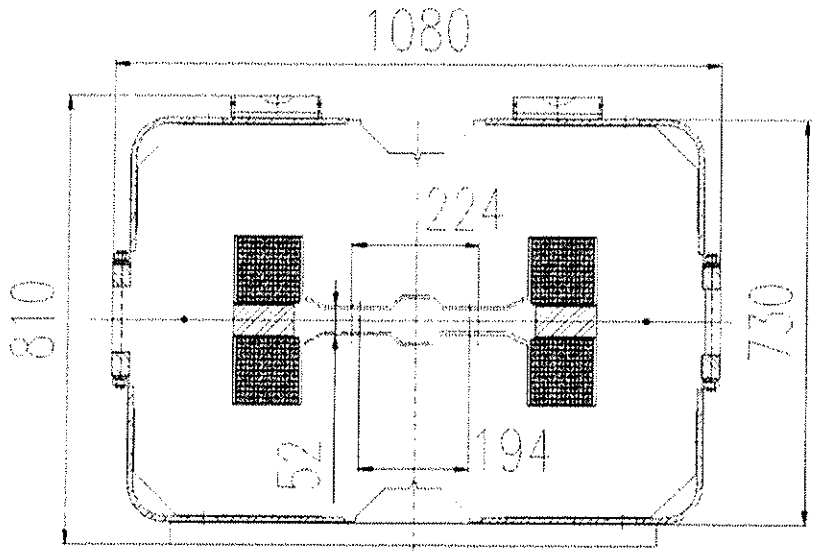

Figure 8.14: Cross-section of the normal conducting separation dipole MBW.

MBXW

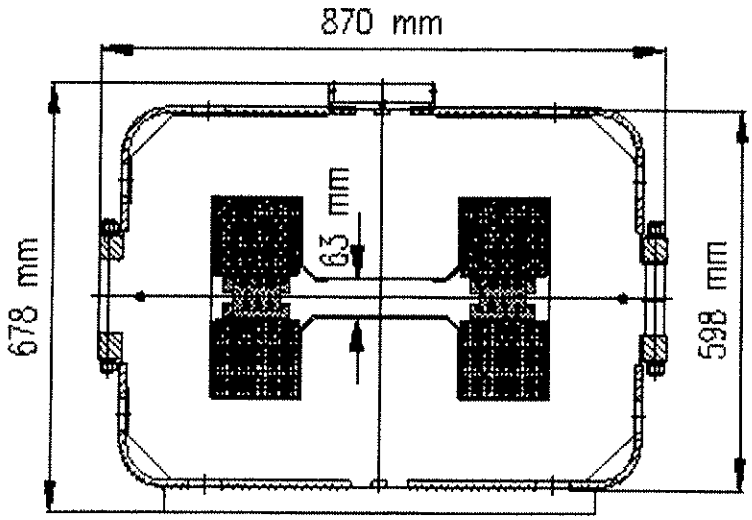

Fig. 8.15: Cross-section of the normal conducting separator dipole magnet MBXW.

The cross-section of the MBXW is shown in Fig. 8.15. It features a coil with three pancakes with 16 turns each, wound using the same copper conductor as for the MBW. Since both beams run through a single pipe, the pole region is 120 mm wide with a gap height of 63 mm. Small shims, placed along the sides of the pole, are part of the punched laminations and homogenize the field in the aperture. The total number of MBXW magnets built by BINP is 29, including 4 spares. A view of such a magnet seen from the connection end is shown in Fig. 8.16. The expected field quality is given in [15].

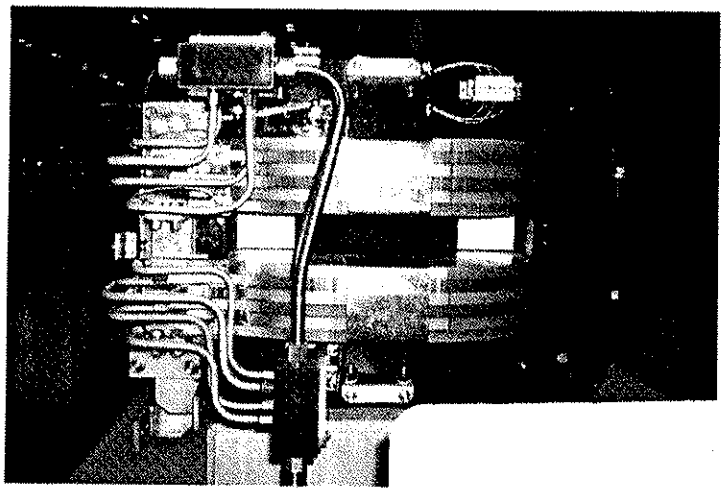

Figure 8.16: View of the connection end of the normal conducting separation dipole MBXW

8.5 LOW-BETA TRIPLETS

The low-β triplet, Fig. 8.17, is composed of four single-aperture quadrupoles with a coil aperture of 70 mm. The magnets are cooled with superfluid helium at 1.9 K using an external heat exchanger system capable of extracting up to 10 W/m of power deposited in the coils by the secondary particles emanating from the proton collisions. Two types of quadrupoles are used in the triplet, 6.6 m long MQXA magnets designed and developed by KEK (Japan) and 5.7 m long MQXB magnets designed and built by FNAL (USA). The magnets are powered in series with 7 kA, with an additional inner loop of 5 kA for the MQXB magnets. Together with the orbit correctors MCBX, skew quadrupoles MQSX and multipole spool pieces supplied by CERN, the low-β quadrupoles are completed in their cold masses and cryostated by FNAL. The cryogenic feed-boxes (DFBX), providing a link to the cryogenic distribution line and power converters, are designed and built by LBNL (USA).

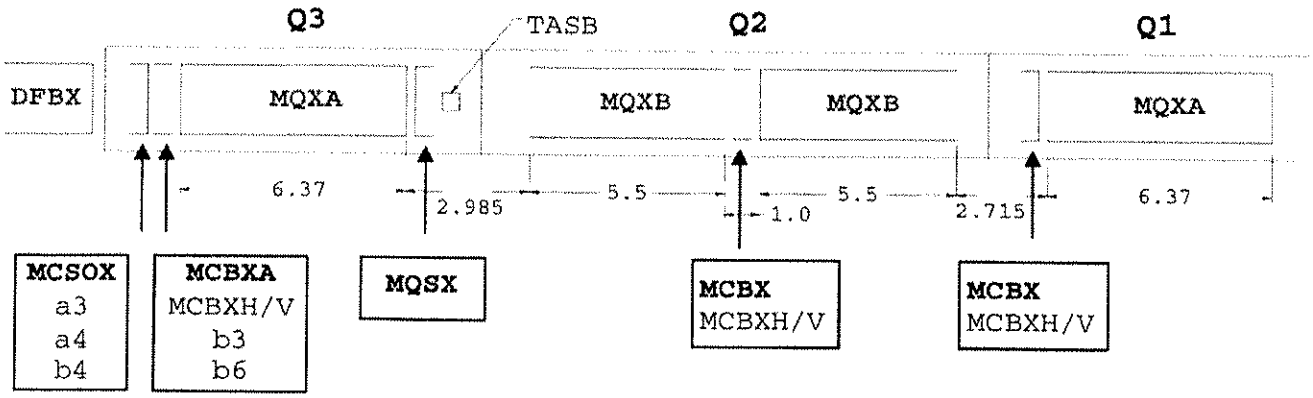

Figure 8.17: Schematic Layout of the low-β triplet.

Alongside the LHC main dipoles, the high-gradient, wide-aperture low-β quadrupoles are the most demanding magnets in the collider. They must operate reliably at 215 T/m, sustain extremely high heat loads in the coils and high radiation dose during their lifetime and have a very good field quality within the 63 mm aperture of the cold bore. In order to validate their design choices, KEK and FNAL have launched comprehensive R&D programmes comprising a number of short model magnets, [16] and [17]. Both programmes were successful in fulfilling the design goals and demonstrating the LHC operational requirements. An important result of the programmes, confirmed by the quadrupole prototypes, is that the field quality is considerably better than initially expected. As a result, the expected field error tables of the magnets were revised [18, 19] and the number and strength of the multipole correctors in the low-β triplet reduced and their arrangement simplified.

8.5.1 MQXA low-β Quadrupole

The design of the MQXA quadrupole is based on a four-layer coil using 11 mm wide Rutherford-type graded NbTi cables. The coils are wound and cured in two double layers and are assembled using 10 mm wide spacer-type collars, Fig. 8.18. The pre-stress in the coils and their rigidity is provided by the yoke structure, which consists of horizontally split laminations keyed at the mid-plane. The main parameters of the magnet are given in Tab. 8.12.

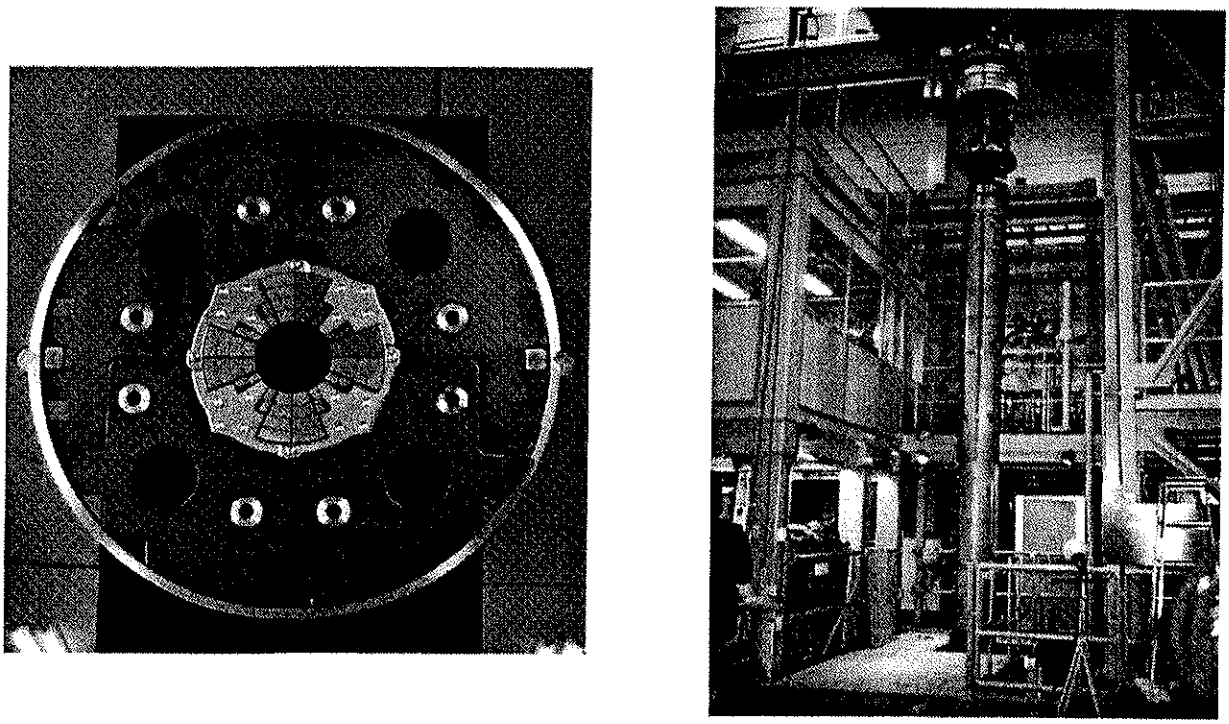

Figure 8.18: (Left) Cross-section of the MQXA low-β quadrupole. (Right) MQXA quadrupole ready for tests in the vertical cryostat in KEK.

Table 8.12: Main parameters of the MQXA low-β quadrupole

Coil inner diameter	70 mm
Magnetic length	6.37 m
Operating temperature	1.9 K
Nominal gradient	215 T/m
Nominal current	7149 A
Cold bore diameter OD/ID	66.5/62.9 mm
Peak field in coil	8.6 T
Quench field	10.7 T
Stored energy	2300 kJ
Inductance	90.1 mH
Quench protection	Quench heaters, two independent circuits
Cable width, cable 1/2	11/11 mm
Mid-thickness, cable 1/2	1.487/1.340 mm
Keystone angle, cable 1/2	2.309/1.319 deg.
No of strands, cable 1/2	27/30
Strand diameter, cable 1/2	0.815/0.735 mm
Cu/SC Ratio, cable 1/2	1.2/1.9
Filament diameter, cable 1/2	10/10 μm
j_c, cable1/2, (4.2 K and 6 T)	2200/2160 A/mm^2
Mass	9600 kg

KEK has completed the production of the total of 16 MQXA magnets, for eight Q1 and eight Q3 quadrupoles. In addition, two magnets have been built as spares. All magnets have been tested in the vertical testing facility in KEK, Fig. 8.18. The magnets were systematically trained to 230 T/m, well above the ultimate gradient in the LHC, to guarantee the temperature margin. The acceptance criterion was that following training and a full-energy dump, the magnets should be powered to 225 T/m without quench. All magnets passed this criterion. In addition to training, all magnets were systematically measured for static and dynamic field effects. The field quality of the production is given in Tab. 8.13, where reference values are also shown [18].

Table 8.13: Field quality of the MQXA low-β quadrupole at 205 T/m (units of 10^{-4} at 17 mm).

	Measured average	Reference Table <b> ± Δb		Measured rms	Reference σ(b)
b3	0.040 ± 0.080	0.000 ± 0.680	b3	0.330	0.096
b4	1.290 ± 0.030	-0.170 ± 0.920	b4	0.100	0.066
b5	-0.010 ± 0.010	0.000 ± 0.130	b5	0.040	0.250
b6	0.350 ± 0.020	0.330 ± 0.890	b6	0.090	0.440
b7	-0.002 ± 0.002	0.000 ± 0.031	b7	0.009	0.055
b8	0.022 ± 0.001	0.003 ± 0.041	b8	0.003	0.028
b9	-0.001 ± 0.002	0.000 ± 0.012	b9	0.008	0.019
b10	-0.016 ± 0.002	-0.002 ± 0.058	b10	0.007	0.037
	Measured average	Reference Table <a> ± Δa		Measured rms	Reference σ(a)
a3	0.220 ± 0.090	0.000 ± 0.680	a3	0.330	0.096
a4	-0.010 ± 0.080	0.000 ± 0.330	a4	0.290	0.510
a5	0.010 ± 0.010	0.000 ± 0.130	a5	0.040	0.240
a6	-0.020 ± 0.010	0.000 ± 0.070	a6	0.020	0.120
a7	0.002 ± 0.002	0.000 ± 0.031	a7	0.007	0.055
a8	0.001 ± 0.004	0.000 ± 0.021	a8	0.014	0.028
a9	-0.001 ± 0.001	0.000 ± 0.012	a9	0.004	0.019
a10	-0.004 ± 0.001	0.000 ± 0.012	a10	0.003	0.009

8.5.2 MQXB low-β Quadrupole

The MQXB design features a two-layer coil, with each layer individually wound using a 15.4 mm wide Rutherford-type NbTi cable, Fig. 8.19. The coils are assembled using free-standing collars, which provide the pre-stress and counteract the magnetic forces. The collared assembly is aligned in the yoke structure with precision keys and the magnet enclosed in a stainless steel helium vessel consisting of half-shells welded at the pole plane. The design parameters of the magnet are given in Tab. 8.14.

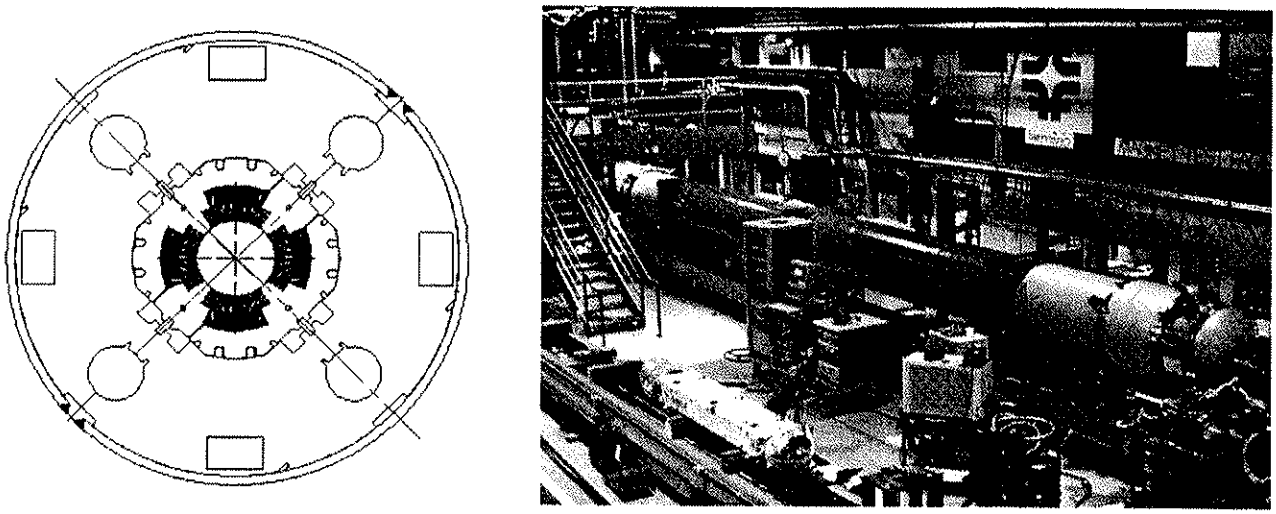

Figure 8.19: (Left) Cross-section of the MQXB low-β quadrupole. (Right) Q2 quadrupole on test in FNAL.

Table 8.14: Main parameters of the MQXB low-β quadrupole

Coil inner diameter	70 mm
Magnetic length	5.5 m
Operating temperature	1.9 K
Nominal gradient	215 T/m
Nominal current	11950 A
Cold bore diameter OD/ID	66.5/62.9 mm
Peak field in coil	7.7 T
Quench field	9.2 T
Stored energy	1360 kJ
Inductance	19.1 mH
Quench protection	Quench heaters, two independent circuits
Cable width, cable 1/2	15.4/15.4 mm
Mid-thickness, cable 1/2	1.456/1.146 mm
Keystone angle, cable 1/2	1.079/0.707 deg.
No of strands, cable 1/2	37/46
Strand diameter, cable 1/2	0.808/0.650 mm
Cu/SC Ratio, cable 1/2	1.3/1.8
Filament diameter, cable 1/2	6/6 μm
j_c, cable 1/2 (4.2 K and 5 T)	2750/2750 A/mm2
Mass	5700 kg

In total, 18 MQXB magnets are built by FNAL for the nine Q2 assemblies, one of which is a spare. FNAL tests all quadrupoles as cryostated magnets in a horizontal test stand, as shown in Fig. 8.19. Like the MQXA magnets, all quadrupoles are trained to 230 T/m at 1.9 K to guarantee ultimate gradient in LHC in presence of dynamic heat load induced by beam collisions. The quadrupoles are also tested for field quality and alignment. On the basis of the first half of production, a comparison of the measured and expected field multipoles is given in Tab. 8.15.

Table 8.15: Field quality of the MQXB low-β quadrupole at 205 T/m (units of 10^{-4} at 17 mm)

	Measured average	Reference Table <b> +- Δb		Measured rms	Reference σ(b)
b3	0.68 +-0.12	0.00 +-0.64	b3	0.27	0.25
b4	0.13 +-0.22	0.00 +-0.22	b4	0.49	0.25
b5	0.02 +-0.04	0.00 +-0.18	b5	0.08	0.10
b6	-0.16 +-0.13	0.21 +-0.42	b6	0.29	0.17
b7	-0.012 +-0.012	0.000 +-0.048	b7	0.027	0.018
b8	0.007 +-0.007	0.000 +-0.011	b8	0.015	0.017
b9	0.018 +-0.016	0.000 +-0.008	b9	0.036	0.009
b10	-0.015 +-0.005	-0.007 +-0.011	b10	0.012	0.009
	Measured average	**Reference Table <a> +- Δa**		**Measured rms**	**Reference σ(a)**
a3	-0.57 +-0.29	0.00 +-0.32	a3	0.65	0.25
a4	0.06 +-0.13	0.00 +-0.27	a4	0.29	0.25
a5	-0.35 +-0.11	0.00 +-0.18	a5	0.24	0.10
a6	0.02 +-0.03	-0.03 +-0.09	a6	0.06	0.17
a7	0.007 +-0.017	0.000 +-0.040	a7	0.039	0.018
a8	0.005 +-0.011	0.000 +-0.011	a8	0.025	0.017
a9	-0.032 +-0.009	0.000 +-0.008	a9	0.020	0.009
a10	-0.026 +-0.015	0.000 +-0.008	a10	0.034	0.009

8.5.3 Inner Triplet Cold Masses and Cryostats

The MQXA and MQXB magnets are completed with MCBX, MQSX and higher-order correctors to form the Q1, Q2 and Q3 quadrupoles. The Q1 quadrupole houses an MQXA and a single MCBX orbit corrector on the non-IP side, while the Q2 quadrupole includes two MQXB magnets with an MCBX corrector in between. The Q3 quadrupole has an MQXA and a skew quadrupole MQSX on the IP side and on the non-IP side an MCBX orbit corrector with a b_3-b_6 insert (MCSTX), followed by the a_3-a_4-b_4 (MCSOX) assembly.

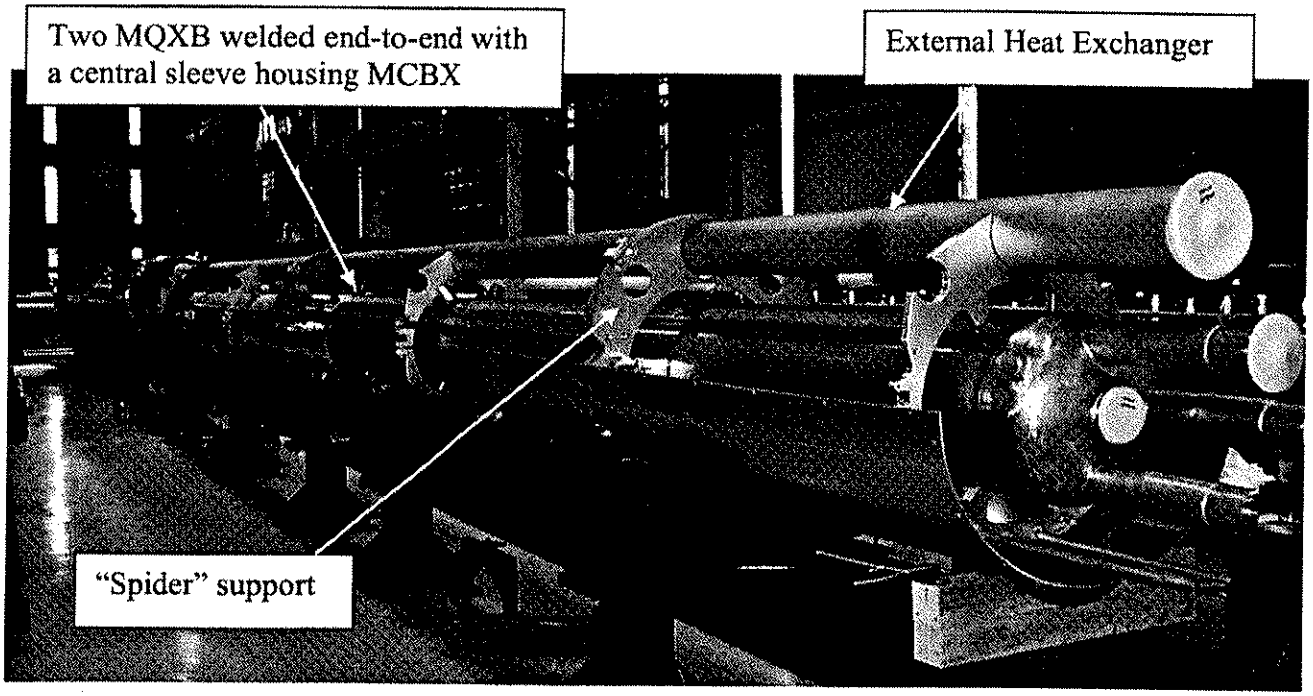

Figure 8.20: Q2 cryo-magnet assembly.

The high heat load expected in the high-luminosity insertions and the alignment requirements for the quadrupole positioning determined the design of the inner triplet cryostat [20]. The positioning of the cold mass and its stability is assured by a system of ring supports ("spiders"), locked to the reinforcements of the 914 mm diameter vacuum vessel, as shown in Fig. 8.20. Two spiders are used in Q1 and Q3 quadrupoles, which are 7.7 m and 8.4 m long, while the 12.5 m long Q2 quadrupole is supported with three spiders. The spiders also serve to guide the cryogenic pipes, in particular the external heat exchanger, which runs above the quadrupole cold masses. It also serves as an adapting element to slightly different outer dimensions of the MQXA and MQXB magnets.

The interconnections between inner triplet cryo-magnets are determined on the basis of power deposition and optics studies and consist of two long drift spaces in between Q1-Q2 and Q2-Q3 and a short interconnect Q3-DFBX. The longitudinal space in-between Q1-Q2 and Q2-Q3 is used for mounting a beam position monitor BPMS and an additional absorber, TASB. The design of interconnecting elements and absorbers takes into account the cooling and beam vacuum requirements of the long drift tubes and the constraints of mounting on the test bench and in the tunnel.

8.6 ORBIT AND MULTIPOLE CORRECTORS IN THE INSERTIONS

Most of the corrector magnets in the insertions are superconducting, except the corrector magnets in the cleaning insertions associated with Q4 and Q5 which are normal conducting magnets of type MCBW (see Sec. 8.6.3). The general design and fabrication principles of the superconducting correctors of the insertions [21] are similar to those of the arcs and are made also from similar strands as described in Sec. 7.6. The list of the superconducting correctors used in the insertions is given in Tab. 8.16.

Table 8.16: Overview of superconducting corrector magnet in the insertions.

Name	Description	Location
MCBC, MCBY	Dipole orbit correctors	Dispersion suppressors & matching sections
MQTL	Long trim quadrupole	Dispersion suppressors & matching sections
MCBX	Nested horizontal & vertical dipole orbit corrector.	Inner Triplets
MCBXA= MCBX+MCSTX	MCBX with a nested 6-pole, 12-pole multipole corrector insert	
MQSX	Skew quadrupole	Inner Triplets
MCOSX+MCOX +MCSSX	Nested skew sextupole, octupole, skew octupole corrector package	Inner Triplets

8.6.1 Orbit Correctors MCBC/Y and Long Trim Quadrupoles MQTL

MCBC and MCBY

The LHC insertion regions are equipped with 6 different types of twin-aperture dipole orbit corrector assemblies. The MCBC (four different types) and the MCBY (two different types) are twin-aperture assemblies consisting of two superconducting dipole modules mounted in a common support structure. These magnet modules are individually powered and arranged so that the field in one aperture is vertical (horizontal correction) and the other horizontal (vertical correction).

The MCBC assemblies are associated with MQM and MQ type quadrupoles, whereas the MCBY assemblies are associated with the MQY quadrupoles. Consequently, the modules of the MCBC assemblies have a 56 mm bore diameter whereas the MCBY modules have a 70 mm bore diameter. Both types of modules are of similar construction and dimensions, using the same superconducting wire. Since the MCBC assemblies are associated with two different types of quadrupoles, two versions of support structures are required, which differ in their outer contour and diameter. The MCBC correctors used in the MQM-type cold mass configuration, which is based on a welded half-shell design, have the same outer contour as the MQM quadrupoles. These correctors are either MCBCA or MCBCB types, depending on the orientation and polarity of their modules. The MCBC correctors used in the MQ-type cold mass configuration, based on the inertia tube design, have the same outer contour as the MSCB correctors (see Sec. 7.6.3). These correctors are either MCBCC or MCBCD, depending on orientation and polarity of their modules. The MCBY correctors are used in the MQY cold mass configuration, which is based on the welded half-shell design and therefore has the same outer contour as the MQM quadrupoles. The main parameters of MCBC and MCBY orbit correctors are shown in Tab. 8.17 and their cross-sections are shown in Fig. 8.21.

Table 8.17: Main parameters of the MCBC and MCBY orbit correctors.

	MCBC	MCBY
Coil inner diameter	56 mm	70 mm
Magnetic length	0.904 m	0.899 m
Operating temperature	1.9 K	1.9/4.5 K
Nominal field (at 1.9/4.5 K)	3.11/2.33 T	3.00/2.50 T
Nominal current (at 1.9/4.5 K)	100/74 A	88/72 A
Peak field in coil (at 1.9/4.5 K)	3.65/2.68 T	3.60/2.96 T
Superconductor	Type 2	Type 2
Theoretical quench current (at 1.9/4.2 K)	172/127 A	162/120 A
Stored energy (at 1.9 K)	14.2 kJ	13.6 kJ
Self inductance	2.84 H	5.27 H
DC resistance (RT)	375 Ω	501 Ω
Overall length	1100 mm	1100 mm
Outer diameter of assembly	452 mm	475 mm
Magnet module mass	203 kg	193 kg
Total mass including the support structure	1234 kg	1247 kg

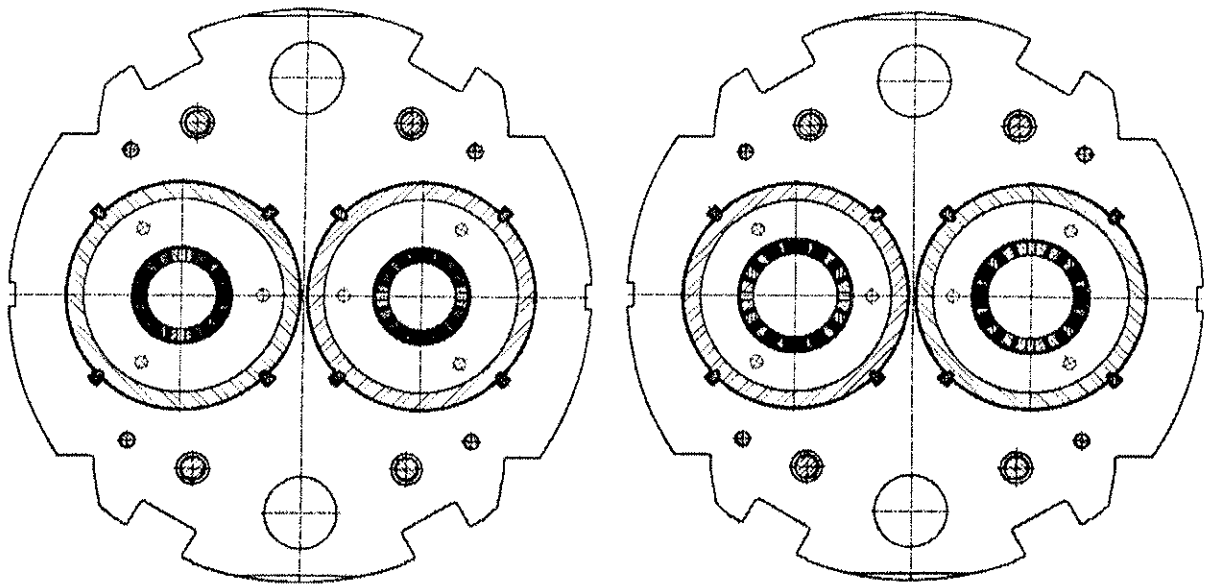

Figure 8.21: Cross-section of MCBC (left) and MCBY (right).

Each dipole module consists of two vacuum impregnated dipole coils, a laminated iron yoke, aluminium shrinking cylinders and an end plate, which supports the electrical connections. The superconducting wire has a rectangular cross-section and is enamel insulated. The dipole coils are made by winding either 14 (MCBC) or 15 (MCBY) such wires, pre-assembled as a flat ribbon, around a copper central post with composite end-spacers. The individual wires of the flat ribbon are connected in series on the end plate. All interconnections are done by soft soldering.

Pre-compression is applied to the coils by shrink fitting an aluminium cylinder over the steel laminations that make up the yoke [22]. The pre-compression is determined by the interference fit between the aluminium shrink ring and the yoke laminations around the coils. The end plate provides the reference for an accurate machining of the keyways along the outer diameter of the shrinking cylinder, which accurately locate the modules precisely within the twin-aperture support structure. The support structure is assembled from stacked steel laminations dowelled together and locked in position with tie-rods between thick steel end plates

MQTL

Each long trim quadrupole assembly consists of a pair of single-aperture quadrupole modules mounted in a twin-aperture support structure. They are used to tune the optical parameters of a certain number of quadrupoles in the dispersion suppressors and matching sections. In the dispersion suppressors one MQTL is placed alongside the MQ quadrupole in all Q11. In addition, in IR3 and IR7 one MQTL is placed alongside the MQ quadrupole in Q7 to Q10, except in Q9, where two MQTL are used. In all these cases, the MQTL assemblies are mounted in an inertia-tube type cold mass and their common support structure has the outer contour of the MSCB correctors (see Sec. 7.6.3). Further, the Q6 quadrupoles in IR3 and IR7 consists of six MQTL mounted together in a half-shell type cold mass and the common support structure has the same outer contour as the MQM. Consequently, the MQTL have two types of support structures, MQTLI for the inertia-tube type and MQTLH for the half-shell type, as shown in Fig 8.22. Both types of assemblies use the same single-aperture modules, MQTLC. The design parameters of the MQTLH and MQTLI quadrupoles are given in Tab. 8.18.

Each magnet module (MQTLC) consists of four epoxy vacuum-impregnated coils, a laminated iron yoke, an aluminium shrinking cylinder in six sections and an end plate that supports the electrical connections. The superconducting wire has a rectangular cross-section and is enamel insulated. The coils are made by counter-winding three such wires, pre-assembled as a flat ribbon, around a G11 central post with composite end spacers and subsequently wrapped with a glass-fibre/epoxy bandage. The module and final magnet assembly is similar to the MCBC and MCBY corrector magnets. The coil inter-connections are made by ultrasonic

welding. Quench protection resistors are connected in parallel with each module and mounted on the support-structure end plate at the connection end of the magnet assembly.

Table 8.18: Main parameters of the MQTL corrector magnets

	MQTLH	MQTLI
Coil inner diameter	56 mm	
Magnetic length	1300 mm	
Operating temperature	4.3 K	1.9 K
Nominal gradient	129.4 T/m	
Nominal current	550 A	
Peak field in coil	4.1 T	
Superconductor type	3	
Theoretical quench current at 4.2 K/1.9 K	670/945 A	
Stored energy	18.15 kJ	
Self inductance	0.12 H	
Overall length	1400 mm	
Module mass	95 kg	
Mass including the twin aperture support structure	1850 kg	1250 kg

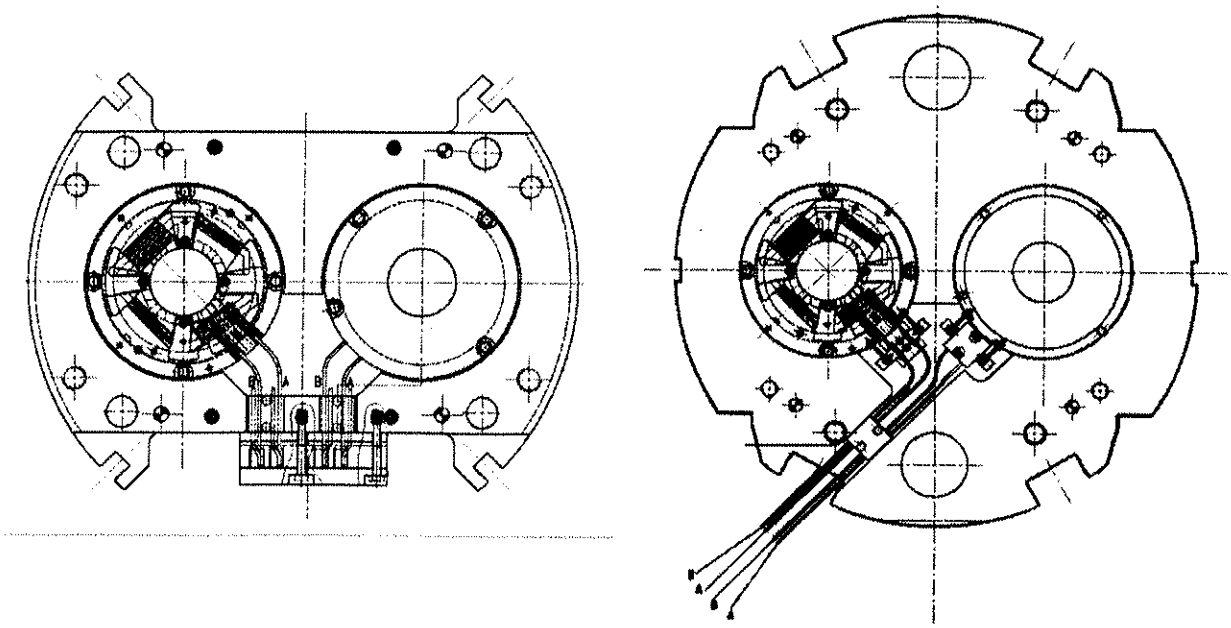

Figure 8.22: MQTLH cross-section (left) and MQTLI cross-section (right).

8.6.2 Correctors for the Inner Triplet

MCBX

Each of the eight inner triplets of the LHC is equipped with three combined horizontal and vertical correction dipoles for closed orbit correction [23]. The MCBX have nested coils and a single-aperture of 90 mm bore diameter, thus providing space for the MCSTX insert. The MCBX magnets are flanged to the end plate of the high-gradient inner triplet quadrupoles (MQXA and MQXB). The main parameters of the MCBX are shown in Tab. 8.19 and the cross-section in Fig. 8.23.

The MCBX magnet consists of two nested dipole coil layers, surrounded by an aluminium shrinking cylinder, a laminated iron yoke, a stainless steel outer shell and an end plate, which supports the electrical connections. The superconducting wire has a rectangular cross-section and is enamel insulated. The dipole coils are made by winding eight superconducting wires, pre-assembled as a flat ribbon, around a copper central post with composite end-spacers. The coils are individually vacuum impregnated with epoxy. The

completed coil assembly consisting of two coil layers and a dry glass-fibre bandage is again vacuum impregnated with epoxy to provide sufficient mechanical strength to resist the shear forces arising from the combined excitation of the horizontal and vertical dipoles.

Table 8.19 Main parameters of MCBX inner triplet orbit corrector.

	MCBXV	**MCBXH**
Coil inner diameter	90 mm	120.8 mm
Magnetic length	0.48 m	0.45 m
Operating temperature	1.9 K	
Nominal field	3.26 T	3.35 T
Nominal current	550 A	
Turns per coil	360	440
Peak field	3.71 T	4.02 T
Superconductor type	4	4
Theoretical quench current at 1.9 K	1240 A	1175 A
Stored energy	26.5 kJ	43.4 kJ
Self inductance	175.2 mH	287.2 mH
Overall length	730 mm	
Outer diameter of assembly	350 mm	
Aperture	90 mm	
Mass	465 kg	

Precompression is applied to the coils by shrink fitting of the aluminium cylinder over the coil assembly. The magnitude of the pre-compression is mainly determined by the interference fit between the aluminium shrinking cylinder and the coil assembly. The iron yoke, which is made of steel laminations surrounded by a stainless steel outer shell, centres the coil assembly and provides support against the electromagnetic forces. The magnetic performance of a MCBX prototype magnet is described in [24].

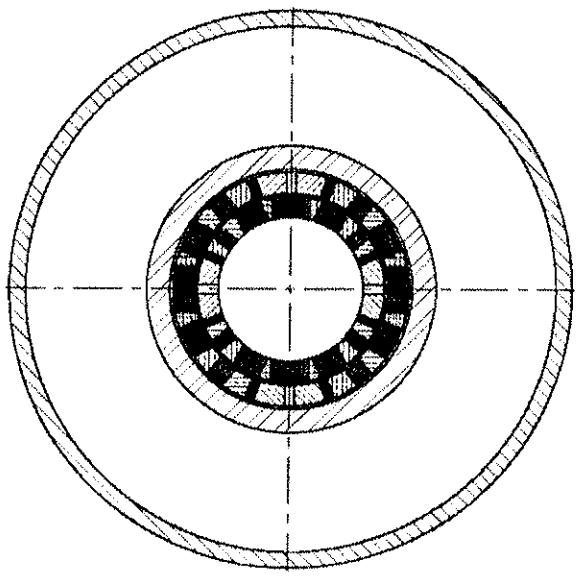

Figure 8.23: MCBX cross-section, without MCSTX insert.

MCSTX Corrector Package

One MCBX corrector in each inner triplet houses an MCSTX corrector magnet inside its aperture. The MCSTX insert consist of a nested superconducting sextupole (MCSX) and dodecapole (MCTX) windings. These single-aperture inserts have inner and outer bore diameters of 70 and 89 mm, respectively. The MCBX correctors mounted with a MCSTX corrector package are designated as MCBXA. The design parameters of MCSTX are given in Tab. 8.20.

Table 8.20: Main parameters of b_3 and b_6 windings of the MCSTX corrector package insert.

	MCTX		MCSX	
Nominal field at 17 mm radius	0.0103 T		0.015 T	
Magnetic length	0.615 m		0.576 m	
Operating temperature	1.9 K			
Nominal operation current	80 A		50 A	
Turns per coil	128		36	
No of coils	6		6	
Peak field in coils	4.1 T	1)	4.2 T	1)
Superconductor type	2		2	
Theoretical quench current at 1.9 K	208 A	1)	220 A	1)
Theoretical quench current at 1.9 K	294 A	2)	325 A	2)
Stored energy at nominal current	93.6 J		5.9 J	
Self inductance	29.2 mH		4.7 mH	
Inner diameter of insert	70 mm			
Outer diameter of insert	89.5 mm			
Total mass (approx.)	4 kg			

1) With background field of 3.9 T from the MCBX

2) Individual powering

The MCSTX insert consists of two nested coil layers (sextupole and dodecapole), a composite support tube, an aluminium outer shell and end plates which support the electrical connections. The superconducting wire has a rectangular cross-section and is enamel insulated. The dodecapole coils are made by counter-winding two superconducting wires, pre-assembled as a flat ribbon, around a copper central post. The sextupole coils are wound as a single layer around a composite central post. Each coil is impregnated with epoxy and subsequently cured.

The insert is assembled into the bore of the MCBX with its connection plate dowelled to the end plate of the MCBX. At the non-connection end the insert is centred by means of an aluminium disc fitted to the return end of the MCBX coil assembly.

MQSX

Table 8.21: Main parameters of the inner triplet skew quadrupole corrector MQSX

	MQSX
Coil inner diameter	70 mm
Magnetic length	0.223 m
Operating temperature	1.9 K
Nominal gradient	80 T/m
Nominal current	550 A
Peak field in coil	3.94 T
Superconductor	Type 3
Theoretical quench current	926 A
Stored energy	2116 J
Self inductance	14.0 mH
Overall length	300 mm
Total mass (approx.)	50 kg

Each inner triplet houses a skew quadrupole corrector, MQSX. The MQSX assemblies are flanged to the end of an inner triplet quadrupole MQXB. The main design parameters of this corrector magnet are given in Tab. 8.21.

The MQSX magnet assembly consists of four coils, a laminated iron yoke, a stainless steel outer shell and end plates which support the electrical connections. The superconducting wire has a rectangular cross-section and is enamel insulated. The coils are made by counter-winding two such wires, pre-assembled as a flat ribbon, around a composite epoxy central post. Each coil is impregnated with epoxy and cured. The end

plate supports the electrical connections and provides a reference for the angular alignment of the magnet assembly. Coil inter-connections are soft-soldered.

Pre-compression is applied to the coils by shrink fitting a stainless steel outer shell over the yoke laminations. The pre-compression is determined by the interference fit between the outer shell and the yoke laminations around the coils.

MCSOX Corrector Package

Each inner triplet houses a combined corrector magnet package of type MCSOX. It comprises a nested skew octupole (MCOSX), an octupole (MCOX) and a skew sextupole (MCSSX) magnet [25]. This assembly is flanged to the end of the MCBXA corrector. The main design parameters of the MCSOX corrector package are given in Tab. 8.22.

Table 8.22: Design parameters of the inner triplet corrector package, MCSOX.

	MCOSX	**MCOX**	**MCSSX**
Bore diameter of assembly		70 mm	
Magnetic length	0.138 m	0.137 m	0.132 m
Operating temperature		1.9 K	
Nominal field at 17 mm radius	0.0475 T	0.0453 T	0.1089 T
Nominal current	100 A	100 A	100 A
Peak field in coils	1.34 T	1.37 T	1.32 T
Superconductor		Type 2	
Theoretical quench current at 1.9 K	267 [1]	262 [1]	257 [1]
Stored energy	15.9 J	21.8 J	38.8 J
Self inductance	3.2 mH	4.4 mH	7.8 mH
Overall length		175 mm	
Total mass (approx.)		30 kg	

[1] With two other layers powered at the nominal current

The MCSOX corrector package consists of the three nested winding layers mentioned above, a laminated iron yoke, a stainless steel outer shell and an end plate. The superconducting wire has a rectangular cross-section and is enamel insulated. The three types of coils are made by counter-winding a single superconducting wire around a composite epoxy central post. Each coil is impregnated with epoxy and subsequently cured. The end plate supports the coil interconnections and also provides a reference for the angular alignment of the magnet assembly. The coil inter-connections are soft-soldered.

Pre-compression is applied to the coils by shrink fitting the stainless steel outer shell over the eccentric steel laminations that make up the yoke. The pre-compression is determined by the interference fit between the outer shell and the yoke laminations around the coils.

Table 8.23: Main parameters of the MCBW normal conducting correction dipoles.

Magnet type	**MCBW**
Magnetic length	1.7 m
Beam separation	224 mm
Gap Height	52 mm
Coil Protection temperature	<65° C
Nominal field	1.1 T
Nominal current	550 A
Inductance	50 mH
Resistance	60 mΩ
Conductor X-section	16 x 10 mm²
Cooling hole diameter	5 mm
Number of turns per magnet	2 x 42
Minimum water flow	9 l/min
Dissipated power at I_{nom}	14 kW
Mass	4500 kg

8.6.3 Normal Conducting Orbit Correction Dipoles in IR3/7

The MCBW dipoles are designed and built by BINP (Novosibirsk, Russia). The MCBW dipoles come in two versions - MCBWH and MCBWV - as horizontal and vertical orbit corrector magnets, shown in Fig. 8.24. The magnet acts only on one beam, while the other passes through a passive aperture in the horizontal version and outside the magnet in the vertical version. The power and water distribution as well as the position of the supports and target holders are specific to each version, while the rest of the design is identical. A total of 20 MCBW corrector magnets are built including two spares of each type. A view from the end of a MCBWH is shown in Fig. 8.25. The main parameters of the MCBW magnet are given in Tab. 8.23. The construction and expected field quality are described in [26].

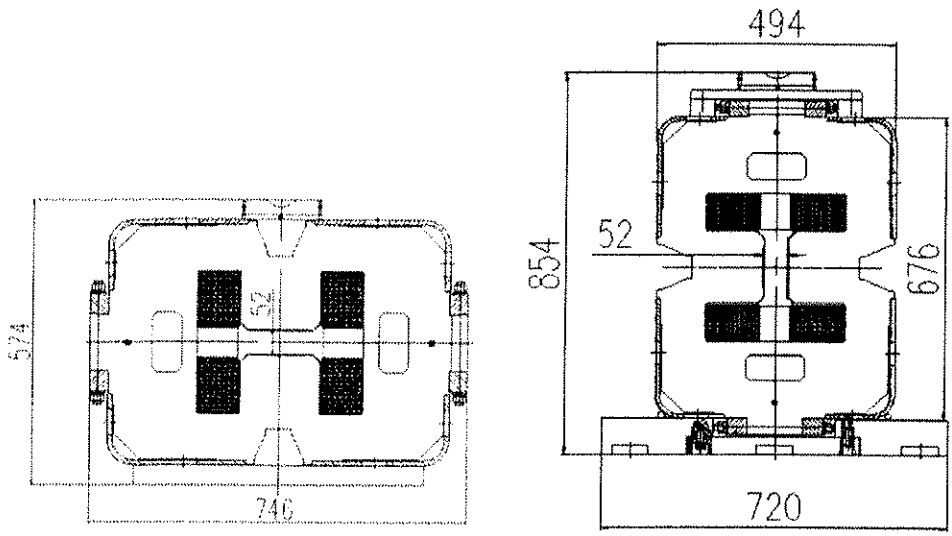

Figure 8.24: Cross section of the normal conducting orbit correction dipole MCBW in a horizontal (MCBWH) and in a vertical configuration (MCBWV).

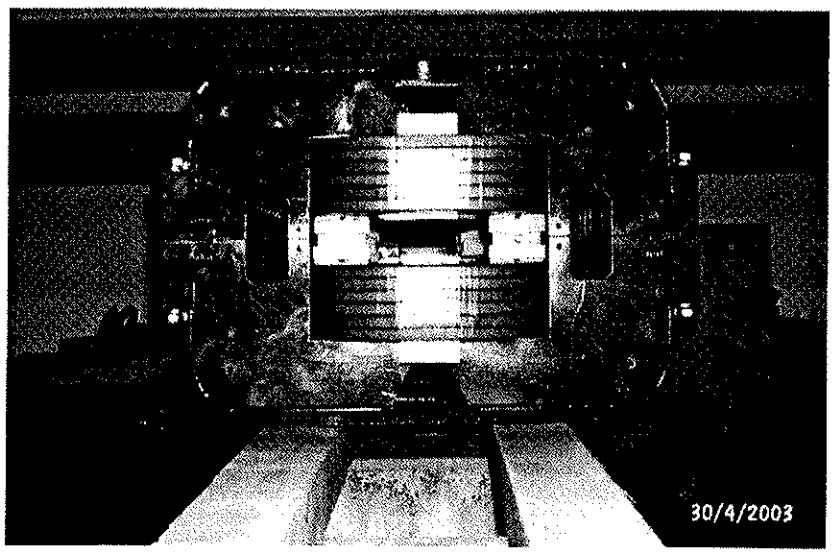

Figure 8.25: End view of the normal conducting orbit correction dipole MCBWH

8.7 COMPENSATOR DIPOLES IN ALICE AND LHCb EXPERIMENTS

The effect of spectrometer dipoles in ALICE (IR2) and LHCb (IR8) experiments on the beam is compensated in both cases with three dipoles, one placed symmetrically with respect to the IP and two weaker dipoles placed next to the inner triplets. The dipole field of the ALICE spectrometer, which produces a vertical kick on the beam, is compensated with a MBWMD and two MBXWT magnets. The MBWMD is a

magnet from the SPS complex, originally built for the ISR beam lines (type HB2 turned vertical). Its main parameters are shown in Tab. 8.24 and its cross section is shown in Fig. 8.26. The LHCb dipole, which produces a horizontal kick on the beam, is compensated by an MBXWH magnet and two MBXWS magnets. The MBXWH is in fact an MBXW separation dipole, discussed in Section 8.4.2 and the MBXWT and MBXWS magnets are short versions of the MBXW dipole. The parameters of these magnets are given in Tab. 8.24. All MBXW type magnets are designed and built by BINP (Russia).

Table 8.24:Main parameters of the compensator dipoles for ALICE and LHCb. The magnets of the first three columns have all the same cross-section as MBXW.

Magnet type	**MBXWH**	**MBXWT**	**MBXWS**	**MBWMD**
Magnetic length	3.4 m	1.5 m	0.8 m	2.6 m
Gap height		63 mm		80 mm
Coil protection temperature		< 65° C		< 65° C
Nominal field	1.24 T	1.20 T	1.33 T	1.32 T
Current at nominal field	670 A	630 A	780 A	475 A
Inductance	145 mH	70 mH	35 mH	639 mH
Resistance	60 mΩ	40 mΩ	20 mΩ	172 mΩ
Conductor X-section		18 x 15 mm²		16.3 x 10.8 mm²
Cooling hole diameter		8 mm		6.6 mm
Number of turns per magnet		2 x 48		2 x 102
Minimum water flow	19 l/min	5 l/min	7 l/min	20 l/min
Dissipated power at I_{nom}	27 kW	16 kW	12 kW	39 kW
Mass	11500 kg	5800 kg	3700 kg	20500 kg

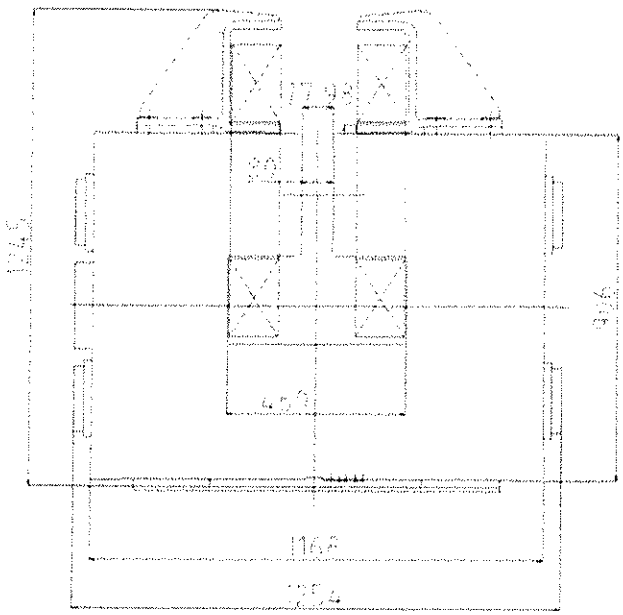

Fig. 8.26: Cross-section of the normal conducting compensation dipole MBWMD for ALICE.

REFERENCES

[1] J. Lucas *et al*, "Performance of the Final Prototype of the 6-kA Matching Quadrupoles for the LHC Insertions and Status of the Industrialization Program" , *IEEE Trans. Appl. Superconductivity*, Vol. 13 (2003), No.2, pp. 1309-1312.

[2] G. A. Kirby *et al.*, "Performance of the 1 m Model of the 70 mm Bore Twin-Aperture Quadrupole for the LHC Insertions", *IEEE Trans. Appl. Superconductivity*, Vol. 11 (2001), No.1, pp. 1641-1644.

[3] LHC Engineering Specification, "Types of Special Short Straight Sections", in preparation.

[4] LHC Functional Specification, "Triumf Specification No. 2604-02-99-2 The Series Production of the Twin Aperture Quadrupole for CERN", LHC-MQW-CA-0001

[5] E. Boter *et al.*, "Modelling in 3D and Shimming of Magnetic Field of the MQW Magnet for the Series Production", SL-Note-2002-026 MS, CERN, 20 Aug 2002

[6] E. Boter *et al.*, "Modelling in 2D of Magnetic Field of the MQW Magnet for the Series Production", SL-Note-2002-010 MS, CERN, 20 Mar 2002

[7] E. Willen *et al.*, "Superconducting Dipole Magnets for the LHC Insertion Regions", Proc. EPAC'2000, Vienna, Austria, June 2000, pp. 2187-2189.

[8] LHC Interface Specification, "LBX-D1 Dipole", LHC-MBX-ES-0002, EDMS doc. 248583.

[9] LHC Functional Specification, "Superconducting Beam Separation Dipoles", LHC-MBR-ES-0001, EDMS doc. 110392.

[10] LHC Engineering Chane Order, "Modification of Cold Bore Separation in D3 and D4 Dipoles", LHC-MBR-EC-0002, EDMS doc.364935.

[11] LHC Interface Specification, "LBRC Cryo-Assemblies - D2 Dipole", LHC-MBR-ES-0003, EDMS doc.306513.

[12] LHC Interface Specification, "LBRS Cryo-assemblies – D3 dipoles", LHC-MBRS-ES-0003, in approval.

[13] D. Gerard *et al.*, "Warm Separation Dipoles: Status and Production Plan", Proc. LHC days 2003, LHC-Project-Report-672, pp. 69-71

[14] LHC Functional Specification, "MBXW Resistive Dipole Magnets for the LHC Cleaning Insertions", LHC-MBW-CA-0001

[15] LHC Functional Specification, "MBXW Resistive Dipole Magnets for the LHC Insertions", LHC-MBXW-CA-0001

[16] T. Shintomi *et al.*, "Progress of the LHC Low-b Quadrupole Magnets at KEK", *IEEE Trans. Appl. Superconductivity*, Vol.11 (2001), No.1, pp.1562-1565.

[17] N. Andreev *et al.*, "Status of the LHC Inner Triplet Quadrupole Program at Fermilab", *IEEE Trans. Appl. Superconductivity*, Vol. 11 (2001), No.1, pp. 1558-1561.

[18] LHC Functional Specification, "Inner Triplet Quadrupole MQXA", LHC-MQXA-ES-0001, EDMS doc. 313715.

[19] LHC Functional Specification, "Inner Triplet Quadrupole MQXB", LHC-LQX-ES-0002, EDMS doc. 256806.

[20] T. Nicol *et al.*, "LHC Interaction Region Quadrupole Cryostat Design and Fabrication", *IEEE Trans. Appl. Superconductivity*, Vol. 12 (2002), No.1, pp. 179-182.

[21] M. Allitt *et al.*, "Principles Developed for the Construction of the High Performance, Low-cost Superconducting LHC corrector Magnets", LHC-Project-Report-528, Mar 2002.

[22] A. Ijspeert, J. Salminen, "Superconducting coil compression by scissor laminations", EPAC-96, Sitges, Spain, June 1996

[23] M. Karppinen *et al.*, "Development of the Inner Triplet Dipole Corrector (MCBX) for LHC", LHC-Project-Report-265.3, Feb 1999.

[24] Z. Ang *et al.*, "Magnetic Performance of First low-beta dipole corrector prototype MCBX", LHC-Project-Report-237, 25 Sep 1998.

[25] M. Karppinen, J. C. Pérez, R. Senis, "Inner Triplet Corrector Package MQSXA for the LHC", LHC-Project-Report-529, 06 Mar 2002 ; *IEEE Trans. Appl. Superconductivity*, Vol. 12 (2002) no. 1, pp.102-106.

[26] LHC Functional Specification, "MCBW Resistive Magnets for the LHC Insertions", LHC-MCBW-CA-0001

CHAPTER 9

POWERING AND PROTECTION

9.1 OVERVIEW

A very large number of both superconducting and conventional copper conductor magnets will be installed in the LHC. The demanding requirements on the quality of the magnetic fields require a large number of distributed corrector magnets around the circumference the main magnets for bending and focusing. Most magnets of the same type in one of the eight symmetrical sectors are combined to form families, powered in series. In total, the LHC will have 1612 different electrical circuits of superconducting and normal conducting magnets. In order to limit the stored magnetic energy and the voltages during energy extraction, magnet families do not extend over more than one sector. The stored energy is mostly sufficient to damage magnets hence their protection is essential. However, the large amount of protection equipment will reduce the availability of the accelerator.

9.2 POWERING CIRCUITS

The magnets of the LHC are powered in eight independent and symmetric sectors (see Fig. 9.1). Within these sectors, more than 40 different cryostats house the superconducting magnets, while the normal conducting magnets are located in the long straight sections (LSS) close to the interaction points (except for IR4 where there are no normal conducting magnets). The higher radiation levels in the cleaning insertions (IR3 and IR7) and around experiments with high luminosity (IR2 and IR8) prevent the use of superconducting magnets. Here normal conducting magnets are employed.

Eight long arc cryostats span the major part of the circumference and contain the main bending and focusing magnets. Smaller cryostats located around the interaction points house magnets that are specifically required for this insertion.

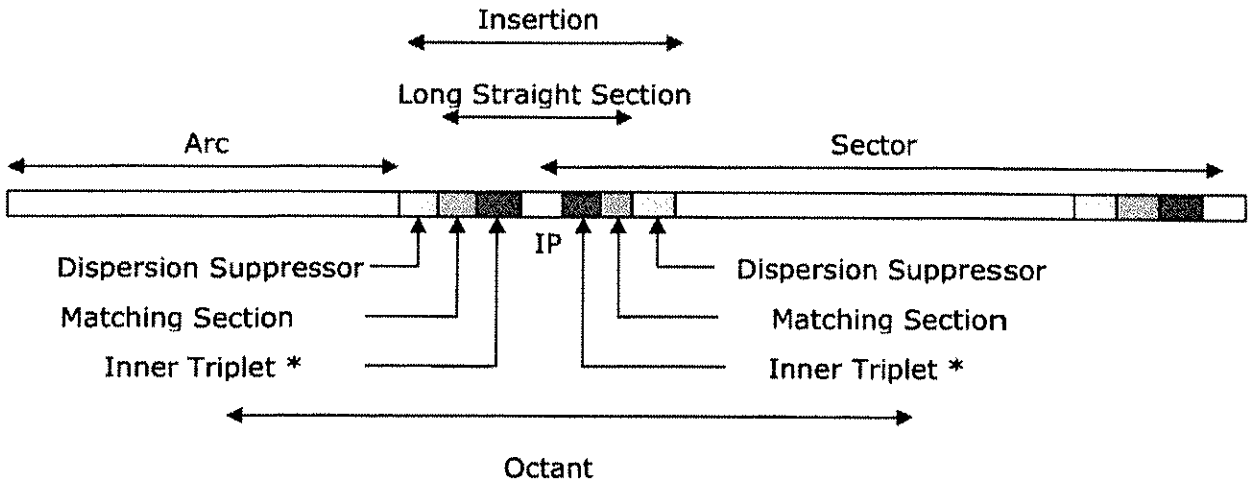

* Inner triplets are only present in insertions with physics experiments

Figure 9.1: Sectors and Octants in the LHC

The total of 1612 electrical circuits is composed of 131 different types, connecting main bending magnets, magnets for beam focusing, dipole field correctors, or higher order correctors. Some types appear in each of the eight sectors (e.g. the main dipole circuit) while others are only present in dedicated insertions (as for example a warm compensator for the ALICE experiment). The detailed description of this complex electrical system is available in the LHC Reference Database [1] which also contains the connection information of all 1612 electrical circuits. In addition the system is described in a set of 40 circuit drawings [2].

9.2.1 The Concept of Powering Subsectors

The segmentation of the powering of such extended electrical systems reduces the stored energies in the circuits and the voltages during extraction. It also allows for easier installation, testing and commissioning. On the other hand, a larger inventory of components for powering of the electrical circuits (power converters, current leads, warm cabling...) is required and operation may be more complicated.

The eight sectors have been subdivided into 28 powering subsectors of four different types, as shown in Fig. 9.2.

- 8 Arc Powering Subsectors, containing all powering equipment related to magnets in the arc cryostats.
- 8 Powering Subsectors for powering of the inner triplet cryostats, housing the magnets for Q1 to Q3 for the insertions with physics experiments and additionally D1 in the insertions 2 and 8.
- 12 Powering Subsectors to power magnets in smaller cryostats in the matching sections, containing individually powered quadrupoles and separation and combination dipoles.
- 7 Powering Subsectors for powering of normal conducting magnets left and right of an IP.

Every electrical circuit and the associated electrical components in the LHC tunnel is allocated to one powering subsector. As such, the powering in each of the powering subsectors is independent of the powering of the other subsectors (see Chap. 15.3.1 for details on the allocation of cryostats to the powering subsectors).

9.2.2 Main Circuits

Each of the eight symmetrical LHC sectors will contain one electrical circuit (called RB), connecting all main bending magnets in series. The main quadrupoles are powered in each sector in two electrical circuits (RQF and RQD) dedicated to focusing and defocusing the two beams. The power converters for these three main circuits in each of the eight sectors are located in an underground area (UA) close to the even insertion regions. The currents enter the cryostat through a nearby DFBA feedbox. The stored energy in these circuits amounts to 1.22 GJ for the main dipole[1] and 20 MJ for each of the main quadrupole circuits. For the main dipole circuit an energy extraction system (consisting of a high current switch in parallel with the extraction resistor) is placed on either side of the arc cryostat, while only one system for either of the quadrupole circuits is sufficient. Fig. 9.2 illustrates the powering layout for the eight long arc cryostats.

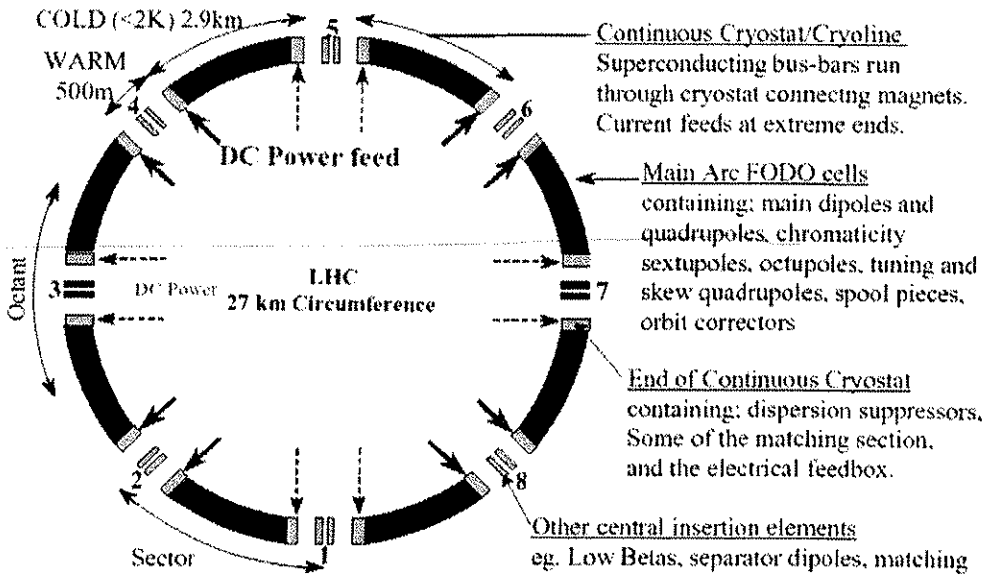

Figure 9.2: Powering of the eight arc cryostats

[1] At ultimate energy and using the measured value for the inductance (100 mH)

9.2.3 Dipole Field Correctors

A number of higher order correctors will be installed as part of every dipole assembly in the long arc cryostat to compensate the field errors of the main dipoles. Two different types of dipole assemblies will be installed alternately in the LHC arcs. In addition to the main dipole coil on each of the two beam pipes the MBA type provides a combined decapole-octupole-corrector (MCDO) at the connection side of the cryo-assembly and a sextupole corrector (MCS) at the far end of the cryo-assembly. The MBB type only contains a sextupole corrector at the far end beside the main dipole coil

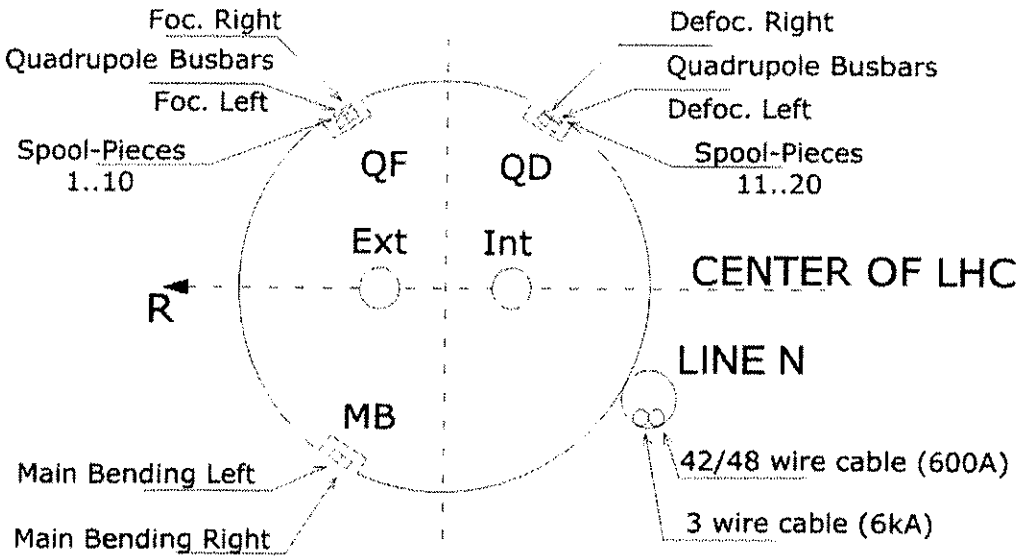

Figure 9.3: Cross-section of LHC arc cryo-assembly with bus-bars

All correctors of a family are connected in series for each of the two beams. The circuit families RCS, RCO and RCD are connected throughout the cryostat via 20 so-called spool-piece bus-bars, (grouped in bundles of five bus-bars), located on top of the two main quadrupole bus-bars (see Sec. 9.3.3 and Fig. 9.3). The circuits are always connected using neighbouring wires (e.g. wire number 1 and 2). Correctors are connected either to wires 1 to 10 or to wires 11 and 20, depending on the beam the corrector family is acting on. The mid-point of the sextupole circuit is connected to a spare current lead on the DFBA by using one of the spare spool-piece wires. Six spool-piece wires are left floating. The power converters are located at the end of the arc close to the even insertion and enter the cryostat via current leads located on the nearby DFBA.

9.2.4 Short Straight Sections (SSS)

Arc Short Straight Sections

The Short Straight Section in the LHC arcs contains two independent main quadrupole magnet coils, two higher order corrector magnets at the upstream connection side and two orbit corrector dipoles as well as two sextupoles at the downstream side.

The orbit corrector magnets are powered with currents of up to 60A (120A for SSS in the dispersion suppressor regions) and are connected to the power converter via current feedthroughs, mounted on a flange of the SSS service module.

The correctors on the so-called "connection end" of the SSS are routed throughout the arc cryostat via a special cable, consisting of 42 (sometimes exceptionally 48) superconducting wire cables. This cable does not run through the magnets but through a special pipe (line N), which is attached to the outside of the cold masses. This special cable is connectable only in the upstream interconnection plane of each SSS in the arc (see Fig. 9.4). To limit the number of wires and hence the size of this cable, each wire will be used in two different electrical circuits as shown in Fig. 9.4. An overview of the corrector family types in the arc SSS can be found in Tab. 9.1.

Table 9.1: Correctors in the arc SSS

Circuit Function	Families	Magnet Type	Circuit Type
Tuning Quadrupoles	2 families/arc	MQT	RQTF, RQTD
Skew Quadrupoles	In even sectors, Beam 1 & in odd sectors Beam 2: 2 families/arc	MQS	RQS
	In odd sectors, Beam 1 & in even sectors Beam 2: 1 family/arc	MQS	RQS
Chromaticity Sextupoles	4 families/arc	MS	RSF1, RSF2, RSD1, RSD2
Skew Sextupoles	1 family/arc	MSS	RSS
Octupoles	2 families/arc	MO	ROF, ROD

The layout of the electrical circuits for SSS correctors can be derived for each sector using the following set of rules:

- The tuning quadrupoles are installed in all sectors in cells 14 to 21 and are connected in families for each beam. In each sector there are four independent circuits in terms of powering, while the power converters are always installed in the even IR end of the sector.
- Skew quadrupoles are installed in cells 23 and 27 (left and right). In the even sectors (12, 34, 56, 78), the four magnets for Beam 2 will be combined in one single family with the corresponding power converter installed in the odd IR. On Beam 1, the magnets will form 2 families of 2 magnets each with a power converter at either side of the sector. In the odd sectors (23, 45, 67, 81), the layout will be inversed with respect to the two beams. The four magnets on Beam 1 will be powered in one single family with the power converter installed in the odd IR at one end of the sector. On Beam two 2 families consisting of 2 magnets each will be powered by 2 individually power converters at both ends of the sector.
- Chromaticity correction will be performed in each sector with four independent sextupole circuits per beam. The corresponding power converters are always installed in the even IR at one end of the sector. Beam 1 enters on the right of an IR at Q11 fitted with SF1 or SD1 depending on the sector, and exits on the left of the next IR at Q11 equipped with SF2 or SD2, respectively. If one sextupole is "focusing" on one beam, it is "defocusing" on the other. By definition Beam 1 starts with a focusing sextupole (SF1) in arc 12, while the sequence is always the following:
  - SF1, SD1, SF2, SD2 or
  - SD1, SF1, SD2, SF2
- The two **skew sextupole** circuits combine the magnets in a single family for each beam. The power converters feeding these circuits are installed in the odd IR at one end of the sector. If a cell contains a skew sextupole, it will replace the normal focusing sextupole. Whenever possible the skew sextupoles are centred on Q34. If this is not possible it is shifted one half-cell clockwise.
- **Octupole** magnets are the highest order of correction in the SSS. They form two families per beam in every sector and are independent in terms of powering. The power converter feeding each family is always installed in the odd IR at one end of the sector. The octupole correctors are installed in the SSS assemblies in the cells 22 to 34, left and right, with the exception of cell 23 and 27.

Fig. 9.4 shows as an example the complete corrector circuit layout for sector 12. This figure and the figures for the other sectors can be found in Ref. [3]. The drawing contains information about the

- Number, position (internal, external) and direction of beams.
- Position of the arc DFBA for the sector.
- Position and function of corrector magnets in the sector.
- IR number in which the power converter feeding a magnet or magnet family is installed.
- Number of wires or bus bars entering a sector and connected to a DFBA.

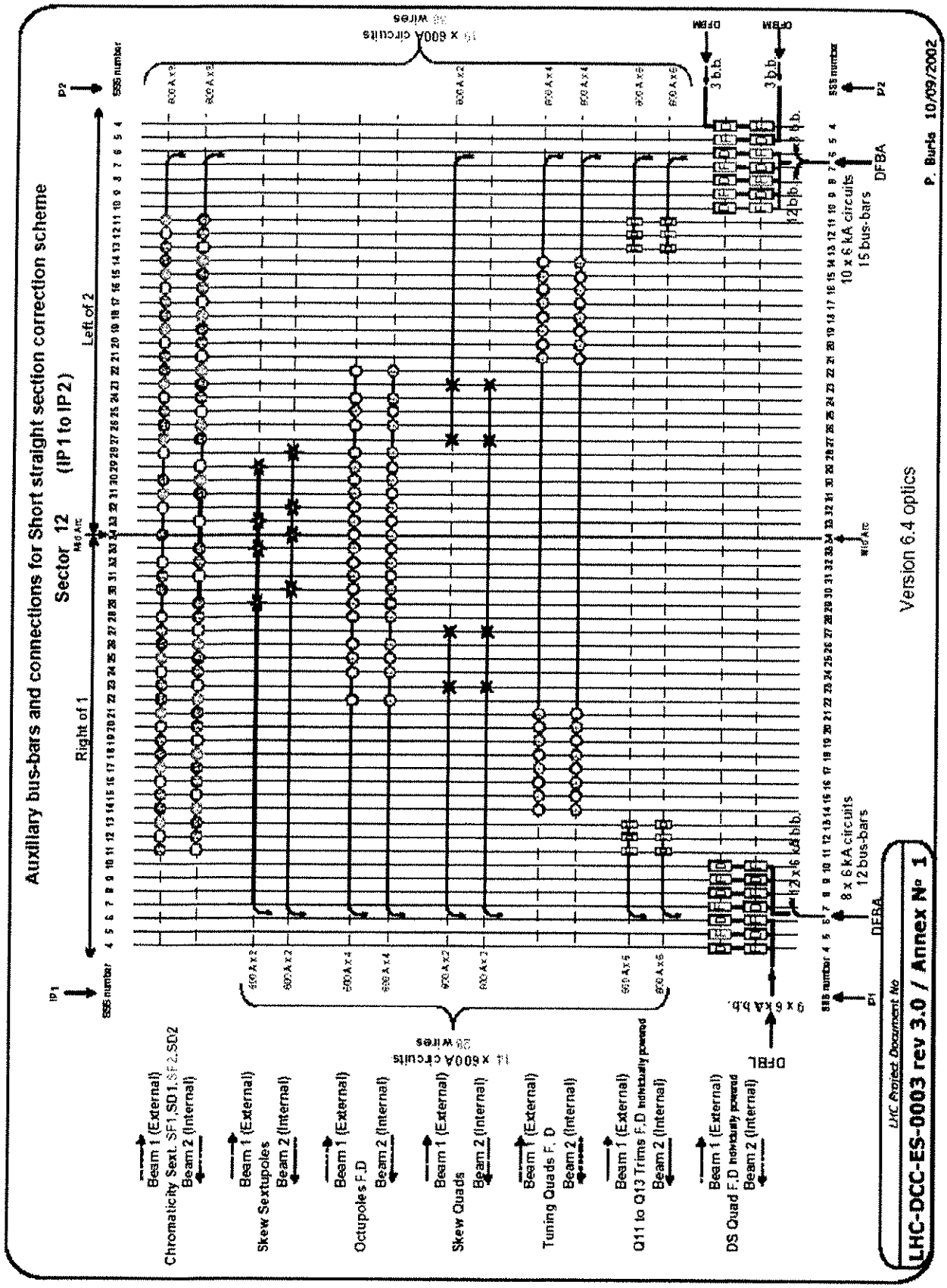

Figure 9.4: Example of the correction circuit layout (sector 12)

Dispersion Suppressor Extension (Q12-Q13)

The dispersion suppressor extension regions consists of Q12 and Q13 (see Tab. 9.2), containing main quadrupole magnets of the type MQ, powered as the quadrupoles in the arc and individually powered MQT type corrector magnets on each beam.

Dispersion Suppressor (Q8 - Q11)

Magnets for the dispersion suppressors are installed at both ends of the long arc cryostats,. The final elements are two DFBAs, one at each end of the arc cryostat.

In all sectors, except in the insertions dedicated to betatron and momentum cleaning (IR3 and IR7), most of the dispersion suppressor short straight sections are built around individually powered quadrupoles of the MQM type (see Tab. 9.2). No additional quadrupole correctors are required when individually powered quadrupoles are used.

Table 9.2: Dispersion Suppressor and Matching Section quadrupole magnets

	Q4	Q5	Q6	Q7	Q8	Q9	Q10
IP1 left	MQY	MQML	MQML	2xMQM	MQML	MQMC + MQM	MQML
IP1 right	MQY	MQML	MQML	2xMQM	MQML	MQMC + MQM	MQML
IP2 left	2xMQY	2xMQY	MQM + MQML	2xMQM	MQML	MQMC + MQM	MQML
IP2 right	2xMQY	2xMQM	MQM + MQML	2xMQM	MQML	MQMC + MQM	MQML
IP3 left				MQ + MQTL	MQ + MQTL	MQ + 2xMQTL	MQ + MQTL
IP3 right				MQ + MQTL	MQ + MQTL	MQ + 2xMQTL	MQ + MQTL
IP4 left		MQY	MQY	MQM	MQML	MQMC + MQM	MQML
IP4 right		MQY	MQY	MQM	MQML	MQMC + MQM	MQML
IP5 left	MQY	MQML	MQML	2xMQM	MQML	MQMC + MQM	MQML
IP5 right	MQY	MQML	MQML	2xMQM	MQML	MQMC + MQM	MQML
IP6 left	MQY	MQY			MQML	MQMC + MQM	MQML
IP6 right	MQY	MQY			MQML	MQMC + MQM	MQML
IP7 left				MQ + MQTL	MQ + MQTL	MQ + 2xMQTL	MQ + MQTL
IP7 right				MQ + MQTL	MQ + MQTL	MQ + 2xMQTL	MQ + MQTL
IP8 left	2xMQY	2xMQM	MQM + MQML	2xMQM	MQML	MQMC + MQM	MQML
IP8 right	2xMQY	2xMQY	MQM + MQML	2xMQM	MQML	MQMC + MQM	MQML
	Matching Section				**Dispersion Suppressor (DS)**		
Local individual cryostats				**Long continuous cryostat**			

However, the Q11 (and Q7 to Q11 in IR3 and 7) are of the same type (MQ) and are powered in series together with the arc quadrupoles. In this case, the quadrupoles of the two beams are fitted with individually powered MQTL type corrector magnets.

The connections between the power converters and the individually powered MQM magnets are made by means of a three-conductor cable routed through line N. The central conductor of this arrangement carries only the difference of currents flowing in the two magnets, keeping in mind that the two magnets are connected with reversed polarities.

Matching sections (Q4 - Q7)

Except left and right of IR3 and IR7, the Matching Sections are built with individually powered quadrupoles of the types MQM and MQY. No additional correctors are required when these types of magnets are used.

Connections between the power converters and the individually powered MQMs or MQYs are made with a three-conductor cable routed through line N (in case of the Q7) or the DFBM/DFBL and the occasional cryogenic links. The central conductor of this arrangement carries only the difference of currents flowing in the two magnets, because the two magnets are connected with reversed polarities.

The configuration of the matching sections depends on the special features of the insertion. From Q4 to Q6, the magnets are fitted in individual cryostats whereas Q7 is located at the end of the long continuous arc cryostat beside the electrical feedbox DFBA.

Left and right of IR3 and IR7 (cleaning insertions), several normal conducting magnets replace the superconducting magnets used in other insertions due to higher radiation levels of these regions. The Q6 quadrupoles of IR3 and IR7 are built as six superconducting low current (600 A) magnets of the MQTL type, connected in series. The six magnets share one individual cryostat.

9.2.5 Separation Dipoles and Final Focus

While the sectors already differ in the matching sections, the differences are even more pronounced in the separation regions and close to the interaction points. Special insertion triplets are installed in the insertion regions 1, 2, 5 and 8. They consist of 2 MQXA magnets (8 kA) from KEK and 2 MQXB magnets (13 kA) from FNAL, forming the quadrupoles Q1 to Q3. The four magnets are powered in series via an 8 kA power converter, while an embedded power converter of 4 kA will superimpose additional current to the two MQXB magnets located between the two MQXA magnets. A third but smaller power converter of 600 A will be used as a trim converter over the Q1 magnet. Hence only four current leads for the high current connections of the four quadrupole magnets have to be installed in the DFBX feedbox close to the inner triplet.

Table 9.3: Magnets in the Separation Region and the Final Focus

	Q5	**Q4**	**D2**	**D1**	**Q3**	**Q2**	**Q1**	
IP1	MQML	MQY	MBRC	6MBXW	MQXA	2MQXB	MQXA	
IP2	2MQY	2MQY	MBRC	MBX	MQXA	2MQXB	MQXA	
IP3	6MQW	6MQW	-	-	-	-	-	
IP4	MQY	-	-	-	-	-	-	
IP5	MQML	MQY	MBRC	6MBXW	MQXA	2MQXB	MQXA	
IP6	MQY	MQY	-	-	-	-	-	5MSDA/B/C
IP7	6MQW	6MQW	-	-	-	-	-	
IP8	2MQM	2MQY	MBRC	MBX	MQXA	2MQXB	MQXA	MBXWS, MBXW [1]

[1] CMS compensator magnets, left side only

Separation and combination for the interaction of the two beams will be done via two bending magnets (D1 and D2) installed in the long straight section between the inner triplet and the beginning of the matching section. In the insertion regions for ALICE and LHCb (IR2 and IR8) superconducting D1 magnets (from BNL) are installed to separate the beams. In such a case, two more 8 kA current leads will be present on the DFBX of this insertion region as the D1 will be fed via the inner triplet feedbox. For insertions with high luminosity experiments (ATLAS and CMS in IR1 and IR5) there are six normal conducting magnets

powered in series on both sides of the IR with one single power converter located in the surface building of these insertions. Tab. 9.3 summarizes the magnets that can be found in the insertion regions of the LHC [4, 5].

In the cleaning insertions (points 3 and 7) and in the RF insertion (point 4) the beams are further separated or brought back to the normal separation by dog-leg combinations of normal conducting bending magnets (D3 and D4).

9.3 POWERING EQUIPMENT

9.3.1 Current Leads

For the 1612 electrical circuits in the LHC a total of 3286 current leads are needed to connect the superconducting wires or cables to the power supply cables, which are at ambient temperature. The design of these leads aims at high reliability and low heat load.

A total of 1070 leads, operating between 600 A and 13 kA, incorporate a section with high temperature superconducting (HTS) material. The higher investment costs are small compared to the savings due to the exceptionally low heat load. All other leads use copper as conductor. To feed the electrical circuits of the Inner Triplet magnets with up to 600 A, 112 gas cooled leads are used. The remaining 2104 leads feed the 60 A or 120 A electrical circuits of the orbit corrector dipoles, the sextupole in the Inner Triplet, and the octupole and dodecapole correctors

HTS leads

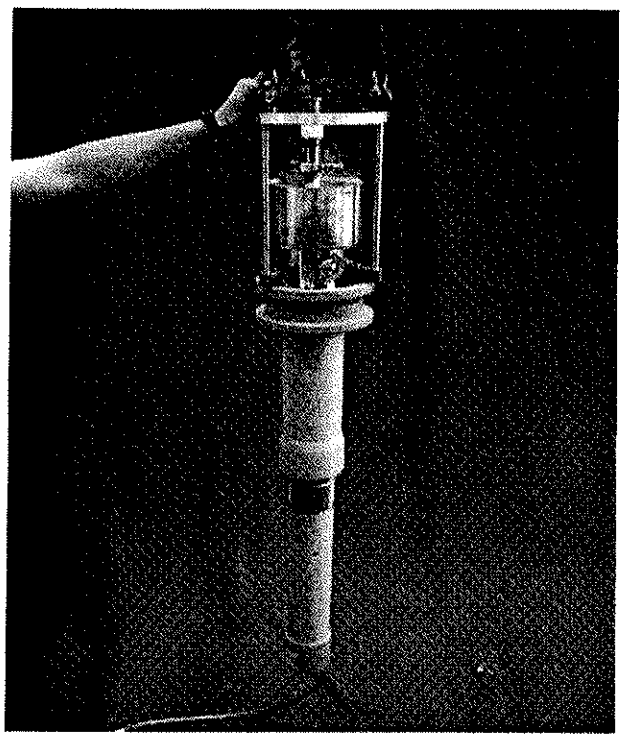

Figure 9.5: 13 kA CERN prototype lead

Optimised conventional self-cooled leads conduct about 1.1 W/kA into the liquid helium bath. The availability of 20 K helium gas in the cryogenic system makes it possible to reduce this heat influx by a factor of ten. In total the cooling power requirements are reduced by about a factor of 3 [6, 7, 8].

An HTS current lead consists of a resistive and a superconducting part. The resistive part operates between room temperature and about 50 K. It is convection cooled by the cold helium gas, available in the LHC cryogenic system, entering the leads at about 20 K and 1.3×10^5 Pa. The resistive part of the lead consists of a copper fin-type heat exchanger. A vacuum jacket insulates it thermally from the cryostat environment.

The superconducting part operates between 50 K and the liquid helium temperature. The vapour, generated by the conduction of the lead at 4.5 K, cools it (self-cooling). The 20 K circuit and the 4.5 K circuit are

hydraulically separated inside the lead. The HTS part of the lead consists of stacks of BSCCO 2223 tapes soldered onto a stainless steel structure.

The HTS leads are classified in three types, according to their nominal current carrying capability: 600 A, 6 kA and 13 kA leads. The 13 kA leads are used to feed current to the main dipoles and quadrupoles. The 6 kA type leads are used for circuits with ultimate currents between 3900 A and 6500 A, feeding current to single powered quadrupoles and dipoles. The 6 kA and the 13 kA current leads are built as single units, while the 600 A current leads come in groups of four leads mounted on a common flange.

A total length of 31 km of BSCCO 2223 tape in the form of spools of multi-filamentary BSCCO 2223 tape in a silver-gold (Au ≈ 5.3 wt %) alloy matrix is needed. The tapes are vacuum soldered at CERN to form stacks, containing 4-7 or 9 tapes, according to the requirements. These stacks are supplied to the leads manufacturer.

The cryogenic performance, measured on prototype current leads at CERN, is summarized in Tab. 9.4. $Q_{4.5K}$ represents the heat load into the liquid helium bath, while m_{20K} indicates the 20 K gas flow and T_{HTS} stands for the temperature at the warm end of the high temperature superconductor.

The resistive and the HTS part of the lead are protected separately at 100 mV and 3 mV respectively. Within 5 seconds after reaching either voltage, the discharge of the magnet or magnets chain starts at its nominal current decay rate.

Table 9.4: Thermal performance of HTS current leads

CURRENT LEAD RATING (A)	**I=0 A**		**$I=I_{MAX}$**	
	T_{HTS} =70 K		**T_{HTS} =50 K**	
	m_{20K} (g/s)	**$Q_{4.5K}$ (W)**	**m_{20K} (g/s)**	**$Q_{4.5K}$ (W)**
600	≤ 0.015	≤ 0.090	≤ 0.04	≤ 0.090
6000	≤ 0.2	≤ 0.7	≤ 0.39	≤ 0.7
13000	≤ 0.3	≤ 1.5	≤ 0.85	≤ 1.5

Normal conducting leads

The 60A leads, 1504 in total, are conduction cooled leads integrated into the densely packed service module (QQS) of the Short Straight Section. They transport the current, through the cryostat main vacuum insulation, from room temperature to the 1.9 K superfluid liquid helium bath.

The conductor consists of a copper plated brass rod [9]. The copper carries the current while the brass assures stability against a thermal run-away and mechanical stability, while contributing negligibly to the heat conduction. The conductor, insulated by a Kapton® tube, is inserted in a stainless steel tube and pre-shaped as required for the installation in the cryostat. The tubes are welded in groups of four to the supporting stainless steel flanges. The leads are clamped twice between two metallic plates and fixed to the cryogenic lines E (50 K-75 K) and C′ (4.5 K-20 K), respectively. These plates are heat sinks, optimised to adsorb the heat conducted by the lead at intermediate temperatures. To further optimise the thermal performance of the electrical conductor, the copper thickness decreases along the lead length. The compact assembly of four leads is mounted as the last component in the SSS cryostat.

The 340 current leads rated at 120A, which are needed in the SSS in the Dispersion Suppressor and Matching Section parts of the LHC, are similar to the 60A conduction cooled leads. Additional 120A conventional self-cooled leads are used in the DFBX cryostats.

9.3.2 Electrical Feedboxes

The HTS current leads described in the previous chapter are mounted in cryogenic electrical distribution feedboxes (DFBs). The limited space in the LHC tunnel requires the use of two different classes of feedboxes. If the space is sufficient, the current is transferred to the arc magnets or to standalone magnets through locally installed DFBs. When the integration of a DFB close to the superconducting magnets is not possible, the magnets are powered through superconducting links (DSL) that connect the DFBs and the superconducting magnets at distances between 70 m and 500 m.

Table 9.5: List of DFB and their current leads

DFB type	Number	Type of leads (nb/DFB)
DFBA	16	13kA (2-6), 6kA (0-15), 600A (0-52), 120A(0-8)
DFBM	23	6kA (0-5), 600A(0-4)), 120A(0-12)
DFBL	5	6kA (0-5), 600A(0-44), 120A(0-12)
DFBX	8	7.5kA (4-6), 600A (10), 120A (14)

There are four different types of electrical distribution feedboxes listed in Tab. 9.5:

- The 16 DFBAs, connected to the ends of the LHC sectors, ensure also the functions of arc termination.
- Through the 23 DFBMs power is fed to the standalone magnets in the long straight sections.
- Five DFBLs supply a cryogenic interface to the connected superconducting links. Via these links power is fed to standalone magnets around point 1 and 5 as well as to the correctors in the arc cryostat right of point 3.
- The inner triplet magnets are fed via one of 8 DFBXs, located always next to Q3.

Except for the DFBAs, which also ensure the termination of the LHC arcs, the main function of the DFBs is to house the current leads described above which transfer high currents from room temperature cables to superconducting bus-bars via current leads. The variants of DFBs, the types of current leads and their respective number for each type of DFB are summarized in Tab. 9.5.

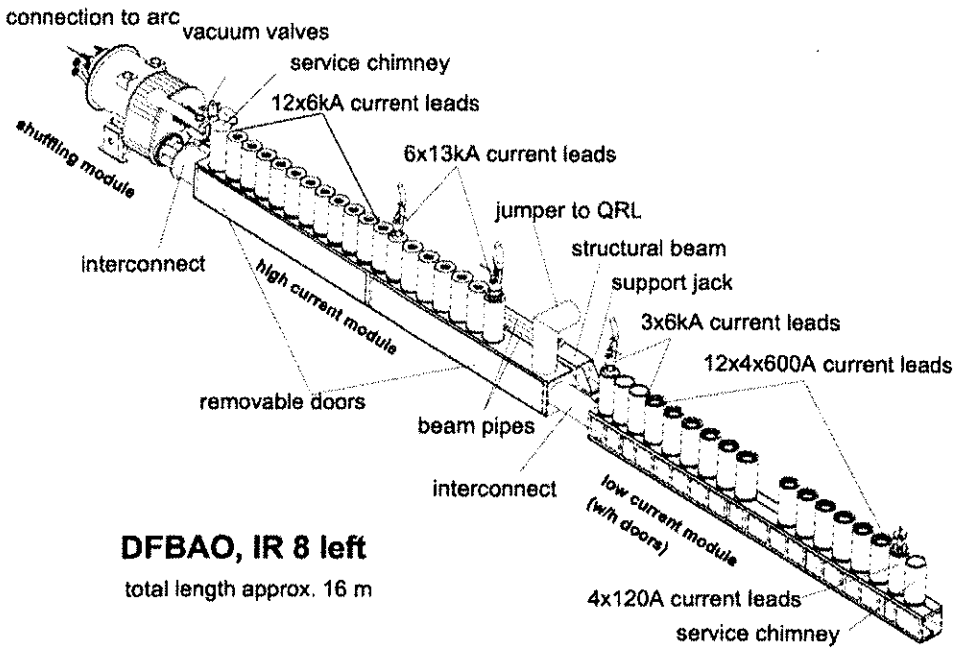

Figure 9.6: DFBA of IR 8 left, powering sector 7-8 of the LHC.

Design of the DFBAs, DFBLs and DFBMs

These DFBs are of modular design [10]. They consist of two types of current lead modules, assembled together with interfaces and other specific equipment that depend on the configuration required. The high current module integrates 13 kA and 6 kA leads while the low current module integrates 6 kA, 600 A and 120 A leads. The number of leads and their arrangement is different for each DFB as described in the references [11] and [12].

A view of the DFBA, located at the left side of IR8, therefore powering sector 7-8, is shown in Fig. 9.6. This DFBA, a typical example of the above-cited modular design, consists essentially of:

- The shuffling module: this equipment ensures the arc termination functions and also allows the rerouting of the bus bars to the current modules. It withstands all forces resulting from its position at the end of the arc, while ensuring a very precise positioning of the beam pipes.
- A high current module connected to the shuffling module and integrating a jumper connection to the QRL.
- A low current module.

These DFBs are all built by combining the two types of current lead modules and equipment specific to each DFB.

Superconducting links

Whenever it is impossible to mount a DFB close to the magnets, the electrical current is transferred from the DFBs to the LHC magnets through superconducting links (DSL).

The links carry currents in the range of 120 A to 6 kA. The nominal operation temperature ranges from 4.5 K to 6 K for the part which houses the superconducting cable and is about 70 K for the heat shielding.

Five superconducting power transmission lines (DSLs) will be needed in LSS 1, 3, and 5. Two types of DSLs are distinguished. Equipment of type-1: DSLA, DSLB, DSLD and DSLE, and of type-2: DSLC. The DSL tag naming, description and respective powering layout references are summarized in Tab. 9.6. The four type-1 DSLs are of similar design, differing only in the precise mechanical layout of their routing in the LHC tunnel. Their length is about 70 m with two intermediate branches of about 3 m. They are located at LSS 1 and 5 on either side of the IRs and connect a link current feedbox (DFBL) to the Q6, Q5 and Q4D2 magnet cryostats. The type-2 DSL serves as a superconducting power transmission line between two current feedboxes. It is exceptionally long, about 500 m, without any intermediate branches. It is located in point 3 and connects the DFBLC in UJ33 to the arc current feedbox (DFBAF) on the right side of IR3. In addition to the power transmission function, it provides the cryogenics for DFBLC.

Table 9.6: DSL summary

Name	Description
DSLA	Type-1: connects the DFBLA current feedbox located in alcove RR13 to the three magnet cryostats of Q6, Q5, and Q4D2 in the LHC main tunnel.
DSLB	Type-1: connects the DFBLB current feedbox located in alcove RR17 to the three magnet cryostats of Q6, Q5, and Q4D2 in the LHC main tunnel.
DSLC	Type-2: connects the DFBLC current feedbox located in the UJ33 alcove to the DFBAF current feedbox located in the LHC main tunnel. The routing is from the UJ33 alcove through the UP33 tunnel (about 46 m long) and then through a part of the LHC main tunnel (about 462 m long).
DSLD	Type-1: connects the DFBLD current feedbox located in alcove RR53 to the three magnet cryostats of Q6, Q5, and Q4D2 in the LHC main tunnel.
DSLE	Type-1: connects the DFBLE current feedbox located in alcove RR57 to the three magnet cryostats of Q6, Q5, and Q4D2 in the LHC main tunnel.

DSLs of type-1 house two cryogenic process pipes while the DSL of type-2 houses three cryogenic process pipes. Both DSL types will be made up of straight pipe sections in order to limit heat loads and to limit space occupancy. Flexible sections will only be employed for very short lengths to resolve possible tolerance or thermal contraction issues. Space for thermal contraction compensation systems for type-1 DSLs is foreseen at each of the interface and branching locations. Space for thermal compensation systems for the type-2 DSL, not exceeding the vacuum envelope of the other pipe sections, is foreseen at intervals of 50 m maximum. At each of the thermal compensation locations, the superconducting cable needs to be clamped.

The superconducting cables are cooled by a flow of supercritical helium at about 3.6×10^5 Pa and 4.5-6 K. The 600 A and 6 kA superconducting cables will mostly be of the standard type used elsewhere in the LHC (e.g. Line N). Only the 500 m long cable bundle of 600 A wires for DSLC will be a special production consisting of 48 instead of 44wires. The connections are defined in [13].

DFBX

The DFBXs are provided by the USA-CERN collaboration and differ from the other DFBs [14]. The purpose of the DFBXs is to feed the inner triplets at the interaction points 1, 2, 5 and 8. At points 1 and 5 the separation dipole D1 is normal conducting. Hence these DFBXs differ from the DFBXs at the points 2 and 8, where the D1 is superconducting.

The cryogenic connections provide the distribution of the cryogenic fluids for cooling and maintaining the MQX magnets and their correctors at 1.9 K. The cooling of the radiation absorbers (TAS2 and TAS3) is also provided, as well as the cooling for the current leads, which differ from the leads described earlier. Finally, the thermal shields are cooled and in case of a quench, venting lines are included.

The electrical connections [15] provide the current to the MQX magnets, with the possibility to trim as required. In addition the current for the corrector magnets is fed through the DFBX. Unlike the other DFBs, the DFBXs also feed the current to the quench heaters and provide all signals from the magnets for monitoring and protection.

The DFBXs at the interaction points 2 and 8 do not have a warm to cold transition of the beam tube as the D1 is superconducting here. Instead a connection to cool the beam screen is foreseen, as well as everything needed to operate the D1 magnet at 1.9 K.

9.3.3 Bus-bar Systems

The superconducting magnet families extend across the sectors. To connect the individual magnets with each other or the current leads superconducting bus-bars are used as mentioned in 9.2.3 and sketched in Fig. 9.3. Operated in the superconducting state, they may quench and hence a quench protection is needed as well. There are four distinct classes of bus-bars. The high current connections are highly stabilized and quite rigid, while all 600 A connections to the correctors in the SSS are made using a 42 or 48 wire cable running outside the main cryostat in line N. The same pipe is also used to hold a cable of 6 kA conductors feeding the individually powered magnets in the continuous cryostat in the matching section and dispersion suppressor. The current for the spool pieces, however, runs through straight wires mechanically attached to the quadrupole bus-bars.

Main Bus-Bars

Superconducting (SC) bus-bars carrying a maximum current of 13 kA connect the main magnets. They consist of a superconducting cable, which is thermally and electrically coupled to a copper tube all along its length. The copper provides an alternative path for the magnet current in case the superconducting cable quenches following a transient system disturbance or a normal conducting zone propagating from one of the neighbouring magnets. The temperature during a quench always has to stay safely below 100°C. In the case of a quench the current is switched off and the beams are dumped.

Inside a magnet cold mass each magnet has its own pair of superconducting bus-bars which allow electrical series connections of this element with other elements of adjacent cold masses. A pair consists of a continuous bus-bar from one end to the other of the cold mass and a two-section bus-bar connected to the winding terminals. Other bus-bar pairs, which are not associated with any element in the particular cold mass, pass through it to ensure the electrical continuity. All these pairs of bus-bars of a particular coldmass type form a set. The maximum length of a bus-bar is close to 17 m. The total length of 13000 A rated current superconducting bus-bars reaches about 150 km. Tab. 9.7 gives the number of bus-bar sets needed to interconnect the main dipoles and the main quadrupoles for the arcs and dispersion suppressor regions.

Table 9.7: Summary of the main bus-bars

Type of bus-bar sets	Number of sets (without spares)
Dipole	1232
Short straight section (in the arcs)	370
Main quadrupole magnet (Specially powered Quads in the LSS)	46
Short straight section of the dispersion suppressors	32
Connection Cryostat (Empty Cryostat)	16
DFBA	16

The bus-bars are produced at the Budker Institute (BINP) in Novosibirsk by inserting the superconducting cable into a rectangular and straight copper tube, on which all the brazing and machining operations that might be harmful to the superconducting cable are completed. The copper tube is suitable for the various forming, soldering and welding operations necessary for manufacture and shows a low residual electrical resistance at low temperature after completion of the bus-bar manufacture. High temperature annealing in a protective atmosphere removes all oil traces from the inner surface to ease the soldering. This final annealing also increases the residual resistance ratio of the copper section and it allows the packing of the sections in flat pancake coils to ease the transport of the 260 t copper sections required for the bus-bars. Once the superconducting cable has been inserted, the whole assembly is bent and twisted to shape. The gap inside the copper tube is then filled with a tin-silver solder to provide both thermal and electrical contact between the superconducting cable and the stabilizing copper. Each individual bus-bar is insulated with a polyimide tape. An assembly of the insulated bus-bars inside a charged epoxy resin profile provides a compact set ready to be installed inside the cold mass.

The copper cross section area of a bus-bar pair is optimized for the current decay rate of the corresponding electrical circuit. Consequently the cross-section of the copper profile for the dipole connections (≤120 A/s) amounts to 269 mm^2, while the quadrupole connection (420 A/s) has only 148 mm^2 of copper.

The bus-bar insulation has a breakdown voltage to ground of more than 4 kV in helium gas under all conditions. The insulation is transparent to both superfluid helium and gaseous helium gas to allow cooling and venting.

Spool piece bus-bar wires (600 A)

120 kilometres of superconducting multi-wire cable are required to interconnect the corrector magnets of the LHC main dipoles. This multi-wire cable is made of a flat parallel assembly of five insulated, monolithic niobium titanium superconducting wires. The current rating of each wire is 1200 A at an operating temperature of 4.2 K and in a magnetic field of 2 T. The cross section of the copper is equal to or greater than 3 mm^2 , while the filament diameter is ranging between 20 μm and 40 μm. The filaments are twisted with a pitch of 25 mm. Each wire is separately wrapped with polyimide tape (50% overlap). Five wires are placed side by side and wrapped again with a polyimide tape without overlap and in the opposite sense of the first layer. In total 4 such assemblies of 5 wires each are then attached to the two bus-bars, carrying the quadrupole currents (see Fig. 9.3).

The 600 A and 6 kA flexible, superconducting bus-bar cables

A 42-conductor cable connects the correctors in the SSSs. Because connections are required only in the SSS interconnects, the cable spans the entire half cells (54 m). The cable (Fig. 9.7 left) is flexible. After the magnets of a half-cell have been placed into their final positions in the tunnel, 54 m long sections of this cable are inserted into the Line N tube and connected in a stainless steel cylinder next to the quadrupoles to the neighbouring section and to conductors leading to the magnets inside the SSS cold mass. The cables have to pass through so called plugs, which are electrically insulated obstacles for the helium flow. To meet the increased demand for corrector magnets around point 3 and 7, the 42 wire cable in the first half-cell on either side is replaced by a 48 wire cable (which, except for the increased number of wires, has the same properties as the 42 wire cable). The technical parameters of the commercial product used for NMR magnets is summarised in Tab. 9.8.

Each strand of the cable is insulated with two wraps of polyimide film (66 % overlap). The copper cross-section of 1.8 mm^2 prevents an unacceptable increase of temperature after a quench while the current decays. Numerical simulations of the quench process taking the heat flow through the insulation into account and tests on prototype cables show that the conductor is cryostable at 1.9 K for currents below about 250 A. Below about 500 A a metastable state exists with a maximum temperature below 30 K. The temperature of a quenched wire will not exceed 300 K provided the quench detection and energy extraction, works properly.

A number of main quadrupoles (MQMs and MQYs) and 12 beam separation dipoles in the insertion and dispersion suppressor regions are powered individually with currents of up to 6 kA. In the case of a quench in one of these magnets or the superconducting components connected to it, quench heaters are activated, leading to an energy extraction time of less than 0.3 s. The maximum extraction time occurs in circuits containing MQY magnets. This short extraction time allows conductors with a relatively small copper cross-

section (~9 mm^2) and thus the design of a flexible and compact cable, which can be routed in Line N without joints over lengths of up to 140 m.

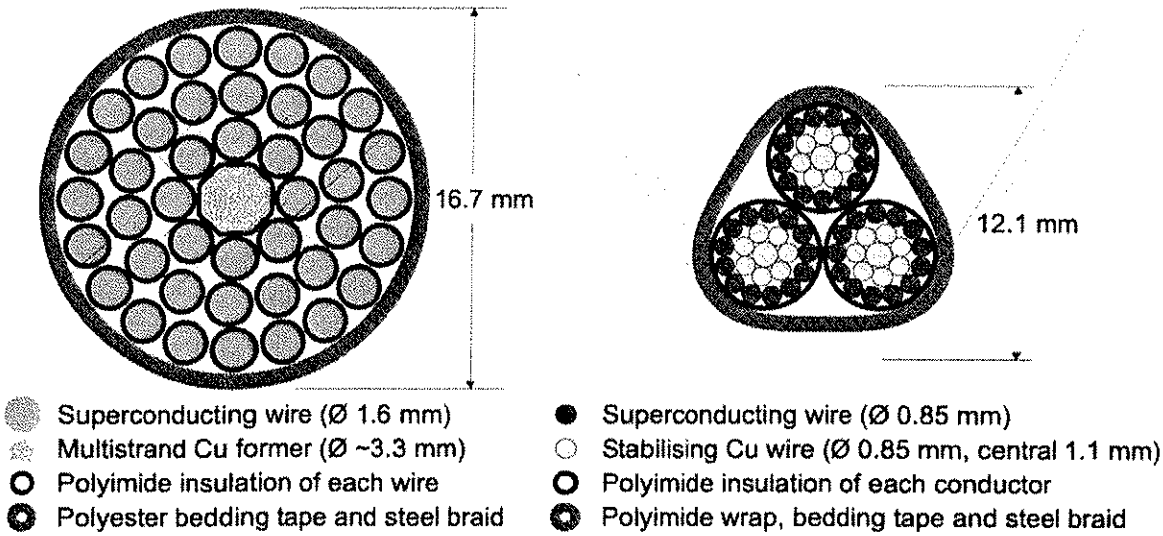

Figure 9.7: Cross sections of the 42 × 600 A cable (left) and the 3 × 6 kA cable (right)

Table 9.8: Technical parameters of the 600 A and 6 kA cables

	600 A cable	6 kA cable
I_c per conductor	> 1000 A	> 10 kA
A_{Cu}	1.8 mm^2	9.6 mm^2
Minimum RRR	100	70
A_{Cu}/A_{sc}	9	3.7
Wire / Strand diameter	1.6 mm	0.85 mm
Source of wire/strands	NMR magnet wire	UNK strands, IHEP, Protvino
Number of conductors	42	3
SC + Cu strands per conductor	1 + 0	13 + 8
Polyimide insulation	4 × 50 μm	4 × 50 μm
Bedding tape	woven polyester tape	
Outer protective covering	stainless steel braid 0.2 mm	
Total diameter	16.7 mm	12.1 mm
Pitch lengths (short)	8 × layer diameter	

A_{Cu} calculated with adiabatic estimates and the time constant of the current decay, strong former (central, electrically unused conductor), wrapped insulation not glued on copper

The design selected for the 6 kA flexible cable (Fig. 9.7, right) contains three insulated conductors, each with 13 superconducting and 8 pure copper strands. The availability of a sufficient quantity of suitable superconducting wire at the Institute of High Energy Physics in Protvino, Russia, motivated this choice and led to collaboration in the design and the production of the cable. Extensive tests at the String 2 installation at CERN showed that the mixture of superconducting and pure copper strands leads to an increase of the quench propagation velocity compared to single strand conductor with the same cross-section, helping to reduce the quench detection time[17].

9.3.4 Normal Conducting Cables

Normal conducting cables are used to connect the current leads or the normal conducting magnets to the power converters. In general, the power converters are located in underground areas close to the corresponding magnet or DFB in order to keep costly normal conducting connections as short as possible.

However, in the case of certain warm magnets no space is available in the underground areas and the power converter is located in the surface building of this IR.

The heat losses of all the normal conducting magnets have a major impact on the installed cooling power in the tunnel and underground areas of the LHC. Cables and tubes carrying very high currents for the LHC main circuits and several other connections are therefore additionally water cooled to decrease heat losses into the air. As for the other LHC components, data for the normal conducting cables have been collected in a database, which is used for integration studies and installation.

9.4 PROTECTION EQUIPMENT

As mentioned elsewhere, in most circuits the stored magnetic energy is sufficient to destroy magnets and bus-bars. The protection relies, as in all previous superconducting accelerators, on the fast and reliable detection of resistive voltages, on a bypass of the current around the quenching parts of the magnet chain and on fast and reliable extraction of as much energy as possible. The large inductive voltages caused by current changes and the electrical noise in an accelerator environment, along with the high level of ionizing radiation present the basic difficulties for detection.

The energy bypass for the main LHC magnets is achieved using cold diodes in parallel to the magnet coils. At low temperatures the turn-on voltage is normally high enough to prevent a bypass leakage current. However, if the voltage across the diode reaches a few volts the diode is turned on and heated up. At elevated temperatures the turn-on voltage rapidly reaches the usual room temperature value of 0.7 V. Here the main difficulty is to avoid a partial overheating of the diode, which would result in an unequal current distribution over the junction area of the diode (current crowding). This in turn results in thermal run-away and a fusion of the pn junction.

It is necessary to discharge the stored magnetic energy as quickly as possible, mainly to protect the diodes. The enormous amount of energy to be transferred into heat and the large inductive voltages, which may endanger the electrical insulation, require special attention.

All parts of the quench protection system are required to be safe and reliable. Moreover, in view of the large number of items, the number of false triggers has to be kept as low as possible.

9.4.1 Quench Protection Electronics

The quench detection systems for the main dipoles are based on a floating bridge detector, which continuously compares the voltages of the two apertures. The two magnet apertures of equal inductance and two balancing resistors form the bridge. These resistors protect also against over-currents through the instrumentation wires. The same kind of detector compares the voltage drops across two different poles of the lattice quadrupole magnet, because here the two apertures are powered separately. In the case of a quench, the floating bridge will become unbalanced and the detector will activate directly the associated quench heater power supplies. These devices are located in racks under the main dipoles inside the LHC tunnel. In addition, these racks house the quench heater power supplies.

Each of the of HTS current leads is protected by a specially designed detector, which compares voltages across the resistive as well as over the superconducting part of the lead with expected values. The hardware is based on an analogue input stage built up with precision instrumentation amplifiers and a micro-converter of the ADuC834 type, which incorporates a 24 Bit $\Sigma\Delta$ ADC with an 8052 compatible microcontroller core.

Differential voltage detectors with dedicated current sensors protect all superconducting circuits up to a nominal current of 600A. The differential voltage is picked up at the cold ends of the superconducting current leads. The DSP based numerical detector is equipped with a dedicated current sensor enabling it to measure the current and to calculate the derivative (Fig. 9.8). The same kind of hardware but in a different configuration is used for the protection of the insertion region magnets including the inner triplets. A dedicated current sensor for the quench detector is not feasible for space and cost reasons due to the higher current rating of these magnets (up to 7.5kA). Voltage taps connected to the midpoints of the circuits and the cold ends of the current leads however offer the possibility of using a floating bridge type quench detector. In this type of detector the superconducting bus bars will also be part of the bridge. The quench detector is based on a DSP, as for the corrector magnet circuits. This allows the implementation of digital filters and compensation of inductances. In the case of a quench, the detector transmits the quench status signal and fires the associated quench heater power supplies.

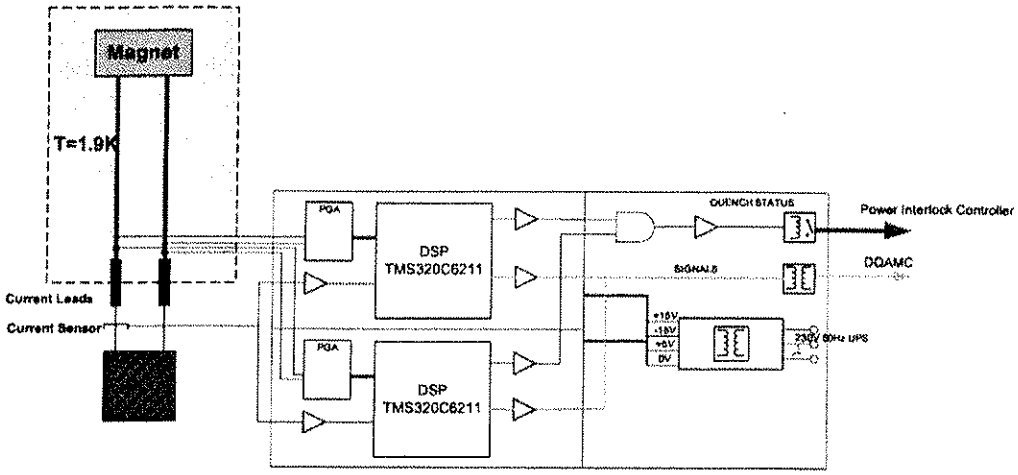

Figure 9.8: DSP based Protection system for 600A corrector circuits.

The protection of the 13kA main bus-bars is a special case. Unlike the superconducting bus-bars of the corrector and insertion region magnets, which are included in the protection of the attached magnets, the main bus-bars require a dedicated quench detector. It is built up with a cluster of digital voltmeters measuring the differential voltage drops at the cold ends of the current leads as well as across selected magnets. All voltmeters communicate their signals to a master device via a WorldFip fieldbus link, which calculates the resistive voltage of the superconducting bus-bars. This fieldbus link must operate properly to make the powering of the main circuits possible.

One part of the quench detection system for the 13 kA superconducting bus-bars will be installed in the alcoves. The rest, as well as other digital quench detectors, will be installed in the LHC underground areas close to the corresponding power converters, as summarised in Tab. 9.9.

Table 9.9: Distribution of the global quench protection electronics in the LHC underground areas

Number of Racks	In Building
2	UJ16
3	RR17
9	UA23
8	UA27
3	UJ33
8	UA43
8	UA47
3	RR53
2	USC55
2	UJ56
3	RR57
3	UA63
3	UA67
1	RR73
1	RR77
9	UA83
8	UA87
3	RR13
2	UJ14

No dedicated quench protection equipment is foreseen for circuits containing superconducting magnets powered with currents lower than 600A. The power converter directly protects the magnet. In the case of a quench, the power converter detects an over-voltage in the circuit and informs the machine protection system (see Chap. 10 for details).

9.4.2 Quench Heater Power Supplies

The quench heater power supplies store the electrical energy necessary to artificially quench a magnet. The quench heater strips, mounted on the coils of many LHC superconducting magnets, are heated up and spread the quench rapidly. This in turn decreases the energy density, and hence the maximum temperature in the quenching coils. Basically a triggered thyristor discharges an aluminium electrolytic capacitor bank, which is normally kept charged. The thyristor has ratings of 1.8 kV and 100 A while the capacitor bank is formed with 2 × 3 capacitors of 4.7 mF / 500 V rating. These components have been extensively tested with respect to reliability, useful lifetime and radiation tolerance. Several completed power supply units have been submitted to radiation tests and confirmed the validity of the design with respect to the required radiation tolerance of 200 Gy. The useful lifetime of the power supply under radiation is therefore mainly limited by the two thyristors used for the discharge of the capacitor bank. Tab. 9.10 lists the quantities of electronics needed

Table 9.10: Quench Protection Electronics, Summary

Device	**Qty.**
Quench heater power supply	6076
Local quench detector (for MB and MQ magnets)	2016
Protection system for 600A corrector circuits	418
Protection system for insertion region magnets	172
Protection system for inner triplets	8
Protection system for 13kA superconducting busbars	80 slave + 8 master
Protection system for superconducting current leads	1198
Acquisition and monitoring controllers	2070

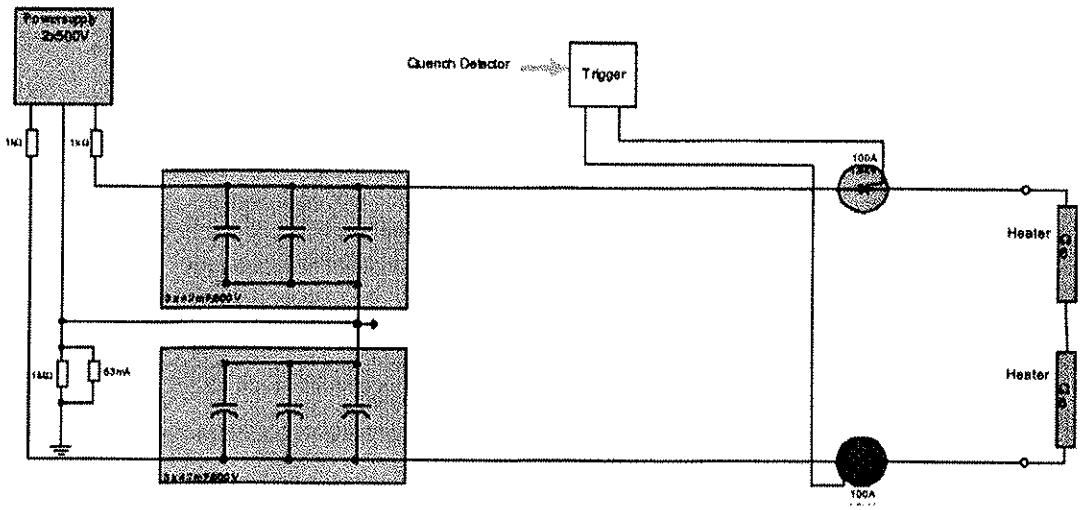

Figure 9.9: Quench heater power supply functional diagram.

9.4.3 Energy Extraction Systems

The quench heaters spread the energy released in a quench over a larger volume, thereby reducing the maximum temperature. This is often sufficient to protect a single magnet. However, the energy stored in the other magnets, which are connected in series, might be too large to be absorbed. In this case as much current as possible has to be routed around the quenching magnet by using a diode but such a diode may not be able to absorb the total energy of the circuit. Also, energy absorbed by the diode has to be removed at cryogenic

temperatures, which is more expensive and time consuming than at room temperature. On top of that, dumping the energy in the diodes takes a very long time. Therefore all major energy dumping systems have an external switch, bypassed by a dump resistor [18].

The energy extraction impacts on other systems in the power circuit. Voltage waves are created by the opening of the switches, sweeping through the magnet chains. The amplitudes of the waves would exceed the ramping voltage by far and individual damping of each magnet achieves sufficient attenuation. For the MB strings 100 Ω resistors connected across the dipole terminals serve this purpose. The effect on the precision of the current due to the leakage during current changes is negligible.

13 kA Circuits

The maximum rate of current change must be limited to prevent eddy current induced quenches (quench-back), while ramping down the current in the main dipoles. The limit has been estimated to be at above 125 A/s for the LHC dipole circuits. Assuming an exponential current decay down from 13 kA, this corresponds to a time constant of 104 s. The inductance of all dipoles[2] in a sector is about 15.1 H. Hence the maximum voltage over a sector would be about 1900 V. With two, identical, series-inserted sub-systems, one with the circuit earthing at its mid-point (through 1 Ω), the maximum voltage to ground is limited to about ±475 V. The system requires the presence of bypass thyristors across the converter terminals to ensure circuit continuity after switch-off of the power source.

The basic criteria for the choice of extraction switch for the various circuits are reliability, lifetime, voltage drop (losses) and radiation hardness (for the units in the tunnel).

The CERN/Russia development resulted in a breaker with the following features:

- Two independent release systems, one completely passive, based on under-voltage release, the other active, based on a discharge pulse trigger.
- Magnetic displacement of the arc into the arc-shute, driven by the main current itself, providing fast and reproducible arc extinction, even at low currents.
- No mechanical catch and latch, the 'on' state being maintained entirely by the excitation of the holding coil.
- Arc-free separation of the main contacts, i.e. opening prior to separation of easily replaceable arc contacts.
- High overload and high current breaking capability combined with low 'on'-state losses.

A 1500 V dipole version and a 200 V type for the quadrupoles exist. They differ in the construction of the arc-shute and the electrostatic, de-ionising muffler. The rated current is 4.0 kA with a continuous overload at 4.5 kA. The total opening time amounts to 5 ms ±1 ms for the fast (pulsed) release and 20 ms ± 1 ms for the slow (under-voltage) release. Triggering of the two systems will always happen simultaneously.

Each extraction facility is composed of eight breakers, in four parallel branches, with two series-connected units each to recover some of the redundancy lost by the parallel connection. All four branches must be closed in order to generate the 'power permit' for the circuit. A minimum of three branches is required for safe operation of the breakers; consequently one branch may open accidentally during operation without forcing a beam abort. In case of accidental opening of a second branch, a 'power abort' is generated, opening all the switches for extraction in the circuit and dumping the beam.

In spite of the large energy difference, the dipole and quadrupole extraction resistors have many common design features. The basic principles for both types are:

- The absorber material has a low inductance and a low temperature coefficient.
- The operating temperature stays below 350°C at the end of the energy deposit.
- The equipment must always be available for extraction during powering of the magnet chain. It cannot rely on any external infrastructure, such as mains power or cooling water, for accepting the energy deposit.
- The resistor body is cooled by forced air and the air is cooled by water. The units contain an air-to-water heat exchanger and a water reservoir with sufficient capacity to ensure worst-case no-boiling conditions.

[2] Using the measured value of 100 mH per dipole

- The cooling period is below two hours. Re-powering of the magnet chain is possible only after cooling of the resistor body.
- The material for the dipole resistors is radiation tolerant.

With an energy deposit of (ultimately) 625 MJ, a single 75 mΩ dipole unit would be 11 m long and have a mass of 8 tons. For reasons of handling and space an alternative solution with three individual, parallel-connected sub-units of 225 mΩ, 220 MJ has been adopted.

The resistor body consists of 84 series-connected stainless steel plates. Particular attention was paid to the need for free expansion-contraction and for a uniform cooling across the resistor body to avoid buckling, twisting and other deformation during the fast energy deposit and the slow cooling. The 6.6 mΩ (and 7.7 mΩ), 22 – 24 MJ quadrupole extraction resistor is small enough to be housed in a rack-sized cubicle.

600 A Extraction Equipment

The MCS, MCD, MO, MQS, MQT, MQTL and MS corrector circuit families are equipped with extraction systems for stored energy ranging from 2 to 108 kJ. In this case the extraction equipment consists of two series-connected, high-speed electromechanical, 3-phase ac breakers with common and simultaneous operation of the three poles. In addition, the breakers are fitted with special dc arc-shutes. The total opening time is 17 ms (pulsed release) and 25 ms (zero-voltage release). For the corrector magnets and their bus bars the extraction time is a critical parameter because of the limited amount of stabilising copper in the superconductors. Capacitive snubbers (typically 320 μF, bi-polar) are used for arc suppression, reducing the contact erosion, the total opening time (by 20%) and the acoustic noise (by 15-20 dB). The extraction resistors, 0.7 Ω or 0.2 Ω, are made from a low temperature coefficient material, such as Fe-Cr-Al.

9.4.4 Cold Diodes

The main magnets are bypassed, as in HERA and RHIC, by diodes operating at cryogenic temperatures. During normal standby operation the diodes have a low temperature turn-on voltage of a few volts, sufficiently high for the anticipated ramp rates. Once a quench has created sufficient resistance in a magnet and the corresponding voltage exceeds the diode turn-on voltage, the diodes start to conduct. They warm up and the knee-voltage drops to lower values. It is important to achieve a knee-voltage and resistance during the bypass operation which is as low as possible. The lower the effective resistance the more current will be transferred out of the coil.

All dipoles or quadrupoles of a sector may be quenched during a discharge due to a malfunction. The non-uniform quench behaviour will cause the last quenching magnet and its diode to see a reverse voltage of 2100V (140 V for quadrupoles). Since there is no diode with such a blocking voltage, the diode will be destroyed. However, it will still protect the magnet. Clearly, the maximum reverse voltage is an important design parameter, along with the resistance to radiation.

A special diffused diode was developed with a cold turn-on voltage of about 6 V, which falls to 0.96 V at room temperature (I=15 kA). The cold reverse voltage is typically around 250 V.

Corrector magnets are protected by parallel resistors. The bypass currents during current changes are negligibly small.

9.4.5 Controllers

Acquisition and monitoring controllers enable the supervision of all electronic devices belonging to the quench protection system and transfer the data via a fieldbus link to the higher-level LHC control systems. These controllers exist in three different variants, differing only in the number of analogue and digital I/O channels. The hardware is based on a micro-converter of the ADuC831 type, which incorporates a 12 Bit 8 channel ADC with an 8052 compatible microcontroller core, and an ASIC of the VY27257 type implementing the WorldFip fieldbus protocol. All controllers are equipped with 62kByte Flash EEPROM memory and 32kByte static RAM. All controller boards have been successfully tested with respect to the radiation tolerance levels required in the LHC tunnel of 200 Gy.

9.4.6 Supervision of the Quench Protection System

The QPS supervision software layer links the gateways (DQGTW) to the LHC general purpose software modules (LHC Alarms, LHC Logging, LHC Post Mortem, Machine Protection System, etc.). The software is presently under development. Some key features are listed below:

- The access to the data is based on views.
- It will be possible to access to the QPS Supervision from an office with W2000/WXP computers, from the control room and from the tunnel area.
- The interface to the hardware controllers is done by command/result data.
- This supervision handles the test mode, where all the QPS hardware can be checked with respect to their proper function.
- The QPS Supervision will always be available. Possible upgrades will be planned for shutdown periods.
- The QPS Supervision will be built in stages. The QPS architecture will support this.

9.5 OPERATIONAL ASPECTS AND RELIABILITY

The operation of the LHC depends, among other things, on the proper connection of all magnet families and on reliable protection and energy extraction electronics. As all magnets are tested and the electrical connections are repeatedly verified, the main risk for faulty connections comes from the interconnections, created during installation.

The main bus-bars are very stiff and bulky. Hence, there is no space in the interconnection regions to make a mistake, except for bad soldering. The connections of the spool pieces are likewise rather difficult to confuse. The other corrector connections, however, can easily be incorrectly wired. The consequences may only show up at a later stage of machine commissioning, when the proper functioning of all correctors is required. Under operating conditions, however, it is quite difficult to spot the fault. Hence a systematic check will be performed during and after the installation.

The quench electronics must never miss signalling a quench and initialising the abort of the beam and the magnetic energy. Likewise the energy dumping system must be available at all times. Ideally, both systems should never react without detecting a real quench. However, component failures, electromagnetic noise and hum (from the mains) cannot be excluded in the LHC environment. In any case the number of "false quenches" must be minimised, to ensure reliable operation.

9.5.1 Electrical Quality Assurance

An electrical quality assurance plan is defined for the LHC machine environment in order to ensure the safe and correct functioning of all superconducting electrical circuits during its commissioning and operation. Such a plan has been worked out in close collaboration with all parties concerned with the installation and commissioning (i.e., the hardware commissioning working group). The electrical interconnection in between segments will be performed by a specific team, the verification will start as soon as the interconnection is finished and several verification crews will check the compliance from the electrical point of view during the assembly and commissioning period. During machine operation and shutdowns these activities will be done by CERN staff.

The steps in the electrical quality assurance plan for the machine assembly, commissioning, operation and shutdown phases are as follows:

- Continuity, polarity, electrical integrity verification during machine assembly until the closure of the helium enclosure of each subsector.
- Electrical measurements at ambient temperatures of reference parameters for each individual electrical circuit part of a subsector. These measurements are performed from the corresponding distribution feedbox.
- On-line monitoring during the cool-down of the integrity of electrical insulation of circuits and instrumentation for magnet protection.

- Electrical measurements of reference parameters at cold conditions before the powering of each individual electrical circuit of a subsector.
- Diagnostic measurements and verifications during subsector commissioning and machine operation.
- Yearly verification during shutdown periods of cold electrical components such as the by-pass diodes.
- Verification after in-situ repairs of electrical circuit segments as well as after an exchange of electrical components.

One of the most important challenges during installation will be to ensure the correct interconnection of the superconducting bus bars powering the LHC cryo-magnets. Between each main magnet there are six main bus-bar interconnections (MB, MQF and MQD circuits) and 20 auxiliary bus-bar interconnections (spool-piece correctors of the main dipoles). At the interconnection of the short straight sections (SSS), flexible bus bars with 42 superconducting wires have to be connected for the powering of the correctors in the MQ cold mass. For the quality assurance of these interconnections an automatic system for test and verification with the LHC electrical reference database has been developed. For the matching section it is foreseen to manually perform the verification during the assembly. This choice is based on the acquired experience on String 2 where the circuits are comparable to the matching section subsectors.

Once the assembly is completed and before starting the cool down of the machine, each subsector circuit will be electrically tested. The resistance, the transfer function and the insulation to ground and to other electrical components are checked. The same type of measurements will also be performed once the subsector has been cooled down.

During the cool down, thermal contraction and transitory displacements inside the cold masses might temporarily or permanently damage the integrity of an electrical circuit. To detect such a problem an on-line system will measure the resistance to ground of the circuit and with respect to other electrical components. In the same way the evolution of the electrical continuity of some specific instrumentation necessary for the protection of segments of superconducting circuits will be followed online.

9.5.2 Quench Protection Availability

The Quench Protection System (QPS) prevents hardware damage during quenches. Hence the availability is of paramount importance. On the other hand, noise and too sensitive equipment can fake a quench, resulting in considerable downtime. Around 4000 internal trigger channels coming from the QPS will be able to generate power aborts and block the Power Permit. The QPS design balances between availability and noise immunity. To understand how likely it is that the QPS misses a quench or creates an artificial quench, a reliability study was carried out [19] comprising the following parts:

- Experimental and/or theoretical study of the protection strategies.
- Check of the components under the expected radiation environment.
- Building a reliability model of the different quench protection subsystems.
- Optimisation of the subsystem designs to minimize risk of hardware damage and unscheduled machine downtime, taking into account redundant topologies, maintenance policies, spatial constraints, machine operation and cost.

The two main sets of input parameters are the reliability data of the components and the expected quench rate. The first set is taken from the Military Handbook (MIL-HDBK-217F) and the data provided by the manufacturers. 24 quenched main magnets per week are assumed, as estimated in [20].

The protection system can be:

- Fully functional. This is the level usually reached after a repair or at the very beginning of operation after commissioning. After a Power Abort, the QPS requires all the components in the subsector to be set at this stage.
- Available: the system is performing well although some components have failed with consequent loss of redundancy level. The acceptable loss of redundancy during the powering phase is defined for each subsystem.

It can show:

- Safe Failure: generation of one or more false protection signals that trigger the protection procedure (e.g. false quench detector signal). The integrity of the protected system will not be compromised, and the only consequence will be unscheduled downtime.
- Dangerous Failure: the protection system becomes unavailable and the facility unprotected. Although this is a highly undesired situation, this failure has no cost.
- Major Failure: the initiator from which the system has to be protected (e.g. quench) shows up while the system is in the Dangerous Failure state. Hence the protection system does not accomplish the task for which it was designed.

The dependability study focuses on the active elements of the QPS (i.e. quench detectors, quench heater power supplies – not the power converters – and energy extraction). The cold diodes and the quench heaters as passive elements are not considered. Collective effects which act on several parts of the system simultaneously and coherently (like faulty software or the fieldbus link) are not considered either.

Quench Detectors

In order to increase the availability of each of the detection systems it is foreseen to use the coherence of the two independent channels continuously, thereby reducing the probability for false quenches. Moreover, a simulated quench signal is sent from the control room. If one or more channels fail the test of the coherency will generate a warning. Since this test implies the discharge of the quench heater power supplies, it can only be performed when the magnets are cold and not powered.

When Quench Tests are performed monthly and repairs are carried out before re-powering the circuits (see below), the probability of missing a quench during 20 years of operation is below 1%.

The expected number of false quenches is around 10 per year. Since the powering of the detectors is not redundant, it is not possible to improve its reliability via checks. However, the number of false quenches will drop to less than 1 per year, if two supplies are connected in parallel. Due to the large investment required to double all the power supplies, it has been decided to install one power supply per local quench detector and provide the necessary space and cabling to install a redundant unit if operation experience shows it to be necessary.

The quench protection of the main bus-bars relies partially on the fieldbus. This seems not very reliable. However, the expected rate of bus-bar quenches without a magnet quench is extremely low, provided all connections are done properly.

Tab. 9.11 summarises the results for all the LHC quench detectors if monthly checks are carried out (see below). The expected probability of not missing any quench along the machine over 20 years is above 95%.

Table 9.11: The probability to miss one quench in 20 years (RMQ) and the expected number of False Quenches with a 95% confidence level for the different detector families.

Detector		Units	RMQ	False Quenches
DQQDL	Local	2016	0.991	197-238
DQQDI,T	Insertion and Inner Triplets	316	0.991	89-145
DQQDG	Correctors	351	0.997	120-187
DQQDC	Current Leads	1198	0.974	132-165

Quench Heater Power Supplies (DQHDS)

Each of the 6076 quench heater power supplies contains two banks of three capacitors each connected in parallel. These are discharged in the quench heaters by triggering two thyristors in series with the strips. Four power supplies are installed per dipole. At least two have to be properly discharged to ensure the integrity of the coil. The quench heaters in the 13 kA and 6 kA quadrupoles are fed by two power supplies (except in the case of the MQY magnets, where four power supplies are required) and at least one of them (two for the MQY) has to be correctly fired to protect the magnet.

The reliability analysis of the quench heater power supplies shows that quench tests on a regular time scale improve the reliability of the system. Monthly tests (and repairs) boost the reliability to react properly to all

quenches during 20 years 99.7% (99.9% for the quadrupoles). Incidentally, a high rate of quenches would have a benign effect on the reliability for this highly redundant system.

Energy Extraction

As described in Sec. 9.4.3 the energy extraction systems are based on electro-mechanical breakers with high redundancy using series and parallel connected current paths.

During a machine run one branch may open by accident without compromising operation. In the case that more than one branch is opened, all the other breakers of the facility will be forced to open. In the case of the main dipoles, the system at the other end of the arc is also opened. In the unlikely, but most dangerous event that one branch of a system remains closed after an opening command, several cold diodes in the main magnets or resistors in the corrector magnets could be damaged because the stored energy will not be dumped properly. In this case several pre-selected magnets will be fired. This will, unfortunately, lead to a huge load on the cryogenic system.

The probability of one such failure in 20 years is about 0.03% in case of the 13 kA energy extraction systems, assuming a realistic failure rate of the breakers of 0.0001. This requires monthly checks and using the post-mortem information of all energy extractions which occur. Four power aborts due to quenches in the main magnets per operational week have been assumed.

For the 600 A, the space conditions allow the use of a third switch, which decreases the failure rate. In this case the result is <0.01 failure probability.

In summary, only regular maintenance can keep the QPS alert, not to miss a quench, and also not to have a false trigger. Failing to provide regular maintenance means failure in operation of the accelerator. Some checks can be done while running, others require normal operation to be stopped. Finally a check will be done automatically, for example due to "normal" quenches. Tab. 9.12 summarises the required maintenance policy.

Table 9.12: Maintenance Policy

		Check	Inspection	Repair	Affected
Quench Detectors	DQQDL	Quench Test	Monthly	Monthly	All
		Post Mortem	After Quench	Before Power Permit	Quenched Magnet
		Coherency Test	On-line	Monthly	All
		Power Permit	On-line	Before Power Permit	Subsector
	Other	Quench Test	Monthly	Monthly	All
		Post Mortem	After Quench	Before Power Permit	Circuit
		Powering Test	On-line	Monthly	All
		Power Permit	On-line	Before Power Permit	Subsector
Heaters		Discharge Test	Monthly	Monthly	All
		Post Mortem	Quench	Before Power Permit	Quenched Magnet
Extraction	13kA	Open Check	Monthly	Monthly	All
		Post Mortem	Quench	Before Power Permit	Subsector
		False Opening	On-line	Monthly	All
		Power Permit	On-line	Before Power Permit	Subsector
	600A	Open Check	Monthly	Monthly	All
		Post Mortem	Quench	Before Power Permit	Subsector

With all maintenance properly done and assuming the parameters mentioned above an overall main failure probability over 20 years of 0.914 is to be expected.

Clearly, the maintenance will take time. The exact time will depend on the number and distribution of quenches happening during operation, which do not need to be tested any more. The strategy for the quench tests will then fully exploit the cryogenic capacity and the voltage rating of the various circuits in order to gain time. After a careful analysis of the data, repair or replacement of parts may be needed. Hence, to keep the systems alert several days per month of intensive tests and repairs should be anticipated. It should be noted that access to the sectors under test will normally not be possible.

REFERENCES

[1] LHC-LD-ES-0003 rev 1.0 (EDMS 355662), The Electrical Circuits in the LHC Reference Database
[2] LHCLSDa_000b, a=1…8, b=1…5, CDD, Electrical Diagram of LHC Magnets
[3] LHC-DCC-ES-0003.00 rev 3.0 (EDMS 104157), Powering Layout of the SSS Correction Scheme
[4] LHCLSXG_0001, CDD, Layouts of LHC Insertions IR1, IR2, IR3, IR4, Optics Version 6.4
[5] LHCLSXG_0003, CDD, Layouts of LHC Insertions IR5, IR6, IR7, IR8, Optics Version 6.4
[6] LHC-DFL-ES-0001, EDMS No 350602, LHC High Temperature Superconducting Current Leads
[7] A. Ballarino, HTS Current Leads for the LHC Magnet Powering System, Physica C 372-376 (2002) 1413-1418
[8] A. Ballarino, Current Leads for the LHC Magnet System, LHC Report 526
[9] A. Ballarino, Dipole Corrector 60 A Resistive Current Leads, LHC Project Note (to be published)
[10] A. Perin, V. Benda, R. van Weelderen, The Cryogenic Electrical Distribution Feeboxes and the Superconducting Links of LHC, Proceedings of the LHC DAYS 2003, to be published
[11] LHC-DFBA-ES-0002 rev. 1.1 (EDMS 355582), Current Lead Assignments on the DFBA's
[12] LHC-DFBM-ES-0001 rev. 1.1 (EDMS 355562), Current Lead Assignment on the DFBM's
[13] LHC-DFBL-ES-0001 rev. 1.0 (EDMS 386685), Current Lead Assignment on the DFBLs
[14] LHC-DFBX-ES-0100.00 rev 1.0 (EDMS 108974), Inner Triplet Feedboxes
[15] LHC-DFBX-ES-0250.00 rev 1.1 (EDMS 313365), Inner Triplet Feedboxes: DFBX-Power Converters
[16] R. Herzog, M. Calvi and F. Sonnemann, Quench Propagation and Heating in the Superconducting 600 A Auxiliary Busbars of the LHC, Advances in Cryogenic Engineering, Vol. 47 p575
[17] R. Herzog, M. Calvi, F. Sonnemann and J.M. Pelegring-Carcelen, Quench propagation in the Superconducting 6 kA Flexible Busbars of the LHC, Advances in Cryogenic Engineering, Vol. 47 p583
[18] K. Dahlerup-Petersen, CERN, B. Kazmine, V. Popov, V. Sytchev, L. Vassiliev and V. Zubko, IHEP, Energy Extraction Resistors for the Main Dipole and Quadrupole Circuits of the LHC, EPAC2000.
[19] A. Vergara, Reliability of the Quench Protection System for the LHC Superconducting Elements. PhD Thesis, March 2003.
[20] LHC-PM-ES-2.00 rev 1.1 (EDMS 100513.00 rev. 1.1), General Parameters for Equipment installed in the LHC

CHAPTER 10

POWER CONVERTER SYSTEM

10.1 INTRODUCTION, DESIGN CONSTRAINTS

While LEP required high voltage and low current for its loads, LHC will require very large currents and rather low voltages for its superconducting magnets. Although it was relatively easy and inexpensive to install the power converters for LEP on the surface and cable them to their underground loads, such an approach would have been prohibitive for LHC because of the high dc currents. Fortunately, LHC will not need the large RF complex used for LEP2 at the even points. Thus the large RF galleries, parallel to the tunnel (UA), have been vacated to allow the underground installation of high current power converters very close to the current feedthroughs. In the odd points, special enlargements of the tunnel (RR) are required to install auxiliary power converters (dispersion suppressors, insertion quadrupoles, insertion orbit correction, with current range from 6 kA to 120 A converters). In the cleaning insertions of points 3 and 7, the insertion quadrupoles and dipole separators use warm magnets which can be powered from the surface using the existing surface buildings and cabling of LEP.

The re-use of the LEP infrastructure and the underground installation is the driving force for reduced volume and high efficiency of the power converters. It should be noted that a lot of power converters will be installed back-to-back (Fig. 10.1). The difficult and restricted access to the underground zones imposed a modular approach for the converter design, allowing quick replacement of faulty modules and off-line repair in surface workshops. To minimise the ventilation installation, low air losses was an important requirement for the design of the power converters. All the power converters will be water cooled, except the orbit correctors, [±60 A, ±8 V] and [±120 A, ±10 V].

Due to the compact installation of the power converters and the close vicinity to all the other equipment (magnet protection, beam injection and beam extraction systems, experiments,...), the Electro Magnetic Compatibility (EMC) has been a severe design constraint for the power converters and needs to be studied and measured when all other equipment has been installed.

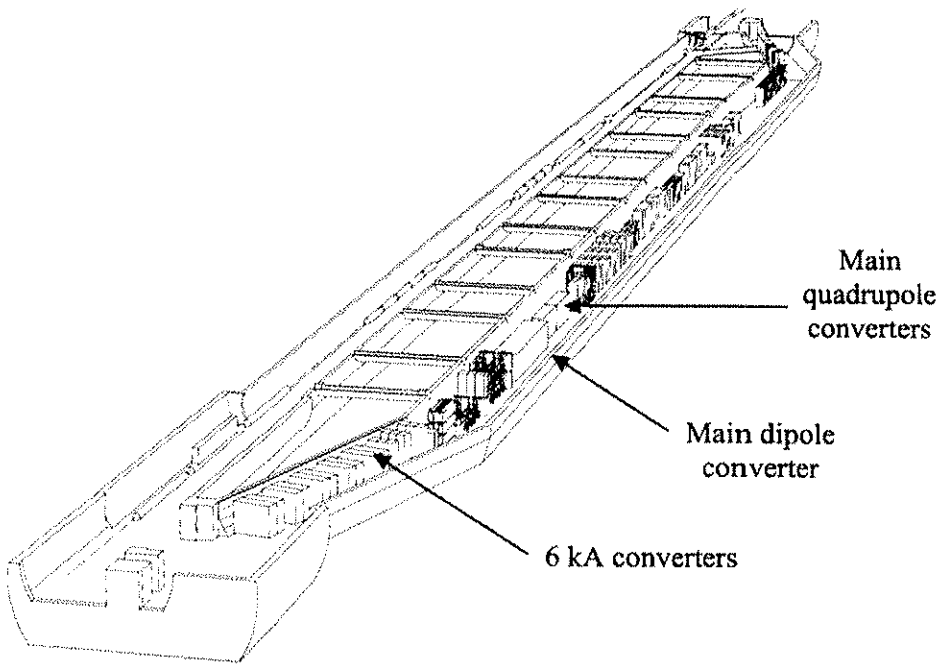

Figure 10.1: UA layout example

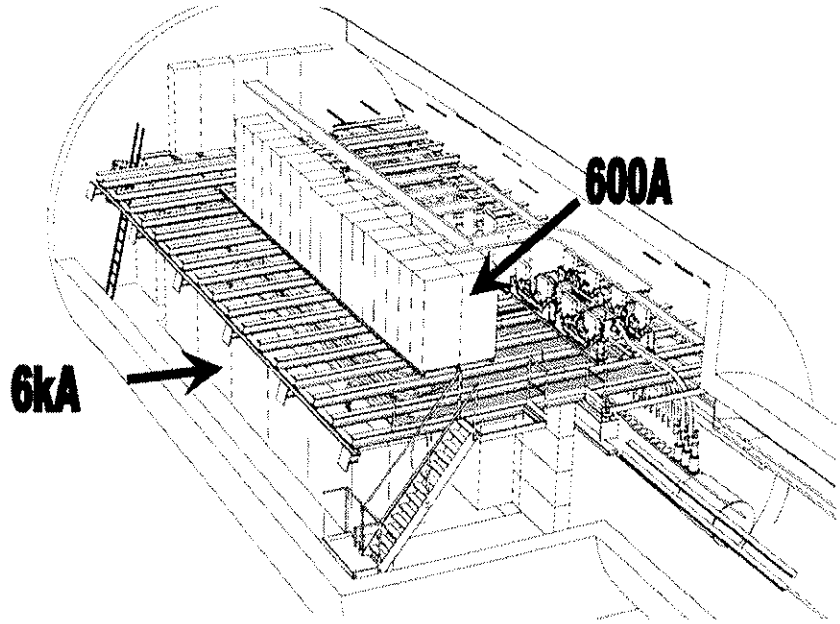

Figure 10.2: RR layout example

In all, there will be 1720 power converters having a total steady state input power of 63 MW and a peak power of 86 MW. They will supply a total current of about 1850 kA and are, in general, characterised by having high current and low voltage (see Sec. 10.3).

The performance of the powering system is dominated by the tune tolerance which ultimately should reach 0.003. This is made more complex by the segmentation of the machine (see Chap. 9) and the fact that the field-to-current relationship in a superconducting magnet is a complex function of many parameters, both static and dynamic [1]. It is particularly delicate at the low currents of injection where great care must be taken to precisely cycle and set the magnets to take into account the effects of DC and AC magnetisation and snap-back of the persistent currents. Initial studies have shown that the overall performance of the main circuits, in order to bootstrap the machine, needs to attain a maximum of about 1.5×10^{-5}. However, a resolution and short term stability of the power converters in the order of few 10^{-6} will be needed to allow precise cycling and fine adjustment. Because the sectors are basically optically autonomous, the sector-to-sector tracking tolerance is of the same order as that of the global requirements.

To achieve these very difficult goals, great development effort was needed and continues in the following domains: Analogue-to-Digital Conversion techniques, high-current DC current measurements, digital control technologies and new soft-switching power converter topologies (see Sec. 10.4)

The accelerator physics requirements translate into an overall high precision [2] which will be presented in the next section.

10.2 POWER CONVERTER PERFORMANCE: PRECISION

The term Precision is only a generic term, covering accuracy, reproducibility and stability.

Before defining these terms, it is useful to recall several basic definitions:

a) Nominal current ($I_{nominal}$): Normal maximum value for a circuit.
b) Rated current (I_{rated}): Maximum current of the power converter
c) Calibration current ($I_{calibration}$): Calibration value = software decided maximum current ($\leq I_{rated}$)
d) Overload Current ($I_{overload}$): A hardware protection setting, tripping the converter if exceeded.
e) Ultimate current ($I_{ultimate}$): Current required for the ultimate main dipole field 9.0 T.

For LHC, the nominal current of the power converter is chosen to be equal to the ultimate current and for all the converters with a nominal current above 1 kA:

$I_{calibration} = I_{LHC\text{-}nominal}$ = current required for nominal operation of the machine (8.33 T in the main dipole)

$I_{overload} = 1.1 * I_{calibration} = 1.1 * I_{LHC\text{-}nominal} \cong 1.03 * I_{LHC\text{-}ultimate}$

Accuracy

The accuracy is defined as the long-term uncertainty in the setting, taking into consideration the full range of permissible changes of operating and environmental conditions.

The environment is defined in various LHC Engineering Specifications:

- General parameters for equipment installed in the LHC [3] (e.g. $\Delta T = \pm 4°C$ in UAs) [27]
- Main parameters of the LHC 400/230 V distribution system [8].

The accuracy is defined for a period of one year and is expressed in ppm (Parts Per Million) of $I_{nominal}$.

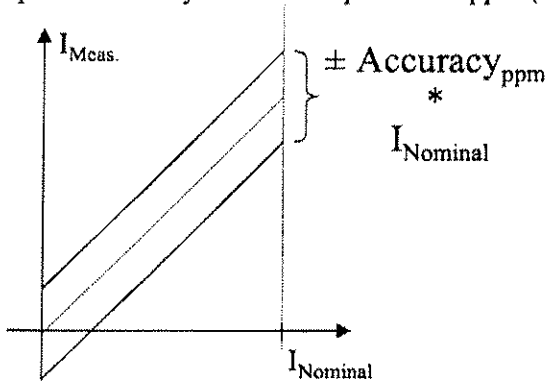

Figure 10.3: Accuracy illustration

If the one year accuracy is not sufficient, the calibration process must be performed more often (e.g. every month). An in-situ quasi-on-line calibration system has been developed for this purpose (see Sec. 10.4.5) Eight of these systems will be installed for the 24 main circuits (main dipoles and main quadrupoles) and eight more systems for the inner triplet quadrupoles.

Reproducibility

The reproducibility is defined as the uncertainty in returning to a set of previous working values from cycle to cycle of the machine.

The reproducibility is defined for a period of one day, without any adjustment of the calibrated parts (e.g. DCCT, ADC). The reproducibility is expressed in ppm of $I_{nominal}$.

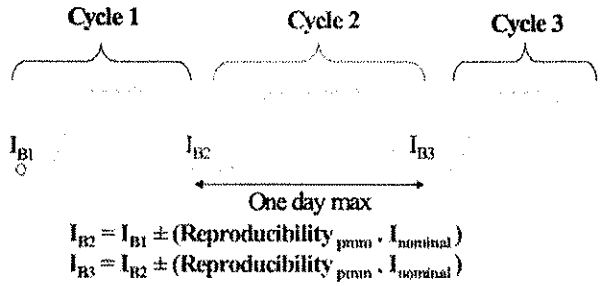

Figure 10.4: Reproducibility illustration

Stability

The stability is defined as the maximum deviation over a period of half an hour, with no changes in operating or environmental conditions other than mains network. The stability is expressed in ppm of $I_{nominal}$

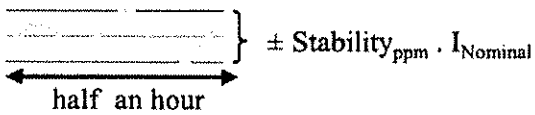

Figure 10.5: Stability illustration

Resolution

The resolution is defined as the smallest increment in current that can be induced or discerned. The resolution is expressed in ppm of $I_{nominal}$. Resolution is directly determined by the A/D system.

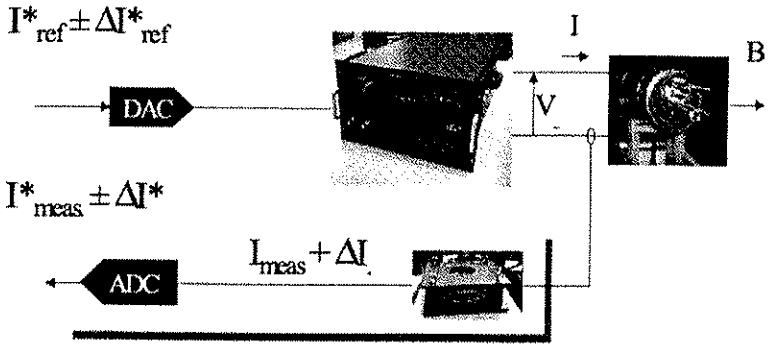

Figure 10.6: Resolution illustration

Tab.10.1 gives a summary of the precision performance of the LHC power converters. These parameters were discussed and defined in the frame of the Dynamic Effects Working Group [4].

Table 10.1: Power Converter Tolerances for LHC

Circuit Type	Nominal Current (A)	Current Polarity	One Year Accuracy (ppm of Inominal)	One day Reproducibility (ppm of Inominal)	1/2 hour Stability (ppm of Inominal)	Resolution (ppm of Inominal)
Main Bends, Main Quads	13000	Unipolar	± 50 ± 20 with calibration	± 5	± 3	1
Inner triplet	8000/ 6000	Unipolar	± 100 (± 20 with calibration)	± 20	± 10	15
Dispersion suppressor	5000/ 6000	Unipolar	± 70	± 10	± 5	15
Insertion quadrupoles	4000/ 5000/ 6000	Unipolar	± 70	± 10	± 5	15
Separators (D1,D2,D3,D4)	5000/ 7000	Unipolar	± 70	± 10	± 5	15
Trim quadrupoles	600	Bipolar	± 200	± 50	± 10	30
SSS correctors	600	Bipolar	± 200	± 50	± 10	30
Spool pieces	600	Bipolar	± 200	± 50	± 10	30
Orbit correctors	120/60	Bipolar	± 1000	± 100	± 50	30
Warm magnets	850/1000	Unipolar	± 200	± 50	± 10	15

10.2.1 Power Converter Tracking

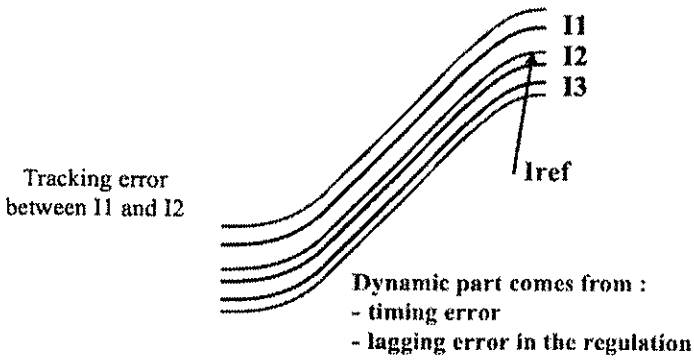

Figure 10.7: Tracking error

Tracking

The tracking is defined as the ability of a converter to follow the reference function. This definition is valid for static and dynamic references. The static part is covered by the static performance: accuracy and reproducibility.

The dynamic part of the tracking error comes from any timing error or lagging error in the regulation.

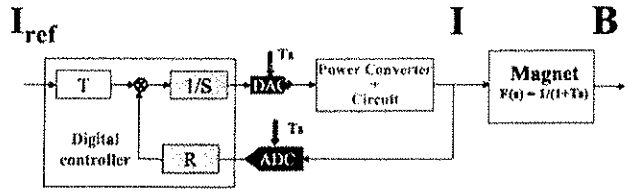

Figure 10.8: Digital control loop principle

To limit the timing error, the measurement and the reference must be synchronised. With a dI/dt equal to 10 A/s, 1 ms timing is necessary to limit the contribution of the timing to the dynamic tracking error to less than 1 ppm.

The digital current loop of the power converters is designed with no lagging error; i.e. independence of the load time constant. The lagging error between the current and the field must be known to be corrected by a timing shift at the start of the ramp. These errors depend mainly on the vacuum chamber and the beam screen.

Tracking between the 8 main dipole converters

Due to the electrical segmentation of the machine in eight independent arcs, a good tracking of the main dipole converters is vital for the LHC beam quality.

With an accuracy of 20 ppm for the main dipole converters [6], the energy error in the LHC machine is given by:

$$\Delta B/B_{nom} = \Delta I/I_{nom} = 20 \text{ ppm}$$
$$\text{where } B_{nom} = 9 \text{ T and } I_{nom} = 13 \text{ kA}$$

Then:

$$\Delta B = 9 * 20\ 10^{-6} = 1.8\ 10^{-4} \text{ T}$$
$$\Delta B/B_o = 3.3\ 10^{-4}.$$

This error in the machine leads to an orbit excursion:

$$\Delta X = D_x \,.\, \Delta B/B_o \approx 0.7 \text{ mm with } D_x \approx 2 \text{ m}.$$

This excursion could be corrected with a pilot run. Then after a machine cycle, reproducibility performance defines the orbit excursion. With a reproducibility of 5 ppm, an orbit excursion, better than 0.2 mm, could be achieved. This 20 ppm accuracy and 5 ppm reproducibility are very difficult performance parameters. To reach this performance, high-precision DCCTs (Direct Current Current Transformer) and ADCs (Analogue Digital Converter) as well as in-situ calibration systems are required.

Tracking between the dipole and quadrupole converter

With an accuracy of 20 ppm for the main dipole and quadrupole converters, the energy error in the machine is:

$$\Delta B/B_{nom} = \Delta I/I_{nom} = 20 \text{ ppm}$$
$$\text{where } B_{nom} = 9 \text{ T and } I_{nom} = 13 \text{ kA}$$

Then:

$$\Delta B = 9 * 20\ 10^{-6} = 1.8\ 10^{-4} \text{ T}$$
$$\Delta B/B_o = 3.3\ 10^{-4}$$

This energy error in the machine leads to a tune change given by:

$$\Delta Q = Q'_{nat} \,.\, \Delta p/po = Q'_{nat} \,.\, \Delta B/Bo.$$

With a natural chromaticity Q'_{nat} equal to 100: $\Delta Q \approx 100 * 3.3\ 10^{-4} = 0.033$

As the tuning quadrupoles can correct up to $\Delta Q = 0.3$, this tracking error between main dipole and main quadrupole converters is acceptable.

10.3 OVERVIEW OF SYSTEM

The list of power converters with their main characteristics is given in Tab. 10.2. More characteristics can be found in the powering database [10]. This list is the result of an optimisation process to reduce the number of power converter types to a minimum.

Table 10.2: List of the LHC power converters

Equipment code	Current		Voltage			Mains Input		Power losses		Qty
	Ultimate A	Minimum A	Steady V	Boost V	Peak V	Peak kW	Peak kVA	Water kW	Air kW	
RPTE	13000	350	10	±180	190	2681	3540	150	50	8
RPHE	13000	350	13	±5	18	265	288	28	3	16
RPHF	8000	160	6	±2	8	78	85	13	1.5	21
RPHG	6000	120	6	±2	8	59	64	10	1.2	132
RPHH	4000	80	6	±2	8	40	42	6.5	0.7	40
RPMB	600	Bipolar	±8	±2	10	8.5	9	2	0.2	330
RPMC	600	Bipolar	±35	±2	40	27	30	3	0.3	24
RPMB	600	0	8	2	10	8.5	9	2	0.2	70
RPMC	600	0	35	5	40	27	30	3	0.5	2
RPLB	120	Bipolar	±8	±2	10	1.7	108	0	0.5	290
RPMC	120	Bipolar	±35	±5	40	5.5	6	0	0.1	10
RPLA	60	Bipolar	±2	±6	8	0.7	0.8	0	0.2	752
RPTL	650	60	160	0	160	113	141	0	25	3
RPTF	810	70	450	0	450	390	490	0	50	4
RPTG	810	70	950	0	950	820	1025	0	40	4
RPTM	1000	50	600	0	600	640	800	0	395	2
RPTI	6500	350	950	0	950	6570	8220	0	14	2
RPTN	1000	50	±180	0	180	195	210	0	26	3
RPTJ	20000	1000	±26	0	26	620	795	76	5	1
RPHK	20500	1000	18	0	18	420	455	44	5	1
RPTH	33000	2000	170	0	170	6060	7610	340	60	1
RPTK	40	n.a.	100000	0	100000	4240	5300	180		4
TOTAL										1720

This process converged towards five main types of converters:

a) The first type of converter (RPTE) is the main dipole magnet converter. The LHC machine is divided in eight sectors, each powered by a separate power converter (see Chap. 9). These eight power converters need to have a very large dynamic range to supply ±190 V during acceleration and normal de-excitation of the machine within reasonable time (20 minutes), but only about 1 V while at injection energy. The steady state specification for physics is 13 kA, 10 V. Thyristor line-commutated technology will be used for these converters.

b) The second type of converter (RPHE, RPHF, RPHG, RPHH) corresponds to the converters for the main quadrupoles, the insertion quadrupoles, the separators, etc. The output rating specifications are [13 kA, 18 V], [8 kA, 8 V], [6 kA, 8 V] and [4 kA, 8 V]. Switch-mode technology will be used for these converters. Taking into account that the state-of-the-art for dc-dc power converter modules is in the range of 30 to 50 kW, these converters will be made up using a modular concept where several high-current sources ([3.25 kA, 18 V] or [2 kA, 8 V]) are placed in parallel; this concept can also provide redundancy. A total of around 700 modules will be used for the LHC.

c) True bipolar power converters [±600 A, ±10 V], [±600 A, ±40 V] and unipolar [600 A, 10 V], [600 A, 40 V] (RPMB, RPMC) are required to power the sextupoles, the sextupole and decapole spool piece circuits,

the octupoles and some warm quadrupoles in the cleaning regions. In total there are 436 converters (10 V: 400; 40 V: 36): 354 bipolar (10 V: 330; 40 V: 24) and 72 unipolar (10 V: 70; 40 V: 2). Based on these ratios and financial considerations, it was decided to have only bipolar converters: [±600 A, ±10 V] and [±600 A, ±40 V]. Furthermore, the [±600 A, ±40 V] converter will be used for the powering of the dispersion suppressor and matching correction dipole in Point 3, instead of [±120 A, ±40 V], which would have needed special development for only 10 units. Switch-mode technology will be used for these converters.

d) Each quadrupole and each aperture of the LHC machine has a small dipole orbit corrector associated with it. In total there are 752 for the arcs (RPLA) and 290 in the dispersion and insertion regions (RPLB). The best solution is to locate the 60 A converters in the LHC tunnel close to the quadrupole magnets: reduction of the cabling costs and of the converter power (±8 V instead of ±115 V for a surface location). The underground installation implies a very high reliability and radiation hardened devices (~10 Gy in 10 years). Switch-mode technology will be used for these converters.

e) For all warm magnets and septa with voltage above 40 V, conventional thyristor, line-commutated, converters will be used.

The actual intention is to reuse the present magnet test bench power converter supply reference magnets. Tab. 10.3 gives the voltage ripple requirements for the different types of power converters.

Table 10.3: Power Converter Voltage Ripple

Power converter type	50 HzRipple pk-pk (mV)	300 HzRipple pk-pk (mV)
[13kA, 18V]	60	350
[8kA,8V]	5	30
[6kA,8V]	5	30
[4kA,8V]	5	30
[±600A,±10V]	5	20
[±600A,±40V]	5	20
[±120A,±10V]	5	20
[±60A,±8V]	30	120
		600 HzRipple
[13kA, ±190V]	60	350
[810A,450V]	40	250
[810A,950V]	80	450
[1000A,600V]	600	3000
[650A,160V]	200	1000
[1000A,180V]	200	1000

The underground installation is the driving force for reduced volume and high efficiency of the power converters.

The main characteristics of these converters are:

- high efficiency (> 80% for the unipolar converters and > 70% for the bipolar converters).
- water cooling of converters with power above 5 kW.
- galvanic isolation between mains and output.
- wide output current range ($I_{max}/I_{min} \sim 100$).
- very high reliability and operational redundancy; no access to the underground during operation with beam and access underground will take a long time.
- repairability: all converters will be designed with fast plug-in modules or fast exchange parts. The weight of each module will be between 25 and 65 kg to allow one or two operators to carry out a fast exchange with spare modules.

To meet these requirements switch-mode technology will be used in most cases. Operation at high frequencies results in a considerable size reduction (volume and weight) for transformers and filter and

improved dynamics. It also gives a better rejection of the mains perturbations and a lower ripple of the output voltage. However, losses associated with high-frequency operation have to be kept as low as possible to achieve efficient power conversion. Therefore switch-mode power conversion technologies have evolved from the basic PWM converters to a new emphasis on switch commutation currently called soft commutation.

The strategy for the design, production and test of the LHC power converters was based on the following considerations:

- Identify subsystems that are suitable for industrial design and production.
- Place development and production contracts.
- Design and build prototypes of remaining subsystems.
- Place production contracts with industry.
- Assume system integration responsibility.
- Carry out integration and system test at CERN before installation.

To fulfil the aims of this strategy, all the power converters were split in three independent parts (Fig. 10.7):

- A power part acting as a voltage source (see Sec. 10.4.1).
- Current transducers (all converters will be equipped with two independent current transducers (see Sec. 10.4.2).
- A digital electronics control module, which performs the current regulation and makes the link with the slow control network (see Sec. 10.4.3 and 10.4.4). A special effort has been made towards standardisation, using the same electronic control modules for all types of converter.

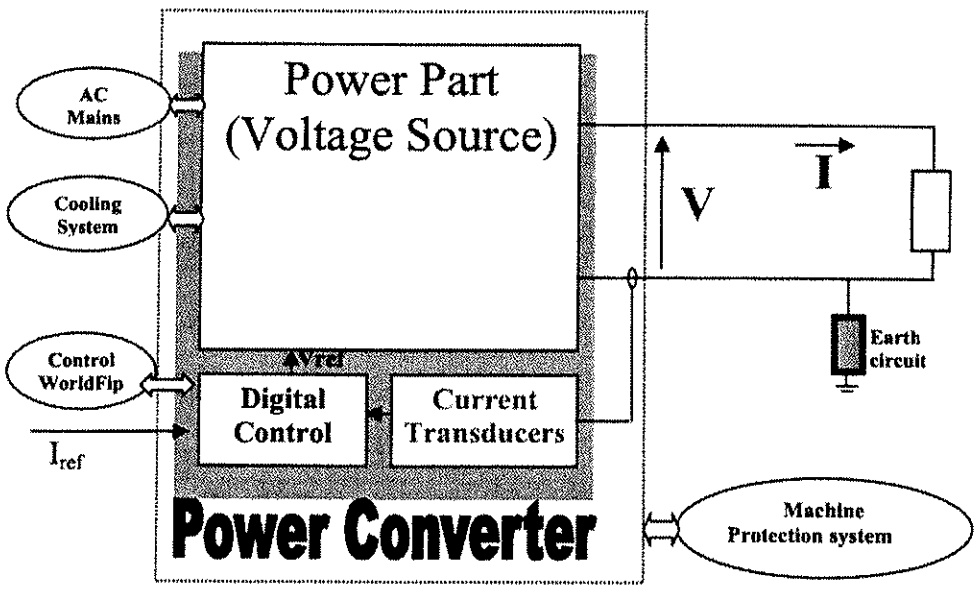

Figure 10.9: Power Converter Structure

The next section describes the design of these equipment subsystems and section 10.5 presents the specific requirements placed on other systems and the interfaces with them.

10.4 EQUIPMENT SUBSYSTEMS

A power converter for LHC is composed of three main blocks: a voltage source, a current transducer (DCCT) and a function generator/controller (FGC) with built-in analogue/digital converter (ADC). This logical and physical separation was created to subcontract the largest possible portion of the work to industry.

The voltage source is the main power part of the power converter. It is built either with switch-mode, soft-commutated, technology or with thyristor, line-commutated, technology. The task of the voltage source is to receive the mains power and convert it to a suitable dc output voltage, controlled by a reference input.

The output current to the load is measured by a high-precision DCCT, which gives an output voltage of 0-10 V proportional to the output current 0 – 100 %.

The ADC converts the analogue 10 V signal from the DCCT to a digital word stream with sufficient sampling rate and bit resolution for the speed and accuracy of the converter concerned.

The FGC receives control vectors from the central accelerator control computers and converts them to an output current reference value every millisecond. A digital regulation loop also resides in the FGC comparing the reference value and the ADC output to calculate the appropriate control value for the voltage source periodically (10-100 ms). This digital value is converted by a digital/analog converter (DAC) to a 0-10 V analogue control signal, which is sent as a reference voltage to the voltage source, thereby closing the loop. This current control loop is designed to make the complete system behave like a "perfect" current source.

The overall accuracy requirements for the magnet current in the different circuits were established between the Accelerator Physics and the Power group, Tab. 10.1. This requirement was then broken down in an accuracy budget for the different subsystems concerned. An example is shown in Tab. 10.4

Table 10.4: Accuracy budget for 13kA converters

Device	**Device specification**		**LHC machine impact**		
	ppm of FS	ppm of value	Stability 1/2 hr	Reproducibility 1-day	Accuracy 1 year
DCCT					
Zero uncertainty (hyst etc.)	2	0	0	0	2
Repeatability	1	0	0	1	1
Uncomp non-linearity	2	0	0	0	2
LF noise, 0.1-10 Hz	0.5	0	0.5	0.5	0.5
Stability 1/2 hr, 1-100 mHz	0	1.5	1.5	0	0
Gain drift 24 hr	0	0.5	0	0.5	0
Gain drift 1 year	0	5	0	0	5
Gain Temperature Coefficient	0	1	0	1	1
Offset drift 24 hr	0.5	0	0	0.5	0
Offset drift 1 year	3	0	0	0	3
Offset Temperature Coefficient	1	0	0	1	1
DCCT total			**2**	**4.5**	**15.5**
A/D converter, 22 bit Sigma-delta					
Uncomp non-linearity	0.5	0	0	0	0.5
LF noise, 0.1-10 Hz	0.6	0	0.6	0.6	0.6
Stability 1/2 hr, 1-100 mHz	0	1	1	0	0
Gain drift 24 hr	0	0.5	0	0.5	0
Gain drift 1 year	0	10	0	0	10
Gain Temp Coeff	0	0.15	0	0.15	0.15
Offset drift 24 hr	1	0	0	1	0
Offset drift 1 year	10	0	0	0	10
Offset Temp Coeff	0.15	0	0	0.15	0.15
A/D total			**1.6**	**2.4**	**21.4**
Miscellaneous			0.3	1	5
Total			**3.9**	**7.9**	**41.9**
Conditions Temperature change (K) Special temperature control cabinet			0	1	1

It was clear from the outset that the accuracy required in the main 13 kA circuits would not be attainable by conventional means. In particular, to achieve, the severe tracking requirement between all the machine sectors, new technology was necessary. DCCTs are being developed by industry with a built-in calibration winding. An entirely new approach for the A/D conversion and the use of digital control loops were also necessary to handle the unprecedented accuracy and the extremely large load time-constants due to the superconducting magnets. The very high precision needed for the sector tracking also means that an automatic calibration system is necessary to periodically monitor and adjust the calibration of the main dipoles, quadrupoles and other critical converters.

10.4.1 Power Part – Voltage Sources

Main dipole converter: 13 kA, 190 V, thyristor converter

The eight main dipole voltage sources consist of thyristor, line-commutated, power converters to which a parallel injection active filter is added to improve mains rejection and ripple performance. To achieve the 13 kA 190 V output rating, a parallel topology (Fig.10.10) is used consisting of *two* sub-converters, each containing an 18 kV – 2 MVA cast resin transformer, a six-pulse thyristor rectifier and a passive filter. The rectifiers are phase-shifted by 30° and connected in parallel. For installation purposes the power converters are made of seven modules: two transformer modules, two thyristor bridge modules, two filter choke modules and one central module containing the filter capacitors and the output current measurement transducer (DCCT). The power converter is supplied via 18 kV switchgear located in the power distribution surface building (SE). For safety reasons, a manual off-loaded 18 kV switch is provided close to the power converter.

The thyristor bridges and the filter chokes are water cooled, while the rest of the equipment is air-cooled. For each converter, the losses to the air are ~40 kW, while the losses to the cooling water are ~80 kW.

In order to handle the magnet current run-down under the worst fault condition, e.g. power cut and no cooling water flow, the power converter is equipped with free-wheel thyristors. This free-wheeling system is rated to handle the 13 kA up to 104 s without water-cooling. This represents the time constant of the magnet discharge with its dump resistor inserted.

In normal operation, the magnet current run-down is made under feedback control with the thyristor bridges used as reverse voltage source, or through the free-wheel thyristors.

The active filter, connected in the passive filter capacitor branch, has a working range of 4% of the total output voltage. This provides rejection of mains transients and gives a wide dynamic range for the control loops.

The main output performance parameters for the main dipole voltage sources are:

- Voltage ripple without active filter: 1×10^{-3} @ 50 Hz; 5×10^{-3} @ 600 Hz
- Voltage ripple with active filter: 25×10^{-6} @ 50Hz; 0.5×10^{-3} @ 600 Hz
- Low frequency (5 - 20Hz) mains rejection without active filter: 10-20 dB
- Low frequency (5 - 20Hz) mains rejection with active filter: 50-60 dB
- Small signal bandwidth without active filter: 70 Hz
- Small signal bandwidth with active filter (up to 4% of Vmax): 5 kHz.

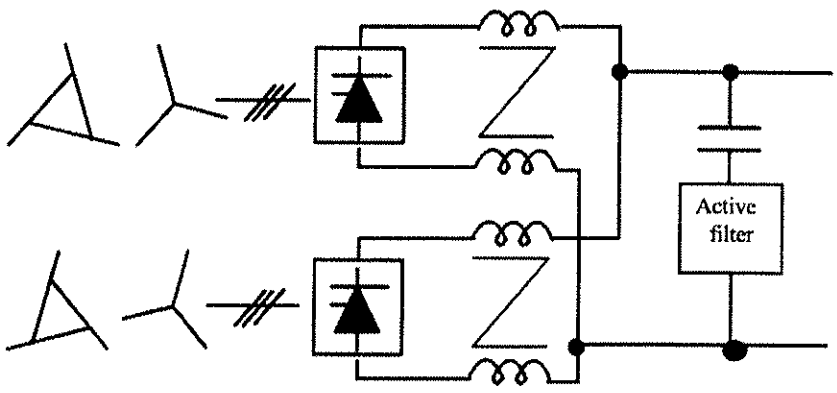

Figure 10.10: Thyristor converter topology

One-quadrant converters using [3.25 kA, 18 V] and [2 kA ,8 V] switch-mode sub-converters

The 1-quadrant switch-mode converters are designed as modular water-cooled converters, each one with a number of sub-converters, whose outputs are connected in parallel. To improve system availability, each converter uses one sub-converter more than required by the load current. Each sub-converter is identical for all power converter output current ratings.

Tab. 10.5 defines for the 1-quadrant converters the number and the rating of their associated sub-converters.

Table 10.5: Sub-converter rating

Equipment code	Converter rating		Sub-converter rating		Number of sub-converters
	Current	Voltage	Current	Voltage	
RPHK	20.5 kA	18 V	3.25 kA	18 V	8
RPHE	13 kA	18 V	3.25 kA	18 V	5
RPHF	8 kA	8 V	2 kA	8 V	5
RPHG	6 kA	8 V	2 kA	8 V	4
RPHH	4 kA	8 V	2 kA	8 V	3

Each sub-converter can be considered as a controllable stabilised unipolar current source. Under normal conditions, all the sub-converters are working in parallel.

The topology of each sub-converter is split into different stages:

- An input stage with a magnetic and thermal protection, an ac contactor, a diode rectifier, a three-phase six-pulse diode rectifier, the necessary filtering on the ac and dc sides and a soft-start circuit to limit the inrush current.
- An inverter stage with a Full-Bridge Zero-Voltage Zero-Current Switching Phase-Shift inverter (FB-ZVZCS-PS) with a switching frequency around 20 kHz.
- An output stage with high-frequency (HF) transformers for insulation and adaptation, a rectifier stage and an output filter.

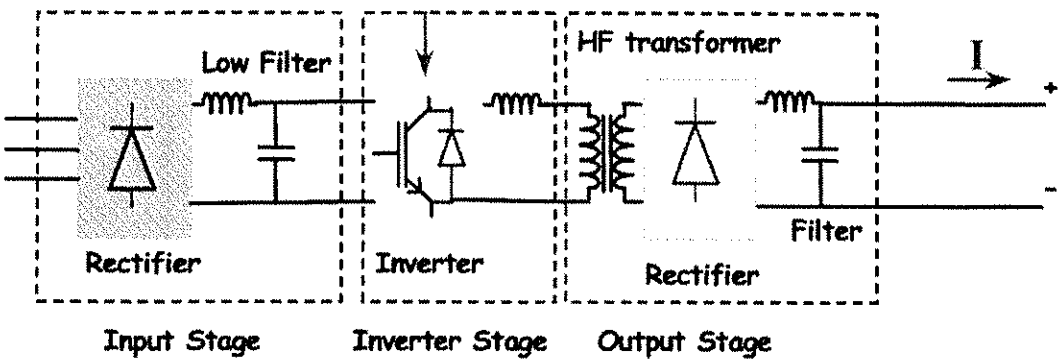

Figure 10.11: Sub-converter topology

Separate common control electronics handles the regulation of the whole converter as a voltage source and provides the reference and other control signals for all the sub-converters. If one or more of the sub-converters fail, the on-state sub-converter reference (even down to one single sub-converter) will increase, so that the current and the voltage of the load do not change.

A water-cooled free-wheel diode circuit provides a bypass path for the current when the converter is stopped. Diagnostic Modules are integrated in the voltage source to collect many status signals (fault list, warning list, status of the sub-converters, etc...) and make them available for diagnostic purposes to FGC through the diagnostic serial bus.

An earthing circuit is connected to the output of the converter to fix the potential of the output circuit versus earth. This circuit detects an earth fault and limits the earth current in case of a fault.

A switch on the front panel provides an adjustable maximum current (five steps up to the nominal current).

Each sub-converter is housed in a 19" rack with individual ac mains, water circuit, dc output, control and protection electronics, such that any sub-converter can work alone. The [3.25 kA, 18 V] sub-converter is housed in a full 19" rack and the [2 kA, 8 V] in half a rack. For rapid exchange of the parts (volume and weight constraints), the sub-converter functions are housed in several plug-in modules. The output stage is also physically duplicated in modules whose outputs are connected in parallel. Tab. 10.6 defines for the 1-quadrant sub-converters the different types of modules and the number used to assemble a sub-converter.

Table 10.6: Sub-converter module rating

Module type	Function	3.25 kA, 18 V modules	2 kA, 8 V modules
Input	Contactor, Rectifier, Filtering	1	1
Inverter	Inverter	1	
Output	HF transformer, Rectifier, Filtering	3	2

The ac mains and the water used for the converter cooling are distributed from a central point located in the central rack. This rack includes the earthing circuit and both DCCT transducer heads.

Busbars placed above the racks connect the outputs of the sub-converters in parallel. A dc connection system connects the converter to the water-cooled load cables.

The common control electronics and the FGC are placed in a separate electronics rack.

All the racks are placed on a steel frame to create a single unit for transport and facilitate installation.

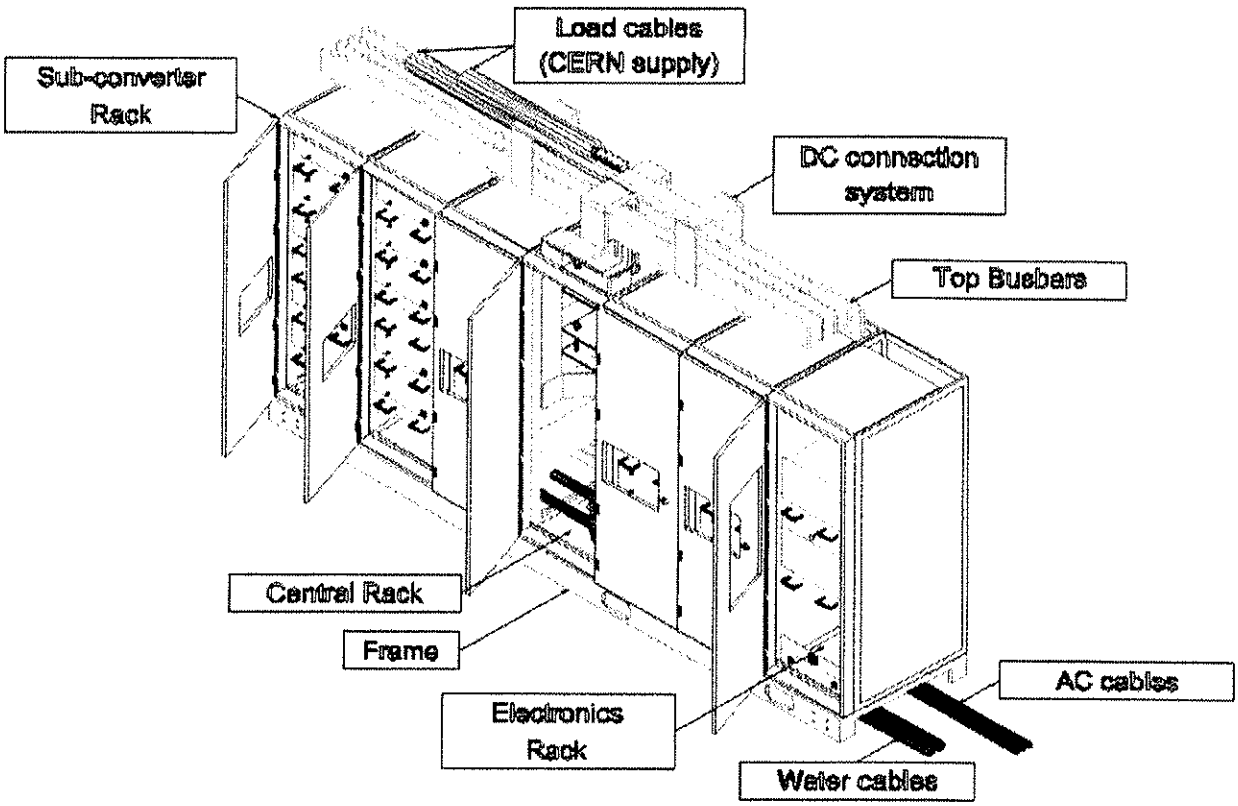

Figure 10.12: 1-quadrant converter enclosure (13 kA configuration)

Note: For the (13 kA, 18 V) converter and the Inner Triplets, the DCCT electronics, associated with the DCCT heads, as well as the Sigma-Delta ADC electronics are placed in a temperature controlled rack with its own mains (UPS).

The main parameters are:

- Small signal bandwidth (200 mV amplitude) over the full voltage range > 800 Hz (-3dB)
- Maximum voltage drop when a sub-converter fails 100 mV during 5 ms
- Voltage output ripple, under normal mains supply conditions:
  - 10 mV peak-peak up to 130 kHz
  - according to IEC 478-3C above 130 kHz
- Free-wheel diode circuit:

(13 kA, 18 V) type - with water	13 kA
- without water	$I_{max}\, e^{-t/\tau}$ with I_{max} = 13 kA, τ = 100 s.
(20.5 kA, 18 V) type - with water	20.5 kA
- without water	20.5 kA during 1 s.
(8 kA, 8 V) type - with water	8 kA
- without water	$I_{max}\, e^{-t/\tau}$ with I_{max} = 8 kA, τ = 70 s.
	τ: the time constant of the magnet discharge.
(6 kA, 8 V) type for the Inner Triplets - with water	11.5 kA
- without water	$I_{max}\, e^{-t/\tau}$ with I_{max} = 11.5 kA, τ = 30 s
(6 kA, 8 V) type for other circuits - with water	6 kA
- without water	$I_{max}\, e^{-t/\tau}$ with I_{max} = 6 kA, τ = 160 s
(4 kA, 8 V) type - same as for the (6 kA, 8 V) for other circuits	
	τ the time constant of the magnet discharge with the faster energy extraction.

More details may be found in the following references: Technical Specifications of the 1-quadrant converters [13], [14], the Workshop on LHC Powering [11] and the Review of LHC Power Converters [12].

Special powering of inner-triplet magnets

In 1999, the decision was taken that the inner triplet quadrupole magnets MQXA and MQXB will be "mixed" in the four insertions. The magnet types are of different design and thus exhibit different parameters (Chap. 8).

To optimise the powering of these mixed quadrupoles, it was decided to use two nested high-current power converters: [8 kA, 8 V] and [6 kA, 8 V]. A [±600 A, ±1 V] trim power converter, connected across the Q1 magnet, allows the correction of the difference in the integrated gradients of the Q1 and Q3 magnets. Furthermore, the possibility to change only the gradient of the Q1 magnet will facilitate the β^* measurements [25]. A schematic of the powering is shown in Fig. 10.13.

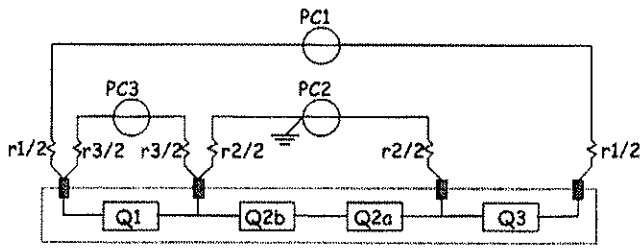

Figure 10.13: Inner triplet powering scheme

Table 10.7: Circuit parameters

PC1	[8 kA, 8 V]
r1	0.6 mΩ
τ1	380 s
PC2	[6 kA, 8 V]
r2	0.8 mΩ
τ2	50 s
PC3	[±600 A, ±10 V]
r3	1.4 mΩ
τ3	65 s

The consequence of this economical powering layout is the interaction between the three galvanically coupled circuits. A control strategy to decouple the three systems has been developed, using three independent standard LHC digital controllers. The converter protection during the discharge of the magnet energy due to quenches or interlocks of the magnets has been studied [24].

Four-quadrant switch-mode converters

The topology of the 4-quadrant switch-mode converters is almost the same for the [±600 A, ±10 V], [±600 A, ±40 V], [±120 A, ±10 V] and [±60 A, ±8 V]. It includes:

- A mains rectifier stage with a magnetic and thermal protection, an AC contactor, a diode rectifier, a three-phase six-pulse diode rectifier, the necessary filtering on the AC and DC sides and a soft-start circuit to limit the inrush current.
- An inverter stage using a soft-commutated bridge with IGBT switching at high frequencies >20 kHz.
- A high frequency transformer and a bipolar output stage: this part comprises a high-frequency transformer for insulation and adaptation. A bipolar output stage provides reversal of the polarity. The magnet energy, during the ramp-down of the current, is dissipated by the converter or sent back to the mains.
- An output circuit with a free-wheel safety and discharge circuit (also called crowbar), both DCCT transducer heads and the earthing circuit.
  The crowbar is composed of a resistor and a switch. This device turns on when an over-voltage appears across the voltage source output terminals. It assures a safe path for the magnet current if the bipolar output stage is stopped whilst current is supplied to the load. During a discharge, the device does not need cooling-water, or an auxiliary power supply, making it autonomous in case of simultaneous mains failure.
  The earthing circuit is connected to the output of the converter to fix the potential of the output circuit versus earth. This circuit detects an earth fault and limits the earth current in case of a fault.

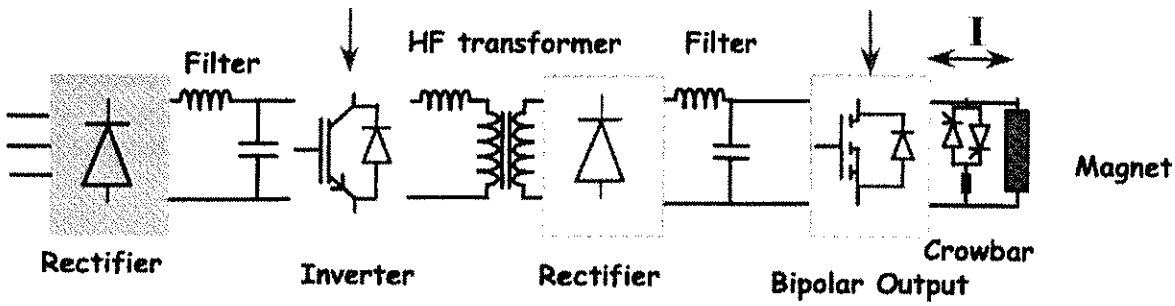

Figure 10.14: 4-quadrant converter topology

±600 A, ±10 V switch-mode converter specifics

The main enclosure of this type of converter is a 19" rack, housing one or two converters, a common mains input with an RFI filter, common inlet/outlet water cooling connections and terminals to connect the loads. The mains rectifier stage, the inverter stage, the transformer and the bi-polar output stage are contained in one 6 U high 19" module. The output circuit with the dc contactor, the crowbar and the DCCTs are fixed in the rack. The FGC for the two converters are located in the same crate inside the rack, independent of other electronics.

A switch on the front panel provides an adjustable maximum current (from 120 A to 600 A in five steps).

For circuits operating with very low voltage and small stored energy, the energy extraction system will be a part of the power converter [26]. Such systems consist of a combination of a semiconductor crowbar in series with a 50 mΩ resistance. Installing low-voltage extraction units at the power converters allows a reduction of cost and space in the packed zones where this equipment will be located in the LHC machine. A dc arc-chute contactor rated at 600 A is put between the converter output and the discharge device. It will protect the load against a short circuit in any output stage component by isolating the discharger and the load from the voltage source output. To maximise reliability of the command of this contactor, a redundant way to

open the contactor has been implemented. All of these converters will be equipped with a crowbar and 50 mΩ resistors, whereas 136 circuits will be equipped with the dc contactor.

The main parameters are:

- Small signal bandwidth (amplitude 160 mV) over full voltage range:> 1 kHz
- Voltage output ripple, under normal mains supply conditions:

  1.8 mV r.m.s. up to 50 Hz
  (without precision current control loop)
  7 mV rms in the 300 Hz-60 kHz range
  above 60 kHz according to IEC 478-3C.

- Discharge circuit:

Crowbar resistor	50 mΩ
Crowbar activation level	13 V
Maximum power to absorb by the resistive output circuit	18 kW
Maximum energy to dissipate	108 kJ.

More details may be found in the following references: [±600A, ±10V] converter Technical Specification [15], the Workshop on LHC Powering [11] and the Review of LHC Power Converters [12].

±600 A, ±40 V switch-mode converter specifics

The main enclosure of this type of 4-quadrant converter is a 19" rack, housing one converter, mains input with an RFI filter, inlet/outlet water cooling connections and terminals to connect the load.

The mains rectifier stage, the inverter stage, the transformer as well as the bi-polar output stage is housed in two 6 U high 19" modules. The output circuit with the crowbar and the DCCTs are fixed in the rack. The FGC for the converter is located in a separate crate inside the rack.

A switch on the front panel provides an adjustable maximum current (from 120 A to 600 A in five steps).

An additional function is added for this type of converter, used for the [±120 A, ±40 V] LHC circuit concerning the protection of the current leads (see Sec.10.5 Interlocks and Quench Protection).

The main parameters are:

- Small signal bandwidth (amplitude 160 mV) over full voltage range : > 1 kHz
- Voltage output ripple, under normal mains supply conditions:

  1.8 mV rms up to 50 Hz
  (without precision current control loop)
  7 mV rms in the 300 Hz-60 kHz range
  above 60 kHz according to IEC 478-3C.

- Discharge circuit:

Crowbar resistor	50 mΩ
Crowbar activation level	52 V
Maximum power to absorb by the resistive output circuit	18 kW
Maximum energy to dissipate	108 kJ.

More details can be found in the following references: [±600 A, ±40 V] converter Technical Specification [15], the Workshop on LHC Powering [11] and the Review of LHC Power Converters [12].

±120 A, ±10 V switch-mode converter specifics

This 4-quadrant converter type is forced air-cooled. The main enclosure is a 19" rack, housing up to four converters, a common mains input with an RFI filter, and terminals to connect the loads. The mains rectifier stage, the inverter stage, the transformer, the bi-polar output stage as well as the DCCT are located in one 6U high 19" module. The crowbar as well as the earthing circuit is fixed directly in the rack. The 4 FGC electronics for the 4 converters are located in two separate crates inside the rack, independent of the other electronics. A switch, placed in the rack, provides an adjustable maximum current limit (60 A instead of 120 A).

The voltage detection across the resistive current leads is part of the converter electronics (see Sec.10.5 Interlocks and Quench Protection).

The main parameters are:

- Small signal bandwidth (amplitude 160 mV) over full voltage range: > 800 Hz
- Voltage output ripple, under normal mains supply conditions:
  1.8 mV r.m.s. up to 50 Hz
  (without the precision current control loop)
  7 mV rms in the 300 Hz-60 kHz range
  above 60 kHz according to IEC 478-3C.
- Discharge circuit:

Crowbar resistor	83 mΩ
Crowbar activation level	15 V
Maximum power to absorb by the resistive output circuit	1800 W
Maximum energy to dissipate	13 kJ.

More details can be found in the following references: [±120 A, ±10 V] converter Technical Specification [16], the Workshop on LHC Powering [11] and the Review of LHC Power Converters [12].

±60 A, ±8 V switch-mode converter specifics

This 4-quadrant converter type is forced air-cooled. These converters are used as dipole orbit correctors for the arc regions. They are located under the magnet and are in radiation areas (~10 Gy in 10 years). The main enclosure of this type of converter is a special horizontal rack, housing up to four converters, a common mains input with an RFI filter, and terminals to connect the loads.

The mains rectifier stage, the inverter stage, the transformer, the bi-polar output stage, the crowbar and the DCCTs are located in one 6 U high 19" module. The FGC electronics for each converter is located in each module.

The voltage detection across the resistive current leads is part of the converter electronics (See Sec.10.5 Interlocks and Quench Protection).

The main parameters are:

- Small signal bandwidth (amplitude 160 mV) over the full voltage range : > 500 Hz
- Voltage output ripple, under normal mains supply conditions:
  10 mV rms up to 50 Hz
  (without the precision current control loop)
  40 mV rms in the 300 Hz-60 kHz range
  above 60 kHz according to IEC 478-3C.
- Discharge circuit:

Crowbar resistor	100 mΩ
Crowbar activation level	8.4 V
Maximum power to absorb by the resistive output circuit	504 W
Maximum energy to dissipate	12.6 kJ.

More details can be found in the following references: [±60 A, ±8 V] converter Technical Specification [17] the Workshop on LHC Powering [11] and the Review of LHC Power Converters [12].

Converters for warm magnets

This family of power converters powers the following circuits:

- Two dump septa, 1000 A, 600 V.
- Four twin aperture, warm insertion quadrupoles in the cleaning regions, 810 A, 450 V.
- Two twin aperture warm separation dipoles in 3 and 7, 810 A, 950 V.
- Two single aperture recombination dipoles in 1 and 5, 810 A, 950 V.

The topology is similar to the one used for the main dipole converters, e.g. thyristor line-commutated 12-pulse parallel with passive filter and parallel active filter injection. The power converters will be installed in

the existing SR surface buildings. The twin aperture warm quadrupole converters are housed in a single cubicle and fed from the 400 V network. The separation recombination dipoles and the dump septa fed from the 18 kV network are composed of two modules, one containing the two 18 kV transformers and one rectifier filter module. The complete converter is air-cooled. The low time constant of the magnet allows energy discharge by a free-wheel diode. The air losses are ~ 20 kW per converter.

The main output performance parameters of the warm magnet voltage sources are:

- Voltage ripple without active filter: 1×10^{-3} @ 50 Hz; 5×10^{-3} @ 600 Hz
- Voltage ripple with active filter: 25×10^{-6} @ 50 Hz; 0.5×10^{-3} @ 600 Hz
- Low frequency (5-20 Hz) mains rejection without active filter: 10-20 dB
- Low frequency (5-20 Hz) mains rejection with active filter: 50-60 dB
- Small signal bandwidth without active filter: 70 Hz
- Small signal bandwidth with active filter (up to 4% of V_{max}): 5 kHz.

The ATLAS converters

The superconducting magnets of ATLAS will be powered by the same 1-quadrant switch-mode converters as those used for the LHC machine.

The power system of ATLAS includes two electrical circuits:

- 20.5 kA circuit for the Toroid magnet (converter based on [3.25 kA, 18 V] sub-converters).
- 8 kA circuit for the Solenoid magnet (converter based on [2 kA, 8 V] sub-converters).

The ALICE and LHCb dipole converters

Both the Alice and LHCb experiments require a 950 V, 6500 A power converter to supply spectrometer dipole magnets. The same topology as the machine main dipoles is used, i.e. 12-pulse parallel rectification with passive filter (Fig.1). The two 4.8 MVA cast resin rectifier transformers are supplied from the 18 kV network. The power converter output is equipped with a mechanical reversal polarity switch, which can only be operated when the power converter is off. The power converters are installed in building SR2 for Alice and SR8 for LHCb. They are composed of two transformers housed in one cubicle, two rectifier modules, two filter-choke modules, one capacitor module and one output module. Cooling is achieved partly by direct cooling and partly by forced-air cooling. The total air losses per converter are ~100 kW.

The main output performance parameters of this voltage source are:

- Voltage ripple: 1×10^{-3} @ 50 Hz; 5×10^{-3} @ 600 Hz
- Low frequency (5-20 Hz) mains rejection (without active filter): 10-20 dB
- Small signal bandwidth: 70 Hz.

The Alice and LHCb solenoid converter

The voltage source for the Alice solenoid is the refurbished LEP L3 power converter. The output ratings are 31 kA, 150 V. The high current is obtained by paralleling of six sub-converters. Each one is rated 5.2 kA, 150 V and composed of an oil-immersed 18 kV transformer, a 6-pulse thyristor bridge and a passive filter. A 30° phase-shift is applied to three sub-converters resulting in a classical 12-pulse configuration.

The converter modules are installed in the surface building SX2, while the six oil-immersed transformers are located in two tanks outside the building. The thyristor bridges are water-cooled, while the rest of the equipment is air-cooled. The total water losses are ~70 kW and are evacuated by a dedicated cooling station. The air losses are ~ 40 kW for the converter part inside SX2.

The main output performance parameters of the voltage source are:

- Voltage ripple 5×10^{-3} @ 50 Hz; 2×10^{-2} @ 600 Hz
- Low frequency (5-20 Hz) mains rejection without active filter: 10-20 dB
- Small signal bandwidth: 70 Hz.

The Alice and LHCb compensator converters

Alice and LHCb each require three compensation circuits: one central compensator and two outer correctors, left and right. The three converters are rated 600 A, 160 V for Alice and 1000 A, 180 V for LHCb.

The basic topology of this family is the same as for the main dipole power converter e.g. thyristor line-commutated 12-pulse parallel system with passive filter. No active filters are required. The power converters are supplied from the 400 V network and, like the Alice and LHCb dipoles, are also equipped with a mechanical polarity reversal switch. They will be installed in buildings SR2 and SR8. They are directly air-cooled and their total losses are ~12 kW per converter.

The main output performance parameters of the voltage sources are:

- Voltage ripple: 1×10^{-3} @ 50 Hz; 5×10^{-3} @ 600 Hz
- Low frequency (5 – 20 Hz) mains rejection without active filter: 10-20 dB
- Small signal bandwidth: 70 Hz.

The CMS solenoid converter

The power converter for the superconducting CMS solenoid is rated 20 kA, 26 V. The high current is obtained by the mounting four sub-converters in parallel. Each one is rated 5 kA, 26 V and composed of a 400 V transformer, a 6-pulse thyristor bridge, and a passive filter choke. A 30° phase-shift is applied to two sub-converters resulting in a classical 12-pulse configuration. The filter capacitors are common for the four sub-converters, acting as current sources. The complete converter is composed of the four sub-converter modules and a central module containing the capacitor and the control electronics. It will be installed underground next to the solenoid in USC55. The thyristor bridges and the filter chokes are water-cooled, while the rest of the equipment is air-cooled. The total water losses are ~70 kW. The total air losses are ~40 kW.

In order to handle the magnet current decay under worst fault conditions, i.e. power cut and no cooling water flow, the power converter is equipped with a free-wheel thyristor. This free-wheeling system is rated to handle the 20 kA up to 180 s without damage.

The main output performance parameters of the voltage source are:

- Voltage ripple: 5×10^{-3} @ 50 Hz; 2×10^{-2} @ 600 Hz
- Low frequency (5 – 20 Hz) mains rejection without active filter: 10-20 dB
- Small signal bandwidth: 70 Hz.

The RF Klystron Power Converters

This consists of four units, each rated 100 kV, 40 A and one spare. The complete LEP PA4 installation will be re-used as it was for LEP2 – see LEP Design Report, Vol. 2, Chap. 7.2, for a detailed description. Minor modifications will be made to the electronics to adapt it to the LHC power converter control system. Specific maintenance will also be carried out on all transformers and diode tanks.

10.4.2 DC Current Transducers

A dc current transducer is required to measure the converter output current in order to control it accurately. Presently there is only one technology that will fulfil the LHC accuracy requirements, the zero-flux dc current transducer. The primary current is passed through a toroidal transducer core of special high-μ magnetic material creating a one-turn transformer.

In the first stage the current is divided with a fixed ratio to a low level. Its bandwidth is extended down to dc through a feedback loop, measuring the dc flux in the core and producing a compensation current, which will balance the flux to zero at all times. The ratio can be established to the ppm (part per million) level.

In the second stage the low-level compensation current is passed through a high-precision burden resistor. The voltage chosen is a compromise between power dissipation and producing enough voltage to overcome noise and thermal emf effects. This voltage is then amplified in a high precision amplifier providing 10 V output at the nominal primary current.

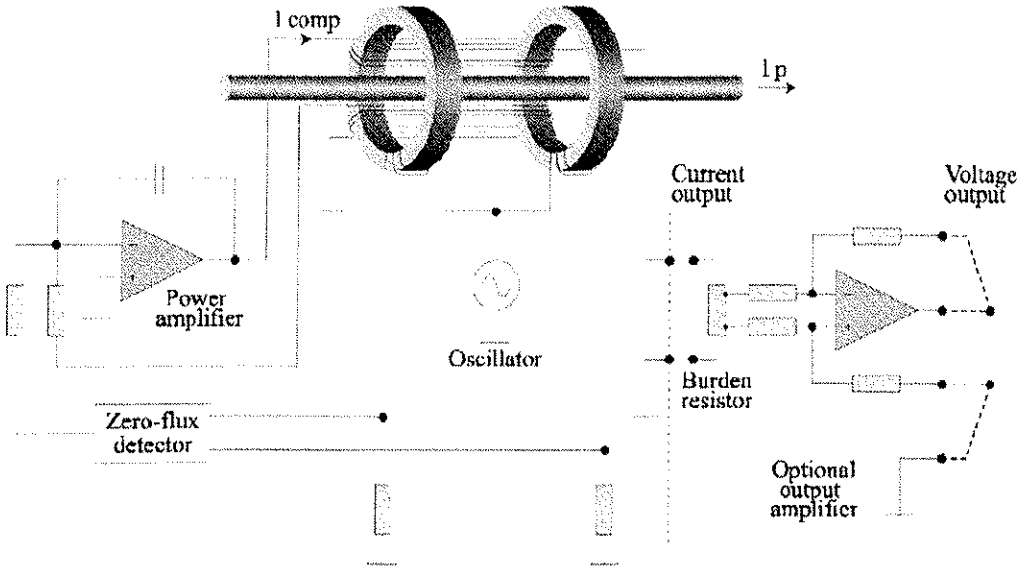

Figure 10.15: DCCT principle

The long-term accuracy of a DCCT depends on several factors and needs periodic re-calibration if the highest performance is required. A complete system has been developed to perform calibrations on-site in a fully automated fashion (See Sec. 10.4.5). The principle requires that the DCCTs in question are equipped with an integral calibration winding in the transducer head.

Following the standardisation of converters in groups, minimising the number of different types, the DCCTs are also chosen in a small number of standard sizes and ratings. The groups with the largest quantities and the highest precision are in the main ring and all other types including the beam transfer are put together in the last class.

4-13 kA DCCT with calibration windings

The high current DCCTs have a separate transducer head including a calibration winding. The compensation current is either 2 or 5 A and the calibration current is standardised to 5 A for nominal ampere turns.

The electronics is housed in a 3U, 19" chassis, powered by 400/230 VAC. The burden resistor is a proprietary design employing specially processed wire to achieve a temperature coefficient of <1 ppm/K.

600 A DCCT, main ring multipole correctors

The medium current DCCTs employ a separate transducer head with a compensation current of 0.5 A. The electronics is housed in an 8TE Europa chassis module, powered with ±15 VDC from dedicated power modules located in the same 19" electronics chassis. The burden resistor is a special development, housed in a TO-3 package.

120 A DCCT, main ring orbit correctors

The low current DCCTs are fully integrated with the head and electronics in one box, powered with ±15 VDC from the converter electronics. The burden resistor is a standard high precision resistor.

When used in the 60 A corrector converters, the primary current is passed through the centre hole twice.

800 – 8000 A DCCT, beam transfer, "warm converters" and experiments

Originally aimed at the needs of the beam transfer, this DCCT requirement was very close to existing standard products on the market. The transducer head is separate with a compensation current of 1 A. The electronics is housed in a 1U, 19" chassis, powered by 230 VAC. The burden resistor is a special development from the DCCT manufacturer, optimising price and accuracy for this application.

For ATLAS and CMS, older 20 kA DCCTs are re-used to minimise cost.

10.4.3 Analogue-Digital Converters

The LHC demands an order of magnitude improvement in accuracy over previous CERN accelerators. New technology had to be developed also for the ADCs to satisfy this need and the Sigma-Delta conversion principle was judged to be the most promising to meet this aim. An industrial product was found for the medium precision, but an entirely new circuit had to be developed for the highest precision. A sigma-delta converter is basically a 1-bit analogue-digital converter with a very high conversion rate producing a high frequency bit-stream. This bit-stream is decimated and digitally filtered to obtain the desired word-stream at a much lower data rate. It is inherently monotonic, has a high noise rejection due to the integration stages and requires few high-precision components. The design of the digital part was made so that it is the same for the high-precision and medium-precision versions.

The medium precision converters are integrated in the FGC (Function Generator/Controller) design, but the high-precision version needs its own housing due to size, temperature control, power supply etc. All A/D converters are designed for 10 V full-scale input voltage and are bipolar.

The LHC tunnel environment presents a certain radiation level, which will affect some electronic components. An alternative ADC design, employing successive approximation technology, was also developed for use in the closed orbit correctors. This design has been tested at radiation levels significantly higher than LHC and was found to function correctly.

22-bit Sigma-Delta ADC

The analogue portion consists of an input buffer, 3 high-speed integrator stages, a comparator and a switched high-precision voltage reference. Matched precision resistors convert the reference voltage to a current fed back to the input integrator. The comparator produces a 1 MHz bit-stream to an optical fibre driver. Control logic monitors the operation and will reset the integrators if an out-of-range condition is detected. The analogue portion is completely enclosed in its own electrostatic shield box with thermal insulation. The high-precision components are temperature-controlled, the Zener reference at the semi-conductor chip-level and the others by a Peltier system. The unit is designed to minimise EMC problems through further power supply shielding and the use of optical isolation. The design is described in [28].

The digital portion located in the FGC consists of a fibre-optic input, a four-stage decimator/filter and control logic. It produces a 22-bit data word with 5 kHz data rate and a status word signalling validity and error conditions.

16-bit Sigma-Delta ADC

The analogue portion is based on a commercial integrated circuit, ADS1201, preceded by a multiplexer to enable monitoring of other analogue signals, including a separate precision voltage reference for periodic calibration to maximise accuracy. A temperature control is provided on the PCB for critical components to improve the temperature characteristics. The ADC produces a 16-bit word with 1 kHz data rate. Two identical channels are located together with the digital filters on a PCB in the FGC assembly. An FPGA contains all the control logic for handling both ADCs and multiplexers.

16-bit Successive Approximation ADC

The successive approximation design is made as similar as possible to the 16-bit Sigma-Delta design to simplify the design and the deployment. The analogue front-end is virtually identical with the same multiplexer and signal conditioning. The same data rate and control was adopted to ensure full compatibility with the FGC environment. A significant difference from the sigma-delta version is that there are no memories or control registers prone to single-event upset from radiation.

10.4.4 Power Converter Control System

The control system for the LHC power converters will follow the architecture used for LEP, with a dedicated controller embedded in every power converter. The controller will be responsible for function generation (current vs. time), current regulation and power converter state monitoring and control (on, off, reset). As a result, it is known as the Function Generator/Controller (FGC) and is a dedicated design with the following features:

- Compact, robust form, enclosed in an industrial quality metal cassette (6U x 20TE).
- Radiation tolerant design based on two microprocessors (M68HC16Z1 and TMS320C32) and 576KB of error corrected memory.
- WorldFIP 2.5Mbps network interface.
- RS232 9600 baud interface.
- Twin channel analogue inputs for DCCT current measurements.
- High resolution analogue output for voltage reference.
- Direct digital inputs for voltage source status monitoring.
- Direct digital outputs for voltage source and polarity changer control.
- Twin serial diagnostic input buses to collect analogue and digital voltage source signals.
- Dallas 1-wire identification bus to collect identity and, where needed, temperature information.

A small number of FGCs will also be used for function generation only by LHC RF. The FGC cassette will plug into a chassis.

- In the case of the 60 A power converter, the chassis will also contain the power electronics and its control card. The chassis will include a backplane that will have connectors for the FGC cassette, the control card and cables leading to the power electronics and the power supply for the FGC.
- For all the other types of power converter, a dedicated electronics chassis will hold either one or two FGCs, together with a high reliability power supply. This supply will be driven from 48 VDC, derived from 3-phase 400 VAC by an external power module. For the 120 A and 600 A power converters, a second power supply (also using 48 VDC) will be included for the DCCT electronics, and for the 600 A systems, the chassis will actually hold the DCCT electronics cards. The backplane in the chassis will combine DIN connectors on the front and Burndy connectors on the back, and in this way, all intermediate cabling will be avoided.
- There will be a backplane designed for each type of converter: 60 A, 120 A, 600 A, multi-kA switch mode, and thyristor. The FGC will be able to read a code that identifies the type of backplane it is plugged into.

Function Generation

In normal operation, each FGC will regulate the current in its circuit. During testing, open loop operation is possible, in which the voltage reference is set directly. In either case, a reference value must be derived as a function of time [37]. The FGC software supports a number of ways to do this by combining a predefined waveform with a real-time value received via the WorldFIP network.

The predefined wave-form can take various forms:

- Steps
- Sine wave
- Square wave
- PELP function (Parabolic Exponential Linear Parabolic)
- PLEP function (Parabolic Linear Exponential Parabolic)
- Table.

The PELP and PLEP functions are standard waveforms, defined by five parameters that combine parabolic start and end segments with linear and exponential middle segments.

A Table is defined by arrays of delta-time (milliseconds) and delta-reference (milliamps or millivolts depending upon the mode). The FGC will use linear interpolation in real-time to generate intermediate reference values. Since all the table values are relative, the complete waveform will also be relative to the reference value present at the moment when the table is armed. The number of points in a table will be limited to about 8000.

In all cases, the reference value is either constant or changing. When it is constant, the definition of the next change (e.g. a PELP or Table, etc...) can be downloaded and armed. The change will be triggered by a timing event. Once the change has been executed, the reference will hold the last value and the change is forgotten.

The actual reference at any moment can combine the predefined reference with a real-time value. Four options are supported:

- Ref. = F(t) Predefined waveform is the reference, no real-time contribution.
- Ref. = F(t) + dF_{rt} Real-time value is an offset from the predefined reference.
- Ref. = F(f)(1 + G_{rt}) Real-time value is the fractional gain for the predefined reference.
- Ref. = F_{rt} Real-time value is the reference, no predefined reference.

Current Regulation

A key task for each FGC is current regulation. It transforms a voltage source into a current source, which is what the global LHC control system requires for each circuit. In LEP, this was achieved using an analogue circuit; however, this was not an option for LHC. Many circuits have very large time constants (many hours) and yet require very high accuracy, and this can only be achieved with digital regulation. This was the main reason to include a second processor in the design. The device chosen is a low-cost floating-point digital signal processor (DSP) from Texas Instruments. It operates as a coprocessor for the Motorola microcontroller, performing the real-time tasks of function generation, digital filtering and current regulation.

WorldFIP Gateways

All the FGCs in the LHC will need to be controlled synchronously from the LHC control room. This will be done using 80 WorldFIP segments. WorldFIP is a 2.5 Mbps transformer coupled real-time fieldbus, based on twisted pair cabling. It can support 500m copper segments and up to 32 nodes between repeaters. gateway systems are needed to link the LHC IP technical network with the WorldFIP segments. The gateways will be based on LynxOS running on a PC platform. They will be installed in the LHC surface buildings. Each Gateway will include a timing receiver interface, connected to the LHC general machine timing network. This will provide the gateway with accurate date/time and millisecond level machine events. It will also generate precise timing pulses to synchronise the WorldFIP interface. Each gateway will drive a single segment with a maximum of 30 FGCs connected. In some cases, the cable will need to be more than 500 m long, in which case a repeater will be included.

The software in the gateway will support operational client applications via the LHC controls middleware (based on CORBA) as well as expert diagnostic client applications via TCP/UDP. It will also publish status information to the LHC alarm system via a central alarms gateway.

Timing and events

Each FGC has a 32 MHz quartz oscillator to generate its processor clocks. This can have a frequency error of up to 100 ppm. The WorldFIP network has a real-time behaviour enabling its 50 Hz transmission cycle to be triggered by an external signal, derived from the LHC general machine timing network. The error in the trigger signal will be less than one microsecond, and the jitter of the WorldFIP traffic will be less than 10 microseconds. This enables the FGC to run a software phase-locked loop to discipline a local digital real-time clock, based on the 32 MHz quartz oscillator. This allows frequency errors to be reduced to less than 0.1 ppm if the temperature is stable. If the WorldFIP traffic is lost for a period, the local FGC real-time clock will continue unaffected, smoothly re-synchronising when the traffic returns.

The first transmission of each WorldFIP cycle is a broadcast time/events variable. This includes UTC and event information, if an event is active. All events destined for the LHC FGCs must be warning events, indicating that a change of state should take place at a fixed time (typically 100 ms) in the future. This gives the gateways time to distribute the event via the fieldbus.

FGC configuration

Each FGC must be correctly configured for the power converter it is controlling. A subset of the FGC's properties are flagged as non-volatile, meaning they are stored in non-volatile (FRAM) memory within the FGC, and are also maintained in a central database. The local copy enables an FGC to reboot and re-establish control of a power converter in less than two seconds. However, following a reboot, the FGC signals via the gateway that it has been restarted, and a central FGC configuration manager program will interrogate the system during the following minute to check its validity. If an FGC is replaced, the configuration will no longer be correct, so the configuration manager will send the correct values from the database.

Configuration properties include:

- Circuit characteristics (e.g. resistance and inductance, maximum and minimum current and rate of change of current).
- Voltage source characteristics (e.g. maximum and minimum voltage and rate of change of voltage)
- ADC, DAC and DCCT calibrations.
- Current loop parameters (e.g. closed loop bandwidth).

The FGC configuration manager will also maintain the online equipment inventory, based on the Dallas 1-wire ID chips embedded in every FGC card and throughout the voltage sources and DCCT systems. More than 30'000 individual items will be tracked in this way, enabling reliable equipment management.

FGC software management

The FGC software is expected to evolve up to and beyond the startup of the LHC. To make this possible, the FGCs include non-volatile Flash memories for their Firmware. These can be reprogrammed as often as needed via the WorldFIP fieldbus or via the RS232 serial interface. Each system includes three separate Flash memory devices, one for the boot programs and two for the main program (the main program has two parts, one for each processor). Two Flash devices are needed so that the system can be running out of one while reprogramming the other.

The boot Flash is divided into two parts so that two different boot programs can be stored:

- Basic boot – this is as simple as possible and is the boot of last resort. It will be written into the boot Flash when the FGC processor boards are manufactured, and will never be changed. It cannot be rewritten over the WorldFIP or serial interface.
- Main boot – this will be a big program with two main objectives:
  1. In normal operation, to launch the main program on the two processors.
  2. When required, to provide extensive self-test functionality, enabling every aspect of the FGC to be tested.

The main program will be able to reprogram the main boot from the WorldFIP. If the reprogramming fails for any reason, the basic boot is always there to enable the system to recover.

The gateways will transmit the main boot and main programs continuously via four bytes of the time/events broadcast variable. It will take about twenty minutes per transmission (100 bytes/second). Both the basic boot and main boot will be capable of receiving this data and reprogramming one or other of the main firmware flash memories. The main program will also be able to receive this data stream in order to reprogram either the main boot, or a new version of the main program (into the other firmware flash memory).

A central FGC firmware manager program will permanently survey software versions, and will be responsible for the distribution of updates.

Diagnostic system

The vast majority of LHC power converters will be in underground areas, with nearly a half actually in the tunnel under the cryostat. This will make interventions difficult, so there is a strong need for high quality remote diagnosis of the power converter electronics. This need has been met using a serial diagnostic bus that threads its way through the power converter. Diagnostic Interface Modules (DIMs) can be connected to the bus to collect information. Each DIM has four analogue inputs (converted using a 12-bit ADC) and 24 digital inputs (two banks of 12). The FGC supports two DIM buses, each scanned at 50 Hz and each capable of supporting 15 DIMs for a maximum of 30 per power converter (i.e. 120 analogue inputs and 720 digital inputs). All the diagnostic signals are logged in circular buffers by the FGC, and are also available in real-time via four RT streams exported over the WorldFIP or serial interface. Each stream can send one analogue signal or one bank of 12 digital signals per 20 ms, for a total of 200 channels per second. Diagnostic interfaces are written in Labview to visualise this information. The interface can either run remotely via a gateway, or locally via an RS232 link.

A fundamental requirement of the diagnostic system is to identify the reason for any unsolicited power converter trips. It is common for the initiating fault to trigger a cascade of other faults, masking the original cause. The DIMs are designed to solve this problem by including a trigger input that freezes the state of the 24 digital inputs at the instant of the trigger (analogue inputs are not frozen). An 8 μs resolution counter is also frozen, so that the time of the trigger can be identified. In this way, the trigger order for different DIMs can be determined, and the first fault identified.

10.4.5 Current Calibration System

To maintain the high accuracy of the critical sub-systems (DCCTs and ADCs), periodic calibration is necessary. For high current DCCTs this becomes very difficult and cumbersome due to the physical size and adverse effects of transport. In LHC the situation is further complicated by the underground location and difficult access. High accuracy ADCs have similar constraints and are better calibrated in-situ under the typical environmental operating conditions.

A novel principle has been employed [25], calibrating the two devices together as a pair. The DCCT is equipped with a calibration winding, in which an accurate calibration current is injected producing the full nominal ampere-turns. The resulting digital value from the ADC is recorded and used to correct the value used for converter control. The evolution of this correction will determine the maximum interval necessary to achieve the target accuracy.

The problem of calibrating DCCTs and ADCs in the field has now been transformed into one of generating an accurate calibration current in the field, but of a reasonable value. This problem has been solved by the creation of a new 10 mA dc current standard and a remote-controlled, programmable current multiplier, the current calibrator, providing the necessary 5 A calibration current. A voltage booster has been added externally to provide the power necessary for the winding resistance without incurring excessive power dissipation in the sensitive environment of the calibration current source.

A computer will be part of each calibration cluster to manage the full remote control of the current calibrator, the voltage booster and the switching matrix. It will have a network connection to receive and return calibration data from the operations database for each converter under its control. In this way full tracking of calibration history can be maintained for each calibrated sub-system and can be used for further performance improvements over time. The local computer will only have full freedom to perform calibration operations during the calibration mode of the LHC.

Current Calibrator

The current calibrator is essentially a current multiplier providing extremely precise current ratios [30]. The input current is 10 mA dc, provided by a current source known as the PBC, see below. The heart of the device is a transformer with primary windings in a binary succession from 1 to 2048, Fig. 10.16, giving a maximum of 40.96 ampere-turns. These primary windings can be switched in and out at will with relays, providing the 12 most significant control bits. An additional 1-turn winding is fed from a DAC with 10 mA full-scale output, providing another 16 bits. The total theoretical resolution is 28 bits, but noise reduces the practical resolution to around 24 bits.

Secondary windings are provided with 4 to 40 turns, giving secondary output current ranges from 1 to 10 A. The compliance of the device is only a few volts at the output terminals.

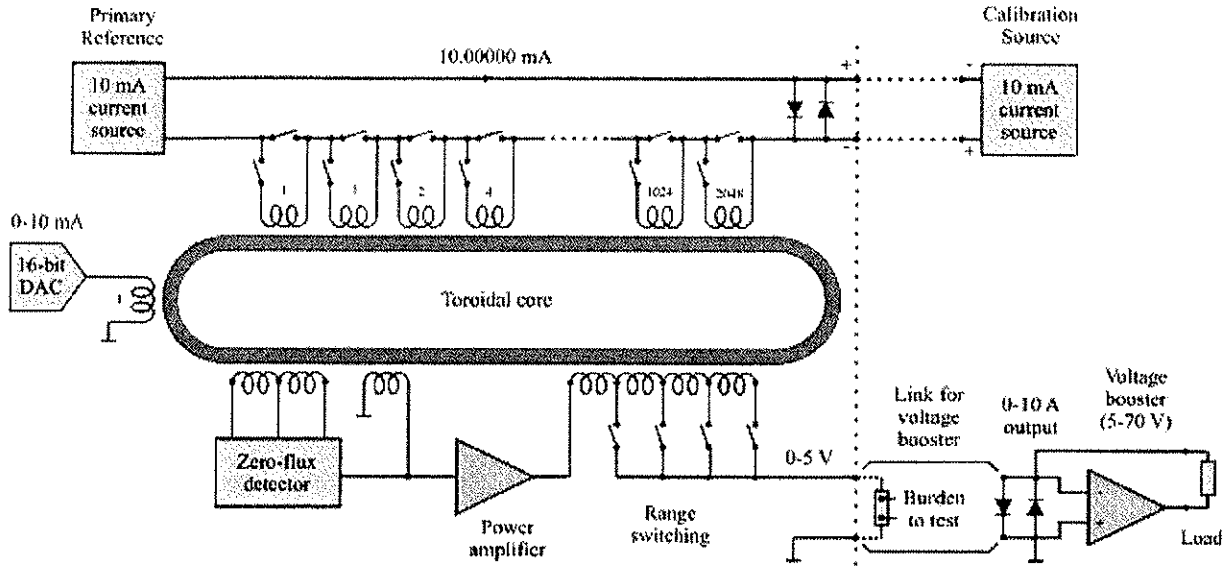

Figure 10.16: Current calibrator principle

Primary standards and calibration infrastructure

Any calibration structure starts with the traceability to national standards. The CERN standards lab has several sets of reference voltage and resistance standards. Mobile standards are employed to transport the Volt and the Ohm from the Swiss National Standards Laboratory (METAS) in Bern to Geneva. Fixed standards, maintained in a well controlled environment, provide the local calibration platform at CERN. Intercomparison with METAS is performed at least once per year and provides a local accuracy of better than 0.5 ppm for both voltage and resistance.

At CERN's initiative a new 10 mA dc current standard (named PBC) was developed and has already been produced and proven in sufficient numbers [31]. Through the use of 10 V voltage standards and 1 kΩ resistance standards, the PBC can be calibrated to better than 0.5 ppm uncertainty and is the beginning of the current calibration chain. Certain PBCs are assigned as mobile transfer standards and move the 10 mA to the different LHC locations. There the 10 mA is transferred to the PBCs located in the current calibrators described earlier. The transfer procedure maintains the highest accuracy and is well adapted to field use. The aim is to maintain the local 10 mA with an uncertainty better than 1 ppm.

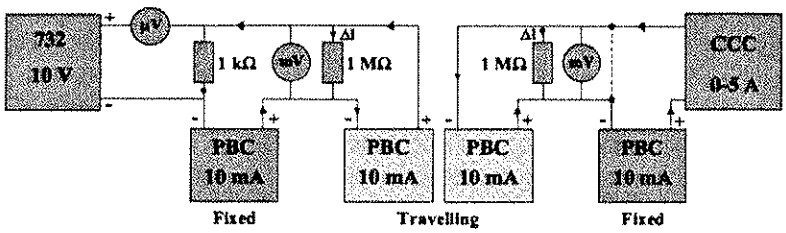

Figure 10.17: Calibration transfer chain

Ancillary equipment – Voltage booster

The current calibrator has a compliance of only a few volts, to limit internal power dissipation and its variation. The calibration windings in the DCCT heads have a resistance of several Ohms so the voltage drop will be substantial. A voltage booster has been designed to bridge this gap, also considering that a calibration

winding has to be driven from a high-impedance source not to disturb the DCCT zero-flux detector and control loop. The booster output voltage is controlled by a loop maintaining zero voltage at the output of the current calibrator. The output stage is a trans-conductance amplifier with a compliance voltage of up to 70 V.

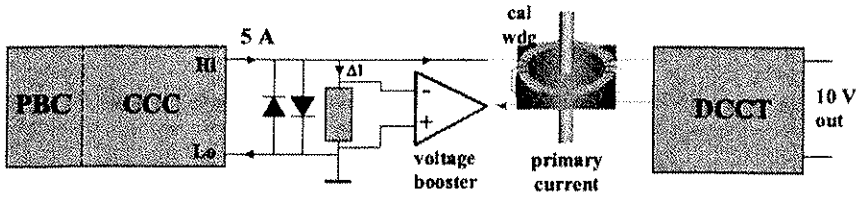

Figure 10.18: Voltage booster configuration

This configuration will ensure that all of the current delivered by the current calibrator will pass through the calibration winding and that problems of leakage currents are virtually eliminated.

Ancillary equipment – Switching matrix

Several DCCTs have to be handled by each cluster and its current calibrator. The booster output voltage will therefore be routed through a relay switching matrix. The relays will determine which DCCT(s) will be connected and which will be bypassed. An output voltage measurement and a zero-current measurement are also included to provide some self-checking of the calibration operation.

Ancillary equipment – Air-conditioned racks

All the high-precision equipment will be located in air-conditioned 19" racks to provide a temperature-controlled environment with predictable accuracy in the calibration results. The temperature control is fixed to 23 ±1°C. Industrial air-conditioning equipment fed with CERN's chilled water. The controller is of PID type, steering a proportional valve for best performance and to minimise EMC problems.

The racks are designed with consideration to the potential EMC problems in the vicinity of high-power switch-mode converters.

10.5 SPECIFIC REQUIREMENTS PLACED ON OTHER SYSTEMS AND THEIR INTERFACES

AC Power Requirements of the Power Converter System for the LHC magnets

All power converters located underground are fed from a 3-phase 400 V source with the exception of the eight power converters for the main dipole circuits which are fed directly from 18 kV. The electrical input parameters for each type of converter are given in LHC Powering Database.

To be able to monitor the magnet current even in case of mains failure, the FGC as well as the DCCT and the Sigma-Delta ADC are supplied by UPS for circuits above 4 kA [32]. It concerns the 1-quadrant converters (type RPHE, RPHF, RPHG, RPHH) and the main dipole converters.

All the power converters conform to the Engineering Specification concerning the main parameters of the LHC 400 V/230 V distribution system [8]. This document defines the main parameters of the 400 V and the user requirement.

For the UPS grids, the power converters conform to the Engineering Specification concerning the Underground Uninterrupted Power Supply (UPS) for LHC [34].

For more details of the harmonics generated by the switch-mode converters, see technical notes [22] and [23].

Tab. 10.8 gives the power consumption of the power converters for the machine in steady-state (collision) and peak (just at the end of the energy ramp) for a main dipole field of 9 Tesla. They are given for the eight points of the machine and various areas within those points. Tab. 10.8 corresponds to the LHC Powering Database V6.4.

Table 10.8: AC power consumption

Location(s)		Steady State Power		Peak Power		UPS
		Real kW	Apparent kVA	Real kW	Apparent kVA	Apparent kVA
Point 1	RR13/RR17	407/407	443/443	457/457	488/488	16.5/16.5
	UJ14	124	135	142	152	4.3
	UJ16	125	136	143	153	4.3
	SR1	462	917	465	917	---
	Octant *	25	27	58	62	---
	Total	**1550**	**2101**	**1722**	**2260**	**41.6**
Point 2	UA23 **	1408	1536	3745	4877	26.5
	UA27 **	1443	1573	3780	4914	26.5
	UJ23	6	7	8	9	---
	SR2	180	412	181	412	---
	Octant *	25	27	58	62	---
	Total	**3062**	**3555**	**7772**	**10274**	**53.0**
Point 3	UJ33	603	652	629	676	---
	SR3	1367	2000	1375	2000	---
	Octant *	25	27	58	62	---
	Total	**1995**	**2679**	**2062**	**2738**	**0.0**
Point 4	UA43 **	1314	1435	3622	4747	20.1
	UA47 **	1314	1435	3616	4740	20.1
	UJ43/UJ47	8/8	9/9	11/11	11.5/11.5	---
	Octant *	25	27	58	62	---
	Total	**2669**	**2915**	**7318**	**9572**	**40.2**
Point 5	RR53/RR57	407/407	443/443	457/457	487/487	16.5/16.5
	UJ56	131	142	149	159	4.3
	USC55	146	159	164	176	4.3
	SR5	463	917	466	917	---
	Octant *	25	27	58	62	---
	Total	**1579**	**2131**	**1751**	**2288**	**41.6**
Point 6	UA63 **	859	936	3127	4213	15.7
	UA67 **	859	936	3133	4219	15.7
	UJ63/UJ67	152/152	1677167	169/169	181/181	---
	SR6	1117	1585	1135	1585	---
	Octant *	25	27	58	62	---
	Total	**3164**	**3818**	**7791**	**10441**	**31.4**
Point 7	RR73	80	86	92	97	---
	RR77	81	87	93	98	---
	UJ76	264	286	265	287	---
	SR7	1063	2000	1069	2000	---
	Octant *	25	27	58	62	---
	Total	**1513**	**2486**	**1577**	**2544**	**0.0**
Point 8	UA83 **	1391	1518	3725	4855	26.5
	UA87 **	1411	1540	3749	4881	26.5
	UJ83	8	9	11	12	---
	UJ87	7	8	10	11	---
	SR8	149	160	149	161	---
	Octant *	25	27	58	62	---
	Total	**2991**	**3262**	**7702**	**9982**	**53.0**
Power Converters* **	**Total**	**18523**	**22947**	**37695**	**50099**	**260.8**

* Orbit corrector Power Converters distributed along the tunnel

** Including power taken directly from 18 kV

*** Only Power Converters for the magnets of the LHC machine. Does not include RF system nor the main experiment's magnets (central and outer compensators for Alice and LHCb are included)

Cooling Requirements of the Power Converter System for the LHC magnets

Considering the large currents involved, most of the power converters used for the LHC magnets are water-cooled. However, it is impossible to capture all losses in water and it is estimated that approximately 10% of the total losses are lost to air. The power converters of 120 A and less which are installed underground, are only air-cooled, as are all power converters installed on the surface. The losses for each type of converter are given in LHC Powering Database.

The rack housing the DCCT electronics and the Sigma-Delta for the high precision circuits (Main Dipoles and Inner Triplets) are cooled by chilled water. All water-cooled converters are tested at 22 bars pressure for half an hour. All the power converters conform to the Engineering Specification concerning the LHC demineralised water circuit [21]. The rack housing the DCCT electronics and the sigma-delta for the circuits with high precision, conform to the engineering specification for the LHC chilled and mixed water circuit [27]. This document defines the main parameters of the demineralised water circuits and the user requirement. All power converters conform to the Engineering Specification concerning the Air Handling of the LHC Tunnel and its Underground Areas [27].

Tab. 10.9 gives the water consumption and air losses of the power converters for a main dipole field of 9 Tesla. They are given for the eight points of the machine and various areas within those points. Tab. 10.9 corresponds to the LHC Powering Database V6.4 [10].

Table 10.9: Water and air losses

Location(s)		Mixed Water Consumption (m^3/h)	Water Losses (mixed water) kW	Air Losses kW
Point 1	RR13	---	150.9	32.2
	RR17	---	150.9	32.2
	UJ14	0.4	39.5	8.7
	UJ16	0.4	39.5	8.7
	SR1	---	---	39.9
	Octant*	---	---	22.0
	Atlas	---	44.0	4.9
	Total	**0.8**	**424.8**	**148.6**
Point 2	UA23	1.0	428.4	102.1
	UA27	1.0	430.0	106.7
	UJ23	---	---	4.4
	SR2	---	---	347.2
	Octant *	---	---	22.0
	Alice	---	---	12.0
	Total	**2.0**	**858.4**	**594.4**
Point 3	UJ33	---	135.3	32.6
	SR3	---	---	99.6
	Octant *	---	---	22.0
	Total	**0.0**	**135.3**	**154.2**
Point 4	UA43	0.6	380.8	88.5
	UA47	0.6	380.8	88.5
	UJ43	---	---	4.4
	UJ47	---	---	4.4
	Octant *	---	---	22.0
	Total	**1.2**	**761.8**	**207.8**
Point 5	RR53	---	150.9	32.2
	RR57	---	150.9	32.2
	UJ56	0.4	39.5	8.7
	USC55	0.4	39.5	8.7

Location(s)		Mixed Water Consumption (m^3/h)	Water Losses (mixed water) kW	Air Losses kW
	SR5	---	---	39.9
	Octant *	---	---	22.0
	CMS	---	70.0	40.0
	Total	0.8	450.8	183.7
Point 6	UA63	0.6	286.9	77.4
	UA67	0.6	286.9	77.4
	UJ63	---	55.5	8.6
	UJ67	---	55.5	8.6
	SR6	---	---	78.3
	Octant *	---	---	22.0
	Total	1.2	684.8	272.3
Point 7	RR73	---	49.7	12.8
	RR77	---	49.7	12.8
	UJ76	---	34.6	4.9
	SR7	---	---	99.6
	Octant *	---	---	22.0
	Total	0.0	134.0	152.1
Point 8	UA83	1.0	430.0	102.3
	UA87	1.0	428.4	102.1
	UJ83	---	---	4.4
	UJ87	---	---	4.4
	SR8	---	---	346.0
	Octant *	---	---	22.0
	LHCb	---	---	12.0
	Total	2.0	858.4	593.2

* Orbit corrector Power Converters distributed along the tunnel

Interlocks and quench protection

In addition to circuits for its own protection, the converters also include:

Machine protection

- All converters are part of the LHC machine protection, managed by the powering interlock system. The interface between power converters and powering interlock system depends on the type of electrical circuit (energy stored in the circuit and function of the magnets).
- A "green light" for powering, PC_PERMIT, is required for all circuits. This signal interlock will inhibit any start command, if not present.
- In case of a failure noticed by the power converter, a POWERING_FAILURE signal is issued. Such failures include failures of the power converter itself, failures in the supply (water, electricity) etc. This signal could, depending on the type of circuit, request a beam dump.
- For an emergency stop of the power converter, for example after a quench, the power converter receives the PC_FAST_ABORT signal. Due to the fact that the emergency stop must be as reliable as possible, a redundant way to switch off the converter is implemented in each converter managing this signal.
- To verify if the connection between power converter and powering interlock system is made, a PC_CONNECT signal will be used by the powering interlock system.

For more details, see the converter Technical Specification [13, 14, 15, 16, 17] and the Engineering Specifications on the Powering Interlock System [18].

Earth fault detection

The earthing circuit is part of the power converter electronics. This circuit has 4 roles:

- earthing of the load circuit (DC side) for safety reasons.

- detection of an earth fault.
- monitoring of the leakage current.
- limitation of the earth current in case of an earth fault to avoid damaging the circuit elements.

Earthing of the circuits is made with active detection so that an earth fault can be detected before powering the circuits.
For more details, see the converter Technical Specifications [13, 14, 15, 16, 17] and the Engineering Specification on the Earthing Circuit [36].

Water-cooled load cables for the 1-Quadrant converters
A flow-meter signal is transmitted to the 1-Quadrant converters for the protection of the water-cooled cables going from the output of the converter to the DFB to avoid a burnout of the cable in case of water-cooling failure. Should this event occur, each converter will receive an open contact indicating no water flow in the cable. The converter will switch off immediately and trigger the fastest extraction of the magnet energy (dump resistor insertion or quench heater firing).
For more details, see the converter Technical Specifications [13, 14].

Over-current
All converters types will switch off when an over-current condition is detected. In most cases, the threshold is adjustable in a series of steps.
For more details, see the converter Technical Specifications [13, 14, 15, 16, 17].

Resistive Current lead protection
In order to determine the electrical resistance and the heat dissipation of the resistive current leads, voltage taps are used at the warm and cold ends of the current leads (Fig. 10.19). The voltage drop between the warm and cold ends of a current lead is measured by the converter. If the voltage drop across one of the leads goes beyond a certain threshold, the power converter will switch off within 100 ms. Special hardware will be installed in the (±600 A, ±40 V) used as (±120 A, ±40 V), the (±120 A, ±10 V) and (±60 A, ±8 V) converters that are used for powering LHC circuits up to 120 A.
In addition, a test routine will be performed periodically to verify the validity of the measurement, i.e. whether the voltage tap connections are open-circuit or in short-circuit. The test routine consists of delivering maximum current to the magnet and checking if the voltage drop across the lead is above a certain threshold (which is lower than the normal trip threshold).
For more details, see the Engineering Specification on the Current Leads protection for LHC circuits up to 120 A [35].

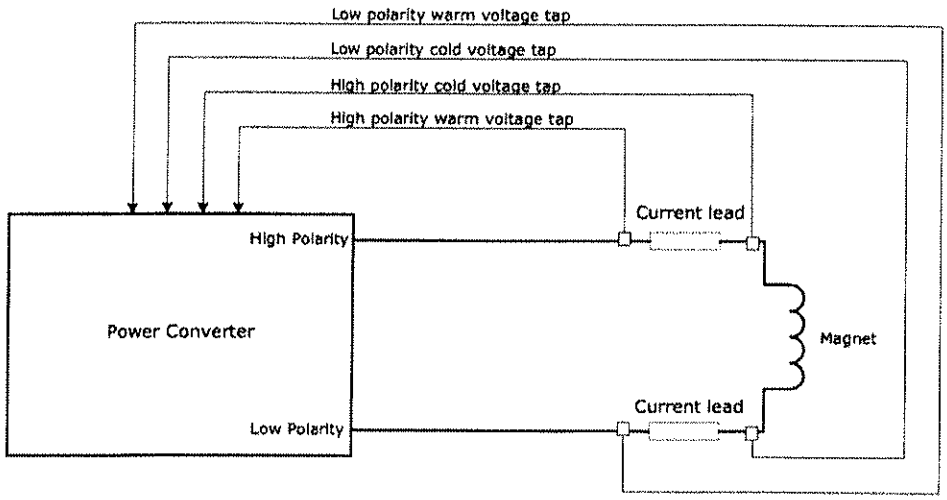

Figure 10.19: Current lead voltage taps

EMC

The power converters fulfil EMI standards for the immunity of the equipment and for conductive noise emission.

- Electrical fast transient/Burst immunity test — IEC 6100-4-4, level 4
- Conductive noise emission

Common Mode (AC and DC sides)	IEC 478-3, curve C (1mV above 0.5 MHz)
Differential Common Mode under 130 kHz	See the ripple requirement depending of the converter type (See Sec. 10.4)
above 130 kHz	IEC 478-3, curve C (1 mV above 0.5 MHz).

10.6 OPERATIONAL ASPECTS

Unlike the LEP power converters, the LHC power converters will be installed underground, where access is difficult. As a consequence, the various systems will not be accessible during the machine runs. It will also be very difficult to repair them in the tunnel as large quantities of equipment will be installed in areas with limited access (radiation and cryogenic risks).

To meet these new constraints, different strategies have been developed depending on the type of equipment installed (Voltage source, DCCT or Function Generator Controller FGC).

10.6.1 Voltage Sources

The voltage sources (VS) MTBFs are estimated to be 100'000 hours. From this we obtain the fault frequencies versus the voltage sources categories.

Table 10.10: Voltage sources

VS categories	Number of VS	Fault frequencies
Thyristors	32	130.21 days
High Current (2 kA et 3.25 kA)	208	20 days
Medium Current (600 A et 120 A)	726	5.7 days
Corrector (60 A)	752	5.5 days

According to the voltage source categories, different operating strategies will be chosen.

a. Thyristor voltage sources

The thyristor voltage sources are easy to repair and the failures usually occur in the control electronics. It is planned to have spare units for main power elements (transformer, inductance, capacitors and semiconductors). In addition only the main dipole power converters and the CMS power converter are installed underground – all others are installed on the surface in the SR buildings. In the event of failure (once or twice per year) the operator will repair the voltage source by simply changing an electronics card. A major problem would be the exchange of an 18 kV transformer or a passive filter choke in the main dipole converter. This event could take 2 or 3 days, but the probability of such an event is only one in ten years.

b. 2 kA/3.25 kA voltage sources

The 2 kA/3.25 kA voltage sources are switch-mode power converters with several sub-converters in parallel to achieve the high output currents. These voltage sources were designed with an additional sub-converter as an active spare. If one sub-converter fails, the other sub-converters are able to deliver the required output current. The operator may then wait until the end of the run to change the failed module. The travel and the access procedure could take up to 1h30min and the change of the module will take around 15 minutes. The maintenance of the failed module will be performed on the surface without any operational constraints. Furthermore this redundancy strategy leads to less stress on the module components: normal operation will be at 75 to 80% of rated power.

c. 600 A and 120 A voltage sources

These voltage sources are modular (as are the other power converters installed in the tunnel), however it is not possible to have an active spare for these voltage sources due to cost and volume constraints. Although a large number of interventions will be required, these will be short as the failed module will simply be replaced, taking very little time.

d. 60 A voltage sources

The 60 A voltage sources will cause a large percentage of the total voltage source interventions. The LHC is however designed to work with 2 - 4% of the corrector power converters out of operation. A monthly campaign is scheduled for the replacement at the same time of all faulty corrector converters; critical cases will have to be replaced immediately. To make this strategy possible, at least 10% of the total 60 A converter quantity must be kept ready as spares.

10.6.2 DCCTs

In each power converter there are two DCCTs. With digital current regulation, the FGC is able to automatically change to the second DCCT for regulation, if the first one fails. Some types of DCCT failures can be detected and signalled. Other failures are of such character that it will be impossible to tell which one of the two DCCTs has failed. This strategy should minimise the downtime in case of a DCCT failure.

In line with other power equipment, the DCCTs are of modular design to minimise the intervention time. The only lengthy operation is the change of a DCCT head (this operation could take up to 5 hours for the high current DCCTs) but it should be very rare (one change every 3 years).

10.6.3 Function Generator Controller (FGC)

The FGC has been designed with an MTBF of 1'000'000 hours. With approximately 1750 units installed in the machine, the fault rate will be in the order of one every 24 days. However, with half of the FGC systems being installed in the 60 A correctors, it is estimated that an FGC failure will only cause a machine shut down once every 48 days. It is virtually impossible to design in full redundancy to eliminate this problem.

10.6.4 Diagnostic Interface Module (DIM)

A diagnostic system has been developed to optimise efficiency of interventions. This system identifies the failure prior to sending personnel on site and interventions can be better planned to limit the downtime. The second functionality of this system is to follow the power converter parameters during machine running and identify areas requiring maintenance before a failure occurs.

10.6.5 Radiation

It is well understood that radiation has an adverse affect on electronics and that some technologies are more vulnerable than others. Both the 60 A voltage source and the FGC control electronics have been designed taking this into consideration, thus failures due to radiation damage are simply an additional factor contributing to the MTBF mentioned in Chaps. 10.6.1 and 10.6.3. Tests conducted both at CERN and at a Belgian cyclotron facility have demonstrated an acceptable tolerance to the doses and fluences predicted for the LHC tunnel. However, a significant number of larger power converters will be installed in the RR and UJ underground areas, where recent studies indicate that while the cumulative radiation dose will be low, there will be a non-zero neutron fluence that may cause disruption to electronics due to Single Event Upsets. Extra shielding is now being designed to reduce the levels in these areas, and the FGC electronics are not expected to have a problem. However the larger voltage sources and DCCTs have not been designed to withstand radiation of any sort, so there is some level of uncertainty in the performance of these systems. These designs will shortly be audited to determine the expected levels of susceptibility, following which an action plan will be developed.

REFERENCES

[1] L. Bottura, "From the LEP warm magnets to the LHC superconducting magnets", Proceedings of the workshop on LEP-SPS performance, Chamonix X , January 2000.

[2] O. Brüning, "Accelerator physics requirements at commissioning", Proceedings of the LHC, Chamonix XI, January 2001.

[3] P. Cruikshank, P. Proudlock, G. Riddone, R. Saban, R. Schmidt, "General parameters for equipment installed in the LHC", LHC-PM-ES-0002.00, April 1999.

[4] Dynamic Effects Working Group: http://lhc.web.cern.ch/lhc/org/wg.htm

[5] F. Bordry, A. Dupaquier, "High Current, Low Voltage Power Converters for LHC", EPAC'96, Sitges, June 1996.

[6] F. Bordry, "LHC Power Converters : Performance requirements ", Proceedings of the LHC, Chamonix XI , January 2001.

[7] F. Bordry, "LHC Powering from String 2 to Sector Test", Proceedings of the LHC, Chamonix XI , January 2001.

[8] G. Fernqvist, J. Pedersen, "Main parameters of the LHC 400/230 V", Engineering Specification, LHC-EM-ES-0001, August 2000.

[9] F Bordry, H. Thiesen an, "RST Digital Algorithm for controlling the LHC magnet current", Electrical Power Techonology in European Physics Research EP2, Grenoble, October 1998.

[10] LHC Powering database Version 6.4. Http://lhc-new-homepage.web.cern.ch/lhc-new-homepage

[11] "Workshop on LHC Powering", CERN, 27-29 November 2000: http://lhcp.web.cern.ch/lhcp/TCC/PLANNING/TCC/Power2000/welcome.htm.

[12] "Review of LHC Power Converters", CERN, 6 June 2001 http://lhcp.web.cern.ch/lhcp/TCC/PLANNING/TCC/PowerReview/welcome.htm.

[13] F. Bordry, V. Montabonnet, "Technical Specification for 13 kA and 20.5 kA, 18 V Switch-Mode Power Converters using Sub-converters of 3.25 kA each" LHC-RPH-CI-0001, N°EDMS 315004, August 2002.

[14] F. Bordry, V. Montabonnet, "Technical Specification for 6-8 kA Switch-Mode Power Converters using Sub-converters of 2 kA each" LHC-RPH-CI-0002, N°EDMS 314993, November 2002.

[15] A. Dupaquier, Y. Thurel, "Technical Specification for Four-Quadrant Switch-Mode Power Converters (±600 A,±10 V) and (±600 A, ±40 V)" LHC-RPM-CI-0001, N°EDMS 305488, July 2002.

[16] Y. Thurel, "Technical Specification for the Production of Four-Quadrant Switch-Mode Power Converters (±120 A,±10 V)" LHC-RPLB-CI-0001, N°EDMS 377945, April 2003.

[17] A. Dupaquier, "Technical Specification for the Production of Four Quadrant Switch-Mode Power Converters (±60 A,±8 V)" LHC-RPLA-CI-0001, N°EDMS 378088, April 2003.

[18] B. Puccio, R. Schmidt, M. Zerlauth "The Hardware Interfaces Between Powering Interlock System, Power Converters and Quench Protection" LHC-D-ES-0003, N°EDMS 368927.

[19] A. Dupaquier, V. Montabonnet, Y. Thurel "Interface between Power Converter, Powering Interlock System and Current Lead protection for circuits up to 120 A".

[20] A. Dupaquier, V. Montabonnet, Y. Thurel "Earthing of the LHC DC Electrical Circuits" LHC-D-ES-0001, EDMS N°309372, October 2002.

[21] L. Annila "LHC Demineralised Water Circuit" LHC-FW-ES-0001, EDMS N°335008, July 2002.

[22] V. Montabonnet, "Courants harmoniques générés par des convertisseurs à pont de diodes" Note Technique SL-PO N°40, December 2000.

[23] K. Kahle, "Harmonics Studies for LHC UA23, UA43, UA63, UA83, RR13, RR17, RR53, RR57, RR73, RR77, UJ33, UJ56, UJ76 " CERN/ST-EL/KK (2002-075), August 2002.

[24] F. Bordry, H. Thiesen, "LHC INNER TRIPLET POWERING STRATEGY", Particle Accelerator Conference PAC'01, June 2001, Chicago.

[25] O. Brüning, 6th LHC commisioning committee, May 2001.

[26] K. Dahlerup-Petersen, F. Rodriguez-Mateos, R. Schmidt , F. Sonnemann, "General parameters for energy extraction of the LHC superconducting circuits", Engineering Specification, LHC-DQ-ES-0001 rev 1.0.

[27] C.Martel, "Air Handling of the LHC Tunnel and its Underground Areas" LHC-UA-ES-0001, EDMS N° 344211, May 2003.

[28] J.G. Pett, "A high accuracy 22-bit sigma-delta converter for digital regulation of superconducting magnet currents", 3rd International Conference on Advanced A/D and D/A Conversion Techniques and their Applications , Glasgow, UK , 27 - 28 Jul. 1999 - Pages 46-49.
[29] G. Fernqvist, "The measurement challenge of the LHC project", IEEE Trans. Instrum. Meas., vol. 48, April 1999.
[30] G. Fernqvist et al, "A novel current calibration system up to 20 kA", IEEE Trans. Instrum. Meas., vol. 52, April 2003.
[31] G. Fernqvist et al, "Design and evaluation of a 10 mA dc current reference standard", IEEE Trans. Instrum. Meas., vol. 52, April 2003.
[32] Minutes of the EEWG Meeting held on 24 January 2003: http://lhcp.web.cern.ch/lhcp/tcc/powering/eewg/eewg.htm.
[33] L. Annila "LHC chilled and mixed water circuit" LHC-FG-ES-0001, EDMS N°3469363, September 2002.
[34] J. Gomez, J. Pedersen, "Underground Uninterrupted Power Supply (UPS) for LHC" LHC-EO-ES-0001, EDMS N°356521, July 2003.
[35] A. Dupaquier, V. Montabonnet, Y. Thurel "Interface between Power Converter, Powering Interlock System and Current Lead protection for circuits up to 120 A".
[36] A. Dupaquier, V. Montabonnet, Y. Thurel "Earthing of the LHC DC Electrical Circuits" LHC-D-ES-0001, N°EDMS 309372, October 2002.
[37] L. Bottura, P. Burla and R. Wolf, LHC Main Dipoles Proposed Baseline Current Ramping, CERN-LHC-Project-Report-172, March 1998.

CHAPTER 11

CRYOGENICS

11.1 OVERVIEW

The LHC is unique among superconducting synchrotrons [1, 2, 3] because its operating temperature is below 2 K in order to maximise the field strength of the superconducting magnets with NbTi windings. The evolution of the basic design criteria and constraints as well as the main technical choices for the LHC cryogenic system are described in Chapter 6 of the 'Pink Book' [4], in Part III, Section 2 of the 'White Book' [5] and in Part III, Section 2 of the 'Yellow Book' [6]. This chapter describes the design of the LHC cryogenic system as it stands in 2004.

11.2 FUNCTIONS, CONSTRAINTS, ARCHITECTURE

11.2.1 General Functions

The superconducting magnet windings in arcs, dispersion suppressors and inner triplets will be immersed in a pressurised bath of superfluid helium at about 0.13 MPa (1.3 bar) and a maximum temperature of 1.9 K [7, 8]. This allows a sufficient temperature margin for heat transfer across the electrical insulation. As the specific heat of the superconducting alloy and its copper matrix fall rapidly with decreasing temperature, the full benefit in terms of stability margin of operation at 1.9 K instead of at the conventional 4.5 K may only be reaped by making effective use of the transport properties of superfluid helium, for which the temperature of 1.9 K also corresponds to a maximum in the effective thermal conductivity [9]. The low bulk viscosity enables the coolant to permeate the heart of the magnet windings, while the very large specific heat (typically 10^5 times that of the conductor per unit mass, 2×10^3 times per unit volume), combined with the enormous heat conductivity at moderate flux (3000 times that of cryogenic-grade OFHC copper, peaking at 1.9 K) can have a powerful stabilising action on thermal disturbances. To achieve this, the electrical insulation of the conductor must preserve sufficient porosity and thermal percolation paths while still fulfilling its demanding dielectric and mechanical duties. This cooling requirement applies during both ramping and stored-beam operation. In the case of fast current discharge, the temperature excursion may be larger but must still remain below the helium II/helium I phase transition (lambda line). In the long straight sections, with the exception of the inner triplets and the superconducting dipoles D1, the field strength and heat extraction requirements are such that operation at 1.9 K is not necessary. These magnets will have their superconducting windings immersed in a bath of saturated helium at a temperature of 4.5 K.

The cryogenic system [10, 11] must cope with load variations and large dynamic range induced by operation of the accelerator.

The LHC cryogenic system must also be able to cool-down and fill the huge cold mass of the LHC, 37×10^6 kg in a maximum time of 15 days while avoiding thermal gradients in the cryo-magnet structure higher than 75 K. This limit in thermal gradient and time also applies to the forced emptying and warm-up of the machine prior to shutdown periods.

The cryogenic system must be able to cope with the resistive transitions of the superconducting magnets, which occasionally will occur in the machine, while minimising loss of cryogen and system perturbations. It must handle the resulting heat release and its consequences, which include fast pressure rises and flow surges. It must limit the propagation to the neighbouring magnets and recover in a time that does not seriously detract from the operational availability of the LHC. A resistive transition extending over one lattice cell should not result in a down time of more than a few hours.

In addition to these basic operational duties, the LHC cryogenic system should allow for rapid cool-down and warm-up of limited lengths of cryo-magnet strings, e.g. for repairing or exchanging a defective unit. It should also be able to cope with the resistive transition of a full sector - this defining the maximum credible

incident - without impairing personnel or equipment safety. Finally, to ensure reliable operation, it should provide some redundancy among its components and sub-systems.

11.2.2 Design Constraints

The main constraints result from the need to install the system in the existing LEP tunnel and re-use its facilities, including the four existing LEP refrigerators [12] and their cryogenic infrastructure. The limited number of access points to the underground areas is reflected in the architecture of the LHC cryogenic system. The cooling power required at each temperature level will be produced in eight refrigeration plants and distributed to the adjacent sectors over distances of up to 3.3 km. For reasons of simplicity, reliability and maintenance, the number of active cryogenic components distributed around the ring is minimised.

To simplify the magnet string design, the cryogenic headers distributing the cooling power along a machine sector as well as all remaining active cryogenic components in the tunnel are contained in a compound cryogenic distribution line (QRL). The QRL runs alongside the cryo-magnet strings in the tunnel and feeds each 106.9 m-long lattice cell in parallel via a jumper connection (Fig. 11.1). Choosing spacing of the jumper connections to be one full cell length was the result of an optimisation exercise [13].

The LHC tunnel is inclined at 1.41 % with respect to the horizontal, thus giving rise to elevation differences of up to 120 m across the tunnel diameter. This will generate hydrostatic heads in the cryogenic headers and could generate flow instabilities in two-phase, liquid-vapour, flow. To avoid these harmful instabilities, all fluids should ideally be transported over large distances in mono-phase state, i.e. in the superheated-vapour or supercritical region of the phase diagram. Local two-phase circulation of saturated liquid can be tolerated over limited lengths, in a controlled direction of circulation.

Equipment is installed as much as possible above ground to avoid the need for excavation of further large underground caverns. However, certain components which must be close to the cryostats or which cannot be installed on the surface because of the hydrostatic head will be installed underground.

For reasons of safety the use of nitrogen in the tunnel is forbidden and discharge of helium is restricted to small quantities only. These safety aspects are reflected in specific operational design features of the system, such as the inclusion of a large acceptance cold recovery header inside the QRL.

The cryogenic system is designed for fully automatic operation during nine consecutive months followed by three months of shutdown during which maintenance will be performed.

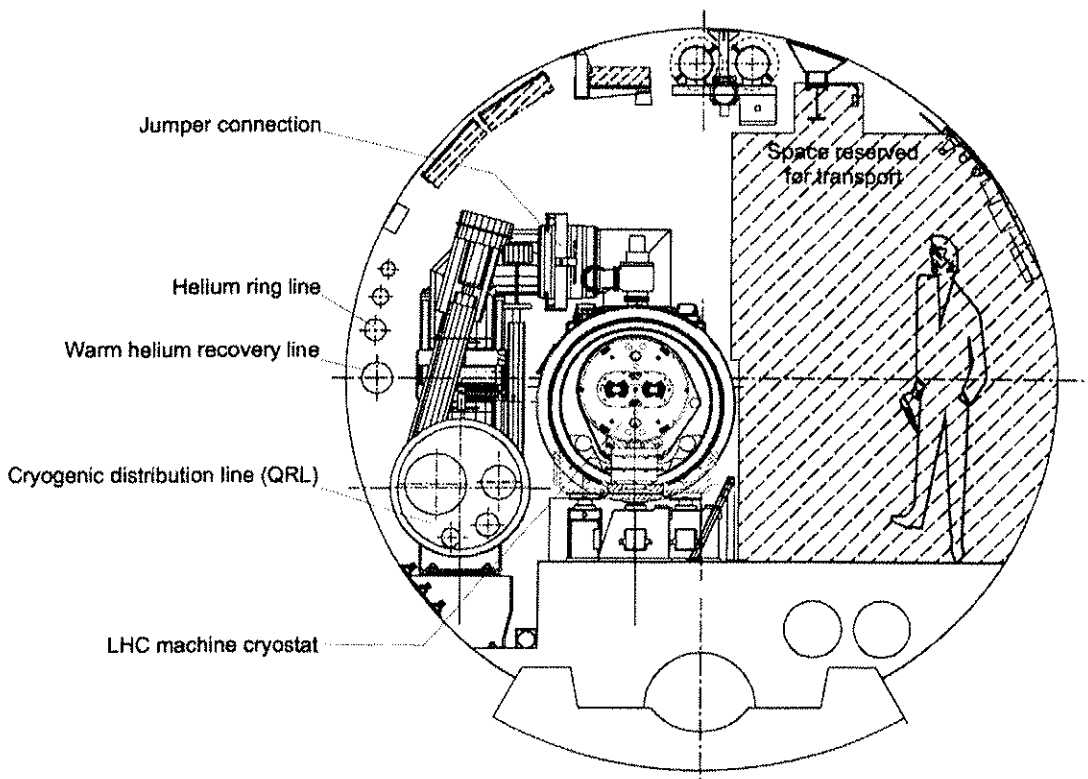

Figure 11.1: Transverse cross-section of the LHC tunnel

11.2.3 General Architecture

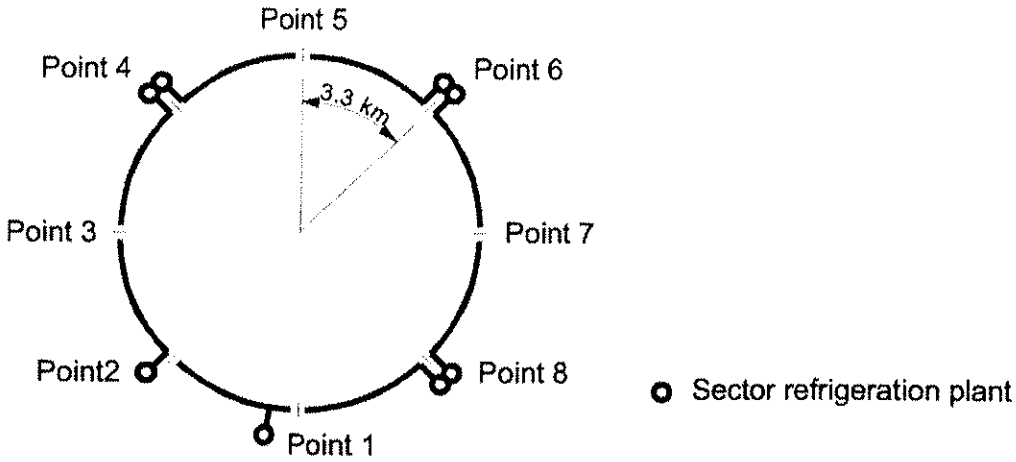

Figure 11.2: General layout of the cryogenic system

A direct consequence of the site constraints is the cryogenic layout of the machine (Fig. 11.2), with five cryogenic "islands" at access points 1.8, 2, 4, 6 and 8 where all refrigeration and ancillary equipment is concentrated. Equipment at ground level includes electrical substation, warm compressor station (QCS_A,B,C), cryogen storage (helium and liquid nitrogen), cooling towers, cold-boxes (QSR_A,B) and underground are the lower cold-boxes (QURA), 1.8 K refrigeration unit boxes (QURC), interconnecting lines, and interconnection boxes (QUI_A,B,C). Each cryogenic island houses one or two refrigeration plants that feed one or two adjacent tunnel sectors, requiring distribution and recovery of the cooling fluids over distances of 3.3 km underground. Fig. 11.3 shows the general architecture of the cryogenic system. A refrigeration plant comprises one 4.5 K refrigerator and one 1.8 K refrigeration unit. The 4.5 K refrigerator is either one of the four split-cold-box refrigerators recovered from LEP or one of the four new integrated-cold-box refrigerators. At each cryogenic island, an interconnection box couples the various refrigeration equipments and the cryogenic distribution line. They also permit, when possible, redundancy in between the refrigeration plants.

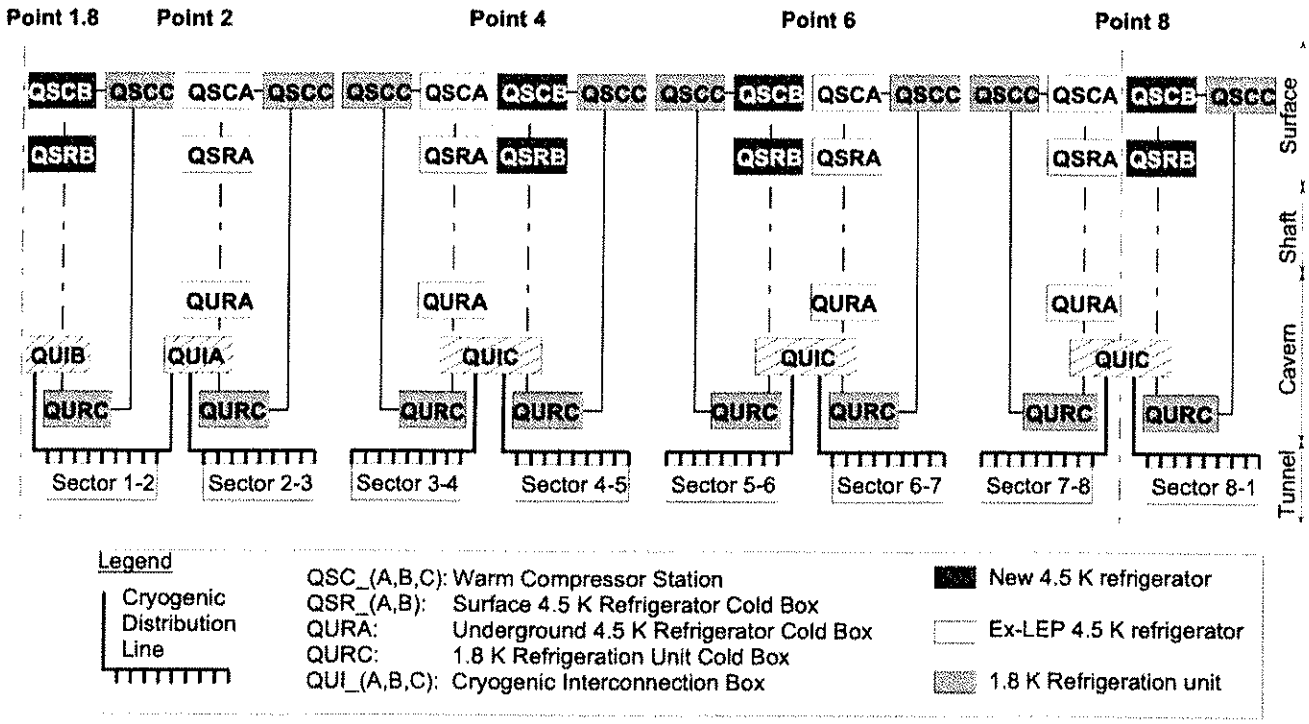

Figure 11.3: General architecture of the cryogenic system

Due to the lack of space for two refrigeration plants at Point 2 and the need at Point 1.8 for large refrigeration capacity for cryo-magnet testing, the 4-point symmetry was broken and two refrigeration plants at points 4, 6 and 8 and only one refrigeration plant at points 1.8 and 2 were installed. The drawback of this architecture concerns sector 2-3, which only benefits from limited redundancy.

To limit the environmental impact as well as the pressure build-up during helium discharge in the case of quench of a magnet sector, helium storage is provided at all eight access points.

11.3 TEMPERATURE LEVELS

In view of the high thermodynamic cost of refrigeration at 1.8 K, the thermal design of the LHC cryogenic components aims at intercepting the largest fraction of applied heat loads at higher temperature, hence the multiple, staged temperature levels in the system. The temperature levels are:

- 50 K to 75 K for thermal shield as a first major heat intercept, sheltering the cold mass from the bulk of heat in-leaks from ambient.
- 4.6 K to 20 K for lower temperature heat interception and for the cooling of the beam screens which protect the magnet cold bore from beam-induced loads.
- 1.9 K quasi-isothermal superfluid helium for cooling the magnet cold mass.
- 4 K at very low pressure (VLP) for transporting the superheated helium flow coming from the distributed 1.8 K heat exchanger tubes across the sector length to the 1.8 K refrigeration units.
- 4.5 K normal saturated helium for cooling special superconducting magnets in insertion regions, superconducting acceleration cavities, and the lower sections of high temperature superconductor (HTS) current leads.
- 20 K to 300 K cooling for the resistive upper sections of HTS current leads [14].

To provide cooling at these temperature levels, the LHC cryogenic system makes use of helium in several thermodynamic states, shown in Fig. 11.4 on a pressure-temperature phase diagram.

The cryostats [15] (see Chap. 7) and cryogenic distribution line [16] combine several low-temperature insulation and heat interception techniques, which will have to be reliably implemented on an industrial scale. These include low-conduction support posts made of non-metallic glass-fibre/epoxy composite [17], low-impedance thermal contacts under vacuum for heat intercepts and multi-layer reflective insulation wrapping the some 80,000 m^2 of cold surface area below 20 K [18]. Each of these techniques was investigated and validated separately in the laboratory [19], and the complete cryostats were then modelled by thermal network analysis and optimised in standard as well as off-design operation [20]. Precision experimental measurements confirmed the soundness of the adopted design and its suitability for industrial construction [21].

Besides their primary function of intercepting beam-induced heat loads at a temperature well above that of the magnets, the beam screens also act as an intermediate-temperature baffle for the cryo-pump constituted by the 1.9 K surface of the magnet bores, thus sheltering the cold surface from synchrotron radiation, preventing desorption of the trapped gas molecules and avoiding breakdown of the beam vacuum [22] (see Chap. 12). In order to limit resistive heating as well as residual heat in-leaks to the magnets, the beam screens must operate below about 30 K. To match the available temperature levels in the existing refrigerators, they are cooled non-isothermally by a forced flow of weakly supercritical helium, between 4.6 K and 20 K, which reduces the entropic load by a factor 8 with respect to 1.9 K isothermal refrigeration. The choice of mono-phase, supercritical helium aims at avoiding the potential problems of two-phase flow in long, narrow channels. However, the strongly varying properties of helium close to the critical point may nevertheless create thermo-hydraulic instabilities, while the large aspect ratio of the cooling channels induces long control delays. These problems have been investigated both theoretically and experimentally on a full-scale test loop [23] and on prototype magnet string [24, 25], thus permitting the identification of critical parameters and the validation of the adequate steady-state and transient performance of the solution proposed [26].

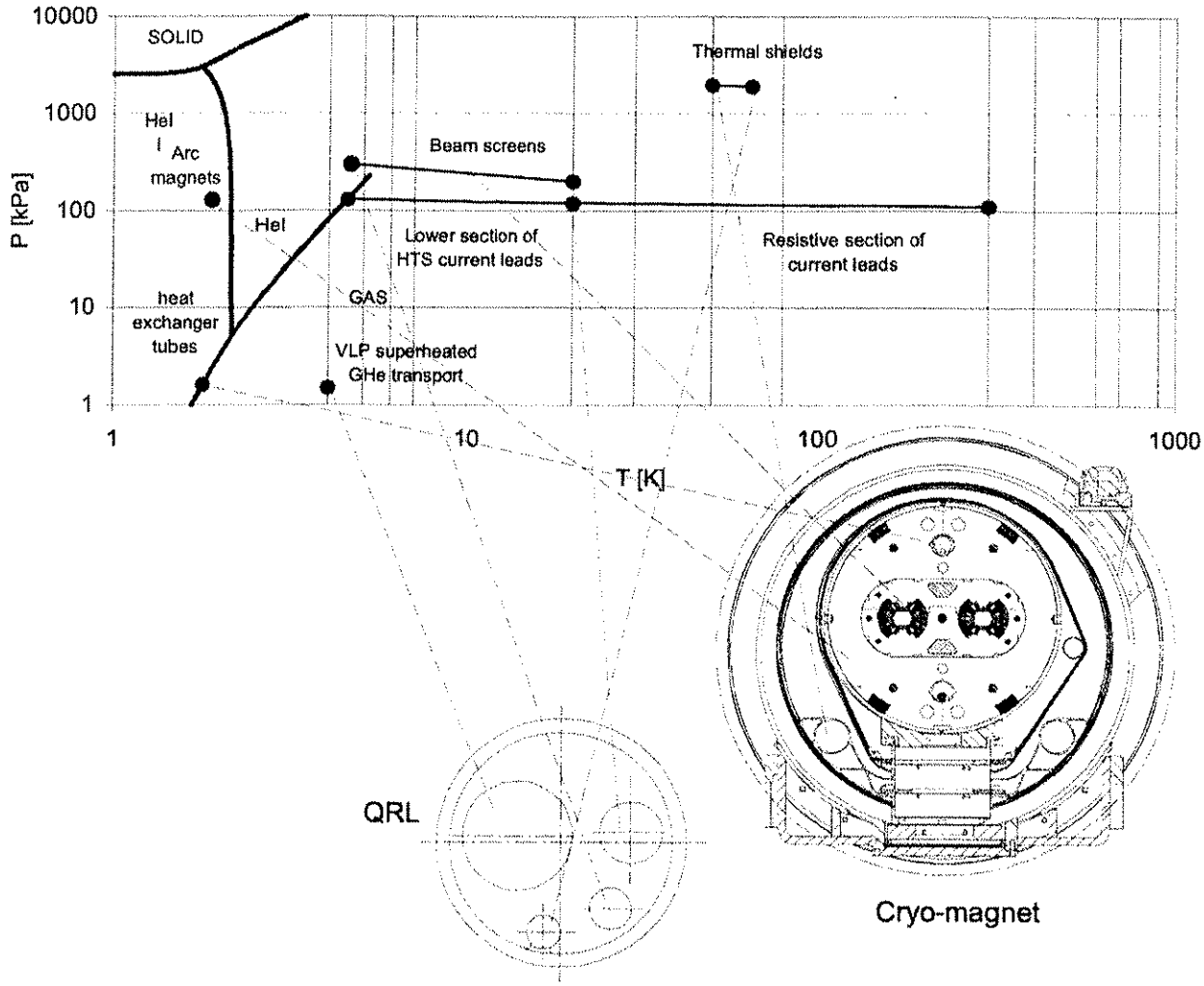

Figure 11.4 Thermodynamic states of helium in the LHC cryogenic system

11.4 HEAT LOADS

11.4.1 Steady Operation

Heat in-leaks

Static heat in-leaks are a function of the design of the cryostats and originate at the ambient temperature environment. Thermal calculations, conducted on the basis of the detailed construction drawings, precise heat in leak measurements on critical components and global measurements performed on prototype cryo-magnets, test string and a full-scale thermal model, have allowed the heat in-leaks to be evaluated. This has confirmed the technical feasibility of efficient compound cryostats [27, 28, 29, 30, 31, 32], housing long superconducting magnets operating in superfluid helium. Tab. 11.1, 2 & 3 give the steady-state heat in-leaks in standard cells, arcs, dispersion suppressors (DS), long straight sections (LSS), QRL sectors and associated distribution equipments.

Table 11.1: Distributed static heat in-leaks in a standard cell [W m^{-1}] (no contingency)

Temperature level	50-75 K	4.6-20 K	1.9 K LHe	4 K VLP GHe
Magnet side	4.5	0.14	0.19	0
QRL side	3.2	0.09	0.02	0.11

Table 11.2: Static heat in-leaks in standard cell, arc, DS and LSS (Magnet side) (no contingency)

Temperature level	50-75 K [W]	4.6-20 K [W]	4.5 K LHe [W]	1.9 K LHe [W]	20-300 K [g/s]
Cell	482	14.0	-	20.4	-
Arc (23 cells)	11090	323	-	470	-
DS 1, 2, 4, 5, 6 & 8 *	788	28	0	34	-
DS 3 & 7 *	794	28	0	34	-
LSS 1 & 5 *	658	15	73	33	9.0
LSS 2 & 8 *	791	14	86	45	9.0
LSS 3 & 7 *	130	3	19	7	1.5
LSS 4 *	508	5	313	11	8.7
LSS 6 *	232	0	49	7	6.1

* Half insertion

Table 11.3: Static heat in-leaks in distribution system (no contingency)

Temperature level		50-75 K [W]	4.6-20 K [W]	4.5 K LHe [W]	1.9 K LHe [W]	4 K VLP GHe [W]
Sector 1-2	QRL	10325	245	11	51	311
	Other *	500	190	-	-	45
Sector 2-3	QRL	9894	235	9	49	296
	Other *	95	67	-	-	29
Sector 3-4	QRL	9853	237	12	43	296
	Other *	156	93	-	-	34
Sector 4-5	QRL	10353	247	14	45	310
	Other *	746	198	-	-	34
Sector 5-6	QRL	10300	245	10	45	309
	Other *	586	183	-	-	34
Sector 6-7	QRL	9723	231	6	42	294
	Other *	156	93	-	-	34
Sector 7-8	QRL	9740	232	7	48	294
	Other *	156	93	-	-	34
Sector 8-1	QRL	10733	248	10	51	315
	Other *	586	183	-	-	34

* Interconnection boxes, local transfer lines and vertical transfer lines

Resistive heating

Resistive heating occurs in the non-superconducting sections of the magnet excitation circuits, essentially in splices of the superconducting cables and in current leads [33]. The heat load due to magnet splices has to be taken by the cold-mass helium bath. The residual resistances per splice assumed for heat load evaluation purposes depend on the type of circuit and on its location (Tab. 11.4). Resistive heating in current leads has to be taken by dedicated cooling circuits and helium baths in the electrical distribution feed boxes (DFBs). Tabs. 11.5 and 11.6 give the steady-state resistive heating in standard cells, arcs, dispersion suppressors (DS) and long straight sections (LSS) for nominal and ultimate operating conditions (see Sec. 11.6.1).

Table 11.4: Residual splice resistance assumed for heat load evaluation purposes [nΩ]

Magnet circuit	Nominal current [A]	Location		
		Inside magnet	Interconnection	
			Main	Others
MB	11850	0.5	0.6	-
MQ	11870	0.5	0.6	-
MCB	55	65		10
MS	550	1.4	7	10
MCBC	100	10	-	10
MCBR	100	10	-	10
MCBY	100	10	-	10
MCBXH	550	1	7	10
MCBXV	550	1	7	10
MQS	550	13	7	10
MQTL	550	1.4	7	10
MO	550	1.4	7	10
MCS	550	1.4	7	10
MCD	550	1.4	7	10
MCO	100	10	-	10

Table 11.5: Distributed steady-state resistive heating heat load in a standard cell [W.m^{-1}]

Temperature level	50-75 K	4.6-20 K	1.9 K LHe
Resistive heating nominal	0.02	0.003	0.10
Resistive heating ultimate	0.062	0.008	0.10

Table 11.6 : Steady-state resistive heating in cell, arc, DS and LSS

Temperature level		50-75 K [W]	4.6-20 K [W]	4.5 K LHe [W]	1.9 K LHe [W]	20-300 K [g/s]
Cell	nominal	2	0.3	-	11	-
	ultimate	7	1	-	11	-
Arc	nominal	43	7	-	248	-
	ultimate	153	19	-	251	-
DS 1, 2, 4, 5, 6 & 8 *	nominal	7	1	-	19	-
	ultimate	27	3	-	20	-
DS 3 & 7 *	nominal	7	1	-	18	-
	ultimate	27	3	-	19	-
LSS 1 & 5 *	nominal	1	0	24	3	8.0
	ultimate	3	0	24	3	8.0
LSS 2 & 8 *	nominal	1	0	26	3	8.3
	ultimate	3	0	25	4	8.3
LSS 3 & 7 *	nominal	1	0	2	1	2.4
	ultimate	3	0	2	1	2.4
LSS 4 *	nominal	1	0	16	2	8.5
	ultimate	3	0	16	2	8.5
LSS 6 *	nominal	-	-	11	1	6.3
	ultimate	-	-	11	1	6.3

* Half insertion

Beam-induced loads

Beam-induced heat loads are deposited in the cryo-magnets through several processes and by the circulating and colliding proton beams themselves. They depend strongly on the energy, the bunch intensity, number and length of the circulating bunches as well as on the luminosity in collision (Tab. 11.7). The various beam-induced loads are:

- synchrotron radiation from the bending magnet, mostly absorbed by the beam screens,
- resistive dissipation of beam image currents induced in the resistive walls and geometrical singularities of the beam channel,
- impingement of photo-electrons accelerated by the beam potential ("electron clouds"), mostly adsorbed by the beam screen,
- nuclear inelastic beam-gas scattering corresponding to a continuous distributed loss of particles from the circulating beam, mostly absorbed by the cold mass helium bath; this value is expected to decrease with running time due to improvement of the vacuum by beam cleaning,
- continuous random loss of particles escaping the collimation system, mostly absorbed by the cold mass helium bath over a length of a few tens of metres corresponding to the region of aperture restriction; in nominal conditions, the maximum random loss of particles per arc is 33 W with a maximum spread per cell of 3.4 W; in nominal conditions, the particle losses in the dispersion suppressor of the cleaning insertion (IR3 and IR7) is 33 W per half insertion.
- Losses of secondary particles, mostly absorbed at 1.9 K in the magnet cold-mass helium bath close to the high-luminosity experimental areas (inner triplet and dispersion suppressor cold masses); in nominal operation in a high-luminosity insertion secondaries are expected to deposit 182 W per half insertion in the inner triplet and 37 W per half-insertion in the dispersion suppressor;
- RF losses in superconducting acceleration cavities; in nominal conditions, RF losses are 200 W per half-insertion.

Tab. 11.8 gives the distributed steady-state beam-induced loads in and LHC cell for nominal and ultimate conditions. Tab. 11.9 gives the steady-state beam-induced loads in standard cells, arcs, dispersion suppressors (DS) and long straight sections (LSS).

Table 11.7: Scaling laws of beam-induced loads

Beam parameter	Energy E	Bunch current I_{bunch}	Bunch number n_{bunch}	Bunch length σ_z [r.m.s.]	Luminosity L
Resistive heating	E^2	-	-	-	-
Synchrotron radiation	E^4	I_{bunch}	n_{bunch}	-	-
Image current	-	I_{bunch}^2	n_{bunch}	$\sigma_z^{-3/2}$	-
Photo-electron cloud	-	I_{bunch}^3	n_{bunch}	-	-
Beam gas scattering	-	I_{bunch}	n_{bunch}	-	-
Random particle loss		I_{bunch}	n_{bunch}		
Secondaries	E	-	-	-	L
RF losses	-	I_{bunch}^2	n_{bunch}	-	-

Table 11.8: Distributed steady-state beam-induced loads in an LHC cell [mW m^{-1}]

Mode	Nominal		Ultimate	
Temperature level	4.6-20 K	1.9 K LHe	4.6-20 K	1.9 K LHe
Synchrotron radiation	330	1	500	1
Image current	360	1	820	2
Photo-electron cloud *	890	9	3040	30
Beam-gas scattering	0.4	48	0.4	48
Random particle loss	0-0.1	0-32	0-0.3	0-48
Total beam-induced *	1580	59-91	4360	82-130

* After beam cleaning

Table 11.9: Steady-state beam-induced loads in cell, arc, DS and LSS

Temperature level		4.6-20 K [W]	4.5 K LHe [W]	1.9 K LHe [W]
Cell	Nominal	169	-	6.3-9.7
	Ultimate	466	-	8.8-13.9
Arc	Nominal	3880	-	211
	ultimate	10740	-	284
DS 1 & 5 *	nominal	319	-	48
	ultimate	915	-	109
DS 2 & 8 *	nominal	319	-	12
	ultimate	914	-	18
DS 3 & 7 *	nominal	354	-	44
	ultimate	1037	-	70
DS 4 & 6 *	nominal	319	-	11
	ultimate	914	-	16
LSS 1 & 5 *	nominal	45	10	193
	ultimate	118	22	440
LSS 2 & 8 *	nominal	37	6	41
	ultimate	100	12	95
LSS 3 & 7 *	nominal	21	1	0
	ultimate	61	1	1
LSS 4 *	nominal	31	214	2
	ultimate	87	529	2
LSS 6 *	nominal	3	7	-
	ultimate	4	14	-

* Half insertion

11.4.2 Transient Modes

Ramping the magnetic fields up and down will generate additional transient heat loads in the superfluid helium due to the eddy currents developed in the superconducting cables and in the mechanical structure of the magnets. Raising the current to its nominal value in 1200 s is expected to dissipate 480 J of energy per metre length of main dipole. This represents a power of approximately 0.4 W per metre. In the case of a resistive transition or in an emergency, it must be possible to ramp the full current down to zero in 80 s. This will result in an energy dissipation of 3000 J per metre of magnet. This represents a power of approximately 38 W per metre.

The only practical way to absorb these transient heat loads and keep the temperature below 1.9 K during ramping-up and below the lambda line during fast ramp-down is to make use of the heat capacity of the liquid helium contained in the magnet cold-masses. About 15 l of liquid helium per metre length is sufficient to cope with the loads to be buffered.

11.5 COOLING SCHEME

11.5.1 Arc and Dispersion Suppressor Cooling Loops

The corresponding flow-scheme of a lattice cell appears in Fig. 11.5. The first level of thermal shielding and heat interception in the magnet cryostats and the distribution line is provided by forced circulation of gaseous helium under pressure at a temperature between 50 K and 75 K, through headers E and F respectively. The cryo-magnets operate in a static bath of pressurised helium II (grey area), cooled by heat exchange with flowing saturated helium II. Low-pressure vapour resulting from the vaporisation of the saturated helium II is returned to the refrigerator by header B. Supercritical helium is distributed by header C and is used to; a) fill the cryo-magnet baths, b) produce - after subcooling and Joule-Thomson expansion -

the saturated helium II flowing in the full cell length heat exchanger tube and c) feed line C' that cools the cold heat intercepts in the support posts at about 5 K, in series with the beam screens that operate between about 5 K and 20 K. The resulting gaseous helium is returned to the refrigerator by header D.

The large, but finite bulk thermal conductivity of static pressurised superfluid helium has been successfully applied for cooling devices below 2 K and transporting their heat loads over distances of up to a few tens of metres. Cooling the kilometre-long strings of magnets in the LHC sectors within a narrow temperature range, say 0.1 K, is however beyond the capability of helium-II thermal conduction alone [34]. In order to maintain the furthest magnet of each sector below 1.9 K, each 106.9 m-long LHC cell is composed of a single bath of static pressurised superfluid helium, cooled from a quasi-isothermal heat sink in the form of a bayonet heat exchanger running through the magnet string [35] and in which the latent heat of a stratified two-phase flow of saturated helium II absorbs the applied heat load, about 0.4 Wm^{-1} in the LHC arc.

The performance of such a scheme critically depends on the thermo-hydraulic behaviour of two-phase helium II flowing in quasi-horizontal tubes: this has been the subject of theoretical modelling and experimental studies at CERN [36] and CEA Grenoble (France) [37, 38, 39]. These studies have demonstrated that over a large range of vapour quality, most of the tube cross-section is occupied by the vapour flow, which then controls the overall pressure drop. For vapour velocities of up to a few m s^{-1}, the drag between the two phases remains small, so that the liquid flows separated from the vapour, almost as if in single phase and open channel. In this condition, the heat transfer is mainly controlled by the wetted area inside the tube, which can be adequately predicted by simple models for engineering purposes. Other important factors controlling the heat transfer across the tube wall are the conductivity of the tube material and the Kapitza thermal resistance at the solid-liquid interfaces [40]. By using a 53.4 mm inner diameter tube of OFHC copper with a wall thickness of 2.3 mm, the total transverse impedance when fully wetted can be kept down to about 0.3 mK m^2 W^{-1}, and the practical heat transfer capability of the partially wetted bayonet heat exchanger is thus typically a few mK m W^{-1}. The final validation of this cooling scheme was performed on a full scale magnet string which has accumulated about 8'000 hours operation at 1.9 K, successfully undergoing all possible nominal and off-design operating conditions [41]. This full scale working model of a LHC cell enabled the dynamic control aspects to be addressed. These are particularly demanding on this system characterised by strong non-linearities - including initial inverse response - and long time delays induced by the low velocity of the liquid flow. To cope with this, advanced automation techniques [42] such as linear model-based predictive control [43] is considered as an alternative to standard PID controllers.

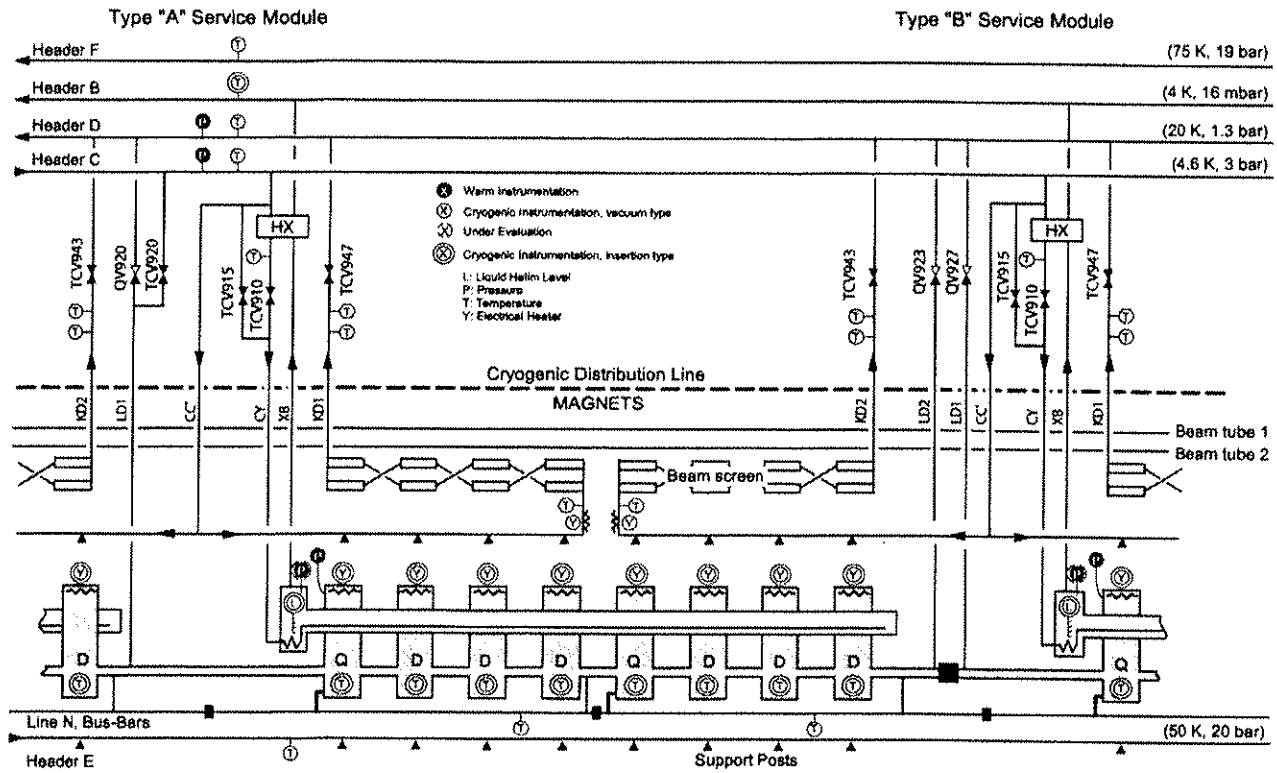

Figure 11.5: Cryogenic flow-scheme and instrumentation of a LHC lattice cell

Cryogenic sub-sectorisation

Within a sector the tunnel slope results in elevation differences up to 50 m, which would develop a large hydrostatic head of up to 70 kPa (700 mbar) in the corresponding string of cold masses, if the cold masses were to remain hydraulically connected. Depending on the pressure normalisation point, this hydrostatic head could increase the helium leak rate across the seat of cold safety relief valves and consequently the heat load on the cold-masses. It could also create sub-atmospheric pressure in some part of the magnet string with risk of the pollution by air in-leaks. To limit the enhancement of valve leak rate and to avoid parts of the cold mass going sub-atmospheric, the cold mass volume within a sector has been sub-sectorised by adding hydraulic restrictions every two or three cells (Fig. 11.6). These hydraulic restrictions also restrict the propagation of resistive transition, caused by warm helium flow from magnet to magnet, to the magnets of one hydraulic sub-sector.

The cryogenic vacuum is also sub-sectorised in order to limit the extent of a degraded vacuum zone created by a possible helium leak of the internal circuit. On the cryo-magnet side, vacuum barriers are integrated in the Short Straight Section cryostats every two cells. On the cryogenic distribution line side, vacuum barriers are integrated every four cells. The jumper connection between QRL and magnet cryostats always contains a vacuum barrier.

Together, these two sub-sectoring schemes for cold mass and insulation vacuum allow a limited length of cryo-magnets (up to 600 m) to be warmed up and short interventions on the cold-mass components (splices, diodes, 60 A current leads...) to be made. In this case, the warm-up and re-cool-down time is reduced by a factor three with respect to the normal full sector warm-up and cool-down times. However, for removing cryo-magnets, which require the opening of cold bores or bayonet heat exchangers or main headers, the complete sector has to be warmed up and re-cooled.

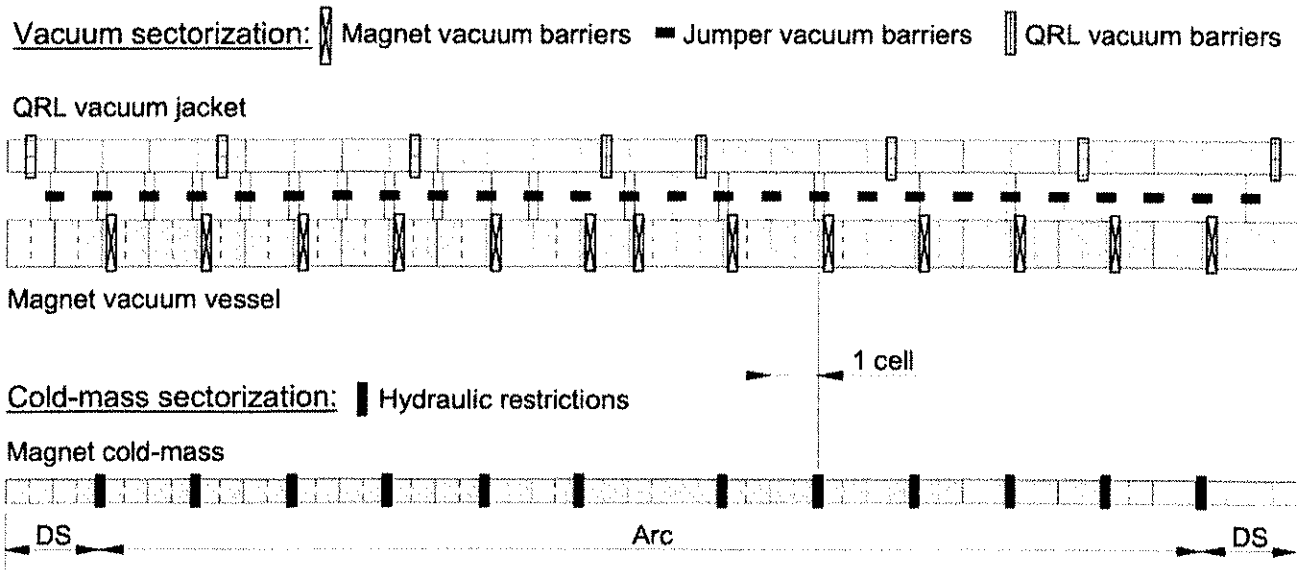

Figure 11.6: Cold-mass and cryogenic vacuum sub-sectorisation

11.5.2 Matching Section Cooling Loops

The special magnets of the matching section (see Chap. 8), which do not require cooling at 1.9 K for field strength and heat extraction, operate in baths of saturated helium I at 4.5 K. The cryostats are referred to as standalone or semi-standalone, because they generally never consist of more than one quadrupole or dipole magnet cryostat plus correctors (standalone) or a quadrupole and dipole magnet cryostat in series plus correctors (semi-standalone). The quadrupole and dipole magnets themselves are very diverse, corresponding to their specific functions in the LHC machine optics. Although the detailed cryogenic schemes have to be in accord with this diversity they all share the characteristics depicted in Fig. 11.7. There is an actively cooled heat intercept at about 70 K. The cold mass is filled and the liquid level actively maintained by helium supply from QRL header C. The vapour outlet is into QRL header D, whose pressure of about 0.13 MPa

(1.3 bar) directly determines the corresponding magnet's saturated liquid bath temperature at about 4.5 K. The vapour outlet is always in open connection to QRL Header D, thereby eliminating the need for a safety valve. If a magnet experiences a resistive transition, the helium is expelled directly into header D. The open connection does, however, require collective warm-up of all 4.5 K operated magnets of the corresponding sector when header D becomes exposed to atmosphere, e.g. due to repair. In nominal operation the beams screens are actively maintained in a temperature range of 5 K to 20 K by a flow of supercritical helium at about 0.3 MPa (3 bar) taken from header C and exiting into header D. To prevent unbalanced cooling of the apertures, the beam screen cooling circuits are always in series.

Instrumentation for temperature and/or pressure of the helium streams is placed in the QRL service module whenever possible. The liquid level gauge and temperature sensor in the magnet cryostat are extractable which eliminates the need for installing redundant ones. The temperature sensor is required only for monitoring the cool-down speed. Furthermore, there is a warm-up heater inside the cold mass and a heater plus its corresponding temperature sensor on the beam screen cooling circuit inlet. In nominal operation the beam screen heater serves to prevent density wave oscillations in the beam screen flow.

The standalone and semi-standalone magnets receive their powering through a dedicated interface which in the majority of cases connects to a local current feed box (DFBM) or else to a superconducting link (DSL). The electrical connection is via a special feed-through that as well as providing electrical insulation also hydraulically separates the magnet's helium bath from the helium in the DFBM and/or DSL. All necessary cryogens for the DFBM and part of the cryogens for the DSL are routed through the magnet cryostat to the QRL.

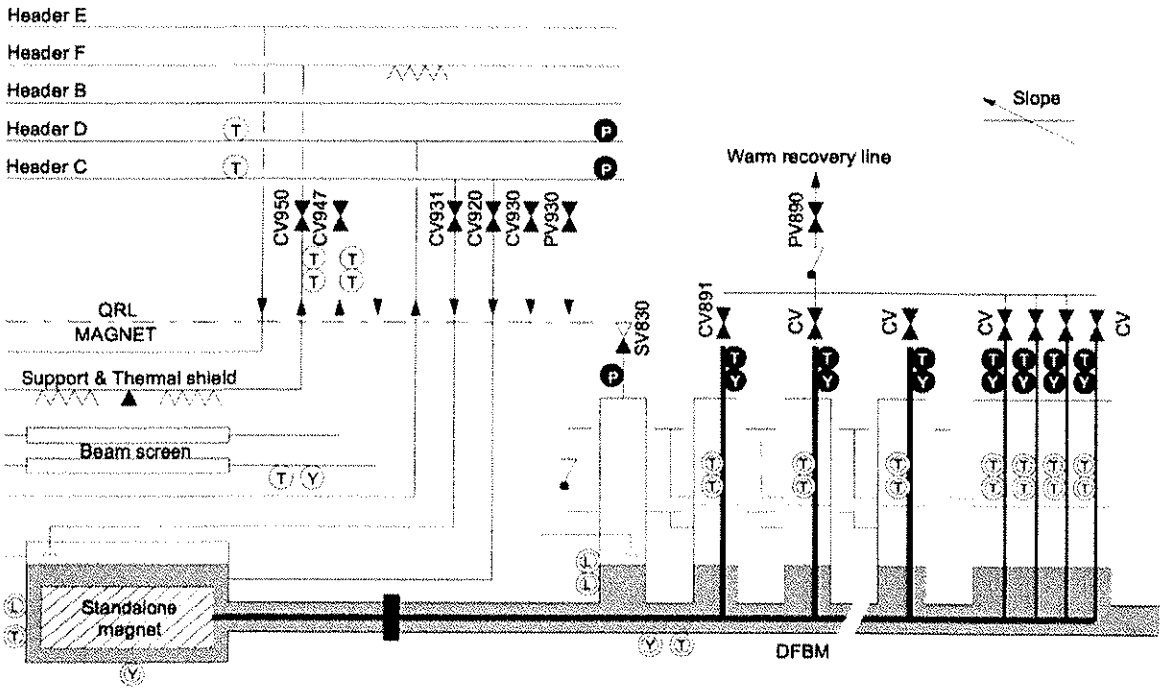

Figure 11.7: Cryogenic flow-scheme and instrumentation of a 4.5 K standalone magnet

11.5.3 Inner Triplet Cooling Loops

The inner-triplet quadrupoles in the insertion regions are subject to dynamic heating from secondaries of up to 10 W m^{-1} at each of the high luminosity insertions 1 and 5 and up to about 2 W m^{-1} at the low luminosity insertions 2 and 8 from the particle interactions. Although this represents a much higher heat load than the magnets in the arc and DS receive, they can be cooled by a scheme similar to the standard cell. A large-diameter, corrugated copper heat exchanger tube inside a stainless steel pipe will be placed outside of and parallel to the cold mass in the cryostat [44]. A full-scale experimental set-up modelling this cooling loop, designed and built by FNAL Batavia (U.S.A.), has validated the cooling method [45]. The present implementation is more than sufficient for nominal LHC luminosity. For ultimate luminosity the system needs to be upgraded. The bottlenecks are mostly in the longitudinal conduction path from the magnet coil to the overcrowded interconnect and then to the parallel heat exchanger.

The superconducting single aperture beam separation dipoles D1 installed in the low luminosity insertions will operate at 1.9 K and will be cooled almost exactly as the arc and DS magnets. The only notable difference is that because of space limitations, two parallel bayonet heat exchangers of straight copper pipe but of smaller diameter will be used instead of a single one. The choice of operating temperature is mainly determined by maximum aperture requirements. Using a RHIC type dipole (originally designed to operate in forced flow supercritical helium of about 5 K) at 1.9 K, it was possible to safely increase the beam pipe diameter to the mechanical maximum.

Fig. 11.8 shows the cryogenic flow-scheme and instrumentation for a high luminosity insertion inner triplet.

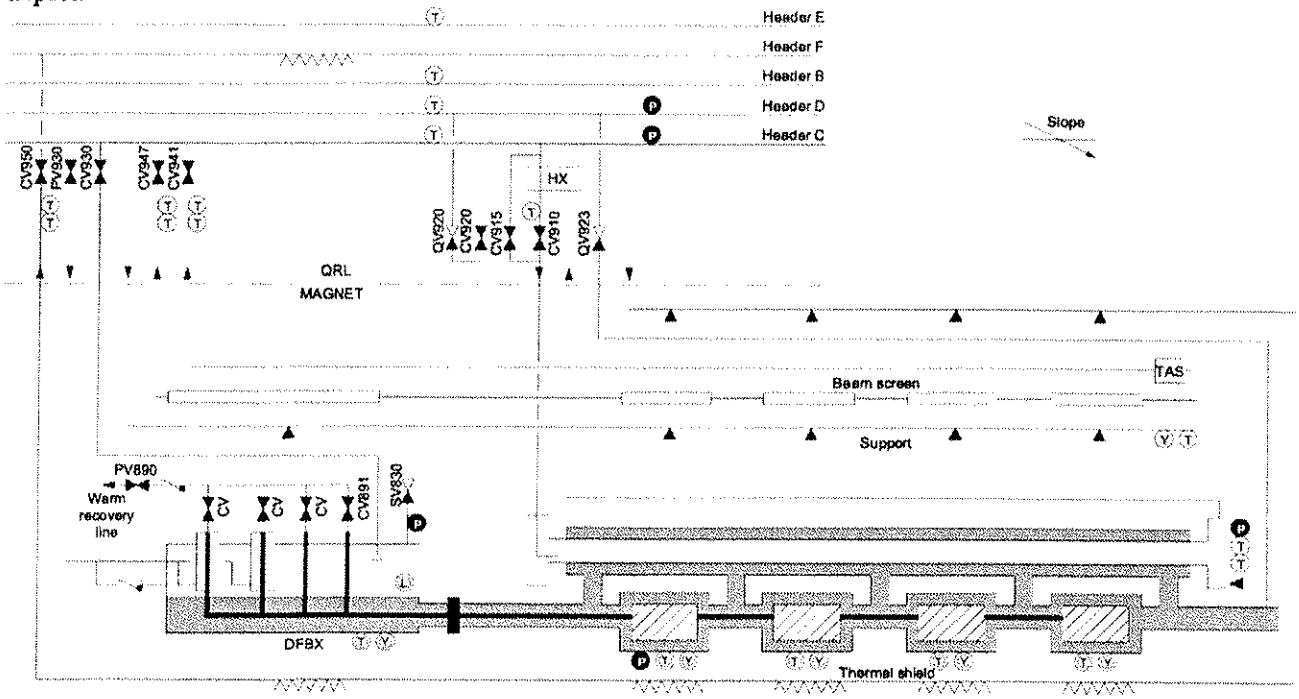

Figure 11.8: Cryogenic flow-scheme and instrumentation of an inner triplet cell

11.5.4 Electrical Distribution Feed Box and RF Cavity Cooling Loops

The electrical distribution feed boxes (DFBAs, DFBMs, DFBLs and DFBXs) (see Chap. 9) and the RF cavities (see Chap. 6) are low design pressure equipment (0.35 MPa for the DFBs and 0.25 MPa for the RF cavities) connected to high design pressure (2 MPa) equipment and cryogen supplies. This peculiarity has specific consequences for their cryogenic implementation. A typical DFB and the RF flow scheme are given in Figs. 11.9 and 11.10.

With the exception of the DFBMs all DFBs have an actively cooled 70 K thermal screen. The lower part of the DFB current leads [46] and busbar bundles are in saturated liquid helium baths which have a common liquid level regulation. The upper, resistive part of the HTS leads is cooled by gaseous helium between 20 K and ambient temperature. Liquid for the saturated helium baths is taken from QRL header C, and vapour is returned to a collector which connects QRL header D to the 20 K gaseous helium inlet of the HTS leads. A non return valve is placed between this collector and the saturated liquid bath to prevent high temperature gas inadvertently entering the liquid bath space. The 20 K helium supply for the resistive part of the HTS leads consists of the bath evaporation complemented with helium from QRL header D. The helium is returned at ambient temperature to the warm recovery line. These flows are controlled at ambient temperature by lead specific valves. To protect the DFBs from overpressure from header D a pressure controlled shut-off valve is placed in the connection to QRL header D. Protection from overpressure in the warm recovery line is provided by a non-return valve. Protection from pressure differences over the control valve in excess of 50 kPa (500 mbar) is provided by a pressure control valve in the warm recovery line connection. Discharge of any helium contained in enclosed DFB spaces will be into the LHC tunnel. In the event of header D pressure shut-off valve failing, the flow rate from header D into the tunnel and the DFB pressure build up are restricted by design of the connecting piping.

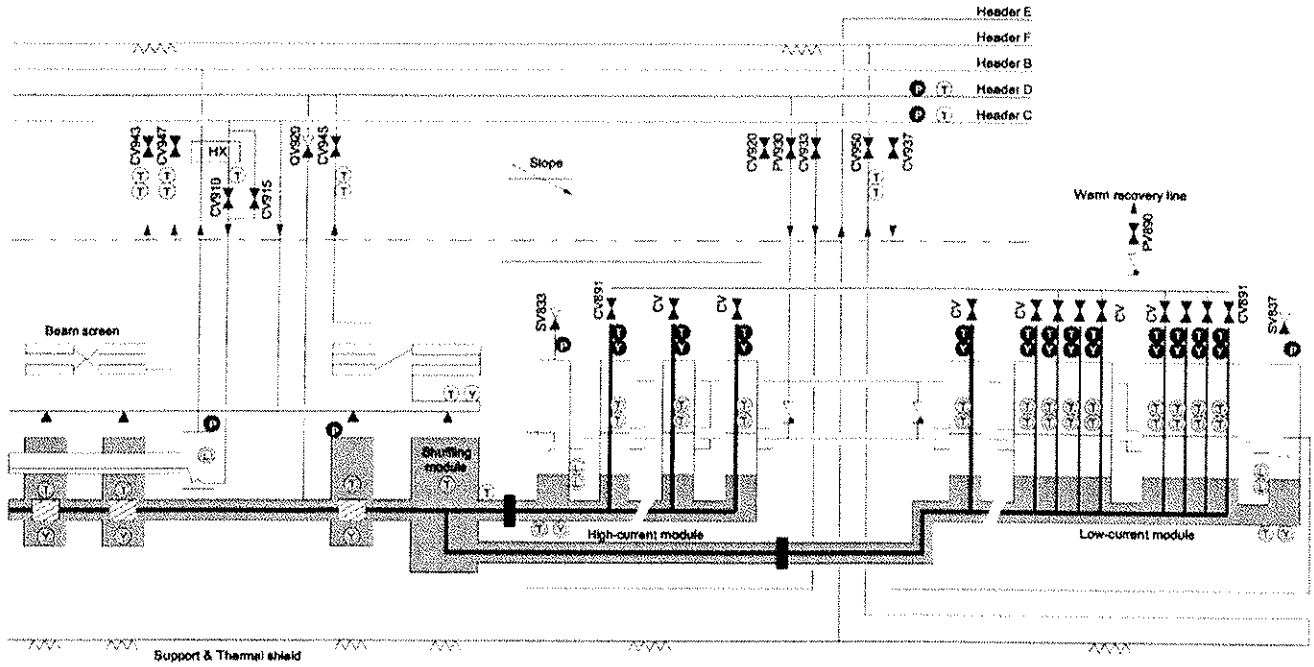

Figure 11.9: Cryogenic flow-scheme and instrumentation of a DFBA type electrical distribution box

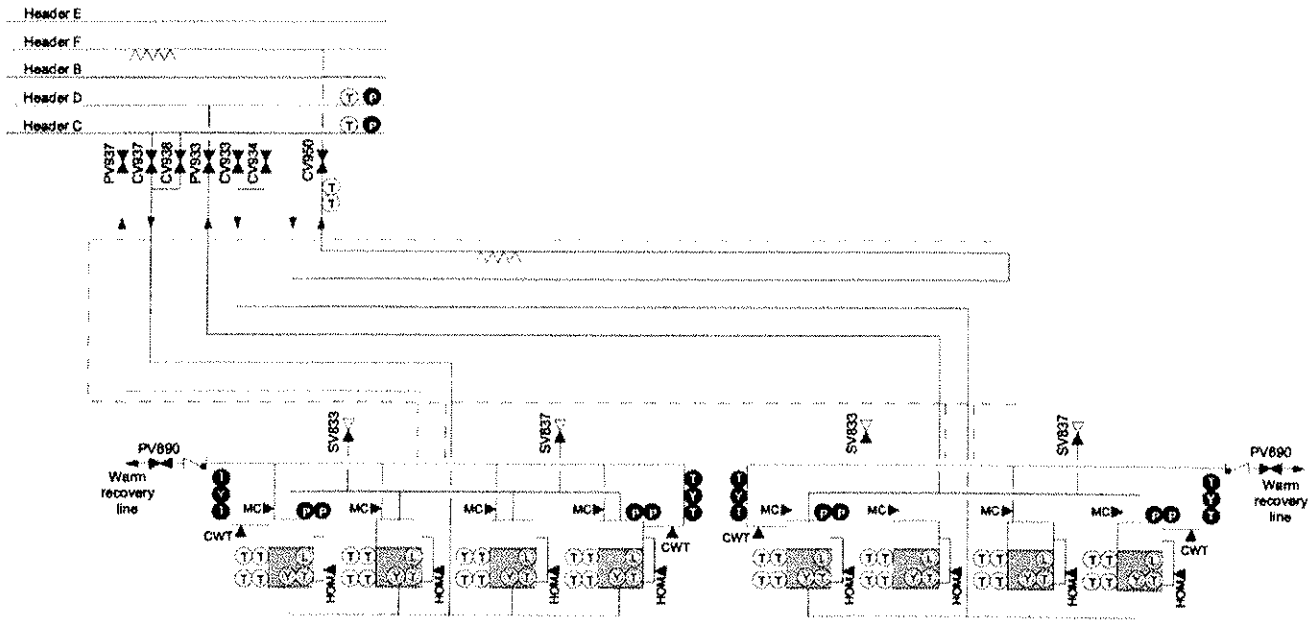

Figure 11.10: Cryogenic flow-scheme and instrumentation of an RF cavity assembly

11.6 OPERATING MODES

11.6.1 Steady-state Operation

Four steady-state operating modes and their corresponding requirements for the cryogenic operation of the machine are considered:

- 'nominal operation' at 7 TeV beam energy, 2 × 0.582 A beam current and 10^{34} cm^{-2} s^{-1} luminosity.

- 'ultimate operation' at 7 TeV beam energy, 2 × 0.86 A beam current and $2.5 \cdot 10^{34}$ cm^{-2} s^{-1} luminosity, assuming a two-fold reduction of residual pressure in the beam channel over long term operation.
- 'low beam intensity operation', characterised by negligible beam-induced heat loads in the magnets but still with full beam energy and thus full excitation current in the magnets.
- 'injection standby' characterised by negligible resistive dissipation and beam-induced heat loads in the magnets.

Cryogenic cooling powers required for each operation mode are given in Tab. 11.10. For efficient operation, large turndown capability is required for the refrigeration plants.

From Tab. 11.10, two sector types are identified. The sectors 1-2, 4-5, 5-6 and 8-1, which include high-luminosity insertions are identified as 'high-load' sectors. The other sectors, less demanding in cryogenic capacity are identified as 'low-load' sectors.

The temperature profiles of the LHC sectors can be calculated with confidence for the various operation modes based on the measured performance of the cooling loop (Fig. 11.11). This shows that the demanding requirement of 0.1 K in nominal operation between the furthest cryo-magnet and the sector refrigerator can be met.

Table 11.10: Cryogenic capacity requirements for each steady-state operating mode (no contingency)

Temperature level		50-75 K [kW]	4.6-20 K [W]	4.5 K LHe [W]	1.9 K LHe [W]	4 K VLP GHe [W]	20-300 K [g/s]
Injection Standby	Sector 1-2	24.9	843	170	667	356	18
	Sector 2-3	23.6	698	114	639	325	11
	Sector 3-4	23.3	717	344	599	330	10
	Sector 4-5	24.9	844	400	627	344	18
	Sector 5-6	24.4	822	132	623	343	15
	Sector 6-7	22.9	706	74	594	328	8
	Sector 7-8	23.5	721	112	638	328	11
	Sector 8-1	25.4	839	169	667	349	18
Low beam-intensity	Sector 1-2	25.0	852	220	959	356	34
	Sector 2-3	23.6	707	142	928	325	21
	Sector 3-4	23.4	726	362	887	330	21
	Sector 4-5	25.0	853	440	918	344	34
	Sector 5-6	24.5	831	167	913	343	29
	Sector 6-7	23.0	715	87	881	328	16
	Sector 7-8	23.5	730	140	927	328	21
	Sector 8-1	25.5	848	197	956	349	29
Nominal	Sector 1-2	25.0	5450	236	1460	356	34
	Sector 2-3	23.6	5320	149	1240	325	21
	Sector 3-4	23.4	5330	577	1160	330	21
	Sector 4-5	25.0	5450	664	1380	344	34
	Sector 5-6	24.5	5400	184	1380	343	29
	Sector 6-7	23.0	5290	95	1150	328	16
	Sector 7-8	23.5	5340	147	1240	328	21
	Sector 8-1	25.5	5450	213	1460	349	29
Ultimate	Sector 1-2	25.0	13600	254	1910	356	34
	Sector 2-3	23.6	13600	155	1400	325	21
	Sector 3-4	23.4	13600	892	1260	330	21
	Sector 4-5	25.0	13600	991	1770	344	34
	Sector 5-6	24.5	13500	203	1760	343	29
	Sector 6-7	23.0	13500	102	1250	328	16
	Sector 7-8	23.5	13600	153	1400	328	21
	Sector 8-1	25.5	13600	231	1900	349	29

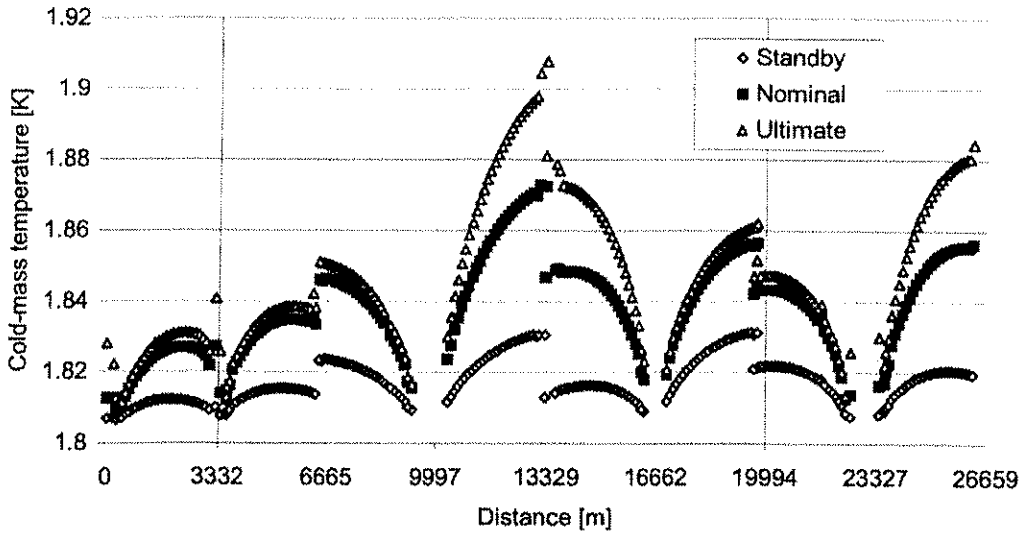

Figure 11.11: Calculated temperature profiles of LHC magnets

11.6.2 Transient Modes

Four transient modes are considered: cool-down from 300 K to 4.5 K, magnet filling and cool-down from 4.5 K to 1.9 K, resistive transition and warm-up from 4.5 K to 300 K.

Cool-down from 300 K to 4.5 K

Cooling of the magnets from ambient temperature is carried out by forced circulation of gaseous helium. To be able to cool-down the cold mass of a LHC sector in a maximum time of 15 days, liquid nitrogen pre-coolers with a maximum capacity of 600 kW are installed in each refrigeration plant. They are either integrated into the new 4.5 K refrigerator cold-boxes or added as auxiliary equipment to the upper cold-boxes (in the 4.5 K refrigerators recovered from LEP). These pre-coolers progressively decrease the temperature of a 770 g s^{-1} gaseous helium flow, with a maximum temperature difference between the supply and return streams of 150 K. The pre-coolers produce effective refrigeration capacity down to 80 K. Below this temperature, the cool-down capacity is provided by the turbo-expanders of the refrigerators. To avoid a longitudinal thermal gradient in the cryo-magnet structure higher than 75 K, a progressive initial ramp-down on the inlet temperature is applied. Normal cool-down is performed using one refrigeration plant (Fig. 11.12). Fast cool-down, reducing by two the normal cool-down time, can also be performed by using two refrigeration plants coupled to one sector, except in sector 2-3 [47, 48].

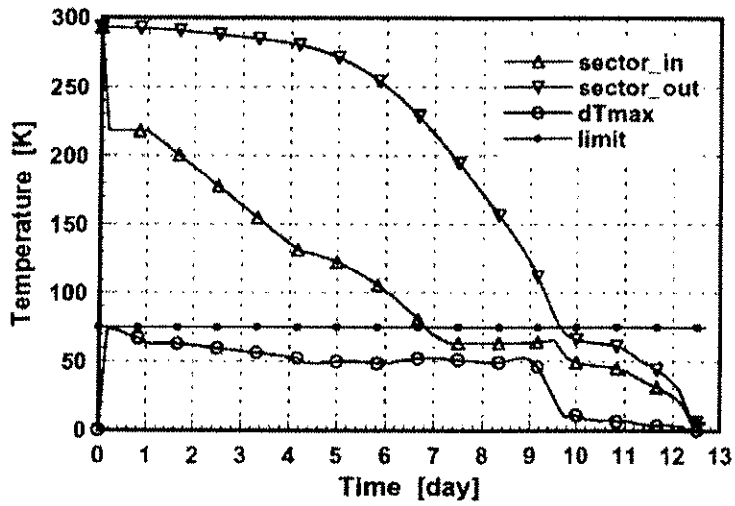

Figure 11.12: Normal cool-down from 300 K to 4.5 K of LHC sectors

Magnet filling and cool-down from 4.5 K to 1.9 K

The filling of the magnets is performed in two steps. The first step uses the liquefaction capacity of the 4.5 K refrigerators to partially fill the cold mass volume with saturated helium at 4.5 K up to the level determined by the position of the highest interconnecting pipe. The filling of the remaining dead volume is performed using the 1.8 K refrigeration unit which condenses the remaining gaseous helium at constant pressure of about 0.1 MPa (1 bar).

Once the magnets are filled, the cool-down to 1.9 K is performed using the 1.8 K refrigeration units. Depending of the number of refrigeration plants coupled to one sector, normal or fast operation can be performed (Fig. 11.13) as is the case for the cool-down from ambient,.

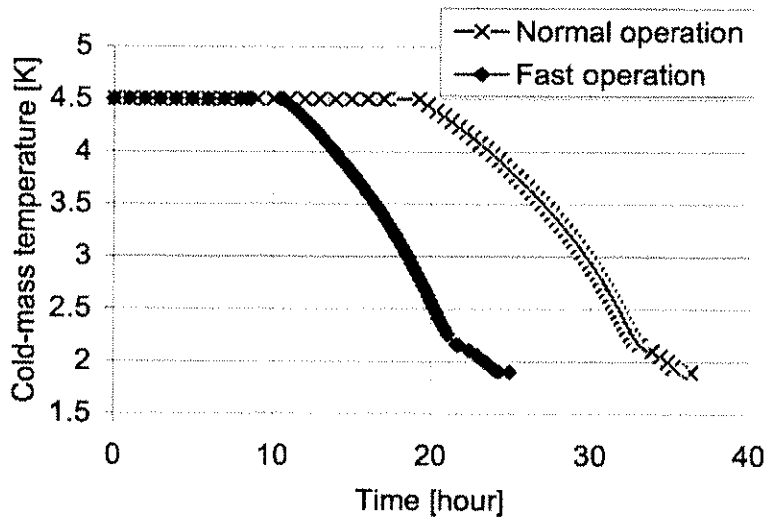

Figure 11.13: Magnet filling and cool-down down from 4.5 K to 1.9 K

Resistive transition

In the first few tenths of a second following the transition of a dipole magnet, the 500 kJ m^{-1} stored magnetic energy is dissipated in the resistive windings, and part of it eventually released to the static helium in the cold mass on a much longer time scale. To contain the resulting pressure rise within the 2 MPa (20 bar) design pressure of the helium enclosure, helium has to be discharged at high flow-rate into header D, normally kept cold by the 20 K bleed from the beam-screen cooling circuits. The large acceptance of this header enables it to perform as a temporary buffer storage, thus avoiding the need for further helium discharge in case of resistive transitions affecting limited stretches of magnets (one to several lattice cells) [49,50]. For generalised resistive transitions, cold gaseous helium is discharged and recovered, though at much lower flow-rates, from header D into the 2 MPa (20 bar) gas storage vessels at ambient temperature which are located in the service areas at the surface areas around the LHC circumference [51].

The discharge of helium from the magnet cold mass is made possible, every 106.9 m, by some 400 cold safety relief valves, normally closed, with their inlet under pressurised helium II. Such components, which are not available off-the-shelf, had to be developed by industry following CERN specifications [52] and their performance assessed on a specially designed test facility [53].

The thermo-hydraulic consequences of resistive transitions in the cryo-magnets may constitute a significant, but not exclusive source of risk to personnel or equipment. Its mechanism however is well understood and the cryogenic infrastructure is designed to cope with it. A systematic risk assessment in the cryogenic system, based on an analysis of the occurrence of accidental events and the gravity of their consequences, has been recently conducted [54, 55, 56, 57, 58]. It confirmed the strong contribution to the intrinsic safety of the specific design features of the system, such as the large acceptance of the cold recovery header D, the absence of liquid nitrogen underground and of helium pumps in the cooling loops.

The re-cool-down time after a resistive transition of limited stretches of magnet is between 2 and 6 hours (Fig. 11.14).

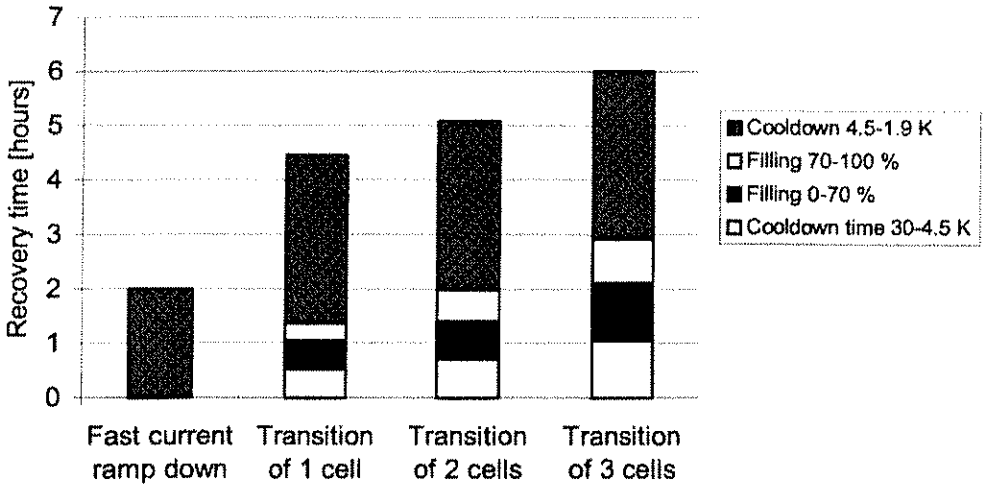

Figure 11.14: Magnet re-cool-down after a limited resistive transition

Warm-up from 4.5 K to 300 K

Warming of the magnets to ambient temperature is carried out by forced circulation of gaseous helium. To be able to warm-up the huge cold mass of a sector in a maximum time of 15 days, electrical heaters with a maximum capacity of 600 kW are integrated into the interconnection boxes of the refrigeration plants. These heaters progressively increase the temperature of a 770 g s^{-1} gaseous helium flow with a maximum temperature difference between the supply and return streams of 150 K. To avoid longitudinal thermal gradients in the cryo-magnet structure higher than 75 K, a progressive initial ramp-up on the inlet temperature is applied. Normal warm-up uses one refrigeration plant (Fig. 11.15). With the exception of sector 2-3, fast warm-up in half the normal warm-up time can also be performed by using two refrigeration plants coupled to one sector.

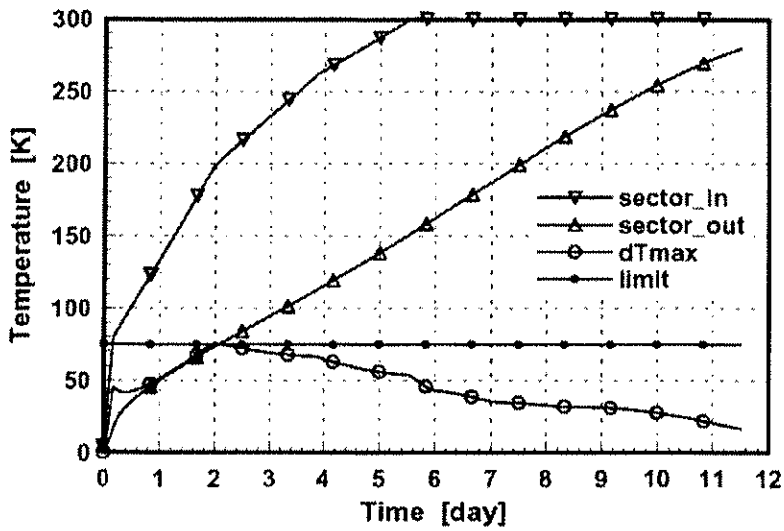

Figure 11.15: Normal warm-up of LHC sectors

11.7 CRYOGENIC DISTRIBUTION

The central nodes of the cryogenic distribution system are situated in the underground caverns. These are the cryogenic interconnection boxes (QUIs) which provide the connection between the different cryogenic sub-systems at each of the five feed-points: surface 4.5 K cold boxes (QSRB) underground 4.5 K lower cold-boxes (QURA), 1.8 K refrigeration unit boxes (QURC), and cryogenic distribution line (QRL).

The upper cold boxes of the new 4.5 K refrigerators are linked to the interconnection boxes via four vertical helium transfer lines (QPLB) passing through the main LHC shafts. These QUIs are located between 80 m and 145 m underground depending on the access point. The lower cold boxes of the refrigerators recovered from LEP and those of the 1.8 K refrigeration units are connected to the interconnection boxes via 12 underground helium transfer lines (QUL). A cryogenic distribution line (QRL) feeds helium at different temperatures and pressures the elementary cooling loops of the cryomagnets and other devices for each of the eight sectors, starting from the QUI and running all along the tunnel. The QUL, QPLB and QRL consist of three, four or five internal process pipes, hereafter referred as headers. The headers are housed in a common vacuum jacket and a common actively-cooled thermal shield. To reduce the heat in-leaks from ambient, the thermal shield and the cold supply headers are wrapped with blankets of reflective multilayer super-insulation and the supporting spacers made of fibre-glass composite materials.

The QPLB (vacuum jacket DN600) [59] are between 90 m and 190 m long and each of them has four headers (DN80 to DN150). The main part of the QPLB is a vertical straight segment between 75 and 125 m long. Because of limited accessibility and for maximum reliability, no internal or external bellows or bends have been accepted in this part. Hence, all thermal contraction is taken in a thermal compensator specified to be at ground level. For the longest line, the thermal compensator must take more than 35 cm displacement. Each header will be equipped with two horizontal angular bellows and one vertical angular bellows. The vertical part of the line has a sliding point directly below the compensator and a fixed point at the bottom 125 m below.

The QUL vacuum jacket which is connected to the 1.8 K refrigerator units (DN500) houses three headers (DN40 to DN250). The QUL vacuum jacket linked to the refrigerators recovered from LEP (DN600) houses four headers of the same dimensions as for the QPLB. Depending on the relative position of the components to connect, the length of these lines can vary from 5 m to 30 m. Dedicated shuffling boxes are needed at the interface to the cold boxes as the lines coming out of them are not grouped on a common standard interface, but in six different outlets. Each of the outlets consists of a single cryogenic line housing one or two process pipes. These shuffling boxes comprise separate single cryogenic lines as well as vacuum barrier(s), elbows and DN700 line portions necessary to bring together the different outlets in one compound transfer line which is then connected to the QUI. At the interfaces to the QUI and QURC, smaller shuffling boxes may be needed allowing for a re-arrangement of the position of the headers within the vacuum enclosure according to the orientation of the interfaces defined for CERN equipment.

The QRL sector [60] is a continuous cryostat of about 3.2 km length without any header sub-sectorisation, but divided into nine vacuum sub-sectors. A QRL sector starts at the QUI and ends at the return modules on the opposite side where the different headers are interconnected to form continuous cooling loops. The QRL, following the LHC lattice, is a repetitive pattern of pipe modules (about 100 m) and service modules (about 6.6 m), which link the QRL to the magnet cryostats once at every full cell (see Fig. 11.1). The arc is made of 22 identical cells, each of 106.9 m length. The DS is made up of four QRL cells of with lengths varying from 79 m to 93 m. The LHC lattice in each LSS is very different, with QRL cell lengths from about 10 m to 115 m. Five headers (inner diameters 80 mm to 269 mm) are housed in the QRL (outer diameter 650 mm) running along the LSS. Inside the arc and DS the supply header E is housed inside the LHC magnet cryostats while the return header F is always inside the QRL. A service module houses the subcooling heat exchanger, all cryogenic control valves for the local cooling loops, one or two cold safety relief valves as well as the necessary monitoring instrumentation. The so-called jumper connection, part of the service module, houses up to nine tappings (diameter 10 mm to 80 mm) to and from the magnet cryostats and a transverse vacuum barrier separating the QRL from the magnet string vacuum systems. All interconnecting pipes as well as the vacuum jacket are equipped with flexible elements to minimise forces applied to the precisely aligned cryo-magnets by the QRL and to allow re-alignment of the magnet strings without displacement of the QRL. In order to realign machine elements without moving the QRL, the jumper connections must be able to compensate for movements of the beam tubes relative to the QRL up to ± 25 mm in the horizontal plane and ± 50 mm in the vertical direction.

Due to different cryogenic users and flow-scheme peculiarities, 44 different types of service modules are required. Most of the variants are inside the LSS.

A QRL sector comprises about 240 straight pipe elements, 40 fixed point/vacuum barrier elements, 37 service modules, 1 test module (used for reception test only), one return module, two to three doglegs, two elbows and 320 interconnections (including about 400 compensation units). A standard pipe module consists of eight straight pipe elements (about 11.3 m), one fixed point element (about 6.6 m) located in the

centre and compensation units. Different QRL cell lengths and routing singularities (e.g. departure from the LHC tunnel towards the QUI located inside a cavern) will be accommodated by special pipe elements of non-standard length or an elbow. To match the tight thermal budget the design had to be highly optimised. The QRL is a largely modular ensemble of pipe and service modules and therefore it allows a high degree of standardisation and consequently series production of various elements.

11.8 REFRIGERATION PLANTS

11.8.1 Installed Refrigeration Capacity

The refrigeration capacity of the sectors [61], listed in Tab. 11.11, includes contingency for excess capacity and uncertainty in heat load budgets for the nominal operation mode and allows the ultimate operation mode according to the heat load level assumed in 1997 without contingency. These values were used for specifying the new 4.5 K refrigerators and the 1.8 K refrigeration units. Since the ordering of the refrigerators, the electron cloud heat load prediction has increased by more than a factor 4. Consequently, the installed capacity for the temperature level 4.6-20 K does not cope with the presently estimated demand in ultimate conditions (about 13.5 kW per sector), but still fulfils the nominal demand (about 5.3 kW per sector).

Table 11.11: Installed refrigeration capacity in the LHC sectors

Temperature level		High-load sector	Low-load sector
50-75 K	[W]	33000	31000
4.6-20 K	[W]	7700	7600
4.5 K	[W]	300	150
1.9 K LHe	[W]	2400	2100
4 K VLP	[W]	430	380
20-280 K	[$g.s^{-1}$]	41	27

11.8.2 4.5 K Refrigerators

The refrigeration of the LHC sectors requires mixed-duty operation of the cryogenic helium refrigerators, in order to fulfil a variety of isothermal and non-isothermal cooling duties. This amounts to a total equivalent entropic capacity of 144 kW at 4.5 K, thus making the LHC the world's most powerful helium refrigeration system.

Previous experience at CERN with large cryogenic helium plants delivered by European industry in the framework of turn-key contracts, has demonstrated their dependable performance, good efficiency and high operational reliability [62]. Consequently in 1997 CERN issued a functional and interface specification for the procurement of four new such refrigerators to equip the "high-load" sectors [63], to complement the existing LEP refrigerators, which have been upgraded in capacity and will feed the "low-load" sectors of the LHC. The adjudication rule took into consideration, besides capital investment, the integrated costs of operation over a period of ten years, thus giving a premium to efficiency, and – indirectly – compactness [64]. On the basis of the offers received two contracts were placed for the supply of two refrigerators each. Although based on different variants of the Claude cycle, both types of machines are designed to reach similar efficiencies, around 29 % with respect to the Carnot cycle [65, 66], corresponding to a coefficient-of-performance around 230 W per W. Based on three pressure cycles (typically 0.1-0.4-2 MPa), the refrigerators comprise a compressor station and a cold box. Each compressor station has five to eight oil-lubricated screw compressors, water refrigerant for helium and oil as well as a final oil removal system achieving an oil content of a fraction of ppm. The installed electrical input power is about 5 MW per refrigerator. The cold boxes are vacuum insulated and house the aluminium plate-fin heat exchangers and from eight to ten turbo-expanders to provide the cooling capacity. The built-in pre-cooler of 600 kW capacity, which is mainly provided by boiling-off liquid nitrogen is only used for the cool-down to 80 K [67]. Switchable 80 K absorbers remove up to 50 ppm of air and a 20 K adsorbed removes remaining traces of hydrogen and neon. In addition, switchable dryers are connected at the ambient temperature cold box inlet to remove humidity.

11.8.3 1.8 K Refrigeration Units

The efficient production of 1.8 K refrigeration in the multi-kW range [68, 69] – a novel requirement set by the LHC project – may only be achieved practically through combined cycles making use of sub-atmospheric cryogenic compressors and heat exchangers [70]. To foster the development of these technologies, CERN procured prototype low-pressure heat exchangers of different designs from industry as well as three hydrodynamic compressors, each handling 18 g s^{-1} at 1 kPa (10 mbar) suction pressure, with a pressure ratio of 3 all of which were evaluated by CEA, Grenoble (France), [71]. The thorough test campaigns performed on the latter have permitted the investigation of such critical issues as impeller and diffuser hydrodynamics, mechanical and thermal design, drive and bearing technology, as well as their impact on overall efficiency. Design and optimisation studies have also been performed in liaison with industry on refrigeration cycles matched to the expected performance of full-size machinery and meeting the requirements and boundary conditions of the project [72, 73]. This preparatory work permitted the launch of the procurement for the eight 1.8 K refrigeration units in 1998, through a successful call for tenders based on a functional and interface specification [74]. Two contracts have placed for the delivery and installation of four units each. The overall coefficient-of-performance of these 1.8 K refrigeration units, once attached to the main 4.5 K refrigerators of the LHC, is expected to be around 900 W per W [75, 76]. The first unit of each supplier has been tested [77].

Although being relatively simple, the cycle of these 1.8 K refrigeration units is somehow particular, as they have to be interconnected to 4.5 K refrigerators to allow production of cooling capacity at 1.8 K. A set of three or four centrifugal cold compressors delivers gas through heat exchangers to screw compressors, at a pressure between 30 and 50 kPa (300 and 500 mbar) to minimise the volumetric capacity of the latter. The cold compressors are equipped with active magnetic bearings operated at ambient temperature with rotational speeds from 200 to 800 Hz for the warmest stages. Isentropic efficiency of 75 % has been achieved reproducibly on several sets of cold compressors. As the return temperature to the 4.5 K refrigerator was imposed at 20 K, re-cooling after the heat exchangers with a turbo expander was necessary within the 1.8 K refrigeration units. The cooling capacity to be achieved defines the delivery pressure of the warm compressors (typically 0.3 to 0.6 MPa). Switchable 80 K absorbers are provided to remove up to 50 ppm of air as for other refrigerators.

11.9 INSTRUMENTATION

The cryogenic operation of the LHC requires a large number of sensors, electronic conditioning units and actuators, most of which are located inside the machine tunnel and must therefore withstand the radiation environment. This environment imposes strict radiation qualification procedures for the instrumentation located inside the tunnel. An inventory of the cryogenic instrumentation is shown in Tabs. 11.12 and Tab. 11.13 indicates the range and accuracy requirements for the whole data acquisition and processing chain. While a large number of sensors and actuators in this table are commercially available, specific tests on prototypes have been performed to select the suitable instrumentation. Furthermore all tunnel electronics are custom designed to be radiation tolerant.

The tight temperature margins allowed along the cryo-magnet strings require the implementation of precision cryogenic thermometry (overall measurement uncertainty down to ±10 mK, see Tab. 11.13) on an industrial scale (several thousand channels) with long-term robustness and reliability. Following the construction and commissioning of cryogenic calibration facilities of metrological class at CERN [78] and CNRS Orsay (France) [79], several types of sensors have been tested for performance in LHC environmental conditions on statistically significant ensembles. In particular, the effects of neutron irradiation at cryogenic temperature [80, 81] and of thermal cycling [82] have been investigated on several hundred thermometers, in order to select appropriate solutions for the project.

The stringent requirements on temperature measurements, once applied to signal conditioning, cannot be met by commercially available equipment. Several conditioner architectures, which could simultaneously provide the large dynamic range, accuracy, stability and tolerance to radiation levels as encountered in most of the LHC areas, have been investigated and prototyped in discrete component and ASIC versions [83].

During final helium filling and normal operation it is very important to know when the cryo-magnet cold-mass is completely filled with pressurised superfluid helium. This information is obtained from warm

pressure transducers hydraulically connected to the cold-mass enclosures via the instrumentation feedthroughs.

As a rule, instrumentation sensors used for control and that are not exchangeable without breaking the vacuum, are duplicated for redundancy. An exception is the cold mass temperature sensors, where redundancy is provided by the adjacent cold-mass temperature sensor.

Table 11.12: Cryogenic instrumentation inventory

Sensor type	Quantity	Redundancy	RadTol quantity
Temperature CX	4,500	1,153	3,347
Temperature Pt100	2,400		450
Pressure Low	230		230
Pressure Mod/High	900		900
Level Gauges	300		300
Electrical Heater	2,500		2,000

Table 11.13: Measurement uncertainty requirements versus temperature.

Temperature Range	1.6-2.2 K	2.2-4 K	4-6 K	6-25 K	20-300 K
Uncertainty [K]	± 0.01	± 0.02	± 0.03	± 1	± 5

11.10 PROCESS CONTROL

The process control system follows an industrial approach and is composed of Programmable Logic Controllers (PLCs) and a Supervisory Control and Data Acquisition (SCADA) systems. These are used in the operator interface and data logging system in three different layers based in a pyramidal organization.

The LHC cryogenic system uses equipment that is either localised in five geographical locations or distributed around the 27 km LHC tunnel. The corresponding control hardware architecture is different in order to save cabling costs and keep subsystems with a certain degree of autonomy. Local cryogenic equipment (e.g. refrigerators, interconnection boxes, storage, etc) has always been interfaced with industrial controllers and the solutions adopted are based in the previous experience with the LEP cryogenics.

However, the wide distribution of the cryogenics and the late availability of complete system require the development of off-line dynamic models and running them in simulation in order to start the machine operation in an optimal way.

The tunnel hardware is composed of standard industrial equipment and of distributed, radiation tolerant, Input/Output (I/O) units. The industrial equipment is installed in protected areas (16 alcoves and 8 IPs) and it is composed of PLCs, Ethernet gateways, fieldbus gateways, "intelligent" valve positioners and ancillary equipment. The distributed I/O units are custom designed to withstand the radiation in the arcs and the DS regions. Data exchange between PLCs and distributed I/O elements is performed via an industrial fieldbus [84].

Control algorithms have been designed, implemented and validated in the LHC test string and will be extended to simulate the LHC interconnected cell of a whole sector. The main control challenge is to regulate the LHC magnets temperature within the very tight margins in spite of it being a strongly non-linear process that exhibits a very large inverse response and a variable dead time [85]. The final choice of strategy, between absolute and relative temperature control, is not made and selection factors like the availability of the saturated pressure sensor or the change in the process dynamics are now under study. An expert tuning tool is required because of the impracticality of manually tuning all the closed control loops in the 216 LHC cells. LHC test string results showed the poor performance of the PID regulation when it is tuned too conservatively to avoid instabilities and demonstrated the improvement achieved by implementing advanced controllers.

11.11 CRYOGEN STORAGE AND MANAGEMENT

11.11.1 Helium

Helium inventory

Helium is mainly contained in the magnet cold masses which require a minimum filling ratio of 15 $l.m^{-1}$ of superfluid helium for enthalpy buffering (measured cold masses filling ratio is about 20 $l.m^{-1}$) and in the header C of the cryogenic distribution line. Header C requires a DN100 diameter for cool-down and warm-up operation and is filled with dense supercritical helium in normal operation. Fig. 11.16 shows the helium inventory per sector. The total helium inventory of the whole machine is about 96×10^3 kg. The complete storage of this inventory would cost about 20 MCHF for vessels and require a large implantation area. To limit costs and reduce the environmental impact, it was decided to provide gas storage for only half of the inventory.

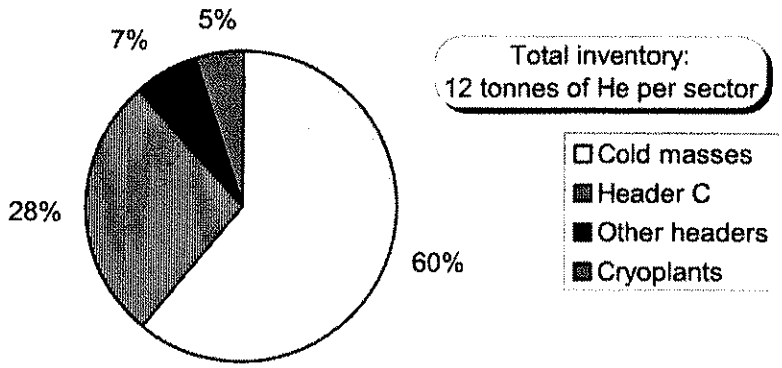

Figure 11.16: Helium inventory per sector

Gas storage management

The cryogenic system of LHC reuses the infrastructure recovered from LEP, which is composed of 40 vessels with a capacity of 75 m^3 each. These vessels with a diameter of 3 m and a height of 12 m have been installed in the shadow of the buildings. To complete this storage, additional vessels have been ordered in two steps in European industry. These additional vessels of 250 m^3 capacity each, a length of 28 m and a diameter of 3.5 m, are installed horizontally to limit their environmental impact. All vessels are in carbon steel. The gaseous helium is stored at a maximum working pressure of 2 MPa (20 bar) and ambient temperature. Fig. 11.17 shows the type and number of vessels distributed on the eight sites around the LHC ring [86].

At each point, four 250 m^3 vessels are used as buffer in case of resistive transition of multiple magnets during operation. These vessels must remain empty during normal operation and may only be used as storage capacity during shutdown. Helium at a temperature down to 10 K may be discharged into the buffer. In order to avoid cold spots on the carbon steel surface, the cold helium is diffused via a 26 m long stainless steel inlet pipe perforated with 41 holes that are 5 mm in diameter; this diffuser is connected to the buffer wall by means of a stainless steel cold finger. The lowest possible temperature of the buffer walls in case of resistive transition of a complete LHC sector is estimated to –35 °C.

The remaining vessels will be used as make-up gas storage for the cryogenic system. The filling of these vessels will be made with helium taken at the full flow dryer discharge, guaranteeing water and oil-free helium in the storage.

The storage vessels are not equally distributed reflecting the available space at the different points. The easy accessibility for helium delivery to some points like e.g. Point 1.8 is also taken into consideration. A helium line interconnecting the different storage areas will be installed in the tunnel and the access shafts. Each sector refrigerator is directly connected to its make-up storage. At Point 3 and 7, where no refrigerators

are installed, make-up storage vessels are also available. Make-up storage can be interconnected by opening the V1 valves.

In the case of resistive transition, helium leaves the cold environment via the interconnection box (QUI) and the return modules (QRLR) of the cryogenic distribution line; the buffers are filled via valves V2. The helium then returns to the sector refrigerator via valves V3 or V4. These are also used during a partial LHC warm-up to store one part of the inventory in the buffers. In this case, no electrical powering of the adjacent sectors is allowed. To minimise the dead volume in the buffers, it is also possible to finish their emptying by connecting them via the helium ring line and valves V5 to the low pressure (LP) of one refrigerator. The hydraulic impedance of the helium ring line (DN100 diameter pipe) does not diminish the liquefaction capacity of the refrigerator during re-cool-down of a sector.

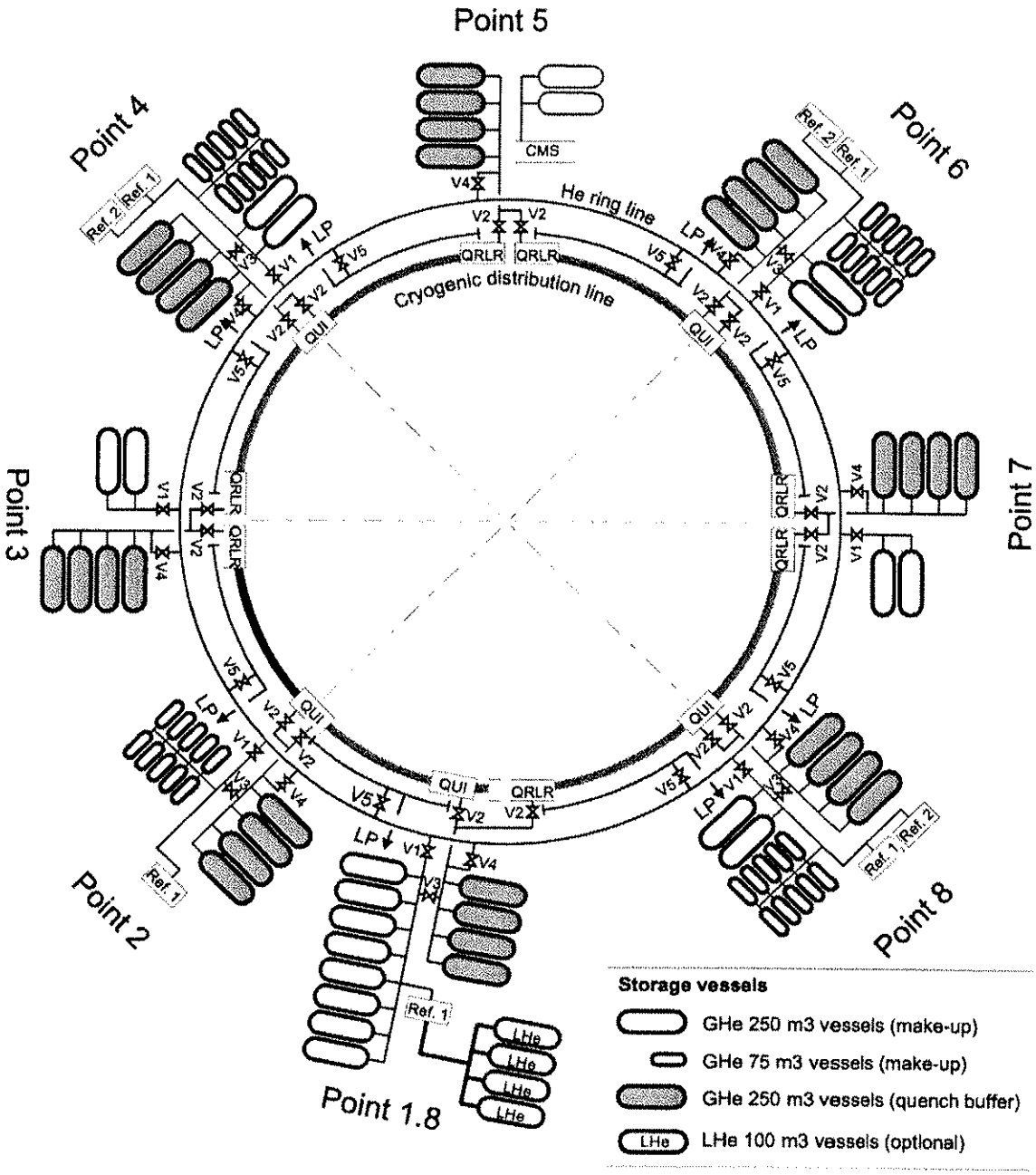

Figure 11.17: Helium storage management

"Virtual" or liquid storage

As the gas management allows storing only half of the inventory, during winter shutdown the excess (50 tonnes or about 400000 litres of liquid helium) has to be either "virtually" recovered by a gas distributor in the framework of an ad hoc contract ("virtual storage") or stored in liquid state in a central storage. Losing this helium to atmosphere, which corresponds to a cost of about 1.5 MCHF per shutdown, is economically not acceptable.

In the "virtual" storage contract, given notice, the company has to place at CERN's disposal standard 11000-gallon (about 40000 litres) industrial containers compatible with liquid helium handling by European distributors. Using the new 4.5 K refrigerators located at ground level, CERN will liquefy the exceeding inventory directly in the containers. During the shutdown period, the gas distributor will put the helium back on the market. During the re-cool-down phase following the shutdown, the distributor is committed to re-supply CERN with the same liquid amount. Studies are also under way about the possible contamination of the helium by activated solid particles or by transmutation of helium into tritium. The conclusion of these studies could impose that the helium inventory has to stay on the CERN site and consequently to immobilise the distributor containers for several months and preclude the "virtual" storage contract.

The best location of this central storage is at Point 1.8 in the vicinity of the new 4.5 K refrigerator in SD18. This central storage could comprise four 30000-gallon (about 110000 litres) containers for fixed storage. These containers with a diameter of 3.5 m and a length of 21 m have to be installed horizontally. The corresponding storage footprint of about 500 m^2 seems compatible with the impact study of Point 1.8. The loss rate of these containers is about 0.09 % per day, i.e. about 8 % per shutdown period. To avoid this loss, which corresponds to about 120 kCHF per shutdown, permanent re-liquefaction could be envisaged using a small liquefier (0.5 g s^{-1}). This storage option, which is under study, is not yet approved by the project management.

11.11.2 Liquid Nitrogen

Cooldown and purification

Nitrogen is only used for the cool-down operation and for regeneration of purifiers. For safety reasons, distribution of nitrogen in the LHC tunnel is forbidden. In addition, to avoid heavy operational logistics, permanent nitrogen consumption is avoided. In normal cool-down of a sector, the 600 kW pre-cooler will use a maximum liquid nitrogen flow-rate of 2.8 l s^{-1} and consume a total amount of liquid nitrogen of 1260 tonnes. Warm gaseous nitrogen is periodically used to regenerate dryer and absorber beds. Tab. 11.14 gives the corresponding flow-rate consumption and the duration of the cool-down and regeneration operations. Liquid nitrogen is also used in some type of refrigerators to regenerate absorbers, but the quantities are negligible on this scale.

Table 11.14: Liquid nitrogen requirements

Operation	Maximum LN2 flow rate [l s^{-1}]	Operation duration [h]	Expected frequency [operation/year]	Total per operation [ton]
Sector cool-down	2.8	200	1	1260
Dryer regeneration	0.36	50	8	324

Logistics

At each of the five cryogenic islands, two liquid nitrogen reservoirs having a unit storage capacity of 50000 l are installed close to the SD refrigerator buildings. For the purpose of producing gaseous nitrogen, an atmospheric heater is coupled to the liquid nitrogen reservoir. In the case of a parallel cool-down of the LHC sectors, the liquid nitrogen consumption would correspond to about 50 full liquid nitrogen standard containers per day, i.e. one container delivery every 2 hours (day and night) at a cryogenic island with two refrigeration plants. The logistics concerning the liquid nitrogen delivery is essential for a continuous cool-down operation. The two reservoirs will be filled alternately in less than one hour to match the volume

required. To relax this logistics constraint, the machine cool-down could be staged by operating some sectors in series. During the winter shutdown, if no intervention on the installation requiring circuit opening is needed, the sector can stay cold floating, thus reducing the re-cool-down time and simplifying the liquid nitrogen logistics.

REFERENCES

[1] L. Evans, LHC Accelerator Physics and Technology Challenges, PAC'99, New York (1999).

[2] Ph. Lebrun, The Large Hadron Collider, A Megascience Project, CERN-LHC-Project-Report-374.- Geneva, 5 Apr 2000.

[3] The LHC study group, Design study of the Large Hadron Collider (LHC), CERN Report 91-03 (1991).

[4] Ph. Lebrun, Advanced Superconducting Technology for Global Science : The Large Hadron Collider at CERN, CERN-LHC-Project-Report-499.- Geneva, 27 Aug 2001.

[5] The LHC study group, The Large Hadron Collider Accelerator Project, eds. Y. Baconnier, G. Brianti, Ph. Lebrun, A. Mathewson and R. Perin, CERN/AC/93-03 (LHC) Report (1993).

[6] The LHC study group, The Large Hadron Collider, Conceptual Design, eds. P. Lefèvre and T. Pettersson, CERN/AC/95-05 (LHC) Report (1995).

[7] Ph. Lebrun, Superconductivity and Cryogenics for the Large Hadron Collider, CERN- LHC-Project-Report-441.- Geneva, 27 Oct 2000.

[8] Ph. Lebrun, Superfluid helium cryogenics for the Large Hadron Collider project at CERN, Proc. ICEC15 Genova, Rizzuto and Federghini editors, Butterworth-Heinemann (1994) pp. 1-8

[9] G. Bon Mardion, G. Claudet and P. Seyfert, Practical Data on Steady-State Heat Transport in Superfluid Helium at Atmospheric Pressure, Cryogenics, Vol. 19 (1979) 45-47.

[10] Ph. Lebrun, Advances in Cryogenics at the Large Hadron Collider, ICEC17, Bournemouth (1998).

[11] Ph. Lebrun, Cryogenics for the Large Hadron Collider, IEEE Trans. Appl. Superconductivity 10 1 (2000) pp. 1500-1506

[12] S. Claudet et al., Four 12 kW / 4.5 K Cryoplants at CERN, Cryogenics 34 ICEC Supplement (1994) 99-102.

[13] M. Chorowski et al, A Simplified Cryogenic Distribution Scheme for the Large Hadron Collider, Adv. Cryo. Eng. 43A (1998) 395-402.

[14] A. Ballarino, A. Ijspeert and U. Wagner, Potential of High Temperature Superconductor Current Leads for LHC Cryogenics, Proc. ICEC16, Elsevier Science, Oxford, UK (1997) 1139-1142.

[15] J.C. Brunet et al., Design of the Second-Series of LHC Prototype Dipole Magnet Cryostats, Adv. Cryo. Eng. 43A (1998) 435-441.

[16] W. Erdt, G. Riddone and R. Trant, The Cryogenic Distribution Line for the LHC: Functional Specification and Conceptual Design, CEC'99 Montreal (1999).

[17] M. Mathieu et al., Supporting Systems from 293 K to 1.9 K for the LHC Cryomagnets, Adv. Cryo. Eng. 43A (1998) 427-434.

[18] G. Ferlin et al., Comparison of Floating and Thermalised Multilayer Insulation Systems at Low Boundary Temperature, Proc. ICEC16, Elsevier Science, Oxford, UK (1997) 443-446.

[19] D. Camacho et al, Heat Inleak Measurements on LHC Components, CEC'99 Montreal (1999).

[20] G. Riddone, Analisi teorica e Verifica Sperimentale delle Prestazioni Termiche dei Criostati Prototipi del Progetto LHC, Doctoral thesis, Politecnico di Torino, Italy (1997).

[21] V. Benda et al., Measurement and Analysis of Thermal Performance of LHC Prototype Cryostats, Adv. Cryo. Eng. 41A (1996) 785-792.

[22] O. Grobner, The LHC Vacuum System, Proc. PAC'97 3, IEEE Piscataway, NJ, USA (1998) 3542-3546.

[23] E. Hatchadourian, Ph. Lebrun and L. Tavian, Supercritical Helium Cooling of the LHC Beam Screens, Proc. ICEC17, IoP, Bristol, UK (1998) 793-796.

[24] R. Saban et al, First Results and Status of the LHC Test String 2, CERN-LHC-Project-Report-568.- Geneva, 02 Jul 2002.

[25] E. Blanco et al., The Cryogenic System for the LHC Test String 2: Design, Commissioning and Operation, CERN-LHC-Project-Report-614.- Geneva, 15 Nov 2002.

[26] E. Hatchadourian, Stability and Control of Supercritical Helium Flow in the LHC Circuits, CEC'99 Montreal (1999).
[27] J.B. Bergot et al., Thermal Performance of the LHC Short Straight Section Cryostat, CERN-LHC-Project-Report-571, 02 Jul 2002.
[28] L. Dufay, C. Policella, J.M. Rieubland and G. Vandoni, A Large-scale Test Facility for Heat Load Measurements down to 1.9 K, CERN-LHC-Project-Report-510, 19 Oct 2001.
[29] M. Chorowski, P. Grzegory, C. Parente and G. Riddone, Experimental and Mathematical Analysis of Multilayer Insulation below 80 K, CERN- LHC-Project-Report-385, 26 Jul 2000.
[30] M. Chorowski, P. Grzegory, C. Parente and G. Riddone, Optimisation of Multilayer Insulation : an engineering approach, CERN-LHC-LHC-Project-Report-464, 12 Feb 2001.
[31] J. Livran et al., A Cryogenic Test Set-Up for the Qualification of Pre-Series Test Cells for the LHC Cryogenic Distribution Line, CERN-LHC-Project-Report-380, 26 Jul 2000.
[32] G. Riddone, D. Rybkowski and R. Trant, Results from the Qualification of the three Pre-series Test Cells for the LHC Cryogenic Distribution Line, CERN-LHC-Project-Report-610, 15 Nov 2002.
[33] A. Ballarino et al., A Low Heat Inleak Cryogenic Station for Testing HTS Current Leads for the Large Hadron Collider, CEC'99 Montreal (1999).
[34] Ph. Lebrun, Superfluid helium as a Technical Coolant, Atti XV Congresso Nazionale sulla Trasmissione del Calore, Edizioni ETS, Politecnico di Torino, Italy (1997) 61-77.
[35] Ph. Lebrun, L. Serio, L. Tavian and R. van Weelderen, Cooling Strings of Superconducting Devices below 2 K: The Helium II Bayonet Heat Exchanger, Adv. Cryo. Eng. 43A (1998) 419-426.
[36] J. Casas et al., Design Concept and First Experimental Validation of the Superfluid Helium System for the Large Hadron Collider, Cryogenics 32 ICEC Supplement (1992) 118-121.
[37] A. Gauthier et al., Thermohydraulic Behaviour of He II in Stratified Co-current Two-phase Flow, Proc. ICEC16, Elsevier Science, Oxford, UK (1997) 519-522.
[38] B. Rousset et al., Thermohydraulic Behaviour of HeII in Stratified Co-Current Two-Phase Flow at High Vapor Velocities, CERN-LHC-Project-Report-617, 15 Nov 2002.
[39] E. Di Muoio et al., Optical Investigations of HeII Two Phase Flow, CERN-LHC-Project-Report-516, 19 Oct 2001.
[40] D. Camacho et al., Thermal characterisation of the LHC HeII heat exchanger tube, Proc. ICEC17, IoP, Bristol, UK (1998) 647-650.
[41] J. Casas-Cubillos et al., Operation, Testing and Long-Term Behaviour of the LHC Test String Cryogenic System, Proc. ICEC17, IoP, Bristol, UK (1998) 747-750.
[42] B. Flemsaeter et al., Applying Advanced Control Techniques for the Temperature Regulation of the LHC Superconducting Magnets, Proc. ICEC17, IoP, Bristol, UK (1998) 631-634.
[43] E. Blanco-Viñuela, J. Casas-Cubillos and C. de Prada-Moraga, Linear Model-Based Predictive Control of the LHC 1.8 K Cryogenic Loop, CEC'99 Montreal (1999).
[44] E. Blanco et al., He II Heat Exchanger Test Unit for the LHC Inner Triplet, CERN-LHC-Project-Report-505, 19 Oct 2001 (Published in: AIP Conf. Proc.: 613 (2002) no. 1, pp.147-154).
[45] R. Byrns et al., The Cryogenics for the LHC Interaction Region Final Focus Superconducting Magnets, Proc. ICEC17 Bournemouth, Dew-Hughes, Scurlock and Watson editors, IoP (1998) pp. 743-746
[46] A. Ballarino, HTS Current Leads for the LHC Magnet Powering System, CERN-LHC-Project-Report-608, 15 Oct 2002.
[47] L. Liu, G. Riddone and L. Tavian, Update of a Cooldown and Warmup Study for the Large Hadron Collider, CERN-LHC-Project-Report-507, 19 Oct 2001.
[48] L. Liu, G. Riddone and L. Tavian, Refined Studies of Cooldown and Warmup for the Large Hadron Collider, CERN-LHC-LHC-Project-Report-618, 15 Nov 2002.
[49] M. Chorowski, Ph. Lebrun, L. Serio and R. van Weelderen, Thermohydraulics of Quenches and Helium Recovery in the LHC Prototype Magnet Strings, Cryogenics 38 (1998) 533-543.
[50] M. Chorowski, P. Grzegory, L. Serio, and R. van Weelderen, Modelling of Helium-mediated Quench Propagation in the LHC Prototype Test String-1, CERN- LHC-Project-Report-468, 23 Mar 2001.
[51] M. Chorowski and B. Skoczen, Thermo-Mechanical Analysis of Cold Helium Injection into Gas Storage Tanks Made of Carbon Steel Following Resistive Transitions of the LHC Magnets, Proc. ICEC17, IoP, Bristol, UK (1998) 755-758.

[52] L. Dufay, A. Perin and R. van Weelderen, Characterisation of Prototype Superfluid Helium Safety Relief Valves for the LHC Magnets, CEC'99 Montreal (1999).
[53] A. Bézaguet et al., A Facility for Accurate Heat Load and Mass Leak Measurements on Superfluid Helium Valves, CEC'99 Montreal (1999).
[54] M. Chorowski, Ph. Lebrun and G. Riddone, Preliminary Risk Analysis of the LHC Cryogenic System, CEC'99 Montreal (1999).
[55] M. Chorowski, G. Konopka and G. Riddone, Helium Discharge and Dispersion In the LHC Accelerator Tunnel in Case of Cryogenic Failure, CERN-LHC-Project-Report-381, 26 Jul 2000.
[56] M. Chorowski, W.K. Erdt, G. Konopka and G. Riddone, Oxygen Deficiency Hazard (ODH) Monitoring System in the LHC Tunnel, CERN-LHC-Project-Report-523, 13 Dec 2001.
[57] M. Chorowski, G. Konopka and G. Riddone, An Experimental Study of Cold Helium Dispersion in Air, CERN-LHC-Project-Report-508, 19 Oct 2001.
[58] M. Chorowski, G. Konopka, G. Riddone and D. Rybkowski, Experimental Simulation of Helium Discharge into the LHC Tunnel, CERN-LHC-Project-Report-611, 15 Nov 2002.
[59] H. Grünhagen, H. Posselt, J. Weber and H. Ahlers, Long, Bellows-Free Vertical Helium Transfer Lines for the LHC Cryogenic System, CERN-LHC-Project-Report-615, 15 Nov 2002.
[60] G. Riddone and R. Trant, The Compound Cryogenic Distribution Line for the LHC : Status and Prospects, CERN-LHC-Project-Report-612, 15 Nov 2002.
[61] Ph. Lebrun, G. Riddone, L. Tavian and U. Wagner, Demands in Refrigeration Capacity for the Large Hadron Collider, Proc. ICEC16, Elsevier Science, Oxford, UK (1997) 95-98.
[62] M. Barranco-Luque et al., Conclusions from Procuring, Installing and Commissioning Six Large-Scale Helium Refrigerators at CERN, Adv. Cryo. Eng. 41A (1996) 761-768.
[63] S. Claudet, Ph. Gayet and U. Wagner, Specification of Four New Large 4.5 K Refrigerators for the LHC, CEC'99 Montreal (1999).
[64] S. Claudet, Ph. Gayet, Ph. Lebrun, L. Tavian and U. Wagner, Economics of Large Helium Cryogenic Systems: Experience from Recent Projects at CERN, CEC'99 Montreal (1999).
[65] P. Dauguet, G.M. Gistau-Baguer and P. Briend, Two Large 18 kW (equivalent power at 4.5 K) Helium Refrigerators for CERN's LHC Project, Supplied by Air Liquide, CEC'99 Montreal (1999).
[66] J. Bösel, B. Chromec and A. Meier, Two Large 18 kW (equivalent power at 4.5 K) Helium Refrigerators for CERN's LHC Project, Supplied by Linde Kryotechnik AG, CEC'99 Montreal (1999).
[67] U. Wagner, Solutions for Liquid Nitrogen Pre-Cooling in Helium Refrigeration Cycles, CERN-LHC-Project-Report-387, 27 Jun 2000.
[68] Ph. Lebrun, L. Tavian and G. Claudet, Development of Large-Capacity Refrigeration at 1.8 K for the Large Hadron Collider, Proc. Kryogenika'96, Icaris, Praha, Czech Republic (1996) 54-59.
[69] L. Tavian, Large Cryogenics Systems at 1.8 K, CERN-LHC-Project-Report-412, 23 Sep 2000.
[70] P. Roussel, B. Jäger and L. Tavian, A Cryogenic Test Station for Subcooling Helium Heat Exchangers for LHC, CERN-LHC-LHC-Project-Report-386, 26 Jul 2000.
[71] A. Bézaguet, Ph. Lebrun and L. Tavian, Performance Assessment of Industrial Prototype Cryogenic Helium Compressors for the Large Hadron Collider, Proc. ICEC17, IoP, Bristol, UK (1998) 145-148.
[72] F. Millet, P. Roussel, L. Tavian and U. Wagner, A possible 1.8 K refrigeration Cycle for the Large Hadron Collider, Adv. Cryo. Eng. 43A (1998) 387-393.
[73] S. Claudet, Ph. Lebrun and L. Tavian, Towards Cost-To-Performance Optimisation of Large Superfluid Helium Refrigeration Systems, CERN-LHC-LHC-Project-Report-391, 27 Jun 2000.
[74] S. Claudet et al., Specification of Eight 2400 W at 1.8 K Refrigeration Units for the LHC, CERN-LHC-Project-Report-392, 26 Jul 2000.
[75] Hilbert, B., Gistau-Baguer, G. and Dagut, F., 2.4 kW at 1.8 K Refrigeration Units for CERN LHC Project Supplied by Air Liquide, ICEC18 Mumbaï 2000, India.
[76] H. Asakura et al., Four 2400 W / 1.8 K Refrigeration Units for CERN-LHC: the IHI/Linde System, ICEC18 Mumbaï 2000, India.
[77] S. Claudet et al., A Cryogenic Test Station for the Pre-series 2400 W at 1.8 K Refrigeration Units for the LHC, CERN-LHC-Project-Report-616, 15 Nov 2002.
[78] C. Balle, J. Casas and J.P. Thermeau, Cryogenic Calibration Facility at CERN, Adv. Cryo. Eng. 43A (1998) 741-748.
[79] E. Chanzy et al., Cryogenic Thermometer Calibration System using a Helium Cooling Loop and a Temperature Controller, Proc. ICEC17, IoP, Bristol, UK (1998) 751-754.

[80] J.F. Amand, J. Casas-Cubillos, T. Junquera and J.P. Thermeau, Neutron irradiation Tests in Superfluid Helium of LHC Cryogenic Thermometers, Proc. ICEC17, IoP, Bristol, UK (1998) 727-730.
[81] J. Casas-Cubillos et al., SEU Tests Performed on the Digital Communication System for LHC Cryogenic Instrumentation, CERN-LHC-LHC-Project-Report-503, 17 Oct 2001 (Published in Nucl. Instrum. Methods Phys. Res.).
[82] Ch. Balle et al., Influence of Thermal Cycling on Cryogenic Thermometers, CEC'99 Montreal (1999).
[83] J. Casas et al., Signal Conditioning for Cryogenic Thermometry in the LHC, CEC'99 Montreal (1999).
[84] T. Bager et al., Instrumentation, Field Network And Process Automation for the LHC Cryogenic Line Tests, CERN-LHC-Project-Report-395, 26 Jul 2000.
[85] E. Blanco-Viñuela, J. Casas-Cubillos, C. De Prada-Moraga and S. Cristea, Non-Linear Advanced Control of the LHC Inner Triplet Heat Exchanger Test Unit, CERN-LHC-Project-Report-506, 19 Oct 2001 (Published in: AIP Conf. Proc.: 613 (2002) no. 1, pp.1597-1604).
[86] M. Barranco-Luque and L. Tavian, Gaseous Helium Storage and Management in the Cryogenic System for the LHC, CERN-LHC-Project-Report-383, 26 Jul 2000.

CHAPTER 12

VACUUM SYSTEM

12.1 OVERVIEW

LHC has the particularity of having not one, but three vacuum systems: insulation vacuum for cryomagnets, insulation vacuum for helium distribution line (QRL) and beam vacuum. The vacuum levels are of course very different. Driven by the requirements for the cryogenic system, the room temperature pressure of the insulation vacuum before cool-down does not have to be better than 10 Pa (10^{-1} mbar). At cryogenic temperatures, in the absence of any significant leak, the pressure will stabilise around 10^{-4} Pa (10^{-6} mbar). The requirements for the beam vacuum are much more stringent, driven by the requested beam lifetime and background to the experiments. Rather than quoting equivalent pressures at room temperature, the requirements at cryogenic temperature are expressed as gas densities and normalised to hydrogen taking into account the ionisation cross sections for each gas species. Equivalent hydrogen gas densities should remain below 10^{15} H_2 m^{-3} to ensure the required 100 hours beam lifetime [1]. In the interaction regions around the experiments the densities will be below 10^{13} H_2 m^{-3} to minimise the background to the experiments [2]. The requirements for the room temperature part are driven by the background to the experiments as well as by the beam lifetime and call for a value in the range from 10^{-8} to 10^{-9} Pa (10^{-10} and 10^{-11} mbar).

All three vacuum systems are subdivided into manageable sectors by vacuum barriers for the insulation vacuum and sector valves for the beam vacuum. Sector lengths are 428 m in the QRL and 214 m for the magnet insulation vacuum. The beam vacuum is divided into sectors of various lengths, in most cases the distance between two stand-alone cryomagnets. However, there are no sector valves in the cold arc, leading to a length for this single sector of approximately 2900 m.

A number of dynamic phenomena have to be taken into account for the design of the beam vacuum system. Synchrotron radiation will hit the vacuum chambers in particular in the arcs; electron clouds (multipacting) could affect almost the entire ring. Extra care has to be taken during the design and installation to minimise these effects, but conditioning with beam will be required to reach nominal performance.

12.2 BEAM VACUUM REQUIREMENTS

The LHC presents several original requirements with respect to classical vacuum systems. It has to provide adequate beam lifetime in a cryogenic system, where heat input to the 1.9 K helium circuit must be minimised and where significant quantities of gas can be condensed on the vacuum chamber. The following four main heat sources have been identified and quantified at nominal intensity and energy:

- Synchrotron light radiated by the high energy circulating proton beams (0.2 W m^{-1} per beam, with a critical energy of about 44 eV);
- Energy loss by nuclear scattering (30 mW m^{-1} per beam);
- Image currents (0.2 W m^{-1} per beam);
- Energy dissipated during the development of electrons clouds, which will form when the surfaces seen by the beams have a secondary electron yield which is too high.

Reducing the heat input to the cryogenic system introduces constraints on the design (e.g. the necessity of a beam screen), on the materials (e.g. the introduction of a copper layer) and on the gas density to be achieved in the LHC vacuum system. In addition, other more classical constraints are set by the lifetime, the stability of the beams, which in turn sets the acceptable longitudinal and transverse impedance [3, 4] and locally by the background conditions in the interaction regions.

The vacuum lifetime is dominated by the nuclear scattering of protons on the residual gas. The cross sections for such an interaction at 7 TeV vary with the gas species [5, 6] and are given in Tab. 12.1, together with the gas density and pressure (at 5 K) compatible with the requested 100 hour lifetime. This number ensures that the contribution of beam-gas collisions to the decay of the beam intensity is small as compared to other loss mechanisms; it also reduces the energy lost by scattered protons in the cryomagnets to below the nominal value of 30 mW m^{-1} per beam.

Table 12.1: The nuclear scattering cross sections at 7 TeV for different gases and the corresponding densities and equivalent pressures for a 100 h lifetime

GAS	Nuclear scattering cross section(cm^2)	Gas density (m^{-3}) for a 100 hour lifetime	Pressure (Pa) at 5 K, for a 100 hour lifetime
H_2	$9.5\ 10^{-26}$	9.810^{14}	6.710^{-8}
He	$1.26\ 10^{-25}$	7.410^{14}	5.110^{-8}
CH_4	$5.66\ 10^{-25}$	1.610^{14}	1.110^{-8}
H_2O	$5.65\ 10^{-25}$	1.610^{14}	1.110^{-8}
CO	$8.54\ 10^{-25}$	1.110^{14}	7.510^{-9}
CO_2	$1.32\ 10^{-24}$	$7\ \ 10^{13}$	4.910^{-9}

12.3 BEAM VACUUM IN THE ARCS AND DISPERSION SUPPRESSORS

The two beams are confined in independent vacuum chambers from one end of the continuous cryostat to the other, extending from Q7 in one octant to Q7 in the next octant. Cold bores of an inner diameter of 50 mm, part of the cryomagnets, are connected together by so-called cold-interconnects which compensate length variations and alignment errors. A beam position monitor, with an actively cooled body, is mounted on each beam at every short straight section. An actively cooled beam screen is inserted into the cold bore of all magnets, connection cryostats and shuffling modules. Initially foreseen to intercept the power deposited by the synchrotron radiation at a temperature higher than 1.9 K, it will also collect the power deposited by electron clouds during the conditioning phase and limit the condensed gas coverage on the surfaces exposed to the impact of energetic particles.

12.3.1 Beam Screen

A racetrack shape has been chosen for the beam screen, which optimises the available aperture while leaving space for the cooling tubes. The nominal horizontal and vertical apertures are 44.04 mm and 34.28 mm, respectively. Slots, covering a total of 4% of the surface area are perforated in the flat parts of the beam screen to allow condensing of the gas on surfaces protected from the direct impact of energetic particles (ions, electrons and photons). The pattern of the slots has been chosen to minimise longitudinal and transverse impedance and the size chosen to keep the RF losses through the holes below 1 mW m^{-1}. A thin copper layer (75 μm) on the inner surface of the beam screen provides a low resistance path for the image current of the beam [7].

The manufacturing process starts by co-laminating a specially developed low permeability 1mm thick austenitic stainless steel strip with a 75 μm copper sheet and rolling a saw-tooth structure which will intercept photons at normal incidence, thereby reducing the amount of reflected photons. The pumping slots are punched into this composite strip, which is then rolled into its final shape and closed by a longitudinal weld.

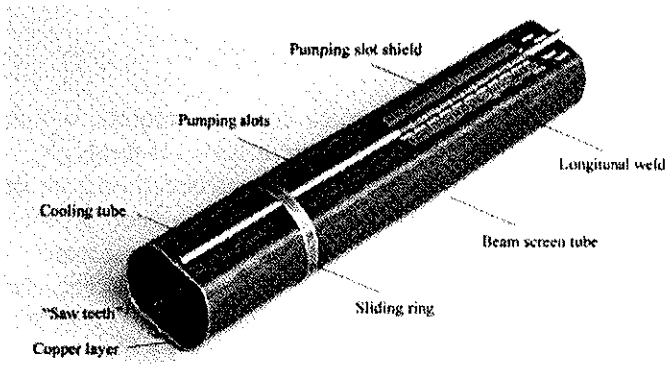

Figure 12.1: Conceptual design of the LHC beam screen

The beam screen is cooled by two stainless steel tubes with an inner diameter of 3.7 mm and a wall thickness of 0.53 mm, allowing for the extraction of up to 1.13 W/m in nominal cryogenic conditions [8]. The helium temperature is regulated to 20 K at the output of the cooling circuit at every half-cell (see Chap. 11 of this report), resulting in a temperature of the cooling tubes between 5 and 20 K for nominal

cryogenic conditions. The cooling tubes are laser welded onto the beam screen tube and fitted at each end with adaptor pieces which allow their routing out of the cold bore without any fully penetrating weld between the helium circuit and the beam vacuum (Fig. 12.2).

So-called sliding rings with a bronze layer towards the cold bore are welded onto the beam screen every 750 mm to ease the insertion of the screen into the cold bore, to improve the centring in the cold bore and to provide good thermal insulation [9].

Finally, as it was recognised that electron clouds could deposit significant power into the cold bore through the pumping slots, the latter are shielded with a structure made of copper beryllium and clipped onto the cooling tubes. The net pumping speed for hydrogen is reduced by a factor of two [10], which remains acceptable.

The beam screen is fixed onto the cold bore at one extremity of the cryomagnet. At the other extremity, a bellows is inserted between the beam screen and the cold bore, to allow for differential expansion between the two. The extremities of the beam screen are gold plated to satisfy the requirement of low electrical resistance of the interconnection.

During operation, in particular when a quench occurs in the magnet, the beam screen is submitted to two types of loads due to the eddy currents induced by the rapidly changing field and the very low resistance of the copper layer at cryogenic temperatures [11]. On one hand, the beam screen is submitted to a horizontal expansion force and on the other hand it is pushed laterally against the cold bore. The latter is the consequence of an asymmetry of the magnetic field integrals in the magnet yoke. Both aspects have been tested under representative conditions in the test String and the design was validated.

12.3.2 Cold Interconnects

Beam vacuum interconnects ensure the continuity of the beam vacuum envelope and of the helium flow in the cooling tubes, as well as a smooth transition between beam screens along the 1642 twin aperture superconducting cryomagnets installed in the continuous cryostat. The physical beam envelope must have a low electrical resistance to carry the image current and minimise coupled bunch instabilities [3]. It also must have a low inductance to minimise the longitudinal single bunch instability. The maximum dc resistance allowed at room temperature for a complete interconnect is 0.1 mΩ. In order to meet these requirements, a complex interconnect module which integrates a shielded bellows to allow thermal expansion as well as for compensation of mechanical and alignment tolerances between two adjacent beam screens, is required.

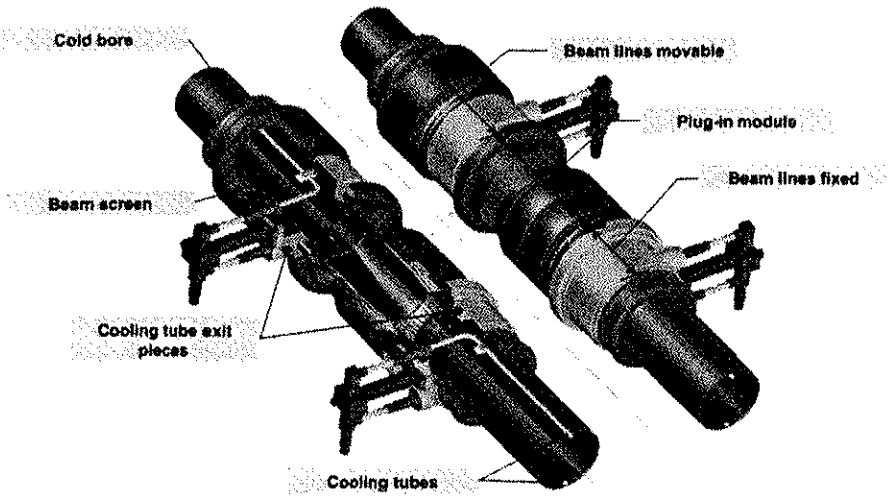

Figure 12.2: Layout and components of the interconnects for the LHC arc beam vacuum

The shielding of the bellows is achieved by means of a set of sliding contact fingers made out of gold-plated copper-beryllium, which slide on a rhodium-coated copper tube. A set of machined copper pieces is used to adapt the racetrack shape of the beam screen to the circular shape of the shielded bellows module. These adaptation pieces also allow the routing of the cooling tubes in and out of the cold bore. The chosen design allows for mounting all adaptation pieces when the beam screen is inserted into the cold bore, before lowering the cryomagnet to the LHC tunnel, leaving the installation and welding of the shielded bellows

module, also called the "plug-in module", as the only in-situ operation. It also satisfies the design criterion which excludes any welds between liquid helium and beam vacuum.

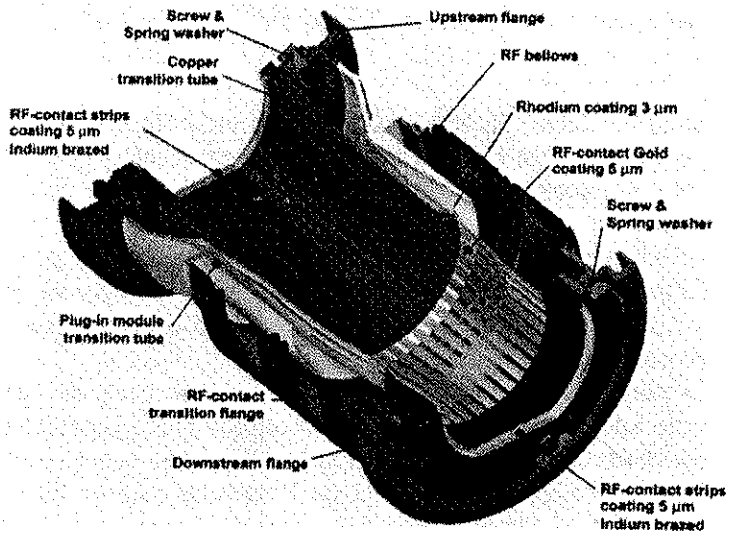

Figure 12.3: Details of the interconnect "plug-in module"

12.3.3 Beam Position Monitor Bodies and Supports

A beam position monitor (BPM) equipped with four button electrodes will be installed on each beam at every short straight section in the continuous cryostat of the arc. In a few places, a strip-line monitor replaces the button type.

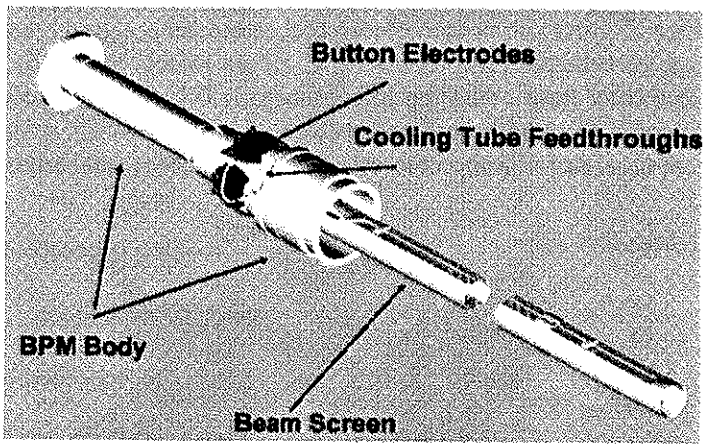

Figure 12.4: Principle layout of an arc beam position monitor

The body holding the electrodes and the connecting "drift length" to the cold bore form an integral part of the beam vacuum chamber, by extending the cold bores of the quadrupole magnets. In this configuration, the beam screen is welded to the BPM body at one extremity and to the cold bore of the magnet, via an expansion bellows, at the other extremity. The BPM body is actively cooled in series with the beam screen, which makes it a rather complex item. A thin copper layer (100 µm) is electrodeposited on both the BPM body and the support to ensure low DC resistance and uniform cooling of the drift length [12].

12.3.4 Pumping and Diagnostics

Initial pumping of the beam vacuum pipe in the arcs and dispersion suppressor is made using mobile pumping groups, connected at regular intervals. Two access ports are available at most of the short straight sections, one for each beam pipe. The number of pumping groups to be connected as well as the required pumping time before cooling down is still under study. The final choice will be made based on the requirement to minimise the initial gas quantity condensed on the inner wall of the beam screen. During

operation at cryogenic temperatures, the pumping solely relies on cryopumping of the cold bore and beam screen.

In the cold beam vacuum system, the strong distributed pumping of the beam pipe and the small conductance between the measuring equipment and the beam vacuum drastically reduce the value of systematic pressure measurements. Therefore, the pressure will be checked during the pre-evacuation stage to prevent condensing a gas layer which is too thick on the cold surfaces due to insufficient pump-down. Under normal operating conditions, the pressure will not be recorded, but in the case of perturbed beam conditions, a mobile diagnostic equipment can be connected to the beam vacuum system through roughing valves mounted at every straight section.

12.4 BEAM VACUUM IN THE INSERTIONS

Room temperature chambers alternate with stand alone cryostats in the Insertion Regions (IRs). The room temperature (RT) part includes beam instrumentation, accelerating cavities, experiments, collimation equipment, the injection and ejection kickers and septa, as well as some of the dipole and quadrupole magnets when superconducting elements are not used. In these regions, the vacuum systems for the two beams sometimes merge, notably in the four experimental insertions, but also in some special equipment like the injection kickers and some beam stoppers.

12.4.1 Beam Screen

The beam screen is only required in the cold bores of the stand-alone cryostats. It is derived from the arc type, but uses a smaller (0.6 mm) steel thickness and comes in various sizes, to match different cold bore diameters. The orientation of the beam screen in the cold bore has to be adapted to the requirements for apertures, which means that the flat part with the cooling tubes can also be vertical, as opposed to the horizontal orientation in the arc. Furthermore, the orientation is different for the two beams in the same twin-aperture magnet in most cases [13]. Tab. 12.2 shows the orientation of the beam screens. For example, HV indicates that beam 1 has the smallest beam screen aperture in the horizontal direction and beam 2 has the smallest beam screen aperture in the vertical direction, as illustrated in Fig. 12.5.

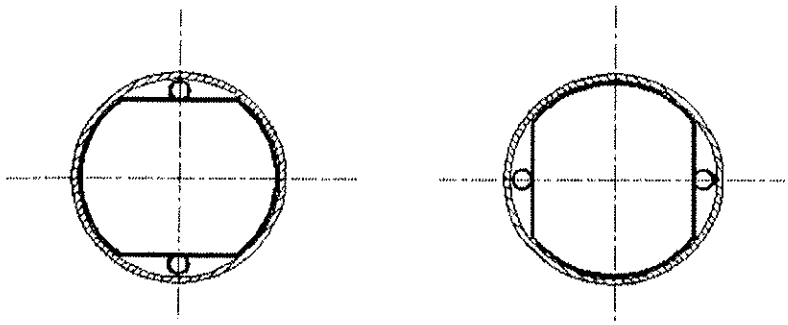

V orientation **H** orientation

Figure 12.5: Definition of beam screen orientation

The saw-tooth structure has been abandoned for these beam screens, since synchrotron radiation hitting the screen in these regions is at least ten times less intense than in the arc and because fitting the saw teeth at the appropriate location of the beam screen would be too expensive [14].

Some stand-alone magnets will operate at 4.5 K instead of 1.9 K. In this case, provisions must be made to pump the hydrogen out of the beam path. This is achieved by fixing a cryosorber on the pumping slot shields. Recent developments at BINP (Novosibirsk, Russia) have resulted in a carbon fabric, easier to use than charcoal, which is likely to provide the required pumping speed and capacity [15].

Table 12.2: Cold bore and beam screen sizes, beam screen orientations

Cold Bore		*Interaction Region*							
Operating Temp (K)	Nominal ID/OD (mm)	**1**	**2**	**3**	**4**	**5**	**6**	**7**	**8**
4.5	#50/53 (replaces 46/49)	$Q6L^{VH}$ $Q5L^{HV}$ $Q5R^{VH}$ $Q6R^{HV}$	$Q6L^{HV}$ $Q5R^{HV}$ $Q6R^{VH}$	$Q6L^{VH}$ $Q6R^{HV}$		$Q6L^{VH}$ $Q5L^{HV}$ $Q5R^{VH}$ $Q6R^{HV}$		$Q6L^{VH}$ $Q6R^{HV}$	$Q6L^{HV}$ $Q5L^{VH}$ $Q6R^{VH}$
1.9	50/53	$Q7L^{HV}$ $Q7L^{VH}$	$Q7^{VV}$	$Q7^{VV}$ $\&SML^{VV}$ $\&SMR^{VV}$	$Q7^{VV}$ $\&SML^{VV}$ $\&SMR^{VV}$	$Q7L^{HV}$ $Q7L^{VH}$	$\&SML^{VV}$ $\&SMR^{VV}$	$Q7L^{HV}$ $Q7L^{VH}$	$Q7^{VV}$
1.9	53/57	$Q1^{H}$	$Q1^{H}$			$Q1^{V}$			$Q1^{V}$
4.5	#62.98/66.7 (replaces 60/64)	$Q4^{VV}$	$Q5L^{HH}$ $Q4^{HH}$		$Q6L^{HV}$ $Q5L^{VH}$ $Q5R^{HV}$ $Q6R^{VH}$	$Q4^{VV}$	$Q5L^{VH}$ $Q4L^{HV}$ $Q4R^{VH}$ $Q5R^{HV}$		$Q5R^{HH}$ $Q4^{HH}$
1.9	62.98/66.7	$Q2^{H}$ $Q3^{H}$ $\&SML^{VV}$ $\&SMR^{VV}$	$Q2^{H}$ $Q3^{H}$ $\&SML^{VV}$ $\&SMR^{VV}$			$Q2^{V}$ $Q3^{V}$ $\&SML^{VV}$ $\&SMR^{VV}$		$\&SML^{VV}$ $\&SMR^{VV}$	$Q2^{V}$ $Q3^{V}$ $\&SML^{VV}$ $\&SMR^{VV}$
4.5	69.08/73	$D2^{VV}$	$D2^{HH}$		$D4L^{VH}$ $D3L^{VH}$ $D3R^{VH}$ $D4R^{HV}$	$D2^{VV}$			$D2^{HH}$
1.9	74/78	$DFBX^{H}$	$D1^{V}$ $DFBX^{H}$			$DFBX^{V}$			$D1^{V}$ $DFBX^{V}$

Increased cold bore diameter as recommended by LCC. Cooling efficiency with reduced gap to be confirmed by July 2003
& DFBA shuffling module

12.4.2 Cold Interconnections and Cold-Warm Transitions

The required interconnections between multiple magnets in a single stand alone cryostat (e.g. the inner triplet) are based on the design of the arc type. In some cases, however, they not only have to compensate for thermal expansion and minor alignment errors, but also for beam separation and cold bore diameter transitions in the adjacent beam pipes. Another complication comes from the fact that the beam screens are rotated in some locations by 90° as compared to the arc, leading to non-standard solution for the routing of the cooling tubes (see Fig. 12.6). It is also sometimes required to integrate pumping ports into interconnects.

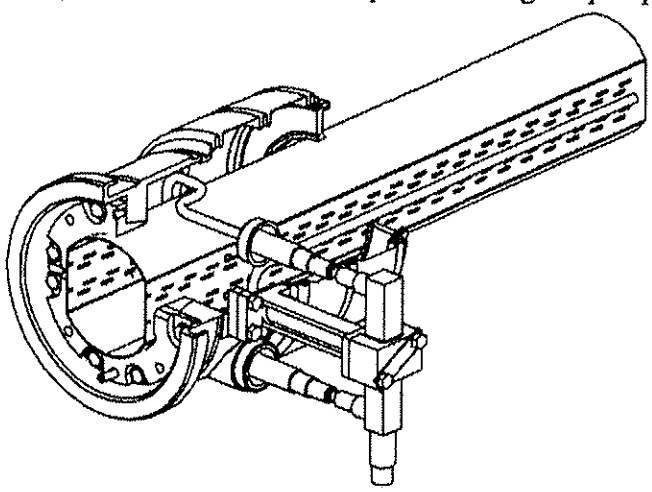

Figure 12.6: Example of non-standard routing of the cooling tubes when the beam screen is rotated by 90°.

The combined interface variations result in 24 different interconnect assemblies to be used in the 278 cold beam vacuum interconnects of the LHC Dispersion Suppressors and Long Straight Sections. The use of modular subassemblies and components shared among design variants, has optimised the design and reduced the number of different pieces to a minimum.

A cold-to-warm transition (CWT) has to be installed for the beam vacuum tubes at the end of every cryostat (Fig. 12.7) as an interface between the cryogen-cooled beam pipes and the room temperature beam pipes. Each circulating beam will pass 108 CWTs per turn (superconducting cavities excluded). In total there will be 200 individual CWTs taking into account that most elements have two apertures.

On the cold side, the CWT connects either to a beam screen and cold bore or to a beam position monitor. On the room temperature side, it connects to the insulation vacuum end cover and a pumping station for the beam vacuum. A thermal anchor at a temperature below 100 K on the CWT intercepts a major part of the conductive heat from room temperature. This thermal anchor is connected to the thermal shield of the cryo-assembly.

The CWT compensates for the longitudinal and transverse thermal displacements of the cold bores and beam screens with respect to the insulation vacuum end cover. It also allows the differential thermal displacements between the beam screen and the cold bore. The concept of the beam vacuum interconnects for the arcs has been adopted and the design will be adapted to the corresponding cold bore dimensions in each case. The final design of the CWT is a compromise between beam impedance and thermal impedance requirements. The heat load to be intercepted by the thermal anchor at 100 K will be less than 6 W per CWT, while the static heat load to the 20 K level must remain below 2.5 W per CWT (1.3 W by thermal radiation and 1.2 W by thermal conduction) [16].

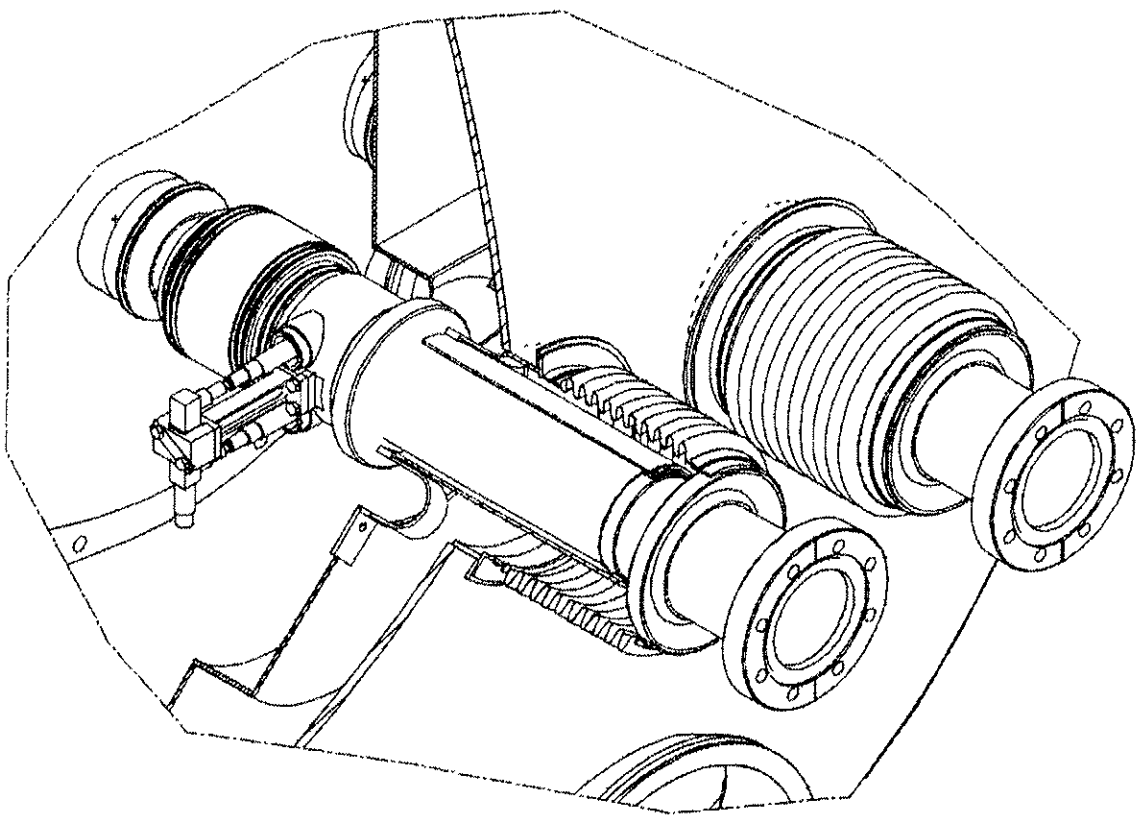

Figure 12.7: Details of a cold-to-warm transition

12.4.3 Room Temperature Beam Vacuum in the Field Free Regions

The baseline for the room temperature (RT) beam vacuum system is to use 7 m long OFS copper chambers, with an inner diameter of 80 mm and fitted with standard DN100 Conflat™ flanges. The

thickness of the copper is 2 mm and the chambers are coated with TiZrV non evaporable getter (NEG) [17], which after activation at low temperature (200°C) provides distributed pumping and low outgassing to maintain a low residual gas pressure, as well as a low secondary electron emission yield to avoid electron multipacting. These chambers will be connected by means of shielded bellows modules, some of them including pumping and diagnostic ports. A significant effort has been put into the design to build up the RT beam vacuum system with a much reduced number of variants for the different components. In particular, the interconnects, based on the design of the cold parts, come with only three lengths of bellows and three different diameters. The adaptation for changing diameters is made out of a set of inserts. Fig. 12.8 gives an overview of the main components used.

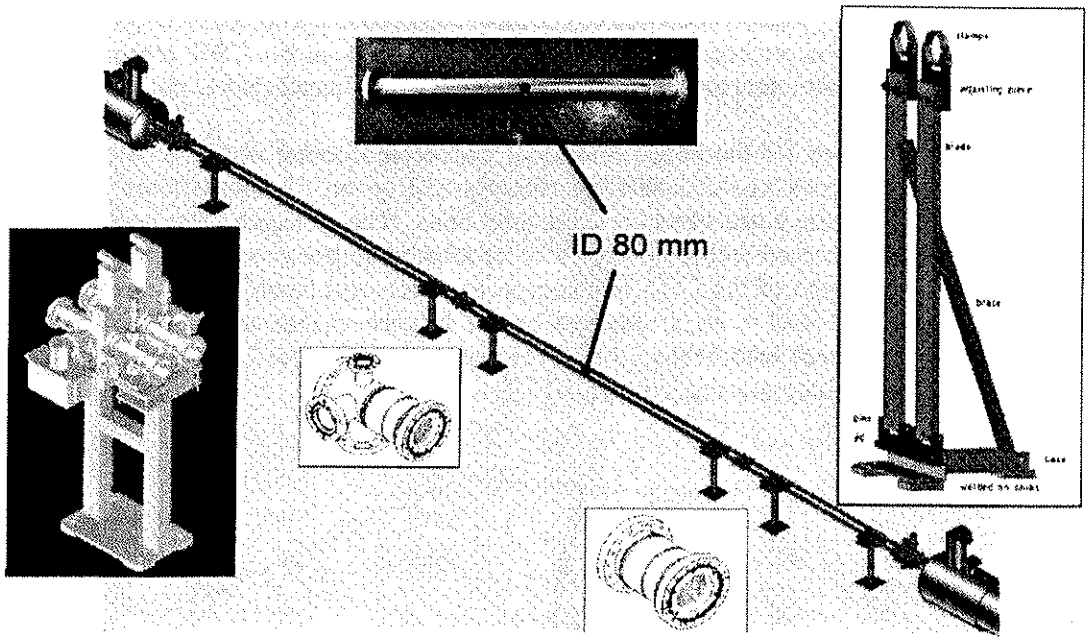

Figure 12.8: Standard layout of the RT beam vacuum system between two cryostats.

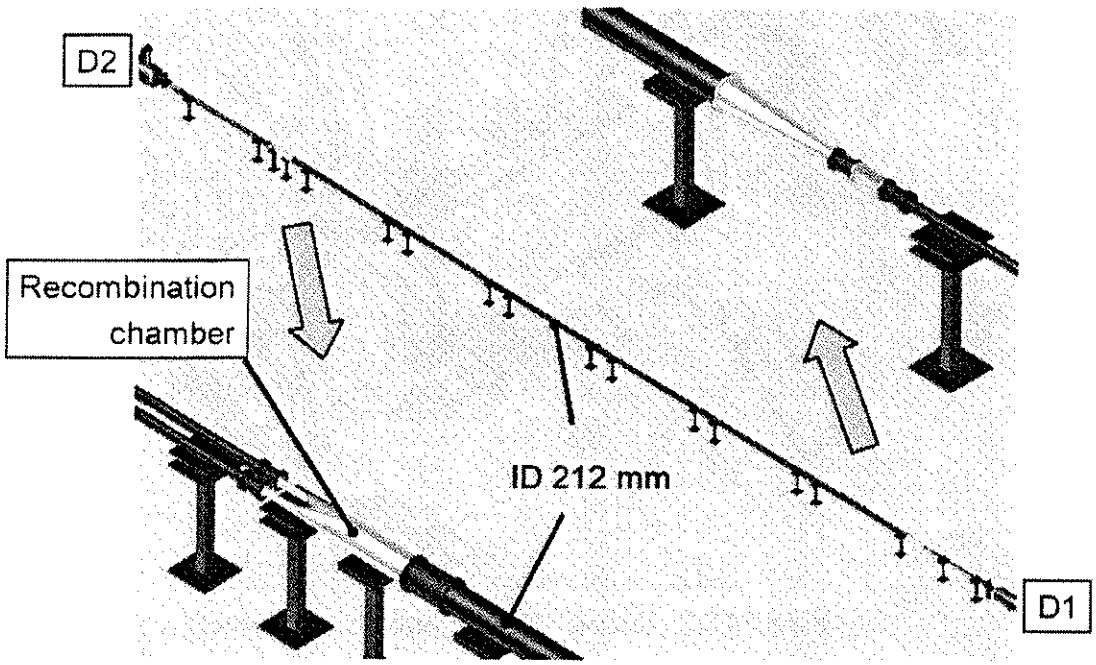

Figure 12.9: Layout of the RT beam vacuum system at left of IR point 8

The 7 m long chambers are supported by three supports, one fixed and two mobile. A removable adjustment system allows the alignment of the chambers, without having to integrate the alignment means into the supports. The required sector valves are installed in the RT part of the vacuum system, in most cases

next to a stand-alone cryostat. They are combined with a pumping and diagnostic port, for a set of gauges, an ion pump and a roughing pump port.

Unfortunately, this simple baseline design cannot be used everywhere. Two examples of more complicated layouts are given in Figs. 12.9 and 12.10, showing the portion of the LSS where two beam lines merge into a single one, for IR8L and IR2R. For the latter, the requirements of the Zero Degree Calorimeter (ZDC) ask for an inner diameter of the vacuum chamber upstream of the experiment as large as 797 mm. For the four insertion regions with experiments, a special vacuum chamber must merge the two physical beam tubes into a single one. In IR 1 and 5, this is done in the neutron absorber (TAN), whereas for IR 2 and 8 a special chamber has to be designed. In all cases, great care was taken to keep the beam vacuum chamber as smooth as possible.

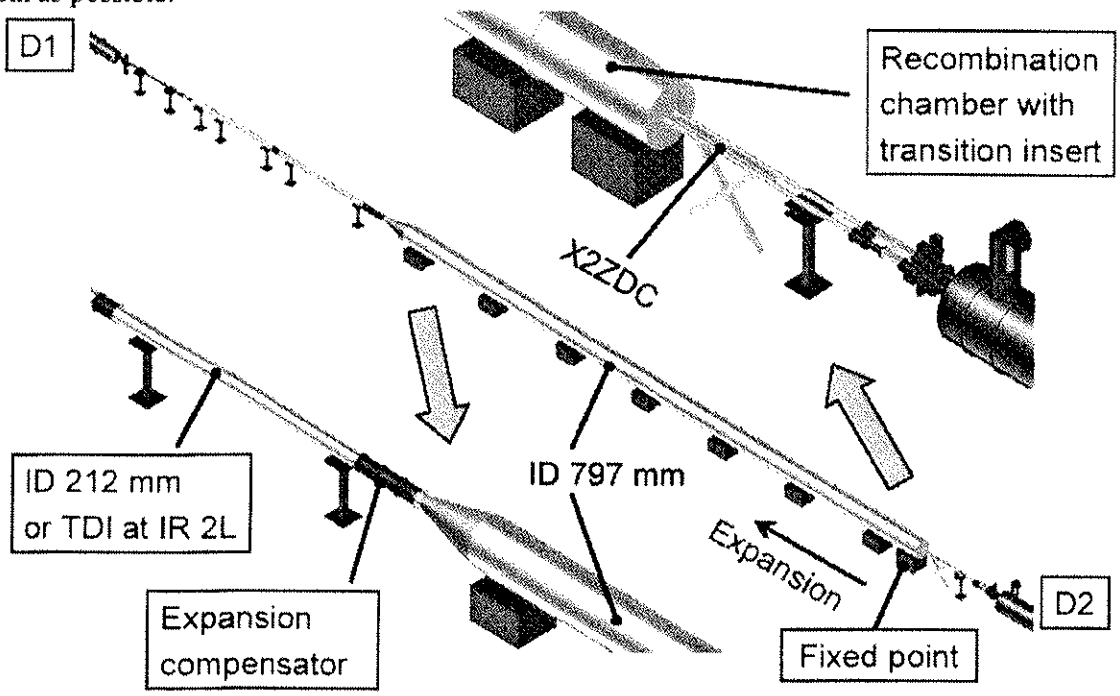

Figure 12.10: Layout of the RT beam vacuum system at right of IR point 2

12.4.4 Beam Vacuum in Room Temperature Magnets

A number of room-temperature magnets, most of them located in the cleaning insertions (IR3 and IR7), will be equipped with extruded OFS copper chambers with either elliptic or circular cross-sections and fitted with standard DN100 Conflat™ flanges. The thickness of the copper is 2 mm and the chambers are NEG coated. The MBXW (also referred to as D1) chambers are an exception in so far as they have a wall thickness of 3 mm and are fitted with DN150 flanges. The initial cruciform shape in the MQW magnets was abandoned for an elliptic cross-section to provide sufficient aperture and allow baking the vacuum chamber to 250°C while keeping a sufficiently low temperature on the magnet yoke. However, as for the beam screen, the orientation of the elliptical chambers will vary depending on the location in the machine.

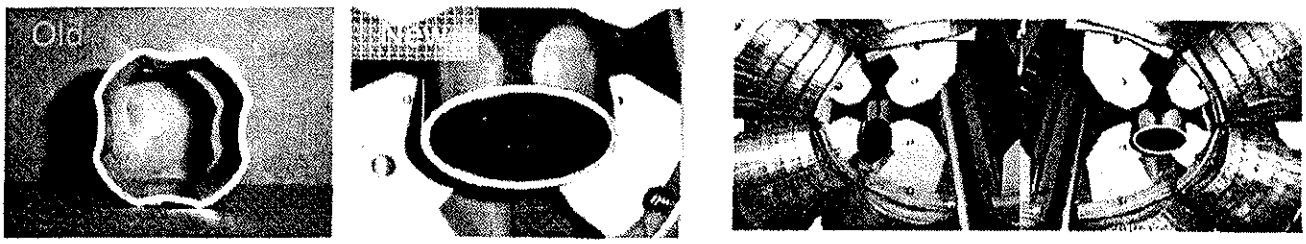

Figure 12.11: Initial and final cross-section for MQW chambers and example of orientation in the magnet yoke.

In the case of the MQW magnets, where the magnets cannot be reopened, the chambers must be inserted into the magnet yoke for installation. This requires that one flange be welded in situ, with very little space available between the magnet coil and the flange.

12.4.5 Beam Vacuum in Special Equipment and Experimental Areas

The details of the beam vacuum in special equipment (RF cavities, septa and kickers, etc.) can be found in the chapters of this report describing the specific equipment. Their design must comply as much as possible with the technical choices made for the standard RT parts, in particular in terms of flanges and bake-out temperatures.

The description of the vacuum system in the experiments is in Chap. 19 of this report.

12.4.6 Pumping

Pumping ports will be integrated in the interconnect modules, in most cases close to a sector valve. Initial pumping is made with mobile, bakeable, pumping stations. The permanent pumping is done with a limited number of sputter ion pumps (typically one every 28 metres) and the NEG coating.

12.4.7 Diagnostics

The room temperature part of the beam vacuum system is baked and very efficiently pumped by the NEG. It therefore requires reliable measurement of low pressures (10^{-9} Pa range) and gas composition to check the background conditions for the adjacent experiments (IR 1, 2, 5and 8) or to have early detection of anomalies such as the development of a leak or the saturation of the NEG coating. On the other hand, the pressure detection system triggering the interlocks for the valves needs reliable sensors in a higher pressure range, typically 10^{-7} to 10^{-4} Pa.

One Pirani gauge per sector is used to monitor the pressure evolution during the initial pump down from atmospheric pressure. It can also be used as a source of an interlock for the sputter ion pumps and the cold cathode gauges. Every sector is equipped with two cold-cathode gauges, installed in the vicinity of the sector valves. Hot cathode gauges, either permanently installed or available on mobile diagnostic stations, will allow measurement of pressures below the reliable operational range of the cold-cathode gauges, typically below 10^{-8} Pa. Finally, residual gas analysers, most likely mounted on mobile stations, will allow qualitative measurement of the beam vacuum after bake-out and NEG activation. They may also provide useful information about the saturation level of the NEG coating.

12.4.8 Bake-out and NEG activation

The required pressures in the insertion regions and the need to activate the NEG coating, call for a bake-out system able to heat every component to 250°C (300°C for uncoated chambers). The final choice on how to heat the standard chambers is not made yet. The baseline is to have mobile heating and regulation equipment. However, as it becomes more and more evident that there will be many very highly radioactive areas around the ring, permanently installed heating equipment may become mandatory to reduce the radiation dose to the personnel during maintenance activities.

For the standard chambers, classical methods, like heating tapes and insulation shells are likely to be the cheapest for permanently installed equipment, heating jackets can be used for removable heating equipment. Although more expensive than tapes, jackets are much more robust when it comes to mounting and dismounting them. They also need significantly less manpower.

For the chambers in the room temperature magnets, an original concept of a wound sandwich made out of stainless steel as heating elements and polyimide foils as insulation material has been developed and validated. This technique allows the space required for heating and insulation to be reduced to less than a mm (typically 0.3 mm). Aluminising the top layer of the polyimide further reduces the radiated power. A considerable cost reduction can be obtained compared to using coaxial heaters.

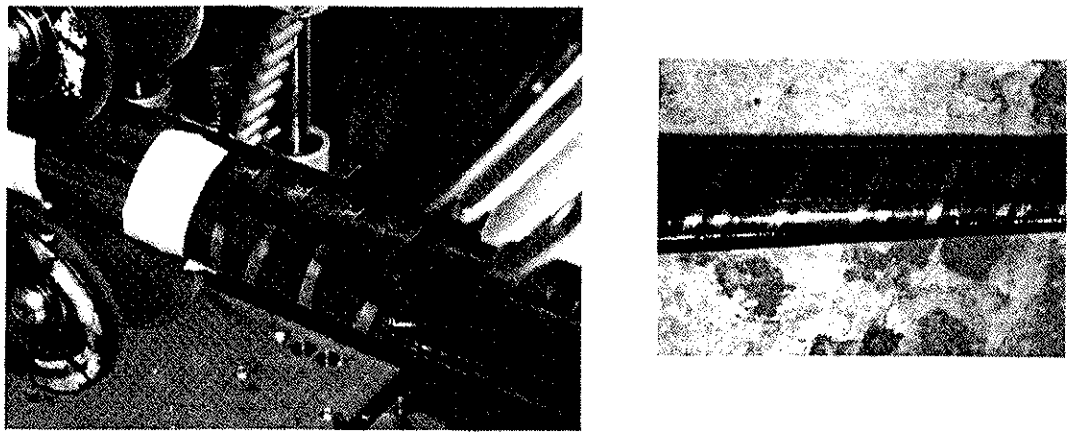

Figure 12.12: Wrapping of the stainless steel strips as bake-out heaters and a close up view of a finished chamber before the addition of the aluminised layer

The proposed bake-out sequence must be optimised to take into account the NEG activation. In the first part of the bake-out cycle, all non-coated elements will be heated to 300°C (gauges and gas analysers to 350°C) for 24 hours, while the coated parts are left at 80°C to prevent absorption of water without an early activation of the NEG. The temperature of the non-coated parts is then reduced to 150°C and 24 hours of NEG activation at 200°C can start. The whole process (Fig. 12.13) takes some 65 hours [18].

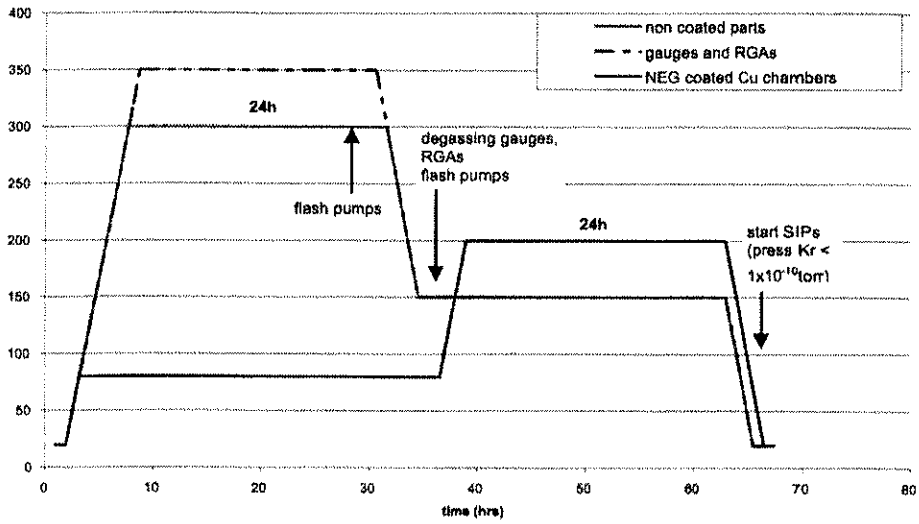

Figure 12.13: Proposed bake-out cycle with NEG activation

12.4.9 Sectorisation

The proposed sectorisation is a compromise between costs, complexity and a number of operational and safety requirements [19]. The strategy used was to start by protecting the arcs, the experimental areas and delicate equipment. In addition, considerations like power limitations for bake-out or reducing the number of potential interventions in high radiation areas were taken into account. Finally, whenever there was a need for a sector valve based on the above-mentioned criteria, the valve was moved close to the cold-to-warm transition leading to a sector valve at each cold-to-warm transition. The result of this approach is that the beam vacuum system will be split into 230 sectors of varying length. All sectors belonging to stand-alone cryostats in the LSS can be isolated and impose no constraints on cool-down or NEG activation cycles.

Only two different types of sector valves are required (DN63 and DN100), some of them are recuperated from LEP, the others are off-the-shelf equipment procured in industry.

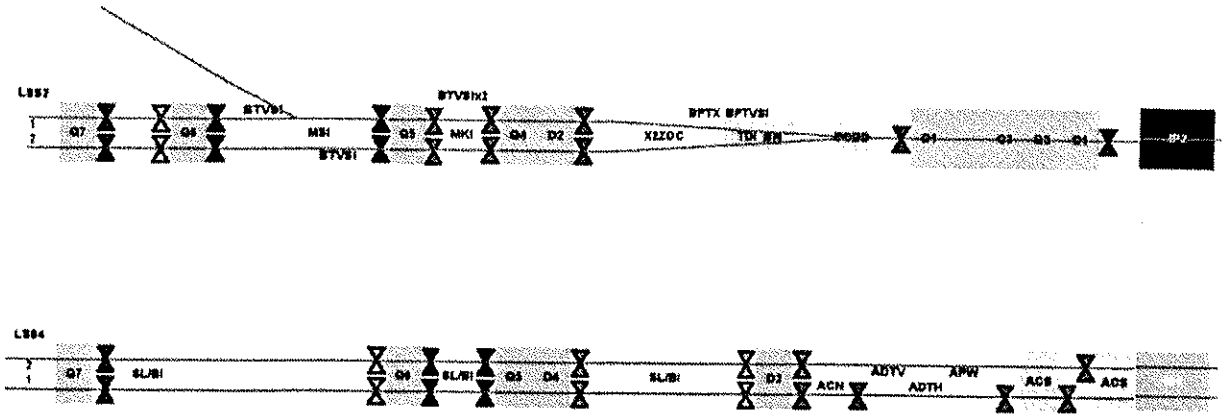

Figure 12.14: Example of sectorisation: left side of IR2 (ALICE experiment) and IR4 (RF equipment)

12.5 BEAM DUMP LINES

The two beam lines designed to transport the proton beams to the dump (TDE), are located in the underground tunnels TD62 and TD68. The beams are kicked out of their circulating orbit by the extraction kickers (MKD) in the horizontal plane and extracted vertically from the ring by the septa (MSD). The beams are then blown-up by the diluters (MKB, see Chap. 17 of this report) before reaching the dump blocks (TDE) at the end of the dump lines. After the diluters, the beam will follow a spiral with an increasing radius (from 50 mm up to 300 mm). Therefore, the vacuum envelope has an increasing cross section up to the dump located at about 630 m downstream from the diluters. The beam dump lines are designed such that the beam never interacts with the vacuum chamber.

The LHC beam dump vacuum system has been designed to be simple, reliable, maintenance free and inexpensive. A pressure below 10^{-3} mbar is enough to satisfy the requirements in terms of acceptable radiation doses produced from beam-gas scattering. However, in order to allow the use of maintenance free sputter ion pumps without decreasing dramatically their lifetime, the pumping system was designed to maintain a pressure of 10^{-6} mbar [20].

In total 33 sputter ion pumps are installed in each line on pumping ports welded to the standard tubes (Fig. 12.15). The first pump down to 10^{-6} mbar will be made using mobile turbo-molecular pumping stations connected to roughing ports.

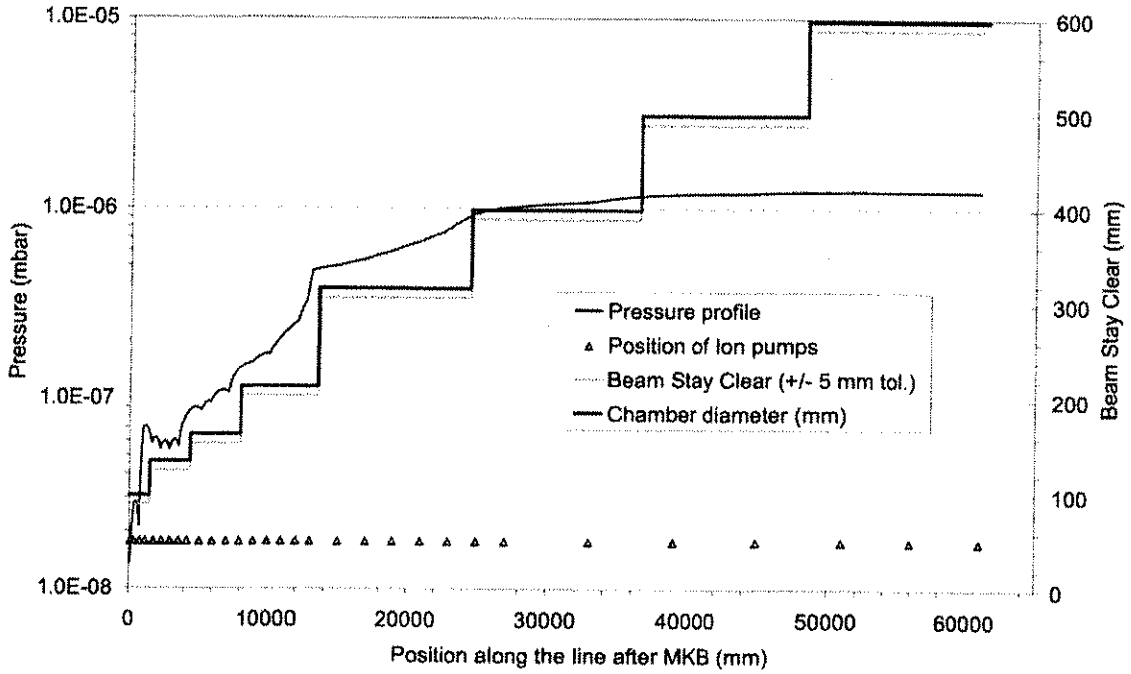

Figure 12.15: Pressure profile, distribution of ion pumps, vacuum chamber diameters and beam stay clear along the beam dump line starting downstream of the diluters (MKB) down to the dump (TDE).

The vacuum line will be made by in situ welding of stainless steel 304 L tubes of suitable diameters chosen from the industrial standards available. Bellows will be used approximately every 12 m, in order to cope with misalignments (±5 mm) and tilts between adjacent elements.

The supporting structure is designed to take the weight of the vacuum line and its instrumentation. In total, about 60 supports will be used per dump line.

The leak detection will be made using a special tooling developed for the leak testing of the welds in the interconnection of the cold magnets. A "clamshell" will be fixed around the weld to be leak tested, pumped down by a mobile turbo-molecular pumping station connected to a leak detector and, finally, the helium will be injected inside the tube directly onto the weld. No leak must be detectable on any joint of the vacuum chamber when measured with a calibrated helium detector with a sensitivity of better than 10^{-9} Pa m^3 s^{-1}.

12.6 INSULATION VACUUM

The insulation vacuum system includes the magnet cryostats and the QRL. Vacuum barriers at the jumper connections maintain separation of the two systems, however, longitudinal vacuum barriers can be by-passed. The configuration of the insulation vacuum barriers and cryogenic circuits permit warming of individual machine cells [21]. The insulation vacuum is characterised by the large volumes that need to be pumped and the large amount of multilayer reflective insulation (MLI), which introduces a high gas load. This requires high-capacity mobile pumping groups (64 m^3 h^{-1}) and an appropriate strategy for leak detection to provide an acceptable pump-down time.

Table 12.3: Main characteristics of the insulation vacuum sectors

	Cryomagnet	QRL
Volume (m^3)	80	85
Length (m)	214	428
MLI (m^2/m)	200	140
Sectors per arc	14	7

The vacuum instrumentation is classified as either permanent or mobile and its layout is similar on the cryomagnet and QRL vacuum systems [22]. Mobile instrumentation has been designed to avoid intrusion into the equipment transport zone in the tunnel ('stay-clear' area). The choice of permanent instrumentation is constrained by the expected radiation dose in the LHC tunnel. Typical vacuum instrumentation requirements per vacuum sector are shown in Fig. 12.16.

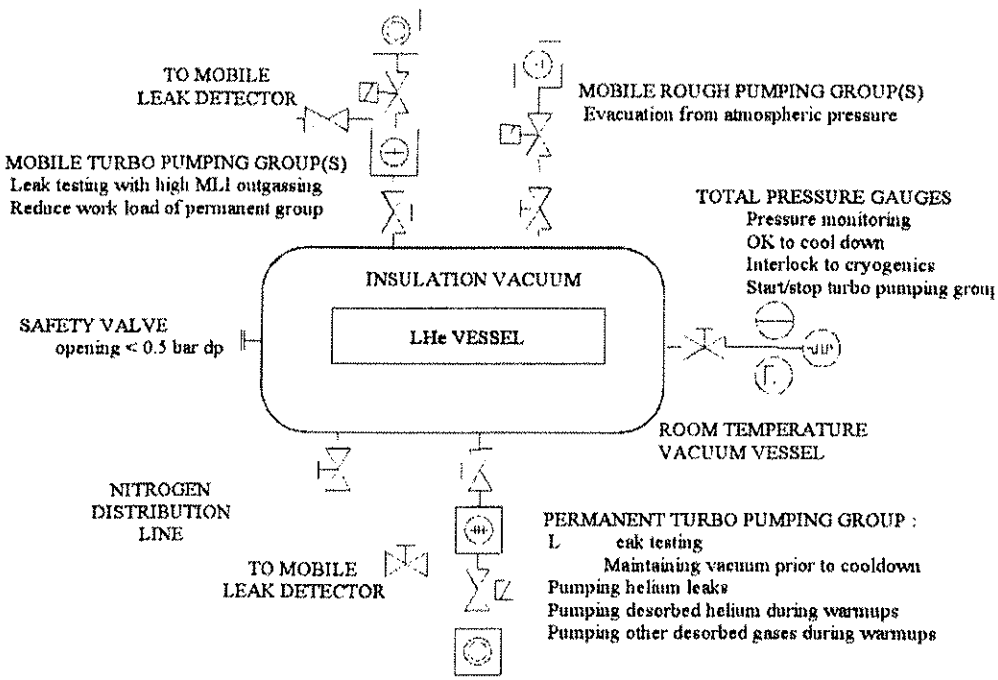

Figure 12.16: Typical insulation vacuum instrumentation

Table 12.4: Proposed leak test scenario for the arc insulation vacuum

Leak Test Scenario	Time per arc	Comments
Weld all interconnects		
Leak test V1 & V2 after each 214 m	2 days x15 sectors	Volume gets big!
Close W bellows – without shields, MLI		To localise He leaks
1st pumping of insulation vacuum sector	4 days x 15 sectors	
Leak test RT envelope of vac sector	2 days x 15 sectors	
Complete Arc (or Sector)		
Leak test (low pressure) He circuits of arc	8 days	Many leak detectors
Leak/pressure test He circuits of arc	2 days	
Vent ins.vacuum & open all W bellows		Many repairs?
Repair leaks on He circuits (clamshells)		
Close all W bellows – with shields, MLI	2 days x 15 sectors	
Re-pump insulation vacuum sector	1 day x 15 sectors	
Leak test RT envelope (W bellows only)	2 days	
Repeat pressure test if necessary		

The permanent turbo-molecular pumping group is placed at the vacuum barrier by-pass, giving the advantage that two permanent groups can pump a single vacuum sector and providing redundancy in case of pump failure. During steady-state LHC operation, the pumping group only operates if helium leak rates are above the design values [23].

The leak test sequence is shown in Tab. 12.4. In order to apply the time-of-flight (TOF) technique, the thermal shields and MLI are not immediately installed. Once the installation of the arc is complete, the helium circuits can be leak tested using the hood-global technique. The circuits are collectively evacuated to <1 mbar and then individually or collectively vented to helium via the QRL. The pressure can then be increased in each circuit to the test pressure. Both remote and manual operation of the QRL cryo-valves will be necessary during these activities. Any unacceptable leak will be localised longitudinally within the 214 m vacuum sectors [24].

After the necessary repairs, all the bellows of the outer envelope must be reopened to install the radiative insulation, thermal shields and MLI, followed by a leak test of the bellows seals. If a vacuum sector has no helium leaks, the reopening activities can be made in the shadow of repair activities in another vacuum sector.

12.7. VACUUM CONTROLS

The controls for the three vacuum systems are based on an industrial solution using PLCs and a central SCADA supervision system connected via Ethernet to the master PLCs.

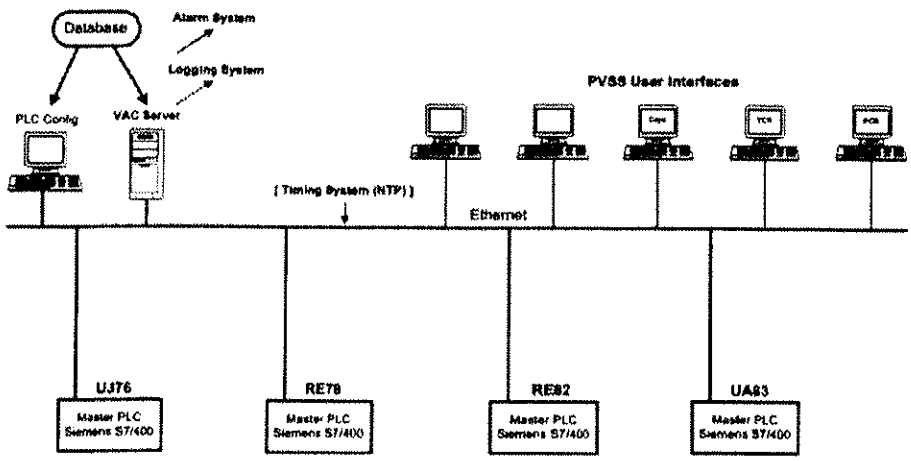

Figure 12.17: Architecture of the higher level of the vacuum control system, example for sector 7-8

A Profibus™ link is used to connect slave PLCs and mobile equipment to the master PLCs. The slave PLCs control off-the-shelf or CERN developed hardware control crates, which are hardwired to pumps, gauges and valves in the tunnel. In order to minimise the cabling costs, signal and control wires are grouped into large multicore cables and locally dispatched to the equipment via junction boxes. Most of the control equipment is located in radiation free areas, such as the alcoves. However, the gauges in the arcs are supplied by local equipment situated in areas where the expected annual dose remains below 10 Gy per year.

Extensive tests have been performed in the North Area of the SPS on the radiation resistance of commercially available vacuum control equipment. Based on these tests and on the requirement to minimise the cables, the power supplies for the cold cathode gauges can be bought from industry, while those for the Pirani gauges have been developed in house. The turbo-molecular pumps needed for the insulation vacuum can also be supplied by industry.

One specificity for the vacuum controls is the requirement to dynamically reconfigure the layout. This is a consequence of using mobile pumping and diagnostic equipment. It must be possible to detect equipment

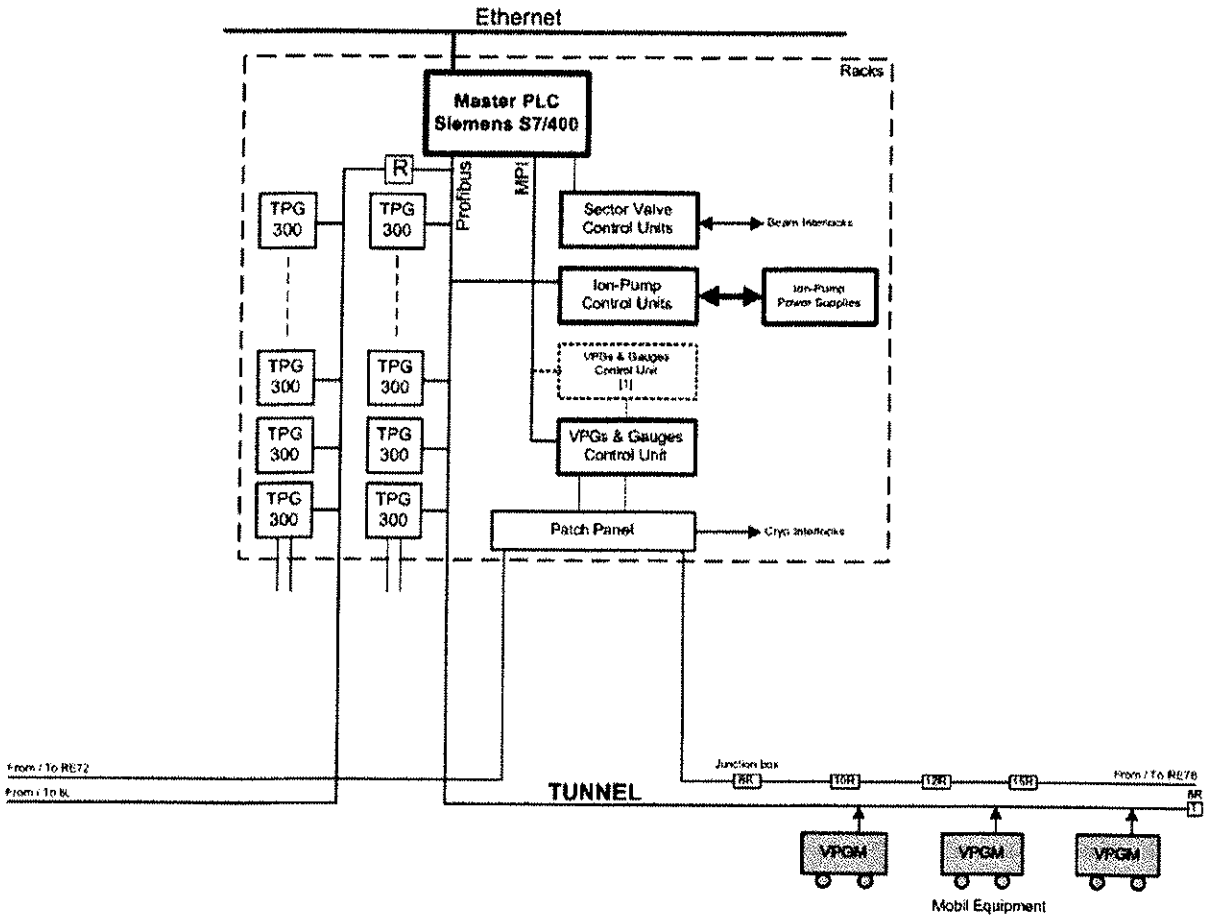

Figure 12.18: Architecture of the lower level of the vacuum control system, also showing the integration of mobile equipment.

when it is connected or disconnected from the Profibus™ link, without having to manually update a database. A prototype link with mobile equipment has been successfully tested in the laboratory. The general architecture and the SCADA program have been operational in the SPS since 2002, thus validating the concept.

12.8 OPERATIONAL ASPECTS

In the cold part of the LHC vacuum system, running at 1.9 K, all gases except hydrogen have a low enough vapour pressure (4 10^{-13} Pa for CO at 20 K) when condensed on the beam screen surface, as long as the beam screen surface is kept at a temperature below 20 K. Hydrogen will be pumped on the 1.9 K surface of the cold bore through the pumping slots of the beam screen. The strong dynamic effects that the LHC vacuum

system will experience, as well as the usage of "saturable" pumping elements like NEG or cryosorbers, impose some running-in and operational constraints.

12.8.1 Beam Screen Cool-Down

To minimise transient effects linked to temperature variations of the beam screen, it is therefore important to begin an annual run with as low a coverage of the surface as possible [25]. This can be achieved by keeping the temperature of the beam screen above 90 K (temperature at which CO_2 is no longer cryopumped) during the full cool-down cycle of the magnets, implying a "plateau" at the end of the cool-down sequence [18]. This procedure has been tested in String2 and does not require additional time, as it is done in the shadow of the cool-down sequence.

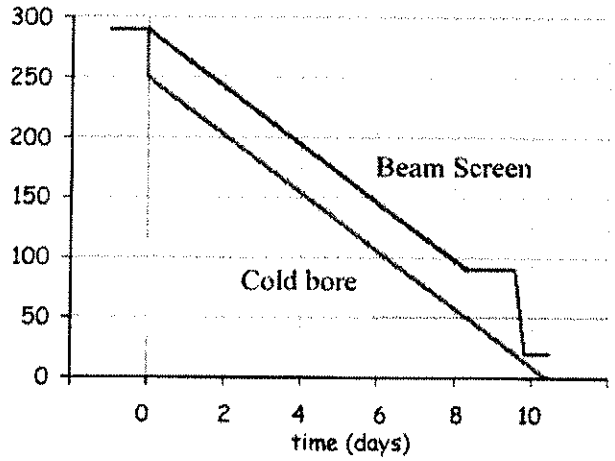

Figure 12.19: Proposed cool-down sequence to minimise initial gas coverage on the beam screen surface

12.8.2 Beam Screen Warming-up

In order to remove physisorbed gas layers accumulated on the beam screen, desorbed from the cold bore during a magnet quench and to avoid any transient effect, it must be possible to heat the beam screens in adjacent magnets. The temperature of the beam screen during this operation must be at least that reached by the cold bore after a quench at ultimate conditions. The present running-in and commissioning scenarios should avoid that warming up of the beam screen in a complete arc is required between two long shutdowns. However, in the unwanted case of oscillations of the beam screen temperature around 25 K, intermediate warming up of the beam screen would be required [26].

12.8.3 NEG Reactivation

NEG surfaces have a limited capacity for gas molecules [17], and the pumping speed reduces as the saturation coverage is reached. If the performance of the NEG has noticeably deteriorated during machine operation, NEG coated surfaces can be reactivated by raising their temperature to 200°C for 24h or 250°C for 2h [18].

12.8.4 Vacuum Conditioning

As mentioned in Sec. 12.1, beam conditioning will be required to achieve the design gas densities. A tentative running-in and commissioning scenario has been studied [25].

The vacuum conditioning of the cryoelements is divided into three phases: operation below electron cloud threshold, scrubbing of the vacuum chamber to reduce electron cloud effects and nominal operation. Gas load due to synchrotron radiation has been shown to require little or no vacuum conditioning [27]. Electron-stimulated molecular desorption, triggered by the electron cloud, has been shown to decrease with increasing

beam time. In the SPS, experimental results indicate that the design conditions could be reached in LHC within a few days [28].

Due to the NEG properties, the electron cloud as observed in the SPS [29] should not appear in the LHC room temperature elements. Thus only gas desorption due to synchrotron radiation exist. Provided adequate lumped pumping of hydrocarbons is available, very little or no vacuum conditioning of the NEG vacuum chambers will be required [30].

REFERENCES

[1] O. Gröbner, Vacuum 60 (2001) 25-34

[2] N. Hilleret, A. Rossi, "Estimations of the Residual Gas Densities in the LHC Experimental Interaction Regions", LHC-Project Note 2003-xx

[3] D. Angal-Kalinin, L. Vos. "Coupled Bunch Instabilities in the LHC", 8th European Particle Accelerator Conference. 2002. Paris.

[4] D. Brandt, L. Vos, "Resistive wall instability for the LHC: intermediate review", LHC Project Report No 257. 2001

[5] K. Eggert, K. Honkavaara and A. Morsh, "Luminosity considerations for the LHC", LHC note 263. 1994.

[6] O. Grobner, "The LHC vacuum system", PAC'97, 1997, Vancouver, B.C., Canada.

[7] I. Collins, P. Cruikshank, B. Jenninger and N. Kos, "Beam Screens for the LHC Arc Magnets", Functional Specification LHC-VSS-ES-0001 rev. 1.0

[8] E. Hatchadourian et al., LHC Project Report 212

[9] N. Kos, "Co-Laminated Sliding Rings for the LHC Beam Screens", Vacuum Technical Note 01-13, October 2001

[10] A. Krasnov, "Molecular pumping properties of the LHC arc beam pipe and effective secondary electron emission from Cu surface with artificial roughness", LHC Project Report 671, August 2003.

[11] C. Rathjen, "Mechanical behaviour of vacuum chambers and beam screens under quench conditions in dipole and quadrupole fields", Proceedings of the 2002 European Particle Accelerator Conference, Paris, p. 2580-2582, paper WEPDO039; also LHC Project Report 582

[12] G. Schneider, "Beam Position Monitor Body and Support", Engineering Specification LHC-BPM-ES-0002 rev. 2.0

[13] V. Baglin, I. Collins, N. Kos, "beam Screens for the LHC Long Straight Sections, Functional Specification LHC-VSS-ES-0002 rev 1.0

[14] R. Veness, "Design Review on the Cold IR Vacuum System – conclusion of the review committee", Engineering minutes LHC-V-EM-001, EDMS 397114.

[15] V.V. Anashin, R.V. Dostovalov, A.A. Krasnov, "Charcoal and Carbon Fibre as the Proposed Cryosorbers for Application in the KHC LSS Cold Beam Vacuum Chamber", Vacuum Technical Note 03-14, August 2003

[16] I. Collins, B. Jenninger, J. Knaster Refolio, "Longitudinal Cold Warm Transitions for the LHC Beam Vacuum System", Functional Specification LHC-VST-ES-0001 rev. 1.0

[17] C. Benvenuti et al., Vacuum 60 (2001) 57-65

[18] A. Rossi, "Operating / regenerating the beam screen and the NEG", LHC days 2003

[19] J.M. Jimenez, P. Cruikshank, "Vacuum Sectorisation of the LHC Long Straight Sections", Functional Specification LHC-LVW-ES-0003 rev 0.1

[20] I.R. Collins, P. Strubin, "Technical Specification for the Design of the Vacuum System for the LHC Beam Dump Lines", Addendum J1 to the Collaboration Agreement between CERN and India, 2002

[21] J.C. Brunet et al., "Update of the LHC Arc Cryostat Systems Layouts and Integration", LHC Project Report 280, April 1999.

[22] R. Schmidt et al., "Instrumentation in the arcs and dispersion suppressors of the LHC", Engineering Specification LHC-PM-ES_0003 rev 0.3

[23] P. Cruikshank, "Leak tightness requirements for LHC arc vacuum systems", Engineering Specification LHC-VQ-ES_0001 rev 1.

[24] P. Cruilshank, LHC Days, 2001.

[25] V. Baglin. "Running in – Commissioning with beam". LHC Performance Workshop – Chamonix XII, 2003.

[26] V. Baglin, I.R. Collins, O. Gröbner, C. Grunhagel and B. Jenninger."Synchrotron radiation studies of the LHC dipole beam screen with COLDEX". LHC Project Report 584, July 2002.
[27] V. Baglin, I. Collins, O. Gröbner, C. Grunhagel and B. Jenninger. "Molecular desorption by synchrotron radiation and sticking coefficient at cryogenic temperatures for H2, CH4, CO and CO2", LHC Project Report 518, November 2001
[28] V. Baglin, I.R. Collins, and B. Jenninger. "Performance of a cryogenic vacuum system (COLDEX) with a LHC type proton beam," LHC Project Report 667, August 2003
[29] J.M Jimenez, G. Arduini, V. Baglin, P. Collier, G. Ferioli, B. Henrist, N. Hilleret, L. Jensen, B. Jenninger, J.M. Laurent, A. Rossi, K. Weiss, F. Zimmermann, "Electron cloud studies and analyses at SPS for LHC-type beams", PAC'03, 2003, Portland, USA
[30] I.R. Collins, V. Ruzinov, O.B. Malyshev, V. Anashin, R. Dostovalov, N. Fedorov, A. Krasnov, "A photodesorption study of a TiZr coated stainless steel vacuum chamber", EPAC'02, June 2002.

CHAPTER 13

BEAM INSTRUMENTATION

13.1 BEAM POSITION MEASUREMENT

A complete list of the beam position monitors associated with orbit and trajectory measurements is given in Tab. 13.1. There are three types of monitor: 24 mm button electrode monitors, 34 mm button electrode monitors and 120 mm stripline monitors. These are assembled in 13 different types of housing depending on the vacuum chamber dimension and interface with neighbouring equipment.

13.1.1 Beam Position Monitors

The LHC orbit and trajectory measurement system has been developed to fulfil the functional specifications described in [1]. The system consists of 516 monitors per LHC ring, all measuring in both horizontal and vertical planes. The acquisition electronics is capable of 40 MHz bunch-by-bunch measurements and will provide closed orbit feedback at 1 Hz.

Table 13.1: List of beam position monitor types in LHC

Type	Electrode Type	Name	Number
Standard Arc	24mm Button	BPM	720
Dispersion suppressor & Q7	24mm Button	BPM	140
Standard BPM for vertical beam screen	24mm Button	BPMR	36
Enlarged Aperture BPM for horizontal beam screen	34mm Button	BPMYA	24
Enlarged Aperture BPM for vertical beam screen	34mm Button	BPMYB	12
Warm LHC BPM for MQWA	34mm Button	BPMW	36
Enlarged Warm LHC BPM for ADTV/H	34mm Button	BPMWA	8
Enlarged Warm LHC BPM for D2	34mm Button	BPMWB	16
Combined Button & Shorted Stripline BPMs	24mm Button + 150mm Stripline	BPMC	16
Cryogenic Directional Stripline Coupler for Q2	120mm Stripline	BPMS	8
Warm Directional Stripline Coupler for Q1	120mm Stripline	BPMSW	8
Warm Directional Stripline Coupler for D1	120mm Stripline	BPMSX	4
Warm Directional Stripline Coupler for DFBX	120mm Stripline	BPMSY	4
	TOTAL		1032

Standard Arc Quadrupole Monitors

The majority of the LHC beam position monitors (860 of the 1032) are of the arc type. These consist of four 24 mm diameter button electrode feedthroughs [2] mounted orthogonally in a 48 mm inner diameter beam pipe. The electrodes are curved to follow the beam pipe aperture and are retracted by 0.5 mm to protect the buttons from direct synchrotron radiation from the main bending magnets. Each electrode has a capacitance of 7.6 ±0.6 pF, giving a Z_{inf} of 1.4, and is connected to a 50 Ω coaxial, glass-ceramic, UHV feedthrough.

The button feedthroughs are connected to the cryostat feedthoughs via semi-rigid, 50 Ω coaxial cables capable of coping with cryogenic temperatures and high radiation environments [3]. These semi-rigid cables

are constructed from copper-clad stainless steel inner and outer conductors to give good electrical conductivity and poor thermal conductivity, and use a silicon dioxide foam dielectric. The N-type connectors on either end use a glass-ceramic dielectric seal. The cables work in a frequency range up to 2 GHz, with the electrical length difference in each quadruplet (the four cables associated with a BPM) being less than 10 ps.

The cryostat feedthrough will consist of four 50 Ω ports with less than 4 ps electrical length difference between them and capable of resisting a high radiation environment [4].

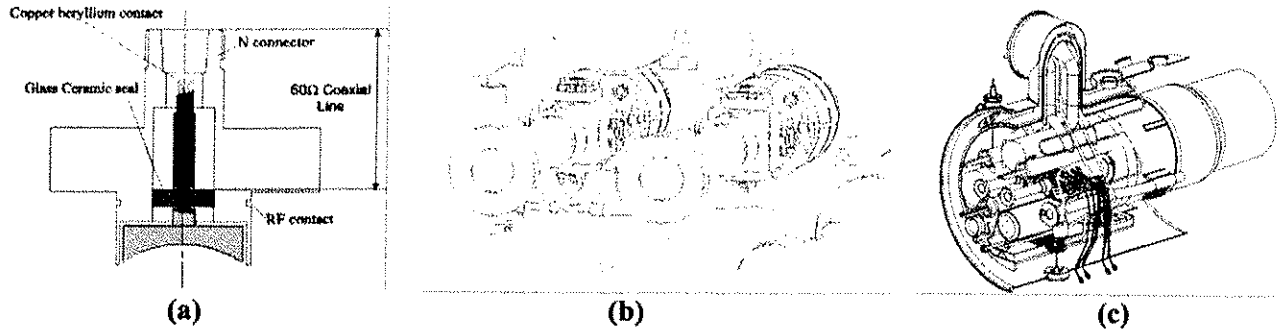

Figure 13.1: (a) 24 mm button electrode, (b) Mounted BPM bodies, (c) Location in the SSS cryostat including semi-rigid coaxial cables.

Non-standard Insertion Region Monitors

The inner triplet BPMs in all interaction regions are equipped with 120 mm, 50 Ω directional stripline couplers (BPMS×), capable of distinguishing between counter rotating beams in the same beam pipe. The location of these BPMs (in-front of Q1, in the Q2 cryostat and after Q3) was chosen as far as possible from a parasitic crossing to optimise the directivity. The 120 mm stripline length was chosen to give a signal similar to the button electrode, so allowing the use of the same acquisition electronics as for the arcs. The BPMs located in the Q2 cryostat is cold and rotated by 45° because of installation constraints. All cold directional couplers use an Ultem® dielectric for use in a cryogenic environment, while the warm couplers use a Macor® dielectric to allow bake-out to over 200°C.

The cleaning insertions in point 3 and 7 are equipped with warm, 34 mm diameter button electrode BPMs (BPMW) fitted either side of the MQWA magnets. The electrodes are an enlarged version of the arc BPM button described in section "*Standard Arc Quadrupole Monitors*". Such button electrodes are also used for the cold BPMs in the matching sections either side of the four interaction regions as well as for the warm BPMs located near the D2 magnets and either side of the transverse damper (ADTV/H).

The BPMC, installed in point 4, are combined monitors consisting of one BPM using standard 24 mm button electrodes for use by the orbit system, and one BPM using 150 mm shorted stripline electrodes for use in the transverse damper system (see Chap. 6.4).

13.1.2 Trajectory Acquisition System

The LHC orbit and trajectory acquisition system is based on a Wide Band Time Normaliser (WBTN) [5] capable of processing the analogue signals from the pick-up at 40MHz. The resulting signal is transmitted via a fibre-optic link, treated, digitised using a 10-bit ADC and processed by a VME64x Digital Acquisition Board (DAB) developed by TRIUMF, Canada [6].

Front-end Chassis

The front-end chassis for the majority of the LHC monitors will consist of four WBTN front-end cards, an intensity card and a WorldFIP control card. The chassis will be located below each SSS cryostat and is capable of processing the two planes from the BPMs of the counter rotating beams. The position information for each passing bunch is encoded in pulse width modulation using the wide band time normalisation principle [5] before being sent over a single mode fibre-optic link using a 2 mW, 1310 nm laser transmitter. In this way the radiation sensitive digital electronics can be separated from the more robust analogue electronics which will be subjected to 12 Gy or more per year during nominal LHC running.

The fibre-optic network linking the front-end electronics in the tunnel to the acquisition electronics located in surface buildings is comprised of ~125 km of ducting containing seven guide tubes. A mini-optical fibre-cable containing six or more fibres is blown into each guide tube and serves a single BPM front-end crate, leading to over 5000 km of installed fibre-optic links. A description of the characteristics and layout of the fibre-optic cabling can be found in Chap. 7 of Volume 2.

The intensity card installed in each chassis allows the simultaneous acquisition of both position and intensity (at the level of a few percent) for a single ring, with the intensity sent by the transmission system of the other ring.

The working mode, WBTN calibration and power supply surveillance of the front-end chassis is controlled via a WorldFIP receiver card using the single 31.25 kbit link serving each LHC sector.

For the insertion region BPMs the front-end chassis is located in neighbouring underground areas due to the high radiation doses around the BPM. In these cases highly phase-stable, ½ inch, 50 Ω, cellular polyethylene dielectric coaxial cable is used to connect the BPM electrodes to the front-end electronics.

VME64x Acquisition Chassis

The VME64x acquisition chassis of the LHC orbit and trajectory system are located in the SR buildings at each access point. The chassis is comprised of a PowerPC, a TTC receiver (see Sec. 13.9) and up to 18 Digital Acquisition Boards (DABs), all linked via a custom AB/BDI VME64x backplane.

Each DAB is capable of processing the data from two WBTN mezzanine cards. A single WBTN mezzanine card receives treats and digitises the pulse modulated signal sent by a single front-end card, providing the DAB with a 40 MHz flow of 10-bit position data.

The DAB is capable of working in parallel in three different modes: orbit, capture (or trajectory) and post mortem. In orbit mode the incoming data is validated, calibrated and summed for 20 ms to eliminate 50 Hz noise. The result is retrieved by the PowerPC which calculates the average orbit for each plane and corrects the result for BPM geometrical non-linearity. This is repeated at 10 Hz, thus allowing the possibility of a 1 Hz closed loop orbit feedback. At the same time the incoming data is histogrammed to provide a standard deviation for each orbit reading.

In capture or trajectory mode the user is free to choose when, for which bunch(es) and for how many turns the DAB stores the position data, while the post-mortem mode stores the last 1000 orbits and 1000 turns in a circular buffer which is frozen by the beam abort system.

13.1.3 Expected Performance

The performance of the WBTN electronics with intensity is shown in Fig. 13.2. The system is expected to function with between 2×10^{9} and 2×10^{11} charges per bunch. A summary of the expected performance of the complete acquisition system for standard arc BPMs is presented in Tab. 13.2.

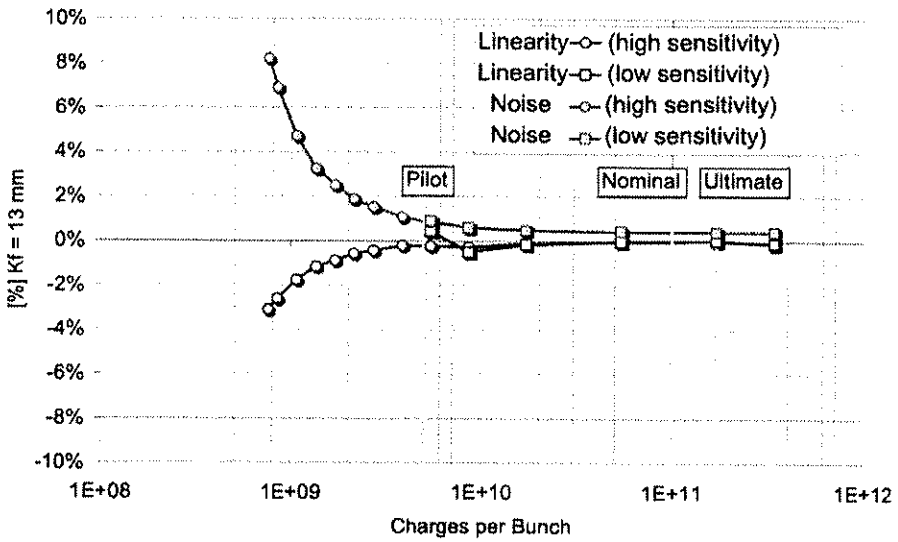

Figure 13.2: Performance of the LHC WBTN system with intensity.

Table 13.2: Expected performance of the LHC BPM system for standard arc BPMs

Range of Operation (±6mm)	Pilot Bunch (5×10^9)		Nominal Bunch (1.1×10^{11})		Ultimate Bunch (1.7×10^{11})	
	Single	Average over 224 turns	Single	Average over 224 turns	Single	Average over 224 turns
Resolution (μm rms)	130	9	50	5	50	5
Non-Linearity (±μm)	100					
Scale Error (±%)	1					
Calibrator Offset (±μm)	50					
Intensity Offset (±μm)	25					
BPM & Gauge Mechanical Offset (±μm)	125					
Survey Measurement Precision (μm rms)	50					
Electrical Axis Offset (±μm)	113					
Uncertainty of MA wrt GA (μm rms)	150					
Geometric Non-Linearity (±μm)	100					
Total Offset (±μm)	363					
Relative Accuracy (offset ignored) (±μm)	302	155	183	154	183	154
Global Accuracy (±μm)	472	394	406	393	406	393

13.2 BEAM CURRENT TRANSFORMERS

Beam current transformers of two different kinds will provide intensity measurements for the beams circulating in the LHC rings as well as for the transfer lines from the SPS to LHC and from LHC to the dumps. The transformers will all be installed in sections where the vacuum chamber is at room temperature and where the beams are separated.

13.2.1 Fast Beam Transformers

The fast beam current transformers (FBCTs) will be capable of integrating the charge of each LHC bunch. This provides good accuracy for both bunch to bunch measurements and average measurements, intended mainly for low intensity beams for which the DCCT accuracy will be limited. For redundancy, two transformers with totally separated acquisition chains will be placed in each ring. These will be located in IR4. Each beam dump line will also be equipped with 2 redundant FBCTs, using the same acquisition electronics, for monitoring the ejected beam. In order to get good performance, there will be a dc restoration with a successive integrator and S/H circuitry used in the ring. The result of integration is digitized and stored in memory. Beam synchronous timing with 40 MHz frequency is used to trigger the system. The measurement precision for the pilot beam of 5×10^9 protons in a single bunch is expected to be around 5 % (worst-case 10%), for the nominal beam below 1%. The transformer cores will use low droop, radiation hard material with a specified droop below 2%/μs and with the sensitivity approx. 1.25 V/A. Once injection is completed the transformers will be used to measure the circulating bunches by averaging the acquired bunch intensities over 20 ms yielding to approximate precision of 1% for pilot beam

13.2.2 DC Beam Transformers (BCTDC)

DC current transformers are based on the principle of magnetic amplifiers and will measure the mean intensity or current of the circulating beam and they can be used to measure the beam lifetime. Because of their operational importance, two of the devices will be installed in each ring. Currently a resolution of 2 μA can be reached but a 1 μA is targeted corresponding to 5×10^8 circulating particles. The temperature dependence of the output current is ~5 μA per degree which makes either temperature stabilisation or frequent re-adjustment of the offset a necessity.

With an intensity of 4.8×10^{14} protons and a lifetime of 25 h driven by pp collisions the decay rate is 5×10^9 protons/s. With a measurement time of 10 s this decay should be seen with 1% precision.

A resolution of 1 μA is, however, insufficient for measurement of the pilot beam which can only be achieved with the fast transformers.

The front-end electronics generating the dc transformer feedback current should be placed as close as possible to the sensor in the ring. However, the radiation induced by the beam and by the RF cavities during their conditioning will be an issue. If the finest resolution is required for measuring the beam over the whole dynamic range, then an ADC of at least 20 bits, located in the front-end electronics is required. The data will be transmitted to the front end computer (DSC) installed in a surface building.

13.3 BEAM LOSS SYSTEM

13.3.1 Beam Loss Monitors

The loss of a very small fraction of the circulating beam may induce a quench of the super-conducting magnets or even physical damage to machine components. The detection of the lost beam protons allows protection of the equipment against quenches and damage by generating a beam dump trigger when the losses exceed thresholds. In addition to the quench prevention and damage protection, the loss detection allows the observation of local aperture restrictions, orbit distortion, beam oscillations and particle diffusion, etc. Since a repair of a superconducting magnet would cause a down time of several weeks, the protection against damage has highest priority.

The measurement method

The measurement principle is based on the energy deposition detection of secondary shower particles using ionisation chambers located outside of the magnet cryostats. The secondary particle energy flux is linear with the initiating protons parameters. To observe a representative fraction of the secondary particle flux detectors are placed at likely loss locations. The calibration of the damage and quench level thresholds with respect to the measured secondary particle energy deposition is simulation based.

Dynamic range, resolution and response time

The criteria used to define the dynamic range are given by the calculated damage and quench levels and the expected usage. The observation time range is defined by the fastest possible use of a beam dump trigger signal by the beam dump itself and the response time of the helium temperature measurement system.
Different families of BLM monitors are defined to ease the monitor design (see Tab. 13.3) [7].

Table 13.3: Functional families of BLM

Type	*Area of use*	*Dangerous consequences in the case of failures*	*Time resolution*
BLMC	Collimation sections	yes	1 turn
BLMS	Critical aperture limits or critical positions	yes	1 turn
BLMA	All along the rings	no	2.5 msec
BLMB	Primary collimators	no	1 turn bunch-by-bunch

There are basic criteria common to the BLMA, BLMS and BLMC:

- The high end of the dynamic range is set at three times the quench level. This takes into account the uncertainty of the evaluation of the quench level (factor of two). It also leaves a safety margin of a factor of nine (7.5) between the dump threshold and the high end of the BLM dynamic range at 450 GeV (7 TeV).
- The low end will be 5% of the quench level.
- For long integration times, the low end of the dynamic range is significantly reduced at 450 GeV to allow for extrapolation of the losses. The extrapolation from the pilot beam to the intermediate intensity beam requires a factor of 430 and an additional sensitivity factor of 10 is used.

13.3.2 BLMA

The dynamic range is specified in Fig. 13.3 and Tab. 13.4. The predicted quench levels depend on the loss duration and the beam energy. A continuous change of quench level thresholds is required during the beam energy ramp.

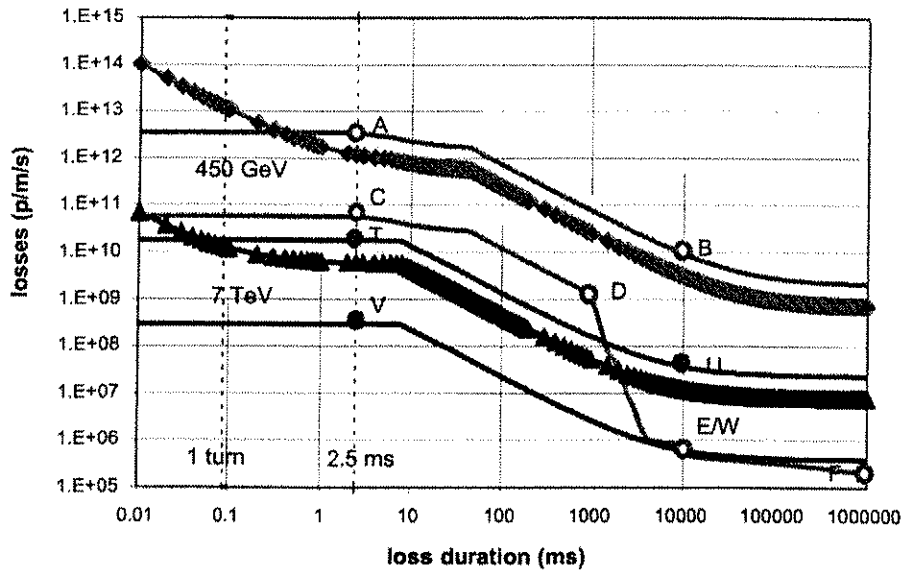

Figure 13.3: Quench levels as a function of the loss duration for the LHC arc bending magnet (marker + line) for 450 GeV (green squares) and for 7 TeV (blue triangles). The dynamic range is indicated by lines limiting either quench level curves. The loss rates marked by letters appear in Table 13.4, with their corresponding numerical values.

Table 13.4: Dynamic range for the BLMA and BLMS in units of Protons/m/s

	2.5 ms (BLMA) 0.1ms (BLMS)		1 s		10s		100s	
	MIN	*MAX*	*MIN*	*MAX*	*MIN*	*MAX*	*MIN*	*MAX*
450 GeV	6×10^{10} (C)	3.6×10^{12} (A)	1.3×10^{9} (D)		8×10^{5} (E)	9.6×10^{9} (B)	2×10^{5} (F)	
7 TeV	3×10^{8} (V)	1.8×10^{10} (T)			6.25×10^{5} (W)	3.7×10^{7} (U)		

13.3.3 BLMS

The BLMS has the same requirements as the BLMA, given in Fig. 13.3 and Tab. 13.3, except for their faster time response (1 turn, which corresponds to 89 us).

13.3.4 BLMC

The BLMC also have a time resolution corresponding to one turn. Their dynamic range must take into account the loss enhancement due to the collimation efficiency. This loss enhancement corresponds to a factor of between 3×10^{3} and 1×10^{4} (see Fig. 13.4).

Table 13.5: Dynamic range for the BLMC in units of Protons/s assuming a length of 1 meter.

	0.1 ms		1 s		10s		100s	
	MIN	*MAX*	*MIN*	*MAX*	*MIN*	*MAX*	*MIN*	*MAX*
450 GeV	6×10^{14} (C)	3.6×10^{17} (A)	1.3×10^{12} (D)		4×10^{9} (E)	9.6×10^{13} (B)	1×10^{9} (F)	
7 TeV	6.5×10^{11} (V)	3.9×10^{14} (T)			6.25×10^{8} (W)	3.7×10^{11} (U)		

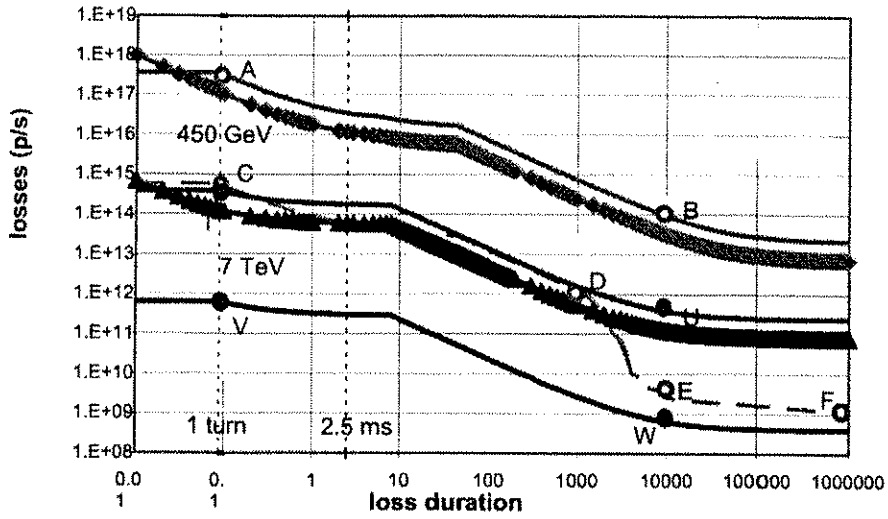

Figure 13.4: Total loss thresholds at all collimators (marker + line) for 450 GeV (green squares) and for 7 TeV (blue triangles) as function of the loss duration. The dynamic range for the BLMC is indicated by lines limiting either quench level curves. The loss rates marked by letters appear in Tab. 13.5, with their corresponding numerical values.

13.3.5 BLMB

The nominal functionality of the BLMB is to monitor any bunch-to-bunch variations. Their dynamic range is specified in Tab. 13.6.

Table 13.6: Dynamic range of BLMB

	Lower limit	*Upper limit*
BLMB	10% of the nominal steady losses at the collimators:	Warning level:
	3.5×10^{6} p/s per bunch (450 GeV)	3.5×10^{8} p/s per bunch (450 GeV)
	1×10^{5} p/s per bunch (7 TeV)	7×10^{6} p/s per bunch (7 TeV)

Accuracy and reliability

The damage and quench level prediction uncertainties are given by:

- Inaccuracy in the ionisation chamber particle flux measurements.
- Inaccuracy in the prediction of the secondary particle flux.
- Inaccuracy in the assumptions and predictions of the topology of proton particle loss distribution.
- Inaccuracy of the damage and quench level predictions.

Given the difference between the quench and damage levels of a factor of 5 at 450 GeV for loss duration larger as 10 s, the ultimate goal will be to calibrate the loss scale to within ±50% (see Tab. 13.7).

Table 13.7: Precision of the detectors

Absolute accuracy (calibration)	< factor 2 (initial < factor 5)
Relative accuracy (to quench levels) for quench prevention	< ± 25%
Resolution for extrapolation	< quench level at 7 TeV/50

The target probability for magnet damage and the probability for a false dump are calculated using the SIL (Safety Integrity Level) approach [8]. The assumption of an LHC downtime period of 30 days as a consequence of magnet damage leads to a target probability for not detecting and dumping the beam in case of a dangerous loss of 10^{-7} to 10^{-8} per hour. A further analysis is required to determine if this low probability is required for every BLM channel.

The false dump probability of 10^{-6} to 10^{-7} is mainly driven by the assumption that ten unjustified dumps (dump requests from the system due to false triggers) could be accepted in one operational year.

Secondary shower particles

Beam protons are likely to be lost at the location where the aperture is minimal: at 450 GeV this occurs at every arc quadrupole magnet and at 7 TeV at the triplet magnets. The beam loss monitors are located on either side of the magnets, in the horizontal plane defined by the beam vacuum tubes. Their longitudinal positions are about 1 m downstream of the most likely loss locations (see Fig. 13.5) [9, 10]. The centre of the quadrupole magnet and the bellows locations between quadrupole magnet and bending magnets are the anticipated loss locations. The optimisation of the location of the monitors is done using the criteria of maximum signal detection and the ability to distinguish between Beam 1 and Beam 2. A summary listing of the monitor locations is shown in Tab. 13.8.

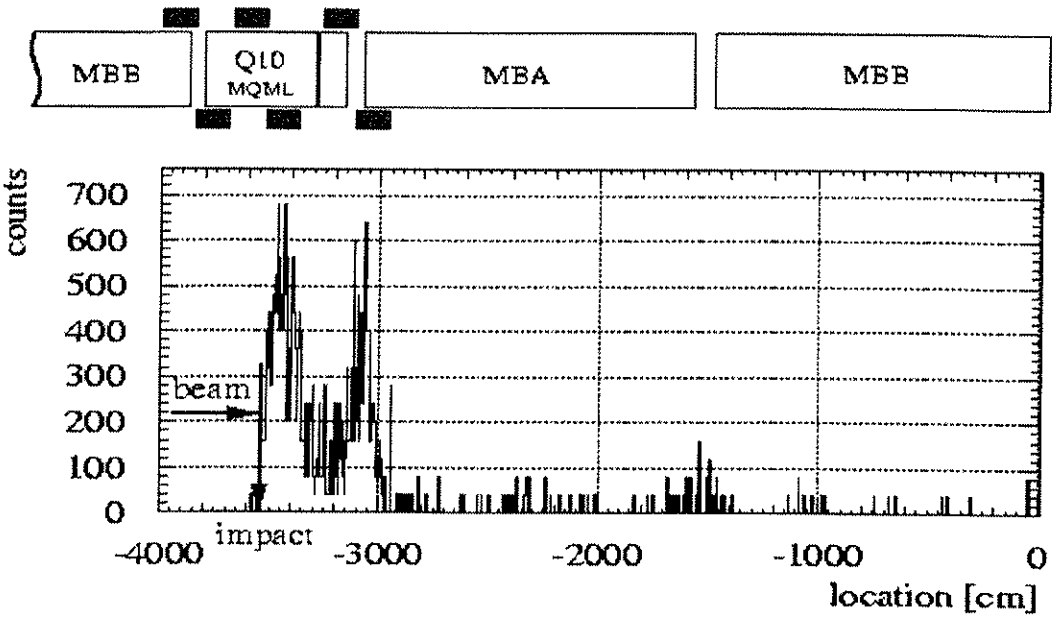

Figure 13.5: Scheme of the beam loss monitor locations in the vicinity of a quadrupole magnet (top). The simulated longitudinal particle shower distribution at the outside of the cryostat surface traversing a stripe with a height of ±5 cm in respect to the horizontal plane (bottom) is shown. The initiating proton impact position is at the centre of the quadrupole magnet.

The Monitor

The basic layout for the BLMA, BLMS and BLMC is shown in Fig. 13.6. The BLMB monitors are not yet defined.

The ionisation chamber signal is proportional to the energy loss of the traversing particles. The ionisation chamber has a volume of about 1 litre and the inner parallel electrodes are separated by 5 mm. The chamber is filled with N_2 under normal pressure and a bias voltage of 1500 V is applied.

The chamber current for the BLMA and BLMS monitors varies between a few 10^{-12} A and almost 10^{-3} A. The BLMC ionisation chamber is not defined yet.

Table 13.8: Location and number of monitors.

	Location		*Number*	*Comments*
BLMC	IR3	1 primary, 6 secondaries	7 × 2	At about 0.2 m downstream of each collimator
	IR7	4 primaries, 16 secondaries	20 × 2	
BLMS	IR3	Cryobox DFBA	2 × 2	Monitoring of the losses on the cryogenic feed-box
	IR7	Cryobox DFBA	2 × 2	
	IR2,IR8	Septum MSI, Target TDI, TCDD, 2 collimators,D1	6 × 2	Monitoring and protection against injection errors
	IR1, IR5	Absorbers: 2 TAS,	4	Monitoring of the losses at the TAS
	IR1,IR2, IR5, IR8	Triplets (2 per triplet) + BPM.Q1	16×2×2 8 × 2	Maximum of beam size Exit of IP
	IR1, IR5	2 TAN absorbers, 4 experimental collimators	12 × 4	Monitoring at the targets around the experiments
	IR6	Septum MSD, TCDQ, TCDS, DFBA	4 × 2	Monitoring of the ejection to the dump channel
	DIS	MB adjacent to Q8 between Q7/Q8 + last MB before Q11, all DS's	8 × 4 × 2	Aperture limit in dispersion suppressors (momentum)
BLMA	LHC	At every quadrupole	368 × 2	At the local maximum of the beam size
	movable		1	Movable goniometer covering a half-cell to be used in case of suspected aperture restriction
BLMB	IR7	At one primary collimator per plane	2 × 2	Monitoring of the losses at 40 MHz

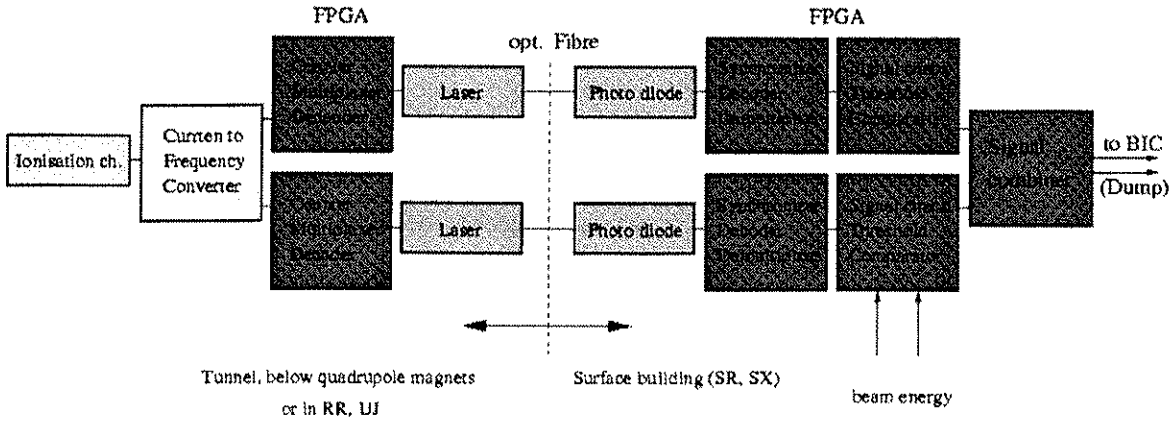

Figure 13.6: The schematic view of the ionisation chamber signal transmission and treatment chain.

The cable length between chamber and front end electronics (BLMCFC) varies between 10 m for the BLMA (below quadrupole magnets) and maximum 400 m for the BLMS (RR and UJ locations). The chamber current is converted to a corresponding frequency and these pulses are counted over a period of 40 μs. The counter value is transmitted every 40 μs to the surface analysis electronics (BLMTC) using a

dedicated fibre link. The BLMTC compares the measured loss values with the loss duration and energy depending threshold values. The warning information is transmitted by a software protocol and the dump signals are transmitted to the dump kicker magnets using the beam interlock controller (BIC). The energy information is received over a dedicated redundant fibre link. The signal treatment and transmission chain is redundant after the current to frequency conversion to meet the required dangerous consequence probability of 10^{-7} to 10^{-8} per hour.

13.4 TRANSVERSE PROFILE MEASUREMENT

The analysis of the anticipated uses allows the definition of four functional modes to be mapped on the different types of hardware monitors:

- A single-pass monitor of high sensitivity (pilot beam) with a modest demand on accuracy and few restrictions on the beam blow-up due to the traversal.
- A "few-pass monitor" (typically 20 turns) dedicated for the intermediate to nominal intensity range of the injected beam for calibration or matching studies. The blow-up per turn should be small as compared to the effect to be measured.
- A circulating beam monitor, working over the whole intensity range. No blow-up is expected from such a monitor.
- A circulating beam tail monitor optimised to scan low beam densities. In this mode one may not be able to measure the core of the beam. The measurement should not disturb the tail density significantly.

IR4 is the default location for all instrumentation.

13.4.1 Single Pass Monitors

Five monitors are planned at each injection point into LHC, and an extra monitor will be installed between quadrupoles Q6 and Q7 at the exit of the first arc after injection. Its location is in the middle of the drift where both the H and V amplitude functions have same value (about 100 m), thus providing equal beam size in either plane. The position of the single-pass-monitors in each LHC ring is summarised in Tab. 13.9.

Table 13.9: Layout of single-pass monitors

Entry septum MSI
Exit septum MSI
Entry kicker MKI
Exit Kicker MKI
Entrance TDI absorber
Between Q6 and Q7
in LSS3 left (for Ring1 and Ring2, also needed for matching studies)
in LSS7 right for Ring2
Between Q5 and Q6 in LSS4 for Ring1 & Ring2 (used also for matching studies)

13.4.2 Few-pass Matching Monitors

For matching studies at injection a matching monitor is needed in each ring at a position where the dispersion is significant (> 1 m) and the horizontal and vertical beam sizes are both large enough to offer the best sensitivity, i.e. in the middle of a drift. The nominal matching monitor will be installed in IR3 between Q6 and Q7 (Tab. 13.9). Optional matching monitors (dispersion free) can be installed in IR4 between quadrupoles Q5 and Q6 (Tab. 13.9 and Fig. 13.7), where rms values of 1.25 mm at 450 GeV will be measured. Another application of these monitors would be first turn observation during injection studies (Tab. 13.9).

13.4.3 Circulating Beam and Tail Monitors

For the best performance, this type of monitor should be placed at large β-values. In addition, with a β-ratio of 2 or more between planes, the tilt due to the coupling of a round beam becomes observable. The following positions have been selected and fulfil the requirements both for the baseline program and for extensions allowing more precise monitors if the need arises:

IR4 synchrotron light monitor

In each ring a synchrotron radiation monitor is under development, using a signal provided by superconducting (SC) undulators installed upstream of the D3 separator magnet, as shown in Fig. 13.7. Profiting from the beam deflection generated by D3, the light is extracted 10 m downstream of D3, providing a two dimensional transverse image of the beam.

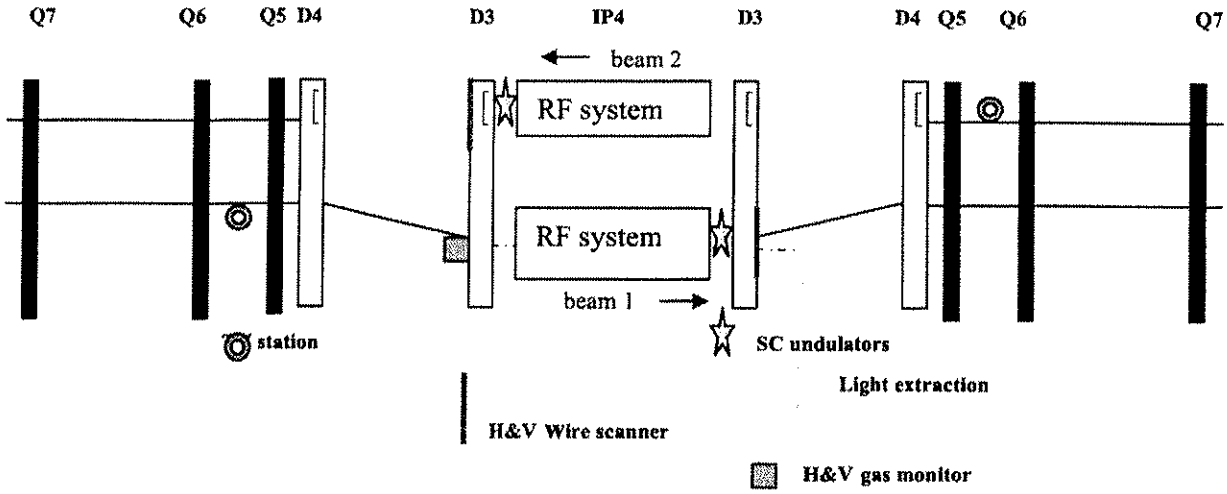

Figure 13.7: Configuration of transverse profile monitors in IR4.

IR5 synchrotron light monitor

This location will be kept as an option. It provides the best resolution for flat top energy operation on the collision optics, with local amplitude functions of 590 m and 1600 m, respectively, in the horizontal and in the vertical planes. The monitor uses the light emitted by the beam within the magnet D2, which is extracted 20 m later. The setup here is shown schematically in Fig. 13.8.

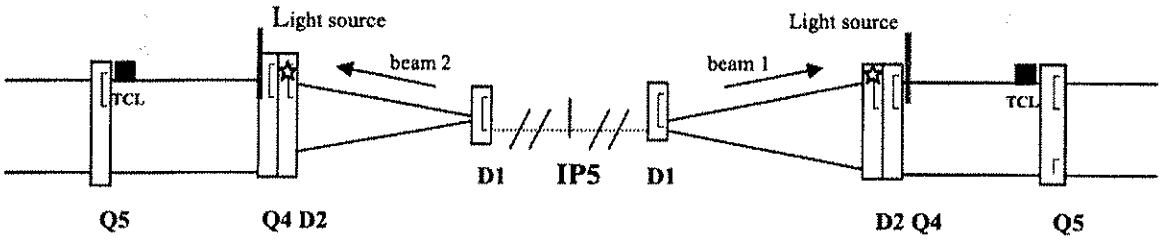

Figure 13.8: Telescope configuration in IR5.

IR4 Gas monitors

Gas monitors, exploiting either the rest gas ionisation signal or looking at the luminescence light resulting from de-excitation of the gas atoms, are being considered. For each beam one monitor with good resolution in each transverse plane is required. A location close to D3 is favourable, where the separation between the beams is largest and where the amplitude functions are close to 250 m. These locations are shown on Fig. 13.7.

Table 13.10: Accuracy and resolution necessary

Mode		Beam scenario	Observation mode	Precision
Single-pass to Few-pass	Beam spot	1 pilot to 1 nominal SPS batch	Turn-by-turn	Accuracy: • 20% rms on σ • average position: $\approx$ 300 μm rms
	matching	1 intermediate bunch to SPS batch	Turn-by-turn over 20 turns	Resolution: ± 20% on σ
Circulating		Intermediate to ultimate SPS batch		
	beam size and profile	Pilot to intermediate beam	10^3 turns	Resolution: 10% rms on beam σ
		intermediate to ultimate beam		Resolution: • 1% rms on beam σ • 5% rms on bunch σ • 10% rms on transv. distribution points • (± σ/10 in beam position)
			10^2 turns	Resolution: 5% rms on beam σ
	Beam emittance		10^3 turns	Accuracy: ± 5% on beam σ
	tail	intermediate to ultimate beam	10^4 turns	Resolution: 10% rms on transv. distribution points
	dynamic aperture	1 pilot to one intermediate bunch	10^3 to 10^4 turns	Resolution: ± 10% on transv. distribution points
	calibration	Pilot bunch to nominal PS batch	No constraint	Accuracy: 1% rms on σ

IR4/IR5 Wire scanners

Wire scanners will be installed in IR4. Their position is illustrated schematically in Fig. 13.7. They will be used principally for absolute calibration of the other monitors, but also as tail monitors. Their use for calibration purposes imposes the most demanding accuracy; typically 1%. To overcome uncertainties related to β-beating, they would ideally be at the same location as the SC undulators or the other emittance monitors. However, in order to minimise the risk of quenching the D3 magnet when they are used, they will be installed immediately downstream of this magnet as shown in Fig. 13.7. The installation of a Synchrotron Light telescope in IR5, would also be complemented by the installation of wire scanners (Fig. 13.8) for the absolute calibration.

The accuracy and resolution to be achieved in the various modes is summarised in Tab. 13.10.

13.5 LONGITUDINAL PROFILE MEASUREMENT

This instrument profits from the Transverse Profile Monitor light source [11] with the aim of using synchrotron light to measure bunch profiles with a dynamic range of 10^5, enabling measurements and monitoring of bunch lengths, tails, un-bunched beam, ghost bunches and the abort kicker rise time gap.

A part of the synchrotron light generated by the superconducting bending and undulator magnets of the Transverse Profile Monitor is collected by a separate fixed mirror offset behind the transverse optics. It is estimated [12] that 2×10^6 photons will be collected per passage of each 1.1×10^{11} proton bunch; this intensity remains reasonably constant from injection energy up to 7 TeV. However, the spectral distribution changes with beam energy, at injection energy the undulator produces a distribution peaked around 950 nm but at

higher energies the spectral profile is from 200 nm to 2000 nm, although only a part of this range can be used by the instrument.

The photon flux reliably mimics the beam in both time and intensity, the specification [13] calls for the photons to be detected with 50 ps precision: two detection methods are under study at Lawrence Berkeley Lab, who will produce the instrument as part of the LARP collaboration. One possible system is to use a laser oscillator which generates ~20 ps pulses at a high repetition rate (40 MHz), synchronised to sample the entire LHC rotation at 50 ps intervals. The synchrotron light can be mixed with a laser pulse, the amplitude of the resulting wavelength-shifted pulse can then be measured by a fast detector, and data is then accumulated in registers to build up the required data profiles. A prototype Laser-Mixing (LM) system has been successfully used to measure beam profiles at the Advanced Light Source at LBNL.

An alternative system is to use an array of fast Single Photon Detectors (SPD) and time-of-flight recorders, continuously detecting the photon flux with the data being accumulated into registers as before. A decision on the best system for LHC will be made in 2004.

The need to sample the entire LHC circumference with 50 ps intervals would lead to 2 million data bins: a serious data handling task. This can be minimised by coding each sample point with the relevant measurements: for example, of the ~35,500 RF buckets, only 2808 should contain bunches, so the data from the majority of sample points will accumulate into the measurement of ghost bunch current or debunched beam.

At injection energy the LPM will monitor the intensity of the debunched beam to ensure safe conditions before the acceleration ramp starts, the maximum safe level being 1500 times lower than the nominal bunch intensity. It is also necessary to ensure that the abort kicker rise time gap remains empty; here the 3 μs gap is divided into 30 measurement bins of 100 ns length.

Individual bunches, groups of bunches, or the entire fill can be targeted to provide the bunch centre of gravity, length, core distribution and distribution in the low intensity tails, the sensitivity and range of the measurements will depend on the integration time available. An absolute intensity calibration can be made by comparing the total integrated beam intensity with a beam current monitor.

13.6 LUMINOSITY MONITORS

13.6.1 Introduction

The nominal LHC luminosity for IR1 (ATLAS) and IR5 (CMS) is 10^{34} $cm^{-2}s^{-1}$, for beams of 2808 bunches of 1.1×10^{11} protons each. The other two interaction regions will have lower nominal luminosities of the order of 10^{32} cm^{-2} s^{-1} for IR8 (LHCb) and 10^{30} $cm^{-2}s^{-1}$ for (IR2) ALICE. With different filling patterns and optics, the global range of luminosities goes from 10^{26} to 10^{34} $cm^{-2}s^{-1}$ and for the ion runs between 10^{24} $cm^{-2}s^{-1}$ and 10^{27} $cm^{-2}s^{-1}$.

The proton beams are bunched with a bunch-to-bunch distance of 25 ns (or a multiple of 25 ns). This corresponds to a maximum bunch crossing frequency of 40 MHz. In nominal conditions the beams do not collide head on, but with a small angle of the order of 150-200 μrad to avoid unwanted collisions near the IP. The plane containing the two beams (collision plane) can be rotated and be different in the four interaction regions.

13.6.2 Machine Requirements

The aim of the machine luminosity monitors [14] is to measure the interaction rates for the setup, the optimisation and the equalisation of the beams at the interaction regions. For this purpose they must be simple, fast and robust and preferably be of one design for all four IR's. These instruments are required to measure the interaction rate with a good relative accuracy; the absolute value can be obtained with frequent cross calibrations with the luminosity monitors installed in the experiments, or other methods. The calibration factor must remain stable over a reasonable amount of time and must not be influenced by the machine parameters (steering, optics etc.)

The requirements on the accuracy go from around 10% for the beam finding mode to 0.25 % for the collision feedback. Measurement times also vary from minutes in beam finding mode (very low luminosity) to one second at nominal luminosity. The monitors should also allow the measurement of the crossing angle with accuracy better than 10 μrad in the range 0-200 μrad.

In order to detect and correct eventual bunch-by-bunch effects the bunch-by-bunch luminosity measurement is required. The detectors, readout and acquisition systems must thus be capable of operating with a useful bandwidth of 40 MHz. The bunch-by-bunch measurements, the average luminosity and crossing angle should be sent to the main control room and also dispatched to the experiments.

13.6.3 Instrument Description

The machine luminosity monitors are in fact flux monitors. They are installed in the TAN absorbers 141 m away on both sides of the high luminosity IR's (1 & 5) and equivalent positions in IR2 and IR8. They measure the flux of the showers generated by the neutral particles created in the collisions (neutrons and photons). Neutral particles are chosen in order to suppress the background related to beam losses. The radiation dose to the detectors is very large, 170 MGy/yr, and poses a constraint on the choice of the technology.

The detectors have a rectangular surface ~10 cm × 10 cm. Each detector consists of four rectangular fast, pressurised, gas ionisation chambers, assembled in a 2×2 array, and are placed behind ~30 cm of copper at the shower maximum inside the TAN [15].

An alternative technology still under investigation consists of the use of polycrystalline CdTe discs in a 2×5 array. This solution offers a better sensitivity, time resolution and angle measurement. The radiation hardness of this type of technology is however still under investigation.

In both cases the signals have to be transported using radiation resistant cables to a less radioactive area behind the TAN where the first stage of the electronic system is installed and then from there sent to the counting room where they will be acquired using the DAB (Digital Acquisition Board) developed at the TRIUMF Laboratory for the orbit measurement system.

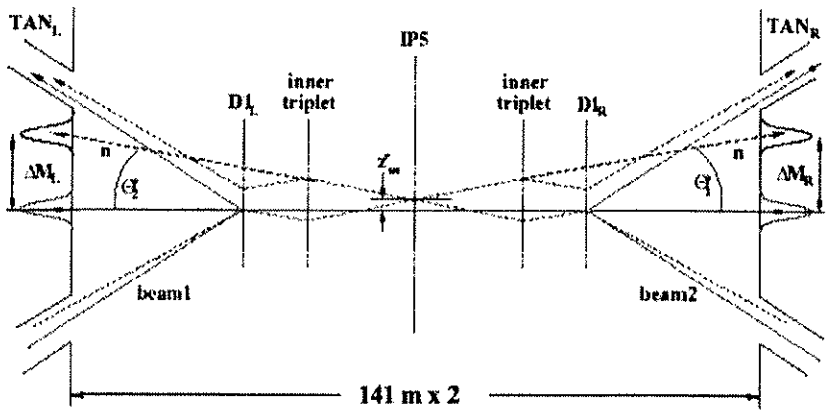

Figure 13.9: Schematic layout of the interaction region at IP5 (CMS).

13.7 TUNE, CHROMATICITY AND BETATRON COUPLING

The reliable measurement of betatron tune, Q (and the related quantities tune-spread, chromaticity and betatron coupling), will be essential for all phases of LHC running from commissioning through to ultimate performance luminosity runs. For injection and ramping, the fractional part of the betatron tune must be controlled to ±0.003, while in collision the required tolerance shrinks to ±0.001. With the exception of Schottky scans (see Sec. 13.9) and the "AC-dipole" excitation outside the tune peak (Sec 13.10), all Q measurement techniques involve some disturbance to the beam. The resulting emittance increase, while acceptable for some modes of running, e.g. with pilot bunches, will have to be strongly limited for full intensity physics runs. Two distinct tune measurement systems are therefore envisaged, as described below.

13.7.1 General tune Measurement System

This system will allow the measurement of tune via standard excitation sources (single kick, chirp, slow swept frequency, and noise). It should operate with all filling patterns and bunch intensities and be commissioned early after the LHC start-up. Even with oscillation amplitudes down to 50 μm, a certain

amount of emittance increase will result, limiting the frequency at which measurements can be made. It will therefore probably be unsuitable for generating measurements for an online tune feedback system.

Detectors

Dedicated stripline couplers will be mounted on 2-3 m long motorised supports that can be displaced horizontally or vertically with a resolution of 1 or 2 microns. There will be two such supports near Q6 and Q5 left of IR4 and another two at Q5 and Q6 right of IR4. They will measure in one plane only to profit from the high β_h or β_v near each quadrupole (typically 400 m). Also mounted on each support will be the resonant pick-up (see Sec. 13.7.3) and a standard warm button BPM dedicated to providing positions for a slow feedback loop keeping the BPM centred about the beam. This will allow the electrical aperture of the tune coupler to be reduced to measure small position deviations about the closed orbit. Also, taking into account the higher signal level from the coupler design, the dedicated tune pick-ups will have a much higher sensitivity than the normal closed orbit BPMs for transverse oscillation measurements. If necessary, electronic common mode rejection could also be included in the processing chain. Measurements of individual bunch positions have been requested for this system.

When the oscillation amplitude is sufficiently large, the orbit BPMs can also be used for tune measurement. It will be possible to measure the betatron function and phase advance all around the ring with them.

Kickers

Four kicker magnets will be installed around IR6 (one for each plane and each beam) to excite coherent oscillations of part of the beam with a short kick pulse. The current specification calls for a Q-kick generator producing 9 μs base half-sine pulses with a superimposed 3rd harmonic to make the pulse more square. The length has been optimised to kick 3 x 72 bunches, with limited disturbance of the neighbouring batch. The maximum oscillation amplitude produced corresponds to $2.6\sigma_T$ at 450 GeV and $0.7\sigma_T$ at 7 TeV. A kick repetition rate of 1 Hz should be possible. The minimum kick available at 450 GeV will be 50 μm. The kicker magnets (identical to a dump-kicker module) will also be driven by a more powerful "aperture" generator producing an 89 μs base half-sine pulse corresponding to up to $8\sigma_T$ at 7 GeV.

An alternative scheme using only one generator per magnet with a maximum kick of 6 σ_T at 450 GeV and $1.7\sigma_T$ at TeV is presently under study. If accepted, this would facilitate kick-based Q measurement at 450 GeV and 7 TeV and the exploration of the dynamical aperture at only 450 GeV. If an $8\sigma_T$ kicker were really required at 7 TeV, then this could be retro-fitted in about one year, once the LHC start-up has taken place. The disadvantage for Q measurement is that three times more beam is kicked at a time and so, on a completely filled machine, fewer kicks would produce a given emittance increase of the whole beam.

Use of transverse feedback kickers

The general tune measurement system will make use of the transverse feedback kickers, as is done in the SPS. Reducing the feedback gain in unstable beam conditions, and injecting noise, chirps (fast frequency sweep), or slow swept frequency are all possibilities that can be exploited for tune measurement. Cabling and patch panels for introducing signals into the feedback loops in SR4 and also in UX45 have been planned.

It is clear that there exists a certain incompatibility between transverse feedback and precision tune measurement: namely that the damping action will broaden the tune resonance to an extent precluding the desired precision of 0.001 of the tune measurement. It is to be hoped that short intervals (some 10's of ms) with reduced feedback gain can be tolerated while a tune measurement is made. An alternative approach using frequencies near the top limit of the transverse feedback bandwidth is described in the next section.

13.7.2 AC Dipole

Principle of the AC-dipole excitation

The emittance-conserving beam excitation was studied at BNL for adiabatic resonance crossing with polarised hadron beams. It was realised that the same principle can be used to diagnose the linear and non-linear transverse beam dynamics.

The principle is as follows: the beam is excited coherently at a frequency close but outside its eigenfrequencies by an oscillating dipole field. Hence the name AC dipole is given to the exciter. In the simplified model of a linear oscillator, the beam is expected to oscillate at the exciter frequency with a phase shift of $\pi/2$. The energy of the coherent oscillation does not couple with the incoherent oscillations of the individual beam particles. There is therefore no change of beam emittance.

It is important to note that the forced beam oscillation amplitude is inversely proportional to the difference of the betatron tune and the exciter frequency, which is the major parameter in the design of the AC-dipole force:

- One would like to create big oscillation amplitudes, which demand the excitation frequency to approach the betatron tune.
- One wants to preserve beam emittance, which in practice demands a minimum difference between exciter frequency and betatron tune of about $0.02 * f_{ref}$.

More details in particular on the excitation scheme can be found in [16] and in the references therein.

Requirements of an AC-dipole for the LHC

At present, the functional specifications for an AC-dipole beam excitation are not complete. The following issues are clear:

- Accelerator physicists would like to use this tool in order to excite sizable beam oscillations at 7 TeV beam energy for diagnostics purposes (several sigma).
- For such extreme cases the minimum frequency difference between exciter and betatron tune could be chosen smaller and one would expect some beam blow-up.
- One has to be able to change the frequency of the AC-dipole by about 10% in order to adapt to changes of the machine tunes.
- An AC dipole excitation for both planes and both rings is requested.

Technical solutions

No work has so far been invested in a detailed design and therefore only a few things can be listed:

- The exciter frequency will be around 3 kHz, which precludes a superconducting magnet or a steel magnet. The skin effect is not yet very important at that frequency, such that an air core magnet with cosine density distribution of the windings can be envisaged.
- By adding a parallel capacitor to the magnet winding a resonant circuit will be created, which will be driven by a power amplifier. The time envelope of the excitation will be created in the low power part driving the amplifier.
- First estimates [17] of the power necessary show an enormous reactive power of more than 10 MVA needed in the AC-dipole, if the requirements on the kick strength are maintained. This value is for a magnet of about 10 m length.
- It is very difficult to achieve a 10 % tunability of such a high power device. Movable ferrite blocks to change the inductance of the coil have been studied at RHIC, but have not been realized. DC polarisation of the coil ferrite material is possible, but will require huge dc currents. As an alternative, the use of a second amplifier, which will act as variable capacitance in a circuit called "gyrator" is being studied.

13.7.3 High Sensitivity Tune Measurement System

The beam is excited by applying a signal of low amplitude and high frequency, f_{ex}, to a stripline kicker. f_{ex} is close to half the bunch spacing frequency, f_b, (for the nominal 25 ns bunch spacing f_b = 40 MHz). The equivalent oscillation amplitude should be a few micrometers or less at a β-function of about 200 m. A notch filter in the transverse feedback loop suppresses the loop gain at this frequency, where instabilities are not expected to be a problem. If the excitation frequency divided by the revolution frequency corresponds to an integer plus the fractional part of the tune then coherent betatron oscillations of each bunch build up turn by turn (resonant excitation).

A batch structure with a bunch every 25 ns "carries" the frequency f_{ex} as sidebands of the bunch spacing harmonics (i.e. at (N × 40 MHz) ± f_{ex}). A beam position pick-up is tuned to resonate at one of these frequencies. By linking the generation of the excitation signal and the processing of the pick-up signal in a phase-locked loop (PLL) feedback circuit, the excitation can be kept resonant and the tune can be determined continuously. Emittance growth is controlled by maintaining the excitation level as small as possible, compatible with the required measurement precision and rate. Since the first derivative of the phase as a function of frequency goes through a maximum at the central value of the tune, this method gives the highest precision for a given oscillation amplitude. The tune values produced could be used as input to a tune feedback loop.

It must be emphasized though that the present design of the system is optimised for luminosity runs with batched beams with 25 ns bunch spacing. The handling of other bunch spacings at multiples of 25 ns should be possible, but the magnitude of the pick-up signal diminishes with increasing bunch spacing.

The development of a PLL tune measurement system for the LHC is being done in collaboration with Brookhaven National Laboratory, where a similar system has been installed in RHIC. It is clear that the system will not be operational during the early stages of commissioning the LHC. Indeed, the beams planned for initial commissioning (single bunch, 43 equally spaced bunches, etc.) are incompatible with this method.

13.7.4 Chromaticity Measurement

At injection it is expected that the linear chromaticity must be controlled to better than $\Delta Q' = \pm 1$ unit. This relaxes to ±3 units in collision. During the "snap-back" phase of the magnet cycle at the beginning of the ramp the b_3 multipole in the main dipoles can generate a chromaticity change of up to 2.7 units per second. Feed-forward, on-line reference magnet measurements and modelling should reduce this rate, but not to zero. At the time of writing there is no proven chromaticity measurement system that can produce data for a feedback loop at these rates for full intensity physics beams.

Energy modulation

Since chromaticity is proportional to the rate of variation of tune with beam energy, the classical measurement method consists of varying the beam momentum and measuring the induced changed in betatron tune. The beam momentum is most conveniently changed by modulating the RF frequency. The drawbacks for use in the LHC are the relatively slow rate of RF frequency modulation (of the order of 0.1 Hz) and the magnitude of the consequent orbit changes. The method will be available for machine setting up, but is incompatible with normal operation.

A promising alternative method of modulating the energy that has been proposed recently is fast RF phase modulation. In the LHC, a 3° RF phase change seems feasible, corresponding to $\Delta E/E$ of 5×10^{-5}. The modulation rate must be significantly higher than the synchrotron frequency (20-60 Hz in the LHC). Experiments are under way in the SPS [18]. Unlike the head-tail method described below, this method does not suffer from the problem of producing an excessive emittance increase.

Head-tail phase shift measurements

The so-called "Head-Tail" chromaticity measurement allows the chromaticity to be calculated from several hundred turns of data after a transverse kick. The measurement relies on the periodic de-phasing and re-phasing that occurs between the head and tail of a single bunch for non-zero chromaticity. By measuring turn-by-turn position data from two longitudinal positions in a bunch it is possible to extract the relative de-phasing of the head and the tail, and so to determine the chromaticity.

Couplers with striplines sufficiently long to allow separation of the principal and reflected beam pulses (~50 cm) will be installed on motorised supports near Q5 and Q6 left of IP4. As for the tune pick-ups, a slow position feedback will keep the detectors centred on the beam, maximising the precision of the oscillation measurements. The beam signals will be digitised with fast ADCs sampling at 2 Gs/s or more, with analogue bandwidth above 1 GHz.

A system has been installed in the SPS and encouraging results obtained [19]. However, although the measurement can be repeated at a reasonable rate (0.5 Hz has been obtained, but a faster rate is possible), the use of oscillations in the mm range would probably produce an unacceptably large emittance increase on beams for physics. This instrument seems best suited for producing feed-forward type corrections.

13.7.5 Betatron Coupling Measurement

The working point of the LHC will be very close to the diagonal, so that insufficient compensation of the betatron coupling will make tune and chromaticity measurement very difficult. Two classical methods that can be used to measure betatron coupling are the closest tune approach and the kick method. In the former method, both betatron tunes are measured continuously during a linear power converter ramp that crosses the values of the horizontal and vertical tunes. The remaining separation of the tune traces is a direct measure of the total coupling coefficient. In the latter method, a single kick is applied in one plane and the time evolution of the betatron oscillations in both planes observed. Other methods are under study.

13.8 APERTURE AND NON-LINEAR MEASUREMENTS

According to simulations, the single particle motion is naturally unstable in the nominal LHC unless some non-linear field harmonics are properly corrected (sextupole to dodecapole). There is therefore a requirement to give access to the beam observables related to the non-linear beam motion to allow deterministic corrections. The measurement principles are sometimes new but more often take advantage of existing ones provided their accuracy can be significantly increased. The methods anticipated for LHC and the requirement they put on the instruments are reviewed below.

13.8.1 Measurement of the Dynamic Aperture by the Kick Method

This well-known method may be hazardous at LHC at 7 TeV as the damage limit could be approached or reached, even for a pilot bunch. The non-linear fields localised in the triplets can however be studied by other methods (see Sec. 13.8.7). At 450 GeV, the non-linear fields are diffuse in the whole machine and the kick method appears the most suitable. It was therefore decided to increase the strength of the Q-kickers to allow a maximum oscillation amplitude of 8σ at 450 GeV (2 σ at 7 TeV) [20] whilst keeping an upgrade at 7 TeV possible. Interlocks on the beam intensity will be provided to prevent too high beam losses that could induce quenches. Combining functionalities in the Q-kickers implies that 25% of the 2808 bunches are deflected at each kick.

13.8.2 Measurement of the Dynamic Aperture by the Blow-up Method

This method involves blowing up the beam transversely by successive sweeps through its eigen-frequencies and measuring the cut in the transverse density profile caused by the dynamic aperture. The blow-up can be provided by the LHC damper system driven by an external sweeping or noise source. The dynamic range of the transverse profile monitors is specified to measure 1% of the density provided by a single pilot bunch diluted over the expected aperture with an accuracy of 10% [21].

13.8.3 Measurement of the Amplitude Detuning

A single kick to large amplitude will cause 25 % of the beam to oscillate at amplitudes between 0 and 8σ at 450 GeV and 0 to 2σ at 7 TeV. The bunch-by-bunch Q-meter will be able to directly measure the tunes versus amplitudes. The accuracy will be limited by the de-coherence time rather than the instrument and can be maximised by modern processing techniques, e.g. [22]. Other methods may be contemplated, using coherent oscillations or dc orbit oscillations. With collisions, the tune-spread becomes a more relevant and accessible observable.

13.8.4 Measurement of Average b_5 Using the Third-order Chromaticity

The dominant non-linear term at injection is b_3. It originates in the dipoles and must be corrected to better than 20 % by decapole correctors. The beam observable is the third-order chromaticity. A PLL tune-meter with a resolution of 10^{-5} or better is needed [23]. This, however, can be provided with a relatively slow response time (seconds) [24].

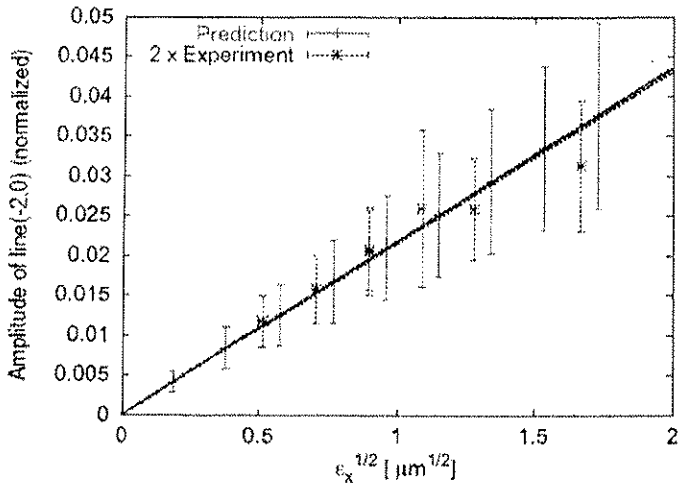

Figure 13.10: Normalized amplitude dependence of the 3Ox driving term [19]

13.8.5 Measurement of the Chromatic Coupling Related to a_3

The parasitic skew sextupole fields create by feed-down a linear coupling whose strength varies during the synchrotron oscillation, modulating the betatron tunes [25]. The correction will be based on the measurement of linear coupling for different dc momentum offsets.

13.8.6 Measurement of the resonance excitation terms

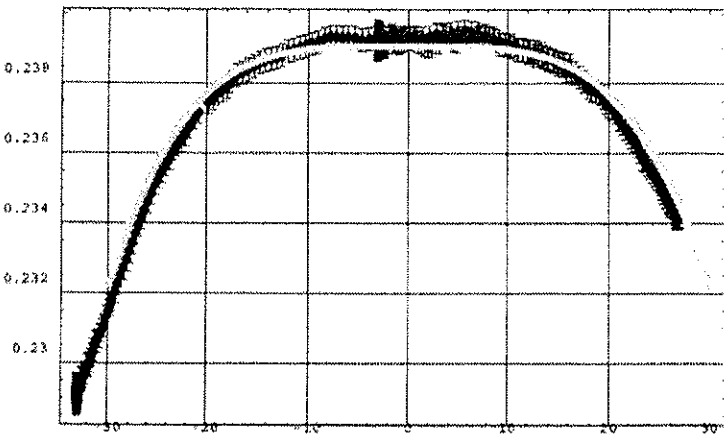

Figure 13.11: Signature of a dodecapole in RHIC. (tune-shift versus bump amplitude [18]

In the presence of non-linearities, the spectrum of the beam oscillation after a kick exhibits harmonics whose strength are related to the dominant resonance driving terms [26]. The method can be implemented in LHC using the Q-kicker as exciter and the turn-by-turn capability of the BPM. The resolution and linearity of the BPM's are consistent with an accurate measurement of third-order resonances. This kick method has the same limitation at 7 TeV (kicker strength, safety) as formerly mentioned.

13.8.7 Measurement of the Higher Order Multipoles by Feed-down to the Tunes

The measurement of localised high-order multipoles (or rather action kick) can be made by an accurate measurement of the feed-downs, e.g. the tunes, when applying dc bumps of varying amplitudes at the azimuth of the non-linearity (an example of such a measurement made at RHIC is shown in Fig. 13.11). The method requires a PLL tune meter with a resolution of 10^{-5} or better to detect the highest-order multipole to

be corrected, i.e. b_6 [27]. The anticipated slow time response is perfectly acceptable. The method requires an efficient coordination between instruments and orbit correctors.

13.8.8 Measurement of the Frequency Maps

To study the tune diffusion versus oscillation amplitude in the frequency domain, it is necessary to measure the tune to high accuracy (10^{-5}) in less than 1000 turns. The method [23] relies on windowing and interpolation in the frequency domain and can take advantage of all BPMs. It has the same constraints as the other kick methods. An example of this type of measurement is shown in Fig. 13.12.

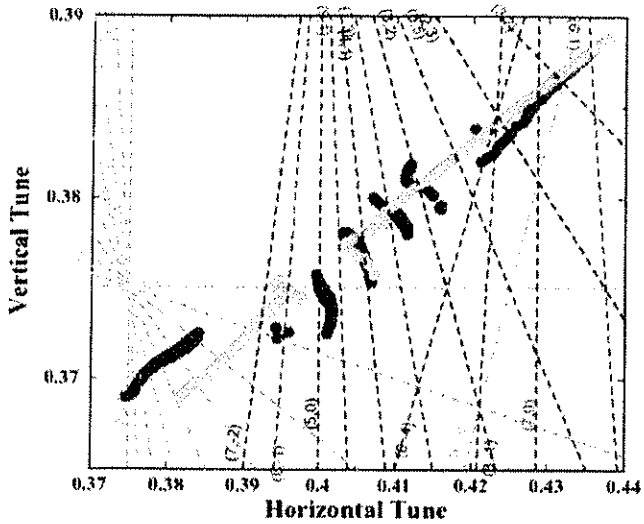

Figure 13.12: Experimental frequency map of the ESRF

13.8.9 Measurement of Longitudinal and Transverse Distribution Tails

A consequence of the non-linear motion is the existence of tails of very low densities in the beam distributions. A synchrotron light-based longitudinal profile monitor is planned to provide the longitudinal tails by single-photon counting down to 10^{-4} of the core density [28]. In the transverse plane, a wire-scanner at a steady but controllable position is anticipated to fulfil the requirement of detecting tails down to 10^{-5} of the core density [21].

13.8.10 Measurement with an AC Dipole

Recent theoretical studies [29] show the high potential of exciting the beams outside their eigen-frequency spectrum for the measurement of the optics parameters (coupling, de-tuning and resonance driving terms). See Sec. 13.7.2.

13.9 OTHER BASELINE INSTRUMENTS / SYSTEMS

13.9.1 Dedicated BPMs

The BPMs which do not form part of the main orbit system are listed and briefly described below:

- BPMC – a cold BPM located in the Q7-Q10 cryostats in IR4 comprised of a 24 mm button electrode monitor which is used by the orbit system and a 150 mm shorted stripline coupler used by the transverse damper system (Sec. 6.4).
- BPRS – a warm, resonant, stripline coupler for PLL tune measurement at IR4 (Sec. 13.7).
- BPLS – a warm, long, stripline coupler used for Head-Tail chromaticity measurement in IR4 (Sec. 13.7).
- BPQS – a warm, stripline coupler for standard, single kick tune measurement at IR4 (Sec. 13.7).

- BPTX – a 34 mm button electrode monitor (Sec. 13.11) located on the incoming beam at the end of the D2 magnet either side of each of the four main experiments. The BPPTX is used to provide a beam signal to the experiments with which they can verify their trigger timing.
- BPMRF – a warm, stripline coupler located in IR 4 and provided to the RF group for beam diagnostics in the transverse plane.
- Each motorised support used for transverse beam diagnostics (Sec. 13.7) is equipped with a warm, 34 mm button electrode BPM for closed orbit offset compensation.
- The beam dump insertion in point 6 is equipped with four warm, 34 mm button electrode interlock BPMs per ring, intended to ensure that the beam never drifts outside the limited beam dump extraction channel aperture.

13.9.2 High Frequency Pickup

The following special pick-ups have been discussed for dedicated studies:

High frequency pick-up

The purpose of a high frequency pick-up is to detect position and intensity signals for a high band of frequencies (~0.5 to 8 Ghz) centred on the cut-off frequency of the LHC vacuum chamber. These pick-ups could be used for the observation of head-tail instabilities. A smooth-response exponential coupler connected via passive hybrid circuits to short, large diameter, air core cables is proposed. The pick-up will be equipped with electrodes in both planes.

Quadrupolar pick-up

The state of betatron matching at injection can be checked with two such monitors per ring, one where β_H is large and β_V is small and there other where the situation is the other way round. This function is important because emittance conservation in the LHC injection is a critical issue. A quadrupolar pick-up has been developed for the PS but due to the different bunch structure a re-design of the sensor will be necessary.

13.9.3 Schottky System

Recent observations from FNAL and BNL indicate that it should be possible to make some basic measurements (tune, momentum spread) at 7 TeV using Schottky pick-ups. It is proposed to use a waveguide structure similar to that tested at FNAL at a frequency around 6 GHz where the width of the transverse sidebands is wide enough to obtain 10^{-3} precision in the tune measurement. At such a high frequency and with sufficient front-end filtering, the observed coherent lines that polluted the Schottky signals in previous stochastic cooling tests should be reduced to a level where the problem is under control and does not lead to head amplifier saturation.

13.9.4 Beam Synchronous Timing Receiver

The beam synchronous timing (BST) for the majority LHC beam instrumentation orbit will be distributed via a fibre-optic network, using the Timing, Trigger and Control (TTC) system designed for the LHC detectors [30]. The TTC infrastructure allows the 40 MHz bunch clock, 89 μs turn clock and arbitrary control data for each ring to be recuperated at each beam instrumentation station by a BST receiver card (BOBR) [31]. This VME64x card is fitted with either one or two (if timing from both rings are required in the same crate) TTCrm mezzanine cards containing the TTCrx receiver ASIC developed as part of the TTC project [32]. The BOBR has the task of distributing the 40 MHz bunch clock and the 89 μs turn clock throughout the VME crate using user defined pins on the P0 connector. In addition the module decodes the message sent on every turn, generating hardware triggers when required or updating software settings. A single command is composed of an 8 bit sub-address and 8-bits of data, allowing up to 256 identified bytes of data to be broadcast. The message transmitted on each turn contains up to 32 such commands, including the machine mode, beam type, beam energy and the GPS absolute time as well as beam instrumentation specific settings and triggers.

13.10 NON-BASELINE, STAGED OR PROPOSED INSTRUMENTS

13.10.1 Long-Range Beam-Beam Compensation

Due to the small bunch spacing, the LHC beams experience 15 'near-misses' on each side of every collision point. In IP1 and IP5, the beam separation is 9.5σ on average. In the other two collision points, the normalised separation is larger and their contribution to the long-range beam-beam effect can be neglected. The non-linear part of the long-range interactions appears to be the dominant mechanism for single particle instability [33], even though the tune spread is small enough (footprint criterion). A very fast diffusion in amplitude is observed for beam amplitudes of 6 to 8σ.

The topology of the long-range interactions in LHC makes it possible to devise a simple but accurate weak-strong model where the weak beam, assumed round, is perturbed by currents flowing in wires on either side of the crossing points (strong beam). This model leads naturally to a compensation system [34] made of genuine wires excited by a constant current for the compensation of the normal bunches or by a pulsed current in an option where the PACMAN bunches would be individually corrected.

These wires run along the beam at positions where the beams are already in separate channels. They should be placed between the two channels for a horizontal crossing and above or below for a vertical crossing. The beam-wire distance should be equal to the beam separation at the long-range interaction points (9.5σ). Studies of robustness show that they can be further retracted to 12σ, i.e. well in the shadow of the collimators. The wire excitation is 83 A·m on each side of every crossing point. The β-function is not relevant (provided it is the same in both planes). The phase advance between perturbation and correction must be as small as possible to correct all non-linear terms, not only the detuning. The strong focusing of the LHC low-β sections allows suitable positions to be found at 112 m from the crossing points and space has been reserved at them. The phase shift is only 2.6° and the beam channels already sufficiently separated. Numerical simulations [35] show that particles up to 7σ are stabilised by the compensation system, i.e. all particles within the collimator acceptance. The robustness of the scheme appears high for all dc effects (errors in excitation and position). The ripple must not exceed 1 per mil to prevent heating the beam.

A 1.25 mm radius (about 1 beam σ) hollow Cu wire was installed in the SPS to test both the physics and the technology. The wire is brazed on alumina insulators themselves brazed on stainless steel supports. Each of the two devices has an active length of 60 cm. The high current density (~100 A/mm^2) requires cooling. Water cooling was chosen for the SPS to meet a tight schedule. Purely passive cooling by conduction appears possible and is preferred for LHC, unless super-conducting wires can be used. The onset of strong diffusion in a situation representing the nominal LHC seems now detected [36]. Confirmation will be obtained in 2004 by adding other such devices to compensate the perturbation in a situation close to that of the LHC.

REFERENCES

[1] "Measurement of the Beam Position in the LHC Main Rings", LHC-BPM-ES-0004 v.2 (EDMS Id: 327557), Ext. Ref. Div. SL-BI.

[2] "The Supply of Button Feedthroughs for the LHC Beam Position Monitors", LHC-BPM-CI-0004 v.1 (EDMS Id: 108428), Ext. Ref. IT-2530/SL/LHC.

[3] "Supply of Cryogenic Semi-rigid Coaxial Cables for the LHC Beam Position Monitors", LHC-BPM-CI-0005 v.1 (EDMS Id: 110698), Ext. Ref. IT-2529/SL/LHC.

[4] "Technical Specification for the Supply of Feedthrough Assemblies for the LHC Beam Position Monitors", LHC-BPM-CI-0008 v.1 (EDMS Id 309289), Ext. Ref. CERN - Div. SL.

[5] D. Cocq, "The Wide Band Normaliser: a New Circuit to Measure Transverse Bunch Position in Accelerators and Colliders", Nucl. Instrum. Methods Phys. Res., A 416, 1998.

[6] "Digital Acquisition Board for the LHC Trajectory and Closed Orbit System", LHC-BI-ES, to be published.

[7] B. Jeanneret and H. Burkhardt. "Measuremnts of the Beam Losses in the LHC Ring", LHC-BLM-ES-0001.00

[8] B. Dehning, "Beam Instrumentation for Machine Protection", Proc. of the LHC Performance Workshop, Chamonix XII, CERN-AB-2003-008-ADM.

[9] A. Arauzo and C. Bovet, "Beam loss detection system in the arcs of the LHC", CERN-SL-2000-052-BI.
[10] A. Arauzo and B. Dehning, "Configuration of the beam loss monitors for the LHC arcs", LHC Project Note 238.
[11] R. Jung, et al.: The LHC 450 GeV to 7TeV "Synchrotron Radiation Profile Monitor", CERN-SL-2002-015 BI
[12] M. Facchini, "Long. Diagnostics Mirror Configuration for the LHC Beam" unpublished
[13] LHC-B-ES-0005.00 - EDMS 328145
[14] R. Assmann et al., "Measurement of the relative luminosity at the LHC", LHC-B-ES-0007, CERN, 2003
[15] E. Gschwendtner, M. Placidi, "Baseline and Requirements for a Luminosity Monitoring at the LHC", to be published.
[16] J.P. Koutchouk et al., "Excitation of Transverse Beam Oscillations Without Emittance Blow-Up Using The AC-Dipole Principle", Proc. of DIPAC 2001, Grenoble, p.82ff
[17] F. Bordry, CERN-AB-PO, private communication.
[18] O.S. Brüning. W. Höfle, R. Jones, T. Linnecar, H. Schmickler, "Chromaticity Measurements via RF Phase Modulation and Continuous Tracking", Proc of 8th European Particle Accelerator Conference, Paris, June 2002, pp 1852-1854.
[19] R. Jones, H. Schmickler, "The Measurement of Q' and Q" in the CERN-SPS by Head-tail Phase Shift Analysis", Proc. of 2001 Particle Accelerator Conference, Chicago, June 2001, pp 531-533.
[20] S. Fartoukh et al., Funct. Spec. of the Transverse Measurements, in work, 2003.
[21] C. Fischer et al., Funct. Spec. of the Transverse Profile Measurements, LHC-B-ES-0006, EDMS328147, 2003.
[22] J. Laskar, "Frequency Analysis for Multi-Dimensional Systems", Physica D67 (1993) 257-281 & R. Bartolini et al., "Precise Determination of the Betatron Tune", EPAC'96, Sitges, 1996.
[23] S. Fartoukh, in PLL Workshop, CERN 2002.
[24] P. Cameron et al., "PLL Tune Measurement during RHIC 2001", EPAC'02, Paris, 2002 & PLL Workshop, CERN 2002.
[25] J.P. Koutchouk, "Chromatic properties of the LHC lattice", LHC Project Note 113, 1997 & S. Fartoukh, 'Chromatic coupling due to a3 and correction', LHC Project Report 278, 1998.
[26] M. Hayes, F. Schmidt, R. Tomas, "Measurement of Resonance Driving Terms at SPS", Proc. of EPAC'02, Paris, 2002.
[27] F. Pilat et al., "Linear/Nonlinear Corrections in the RHIC Interaction Regions", Proc. of EPAC'02, Paris, 2002.
[28] C. Fischer et al., Funct. Spec. of the Longitudinal Profile Measurements, LHC-B-ES-0005, EDMS 328145, 2003.
[29] S. Peggs, PAC'99, New York, 1999. & S. Fartoukh, "Linear Coupling Coefficients via AC dipole excitation", CERN-SL-2002-059 AP, 2002.& R. Tomas, "Normal Form of Particle Motion under the influence of an AC-dipole", Phys. Rev ST Accel. Beams, vol.5 54001 (2002).
[30] B.G. Taylor, "TTC Distribution for LHC Detectors", IEEE Trans. Nuclear Science, Vol. 45, No. 3, pp. 821-828, 1998.
[31] "BOBR - The Beam Synchronous Timing Receiver Interface for Beam Observation Systems", LHC-BI-ES, to be published.
[32] J. Christiansen, A. Marchioro, P. Moreira; "TTCrx: an ASIC for timing, trigger and control distribution in LHC experiments" in 2nd Workshop on Electronics for LHC Experiments, Balatonfüred, Hungary, September 1996, p. 161-165.
[33] Y. Papaphilippou, F. Zimmermann, "Weak-strong beam-beam simulations for LHC", CERN-SL-99-039 AP, 1999.
[34] J.P. Koutchouk, "Correction of the Long-Range Beam-beam Effect in LHC", Proc. of IEEE PAC2001, Chicago (2001).
[35] F. Zimmermann, "Weak-strong simulations studies for the LHC long-range beam-beam compensation", Proc. of beam-beam Workshop, Fermilab, June 2001.
[36] J.P. Koutchouk, J. Wenninger, F. Zimmermann, in work.

CHAPTER 14

CONTROL SYSTEM

14.1 INTRODUCTION

The LHC control system will be an extension of the infrastructure in use today for the Injector Chain and the Technical Services. Controls projects are underway for additions and upgrades to the existing CERN accelerators – the LEIR reshuffling as an ion accumulator for LHC – the CNGS and the LHC transfer lines at the SPS. Evolving control technologies and diminishing costs are already leveraged in the infrastructure.

Nevertheless the LHC will present unique challenges for the control system. The hardware will be of unprecedented complexity and will require a precise and unambiguous description. Failures will lead to long cryogenic recovery times and long magnetic conditioning cycles. Operational efficiency will depend on both the technical services and the accelerator hardware control systems. The high stored energies and beam powers will impose rigorous operational procedures and sophisticated diagnostics, while the challenging design parameters and the large dynamic effects will only be mastered by a flexible control strategy, adapted to changing circumstances as the knowledge of the LHC improves.

In order to achieve good beam performance and safe operation the beam control system must provide for real-time automation which is a novel requirement at CERN.

This chapter presents an overview of the control system architecture, a review of the different layers starting at the hardware level and concludes with an outline of some important high level services. Particular emphasis is given to software frameworks and the impact of modern industrial control technology.

It is anticipated that the LHC will be commissioned and operated from a new CERN Control Room (CCR). This will bring together control and operation of the site services, cryogenics, injector chain and the new machine. The impact of the reorganisation of the existing control rooms is not discussed in this report.

14.2 ARCHITECTURE

The LHC control system architecture is largely based on standard components employed worldwide for the control of accelerators and used during recent years of efficient operations of the CERN injectors (PS, SPS) and of the LEP machine. However, two major changes will take place for the LHC era:

- The consistent use of object oriented technologies and design principles for the control of beam-related systems,
- The wide use of industrial controls solutions for the supervision of complete subsystems of the LHC.

14.2.1 Overall Architecture

As shown in Fig 14.1, the LHC control system has three hierarchical layers of equipment communicating through the CERN Technical Network, a flat Gigabit Ethernet network using the TCP-IP protocol (Sec. 14.2.2).

Starting from the bottom of Fig 14.1:

- At the equipment level, the various actuators, sensors and measurement devices are interfaced to the control system through three different types of front-end computers :
  - VME computers dealing with high performance acquisitions and real-time processing; these employ a large variety of I/O modules. Typically, the LHC beam instrumentation and the LHC beam interlock systems use VME front-ends.
  - PC based gateways interfacing systems where a large quantity of identical equipment is controlled through fieldbuses, such as the LHC power converters and the LHC Quench Protection System.
  - Programmable Logic Controllers (PLCs) driving various sorts of industrial actuators and sensors for systems such as the LHC Cryogenics systems or the LHC vacuum system.
- At the heart of the control system, powerful UNIX servers host the operational files and run the LHC applications:
  - Application servers hosting the software required to operate the LHC beams and running the Supervisory Control and Data Acquisition (SCADA) systems.

- Data servers containing the LHC layout and the controls configuration as well as all the machine settings needed to operate the machine or to diagnose machine behaviours.
- Central timing which provides the cycling information of the whole complex of machines involved in the production of the LHC beam and the timestamp reference.

Processes running in these servers will communicate with the equipment access machines using various mechanisms and protocols such as the Common Object Request Broker Architecture (CORBA) and TCP-Modbus.

- At the control room level, consoles running the Graphical User Interfaces (GUI) will allow machine operators to control and optimise the LHC beams and to supervise the state of key industrial systems. Dedicated fixed displays will also provide real-time summaries of key machine parameters.

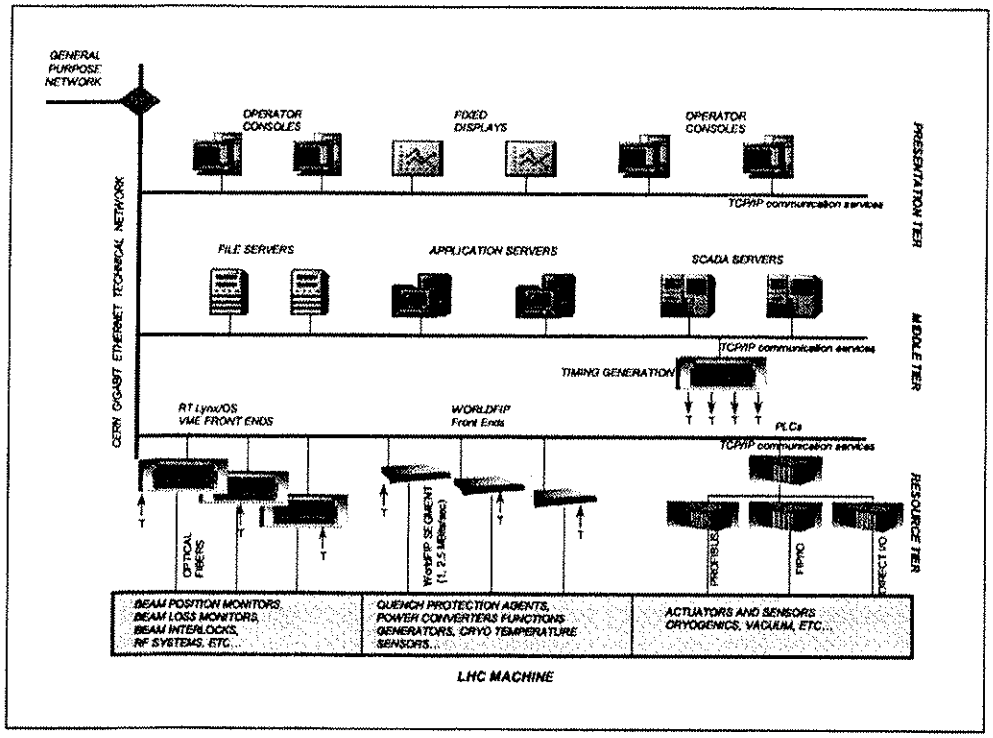

Figure 14.1: Control System Architecture

14.2.2 Network

The control system for LHC relies on the CERN Technical Network. This network uses IP addresses of the form *172.18.xxx.xxx*. This address prefix prevents any direct communication between the technical network and the Internet. The infrastructure is interconnected with the General Purpose Network so that communications from within the Organization are still possible; however, the technical network can be completely isolated if required.

The technical network is a highly sub netted, routed network that implements a high performance redundant backbone, reduces parasitic traffic and keeps the overall structure maintainable. As shown in Fig 14.2, the basic distribution is based on a redundant Gigabit Ethernet backbone using fibre optical distribution. The core consists of two redundant backbone routers located in the CERN computer centre and in the Prévessin control room, where most of the fibres terminate. These two central routers are interconnected in a redundant way to a series of regional routers located in the following buildings:

- The computer centre (building 513) for central services like Oracle databases and main file servers,
- The Meyrin control room (building 354) for the control of accelerators located on Meyrin site,
- The technical control room (building 212) for the supervision of the 2 CERN sites,
- The Prévessin control room (building 874) for the SPS control and other technical services located on the Prévessin site.
- Each LHC pit (SR building) for the LHC machine and technical services control.

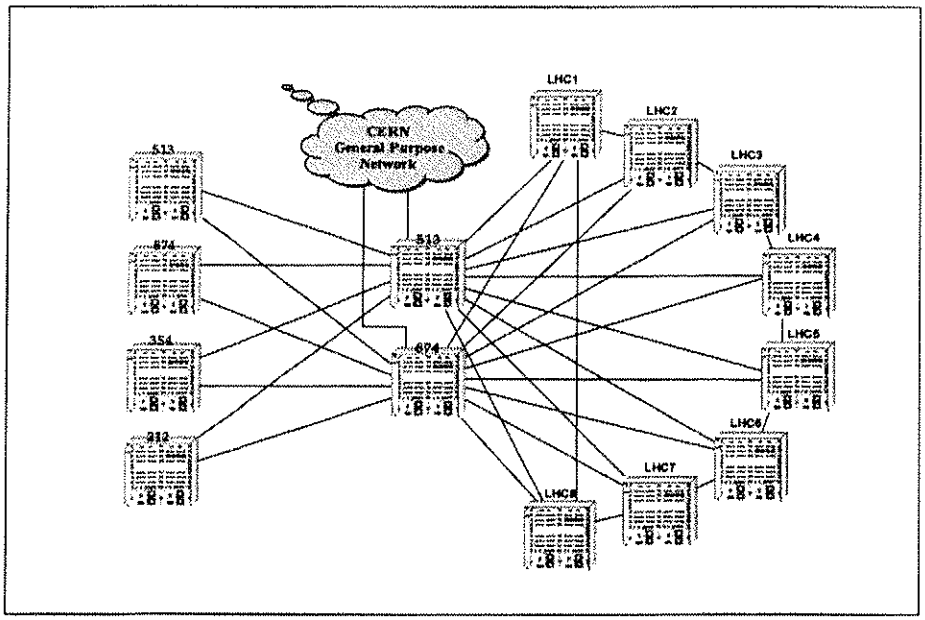

Figure 14.2: The CERN Technical network

In each technical building we find one or more "star points" in order to respect the maximum cable length of 100 m for 100-BaseT connections between the end-node and a high performance Fast-Ethernet switch. This usually has a 100Mbps uplink to the closest regional router that may be upgraded to Gigabit if needed. Close to regional routers, 1Gbit/s Ethernet may easily be made available if needed.

Active equipment in the network architecture is installed with a double power supply connected to two independent power sources (normal and secured) in order to ensure proper connectivity even in case of a power-cut on either 220V distribution.

Because the technical network can be completely isolated from the external world, independent dedicated redundant name and time servers have been implemented. These servers are installed at different locations and connected to different regional routers to ensure full redundancy of the system.

It must be noted that because the technical network infrastructure is interconnected with the general purpose network, security break-ins can be attempted on the devices connected to this infrastructure. End nodes security survey and updates must not be forgotten.

14.3 EQUIPMENT ACCESS

14.3.1 The VME and PC Front End Computers

Most of the non-industrial accelerator hardware in the PS, SPS and LHC sites is already connected to the control system via VME or PC based Front End Computers (FEC). These systems run a real-time operating system called LynxOS from LynuxWorks [1] or Red Hat Linux [2].

There will be several hundred FECs distributed in the surface buildings of the LHC and in some cases in the underground areas. Wherever possible they will be diskless to increase reliability and will boot over the network. They will be connected to the remote reboot and terminal server systems so that they can be managed remotely by the operators and system administrators.

A set of commercial or CERN made hardware interface boards is being standardised for the LHC, together with the necessary device drivers (e.g. timing generators, timing receivers, beam interlock controllers, digital acquisition boards, WFIP cards, digitisers, etc.). The type of hardware (VME or PC), as well as the Operating System (Linux or LynxOS), will be selected according to the performance needed and to the availability of the specific drivers.

These FECs will execute the equipment access software which is part of the *resource tier* (Fig. 14.1). This software accesses data of the hardware interface boards and provides it either via subscription or command/response to any software agent in the control system.

A dedicated FEC software framework (Sec. 14.7.1) has been developed in order to simplify and standardise the software running in the FECs.

14.3.2 The PLCs

PLCs are increasingly used for controlling industrial equipment for LHC. This type of controller can be chosen when the process is not synchronised to accelerator timing and when the sampling period required is not smaller than 100 msec.

PLCs offer ease of programming process logic via standard high-level languages (IEC-61131-3), cost efficiency, high reliability and adaptation to industrial environment. They are used in typical industrial controls fields such as electricity, water, gas, cooling, ventilation, but also in accelerator-specific fields of machine cryogenics, interlocks, vacuum, radio-frequency and beam extraction.

PLCs are generally part of a complete subsystem including supervision (Sec. 14.7.4). In a few cases they are accessed through VME FECs. As with any other FEC in the Controls Infrastructure, PLCs benefit from generic facilities such as remote reset, monitoring and optionally clock synchronisation.

Only PLCs from Schneider and Siemens are used for LHC as recommended by the CERN Controls Board.

14.3.3 The Supported Fieldbuses

The two fieldbuses used in the LHC accelerator, namely WorldFIP and Profibus, are part of the three fieldbuses recommended at CERN. They are both supported by an internal CERN service. These fieldbuses typically allow longer distance and more robust protocols than Ethernet. In addition they are the only means to connect equipment located in the LHC tunnel or other radioactive areas.

The WorldFIP Fieldbus

Tab. 14.1 summaries the LHC WorldFIP installation needs. WorldFIP is selected when the following features are required:

- Determinism (up to10μs); is required for:
  - The real-time control and synchronisation of LHC equipment,
  - High precision time distribution,
  - The management of periodic data.
- Robustness in severe environments and in particular:
  - Its resistance to electromagnetic noise (level 3),
  - Its good resistance to high radiation levels (based on robust semiconductors and a magnetic coupling ensuring galvanic isolation).
- Data Rates:
  - WorldFIP will be used to control largely distributed LHC systems at high data rates (1MBits/s and 2.5 MBits/s),
  - High load factor possible (70 to 80% of the network bandwidth)

Table 14.1: WorldFIP Needs for the LHC machine

LHC System	Required Time precision (ms)	Cable length (km)	Data rates
Magnet Protection	1	61	1 MBit/s
Power Converters	0.01	45	2.5 MBit/s
Beam Instrumentation	500	50	31.25 KBit/s
Radio Frequency	1	5	1 MBit/s
Cryogenics	500	90	1 MBit/s
Survey	1000	44	31.25 KBit/s

The Profibus Fieldbus

Profibus has been selected for several applications in the LHC, such as fast kicker magnets, cooling and ventilation, vacuum, cryogenics, magnet and power interlock controllers.

The main reasons to select Profibus for these applications are:

- The robustness of the protocol and simplicity of configuration.
- The large variety of remote I/O systems available with Profibus.
- The ease of integration with Siemens PLCs.
- The availability of radiation-tolerant remote I/O on Profibus.
- Its capacity to be used as an instrumentation bus (Profibus-PA) with a wide range of instrumentation products offering Profibus as standard means of connection.

14.4 SERVERS AND OPERATOR CONSOLES

The upper layers of the LHC control system (Fig. 14.1) will be deployed on operation consoles and fixed displays, files and applications servers to meet the requirements of the LHC applications software.

The servers will be used to run the LHC middle-tier software, to host operational programs and data files, and also to offer specific services (web services for operation, fixed displays, SCADA servers, Database servers, etc.). The servers will run the Linux operating system. Emphasis will be put on the hardware reliability and availability issues by selecting multi-CPU architectures with redundant and hot swappable power supplies, discs and fans. Mirroring and RAID techniques will be used to ensure data integrity and error recovery.

The UCR fixed displays and operator consoles will both be based on desktop PCs with a large amount of memory. They will run GUI applications from their local disks and use one to three screens to display the data. At present the choice of the Operating System between Linux and Windows has not yet been made.

More than 20 fixed displays and around 10 consoles will be needed in the CCR control room to operate the LHC machine. Around 50 servers located nearby and in the LHC surface buildings will be used to deploy and run the operational LHC software.

14.5 MACHINE TIMING AND UTC

14.5.1 Central Beam and Cycle Management

The LHC beam production involves a long chain of injectors which need to be tightly synchronised. Moreover, the different types of beam to be produced for LHC are only a subset of the beams that the injectors have to produce, e.g. beams for fixed target physics, for Isolde, for AD. All these beams are produced in sequences of typically a few tens of seconds. The composition of these sequences changes many times a day and the transition between different sequences has to be seamless.

To manage the settings of the machines and to synchronise precisely the beam transfer from one injector to the other up to the LHC, a Central Beam and Cycle Manager (CBCM) is required. The CBCM will:

- Deliver General Machine Timing (GMT),
- Provide Beam Synchronous Timings (BST),
- Elaborate the "telegrams" specific to each machine and broadcast over the GMT networks.

A "telegram" describes the type of beam that has to be produced and provides detailed information for sequencing real-time tasks running in the FECs and for setting up equipment.

The CBCM drives seven separate GMT networks dedicated to the different CERN accelerators, including the LHC and four BST networks of which three are for the LHC and one for the SPS. To achieve extreme reliability, a CBCM is running in parallel on two different machines, with a selector module capable of seamlessly switching between them.

14.5.2 Timing Generation, Transmission and Reception

Several hardware timing modules are being built either to produce reference clocks and timing events or to extract the timing pulses or the interrupts needed to drive the equipment from the distributed timing data. The deployment of these modules will start on the PS and on the SPS in 2004:

- The CTSYNC module provides the "master" clocks from a 10MHz oscillator which has a stability which is better than 10^{-10}.

- The CTGU module encodes events to be transmitted over the GMT network: the millisecond events, machine timing events, telegrams, and the Universal Coordinated Time (UTC) events.
- The CTGB is the driver module for the BST network; it uses the TTC technology [3]. The CTGB will also send the 1 Pulse per Second (1PPS) UTC time and some telegram events over these networks, hence its inclusion into the CBCM.
- The CTRP is a GMT multi-channel reception module. It comes in three formats: PMC, PCI, and VME and can generate timing pulses with very low jitter. The CTRP recognises the various types of timing events: UTC time, the telegrams, the millisecond and other machine events, and can use them to trigger pre-programmed actions.

14.5.3 UTC for LHC Time Stamping

A key requirement for the LHC control system is the need for a timing reference to timestamp the accelerator data. UTC has been adopted as the standard of date and time for all CERN accelerators [4, 5]. UTC is the basis for the worldwide system of civil time. The motivation behind this decision was to eliminate the problems associated with the changes between the winter and summer standards, particularly for the change in October (CET changes from UTC+2H to UTC+1H) when the time is repeated for one hour.

14.5.4 UTC Generation, Transmission and Reception

The source of date and time for all CERN accelerators will be a Global Positioning System (GPS) time receiver connected to the CTGU. The GPS provides UTC referenced date and time plus a very accurate 1 PPS tick, which is used by the CTGUs to synchronise the UTC time.

At initialisation the CTGUs receive the date and time information from the GPS receiver then run independently, using the clock delivered by the CTSYNCH until a manual resynchronisation is made. CTGUs provide the time every second in UNIX standard format. UNIX time can then easily be converted by software into year, month, day, hour, minute and second.

UTC time can be provided by the CTRP modules to timestamp the data to be logged with a 25 ns resolution. Using an optional CERN-developed chip the resolution can be brought down to 1 ns. The required time-stamping granularity for the different LHC systems [6] is shown in Tab. 14.2. The 1 ns performance is required principally in the injector chain.

Table 14.2: Required LHC time stamping accuracy

System	Timestamp Accuracy
Beam Dump	< 0.05 ms
Beam Instrumentation	
Radio Frequency	
Injection (Kickers...)	
General Machine Timing	
Machine Interlocks	1 ms or better
Quench Protection	
Power Converter	
Feedbacks (orbit, tune ...)	1 – 10 ms
Cryogenics	
Vacuum	
All other systems	

14.5.5 NTP Time Protocol

PLCs will use the Network Time Protocol (NTP) [7] to synchronise the time (Sec. 14.2.2). NTP provides accuracies typically within a few milliseconds on LANs and up to a few tens of milliseconds on WANs. This accuracy is sufficient to properly tag most of the PLC data. Some PLCs that require higher precision for time-stamping their data will use the high precision 1PPS tick from the CTRP; in this case NTP will be used only to relate this tick to UTC time.

14.6 DATA MANAGEMENT

The LHC Machine will be of unparalleled complexity in terms of number of components and in the manipulation of operational parameters. A large number of signals will be made available to the control room, including over 100,000 from the cryogenics, machine protection and beam monitoring systems. Over 1600 electrical circuits will power a wide variety of magnet systems. The quantity of data to be recorded for diagnostics after a "beam abort" has been estimated as a few gigabytes; during Hardware Commissioning it is anticipated that 1 terabyte of information will be accumulated. Operation of the machine will rely on stringent control of the hardware settings. A complete beam operational history will be created in order to build a long term understanding on the accelerator performance.

Such a variety and volume of data cannot be exploited without data management tools. Building on the experience of LEP construction and operation [8] Oracle has been selected as the strategic choice for data management at the LHC.

14.6.1 Offline and Online Data Repositories

As shown in Fig 14.3, the LHC Reference Database is being populated during the machine construction in order to manage the information essential for integration studies, installation and hardware commissioning [9]. This offline Database will be one of the sources of data that is required to configure the online LHC control room application software providing essential information such as the layout, accelerator optics and calibration information. The electrical circuit data, described in the next section, are an example of the use of the database both during construction and operation.

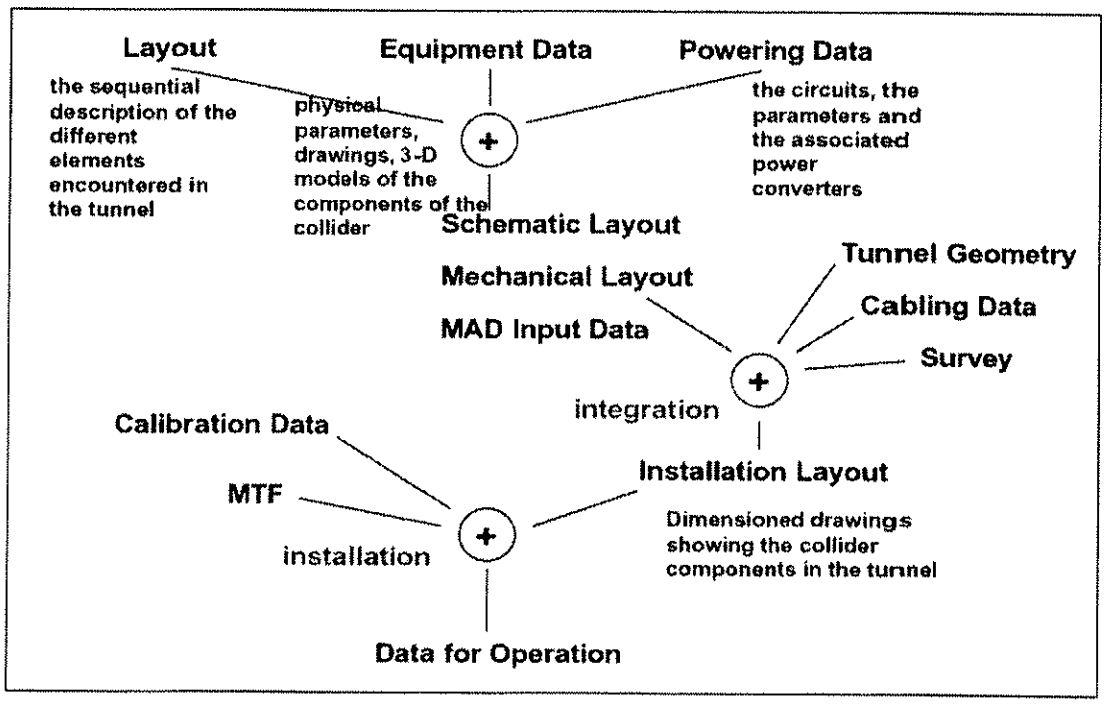

Figure 14.3: LHC Reference Database

While the Reference Database will be an offline source of information during machine operation, several online databases - alarm archives, periodic data logging, Post Mortem event archive and accelerators settings management - will be required to capture the operational history. These are described in the later sections of this chapter.

14.6.2 Electrical Circuits

The powering layout of the LHC is extremely complex, comprising 1232 main dipole magnets, about 450 quadrupole magnets and several thousand corrector magnets, powered in 1612 electrical circuits. The current feeding the magnets ranges from 60 A (for small correctors) to 12 kA for main dipole and quadrupole

magnets, while the energy stored in the superconducting magnets is about 10 GJ. About 80,000 high current connections have to be made and tested in the tunnel during the installation and commissioning phases.

To ensure the connection correctness of the superconducting bus bars around the 27-km long machine, a detailed description of the electrical circuits and their elements has been added to the layout description of the machine in the LHC Reference Database [10]. This description has been linked to the existing data describing the physical and magnetic layouts. Changes of this powering information are very rare (static data) and updates have to be performed only if there are major changes in the physical or powering layout of the machine.

Information about the powering will be provided to users to:

- Perform the interconnections between cryo-assemblies in the long arc cryostats,
- Configure the powering interlock PLCs (section 15.3.7),
- Create MAD input files to calculate the beam optics,
- Display detailed circuit and equipment information via the web and the LHC equipment catalogue,
- Configure hardware state and beam parameter control room application software.

Integrity will be ensured by using the same information to generate the machine optics, make the circuit connections during assembly, configure the behaviour of the interlock system and operate hardware and beams.

14.6.3 Control System Configuration

The control system is composed of a large number of application programs, a middleware layer, VME- and PC-based FECs with control software, industrial PLCs, fieldbuses, and hardware interface modules. These components have shared characteristics, associated with their type or class, and specific addresses and parameters associated with their instances. All these data will be stored and described in an Oracle relational database, the *Controls Configuration Database*.

This centrally managed configuration information permits the use of generic software on all levels. A layer of Java and C++ interfaces will enable all control room software to be data-driven, by fetching at runtime the layout, interconnection, access methods, and parameters of remotely controlled LHC equipment. All FECs can be automatically configured and bootstrapped with files generated from the database.

Thanks to a generic design, the database also holds the controls configuration of the injection accelerator chain of the PS and SPS complexes. This common source of data will make it possible to have uniform controls data management throughout the accelerator chain, as well as effective sharing of tools and methods that use this data [11].

On top of the Configuration Database, a Web browser service will allow exploration of all the information about the underlying controls hardware and software.

14.7 COMMUNICATION & SOFTWARE FRAMEWORKS

14.7.1 FEC Software Framework

The software running in the LHC FECs will be developed using a specific framework, known as FESA. This framework is a complete environment for the equipment specialists to design, develop, test and deploy real-time control software for the FECs. This framework is also the new standard for the LHC injector chain.

The recurrent components of the equipment control software have been formalised into a generic model. It defines the structure of the real-time part of the software which handles hardware and interrupts together with the structure of the server task that handles external requests. In order to enhance the productivity and the maintainability of the code, a clear separation between the generic and the equipment specific parts is enforced and automatic code generation is extensively used. As a result, the ratio between the generic/generated code and the developer specific code is usually around 10 to 1. An object-oriented design and a C++ implementation have been used for supporting this approach.

For building the control software, the programmer is provided with a set of configuration tools for the creation and evolution of any FESA component. These tools are directly linked to the control system configuration DB (Sec. 14.6.3). They are used for the definition of internal data structures, syntax of the external command and binding between hardware events or external requests and treatment code.

External requests are handled by dedicated server tasks that fully implement the device access model of the Controls Middleware, which is described in the next section. Compound data types are supported for data coherency and for performance purposes.

System-level services are provided for the operation of the FECs: handling of errors from the equipment software, monitoring of the processes, etc. These dedicated services are made for preserving the real-time behaviour of the FECs and they support remote control for adjusting parameters, such as the trace level of a task, or executing corrective action like restarting a process.

The developers and the users (equipment-specialists, operators, and maintenance team) are also provided with a set of interactive tools, test programs and Java libraries which allow immediate testing of all the functionality of the software during its development and operation. These facilities are all generated in an automatic manner, without any specific code required.

The FESA framework is built for LynxOS and Linux platforms. The software tools are written in Java and are thus platform independent. No commercial software requiring a run-time license has been used.

14.7.2 Controls Middleware

The Controls Middleware (CMW) [12] is the ensemble of protocols, Application Programming Interfaces (API) and software frameworks, which allow seamless communication between the software entities of the control system. Two conceptual models are supported: the device access model and the messaging model. The device access model is mainly used in the communication between the resource and middle tiers while the messaging model is mainly used within the business tier or between the business tier and applications running in the presentation tier.

Device Access Model

Fig. 14.4 depicts the full architecture of the CMW device access model. The typical use of this communication model is between Java applications running in the middle tier and CMW equipment servers running in FECs. These processes communicate together through the Remote Device Access (RDA) API [13] which is available for both Java and C++ languages.

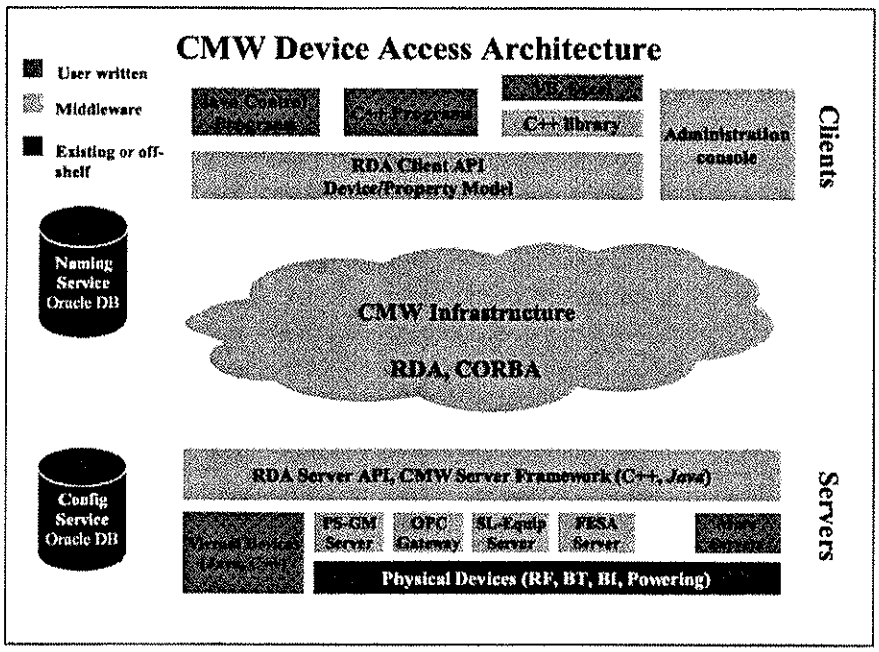

Figure 14.4: The Device Access Model

Within the device access model all accelerator equipment can be accessed as "devices". A device is a named entity within the control system, which normally corresponds to a physical device (e.g. beam position monitor, power converter) or to a virtual controls entity (e.g. transfer line). Conceptually each device has a number of properties that characterise its state. By getting the value of a property, the state of the device can be read. Accordingly, a device can be controlled by setting one of its properties with the required value. Get

and Set operations can be either synchronous or asynchronous. In addition to the Get and Set operation on device properties, it is possible to monitor changes to the property via listeners (callbacks).

It is often necessary to specify under which conditions the operation has to take place, for instance to which cycle of the machine the operation applies. These conditions are commonly referred to as context or filter.

A list of properties, together with their type description and the semantic of the assessors, is referred to as a contract. Contracts typically serve a specific purpose such as measurements or settings of a device.

Messaging Model

Complementary to the device access model, the messaging model allows any software process to send and receive asynchronous messages in a loosely coupled way. Various application programs for accelerator controls naturally exchange data via asynchronous messages: timing and logging events, notifications and alarms are typical examples of data which is asynchronously generated from a various set of producers, which is potentially of interest for multiple consumers.

The LHC control system software relies on the Java Message Service (JMS) [14] as the messaging solution for Java based controls application. The JMS specification adds a standard and vendor-independent API that enables the development of portable, message-based applications in the Java programming language. Moreover, JMS is a strategic technology for the Java 2 Platform Enterprise Edition (J2EE).

The LHC Alarm Service [15] is a typical example of a messaging system relying on the publish-and-subscribe paradigm: it subscribes to alarm notifications being published by several processes and, after processing, redistributes the result to dedicated consoles and any other controls software component that subscribed to the appropriate alarm content hierarchy.

14.7.3 The J2EE Framework for Machine Control

Applications controlling the LHC beams must handle a great variety of tasks such as visualisation of data and significant computation, together with database and equipment access. These applications rely on several services such as security, transactions (to make sure that complex operations are performed atomically), and remote access or resource management. Those requirements dictate a move towards a modular and distributed architecture. Such architecture offers a clear separation between the GUI (the user interface), the control (the core business of the application), the model (the abstract model of the accelerator control) and the devices (the physics equipment) that are controlled.

For LHC, a 3-tier architecture is being implemented where the middle-tier is responsible for providing all services and for coordinating the client applications running on the operator consoles. In this architecture shown in Fig. 14.4, applications are running both in the operational consoles of the presentation tier and in dedicated servers of the middle-tier. The consoles are responsible for the GUI applications and translate operator's actions into commands invocation in the middle-tier. The middle-tier, through its centralised and shared processing power is in charge of accessing databases and accelerator devices. The middle-tier also ensures the coherency of operator actions and shelter resources. It enforces separation between presentation and application logic and provides shared services to many clients.

To achieve this new programming model, a platform is needed, to support the middle-tier. The platform provides the infrastructure with all the necessary common basic services, i.e. all parts of a control system that are not specific to accelerator controls. By using such a platform, the developers can concentrate on writing code for the accelerator controls components such as parameter management, setting generation, cycle handling, trim management; they do not have to write system level services. The platform of choice today is the J2EE [16]. J2EE is an industrial standard defined by a set of specifications and APIs, implemented by many vendors. J2EE is based on the Java programming language and on a component model known as Enterprise JavaBeans (EJB). Components are the key technology to write a modular object-oriented distributed application. EJB components are "Lego pieces" that implement a set of interfaces allowing them to run inside a so-called "EJB container".

As shown in Fig 14.5, developers write accelerator-specific code in the form of EJB components, and the EJB container provides the necessary infrastructure to run them, such as remote accessibility, components management, concurrency support, fault tolerance, high availability, scalability, resources pooling, transaction management and security.

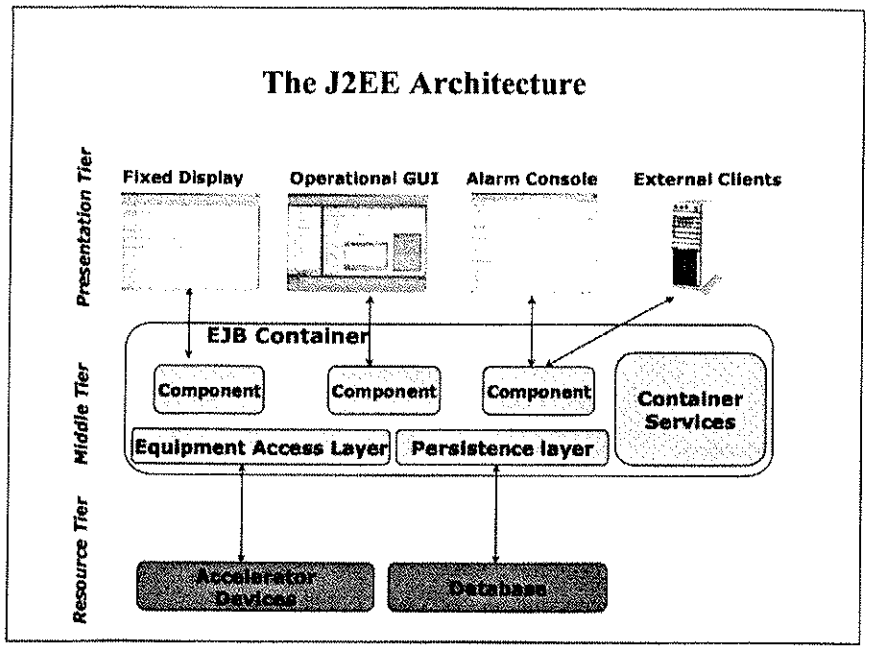

Figure14.5: The J2EE Architecture

To summarise, the 3-tier approach and the J2EE framework are the basis on which to build the control for the LHC. Efforts may be focused on the LHC control challenges and not on the infrastructure. It exploits existing technology and provides the modular and distributed architecture needed.

14.7.4 The UNICOS Framework for Industrial Controls

In the past decade many CERN control systems, particularly those for technical services, have been built with standard industrial control components, often by industry following a technical or functional specification. Reflecting this trend, a single industrial supply has been made for the procurement of the hardware and software for the control of the cryogenic equipment and experimental magnets installed in the LHC accelerator complex. This control system is referred to using the acronym UNICOS, standing for UNified Industrial COntrol System.

UNICOS builds on a classic industrial controls architecture using the PVSS [17] SCADA in the Supervision layer, Schneider Quantum PLCs for process control at the Control layer and Schneider Premium PLCs to connect process channels in the Field layer (an alternative is Quantum remote I/O). Communication is based on Ethernet and FIPIO. The software design is an evolution of an object oriented philosophy used with former control systems [18, 19]. In this approach each process device - sensor, actuator, or set of devices constituting a process entity - is modelled in an object. This object integrates the process behaviour and the GUI.

The UNICOS Object Model

In the UNICOS concept the object implementation is split into two parts:

- The GUI functionality - programmed in the SCADA,
- The process behaviour - programmed in the PLC.

The GUI part includes the interaction with the operator by means of graphical components and dedicated panels called "faceplates"; these GUIs inform the operator of the object status, and allow him to send orders. The PLC part contains the process behaviour of the object. The object is linked to the plant through I/O channels that may be linked to the PLC via either a fieldbus or a direct I/O connection. The SCADA and PLC object parts are connected together by the communication layer based on the TCP-Modbus protocol.

As shown in Fig. 14.6, each object has several interfaces and receives the following information:

- Requests from the operator via the SCADA object. These requests are transmitted to the PLC by the manual requests through the communication middleware.
- Configuration parameters (GUI or PLC) set during the programming phase and accessible for modification by a program specialist.
- Information from the process (process inputs), consisting of analogue or binary values from sensors and status of other objects.
- Orders from the control logic programmed into an object of a higher hierarchical level via the Auto Requests.

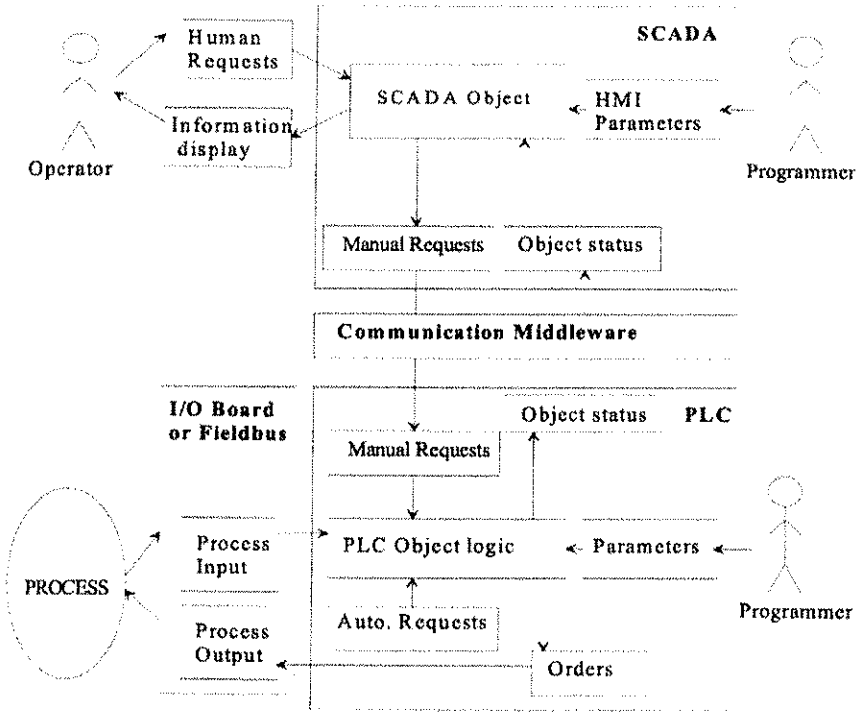

Figure 14.6: The UNICOS Object Model

Three main types of object are defined in the UNICOS architecture:

- Input-output objects which provide the interface to the plant. They link the devices and actuators to the control system. Some basic treatments may be embedded in these objects. Input/output channels are exclusively accessed through such objects.
- Field objects that represent hardware elements such as valves, heaters, motors, and other devices. Each type of field object has its own associated process logic. This logic integrates specific functions (alarm generation, transition between set points, interlocking).
- Process control objects that control equipment units grouping several field objects and/or other process control objects. The process logic of these objects is split between a standard part insuring a homogeneous interface to the environment, and a specific part to handle the process to control.

Implementation

The industrial supply includes the development of the PLC and SCADA components for each type of object as well as the communication mechanisms between the PLCs and the SCADA. It also includes a SCADA framework offering homogeneous user interfaces and accelerating application development for the supervision layer. The PLC objects were developed in IEC-61131-3 languages and all SCADA modules have been developed using ActiveX and proprietary PVSS scripts. In order to optimise the communication bandwidth between the PLCs and the SCADA, an event-driven protocol based on TCP-Modbus has been developed by the supplier.

The user application development process is considered as an integral part of the software framework. This is split into 3 distinct phases: specification, software development and acceptance/maintenance.

14.7 CONTROL ROOM SOFTWARE

14.7.1 Software for LHC Beam Operation

The LHC control room applications will be based on a set of common control system services and components, in order to avoid duplication of effort and solutions. The operational software development process relies on common development tools, guidelines and procedures for the construction, testing, integration, deployment and change management.

UCR Software Requirements

The LHC aims at injecting, accelerating and then colliding beams with well controlled beam parameters in an efficient, reliable and reproducible manner. This is a non-trivial task, since the small aperture, the high stored beam energy and the sensitivity of the machine to beam losses impose very tight accelerator physics constraints. The superconducting magnets will generate field errors that have large static and dynamic components. Thus, the destructive power of the LHC beams and the low tolerances to beam losses will place very stringent demands on the LHC control system. A non-exhaustive list of the main software applications for LHC is outlined below:

- **On-line monitoring** of the state and tolerances of every LHC component and interlock systems.
- **Measurements** to allow for synchronised measurement acquisition as part of scans, feedback, or at a given point in the ramp.
- **Real time control** to implement feedback on key beam parameters (orbit, tune, chromaticity) plus the feed-forward of corrections from the reference magnets.
- **On-line model** including calculation of parameter variations and feed-forward from machine into model.
- **Automatic sequencer** to allow complicated sequences for injection and ramp to be performed systematically.
- **Fixed displays** including transfer lines, beam sise, bunch currents, mountain range turn-by-turn, tune FFT, beam loss monitors, global orbit plus crossing angles, beam separation, transverse position along a batch.
- **Settings management system** to deal with the generation and management of complex settings.
- **Control of the main beam parameters** implying fast, accurate control in terms of appropriate parameters in both the physics coast and during injection and ramping.
- **Trim facility** to allow for trim incorporation, persistent versus geometric correction, scaling, accumulation, and smoothing out of errors and corrections, time and history dependency of errors.
- **Communication with experiments** and other major systems (cryogenics, vacuum, technical services).
- **Scripting environment** for ad-hoc rapid application development for machine development.
- **Miscellaneous support applications** such as Electronic Logbook.
- **Console Manager** to launch and manage controls applications in a unique manner.

The Software Development Process

The current software development follows the Unified Software Development Process [20]; a practical software process model followed by many industrial OO projects. Java is the programming language chosen for the implementation of the high-level services and control room applications, as it enables platform independent development. XML is playing an increasingly important role in the exchange of data.

A suite of selected software tools for code optimisation, quality insurance and testing is provided to the developers to guarantee the quality of the control room software. Software configuration management facilities are provided on top of the archive engine (RCS) to provide version management services, making it possible to trace and identify any component of an operational application, and to deliver consistent operational software releases. In addition tools for code building and distribution are available to release operational software components in a multi-versioned repository residing on dedicated fileservers (Sec. 14.4).

Operational software, once released, is deployed locally to the operators' consoles using standard Java distributed deployment technology (e.g. Java Web Start) [21], which guarantee automatic delivery of

software updates without operator intervention. Local deployment ensures the speed and performance required by operations.

14.8.2 Software for LHC Industrial Systems

Several LHC accelerator industrial subsystems will be accessible from the UCR consoles via a SCADA supervision interface. SCADA systems are used in a wide variety of industrial domains and therefore typically provide a flexible, distributed and open architecture to allow customisation to a particular application area. In addition to a set of basic SCADA functionality, these systems also provide a strong support for GUI tools, a set of standard interfaces to hardware as well as an API to enable integration with other applications or software systems. PVSS [17], the industrial SCADA product recommended at CERN, has the following specific features:

- It can run in a distributed manner.
- It has multi-platform support (Linux and Windows).
- It is device oriented with a flexible structural concept.
- It has advanced scripting capabilities.
- It has a flexible API allowing access to all features of PVSS from an external application.

The SCADA development process, in particular when based on frameworks such as UNICOS (Sec. 14.7.4), can be based mostly on configuration and graphic editors rather than programming. A unique device configuration database contains all characteristics of the devices, including device addressing, alarm and data logging parameterisation.

14.9 SERVICES FOR OPERATIONS

14.9.1 Analogue Signals Transmission

While most signals from the LHC will be digitised for internal usage by the respective accelerator systems there are a number of them which are required for visualisation during tuning and measurement. These include some 200 signals, mainly in the 0 to 10 kHz range from the RF system and over 300 signals with a typical bandwidth of 50 MHz from the kicker systems for injection and beam extraction. In the injector chain, the nAos system [22] is successfully used to fulfil the need for coherent acquisition and display of analogue signals. The system's main feature is the digitisation of signals in acquisition crates as close as possible to their sources, therefore ensuring optimal fidelity. Whenever possible, in order to save costly oscilloscope modules, signals are multiplexed allowing some 100 signals to be serviced by one crate containing four two-channel oscilloscope modules. The triggers for all the oscilloscope modules are elaborated from the GMT distribution (Sec. 14.5.1), ensuring a precise time-correlation between signals. The digitised signals are sent through Ethernet to control room consoles, where a GUI application (Fig. 14.7) allows operators to monitor them in four-channel "virtual oscilloscope" screens.

The nAos system is currently being upgraded to more modern, commercial hardware and software platforms. The new version of the system is called Open Analogue Signals Information System (OASIS) [23]. It will implement all the above features, including arbitration of resource (i.e. oscilloscopes), allocation to clients and the additional functionality for the LHC requirements. This approach will ensure that signals from the injector chain may also be integrated into the LHC operation; the older, lower energy machines are more richly instrumented by this system. As with all LHC systems OASIS must provide information to the Logging (Sec. 14.9.3) and Post Mortem (Sec. 14.9.4) systems. This offers a very attractive possibility of flexibly connecting signals which should prove very useful in understanding malfunctioning of complex systems. Analogue signals will be monitored by Compact PCI-based acquisition systems; the total number of crates will depend on the amount of multiplexing achievable with regard to the number of clients.

14.9.2 Alarms

Operating the LHC will require many services to help both operators and equipment specialists to understand the many complex situations which will arise during maintenance or operation of the CERN accelerator complex. The detection, collection, management and distribution of information concerning

abnormal situations ranging from severe alarm states to warning states, hereafter referred to as Fault States (FS), will require one global system. The system will accept information concerning any problem associated with the CERN accelerator complex and offer this information, in a structured way, to any interested party. The core part of this system will be the LHC Alarm SERvice (LASER), [15, 24]. As a result of a detailed technology survey, a 3-tier architecture was chosen and is now being implemented according to the J2EE specification (see 14.7.3).

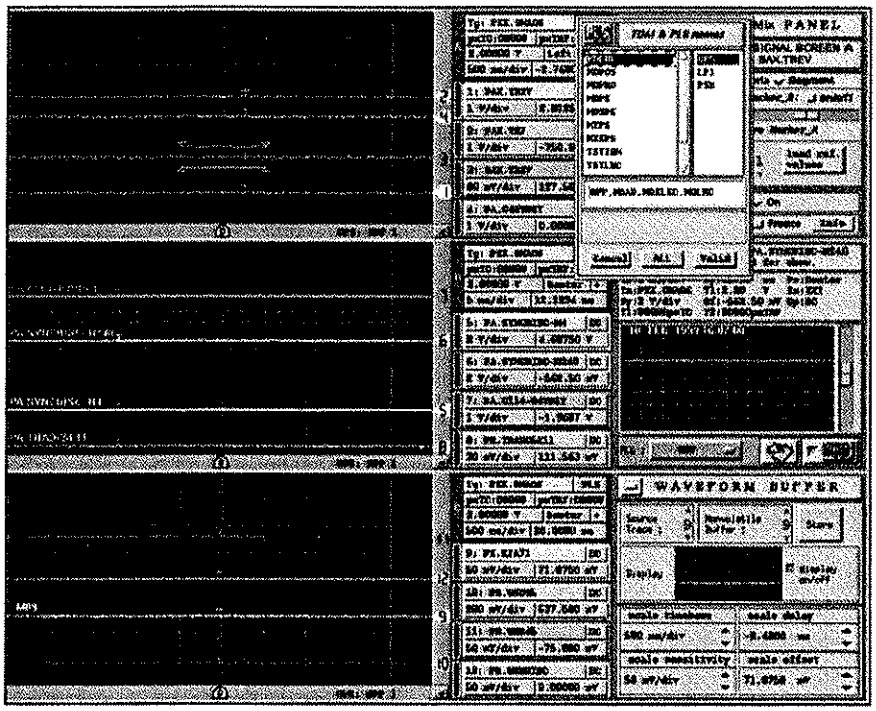

Figure 14.7: Snapshot of nAos GUI

Fault State (FS) detection is performed (Fig. 14.5) in the resource tier by surveillance software written by equipment specialists, application programmers and operators. The LASER system offers a standard interface for these sources to push a FS, by means of either a C or Java API [25] based on the messaging system. FS time stamping at the point of detection, using UTC time, down to the microsecond level if needed, will be crucial in correlating data. The middle-tier will collect the FS by subscribing to all FS sources. A number of services and facilities will be offered at this level including:

- FS persistence;
- Logging of FS transitions using the LHC Logging facility;
- FS dependency and reduction management;
- FS browsing and interaction;
- Administration of the overall system;
- User and configuration management;
- Scaling, using clustering facilities;
- FS distribution according to a FS hierarchy, representing the interest of users.

Finally, the presentation tier will cater for clients interested in those services via a Java client interface. The major user of this interface will be the alarm console, which will be used by equipment groups and control centres to select, receive and display FS, and in order to access all LASER services. Important configuration facilities will allow the alarm console to be personalised.

14.9.3 Logging

The process of capturing and recording information on the operation of the LHC is generally referred to as *"LHC Logging"*. Logging of information in a centralised storage medium is an operational requirement and has proven to be essential in previous projects, including LEP and the String2 installation.

The information of interest that needs to be *logged* is various and heterogeneous, but usually concerns values of variables that evolve over time, for example cryogenic temperatures, vacuum pressures, magnetic field measurements, bunch intensities, or beam profiles. The total number of logging variables will be in the order of 10^5-10^6 with logging frequencies up to 0.1 Hz.

The main purpose of LHC logging is to improve the machine performance and that of the individual subsystems. Therefore the recorded data will be stored and kept accessible over the consecutive years, in order to permit comparison of historical data, off-line analysis to search for data correlations, and compilation of operational statistics.

For each of the logged records of the data variables, the date-time value is a key attribute, and therefore correct *"time stamping"* is vital for the exactness of the data. For time stamping, the usage of UTC is endorsed throughout the LHC Logging system (Sec. 14.5.3), with microsecond precision where applicable.

In order to enable effective exploitation of the logged data by users such as equipment engineers, control room operators, machine physicists and CERN managers, the LHC Logging system will employ web-enabled interfaces to graphically visualise the information and to extract it to common desktop tools. It will be essential to be able to correlate logging data to the other major operational data systems: Alarms and Post-Mortem.

The functional specification [26] and architectural design [27] of the LHC Logging system have been documented. The central storage medium will be a dedicated Oracle database instance. Input of the logging data and its description will be done through formally defined XML files, which may be generated from Java, C or C++ programs.

Logging of data will start as of the commissioning of the first QRL sector and will ultimately cover the complete lifetime of the LHC.

14.9.4 Post Mortem

The LHC will be protected by over 10000 interlock channels, thousands of quench detectors and around 3000 beam loss monitors. Many tens of thousands of signals will be available for the operators and engineers to interpret the circumstances of Beam and Power Aborts. The Quench Protection System alone will provide around 80000 signals for Alarms, Logging and Post Mortem purposes. Recovery from a perturbation to the nominal magnet cycling will require a minimum of 2 hours (7 TeV back to 7 TeV) which precludes learning by trial and error as practiced with normal conducting machines.

The LHC Post Mortem System (Fig. 14.8) [6, 28, 29] is required as a suitable diagnostic tool. The purpose of this system is:

- To ensure comprehensive monitoring of machine protection systems.
- To improve the operational efficiency of the LHC by:
  - Providing diagnostics of power and beam aborts - the aim is to quickly identify the origin of failures in order to initiate appropriate actions and restore operation,
  - Building long term understanding of accelerator operation,
  - Providing diagnostics for beam losses resulting from equipment malfunction.
- To explain the mechanism if damage occurs.

To achieve these aims the post mortem data must be *complete* and *coherent* across systems.

Whilst it is intended to make full use of diagnostics from Alarms and Logging these systems will not provide all the facilities required for the understanding of quenches and beam losses in the LHC. In particular the underlying hardware must capture transient data pertaining to conditions prevailing before, during and after such events. These transients may be relatively slow when they are provoked by quenches; indeed the Logging system will gather some pertinent information, such as cryogenic temperatures. However in the case of beam losses the timescales are extended downwards to turns of the machine.

In order to satisfy the essential aims of being complete and coherent across all LHC systems the following essential ingredients are required:

- Every LHC equipment and diagnostics system must implement a circular Post Mortem buffer of appropriate depth holding the latest data (for example 1000 turns for beam instrumentation).
- This data must be time stamped using a common clock with a precision related to the corresponding process (see Tab. 14.2).

- The Post Mortem buffers must be frozen by the Post Mortem timing event or by self-triggering in the case of the protection systems.
- Data must be self describing so that it can be managed by the event builder and analysed by generic tools.

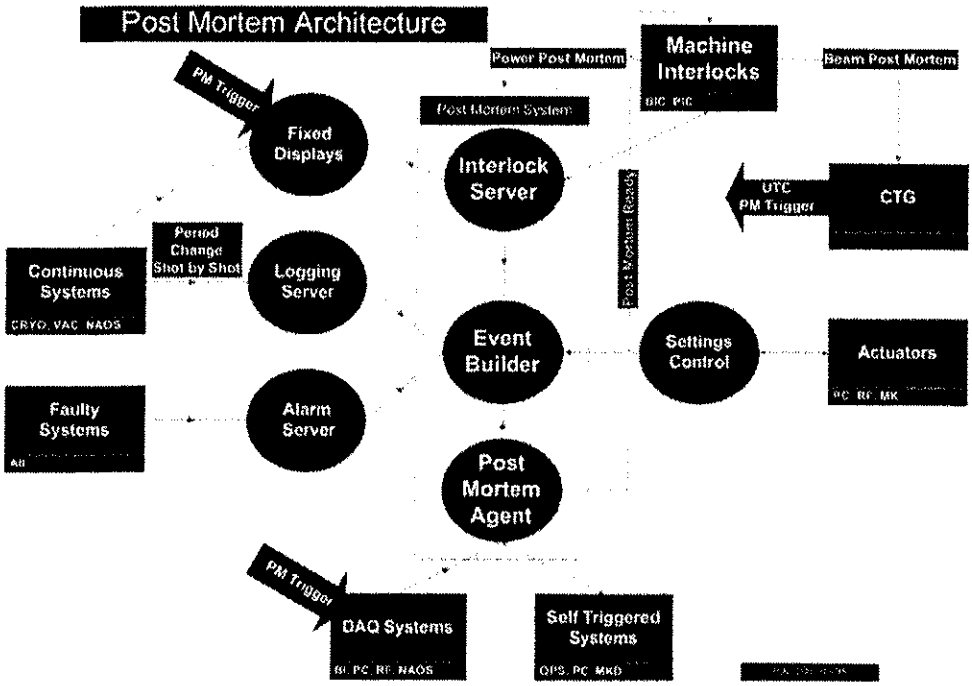

Figure 14.8: The LHC Post Mortem Architecture

The Post Mortem events will be large - several gigabytes - and therefore analysis must be automatic in order to generate digested information for operators. After analysis the information must be stored in order to build up the longer term history and understanding of the machine. The most relevant data will be stored for the lifetime of the LHC.

14.9.5 Support for Real-Time Feedback Loops

To operate the LHC efficiently with high intensity beams, a number of key beam parameters must be stabilised using digital real-time feedbacks and fast feed-forward from reference magnet measurements. It is anticipated [30] that an 80% reduction of the persistent current decay effects can be achieved with feed-forward but that real-time feedbacks will be required for orbit, tune and chromaticity. The expected sampling frequencies of the feedbacks lie in the range of 10 to 100 Hz. For chromaticity the main difficulty lies presently in the possibility to measure this parameter in a non-destructive way at a reasonably high frequency.

It has been shown [31] that a properly designed feedback loop can control orbit distortions during injection and at the beginning of the ramp. For example, a proportional–integral control loop that samples at 10 Hz and that has a total time delay of 100 ms can reduce orbit errors at a frequency of 0.1 Hz with a gain of 8. A considerably better performance can be obtained when the sampling frequency is increased and/or when the total time delay is reduced.

From the point of view of infrastructure, robust operation of feedbacks mainly concerns networks and FECs. A global orbit feedback in particular will involve more than 100 FECs of the beam instrumentation and power converters. Despite the large size of the LHC ring and the distribution of the equipment over the machine, the network performance must be stable and guarantee delays in the range of a few milliseconds for data sent between any points of the LHC. Large variations of time delays due to the computation, control or communication must be avoided, if necessary by allocating dedicated resources to feedback operation.

The LHC FECs will provide good real-time support based on the LynxOS operating system. Networking topology and resources will be organised to meet the service requirements. At present no specific infrastructure for feedback is foreseen.

14.9.6 Control System Monitoring and Diagnostic Tools

The monitoring tools used by accelerator operators, experimental areas operators, technical services operators and system administrators allow operators to detect, understand and repair faults or remotely reboot the computers. The current system (Fig 14.9) monitors a few hundred UNIX, Linux and LynxOS computers, 365 days a year, 24 hours a day.

In order to cope with the growing and evolving controls environment as well as to conform to the new application software standards (Sec. 14.7.3) a new design of the monitoring tools is currently underway. A new surveillance program will inject alarms directly into the LASER system (see 14.9.2). The new operator interface will be based on the same technology as the LHC Alarm Console and will allow the operator to view the state of all the computers being monitored, either good or bad. The operator can then select one of them to perform more detailed checks or restart a failing program or even reboot the computer.

The LASER archive will store all these monitoring alarms. So, after a major event for example a UPS failure on an LHC site, the operators and system administrators will be able to check at what time computers stopped functioning due to loss of power and when the control system was restored.

As part of the upgrade, the surveillance will be extended to Sun Workstations, Windows Servers and PLCs in order to cover all the main components of the LHC Control System.

REFERENCES

[1] http://www.lynuxworks.com
[2] http://www.redhat.com
[3] http://ttc.web.cern.ch/TTC/intro.html
[4] http://lhc-proj-timwg.web.cern.ch/lhc-proj-timwg/
[5] http://www.its.bldrdoc.gov/fs-1037/dir-009/_1277.htm
[6] E Ciapala, F. Rodriguez Mateos, R. Schmidt, J. Wenninger, "The LHC Post Mortem System", LHC Project Note 303, October 2002
[7] www.ntp.org
[8] 'Building, running and dismantling world's largest scientific instrument with the same database tools', R. Billen, J. Schinzel, CERN, Switzerland, SL-Note-2001-011 MR.- : CERN, 30 Mar 2001
[9] Installation and Integration Database. R. Saban Presented at the 16th Meeting of the LHC Controls Project, CERN. September, 2001
[10] M. Zerlauth, A. Jimeno, G. Morpurgo, R. Schmidt, "The Electrical Circuit Description for the LHC", Proc. of EPAC 2002, Paris, France
[11] The Configuration Database for the CERN Accelerator Control System, ICALEPCS 2003
[12] Controls Middleware - The New Generation, EPAC 2002
[13] http://wwwpsco.cern.ch/private/mw/RDA/cppapi-1.1/html/index.html
[14] http://java.sun.com/products/jms/
[15] http://proj-laser.web.cern.ch/proj-laser/
[16] http://java.sun.com/j2ee/
[17] http://www.etm.at/english/index.htm
[18] http://ab-project-unicos.web.cern.ch
[19] P. Gayet et al., "Application of Object-based Industrial Controls for Cryogenics", Proc. of EPAC2002, PARIS
[20] The Unified Software Development Process, by Ivar Jacobson, et al
[21] http://java.sun.com/products/javawebstart/
[22] http://srv1ps.cern.ch/psop/nAos/index.htm
[23] http://project-lhc-cp-sigwg.web.cern.ch/project-lhc-cp-sigwg/
[24] F. Calderini et al., "LHC Alarm System User Requirements Document", SL-Note-2002-004(CO)
[25] http://proj-laser.web.cern.ch/proj-laser/development/laser-source/index.html
[26] The LHC Logging System, functional specification, EDMS Id 358869
[27] The LHC Logging, design specification, EDMS Id 367787
[28] R. J. Lauckner, "What Data is needed to Understand Failures during LHC Operation?", Proc. Chamonix XI, CERN-SL-2001-003-DI, January 2001

[29] R. J. Lauckner, "What Do we see in the Control Room?", Proc. Chamonix XII, CERN-AB- 2003-008-ADM, April 2003
[30] T. Wijnands, L. Bottura, A. Burns, M. Lamont, L. Vos, "Requirements for Real Time Correction of Decay and Snapback in the LHC Superconducting Magnets", LHC Note 221, 1999-04-10
[31] T. Wijnands, J. Wenniger, B. Srinivasan, "Prototyping LHC Orbit Control", LHC Note 278, 2002-01-22

CHAPTER 15

MACHINE INTERLOCK SYSTEMS

15.1 INTRODUCTION

The energy stored in the LHC superconducting magnets and in the circulating beams is unprecedented. For nominal beam parameters at 7 TeV, each proton beam will have an energy of about 340 MJ. The energy stored in the magnet system amounts to about 10 GJ. An uncontrolled release of energy could lead to serious damage of equipment. Major damage of equipment inside the cryostats will result in long repair times, as the equipment is delicate and difficult to access.

When a failure occurs while powering the magnets, for example in case of a quench or a power converter fault, the energy stored in the magnets must be extracted. For a failure during beam operation, for example when beam losses become unacceptable or after failure of equipment, the beams must be dumped as fast as possible.

The main objective for the machine protection system is to protect the machine in case of failure; the necessary steps should be taken to dump the beam and to dissipate the stored energy in the magnets in a safe way [1]. Furthermore the system should:

- Protect the beam: The system should not generate beam dumps if this is not strictly necessary. Faulty trigger signals that lead to a beam dump should be avoided.
- Provide the evidence: In case of beam dump or failure in the powering systems, correct diagnostic messages should get to the operator. In case of multiple alarms when one initial failure causes subsequent failures, the system should support identifying the initial failure.
- Assist the operation of the machine: The diagnostics for failures should be easy to understand. The status of the system must be presented clearly to the operator in the control room and should be transparent.

15.2 MACHINE PROTECTION AND INTERLOCK SYSTEMS

Several systems are required in order to protect the complex equipment of the LHC accelerator. The machine interlocks are part of the protection and include two systems, the powering interlock system and the beam interlock system (Fig.15.1 and [1]).

Protection during magnet powering prevents damage to the elements in the electrical circuits, such as magnets, normal conducting and superconducting cables, current leads and power converters (see Chap. 9). Protection requires dedicated equipment such as the quench protection system, energy extraction system and the powering interlock system. It had also a strong impact on the design of the power converters.

The powering interlock system permits powering of magnets if several conditions are met. In the case of a failure, the powering interlock system must ensure a safe stop of powering ("power abort") and a discharge of the magnet energy and request a beam dump if necessary.

Magnets can be powered independently of beam operation, for example during commissioning and for tests. The full functionality of the protection systems is required for the start of commissioning the magnet powering system.

The beam interlock system permits beam operation. Firstly, it permits injection into the LHC when all systems are ready for beam. Secondly, with circulating beam, the beam interlock system transmits any beam dump request from other systems to the beam dumping system.

The systems that are essential for protection during beam operation are the beam dumping system, collimators and beam dilutors and beam monitors and all of these have an interface to the beam interlock system. Other systems with an interface to the beam interlocks are the powering interlocks, RF, injection kickers, vacuum system, access safety system, controls system and the LHC experiments.

For the machine interlocks several principles have been adopted:

- To prevent damage of equipment, fail safe hardwired links are used. No interlock signals are transmitted via the control system.

- To understand the current status of the LHC, the general status of the systems connected to the machine interlocks be will displayed.
- To understand the events leading to a power or beam abort, recording of parameters of the interlock systems will be made available for later analysis (Post Mortem). Time stamping of the recording is synchronised across all systems in the LHC by using the same clock [2].

The access safety system and the access control system are separate from the machine interlocks and discussed elsewhere [3, 4].

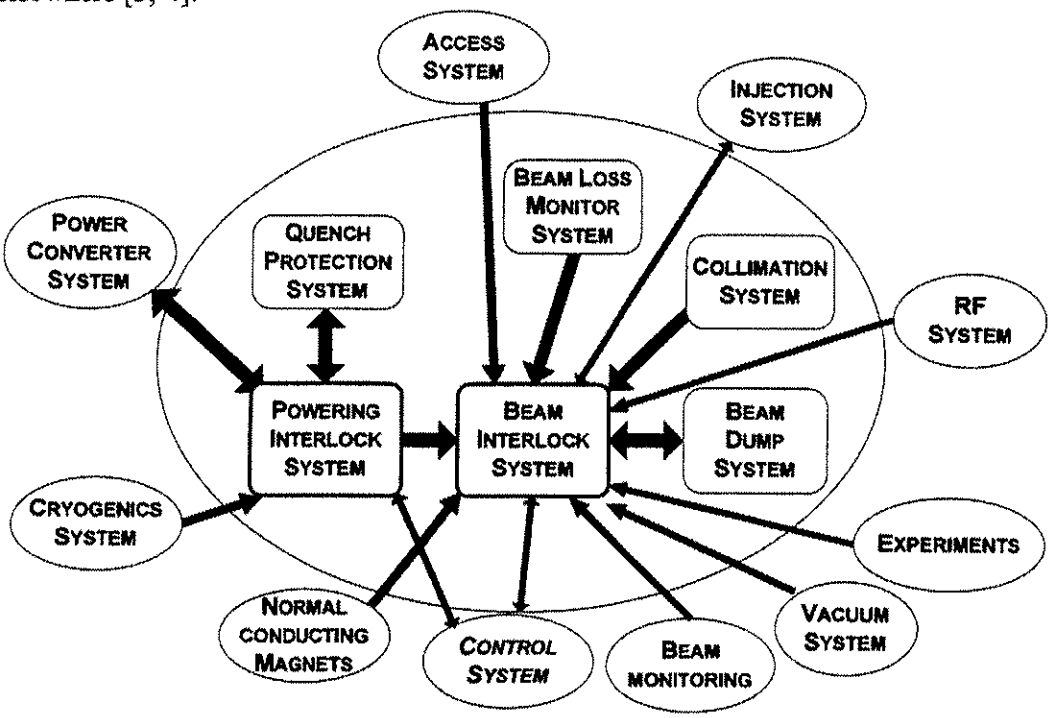

Figure 15.1: Relationship between the powering interlock system, the beam interlock system and other main LHC systems. The systems dedicated to protection are within the grey zone.

15.3 THE POWERING INTERLOCK SYSTEM

In the LHC, superconducting as well as normal conducting magnets are used. The requirements for protection from failures are somewhat different. Therefore the powering interlock system is composed of two sub-systems: one is in charge of the protection of the electrical circuit with superconducting magnets, and the other is in charge of the protection of the circuits with normal conducting magnets.

15.3.1 Basic Functionality and Response Time of the Interlock System for Superconducting Magnets

The powering interlock system permits powering of an electrical circuit with superconducting magnets when the required conditions are met.

- The superconducting magnets must be at operating temperature.
- The quench protection system must be ready for powering.
- The electrical supplies for the protection systems, backed up by uninterruptible power supplies (UPS), must be fully operational.

In the case of a failure in the electrical circuits, the powering interlock system, together with the quench protection and power converter systems, ensures that powering is aborted correctly:

- The energy stored in the magnets is safely discharged for circuits with large stored energy.
- The power converters are stopped, by removing the permit and issuing a fast abort for the power converters.

- When operating with beam, the powering interlock system informs the beam interlock system of any failures in the powering system. The beam interlock system decides if a beam dump is required.

Numerous failure scenarios were considered during the design phase. The most likely failure is a quench of a magnet. Other failures are quenches of bus-bars, quenches of high temperature superconductor (HTS) current leads, and failures in the powering system for example, a fault in a power converter or in the water cooling of a normal conducting power transmission cable.

As discussed in Chap. 9, in the case of a quench in one of the superconducting magnets with large stored energy, the quenching magnet can absorb its own energy. The energy of the other magnets in the electrical circuit is discharged as fast as possible by switching a resistor into the circuit. The time constant for the current decay is between about 0.1 s for some of the corrector magnet circuits and 100 s for the main dipole magnet circuits. For the electrical circuits with superconducting magnets the response time required to start discharging the energy and stopping the power converters is some tens of milliseconds [5]. In the case of a power converter failure after a water cooling fault, for example, the requirements are similar.

15.3.2 Powering Subsectors

The LHC superconducting magnets are powered separately in each of the eight sectors. When operating at 7 TeV, the energy in each sector of the LHC amounts to about 1.2 GJ: sufficient to warm up and melt 1900 kg of copper.

In each sector there are several cryostats, in total more than 40. To simplify installation, commissioning and operation, the electrical circuits with superconducting magnets are grouped into 28 powering subsectors (see Tab. 1Table 1 for the inventory of powering subsectors) [6]. One power converter is always powers magnets that are installed in only one cryostat. There are no electrical circuits powering magnets in several cryostats.

The powering subsectors are defined according to the layout of the cryostats:

- Arc cryostats: Eight long cryostats span the major part of the sectors and are electrically fed from both sides. The MB, MQD and MQF magnets are powered from converters installed at even points, as are the energy extraction systems for the MQF and MQD magnets. For the MB electrical circuit there is one energy extraction system at each end of the arc cryostat. The arc powering subsectors need two powering interlock controllers, one at each side of the arc. In IR3 and IR7 there is only one additional cryostat housing the Q6 magnet left and right of the insertion. Therefore the corresponding electrical circuits in these insertions are interlocked by the controller for the adjacent arc powering subsectors.
- Triplet cryostat: At each interaction point with an experiment, several quadrupole magnets and the D1 magnet (for IR2 and IR8) are installed in a cryostat at each side of the interaction point. Each triplet cryostat is a powering subsector managed by one powering interlock controller.
- Cryostats in matching sections: In some of the long straight sections several other cryostats are installed, with magnets for matching and for separating the beams. These cryostats are combined to one powering subsector with one powering interlock controller.

In total, there are 28 powering subsectors and 36 powering interlock controllers for the superconducting magnets. The powering interlock system must allow for independent operation of each powering subsector.

15.3.3 Powering Interlock Controllers for Superconducting Magnets

A powering interlock controller for superconducting magnets is in charge of the interlocks of one powering subsector. It exchanges several hardware signals with the power converters and the quench protection system for each electrical circuit [7]. Each controller also has an interface to the UPS [8] and to the general emergency stop [9]. Other signals, transmitted via the control system, are only used to evaluate if powering of the electrical circuits in the subsector can be permitted:

Table 15.1: List of the Powering Subsectors and Powering Interlock Controllers (for superconducting magnets)

	Powering Subsectors		Name of DFB	PIC		
	Number	Purpose		Name	Location	No.Circuits
Sector 1-2	1	Inner triplet in R1	DFBXB.3R1	CIPCX.R1	UJ16	*16*
	2	Matching section in R1	DFBLB.RR17	CIPCL.R1	RR17	*17*
	3	Arc 1-2 cryostat (right side)	DFBAB.7R1	CIPCA.R1	RR17	*30+48 (+94)*[1]
		Arc 1-2 cryostat (left side)	DFBAC.7L2 + DFBAC.6L2	CIPCA.L2	UA23	
	4	Matching sections in L2	DFBMC.5L2 + DFBMA.4L2	CIPCM.L2	UA23	*17*
	5	Inner triplet in L2	DFBXC.3L2	CIPCX.L2	UA23	*16*
Sector 2-3	6	Inner triplet in R2	DFBXD.3R2	CIPCX.R2	UA27	*16*
	7	Matching sections in R2	DFBMB.4R2 + DFBMC.5R2	CIPCM.R2	UA27	*17*
	8	Arc 2-3 cryostat (right side)	DFBAD.6R2 + DFBAD.7R2	CIPCA.R2	UA27	*48+34 (+94)*[1]
		Arc 2-3 cryostat (left side) + Matching section	DFBAE.7L3 + DFBMD.6L3	CIPCA.L3	UJ33	
Sect. 3-4	9	Arc 3-4 cryostat (right side) + Matching section	DFBAF.7R3 + DFBMD.6R3 + DFBLC.UJ33	CIPCA.R3	UJ33	*34+44 (+94)*[1]
		Arc 3-4 cryostat (left side)	DFBAG.7L4	CIPCA.L4	UA43	
	10	Matching sections in L4	DFBMG.6L4 + DFBMF.5L4 + DFBME.3L4	CIPCM.L4	UA43	*11*
Sector 4-5	11	Matching sections in R4	DFBMK.3R4 + DFBML.5R4 + DFBMG.6R4	CIPCM.R4	UA47	*11*
	12	Arc 4-5 cryostat (right side)	DFBAH.7R4	CIPCA.R4	UA47	*44+30 (+94)*[1]
		Arc 4-5 cryostat (left side)	DFBAI.7L5	CIPCA.L5	RR53	
	13	Matching section in L5	DFBLD.RR53	CIPCL.L5	RR53	*17*
	14	Inner triplet in L5	DFBXE.3L5	CIPCX.L5	USC55	*16*
Sector 5-6	15	Inner triplet in R5	DFBXF.3R5	CIPCX.R5	UJ56	*16*
	16	Matching section in R5	DFBLE.RR57	CIPCL.R5	RR57	*17*
	17	Arc 5-6 cryostat (right side)	DFBAJ.7R5	CIPCA.R5	RR57	*30+40 (+94)*[1]
		Arc 5-6 cryostat (left side)	DFBAK.5L6	CIPCA.L6	UA63	
	18	Matching sections in L6	DFBMG.5L6 + DFBMG.4L6	CIPCM.L6	UA63	*8*
Sect. 6-7	19	Matching sections in R6	DFBMG.4R6 + DFBMG.5R6	CIPCM.R6	UA67	*8*
	20	Arc 6-7 cryostat (right side)	DFBAL.5R6	CIPCA.R6	UA67	*40+34 (+94)*[1]
		Arc 6-7 cryostat (L) + Matching section	DFBAM.7L7 + DFBMH.6L7	CIPCA.L7	RR73	
Sector 7-8	21	Arc 7-8 cryostat (R) +Matching section	DFBAN.7R7 + DFBMH.6R7	CIPCA.R7	RR73	*34+48 (+94)*[1]
		Arc 7-8 cryostat (left side)	DFBAO.6L8 + DFBAO.7L8	CIPCA.L8	UA83	
	22	Matching section in L8	DFBMA.4L8 + DFBMC.5L8	CIPCM.L8	UA83	*17*
	23	Inner triplet in L8	DFBXG.3L8	CIPCX.L8	UA83	*16*
Sector 8-1	24	Inner triplet in R8	DFBXH.3R8	CIPCX.R8	UA87	*16*
	25	Matching sections in R8	DFBMB.4R8 + DFBMI.5R8	CIPCM.R8	UA87	*17*
	26	Arc 8-1 cryostat (right side)	DFBAP.7R8 + DFBMJ.6R8	CIPCA.R8	UA87	*48+30 (+94)*[1]
		Arc 8-1 cryostat (left side)	DFBAA.7L1	CIPCA.L1	RR13	
	27	Matching section in L1	DFBLA.RR13	CIPCL.L1	RR13	*17*
	28	Inner triplet in L1	DFBXA.3L1	CIPCX.L1	UJ14	*16*

- From the cryogenics system ("Cryogenics OK") when the operating temperature in the cryostat is reached.
- From the quench protection system ("Quench Protection Permit") when the quench heater power supplies are charged and the energy extraction system is ready. This also requires that the system is ready to record data in case of failures ("Post Mortem Ready").

Two types of electrical circuits are defined:

- Circuits with main magnets having large stored energy. This includes all the main dipoles and main quadrupoles in arcs and insertions. In the case of a quench of such a magnet, the quench could travel to magnets or bus bars in other circuits and therefore all circuits in the cryostat will be discharged (fast power abort of all electrical circuits in the subsector).
- Circuits that only include magnets with low stored energy. A quench of a magnet in such circuits would normally not travel to magnets in other circuits (power abort only for the circuit with the quenching magnet).

The powering interlock controller sends the "PC_PERMIT" signal to the power converter to permit powering of an electrical circuit. Absence of this signal causes a slow abort of the power converter.

Most circuits are equipped with quench detectors. In the case of a quench, the quench protection system opens a current loop (see Fig. 15.2 – Circuit Quench Loop). This informs the powering interlock controller and the power converter about the quench. The power converter performs a fast power abort.

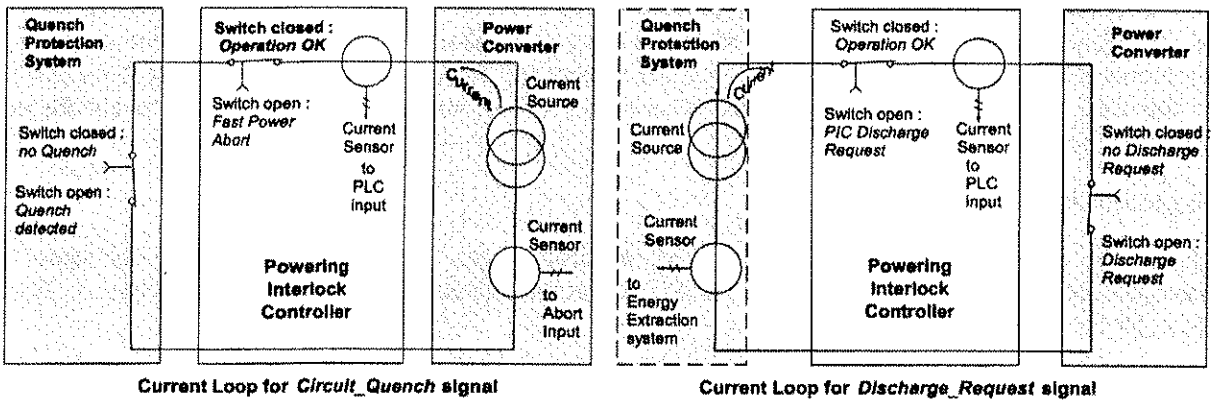

Figure 15.2: Interfaces between powering interlock controller, power converter and quench protection system. Two current loops, the Circuit Quench Loop and the Discharge Loop are shown.

For circuits with high stored energy, the energy is discharged by the quench protection system requiring no action by the powering interlock controller. To avoid quench propagation to other magnets in the same cryostat, all circuits must be discharged. Therefore the powering interlock controller requests a fast abort of all power converters in the subsector, and removes the power permit.

Some circuits have a very long time constant for current decay and it may be necessary to discharge the energy after a failure in the water cooling of the free-wheel diode, for example. To request such discharge, the power converter opens a second current loop (see Fig. 15.2 – Discharge Loop). The quench protection system detects that the loop is open and initialises the energy discharge.

For some circuits with low stored energy, the energy discharge is done either by the power converter or by a system installed in a rack beside the power converter. For these circuits, the power converter triggers the discharge of energy after receiving a request for fast abort.

In the case of a failure detected by the power converter, the "POWERING_FAILURE" signal is sent to the powering interlock controller.

Time stamping of all these events with an accuracy of 1 ms is required, with the common LHC clock derived from the NTP (Chap. 14.5.5).

Hardware platform

The powering interlock system will interface with power converters for about 800 electrical circuits, with the quench protection system for 700 circuits, etc. There are about 1400 input signals and 1500 output signals in total. The response time required is ~10 ms. The controllers will be built with industrial PLC's that are well suited for such applications. The exchange of signals with the other systems will use commercial I/O modules.

Since some of the powering equipment is located in tunnel enlargements (RR's) close to the accelerator, a radiation dose in the order of 0.1 Gy/year is expected. It has been shown that the CPU in a PLC does not work correctly in such environment [10]. However, after extensive tests it has been demonstrated that some of the commercially available I/O modules are sufficiently radiation tolerant. The I/O modules are linked via PROFIBUS to the CPU, which is installed in a location better protected from radiation.

Interface to UPS and general emergency stops

UPS systems are installed in various underground areas to take over the supply of safety critical systems around the LHC ring in the case of mains failure. In the case of a failure of the redundant UPS system, followed by failure of the mains (for example during a thunderstorm), there will be no safe way to stop the machine as all safety systems will be without power. It is envisaged to transmit a signal to the interlock controller, which will trigger the discharge of energy in all concerned powering subsectors when the redundant UPS system fails [8].

In the case of a general emergency stop, i.e. Arrêts d'Urgence Généraux (AUG), the electrical power and other sources of energy that are likely to present a risk must be stopped. In order to meet this requirement, the magnetic energy of the MB, MQF and MQD must be discharged after a delay of some seconds [9]. For this purpose a link is proposed between the AUG system and the powering interlock controllers involved. As for the UPS link, it is envisaged to transmit a signal which will abort the powering in all the powering subsectors concerned.

Interface to beam interlock controller

A failure in an electrical circuit will have an impact on operation with circulating beam and the consequences will depend on the state of the accelerator (beam energy, beam intensity...). Hence, the criticality for beam operation is defined:

- Essential circuits are required for beam operation under all circumstances. In the case of a failure, the beams are dumped. All circuits with main dipole and quadrupole magnets fall into this category.
- Non-essential circuits are not necessarily required. Their use depends on machine and beam parameters. A failure should not automatically generate a beam dump. Examples of such circuits are those of the multipole correction magnets.

Each powering interlock controller will have a link to a nearby beam interlock controller to transmit two separate signals to distinguish the level of criticality. After a failure of an essential circuit, the beam will be unconditionally dumped. After a failure of a circuit that is not considered to be essential, the beam interlock controller will only request a beam dump if continuing operation with beam could endanger machine equipment.

Interfaces to other systems

The interlock controllers are linked to the control systems via Ethernet. In order to get precise time stamping information, the synchronisation of the controllers is performed either with Ethernet, or a special link to the LHC timing system. This needs still to be defined. A resolution of about one ms is required.

15.3.4 Electrical Circuits with 60 A Orbit Corrector Magnets

In the arcs of the LHC 752 orbit corrector magnets are locally powered by 60 A power converters. In the case of a magnet quench, the power converter switches off due to an over voltage in the circuit. There is no risk for the magnet [11]. There are no hardware links between the converters and the powering interlock controllers.

In order to start powering the orbit corrector magnets, the same external conditions as for other superconducting magnets in the same cryostat are required. The powering interlock control system will inform the power converters via the control system.

The failure of an orbit corrector magnet that significantly deflects the beam can lead to beam losses and to a quench. The beam loss monitor systems are being designed to measure the increased losses and request a beam dump via the interlock system. However, another mechanism of requesting a beam dump might be required. The status of all power converters will be available every 10 ms. If necessary, a beam dump request could be issued if one of the corrector magnet power converters goes to fault state. The details and the time constants that are required have not defined at the time of writing.

15.3.5 Programming of the Powering Interlock Controllers

The number of circuits to be managed by one powering interlock controller varies between 8 and 48. Thus the hardware of every powering interlock controller is specific, with between 20 and 160 inputs and outputs managed by the PLC.

To avoid a large number of different programs running in the PLC's, a generic program has been developed. The software will obtain the information about its layout from configuration files located in the LHC Reference Database [12].

Depending on the type of electrical circuit and the circuit parameters, such as the stored energy in the circuit and its importance for beam operation, four different procedures for handling a failure have been defined. For each circuit, the configuration data defines the procedures to be used. Depending on the state of the signals received from the power converter and quench protection system, the powering interlock controller will initiate or remove the signals to permit powering in the circuit, or safely abort powering and discharge the energy.

In the configuration file, two additional parameters for each electrical circuit are included. One parameter defines if the beam will be dumped in case of circuit failure. The other parameter defines if powering abort of all circuits in the powering subsector is required in case of circuit failure.

Starting from the initial state, powering in the circuit can be permitted on operator request if no quench signal is received from the quench protection system and if all other systems are ready. During normal operation powering is permitted until either a request from the operator or a failure in the powering leads to a slow or fast power abort. As soon as one of these abort mechanisms is activated, a beam dump request will be sent to the beam interlock controller and in the case of a fault in a major circuit, the powering of the complete subsector will be aborted.

The input and output states of each circuit will be continuously monitored by the PLC. The cycle time depends on the number of electrical circuits that are managed by the PLC. In each cycle all circuits in the powering subsector are processed sequentially. The maximum response time of the system of about 10 ms will not be exceeded in any of the configurations. All state changes will be recorded in a history buffer together with a time stamp with an accuracy of about one ms.

15.3.6 Powering Interlock System for Normal Conducting Magnets

The interlock system is required to avoid overheating water cooled magnets and therefore several temperature probes are installed on each magnet,. If the temperature exceeds a predefined value, a relay opens and the signal is sent to the interlock controllers. The controller has the task of removing the permit for the power converter, thus stopping the converter.

Normal conducting magnets in one electrical circuit which are powered in series by one power converter can be installed at both sides of one interaction point, (for example, the D1 magnets in IR1 and IR5). The interlocks for all normal magnets in one insertion are managed by one powering interlock controller. In IR4 no such controller is required since there are only superconducting magnets.

The required response time for switching off the power converter to avoid overheating is of the order of seconds. In general, normal conducting magnets have a large resistance and a low inductance. The time decay for the current is much shorter than for superconducting magnets and is of the order of some seconds. Switching off such magnets could lead to beam loss within a very short time, for the D1 magnet only a few turns (see Sec. 15.4.1). Before the power converter is switched off, a signal is sent to the beam interlock controller that will trigger a beam dump.

Table 15.2: List of the Powering Interlock Controllers (for normal conducting magnets)

	Controller			Number of		
	Number	Name	Location	Converters	Magnets	Magnets Name
IR1	1	CIPW.LR1	US15	1	12	MBXW(2x6)
IR2	2	CIPW.LR2	UA23	3	3	MBXWT(x2), MBWMD
IR3	3	CIPW.LR3	UJ33	3+12	44	MBW(x12), MCBW(x8), MQWA(x20), MQWB(x4)
IR5	4	CIPW.LR5	USC55	1	12	MBXW(2x6)
IR6	5	CIPW.LR6	US65	2	30	MSDA(2x5), MSDB(2x5), MSDC(2x5),
IR7	6	CIPW.LR7	UJ76	3+12	40	MBW(x8), MCBW(x8), MQWA(x20), MQWB(x4)
IR8	7	CIPW.LR8	US85	3	3	MBXWS(x2), MBXWH

Hardware platform for the normal conducting magnet interlock system

The powering interlock controllers for the normal conducting magnets are similar to those used in the SPS-LHC transfer lines. The powering interlock system will interface to power converters for 40 electrical circuits and 144 magnets (the two main magnets of the ALICE and LHCb experiments are not under the responsibility of the machine interlock and as such are not included in these numbers). There are in total 144 input signals, one for each magnet grouping all thermal switches for this magnet in series. 40 output signals will be transmitted by the system to the power converter. The required response time is of the order of several seconds. As for the interlock controllers for superconducting magnets, the controllers will be implemented with industrial PLC's. The exchange of signals with the other systems is via input/output modules.

15.3.7 Magnet Powering System and Interlocks in the LHC Reference Database

The data for all electrical circuits for powering magnets and their components have been introduced into the LHC Reference Database [12, 13, 14]. The data is used to provide the powering interlock controller with consistent data about the magnet powering system [15].

Every electrical circuit with its electrical circuit elements (power converters, normal conducting cable, current leads, superconducting busbars, magnets, energy extraction facilities etc.) is assigned to one of the 28 subsectors for superconducting magnets, or one of the seven insertions with normal conducting magnets. The LHC Reference Database will provide the interlock controllers with the name and type of all electrical circuits it will have to manage. Four different types have been defined, depending on the hardware interfaces with quench protection system, power converters and energy extraction. Two variables define whether a failure in the powering will lead to a beam dump and an abort of the powering in the complete subsector. This information will be downloaded from the LHC Reference Database to the interlock controllers and to the supervision software. An example of such configuration data is shown here for three circuits of the inner triplet powering subsector right of IP1:

ID	CIRCUIT NAME	CONFIGURATION_TYPE	PAR_POWSUBOFF	PAR_BEAMDUMP
1	RQX.R1	A	1	1
2	RCBXH1.R1	B1	0	0
3	RCBXH2.R1	B1	0	0

.....etc...

The configuration file is generated taking into account the grouping of signals between the quench protection system and the power converters on one hand, and the powering interlock controllers on the other hand. The information in the LHC Reference Database includes detailed data about the location of quench detectors and power converters as well as the cabling between the three systems.

15.3.8 Supervision of the Powering Interlock System

Hardware commissioning of the LHC systems is expected to take about two years. During most of this time, the powering subsectors are independent and individual supervision of each powering subsector is required. The requirements for the supervision of powering interlock controllers for normal conducting magnets are less complex than those for the supervision of the controllers for superconducting magnets.

In order to operate with beam, all electrical circuits for magnet powering must be fully operational. Therefore the supervision system must combine the data from all powering interlock controllers and indicate if the magnet powering system is ready for beam. At this level, the supervision of the powering interlock controllers for normal conducting magnets and superconducting magnets will be combined.

The use of a commercial SCADA system is envisaged, motivated by the following operational and technical requirements:

- The powering interlock system is based on industrial PLC's.
- In total, 36 controllers for superconducting magnets and seven controllers for normal conducting magnets will be supervised using the same tool.
- From the point of view of its supervision, the system is rather complex.
- The time and safety critical control is done in the PLC software and the associated hardware.
- The required response time on the supervision level is in the order of one second.

The tool should be able to provide an interface to the PLC. Database support (ORACLE) and networking (Ethernet, PROFIBUS, etc) is required. The data from the powering interlock controllers will be integrated into the logging, alarm and post-mortem systems.

15.4 THE BEAM INTERLOCK SYSTEM

15.4.1 Beam Losses and Strategy for Beam Dumps

The most probable causes for beam losses are failures in the magnet powering system, with about 10000 magnets powered in 1612 electrical circuits with 1712 power converters. However, there could be many other types of failures [16, 17]. There could be also aperture restrictions, with two beams circulating through 53 km of beam vacuum pipe containing the beam screen, helium feedthroughs, interconnects, RF shielding etc., many vacuum valves and more than 100 collimator jaws could obstruct the beam passage.

The time after a failure at which particle losses become unacceptable was evaluated for many types of failures. This time depends on the failure and several other parameters such as energy, optics and collimator settings and falls into three categories [18]:

- One turn failures are ultra-fast losses due to a failure during injection or beam dump.
- Very fast losses in less than 5 ms.
- Fast losses in more than 5 ms.
- Steady losses are continuous losses, the lifetime is one second or more.

One turn failures could happen during injection and extraction. Protection relies on collimators and beam dilutors which must be correctly positioned with respect to the beam. The beam interlock system ensures that no beam can be injected if the collimators and dilutors are not correctly positioned.

Very fast losses: The failure of a D1 normal conducting bending magnet in IR1 and IR5 has been identified as the fastest mechanism for multi-turn failures [19]. The beam moves and could touch a collimator after a few turns. Another very fast beam loss is expected after a quench of a superconducting dipole magnet. In this case the beam is expected to touch collimator jaws after several 10's of turns. For failures causing very fast beam movements or emittance blow-up, the beam losses close to aperture limitations (collimators, beam dilutors, low-beta quadrupoles, etc.) are detected by beam loss monitors. The loss monitors request a beam dump if the beam loss exceeds a pre-defined threshold [20, 21]. It is also planned to detect rapid beam position changes. If beam orbit movements exceed a predefined value of say, ~0.2 mm/ms, the beams are dumped.

Fast Losses: Beam loss monitors around the machine and signals from equipment in case of hardware failure will be used to generate beam dump requests and complement fast beam loss and beam position monitors.

Steady losses: the beam losses and heat load at collimators will be monitored. A beam dump in case of unacceptable lifetime is also being considered.

15.4.2 Basic Functionality and Response Time

The beam interlock system provides beam permit flags for each beam. It receives status information from many "client systems" that can request the removal of the beam permit flags. Only if all systems indicate that they are ready for beam will the beam interlock system give beam permit. For example, in order to inject beam, the beam dumping system must be ready, all vacuum valves in the beam tube must be in the "open" position and magnets in the LHC and the transfer line must be powered, etc. The beam interlock controllers ensure that these conditions are met before giving beam permit. If the operation of the machine becomes unsafe and beam losses exceed the acceptable threshold or are imminent due to equipment failure, the beams have to be dumped as fast as possible. There is a minimum delay between such requests received by the beam interlock controller and the end of the beam dump [5]:

- The beam interlock system needs to inform the beam dumping system, which takes up to 50 μs if the signal travels half around the ring.
- The synchronisation of the extraction kicker with the particle free gap takes up to one revolution (89 μs).
- It takes about one turn from the start of the extraction to dump all bunches circulating in the LHC.

This determines the achievable response time of up to 270 μs between reception of a beam dump request by the beam interlock controller and the completion of a beam dump.

Systems that are critical for beam operation will always be in the interlock chain. It will be possible to disable some less critical input signals. A so-called "safe beam flag" will be derived from the circulating beam current and the energy and it will be distributed around the machine. If the stored energy in the beam is low and there is little risk of damage, the flag is set to logical one. A beam interlock controller receives the flag. Only when the safe beam flag is one (= safe beam), disabling of inputs is tolerated.

The beam interlock system provides monitoring of all inputs and outputs with precise time-stamps for post-mortem information. The accuracy of the time stamps should be about 1 μs.

15.4.3 Architecture of the Beam Interlock System

One beam interlock controller will be installed right of each IP, and one controller left of each IP. The beam interlock system therefore has 16 controllers. The controllers are connected by "beam permit loops" (one redundant loop for beam 1, and one redundant loop for beam 2). A high frequency signal (10 MHz) is transmitted across the loop. The presence of the signal indicates beam permit. If the signal is not present or has a different frequency, this means "no beam permit". If one of the controllers receives a dump request from a client system, it interrupts the loop. Both beam interlock controllers in the insertion with the beam dumping systems (IR6) receive the beam permit signal. When the loops are interrupted, the signal disappears. The two controllers detect the loss of signal, and instantaneously send hardware signals to extract the beam by the extraction kickers (Fig. 15.3).

The beam interlock system allows breaking of only one of the loops leading to a dump of only one beam. As an example, a failure during injection is considered: assume that the first ring has already been filled successfully and the second ring is partially filled. An attempt to inject a batch leads to unacceptable beam parameters for Beam 2. In this case it is sufficient to dump the beam in the second ring. Another example is an obstruction in the beam tube of one ring, when operation with beam in the other ring should still be possible.

Optical fibres will be used for the beam permit loops. Two signals run in clockwise and counter-clockwise direction for each beam. This ensures that the dump signal reaches the kickers as fast as possible, and adds redundancy to the beam interlock system. It is sufficient that one signal is missing in IR6 to dump the beams.

The optical links will only be used for the beam permit signal despite the available bandwidth, assuming that simplicity will lead to enhanced reliability

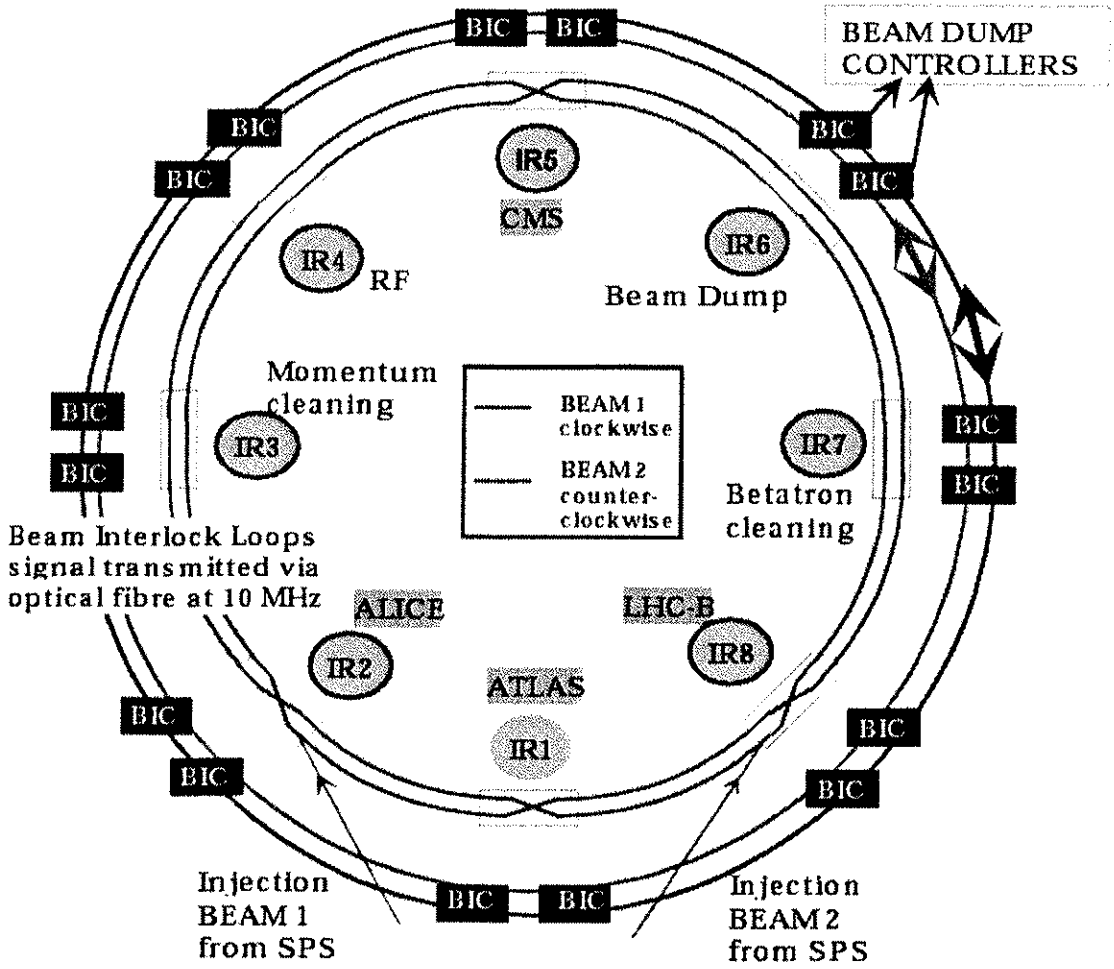

Figure 15.3: Architecture of the beam interlock system with its 16 beam interlock controllers

15.4.4 Beam Interlock Controller and its Interfaces

A beam interlock controller receives one signal from each of the following client system in the vicinity:

- Powering interlock controllers for superconducting magnets: each controller sends two signals to the beam interlock controller.
- Powering interlock controllers for normal conducting magnets: a failure of the normal conducting magnets in the insertions could occur due to overheating of the magnet or due to a failure of the power converter.
- Beam dumping system: If it is not ready, injection of beam is inhibited. In the presence of circulating beam, the beam dumping system is continuously monitored. If an equipment fault that could lead to a failure during the next extraction is detected, the beams are dumped immediately.
- LHC experiments: They can prevent beam injection and issue beam dump requests during operation. Injection is only possible if movable detectors (Roman pots, or the LHC-B Velo detector) are in the position far away from the beam centre. During physics operation (top energy, luminosity operation, with stable beams) experiments are authorised to move detectors closer to the beams.

- RF and transverse feedback: A signal to dump the beam is required from the RF system if debunching due to a failure is anticipated. The time constant for debunching is in the order of several 100 ms [22, 23]. A failure of the transverse damper might cause a beam loss within a very short time. Incorrect operation of the transverse feedback must trigger a beam dump.
- Beam loss monitors: There will be many beam loss monitors distributed around the ring close to each quadrupole, each with a response time in the order of one millisecond. Near the collimators and other aperture restrictions the BLMs will have a response time of less than 0.1 ms. The BLMs are the most important monitors for protection against damage from beam losses.
- Access safety system: The system for safety of personnel has to conform to legal requirements, independent of equipment protection considerations. There is a direct link from the access system to the beam dumping systems. For redundancy, the access status is also transmitted to the beam interlock system.
- Vacuum system: There will be many valves that could obstruct the beam passage. If a valve is in a position defined as "not open", beam permit cannot be given. The vacuum system will read the beam permit flags, and only close a valve if there is "no beam permit".
- Input from the beam dilutors and collimators: Collimators and beam dilutor must be in the correct position for each phase of the operation. Only if the conditions are correct will such devices give beam permit to the beam interlock system [24].

Each beam interlock controller knows the state of the beam permit loops: either no beam permit, or beam permit. The status of each beam permit loop (beam permit flags) will be provided for the client systems:

- The beam dumping system for each beam is one client and will receive the beam permit flag from both beam interlock controllers in IR6, for redundancy. If one of the signals disappears, the beam is extracted.
- Each injection kicker is a client. The kicker can only fire if the beam permit is granted.

15.4.5 Hardware Platform for the Beam Interlock Controller

VME was selected as hardware platform for the beam interlock controller because:

- The response time required of the order of some μs requires fast processing.
- VME is one of the standards supported at CERN.
- The connection to the control system is simple and supported by the Controls Group.

The VME crate will house several modules (see Fig. 15.4):

- A core module with the central logic for the decision on a beam permit. This will use a module made in-house with programmable logic that can easily be integrated in a VME crate. The interface via the VME bus allows reading of the status and recording the history of state changes. It allows disabling some of the inputs. In addition, the module includes an interface to the LHC timing system.
- The interface to the client modules. This module will also be used to simulate permission from clients during testing of the beam interlock system.
- The link of the controller to the other beam interlock controllers via the optical fibres.

The controller is connected to the control system via Ethernet for monitoring, setting the masks, testing and post mortem data. All input and output state changes and the time of occurrence are recorded and stored into memory.

15.4.6 Beam Interlock Client Interface

The beam interlock controllers are distributed around the LHC. The distance to the client systems is between several metres and several hundred metres. For each client, a "beam interlock interface" is provided to be installed in the client's rack (as a one unit, mountable, module). The client's system should provide a signal to this interface box using a TTL level (+5 Volt) or a PLC compatible level (+24 Volt). To be fail safe, the signal must always be present to get the beam permit. If the signal is lost, the beam permit loops will be broken by the corresponding controller and consequently the beams will be dumped.

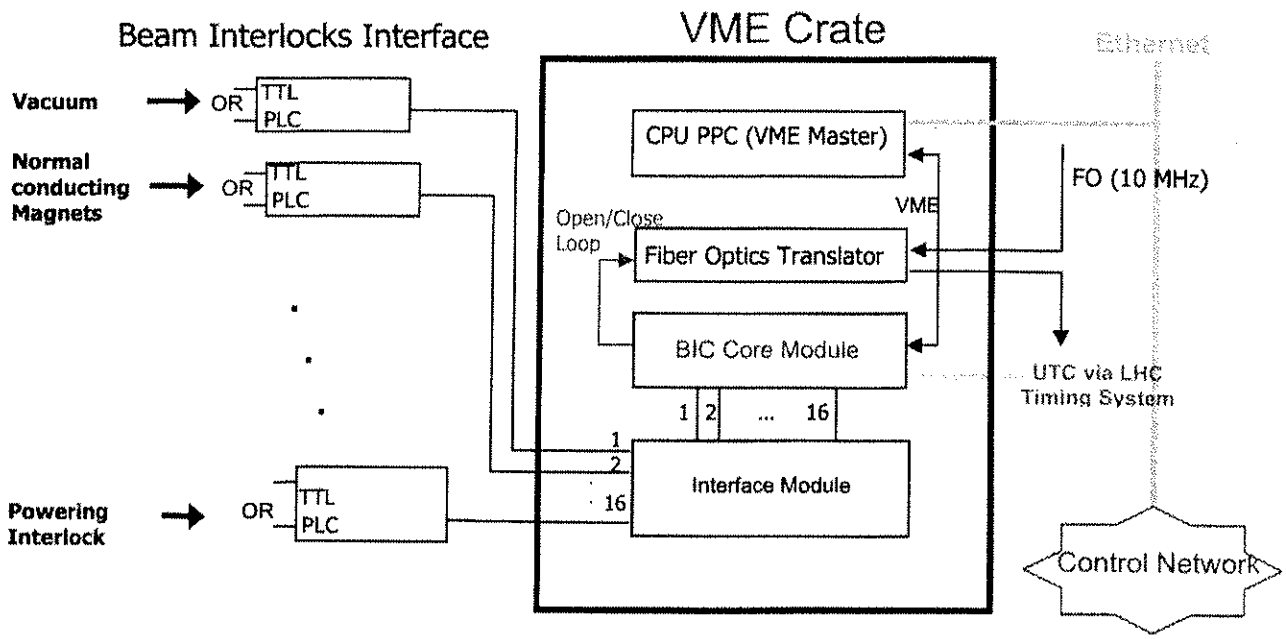

Figure 15.4: Architecture of the Beam Interlock Controller

As each beam interlock controller knows the state of the beam permit loops, the status of each beam permit loop (beam permit flags) will be provided for the client systems via this "beam interlock interface" box. The two status flags are delivered to the user via TTL signals and via PLC compatible signals.

In addition, the "beam interlock interface" box includes some internal self-test parts for remote use via the beam interlock controller.

15.4.7 Operation of the Beam Interlock System

Before injecting beam into the LHC, the beam interlock system must receive the beam permit from all client systems that are not disabled. When all clients give permission, the 10 MHz signal on the beam permit loop is established and only then beam can be transferred and injected into the LHC.

It is possible to close one of the two loops for each beam in test mode, by simulating a beam permit for each client system. In this mode the second loop will be forced to remain open, it is not possible to close both loops in this mode at the same time. This facilitates verification of the complete functioning of the beam interlock system without the risk of giving beam permit.

The efficiency of beam operation and the reliability of the protection systems can be improved using beam dump requests or power aborts via the controls system. Such requests can be disabled. If a soft abort is disabled or fails, there is always a second level of protection against damage by the machine interlock system. For example, if the cryogenic system signals that the temperature cannot be kept at the required level, the overall performance is improved by dumping the beam and discharging the circuit before a magnet quenches. This action will reduce the downtime. It is not required that the action is fail safe, since the quench protection system, beam loss monitor and the interlock system would trigger a beam dump and the discharge of the magnet energy.

15.4.8 Supervision of the Beam Interlock System

The most relevant information from the beam interlock system to be displayed in the control room is the status of the beam permit for each beam. The supervision for the beam interlock system will also read and display the status of all input signals from the clients for each beam interlock controller, as well as the output status.

The supervision system will allow disabling some of the channels. The status of the hardware will be displayed, showing, for example, which channels are disabled. All state changes and the associated time stamps that are recorded in the controllers will be read and archived via the supervision system.

The beam and powering interlock systems have different requirements and use different hardware platforms. The main operational and technical features of the beam interlock system that determine a proper supervision tool are:

- VME based.
- 16 beam interlock controllers.
- Hardware-based control + embedded real-time application.
- Faster than powering interlock controller (in the order of microseconds).
- Simplicity from the point of view of supervision.

The supervision system must provide the interface to the VME base beam interlock controllers, and to the LHC control system. The data from the beam interlock system will be integrated into the logging, alarm and post-mortem systems.

15.4.9 Injection Procedures and Interfaces to SPS

During operation with circulating beam, protection relies mainly on fast monitors to detect beam losses early and issue a beam dump request immediately if the losses exceed the acceptable level.

During injection of high intensity beam there is a risk that equipment in the LHC is not in the correct state. To avoid damage of equipment if there is no beam in the LHC, a procedure for injection has been defined [25]. Without beam, only beam with limited intensity ("pilot beam") can be injected. The pilot beam is used to verify that there are no obstructions and no magnet wrongly powered etc. The presence of beam in the LHC will be monitored by a beam current transformer. Only when beam is circulating, injection of beam with higher intensity is permitted. If the LHC requests beam with high intensity in the presence of circulating beam, it is still possible that the beam is lost before injection. In this case the beam current transformer will indicate that no beam circulates, and veto injection of high intensity beam. Injection must restart with low intensity beam.

15.5 RELIABILITY ISSUES

The correct functioning of powering and beam interlock systems is essential to avoid damage of machine equipment. As such they have to be designed as highly reliable and fail safe systems.

15.5.1 Powering Interlock System

Current loops are used to connect the quench protection system, the power converter and the powering interlock controller. If one system opens the loop, the two other systems detect the loss of current, and react accordingly. Fail safe logic is used for the transmission of signals. A faulty system or a cable that is not connected is detected and will result in a fast abort of powering and discharge of the magnet energy. After a complete failure of the PLC used for the powering interlock controller, the equipment would still be protected. The functionality of a power abort in the complete subsector after a quench in a major circuit would be lost, but this is acceptable. The assessment of the Safety Integrity Level (SIL) of the powering interlock system is planned.

15.5.2 Beam Interlock System

Beam dump requests will be transmitted via the beam interlock system that must have a similar Safety Integrity Level (SIL) to the beam dumping system. The beam dumping system requires SIL 3 (see Chap. 17).

The beam interlock system is therefore designed in a redundant way. Each client will provide the signal for beam dump requests via a fail safe interface. The beam interlock system provides two independent paths for a dump request including two beam permit loops for each beam. Redundancy is provided for the reception of a beam dump request issued by a client to the beam dumping system.

For most type of failures that have been considered, several beam dump requests will reach the beam interlock system. It is likely that the requests will arrive at several beam interlock controllers. As an example, a quench of a superconducting dipole magnet is considered:

- The beam will be deflected due to the decreasing magnetic field in the magnet. The tail of the beam distribution will touch one of the collimators after several 10 turns. The beam loss monitor close to the collimator will issue a beam dump request.
- Assume that due to an equipment failure the dump request from the first beam loss monitor is not transmitted to the beam dumping system. The beam would move further out and touch another collimator or an aperture limit and another beam loss monitor would request a beam dump.
- The quench protection system will inform the powering interlock system about the quench. The powering interlock system will abort powering in the powering subsector with the quenched magnet and request a beam dump via the beam interlock system.

Several other ideas are being studied to better protect LHC equipment from damage due to beam losses:

- Fast beam position changes could be detected by several beam position monitors covering the horizontal and the vertical plane, installed with a phase advance of 90°. For two rings and two planes, eight of such monitors are required.
- For the D1 normal conducting magnet, the time between detection of a loss of 10^9 protons and about 10^{12} protons hitting the collimator is in the order of 6-10 turns (less than one ms). This time could be increased by about a factor of three by installing industrial superconducting solenoid magnets in series with the normal conducting D1 magnets.
- Several techniques for a fast detection (in the ms range or even below) of a changing magnetic field in the normal conducting D1 magnets are being considered.

For a safe beam operation all systems for machine protection need to operate properly. The Safety Integrity Level for all these systems functioning together will be assessed. After such assessment, a decision will be taken if an improvement of the reliability of the protection systems is required.

REFERENCES

[1] F. Bordry et al., "Machine Protection for the LHC: Architecture of the Beam and Powering Interlock System", CERN-LHC Project Report 521, December 2001

[2] E. Ciapala, F. Rodriguez Mateos, R. Schmidt, J. Wenninger, "The LHC Post-mortem System", CERN-LHC Project Note 303; 15 Oct 2002

[3] E. Cennini, G. Roy, "The LHC Access Control System", LHC-Y-ES-0006 v.0.3, EDMS Doc. 386759

[4] F. Balda, E. Cennini, "Système de Sûreté d'Accès du LHC", LHC-Y-ES-0005 v.1.0, EDMS Doc. 362437

[5] B. Puccio, "Interlock channels and their timescales", Proc. Chamonix XII, CERN-AB-2003-008 ADM

[6] B. Puccio, R. Schmidt, "Powering Subsectors", LHC-D-ES-0002 v.1.0, EDMS Doc. 361532

[7] B. Puccio, R. Schmidt, M.Zerlauth, "The Hardware Interfaces Between Powering Interlock System, Power Converters and Quench Protection System", LHC-D-ES-0003 v.0.5

[8] J.Gomez, J.Pedersen, "Underground Uninterrupted Power Supply (UPS) for the LHC", LHC-EO-ES-0001 v.1.0, EDMS Doc. 356521

[9] K.H. Mess, P. Proudlock, "General Emergency Stop Policy for the Underground Areas of the LHC Machine", LHC-SU-ES-0001 v.1.0., EDMS Doc. 361856

[10] R. Rausch, C. Pignard, T. Wijnands, "Qualification of electronic components and systems in a LHC Tunnel Radiation Environment", CERN-SL-2002-025-CO; May 2002

[11] R. Schmidt et al., "Protection of the Superconducting Corrector Magnets for the LHC", CERN-LHC Project Report 419, Geneva, CERN, September 2000

[12] M. Zerlauth, A. Jimeno, G. Morpurgo, R. Schmidt, "The Electrical Circuit Description for the LHC", Proc. EPAC'02, La Vilette, Paris, 3-7 June 2002

[13] A. Jimeno-Yepes, M. Zerlauth, "Electrical Circuit Elements in the LHC Reference Database", LHC-LD-ES-0001 v.1.0

[14] A. Jimeno-Yepes, M. Zerlauth, "Interfaces between the Circuit Description and the LHC Reference Database", LHC-LD-ES-0002-10-00

[15] M. Zerlauth, A. Garcia Lopez, "Using the Description of Electrical Circuits in the LHC Reference Database as the Input for the Generation of the Mad Input File", LHC-D-ES-0004 v.0.2, EDMS Doc. 395088

[16] R. Schmidt, "How can we lose the beam? Beam loss scenarios and strategies for the design of the protection systems", Proc. Chamonix XII, CERN-AB-2003-008 ADM

[17] R. Schmidt, V. Kain, "Equipment failures and Beam Losses in the LHC", Proc. EPAC 2002, Paris, June 2002

[18] R. Schmidt et al., "Beam Loss Scenarios and Strategies for Machine Protection at the LHC", 29th ICFA Advanced Beam Dynamics Workshop on Beam-Halo Dynamics, Diagnostics and Collimation, Montauk, Long Island, New York , 19 - 23 May 2003 and CERN-LHC Project Report 665, 2003

[19] V. Kain, "Power converter failure of the normal conducting D1 magnets at experimental insertions IR1 and IR5", LHC Project Note 322, September 2003

[20] B. Jeanneret, H. Burkhardt, "Measurement of the Beam Losses in the LHC Rings", LHC-BLM-ES-0001 v.1.1, EDMS Doc. 328146

[21] B. Dehning, "Beam Instrumentation for Machine Protection", Proc. Chamonix XII, CERN-AB-2003-008 ADM

[22] E. Shaposhnikova, "Abort gap cleaning and RF system", Proc. Chamonix XII, CERN-AB-2003-008 ADM

[23] J.B. Jeanneret et al., "Beam loss and collimation at LHC", 29th ICFA Advanced Beam Dynamics Workshop on Beam-Halo Dynamics, Diagnostics and Collimation, Montauk, Long Island, New York , 19 - 23 May 2003, and CERN-LHC Project Report 663, 2003

[24] R. Assmann et al., "Designing and Building a Collimation System for the High-Intensity LHC Beam", CERN-LHC Project Report 640, CERN, June 2003

[25] R. Schmidt, J. Wenninger, "LHC Injection Scenarios", LHC Project Note 287, CERN, March 2002

CHAPTER 16

INJECTION SYSTEM

16.1 OVERVIEW AND MAIN PARAMETERS

16.1.1 Introduction

Injection into LHC is performed in the combined experimental and injection insertions IR2 and IR8. The transfer line TI 2 brings the beam to a point ~150 m left of IP2 for injection into Ring 1 and TI 8 delivers the beam ~160 m right of IP8 for injection into Ring 2, as this IP is displaced 11.22 m from the injection point. The transfer lines with the injections are described in more detail in [1].

A schematic layout of the injection region near IP8 is given in Fig. 16.1. In both insertions the beam approaches the LHC from outside and below the machine plane. The beam is directed by a last series of dipoles, already located in the LHC tunnel, towards a series of five Lambertson type septum magnets which deflect the beam horizontally by 12 mrad under the outer ring. A series of four MKI kicker magnets deflects the beam vertically by 0.85 mrad onto the orbit. In order to allow a proper injection setup with pilot bunches and to protect the LHC in case of malfunctioning of the injection kickers, an injection beam stopper, TDI, is placed 15 m upstream of the superconducting recombination dipole D1, supplemented by an additional shielding element, TCDD, 3 m upstream of D1. The protection against injection errors is further complemented by two collimators, TCLI, near the superconducting quadrupole Q6 on the other side of the insertion.

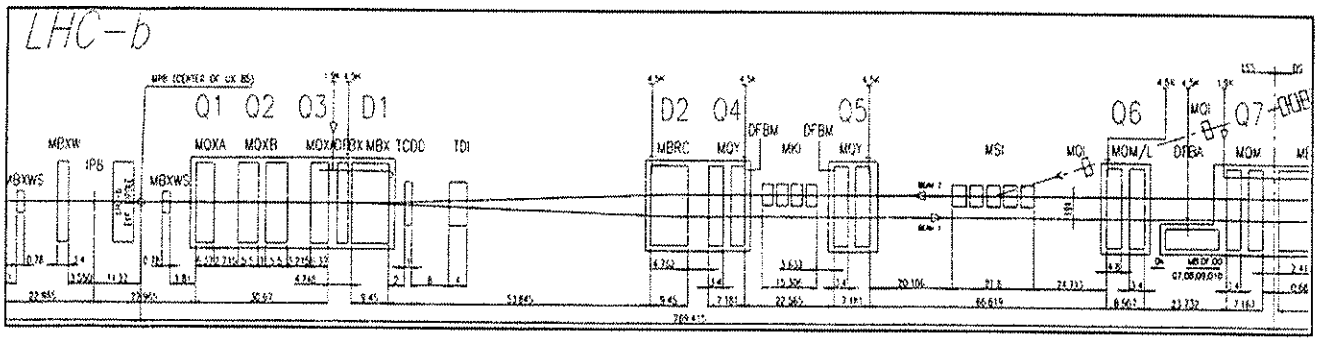

Figure 16.1: Schematic layout of the injection region right of IP8

The geometrical layout and arrangement of MSI, MKI and TDI/TCDD among each other and, within a few mm, also with respect to the adjacent machine elements is identical for both injections. However, despite being based on the same design criteria, the optics varies between IR2 and IR8 due to the displaced interaction point in IR8. The vertically defocusing quadrupole Q5 between the MSI and the MKI provides, through its kick enhancement, about one quarter of the required total vertical deflection. It should be noted that, although this is not apparent in the schematic layout above, the size of the Q6 cryostat is reduced to leave space for beam to be injected. The precision of the injected beam's position with respect to the LHC closed orbit is specified to be less than $\pm 1.5\sigma$, including SPS closed orbit errors at extraction, ripple and drifts of power supplies and injection kicker ripple. Further parameters can be found in the descriptions of the individual components.

16.1.2 Scope and Chapter Organisation

Each of the following sections is devoted to a major injection specific equipment, following the order seen by the beam to be injected – septa, kickers, and stoppers. This is followed by a discussion of the injection related beam instrumentation. A further section discusses the relations between the injection and other machine systems and the requirements put upon them. The description of general accelerator-wide systems or services like vacuum is restricted to the extent that a sufficient degree of self-containment for the

component under consideration is produced; for a more in-depth treatment the reader is referred to the relevant chapters. A discussion of the auxiliary injection collimators, TCLI, can be found in the chapter describing the collimation system. The transfer lines collimators, TCDI, are only briefly mentioned as to their protection function for the injection septa. Even though their main role is to protect LHC elements against beam arriving with too large transverse or angular offsets, the main discussion about them is deferred, owing to their physical location, to the chapter describing the injection transfer lines.

16.2 INJECTION SEPTA

16.2.1 Machine Layout and Main Parameters

Five septum magnets (MSI) of two different types (MSIA and MSIB) deflect the beam to be injected horizontally by 12 mrad under the outer ring. For injection into Ring 1 the septa are located in RA23 between Q6 and Q5, and similar for Ring 2 in RA87. MSIA and MSIB magnets differ in the septum thickness (the distance of the holes for the circulating beams from the pole) and the coil configuration and, consequently, the field in the gap. In the direction of the beam to be injected three MSIB magnets are followed by two MSIA magnets and including the inter-magnet gaps, the whole system stretches over 21.8 m. The main parameters of the injection septum magnets are given in Tab. 16.1.

Table 16.1: Main parameters of the injection septum magnets

	MSIA	**MSIB**	
Septum core length	4000	4000	mm
Coil core length	3650	3650	mm
Core width	734	734	mm
Core height	529	529	mm
Gap height	25	25	mm
Septum thickness	6	15.5	mm
Number of coil turns	16	24	-
Number of coil layers	4	6	-
Number of turns per layer	4	4	-
Electrical coil resistance at 20 °C	10.9	16.4	mΩ
Inductance	10.2	23.7	mH
Dissipated power	10.6	15.9	kW
Water flow per coil	7.9	11.8	l/min
Coil pressure drop	5	5	bar
Design current	950	950	A
Nominal magnetic field in the gap	0.76	1.13	T
Magnet weight	9800	9900	kg

16.2.2 Magnet Design

The magnets were designed and built in a collaboration between CERN and the Institute for High Energy Physics (IHEP) in Protvino, in the framework of the contribution of the Russian Federation to LHC [2, 3]. A view of the connection front face of both magnets is given in Fig. 16.2 and Fig. 16.3 shows a side view.

The laminations are punched from 1.0 mm thick steel sheets with a 10 μm thick Fe_3O_4 layer as electrical insulation. The magnet yokes are an all-welded construction and are assembled from different half cores, the so-called septum core and the coil core. The septum core comprises circular holes for the circulating beams, thus avoiding the need for the careful alignment of the usually wedge-shaped septum blades used in classical Lambertson magnets. The septum core is longer than the coil core to reduce the stray field extending from the field gap to the circulating beam holes. The coil core holds the single pancake coil.

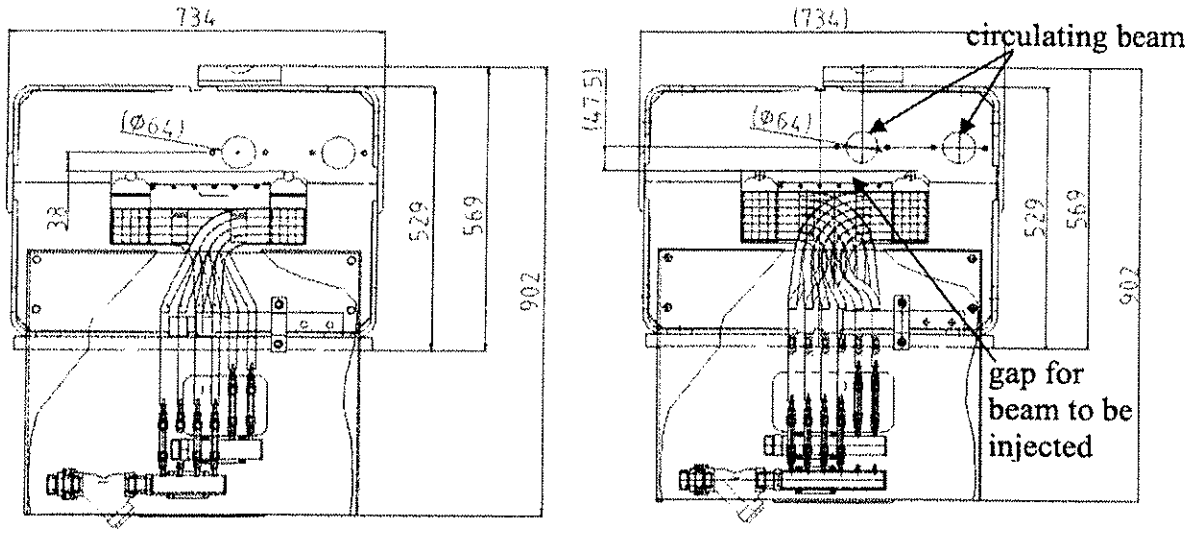

Figure 16.2: MSIA (left) and MSIB (right) connection front face view

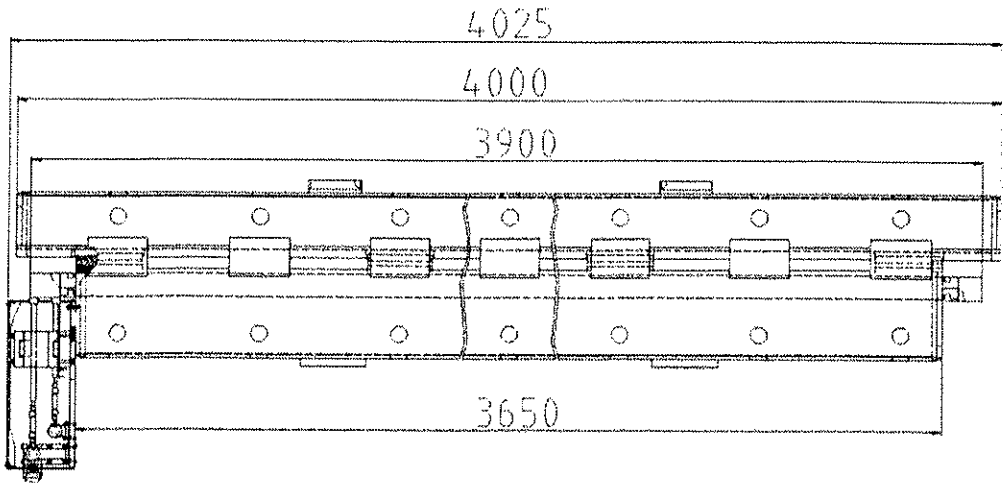

Figure 16.3: MSI side view

The coils are made from a 15 mm wide OFHC square copper conductor with a circular cooling hole of ≈ 4.5 mm diameter, insulated with glass fibre tape and impregnated using a radiation resistant resin. Each coil water outlet carries a thermo-switch to prevent overheating of the coil by switching off the MSI power converter if there is a defect in the cooling circuit. The trip temperature on the switch is 65°C and control is made through the magnet surveillance system,

16.2.3 Vacuum System

The vacuum system of the MSI magnets has to fulfil several stringent requirements. The beam holes in the septum cores have a diameter of 64 mm. The mechanical vacuum system tolerances including their alignment and the alignment of the magnet in general, must be such as not to reduce the available aperture significantly. The circulating beam must be shielded against the stray field leaking from the core into the septum holes, with a measured dipole component of the order of 10 Gauss [4]. The vacuum chambers for the circulating beams should be bakeable to 250°C in situ without heating the magnet yokes to more than 120°C. The combination of all constraints like the beam hole diameter, alignment tolerances, magnet tilt angle, aperture requirements and the need for bake-out led to the choice of a mumetal chamber with an inner diameter of 56 mm and a wall thickness of 0.9 mm [5]. The stray field remaining for the smaller chamber which had been envisaged before was calculated to be of the order of 0.1 Gauss [6].

To reduce the outgassing rate of the chambers to meet the ultra high vacuum requirements, a bake-out at 250 °C using special heaters [7] for at least 24 hours is made [8]. These heaters comprise three layers: a stainless steel heating strip in the centre surrounded by two insulating polyimide films. Wrapped around the chamber the total thickness of such a heater is 0.3 mm. A reflective aluminised polyimide film is wrapped on top of the heater sandwich. Special thermal insulation precautions have been taken to reduce the heat load on the magnet yoke, keeping its maximum temperature below 120 °C.

The inner surface of the chambers is copper coated using electrochemical deposition with a fluid circulation technique which is required due to the length of the tubes (~5 metres). A current delivered by a pulsed power supply is transmitted into the electrolyte through a copper electrode surrounded by a platinum coated titanium grid. The tube is placed in a vertical position to avoid bending problems and a pump drives the electrolyte through the mumetal tube [9]. Preliminary tests demonstrate that a copper thickness of 0.5 mm can be achieved with good resistive characteristics [10] (values of up to 0.85 mm have been obtained). For aperture reasons a baseline thickness of 0.4 mm was chosen [11]. Finally, the circulating chambers are NEG (Ti-Zr-V Non Evaporable Getter) coated to improve the pressure and thus the background for the experiments and to avoid electron cloud build up.

Both ends of the chambers for the circulating beams are fitted with DN200CF flanges (316LN) which are welded after insertion of the chamber in the magnet. The chambers are centred in the septum holes using one stainless steel ring (304L) in two parts, spot welded in the centre. This not fully penetrating spot weld must be made before the copper deposition to avoid the destruction of the copper layer during the welding and to allow the recovery of the magnetic properties by the high temperature thermal treatment (1050°C). Further centring is obtained through two other stainless steel rings (304L) mounted at the ends of the chambers. These three rings, welded on each chamber, must pass through the magnet hole. Two copper coated (0.4 mm) extensions in 316L and are welded at each end of the mumetal chamber to allow the welding of the temporary and the final flanges. The manufacturing tolerances of the mumetal tubes could lead to unacceptable gaps between the tubes and the apertures machined in the flanges. To keep the assembly gap constant and thus to preserve the reliability of the welds between the mumetal and the flanges, the tube ends will be recalibrated (plastically deformed by inserting a high precision machined profile).

The chambers of the beam to be injected are made from 304L stainless steel with an inner diameter of 22 mm and a wall thickness of 1 mm. Mounting is achieved by special form pieces along the gap and welded strips at the ends. The chambers are baked at 85°C for 24 hours to minimise the outgassing onto the circulating beams' NEG coated chambers. The bake-out is performed using the special sandwich heaters developed for the circulating chambers.

A special 300 mm long modular pumping port equipped with a 60 l/s pumping speed ion pump is fitted in the 450 mm inter-magnet gap. All inter-magnet gaps will be equipped with pumping ports to provide the required differential pumping between the chambers for the circulating beams in the order of 10^{-10} mbar and the chambers for the beam to be injected of the order of 10^{-7} mbar, while permitting a reasonably fast exchange of a magnet in case of failure. However, the pumping port configurations are specific to each inter-magnet gap so that the spare magnet could only be equipped after identifying the faulty magnet.

Prototypes fulfilling all requirements mentioned above have been made at CERN and a Functional Specification has been written for the series production [12].

16.2.4 Aperture and Alignment Issues

The effective apertures in the septa are determined by the vacuum chambers, the magnet alignment, the beam sizes and orbit offsets in these locations. To optimise the available aperture without making the vacuum design too magnet specific, the magnets will be tilted with respect to the machine plane and the MSIA and MSIB groups precision aligned with different chamber axis offsets. A qualitative plot of the vertical beam trajectory and the beam envelope, showing the two groups of septa (MSIA left and MSIB right), is shown for the circulating and injected beams in IR2 in Fig. 16.4. For the circulating beam a $9.8\sigma_y$ beam envelope is shown, including 21% beta beating, 27% parasitic dispersion, ±4 mm orbit error and ±2 mm mechanical and alignment tolerance (the mechanical tolerances of the chamber are treated as effective position errors of the beam) . For the injected beam, a $5\sigma_y$ beam size is plotted, including 21% beating and ±1.5 mm mechanical and alignment tolerance.

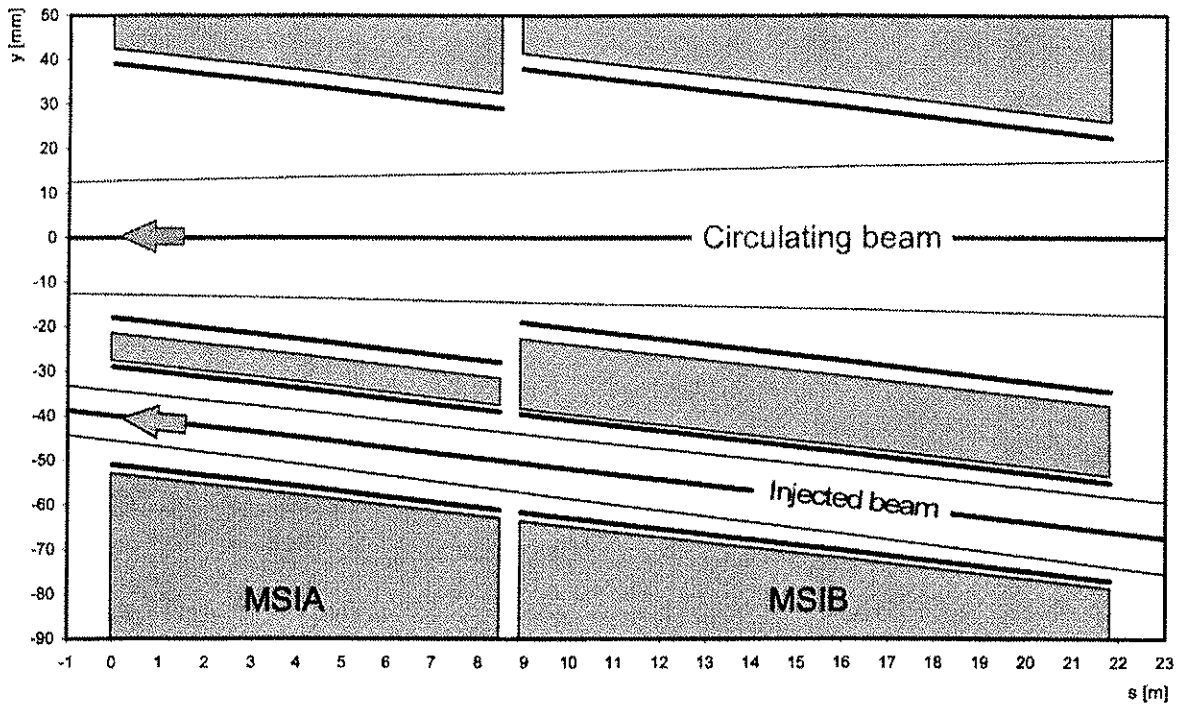

Figure 16.4: Vertical beam trajectory and envelope through the injection septa in IR2

16.2.5 Protection

The last TCDI collimator in each transfer line will be placed just upstream of the first injection septum magnet in order to protect the septa against misdirected beam [13, 14]. Together with the other transfer line collimators it will also protect elements further downstream in the LHC. It will probably consist of a fixed graphite mask of about 3 m length and 5 – 6 σ aperture. The detailed design has not been finalised at the time of writing.

16.2.6 Powering and Control

The MSIA and MSIB septa of one injection line are powered in series using a 1000 A, 200 V power converter, with a nominal current of 950 A. The current precision required ($\Delta I/I_{nom}$) is $\pm 1 \times 10^{-4}$ with an interlock level set at around $\pm 5 \times 10^{-3}$ to prevent damage to the LHC in the event of a converter trip prior to the SPS extraction. The septa will be slowly pulsed for each injection with a rise time of several hundred ms and a similar length flat top. A digital controller (Function Generator Controller, FGC), as used for other LHC magnets, controls and supervises the converter. In the event of a trip or instability prior to injection, the present response time of 5 ms of the surveillance system means that the maximum possible orbit deviation will be ~6 - 7σ in the horizontal plane, which is at the limit of causing problems for the LHC collimation system. It may be necessary to reduce this figure by upgrading the surveillance system for these converters.

16.3 INJECTION KICKERS

16.3.1 Overview and Machine Layout

The injection kicker system (MKI) comprises four fast pulsed magnets per injection. The magnets are housed in a separate vacuum tank comprising both beam pipes which has been recuperated from the LEP separators. For injection into Ring 1 the magnets are located in RA23 between Q5 and Q4, for Ring 2 injection in RA87. The pulse generators and part of the power and control electronics are located in the adjacent underground gallery, UA23 in for IR2 and UA87 for IR8. The transmission cables pass through two existing holes previously used for wave-guides. Fig. 16.5 gives the layout (plan view) around the LHC injection kickers in IR8 and Fig. 16.6 a cross section.

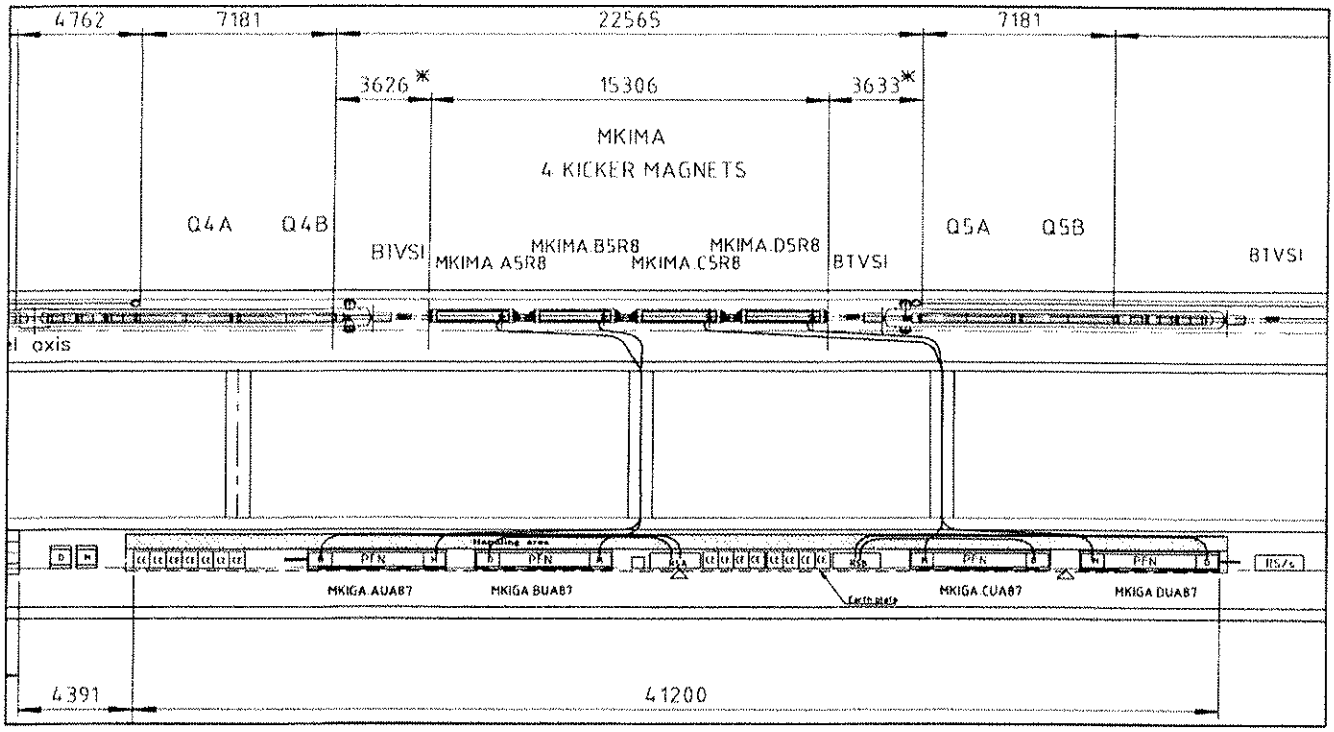

Figure 16.5: Injection kicker layout right of IP8 (plan view)

16.3.2 Main Requirements and Parameters

The beam to be injected approaches the kicker system from below at an angle of 0.85 mrad, requiring a total integrated dipole field of 1.2 Tm for deflection onto the central machine orbit. To limit the emittance blow-up at injection, reflections and flat top ripple of the field pulse must stay below ± 0.5% – a very stringent requirement. The pulse repetition time is imposed by the SPS acceleration cycle, 18 s in case of 3-train extraction. The LHC will be filled with 12 batches of 5.84 μs or 7.86 μs duration, to be deposited successively on the machine circumference, with 11 gaps of 0.94 μs in between them to account for the injection kicker rise time. One final gap of 3.0 μs accounts for the fall time of the injection kickers and allows also for the rise time of the beam dumping kickers. The main parameters are summarised in Tab. 16.2.

Table 16.2: Main MKI system parameters

Item	Value	Unit
Number of magnets per system	4	-
System deflection angle (4 magnets)	0.85	mrad
$\int B\,dl$	0.325	Tm
Magnet beam aperture (diameter)	38	mm
Characteristic impedance	5	Ω
Operating charging voltage (PFN)	54	kV
Field flat top ripple	< ± 0.5	%
Field flat top duration	up to 7.86	μs
Field rise time 0.5 %-99.5 %	0.9	μs
Field fall time 99.5 %-0.5 %	3.0	μs
Yoke length	2.650	mm
Magnet length (mechanical)	3.400	mm

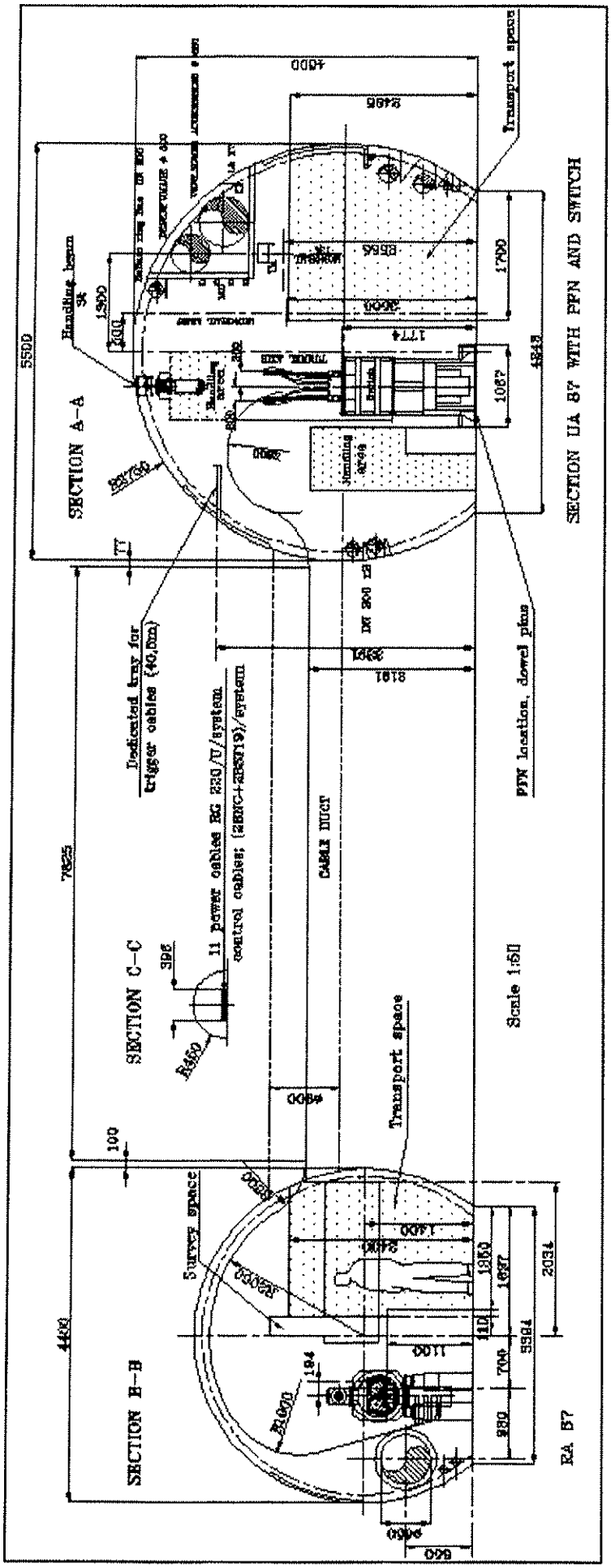

Figure 16.6: Cross section of tunnel section RA87 and underground gallery UA87 around the MKI

16.3.3 Equipment Description

Overview

The schematic circuit diagram of the injection kickers is given in Fig. 16.7. Each magnet is powered by a separate pulse-forming network (PFN). Two PFNs are charged simultaneously from one resonant charging power supply (RCPS). To be able to vary the pulse duration a main switch (MS) and a dump switch (DS) are needed, one at either end of the PFN. A carefully matched high bandwidth system is necessary to fulfil the stringent pulse response requirements. The system is therefore composed of a multi-cell PFN and a multi-cell travelling wave kicker magnet, connected by a matched transmission line and terminated by a matched resistor [15]. To achieve the required kick strength a low characteristic impedance of 5 Ω was chosen.

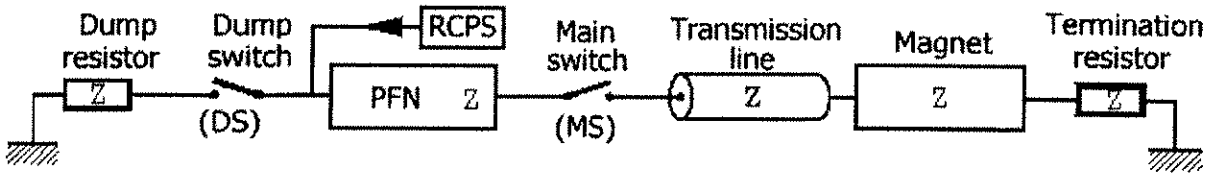

Figure 16.7: Schematic circuit diagram

The design voltage is 60 kV, as in most SPS kicker installations, allowing the use of several proven components such as transmission lines, connectors and termination resistors. The voltage on the magnet is half of the PFN voltage - allowing for overshoot, the design voltage of the magnet is 35 kV. The major components are discussed below in more detail.

Magnet

Each kicker magnet consists of a series of 33 cells: a compromise between bandwidth and cost. Fig. 16.8 shows a cross section of one magnet cell, with matching capacitors mounted between a high voltage and a ground plate. The plates are spaced by three ceramic-metal insulators, which together form an independent cell assembly. To achieve a characteristic impedance of 5 Ω within the space constraint of the 540 mm diameter tanks, two ceramic plate capacitors with 210 mm diameter each and contoured rims have been used leading to a nominal self-inductance and capacitance per cell of 101 nH and 4.04 nF, respectively, including the plate end effect.

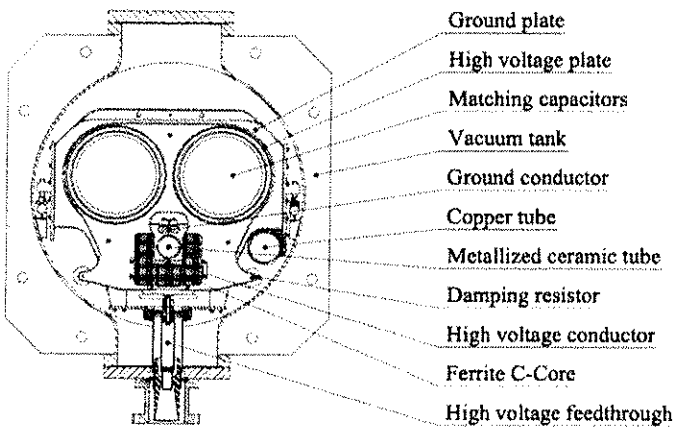

Figure 16.8: MKI magnet cross section

For stability reasons the capacitors are made of a monolithic class 1 ceramic with relative permittivity of about 75. The electrodes are formed by painted and then baked silver layers. In order to avoid surface flash-over problems and to achieve reliable operation at full voltage, the voltage holding capabilities have been

extensively studied using finite element computer codes to simulate the geometry of the transition between the connecting plates and the capacitors. The critical electrical contact is ensured by toroidal spring contacts all around the capacitor rims and an accurate rim geometry. Careful design of the mechanical components (distances and radii) was needed to maintain the electrical fields below 5 MV/m. Deflectors have been added to eliminate the electrical field at the triple junction. High voltage and ground plates have been electro-polished.

The viability of using ceramic capacitors in ultra high vacuum has been demonstrated through outgassing tests. Good vacuum quality of some 10^{-10} mbar in operation is ensured by bake-out at 300°C, vacuum firing and heat treatment in air on most of the parts of the magnet. To be bakeable the magnet has been made of stainless steel, aluminium being unsuitable for such temperature cycles. Low inductance damping resistors have been connected in parallel with the cells. They have been specially developed for UHV compatibility and consist of two counter-wound Kanthal® wires on a ceramic rod.

In order to reduce beam impedance while allowing a fast field rise time, the beam passes through a ceramic pipe with silver stripes on its inner wall. The stripes provide a path for the image current and screen the ferrite yoke against beam induced heating [16]. The stripes are directly connected to the standard vacuum chambers of the machine at one end and via a decoupling capacitor of 300 pF at the other, using the ceramic pipe itself as dielectric. The pipe is made from a 3 m long extruded ceramic tube with a wall thickness of 4 mm. The stripes are produced using a photochemical technique similar to printed circuit boards but complicated by the difficult access to the inside of the tube. Two layers of silver paint are first applied uniformly inside with bake-out at 800°C after each layer. A mask is then held against the inner wall by vacuum while UV light is passed through the pipe. The 200 mm of the tube which extends outside the magnet has its is outer surface uniformly painted silver and the inner surface has the stripes, thus giving the required capacitance between each stripe and the outer layer. The latter is connected to the metallic beam tube of the machine. The other beam traverses the vacuum tank inside a copper chamber.

The ferrite cores are made from high permeability and high resistivity NiZn type, 8C11 grade, and have a C-configuration to allow earthing of the coaxial HV cable input connection and the output connection to the terminating resistor [17]. In addition to their magnetic properties which are specially adapted to this application, they exhibit very good vacuum performance after appropriate treatment [18].

Again, in order to obtain a fully bakeable design, the conductors are made from stainless steel. The shape of the ground conductor has been optimised in order to provide a homogeneous field without having to machine shims on the ferrites.

PFNs

PFN type generators are used to produce rectangular pulses with very low ripple. The top part of the current pulse in the prototype magnet is shown in Fig. 16.9.

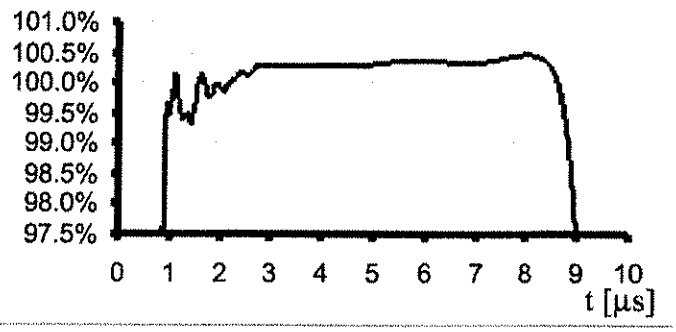

Figure 16.9: MKI prototype current pulse shape (top part)

Since experience had shown that adjusting individual inductances of a PFN would not lead to a flat top ripple smaller than about ± 1 % [19] the inductances are wound as a continuous straight and rigid coil with constant and high precision pitch to guarantee the same self inductance and mutual coupling coefficient for

all cells. A characteristic impedance of 5 Ω with adequate frequency response requires cell inductances of less than 1 μH. As such small inductances cannot be built cost effectively with the required high precision, two networks of 10 Ω impedance are connected in parallel.

Conduction losses along the coil, resulting in droop of the top of the magnetic field pulse in the kicker magnet, are compensated for by grading the values of the capacitors such that they increase in value from the MS end to the DS end of the PFNs [20]. Component values leading to an acceptable field rise time, fall time, and ripple, have been chosen in an iterative way, using the PSpice optimiser [21]. In order to obtain a realistic transient response, most known parasitics were modelled in the simulation of the electric circuit as well as the voltage and frequency dependency of components. For optimum pulse response the component values of the end cells differ from those of the central cells.

The PFNs are housed in a metallic tank and insulated with silicone fluid. The capacitors are mounted vertically and in individual coaxial housings. The two straight and continuous copper coils are tightly wound around a threaded glass reinforced epoxy cylinder to ensure a precise and constant geometry along the coil. A series of holes through the cylinder allows connections to be made to the capacitors mounted below and in line with the coil. Each coil is shielded by a screen connected to the coaxial housing of the capacitors. The coils are connected in parallel, and then to the switches via a common coaxial "plug-in" feed-through.

HV Switches

Main and dump switches have been designed for minimum size and easy maintenance. They use three-gap thyratrons of types CX 2003 and CX 2503, installed in independent tanks with isolating transformers for heaters, reservoirs and grid biasing. These switches are mounted directly onto the PFN to save space and cost as in the SPS injection kicker installation [19]. The post-pulse period is only critical for the last of the 12 injection pulses. The DS is only required for this last pulse.

Transmission Lines

The pulse is transmitted from the PFNs to the magnets through 10 parallel RG220 type coaxial cables of 50 Ω impedance and 35 m total length each. The conductors are drawn from electrolytic copper and low density polyethylene of high purity is used as dielectric. The cable can be exposed to an integrated radiation dose of at least 10^6 Gy. Cable ends are terminated by moulded high voltage connectors as already in use in the SPS.

Matching Resistors

Both matching resistors are assembled from ceramic-carbon discs mounted in a low inductance coaxial housing and insulated with silicone fluid. This type of resistor is extensively used at CERN, but the adjustment to the required value and the resistance stability remain an issue for this very precise application.

Safety Aspects

To reduce the fire hazard, the transmission cables are flame retardant and free from halogens and sulphur in accord with CERN Safety Instruction IS23 and IEC Standard 332-3. The resonant charging power supplies, PFNs, switches and terminating resistors are insulated by a silicone fluid (dimethylsiloxane polymer) with high ignition point. Conventional smoke detection is installed in the pulse generator areas.

The whole circuit has been designed so that personnel cannot come into contact with high voltage. All components are contained in grounded metallic containers or racks. The disconnection of HV cables or opening of the containers is not possible without tools, and the rack doors are locked by key and equipped with micro switches fitted to disconnect the primary power supply and discharge all high voltage capacitors and other stored charges before allowing access. The x-rays produced during the operation of the thyratrons are shielded by their metal housing. Therefore, no access limitation is required during the tests and conditioning. Yellow flashlights, however, are installed in the tunnel and gallery and indicate when the system is operating.

Vacuum Issues

Each tank is equipped with two 400 l/s ion pumps and two 1000 l/s titanium sublimation pumps, all recovered from the LEP separators and re-installed using the previous layout. The tank will be baked up to 300 °C using the separator heating jackets.

Due to the overall size of the vacuum tank the other ring also passes through the tank and for impedance reasons this has to pass through a copper tube which has 60 mm inner diameter. NEG coating has been added for vacuum and electron cloud reasons. The ion pumping of this tube is ensured to a level of 40 l/s by the conductance at each end through RF fingers and to a level of 200 l/s by holes located at 1/3 and 2/3 of the tube for impedance reasons. The NEG coating will be activated during the bake-out of the tank at 300°C.

Each tank is equipped with a Pirani and two Bayard-Alpert gauges (SVT type); only one is cabled and the other serves as spare. The ion pumps also provide the vacuum interlock for the high voltage of the kicker generators by means of a hardwired signal from the pump power supply.

There are vacuum valves at each end of the group of four kicker magnets but no individual vacuum valves between each magnet for cost reasons. An intervention on one of the tanks therefore requires a new bake-out in situ of the whole set of magnets. This takes about 8 days, and must be followed by about four days of reconditioning.

Exploitation and Maintenance Issues

Regular maintenance will be focused on the thyratron switches. Their lifetime under the conditions of use in the LHC is estimated to between five and eight years. Regular adjustments will be required. Based on experience with the SPS injection kicker system and depending on the budget available for preventive maintenance, the expected down-time due to the MKI system should be of the order of 10 to 30 hours per year, not counting the time for access to the underground galleries.

Faults

Note that a more thorough discussion of injection kicker faults and their impact is contained in Sec. 16.4.1, with only some basic information given here for self-consistency.

Owing to their nature as gas tubes the thyratron switches are liable to possible self-firing ("erratic pulses") or not firing when required ("missing pulses"). Non firing of the kicker system can also occur when no RF prepulses are received. In this case the beam to be injected continues straight onto the injection beam stopper (TDI).

In the case of erratic firing of one kicker generator, all kickers are immediately triggered and then beam will be swept over the full deflection range with some 20 bunches escaping the TDI and propagating to the auxiliary injection collimators or the cleaning system [22]. This type of fault is expected to occur a few times per year. It should be noted that the PFNs are only charged 2 ms before injection in order to limit the time during which such errors can occur. After injection the kickers are switched off.

More severe consequences can result from a flash-over inside a kicker magnet, particularly if it occurs in some specific cells. In the worst case almost a full batch can just escape the TDI and end up on the cleaning collimators. From experience with the prototype magnet and several improvements introduced in the series this event is estimated to occur less than once per ten years of operation [23].

16.3.4 Control System

Overview

The kicker control system, schematically shown in Fig. 16.10, comprises three independent entities: one for the control of the equipment state (ON, OFF, STANDBY...), one for the control of the injection process (timing system and operational setting management) and one for the control of the fast signal acquisition and interlock logic (protection of the equipment and of the machine), each implemented in an appropriate technology.

The injection process is composed of two consecutive stages which are repeated for each injection. First a slow stage divided into two phases: a 1000 ms long charging phase of the primary capacitor bank followed

by a 2 ms long resonant charging phase for charging the PFNs with a pulse-to-pulse reproducibility of 0.1%. Then a fast stage of 10 μs duration for synchronisation of the timing system with the circulating and to-be-injected beams, triggering of the thyratron switches, discharging of the PFNs and generation of the magnetic pulse.

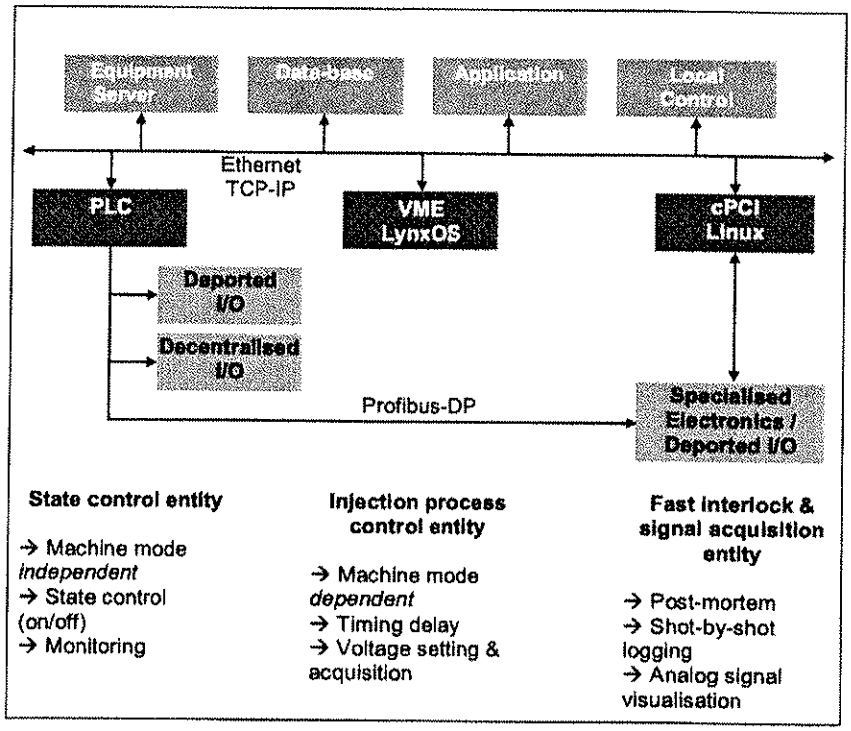

Figure 16.10: MKI control system architecture

State Control

The state control is based on a SIEMENS S7-400 master programmable logic controller (PLC), which is linked through two identical PROFIBUS-DP segments to the various equipment controllers (resonant charging power supply controller, thyratron heater controller, terminating resistor controller, pulse generator controller). They are connected either as deported I/Os or as decentralised I/Os when low-level intelligence is required. A third PROFIBUS-DP segment is used to interface to the resources common to the two generators of one injection, like electrical distribution and temperature measurements. The master PLC is connected to the Ethernet TCP/IP network for communication with the application layer. Modelling of the different controller functionalities at the master level is performed through dedicated functional software blocks. MKI state transition management and state acquisition are implemented through a finite state machine running in the master PLC level.

Injection Process Control

The injection process control consists of a LynxOS VME PowerPC front-end computer including four 1 ns resolution digital delay modules. These are used for trigger pulse generation in phase with injected and circulating beams and for fine timing adjustment, one 16 bit DAC/ADC module for kick strength settings and measurements and one standard LHC timing module (CTX1) for synchronisation with the machine timing. The management of the different operational settings during the injection process is based on a real-time task running in the front-end.

To ensure high reliability of the injection process, the thyratron triggering system is based on a fully redundant architecture up to the primary side of the thyratron trigger transformers. A comprehensive fast monitoring system supervises at each injection pulse the correct operation of the complete system and allows fault tracing on the various active elements (resonant charging system, thyratron erratic or missing pulses, magnet or transmission line sparks, terminating resistor open or short-circuit, timing synchronisation failure,

etc.). In addition, a pre-triggering system ionises the gas tubes 500 ns prior to injection in order to reduce the thyratron turn-on delay and to optimise the turn-on jitter.

Fast Interlock Control

The fast interlock logic, built from specialised electronics, continuously surveys all the critical parameters of the injection process and upon detection of a failure either inhibits the injection process or reduces the impact of the failure and inhibits further injections.

Equipment state failures occurring up to 2 ms before injection inhibit the charging process and the SPS extraction. In this case, beam is dumped in the SPS. If the failure occurs in the 2 ms window before injection, the charging process in progress will not be stopped but the LHC injection and SPS extraction be inhibited until the reason of the failure has been removed.

The injection process can be inhibited up to 250 ns before injection. It has to be noted that there is no possibility to stop the magnetic pulse rapidly once it has been started since the system is not equipped with clipper switches at present. The shortest magnetic pulse length is 3 μs, followed by a fall time of 3 μs.

Remote analogue visualisation of injection related waveforms is based on the OASIS system [24].

Exploitation and Maintenance Related Issues

All control electronics are located in the underground gallery near the pulse generators. Personnel making interventions have at their disposal a complete set of low level monitoring and diagnostic tools. These are available in the galleries, in the surface buildings and also remotely for a continuous surveillance of the whole installation. During machine operation, access to the galleries is required only in case of a hardware failure of an electronics module. All operational parameters, like timing settings, interlock thresholds, etc., are remotely controllable. Each intervention on the installation, e.g. a remote setting change, is logged. Control of critical parameters is password protected.

Preventive maintenance is limited to the verification and re-calibration of electronics modules and the replacement of electromechanical components like relays or fans.

16.4 INJECTION BEAM STOPPER AND SHIELDING

16.4.1 Injection Beam Stopper

Layout

The injection beam stopper (TDI) is used for injection setting-up and machine protection in case of a malfunction of the injection kickers. For maximum efficiency it is located ~70 m downstream of the injection kickers at a vertical phase advance $\mu_v = 90°$, 15 m upstream of the superconducting recombination dipole, D1. It is complemented in its protection function by the supplementary shielding device TCDD, described further below. The TDI is housed in a 5 m long vacuum tank recuperated from the LEP separators.

The active part of the TDI consists of two absorber jaws, ~4.2 m long, one above the beam and one below [25]. The upper jaw intercepts beam arriving from the transfer line which has not been sufficiently deflected by the injection kickers, the lower jaw receives circulating beam kicked away from the orbit. The jaws can move vertically in a range of ±2 - 60 mm from the nominal beam axis by means of two dc servo motors per jaw. The side view of the tank, including the motor assemblies, the ion pumps and the support feet, is given in Fig. 16.11.

Each jaw consists of a sequence of segments of absorbing materials mounted in an aluminium frame. Eighteen hexagonal boron nitride (hBN) blocks, each 157.7 mm long, are followed by one 600 mm long aluminium block and one 700 mm copper block. All segments have a cross section of 58 mm width and 54 mm height. The evacuation by conduction of heat deposited is eased by means of flexible copper strands between the jaws and the tank.

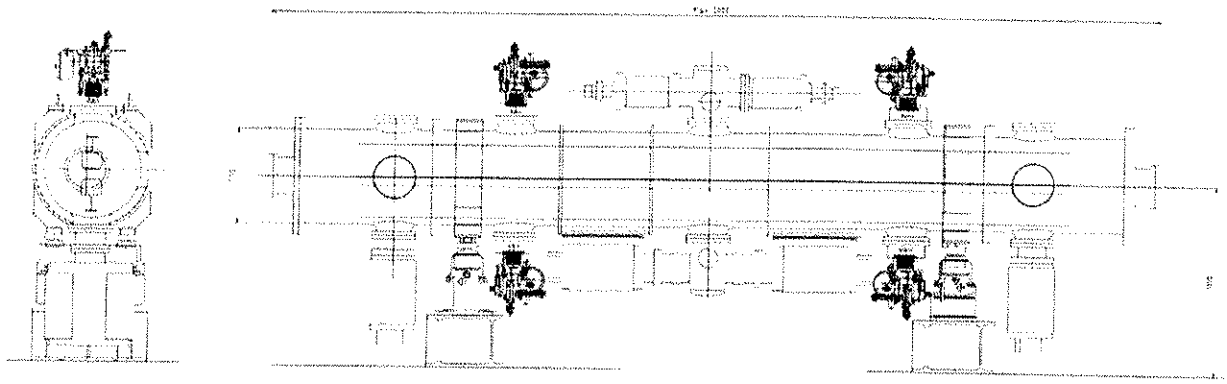

Figure 16.11: TDI cross section and side view

Mechanical Parameters

Table 16.3: Main mechanical TDI parameters

Item	Value	Unit
Tank length	5000	mm
Jaw stroke	± 2 - 60	mm
Jaw flatness	0.3	mm
Jaw position resolution and reproducibility	20	µm
Jaw speed	1	mm/s
Weight per jaw	200	kg

The drive mechanism entails a mechanical backlash of 70 µm. Jaw inclinations as high as 33 mrad are mechanically possible in case one motor is in the innermost position (2 mm from the nominal beam axis) and the other one fully retracted (at 60 mm), but the maximum operational range needs still to be defined.

Impedance Aspects

To reduce beam impedance the hBN blocks are coated with 3 µm of titanium and the aluminium block with 10 µm of copper, like the aluminium frame. To provide a path for the image current and mask off the tank cavity against the beam a complex-shaped 1.5 mm thick stainless steel (316LN) beam screen with 300 µm copper coating is located on each side of the jaws. This beam screen limits both the disturbance to the beam and the local heating caused by losses,

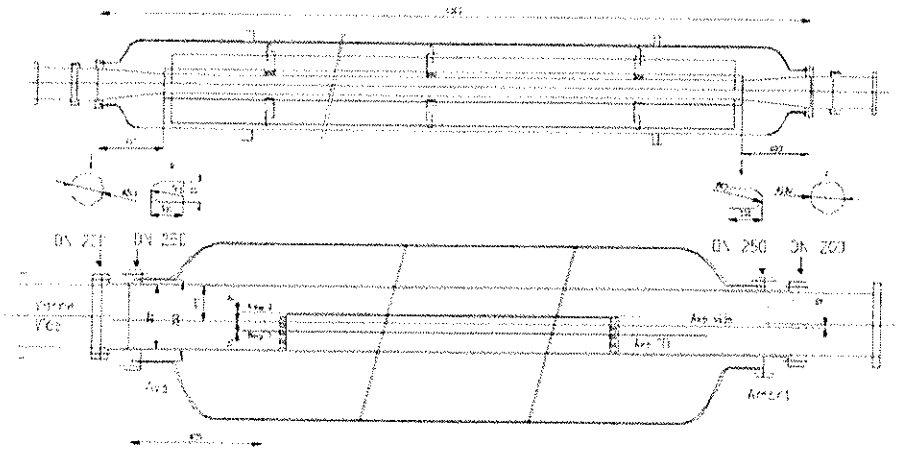

Figure 16.12: Schematic longitudinal cross-section of the TDI with beam screen

Cone shapes at both extremities ensure a smooth transition to the adjacent vacuum chamber segments. The mechanical and electrical connection to the mobile jaws is made with sliding contacts. A longitudinal cross section of the TDI and a cross section of the TDI in IR2, showing the beam screen, are given in Fig. 16.12 and 16.13, respectively.

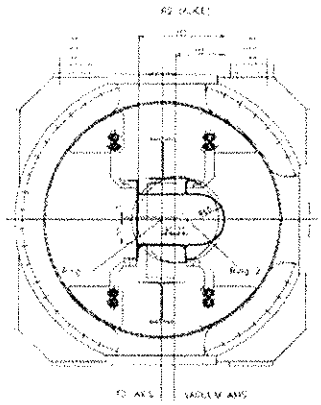

Figure 16.13: TDI cross section at IR2

Vacuum Aspects

Owing to the proximity to the experiments, the background from residual gas scattering in the TDI must be kept small. Two ion pumps of 400 l/s each and two titanium sublimation pumps of 1000 l/s each provide an efficient pumping speed of 1600 l/s in total. The expected residual pressure inside the beam screen is 10^{-8} mbar during normal operation after an in-situ bake-out. Sufficient vacuum transparency of the beam screen, at about 10 % of its surface, is provided through a large number of quasi-irregularly positioned holes which measure 11 × 2 mm.

The suitability of hBN for this quite novel application has been verified through extensive testing of both the mechanical resistance and the vacuum aspects [26]. Prior to mounting, the material undergoes a heat treatment at 400 °C under vacuum. After installation and following any intervention, the tank is baked out at 200 °C using heating jackets. To improve removal of gas emanating from the absorber during bake-out and after interception of significant amounts of beam, the absorber segments contain machined slits and are mounted with 5 mm gaps. The aluminium jaw frame will be heated directly by a resistive wire (stainless steel) mounted inside a groove on both sides of the frame, isolated by ceramic rods. During bake-out the motor drives will be protected from overheating by temporary air cooling. Temperatures will be monitored by PT100 sensors located on each jaw, with an interlock level set slightly above 200 °C to prevent deterioration of the mechanical properties of the aluminium.

The vacuum system has been designed to cope with the outgassing during normal operation, i.e. with a jaw temperature between 20 and 35°C. As thermal outgassing increases dramatically with temperature, a vacuum degradation of the order of 10 will be incurred for a temperature increase of 50°C. Operating temperatures of higher than 50°C will therefore possibly lead to gas density levels exceeding those required near the experiments.

Fault Cases Considered

According to the initial design specification the various circumstances leading the TDI to intercept beam have been investigated and grouped in cases [22], with the same total kick strength seen by the beam. Operational (i.e. intentional) uses of the TDI were considered to imply the repetitive use of single bunches without leading to quenches of the superconducting dipole D1 located downstream, accidental or emergency uses were to proceed from the assumption of full batch intensity, without causing damage to D1.

In case 1 the kick strength is zero. Besides the during commissioning and during re-adjustment of the injection before each fill this could happen when the SPS extraction was launched but the LHC suddenly turned out not to be ready to receive beam. It could also be caused by a missing trigger to the MKI. This could happen several times per year. In this case the beam hits the upper jaw at about 30 mm from the lower edge.

Case 2, the beam sweep occurs when the rise or fall slope of the kicker pulse coincides with the passage of beam to be injected or with the circulating beam. This could occasionally occur as a result of wrong kicker timing, either due to an internal or external reason, or a pre-fire of one of the modules. Several precautions are taken to make this a relatively rare event. The pulse generators are only charged 2 ms before an injection, making the time when a breakdown in the thyratron gas tubes could occur quite short. As soon as one kicker module has pre-fired the other modules are also triggered. In this case close to 100 bunches are distributed on the TDI with various offsets from the jaw edge.

The also quite rare case 3 refers to one of the four MKI modules not firing. In this case the beam hits the upper jaw at about 3.5 mm from the lower edge.

Case 4 is an internal flashover on one of the MKI magnets. The consequences are particularly bad when the flashover occurs in any of a range of 8 out of the 33 cells. In this case beam would just miss the TDI and approximately 90 % of an injected batch could hit the collimators. To reduce the consequences the dump switches will be fired upon detection of such a flashover, terminating the pulse and reducing the intensity leaking into the LHC machine by a factor of 2. Based on the prototype results and several other improvements implemented in the series kickers this case is expected to be a very rare event, happening less than once per 10 years of operation [23].

Protection Performance

The TDI/TCDD/D1 ensemble has been simulated and optimised using FLUKA [27]. The material of the TDI sandwich construct lumps up to about 15 interaction lengths. Considering the TDI alone for case 1 leads to no quench, even at highest intensities. Without the additional shielding provided by the TCDD described in 16.4.2, case 4 would approach the limit for producing damage to the D1 coil for a nominal full batch and surpass it slightly for ultimate intensity. The TCDD reduces the energy deposition in the coil by about two orders of magnitude and thus excludes damage to D1 under all circumstances. Its presence is of course also beneficial for the cases 2 and 3, so that quenching D1 can probably be avoided for the sweep case for nominal intensity.

To ensure this protection the TDI must be set very close to the beam for injection. Details of possible impact of beam missing the TDI or leaking from it onto other machine components are discussed in [22]. Two additional collimators, positioned at a phase advance of $\mu_y \approx \pm 20^\circ$ from the TDI, near Q6 on the other side of the insertion, and set at the same aperture will extend the protection of the TDI in case of phase errors.

Structural Considerations

The mechanical performance of the TDI has been studied using the numerical code ELSE which is based on the Spectral Element Method (SEM) [28]. The structural behaviour of all of the hBN blocks was modelled up to 80 μs after the absorption of a full batch at ultimate intensity for a centred beam load, in order to identify the most critical one. The highest temperature increase and radial thermal gradients are located in the first three blocks, with a maximum $\Delta T = 638$ °C in the third one. The most stressed blocks are the first five, while the last blocks show a more uniform stress field.

Since hBN is an orthotropic material, the maximum stress criterion was selected to assess the structural performance of the absorbing core; this criterion is more conservative than the Stassi (or generalized Von Mises) criterion usually adopted for graphite. The components of the dynamic stress tensor were evaluated at each time step and each node of the SEM model. The ratio between these values and the rupture stress was calculated and a maximum value of 0.32 was found, which gives a stress safety factor of three at ultimate intensity. The most stressed volume is concentrated around the beam axis, though other parts of the block are subjected to relevant stresses due to the propagation and reflection of elastic stress waves.

Because the beam may be intercepted at various distances from the free edge of the absorbing segments (the "impact parameter"), numerical simulations were performed for the most critical third hBN block with a varying impact parameter. For the chosen stress criterion, the maximum stress is approximately constant for the different beam positions and the stress ratio close to the above-mentioned value of 0.32.

The use of fine-grained polycrystalline graphite was investigated as an alternative to hBN. Due to the higher thermal expansion coefficient and lower mechanical resistance, higher stresses ratios were found. Based on the Stassi criterion, a maximum stress ratio of 0.76 was estimated for a centred beam load, giving a

safety factor as low as 1.3. Worse values are expected for off-centre loadings, which substantiates the choice of hBN.

Downstream of the hBN blocks, the estimated temperature rise after interception of one full batch at ultimate intensity is 150°C in aluminium and 190°C in copper. These values, together with the very low thermal gradients, are estimated to be low enough not to require a dedicated structural analysis.

Dose Rates

Tab. 16.4 shows the estimated dose rates of the TDI under the assumption of 10^{15} protons being dumped per year, as a function of the number of years in operation and the cool-down time. The values scale with the intercepted intensity and almost saturate after 10 years of operation. The TDI activation is low enough to allow human intervention around the vacuum tank, and, after an appropriate cool-down time, also on the jaws itself. This holds a fortiori for the TCDD described in 16.4.2.

Table 16.4: Estimated TDI dose rates in mSv/h when intercepting 10^{15} protons per year

Cooling time	*Contact dose at*	**Operation time**	
		1 year	**10 years**
1 min	*Core*	112	120
	Tank	16	16
1 day	*Core*	0.5	0.6
	Tank	0.09	0.09
1 month	*Core*	0.08	0.12
	Tank	0.02	0.03
1 year	*Core*	0.02	0.05
	Tank	0.005	0.015
10 years	*Core*	0.003	0.02
	Tank	0.0003	0.002

Operational Aspects

After dumping the previous circulating beam and prior to the next injection, the TDI jaws are closed to a nominal position of ± 8.5σ (about ±4.3 mm). After injection the TDI jaws are retracted.

Owing to its basic design purpose the TDI core is not actively cooled. The thermal inertia of the TDI jaws allows the absorption of single SPS bunches of ultimate intensity (1.7×10^{11} protons per bunch) during commissioning and adjustment of injection every 18 s for about 8 hours consecutively. For a few consecutive SPS cycles the TDI is able to intercept a full batch of $4 \times 72 = 288$ bunches at ultimate intensity. Normally this case should not occur as further extraction of intense beam towards LHC should be inhibited after one error, until the source of the fault has been removed. The temperature in the TDI absorbers will be monitored and fed back to the SPS extraction system to prevent over heating and thus mechanical deformations leading to loss in TDI precision or even severe malfunctioning.

16.4.2 Supplementary Shielding for D1

The TDI alone is sufficient to prevent damage to D1 in practically all cases of injection kicker malfunction. To prevent damage even in the worst MKI flashover case where a full batch just grazes the TDI jaw, an additional shielding element (TCDD) is placed about 3 m upstream of D1. This also improves the TDI performance for other fault cases.

Its absorbing element consists of two copper jaws placed inside a vacuum tank. In the closed position, they form a cylindrical core ∅ 70 mm × 1000 mm with a rectangular opening of 30 × 50 mm and rounded corners. This assembly shadows the D1 coil with a beam clearance ~15σ. A side view of the TCDD, along with a cross section, is given in Fig. 16.14. Longitudinally, the jaws are wedge-shaped to avoid particle streaming, as shown schematically in Fig. 16.15.

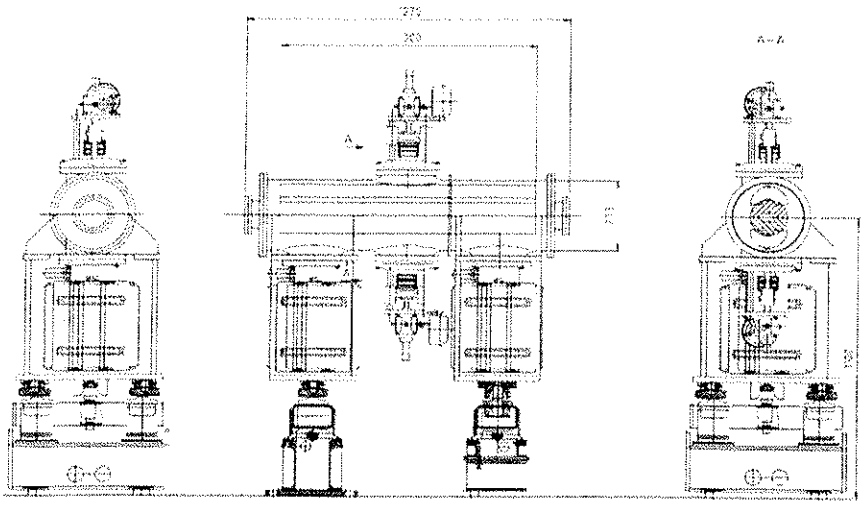

Figure 16.14: TCDD side view and cross section

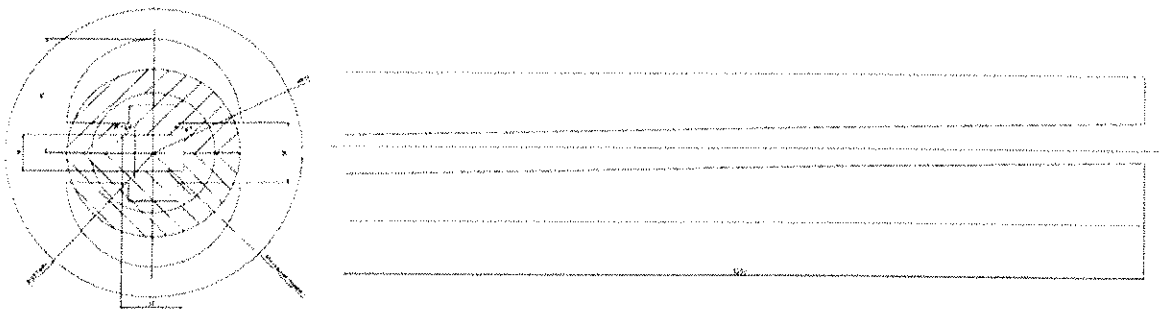

Figure 16.15: TCDD absorber cross section and side view

In IR8 the jaws are always fixed in the closed position and no motorisation is provided. In IR2 the jaws can be opened by ±50 mm to provide appropriate aperture for the ALICE Zero Degree Calorimeter once injection is terminated.

The design of several TCDD sub-components (motorisation, supports) is based on that of the TDI. One ion pump of 400 l/s is mounted on a simple steel tank of 1270 mm length and 273 mm diameter. As 200°C is the maximum bake-out temperature acceptable on the tank, the jaws will be baked directly up to 250°C using the same heaters as in the TDI. The TCDD is not cooled and should see no direct beam.

16.5 BEAM INSTRUMENTATION

16.5.1 Overview

The beam instrumentation around the injection systems is a direct continuation of the transfer line systems in TI 2 and TI 8. Therefore the functional specifications for the transfer lines [29, 30] have been used in the design choices for these systems. A schematic overview of the instrumentation in the injection region is given in Fig. 16.16. Only instruments forming an integral part of the LHC rings are described below; elements being part of the transfer lines (grey shaded in contrast to black filled symbols) and physically separate from the rings are described in Volume 3.

The transfer line beam position monitors (BPMI) allow steering of the beam up to the entry of the septum magnets. The BPMs around the injection elements are standard ring BPMs installed on the superconducting quadrupoles, details of which can be found in Sec. 13.1. Luminescent screens (BTVI) using the optical transition radiation effect (OTR) are used to determine the transverse beam sizes and centre of gravity upstream and downstream of the major injection elements and provide complementary position information during the setting up and steering of the injection. Standard SPS type beam-loss monitors (BLMI) are used to

localise the losses linked to the injection process. Installed instruments can cope with the full variety of LHC beams. For proton operation, the intensity varies from a single pilot bunch, namely 5×10^9 protons, to 4 batches of 72 bunches with up to 1.7×10^{11} protons per bunch.

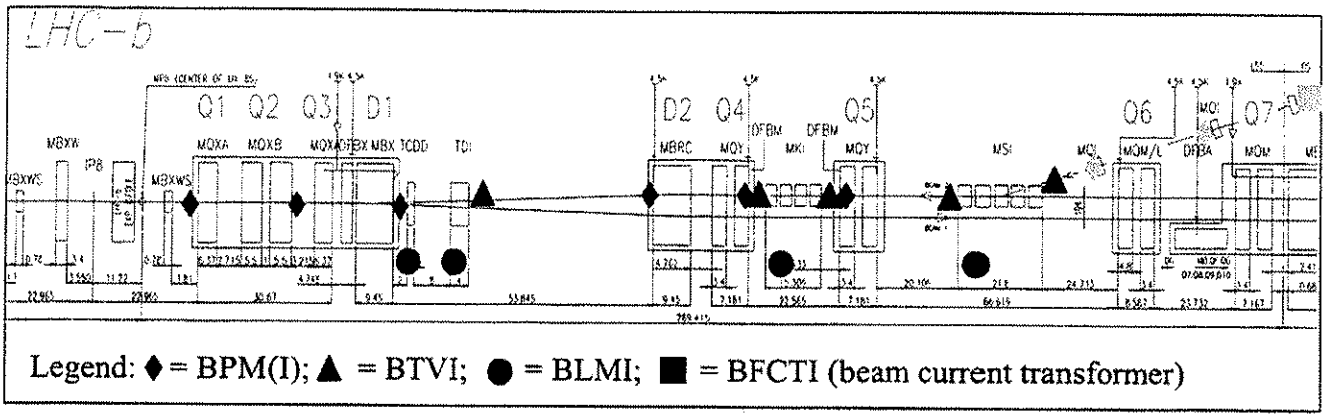

Figure 16.16: Schematic view of injection related instrumentation (case of injection near IP8)

16.5.2 Beam Loss Monitors

The beam-loss monitors around the injection systems are of the SPS type. The ionisation chambers and acquisition system are described in [31, 32]. Acquisitions are triggered using SPS timing events pre-programmed at the correct time in the SPS elementary cycle. The beam-loss server allows returning data either in raw ADC units or calibrated in units of mGy. The calibration of the whole acquisition chain is done with an external source.

Dynamic Range and Precision

The dynamic range to be considered for the LHC beam corresponds to a factor 10^4 if the losses scale linearly with the total intensity. The acquisition cards have 12 bit ADCs which is insufficient to cover this dynamic range. It will therefore be necessary to use the on-board gain switches providing gains between 1 and 2.5×10^4.

16.5.3 Beam Profile Monitors

The BTV mechanisms are of a new type with respect to the existing SPS version, as they have to allow the movement of three different screen holders (one of them being empty) within a very confined space between the transfer line and the LHC ring vacuum chambers. The first physical screen that can be inserted into the vacuum chamber is made of a foil of alumina (Al_2O_3) for low intensity use and the second of titanium for OTR observation at intensities $>10^{11}$ particles. The second screen can alternatively be equipped with a carbon foil believed to withstand even ultimate LHC intensity. The round foils have a diameter of 65 mm and cover therefore the entire acceptance of the vacuum chamber, making it possible to use them for calculating the beam position over a very wide range. Depending on the choice of fixed optics in front of the BTV camera, a part of the screen can be selected for digitisation. This defines in the end the resolution in the range between 60 μm to 120 μm per pixel. The resolution can be user-defined, owing to the trade-off between resolution and screen coverage.

As the aperture near the injection region is restricted, measurements of the beam size and beam position (centre of mass) obtained from the transverse beam profile monitors are mandatory to steer the beam and minimise the injection oscillations. BTV monitors are inserted at the entrance and exit of the MSI and MKI to optimally position the beam inside those devices and check their correct functioning. One monitor is placed in front of the TDI inside the LHC tunnel to obtain correct initial conditions for the trajectory on the first turn.

BTV Acquisition

The acquisition of beam profile data is based on high-resolution CCD cameras linked to a newly developed BTV acquisition card giving a two-dimensional image with a digitisation of 300 × 400 pixels. The screen position, filters and an external lamp can also be controlled from the same VME module. All monitors provide two-dimensional information. For normal batches the integrated beam spot must be made available. By directing the light emitted by the passage of the beam through the screen towards a fast profile acquisition system, bunch-by-bunch profiles (X and Y projections) are possible at selected monitors [33]. The last option requires the installation of further BTV tanks that are not part of the present layout.

Reproducibility on Position and Size Measurements

Measurements on an existing SPS BTV tank [34] have shown that the reproducibility on the measurement of beam size and centre of mass for a spot size equivalent to that of the LHC beam is very good. The beam position (centre of mass) acquired over 10 consecutive screen movements changes by around 100 μm peak-to-peak and the beam size is determined to within 1% which is well within the specifications. Even better results are expected with the newly designed BTV tank if special care is taken during the alignment of the BTV screens.

Acceptance

The BTVs should, if possible, cover a large fraction of the vacuum chamber aperture. The profile monitor optics and readout should be adjustable to cover either a large area at the expense of a loss in accuracy, or to cover a significantly smaller area optimised for optics and emittance measurements. During the first commissioning of the lines, the profile monitors should be tuned to cover the largest possible fraction of the aperture.

16.5.4 Software

The low-level software for all instrumentation systems in the transfer lines and thus also around the injection systems is based on a common front end software architecture [35] which provides a set of generic structures allowing the production of graphical user interfaces for operations as well for expert applications used during the setting-up of these systems.

16.5.5 Interlocks

The beam loss monitors in the transfer lines and in the injection region are part of the SPS extraction interlock. Whenever the rates exceed a given preset threshold, extraction from the SPS is inhibited for the following cycles. A machine operator has the possibility to reset this interlock in order to perform tests and, if required, improve the steering of the line or of the extraction channel. An automatic reset mechanism may be applied to prevent useless machine downtime in case of a spurious problem, as is already done in the SPS ring. There are also ideas to incorporate a software interlock to inhibit further injections into the LHC if the difference between the beam trajectory and its reference exceeds a given threshold. During the injection process, rare but heavy losses are expected that will be associated to either bad beam conditions at the end of the transfer line or to injection kicker faults. Most of the beam losses will occur in the TDI. The beam-loss monitors around these devices are part of the LHC beam-loss system described in the beam instrumentation chapter. The position of the intercepting transverse profile monitors is to be surveyed by the SPS software interlock system. Depending on the operation mode of the LHC, the software interlock system should prevent beam extraction when the profile monitors are intercepting the beam to avoid undesired emittance blow-up of the beam. This interlock can, however, be bypassed for machine experiments and during verifications of the transfer line optics.

16.5.6 Post-Mortem System

Bad injections into the LHC may lead to large beam losses or even to magnet quenches. To understand such a sequence of events in detail, the full beam instrumentation data of each injection is made available to

the LHC post-mortem system. The position of intercepting beam profile monitors are also provided. The history of beam transfer data, in particular beam losses and beam transmission, will be recorded.

16.6 INTERRELATIONS WITH OTHER MACHINE SYSTEMS

16.6.1 SPS Machine and Transfer Lines

Prior to SPS extraction towards LHC various checks are performed on the circulating beam in the SPS. Should the intensity be too high for the LHC to accept in its present mode of operation or should the beam otherwise not meet the required specifications (number of bunches, synchronisation with respect to the foreseen RF buckets) the beam would not be extracted, unless one of the TED beam dumps in the respective transfer line is in its dump position. If the beam position differs too much from its nominal position, it is not extracted but dumped at the end of the cycle.

The state of critical extraction and transfer line equipment is checked shortly before extraction. If the extraction kickers exhibit any significant flaw, the transfer line collimators are not set properly or the vacuum in the transfer lines is too poor, extraction is inhibited. About 20 ms before transfer the currents in all transfer line power converters are measured, including those of the injection septa. Should one be found outside the tolerance window, extraction will again not take place. Extraction can be inhibited by a signal reaching the extraction kickers until about 1 μs before they would be fired. As already mentioned the injection can be inhibited up to 250 ns before the injection kickers would pulse.

16.6.2 LHC Injection Modes

Injecting beam with significant intensity into the LHC can cause severe damage to equipment if one of the critical LHC elements has wrong settings or is in a faulty state. Since it is not possible to observe the resulting losses and to dump the injected beam in less than several turns, typically a minimum of 3 turns, existing safety systems cannot prevent such damage.

A rigorous application of a succession of different injection modes has to be followed in order to increase progressively the beam intensity from a pilot bunch up to a nominal beam. The different injection related operation modes are injection inhibit, inject-and-dump, inject-and-probe, inject-and-dump with an intense beam and inject-and-fill [36].

Inject-and-dump mode permits a pilot beam to be injected and then dumped very early, i.e. within a few turns up to a few tens of milliseconds. This operation mode requires an automatic dump action with a given delay relative to the LHC injection pre-pulse. If the delay is set to its minimum value, the beam will be dumped during its first turn.

Inject-and-probe mode is based on continuous real-time measurements of the current of the LHC and SPS circulating beams and information on what beam intensity the LHC is permitted to receive. Correlations between the two beams are made in order to enable or disable the injection inhibit as listed in Tab. 16.5. The general rule is that a low intensity beam must first be present in the machine before a higher intensity beam can be injected.

Inject-and-fill mode is synchronised with the abort gap frequency as explained in Chap. 17. A gating-off mechanism for injection is implemented in order to avoid filling the beam abort gap with an unsynchronised injection. The filling pattern and the longitudinal beam position during filling is entirely defined by the radiofrequency system through the timing of the injection pre-pulses sent to the injection kickers.

Table 16.5: Injection conditions in "Inject-and-Probe" mode

Beam Intensity in SPS	Beam Intensity in LHC	LHC Injection Inhibit
Pilot Bunch	None	No
Pilot Bunch	Pilot Bunch	No
Intense Beam	None	Yes
Intense Beam	Pilot Bunch	No
Intense Beam	Intense Beam	No

16.6.3 Control System

The injection kicker control system is fully integrated in the LHC controls infrastructure following the standard controls framework. Integration of the different control entities described above is based on dedicated equipment servers implementing the required functionalities through standard communication contracts and low-level threads.

Operational settings management like kick delay, kick length and kick strength is performed at the application layer through accelerator wide standard application programs. Equipment settings management, such as fine timing delay or interlock thresholds are managed by the equipment experts.

The injection kickers are linked to the machine post-mortem system for correlation of injection related data with other accelerator processes in case of faults. Typical signals acquired are the magnet current pulse shape, the currents of the injected and circulating beams, and the beam permit and beam abort gap signals. Triggering of the post-mortem system will be based on the opening of the beam permit loop. The same signals are also acquired and analysed on a shot-by-shot basis at each injection to continuously monitor the injection kickers with the objective to detect any degradation of their performance.

16.6.4 Radiofrequency

The synchronisation of the injection kicker timing system with the injected and circulating beams is performed at the radiofrequency (RF) level through the generation and the distribution of the fast injection pre-pulse. In order to avoid any modification of the pre-pulse distribution delay, dedicated fibre optics links are used between the RF installation in SR4 and the kicker timing systems installed in UA23 and UA87. Despite the fact that this pre-pulse is locked to the SPS/LHC common frequency, the final longitudinal beam injection position in the LHC also depends on the selected SPS extraction turn. A bad selection of the SPS extraction turn can result in filling the beam abort gap in one shot.

As a fixed phase difference with respect to the revolution frequency exists between the beam abort gap position at the injection kicker and at the dump extraction kicker, the injection kicker timing system can be bound to the extraction kicker synchronisation system through the distribution of the beam abort frequency. On the basis of this beam abort frequency and after compensation of beam time-of-flight and signal distribution delay, a 10.8 μs long gating-off window is included within the injection kicker timing system in order to inhibit the injection pre-pulse if it falls within the window. This window starts 7.8 μs before the beam abort gap at the injection kicker and continues up to the end of the abort gap. If an injected pre-pulse falls within this window, the injection will be inhibited and the arriving beam be sent to the TDI.

16.6.5 Machine Protection System

The injection kicker systems are connected to the LHC beam permit loops and injection into LHC is only enabled when the loops are closed. Opening one of the beam permit loops automatically inhibits the injections with a reaction delay of 250 ns. In this case, the incoming beam is automatically sent to the TDI. The LHC injection inhibit interlock signal is also sent to the SPS extraction interlock in order to inhibit extraction, thus preventing intense beam sent repetitively to the TDI, unless the transfer line dumps are in position to intercept them, for instance in the case of transfer line tests.

16.6.6 Beam Dumping System

At injection, the propagation delays between the beam dumping system and the injection kickers must be taken into account in order to avoid the "1-turn-deadlock". Opening the beam permit loop in IR6 will immediately trigger the beam dump and will require ≈100 μs to reach the injection kicker in IR2. If a dump request in IR6 occurs just before a new injection, the circulating beam will be dumped but beam injection will still be allowed during the next 100 μs while the beam dump system is not ready. The full consequences of this "1-turn-deadlock" between beam dumping system and injection kickers still have to be studied in more detail.

16.6.7 Collimator System

As the TDI is normally set to $8.5\sigma_y$ at injection it is well in the shadow of the secondary LHC collimators which are positioned at $7.0\sigma_y$. However, if the TDI jaws are closed by about 1σ (about 0.5 mm), or if the secondary collimator settings are opened by a similar amount, the TDI jaws may start to see a significant particle load from the secondary halo. The settings of the injection collimation system and the main LHC collimators are therefore interdependent and special care is needed in their operation to satisfy both machine protection and performance requirements.

The TDI and associated TCLs also limit the amount of beam impacting the LHC collimators in the event of injection kicker failures. For the LHC collimation system, the failure cases 2 and particularly 4, described in 16.4.1, could result in beam impacting on collimator jaws.

REFERENCES

[1] A. Hilaire, V. Mertens, E. Weisse, "Beam Transfer to and Injection into LHC", Proc. EPAC'1998, Stockholm, 1998.

[2] Technical Specification of the Steel Septum Magnets for the LHC Injection and Beam Dumping Systems, CERN, SL-Spec 98-31 (MS), 1998.

[3] S. Bidon et al., "Steel Septum Magnets for the LHC Beam Injection and Extraction", Proc. EPAC'2002, Paris, June 2002.

[4] D. Cornuet, J. Dutour, P. Leclère, "Magnetic Measurements of the Steel Septum Magnet used for Injection: MSIB01", CERN, LHC Project Note 280, 2001.

[5] B. Goddard, CERN-AB/BT, J.M. Jimenez, CERN-AT/VAC, private communication (note in preparation).

[6] M. Gyr, "Expected Magnetic Field Quality of the LHC Septum Magnets Used for Injection (MSI) and for Extraction to the Beam Dump (MSD)", CERN, LHC Project Note 129/rev., 1999.

[7] B. Henrist, CERN-AT/VAC Technical Note (in preparation).

[8] I. Collins, "Room Temperature Beam Vacuum System for the LHC Long Straight Sections", CERN EDMS rev. 0.2, N°339088, 2002.

[9] A. Gerardin, CERN, Report EST/SM/ME 01-05-16.

[10] A. Gerardin, "Scratch Test on an Electro-deposed Copper Layer of a Mumetal Pipe", EST/SM-ME EDMS 349561 16/07/02.

[11] L. Vos, CERN-AB/APB, private communication.

[12] J.M. Jimenez, B. Henrist, "Vacuum Chamber for the Circulating Beams in the LHC Injection and Extraction Septa", under approval (EDMS).

[13] H. Burkhardt, "Do We Need Collimation in the Transfer Lines ?", Proc. LHC Workshop, Chamonix XII, Chamonix, 2003.

[14] H. Burkhardt, B.Goddard, V.Mertens, "Passive Protection Devices in the Transfer Lines to the LHC", Proc. PAC'2003, Portland, 2003.

[15] L. Ducimetière et al., "Design of the Injection Kicker Magnet System for CERN's 14 TeV Proton Collider LHC", Proc. 10th IEEE Int. Pulsed Power Conference, Albuquerque, 1995.

[16] R.L. Gluckstern, L.Vos, B.Zotter, "Shielding Particle Beams by Thin Conductors", CERN-SL-2002-014-AP, 2002.

[17] L. Ducimetière et al., "The LHC Injection Kicker Magnet", Proc. PAC'2003, Portland, 2003.

[18] B. Versolatto, "Procédure de traitement des ferrites en vue de leur utilisation dans un système UHV", CERN-AT/VAC Note (in preparation).

[19] E. Frick et al., "Fast Pulsed Magnet Systems for Proton and Antiproton Injection into the CERN 400 GeV Proton Synchrotron", Proc. 15th Power Modulator Symposium, Baltimore, 1982.

[20] E. Decailloz, PFN design Department, LCC-Thomson, France, private communication, 1993.

[21] Cadence, 2655 Seely Av., San Jose, CA 95134, USA.

[22] O. Brüning et al., "Impact of and Protection Against Failures of the LHC Injection Kickers", Proc. PAC'1999, New York, 1999.

[23] B. Goddard, "Impact of Injection Kicker Failures", 23th LHC Collimation Working Group Meeting, March 28, 2003.

[24] OASIS, http://project-lhc-cp-sigwg.web.cern.ch/project-lhc-cp-sigwg/ and http://ab-co-fc.web.cern.ch/ab-co-fc/AnalogSignals/nAos_for_TT40/main.htm.
[25] P.R. Sala, S. Péraire, "Conceptual Optimisation of the TDI and TCDD Protections for LHC Injection Lines", CERN AB-Note-2003-059 ATB, 2003.
[26] P. Chiaggiato, CERN-EST/SM, Report on BN Outgassing Measurements, 2001.
[27] A. Fassò et al., "FLUKA: Present Status and Future Developments", Proc. Int. Conf. On Calorimetry in High Energy Physics, La Biodola (Is. D'Elba), Italy, 1993, Eds. A.Menzione and A.Scribano, World Scientific.
[28] L. Massidda, F. Mura, "Thermal and Mechanical Analyses of the LHC Injection Beam Stopper (TDI)", CRS4 – Centre for Advanced Studies, Research and Development, Cagliari, Italy, 2003.
[29] M. Meddahi, "Instrumentation Needs for LTI", Proc. LHC Workshop, Chamonix XI, CERN-SL-2001-003 DI.
[30] J. Wenninger, "Instrumentation for the TI 2 and TI 8 Transfer Lines", Engineering Specification, EDMS Document LHC-B-ES-0004.
[31] G. Ferioli et al., "Protection and Diagnostic Systems for High Intensity Beams", CERN-SL-2000-032-BI.
[32] J. Bosser, G. Ferioli, "Comparative Test Results of Various Beam Loss Monitors in Preparation for LHC", Proc. DIPAC'99, Chester, 1999.
[33] G. Ferioli, "Beam Profile Measurements at 40 MHz in the PS to SPS Transfer Channel", CERN SL-99-043 BI.
[34] Minutes of the 25th BI LHC/CNGS Technical Board.
[35] J.J. Gras et al., "AB Front End Common Software Architecture", https://edms.cern.ch/file/380278/1/FE ComSA_TC.pdf.
[36] E.C arlier, "Safe Injection into LHC", Proc. LHC Workshop, Chamonix XII, Chamonix, 2003.

CHAPTER 17

BEAM DUMPING SYSTEM

17.1 SYSTEM AND MAIN PARAMETERS

17.1.1 Introduction and System Overview

IR6 of the LHC [1] is dedicated to the beam dumping system. The function of the beam dumping system will be to fast-extract the beam in a loss-free way from each ring of the collider and to transport it to an external absorber, positioned sufficiently far away to allow for appropriate beam dilution in order not to overheat the absorber material. A loss-free extraction will require a particle-free gap in the circulating beam, during which the field of the extraction kicker magnets can rise to its nominal value. Given the destructive power of the LHC beam, the dumping system must meet extremely high reliability criteria, which condition the overall and detailed design. The system is shown schematically in Fig. 17.1 and will comprise, for each ring:

- 15 extraction kicker magnets MKD located between the superconducting quadrupoles Q4 and Q5;
- 15 steel septum magnets MSD of three types MSDA, MSDB and MSDC located around IP6;
- 10 modules of two types of dilution kicker magnets between the MSD and Q4;
- The beam dump proper comprising the TDE core assembly and associated steel and concrete shielding, situated in a beam dump cavern ~750 m from the centre of the septum magnets;
- The TCDS and TCDQ diluter elements, immediately upstream of the MSD and Q4 respectively.

Nominal system parameters are given in Tab. 17.1, with details of the equipment subsystems in Section 17.3. The MKD kickers will deflect the entire beam horizontally into the high-field gap of the MSD septum. The MSD will provide a vertical deflection to raise the beam above the LHC machine cryostat before the start of the arc sections. The dilution kickers will be used to sweep the beam in an '*e*' shaped form and after the appropriate drift distance the beam will be absorbed by the TDE assembly. The TCDS and TCDQ will serve to protect machine elements from a beam abort that is not synchronised with the particle-free beam gap.

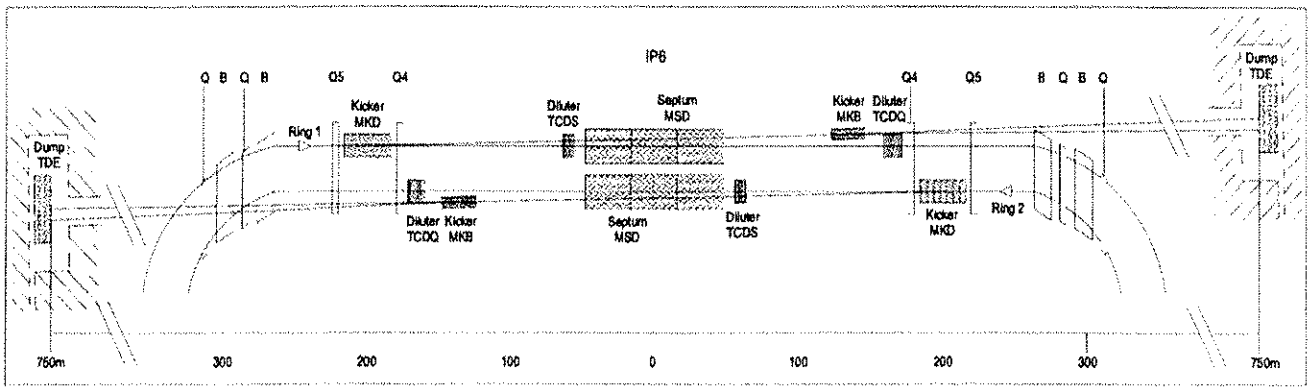

Figure 17.1: Schematic layout of beam dumping system elements around LHC point 6.

17.1.2 Assumed Worst-Case Beam Characteristics

The beam dumping system must be able to accept LHC beams with well-controlled parameters (e.g. during a planned abort at the end of a physics run) and also beams with off-normal parameters (e.g. as arising from an equipment failure or beam instability), in addition to variations imposed by optical effects (beta-beating, power supply ripple, allowed tuning range). The relevant worst-case beam characteristics that can be accommodated [2] by the dumping system are given in Tab. 17.2 for the various LHC beams considered.

Table 17.1: Overall beam dumping system parameters.

Parameter	**Unit**	**Value**
Total horizontal deflection (MKD + Q4)	mrad	0.330
Total vertical deflection (MSD)	mrad	2.400
Dilution horizontal deflection (MKBH)	mrad	±0.14
Dilution vertical deflection (MKBV)	mrad	±0.14
Total beam line length (start MKD – end TDE)	m	975
Required particle-free abort gap length	μs	3.0
System Safety Integrity Level (SIL)		3
Beta function at TDE entrance	m	4990 (H), 4670 (V)

Table 17.2: Assumed worst-case LHC beam characteristics for dumping system design.

Beam	Max ε_n 450 GeV [μm]	7 TeV [μm]	Total Orbit [mm]	Beta variation [%]	Total p+ 10^{14}
Commission	6.0	12.0	±4	42	0.3
Initial	6.0	12.0	±4	42	0.8
Nominal	7.5	15.0	±4	42	3.1
Ultimate	7.5	15.0	±4	42	5.3

17.1.3 Operational Assumptions

For the purposes of estimating radiation and heat loads for the TDE, TCDS and TCDQ and also for the purposes of the reliability analysis, the assumptions shown in Tab. 17.3 were used concerning the operational parameters, dump and fault frequencies [3, 4]. Note that these are generally worst-case assumptions so as to ensure that there is an inherent safety factor in the subsequent calculations.

Table 17.3: Assumptions for activation calculations and reliability.

Number of years of LHC operation	20
Number of days operation per year	200
Number of 7 TeV fills dumped per day (at nominal current)	2
Number of 450 GeV fills dumped per day (at nominal current)	2
Number of dumps at full intensity per beam in LHC operational lifetime	2×10^4
Number of dumps with a missing MKD modules per year	1
Number of asynchronous dumps per year	1
Number of total dump system failures per 100 years	1
Total intensity until staged equipment operational (MKB and TDE cooling)	50% of nominal

17.2 RELIABILITY AND FAULT CASES

17.2.1 System Reliability

A fault with the beam dump system could lead to severe damage to the dumping system itself, to the LHC machine or to the LHC experiments, due to full or partial loss of the beam onto machine components. (The beam dumping system is not, however, formally considered as a critical element of the safety systems, since from the state of the system one cannot determine the presence or absence of beam in the LHC.)

It is assumed that a total beam dump failure (i.e. a failure to execute a correct beam dump upon receipt of a dump request) will not exceed 1 failure in 10^6 hours [5, 6], or roughly one failure in 100 years. Obtaining (and even quantifying) lower failure rates than this (already ambitious) value is very difficult and would be likely to reduce the availability of the beam dumping system. The low assumed failure rate has to be

obtained by using high quality components, introducing redundancy for the most critical elements, provision of redundant signal paths, use of fault tolerant subsystems, continuous surveillance, rigorous follow-up and the imposition of a check list of validation tests before injecting beam in the LHC. It has to be noted that this failure rate needs to be obtained for the complete system, comprising the beam dumping sub-system elements together with the LHC Beam Interlock System (Sec. 15.5), the LHC Beam Energy Meter and the associated signal transmission [7].

The Beam Energy Meter will be one of the critical elements in the chain of equipment required to dump the beam [8], since underestimating the beam energy could send the full LHC beam into one of the arcs adjacent to the beam dump insertion. Severe malfunctioning of the very complex extraction kicker magnets could also result in similar disastrous scenarios and the MKD will therefore also be one of the critical reliability elements in the system.

17.2.2 System Design Regarding Reliability

MKD

First estimates from reliability calculations [5] for the extraction kicker system MKD have shown that the reliability requirement can only be obtained with full redundancy of one complete MKD kicker and its generator: the beam can safely be extracted (albeit with the risk of beam losses on the TCDS) with only 14 out of 15 kicker magnets pulsing [9].

The following additional measures are incorporated in the MKD design specifically for reliability reasons:

- Each MKD generator will consist of two parallel discharge circuits, including two switches, with failsafe triggering [10]. In case of failure to start of one switch, the other will take the full current;
- The switches [11] will use Fast High Current Thyristor (FHCT) solid-state technology which is much more reliable than using conventional gas discharge switches;
- The energy needed for the kickers will be stored in local capacitors of which the voltage will be constantly monitored. If one voltage is outside the specified value, the beam will be dumped immediately (self triggering);
- If a switch closes when not demanded (erratic), a re-trigger system will immediately close all the other 14 switches with a maximum delay of 700 ns (for beam energies above 3 GeV/c). Note that this action will not be synchronised with the abort gap and will therefore produce losses at the LHC collimators, the TCDS and TCDQ;
- A redundant UPS system will ensure that a dump action is correctly triggered and executed in the event of a general power cut;
- All trigger and re-triggering lines will be doubled.

MKB

The diluter kickers MKB will not be critical items from a reliability viewpoint because of the redundancy present [31] and because extraction of the beam from the LHC machine will not rely on their correct operation. Triggering lines will, however, be doubled, since a total dilution failure could lead to damage of TDE core.

MSD

The reliability of the DC septum magnets, MSD, is not regarded as critical since the magnets are based on conventional technology (with current decay time constants in the order of seconds) and the current in the magnet can be constantly monitored, as could the voltage drop across the magnet if required.

Vacuum System and TDE

The vacuum system of the TD dump line and the pressure vessel of the dump block TDE cannot fail in such a way as to threaten the safety of the LHC machine in general, since a loss of TD vacuum or loss of TDE pressure can be detected well in time; in any case the beam can still be dumped under degraded vacuum conditions of these components without risk to the LHC machine proper. The risk of a damaging loss of containment of the TDE will be dealt with by over-pressuring the core with inert gas.

Post-mortem

High reliability will be maintained by performing and analysing a post-mortem of every beam dump. A dump action without beam will take place if the last post-mortem was too long ago, e.g. after a technical stop. It will only be possible to inject beam in the LHC if the post-mortem of the last beam dump and the beam dump status was satisfactory.

Synchronisation

The synchronisation between the RF and the beam dump kickers will be a redundant system and the loss of the synchronisation of one of the two systems will launch a synchronous beam dump. Transmission is via a direct fibre-optic link.

Energy Tracking

The beam energy tracking system will bind the deflection strength of the MKB and MKD kicker magnets and the MSD septum magnets to the measured beam energy in order to get the correct extraction trajectory (the tolerances on the kick angles for the MKD and MSD elements are below one percent). The beam energy tracking system will have two main tasks:

- The generation of the strength reference signals for the power-supplies of the kickers and MSD;
- The verification of the output voltages of the kicker power-supplies and the MSD current.

The measured levels must follow the required levels for the inferred beam energy, within a predetermined tolerance window; otherwise a synchronous beam dump request is issued. The beam energy reference information will be obtained through two redundant Beam Energy Meter systems (BEM) connected to the two main bend power converters located left and right of IR6. The BEM will convert a physical measurement, current or voltage, into a value proportional to the beam energy and will therefore not be a real beam energy measurement.

A BEM Transmitter (BEM_T_x) will be installed in the standard AB/PO main bend power converter function generator controller, in the MSD power converter and in the MKD high voltage generators for monitoring of the equipment settings. The BEM_T_x will send out the measured DCCT value for magnet power converters or the capacitor charging voltage for the kicker as well as 1 mV and 10 V constant reference voltages at 1 kHz. The current measurement signal will be provided by a ±0.1% accuracy DCCT and the capacitor charging voltage by a ±0.1% accuracy high voltage divider. Each data frame sent out by the BEM_T_x will contain the 16 bit measurement signal, the two calibration signals and system status information.

The data frame will be received by the BEM Receiver (BEM_R_x) that will convert the measurement signal to an absolute energy value reconstructed from an internal look-up Table. Different tables will exist for the different types of power converter (main bends, septa or kicker). The frame will then be re-emitted by the BEM_R_x with the two calibration signals, some status bits and the absolute beam energy with an accuracy of 0.2%.

Finally, signals emitted by the different BEM_R_x modules will be received by the Beam Energy Tracking (BET) module and the absolute energy value measured for each equipment will be compared. If one signal falls outside a predefined tolerance window, a dump request will be sent to the Beam Interlock System.

It should also be noted that the MKD power trigger primary voltage will also be connected to the BEM system in order to compensate dynamically the FHCT switch turn-on delay described in 17.3.1.

The RF central frequency and integrated orbit corrector fields will affect the beam energy and possibly need to be taken into account, either via the BEM or via interlocking.

Other Protection

Local damage to components in case of certain fault scenarios will be avoided or reduced by the absorbers TCDS [12] and TCDQ [13]. The local orbit feedback will stabilise the beam in the extraction channel and an interlock on the orbit position will ensure that the beam position remains within tolerable limits to permit a successful abort. Sacrificial absorbers in the TD lines are also possible if the reliability analysis shows a necessity.

17.2.3 Acceptable (Design) Fault Cases

Despite the precautions listed above, certain faults of the dumping system are nonetheless expected to occur and are therefore foreseen in the design of the system and in the load cases for other systems, in particular the LHC collimators. They may result in a loss of efficiency for operation but should not result in equipment damage. These faults are termed acceptable faults and are as follows:

- One missing extraction kicker (MKD). A correct beam dump can be performed with 14 out of the 15 kicker magnets functioning correctly. If this fault occurs simultaneously with other acceptable faults (such as an orbit error of several mm) this can affect the machine operation by producing a quench in the downstream superconducting elements;
- Asynchronous dump. This could be caused by a spontaneous trigger of one of the MKD kickers followed by a re-triggering of the other magnets, or by a fault in the synchronisation with the abort gap [14]. In both cases the majority of the beam swept over the machine aperture will be intercepted by the TCDS and TCDQ absorbers and should not cause any damage, although several superconducting elements in IR6 will probably quench [13];
- Missing diluter kickers. Only one MKB magnet of each type will need to be operational to prevent damage to the beam dump block for nominal beam intensity. In the case of missing MKB magnets a longer cool-down period of the TDE needs to be envisaged before beam can be re-injected. This effect will be exacerbated by the staging of the TDE cooling;
- Self triggering of the system. If the beam dumping system detects an internal fault, like a tracking error of one of the voltages or a fault on one of the generators, the system will be triggered to cause a synchronous beam dump.

17.2.4 Unacceptable (Beyond Design) Fault Cases

The following system faults are unacceptable and could possibly lead to damage to the LHC since they are not foreseen in the design:

- The MKD kickers do not fire when a dump request is made by another system (e.g. the beam loss system). This potentially catastrophic failure could be caused by an undetected fault of the Beam Interlock System or by problems in signal transmission / reception;
- Receiving the wrong energy information, caused by an error in the beam energy system. It is expected that an energy error of more than a few percent for the complete system or for one of the subsystems can lead to severe equipment damage (a detailed analysis of the tolerances and consequences on energy errors remains to be performed). Wrong energy information in one of the sub-systems could be caused by problems in the look-up tables that relate energy to specific equipment settings;
- 13 or fewer out of 15 MKD extraction kicker magnets pulsing correctly. This may result in equipment damage, the extent of which would depend on the number of missing kicker magnets;
- Q4 field out of tolerance. The defocusing Q4 magnet is downstream of the extraction kickers and contributes about 20% of the total deflection angle. If Q4 is out of tolerance by more than about 1%, it is possible that the beam will not be properly extracted from the machine (losses or damage);
- MSD septum magnet field out of tolerance. If the septum field is more than about 0.5 % out of tolerance, losses or damage to the septum magnets, the MKB dilution kickers and the TD vacuum system could result. In addition the containment of the TDE could be threatened;
- If none of the MKB magnets pulse the dump block could be damaged, depending on the beam intensity.

17.2.5 Expected Fault Frequencies

The reliability of the complete beam dumping system remains to be calculated. Initial estimates have been made regarding the MKD generator, which is one of the most critical items. According to [6] an obtainable failure rate of 10^{-4}/h/kicker branch per year results in system failure rate (i.e. fewer than 14/15 generators working) of 1.1×10^{-11} /h. This assumes a fill duration of 10 hours and an 'as good as new' status after maintenance tests, to be made before each beam dump. This is better than the required Safety and Integrity Level (SIL) 4 [15] and much better than the assumed 10^{-6} hours mentioned in Section 17.2.1. Without a redundant MKD system, the failure rate calculated for 14/14 generators is only 1.4×10^{-6} /h, which conforms

only to SIL 1 and is therefore inadequate. Full calculations will be made for the complete system, including the beam energy meter, Beam Interlock System and signal transmission systems.

17.2.6 Reliability Run

After the hardware commissioning of the beam dumping system a 'reliability run' without beam of about three months is planned. This test period should eliminate any teething problems of the system, show up unforeseen faults scenarios and confirm the calculated reliability figures.

17.3 EQUIPMENT SUBSYSTEMS

17.3.1 Fast-Pulsed Extraction Magnets MKD

Two sets of 15 fast-pulsed extraction magnets MKD will form part of the beam dumping system. A pulse generator will power each magnet via a low impedance transmission line. There are several basic design requirements for the MKD system:

- At least 14 out of the 15 kicker magnets must operate simultaneously on request;
- The kicker system field rise time must be at most 3.0 μs and the kicker field 'flat-top' must be at least 90 μs. The current pulse is shown in Fig. 17.2;
- Any spontaneous triggering of one of the pulse generator-magnet systems must be detected and trigger the other generators within 700 ns at energies above 3 TeV;
- The kicker field must track the energy as provided by the Beam Energy Meter to better than ±0.5 %.

The unipolar system voltage will be 30 kV. The individual magnet current pulse (Fig. 17.2) will have an amplitude of 18.5 kA with a rise time of 2.85 μs (to which 150 ns total jitter between magnets must be added) and a 'flat top' duration of 90 μs followed by an approximately exponential decay of 1900 μs. This current corresponds to a magnetic field in the gap of 0.34 T, with up to 0.35 T in the steel. Tab. 17.4 summarises the main parameters of the MKD kicker system.

Table 17.4: MKD system parameters

Number of magnets per system	15	
System deflection angle	0.275	mrad
Kick strength per magnet	0.428	Tm
Vacuum chamber clear aperture (inner diameter)	56	mm
Operating charging voltage range	2 to 30	kV
Magnet field overshoot at 7 TeV	≤7.9	%
Magnet field overshoot at 450 GeV	≤10.0	%
Field flat top duration	≥ 90	μs
Effective magnet length (magnetic)	1.421	m
Yoke length (mechanical)	1.348	m
Magnet vacuum length (mechanical)	1.583	m

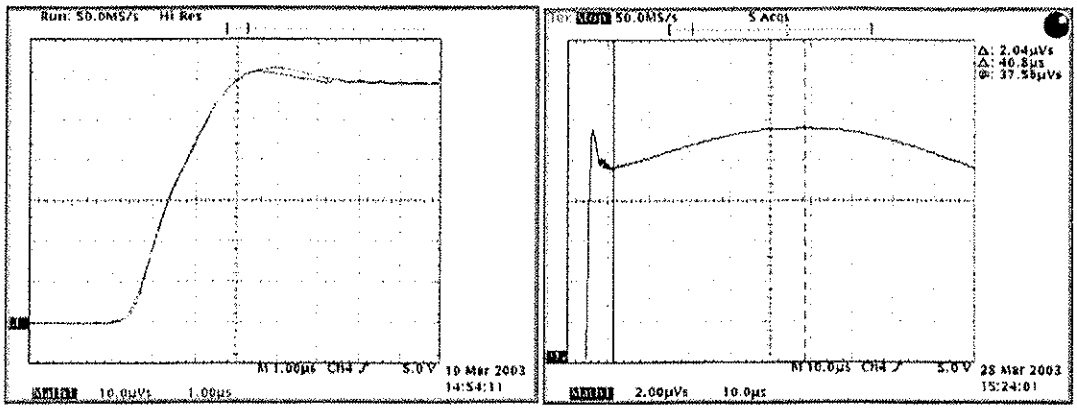

Figure 17.2: Start of MKD magnet current pulse at 450 GeV and 7 TeV with overshoots of 7.5% and 5.2% respectively (left); MKD magnet current pulse over 100 μs at 7 TeV with flat top overshoot of 5.6% (right).

The MKD magnets will consist of a steel yoke with a one-turn HV winding. A mechanical frame will surround the yoke for support and location of the individual components. A metallised ceramic chamber will be placed in the centre of the magnet. The cross-section of the MKD magnet is shown in Fig. 17.3. The service life of the magnets will be at least 20 years and during this period the magnets will be exposed to an estimated integrated radiation dose of 10^6 Gy (10^8 rad), which conditions the choice of materials. The magnet and its excitation coil can be opened horizontally in order to insert a ceramic vacuum chamber, with its two large vacuum flanges at both ends.

1. Insulation of high voltage coil
2. Conductor of high voltage coil
3. Ceramic vacuum chamber
4. C-core
5. Mechanical frame
6. Epoxy moulding

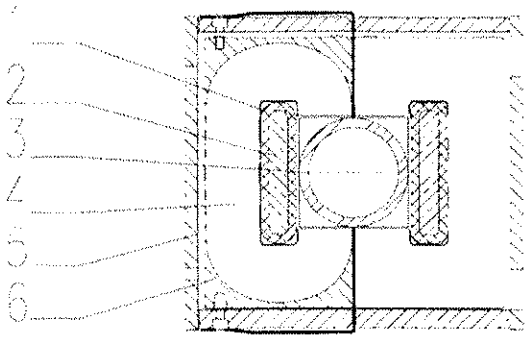

Figure 17.3: Cross-section of the MKD magnet

Yoke

The yoke will be composed of tape-wound C-shaped cores of thin gauge steel in continuous tape form, produced from a cold-rolled grain oriented silicon-iron alloy of at least 3% Si content. Once wound, heat-treated and vacuum impregnated, one leg of the core will be cut to create a gap. Short circuits between adjacent layers are then removed. Two C-cores with insulating sheets will be vacuum moulded in charged epoxy resin to provide mechanical stability and to allow mounting. During the assembly of a magnet, these individual assemblies will be stacked longitudinally.

Conductor

The one-turn coil will be composed of two insulated conductor bars of quasi-rectangular cross-section, with a minimum insulation thickness of 5 mm. The conductors will be made of high conductive electrolytic copper OFE, with hot-pressed mica tapes with a glass carrier and pre-impregnated with an electrically high-grade epoxy resin as insulation. This tape has excellent high voltage properties and adequate radiation resistance. The extremities of the conductors will be epoxy vacuum moulded using a dolomite charged epoxy compound. The surface of the insulation will be coated with a semi-conductive layer and connected to earth.

Vacuum Chamber

The magnets will be equipped with ceramic vacuum chambers, forming part of the vacuum system which will operate in the 10^{-11} mbar range. The ceramic chamber will be composed of a monolithic, isostatically pressed cylindrical Al_2O_3 tube. Fe-Ni-Co alloy sleeves with ceramic back-up rings will be brazed onto both ends of the ceramic tube and stainless steel Ultra High Vacuum (UHV) flanges welded to these sleeves. The total length of the brazed assembly will be 1583 mm. In order to maintain the impedance of the kicker magnets as low as possible [38, 39], the ceramic chamber will be coated on the inner surface of the tube with a thin sputtered titanium layer [41].

The 15 magnets will be divided into 3 vacuum sectors of 5 ceramic chambers each. This sectorisation, which requires 2 additional valves per MKD zone, will limit the extent of failures of the very fragile ceramic vacuum chambers in case of problems during the 24 hour bake-out at 150°C. During bake out the magnets will have to be opened to allow access to the ceramic chamber and installation of the heating jackets. The temperature rise and decrease will be limited to 20°C/h to avoid damaging the chambers.

The circulating beam will pass through a standard copper chamber (ID 80 mm, 2 mm thickness) coated with Non-Evaporable Getter (NEG) and baked up to 250°C. Two 60 l/s ion pumps per vacuum sector mounted on standard pumping ports will ensure the required pressure.

Generator

The generator will consist of a discharge capacitor in series with a solid-state switch operating at 30 kV [16]. In combination with a parallel diode stack, this generator produces the current pulse shown in Fig. 17.2. The circuit will be completed with a flat top current droop compensation network, consisting of a low voltage, low stray inductance, high current discharge capacitor.

For reliability reasons each generator will have a redundant second, parallel branch. The circuitry of the dual branch generator is shown in Fig. 17.4.

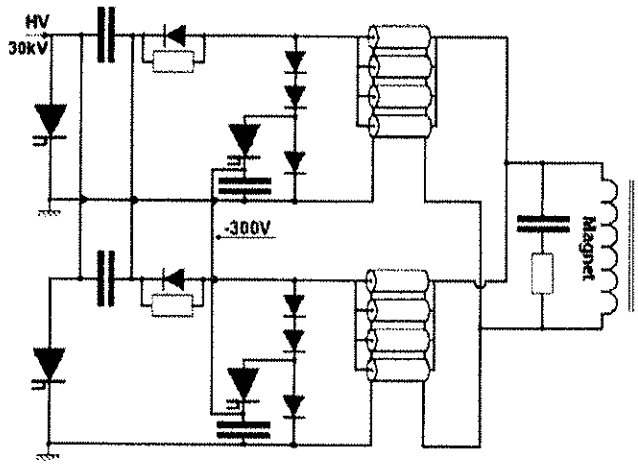

Figure 17.4: Dual branch generator circuit layout.

When both branches operate, each branch will supply only half the current, although in the event of a switch failure each branch will be capable of supplying the nominal current. Before each physics run both branches will be tested. If they are found to be working correctly, the probability that a magnet fails to pulse at the end of the physics run will thus be low enough to meet the reliability requirements.

The system is designed such that the expected failure behaviour of components should not cause a spontaneous trigger. Any spontaneous trigger will be detected using several detectors built into the generator on crucial points and a re-trigger will be immediately forwarded to the other 14 kicker magnet systems.

Due to the low level of the current in the dual main switch branches at 450 GeV (614 A) the anode delay of each switch will be almost 300 ns shorter than at 7 TeV. By decreasing the gate trigger voltage of the switch at 450 GeV, the turn-on speed will be reduced and synchronised with the turn-on at 7 TeV as shown in Fig. 17.2. This means that the voltage of the trigger unit has to be variable and will be a function of the beam energy.

After the magnet current has reached its full amplitude the polarity of the generator will inverse and the freewheel diode stacks, each consisting of two 13.5 kV multi-chip avalanche diodes and one very fast recovery 4.5 kV diode, will start to conduct the magnet current. Simultaneously the 2.5 kV FHCT switch, connected in series with a 3.25 mF, -300 V pre-charged low inductance (<200 nH) self-healing capacitor, will be closed and the current in the fast recovery diode commutated. The capacitor will then be connected in series with the magnet inductance and the current will oscillate with a superimposed half-sine wave. The initial capacitor voltage is determined so that it will compensate the resistive losses of the magnet current freewheel circuit.

The total stray inductance of each freewheel branch has to be kept very low (about 75 nH). This will limit the initial magnet current overshoot to 5.2% at beam energy of 7 TeV, which means a total system overshoot of about 7.5%, when all uncertainties such as charging voltage stability, temperature effects, interpolation errors, differences between generators etc. are included. At 450 GeV the dynamic current conduction and the sum of the threshold voltages of the freewheel diode branch will have a greater influence on the initial magnet current overshoot, which will increase to 7% (corresponding to a system total of 10%). There are two compensation circuits to minimise the magnetic field overshoot.

The generators will be air-insulated and only the capacitors will be impregnated with liquid dielectric. Therefore no significant amount of dielectric fluid will be present in the underground generator areas.

Transmission Lines

In order to respect the 2.85 μs rise time required for each individual magnet, the total inductance of the transmission line between magnet and generator should not exceed 250 nH. This will be achieved by connecting 19 m long, 18 Ω coaxial cables with an inductance of 104 nH/m, in parallel. In order not to influence the droop by more then 30%, the cable resistance will be kept to 3 mΩ. The inner conductor will be a Cu-tube with an outer diameter of 15 mm and a wall thickness of 1.5 mm. The dielectric will be low-density polyethylene of high purity with semi-conducting layers. A number of constraints are imposed on the design of the outer conductor, like low voltage drop between magnet and generator (<100 V), limited free-wheel droop of the current pulse and maximum temperature rise of the cable to about 30 K at a repetition period of 20 s. The outer conductor will comprise 74 spiral-wound Cu-wires of 1 mm diameter. To keep the circular wires in place and to improve the fire barrier, two layers of 40 μm wrapped Cu-foil will be applied over the spiral wires. The cable will be flame retardant and free from halogens and sulphur according to CERN Safety Instruction IS23. It can be exposed to an integrated radiation dose of at least 10^6 Gy without loss of performance. Simplified high voltage connectors that do not require moulding will terminate the cable ends.

Regular Maintenance

Regular maintenance will be concentrated on the generator side, mainly consisting of dust removal and contact cleaning. Regular control of the shape of the pulse will also be required.

17.3.2 Fast-Pulsed Dilution Magnets MKB

For each extracted beam, a set of four horizontal and six vertical dilution fast-pulsed magnets MKB will be used to sweep the beam along an "*e*"-shape path on the upstream face of the absorber graphite core, with a minimum velocity of 10 mm/μs during the dumping process. Each magnet will be sinusoidally powered by a pulse generator via a low impedance transmission line. Tab. 17.5 summarises the main parameters of the beam dump dilution kicker system.

The MKBH and MKBV magnets will be based on the same technology, using similar C-cores to the MKD, although no ceramic vacuum chamber will be required for the magnet which is installed directly in a vacuum tank.

Initially only 2 of each type of magnet will be constructed and installed on each extracted beam. The construction of the remaining staged equipment will take at least two years, installation not included and will be started at a later date.

Table 17.5: MKB System parameters

Horizontal diluter magnet system MKBH		
Number of magnets per system	4	
Max. system deflection angle	0.278	mrad
Kick strength per magnet	1.624	Tm
Magnet beam aperture – horizontal	58	mm
Magnet beam aperture – vertical	32	mm
Operating charging voltage	16.4	kV
Field rise time	18.9	μs
Field oscillating frequency	14.2	kHz
Effective length (magnetic)	1.936	m
Yoke length (mechanical)	1.899	m
Vacuum length (mechanical), 2 magnets	4.582	m
Vertical diluter magnet system MKBV		
Number of magnets per system	6	
Max. system deflection angle	0.277	mrad
Kick strength per magnet	1.077	Tm
Magnet beam aperture – horizontal	66	mm
Magnet beam aperture – vertical	36	mm
Operating charging voltage	22.3	kV
Field rise time	34	μs
Field oscillating frequency	12.7	kHz
Effective length (magnetic)	1.267	m
Yoke length (mechanical)	1.196	m
Vacuum length (mechanical), 2 magnets	4.076	m

The main elements of the horizontal MKBH circuit will be pre-charged oscillating capacitors coaxially connected to the magnets. The capacitors will be discharged through solid-state closing switches to produce an attenuated sinusoid. The vertical MKBV circuit will be more complex because it will require a current phase shift of 90° with respect to the horizontal system for a simultaneous trigger of the two systems.

Fig. 17.5 shows the attenuated discharge currents of both systems. The duration of the resulting "*e*"-shape beam spot, Fig. 17.6, corresponds to one revolution of the beam in the LHC.

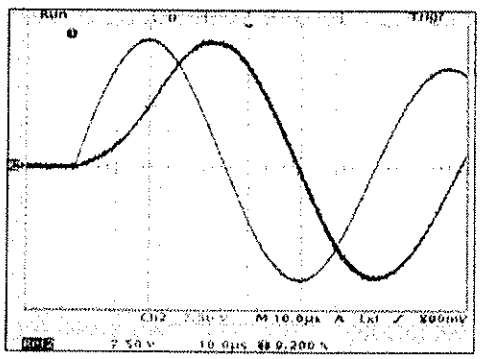

Figure 17.5: Discharge currents of horizontal and vertical (bold) generators (7.5 kA per vertical division).

Generator

The generators [17] will consist of a discharge capacitor in series with a solid state closing switch and completed by auxiliary circuits as shown in Fig. 17.7.

The MKBH system will comprise a pre-charged oscillating capacitor, CH, coaxially connected to the magnet inductance, LMH. The capacitor, CH, will be discharged through a solid state closing switch, SH. The discharge pulse will be an attenuated sinusoidal oscillation of 25 kA maximum amplitude with a period of 70 μs. The required damping coefficient of the magnet current is adjusted with the resistor RH.

The oscillation in the MKBV vertical magnet system is started by resonantly charging capacitor, CV2, from capacitor, CV1, via the fast solid-state closing switch, SV, diode, DV and charging inductance, LV. The resonant charging time is 26 μs. The circuit LMV-CV2 can then swing freely with attenuated oscillations.

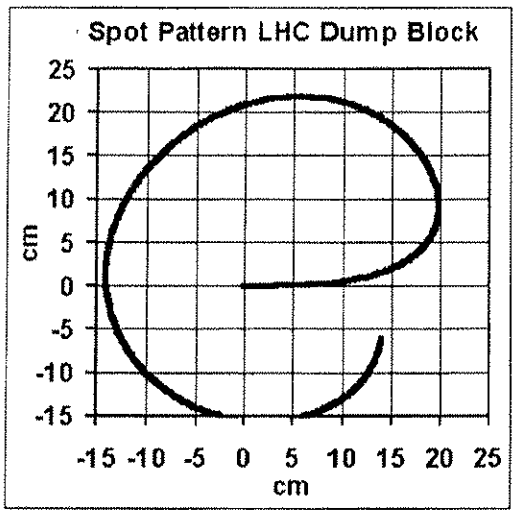

Figure 17.6: Beam spot figure on absorber block.

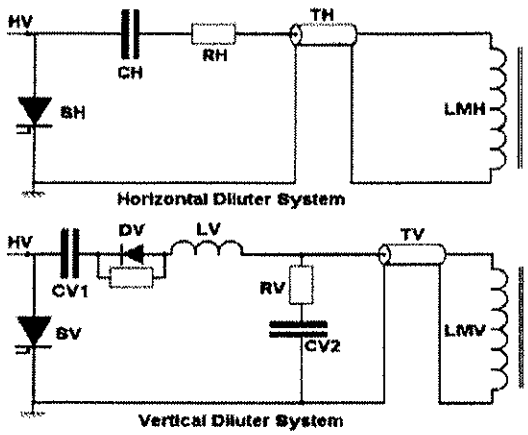

Figure 17.7: Basic circuit diagram for MKBH and MKBV systems.

The damping coefficient of the magnet current will be adjusted with the resistor, RV. The main advantage of the circuit of the MKBV system is the absence of a switch in the oscillation between CV2 and LMV. A current amplitude of 25 kA and a maximum hold off DC voltage of 27 kV will be required. The fast 30 kV solid-state switches, developed for the LHC beam extraction generator, will be used.

All switches and damping diodes will be mounted with grounded cathodes. This will permit the remote checking of the state of each complete stack of FHCTs and diodes by comparing the voltage over the first device at earth potential with the voltage of a separate divider over the complete stack.

Transmission Lines

The low inductive cable link between generators and magnets will use a specially developed coaxial cable. The construction mixes the inner conductor of an RG-220/U cable and the outer conductor of an RG-218/U with two braids of bare copper wires without joints. Each braid will have an optical coverage of 90 %. Two layers of PETP foil are wrapped between the braids. The dielectric is low-density polyethylene of high purity with semi-conducting layers. The cable is flame retardant and free from halogens and sulphur according to CERN Safety Instruction IS23 and must retain its performance after exposure to an integrated radiation dose of 10^6 Gy. Simplified high voltage connectors that do not require moulding will terminate the cable ends.

Regular Maintenance

Regular maintenance will be concentrated on the generator side, mainly consisting of dust removing and contact cleaning. Regular control of the shape of the pulse will also be required.

Vacuum System

The pumping of each tank will be ensured by two 400 l/s ion pumps. Two magnets will be installed per vacuum tank, with no bake out foreseen. The magnets, containing a non negligible amount of organic material, will outgas strongly and the large installed pumping speed (600 l/s effective) will allow operation in the 10^{-5} mbar range, to maximise the lifetime of the ion pumps in this potentially radioactive region.

Differential pumping will be installed between the extraction septa (MSD) and the diluters (MKB) to reduce the gas load onto the NEG coated chambers.

The two circulating beams will pass just below the MKB tanks and a permanent bake out will be installed to reduce personnel radiation exposure in case of intervention. The chambers will be standard copper chambers (ID 80 mm, 2 mm thickness) coated with NEG and baked up to 250°C. The chambers will be supported directly on the ground, independently from the MKB tanks.

17.3.3 Extraction Septum Magnets MSD

The 30 MSD septum magnets [18] will be laminated iron-dominated magnets built using an all welded construction. There will be 3 magnet types, MSDA, MSDB and MSDC, differing in the number of coil layers and the distance of the circulating beam hole from the pole. Transverse and longitudinal sections of the MSD magnet are shown below in Figs. 17.8 and 17.9. The installation of the magnet in the LHC tunnel will be complicated because the magnets will be placed back-to-back (Fig. 17.10). Moreover, access to the magnets for maintenance in the non-tunnel passage side will be limited by the cryogenic feed line (QRL), which will be near the connection box of the magnet. A modification to the connection box shown in Fig. 17.8 will be necessary to avoid an interference with the QRL in this region. The supply of the septum magnets is part of the CERN collaboration with IHEP (Protvino) in Russia. The main parameters of the magnets are shown in Tab. 17.6.

Table 17.6: The main parameters of the MSD magnets.

	MSDA	MSDB	MSDC	
Septum core length	4460	4460	4460	mm
Coil core length	4000	4000	4000	mm
Core width	447	447	447	mm
Core height	854	854	854	mm
Gap height	44	44	44	mm
Septum thickness	6	12	18	mm
Number of coil turns (total)	32	40	48	-
Number of coil layers	4	5	6	-
Number of turns per layer	8	8	8	-
Electrical coil resistance at 20 °C	27.1	33.9	40.7	mΩ
Inductance	36	56	79	mH
Dissipated power	22.7	28.3	34.0	kW
Water flow per coil	16.5	20.7	24.8	L/min
Coil water pressure drop	5	5	5	bar
Design current	880	880	880	A
Nominal magnetic field in the gap	0.80	0.99	1.17	T
Magnet weight	10500	10600	10700	kg

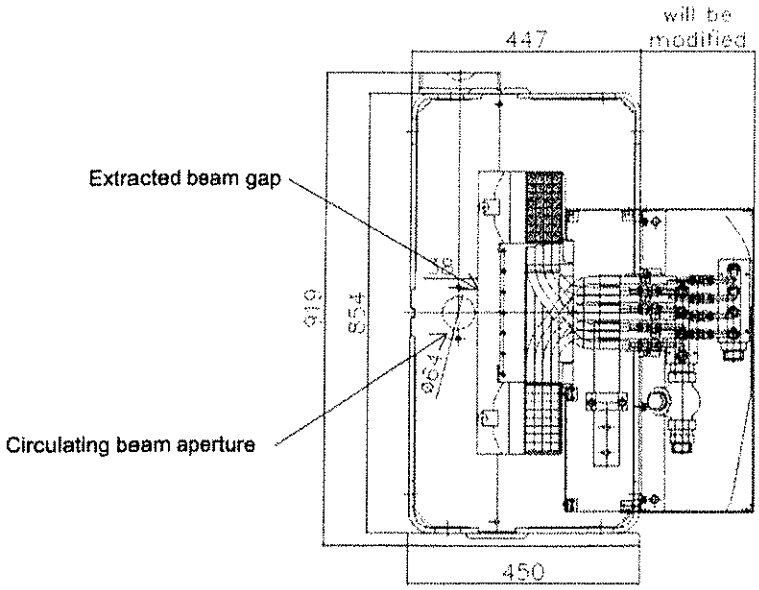

Figure 17.8: Connection end view of an MSIA magnet

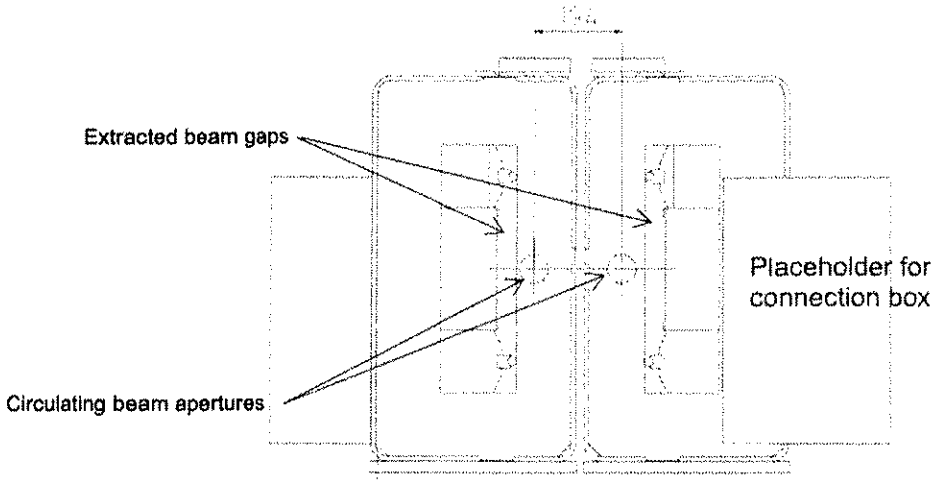

Figure 17.9: MSD in installed positions for Beam 1 and Beam 2.

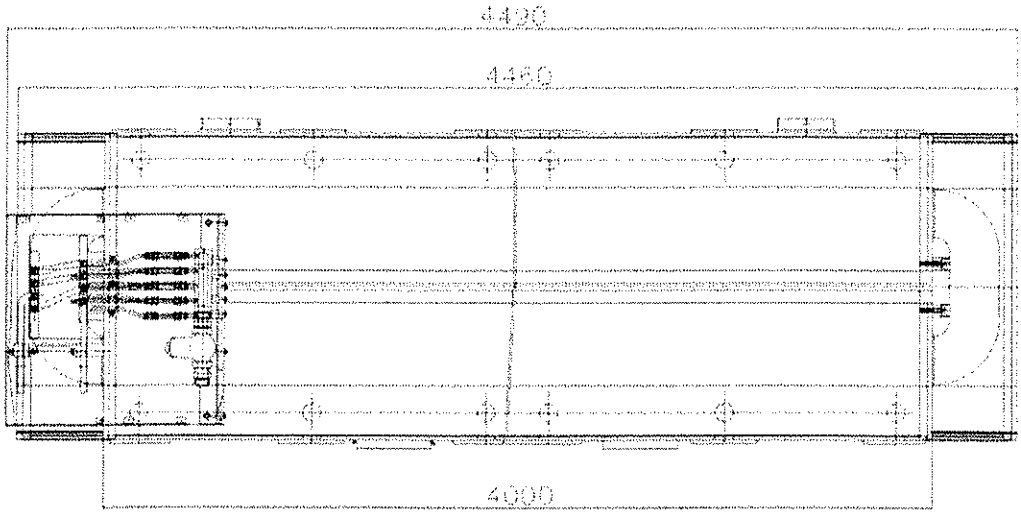

Figure 17.10: Side view of an MSDA magnet

Laminations

The laminations will be made of 1.0 ±0.02 mm steel, with a 10 μm thick Fe_3O_4 layer as electrical insulation, a maximum permeability of 4600±80 and a coercivity of 60±12 A/m. The circulating beam holes will be punched into the individual laminations, to avoid the careful alignment needed for wedge-shaped septum blades as used in classical Lambertson magnets.

Yoke

The yoke will be an all-welded construction made from two half-cores, the coil- and septum cores. The coil-core will contain the single pancake coil; the septum-core will contain the circular hole for the circulating beams. The septum core will be longer than the coil core in order to minimise the stray field extending from the field gap to the circulating beam holes. A μ-metal layer on the vacuum chamber will shield the beam from the residual field in the circulating beam hole [19], such that the residual field level will be lower than 0.5 Gauss.

Coil

The racetrack coils will be made from rectangular OFHC square copper conductor of 15×15 mm section, with a circular cooling hole 7.0 mm in diameter for the MSD. Each layer corresponds to one cooling circuit with a pressure drop of 5 bar and a temperature increase of 20°C. A 0.5 mm thick glass fibre tape, treated with amino silane, will be used as inter-turn and ground insulation. The vacuum impregnation of the coil will be made using radiation-hard epoxy resin. A thermo-switch will be placed to protect against cooling faults on each coil water outlet.

Vacuum and Alignment Issues

The vacuum system for the MSD magnets [20], similar to the one of the injection septa (MSI) described in 16.2.4, will have to fulfil several stringent requirements. With the septum beam hole diameter of 64 mm, the mechanical vacuum system tolerances including their alignment and the alignment of the magnet in general must be such as not to reduce significantly the available aperture. The circulating beams must be shielded against the stray field leaking from the core into the septum holes, which has a measured dipole component on the order of 10 Gauss [21]. The vacuum chambers for the circulating beams should be bakeable in situ (after installation) to 250°C without heating the magnet yokes to more than 120°C.

To fulfil these requirements, a vacuum chamber in 0.9 mm thick μ-metal will be used with a 0.5 mm copper coating [22,23] for impedance reasons. The compilation of all the constraints (magnet and chamber alignment tolerances, angle of tilt of the magnets, aperture requirements) gives an inner diameter (beam stay-clear) of 52.4 mm with a total wall thickness of 1.4 mm. The stray field in the shielded vacuum chamber will be of the order of 0.1 Gauss [24].

The μ-metal vacuum chambers equipped with the heating and insulating elements will be fitted at both ends with DN200CF flanges, welded after insertion in the magnet. The chambers will be centred using stainless steel rings. To reduce the outgassing rates of the vacuum chambers, a bake out at 250°C for at least 24 hours will be made [25]. This will use special heaters developed at CERN [26], which comprise a resistive stainless steel heating strip in the centre surrounded by two insulating polyimide films, wrapped around the tube with a total thickness of 0.3 mm. A reflective aluminised polyimide film will be wrapped on top of the bake out sandwich and special thermal insulation precautions are foreseen to reduce the heat load on the magnet yoke.

The copper coating of the inner surface of the μ-metal vacuum chamber will be made using the electrochemical deposition process. Due to the ~5 m length of the tubes, the deposition will be made using a fluid circulation electrolytic technique [22]. Finally, the circulating chambers will be NEG coated to improve the pressure and to avoid the electron cloud build up.

The extraction beam line chambers will be made from stainless steel with an inner diameter of 41 mm and a wall thickness of 1 mm. Alignment in the gap will be achieved by special form pieces along the gap and welded strips at the ends. The injection chambers will be baked at 85°C using the special sandwich heaters described above to minimise the outgassing flux onto the circulating chambers coated with NEG.

All the 450 mm inter-magnet gaps will be fitted with special modular pumping ports. These will be specific to each gap with a length of 300 mm, equipped with a 60 l/s ion pump to provide the required

differential pumping between the chambers for the circulating beams in the order of 10^{-11} mbar and the chambers for the extracted beam ~10^{-8} mbar, while permitting a reasonably fast exchange of a magnet in case of failure

17.3.4 TCDS Diluter

A fixed diluter block TCDS will be installed immediately upstream of the MSD septum magnets in order to protect them from destruction in the event of an asynchronous firing of the MKD kickers [12, 14]. The TCDS must intercept about 40 LHC bunches (1.7% of the beam) containing about 6.1 MJ of energy and must provide enough dilution such that the temperature in the MSD vacuum chambers does not exceed 300°C and so that the temperature in the MSD yoke does not exceed 100°C.

Several scenarios have been studied [26] for the configuration of the TCDS and a 6m long wedge shaped model has been chosen to optimise the aperture for the extracted beam and to provide adequate protection for the MSD magnets, with a sandwich construction of 1m Graphite (1.77 g/cm^3), 2m C-C composite (1.4 g/cm^3), 1.5m Graphite (1.77 g/cm^3), 1m Aluminium nitride (3.31 g/cm^3) and 0.5m Titanium (4.5 g/cm^3).

A parallel row of diluter blocks, the outer jaw, giving a clear aperture of 30mm, are also envisaged to protect the MSD magnets from bunches with large excursions to the outside. Figure 1. 17.11 shows a schematic of the layout and function of the TCDS absorber system.

The RF heating due to circulating beam will result in a power deposition estimated at about 40W/m. A 1 kW water cooling system is designed to absorb this power. Temperature sensors, flow-meters and temperature gauges for the cooling system will be required.

The diluter and surroundings will be subject to irradiation by protons or heavy ions. The estimated contact radiation dose levels after an asynchronous dump and a cooling period of 1 day reach 3mSv/h. After a cooling period of 30 days these radiation dose levels are estimated to go down to a level of 0.035mSv/h [12].

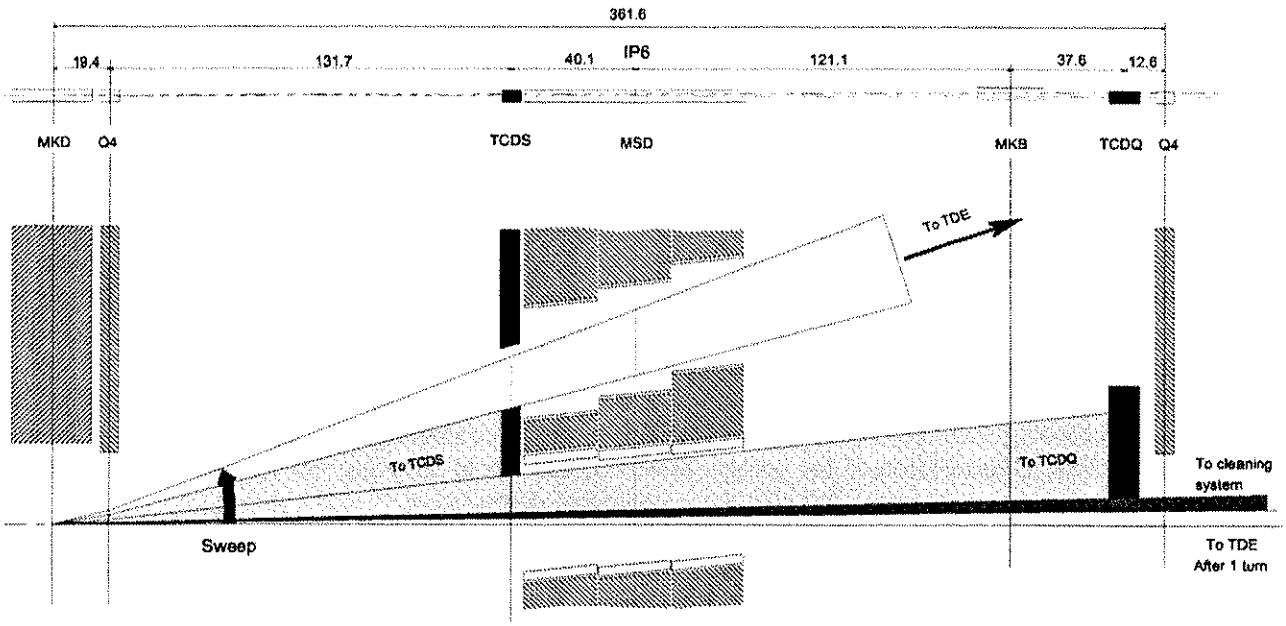

Figure 17.11: Schematic and functional layout of TCDS and TCDQ diluter systems.

Vacuum

The beam gas scattering and the operating pressure in the TCDS must be kept small for beam lifetime issues and also to avoid the saturation of the adjacent NEG coated chambers. Two 400 l/s ion pumps and two 1000 l/s Ti sublimation pumps will provide an effective pumping speed of 1600 l/s. The expected residual pressure inside the beam screen will be 10^{-8} mbar during normal operation after a 24 hour in situ bake out at 250°.

Prior to mounting, the graphite and Carbon-Carbon materials must undergo a heat treatment at 1000°C under vacuum. After installation and any intervention, the tanks will be baked out at 250°C using heating jackets. The vacuum system has been design to cope with the outgassing during normal operation, i.e. with

the jaws between 20 and 35°C. For a temperature increase of 50°C the thermal outgassing increases by a factor of 10 to a point where the gas density levels will be too high for the required beam lifetime.

17.3.5 TCDQ Diluter

In the event of a beam dump that is not synchronised with the abort gap, or after an asynchronous firing of MKD kickers, a part of the beam will not be absorbed by the TCDS and could impact on the Q4 coils [13]. In order to protect these magnets against damage a mobile diluter block TCDQ will be installed immediately upstream of Q4. The TCDQ will also protect the downstream arc at 450 GeV and low β insertion triplets at 7 TeV and will reduce the number of bunches impacting on the LHC collimators [12].

The preliminary TCDQ design is based on nuclear simulations, with 8m of graphite (1.77g/cm^3) followed by 1.5m Aluminium (2.6g/cm^3). The required jaw width was found to be 40 mm. A single jaw configuration will fulfil the protection objectives although for machine protection issues and orbit control, an additional short two-sided collimator may be considered.

The TCDQ will be mobile, to guarantee the nominal setting of 10±0.5σ at injection (450GeV) as well as collision (7TeV). The TCDQ will be at a phase advance of 87° from the MKD kicker magnets. Precise control of the orbit at the TCDQ will be very important to ensure correct protection of the downstream machine elements. A movement of about 30 mm will be required, with a resolution of below 100 μm.

The vacuum considerations are identical to those described above for the TCDS.

17.3.6 Beam Dump Absorber Block TDE

For each ring, the LHC beam dumping system will direct the extracted and diluted beams onto an external beam dump TDE [28]. Approximately 2×10^4 beam aborts at 7TeV and full beam intensity are assumed during an operational lifetime of 20 years. As the TDEs will be permanent fixtures of the accelerator, the LHC ultimate beam intensity (4.69×10^{14} protons per beam) was considered as the reference load case in the design study. Under this ultimate load, about 80% of the corresponding total beam energy (i.e. 428 MJ out of 534 MJ) must be safely absorbed into the dump core. For safety reasons the core must be solid and it must keep its structural integrity under normal operating conditions over the dump lifetime.

TDE Core Design

The TDE design [40] has been substantiated by Monte Carlo energy deposition simulations [29], heat transfer analyses [30] and the structural assessment of the off-normal operating conditions [31]. Carbon was chosen as the most suitable absorbing material for the LHC main beam dump, with highest melting (sublimation) temperature and best thermal shock resistance of the investigated materials.

Localised fracture in the graphite core will not be a concern for the absorber block, as the dump will not lose its absorbing function: fractured graphite will continue to intercept the incident particles exactly as solid graphite does. Optimisation of the design, however, has led to adopting the very conservative constraint of avoiding not only any thermal, but also any mechanical degradation.

Based on numerical analyses, the ambitious goal of preventing fracture within the carbon core can been achieved by carefully selecting the grades of carbon material. The absorber block will be made of consecutive Polycrystalline Graphite (PG) cylinders with 1.73 g/cm^3 density and Flexible Graphite (FG) plates with 1.1 g/cm^3 density. A 0.7 m long section of PG will be followed by 3.5 m of FG and again by 3.5 m of PG. The maximum temperature increase will be limited to 1250 °C in the FG and to less than 1050 °C in the PG [31] under normal beam dilution conditions at ultimate beam intensity.

Based on these requirements, each beam dump core was designed as a segmented carbon cylinder of 700 mm diameter and 7700 mm length, shrink-fitted in a stainless steel jacket (Fig. 17.12). The jacket will incorporate welded tubes for cooling water. The core assembly will be connected upstream to the beam dumping line by a DN700 quick-disconnect flange, while a leak-tight titanium window will close the downstream end.

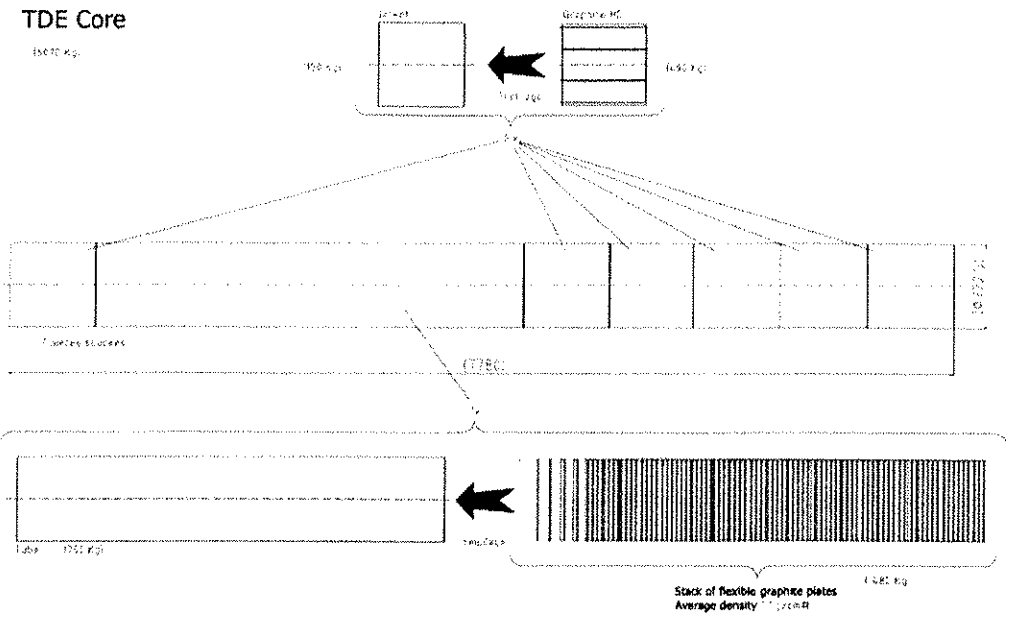

Figure 17.12: Side view of the TDE core.

Shielding

Each dump will be surrounded by ~900 tons of radiation shielding blocks, which have been constructed using decommissioned ISR dipole-yokes, partially filled with concrete [32]. Each block is 1298×1088×2440 mm and weights 24 tons. Thirty-five blocks in total are required per dump, Fig. 17.13.

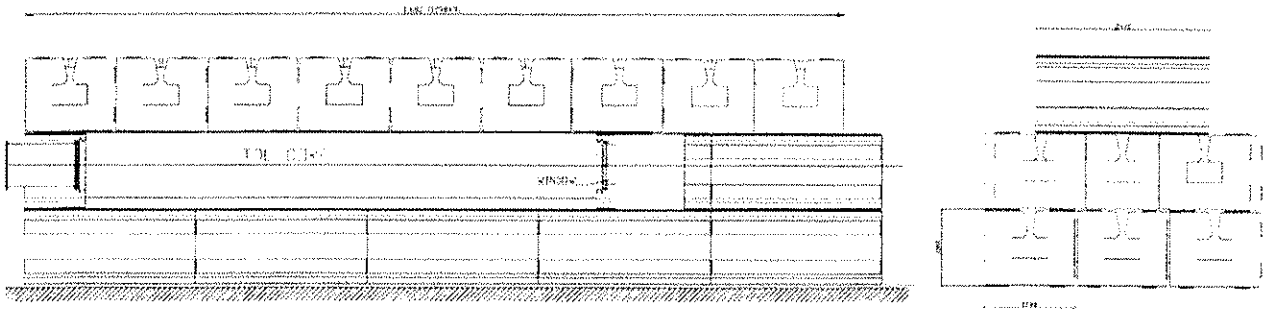

Figure 17.13: Installed TDE core and shielding blocks.

Water Cooling

The dump core has been designed to be actively water-cooled and the core will be equipped with the cooling tubes, but the external cooling circuit will be implemented at a later date as part of the staged equipment. During LHC commissioning, therefore, thermal inertia, conduction and natural convection will define the temperature evolution of the TDE, which will be permanently monitored. The most sensitive elements of the TDE will be the helicoflex joints of its end-flanges. If the temperature approaches the maximum allowable temperature (250°C), an interlock will prevent further operation of the LHC.

Steel Jacket

The steel jacket will be made of a duplex stainless steel tube Ø724/700×710 mm, which will be shrink fitted onto a polycrystalline graphite cylinder Ø700×700 mm. The jacket's functions are: *1)* to provide a beneficial pre-stress; *2)* to better disperse the energy of stress waves; *3)* to protect the lateral surface of polycrystalline graphite; and *4)* to build a vacuum tight containment for the carbon core. Six of these sections

(also called *segments*) will be needed for the 7.7 m-long dump core. In the remaining 3.5 m-long section containing flexible graphite no shrink-fit will be possible. A steel tube Ø724/700×3500 mm will nevertheless be used, which will act as a container for a Ø700×3500 volume of the low-density carbon, providing the necessary mechanical rigidity and ensuring stable shape and dimensions.

Failures

Under almost all conditions and fault scenarios the structure of the graphite block and its concentric steel jacket will remain intact. The 700 mm diameter dump is designed to accept a total offset (misalignment) of the diluted beam of ±50 mm. An optical transition radiation (OTR) beam monitor located in front of the dump [33] will detect off-normal dilutions. Only if the beam was kicked very badly and exceeded the alignment limit, could the steel jacket be damaged. If the risk of this failure mode is found to be non-negligible, a sacrificial absorber placed some distance upstream of the dump and outside the beam pipe could be implemented as a safety upgrade to deal with this scenario.

In case of a total dilution failure (no active dilution kicker), the downstream window of the dump could be penetrated when operating with normal or ultimate beam intensities. From detailed numerical analysis, the central graphite blocks will fail extensively due to tensile unloading. In addition, the graphite density will reduce considerably due to vaporisation along the core axis. However, this failure will remain laterally contained within the steel jacket, with only a negligible amount of graphite material failure in the upstream segment, which will not suffer complete perforation from either mechanical failure or phase transition. The consequences of such a total dilution failure will not, therefore, be catastrophic for the LHC or its environment.

Containment

The initial dump design was based on a vacuum-tight core operating under high vacuum. However, if a massive air entry were to occur in the 6 minutes following a high intensity dump, the graphite could burn releasing a thermal power of up to 2 MW. To avoid this risk, the option of permanently filling the dump with an inert gas with sufficient supply to stop a fire will be implemented. The window at the end of the extraction line, before the dump block, will be able to withstand this differential pressure and the gas pressure in the TDE will be slightly above atmospheric. Monitoring connected to the machine interlock system will dump the beam (or inhibit injection) if the pressure begins to drop and simultaneously cut the ventilation in the beam dump cavern affected.

Activation

From the radiological viewpoint, total activities in different parts of the dump, activities in the surrounding air, rock and ground water, dose-rates close to the core and different parts of the dump have been estimated [40]. For general access to the dump-caverns with all the dump-shielding in position, total dose-rates from all sources (dump, air and walls) will be at relatively low levels. Only 1 hour after dumping the beam, the dose-rates will be typically below 300 μSv/h. However, most of this will be due to the ^{24}Na in the concrete shielding and walls, so allowing several days for this to decay would be preferable. The dismantling of the dump to exchange the core will require strict control and remote handling.

17.3.7 Special Vacuum Systems

The vacuum system for the two beam dump lines TD62 and TD68 between the MKB and TDE, each about 630 metres in length, is described in Chap. 12 of this report.

17.3.8 Beam Instrumentation

The beam instrumentation of the dump extraction lines [34] must ensure that the relevant characteristics of the extracted beam and its impact on the machine components can be properly determined and also must allow correct setting up and commissioning of the extraction system with beam.

The position of the extracted beam must be adjusted inside the extraction channel to ensure the best possible transmission efficiency to the dump block. Beam profile (BTV) and position (BPM) monitors will

be placed at strategic positions around the extraction septa, after the dilution kickers and in front of the dump block to monitor the trajectory along the entire path of the beam. Commissioning will be performed using both profile and position monitors, while for high intensities most of the profile monitors must be retracted (with the exception of the monitor in front of the dump block) to avoid damage due to the large amount of energy deposited.

Beam loss monitors (BLM) [45] will be installed around the septa and along the extraction line to monitor the quality of the extraction and localise aperture restrictions. The loss monitors are mainly concentrated near known aperture limitations.

Two redundant beam current transformers (BCT) will be used to cross-check the intensity of the extracted beam with respect to the circulating beam before dump extraction. The accuracy of the cross calibration is expected to be in the range of 1-2% for nominal filling, which should be sufficient to prove that the beam was indeed correctly extracted from the ring. Due to the limited accuracy of the BCTs, beam loss recordings over the last machine turn and in the extracted channel must be used to verify that the dump action was clean.

An undiluted beam could damage the dump block. It will therefore be mandatory to determine the sweep trace of the beam on the front face of the dump block. The sweep must be recorded by a very large profile monitor in front of the dump block. High resolution will not be critical since no attempt will be made to measure the beam sizes, only the trace of the beam produced by the dilution kickers must be monitored. For redundancy, the bunch-by-bunch position measured by a BPM installed a few meters downstream of the dilution kickers could be used to verify the correct functioning of the dilution kickers.

To ensure clean dumps without losses in the extraction channel, the circulating beam position should not deviate from its nominal position at the MKD kicker and MSD septum by more than 4 mm. To enforce this tolerance under all circumstances, 4 dedicated BPMs will be installed on the IR side of the Q4 quadrupoles (2 per quadrupole and per beam). These BPMs will be dedicated to a position interlock system that will monitor the position on a bunch by bunch and turn by turn basis and which will dump the beam if the threshold is reached.

Finally, all beam instruments must provide post-mortem data. This data must be analyzed to establish that dump action was performed correctly before any beam can be re-injected into the ring and in addition the dumped beam intensity will be logged.

17.3.9 Equipment State Control

The MKD state control entity will be based on a SIEMENS S7-400-F master Programmable Logic Controller (PLC), which interfaces 15 independent PROFISAFE sub-segments through a single PROFISAFE master segment. Each sub-segment will be attached to a single high voltage generator and will be controlled by a SIEMENS S7-315-F slave PLC. The interface between PROFISAFE segments will be based on PROFIBUS DP/DP couplers.

Failsafe PLC technologies will be used to ensure that any failures, hardware or software, occurring in the state control entity will generate a dump request. The state control entity will be in conformity with IEC 61508 International standard for electrical/electronics/programmable electronics safety related systems.

The master PLC will use the Ethernet TCP/IP network for communication with the application layer, but the design will be such that failures in the application layer and Ethernet network will not compromise the safety of the operational behaviour.

The state control entity will be responsible for the control of equipment state (ON, OFF, STANDBY...), the surveillance of the FHCT switches, the generation of the kick strength reference voltage accordingly to the beam energy and personnel safety aspects of the installation. Typical response times will be ~5 ms.

17.3.10 Synchronisation, Trigger and Re-trigger Control

Dump requests will come from different sources including the machine protection system for emergencies, the machine timing system for scheduled dumps and the LBDS itself for internal failures.

The LHC revolution frequency pulse train will have a fixed phase offset relative to the abort gap in the circulating beam and this will be used to synchronise spontaneous requests with the abort gap. Once synchronised, dump requests will be distributed to the power trigger system (PTS) for firing of the kicker

pulse generators. In addition, a re-trigger system (RTS) will be used to increase reliability and protect the machine against spontaneous firing.

The beam dump triggering system will be based on a redundant fail-safe logic [10] up to the beam abort gap synchronisation unit and then on a redundant fault tolerant system up to the high voltage generator power trigger unit, in order to avoid asynchronous beam dumps.

Synchronisation

Locked to the LHC revolution frequency, two independent quartz controlled oscillators (QCO) will continuously produce dump trigger pulses synchronised with the gap in the circulating beam. The distribution of these pulse trains will be inhibited until a beam dump is requested. The pulses which pass the inhibit stage will be then sent via a fan-out system to all power trigger modules. In this way the first pulse after the reception of a dump request will synchronously trigger the system. The time of flight of the circulating beam through the magnets, as well as electronic and high voltage turn-on delays, will be compensated for each kicker magnet individually with the trigger distribution cables.

In case the revolution frequency pulse train is lost for more than one turn, an internally synchronised direct digital synthesiser (DDS), precisely locked on the revolution frequency, will issue a dump trigger, which is still synchronous with the particle free gap in the circulating beam. This mechanism reduces the probability of non-synchronised dumps to almost zero. If the synchronisation of only one of the oscillators fails, a synchronous dump trigger is forced by the redundant system.

In addition, any dump request also generates a dump trigger, delayed by just over one turn, via the re-trigger system to the power trigger modules. This third trigger path guarantees that at least an asynchronous beam dump is initiated, even when both principle systems fail. It has to be mentioned that in the case of spontaneous firing of one of the generators no synchronisation is possible.

The duration of the particle free gap is 3.0 μs and just covers the rise of the magnetic field in the magnets. The tolerance available for the synchronisation at the extraction kicker will be approximately 100 ns. Any delay or jitter in the transmission of the revolution frequency therefore has severe consequences for the synchronisation of the extraction process. For that reason it will be necessary to verify continuously the phase between each revolution frequency pulse and the structure of the circulating beam.

Re-triggering

The main task of the re-triggering system (RTS) will be to immediately re-distribute a trigger request issued from a spontaneous firing of one generator to the remaining 14 generators.

A redundant chained input/output system has been chosen for the RTS. Each pulse generator will have several re-trigger source sensors with enough powering capabilities to trigger all power trigger modules of the other 14 high voltage generators. Due to the architecture of the system, an avalanche mechanism is started after a detection of a spontaneous firing. Since there is no stored energy in the system itself it is difficult to create spurious triggers, neither can a disconnected cable nor a defective trigger source cause triggers. The typical reaction time between detection of a spontaneous firing of one pulse generator and re-triggering of the 14 other generators is 700 ns for energies above 3 TeV.

Trigger

The normal trigger distribution system will be based on two redundant fan-out units triggered independently. The output driver circuit of each fan-out unit will be based on a blocking oscillator circuit with one primary input for 30 circuit secondary outputs.

The dump request distribution will be based on redundant chains of stages using the "domino effect" strategy to trigger the next stage in the chain. The energy required to propagate the trigger request up to the kicker high voltage generator will be stored within capacitors at each stage of the triggering chain. This energy will be used to trigger the next stage of the chain and its level is checked before a beam permit signal is issued.

17.4 PERFORMANCE AND OPERATIONAL ASPECTS

17.4.1 Controls Issues

Triggering and Internal Monitoring

The external signals such as beam loss monitors, quench detectors etc. which can generate a beam dump trigger are listed in Section 15.5. These signals will trigger the Beam Interlock System which will then pass on the dump request. In addition the beam dumping system will continuously monitor its own status [35] and will trigger a synchronous dump if one of the following faults is detected:

- Error in the energy tracking of the MKD, MKB or MSD;
- Beam Energy meter: inconsistency between the two branches;
- Incoherence of one of the two synchronisation systems with the Radio-Frequency system;
- Out of specification of vacuum of the TD lines, overpressure of TDE, or high temperature of TDE;
- Temperature of the absorbers TCDS, TCDQ too high;
- Fault in the water flow of the different cooling circuits;
- Incorrect general status of the beam dumping system (status of the power converters, slow controls, Programmable Logic Controllers).

Post-mortem

A system post-mortem will have to be performed after every beam dump. It is planned that at least the following signals will be recorded and an automated comparison made relative to reference signals:

- Shape of figure on the beam dump block;
- Beam position on pick-ups in TD dump line;
- All MKD and MKB current wave forms;
- Check of redundancy of circuit paths: they should all carry current;
- Comparison of circulating beam currents and current in TD dump lines;
- Radiation levels in the beam dumping system elements (check synchronisation) and behind the TDE block.

After every beam dump the system will pass from a 'ready' state to a 'not ready' state. Only after successfully passing the post mortem tests described above can the system status pass back to 'ready'. The time necessary for the beam dumping system to perform the internal post-mortem analysis is expected to be shorter than 10 seconds.

An 'external post-mortem' will also take place at every beam dump. It should identify the source of the beam dump request and log certain key machine parameters before, during and just after each beam dump request. The time stamp of the beam dump request as generated by the Beam Interlock System will be compared with the time stamp of the beam dump request as received by the beam dumping system.

Logging

Like many other signals in the machine, a number of beam dump signals will be logged continuously:

- Voltages of the different circuits of the MKD and MKB generators;
- Currents in the MSD septa;
- Different temperatures and pressures of the system;
- Beam instrumentation data (profile on the TDE, dumped intensity, ...).

17.4.2 Apertures

The MSD septa and TCDS diluter will be aperture limiting elements for both the circulating and extracted beams. The layout of the TCDS and MSDC vacuum chamber have been optimised [9] according to the allowed LHC beam parameters (Tab. 17.1) and the allowed beam dumping system failure modes (Sec. 17.4.8). The MSD chambers must be shielded by the TCDS in the event of an unsynchronised MKD pre-trigger, which constrains the possible positions of these elements. The maximum aperture for the overall

system (considering the circulating plus extracted beam) is obtained with the TCDS positioned as close as possible to the circulating beam axis.

Circulating Beam Aperture

With a ±4 mm orbit, the nominal TCDS position (upstream) will be set to +16.3 mm, which corresponds to an acceptable *n1* [36] of 6.5. At the MSDC the aperture in terms of *n1* will be 6.9. The plots of available aperture versus orbit at the upstream end of TCDS and the downstream end of the MSDC5 vacuum chamber are shown in Fig. 17.14 for the limiting 450 GeV beam.

Extracted Beam Aperture

For the extracted beam aperture calculation the total overshoot of the MKD kicker waveform is taken to be 10%. For the nominal case with all 15 MKD kickers pulsing correctly, the extracted beam will be centred in the septum gap. The same kick of 0.27 mrad will be imposed from 450 GeV to 7 TeV beam energy, which will ease setting up, post-mortem and energy-tracking. The available aperture at 450 GeV and 7 TeV as a function of orbit is shown in Fig. 17.15. Assuming that for 'loss free' extraction an aperture of 4σ will be sufficient at 450 GeV and 6σ at 7 TeV, the orbit should stay within about ±4 mm and ±7.3 mm, respectively. The control of the orbit in point 6 to better than ±2 mm will be achieved using a feedback system and will provide an essential operational margin in the event of failures.

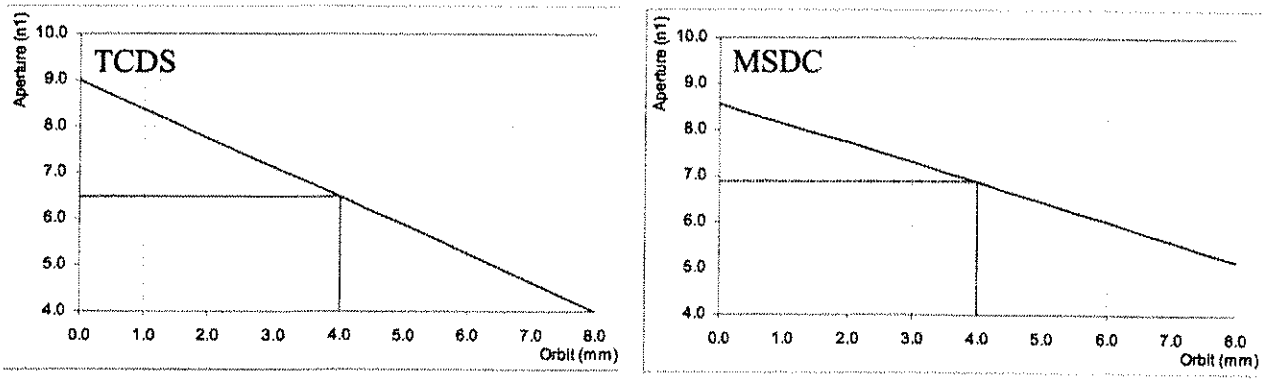

Figure 17.14: Aperture in *n1* at TCDS and MSDC5 for circulating beam as a function of local horizontal closed orbit excursion (±4 mm vertical orbit assumed) for the limiting 450 GeV beam.

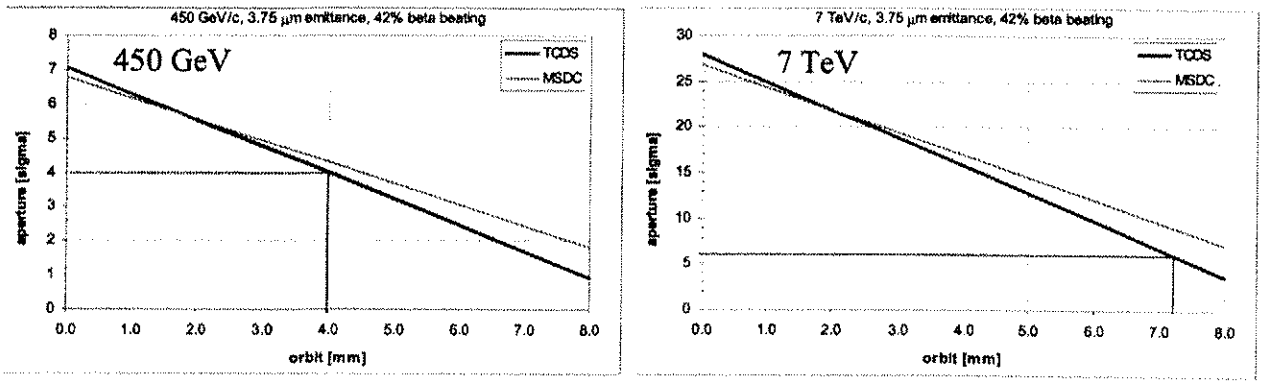

Figure 17.15: Aperture in beam □ at 450 GeV and 7TeV for extracted beam as a function of the orbit in the nominal 15/15 MKD case.

An allowed failure case is where one of the MKD magnets does not pulse. The worst of these modules to miss firing will be MKD1; in this case the effective deflection at the TCDS will be 91.96% of the total and the beam will approach the TCDS. The available apertures at 450 GeV and 7 TeV as a function of orbit are shown in Fig. 17.16. At 450 GeV, even for moderate orbit excursions, the TCDS will receive some beam, with the attendant risk of quenches in downstream superconducting magnets.

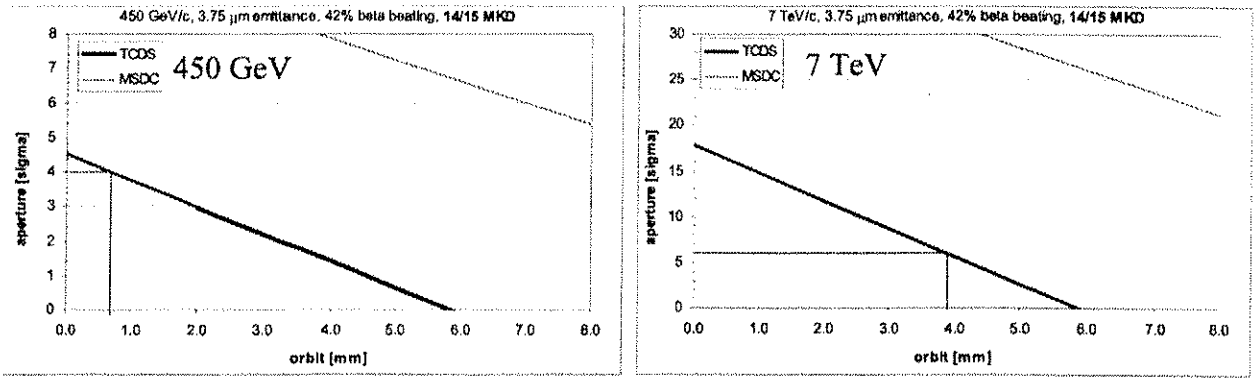

Figure 17.16: Aperture in beam σ at 450 GeV and 7TeV for extracted beam as a function of the orbit in the 14/15 MKD case.

For normal operation, with realistic failure cases, orbit excursions of up to ±4 mm should be tolerable without damage to any elements, up to nominal intensities. In addition, emittance increases of ×2 / ×4 will not result in equipment damage at 450GeV / 7TeV respectively. However, these may produce Q4 quenches at low energy for large orbit excursions. The 14/15 MKD case will produce losses on the TCDS and Q4 quenches but should not result in damage, again provided the orbit is held to better than ±4 mm. To ensure that the dumping system can safely extract the beam, reliable interlocking of the local beam position at a level of ±4 mm in point 6 will be absolutely necessary. The required response time of this interlock and the exact threshold margin will depend on the maximum rate at which the beam will move after an LHC fault, which has been shown to be ~60 μm per turn [37].

17.5 SPECIFIC REQUIREMENTS PLACED ON OTHER MACHINE SYSTEMS

Many of the following items have already been treated in the above; here a summary is given of the specific requirements placed on other LHC machine systems by the beam dumping system, apart from the general services which are not considered here.

- Powering (MSD powering): the MSD current must follow the LHC energy with a tolerance of 0.5%;
- Radio-Frequency (synchronisation): the beam dumping synchronisation will rely on a revolution frequency signal for each beam from the RF system; if this signal is interrupted the beams will be dumped immediately after a few turns using an internally generated synchronisation which will stay in phase with the abort gap;
- RF (abort gap cleaning): the abort gap should be as free as possible of spurious particles in order to minimise the activation of the TCDS, TCDQ and collimators during regular dump actions. If the abort gap population becomes too high, a normal dump could result in a Q4 quench, which is unacceptable from an availability viewpoint. The abort gap population must therefore be kept below 0.3×10^7 protons per m [44] which will require active cleaning using the damper [42];
- Controls (settings, alarms, timing, post-mortem and logging): the logging and post-mortem will be essential to provide the assurance that dump actions have been correctly executed. The relevant data must be available to enable the beam permit;
- Safety (fire detection, access zoning, emergency stops): the availability of standard safety systems will be required for tests and conditioning. In the case of the emergency stop system, it is clear that the beam dump action must be triggered before any power supplies are cut;
- Collimators: there will be a fundamental interdependence of the TCDQ settings with LHC collimation system settings [43], since the TCDQ must be positioned so as to reduce the number of bunches impacting the primary collimators in the event of an asynchronous dump and also because in the planned second phase of the collimation system, the TCDQ must act as a tertiary collimator and completely protect the metallic secondary collimators;

- Machine protection (beam permit): the Beam Interlock System will pass on a dump request generated by other critical systems such as the beam loss monitoring. To ensure the required reliability level for the beam dumping system as a whole, the Beam Interlock System must also meet stringent requirements, concerning the correct transmission of the dump request and its internal status;
- LHC magnets: the tolerance on the Q4 current will be about 1% and for the MSD about 0.5% - beyond these limits an abort signal should be generated. The detection of a short-circuit between MSD coils may require an additional protection, e.g. based on voltage surveillance;
- Localised orbit feedback and position interlock: the beam position in IR 6 should be stabilised to ±2 mm using orbit feedback and a separate interlock system must dump the beam if the orbit exceeds ±4 mm.

REFERENCES

[1] A.Verdier, The LHC IR6 optics, LHC-PROJECT-NOTE-146; 29 Jun 1998.
[2] B.Goddard et al., LHC beam dumping system : Extraction channel layout and acceptance, CERN-LHC-Project-Report-654, 2003.
[3] B.Goddard, http://proj-lbds.web.cern.ch/proj-lbds/parameters/TCD_I_S_Q_load_summary.pdf.
[4] L.Bruno, S.Perraire, Design Studies of the LHC beam dump, CERN-LHC-Project-Report-306, 1999.
[5] J.H.Dieperink, Reliability of the LHC beam dump kicker magnets, presentation in Machine Protection Working Group, CERN, 12 April 2002.
[6] J.H.Dieperink et. al., Design aspects related to the reliability of the LHC beam dump kicker systems, LHC Project Report 113, 1997.
[7] E.Carlier, Information exchange between beam dumping system and other systems, CERN-SL-2001-003
[8] R.Schmidt, Energy tracking for beam dump and other users, presentation in Machine Protection Working Group, CERN, 2 February 2002.
[9] B.Goddard, M.Gyr, The Aperture and Layout of the LHC Extraction Septa and TCDS Diluter with an Enlarged MSDC Vacuum Chamber, CERN-LHC-PROJECT-NOTE-320, 2003.
[10] M.Rampl, Study for a failsafe trigger generation system for the Large Hadron Collider beam dump kicker magnets, CERN-THESIS-99-056
[11] E.Vossenberg, Modular solid-state switch for the SPS and LHC beam dump systems, CERN, 2001
[12] W.Weterings et al., TCDS diluter to protect MSD septum magnets ,LHC-TCDS-ES-0001 rev 0.1, (393973), 2003.
[13] A.I.Drozhdin et al., Status of studies on protecting LHC components against radiation resulting from an unsynchronised beam abort, Fermilab Project Note FN-0724, 2002.
[14] R.Assmann et al., The consequences of abnormal beam dump actions on the LHC collimation system, LHC-PROJECT-NOTE-293, 2002.
[15] F.Balda, Risk Assessment and Safety Integrity Level, presentation in Machine Protection Working Group, CERN, 14 December 2001.
[16] L.Ducimetiere et al., Improved Turn-on Characteristics of Fast High Current Thyristors, CERN-LHC-Project-Report-260, 1999.
[17] E.Vossenberg et al., A high current sinusoidal pulse generator for the diluter magnets of the LHC beam dump system, Geneva : CERN, 2001.
[18] S.Bidon et al., Steel septum magnets for the LHC beam injection and extraction, CERN-SL-2002-019-MS, 2002.
[19] M.Gyr, Estimated residual Magnetic Field acting on the Circulating Beam in the LHC Septum Magnets MSI and MSD - Shielding Efficiency MLHC-PROJECT-NOTE-212, 2000.
[20] J.M. Jimenez, B. Henrist, "Vacuum chamber for the circulating beams in the LHC injection and extraction septa", under approval (EDMS)
[21] D.Cornuet et al., "Magnetic Measurements of the Steel Septum Magnet used for Injection: MSIB01, CERN, LHC Project Note 280, 2001.
[22] Report EST/SM/ME 01-05-16 A.Gerardin
[23] A. Gerardin, "Scratch test on an electro-deposed copper layer of a mumetal pipe", EST/SM-ME EDMS 349561 16/07/02

[24] M.Gyr, Expected Magnetic Field Quality of the LHC Septum Magnets Used For Injection (MSI) and For Extraction to the Beam Dump (MSD), LHC-Project-Note-129, 1998.
[25] Ian COLLINS, "Room Temperature Beam Vacuum System for the LHC Long Straight Sections", CERN EDMS rev. 0.2, N°339088 4/3/2002
[26] B. Henrist, Vacuum technical note, to be published.
[27] M.Sans, Simulations of energy deposition and adiabatic temperature rise in the TCDS, LHC Project Note to be published, 2003.
[28] S.Perraire et al., Beam Dumps and Beam Stoppers for LHC and CNGS Transfer Lines, CERN-LHC-Project-Report-465, 2001.
[29] J.Zazula and S.Peraire, LHC beam dump design study; 1, simulation of energy deposition by particle cascades; implications for the dump core and beam sweeping system, CERN-LHC-Project-Report-80, 1996.
[30] J.Zazula and S.Peraire, LHC beam dump design study; part 2, thermal analysis; implications for abort repetition and cooling system, CERN-LHC-Project-Report-87, 1996.
[31] L.Bruno et al., LHC Beam Dump Design Study - Part III : Off-normal operating conditions, LHC-PROJECT-NOTE-217, 2000.
[32] M.Ross, Recuperation of ISR Dipole Magnet Yokes for Use as Shielding for the LHC Beam Dumps TDE, LHC-PROJECT-NOTE-185; 1 Mar 1999.
[33] A.Variola, L.Bruno, Proposal for the LHC beam dump upstream diagnostics monitor, LHC-PROJECT-NOTE-241, 2000.
[34] B.Goddard, J.Wenninger, Instrumentation for the LHC beam dump lines, LHC DC-ES-0002.00 rev. 0.1 (341034), 2003.
[35] T.Dissing, Fault Detection on the LHC Beam Dump Kicker System, CERN-THESIS-99-006.
[36] J.B.Jeanneret, R.Ostojic, "Geometrical acceptance in LHC version 5.0", LHC note 111.
[37] V.Kain, Studies of Equipment Failures and Beam Losses in the LHC, Diploma Thesis, Wien, 2002.
[38] D.Brandt et al., Experimental Evaluation of the RF Shielding Properties of a Thin Resistive Layer in a Ceramic Chamber, CERN-LHC-Project-Report-403, 2000
[39] F.Caspers et al., RF screening by thin resistive layers CERN-LHC-Project-Report-300, 1999.
[40] L.Bruno, S.Peraire, Design Studies of the LHC Beam Dump, LHC-PROJECT-NOTE-196, 1999.
[41] C.Gonzalez et al., Impedance Measurements on the LHC Dump Kicker Prototype, LHC-PROJECT-NOTE-151; 10 Jul 1998.
[42] T.Bohl et al., Observation of Parasitic Beam and Cleaning with Transverse Damper, AB-Note-2003-021 MD, 2003.
[43] R.Assmann et al, Beam Loss Scenarios and Strategies for Machine Protection at the LHC, LHC-Project-Report-665, 2003.
[44] J.B.Jeanneret et al., Beam loss and collimation at LHC, Presented at Halo 2003, Monthauk, 2003
[45] B.Dehning et al., LHC beam loss monitor system design, AIP Conf. Proc. 648, pp.229-236, 2002.

CHAPTER 18

BEAM CLEANING AND COLLIMATION SYSTEM

18.1 INTRODUCTION

Each of the two LHC rings will handle a stored beam energy of up to 350 MJ (3×10^{14} p at 7 TeV), two orders of magnitude beyond the achievements in the Tevatron or HERA [1]. Comparing transverse energy densities, LHC advances the state of the art by even three orders of magnitude, from 1 MJ/mm^2 to 1 GJ/mm^2, which makes the LHC beams highly destructive. At the same time the superconducting magnets in the LHC would quench at 7 TeV if small amounts of energy (on the level of 30 mJ/cm^{-3}, induced by a local transient loss of 4×10^7 protons) are deposited into the superconducting magnet coils [2].

Any significant beam loss into the cold aperture must therefore be avoided, however, beam losses cannot be completely suppressed. A so-called "primary beam halo" will continuously be filled by various beam dynamics processes and the beam current lifetime will be finite [3]. The handling of the high intensity LHC beams and the associated high loss rates of protons requires a powerful collimation system with the following functionality:

1. Efficient cleaning of the beam halo during the full LHC beam cycle, such that beam-induced quenches of the super-conducting magnets are avoided during routine operation.
2. Minimisation of halo-induced backgrounds in the particle physics experiments.
3. Passive protection of the machine aperture against abnormal beam loss. Beam loss monitors at the collimators detect any unusually high loss rates and generate a beam abort trigger.
4. Scraping of beam tails and diagnostics of halo population.
5. Abort gap cleaning in order to avoid spurious quenches after normal beam dumps.

The collimators must be sufficiently robust to fulfill these tasks without being damaged both during normal and abnormal operational conditions.

Design work on an appropriate LHC collimation system started in 1990 [4] and evolved significantly over the years [5, 6, 7, 8, 9, 10, 11, 12, 13], reflecting both the difficulties to meet the LHC requirements and the challenge of advancing the state of the art in beam cleaning and collimation into a new regime. The latest critical revision of the LHC collimation system started in 2002 [14]. The final collimation design for the LHC has been fixed but not all details have been worked out and this chapter summarises the design status in January 2004.

18.2 DESIGN GOALS

Any possible hardware solution for the collimators can only resist a small fraction of the LHC beam [14, 15]. The maximum beam load that is expected on the collimators must be estimated in order to make an appropriate design. Experience from operating accelerators shows that beam losses are always higher than the theoretical optimum with real-world beam losses which are driven by imperfections, operational problems, unexpected beam physics processes, technical components operating out of specification, human errors and failures of equipment. This section summarises the assumed beam load on the collimators. Based on these estimates the required cleaning efficiency is derived and some design principles for the layout of the collimation system are summarised. The collimation design is described for proton-proton operation of the LHC and the specific design constraints which exist for ions and are discussed in Chap. 21.

18.2.1 Specification of maximum collimator beam load

Beam impact at the collimators is divided into normal and abnormal processes [13, 16, 17]. Normal proton losses can occur due to beam dynamics (particle diffusion [3], scattering processes, instabilities) or opera-

Table 18.1: Specified minimum beam lifetimes τ, their duration T, the proton loss rate R_{loss}, and maximum power deposition P_{loss} in the cleaning insertion.

Mode	T [s]	τ [h]	R_{loss} [p/s]	P_{loss} [kW]
Injection	cont	1.0	0.8×10^{11}	6
	10	0.1	8.6×10^{11}	63
Ramp	≈ 1	0.006	1.6×10^{13}	1200
Top energy	cont	1.0	0.8×10^{11}	97
	10	0.2	4.3×10^{11}	487

tional variations (orbit, tune, chromaticity changes during ramp [18], squeeze, collision). These losses must be minimised but cannot be avoided completely. Abnormal losses result from failure or irregular behaviour of accelerator components. The design of the collimation system relies on the specified normal and abnormal operational conditions and if these conditions are met it is expected that the collimation system will work correctly and that components will not be damaged. It is assumed that the beams are dumped when the proton loss rates exceed the specified maximum rates.

Normal proton losses

Based on the experience with other accelerators it is expected that the beam lifetime during a fill of the LHC will sometimes drop substantially below the normal value. The collimation system should be able to handle increased particle losses, in order to avoid beam aborts and to allow correction of parameters and restoration of nominal conditions. In particular, the range of acceptable lifetime must allow commissioning of the machine and performance tuning in nominal running and for periods of up to 10 s, beam lifetimes of 0.1 h (injection) and 0.2 h (top energy) must be accepted. The peak loss rate at injection energy occurs at the start of the ramp with an expected beam lifetime of 20 s for the first second of the ramp[1]. For continuous losses a minimum possible lifetime of 1 h is specified for injection and top energy [19]. Tab. 18.1 summarises the specified lifetimes and the corresponding maximum power deposition in the cleaning insertion. The collimators should be able to withstand the specified beam load. At injection the protons impact on the material at a few microns from the collimator edge[20]and at 7 TeV this transverse impact parameter can be as small as a few hundred nanometers.

Low beam lifetimes can occur due to orbit and optics changes, e.g. during injection, start of ramp, or squeeze. Proton losses can therefore occur locally at a single collimator jaw, where they develop into nuclear showers and the energy lost is only dissipated in the jaw itself to a small extent with the downstream elements and the surrounding materials absorbing most of the energy.

Abnormal proton losses

A great deal of effort has been invested in a powerful LHC machine protection system which is designed to handle equipment failures [21]. Primary proton losses will occur at the collimators if they are at nominal positions and they will be continuously monitored with fast Beam Loss Monitors [23, 24]. When an abnormal increase of beam loss signal is detected, a beam abort is initiated which will be completed within 2-3 turns (178-267 μs). The beam is dumped before it can damage any accelerator components, including the collimators. The reliability of this process must be very high. For a detailed description see Chaps. 15 and 17. Here it is assumed that in case of equipment failure the disturbed beam will always end up in the beam dump, however, this machine protection philosophy does not protect against single turn problems like irregularities of the beam dump itself and abnormally injected beam.

For these fast losses any jaw can be hit, because the primary collimators only cover one phase space location

[1] About 5% of the total intensity is expected to be uncaptured beam. It will be lost at the start of the ramp. The loss rate can be adjusted by the speed of the ramp.

Table 18.2: The beam deposited in the collimators for a few important one turn failures.

Abnormal condition	Beam energy [TeV]	Intensity deposit [protons]	Energy deposit [kJ]	Transverse dimensions [mm×mm]	Impact duration [ns]	Affected plane
Injection error	0.45	2.9×10^{13}	2073	1.0×1.0	6250	H/V/S
Asynchronous beam dump	0.45	6.8×10^{11}	49	***5.0*** $\times 1.0$	150	H
(all modules)	7.00	4.8×10^{11}	538	***1.0*** $\times 0.2$	100	H
Asynchronous beam dump	0.45	10.2×10^{11}	74	***5.0*** $\times 1.0$	225	H
(1 out of 15 modules)	7.00	9.1×10^{11}	1021	***1.0*** $\times 0.2$	200	H

and the overall LHC tune will vary. The collimator hardware must be designed to withstand the beam impact during abnormal proton losses without damage. The specified one turn beam loads on the collimator jaws are summarised in Table 18.2 for different abnormal conditions. The calculation assumes nominal bunch intensity (1.15×10^{11}), the nominal bunch scheme (2808 bunches separated by 25 ns), an average β_x of 410 m at the extraction kicker (MKD), and impact on the collimators between 5 and 10 σ_x. The energy deposition is integrated in time. The transverse dimensions listed in bold italic font are defined as full width (flat distribution) and all others are Gaussian standard deviations. Two cases of abnormal beam dump actions have been identified [16, 25]:

- The firing of the dump kickers is not synchronous with the beam dump gap, such that the LHC beam is swept across the aperture by the rising kicker voltage ("asynchronous dump").
- When one of the 15 MKD dump kicker modules spontaneously triggers it is followed by a re-trigger for the 14 other modules which will almost certainly be out of phase with the beam abort gap ("single module pre-fire"). The retriggering time is 1.2 μs at 450 GeV and 0.7 μs at 7 TeV [26].

The frequency of such failures is difficult to predict. It is assumed that they will happen at least once per year. A detailed discussion on the beam dump and its reliability is given in Chap. 17.

The impact of 7 TeV protons on a primary collimator for a single module pre-fire with the expected MKD performance is shown in Fig. 18.1. It is assumed that protons between 5 σ_x and 10 σ_x can impact on a collimator (shaded area). Local dump protection devices are assumed to intercept all beam above 10 σ_x. This case is more severe than an asynchronous beam dump and the horizontal beam distribution on the collimator jaw is not flat. For a pre-fire of MKD 15 about 8 nominal LHC bunches impact over 5 σ_x (1 mm), close to the edge of the collimator. Note that abnormal dump actions only affect horizontal collimators, as the dump kick acts on the horizontal plane and to a lesser extent skew collimators can also be hit.

Injection oscillations can originate from the SPS extraction system, the pulsed transfer line magnets, or the LHC injection system (see Chap. 16). The transfer line collimation system (described in Volume 3 of the design report) will protect against several possible injection problems [27], however, there are a number of residual cases which must be considered:

- The initial transfer line collimation system (two betatron collimators per plane) will ideally protect against injection oscillations at 7.5 σ amplitude, if these are generated upstream of the collimation system. Adding additional injection jitter from LHC injection (of the order of 0.5-1 σ) it is seen that primary and secondary collimators can be hit by a full injected batch. It is noted that the cold LHC aperture would be protected. An upgrade phase of the transfer line collimation system could constrain injection oscillations at the end of the transfer line to a maximum amplitude between 5 σ and 6 σ [28].
- Failures downstream of the transfer line collimation system cannot be protected against by this system (see also Chap. 15).
- A special flash-over failure has been identified for the LHC injection kicker. This failure can put 80% of an injected batch onto a collimator jaw. Some further improvement would permit the reduction of the

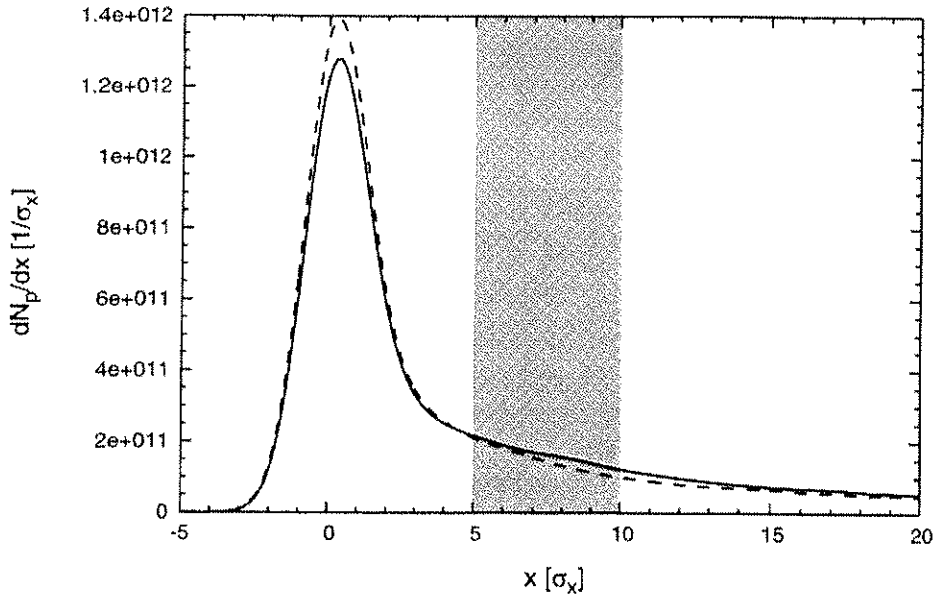

Figure 18.1: Time integrated horizontal distribution of LHC proton beam downstream of the MKD dump kickers, after a single module pre-fire. The two curves refer to a pre-trigger of the first and last kicker module, defining the two extreme cases. The shaded range shows the maximum collimator exposure.

beam impact to 50% of a batch. Expected frequency of a dangerous flash-over failure is about once per 10 years [29].

Based on this analysis of injection failures it is assumed that the amplitude of an oscillation can reach 6-10 σ and can affect both planes and therefore the collimator jaws must withstand the impact of a full injected batch without damage. It is noted that this design decision also decouples operation of the transfer line and ring collimation systems.

18.2.2 Definition of cleaning inefficiency

The following section contains a short introduction to the formal notation and central definitions for beam cleaning (see also Chap. 4). Halo particles are characterised by their normalised offsets $A_{x,y}$ in the transverse coordinates x, y:

$$A_x = \sqrt{\left(\frac{x}{\sqrt{\epsilon_x \beta_x}}\right)^2 + \left(\frac{\alpha_x x + \beta_x x'}{\sqrt{\epsilon_x \beta_x}}\right)^2}\,. \tag{18.1}$$

The same definition applies for A_y. Note that x is the sum of the betatron oscillation x_β and the dispersion offset δD_x, where D_x is the dispersion and δ the energy offset of the particle, similarly for x', y and y'. The terms β, α, and ϵ are the beta and alpha Twiss functions and the emittance. The normalised radial amplitude A_r of a particle is:

$$A_r = \sqrt{A_x^2 + A_y^2}\,. \tag{18.2}$$

The collimation system will capture most particles with large radial amplitudes. However, a secondary halo is generated from the primary collimators and a tertiary halo is leaked from the secondary collimators (see Fig. 18.2). In order to define the cleaning inefficiency η_c a variable normalised ring aperture a_c is considered. For N particles impacting at the collimators the cleaning inefficiency is then defined as the following leakage rate:

$$\eta_c(a_c, n_1, n_2) = \frac{1}{N} \sum_{i=1}^{N} H(A_r - a_c)\,. \tag{18.3}$$

Here, H is the Heaviside step function, returning 1 for $A_r \geq a_c$ and zero otherwise. The cleaning inefficiency gives the fraction of protons impacting on the primary collimators, which escape the collimators and reach at

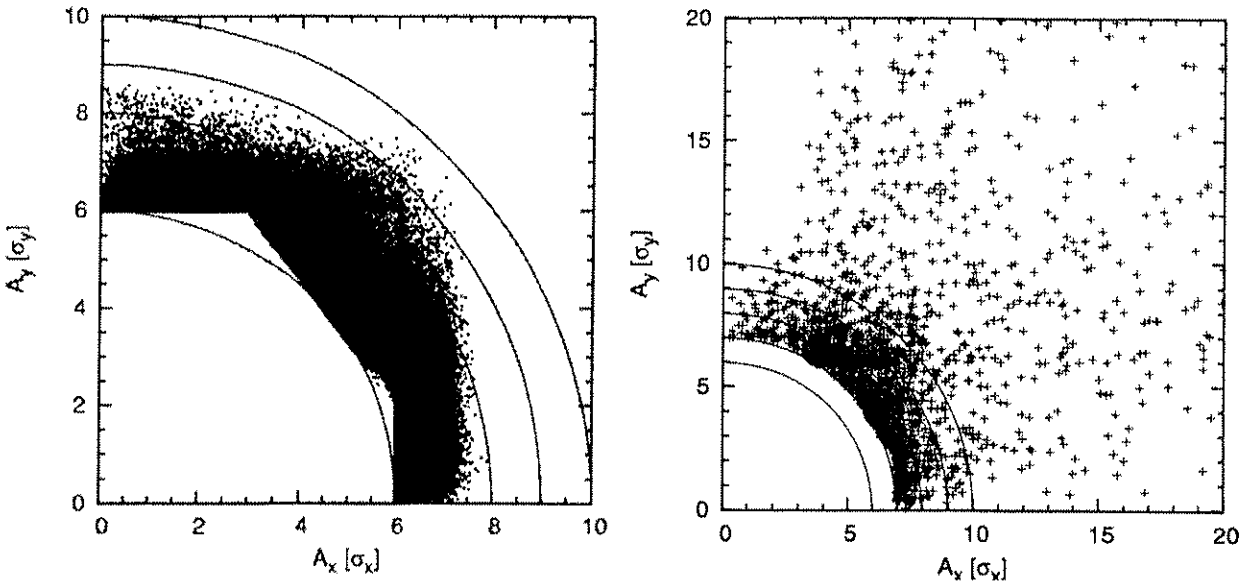

Figure 18.2: Transverse distribution of secondary (left) and tertiary (right) beam halos in normalised units. The primary and secondary collimators have been set to 6 σ and 7 σ in this example.

least a normalised ring amplitude a_c for given settings n_1 and n_2 of primary and secondary collimators. These protons will be lost into the cold aperture around the ring. The losses are diluted over some length L_{dil} and a local cleaning inefficiency $\tilde{\eta}_c = \eta_c / L_{dil}$ is defined and calculated with sophisticated tracking programs [30, 31, 32, 33], tracking over many turns, counting each particle once[2].

18.2.3 Maximum leakage rates for protection against quenches

The maximum leakage rates or in other words the required cleaning inefficiency can be specified from the maximum loss rates, the quench limit, and the dilution length. The quench level R_q is estimated to be 7×10^8 protons/m/s for 450 GeV and for slow, continuous losses [2]. For 7 TeV a value of 7.6×10^6 protons/m/s is obtained (at top energy additional limits can arise for the heat load in an LHC sector). It is noted that transient losses over $\approx$10 turns must be controlled to about 10^{-9} of the total intensity to avoid quenches. It was not possible to specify beam loss processes on this time scale and the required collimation inefficiency is therefore defined for slow, continuous losses. The longitudinal loss distribution is case dependent and for some specific case studies an average dilution length $L_{dil} = 50$ m is assumed. An accurate determination of L_{dil} remains to be completed. The total intensity $N^q_{\rm tot}$ at the quench limit R_q and for an operationally required minimum beam lifetime $\tau_{\rm min}$ is then given by:

$$N^q_{\rm tot} = \frac{\tau_{\rm min} \cdot R_q}{\tilde{\eta}_c} . \tag{18.4}$$

The total intensity allowed at the quench limit is shown as a function of the local collimation inefficiency in Fig. 18.3. It is assumed that a minimum beam lifetime of 0.2 h at top energy and 0.1 h at injection must be ensured for operation (see Tab. 18.1). It is noted that the most stringent requirements on the collimation inefficiency arise at top energy. The nominal intensity of 3×10^{14} protons per beam requires a collimation inefficiency of 2×10^{-5} m^{-1} but injection has less strict requirements. The settings n_1, n_2 and n_3 of primary, secondary and tertiary collimators must be carefully adjusted in order to minimise the leakage rates of the cleaning insertions.

[2]This definition assumes that a particle that reaches a_c is lost within the same turn and cannot perform multiple revolutions.

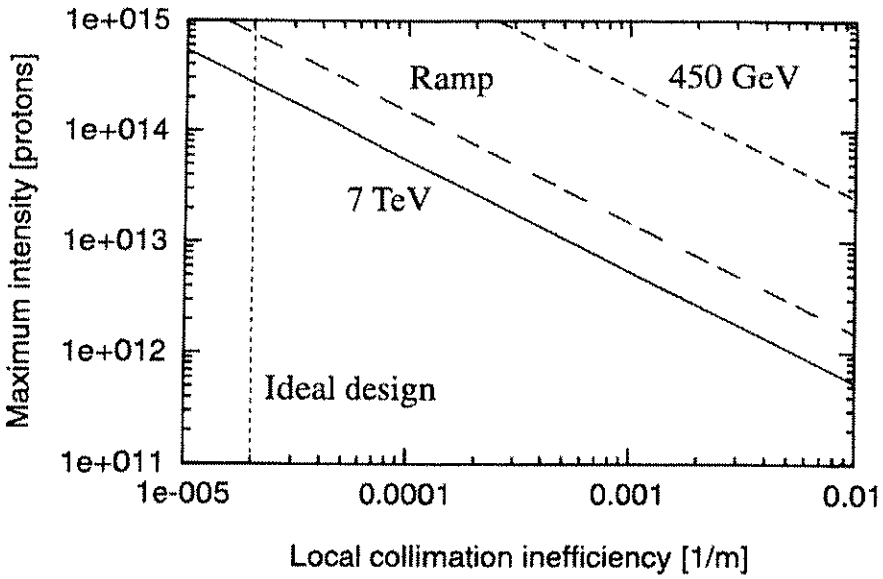

Figure 18.3: The maximum total intensity is shown as a function of the local collimation inefficiency for injection, top energy, and the start of the ramp. A beam lifetime of 0.2 h at top energy and 0.1 h at injection is assumed. The ideal design value for local inefficiency is indicated.

18.2.4 Constraints for collimator settings

The settings for the collimators are specified as the normalised half gap, assuming nominal emittance and the beta functions at the collimators. A setting n_1 of a primary vertical collimator means that the jaws are located at vertical positions of $\pm n_1 \cdot \sqrt{\epsilon_y^{\rm nom} \cdot \beta_y^{\rm coll}}$. This notation should not be taken as an indication that collimator settings depend on beam emittance; they must be decided based on the available machine aperture a_c. Several boundary conditions constrain the settings of the collimators. Collimator settings for nominal intensity are 6 σ for primary and 7 σ for secondary collimators, both at injection and at 7 TeV with nominal β^*.

Machine protection functionality

The collimators in the warm insertions must be the aperture bottlenecks in the LHC ring, therefore they cannot be opened to arbitrarily large gaps. For example, with the injection ring aperture designed for $n_1 = 7$ (aperture notation) the guaranteed minimal vertical aperture is 8.4 σ_y. Vertical protection devices like the TDI must then sit at around 7.5 σ_y and secondary vertical collimators should be set to around 7 σ_y. Betatron collimator settings at injection are constrained to be below 6 σ for primary and 7 σ for secondary collimators. The protection requirements at 7 TeV are a function of the values for β^* in the interaction points and the corresponding aperture bottleneck at the experimental triplets. The maximum allowed collimator gaps can be directly expressed as a function of the lowest β^* in the ring.

Quench prevention

The protection of the LHC aperture against loss of primary protons is not sufficient to prevent quenches of the super-conducting magnets. As seen in Fig. 18.2 primary and secondary collimators generate a secondary and tertiary halo that extends several σ beyond the collimator settings. The collimators are conventionally put to a position such that the secondary halo does not impact on any super-conducting magnet.

Operational and accelerator physics constraints

It is beneficial for machine protection and halo cleaning to close the collimator gaps as far as possible. However, operational and accelerator physics constraints put important limitations on the allowed minimal collimator gap:

- The beam core must not be scraped by collimation, usually requiring collimator settings above 4-5 σ.
- The collimator gap must be wide enough to avoid excessive impedance from the collimators and to maintain beam stability. e.g. it may in most cases not be possible to reduce emittance and to move collimators to smaller gaps with the same normalised setting.
- The two-stage functionality of the collimation system must be maintained during the whole operational cycle, e.g. the primary collimators must always remain primary and the secondary must always remain secondary collimators. Usually a relative offset of 1 nominal *sigma* is required, corresponding to about 200 μm at 7 TeV and operational and mechanical tolerances are specified for this retraction. Maintaining the same normalised collimator gaps (e.g. 6 σ and 7 σ) with smaller than nominal emittances will be challenging.

Abort gap cleaning

Special considerations apply for the momentum collimators which are needed to absorb a flash of losses soon after the beginning of the ramp [34, 35] and to capture off-bucket protons which lose momentum by synchrotron radiation at top energy [36, 37]. Long storage time of particles with large momentum offset must be avoided. Their detuning with momentum can be quite large (the momentum aperture of the ring is $\approx 6 \times 10^{-4}$) and thus the effective aperture may differ from the nominal one. In addition, these particles creep along the bunch structure and invade the abort gap. If their density is too large, a quench will occur in the magnets downstream of the dump system even during normal beam dumps. The phenomenon is similar to the dump error discussed in Sec. 18.2.1. A detailed description of this effect is in preparation [38] and is illustrated in Fig. 18.4. The peak density in the abort gap is given here by the very simplified expression:

$$\hat{\rho}_0 \simeq 0.7 \frac{N_0}{\tau_{\rm long} L_{\rm ring}} \frac{\delta_{\rm cut}}{\dot{\delta}} = 2.2\,10^7 \ \ {\rm p/m}\,, \tag{18.5}$$

with N_0 the number of stored protons, $\tau_{\rm long} = 10$ h a somewhat low longitudinal beam lifetime, $L_{\rm ring} = 26660$ m, $\dot{\delta}_{cut} \simeq 10^{-3}$ the momentum cut made by the momentum collimation system at top energy and $\dot{\delta} = U_0 f_r / E_{\rm beam} = 10^{-5}$ the momentum loss per second by synchrotron radiation with $U_0 = 7$ keV/turn, $E_{\rm beam} = 7$ TeV and $f_r = 1.1 \times 10^4$ Hz the rotation frequency. The coefficient 0.7 is obtained by the integration of the synchrotron motion between $\delta_{\rm bucket}$ and $\dot{\delta}_{\rm cut}$ and by summing over all occupied buckets. This value is case specific and should only be used indicatively, see [38] for a complete formalism. The peak density is reached at the rear side of the abort gap, because particles with negative δ_p creep forward and in this case, the density at the head is $\rho_{\rm head} \approx \hat{\rho}_0/2 = 1.2 \times 10^7$p/m. This value is larger than the critical $\rho_{\rm tol} \approx 0.4 \times 10^7$ p/m, above which a quench is induced behind the dump system [39]. It is intended to make use of the transverse damper (see Chap. 6), used in an excitation mode, in order to increase the betatron amplitude of the particles which are present in the abort gap, and thus accelerate their capture. It is fortunate that the dangerous part of the abort gap is located at its head (this is where the dump kicker starts to rise and sprays the beam at low amplitude), because the creeping protons must traverse the entire gap before reaching the head. This allows the damper to work mostly in the central part of the gap, leaving enough time for turning the excitation mode on and off.

18.2.5 Layout goals

In order to achieve the required low inefficiencies of around 10^{-3} (before dividing by the dilution length) several design principles have been developed and included in the layout of the LHC collimation system:

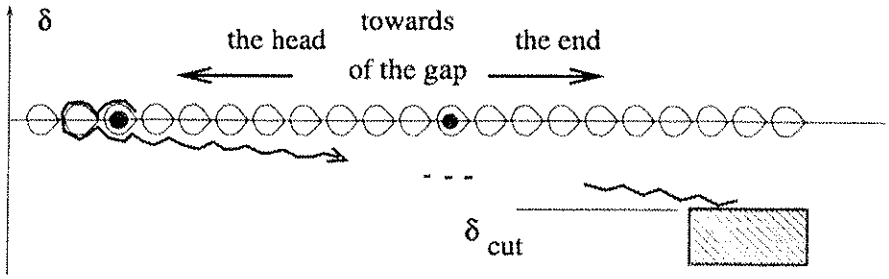

Figure 18.4: The longitudinal motion of a proton which left the bucket. It loses momentum by synchrotron radiation and is finally captured by the primary momentum collimator in IR3.

- A multi-stage cleaning process is implemented. Primary collimators intercept the lost primary protons and generate an on-momentum and off-momentum secondary proton halo. The secondary proton halo is intercepted by the secondary collimators which leak only a small tertiary halo. The tertiary halo is lost in the cold aperture but is populated sparsely enough that quenches are mostly avoided (see Fig. 18.2). Tertiary collimators are used locally to provide additional protection from the tertiary halo (e.g. at the aperture bottlenecks in the triplets).

- The phase advances between different collimators and their orientations are optimised to achieve the best possible coverage in the x-x'-y-y' phase space [40, 41]. An additional optimisation is performed to locate collimators at larger values of the beta function, thus obtaining larger opening gaps and a reduced impedance.

- As far as possible, collimators are located in front of bending magnets so that a large fraction of the proton-induced cascade is then swept out of the machine aperture and neutral particles do not propagate far downstream (see the dogleg description for IR3 and IR7 in Chap. 3).

- Separately optimised cleaning systems are dedicated to the cleaning of protons with high betatron amplitudes (betatron cleaning in IR7) and off-momentum protons (momentum cleaning in IR3). See the description of optics goals for IR3 and IR7 in Chap. 4.

- The collimators have been located in warm sections of the machine because the warm magnets are much more tolerant to local beam losses and can accept the particle showers that exit the collimators.

These constraints are implicitly included in the design of the LHC collimation system.

18.2.6 Radiological considerations

The cleaning insertions will become some of the most activated sections in the LHC. For radiation studies it is estimated that about 30% of all stored LHC protons will be lost in the cleaning insertions at Points 3 and 7. Detailed radiological assessments have been performed and are discussed in Volume 2 of this report. Of particular importance for maintenance are estimates of remanent dose rates from induced radioactivity. As studies have shown, these dose rates depend strongly on various factors, such as on the collimation layout, local shielding, the materials chosen, the cooling time and the location of the collimators within the beamline layout. Close to the collimators dose rates from activated beamline components or shielding typically reach several tens of mSv/h, whereas the dose rate from the collimator jaws (on close contact) can be significantly higher. The design of the collimators and adjacent equipment (high reliability, fast connections, etc.) takes into account the fact that intervention time in these regions will have to be limited. It has been shown for the former layout (LHC layout and optics version 6.2) that the warm magnets and other accelerator equipment in the cleaning insertions can withstand the expected radiation [42]. However, the accumulated dose in the collimator tanks and the surrounding shielding is expected to be 1-100 MGy/year, thus rather radiation hard equipment will have to be installed. This significantly exceeds CERN's acceptable radiation dose to standard cables of 500 kGy as

given in [43]. Since the shielding layout will be different as assumed in preceding calculations [42], further detailed studies might become necessary.

18.2.7 Compatibility with the LHC ultra high vacuum

The choice of collimator design and materials must be compatible with the ultra-high vacuum of the LHC and the collimators must be bakeable and outgassing rates remain acceptable.

18.2.8 Compatibility with the LHC impedance budget

The collimators can produce significant transverse resistive impedance due to the small gaps at 7 TeV (impedance scales inversely proportional to the third power of gap size). Some increase of the LHC impedance can be handled with the LHC octupoles, which provide Landau damping of the rigid dipole modes. The collimator-induced impedance, the impedance limit, and the beam stability with collimators are discussed in detail in Chap. 5. The compatibility of the collimation system with the LHC impedance budget is a limiting design constraint for the collimators.

18.3 THE CONCEPT OF A PHASED APPROACH FOR LHC COLLIMATION

A detailed analysis of possible collimator materials and concepts did not produce any single collimator solution that fulfills all the design goals for LHC collimation (see also discussion in Sec. 18.5). In particular it was found that a trade-off exists between collimator robustness and collimator induced impedance. For example, a collimation system with sufficient robustness (based on graphite material) would introduce peak performance limitations for the LHC (reduced intensity, increased β^*). A system with sufficiently low impedance (copper based) would likely experience regular damage to the collimator jaws with resulting loss in cleaning inefficiency (peak intensity) and efficiency of LHC operation. A beryllium based system would not resist the specified one turn beam loads and in addition would introduce concerns about toxic materials.

In order to meet the LHC design goals, a number of sub-systems have been defined which have specific tasks and can be fitted conveniently into different installation phases. The system for beam cleaning and collimation in the LHC will be constructed and installed in three phases [44]. This phased approach relies on the fact that difficulties and performance goals for the LHC are distributed in time, following the natural evolution of the LHC performance. The phased approach allows initial operation with a collimation system with fewer components than previously anticipated. The following section describes the different phases and the associated philosophy of beam cleaning and collimation.

18.3.1 Phase 1

The initial phase 1 system which will be described in more detail later, will be the central part of the overall collimation system. Essentially this phase presents a collimation system with maximum robustness which includes a reduced two-stage cleaning in IR3 and IR7, tertiary collimators at the experimental insertions, scrapers, and special collimators for injection protection in IR2/IR8 and collision debris in IR1/IR5. The phase 1 collimation system is designed to withstand the specified beam impact and will be the system used for injection and ramp up to nominal or even ultimate intensities. The normalised settings of main collimators and the predicted cleaning inefficiency are listed in Tab. 18.4 and the injection set-up with phase 1 collimation is illustrated in Fig. 18.5. A two-stage cleaning process is performed with primary and secondary collimators at 6 σ and 7 σ (here referring to σ at injection). The cold aperture limitation in the LHC arcs is efficiently shadowed. This set-up is used during the whole lifespan of the LHC. Scrapers can be used for beam forming or halo diagnostics.

During collisions at 7 TeV, the phase 1 collimation system may be operating at the impedance limit, limiting the maximum intensity and thus LHC luminosity. The three-stage 7 TeV set-up during phase 1 collimation is illustrated in Fig. 18.6. The C collimators in IR7 are set for relaxed conditions with half intensity and $\beta^* = 1$ m. A three-stage cleaning process is then performed with primary and secondary collimators at 6 σ and 8.5 σ (here

referring to σ at 7 TeV). Tertiary collimators in the experimental insertions provide additional shadow for the super-conducting triplet magnets.

The technical design of the collimators in phase 1 is demanding but follows conventional concepts. Mechanical and operational tolerances at 7 TeV can be relaxed by a factor larger than 3 with respect to the full performance system, if a higher β^* is accepted.

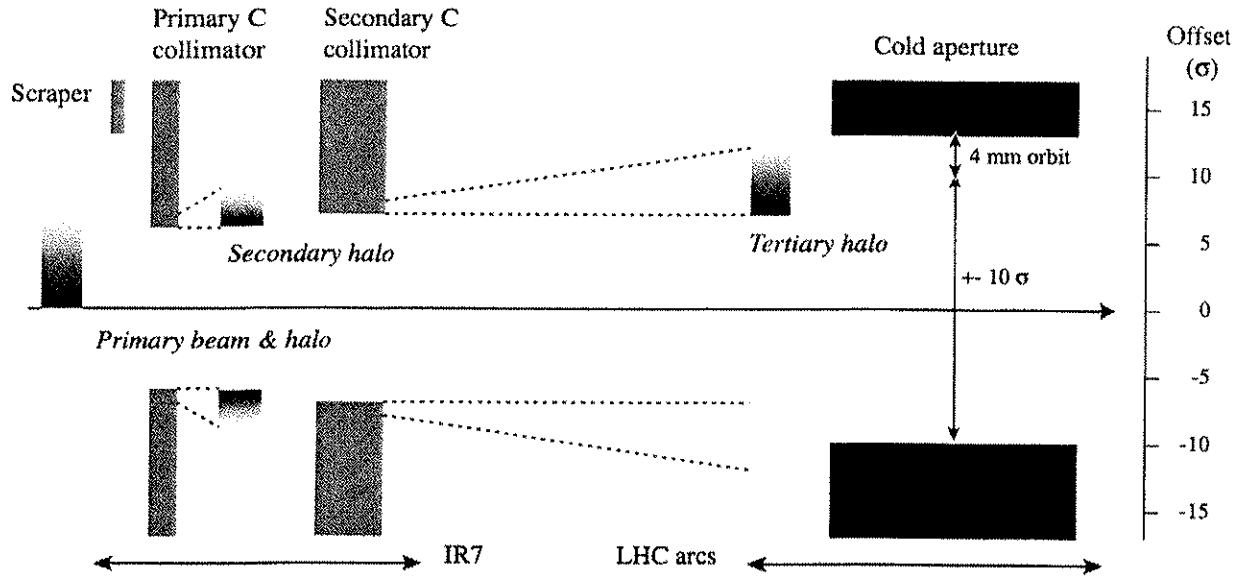

Figure 18.5: Principle of betatron collimation and beam cleaning at *injection energies* and during the ramp.

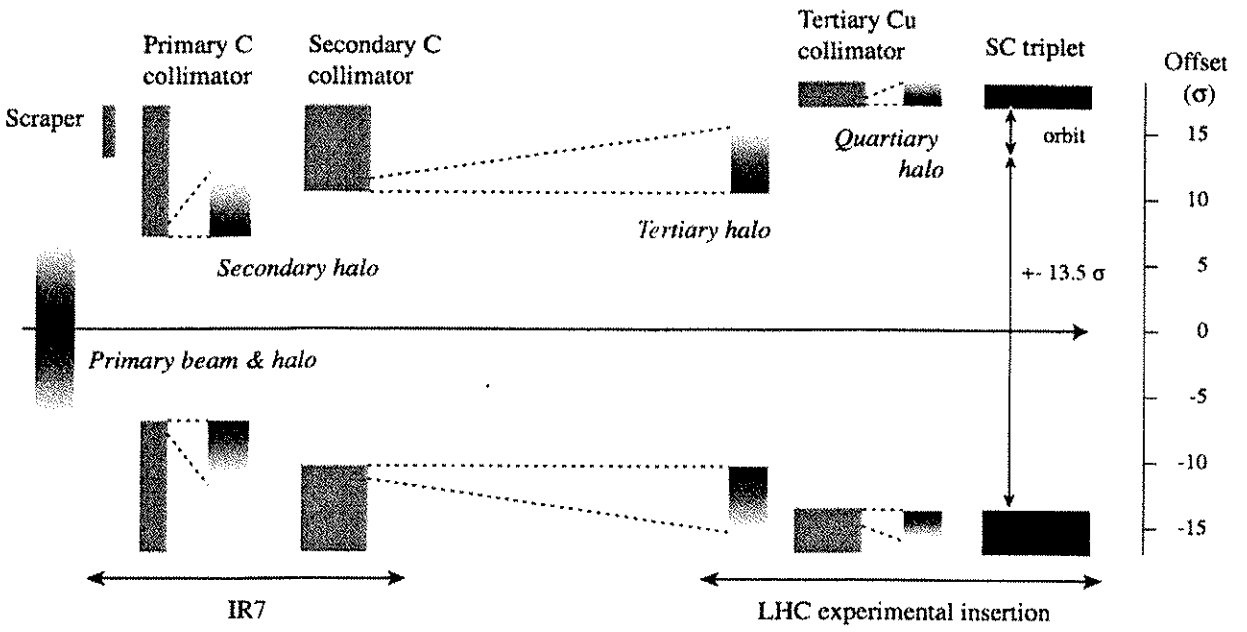

Figure 18.6: Principle of betatron collimation and beam cleaning *during collisions* in phase 1. The C collimators in IR7 are set for half intensity and $\beta^* = 1$ m.

18.3.2 Phase 2

The phase 2 system will complement the high robustness secondary collimators in IR3 and IR7 with 30 low impedance "hybrid" collimators. These hybrid collimators, which will only be used towards the end of the low beta squeeze at 7 TeV and in stable physics, will have a reduced robustness but low impedance and excellent

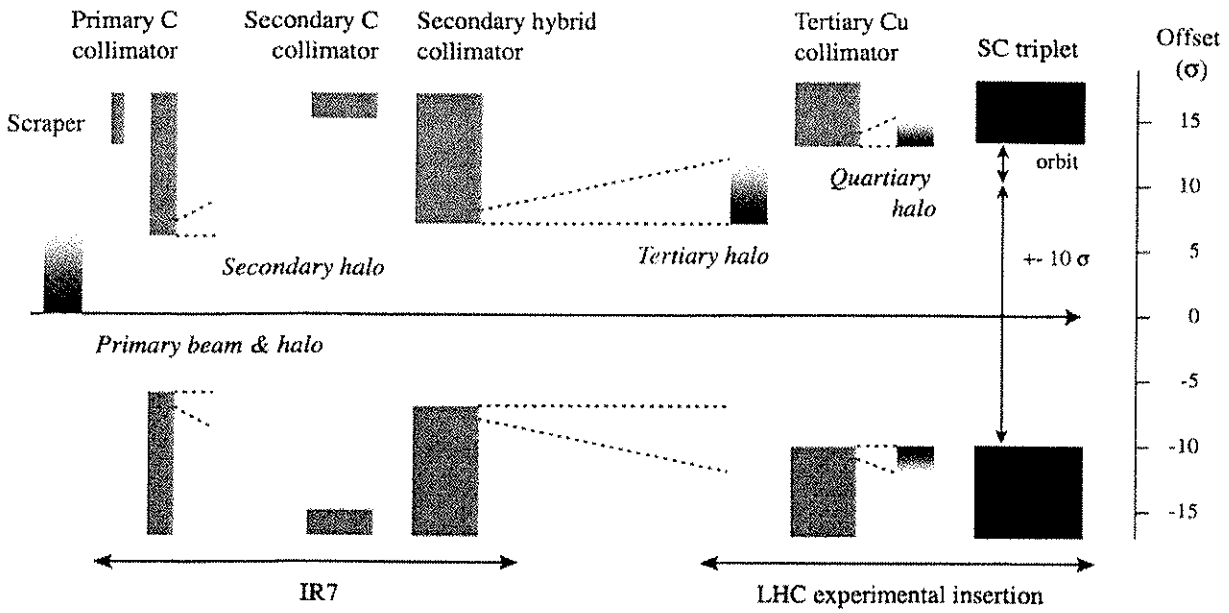

Figure 18.7: Principle of betatron collimation and beam cleaning during *collisions in phase 2*. Hybrid secondary collimators with low impedance are used, allowing nominal intensity and β^* with nominal collimation gaps.

mechanical tolerances and will support nominal performance. The 7 TeV set-up for phase 2 collimation is illustrated in Fig. 18.7. Hybrid secondary collimators with low impedance are used, allowing nominal intensity and β^* with nominal collimation gaps. A three-stage cleaning process is performed with primary and secondary collimators at 6 σ and 7 σ (here referring to σ at 7 TeV). Tertiary collimators in the experimental insertions provide additional shadow for the super-conducting triplet magnets. Scrapers can be used for beam forming or halo diagnostics.

The hybrid collimators will only be used in stable conditions at top energy, when risk of damage is significantly reduced. Only a few horizontal collimators can be affected by abnormal beam loss because several scenarios for abnormal beam impact do not apply at 7 TeV. Either the design of the collimators will be able to cope with possible damage ("consumable" collimator concept) or the critical collimators[3] can be retracted into the protection of the local dump absorber TCDQ (see Chap. 17), accepting reduced cleaning efficiency and higher normal losses on the TCDQ.

The design of the hybrid collimators is not decided yet but possible options include consumable metallic collimators, a graphite material doped with copper, beryllium jaws, thick metallic coating and graphite jaws with a movable metallic foil. For performance estimates a consumable collimator with a 1 m long Cu jaw is used.

18.3.3 Phase 3

Several years after LHC start-up, 4 additional collimators will be installed in order to capture the high luminosity collision debris downstream of IR1 and IR5. These devices will be required once LHC exceeds about 30% of the nominal design luminosity.

18.3.4 Phase 4: Eventual efficiency upgrade

The collimation sub-systems in IR3 and IR7 were reduced by 16 collimators in order to reduce the number of components (total cost, work load for phase 1) and to limit their contribution to impedance. Compared to the full complement of collimators, the associated cost in performance is a factor of 2 loss in efficiency. Placeholders are kept for all suppressed collimators. If LHC operation reveals problems with cleaning efficiency, the best

[3]For a known tune working point it can be predicted accurately which horizontal collimator is exposed to abnormal dumps.

Table 18.3: Overview on the different types of collimators used in the LHC ring collimation system for both beams and for phases 1-3. The jaw length is given without impedance tapering.

Acronym	Material	Length [m]	Number	Locations	Purpose
TCP	C or C-C	0.2	8	IR3, IR7	Primary collimators
TCSG	C or C-C	1.0	30	IR3, IR7	Secondary collimators
TCSM	tbd	1.0	30	IR3, IR7	Hybrid secondary collimators
TCT	Cu	1.0	16	IR1, IR2, IR5, IR8	Tertiary collimators
TCLI	tbd	tbd	4	IR2, IR8	Injection protection
TCLP	Cu	1.0	8	IR1, IR5	Protection luminosity debris
TCSP	tbd	tbd	6	IR3, IR7	Beam scraping

possible cleaning efficiency and protection can be achieved by adding the 16 collimators.

18.4 THE IMPLEMENTATION OF THE PHASED APPROACH

The choice of a phased approach requires significantly more space for collimators than previously planned. For each secondary collimator a space of 4 m must be reserved for phase 1 and phase 2 collimators, almost 6 times more than in the former layout. Fewer collimators will be installed initially while a higher number of components is required for all four phases. A careful optimisation was performed to optimise the cleaning insertions accordingly while maintaining cleaning efficiency and minimising impedance. The phased solution is described in detail in this section.

18.4.1 Number of components, performance and schedule

A list of the collimator types, their material choice and length, number of components, locations, and purposes is given in Tab. 18.3. The number of components in the different phases, the main collimation settings for betatron and momentum cleaning, and predicted inefficiencies are listed in Tab. 18.4. The calculated inefficiency refers to the range of predicted values [45], which does not include the cleaning from the tertiary collimators or any imperfections in collimator settings. About 6 scrapers and a number of absorbers will additionally be installed for phase 1. An optional phase 4 would provide for a modest upgrade in cleaning inefficiency and would only be pursued in the case of unforeseen problems. It is noted that inefficiencies at injection seem adequate, while the situation at top energy cannot be guaranteed to be adequate and therefore the tertiary collimators have been introduced. The phase 1 installation will be available for the LHC start-up and commissioning, phase 2 collimators will be installed in 1-2 years and phase 3 collimators about 3 years after the first physics runs.

18.4.2 IR7 layout

The IR7 insertion contains the betatron collimation system. Optics and aperture properties of the IR7 layout are described in Chaps. 3 and 4. An efficient design process for IR7 took into account the space requirements, all proposed collimators, impedance minimisation and efficiency optimisation. During this process collimators were moved up to 30 m and quadrupoles up to 1 m. Additional design optimisations for vacuum layout and beam instrumentation were included. The finally adopted longitudinal layout is summarised in Fig. 18.8, clearly indicating phase 1 and phase 2 secondary collimators, as well as placeholders for further upgrades.

18.4.3 IR3 layout

The IR3 insertion houses the momentum collimation system which has many fewer components than are used in IR7 and a limited redesign was performed in order to find the space required. Optics and aperture properties of the IR3 layout are described in Chaps. 3 and 4. The longitudinal layout which was finally adopted

Table 18.4: Overview of the planned phases of LHC collimation. The total number of collimators N_{coll}, the settings n_1, n_2, n_3 and the expected ideal cleaning inefficiencies are listed for the different phases and machine states, and for betatron (IR7) and momentum (IR3) cleaning systems.

Phase	N_{coll}	Setting	Stages	n_1 $[\sigma_\beta]$	n_2 $[\sigma_\beta]$	n_3 $[\sigma_\beta]$	Performance	Cleaning inefficiency (ideal)
1	62	Injection IR3	2	8.0	9.3		Initial	
		Injection IR7	2	6.0	7.0			$(6.3...12.6)\times10^{-3}$ at 10 σ_r
		Collision IR3	2	15.0	18.0			
		Collision IR7	3	6.0	8.5	14.0		$(0.5...1.5)\times10^{-3}$ at 14 σ_r
		(β^*=1 m)						
		Collision IR7	3	6.0	7.0	10.0		$(1.1...3.3)\times10^{-3}$ at 10 σ_r
		(β^*=0.5 m)						
2	92	Injection IR3	2	8.0	9.3		Nominal	
		Injection IR7	2	6.0	7.0			$(6.3...12.6)\times10^{-3}$ at 10 σ_r
		Collision IR3	2	15.0	18.0			
		Collision IR7	3	6.0	7.0	10.0		$(0.2...2.0)\times10^{-3}$ at 10 σ_r
3	96	Injection IR3	2	8.0	9.3		High lumi.	
		Injection IR7	2	6.0	7.0			$(6.3...12.6)\times10^{-3}$ at 10 σ_r
		Collision IR3	2	15.0	18.0			
		Collision IR7	3	6	7	10.0		$(0.2...2.0)\times10^{-3}$ at 10 σ_r
(4)	112	Injection IR3	2	8.0	9.3		Maximum	
		Injection IR7	2	6.0	7.0			$(5.7...11.4)\times10^{-3}$ at 10 σ_r
		Collision IR3	2	8.0	9.3			
		Collision IR7	3	6.0	7.0	10.0		$(0.2...2.0)\times10^{-3}$ at 10 σ_r

is summarised in Fig. 18.9, including phase 1 and phase 2 secondary collimators. It should be noted that no placeholders for future efficiency upgrades are required in IR3.

18.4.4 Radiological aspects of phased installation

The collimators will intercept a large fraction of the protons that are lost in the machine during normal operation. The induced showers activate the collimators themselves and the downstream equipment in IR3 and IR7. It is therefore essential to carefully study the radiological consequences and to consider provisions for minimising the environmental impact and personnel exposure (further details are given in Volume 2 of this report). The possibility of installation work and maintenance close to the collimators is an important aspect for the feasibility of the phased installation. Simulation studies have shown that residual activation can be significant, imposing strict limitations on any human intervention [46] and it is a legal requirement to plan each intervention in detail with particular regard to personal and collective doses. An example study of the dose received during the exchange of a collimator showed that the personal dose may reach several tens of mSv [47, 48]. These results strongly depend on the particle losses at that collimator, the collimator material and the surrounding local shielding. As for dose planning more detailed calculations will have to be performed in order to understand and optimise the final layout of the collimators and its implication on collective doses (for example see [49]). During the first two years of LHC operation losses will be smaller and thus dose rates lower by about a factor of two. However, precautions have to be taken for the phase 2 installations in order to keep personal and collective doses as low as reasonably achievable (ALARA). Therefore, a fast installation procedure has been established and will be used from the design phase onward.

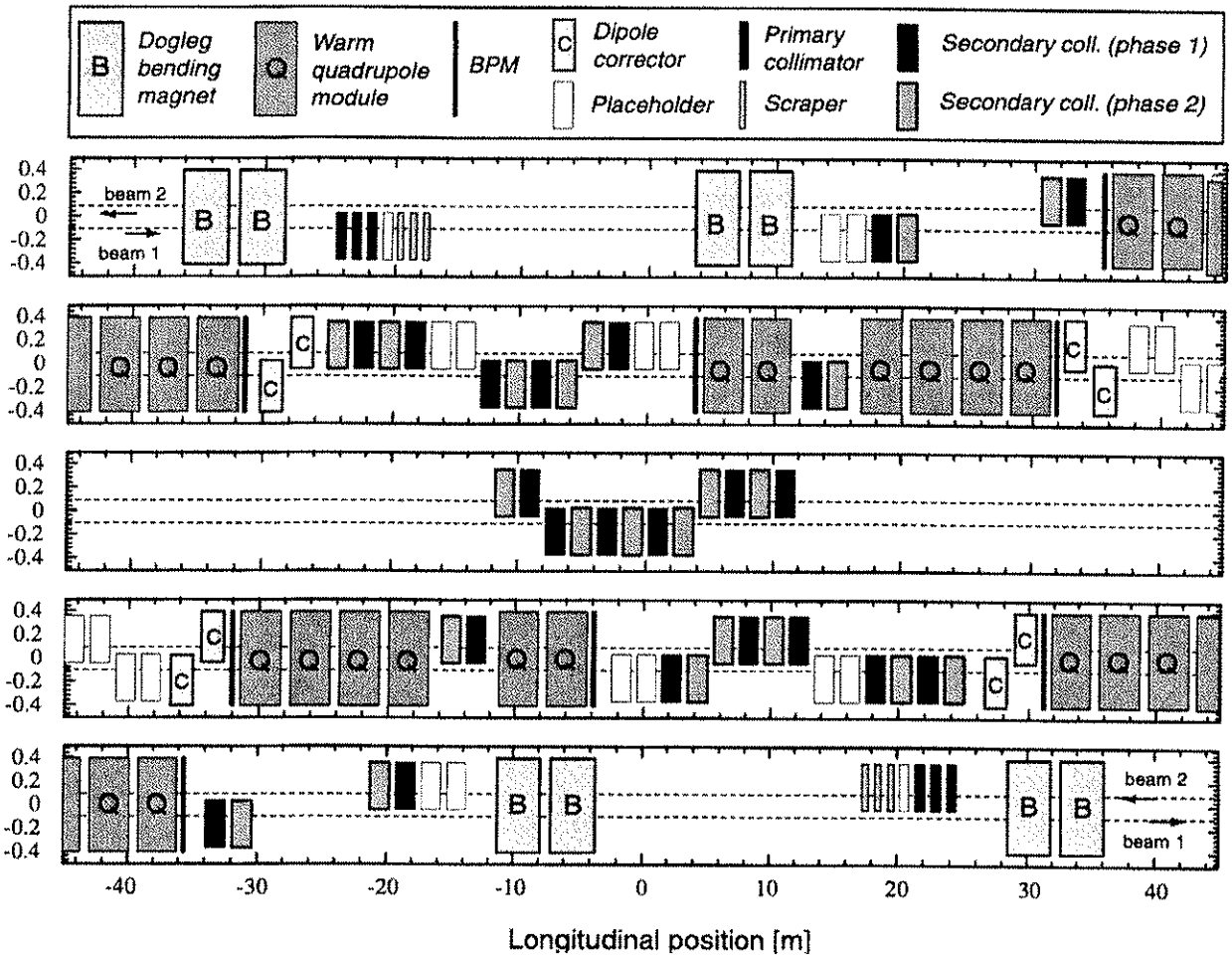

Figure 18.8: Longitudinal layout for the betatron cleaning insertion in IR7.

Table 18.5: Overview on the collimators installed for phase 1 of LHC collimation. The numbers refer to the total number of elements required for both beams. Note that 6 scrapers have been included into this list. This is a sub-set of Tab. 18.3.

Acronym	Number	Locations	Purpose
TCP	8	IR3, IR7	Primary collimators
TCSG	30	IR3, IR7	Secondary collimators
TCT	16	IR1, IR2, IR5, IR8	Tertiary collimators
TCLI	4	IR2, IR8	Injection protection
TCLP	4	IR1, IR5	Protection luminosity debris
TCSP	6	IR3, IR7	Beam scraping

18.5 DESCRIPTION OF PHASE 1 COLLIMATION

Phase 1 of collimation will provide a collimation system with maximum robustness. It has been agreed to operate at the LHC impedance limit and thereby reduce the luminosity reach somewhat below nominal performance. The system must be ready for the start-up of the LHC and will support commissioning and initial luminosity running without a further upgrade: for phase 1 62 collimators and 6 scrapers wil be installed – the numbers and types of components are given in Tab. 18.5. The collimation settings and expected performance have been summarised in the previous section. In this section a detailed list of phase 1 components is given, the basic hardware choices are explained and the mechanical design is presented.

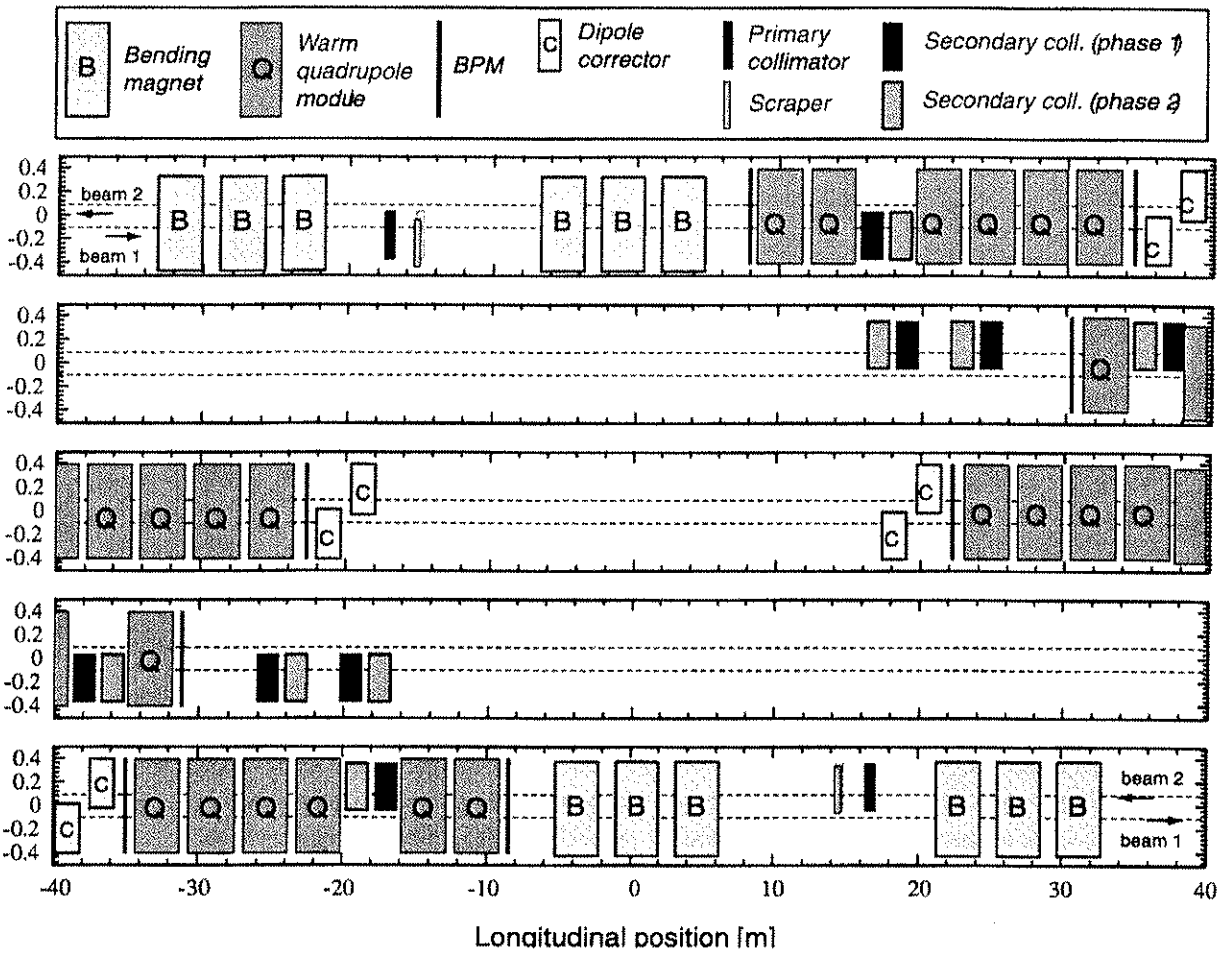

Figure 18.9: Longitudinal layout for the momentum cleaning insertion in IR3.

18.5.1 Components in IR3 and IR7

Detailed lists of phase 1 collimators are given in Tabs. 18.6 and 18.7 for the IR3 and IR7 collimation systems. The list specifies in particular the longitudinal position, the nominal half gap and the azimuthal orientation of the jaws. The nominal half gaps in the betatron cleaning refer to settings of 6 σ and 7 σ for primary and secondary collimators, a beam energy of 7 TeV, the design optics and the nominal 7 TeV emittance. Nominal 7 TeV settings in the momentum cleaning are 15 σ and 18 σ for primary and secondary collimators (expressed in betatron beam size). It is noted that the specified 7 TeV half gaps in both insertions are operationally challenging and cannot be reduced much further without significant effort.

18.5.2 High robustness graphite collimators for phase 1 (TCP/TCSG)

Collimators with maximum robustness are required for the phase 1 system and it was decided [50] that graphite should be used, based on the specified maximum beam load on the collimators (see Sec. 18.2.1). Both fine grain graphite (carbon, C) and fiber-reinforced graphite (carbon-carbon, C-C) have sufficient robustness to withstand all specified beam load cases at injection and top energy without damage. Graphite materials exhibit a significant variation in electrical resistivity, ranging from 7 $\mu\Omega$m to about 30 $\mu\Omega$m: for impedance calculations an electrical resistivity of 14 $\mu\Omega$m (fine-grain graphite) was assumed [51]. The specific variety of graphite will be selected based on measurements to be made at CERN of electrical properties, vacuum performance, and mechanical tolerances.

Table 18.6: Collimators in the momentum cleaning insertion IR3 for beam 1 and beam 2. For each collimator the longitudinal position relative to IP3, the azimuthal orientation of the jaws and the nominal half gap at 7 TeV is listed. The list includes only phase 1 collimators; hybrid TCSM collimators are omitted.

Name	Distance from IP3 [m]	Azimuth [°]	Half gap [mm]
TCP.6L3.B1	-177.35	0	3.87
TCSG.5L3.B1	-142.31	0	2.94
TCSG.A4R3.B1	43.34	0	2.06
TCSG.A5R3.B1	55.20	170.4	2.72
TCSG.B5R3.B1	61.02	11.4	3.05
TCP.6R3.B2	177.45	0	3.64
TCSG.5R3.B2	143.31	0	2.63
TCSG.A4L3.B2	-42.34	0	2.14
TCSG.A5L3.B2	-54.20	170.9	2.60
TCSG.B5L3.B2	-60.02	10.5	2.84

Peak temperature increase

The energy deposition in graphite and other materials due to a single module dump pre-fire at 7 TeV (compare Sec. 18.2.1) was calculated with FLUKA [52, 53] and the results are summarised in Tab. 18.8. It can be seen that graphite and beryllium exhibit a reasonable maximum temperature increase after impact of the 8 out of 2808 LHC bunches. Aluminium, titanium and copper show destructive maximum heating: the heating along the length of a collimator jaw is illustrated in Fig. 18.10. The development of the particle cascade and the longitudinal position with maximum heating are visible. For a graphite secondary jaw (1 m length) the peak temperature is reached at the end of the jaw. Energy deposition was calculated for all specified beam load cases for both protons and ions and the results indicated that graphite jaws meet the requirements of maximum robustness. They must have a transverse depth of at least 15 mm to avoid excessive showering in a higher-Z back plate.

Peak mechanical stress

The results of the FLUKA calculations were input to thermo-mechanical calculations, performed with ANSYS [50]. Tab. 18.9 summarises the calculated peak stress values for load cases at injection and top energy and graphite, carbon-carbon (CFC), and beryllium materials. To compare the structural behaviour of the jaw materials, a stress norm $\sigma_{equiv} = ||s||$ is introduced[54], which for beryllium is a von Mises stress. The isotropic, fine grain graphite is estimated by the Stassi criterion (generalised von Mises). CFC is analyzed with its principal components in each direction. Corresponding to the main fiber orientation in the y-direction, the main calculated values are indicated in Tab. 18.9. The peak stresses are compared to the maximum allowed, which is specific for each material. Calculated peak stress values for graphite and carbon-carbon (fiber-reinforced graphite) are within the tolerances and can be used for maximum robustness collimator jaws, both for primary and secondary collimators. Beryllium does not meet the tolerances for either injection or 7 TeV load cases and cannot be used safely.

Heat load and cooling

During normal operation the collimators will experience a varying heat load from electro-magnetic fields (RF heating) and from direct beam deposition, so an appropriate cooling system is required. The maximum heat load occurs at 7 TeV where up to 4×10^{11} p/s can be lost for 10 s (case of 0.2 h beam lifetime). The lost protons have impact parameters of 0-200 nm and a typical round spot size of 200 μm was assumed. This case was studied using the scattering routines in FLUKA [52, 53] where the energy is deposited in multi-turn interactions. It was found that the longitudinal power density depends on the beam-to-jaw collinearity.

Table 18.7: Collimators in the betatron cleaning insertion IR7 for beam 1 and beam 2 during phase 1. Placeholders for a potential efficiency upgrade are indicated in slanted typeface (these are not installed during phase 1) and phase 2 TCSM collimators have been omitted. For each collimator the longitudinal position relative to IP7, the azimuthal orientation of the jaws and the nominal half gap at 7 TeV is listed.

Name	Distance from IP7 [m]	Azimuth [°]	Half gap [mm]
TCP.D6L7.B1	-204.17	90.0	1.2
TCP.C6L7.B1	-203.17	0.0	1.7
TCP.B6L7.B1	-202.17	135.0	1.4
TCP.A6L7.B1	-201.17	45.0	1.4
TCSG.B6L7.B1	-165.67	41.1	1.7
TCSG.A6L7.B1	-161.67	141.5	1.7
TCSG.B5L7.B1	-102.27	146.7	2.0
TCSG.A5L7.B1	-98.27	40.5	2.0
TCSG.E4L7.B1	-76.97	90.0	1.3
TCSG.C4L7.B1	-47.77	134.4	2.1
TCSG.B4L7.B1	-6.97	0.0	1.9
TCSG.A4L7.B1	-2.97	135.7	1.8
TCSG.A4R7.B1	1.03	44.2	1.8
TCSG.B4R7.B1	49.73	135.7	2.1
TCSG.A5R7.B1	88.23	44.7	2.2
TCSG.B5R7.B1	92.23	134.0	2.2
TCSG.C5R7.B1	104.23	90.0	2.1
TCSG.D5R7.B1	108.23	57.9	2.1
TCSG.E5R7.B1	112.23	122.8	2.0
TCSG.6R7.B1	146.83	0.5	2.9
TCP.D6R7.B2	204.18	90.0	1.2
TCP.C6R7.B2	203.18	0.0	1.6
TCP.B6R7.B2	202.18	135.0	1.4
TCP.A6R7.B2	201.18	45.0	1.4
TCSG.B6R7.B2	165.48	41.7	1.7
TCSG.A6R7.B2	161.48	140.8	1.7
TCSG.B5R7.B2	102.26	146.6	2.0
TCSG.A5R7.B2	98.26	40.3	2.0
TCSG.E4R7.B2	76.93	90.0	1.3
TCSG.C4R7.B2	47.74	135.6	2.1
TCSG.B4R7.B2	11.00	0.0	1.9
TCSG.A4R7.B2	7.00	136.6	1.8
TCSG.A4L7.B2	-9.00	43.4	1.8
TCSG.B4L7.B2	-49.74	136.1	2.1
TCSG.A5L7.B2	-88.26	45.0	2.2
TCSG.B5L7.B2	-92.26	133.7	2.2
TCSG.C5L7.B2	-104.26	90.0	2.1
TCSG.D5L7.B2	-108.26	58.3	2.1
TCSG.E5L7.B2	-112.26	122.3	2.0
TCSG.6L7.B2	-146.72	0.5	2.9

Table 18.8: Density, maximum energy deposition, maximum temperature, and fraction of energy escaping a 1.4 m long collimator jaw of different materials for a single module dump pre-trigger at 7 TeV. Some materials are heated well above their melting point and it is noted that the temperature is given for illustration only.

Material	Density [g/cm^{-3}]	Max. energy deposition [GeV/cm^{-3}]	Max. temperature [°K]	Energy escaping [%]
Graphite	1.77	1.3×10^{13}	800	96.4
Beryllium	1.85	0.9×10^{13}	310	97.0
Aluminium	2.70	5.3×10^{13}	2700	88.8
Titanium	4.54	1.7×10^{14}	>5000	79.5
Copper coating (100μm)	8.96	7.0×10^{14}	>5000	34.4

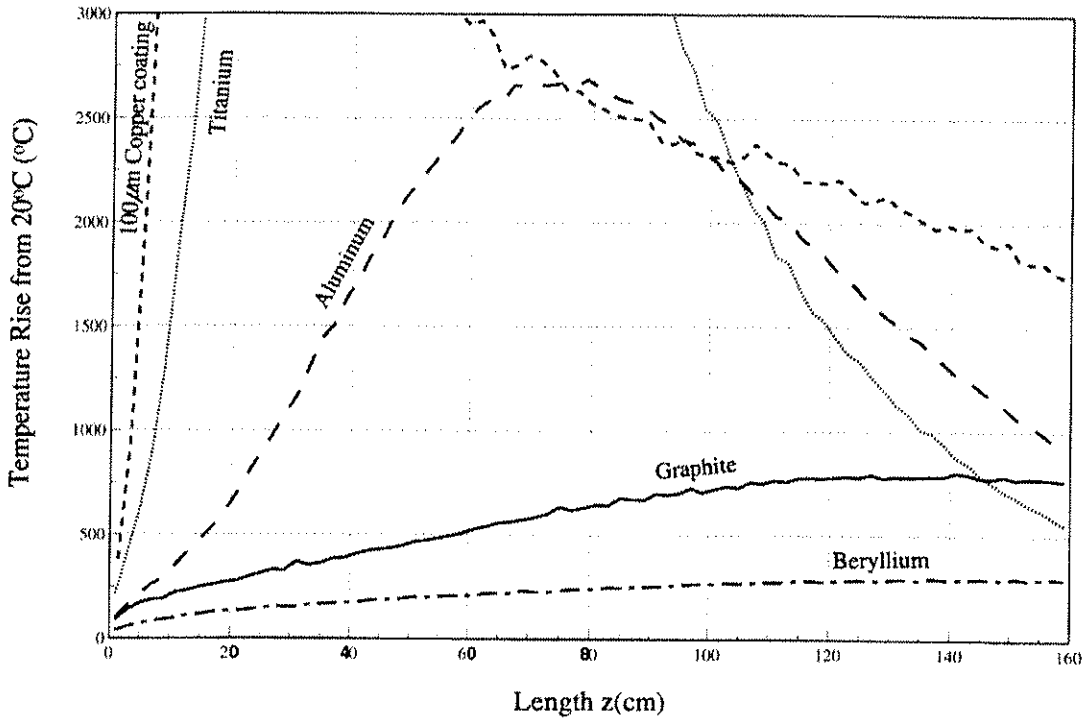

Figure 18.10: Maximum temperature increase for different longitudinal slices of a collimator block and for different materials. A single module dump pre-trigger at 7 TeV is assumed for a typical spot size of 200 μm.

Small misalignments reduce the length of traversal and energy is deposited in a shorter distance, e.g. a 5 μrad misalignment reduces the traversal length to 2 cm; this is illustrated in Fig. 18.11. The proton induced power is then 2960 W which must be compared to a 1785 W for perfect alignment. The maximum possible peak power deposition from primary proton is expected to be close to 3 kW.

RF heating was estimated to be below about 0.5 kW per jaw. The power deposition due to showers that originate in upstream collimators comes in addition. Energy deposition in a secondary collimator was found to be up to 30 kW in phase 1 and 130 kW in phase 2 and the maximum power deposition in a phase 1 collimator amounts to 34 kW for peak losses during 10 s. The maximum continuous power load for a specified beam lifetime of 1 h amounts to about 7 kW.

In conclusion, a secondary collimator with two jaws must withstand a power load of 34 kW during 10 s and 7 kW continuously in phase 1. An appropriate cooling system is under study with the goal to hold the jaw temperature below 50 °C and to prevent significant mechanical deformations.

Dedicated cooling systems which will provide independent control of cooling water for each collimator are required for the two cleaning insertions. It is particularly important that the activated water can be drained and refilled remotely during a collimator bake-out or a collimator exchange.

Table 18.9: Summary of calculated peak stress values σ_{equiv} for *impact of one injected batch* and for *7 TeV impact* of 8 out of 3000 bunches (abnormal dump) on a collimator. Different materials and primary and secondary collimator lengths are compared. The allowable maximum stress σ_{allow} is listed and the suitability is indicated.

Case	Material	Jaw length [cm]	Max. temperature [°C]	Stress σ_{equiv} [MPa]	σ_{allow} [MPa]	Suitability
Injection	Carbon-Carbon	20	335	4.4	86	yes
		100	345	12.7	86	yes
	Graphite	20	335	3.1	18	yes
		100	345	6.2	18	yes
	Beryllium	20	168	334	160	no
		100	200	440	160	no
7 TeV	Carbon-Carbon	20	212	20.8	86	yes
		100	551	82.0	86	yes
	Graphite	20	212	4.4	18	yes
		100	551	17.8	18	yes
	Beryllium	20	116	584	160	no
		100	168	1248	160	no

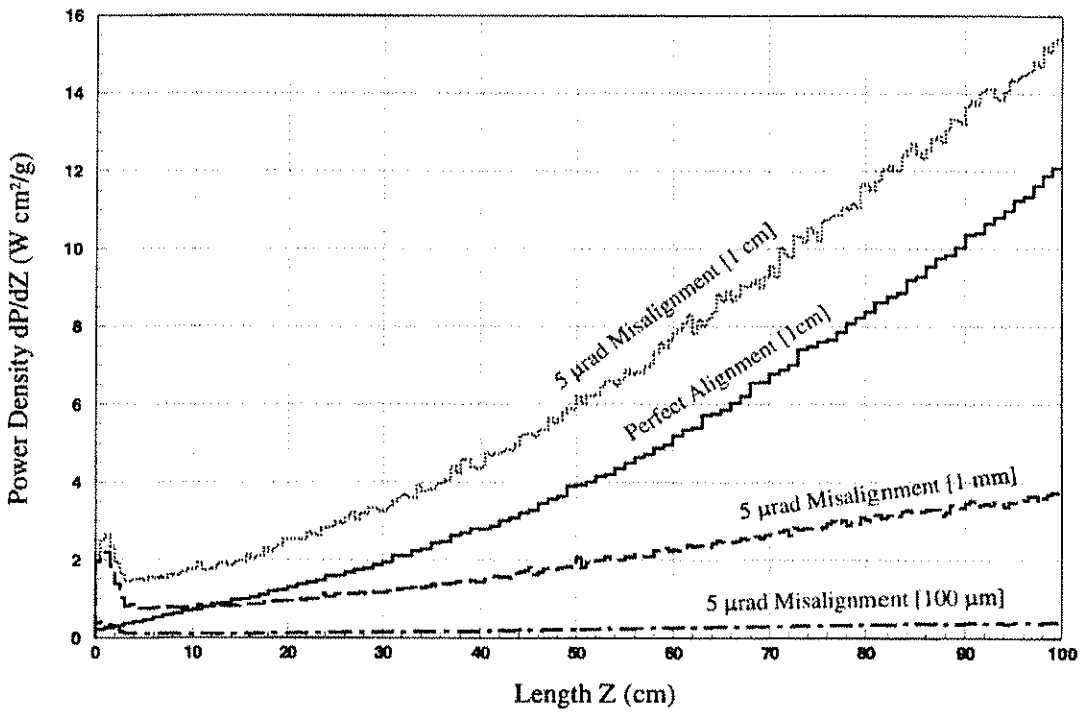

Figure 18.11: Longitudinal power density along a 1 m long graphite collimator, plotted versus the longitudinal position. It is assumed that 4×10^{11} p/s impact at 7 TeV with impact parameters of 0-200 nm (case of 0.2 h beam lifetime). The curves correspond to a perfect parallelism between protons and jaw (perfect alignment) and a 5 μrad misalignment. The power density is integrated in several transverse ranges of 0.1 mm to 10 mm.

Vacuum compatibility

The LHC beam tube is an ultra-high vacuum system and the collimators must not disturb vacuum performance. Several species of graphite were tested for outgassing rates and compatibility with the LHC vacuum requirements [55]:

- Variations in outgassing rate of up to a factor of 10 were observed for the materials tested. Material composition, dimensions and design are essential and each material/design must be examined separately.

- A factor of 10 improvement in outgassing rate can be achieved by heat treatment in a clean vacuum or a high temperature bake-out.
- An in-situ bake-out at above 300°C improves the performance by a factor of 10.
- CH species from the C jaws are only pumped by ion pumps. One cannot rely on NEG or Ti sublimations for these.
- Special treatments can decrease performance (e.g. 2 μm PVD Ti coating by a factor of 6). If followed by a bake out at 250°C during 24 h, the material will recover the initial outgassing values.
- If the graphite material is operated above room temperature then the outgassing rate increases steeply. Outgassing rates are increased about tenfold for a 50°C increase of jaw temperature. The jaw temperature should therefore be kept below 50°C.
- A pressure rise by 4 orders of magnitude is expected in the case of an abnormal beam impact (temperature increase to 1050°C) .
- Recovery following dump errors is good with 3 orders of magnitude in vacuum pressure recovered after 1.5 hours. This is short enough to not impose any delays for the refilling of the LHC.

The vacuum studies show that graphite-based jaws are compatible with the LHC vacuum. The outgassing rates of the C jaws of the collimators will be optimised by material and heat treatment under vacuum, an in-situ bake-out and a proper shape design. A survey in the SPS close to the graphite dump revealed no signs of dust and there is no indication that graphite dust may be a problem for the LHC. The magnitude and possible effects of a local electron cloud are being studied.

Impedance implications (resistivity, coating)

Graphite materials have a relatively high resistivity, ranging from 7 $\mu\Omega$m to about 30 $\mu\Omega$m which results in significant contributions to the LHC impedance from the collimators. In order to minimise impedance it is crucial to select the graphite material with the lowest resistivity, if at all possible. A market survey and measurements are ongoing at the time of writing. A thin 1 μm coating of copper might be placed on all graphite collimators, if it can be shown that this coating will adhere reasonably well and will not damage the graphite jaw in case of abnormal beam impact.

18.5.3 Mechanical collimator design

The mechanical design of collimators that can withstand the high intensity LHC beam is challenging. Collimators do not only need to be very robust but at the same time quite long (high energy protons) and very precise (small collimation gaps). The functional requirements for TCP and TCSG collimators are summarised in Tab. 18.10 [56]. The small minimum gap size of 0.5 mm and the small beam size at the collimators (200 μm rms) implies tight mechanical tolerances and the numbers quoted which refer to nominal running will be relaxed for initial running. Achieving these tolerances would in principle allow closing the TCP and TCSG collimators of phase 1 to 6 σ and 7 σ. For beam-based alignment the jaws must be remotely movable with good precision and reproducibility of settings is crucial in order to avoid lengthy re-optimisations. The absolute opening of the collimator gap is safety-critical and must be known at all times with good accuracy. A movement orthogonal to the collimation plane allows provision of spare surface, e.g. after coating has been locally damaged by the beam.

Technical concept

The present technical concept (see Fig. 18.12) is the result of the analysis of a wide spectrum of options and alternatives [57]; the guiding principle for the mechanical design has been the use and optimisation of proven

Table 18.10: Functional requirements for the TCP and TCSG type collimators. The orientation of objects with one or two parallel jaws is horizontal (X), vertical (Y), or close to 45 degree (S). The required degrees of freedom (DOF) for jaw movements are listed.

Parameter	**Unit**	**TCP**	**TCSG**
Azimuthal orientation		X, Y, S	various
Jaw material		C or C-C	C or C-C
Jaw length	cm	20	100
Jaw tapering	cm	2×10	2×10
Jaw dimensions	mm^2	65×25	65×25
Jaw coating		0-1 μm Cu	0-1 μm Cu
Jaw resistivity	$\mu\Omega$m	minimal	minimal
Surface roughness	μm	≤ 1	≤ 1.6
Surface flatness	μm	25	25
Heat load (peak)	kW	1.5	34
Heat load (continuous)	kW	1.5	7
Max. operational temperature	°C	50	50
Outbaking temperature	°C	250	250
Maximum full gap	mm	60	60
Minimum full gap	mm	0.5	0.5
Knowledge of gap	μm	50	50
Jaw position control	μm	≤ 10	≤ 10
Control jaw-beam angle	μrad	≤ 15	≤ 15
Reproducibility of setting	μm	20	20
DOF movement (hor. collimator)		X, X', Y	X, X', Y
DOF movement (vert. collimator)		Y, Y', X	Y, Y', X
Positional installation accuracy	μm	100	100
Angular installation accuracy	μrad	150	150

technologies, mainly drawn from LEP collimator experience [58]. However, due to the unprecedented specification, it was also necessary to make use of innovative technologies and novel materials, such as Carbon/Carbon composites. The main technical features of the LHC secondary collimators are:

1. An internal alignment system allowing both lateral displacement and angular adjustment.
2. A jaw clamping system to ensure good thermal conductance and free thermal expansion.
3. An efficient cooling system.
4. A precise actuation system including a semi-automatic mechanical return and a misalignment prevention device.
5. A plug-in external alignment system, allowing a quick and simple positioning of the collimator assembly in the machine.
6. A motorisation and a control set.

The system is free from the effect of vacuum force.

The jaw assembly design

The design of the jaw assembly was chosen based on the clamping concept: the graphite or C/C jaw is pressed against the copper-made heat exchanger by a steel bar on which a series of springs is acting. The jaw assembly is held together by steel plates (see Fig. 18.13). To minimise the thermal path from the hottest

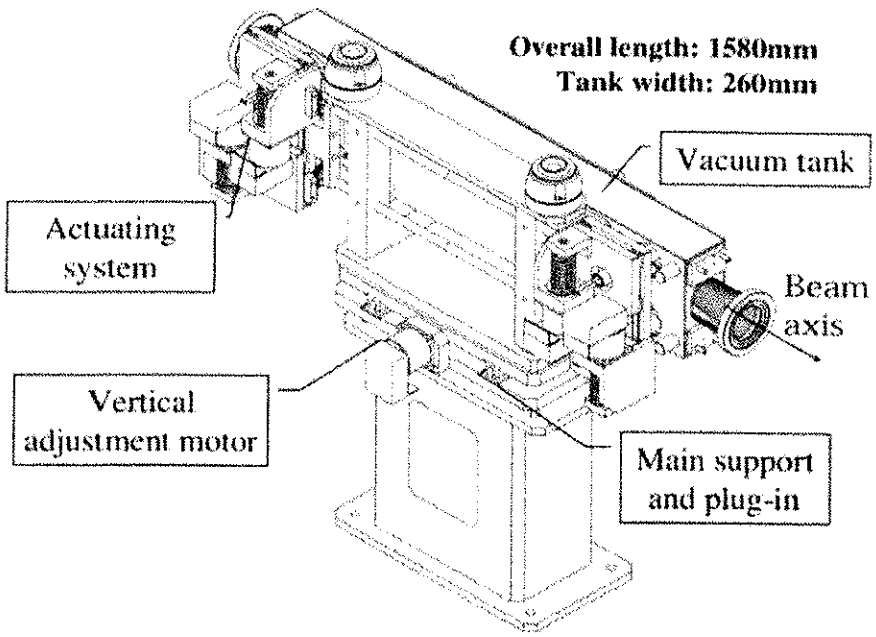

Figure 18.12: General layout and dimensions of the LHC secondary collimator (vertical configuration).

spot, where the beam impact takes place, to the cooling pipes, the jaw width has been reduced to an allowable minimum (25 mm), as demanded by preliminary thermo-mechanical analysis. Since the thermal expansion coefficient of copper is three times (or more) larger than graphite's, a fixed joint between the jaw and the copper plate is not possible, if one wants to avoid unacceptable distortions; hence, the contact must allow for relative sliding between the two surfaces. At the same time, to ensure proper heat conduction at the contact interface, a certain pressure has to be applied between these surfaces. The pressure was estimated through a semi-analytical model developed by Fuller and Marotta [59, 60]. A higher pressure leads to better conductance, but, in turn, it means higher mechanical stresses on the jaw; therefore a trade-off had to be found: the nominal pressure on the interface is set to 5 bar. To minimise the effect of differential thermal expansion on the jaw surface precision, the transverse distance from the two supporting axles to the internal reference surface of the jaw has been reduced to 40 mm.

The cooling system

The heat exchanger is made from two OFE-copper pipes per jaw brazed on one side, to a copper plate and on the other to a stainless steel bar; each pipe has three turns to increase the heat exchange (Fig. 18.14) and the inner diameter of the pipes is 6 mm. To ease the brazing and avoid harmful air traps, the pipe section is square. The measurement of the outgassing rates of graphitic materials led to the specification of a maximum operating temperature of 50 °C for the jaw material which necesitates the use of chilled water. To meet such a strict requirement, the coolant temperature must be as low as possible: the assumed inlet temperature is 15 °C to limit possible condensation problems (to this regard, a certain margin exists, since temperature could be further reduced to 12 °C). The water flow rate is 5 l/min per pipe, leading to a flow velocity of ≈3 m/s. This value is in fact rather high and might lead to erosion-corrosion problems on the soft copper pipe bends; however it is necessary both to ensure the evacuation of the high heat loads anticipated and to limit the thermally-induced deformations. In any case, the flow rate can be adjusted for each collimator by specific flow-fix valves. A cooling system is also planned for the outer surface of the vacuum tank.

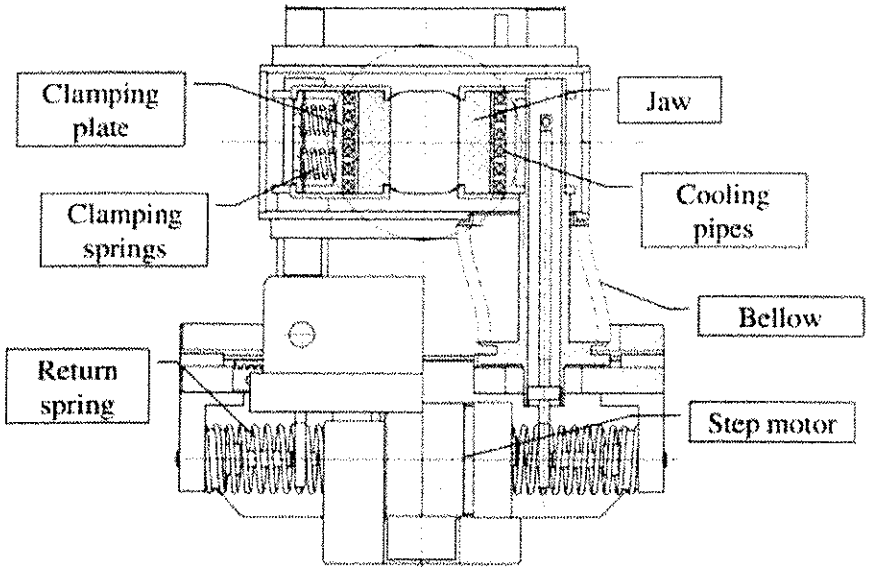

Figure 18.13: Secondary collimator mechanical assembly (cross-section of a horizontal TCSG).

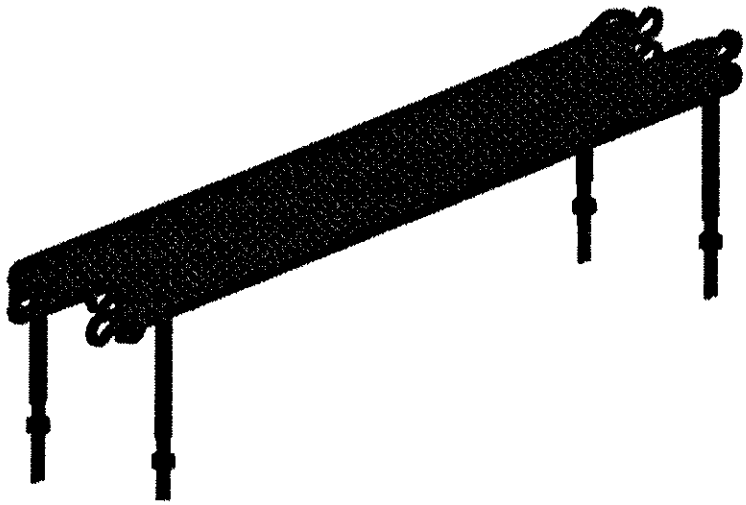

Figure 18.14: Cooling system: the multi-turn cooling pipes and the copper plates.

Motorisation and actuation system

Each jaw is independently actuated by two stepper-motors (Fig. 18.15) which allows both lateral displacement (with a nominal stroke of 30 mm plus 5 mm of extra-stroke) and angular adjustment. Excessive tilt of the jaw is prevented by a rack and pinion system which avoids relative deviation between the two axes larger than 2 mm (i.e. 2 mrad). Each motor directly drives, via a roller screw/nut set, a table which allows the precise positioning of the jaw supporting axle. Each table is mounted on anti-friction linear guide-ways. The advancement for each motor step is 10 μm. Vacuum tightness is guaranteed by four bellows which can be bent sideways (not shown). The system is preloaded by a return spring which makes the system play-free and also ensures a semi-automatic driving back of the jaw in case of motor failure. The position control is guaranteed by the motor encoder and by four linear position sensors. Stops and anti-collision devices for jaw motion are also planned.

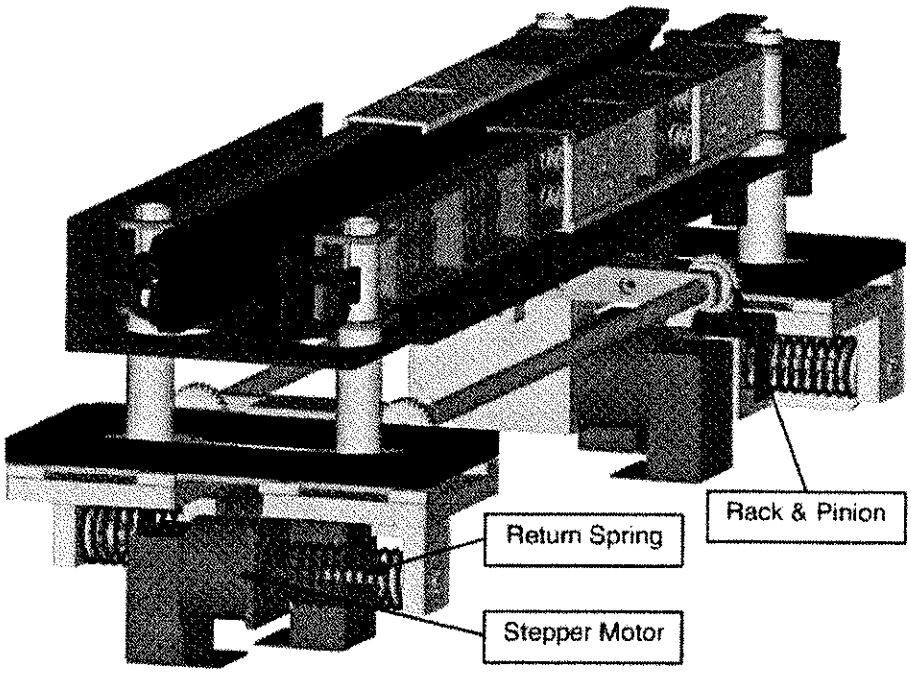

Figure 18.15: Motorisation and actuation system.

The vacuum tank and the external alignment system

The vacuum tank is of a traditional design, is manufactured in AISI 316L stainless steel and is mainly electron-beam welded. The structural design is the same for all the collimator configurations (horizontal, vertical or skew). The tank is supported by brackets the design of which depend upon the orientation and the whole system is pre-aligned and then placed on a support table via a plug-in system. A stepper motor allows the adjustment of the whole assembly by 10 mm in order to move the jaws on the plane of collimation and present a fresher surface in the beam impact area in case the initial impact area is damaged.

Local collimator instrumentation

The collimators will be equipped with sophisticated instrumentation which will provide extensive diagnostics. The main diagnostics information is summarised:

- Position of each motor and jaw support point.
- Independent measurement of collimator gap at both extremities of collimator tank (average gap and angle between the two jaws).
- Independent measurement of one jaw position at both extremities of collimator tank.
- Temperature of each graphite jaw at both of its extremities (start and end).
- Temperature of cooling water at inlet and outlet.
- Signals from various switches (in, out, anti-collision, etc.).
- One microphonic sensor per jaw for detection of beam-induced shock waves.
- Flow of cooling water per collimator.

The extensive diagnostics will allow fail-safe setting of collimator gaps, important checks on self-consistency and detection of abnormal beam load conditions.

18.5.4 Tertiary collimators in the experimental insertions (TCT)

The most stringent requirements for the collimation system occur during collisions at 7 TeV when the stored energy is maximal and local aperture restrictions occur at the experimental triplets. In order to protect the triplets in case of the unlikely event that mis-kicked beams escape the protection systems, it is useful to install local protection. In addition, tertiary collimators can help to fulfill the efficiency requirements by providing a local cleaning stage at the location where it is needed. Local cleaning is highly efficient because global changes of beam parameters (orbit, beta beat) do not perturb the local shadow.

The tertiary collimators are currently planned to be close to D1 on each side of the four experimental insertions and their jaws will be made out of high-Z material. The tertiary halo will be intercepted and diluted, such that less energy reaches the super-conducting triplet magnets. Peaks in tertiary halo (e.g. due to transient drops in beam lifetime) are suppressed and triplet quenches are avoided, even though some background spikes could be expected in the experiments. It is important to realise that these background spikes are the price paid for preventing triplet quenches which would otherwise terminate the physics fill. With tertiary collimators the physics fill can be continued after stable conditions have been restored (perturbations can be as short as a few seconds or minutes). It is expected that significant gains can be made in uptime and integrated luminosity production and if the tertiary collimators generate unforeseen problems they can be moved out from the beam.

In total 16 tertiary triplet collimators will be installed, each made out of copper and with a length of 1.0 m. From Fig. 18.16 it is seen that almost all protons in the tertiary halo will interact inelastically and more than 50% of the energy lost stays in the copper block. Therefore the halo-induced heat load in the triplet will be reduced by at least a factor of 2 (gaining in effective efficiency). In addition, the tertiary collimators add significant flexibility to the system. For example, one could optimise beam-induced background in the experiments versus luminosity.

The tertiary collimators offer important additional protection against beam losses, in particular for operation at 7 TeV with low beta function at the IP and large beta function in the triplet:

1. In the case of an abnormal beam dump, the maximum excursion of bunches in the triplet depends on many parameters, such as the orbit at the TCDQ, the orbit at the triplet, etc. An orbit offset of only 1.5 σ at the TCDQ (0.5 σ is the specified tolerance) could result in an impact of one 7 TeV bunch at the superconducting magnets in the triplet. The setting of the tertiary collimators would be such that they shadow the superconducting coils of the triplet magnets. Particle loss would be restricted to the collimator which can be replaced more easily.

2. A failure that leads to an orbit distortion or emittance growth would first result in beam losses at the collimators. Normally, beam loss monitors would detect the losses and request a beam dump. If the beam was not dumped, the showered beam would touch the triplet aperture a short time later and possibly quench or even damage the magnets. With the aperture restriction of the tertiary collimators, close-by beam loss monitors would request a beam dump and therefore ensure some redundancy in the protection.

18.5.5 Additional collimators, absorbers and scrapers

Scrapers (TCSP)

Scraping of proton beams is an important accelerator technique. It is often used for diagnostics purposes, control of background, or to avoid peaks in loss rate. The LHC primary collimators are specified for a minimum opening of 5 σ (about $\pm$ 1 mm) and because they are crucial for beam cleaning, they should not be used for other purposes. It has therefore been decided to include 6 dedicated scrapers (horizontal, vertical, momentum for each beam) into the LHC design and they will be located at the corresponding primary collimators. Material, length, and detailed design of the LHC scrapers remain to be decided. It is planned to install scrapers for phase 1 of LHC collimation.

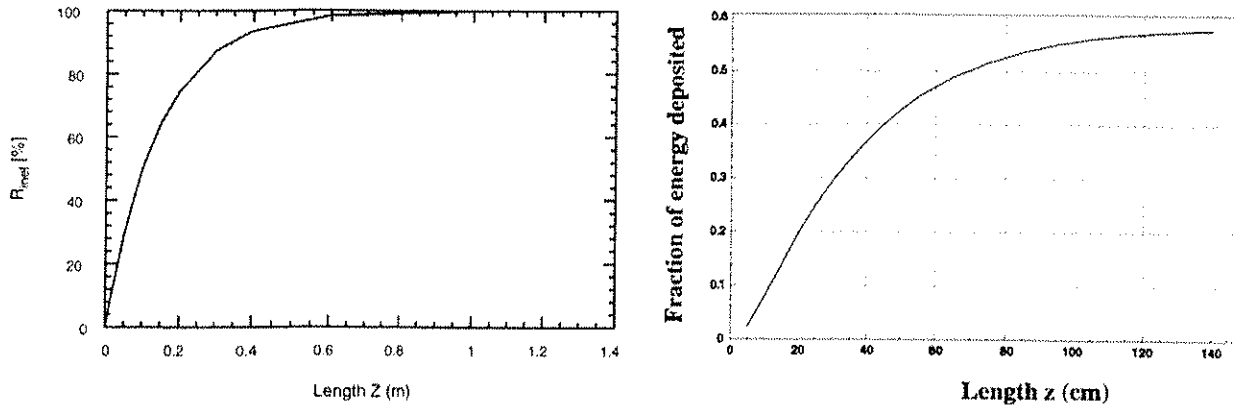

Figure 18.16: Fraction of inelastically interacting protons (left) and fraction of energy deposited (right) in a block of Cu material, plotted as a function of its length. The energy deposition results include the full proton-induced cascade.

Fixed absorbers

The collimators absorb only a small fraction of the energy from the lost protons (of the order of a few %) and the particle showers will exit from the collimator jaws and carry energy downstream. In order to avoid quenches or excessive heating, the particle cascades must be intercepted by additional fixed absorbers downstream of the collimators. Detailed shower calculations will be performed in order to decide the length, location, and eventual cooling requirements for fixed absorbers which will be required for phase 1 of LHC collimation.

Collimators for collision debris (TCLP)

The movable TCLP collimators are used to capture part of the debris from the p-p interactions at the experimental insertions in IR1 and IR5. They will be made out of 1 m long copper jaws and can be installed in two batches of 4 components in phase 1 and phase 3: the detailed design remains to be decided.

Injection collimators (TCLI)

Special TCLI collimators are part of the protection system for LHC injection. These movable devices complement the protection from the TDI device (see Chap. 16) and will intercept mis-kicked beam in IR2 and IR8: a detailed design remains to be decided. TCLI collimators are required for phase 1 of LHC collimation.

18.6 PERFORMANCE REACH WITH PHASE 1 COLLIMATION AND BEYOND

The relevant performance measure of the LHC collimation system is the beam loss rate $R_{sc}(s)$ in any superconducting magnet of the LHC ring. This maximum loss rate should be below the quench limit $R_q(s)$ and is a function of the cleaning inefficiency $\eta_c(a_c, n_1, n_2, n_3)$ (see Eq. 18.3), the minimum beam lifetime at the collimators $\tau_{\min}$, the total beam population N_{tot} and some aperture distribution map $A_{dis}(s, x_0, x_0', y_0, y_0', \delta_0, s_0)$:

$$R_{sc} \approx \eta_c(a_c, n_1, n_2, n_3) \cdot \frac{N_{tot}}{\tau_{\min}} \cdot A_{dis}(s, x_0, x_0', y_0, y_0', \delta_0, s_0) \tag{18.6}$$

The aperture distribution map A_{dis} is a particularly complicated function that depends on the collimator location s_0 where the particle escaped, the particle coordinates (offset in phase space) and the detailed aperture model between the escape location s_0 and the observation point s. Though it is sometimes approximated by the inverse of a so-called dilution length L_{dil}, a reliable determination requires full tracking studies with a detailed aperture model, including aperture imperfections and additional absorbers. These studies are presently not advanced enough to predict local beam loss rate $R_{sc}(s)$ at the 10^{-5} level of primary beam losses ($10^{-8} - 10^{-9}$ level of totally stored intensity).

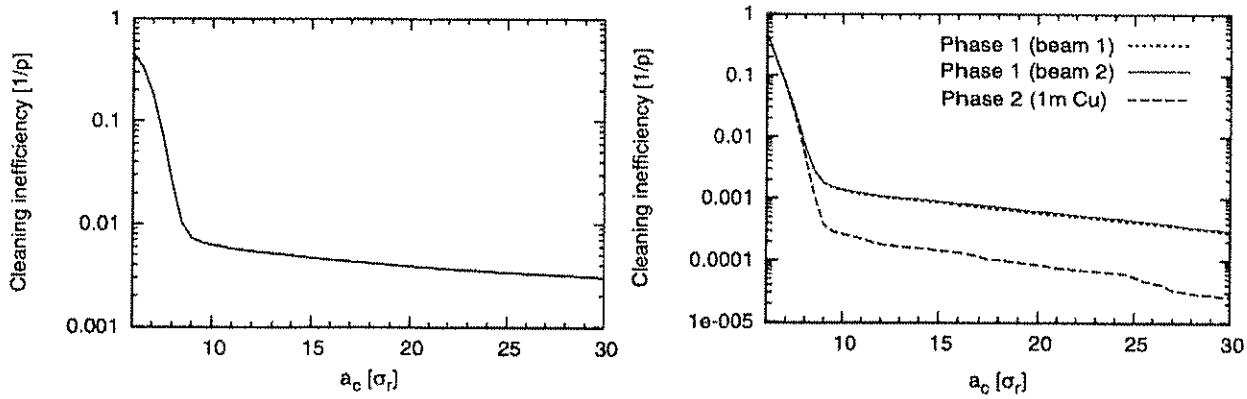

Figure 18.17: Predicted ideal inefficiencies for betatron cleaning at injection (left) and 7 TeV (right) with 6/7 σ settings. The 7 TeV prediction includes phase 1 and phase 2 performance, assuming 1 m Cu jaws for phase 2 collimators.

Even though detailed performance estimates are not yet possible, it is hoped that the design goals for cleaning efficiency can be met. The collimation system is designed to support up to 40% of design intensity with nominal β^* in phase 1. The phase 2 collimation system should allow nominal and possibly even ultimate running conditions.

18.6.1 Estimation of ideal cleaning inefficiency

The cleaning inefficiency $\eta_c(a_c, n_1, n_2, n_3)$ (here generalised to include tertiary collimators at a normalised setting of n_3) can be predicted by tracking programs that are also used in the design process of the cleaning insertions. The expected performances at injection and top energy of the betatron cleaning system in IR7 are shown in Fig. 18.17. Almost a factor of 10 better inefficiency can be reached with phase 2. It is noted that the results apply for an ideal system with some assumptions on the beam halo (see Fig. 18.2) and cannot easily be used to estimate the allowable beam intensity in the LHC ring. Advanced halo tracking in a detailed aperture model must be used for this purpose, as discussed above. Nevertheless it is stated that the design of the collimation systems achieved quite good cleaning inefficiencies that could not be optimised further, given the LHC constraints. The predicted inefficiencies for the ideal betatron collimation at 7 TeV are as low as 11×10^{-4} for phase 1 and 2×10^{-4} for phase 2. The corresponding maximum amplitudes of the on-momentum secondary halo were independently estimated to be 9.3 σ radially and 7.3 σ and 7.4 σ in the horizontal and vertical directions.

The tracking studies provide predictions on other important aspects. Fig. 18.18 shows the calculated multi-turn probability for inelastic interaction and the average impact parameter for the various collimators in the betatron cleaning insertion IR7. The locations of inelastic interactions of lost protons is an important input for understanding the loss distribution and activation in IR7. The impact parameter at the secondary collimators (defined as transverse distance between proton impact point and collimator edge) determines important tolerances, e.g. the required surface flatness and allowable angular imperfections.

18.6.2 Collimation tolerances

A complete and consistent study of collimation tolerances remains to be completed and the numbers listed should be used as preliminary estimates only.

The proper functioning of the LHC collimation system depends on the concept of a two stage cleaning process in IR3 and IR7 which implies that the secondary collimators must never become primary collimators. The relative retraction between the two settings is nominally 1 σ, about 1.2 mm at injection and 0.2 mm at top energy. Several effects can change the relative retraction of collimators with respect to the beam orbit, in particular orbit changes and transient changes in beta beat must be avoided. In addition mechanical deformations of the jaws can cause perturbations. The most severe tolerances apply for 7 TeV where the nominal 200 μm

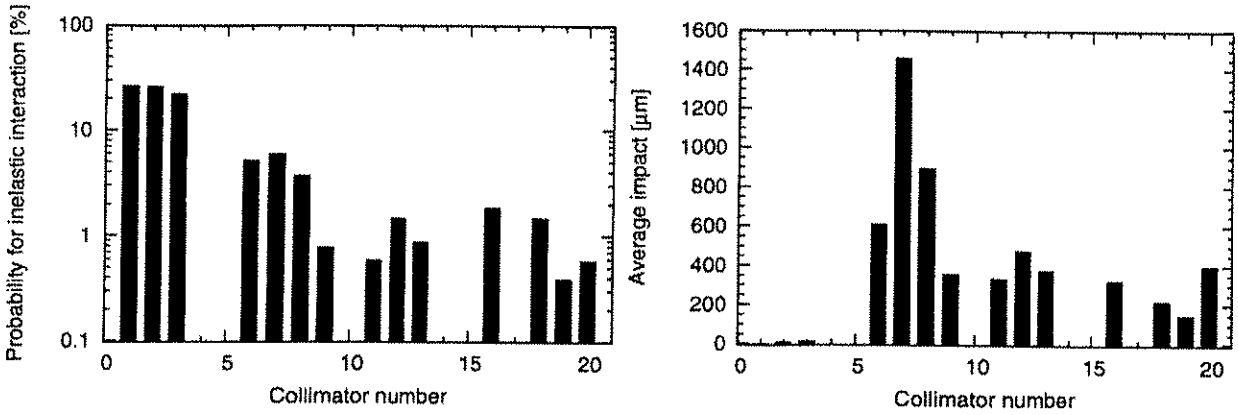

Figure 18.18: Predicted multi-turn probability for inelastic interaction (left) and average impact parameter at the various collimators (right) in the betatron cleaning insertion IR7.

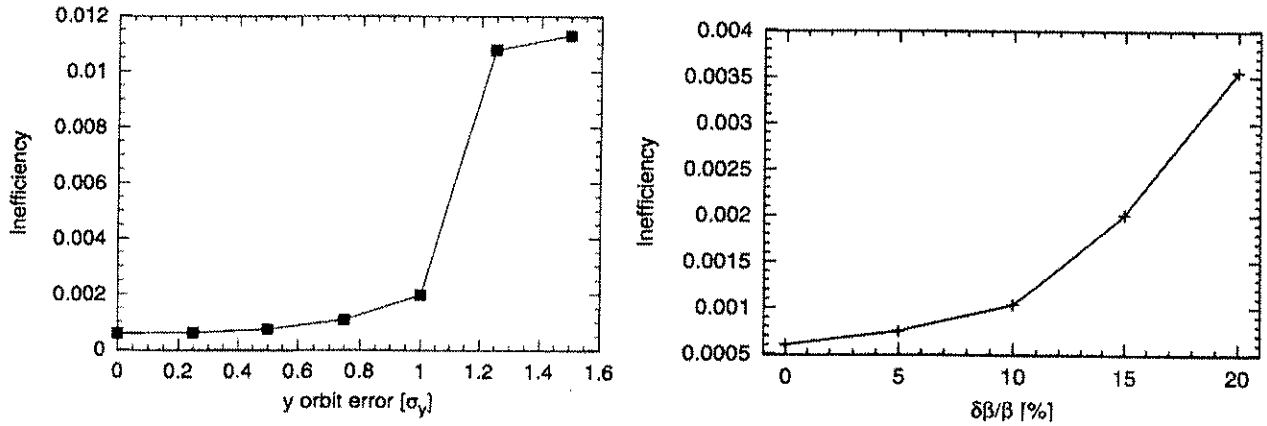

Figure 18.19: Left: Dependence of the collimation inefficiency on an uncontrolled change in vertical orbit (worst phase). Right: Dependence of the collimation inefficiency on an uncontrolled transient beta beat (worst phase).

relative retraction can be reduced by several possible sources of errors. It is noted that this retraction should not be smaller than about 0.5 σ or 100 μm at 7 TeV. The tolerances for mechanical jaw properties were listed in Tab. 18.10 for nominal collimation settings (6/7 σ).

Operational tolerances were preliminarily estimated for the 7 TeV nominal collimation settings (6/7σ), each tolerance leading to a 50% increase in cleaning inefficiency [61]. A consistent and combined treatment of all tolerances remains to be completed. The results of studies are illustrated in Fig. 18.19 and the corresponding tolerances are summarised in Tab. 18.11 for nominal conditions and for an early 7 TeV collimation setting that relaxes operational tolerances. A relaxation of tolerances at 7 TeV is achieved by choosing for example a 3.5 σ retraction between primary and secondary collimators during early collisions (requiring a higher β^* in the range of 1-2 m). The collimation process can thus be made compatible with a natural learning curve in operation and optimisation of the LHC. The tertiary collimators provide an additional gain in operational tolerances at 7 TeV which was not included in the numbers listed. It is noted that tolerances at injection cannot be relaxed, except by accumulating less beam.

18.6.3 Operational conditions for collimation

The operational set-up of the LHC collimation system for significant intensities can be envisaged only after some pre-requisites have been fulfilled by LHC operation. They are listed in order of importance:

- Design aperture has been established (in particular a maximum beta beat of 20% and a maximum peak orbit of 4 mm must be guaranteed during the LHC beam cycle).

Table 18.11: Important operational tolerances for collimation, each defined for a 50% increase in cleaning inefficiency (preliminary estimates). Interdependencies between errors are not yet taken into account. The β^* for relaxed conditions depends on the stored intensity and should be in the range of 1-2 m.

Parameter	Tolerances		
	Nominal injection	Collision (nominal)	Collision (relaxed β^*)
(n_1/n_2)	(6/7 σ)	(6/7 σ)	(7/10.5 σ)
Beam size at collimators	$\approx$ 1.2 mm	$\approx$ 0.2 mm	$\approx$ 0.2 mm
Orbit change	0.6 σ	0.6 σ	2.0 σ
	$\approx$ 0.7 mm	$\approx$ 0.12 mm	$\approx$ 0.4 mm
Transient beta beat	8%	8%	80%
Collinearity beam-jaw	50 μrad	50 μrad	75 μrad

- Nominal beam loss rates have been established (the minimum beam lifetime should not drop below 0.2 h during the full LHC beam cycle).
- Transient changes in orbit and beta beat are under control, fulfilling the collimation injection tolerances (orbit and tune loops have been commissioned).

The margin gained by running with lower intensities would be used for bringing up cleaning efficiency from an initially sub-optimal to a fully optimised situation.

The collimation system will be operationally characterised by the achieved cleaning efficiency and the induced impedance. The operational conditions of the LHC must be adapted accordingly with possible consequences on the stored beam intensity and the β^* in the experimental insertions. Possible operational measures to help collimation performance are described:

- Decrease of stored intensity as a measure to adapt to limited cleaning efficiency or to reduce the effects of collimator induced impedance. For impedance it is important to carefully consider reductions in bunch intensity or number of bunches.
- Increase of β^* at top energy as a measure to adapt to limited cleaning efficiency or to increase the collimator gaps. Wider collimator gaps are helpful to relax operational tolerances (improve collimation efficiency) or to reduce the effects of collimator induced impedance.

It is expected that impedance limitations become apparent only at 7 TeV if more than about 40% of nominal intensity is stored with a 25 ns bunch spacing (see Chap. 5). A careful trade-off will be required to define the optimal operational strategy with collimation, based on the actually observed limitations in the LHC machine. The tertiary collimators increase the operational flexibility and introduce additional ways of optimising performance.

18.6.4 Beam-based optimisation of collimator settings with Beam Loss Monitors

The set-up and optimisation of the collimation system will be done in several beam-based steps, relying on the measurements from Beam Loss Monitors (BLM's) which will be installed near every collimator [24]. Following set-up procedures at other colliders the following logic could apply:

1. Separate beam-based calibration of each collimator: After producing a well-defined cut-off in the beam distribution (e.g. with a scraper), the two ends of each collimator jaw are moved until the beam edge is touched (witnessed by a downstream beam loss signal). This step defines an absolute reference position and angle for each jaw, which is valid for given and hopefully reproducible orbit and optics functions.
2. System set-up: After restoring the reference beam conditions all collimators are set to their target gaps and positions, directly deduced from the absolute reference positions obtained in step 1. The cleaning inefficiency is observed in a few critical BLM's in the downstream areas.

3. Empirical system tuning: The cleaning inefficiency is minimised by empirical tuning on the few relevant BLM's where quenches can occur. The most efficient collimators are optimised first and the optimisation is orthogonal if the beam direction is followed. Possible cross-talk between beams can be avoided by single beam optimisation.

4. Automatic tuning algorithms: Once some experience has been gained with the collimation system a more advanced automatic tuning algorithm may be envisaged, taking into account collimator response matrices.

The detailed process of set-up and optimisation of the collimation system requires further studies and work.

Some effort has already been invested in understanding the BLM response to beam loss in the cleaning insertions. Considering advanced scenarios (all collimators used simultaneously for optimisation) it was found that the data recorded near collimators is difficult to use and to interpret. At high energy, the cascade developed in a jaw and in the surrounding material will induce signals in all monitors which are installed nearby and downstream. In order to understand how to use the signals, a preparatory simulation was done with MARS, which develops cascades into the entire momentum cleaning section, including 7 collimators and BLM monitors, vacuum chambers, magnets with their field, tunnel, ground, etc [62]. A primary impact map was generated. The partial fluences as issued from every collimator were recorded at each monitor, allowing a matrix to be built which allows the computation of the normalised rate s_i at every monitor as a function of the primary rate r_i at each collimator. For nominal working condition at injection energy, for $\vec{s} = \mathbf{M}\,\vec{r}$, $\mathbf{M}$ is equal to:

$$M = \begin{bmatrix} .0178 & .0 & .0 & .0 & .0 & .0 & .0 \\ .4662 & 1.19 & .0 & .0 & .0 & .0 & .0 \\ .0268 & .0291 & 1.081 & .0004 & .0 & .0 & .0 \\ .0432 & .0389 & 1.085 & 1.044 & .0 & .0 & .0 \\ .0079 & .0036 & .138 & .3245 & .9891 & .0 & .0 \\ .0036 & .0017 & .03858 & .1187 & .513 & .9848 & .0 \\ .0012 & .0007 & .0099 & .0349 & .1642 & .5093 & .9445 \end{bmatrix}. \tag{18.7}$$

Further work will include a variation of the jaw depth n_i one by one, in order to map $\mathbf{M}$ as a function of $\vec{n}$. $\mathbf{M}$ may be constructed by sending a pilot bunch on each jaw sequentially. With the high value of many non-diagonal terms in $\mathbf{M}$, it is not yet sure that unambiguous calculations of the loss rate on every collimator can be deduced with this approach. This will only become an issue once it is tried to tune many collimator settings at once, e.g. trying to speed up optimisation procedures after a few years of operation. Initial one-by-one studies will result in easily understandable response matrices.

REFERENCES

[1] R. Assmann. Proc. Chamonix 2003. CERN-AB-2003-008 ADM.

[2] J.B. Jeanneret, D. Leroy, L. Oberli and T. Trenkler. LHC Project Report 44 (1996).

[3] R. Assmann, F. Schmidt, F. Zimmermann, M.P. Zorzano. LHC-PROJECT-REPORT-592. EPAC02.

[4] L. Burnod and J.B. Jeanneret. CERN-SL-91-39-EA. LHC-Note-167 (1991).

[5] P. Bryant and E. Klein. CERN-SL-92-40-AP (1992).

[6] P. Bryant. CERN-SL-AP-92-024 (1992).

[7] P. Bryant et al. CERN-SL-AP-93-015 (1993).

[8] P. Bryant and E. Klein. SL-Note-93-29-AP (1993).

[9] T. Risselada. SL Note 95-32 AP. LHC Note 317 (1995).

[10] J.B. Jeanneret, "Optics of a two-stage collimation system". CERN-LHC-Project-Report-243 (1998).

[11] I.L. Azhgirey, I.S. Baishev, N. Catalan-Lasheras, J.B. Jeanneret, "Cascade Simulations for the LHC Betatron Cleaning Insertion". LHC-Project-Report-184 (1998).

[12] N. Catalan-Lasheras, G. Ferioli, J.B. Jeanneret, R. Jung, D. Kaltchev, T. Trenkler. LHC-Project-Report-156 (1997).

[13] R. Assmann et al. PAC03. CERN-LHC-Project-Report-640 (2003).

[14] R. Assmann, C. Fischer, J.B. Jeanneret, R. Schmidt. LHC-PROJECT-NOTE-282 (2002).

[15] P. Sievers et al. Proc. Chamonix 2003. CERN-AB-2003-008 ADM.

[16] R. Assmann, B. Goddard, E. Vossenberg, E. Weisse. LHC-Project Note 293 (2002).

[17] R. Assmann et al. LHC-PROJECT-REPORT-599. EPAC02.

[18] M. Hayes et al. EPAC02. CERN-LHC-Project-Report-589.

[19] R. Assmann et al. LHC-PROJECT-NOTE-277 (2002).

[20] T. Risselada. SL Note 92-16 AP. 1992.

[21] R. Schmidt. Proc. Chamonix 2003. CERN-AB-2003-008 ADM.

[22] R. Schmidt et al. Proc. HALO03. CERN-LHC-Project-Report-665 (2003).

[23] B. Dehning. Proc. Chamonix 2003. CERN-AB-2003-008 ADM.

[24] J.B.Jeanneret et al., CERN LHC-BLM-ES-0001.00 rev 1.1, EDMS doc 328146, 2003.

[25] L. Burnod and J.B. Jeanneret. AC/DI/FA/Note 92-05 (1992).

[26] J. Uythoven. Reported at the 24^{th} meeting of the Collimation WG (http://www.cern.ch/lhc-collimation).

[27] H. Burkhardt. Proc. Chamonix 2003. CERN-AB-2003-008 ADM.

[28] H. Burkhardt. Reported at the 27^{th} meeting of the Collimation WG (http://www.cern.ch/lhc-collimation).

[29] B. Goddard. Reported at the 23^{rd} meeting of the Collimation WG (http://www.cern.ch/lhc-collimation).

[30] T.Trenkler, J.B.Jeanneret, CERN SL/Note94-105(AP), 1994.

[31] F. Schmidt, "SixTrack, User's Reference Manual", CERN SL/94-56 (AP).

[32] I. Baichev, D. Kaltchev, *Implementation in Dimad of a new Collimator Element (STRUCT module)*, TRIUMF Report (in preparation)

[33] R.V.Servranckx, *User's Guide to the Program Dimad*, TRIUMF Design Note, TRI-DN-93-K233, (1993).

[34] J.B. Jeanneret, SL/Note 92-56 (EA).

[35] I. Baishev et al., CERN LPR 309 (1999).

[36] J.B.Jeanneret, CERN/SL/92-44(EA).

[37] E. Chapochnikova. Proc. Chamonix 2003. CERN-AB-2003-008 ADM.

[38] E. Chapochnikova, S. Fartoukh and J.B. Jeanneret, CERN LPN, to be issued 2003.

[39] A.I. Drozhdin et al., Fermilab Project Note FN-0724,2002.

[40] J.B. Jeanneret, Phys. Rev. ST Accel. and Beams, **1**, 081001, December 1998.

[41] T. Risselada. SL Note 95-67 AP (1995).

[42] I. Ajguirei, I. Baichev, J.B. Jeanneret, I.A. Kourotchkine and G.R. Stevenson. CERN-LHC-Project-Note-263 (2001).

[43] Instruction de securite, Safety instructions, CERN IS 23 (Rev. 2), Edms 335745.

[44] R. Assmann. Proposal to the AB LHC Technical Committee (LTC) on June 25^{th}, 2003.

[45] R. Assmann et al. PAC03. CERN-LHC-Project-Report-639 (2003).

[46] M. Brugger. Proposal to the AB LHC Technical Committee (LTC) on June 25th, 2003.

[47] M. Brugger, S. Roesler, "Remanent Dose Rates in the LHC Beam Cleaning Insertions", CERN-TIS-2003-026-RP-TN, 2003.

[48] O. Aberle. May 2003.

[49] M. Brugger, S. Roesler, "Accumulated Doses during Interventions on the Vacuum System in the LHC Beam Cleaning Insertions", CERN-TIS-2003-027-RP-TN, 2003.

[50] O. Aberle. Proposal to the AB LHC Technical Committee (LTC) on June 25^{th}, 2003.

[51] F. Ruggiero. Proposal to the AB LHC Technical Committee (LTC) on June 25^{th}, 2003.

[52] A. Fasso, A. Ferrari, J. Ranft, P.R. Sala. Proc. of the Int. Conf. Monte-Carlo 2000, Lisbon, Portugal, Oct. 23-26, 2000, p. 955, Springer-Verlag Berlin Heidelberg (2001).

[53] V. Vlachoudis. Proposal to the AB LHC Technical Committee (LTC) on June 25^{th}, 2003.

[54] M. Zyczkowski, Combined Loadings in the Theory of Plasticity, Chapter 11.

[55] M. Jimenez. Proposal to the AB LHC Technical Committee (LTC) on June 25^{th}, 2003.

[56] O. Aberle and R. Assmann. July 2003.

[57] A. Bertarelli and R. Perret. Proc. Chamonix 2004.

[58] R. Perret, Note Technique MT-ESI/94-3, 1994.

[59] E. Marotta, S. Mazzucca, J. Norley. Electronic Cooling, 8 (2003) 3.

[60] J.J. Fuller, E. Marotta. Journal of Thermophysics and Heat Transfer, 15 (2001) 2.

[61] R.W. Assmann, J.B. Jeanneret, D. Kaltchev. EPAC02. LHC-PROJECT-REPORT-598 (2002).

[62] I. Ajguirei, I.S. Baichev, J.B. Jeanneret and I.A. Kourotchkine, CERN LPN, to be issued, 2003.

CHAPTER 19

INTERFACE WITH AND REQUIREMENTS FROM THE EXPERIMENTS

19.1 INTRODUCTION

In order to understand the requirements of the LHC experiments it is helpful to recall the physics which the LHC is expected to reveal and to note that protons are composite particles which means that the parton-parton centre of mass energy covers a wide range and therefore high energy hadron colliders access a much wider range of physics than for example electron-positron colliders. The extremely high design luminosity of the LHC (10^{34} $cm^{-2}s^{-1}$) results in some 10^{16} minimum bias events in a full year, but even with this enormous amount of raw data much of the new physics will be 'discovered' with a few hundred events. The LHC experimental challenge [1] is to find rare events at levels of 1 in 10^{13} or more.

The ATLAS and CMS collaborations are constructing general-purpose proton-proton detectors, which are designed to exploit the full discovery potential of the LHC [2,3]. Their detectors will be operational at the start-up of the LHC and will be able to investigate the physics accessible during the initial lower luminosity running as well as handling the highest luminosity that will be available later from the design machine.

The initial LHC physics programme also includes a general heavy-ion detector ALICE [4], designed to study the physics of strongly interacting matter in nucleus-nucleus collisions at the LHC. ALICE, as well as ATLAS and CMS, will be able to study the products from colliding beams of heavy nuclei such as lead. Collisions between these nuclei will produce 'little bangs' at an equivalent temperature around 100,000 times that at the centre of the Sun and a density up to 20 times that of normal matter. Under these extreme conditions, which mimic those in the period less than 1 s. after the 'Big-Bang', the constituent protons, neutrons and gluons are expected to 'melt' to form a Quark-Gluon Plasma (QGP).

The initial programme also includes the LHCb spectrometer [5] that is dedicated to the study of B-physics and TOTEM [6,7] with detectors designed to measure the total proton-proton cross-section at LHC energies as well as to study elastic scattering and diffractive physics.

These very large and complex experiments are already being installed at the four points around the circumference of the LHC, where the beams can be brought into collision, (IR1, IR2, IR5 and IR8) as shown in Fig. 19.1.

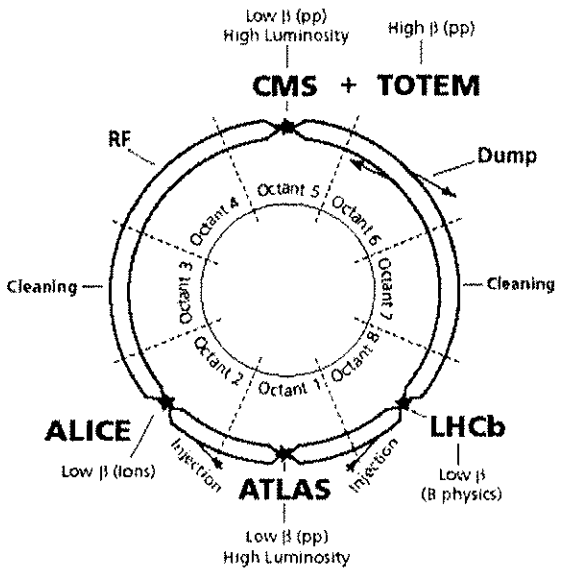

Figure 19.1: Schematic layout of the experiments around the circumference of the LHC.

19.2 REQUIREMENTS OF EXPERIMENTS

The experiments indicated in Fig. 19.1 each have particularities which allow them to focus on different aspects of LHC physics and as a result require different conditions to allow them to fully exploit the potential of the LHC.

19.2.1 The High Luminosity Experiments – ATLAS and CMS

The primary aim of the ATLAS and CMS experiments is to discover the Higgs boson and to search for other new particles predicted in theories beyond the Standard Model such as Supersymmetry. In the framework of the Standard Model, particles acquire mass through their interaction with the Higgs field. This implies the existence of a new particle – the Higgs boson H^0. In extensions to the Standard Model such as the Minimal Supersymmetric Standard Model (MSSM), there are 5 Higgs bosons – h^0, H^0, A^0 and $H^{\pm}$. ATLAS and CMS have been optimised to discover the Higgs boson(s) in the complete expected mass range. Supersymmetry also predicts that for every known particle there is a supersymmetric partner (sparticle) equal in charge but differing in spin. Production of sparticles will reveal itself through distinct kinematical signatures even at relatively low operating luminosities of the LHC machine.

The ATLAS detector is centred on a magnet configuration based on a 2 T inner superconducting solenoid around the inner tracking detector cavity and large superconducting air-core toroids outside the calorimetry. CMS employs a different approach to its detector layout, characterised by a single large 4 T superconducting solenoid magnet. The inner tracking detector and calorimeters are placed within the magnet bore. The iron of the return yoke houses the four layers of muon chambers, resulting in the overall CMS detector design being very compact.

Luminosity and Backgrounds

The design luminosity of 10^{34} cm^{-2} s^{-1} during one effective year of running (10^7 seconds) corresponds to an integrated luminosity of 100 fb^{-1}, which should yield of the order of 1000 Higgs events in each of the ATLAS and CMS experiments. ATLAS and CMS have to be able to identify these events among the total of 10^{16} minimum bias events. Between these two extremes there is a wealth of physics, some of which will be within reach of lower luminosities, but even W and Z production is only at the level of 1 event in 10^6. Therefore, ATLAS and CMS require high average luminosities and very reliable operation so that a sufficient number of rare events are recorded to establish a discovery. The high luminosities should be coupled with low backgrounds coming from both the high flux of secondary particles from the IP and stray particles from the LHC machine tunnel.

The schedule of the first year of LHC operation is not yet defined but an integrated luminosity of ~10 fb^{-1} would be a reasonable target. It is expected that this would yield around 100 Higgs events which would be sufficient to claim a Higgs discovery. Production of sparticles will reveal itself through distinct kinematical spectra even at the relatively low operating luminosities of the LHC machine expected in early 2007.

19.2.2 LHCb Requirements for B-physics

The LHC will be a very copious source of B mesons due to its high luminosity and the high $b\bar{b}$ cross section ($\sigma(b\bar{b}) \sim 500$ μb for $\sqrt{s} = 14$ TeV). The LHCb detector [5] has been designed to specifically exploit the large number of b-hadrons produced in order to make precision studies of CP asymmetries and rare decays in the B-meson systems. The experiment plans to operate with an average luminosity between 1×10^{32} cm^{-2} s^{-1} and 5×10^{32} $cm^{-2}s^{-1}$. The nominal luminosity of 2×10^{32} $cm^{-2}s^{-1}$ corresponds to a production of 10^{12} $b\bar{b}$ events in one year of 10^7 s of data taking. Running at this luminosity has several advantages: the radiation damage will be reduced, the events will be dominated by single pp interactions that are relatively easy to analyse and the detector occupancy will remain low. In addition, this luminosity will allow the experiment to collect data for many years under constant conditions, since it can be obtained at a very early stage in the commissioning of the LHC and can be kept at its nominal value while the luminosities at the other interaction points are being progressively increased to their design values. This will be possible by tuning the low-β insertion with $1\ m < \beta^* < 50\ m$.

The LHCb detector is a single-arm spectrometer with a forward angular coverage from approximately 10 to 300 (250) mrad in the bending (non-bending) plane. The choice of the detector geometry is motivated by the fact that at high energies both the b-hadrons and the $\bar{b}$-hadrons are predominantly produced in the same forward cone, a feature exploited in the flavour tag. The LHCb spectrometer is placed at IP8 in the existing hall that was hosting the DELPHI detector. A modification of the LHC optics, displacing the interaction point by 15 RF wavelengths (which corresponds to 3/2 bunch spacing or 11.25 m) from the centre in the direction of IP7, allows maximum use to be made of the existing cavern by freeing 19.7 m for the LHCb detector components, without the need for substantial civil engineering work. To maintain the symmetry of the beam optics around IP8, approximately 160 m of machine elements on both sides must be displaced. As a result it must be noted that this solution implies that only bunches separated by 25 ns and 75 ns will naturally produce collisions in the LHCb detector.

The LHCb spectrometer dipole [8] is a warm magnet with a high field integral of 4 Tm oriented vertically. The polarity of the field will be changed every run to reduce systematic errors in the CP-violation measurements that could result from a left-right asymmetry of the detector. The dipole magnet is expected to remain at its nominal field and polarity throughout an LHC physics run. It will give the circulating beams a horizontal angular kick, which must be compensated by adding three compensation magnets to the LHC lattice (Chap. 3.2.9). All magnets (spectrometer and compensators) will be ramped up together with the rest of the machine and in step with the beam energy. At injection the currents will be larger than zero.

The LHCb detector can reconstruct a B-decay vertex with very good resolution and provide excellent particle identification for charged particles. Excellent vertex resolution is essential for studying the rapidly oscillating B-mesons and in particular their CP asymmetries. This implies that the extrapolation distance between the first measured point on a track and the primary vertex needs to be reduced to the minimum possible. This is achieved by placing the LHCb Vertex Locator [9] as close as possible to the beam. In practice, this is limited by the aperture required by the LHC machine. During physics running conditions, the minimum distance between the beam and the Vertex Locator is expected to be ~ 5 mm and will be limited by the beam size and safety considerations. During injection, the aperture required by the LHC machine increases and the Vertex Locator needs to be retracted by 3 cm (Sec. 19.3.2).

19.2.3 Heavy-ion Interactions for ALICE, ATLAS and CMS

The ALICE collaboration has designed a dedicated heavy-ion detector to exploit the unique physics potential of nucleus-nucleus interactions at LHC energies [4]. It will study the physics of strongly interacting matter at extreme energy densities, where the formation of a new phase of matter, the quark-gluon plasma, is expected. The existence of such a phase and its properties are a key issue in QCD for the understanding of confinement and of chiral-symmetry restoration.

The ALICE central detector is embedded in a large magnet (the magnet of the LEP L3 experiment) with a weak solenoidal field that will be on during the whole LHC cycle. The ALICE forward muon arm [10], designed to measure the complete spectrum of heavy quark vector mesons via their muonic decay in pp and heavy-ion collisions, is placed outside the L3 magnet. It will consist of a large dipole magnet with a 3 Tm field integral in the horizontal direction that will give the circulating beams a vertical angular kick, that, as in the LHCb case, must be compensated by adding three compensation magnets to the LHC lattice (Chap. 3.2.5). The polarity of the dipole magnet will be changed on a regular basis in order to check systematic effects that could affect the event reconstruction. All magnets (spectrometer and compensators) will be ramped up together with the rest of the machine and in step with the beam energy. At injection the currents will be larger than zero.

The ALICE detector has two sets of zero-degree calorimeters (ZDC) located symmetrically on both sides of IR2 far downstream in the machine tunnel. The ZDCs will provide fast information about the centrality of the collisions and they will be used as a luminosity monitor measuring the rate of mutual electromagnetic dissociation in the neutron channel [11]. The ZDCs will be placed at 116 m from the IP in the IR2 long straight section, between the dipole magnets D1 and D2, where the common beam vacuum pipe in the experimental insertion and inner triplet region is separated into two beam vacuum pipes before entering the D2 magnet. When LHC is operating with heavy ions, the D1 magnet will deflect all lighter ions produced in the interaction region (fragments) and separate them from the ion beam. Neutral particles will follow the bisector of the two ion beams. The best positions of the ZDCs are therefore as close as possible to the entrance of the D2 magnet, where the neutral detector module can be installed in between the two beam

vacuum pipes and the positive detector modules can be installed close to the outside of the beam vacuum pipes. Therefore the beam pipe design in that region has to accommodate the ZDCs and minimise the material in front of them (Sec. 19.3.2).

Moreover, both ATLAS and CMS have shown an interest in heavy-ion physics. Their heavy-ion physics programme can be fulfilled with their baseline detector layout. However, the addition of ZDCs is presently under study in both ATLAS and CMS. The LHC is able to produce heavy-ion collisions in the three interaction regions at the same time. However, the two additional interaction regions will imply a reduction of the beam lifetime [12, 13].

A list of the ALICE luminosity and beam requirements can be found in the following and in reference [13].

Lead-Ion interactions

Collisions of Pb-Pb ions will provide the highest energy density and the first physics pilot run will already provide a wealth of information on global event properties and large cross section observables, particularly in the ALICE detector. For the study of interactions with low cross sections some further 1-2 years of Pb-Pb runs at the highest possible luminosity should provide sufficient statistics. For this physics it is expected that both ATLAS and CMS will also participate.

The luminosity for Pb-Pb collisions has limitations coming from both the detectors and the accelerator. For the ALICE detector, two different limits are coming from the main tracking device, the Time Projection Chamber (TPC) and the Forward Muon Spectrometer. The TPC limits the maximum useful luminosity to 10^{27} $cm^{-2}s^{-1}$ because of event pile-up during the 90 μs drift time. However, it is conceivable that it can be operated at higher luminosities, in particular if the multiplicity turns out to be in the lower part of the expected range. The luminosity limitation of the muon spectrometer comes from the maximum acceptable illumination of the trigger chambers, the Resistive Plate Chambers (RPCs) of 50-100 Hz cm^{-2}. This limit corresponds to a maximum usable luminosity of 2-4 × 10^{28} cm^{-2} s^{-1}. A more stringent limitation on the luminosity is coming from the machine. In the case of electromagnetic dissociation with subsequent electron-capture, the single-charge-changed ion will be lost from the circulating beam in the dispersion suppressors of the machine. In order not to exceed the quench limit of the magnets the luminosity for Pb-Pb will have to be limited to about 1 × 10^{27} cm^{-2} s^{-1}.

The predicted cross-sections for these electromagnetic interactions and the additional experiments participating in the heavy-ion programme are expected to seriously affect the luminosity lifetime, limiting it to only three hours [13] in the case of three experiments. It is then highly desirable to find new methods to maximise the integrated luminosity without exceeding the quench limit in the magnets. The method proposed in the reference [14] called β-squeeze, will not only maximise the integrated luminosity, but will also produce a constant luminosity during the runs that will make it easier to handle the space-charge effects in the ALICE TPC.

Additional Pb-Pb runs at lower energy would allow ALICE to measure an energy excitation function and to connect to results from RHIC. Finally, some rare processes limited by statistics in the early runs could require additional high-energy Pb-Pb running.

Lighter ions and hybrid interactions

Like the SPS and RHIC programmes, a comprehensive heavy-ion programme will be possible at the LHC, not only colliding the largest available nuclei at the highest possible energy, but also by carrying out a systematic study of lighter ions and hybrid collisions.. Such a programme will take several years and will include colliding beams of different ion species as well as ions against protons. The separated RF systems of the two LHC beams make hybrid collisions possible although an upgraded RF control system will be needed.

For a later phase, a number of ion running options will be possible, the relative importance of which will depend on the initial results. For a direct comparison of the Pb-Pb and pp data, a dedicated pp run at the Pb-Pb nucleon-nucleon centre of mass energy, $\sqrt{s_{NN}} = 5.5\text{TeV}$, is also probably advisable.

As for the Pb-Pb collisions, the useable luminosities with lighter ions and hybrid collisions have limitations coming from the LHC injectors and ion sources as well as quench limits in the LHC itself and also in detectors such as the ALICE TPC or the trigger chambers of the muon spectrometer. A list of the maximum acceptable luminosities for the different kinds of collisions can be found in reference [13].

19.2.4 Proton Running for ALICE

The pp collisions are an integral part of the heavy-ion physics programme both because of their intrinsic interest and because they are needed to obtain reference data. Moreover, pp runs will provide low multiplicity, thus simpler, data to commission and calibrate the components of the ALICE detector. Hence, they are needed during the whole period of ALICE operation, both initially as well as in later years for shorter periods prior to every heavy ion run.

The pp runs for ALICE will be in parallel with those for the other experiments, but at much reduced luminosities in IR2 in order to keep the pile-up in the TPC and Silicon Drift Detectors at acceptable levels. The luminosity during the pp runs has to be limited to $\sim 3 \times 10^{30}$ $cm^{-2}s^{-1}$, corresponding to an interaction rate of ~ 200 kHz. At this rate, ALICE records on average, 20 overlapping events, i.e. 95 % of the data volume corresponds to unusable partial events. This has obvious negative consequences both in terms of data storage and offline computing requirements as well as reducing the physics performance of the central barrel detectors because of increased occupancy. The optimal detector operation and physics performance with the TPC, i.e. no pile-up, is at $\sim 10^{29}$ $cm^{-2}s^{-1}$. ALICE will therefore request pp collisions in IR2 with both the maximum acceptable rate (3×10^{30} $cm^{-2}s^{-1}$) in order to maximise integrated luminosity for rare processes as well as with lower luminosity (10^{29} $cm^{-2}s^{-1}$) to collect statistics for large cross section observables and global event properties at optimum DAQ bandwidth and detector performance.

Depending on the beam intensity and emittance, the luminosity reduction can be obtained either with displaced beams or with larger β^* values which, however, are limited by the available aperture in the inner triplet. For nominal beam conditions both methods need to be used. With a β^* of around 10 m, a parallel beam separation of 5 σ is required with otherwise nominal beam parameters. However, during the LHC running-in phase, beam intensities and luminosities are lower than their nominal ones and the reduction in luminosity may be reached by simply increasing the β^* values. If feasible, this is highly desirable since the most stable running conditions are expected without beam displacements.

19.2.5 Dedicated Operation for TOTEM

TOTEM is an experiment dedicated to the measurement of total cross section, elastic scattering and diffractive processes at the LHC [6, 7]. The total cross section will be measured using the luminosity independent method that is based on the simultaneous detection of elastic scattering at low momentum transfer and of inelastic interactions. This method also provides an absolute calibration of the machine luminosity. The measurement of the total cross section is the first objective of the TOTEM collaboration at the earliest stage of operation of the LHC. The experimental apparatus consists of forward inelastic detectors placed in the experimental insertion of IR5 and of three sets of telescopes, called Roman Pots, placed symmetrically on both sides of the IR far downstream in the machine tunnel. The inelastic detectors will measure the overall rate of inelastic reactions while the Roman Pots will detect protons scattered at very small angles in elastic or quasi-elastic reactions.

The Roman Pots are special devices mounted on the vacuum chamber of the accelerator. In its retracted position the Roman Pot leaves the full aperture of the vacuum chamber free for the beam as required at injection. Once the final energy is attained and the circulating beams are stable, the Roman Pot is moved toward the machine axis by compressing the bellows until the inner edge of the detectors are at a distance of the order of one millimetre, or 10 σ from the beam. Particles scattered at very small angles at the IP can therefore be detected. The detectors inside the pots will be silicon detectors which may be operated at cryogenic temperatures. The three sets of telescopes will be placed in IR5 at each side of IP5 in the warm sections between TAN-D2, Q4-Q5 and Q5-Q6. The beam pipe design in this region will easily accommodate the three sets of Roman Pots (Sec. 19.3.2).

Since the cross sections involved are large, the measurements can be performed at the relatively low luminosity of 10^{28} $cm^{-2}s^{-1}$. This is achievable both by reducing the nominal LHC number of bunches to 43 (Chap. 20.6) and the nominal number of protons per bunch to $\sim 0.4 \times 10^{11}$. These two reductions have the very desirable features of allowing a zero crossing angle beam operation and of decreasing the risk both for the Roman Pots and the LHC in case of beam accident.

The measurement of the total cross section can be performed only with special optics at high β^* which allows the detection of particles emitted at very small angles. In fact with optics at high β^* the beam divergence at the IP becomes very small while the beam size is relatively large. As already mentioned the

corresponding loss of luminosity is not a problem because of the large cross sections involved in the measurements. The best configuration for the elastic scattering corresponds to the optics with parallel-to-point focusing from the IP to the Roman Pot location. In this case the displacement of the particle at the detector placed in the Roman Pot is proportional to the scattering angle θ and does not depend on the actual transverse position of the collision point. This has the advantage that measuring the particle position at the Roman Pots allows the scattering angle to be reconstructed in a way that is unambiguous and straightforward. A special optics with $\beta^*= 1540$ m has been designed for the dedicated TOTEM runs (Chap. 4.6). This optics has the advantage that the parallel-to-point focusing is achieved in both the vertical and horizontal plane at the same location.

The study of elastic scattering at large momentum transfer (above $|t| \approx 1\text{GeV}^2$) where the cross section is rather small cannot be achieved with $\beta^*= 1540$ m because of the large reduction in the counting rate due to low luminosity and for acceptance reasons. For this study the optics at $\beta^*=18$ m, which is used when injecting beam into the LHC, is well suited. Given the small cross section, no reduction in the nominal number of bunches is foreseen for this measurement implying that a non-zero crossing angle will be required to avoid unwanted collisions in the part where the two beams share a common beam pipe.

The detection of the particles emitted at very small angles will require moving the Roman Pots as close as possible to the beam. The reduction and the control of the beam halo is therefore of crucial importance, as well as, the reduction of beam-gas interactions. In addition the minimum distance of approach is proportional to the size of the beam at the position of the Roman Pots themselves. Operation with a transverse emittance reduced by approximately a factor of three with respect to the nominal one will then have the two desirable consequences of reducing both the beam size and the beam angular spread. The beam stability at the Roman Pot location has to be of the order of a few microns.

19.2.6 Machine Induced Backgrounds

Stray particle background

Each beam in a hadron collider is accompanied by stray particles outside the beam pipe, which are likely to cause background in detectors in the experimental areas. Simulations for the LHC have been made in order to estimate the importance of this effect and supply to the experiments the particle flux and characteristics, such as energy distribution and type of particles, which they can expect to enter their experimental cavern [15, 16]. All likely sources of stray particles have been included in these simulations, notably, beam-gas interactions at all points around the circumference of the machine, particles originating from the beam cleaning insertions (collimator inefficiency) and secondary particles from one collision point, which if they are transported by the machine structure could in principle create background in an adjacent experiment. The particles in question come mainly from secondary and higher order scattering as for example from the beam pipe in the inner triplet quadrupoles where the exceptionally high β function means that the aperture is limited to about 10 beam sigma and any halo particles outside that will interact in the vacuum chamber wall and produce showers of lower momentum particles. Similarly points of high dispersion will catch off-momentum particles from whatever source and the beam pipes in such regions can become a secondary source of background particles accompanying the beam. It is important to note that the high energy component of these background particles retain a close time correlation with the bunch structure.

It turns out that for reasonable estimates of the residual gas pressure in the LHC, even in the presence of nominal intensity beams, the main source of the machine background described above is scattering of beam particles by residual gas molecules in the proximity of the experiment, the dispersion suppressor and long straight section. The latest residual pressure estimates [17, 18] suggest that the highest residual pressures will exist in cold sections where there is synchrotron radiation and thus these regions such as the D2/Q4 cryostat will be a primary source of background. This is particularly true for ATLAS and CMS as these high luminosity experiments require a very heavy forward shielding around the TAS absorbers and Q1 quadrupoles to avoid backscattering of forward particles from their own collision region. This heavy forward shielding will very effectively close the machine tunnel as seen by the detectors of the experiment and greatly reduce the importance of all stray particles except muons. Sources such as the residual gas in the D2 vacuum chamber 150 m upstream of this shielding are the main sources of these muons. Fig. 19.2 [16] shows the flux of particles entering the ATLAS cavern as a function of radial distance from the beam. All particles

inside a radius of 130 cm are inside the planned forward shielding of ATLAS and many of the hadrons in this region will be absorbed.

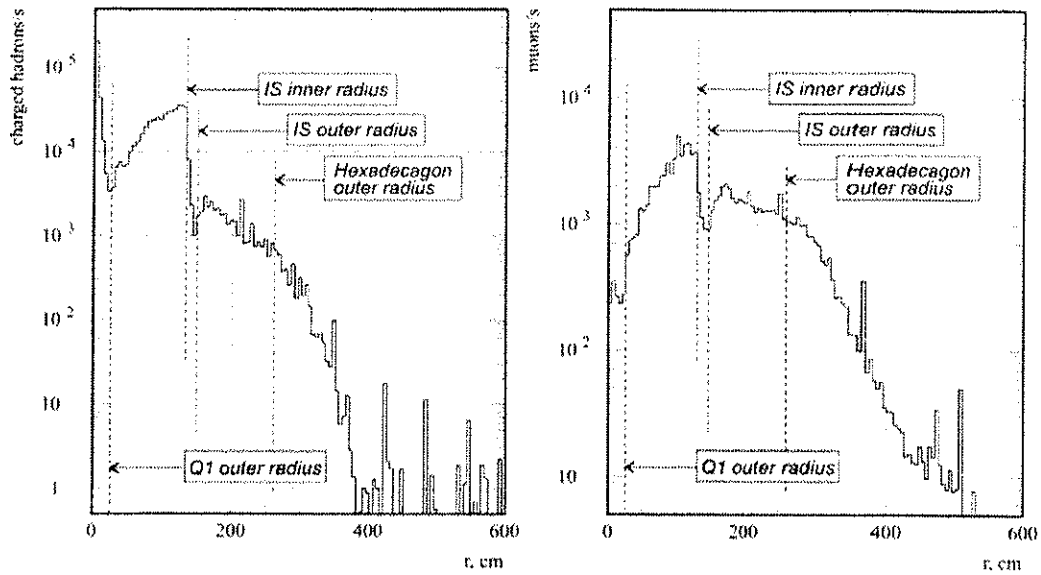

a) b)

Figure 19.2: Distributions of stray particles cm^{-2} s^{-1} entering UX15, the ATLAS experimental cavern, as a function of radial distance r (cm) from the beam, for a) charged hadrons and b) muons. The radial dimensions of the Q1 quadrupoles and various parts of the forward shielding are indicated by the dotted lines.

Tunnel shielding plugs

The low luminosity experiments, ALICE and LHCb do not need TAS absorbers to protect the inner triplet quadrupoles from secondaries and therefore have no need for heavy forward shielding. Both these experiments will have to rely on shielding plugs in the machine tunnel just before the entrance to their experimental cavern. It is impractical to install more than about two metres of iron and these walls will be far from complete. In most cases they have to be built around the inner triplet cryostat and may also have a cryoline passing through them. In practice, the latter is not of any great importance, nor are the services around the tunnel wall, because the important leakage all occurs close to the beam. ATLAS and CMS also benefit from the small aperture of the TAS absorber 34 mm diameter and as a result the background in ALICE and LHCb where there is no such aperture restriction is substantially larger. At Point 2 and Point 8 in addition to the muon background seen in ATLAS and CMS there is a considerable flux of hadrons entering the experimental caverns depending upon the effectiveness of this shielding wall. The levels are around 10^6 hadrons per second and 10^5 muons per second in the absence of shielding. A preliminary study of shielding walls suggests that the hadrons can be reduced by a factor of between three and ten [19]. Example distributions of particles entering UX85 and the effect of different shielding configurations from reference [19] are shown in Fig. 19.3.

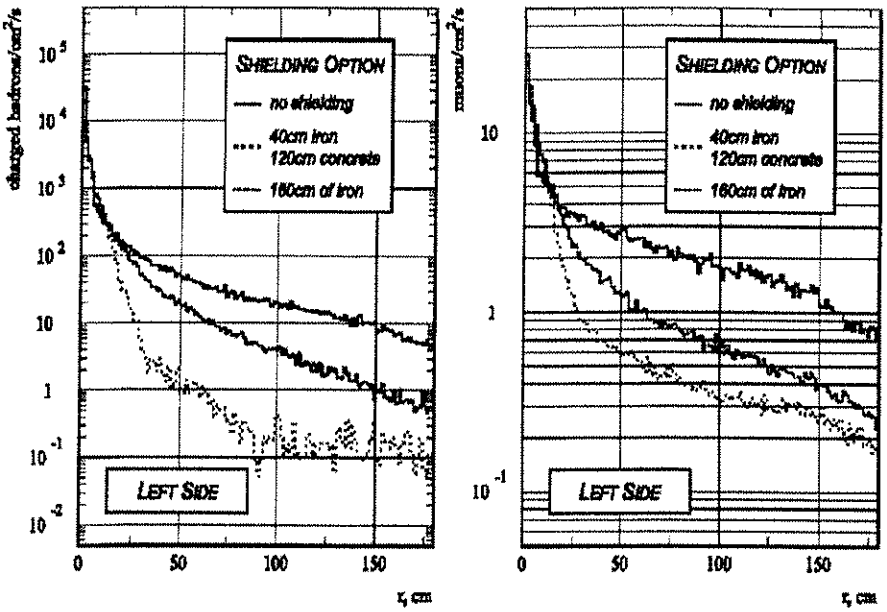

a) b)

Figure 19.3: Example distributions of stray particles entering UX 85, a) charged particles b) muons, as a function of the radial distance r (cm) from the beam with different configurations of iron and concrete shielding in the upstream tunnels.

Background from the TAS absorber

As mentioned above the high luminosity interaction regions of the LHC have a TAS absorber at approximately 19 m from the IP. This 1.8m long block of copper has the smallest beam aperture consistent with the beam size at injection in order to intercept as many secondary particles from the IP as possible. All of these particles would otherwise enter the cold mass of the inner triplet and energy deposition directly into the SC coils or total power into the cold mass would cause the superconducting quadrupoles to quench. At design luminosity some 200 W is deposited in each TAS absorber and almost all of this energy would otherwise reach the inner triplet. The particles that strike the TAS are mostly absorbed, but a few are back scattered and the TAS becomes a major source of background in the muon chambers of ATLAS and CMS [20]. By surrounding the TAS with an equivalent of up to two metres of iron, all but low energy neutrons can be absorbed. The neutron doses have been evaluated for different shielding configurations and the final layouts chosen are a compromise between performance, practicality and cost. The two metres of iron equivalent is needed around the TAS to reduce the background in the large area ATLAS muon chambers to acceptable levels [21]. A somewhat lighter shielding is required by CMS to protect their muon chambers installed in the iron return yoke of their solenoid magnet [22]. Both ATLAS and CMS expect to have to incorporate neutron absorbing layers such as polyethylene or Boron-loaded concrete in the final shielding needed with luminosities above 10^{34} $cm^{-2}s^{-1}$.

Below a luminosity of 10^{33} $cm^{-2}s^{-1}$, TAS absorbers are unnecessary and none need to be installed for either ALICE or LHCb. Both these experiments will have a very much lower background from backscattered particles, as described above, not only because of the lower interaction rate (luminosity), but also because the Q1 quadrupoles are further from the detectors of the experiments and have a larger beam aperture than the TAS absorbers.

19.2.7 Requirements of the LHC Experiments in the First Year of LHC Operation

Physics Impact of Lower Energy Operation at Start-up

For safer and more reliable operation at start-up, the LHC machine may run at lower than the nominal 14 TeV energy by about 10%. It is anticipated that this will not last for more than a few months [23].

Running at lower energy has repercussions on the physics discovery potential. The cross-section times the branching ratio of the Higgs boson is low and the discovery is essentially rate limited. Therefore, in this initial period, the discovery of the Higgs boson will most probably be out of reach. However, the

Supersymmetry processes have strong cross-sections and the discovery of 'sparticles' is not rate limited. Some discoveries can still be made with a few weeks of running at luminosities of 10^{33} cm^{-2} s^{-1}. Hence, a lower rate due to lower cross-sections at lower centre-of-mass energies does not much affect the Supersymmetry discovery potential at start-up.

Therefore, the requirement from ATLAS and CMS to start at the design energy is not a strong one, i.e. start-up can take place at a lower energy. Clearly, running at the design 14 TeV energy must start as soon as possible and in order not to have to combine data from too many different energies, the experiments wish to move to the design energy in one step.

It should be noted that the potential for b-physics can be exploited in ATLAS, CMS and LHCb even at the lower centre-of-mass energies. The effect of lower energies for LHCb is expected to be negligible. In the case of TOTEM, data taking at energies lower than the nominal one is welcome, as it will allow the measurement of elastic scattering at lower momentum transfer.

Impact of Event Pile-up

The number of pile-up events per crossing depends on β^* and the product of the number of protons in each interacting bunch. Understanding the performance of the LHC detectors is easier when there are few or no overlapping events since the track density is low thus making track and energy reconstruction much easier. Furthermore, the quality of calibration, alignment and synchronisation can be checked more easily. Consequently, ATLAS and CMS would like to operate in conditions with no more than ~2 overlapping events during the initial physics data taking until the performance of the detectors is properly understood [23].

As mentioned above, the LHCb experiment expects to have their nominal luminosity of 2×10^{32} cm^{-2} s^{-1} available at a very early stage with a minimum β^* of 1 m. As their B-trigger does not allow any pile-up they will ask for β^* to be increased to maintain this low luminosity and their only concern will be that if commissioning with a 75 ns bunch spacing is not replaced rapidly by 25 ns running they will lose integrated luminosity.

Activities in the LHC Experiments during the commissioning of the LHC

As a reminder, the nominal LHC running conditions for the two high luminosity experiments ATLAS and CMS are: 1.15×10^{11} protons / bunch, a β^*=0.55 m, a bunch crossing interval of 25 ns and a luminosity of 10^{34} $cm^{-2}s^{-1}$ This leads to about 20 overlapping events per crossing.

Activities in ATLAS and CMS will follow developments in the LHC machine leading up to the first physics run according to the possible timeline given in reference [23]. Following the completion of the installation and equipment commissioning, the accelerator will be set up for safe operation. The setting-up will start with one low intensity bunch, increasing to multiple bunches and raising the bunch intensity to close to the nominal.

It should be noted that the superconducting magnets of ATLAS and CMS as well as the solenoid magnet of ALICE will be on throughout all normal operation of the LHC, while the warm dipole spectrometer magnets of ALICE and LHCb, which need special compensation for closed orbit correction, will be ramped proportionally to the main LHC dipole field. This will have to be taken into account at an early stage in the commissioning of the machine.

The experiments will carry-out studies of synchronisation, vacuum quality, beam-gas interactions and their rejection, profile of beam-gas interactions and muon halo triggers and finally catalogue detector problems. Collisions of one bunch on one bunch will then follow rising to collisions with 43 on 43 bunches with bunch intensities rising close to the nominal bunch intensity, all done with zero beam crossing angle. Beam squeezing will then commence to get to low β^*. It should be noted that crossings involving bunches with nominal intensities and nominal β^* lead to 20 pile-up events/crossing, which is considered too high by ATLAS and CMS for these initial phases. The experiments will start recording first pp collisions and will continue the synchronisation studies and the cataloguing of detector problems. Subsequently, a beam crossing angle will be introduced and the running configurations that have been explored could include:

(i) 75 ns bunch-spacing, β^*=1.0 m., 0.9×10^{11} protons/bunch, 936 bunches at a luminosity of a few 10^{32} $cm^{-2}s^{-1}$,

(ii) 25 ns bunch-spacing, β^*=0.55 m., 0.4 × 10^{11} protons/bunch, 2808 bunches at a luminosity of a few 10^{32} cm^{-2} s^{-1}.

The latter running configuration would correspond to the scrubbing runs at 25 ns bunch-spacing required to address the issue of the electron cloud.

The experiments ATLAS and CMS will continue studies of synchronisation, setting-up for physics running and recording first physics events. A three-month shutdown period may then be needed to allow the experiments to install sub-detectors that are ready, but were not installed before start-up, e.g. pixel detectors, and solve problems encountered during the initial running period.

The LHC accelerator and experiments would then be ready for the first physics data run. Starting with an accelerator configuration with a 75 ns bunch-spacing, 936 bunches and a luminosity of 10^{32} cm^{-2}, the experiments will continue verifying their detector synchronisation. The bunch intensities will be increased until pile-up leads to greater than 2 pile-up events / crossing and then move to 25 ns bunch spacing, i.e. to 2808 bunches.

Two options have been identified for accumulating subsequently a large data set:

1. If operation with the 25 ns bunch-spacing is satisfactory, the luminosity should be raised to around 10^{33} cm^{-2} s^{-1} and accumulation of physics data should continue.
2. However, if problems are observed with the 25 ns bunch-spacing operation or if the experiments desire higher integrated luminosities (i.e. they have understood detector operation with >> 2 overlapping events / crossing), running at 75 ns bunch-spacing with > 2 pile-up events / crossing can be considered.

The high luminosity experiments, ATLAS and CMS, prefer to carry-out the bulk of the initial physics data-taking at 10^{33} $cm^{-2}s^{-1}$ and 25 ns bunch spacing.

A potential physics run could last for about seven months integrating a luminosity of up to 10 fb^{-1} per experiment in ATLAS and CMS. At the end of a long physics run, or a long winter shutdown period, a Pb-Pb ion run of approximately two weeks is requested by ALICE, at a lower than nominal luminosity, to yield a few days of good data taking. Any such run will also be used by ATLAS and CMS to obtain a first taste of heavy-ion data.

As mentioned above, the LHCb experiment is expects to be able to reach optimum running conditions of one interaction per bunch crossing rather early in the commissioning of the LHC. With a 75 ns bunch separation this occurs at a luminosity below 10^{32} $cm^{-2}s^{-1}$ and the main concern of LHCb will be to gain a factor of three in integrated luminosity by moving as rapidly as possible to a bunch spacing of 25 ns.

The TOTEM running scenario during the first year of the LHC expects data taking with single beams for calibration and background study purposes. Several one day runs with β^* = 1540 m and β^* = 18 m are needed for the total cross section and the elastic scattering at large momentum transfer measurements. In addition, TOTEM plans to take data with β^* = 0.55 m together with CMS to study diffractive events for $L < 10^{33}$ cm^{-2} s^{-1}.

The physics programme of the LHC, even in its first year, is expected to be extremely fruitful and it will be a considerable challenge to assign priorities and make the best possible use of this early running.

19.2.8 The Collision Region

Calculations have been performed to estimate the collision region around the interaction points taking into account the nominal LHC parameters and also the longitudinal spread of a bunch during a coast. It is estimated that 95% of the luminosity is found within a distance of ± 9 cm around the IP. Studies of the ATLAS Inner Detector reconstruction show that in order to preserve the assumed performance of the experiment, at most 5% of the integrated luminosity may be outside the distance ± 11 cm around the IP. As for CMS, global inefficiencies of 0.2% and 3% were estimated for the Inner and Outer Tracker Barrel detectors, indicating a good coverage of the luminous region by the Tracker. Similarly a good match was determined for the barrel and end-cap Pixel detectors and the end-cap Tracker.

Similar values for the collision region are estimated for ion-ion collisions.

Transverse Centring of the Interaction Point

A collision point well-centred in their detectors is required by the experiments. The maximum transverse variation during a coast is expected to be < 20% of the nominal beam width of $\sigma_{x,y}$ = 16 μm, while the

maximum transverse variation of the beam collision point between coasts is likely to be < 1 mm. Despite this the LHCb collaboration has designed their VELO detector to accommodate maximum transverse shifts of up to ± 5 mm, so as to include alignment errors.

However, there will also be a need for re-alignment of the experiments to the machine. The new cavern floors are expected to move over time due to the settling of the concrete and due to the hydrology of the geology. Estimations for the ATLAS cavern suggest up to 5.5 mm settling of the floor over the 6 months following installation due to the weight of the ATLAS detector, followed by a 1 mm per year lift of the floor due to the hydrostatic pressure.

Some adjustment of the ATLAS detector is possible, but may need to be extended. CMS includes an adjustment mechanism based on jacks and grease pads that allows lateral and vertical adjustments of ± 50 mm during machine shutdown periods. Alternatively, given the survey link between the machine tunnel and experimental areas, the interaction regions can be aligned to the experiments to within about ± 1 mm.

Satellite Bunches

While transferring the beam from one machine to another (PS -> SPS and SPS -> LHC), two phenomena are to be considered:

(a) the uncaptured beam which is lost at the beginning of acceleration and

(b) the beam captured in unwanted locations giving rise to satellite bunches.

At IP1, IP2, IP5 and at IP8, collisions between satellites may occur every 2.5 ns at the same vertex as nominal bunches and in the worst case may occur 9 times more frequently than normal collisions. At IP8, there is an additional possibility of collisions between satellites and normal bunches at the beginning and end of each 72-bunch train. For TOTEM running, since there is no beam crossing angle, there is the possibility of additional collisions between satellite and normal bunches every 37.5 cm on either side of the IP.

A high-sensitivity longitudinal profile monitor should detect satellites at the 0.001% level within minutes in the LHC. However, satellite bunches in the SPS are likely to create satellites in the LHC but measurements in the SPS are difficult and limited only to the percent level. Detection of satellites in the SPS may be used to prevent injection into the LHC, but this would require new instrumentation that is currently not foreseen. The experiments, however, expressed their satisfaction that a satellite frequency at the percent level is acceptable and thus an upgrade to the SPS instrumentation is not needed.

19.3 INTERFACES WITH THE EXPERIMENTS

19.3.1 Data Exchange

Data exchange, both at the hardware and software levels, has the aim of communicating information on the state of the machine, experiments and technical services as a whole and on their various sub-systems, as well as providing a means to understand the causes of error by acting as a recording and diagnostic tool. These communication links will be required to guide the interaction between the collider and experiments when operation of the LHC commences. Emphasis is placed on observables that can provide a measure of the LHC machine operating conditions for the experiments and that can be used by the experiments to give feedback to the machine operation as well as to protect their detectors against damage from spurious operating conditions of the machine. This section discusses the subset of exchanged information most relevant to the data exchange.

Fig. 19.4 shows the conceptual lay-out of the entities considered for data exchange. The exchange is considered to be low frequency, ~1 kbps and therefore should not be limited by bandwidth and have a latency of < 1s. The commercial protocol to be implemented is currently being defined.

The LHC data from the machine and experiments will have an absolute UTC time stamp, which will be derived from several GPS modules. These modules will be located centrally in the PS Complex, with auxiliary modules at each of the other accelerators and at each pit of the LHC from where a fibre will be connected to the experiments.

It should be noted that in addition to the above information, a concise summary of the machine operation status, as has been the case for the PS, SPS and LEP, will be made available on TV monitors throughout CERN and also accessible via the WWW.

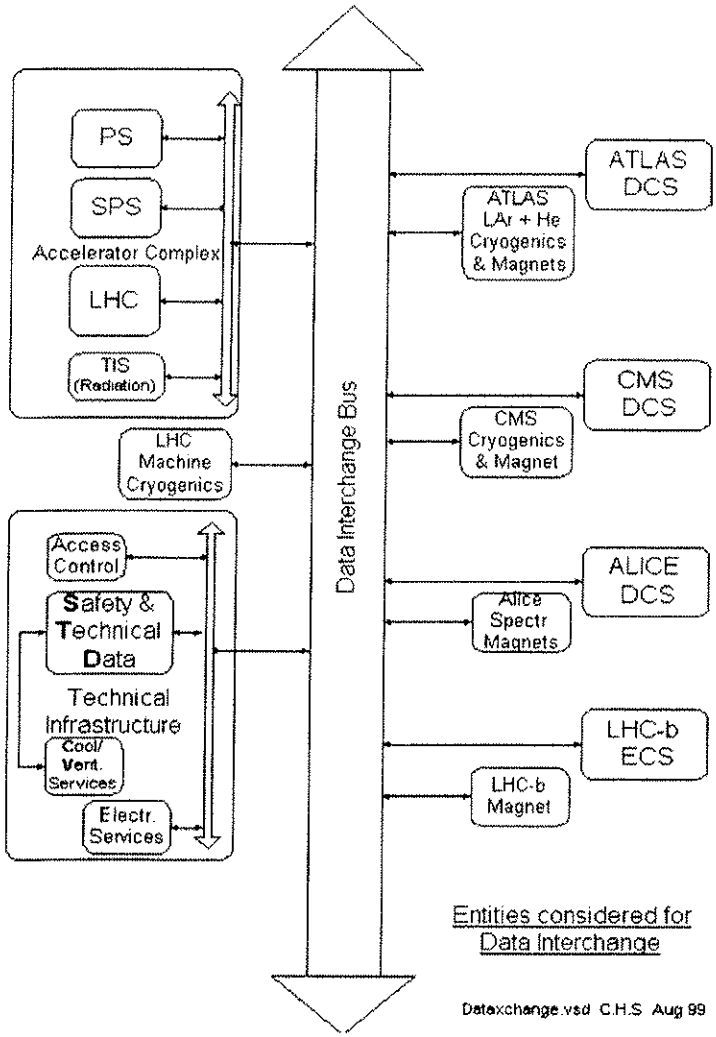

Figure 19.4: Schematic of the exchange of data between the experiments and the LHC

Experiment Measurements of the Collision Parameters

The experiments, ATLAS and CMS, have studied what information might be provided to the LHC machine relating to beam conditions. Each experiment aims to provide at least one estimate of the luminosity, at least one rate measurement sensitive to beam–beam collisions and at least one rate measurement per beam sensitive to beam-related background. Under stable running conditions, each experiment should also be able to provide three-dimensional information on the position and size of the luminous region; this could possibly be supplemented by the average angle of the beams in the horizontal and vertical planes.

The experiments have demonstrated their ability to assess the quality of the collisions based on measuring observables in their detectors. Several trigger rates will be measured continuously by the experiments. For example, the measurement rate of various kinds of clusters and muon candidates above threshold can be integrated over all bunches and can also be measured on a bunch-by-bunch basis. Information from the muon detectors can be used to study the muon halo and the neutron background. Moreover, information from the forward rates and the vertex counting per event in the inner detectors would provide a measurement of the relative luminosity. Finally, a measure of the occupancies in the hadron calorimeter sectors may lead to an estimation of the background imbalance. Transmission of the summary information can be performed at least every minute.

A fast reconstruction of the collision point can also be provided by ATLAS and CMS. A 10 μm transverse position accuracy and a 2 mm longitudinal position and luminous region accuracy can be measured within about 600 s. Such measurements require that the inner detectors, including the pixel detectors, are powered and operational and would only be possible once stable beams are established.

The following table summarises the present ideas. However, it is essential to retain flexibility in the data-exchange system (e.g. in the number and choice of quantities to be exchanged, the production interval and hence the data rate). Note that the numbers given in Tab. 19.1 are for a minimum set of information and that the information ultimately produced might have a larger volume. It is assumed that 4-byte words are used for all quantities.

Table 19.1: Data exchange from experiments to accelerator.

Producer	**Measurement**	**Units**	**Production Volume (Bytes)**	**Production Interval (sec)**	**Data Rate (Bytes/sec)**
ATLAS/CMS	Total luminosity	$cm^{-2}s^{-1}$	4	1	4
ATLAS/CMS	Average rates	Hz	12	1	12
ATLAS/CMS	Luminosity per bunch	$cm^{-2}s^{-1}$	14256	60	238
ATLAS/CMS	Individual bunch rates	Hz	42768	60	713
ATLAS/CMS	Position and size of luminous region (average over all bunches)	cm	24	600	0.04
ATLAS/CMS	Total per experiment				966

Concerning the rates (both average and bunch-by-bunch), the numbers in Tab. 19.1 assume one rate sensitive to beam-beam collisions and one rate per beam sensitive to beam-induced background. Additional rates, e.g. from calorimetric and muon detectors that are sensitive to the radial and phi distributions of beam-related backgrounds, will be developed in collaboration with the machine groups. ATLAS and CMS will endeavour to be flexible in the production and choice of rates to be transmitted as experience with machine operation accumulates.

Data exchange from the accelerator to the experiments

Tab. 19.2 provides an example of data to be distributed from the LHC machine to the experiments, based on measurements taken with the beam instrumentation of the machine.

It is the responsibility of the experiments to measure their own absolute luminosity. Standardised, simple, fast and robust machine luminometers are provided to set up the machine for physics, optimise its performance and make comparisons from run to run. The event rate of these luminometers may be calibrated by comparing with the luminosity from the experiments and by the Van der Meer method, cross-checks will also be possible by calculations using the best available beam parameters. From experience, cross-checks with data from LHC detectors are equally valuable to understand possible differences in the luminosities of LHC IP's. The beam parameters necessary to calculate the luminosity will be transmitted to the experiments (optics parameters, bunch-by-bunch beam emittances and currents).

LHC Timing Signals and Distribution to the Experiments

The LHC RF group is considering three clocks: a stable reference clock at 40.08 MHz delivered from the Faraday Cage at Point 4, which will serve as the reference clock of the LHC machine and which can be used by the experiments to clock their electronics and two clocks which will drive the RF for the two beams. The latter will be locked to the reference clock but will vary since they will be adjusted to follow the bunches in the machine.

Table 19.2: Example data to be distributed by the LHC to experiments

Measurement	units	Production Volume (Bytes)	Transmission rate	Expected Accuracy	Remarks
Total beam intensity	proton	8	~1 sec	1%	
Individual bunch intensities	proton	28,512	~1 min	5%	
Rms beam sizes	mm	16	~1 sec	15%	For transport to IP will require knowledge of β-function
Rms bunch sizes	mm	44,928	~1 min	15%	
Average bunch length	ps	8	~1 sec	1%	
Total longitudinal distribution	proton/bucket	285,120	~1 min		Will be able to detect ghost bunches at the 0.1% level of nominal
Average HOR & VER positions	μm	32	~1 sec	50μm	From the BPMs at Q1 either side of each IP
Luminosity b-by-b		28,512	~100 sec	1% relative	
Beam Loss	proton/s	80	~1 sec	Few % relative	Average over up to 50 selectable BLMs

The experiments rely on collisions being as close as possible to the nominal IP at the centre of their detectors. The jitter of the reference clock is approximated to be ~10 ps at the origin, while the RF clocks will be less accurate and whose phase could differ from that of the reference clock by up to 300 ps. As the jitter affects the average time of collisions in the experiments with respect to the reference clock and the average collision point itself, the latter jitter implies a significant displacement from the nominal IP, since, for example, the CMS calorimeter digitisation requires a timing signal with <50 ps jitter.

The Experiment Beam Position Monitors (BPTX)

A total of 1166 Beam Position Monitors (BPMs) are needed for the LHC and its transfer lines. This includes one experiment BPM (BPTX) timing pick-up per incoming beam in IR 1, 2, 5 and 8. The BPTXs will be located about 150 m from the IP in front of the D2 magnets and will be used exclusively by the experiments. Button electrodes will be used as the pick-up technology.

Two applications of the BPTX timing signals have been identified by the experiments. They may be used to monitor the phase of the clock of the two beams locally at the IRs, thus determining whether the Timing and Trigger Control (TTC) system is synchronised with the actual arrival of the bunch. Moreover, the monitors can be used to identify the location of the gaps in the LHC bunch train, which is considered to be particularly useful during the setting up stage of the experiments.

Beam Abort Signals

Several mechanisms have been identified as leading potentially to beam losses. For example, a magnet quench, a trip of power converters or the RF system, or an unsynchronised beam dump may lead to damage to both machine and experiment elements.

One of the fastest beam loss mechanisms is due to a power converter trip in the D1 warm magnets around the IRs. The time constant, i.e. the time interval from the equipment failure to when the beam loss will occur, is about 5 turns. A fast beam abort signal from the experiments could act on this time scale.

In addition, an accident with the beam dump at the Tevatron has highlighted the danger of an unsynchronised beam dump. In such a scenario, the dump kicker does not hit the dump gap, either because of a loss of timing or control or, as in the case at the Tevatron, a problem with the RF de-bunched the beam, thus eliminating the dump gap. Beam dump malfunctions affect mainly CMS, as it is adjacent to the dump insertion IR6. The accident duration is estimated to be 260 ns, during which up to 10^{12} protons can be lost in IR5 (CMS). The experiment beam abort system will not be able to handle the fast speed of such an accident scenario. The installation of an absorber in IR6 will protect the machine (and CMS).

A dedicated machine protection system is being developed for the machine and the experiments are also studying methods to send an abort signal to the machine on observation of spurious behaviour in their monitors. Diamond and silicon detectors are being evaluated as dedicated detectors in the experimental areas to be used in the beam abort mechanism. They will operate independently from the other experiment sub-detectors and would give a response time of the order of two beam orbits.

It has been agreed that alongside several machine sub-systems, an input from the experiments to the machine Beam Interlock Controller is included in the design of the machine protection system. This would allow a signal from the experiments to give the BEAM PERMIT and a BEAM ABORT if the PERMIT is absent.

19.3.2 Experimental vacuum systems

Introduction

The experimental vacuum system is the part of the LHC main ring that passes through the four experimental interaction points. This is perhaps the most sensitive sector of the LHC vacuum system as it must conform to two markedly different sets of requirements. It must conform to the standard LHC vacuum system specification for dynamic beam vacuum and impedance (Chap. 12). However, it must also cause the minimum of interference with the detection performance of the experiments, which in general means that the material introduced into the path of the secondary particles from the IP must be minimised.

This second requirement has led to the development of a number of specific technologies for the experimental vacuum systems, in particular for the choice of materials and geometries for the vacuum chambers, the optimisation of the mass and size of both vacuum chambers and vacuum equipment.

The designs for the experimental vacuum systems have been the subject of a number of reviews. These have concluded in interface specifications agreed, or under agreement with the experiments [24, 25, 26, 27]. However, in some limited areas the final designs are still under discussion.

The 'very forward' regions between 18 and 22 m from the IP, where the vacuum systems inside the experiments interface with the standard machine long straight sections, also have a number of particular requirements. In the high luminosity experiments, ATLAS and CMS, this region sees a very high radiation flux from the interactions. The TAS absorber [28] and vacuum equipment installed here will become radioactive, requiring special equipment and precautions. In all experimental insertions the space here is very limited and agreement between machine and experiments is necessary before equipment can be installed [29].

Experimental Vacuum Technology

Although the layout of the experiments and hence the vacuum systems are quite different from each other, a number of common technologies have been developed and applied as required by the experiments.

The vacuum chamber directly around the IP of all experiments except LHCb is made from Beryllium, chosen for a combination of excellent transparency to particles, good mechanical properties and compatibility with ultra-high vacuum (UHV). New beryllium technology has been developed for the LHC in

order to improve the leak tightness and minimise the external envelopes of the chambers. Beryllium chamber sections are now machined from solid rod and assembled by welding. Beryllium sections are either welded to aluminium or vacuum brazed to stainless steel. The central parts of ALICE, ATLAS and CMS use similar designs for this beryllium section. The inner diameter of 58 mm was the minimum acceptable for aperture and allows silicon vertex detectors to be as close as possible to the collision region.

The other beam vacuum chambers in the experimental areas are either constructed from stainless steel (with a copper coating to minimise machine impedance) or AA 2219 aluminium. This alloy has been approved at CERN for use in these areas as it maintains mechanical strength at the temperatures required for activation of the NEG (Non Evaporable Getter) coatings, whilst being considerably more transparent to particles than stainless steel.

In order to minimise the background due to the beam pipe in the forward regions, the ALICE, CMS and LHCb experiments have chosen to use conical beam pipe sections with a conical angle originating at the IP. These cones are terminated by thin 'windows', through which the particles pass at a quasi-acute angle.

UHV flanges have been specially designed to minimise the mass of material and external dimensions [30]. They have only 35% of the mass of a standard UHV flange and are used in different diameters in all four experiments.

Due to the estimated contact dose of 45 mSv in front of the TAS [31], a special remotely actuated flange system has been designed and will be used in the two high luminosity insertions.

The vacuum pumping inside the experiments is based on sputtered Non-Evaporable Getter (NEG) pumps, recently developed at CERN [32]. These have the advantage of adding very little mass whilst providing a high local pumping speed. These NEG pumps require periodic re-activation by heating the chamber to 250°C. It is expected to re-activate the NEG once per year during the winter shutdown.

Two special systems have been developed to enable this re-activation in the experimental chambers. In certain areas, access to the chamber will be difficult and the re-activation system will be permanently left in place. Heating systems based on stainless steel conductors laminated in Kapton sheets have been developed and approved for the high temperatures and radiation levels. Insulation will be either silica aerogel or high performance ceramic fibre (Microtherm). The central parts of CMS and ALICE will be re-activated by specially developed removable bake-out furnaces that will be installed on rails and then removed after re-activation.

The ALICE Beam Vacuum

The ALICE experiment being installed in IR2 is asymmetric about the IP. The vacuum chamber shown schematically in Fig. 19.5, can be divided functionally into three different sections: the central part (CP) which needs high transparency to secondary particles; the RB26 side which is a stainless steel cone embedded in a heavy muon absorber and the RB24 side which is upstream of the CP and has no physics requirements from the experiment.

The CP will have a 4 m long beryllium chamber connected to stainless steel extensions and bellows. The removable heating system will be installed each time a NEG re-activation is needed and will require a shutdown of several weeks. The RB26 side will be copper-plated stainless steel sections with increasing thicknesses from 1 to 3 mm. It consists of three beam pipes connected by commercial UHV flanges. These three chambers are supported inside the muon absorber. Each chamber has an axial fixed point inside the absorber bore, sliding supports and bellows. The sliding supports will be made of stainless steel and designed to minimise the heat load into the absorber during NEG re-activation. Due to the difficult access to the beam pipe, a permanent Kapton / Microtherm heating system will be installed. This has been optimised for this application due to the limits on radial space and heat input to the absorber block.

The RB24 section will be installed with standard warm LSS components.

In addition to the experimental area, ALICE has detectors in the LSS of the LHC. The 'Zero Degree Calorimeter' or ZDC is installed ~116 m from IP2, in front of the D2 magnet. This is the recombination region where the single beam pipe that passes through the IP becomes two parallel pipes for the standard LHC twin aperture. ALICE takes advantage of this recombination to install a neutral particle detector in between the twin apertures and a proton detector to the side of the apertures, using the D1 magnet as a spectrometer magnet [11].

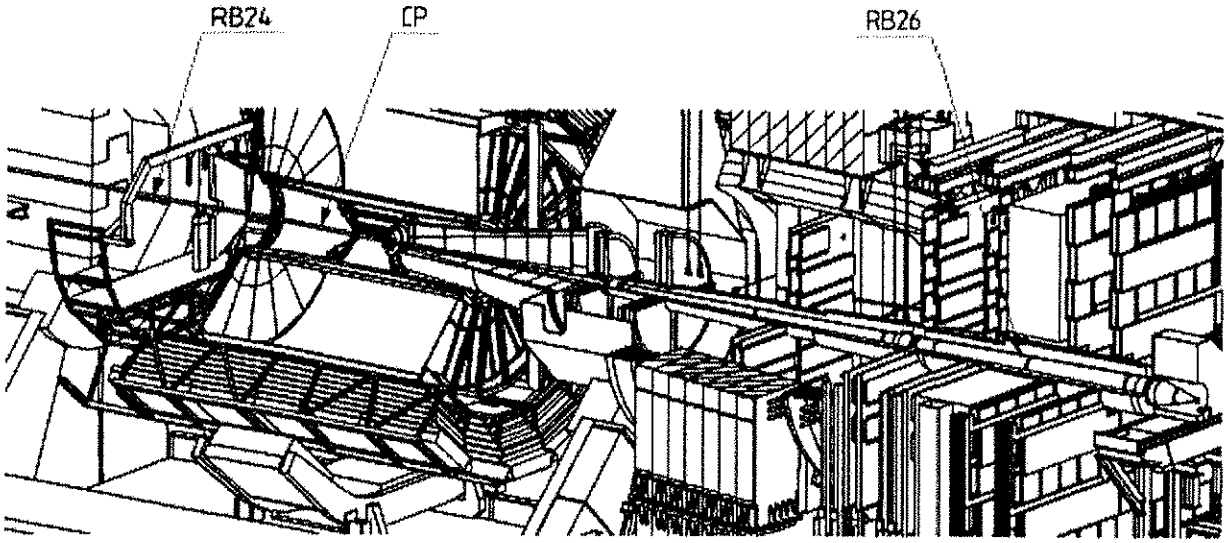

Figure 19.5: The ALICE Beam Vacuum System

The ATLAS Beam Vacuum

The beam vacuum system in ATLAS is functionally symmetric about the IP. It has a 7.3 m long central chamber inside the inner detector, 7 m of which is beryllium with extensions and minimised flanges in AA 2219 aluminium. This chamber is equipped with a permanent Kapton foil / Aerogel NEG activation system. At either end is a specially developed low-mass ionisation pump with 20 l/s nominal pumping speed [33]. This is required due to the small diameter of the ATLAS chambers which gives a poor pumping speed for the gasses not removed by the NEG. The vacuum chamber then passes through the 92 mm bore argon end-cap calorimeter. This restricts the diameter of the beam pipe up to 10 m from the IP. From this point the chamber increases to 80 mm ID and then 120 mm in two steps. At ~19 m from the IP, the diameter drops to 34 mm through the remotely operated flange and into the TAS.

All of the chambers with the exception of the inner detector chamber are made from copper-coated stainless steel. However, studies are under way to replace some sections with AA 2219 aluminium.

The CMS Beam Vacuum

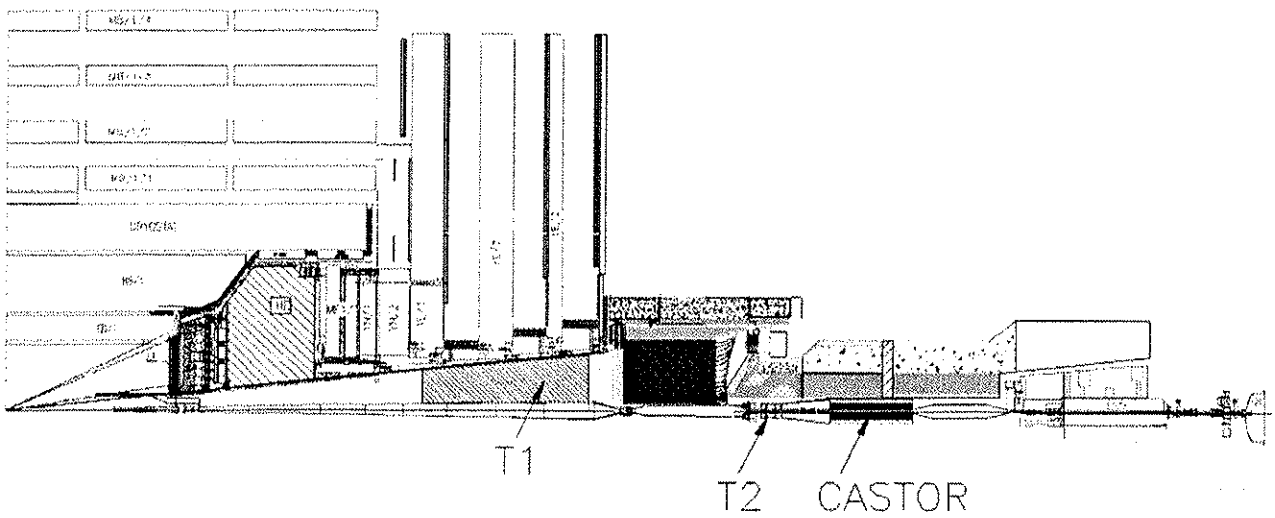

Figure 19.6: Half-section through the CMS beam vacuum system also showing the detectors of both CMS and TOTEM.

The beam vacuum system in the CMS detector is functionally symmetric around IP5. As shown in Fig 19.6 it has a ~6.2 m long central chamber of which 3.8 m is beryllium. Either side of this beryllium tube is a transition to a copper-plated stainless steel cone of ~15 mrad opening angle. This cone continues to the second chamber which passes through the CMS end cap, up to 10.6 m from the IP. There is then a 'window' with a 15° angle as the chamber diameter reduces to pass through the HF calorimeter. In the 'forward' region between 13 and 18 m the chamber will pass through the TOTEM T2 telescope and CASTOR detector before the remotely activated flange assembly in front of TAS. This forward region design is still under discussion with the experiment.

The central chamber is heated for NEG re-activation by a removable system, running on the rails used for PIXEL detector installation. The PIXEL detector must be removed to re-activate the NEG.

The LHCb Beam Vacuum

The IP at Point 8 is offset from the centre of the cavern and the LHCb experiment will be installed on one side only with the vacuum chamber layout illustrated in Fig. 19.7. The silicon Vertex Locator (VELO) detector is installed around the IP inside a 'vertex tank', separated from the beam vacuum by a thin aluminium membrane. The detectors and membrane can be moved close to the IP for data taking [9].

The VELO vertex tank is terminated by a thin aluminium window covering 390 mrad opening angle. From this starts a double conical vacuum chamber with 25 mrad and then 10 mrad opening angles. LHCb will have around 12 m of beryllium or beryllium-aluminium (Al-Be) alloy with increasing thickness from 1 to 2.4 mm. Beryllium is more transparent than the alloy, the final cost/benefit choice between these materials will be made by the experiment. Tests of the Al-Be material have been performed to determine its mechanical behaviour at bake-out temperatures, its creep performance and weldability by electron beam. An aluminium bellows universal joint with 0.4 mm wall thickness has been developed for LHCb and will be used to decouple the beryllium chambers.

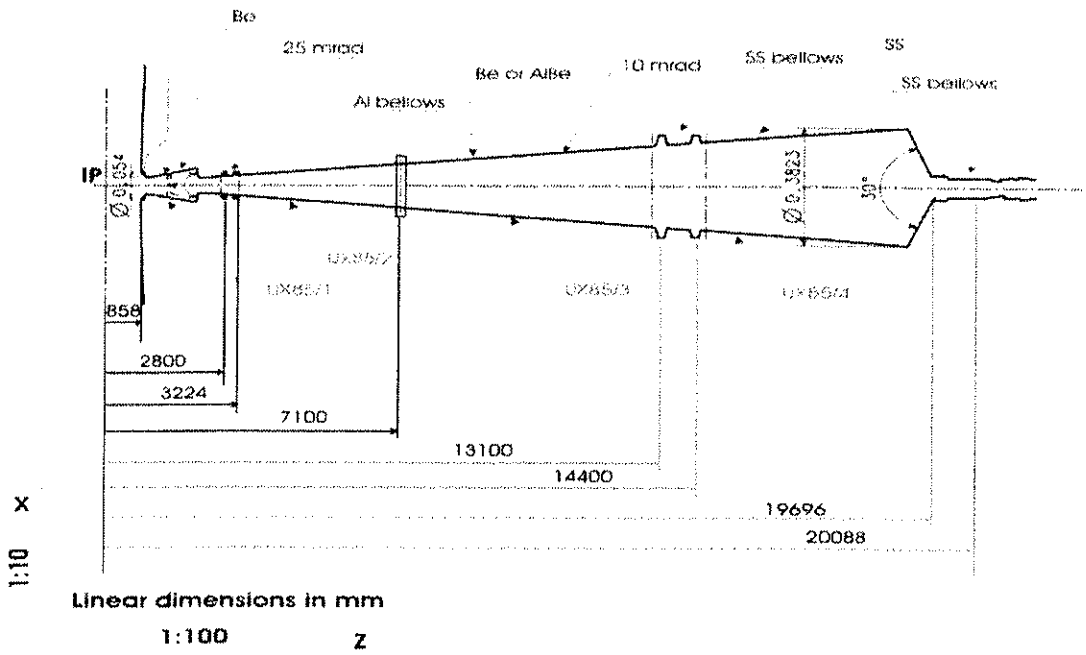

Figure 19.7: Schematic view of the LHCb beam-pipe

A stainless steel cone will be installed inside the muon detectors where the beam pipe transparency is of lower importance. The easier access to the beam pipe compared with the other LHC experiments allows removable bakeout systems for most of its length. Only the stainless steel section UX85/4 will have a permanent system installed. Upstream of the experiment, the beam pipe will consist of standard warm LSS components.

The TOTEM Beam Vacuum

Part of the TOTEM experiment is situated inside the CMS experimental area at IP5 and part in the LSS of IR5. The T1 and T2 telescopes, inside the CMS area are mounted close to the vacuum chamber as shown in Fig. 19.6. A chamber compatible with both CMS and TOTEM has been agreed.

The other part of the experiment consists of pairs of 'Roman Pot' detectors installed at ~150 m, ~180 m and ~215 m from the IP as shown in Fig. 19.8. These Roman Pots allow detectors to be moved close to the accelerated beam whilst remaining outside the beam vacuum. The detectors will be in a secondary vacuum completely separated from the primary beam vacuum by a thin window. For safety and reliability it has been decided to ensure that this thin window can resist a pressure of 1 atmosphere from either side.

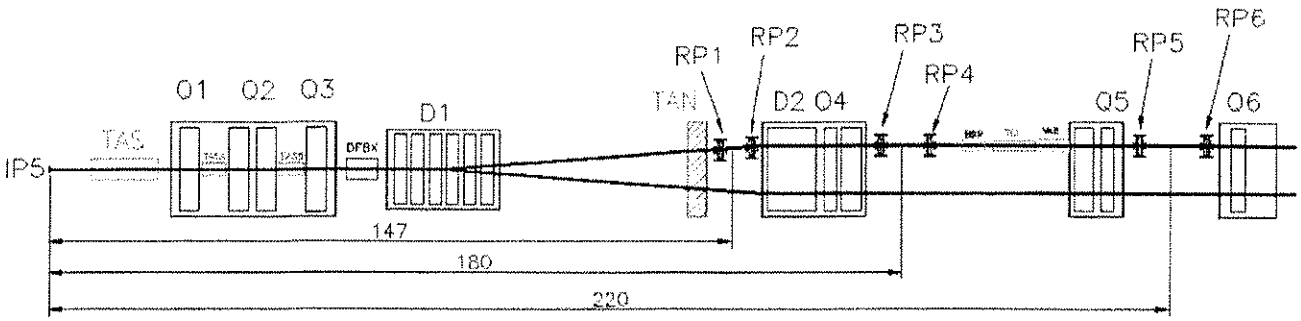

Figure 19.8: The layout around IP5 showing the position of the "Roman Pots" (RP1-6) for the detectors of the TOTEM experiment.

REFERENCES

[1] J. Virdee, "Inaugural Lecture", CMS website http://cmsinfo.cern.ch/Welcome.html/CMSdocuments/JimInaugural/JimInaugural_index.html

[2] The ATLAS collaboration, ATLAS Technical Proposal, CERN/LHCC/94-43, December 1994

[3] The CMS collaboration, CMS Technical Proposal, CERN/LHCC/94-38, December 1994

[4] The ALICE collaboration"ALICE Technical Proposal", CERN/LHCC 95-71,1995

[5] The LHCb Collaboration, "LHCb Technical Proposal", CERN/LHCC 98-4, 1998

[6] The TOTEM collaboration, "TOTEM TP", CERN/LHCC 99-7, March 1999

[7] The TOTEM collaboration "The TOTEM experiment", Proceedings of IV International Symposium on LHC Physics and Detectors,

[8] The LHCb collaboration, "LHCb magnet TDR", CERN/LHCC 2000-007

[9] The LHCb collaboration, "LHCb VELO TDR", CERN/LHCC 2001-011, May 2001

[10] The ALICE collaboration, "ALICE Muon Spectrometer TDR", CERN/LHCC 99-22

[11] The ALICE collaboration, "ALICE : Technical Design Report of the Zero Degree Calorimeter (ZDC)" CERN-LHCC-99-005, March 1999

[12] K. Schindl, "LHC Request and Overview", Proceedings of Chamonix XII, http://ab-div.web.cern.ch/ab-div/Conferences/Chamonix/chamx2003/contents.html

[13] A. Morsch, Internal Note, ALICE-INT-2001-10

[14] D. Brandt, "Review of the LHC Ion Programme", LHC Project Report 450 http://conferences.fnal.gov/lhc2003/index.html

[15] I. Azhgirey et al, Methodical study of the machine induced background formation in the IR8 of LHC, LHC Project Note 258

[16] I Azhgirey et al, Cascade simulations for the machine induced background study in IR1 of the LHC, LHC Project Note in preparation.

[17] I.R. Collins & O.B. Malyshev, Dynamic Gas density in the LHC Interaction Regions1 & 5 and 2 & 8 for Optics version 6.3. LHC Project Note 274, December 2001

[18] A. Rossi & N. Hilleret, Residual gas density estimations in the LHC experimental interaction regions, LHC Project Report 674
[19] I. Azhgirey et al, Evaluation of some options for shielding from machine induced background in IR8, LHC Project Note 307, December 2002
[20] A. Ferrari et al., "Radiation Calculations for the ATLAS Detector and Experimental Hall", Proceedings of the workshop on Simulating Accelerator Radiation Environment (SARE), October 1995 and M. Huhtinen, "The Radiation Environment at the CMS Experiment at the LHC", Report Series HU-SEFT R 1996-14, 1996
[21] ATLAS Collaboration, Technical Co-ordination Technical Design Report CERN/LHCC/99-01, ATLAS TDR 13 31 January 1999
[22] CMS Collaboration, The Muon Project technical Design Report, CERN/LHCC 97-32, CMS TDR 3, 15 December 1997
[23] J. Virdee, Proceedings of Chamonix XII, March 2003
[24] G. Schneider "Interface Specification of ALICE beam vacuum chamber" CERN Specification LHC-VC2-ES-0001, May 2003
[25] R. Veness "ATLAS Beam Vacuum Interfaces" CERN Specification LHC-VC1-ES-0001, to be published
[26] P. Lepeule "CMS Beam Vacuum Interfaces" CERN Specification LHC-VC5-ES-0001, to be published
[27] J. Knaster "LHCb Beam Vacuum Chamber" CERN Specification LHC-VC8-ES-0001, July 2003
[28] E. Hoyer, W. Turner "LHC IP1/IP5 Front Quadrupole Absorbers (TAS)", CERN Specification LHC-TAS-ES-0001, May 2002
[29] R. Veness "Vacuum Equipment between Q1, TAS, ALICE and LHCb" CERN Specification LHC-LV-ES-0001, May 2002
[30] S. Karppinen, R. Veness "Study of Minimised Flanges for LHC Experiments" CERN-LHC Vacuum Technical Note 00-27, November 2000
[31] I. Dawson, G. R. Stevenson "Radiation Studies in the Collimator Regions of the ATLAS Experimental Area", CERN/TIS-RP/IR/98-01, January 1998
[32] C. Benvenuti et al "Vacuum properties of TiZrV non-evaporable getter films [for LHC vacuum system]", Vacuum 60 (2001) 57-65
[33] J. Knaster et al "Optimised Annular Triode Ion Pump for Experimental Areas in the LHC" CERN LHC Project Report 670, August 2003

CHAPTER 20

EARLY PLANS FOR COMMISSIONING AND OPERATION

Plans for commissioning of both hardware and with beam, are sure to evolve with time. The purpose of this chapter is to summarise the current thinking on these issues.

20.1 HARDWARE COMMISSIONING

The mandate of preparing the hardware commissioning was given to Hardware Commissioning Working Group, which started in May 2003 and is composed of staff from the equipment groups (project engineers and system owners). The group will act first as a working group during the study phase (programme, procedures, sequence) and will later evolve into a team deployed in the field when the actual commissioning in the tunnel starts.

20.1.1 General Plans for Commissioning a Sector

The commissioning of the hardware in the eight LHC sectors will be handled in two phases: the individual systems tests and the commissioning of each sector as a single system.

The individual system tests aim at qualifying the various systems for operation. The definition of the procedures, the conditions required for the tests to start, those needed during the tests and those signalling the end of the tests are defined by the system owners. The Hardware Commissioning Working Group then gathers these requirements, makes a refinement of the time required for the commissioning and issues a set of documents describing the commissioning. It then coordinates the tests and their sequencing and follows up the preparation work of the assemblers and the specialised teams.

The commissioning procedures and programme will vary depending on the contents of the sector, for example the presence of special machine systems like RF, warm magnets in the cleaning insertion, injection and the dump system.

The sectors are composed of several cold and warm sub sectors, which are mechanically separated and electrically and cryogenically independent. For the insulation vacuum the sub sectors are independent but coupled by the beam vacuum tubes. These features will impact on the order, the procedures and the usage of the resources during the two commissioning phases. The hardware commissioning of a sector is considered finished when all of the circuits have been powered to nominal current both independently and in unison in a pattern representative for operation. Acceptance tests and specific studies will also be carried-out for the first commissioned sector. The programme for these has not yet been determined but is expected to include performance measurements of the cryogenic control system, heat load measurements and quenching of a substantial part of the sector.

In the present plan, Sector 7-8 will be commissioned first. This sector contains 125 independent electrical circuits, 77 of which traverse the whole of the main arc sub sector; another 94 circuits for the orbit correctors are individually powered locally, two per short straight section. The complexity of these circuits varies greatly both in terms of number of components and the powering scheme: the biggest circuits in terms of components are the main dipole circuits (approximately 600 components), while the most difficult to commission will be the inner triplet circuit with its three nested power converters. Most of the magnets will have been individually tested; however one of the most complex components, the electrical feed boxes (in the arc, matching sections and inner triplet sub sectors), which vary from sector to sector, might be cooled and operated for the first time during the hardware commissioning.

While it is expected to carry out the hardware commissioning of the first sectors from ad-hoc control centres in the tunnel, the aim is to move the activity to the accelerator control room. By involving staff from the accelerator control room in the study and the execution of the hardware commissioning, a first link to commissioning with beam will be made. In addition, close collaboration with the LHCOP project will be maintained. The SPS stop (October 2004 to April 2006) takes place partly during the hardware commissioning (March 2005 to December 2006) and it is agreed that accelerator operators will be deployed for hardware commissioning with the double objective of training the future operators of the LHC and helping the hardware commissioning team.

20.1.2 RF Considerations

The planning of installation around point 4 is still under discussion and some extra time may become available for installation and tests of the RF system. The present schedule implies that installation in UX45 will take place in the last quarter of 2005 and the first of 2006, while installation in the tunnel will be during the second and third quarter of 2006. This means that RF tests without the cavities can take place in the last quarter of 2006 during the general cool-down of the cryogenic system. Full RF commissioning and conditioning of the cavities and couplers can only take place in the first quarter of 2007 and commissioning with beam will start in the April 2007. Conditioning will be time consuming (see below) and so very little time will be available to test and commission the complex loops and interlocks.

As a result, as many tests as possible must be carried out before installation. For this reason extensive full acceleration-chain tests will be done in the test facility building SM18 in 2004 and 2005, in order to test all items under full power and simulated transient conditions.

Using knowledge from LEP and SPS operation together with somewhat limited experience with the LHC cavities and couplers, the following conditioning times can be estimated:

- Cavity conditioning:
    - First conditioning in SM18, requiring 3 weeks per cavity.
    - After installation, before the beam arrives, some conditioning must be re-made, requiring 1 week per cavity. This may be done in parallel on some or all cavities if the total radiation generated does not exceed the safety limits for personnel in UX45.
    - During operation there is nothing special foreseen. However some helium processing may be unavoidable following cavity filling with nitrogen and would need about 1hour.
- Coupler conditioning
    - First conditioning in SR2 and SM18, requiring 7 weeks per coupler.
    - During operation, the polarisation will be on.

Operating the coupler with the polarisation on prevents multipactoring but the coupler slowly becomes contaminated and will eventually break down, catastrophically if left too long. After the coupler is used in this mode for periods of around a month, then a full re-conditioning may take about 1 week. Experience in the SPS with pulsed conditioning in beam-out times suggests that an operationally better approach may be to condition the couplers in between fills. However this remains to be proven. Conditioning will use a significant amount of time during the hardware test period before commissioning with beam.

20.2 BEAM TESTS BEFORE FULL MACHINE COMMISSIONING

As progress is made towards the completion of the LHC, a number of tests with beam are planned to validate the ongoing installation. The tests are; extraction into TT40 (the first part of TI8) in 2003, commissioning of the completed TI8 in 2004, a sector test with beam of LHC sector 7-8 in 2006 and finally commissioning of TI2 in 2007, culminating in the commissioning of the LHC itself in 2007. Two retractable beam stoppers (TEDs) will be installed, one at the SPS end and one at the LHC end of the TI8 and TI2 lines.

20.2.1 TT40

The TT40 extraction tests took place during two 24-hour periods in September and October 2003, with beam transported to the first TED of the TI8 line. Objectives included the verification of equipment functionality in the new extraction zone in LSS4 of the SPS (kickers, septa, beam instrumentation, magnetic elements and power converters) as well as a test of supporting systems such as interlocks and controls [1]. Low intensity beam was used throughout to verify the extraction channel and trajectory in the beginning of the line, to measure the acceptance of the extraction channel and check the reproducibility of the trajectory in the line. Double batch extraction as required for operation in the CNGS era was also demonstrated. Although relatively small in extent the test already posed an interesting integration exercise with issues such as radiation protection and access requiring careful attention.

20.2.2 TI8

The TI8 tests with beam are planned for two 48-hour periods in September and October 2004, with the aim to transport beam as far as the downstream TED in the transfer line. Limited cooling capacity in the line will prevent continuous pulsing during this period. The aims, similar to the TT40 test, are to verify equipment functionality and the proper integration of interlocks, surveillance, access and other systems. LHC pilot intensities (5×10^9) are generally foreseen but higher intensities are considered in the dose estimations. The tests will include trajectory acquisition and correction, reproducibility, commissioning of the beam instrumentation, measurements of the optics in the line and matching between the line and the SPS.

The Radiation Protection Group has produced estimated dose rates [2]. These show that with intensities of 2.5×10^{11} protons per pulse over 24 hours at 50% efficiency, remnant dose rates alongside the TED area would be around 120 μSv/h and around 3 μSv/h on the downstream face of the TED, after a 1-day cool down period. These figures show the need for extra shielding (iron/concrete) after the TED and the area around the TED to be declared a "Simple Controlled Radiation Area" after the tests. This would imply that people working in this zone after the test would be classified as radiation workers and carry film badges.

An access zone from the TED extending through UJ88 to UJ86 towards UX85 and US85, with a gate in the LHC tunnel towards point 1, will be required to prevent access downstream of the TED for the duration of the test and appropriate radiation monitoring will be installed. The impact on ongoing LHC installation still needs to be carefully evaluated.

20.2.3 LHC Injection Test in 2006

The LHC installation schedule (LHC-PM-MS-0005 rev 1.7) includes an injection test in April 2006. This is defined to be the injection of beam down TI8, into the LHC at the injection point right of IP8, traversal of IR8 and LHCb, through sector 7-8 to a temporary dump located near the position of Q6 right of point 7. The test will be made with the final machine configuration.

The motivation for performing this test was outlined at the LHC performance workshop held at Chamonix in 2003 [3], where it was strongly endorsed. However, many consequences and potential problems were also identified [4]. The issues raised included the impact of remnant radiation and INB approval, the need for access and interlock systems, the impact on LHCb, the impact on injectors, the impact on hardware commissioning and installation and the need to install and remove the beam dump. These and others have been carefully examined, shown to be manageable and outweighed by the many benefits [5].

The beam provides a powerful diagnostic tool and will allow checks of the physical aperture, giving a means of checking the field quality in situ. It will be the first exposure to beam of much of the hardware and will potentially allow verification of assumed quench limits and spatial resolution of beam losses. It will also permit polarity checks of the corrector elements and the beam position monitors; key concerns in the installation procedure. First tests of important beam diagnostic systems would also be possible.

Furthermore the injection test will also provide an extremely high-profile milestone forcing large-scale integration of all components, including controls, timing, transfer from the injectors and instrumentation. The test will highlight any oversights, misconceptions and shortcomings. Operationally the exercise will be extremely valuable and the time and effort spent on the test will be more than compensated by a more efficient start-up of the completed machine. Any problems highlighted would have a whole year for resolution before the commissioning of the full machine.

Tests with beam

The aim is to mostly use the LHC pilot beam; that is, a single bunch of intensity between 5 and 10×10^9 protons. This is below the quench limit if losses are diluted over more than 5 m and 2 orders of magnitude below damage threshold. Folding in generous inefficiencies a programme of tests lasting seven days is planned, which, with around 50% operational efficiency gives a total elapsed time of 2 weeks for the test. A maximum of around 3000 shots is foreseen corresponding to a total intensity of 2×10^{13} protons over the two-week period.

Timing of the test

At present the test is scheduled for April 2006. However, for start-up in 2006 both the SPS and PS will be recovering from the 2005 shutdown and it is estimated that 4 weeks will be required for cold checkout and re-commissioning. Also the SPS is presently subject to energy consumption restrictions and should not normally pulse before April. Thus the test will take place in the first two weeks of May 2006 unless provision is made to start the SPS earlier. This is compatible with the requirements of LHCb, who insist that a delay of more than 10 weeks beyond April 2006 would jeopardise the LHCb overall installation and commissioning as foreseen in the current schedule.

Radiation issues

It planned to use LHC pilot intensities (5×10^9) with the strict proviso not to irradiate LHCb; their zone must remain a surveyed area with no restrictions after the test. The clear aim will be to minimise losses everywhere and use beam sparingly throughout the test. For the expected total intensity of 2×10^{13} protons over the two-week period, simulations by the Radiation Protection Group [2] show that activation will be low. Appropriate radiation monitoring will be operational during the test and measures will be taken to minimise does rates and there will be a full survey after the event to check levels of activation. As with TI8 after the 2004 test, however, we must anticipate that particular zones, such as near the injection dump (TDI) and around the position of the temporary dump, may be declared a "Simple Controlled Area" and subsequent work in these areas will require wearing a film badge. It should be noted that the temporary dump itself would be removed after the test.

Access considerations

Gates in tunnel sectors 6-7 and 8-1 will be needed, along with interlocked, restricted access at PM76, PM85 and PZ85. Much of this infrastructure will be necessary in the final LHC configuration and can be made available for the test without too much extra cost [6].

20.3 CONSTRAINTS FOR THE FIRST YEAR OF OPERATIONS

Restrictions during the first year include the need to keep the event rate below or around 2 events per bunch crossing (10^{33} cm^{-2} s^{-1} at 25 ns bunch spacing), a total maximum intensity of 50% of nominal because only 8 out 20 beam dump dilution modules will be installed and a bunch intensity limit of around 1/3 nominal with 25 ns bunch spacing to avoid electron cloud effects [8].

In addition, machine protection and collimation systems will favour initial operation with low beam power and low transverse beam density until multipole effects are controlled and a reproducible operational cycle has been established.

For the vacuum system, 3 phases are foreseen [9]. Firstly there will be a start-up phase below the electron cloud threshold of 3 to 4 x 10^{10} per bunch, followed by a conditioning of the cryo-elements with scrubbing runs and finally a post-conditioning phase. It may prove necessary to remain in phase 1 during the first year of operation.

From a radiation standpoint the lower intensities will favourably reduce the potential impact on equipment, particularly electronics and allow a first look at reliability issues under less severe conditions than those expected later.

For the cryogenics the lower intensity will mean lower heat load: from beam loss (given efficient collimation), from lower synchrotron radiation and lower image currents. The very difficult challenges for the LHC collimation system will be relaxed during commissioning by the lower total beam intensity, by keeping the β^* at reasonable values and by not reducing the emittances below nominal. Lower intensity means that lower cleaning efficiencies can be accepted for a given beam lifetime while still respecting the quench limits.

It is not possible to reduce the heat load on the cryogenics system significantly by reducing the beam energy [10]. Reducing the energy can increase the quench level margin, but in order to gain an order of magnitude in the case of transient losses, a large reduction in energy is needed. There is only a small gain with respect to continuous losses and lower synchrotron radiation. The experiments are prepared to accept a

10% energy reduction for a limited period. This would gain something like a factor of two in the quench margin.

It is anticipated that the first months of LHC operation will be dedicated to commissioning the machine with a single beam before establishing colliding beams, with the goal of a low intensity pilot physics run before a 3-month shutdown requested by some experiments [7]. There would then be a longer physics run with the goal of establishing luminosities of up to 10^{33} cm^{-2} s^{-1} (Sec. 20.7). Bunch intensity for physics will be restricted to around 4×10^{10} protons, in line with the constraints outlined above.

20.4 EARLY COMMISSIONING

20.4.1 Establish Circulating Beam

It is planned to begin with a special magnetic cycle in order to minimise the dynamic effects in the machine components. This cycle has a 'degauss blip' in order to minimise the decay of the multipole components in the dipoles during the injection plateau [12]. While this cycle cannot be used to accelerate the beam, it is expected to be of great advantage in the early commissioning of the machine. Studies have also shown that a similar level of stability can be gained with the normal cycle, by waiting around 30mins before injecting on the 450 GeV plateau.

A key factor in the commissioning will be to identify the simplest possible configuration that allows the beam to be injected, to use this to begin and then to increase the complexity in a controlled way. For the first turn in the LHC relatively few of the magnet power circuits will be needed. Clearly the main lattice circuits must be powered at their nominal values. Among the correction circuits the orbit correctors, trim quads, sextupole spool pieces and skew quadrupoles should suffice, with the skew sextupoles, octupole and decapole spool pieces switched off. Regarding the insertions, the crossing angle, spectrometer magnets, 'experiments' solenoids and separation bumps should be off. Simulations show that under these conditions the injected beam should, on average, traverse about 4 cells and so be seen by the beam position monitors. Threading can then be done, powering orbit correctors as needed. Once a complete turn has been made the trajectory must be closed on itself to form an orbit.

For multiple turns the chromaticity starts to become important. Decoherence of the beam from the huge chromaticity expected without correction make it difficult to measure the tune. Powering the b_3 spool pieces from magnetic measurement data and the lattice correctors to correct for the natural chromaticity should bring the chromaticity down to below 80 units.

A reasonable tune measurement should then be possible even without RF capture. However, feed down from the b_3 spool pieces, together with systematic a_2 in the dipoles and other contributions, lead to a significant coupling in the machine. The use of a special working point would help to minimise coupling, but the a_2 correctors should be powered, again based on magnetic measurement data.

It should be possible in this way to establish circulating beam making tens of turns before any RF is needed. However it is planned to capture the beam with the RF system very soon in the setting up; the commissioning of the RF will be then be interleaved with other ongoing activities.

20.4.2 Flat-bottom Tuning

Once circulating beam is established a campaign of measuring, checking and correcting a large number of parameters and settings can begin. The studies will include:

- Linear optics – model vs. measurements. Feed-down and alignment tolerances will lead to linear optics errors. Correct orbit, Q, Q', coupling, dispersion, β^*, β-beating.
- Compensation for the Experimental magnets – solenoids and dipoles.
- Aperture and collimator optimisation.
- Non-linear optics. There are some 256 corrector circuits from a2 to b6. For some of them, such as b5, the measurement and correction procedure is not yet known.
- RF studies.

Other studies at injection energy may include inner triplet alignment, commissioning of the separation scheme and squeeze pre-commissioning.

20.4.3 RF Capture

The RF system is very complex with nested loops to control the cavities and cope with the beam loading. The commissioning of the RF system will take place over an extended period of time with adjustments each time the bunch intensities and bunch patterns change. This activity will be interleaved with setting up the rest of the machine and a possible procedure is given in section 20.6.

20.4.4 Feedback Systems

Beam feedback systems will be very important in the LHC and several are envisaged, covering orbit, tune, energy, chromaticity and coupling. However, the machine should be setup in such a way as to minimise the errors left for the feedback systems to correct.

From the start, open loop correction using the multipole factory and feed-forward of trims to the next machine cycle will be required. The need here is to establish a reproducible magnetic cycle as early as possible. A powerful software system will also be needed to manage the trims and trim history.

The orbit feedback should be relatively easy to implement. Here the main question concerns the use of global correction algorithms and how these affect the need for local corrections around the collimation and beam dump regions. The energy feedback (using the horizontal orbit correctors) should also be commissioned early. Tune feedback will principally be needed once commissioning of the snapback and ramp begin. Chromaticity and coupling feedbacks are much more complex and will not figure in the early commissioning phase of the LHC.

20.5 COMMISSIONING THE NORMAL CYCLE

Some considerable time will have been spent at injection energy establishing circulating beam, commissioning beam instrumentation and other systems. However, to get beams to high energy it will be necessary to address the problems associated with the normal operational cycle. The following section examines the beam required in this phase, how tolerances may be relaxed and what simplifications can be made to ease operation, with the aim of getting colliding beams at close to full energy in a safe way.

20.5.1 The Baseline Cycle

The nominal LHC ramp has been established [11]. It is composed of a sequence of sections in the form of parabolic, exponential and linear, with a parabolic round off at high energy, designed to mitigate the effects of persistent currents and ramp-induced eddy currents. The power converters give the maximum ramp rate in the linear section. The ramp can be incorporated into a standard cycle as illustrated in Fig. 20.1. The power converters again determine the ramp down rate and the pre-injection plateau is introduced to help minimise the persistent current effects [12]. If the nominal cycle is interrupted for any reason, for example by a quench, a pre-cycle which takes the machine to 7 TeV equivalent for 30 minutes to re-establish the magnetic history is planned.

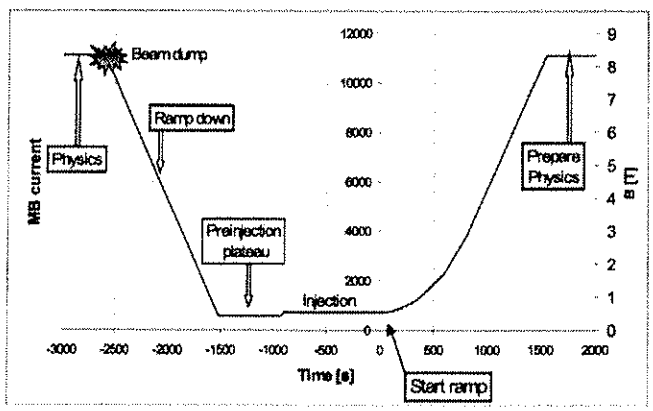

Figure 20.1: The baseline cycle for the LHC

The baseline cycle can be broken down into the main operational phases that make up the nominal cycle. A first version detailing these phases may be found in [13]. Clearly the complete cycle does not need to be commissioned in order to establish first collisions and the phases addressed herein are those which will allow the following to be performed:

1. First optimisation of the machine at 450 GeV; Beam 1, Beam 2, Beam 1 AND Beam 2.
2. Correction of snapback; single beam, ring 1.
3. Ramp; single beam, ring 1.
4. Stop in ramp. Commission beam dump, machine protection in ramp, ring 1.
5. Single beam to 7 TeV, ring 1 (± separation bump).
6. Ramp; single beam, ring 2.
7. Stop in ramp. Commission beam dump, machine protection in the ramp, ring 2.
8. Single beam to 7 TeV, ring 2 (± separation bump).
9. Two beams to 7 TeV and collide unsqueezed.
10. Increase intensity and collide.
11. Single beam partially through squeeze.

20.5.2 Bootstrapping the Cycle

Beam considerations

For commissioning the ramp and beyond a setup beam consisting of a single bunch with an intensity of around 5 to 10 $\times$ 10^9 will be needed. This intensity is below the quench limit at 450 GeV but is, however, above the damage threshold at 7 TeV.

Low emittance of $\varepsilon_n \approx 1.0$ μm.rad gives a beam size of around 0.6 mm at $\beta = 180$ m at 450 GeV, compared to a value of 1.1 mm with nominal emittance. This reduction is useful in two ways; firstly the mechanical aperture in terms of σ increases and the margin for orbit and optics corrections can be relaxed; secondly the dynamic aperture constraints are relaxed and smaller particle amplitudes mean less sampling of the non-linear fields at high amplitudes. The longitudinal emittance should be between 0.5 eV.s and 0.7 eV.s.

The nominal LHC beam parameters have very tight tolerances [14,15], which can be relaxed with the setup beam described. This beam would also be needed later for re-commissioning and debugging.

Reproducibility issues

Establishing reproducible conditions will be essential to LHC operations and at the commissioning stage it is planned to avoid starting the ramp after a variable length of time at injection. Thus there are two choices at injection; either wait each time for the persistent currents to decay fully, or move quickly and avoid the full decay and snap-back by ramping after a short, fixed time interval. Initially it will be easier for the injectors to follow the former option; when reliable filling is possible the latter option should be possible.

To compensate for the effects of snapback, a number of tools are available; the use of a predictive model, cold magnet measurements, on-line measurements from reference magnets and beam-based feedback. Strict procedures will need to be in place in order to establish a reproducible magnetic history.

Ramp

In order to accelerate the beam it will be necessary to use low intensities and even then care is needed since the pilot bunch can cause damage at high energy. It will be necessary to use the simplest possible machine and stop at pre-programmed places in the ramp to measure and correct parameters.

The ramp will be driven by current, voltage and frequency as functions of time, pre-loaded to the power converters and RF, with the start of ramp triggered by a timing event. Before the start of the ramp the TDI and injection collimators are retracted, while the cleaning insertion collimators are left where they are.

Real-time corrections from operator-controlled knobs, feed-forward from reference magnets and beam-based feedback are all planned, but these tools are unlikely to be in place initially.

The main challenge will be anticipating the depth of the snapback and attempting to deal with the associated swing of beam parameters. With the larger tolerances, input from the offline multipole factory, tune and orbit measurements and some rudimentary corrections, it should be possible to get some beam through the snapback.

After snapback and the first 100 GeV it is expected that problems associated with dynamic effects will be considerably reduced. The ramp dependent eddy currents are expected to be reproducible, small and thus to be taken care of in corrector functions.

In the ramp, orbit corrections, tune measurement and operator control of various parameters will be necessary. It is expected that the collimators can remain at fixed positions.

Beam dump

The beam dump system should be commissioned as soon as possible to allow safe extraction of the beam from the machine. It will be necessary to commission the beam dump at a number of intermediate energies. The pilot beam is fairly innocuous at low energies but will need a fully functioning beam dump before pushing too far in energy.

Although the beam dump could be commissioned with a ramping beam, the present plan is to perform a programmed stop of the ramp at intermediate energies. This would give the opportunity to perform measurement checks and to commission the beam loss monitors cleanly before dumping.

A number of systems and parameters are important for the correct functioning of the beam dump and have to be checked. These are;

- Energy tracking calibration (MKD, MSD, MKB).
- Orbit/aperture.
- Extraction trajectory.
- Instrumentation.
- Kicker timings/retriggering.
- Post mortem.

Two beam operation

In the interest of having the simplest possible configuration for the first collisions, it is planned to use one bunch per beam, crossing in ATLAS and CMS. This will require commissioning the separation bumps in points 1 and 5. A cautious approach would be to ramp a single beam with the separation bumps on to check orbit control and closure.

It is envisaged colliding one point at a time. Beams will be put into collisions by extrapolation of the position at the interaction point from the beam position monitors near the first of the triplet quadrupoles, followed by a luminosity scan. At the low luminosity (2.0×10^{26} $cm^{-2}s^{-1}$) expected, integration times will be long but as the exercise is performed with un-squeezed beams with β^* of 18 m, the bigger beam sizes should help in establishing the collision point. Finally, the RF will need phase adjustments and other checks before collisions.

Squeeze

Commissioning of the squeeze will take place with a single beam, one interaction region at a time. The primary and secondary collimators (and TCDQ) will have to follow the squeeze, with relaxed settings in the commissioning stage. Operationally the challenges will be the tune, chromaticity and orbit control, potentially exacerbated by beta beating. Optics and aperture checks will be necessary at each stage.

Conclusions

Commissioning with a low intensity, low emittance and single bunch should allow relaxed tolerances on the critical beam parameters. The machine configuration will be kept as simple as possible.

It will be necessary to anticipate snapback and have the ability to incorporate predictions into the machine settings. This should help to bring tune, chromaticity and orbit within reasonable bounds. Measurement and correction facilities will of course be necessary but fast, real-time feedback should not be obligatory.

It will be necessary to stop in the ramp to commission the beam dump, perform measurement checks and commission beam instrumentation.

This strategy should allow the two beams to be brought safely into collisions for the first time.

20.6 RF COMMISSIONING WITH BEAM

A possible procedure for preliminary commissioning of the RF is given below. Clearly it must be interleaved with the setting up of many other machine elements.

20.6.1 Special Cycle

It is proposed to use the special magnetic cycle designed to minimise dynamic effects for a substantial part of the RF commissioning. This would allow the use of an 'inject and dump' mode where each SPS cycle could be used to inject beam. This will bring advantages in terms of ease of setting up and will therefore minimise the time needed. The total time estimated for RF work on this cycle will be of order 3 weeks. Tab. 20.1 summarises the different beams envisaged and the uses made of them.

Table 20.1 : RF commissioning on the special magnetic cycle

Beam	Purpose
Single pilot bunch $5\ 10^9$, 0.4 eV.s	Find the bunch, set up the phase and synchronisation loops. Set up observation equipment and bunch reference numbers. Set up the beam dump timing and adjust B-field and phase offsets.
Single PS batch from SPS Few 10^{10} per bunch, 0.4 eV.s	Readjust loops with beam, verify and adjust transients in loops.
2,3,4 PS batches from SPS Few 10^{10} per bunch, 0.4 eV.s	Check everything (transients change).
Repeated injections from SPS	Set up injection damping of each batch. Confirm batch position. Confirm effective energy jitter.
Increase intensity to nominal	Observation and adjustment.

20.6.2 Nominal Accelerating Cycle

With the RF now in a solid state with respect to operation with beam induced transients, the problems generated by persistent currents can be addressed. The total time for these procedures is estimated to be of the order of 2 weeks. Tab. 20.2 summarises the different beams envisaged and the uses made of them.

Table 20.2 : RF commissioning on the nominal cycle

Beam	Purpose
Single pilot bunch $5\ 10^9$, 0.4 eV.s	Make multiple injections onto flat bottom with no acceleration. Dump just before the B-field rises. Control B-field correction procedures to obtain $dB/B < 10^{-4}$.
Single pilot bunch $5\ 10^9$, 0.4 eV.s	Make multiple injections onto the flat bottom and accelerate. Beam dump progressively moved up in energy. Control acceleration through snap-back, measure capture losses.
Single PS batch from SPS Few 10^{10} per bunch, 0.4 eV.s	Verify acceleration of a batch.

From this point onwards the number of injected batches and the intensity will be slowly increased. It has also been suggested (Sec. 20.7) that a good commissioning beam for physics would contain 43 (or 86) bunches spaced at ~ 2 μs. This would induce very small transients in the loops even if the bunches were at nominal intensity and so would also be a good initial beam for the RF.

It should not be forgotten that the LHC is basically two machines and everything will have to be repeated for the second beam. In practice this might be interleaved with the first beam setting-up.

20.7 PHYSICS

The constraints outlined in Sec. 20.3 are expected to limit the maximum instantaneous luminosity to about 10^{33} cm^{-2} s^{-1} during the first year of LHC operations. Furthermore the requirement from the experiments to have an event pileup less than 2 limits the luminosity in all modes except 25 ns operation.

20.7.1 Operation with Zero Crossing Angle

It is proposed to begin high energy running without a crossing angle and the associated complexity of parasitic beam-beam interactions. This will allow the beams to cross the inner triplets and matching insertions on-axis. With this configuration, a large amount of beam-based studies can be made and the squeeze to smaller β^* can be made in much cleaner conditions.

The geometry of the interaction regions limits the number of bunches per beam in this mode to under 100. For ease of operation of the injectors, it is proposed to take single (or double) bunches from the PS into the SPS, thereby providing 43 (or 86) bunches in the LHC in a filling scheme closely related to the one needed for operation with high numbers of bunches [16]. In order to provide collisions in LHCb it will be necessary to displace some bunches in one beam by 75ns. These displaced bunches will cause events offset by 11.25 m in the other detectors.

Bringing beams like this into collision would set a clear baseline for luminosity in a simple configuration. Expected performance for parasitic physics with the given parameters at 7 TeV is as follows:

Bunches per beam	Crossing Angle	Bunch Intensity	β^* [m]	Max. Luminosity
43	0	$0.5\ 10^{11}$	1	2×10^{31} cm^{-2} s^{-1}

After having established reasonable performance levels under these conditions, one can bring on the crossing angles, redo the squeeze and re-establish physics conditions.

20.7.2 Operation with 75 ns Bunch Spacing

When running with 75 ns bunch spacing there are fewer parasitic beam-beam encounters than in the 25 ns mode. This allows relaxing the crossing angle. Furthermore, if the β^* is held greater than 0.75 m, any field errors in the triplet are less critical. It is therefore proposed to run with 75 ns spacing, with relaxed parameters, in order to commission multi-bunch operation. No bunch intensity limitations due to electron cloud are expected. Early physics runs could be foreseen at 7 TeV with the following parameters:

Bunches per beam	Crossing Angle [μrad]	Bunch Intensity	β^* [m]	Max. Luminosity
936	250	$0.5\ 10^{11}$	1	5×10^{32} cm^{-2} s^{-1}

20.7.3 Operation with 25 ns Bunch Spacing

Electron cloud effects will limit the bunch intensity in this mode until beam scrubbing has been performed. Otherwise, assuming that the 75 ns operation has allowed reaching all other nominal parameters, the following physics conditions can be expected at 7 TeV:

Bunches per beam	Crossing Angle [μrad]	Bunch Intensity	β^* [m]	Max. Luminosity
2808	285	$0.4\ 10^{11}$	0.55	1.2×10^{33} cm^{-2} s^{-1}

For completeness, the nominal performance at 7 TeV and parameters, with bunch intensities that can only be achieved when the electron cloud has been mastered are:

Bunches per beam	Crossing Angle [μrad]	Bunch Intensity	β^* [m]	Max. Luminosity
2808	285	$1.15\ 10^{11}$	0.55	1×10^{34} cm^{-2} s^{-1}

REFERENCES

1. See, for example, http://proj-lti.web.cern.ch/proj-lti/
2. D. Forkel-Wirth, S. Roesler, G.R. Stevenson, H. Vincke, "Radiation Issues Associated with the LHC Machine Sector Tests", Radiation Safety Officers Committee, May 2003.
3. R. Assmann, Proc. XIIth Chamonix LHC workshop on LHC performance, 2003.
4. F. Rodriguez-Mateos, Proc. XIIth Chamonix LHC workshop on LHC performance, 2003.
5. M. Lamont, http://cern.ch/lhc-injection-test/
6. E. Cennini, private communication
7. J. Virdee, Proc. XIIth Chamonix LHC workshop on LHC performance, 2003.
8. F. Ruggiero, Proc. XIIth Chamonix LHC workshop on LHC performance, 2003.
9. V. Baglin, Proc. XIIth Chamonix LHC workshop on LHC performance, 2003.
10. A. Verdier, Proc. XIIth Chamonix LHC workshop on LHC performance, 2003.
11. L. Bottura, P. Burla and R. Wolf, "LHC main dipole proposed baseline current ramping", LHC Project Report 172, March 1998.
12. L. Bottura, "Superconducting Magnets on Day 1", Chamonix 2001.
13. O. Brüning, A. Butterworth, M. Lamont, J. Wenninger, "The Nominal Operational Cycle of the LHC with Beam (version 1)", LHC Project Note 313.
14. O. Brüning, "Accelerator Physics Requirements at Commissioning", Chamonix 2001.
15. O. Brüning, "Accumulation and Ramping in the LHC", LHC Project Note 218, February 2000
16. R. Bailey, P. Collier, "Standard Filling Schemes for Various LHC Operation Modes", LHC Project Note 323

CHAPTER 21

THE LHC AS A LEAD ION COLLIDER

21.1 INTRODUCTION

Heavy ion collisions were included in the conceptual design of the LHC from an early stage and collisions between beams of fully stripped lead ($^{208}Pb^{82+}$) ions are scheduled for one year after the start-up of the collider with protons. With the nominal magnetic field of 8.33 T in the dipole magnets, these ions will have a beam energy of 2.76 TeV/nucleon, yielding a total centre-of-mass energy of 1.15 PeV and a nominal luminosity of $1.0 \times 10^{27}\,\mathrm{cm}^{-2}\mathrm{s}^{-1}$. Collisions between ion beams will be provided principally at IP2 for the specialised ALICE detector. However the CMS and ATLAS detectors also plan to study ion collisions with similar luminosity.

While the major hardware systems of the LHC ring appear compatible with heavy ion operation, the beam dynamics and performance limits with ion beams are quite different from those of protons in a number of respects. The LHC also enters new territory where, for example, the copious nuclear electromagnetic interactions in peripheral collisions of the ions can directly limit luminosity and beam lifetime. While these phenomena are present in RHIC, for example, they are not straightforward to observe and do not limit performance. Yet they become critical in the LHC because of the combination of its unprecedented energy and magnet technology.

At the time of writing, it is premature to make firm predictions about some of the factors that may limit the performance of the LHC with ions. In particular, there are substantial uncertainties concerning some vacuum issues and the ion beam parameters during ramping. Some effects limiting the luminosity appear more serious now than in earlier discussions although means to alleviate them are under study.

Starting with the first acceleration of ions in the CERN Proton Synchrotron (CPS) in 1976, CERN has built up a wealth of experience in creating and accelerating ion beams. Recent years have seen the successful exploitation of lead and indium ion beams for fixed target experiments at the SPS. The creation, acceleration and injection of ion beams for the LHC, including the new LEIR accumulator ring, are founded in this experience. The ion injectors are covered in Part 4 of Volume III of this report. The present chapter will describe ion beams in the LHC main ring itself.

21.2 PARAMETERS OF THE LHC WITH LEAD IONS

Some aspects of ion beams are similar to the proton beams. For example, the nominal emittance of the ions has been chosen so that the ion beams have the same geometric size as the nominal proton beams (at beam energies corresponding to the same magnetic field in the dipole magnets). Then at least the most basic considerations of beam size and aperture will be the same as for protons, implying that this is a safe operational value. Despite this, the physics of ion beams is qualitatively and quantitatively different from that of protons and the values of some parameters are necessarily very different.

There are two reference sets of parameters for lead ion beams:

Nominal Ion Scheme: A peak luminosity of around $10^{27}\,\mathrm{cm}^{-2}\mathrm{s}^{-1}$ has been the overall performance goal for lead ions for some time [1, 2, 3, 4]. Yet there are several phenomena specific to heavy ions that may turn out to be serious impediments to reaching this level of luminosity. The most important ones will be discussed in Sec. 21.4 and Sec. 21.5 below. The main parameters of the beams at injection and collision energies are given in Tab. 21.1.

Early Ion Scheme: The first period of operation of the LHC as a lead-lead collider, running-in and early physics, will be carried out with identical single bunch parameters but ten times fewer bunches and a larger value of β^*. These relaxed parameters will provide more margin against some of the performance limits discussed in Sec. 21.5 and Sec. 21.4, namely those that depend on the total beam current. The reduced luminosity will nevertheless give access to important physics. Parameters at collision energy are given in Tab. 21.2.

The reasons for the values given will be discussed in the following sections.

Table 21.1: LHC beam parameters bearing upon the peak luminosity in the nominal ion scheme.

		Injection	Collision
Beam parameters			
Lead ion energy	[GeV]	36900	574000
Lead ion energy/nucleon	[GeV]	177.4	2759.
Relativistic "gamma" factor		190.5	2963.5
Number of ions per bunch		$7. \times 10^7$	
Number of bunches		592	
Transverse normalised emittance	[μm]	1.4[a]	1.5
Peak RF voltage (400 MHz system)	[MV]	8	16
Synchrotron frequency	[Hz]	63.7	23.0
RF bucket half-height		1.04×10^{-3}	3.56×10^{-4}
Longitudinal emittance (4σ)	[eV s/charge]	0.7	2.5[b]
RF bucket filling factor		0.472	0.316
RMS bunch length[c]	[cm]	9.97	7.94
Circulating beam current	[mA]	6.12	
Stored energy per beam	[MJ]	0.245	3.81
Twiss function $\beta_x = \beta_y = \beta^*$ at IP2	[m]	10.0	0.5
RMS beam size at IP2	μm	280.6	15.9
Geometric luminosity reduction factor F[d]		-	1
Peak luminosity at IP2	[$cm^{-2}sec^{-1}$]	-	$1. \times 10^{27}$

[a]The emittance at injection energy refers to the emittance delivered to the LHC by the SPS without any increase due to injection errors and optical mismatch.

[b]The baseline operation assumes that the longitudinal emittance is deliberately blown up during, or before, the ramp in order to reduce the intra-beam scattering growth rates.

[c]Dimensions are given for Gaussian distributions. The real beam will not have a Gaussian distribution but more realistic distributions do not allow analytic estimates for the IBS growth rates.

[d]The geometric luminosity reduction factor Equation 3.3 depends on the total crossing angle at the IP. The crossing angle for lead ions is discussed in Sec. 21.3.2

Table 21.2: LHC beam parameters bearing upon the peak luminosity in the early ion scheme. Only those parameters that differ from those in the nominal ion scheme, given in Tab. 21.1 are given.

		Injection	Collision
Beam parameters			
Number of bunches		62	
Circulating beam current	[mA]	0.641	
Stored energy per beam	[MJ]	0.0248	0.386
Twiss function $\beta_x = \beta_y = \beta^*$ at IP2	[m]	10.0	1.0
RMS beam size at IP2 [e]	[μm]	280.6	22.5
Peak luminosity at IP2	[$cm^{-2}sec^{-1}$]	-	5.4×10^{25}

Table 21.3: LHC beam parameters bearing upon the beam or luminosity lifetime in the nominal ion scheme.

		Injection	Collision
Interaction data			
Total cross section	[mb]	-	514000
Beam current lifetime (due to beam-beam)[a]	[h]	-	11.2
Intra Beam Scattering			
RMS beam size in arc	[mm]	1.19	0.3
RMS energy spread $\delta E/E_0$	$[10^{-4}]$	3.9	1.10
RMS bunch length	[cm]	9.97	7.94
Longitudinal emittance growth time	[hour]	3	7.7
Horizontal emittance growth time[b]	[hour]	6.5	13
Synchrotron Radiation			
Power loss per ion	[W]	3.5×10^{-14}	2.0×10^{-9}
Power loss per metre in main bends	$[\mathrm{Wm}^{-1}]$	8×10^{-8}	0.005
Synchrotron radiation power per ring	[W]	1.4×10^{-3}	83.9
Energy loss per ion per turn	[eV]	19.2	1.12×10^{6}
Critical photon energy	[eV]	7.3×10^{-4}	2.77
Longitudinal emittance damping time	[hour]	23749	6.3
Transverse emittance damping time	[hour]	47498	12.6
Variation of longitudinal damping partition number[c]		230	230
Initial beam and luminosity lifetimes			
Beam current lifetime (due to residual gas scattering)[d]	[hour]	?	?
Beam current lifetime (beam-beam, residual gas)	[hour]	-	< 11.2
Luminosity lifetime[e]	[hour]	-	< 5.6

[a]Each "lifetime" in this table is the instantaneous time-constant for the decay of a quantity when the beam current and emittances have their nominal values; it is not a direct indication of the length of a fill. It is assumed that two experiments receive the nominal luminosity.

[b]An IBS growth time for the vertical emittance is not quoted since the direct effect of IBS in this plane is very small.

[c]This is the derivative $dJ_\epsilon/d\delta$ where $\delta = -1/\alpha_c \Delta f_{\mathrm{RF}}/f_{\mathrm{RF}}$ is the fractional momentum difference of the closed orbit with respect to the one for which the closed orbit passes through the centres of the magnet apertures.

[d]Currently under review.

[e]Including the effects of beam-beam, radiation damping and IBS; no accounting for residual gas.

Table 21.4: LHC beam parameters bearing upon the beam or luminosity lifetime in the early ion scheme. Only those parameters which differ from those in the nominal ion scheme, given in Tab. 21.3 are given.

		Injection	Collision
Interaction data			
Beam current lifetime (due to beam-beam)[a]	[h]	-	21.8
Synchrotron Radiation			
Power loss per metre in main bends	$[\mathrm{Wm}^{-1}]$	8.5×10^{-9}	5.0×10^{-4}
Synchrotron radiation power per ring	[W]	1.5×10^{-4}	8.8
Initial beam and luminosity lifetimes			
Beam current lifetime (beam-beam, residual gas)	[hour]	-	< 21.8
Luminosity lifetime (as in Tab. 21.3)	[hour]	-	< 11.2

[a]Assuming that two experiments receive the nominal luminosity.

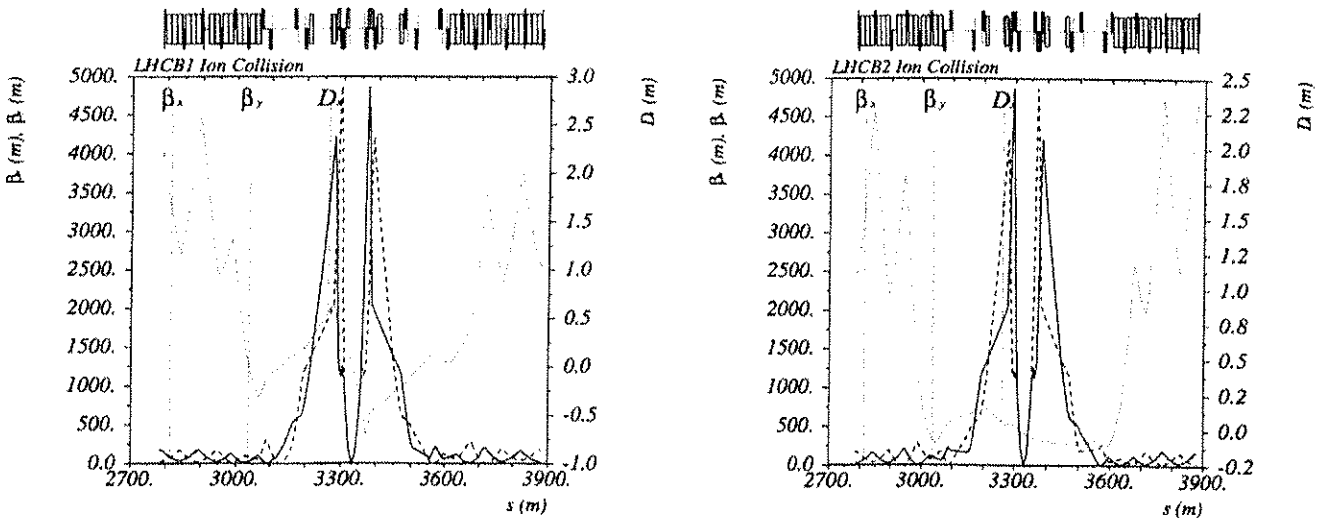

Figure 21.1: Collision optics in IR2 for lead ions with $\beta^* = 0.5\,\mathrm{m}$, showing Beam 1 (left) and Beam 2 (right). As usual, the azimuthal coordinate s is given relative to IP1.

21.3 ORBITS AND OPTICAL CONFIGURATIONS FOR HEAVY IONS

21.3.1 Optical functions

As in Chap. 4, the optical configuration described in this section is the LHC Version 6.4, including the repositioning of the Q3 triplet magnets, which is part of Version 6.5.

The optics in IR2, for head-on collisions of ion beams in the ALICE detector, will be quite different from that used for protons (see Chap. 4) in which $\beta^* = 10\,\mathrm{m}$ and beams are collided with an offset. For ions, collisions will be head-on with β^* values down to $\beta^* = 0.5\,\mathrm{m}$. Moreover, since this value is somewhat smaller than the limit of $\beta^* = 0.55\,\mathrm{m}$ for high-luminosity p-p collisions at IP1 or IP5, the peak values of β_x and β_y in the insertion quadrupoles will be higher in the ion collision optics. The lower value of β^* is possible with ions because the separation bumps are smaller (see the following section), leaving more aperture for the peaks in the β-functions.

For ion collisions in either IP1 or IP5 the optics can be the same as for protons (see Chap. 4) or may be adjusted to $\beta^* = 0.5\,\mathrm{m}$ as in IP2. Otherwise, the pre-collision optics can be maintained in any IP in which the beams do not collide. Thanks to the modularity and independence of the optics in the various interaction regions, it is in principle straightforward to adapt the optics of the LHC to any set of collision points. However it should be remembered that switching between the various possible configurations may require some operational time in order to establish the appropriate corrections. In particular, each configuration will contribute differently to the horizontal and vertical dispersions around the ring.

21.3.2 Beam Separation near the Interaction Points

Compared with the nominal proton beams, the relatively low intensities and larger bunch spacing of the lead ion beams lead to weak beam-beam effects which do not, in themselves, impose any minimum separation around the interaction points. If these were the only considerations, it might be possible to eliminate the crossing angle entirely. However this would create additional head-on beam-beam encounters, reducing the beam lifetime. Moreover the ALICE detector has a spectrometer magnet compensated by its own orbit separation bump around IP2 Sec. 4.2.3. The total separation will be the superposition of this bump and the "external" crossing angle and parallel separation bumps. At the interaction point, the full crossing angle is given by

$$[\theta_c/\mu\mathrm{rad}] \simeq 140 f_{\mathrm{ALICE}} - 340 f_{\mathrm{IP2bump}} \tag{21.1}$$

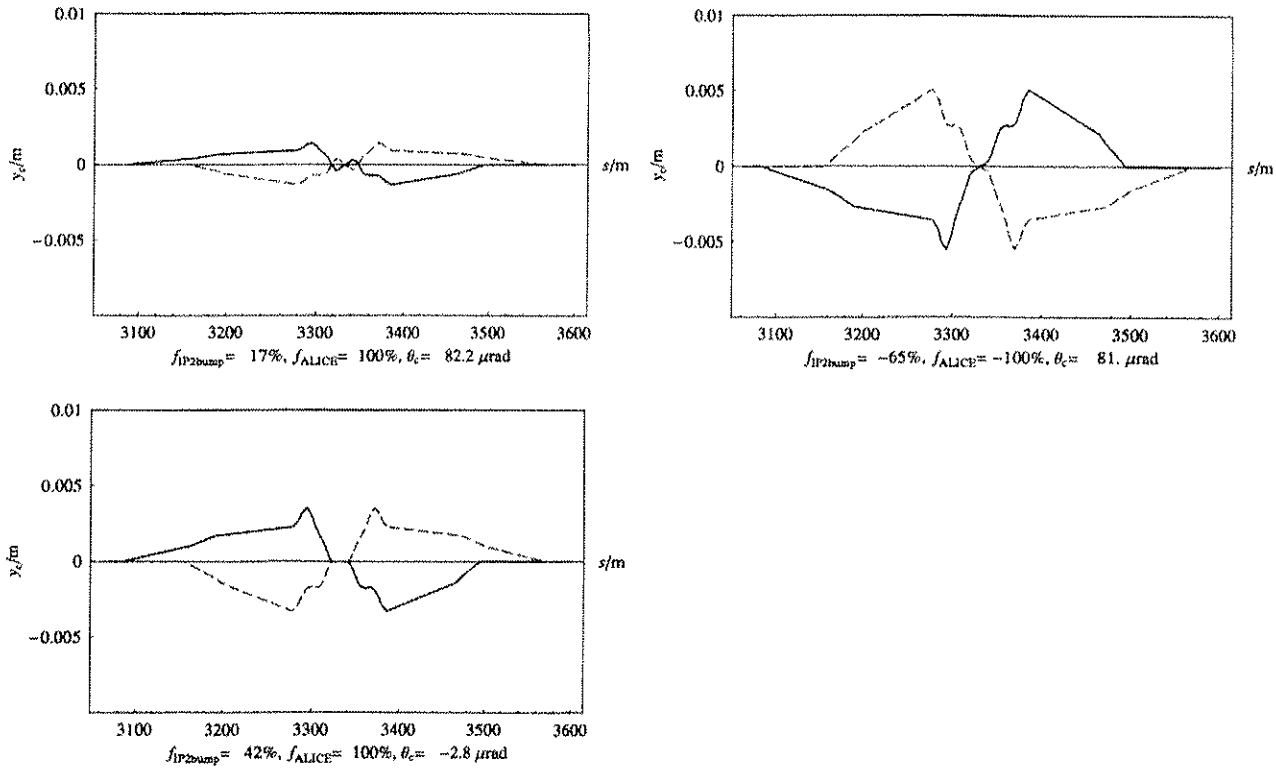

Figure 21.2: Separation of lead ion beams around IP2 for positive and negative polarities of the ALICE compensation bump in an ion collision optics with $\beta^* = 0.5\,\mathrm{m}$. The vertical closed-orbit distortion of Beam 1 is represented by the solid line and that of Beam 2 by the dashed line. In the first two cases, the amplitude of the external bump is chosen to provide a crossing angle of about $80\,\mu$rad at IP2. As usual, the azimuthal coordinate s is given relative to IP1. In the first case, the ALICE bump and the external separation bump generate contributions to the crossing angle of equal sign at the IP; in the second they are opposite, leading to larger separations outside the ALICE bump. In the third case, the bumps are chosen to cancel at the IP, resulting in zero crossing angle.

where f_{ALICE} and f_{IP2bump} are amplitude factors for the bumps (normalised so that $\theta_c = -200\,\mu$rad for $f_{\mathrm{ALICE}} = f_{\mathrm{IP2bump}} = 100\%$. The collisions at additional encounters would also interfere with the trigger for ALICE. It is desirable to use the minimum separation needed to avoid these problems because, with the full separation used for protons, the criteria for minimum aperture Sec. 4.3 are violated. Further discussion of the separation scheme in IR2 can be found in Sec. 4.2.3.

Since the ion collision optics in IR2 has higher maximum values of β_x and β_y in the insertion quadrupoles, the need to observe the minimum physical aperture criteria is another strong reason for reducing the separation bump amplitudes in the collision optics.

Pending final optimisation, some illustrative configurations of the separation bumps around IP2 are shown in Fig. 21.2. The first two arrangements are chosen to provide a similar crossing angle at IP2 but differ in the relative polarities of the external separation bump and the ALICE compensation bump. In the second configuration, where the two bumps cancel each other to a large extent close to the IP, a greater separation, of about $7\sigma_y$ at the first beam-beam encounter (which lies outside the ALICE bump in the nominal ion scheme) is achieved; this could be considered a very safe configuration for the nominal ion scheme where unwanted collisions should be avoided for reasons of beam lifetime and experimental background and triggering. The first configuration gives a minimum separation of about $2.6\sigma_y$ which is marginal.

In the third configuration, the two bumps have been combined in such a way as to achieve an almost zero crossing angle. This arrangement is of particular interest for ion collisions. According to Equation 3.3, reducing the crossing angle to the minimum possible provides some gain in luminosity. Reducing the bump amplitudes

also tends to reduce the vertical dispersion around the ring. In this configuration, the separation at the first parasitic encounter is $2.5\sigma_y$ on both sides. It is probably close to the optimum for the early ion scheme but may be marginal for the nominal ion scheme, in which case the crossing angle could be increased to 20 μrad to give a minimum separation of $3\sigma_y$ at the closest encounter.

The only obvious advantage of a scheme of the first type is the reduction of parasitic vertical dispersion created by the smaller overall amplitude of the bump.

The mechanical acceptance of IR2 in each of these separation configurations is shown in Fig. 21.3. Each of them meets the requirements specified in Chap. 4. It should be noted that a bump amplitude similar to that used in the nominal collision scheme for protons would not meet the requirements with $\beta^* = 0.5\,\mathrm{m}$.

In principle, the overall polarity of each case shown in Fig. 21.2 could also be reversed. However the polarities shown are those most easily accessible by continuous variation from the injection conditions described in Chap. 4.

For collisions of ion beams in IP1 or IP5, the optics may be the same as for protons but the crossing-angles can be reduced, possibly to zero in the early ion scheme.

During injection and ramping, the requirements for the separation of ion beams at the IPs appear even less demanding. The final choice of separations in these conditions is still to be made but is likely to be determined mostly by operational considerations. If, for example, there are well-established corrections of the injection and ramp for protons then it may be most straightforward to simply adopt the same scheme for ions, differing only in the final steps to the collision configuration. The examples given in this section were intended to show that the separation schemes have sufficient flexibility to accommodate the requirements of heavy ion operation.

21.3.3 Longitudinal dynamics

Nominal longitudinal parameters for lead ions at injection and collision energies are given in Tab. 21.1. The relatively small injected longitudinal emittance of $\epsilon_l = 0.7\,\mathrm{eV\,s/charge}$ is necessary for efficient injection as long as the 200 MHz capture system (discussed in the Introduction to Chap. 6) is not installed. All parameters given in this chapter assume these conditions. Because of mismatch and nonlinearities there will likely be some filamentation to a slightly larger value after injection. In these conditions the bunches occupy about half the RF bucket area. The relatively short growth times for the longitudinal emittance with nominal intensity (see Fig. 21.6) imply that, if the bunches have to be kept for some time at injection for any reason, their longitudinal emittance will increase further. At some point, ions may start to spill out of the RF bucket but, since beam-loading is very small with the currents in the ion beams, a reserve of 50 % or the total RF voltage is available to counter this. Controlled blow up to $\epsilon_l = 2.5\,\mathrm{eV\,s/charge}$ is in any case necessary during the ramp to collision energy to reduce the growth of the transverse emittances from intra-beam scattering.

21.4 EFFECTS OF NUCLEAR INTERACTIONS ON THE LHC AND ITS BEAMS

When ultra-relativistic lead ions collide at LHC energies numerous processes of fragmentation and particle production can occur. Some of these have direct consequences as performance limits for the collider.

Besides the hadronic nuclear interactions due to direct nuclear overlap,

$$^{208}\mathrm{Pb}^{82+} + {}^{208}\mathrm{Pb}^{82+} \xrightarrow{\text{nuclear}} X \tag{21.2}$$

for which the cross section is

$$\sigma_{\mathrm{H}} \simeq 8\,\mathrm{barn} \tag{21.3}$$

there is an important class of longer-range, or peripheral, collisions dominated by electromagnetic interactions. In collisions of light ions, the cross sections for these processes are small (some are zero in the case of protons) compared with σ_{H}. For heavy ions (with $Z \gtrsim 30$), and Pb in particular, the cross sections for these electromagnetic interactions are much larger than σ_{H}. While simple elastic (Rutherford) scattering and free $\mathrm{e^+e^-}$ pair production are of little consequence, other processes change the charge state or mass of one of the colliding ions, creating a secondary beam emerging from the collision point. For a change, ΔQ, in the charge, Q, and

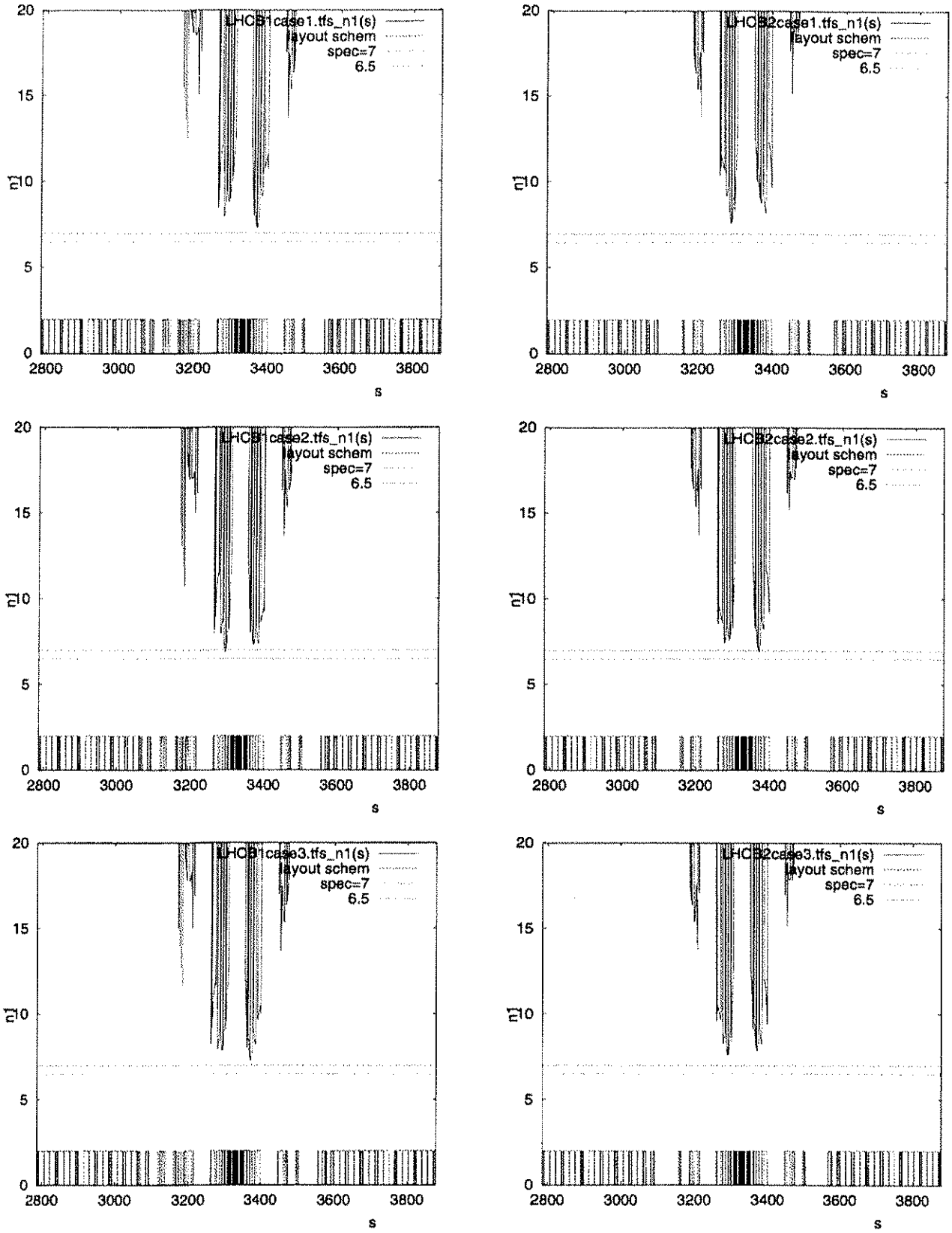

Figure 21.3: Mechanical acceptance in IR2, expressed in terms of the primary aperture quantity n_1, as defined in Chap. 4 at 2.75 TeV/nucleon and $\beta^* = 0.5\,\mathrm{m}$ (ion collision optics with parallel separation switched on), showing Beam 1 (left) and Beam 2 (right) for each of the three separation configurations shown in Fig. 21.2. As usual, the azimuthal coordinate s is given relative to IP1.

ΔA in the number of nucleons, A, the magnetic rigidity of the secondary beam corresponds to an effective fractional momentum deviation given approximately[1] by

$$\delta(\Delta Q, \Delta A) \simeq \frac{1 + \Delta A/A}{1 + \Delta Q/Q} - 1. \tag{21.4}$$

This parametrisation in terms of $\delta(\Delta Q, \Delta A)$ will be used in the following sections and also in the discussion of collimation for ions where similar processes occur in collimator materials.

Recent reviews of the nuclear physics and the calculations of cross sections can be found in [7, 8, 9].

All contributions to the total cross section for ion collisions will of course contribute to the total loss rate and resulting beam lifetime. However certain processes have consequences beyond this.

Electron capture from pair production (ECPP)

In this process, an e^+e^- pair is produced but the electron is captured by one of the nuclei

$$^{208}\mathrm{Pb}^{82+} + {}^{208}\mathrm{Pb}^{82+} \xrightarrow{\gamma} {}^{208}\mathrm{Pb}^{82+} + {}^{208}\mathrm{Pb}^{81+} + e^+ \tag{21.5}$$

The seriousness of this effect hinges on the knowledge of the cross section and many papers have been devoted to its calculation and measurement; some recent references are [10, 11]. Most authors are now in close agreement (the differences with some earlier calculations being understood). The present estimates are based on values from the theoretical calculations in [11] including the sum over final ion-electron bound states as detailed in [12] giving

$$\sigma_{\mathrm{ECPP}} \simeq 281 \text{ barn}. \tag{21.6}$$

Note that the variation of these cross sections with energy is rather weak, of the form $\sigma_{\mathrm{ECPP}} \simeq A \log\gamma + B$ so reducing the beam energy would have little impact on the rate of production of these ions.

According to (Eq. 21.4), the effective momentum deviation of the secondary beam emerging from the collision point is $\delta(-1, 0) \simeq 0.012$, a value well outside the momentum acceptance of the ring. The secondary beam strikes the beam screen inside one of the cryo-magnets of the downstream dispersion suppressor as illustrated in Fig. 21.4. This occurs on each side of every IP where ions collide.

Earlier estimates of the consequences of this effect [13, 14, 15, 12, 16] were based on simplified models using the linear optical functions. However the strong chromatic effects of the insertion quadrupoles modify the size of the secondary beam considerably: the beam size "beats" with respect to the size of the main beam. In more recent studies with new software for localisation of beam losses [17], the ions are tracked in the full optics model to the entrance of the magnet. Inside the magnet, a detailed 3D tracking algorithm has been implemented to localise the impact points of particles on the beam screen. A typical result is shown in Fig. 21.5. Unfortunately, in this case, the secondary beam is somewhat smaller than the main beam at the impact point in the dipole magnet MB.B10R2.B1, resulting in a more concentrated deposition of ion beam energy in the beam screen. The longitudinal RMS spot size is 0.5 m whereas an estimate based on linear optics gives 0.7 m.

The energy deposition will take place over a length corresponding to this distribution, convoluted with the shower length. Pending the results of further study including a proper model of the ion fragmentation, this is estimated to be about 1 m [15], resulting in an effective (2σ) length $l_{\mathrm{eff}} \simeq 1.4\,\mathrm{m}$ for the energy density distribution.

Heating of the beam screen may induce a quench of the superconducting magnet. The quench limit for lead ions at 2.75 TeV/nucleon can be inferred [18] from that of protons at the *same energy*, 2.75 TeV, by dividing by the mass number

$$f_q(\mathrm{Pb}) \simeq \frac{1.7 \times 10^7\,\mathrm{p/m/s}}{A} \simeq 8 \times 10^4\,\mathrm{Pb/m/s}. \tag{21.7}$$

[1] This assumes that the *momentum per nucleon* of all final state components—for example, emitted neutrons—in the laboratory frame remains close to its value in the initial state. It is easy to see that the approximation is good for the electron capture process considered in Sec. 21.4. Detailed calculations [5, 6] show that this holds, in an average sense, to a fairly good approximation in the electromagnetic dissociation processes considered in Sec. 21.4.

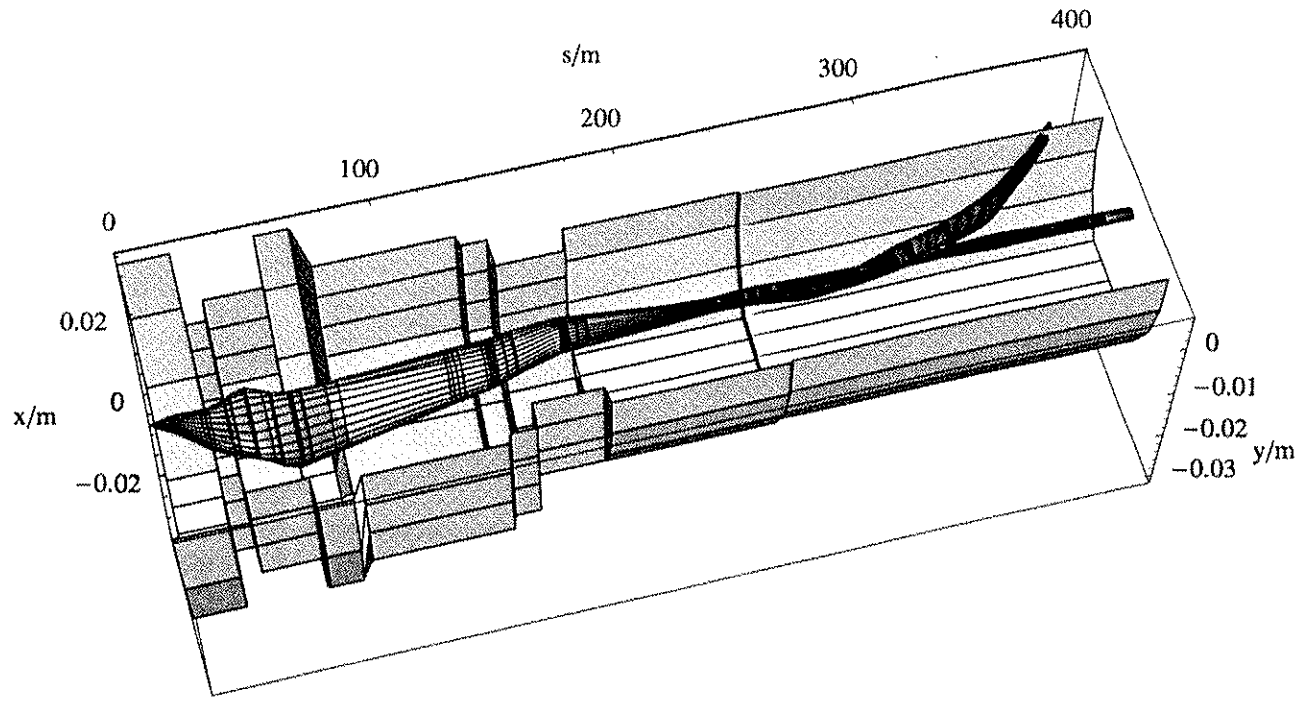

Figure 21.4: Beam screen, seen cut away from above and 5σ envelopes of the main Beam 1 ($^{208}Pb^{82+}$) and secondary beam ($^{208}Pb^{81+}$, shown with a darker surface) created from it by the ECPP process. The coordinate system is the usual beam dynamics system for Beam 1 in which s is the azimuthal coordinate along the reference orbit $x = y = 0$ except that, in this plot, s is given relative to IP2. Both beams travel from left to right in this image. Moving away from the interaction point, the two beams develop very different orbits in both planes because of the dispersive effects of the bending magnets. They *also develop very different sizes* because of the chromatic effects of the quadrupoles. Close to its point of impact in the dispersion suppressor, the $^{208}Pb^{81+}$ beam has a much larger beam size in the vertical plane but is narrower in the horizontal plane, increasing the longitudinal density of the ion flux on the beam screen. The image also illustrates that it is not easy to find a place where the two beams are sufficiently separated for the $^{208}Pb^{81+}$ beam to be effectively stopped or collimated.

Assuming the nominal luminosity, $L = 10^{27}\,\mathrm{cm}^{-2}\mathrm{s}^{-1}$, the flux of lead ions from the ECPP process is then

$$f(\mathrm{Pb}) = \frac{L\sigma_{\mathrm{ECPP}}}{l_{\mathrm{eff}}} = 2 \times 10^5\,\mathrm{Pb/m/s} \gtrsim 2f_q(\mathrm{Pb}), \tag{21.8}$$

i.e., at the nominal luminosity the heating due to this flux of ions on the beam screen is about twice the quench limit. While the quench limit figure certainly contains some reserve, this is currently understood as the most serious limit on luminosity with lead ions.

Measures to reduce this effect are under study. These may work either by intercepting a fraction of the $^{208}Pb^{81+}$ ions before they strike the beam screen or by spreading out the spot size when they do. One way to spread out the secondary beam spot might be to adjust the chromatic effects of the insertion optics. However this is not easy since no sextupolar correction is available in the relevant region. Other possibilities may include special collimators or stripping foils in places where the main and secondary ion beams are sufficiently separated by dispersion in the horizontal or vertical plane. The feasibility of such schemes in a given IR is closely linked to the separation schemes used, not only in that IR but in all the others and requires further detailed study.

Calculations of ion fragmentation and the resulting heat deposition in the environment of the beam screen and cold mass are planned.

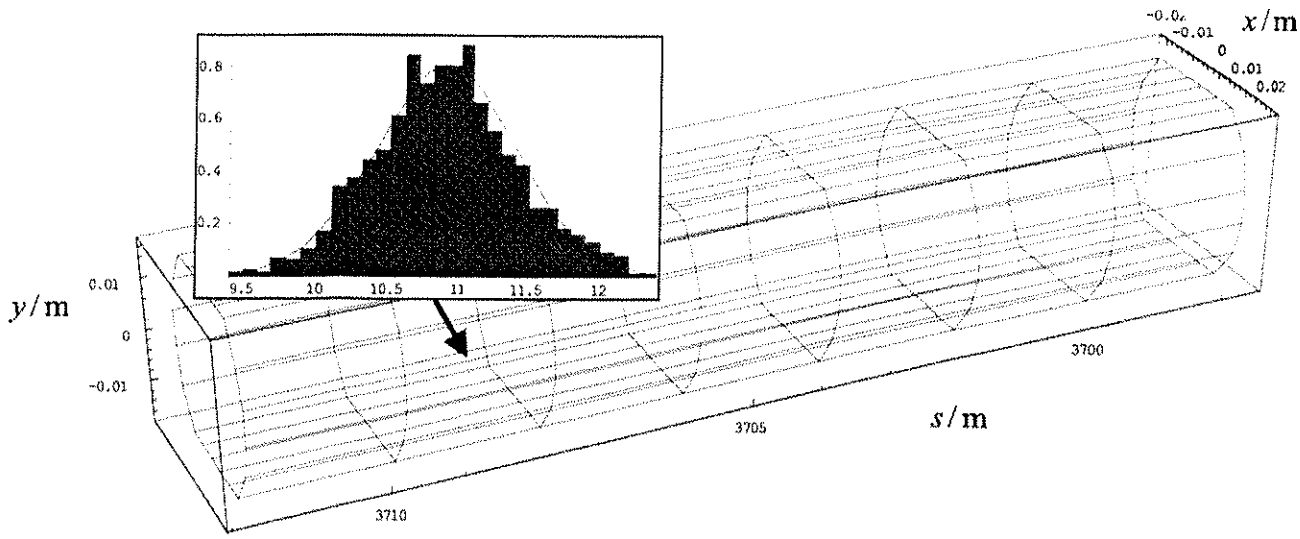

Figure 21.5: Image of the $^{208}Pb^{81+}$ beam spot on the beam screen, just above the median plane of the ring, seen from the outside. The wire-frame image represents the beam screen inside the dipole magnet MB.B10R2.B1 to the right of IP2. The embedded histogram of the longitudinal density of ion flux on the screen (in which the longitudinal coordinate is the distance from the entrance face of the magnet) shows that the beam spot has an RMS length of 0.5 m. The coordinate system is the usual beam dynamics system for Beam 1 in which s is the azimuth along the reference orbit $x = y = 0$. As usual, the azimuthal coordinate s is given relative to IP1.

It has been shown [9, 12] that the rate of Lorentz stripping of the $^{208}Pb^{81+}$ ions back to the fully stripped state in the magnetic fields of the LHC is utterly negligible.

Although the present estimate of the effects of ECPP gives serious cause for concern, it must be emphasised that there are uncertainties and safety margins still in hand, together with reasonable hope for effective cures. Therefore the nominal luminosity of $1.0 \times 10^{27}\,\mathrm{cm}^{-2}\mathrm{s}^{-1}$ has been maintained as a design goal pending the results of further studies.

Electromagnetic dissociation (EMD)

Electromagnetic dissociation processes can be thought of as proceeding in two stages. First, one of the lead ions makes a transition to an excited nuclear state that then decays with the emission of a neutron, leaving a lighter isotope of lead. The dominant process of this sort in lead-ion collisions at the LHC is

$$^{208}Pb^{82+} + {}^{208}Pb^{82+} \xrightarrow{\gamma} {}^{208}Pb^{82+} + {}^{208}Pb^{82+*} \downarrow {}^{207}Pb^{82+} + \mathrm{n}. \tag{21.9}$$

According to calculations using the RELDIS program [5, 6], at the LHC lead beam energy, the cross section for this process is 104 barn out of a total cross section for all electromagnetic dissociation processes of $\sigma_{\mathrm{EMD}} \simeq 226$ barn.

Similar basic processes are important both in the heat deposition and secondary scattering processes that occur whenever ions strike the beam-screen or collimators (see the discussion of the ECPP process above and Sec. 21.7).

According to (Eq. 21.4), the process described in (Eq. 21.9) results in a *negative* effective momentum deviation $\delta(0,-1) \simeq -0.0048$. This places the resulting $^{207}Pb^{82+}$ ion in the band of momenta that should be intercepted by the collimation system (the RELDIS results also show that these ions have a spread in momentum around this value that will tend to increase the longitudinal spread of any heat loss.)

The next most important electromagnetic dissociation process is the production of a secondary beam of $^{206}Pb^{82+}$ with $\delta(0,-2) \simeq -0.0097$ with about 20% of the intensity of the $^{207}Pb^{82+}$ beam. This is outside

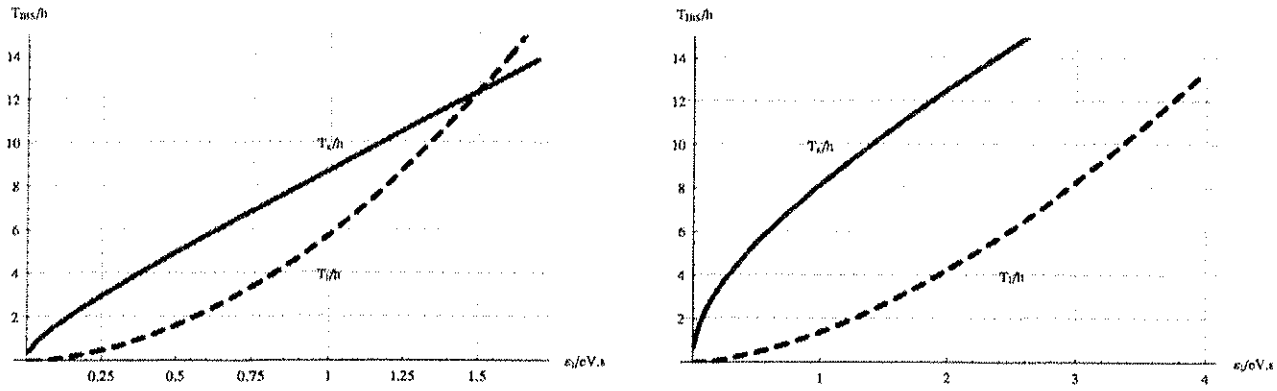

Figure 21.6: Emittance growth times from intra-beam scattering as a function of longitudinal emittance for $^{208}Pb^{82+}$ at injection (left plot) and collision (right plot) energies. The transverse emittances and beam intensities are taken to have their nominal values and the total circumferential voltage from the 400 MHz RF system are $V_{RF} = 8\,MV$ and $V_{RF} = 16\,MV$ respectively. Solid and dashed lines correspond to the growth times for horizontal and longitudinal emittances.

the momentum acceptance of the ring and will result in a beam spot longer than that shown in Fig. 21.5, at a location further downstream but on the *inside* wall of the beam screen. This secondary beam is unlikely to quench a magnet.

The rates of transmutation of the lead ions to isotopes of lighter elements are very small compared with the processes in which the lead ion emits one or two neutrons.

Detailed studies to localise the losses of these ions and evaluate their effects are under way and will be pursued with high priority.

21.5 LUMINOSITY AND BEAM LIFETIME

21.5.1 Intra-beam Scattering

Multiple Coulomb scattering within an ion bunch, known as intra-beam scattering (IBS), is a diffusive process that modifies all three beam emittances. Already significant for protons in the LHC (see Chap. 5), it is even stronger for lead ion beams of nominal intensity and determines the acceptable longitudinal emittance, particularly at injection from the SPS.

The values of the IBS growth times given in Tab. 21.1 refer to the initial bunch parameters and nominal intensity. As the emittances increase, the growth rates will diminish. Fig. 21.6 shows how they depend on longitudinal emittance.

The calculations of emittance growth times from IBS were done with the theory of [19] as implemented in the program MAD [20].

21.5.2 Synchrotron Radiation from Lead Ions

The LHC is not only the first proton storage ring in which synchrotron radiation plays a noticeable role (mainly as a heat load on the cryogenic system, see Sec. 5.6) but also the first heavy ion storage ring in which synchrotron radiation has significant effects on beam dynamics. Surprisingly, perhaps, some of these effects are stronger for lead ions than for protons.

Quantities such as the energy loss per turn from synchrotron radiation and the radiation damping time for ions are obtained from the familiar formulas for electrons by replacing the classical electron radius and the mass by those of the ions[2]. The principal characteristics of the incoherent synchrotron radiation of fully stripped ions of atomic number Z and mass number A can be related to those of protons (assuming the same field in the

[2]The nuclear radius being much smaller than relevant wavelengths, the nucleus radiates coherently, like a single charge Ze

bending magnets) by

$$\frac{U_{\rm ion}}{U_{\rm p}} \simeq \frac{Z^6}{A^4} \simeq 162, \qquad \frac{u^{\rm c}_{\rm ion}}{u^{\rm c}_{\rm p}} \simeq \frac{Z^3}{A^3} \simeq 0.061, \tag{21.10}$$

$$\frac{N_{\rm ion}}{N_{\rm p}} \simeq \frac{Z^3}{A} \simeq 2651, \qquad \frac{\tau_{\rm ion}}{\tau_{\rm p}} \simeq \frac{A^4}{Z^5} \simeq 0.5 \tag{21.11}$$

where U is the energy lost per ion per turn by synchrotron radiation, $u^{\rm c}$ is the critical energy of the synchrotron radiation photons, N is the number of photons emitted per turn and τ is a synchrotron radiation damping time; the numerical values are given for the case of $^{208}\mathrm{Pb}^{82+}$. The critical energy of the radiation from lead ions at collision energy falls in the visible spectrum. Precise values of these quantities are given in Tab. 21.3.

It is notable that radiation damping for heavy ions like lead is about twice as fast as for protons and that the emittance damping times are comparable with the growth times from intra-beam scattering[3]. Since emittance growth due to the quantum fluctuations of the synchrotron radiation is negligible, shrinking transverse emittances are a real possibility below some intensity level. In addition there appears to be some scope for varying damping partition numbers with momentum (see Tab. 21.3) to switch some damping from the longitudinal to the horizontal plane; this comes at the price of a displaced central orbit. It should be remembered that, even when radiation damping overcomes intra-beam scattering, noise in the RF system will ultimately determine the minimum longitudinal emittance; the level at which this occurs remains to be quantified.

21.5.3 Beam loss from collisions

The total cross section for removal of an ion from the beam is

$$\sigma_{\rm T} = \sigma_{\rm H} + \sigma_{\rm EMD} + \sigma_{\rm ECPP} \simeq 514\,\mathrm{barn} \tag{21.12}$$

As discussed in Sec. 21.4, nuclear electromagnetic processes dominate the beam loss rate, leading to a non-exponential decay during a fill. The initial beam (intensity) lifetime due to beam-beam interactions in the nominal ion scheme with beams colliding at $n_{\rm exp}$ interaction points:

$$\tau_{NL} = \frac{k_{\rm b} N_{\rm b}}{n_{\rm exp} L \sigma_{\rm T}} = \frac{22.4\,\mathrm{hour}}{n_{\rm exp}} \left(\frac{10^{27}\,\mathrm{cm}^{-2}\mathrm{s}^{-1}}{L} \right) \tag{21.13}$$

If this intensity loss were the sole mechanism involved in the evolution of the luminosity, the initial luminosity half-life (sometimes quoted) would be $\tau_{L/2} = \left(\sqrt{2}-1\right)\tau_{NL}$.

Given that the intensity decays and the emittance evolves under the influence of radiation damping, IBS and other effects, the formula for luminosity

$$L = \frac{k_{\rm b} N_{\rm b}^2 f_0}{4\pi\sigma^{*2}} = \frac{k_{\rm b} N_{\rm b}^2 f_0}{4\pi\beta^* \epsilon_{\rm n}}\gamma \tag{21.14}$$

suggests that the rapid initial decay of the intensity could be offset by varying $\beta^* \propto N_{\rm b}^2/\epsilon_{\rm n}$ in the course of a fill. This so-called "β^*-tuning" would be very valuable during collision to maximise integrated luminosity—especially if there turns out to be some scope for increasing the initial value of $N_{\rm b}$, whose value is limited at injection into the SPS (see Vol. III of this report). A higher initial value of β^* would also push up the margin for the ECPP quench limit—should this prove necessary—providing further grounds for interest in this capability.

However β^*-tuning is not expected to be a straightforward operational procedure in the LHC as the beams will have a tendency to move apart by distances comparable with the beam size at the IP.

Note that the luminosity lifetimes quoted in (Eq. 21.13), Tab. 21.3 and Tab. 21.4 are those that apply at the beginning of a fill with the full intensity and nominal transverse emittance. Fills with lower initial luminosity will have much longer lifetime and the lifetime will increase in inverse proportion to luminosity as the fill goes on.

[3]Radiation damping of light ions can be up to 16 times *slower* (deuterons) than protons; equality occurs for $Z \simeq 20$.

Table 21.5: $^{208}Pb^{+}$ ion/matter interactions in comparison with proton/matter interactions. Values are for particle impact on graphite.

Physics process	p injection	p collision	$^{208}Pb^{+}$ injection	$^{208}Pb^{+}$ collision
Ionisation energy loss $\frac{dE}{E\,dx}$	0.12 %/m	0.0088 %/m	9.57 %/m	0.73 %/m
Multiple scattering projected RMS angle	$73.5\,\mu\mathrm{rad}/\mathrm{m}^{1/2}$	$4.72\,\mu\mathrm{rad}/\mathrm{m}^{1/2}$	$73.5\,\mu\mathrm{rad}/\mathrm{m}^{1/2}$	$4.72\,\mu\mathrm{rad}/\mathrm{m}^{1/2}$
Electron capture length	-	-	20 cm	312 cm
Electron stripping length	-	-	0.028 cm	0.018 cm
ECPP interaction length	-	-	24.5 cm	0.63 cm
Nuclear interaction length (incl. fragmentation)	38.1 cm	38.1 cm	2.5 cm	2.2 cm
Electromagnetic dissociation length	-	-	33.0	19.0 cm

The evolution of the luminosity during a fill can be predicted and optimised straightforwardly by solving the coupled differential equations for the beam currents and emittances, taking into account the luminosity losses, emittance blow-up due to intra-beam scattering countered by radiation damping, β^*-tuning and any other known loss mechanisms. Pending a full revision of these calculations, previous versions can be found in [21, 4].

21.6 VACUUM

The study of vacuum phenomena specifically related to heavy ions is in an early stage. Unexpectedly high levels of desorption of gas molecules by lost ions have recently been measured at lower energies [22, 23, 24, 25, 26] and have a potential impact on LHC vacuum conditions, particularly in view of the loss mechanisms described in Sec. 21.4. Experiments and further study are planned.

For these reasons, estimates of the beam-gas lifetime from nuclear scattering and the emittance growth rates from multiple Coulomb scattering are not given in Tab. 21.1.

Otherwise, thanks to the reduced intensity and larger bunch spacing and the much lower synchrotron radiation power, there should be no electron cloud build-up as for protons. Desorption induced by residual gas molecules ionised by the beam is expected to be very small.

21.7 COLLIMATION ISSUES FOR ION OPERATION

The purpose, specifications and design of the LHC collimation system are described in detail in Chapter 18 of this report; this section focuses on those system issues specific to operation with ions. Although the stored energy of the nominal ion beam is only 1 % of that of the nominal proton beam (3.81 MJ for ions compared with 362 MJ for protons), some attention has to be paid to the ion collimation because of the different characteristics of the beam-matter interactions. An overview of the main interaction mechanism of high energy ions in the collimator material is given in Tab. 21.5. A discussion of the various processes can be found in [10]. The values for nuclear interaction length and electromagnetic dissociation length are computed with the methods described in [5, 27]

The nominal ion beam hitting a material surface (i.e., a collimator) produces a local heat deposition at the surface comparable with the heat deposition caused by the nominal proton beam. This is due to the much higher

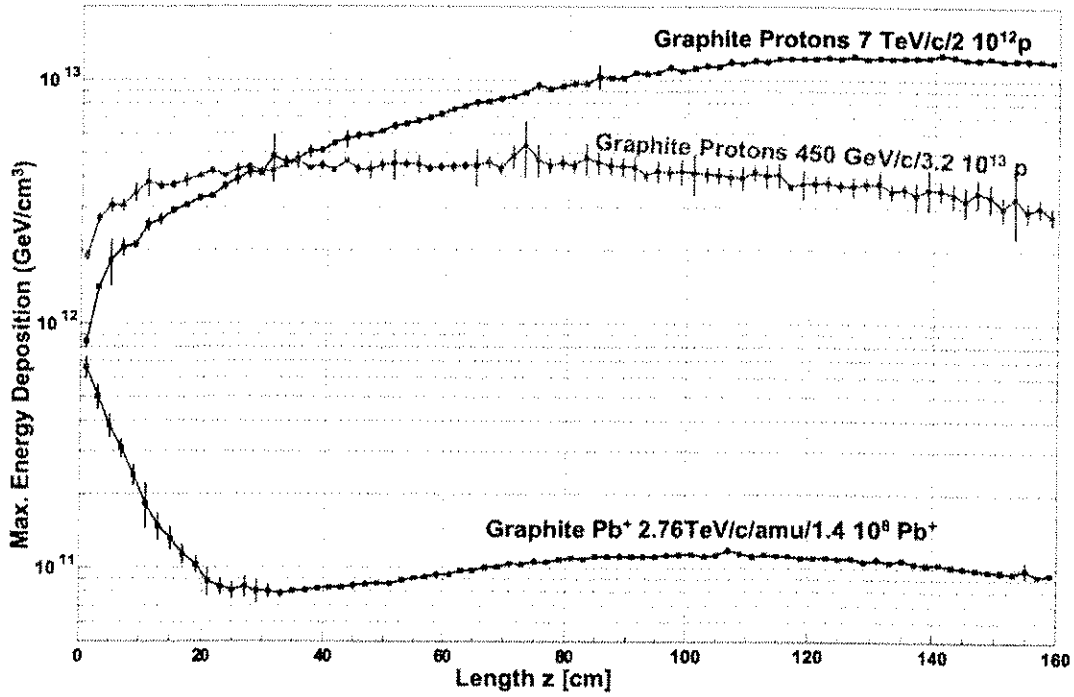

Figure 21.7: FLUKA results for energy deposition of protons and $^{208}Pb^{82+}$ ions in the collimator jaws in case of an erroneous trigger of a dump kicker module.

ionisation energy loss of ions compared to protons. Once the ions have fragmented the resulting hadronic shower behaves similarly for both particle species and the heat deposition is in proportion to the beam energies. Fig. 21.7 shows this behaviour as a result of a FLUKA simulation for the case of an erratic firing of a dump kicker module [28]. From this simulation it can be concluded that the heat deposition of the ions on the collimators nowhere exceeds those of the protons.

Another concern is the local cleaning inefficiency of the collimation system η_c as defined in Equation 18.3. Because the stored beam energy of the ions is lower, η_c can be relaxed from the proton value of $2 \times 10^{-5}\,\mathrm{m}^{-1}$ to $2 \times 10^{-3}\,\mathrm{m}^{-1}$ for ions. However, as explained below it is presently not clear if even this relaxed value can be achieved. The design philosophy of the collimation system is based on a two-stage system. In the first stage, short primary collimators intercept halo particles and off-momentum particles and increase their betatron amplitude by means of multiple scattering. In the second stage these particles are absorbed by long secondary collimators. In comparison with single stage systems, this scheme has the advantages that the fraction of errant particles escaping from the collimators to be subsequently lost elsewhere in the accelerator is very substantially reduced and that the heat load on the collimators is distributed over a larger volume. However, in the present system, which has been so far only optimised for proton operation, it is implicitly assumed that the main action of the primary collimators on an intercepted particle is scattering, while energy loss has a comparably small effect on the particle trajectories. This assumption is no longer valid for heavy ions, because:

1. The relative energy loss due to ionisation is two orders of magnitude larger.

2. Peripheral collisions with collimator nuclei lead to nucleon losses by hadronic fragmentation and electromagnetic dissociation. From a beam dynamics point of view these effects are analogous to a change of longitudinal particle momentum according to (Eq. 21.4), while the related changes of trajectory angle are usually small.

3. The average increase of trajectory angle due to multiple scattering is the same as for protons.

Thus, the collimation system tends to put ions on trajectories characterised by large momentum errors but of moderate betatron amplitude increase. The secondary collimators, however, are designed to cut into the betatron amplitude. In consequence the cleaning inefficiency is substantially greater for ions than for protons.

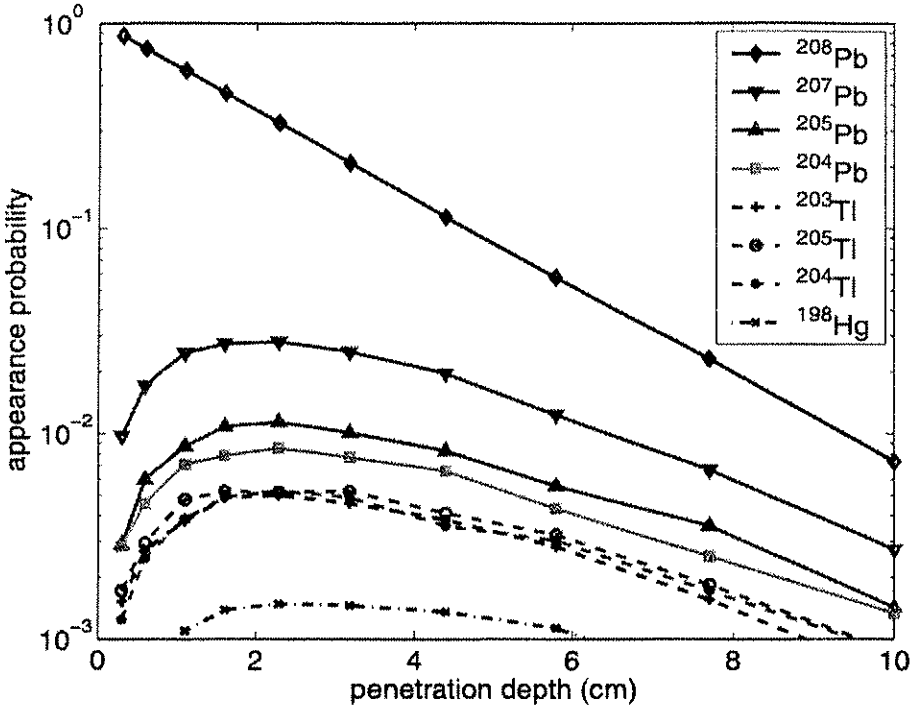

Figure 21.8: The probability to convert a ^{208}Pb nucleus into a neighbouring nucleus as a function of penetration depth. The calculation is performed for ion impact on graphite at LHC collision energy.

A study is underway to quantify η_c for the case of ion beams and to compute the expected particle losses in the superconducting magnets for the scenarios considered in Chapter 18. An important ingredient for this study is a quantitative estimate of the fragment distribution generated in the collimators. For this purpose the cross sections for dissociation and fragmentation of ^{208}Pb ions and their products have been computed with appropriate Monte-Carlo programs [5, 27]. The probability of appearance has been derived from the cross section tables generated by these programs with a simple transport code. Results are shown in Fig. 21.8 for some of the most probable fragments. Apparently the probability of losing a single neutron from the nucleus is particularly high. This is due to the large cross section of electromagnetic dissociation for this process. The change of magnetic rigidity for this dissociation process corresponds to $\delta(0,-1) \simeq -0.0048$, which is of the same magnitude as the LHC momentum aperture (approximately 0.6% for a pencil beam). The transverse momentum transferred in this process is small (<30 MeV/c [6]) and in consequence the ^{207}Pb fragment has a high probability of exiting from the primary collimator without being intercepted by the secondary collimator. To determine the loss pattern and related heat loads for this kind of process, more detailed tracking studies need to be performed.

21.8 OPERATION AND BEAM INSTRUMENTATION

From an operational point of view, the most striking difference between running the LHC with lead ions and with protons is the much smaller beam current and stored energy. While this has obvious advantages—notably the almost total absence of conventional collective and beam-beam effects—there are disadvantages related to the dynamic range of the beam instrumentation (for the specifications, see Chap. 13).

21.8.1 Beam Position Monitors

In order to provide accurate readings, the arc beam position monitors in the LHC require a minimum charge per bunch $\simeq 2.0 \times 10^9$ e, equivalent to some $N_b \simeq 2 \times 10^7$ Pb ions/bunch. Since the lowest range of beam currents will occur in operation with lead ions, this mode of operation determines the specification of their

resolution.

However there is little more than a factor of 3 between the minimum bunch current for which the orbit can be measured and the single-bunch intensity for full nominal performance, implying a very narrow gap between "commissioning" and "design" conditions.

21.8.2 Beam Current Monitors

The LHC has two systems (see Chap. 13) for measuring the beam current:

- The "BCTDC" measures total DC current in each beam and has a typical resolution of $10\,\mu$A on total current
- The "FBCT" measures individual bunch currents. Although there are presently uncertainties in extrapolating the performance of the system tested in a laboratory to operational conditions in the LHC tunnel, the resolution hoped for is about 5% of the proton pilot bunch ($9\,\mu$A). The examples given here are a factor 2 more conservative and assume $1\,\mu$A.

21.8.3 Motivation for Early Ion Scheme

With the full complement of 592 ion bunches of the minimum single-bunch current necessary to measure orbits, commissioning would have to be done dangerously near the ECPP quench limit. These and other reasons related to relaxing the performance requirements on the injector chain, are the motivation for the early ion scheme mode of operation (see also Vol. III of this report) of the injectors, leading to about 10 times fewer bunches in the LHC. This scheme is envisaged for use in an initial period of running with lead ions.

With this many bunches, N_b and β^* (and hence the beam lifetime) could have their nominal values but the ECPP quench limit would be far away, the bunches would be visible on the BPMs, the injector scheme would be simplified and some interesting heavy ion physics would be accessible with the reduced luminosity. To simplify further the value of β^* is raised to 1 m to increase the beam lifetime and generally simplify the operational conditions.

The initial performance parameters in the nominal ion scheme and early ion scheme are summarised in Tab. 21.1 and Tab. 21.2.

Fig. 21.9 gives a global view of the luminosity as a function of single-bunch current in both the early ion scheme and nominal ion scheme, with indications of the thresholds of visibility of the beams on the instruments. The largest single bunch current in the lead ion beam for which the beam would be invisible on the BPMs is about $I_b \simeq 3.6\,\mu$A, corresponding to a stored energy of 1.3 MJ in the nominal ion scheme. This is much smaller than the beam energy in proton beams and is very likely to be safe to keep in collision even without the ability to measure the closed orbit.

It also provides a useful luminosity so one may well wish to continue colliding beams of this intensity. In particular, it is easy to imagine situations where lead ion injection is not available and beams are kept in the LHC for longer than they might otherwise be, allowing the experiments to take data. Such situations are most likely to arise in early operation.

The expected resolution of the BCTDC (see Chap. 13), around $10\,\mu$A total beam current, is adequate for all situations likely to arise with Pb ion beams. It reaches $I_b \simeq 0.02\,\mu$A for all Pb bunches evenly filled in the nominal ion scheme or about $I_b \simeq 0.2\,\mu$A in the early ion scheme. These values correspond to luminosity around $10^{22}\,\mathrm{cm}^{-2}\mathrm{s}^{-1}$, well below what would be useful for physics.

With the assumed resolution of the FBCT fast single-bunch monitor, around $1\,\mu$A in a single bunch, a beam at the threshold of visibility may still yield a luminosity of 10^{24}–$10^{25}\,\mathrm{cm}^{-2}\mathrm{s}^{-1}$. Although modest, these luminosities may be of interest in early running. Resolution at this level will also be useful for checking the injection. It will be possible to verify the absence of unwanted "ghost" bunches only if they have sufficiently high current. However such bunches—should they exist—are not expected to have very adverse effects in ion operation.

It will be difficult to make useful lifetime measurements for individual ion bunches. The situation is somewhat better for lifetime measurements of a multi-bunch beam as a whole.

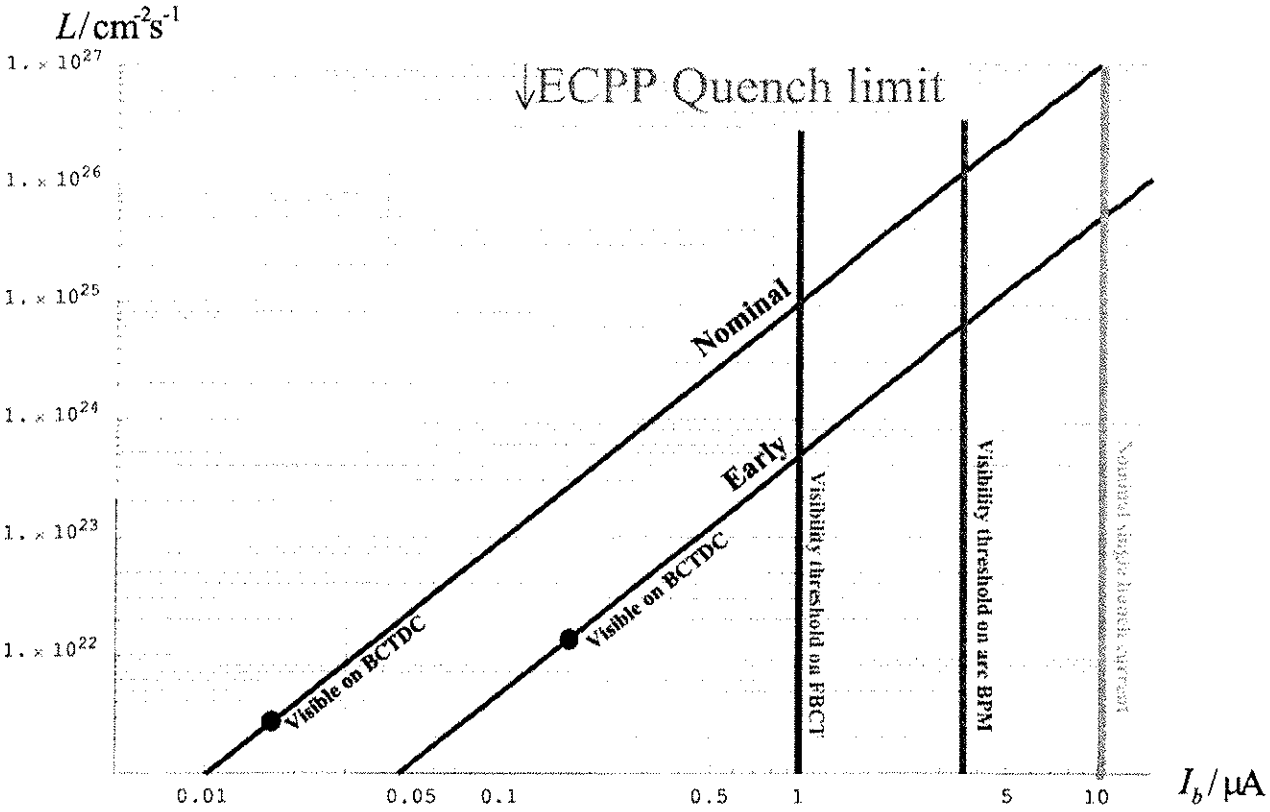

Figure 21.9: Variation of luminosity with single bunch current, I_b, for both the nominal ion scheme and early ion scheme (note that the values of β^* are different in the two cases). Thresholds of visibility on the FBCT and the arc BPMs are shown as vertical lines. Another vertical line indicates the nominal single bunch current. The threshold of visibility on the BCTDC is indicated as points since it occurs at different values of the single bunch current in the two filling schemes. Dipole quenching due to the ECPP effect (Sec. 21.4) is expected to limit the luminosity at some level $\gtrsim 0.5 \times 10^{26}\,\mathrm{cm}^{-2}\mathrm{s}^{-1}$.

In summary, Fig. 21.9 shows the unusually constrained range of operating parameters for lead ion beams. Commissioning and initial adjustment of the beams will have to be done with beam currents within a factor of 3 of the nominal maximum.

REFERENCES

[1] The LHC Study Group, "Design Study of the Large Hadron Collider (LHC)", CERN/AC/91-03 (LHC), 1991.

[2] The LHC Study Group, "The Large Hadron Collider Accelerator Project", CERN/AC/93-03 (LHC), 1993.

[3] The LHC Study Group, "The Large Hadron Collider Conceptual Design", CERN/AC/95-05 (LHC), 1995.

[4] D. Brandt, LHC Project Report 450, 2000.

[5] I. A. Pshenichnov, J. P. Bondorf, I. N. Mishustin, A. Ventura and S. Masetti, Phys. Rev. C **64** (2001) 024903 [arXiv:nucl-th/0101035].

[6] I. A. Pshenichnov, private communication, 2003.

[7] G. Baur, K. Hencken and D. Trautmann, J. Phys. G **24** (1998) 1657 [arXiv:hep-ph/9804348].

[8] Spencer R. Klein in Proceedings of the 18th Advanced ICFA Beam Dynamics Workshop on Quantum Aspects of Beam Physics, Capri, 15-20 October 2000, World Scientific.

[9] G. Baur, K. Hencken, D. Trautmann, S. Sadovsky and Y. Kharlov, "Coherent $\gamma\gamma$ and γA interactions in very peripheral collisions at relativistic ion colliders," Phys. Rept. **364** (2002) 359 [arXiv:hep-ph/0112211].

[10] P. Grafstrom *et al.*, "Measurement of electromagnetic cross sections in heavy ion interactions and its consequences for luminosity lifetimes in ion colliders," CERN-SL-99-009-EA *1999 Particle Accelerator Conference : PAC '99, New York City, NY, CUSA, 29 Mar -2 Apr 1999*

[11] H. Meier et al, "Bound-free electron-positron pair production in relativistic heavy-ion collisions", Phys. Rev. **A**, 63, 032713 (2001).

[12] J. M. Jowett, "Ions in the LHC ring," *12th Chamonix LHC Performance Workshop, Chamonix, France, 3-8 Mar 2003*, CERN-AB-2003-008.

[13] S.R. Klein, "Localized Beampipe Heating due to e–Capture and Nuclear Excitation in Heavy Ion Colliders", arXiv:physics/0005032, LBL-PUB-45566, May, 2000.

[14] S. R. Klein, Lawrence Berkeley National Laboratory Report No. LBNL-45566, e-print physics/0005032.

[15] J-B. Jeanneret, CERN SL-AP Group, Beam Physics Note 41 (2000).

[16] J. M. Jowett, J. B. Jeanneret and K. Schindl, "Heavy ion beams in the LHC," CERN-LHC-PROJECT-REPORT-642, *Particle Accelerator Conference (PAC 03), Portland, Oregon, 12-16 May 2003*

[17] M. Gresham, J. M. Jowett, to be published.

[18] J. B. Jeanneret, D. Leroy, L. Oberli and T. Trenkler, "Quench levels and transient beam losses in LHC magnets", LHC Project Report 44, July 1996.

[19] J. Bjorken and S. K. Mtingwa, Part. Accel. 13, 115 (1983).

[20] `http://cern.ch/mad`

[21] A. Morsch, ALICE/97-13.

[22] E. Mahner, J. Hansen, J. M. Laurent and N. Madsen, "Molecular desorption of stainless steel vacuum chambers irradiated with 4.2-MeV/u lead ions," Phys. Rev. ST Accel. Beams **6** (2003) 013201.

[23] E. Mahner, J. Hansen, D. Küchler, M. Malabaila, M. Taborelli, "Ion-stimulated gas desorption yields of coated (Au, Ag, Pd) stainless steel vacuum chambers irradiated with 4.2 Mev/u lead ions", 8th European Vacuum Conference, 23-26 June 2003, Berlin, Germany and CERN AT/2003-6 (VAC) September 2003.

[24] W. Fischer, M. Bai, J.M. Brennan, M. Blaskiewicz, P. Cameron, H.C. Hseuh,H. Huang,W. MacKay, T. Roser, T. Satogata, L.A. Smart, D. Trbojevic, S.Y. Zhang, "Vacuum pressure rise with intense ion beams in RHIC", in: Proceedings of the European Particle Accelerator Conference EPAC 2002, Paris, 2002.

[25] S. Y. Zhang, M. Bai, M. Blaskiewicz, P. Cameron, A. Drees, W. Fischer, D. Gassner, J. Gullotta, P. He, H.C. Hseuh, H. Huang, U. Iriso-Ariz, R. Lee, W. W. MacKay, B. Oerter, V. Ptitsyn, V. Ponnaiyan, T. Roser, T. Satogata, L. Smart, D. Trbojevic, K. Zeno, "RHIC Pressure Rise and electron cloud", in: Proceedings of the European Particle Accelerator Conference EPAC 2002, Paris, 2002.

[26] E. Mustafin, O. Boine-Frankenheim, I. Hofmann, H. Reich-Sprenger and P. Spiller, "A theory of the beam loss-induced vacuum instability applied to the heavy-ion synchrotron SIS18", Nuclear Instruments and Methods in Physics Research Section A: Accelerators, Spectrometers, Detectors and Associated Equipment, Volume 510, Issue 3, 11 September 2003, pages 199-205.

[27] C. Scheidenberger et al., "Charge-changing interactions of ultrarelativistic Pb ions", to be published.

[28] V. Vlachoudis, presentation in LHC Collimator project meeting, 20.6.2003

List of CERN Reports published in 2004

CERN–2004–001
CERN. Geneva
Ellis, N; Fleischer, R [eds]
Proceedings, 2002 European School of High-Energy Physics, Pylos, Greece, 25 Aug–7 Sep 2002
CERN, 8 March 2004. – 250 p

CERN–2004–002 ; ECFA/04/230
CERN. Geneva
Blondel, A; Buchalla, G; Campanelli, M: et al. [eds]
ECFA/CERN studies of a European Neutrino Factory complex
CERN, 11 March 2004. – 378 p

CERN–2004–003
CERN. Geneva
Brüning, O; Collier, P; Lebrun, P: et al. [eds]
LHC Design Report: Vol I, The LHC main ring
CERN, 4 June 2004. – 556 p

CERN–2004–003
ISSN 0007–8328
ISBN 92–9083–224–0

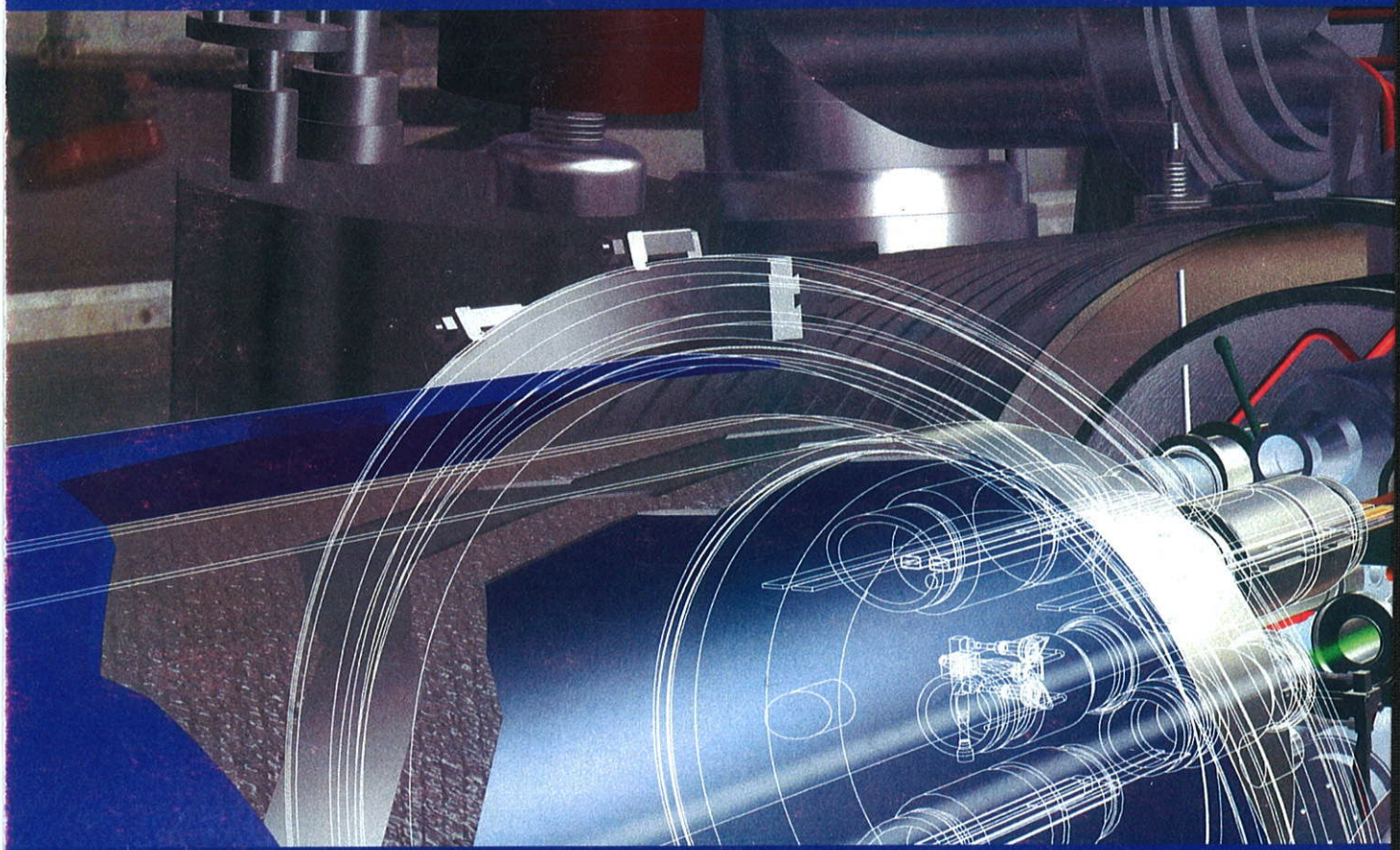

CERN